NIĞDE ÖMER HALİSDEMİR UNIVERSITY 1992

NATIONAL HYDROGEN ASSOCIATION TURKEY

International Association for Hydrogen Energy

International Journal of Hydrogen Energy

IHTEC 2021

www.ihtec2021.org

5th International HYDROGEN TECHNOLOGIES Congress

May 26-28, 2021

Niğde Ömer Halisdemir University, Niğde, Turkey

ONLINE

zoom

PROCEEDINGS

EDITORS

İbrahim Dincer

Adnan Midilli

Bora Timurkutluk

Selahattin Celik

2021

ISBN: 978-605-70717-0-5

5th International HYDROGEN TECHNOLOGIES Congress

May 26-28, 2021
Niğde Ömer Halisdemir
University, Niğde, Turkey

ONLINE

PROCEEDINGS

EDITORS

İbrahim DİNÇER
Adnan MİDİLLİ
Bora TİMURKUTLUK
Selahattin ÇELİK

ISBN: 978-605-70717-0-5

INDEX

Forewords	4
Committees	7
Scientific Program	8
Keynote Speakers	18
Proceedings	23

FOREWORDS

WELCOMING MESSAGE

Participants of 5th International Hydrogen Technologies Congress 26-28 May 2021, Nigde Omer Halisdemir University, Nigde, Turkey

Fossil Fuels (i.e., petroleum, natural gas and coal), which meet most of the world's energy demand today, are being depleted fast. Also, their combustion products are causing the global problems, such as the global warming, climate change, ozone layer depletion, acid rains, oxygen depletion and pollution, which are posing great danger for our environment and eventually for the life in our planet.

Many engineers and scientists agree that the solution to these global problems would be replacing the existing fossil fuel system by hydrogen as the fuel and by fuel cells as the energy conversion devices. Hydrogen is the lightest, most efficient and cleanest fuel. Its use in fuel cells and in other energy conversion devices (such as the heat engines) will produce no greenhouse gases, no ozone layer depleting chemicals, no acid rain ingredients, no oxygen depletion and no pollution. Around the world, there is extensive R&D work on Hydrogen Energy and fuel cells. Many types of fuel cells have been developed. Vehicle manufactures have built several hydrogen fuel cell cars and buses. Mercedes Benz. Hyundai, Toyota and Honda companies started selling hydrogen fuel cell cars. Many bus companies are selling hydrogen fuel cell buses. Internal combustion engines are being modified for hydrogen fuel. Hydrogen fueled appliances based on catalytic combustion have been developed.

There is research and development work on hydrogen hydride refrigeration and air conditioning systems. Siemens Company is building hydrogen fuel cells for submarines. Aircraft manufactures are working on hydrogen fueled subsonic and supersonic transport planes. The preferred fuel of the space programs is hydrogen. Without hydrogen, it would not have been possible to send astronauts to the Moon. Hydrogen made it possible to travel to the moon. It provided the fuel for the rocket engine, electric through the fuel cells for the controls and the cabin, and the by-product from the fuel cells was the drinking water for the astronauts.

Scientists and Engineers from many countries of the world will gather at the IHTEC2021 Congress to present their papers covering the recent advances in hydrogen energy and in hydrogen technologies. All these will no doubt speed up the conversion to the hydrogen economy, eliminate global environmental problems, and provide the humankind with higher living standards. I congratulate the organizers of this Congress and wish all the participants a very fruitful meeting and pleasant days in Niğde, Turkey.



T. Nejat Veziroğlu

Honorary Chair, IHTEC2021

Emeritus President, International Association for Hydrogen Energy

FOREWORDS

MESSAGE FROM THE PRESIDENT

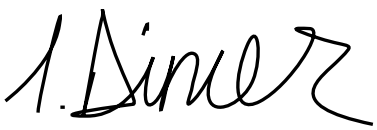
Organizing the Fifth International Hydrogen Technologies Congress is recognized during this COVID-19 pandemic as another milestone in Turkey's hydrogen energy activities under the shelter of the National Hydrogen Energy Association. Due to the increasing interest in implementing carbon free economy, hydrogen energy technologies appear to become the central point to formulate the energy solutions for all sectors, ranging from industrial to transportation and residential to commercial accordingly. During the past a few years, the climate change conferences in various parts of the World have made clear that the renewable energy and carbon-free based solutions will be critical in addressing both local and global environmental issues and provide clean and sustainable options for implementation. Coupling hydrogen technologies with renewable energy systems will solve many issues ranging from intermittency to storage and distribution as well as demand management.

It is also important to note that the National Hydrogen Energy Association was able to secure to organize the 23th World Hydrogen Energy Congress first time in 2022, in Istanbul, Turkey. This is recognized as a true achievement of the Association and the efforts of its Board. The Association is now getting ready to be one of the world's most successful societies in the area of hydrogen technologies. This is of course not easy and requires great efforts from various parties of academia, industry and government agencies, as well as individually from every one of us working in the area of hydrogen and related technologies. It is also equally important for us to primarily focus on coupling renewables and hydrogen energy technologies for implementation.

We are now getting together for our fourth congress in the area of hydrogen technologies, after organizing the first one in Yildiz Technical University in Istanbul, the second one in Cukurova University in Adana, the third one in Alanya Alaaddin Keykubat University in Alanya, the fourth one in Trakya University in Edirne, which aims to bring researchers, scientists, engineers and practitioners, who are working in the subject matter area, to provide a forum to exchange ideas, disseminate new research developments and discuss latest advances, new directions and priorities for a carbon-free future with hydrogen. We are happy to have numerous leading researchers here to share the newest ideas and latest technologies and developments.

Over 137 technical papers selected from 144 papers will provide an ample opportunity to learn about a wide range of topics with distinguished presenters from over ten countries. Furthermore, the conference delegates will benefit from the exchange of ideas, problems and solutions with a large number of technical experts. Many individuals have contributed in significant ways to organize this conference and make the necessary preparations for another successful gathering.

As the Association President, I would like to register my sincere appreciation to the Organizing Committee Members, Executive Organizing Committee Members, and the Honorary Chairs, Dr. T. N. Veziroglu, and Dr. Muhsin Kar (Rector of Nigde Omer Halisdemir University), the Congress Chair, Dr. Bora Timurkutluk and Co-Chair Dr. Selahattin Celik and Secretary General Dr. Adnan Midilli. In addition, I would like to acknowledge the assistance, support and coordination of the Bros Congress Team. Last but not least, I warmly thank the congress keynote speakers, authors, session chairs, and all attendees, whose contributions and efforts will make this conference a great success.



Ibrahim Dincer
President / National Hydrogen Energy Association

FOREWORDS

WELCOME FROM THE CONFERENCE CO-CHAIRS

As conference chairs, we are very happy to serve for "The Fifth International Hydrogen Technologies Congress (IHTEC2021)" hosted by Nigde Omer Halisdemir University in Nigde. This online conference is organized as an annual event under the National Hydrogen Technologies Association. It brings together 7 keynote speakers and over 150 participants from 10 countries for a period of three days to discuss, disseminate and network on various aspects of hydrogen technologies and processes.

We wish to formally put on record our sincere thanks to numerous key people and organizations that have been instrumental in ensuring the success of IHTEC2021 in Nigde Omer Halisdemir University in Nigde.

We would like to thank Professor Muhsin Kar, Rector of Nigde Omer Halisdemir University and his management for their full support.

We would like to register our sincere appreciation to Professor T. Nejat Veziroğlu, Founding President of International Association for Hydrogen Energy, Founding and Honorary Editor of International Journal of Hydrogen Energy (IJHE) and Honorary chair of this congress, and Professor Ibrahim Dincer, President of National Hydrogen Association and his management.

Finally, we would like to thank all keynote speakers, presenters, all participants and the organizing committee members, as well as Bros Congress members for their exemplary contribution and support.

Bora Timurkutluk
(Congress Chair, IHTEC2021)

Selahattin Celik
(Congress Co-Chair, IHTEC2021)

COMMITTEES

Honarary Chairs

Kar, M. / Rector, Nigde Omer Halisdemir University
Veziroğlu, T.N. / Founding President of International Association for Hydrogen Association

General Chair

Dincer, I. / President of HTA in Turkey/Canada

Congress Chair

Timurkutluk, B. / Turkey

Congress Co-Chair

Celik, S. / Turkey

Technical Chair

Midilli, A. / Turkey

Executive Committee

Baykara, S. / Turkey
Colpan, C. / Turkey
Celik, C.T. / Turkey
Eroglu, I. / Turkey
Gokhan, I. / Turkey
Karaosmanoglu, F. / Turkey
Midilli, A. / Turkey
Ozkaya, B. / Turkey
Ozturk, M. / Turkey
Solmaz, R. / Turkey
Tuncer, G. / Turkey
Yazici, S. / Turkey

Organizing Committee

Akbulut, U., / Turkey
Kalinci, Y. / Turkey
Altan, T. / Turkey
Korkmaz, H.G. / Turkey
Onbilgin, S. / Turkey
Gavani, N. / Turkey
Ucar, E. / Turkey
Ozturk, M. / Turkey

International Scientific Board

Amani, Y. / USA
Avaca, L.A. / Brazil
Azbar, N. / Turkey
Baker, R. / UK
Barbir, F. / USA
Baykara, S. / Turkey
Bolcich, J.C. / Argentina
Chen, W.H. / Taiwan
Dincer, I. / Canada
Eroglu, I. / Turkey
Gadalla, M. / UAE
Goltsov, V.A. / Ukraine
Hamdullahpur, F. / Canada
Hepbasli, A. / Turkey
Hirohisa, U. / Japan
Kakac, S. / Turkey
Karakoc, H. / Turkey
Karaosmanoglu, F. / Turkey
Kargı, F. / Turkey
Kendall, K. / UK
Koca, A. / Turkey
Kumbur, E.C. / USA
Li, X. / Canada
Mench, M.M. / USA
Midilli, A. / Turkey
Min, Z. / China
Miranda, P.E. / Brazil
Muradov, N. / USA
Naterer, G.F. / Canada
Ozkar, S. / Turkey
Ozturk, T. / Turkey
Ramenskiy, A.Y. / Russia
Pollet, B.G. / Norway
Rosen, M.A. / Canada
Sahin, O. / Turkey
Sahin, S. / Turkey
Sattler, C. / Germany
Sheffield, J.W. / USA
Spazzafumo, G. / Italy
Srivastava, O.N. / India
Stanislaw, S. / Poland
Stolten, D. / Germany
Veziroglu, A. / USA
Veziroglu, E.A. / USA
Veziroglu, T.N. / USA

SCIENTIFIC PROGRAM

SCIENTIFIC PROGRAM

The times mentioned in the program refer to the GMT+3 timezone.

Wednesday, May 26, 2021		
	HALL A	
09:00-09:30	**Opening Talks** **Bora Timurkutluk**(Congress Chair) **Ibrahim Dincer** (President, National Hydrogen Energy Association) **Muhsin Kar** (Rector, Nigde Omer Halisdemir University)	
09:30-10:00	**Overview Talk- Ibrahim Dincer** NHA, hydrogen energy and future directions	
	Keynote Speakers Chair: **Ibrahim Dincer**	
10:00-10:45	**Keynote Speaker - Laurent Antoni** Recent European Advances in Electrolyzer and Fuel Cell Technologies	
10:45-11:30	**Keynote Speaker - Wei-Hsin Chen** Advances in Hydrogen Separation using Palladium-Based Membranes	
11:30-11:45	**Break**	
	PARALLEL SESSIONS	
	HALL A	**HALL B**
11:45-13:30	**SESSION 1A: Hydrogen Production-1** Chair: **Adnan Midilli**	**SESSION 1B: Fuel Cells/ Electrolysis and Hydrogen Fuel Combustion-1** Chair: **C. Ozgur Colpan**
11:45-12:00	Hydrogen production over Ni-containing MgO supported catalyst: Effect of hydrothermal process duration in catalysts synthesis **Saleh Ahmat Ibrahim, Emine Kaya Ekinci, Birce Pekmezci Karaman and Nuray Oktar**	Development of a Zero-Dimensional Dynamic Model of a Solid Oxide Electrolyzer in Co-Electrolysis Mode Integrated with a PV System **Alper Can Ince, Ozgur Colpan and Mustafa Serincan**
12:00-12:15	Hydrogen Production by Solid Fuels with Different Gasification Methods **Mustafa Tolay, Cemil Koyunoglu and Andre Waterschoot**	Characterization of B-site Fe3+ and Co3+ Substituted La0.2Ca0.8Mn1-xBxO3 (x= 0.2) Type Perovskite for Thermochemical Water Splitting **Ihsan Emre Yigiter, Seyfettin Berk Sanli, Fatih Piskin, Gulhan Cakmak and Berke Piskin**
12:15-12:30	Planning and Analysis of a Double Flash Geothermal Plant for Purpose of the Drying, Hydrogen, Hot Water, and Power Generation Aims **Fatih Yilmaz, Murat Ozturk and Resat Selbas**	NOx Emission Behaviors of Hydrogen/ Syngas/ Ammonia as Alternative and Clean Fuels **Mehmet Salih Cellek**
12:30-12:45	Modeling of the Solar Energy-Based Hydrogen and Freshwater Production System **Fatih Yilmaz, Murat Ozturk and Resat Selbas**	Investigation of Ni-MnxOy Coated SS316 Stainless Steel Mesh as a Gas Diffusion Layer Material for PEM Water Electrolyzer **Murat Kisti and Mehmet Fatih Kaya**
12:45-13:00	Feasibility Report of 5-6 MW Biomass (Forest and Agricultural waste) Power Generation Facility in Manisa Akhisar Region **Mustafa Tolay, Cemil Koyunoğlu and Andre Waterschoot**	Yeast Industry Wastewater Treatment with Microbial Fuel Cells: Effect of Electrode Materials and Reactor Configurations **Haris Nalakath Abubackar, Azize Ayol and Idris Biryol**
13:00-13:15	Effect of Green Synthesized Silver Oxide Nanoparticles on Biological Hydrogen Production **Oznur Yildirim, Dogukan Tunay, Bestami Ozkaya and Ahmet Demir**	Investigation and Modeling of Flow Channels for Direct Borohydride Fuel Cell **Anil Can Turkmen, Kursat Can Ata, Gozde Mentese and Cenk Celik**
13:15-13:30	Photofermentative Hydrogen Production by Agar Immobilized Co-Cultures of Purple Non-Sulfur Bacteria **Gorkem Baysal, Harun Koku, Inci Eroglu and Ayse Meral Yucel**	Low-Cost Membrane-Electrode-Assembly (MEA) Production for Direct Borohydride Fuel Cell **Kursat Can Ata, Ipek Caglayan, Anil Can Turkmen, Tuncay Kadioglu, Ramiz Gultekin Akay and Cenk Celik**

SCIENTIFIC PROGRAM

13:30-14:00	**Break**	**Break**
	HALL A	
	Keynote Speakers Chair: **Suha Yazici**	
14:00-14:45	**Keynote Speaker - John William Sheffield** A Student Design Project for Hydrogen Fuel Cell Electric-Drive Mining Trucks	
14:45-15:30	**Keynote Speaker - Mark Kirby** Update on Hydrogen and Fuel Cell Activity in Canada	
	PARALLEL SESSIONS	
	HALL A	**HALL B**
15:30-17:00	**SESSION 2A: Hydrogen Storage and Hydrogen Purification/Separation-1** Chair: **Tayfur Ozturk**	**SESSION 2B: Hydrogen Energy Technologies-1** Chair: **Sudi Apak**
15:30-15:45	A Two-Stage Metal Hydride Compressor Based on Commercial Alloys **Jussara Barale, Federico Nastro, Paola Rizzi, Carlo Luetto and Marcello Baricco**	Environmental Effects as a Result of The Use of Fuel Cell and as Hydrogen Alternative Fuel in UAVs **Duran Calisir, Selcuk Ekici, Adnan Midilli and T. Hikmet Karakoc**
15:45-16:00	Fundamental Hydrogen Storage Properties of TiFe-Alloy with Partial Substitution of Fe by Ti and Mn **Erika Michela Dematteis, David Dreistadt, Giovanni Capurso, Julian Jepsen, Fermin Cuevas, Michel Latroche and Marcello Baricco**	Electric Taxiing with Fuel Cell Hybrid Power Unit **Mustafa Kececi, Can Ozgur Colpan and Tahir Hikmet Karakoc**
16:00-16:15	Onboard Hydrogen Storage for Ships: An Overview **Omer Berkehan Inal, Caglar Dere and Cengiz Deniz**	Fuel Cell Systems for Submarines **Ibrahim Pamuk, Ugur Aydin, Selahattin Celik, Bora Timurkutluk, Serkan Toros and Yuksel Kaplan**
16:15-16:30	The Optimal Isosteric Heat of H2 Adsorption on Co(II)- and Ni(II)- exchanged ZSM-5 and US-Y **Nurkan Sarohan and Bahar Ipek**	Comparison of PEM Fuel Cell vs. Lithium-Sulfur Battery Systems for Unmanned Aerial Vehicles **Nisa Erisen, Damla Eroglu, Harun Koku and Inci Eroglu**
16:30-16:45	Development of Cost-effective Dense Metallic Membranes for Hydrogen Separation **Fatih Piskin and Tayfur Ozturk**	Energy and Environmental Assessment of Transition to Hydrogen Vehicles **Merve Nur Dinc, Murat Kisti, Saltuk Selcuklu and Mehmet Fatih Kaya**
16:45-17:00	High Temperature Electrochemical Hydrogen Purification Using Polybenzimidazole Membrane **Gizem Nur Bulanık Durmus, Can Ozgur Colpan and Yilser Devrim**	Modeling of Hydrogen and Electric Powered Vehicle Filling Stations Using a Floating Photovoltaic System **Seyfi Bulduk and Mehmet Fatih Kaya**
17:00-17:15	**Break**	**Break**

SCIENTIFIC PROGRAM

	HALL A	HALL B
17:15-18:30	**SESSION 3A: PEM Fuel Cells-1** Chair: **Yilser Devrim**	**SESSION 3B: Hydrogen Storage and Hydrogen Purification/Separation-2** Chair: **Tayfur Ozturk**
17:15-17:30	A Numerical Study on Cooling Performance of Various Flow Field Designs of Cooling Plates **Mahmut Caner Acar and Bahadir Erman Yuce**	Hydrogen Adsorption on Metal (Na, K, Mg, Ca) Porphyrin Complexes: A DFT Study **Ahmet Kose, Numan Yoksel and Mehmet Ferdi Fellah**
17:30-17:45	Preparation of Polybenzimidazole-MOF Composite Membranes with Enhanced Proton Conductivity **Oguzhan Eren, Necati Ozkan and Yilser Devrim**	A Density Functional Theory Study of Hydrogen Adsorption on Ni Doped Carbon Nanocone **Ahmet Kose, Numan Yuksel and Mehmet Ferdi Fellah**
17:45-18:00	Chemically and Thermally Reduced Graphene Oxide Supported Pt Catalysts Prepared by Supercritical Deposition **Meryem Samanci and Ayse Bayrakceken Yurtcan**	Catalyst Development for Viability of Electrochemical Hydrogen Purifier and Compressor Technology **Yasemin Aykut and Ayse Bayrakceken Yurtcan**
18:00-18:15	High Performance Sulfonated Silica-Based Electrospun Membrane-Electrode-Assemblies (MEAs) for PEM Fuel Cells **Begum Yarar Kaplan, Naeimeh Rajabalizadeh, Bilal Iskandarani, Alp Yurum and Selmiye Alkan Gursel**	Surface Modification of 316L by Electrochemical Dealloying **Omer Ozcan and Fatih Piskin**
18:15-18:30	Enhanced Fuel Cell Performance and Durability of PVDF-based Sulfonated Silica-loaded Fibrous Electrodes **Bilal Iskandarani, Selmiye Alkan Gursel and Begum Yarar Kaplan**	Proposal of an Ocean Thermal Energy Conversion Based Subcritical CO2 Power Cycle for Clean Hydrogen Production **Gamze Soyturk, Serpil Celik Toker and Onder Kizilkan**

SCIENTIFIC PROGRAM

Thursday, May 27, 2021		
	PARALLEL SESSIONS	
	HALL A	HALL B
09:00-11:30	**SESSION 4A: Materials for Hydrogen Energy Technologies-1** Chair: **Aysel Kanturk Figen**	**SESSION 4B: Hydrogen Economy** Chair: **Hikmet Karakoc**
09:00-09:15	Radiation-Grafted PVDF based Dual-Electrospun Membranes for Anion Exchange Membrane Fuel Cells **Ahmet Can Kirlioglu, Naeimeh Rajabalizadeh, Selmiye Alkan Gursel and Begum Yarar Kaplan**	Techno-Economic Analysis of a Solar Hydrogen Production Plant Using Textile Wastewater **Murat Emre Demir and Ibrahim Dincer**
09:15-09:30	Investigating the Hydrogen Bake-out Operation of Armor Steels conforming to MIL-DTL-12560 Class 4a and MIL-DTL-46100 Military Standards **Ferdi Caner Bayram, Burak Bal and Barıs Cetin**	Hydrogen as A Renewable Energy Source **Sibel Demiroglu Mustafov**
09:30-09:45	B-site Al Dopant Effect on The Structural Properties of La0.4Sr0.6Mn1-xAlx (x=0.4, 0.5 and 0.6) Perovskite Oxides **Seyfettin Berk Sanlı, Ihsan Emre Yigiter, Fatih Piskin, Gulhan Cakmak and Berke Piskin**	Turkey's Offshore Hybrid Energy Potential and Techno-Economic Analysis in the Eastern Mediterranean **Soner Celikdemir and Mahmut Temel Ozdemir**
10:00-10:15	Hydrogen Evolving Studies over Pellet Type Catalyst for Decomposition of Ammonia Borane Solutions **Bilge Coskuner Filiz and Aysel Kanturk Figen**	The Importance of Hydrogen in Terms of Energy Diversity for Turkey's Energy Projection **Cengiz Amil and Zeki Yilmazoglu**
10:15-10:30	Increasing Activation of Aluminum by Alloying with Zn and Sn for Hydrogen Generation **Sevgin Koymen, Sevim Yolcular and Serdar Karaoglu**	Hydrogen Economy in the Light of Europe's Green Deal Plan and Green Jobs Opportunities **Erhan Atay and Sudi Apak**
10:30-10:45		Design and Economic Optimization of PV/Wind/ Hydrogen Hybrid Power System **Duygu Kemeriz, Yagmur Budak, Serkan Eryilmaz and Yilser Devrim**
10:45-11:00	**Break**	**Break**
	HALL A	**HALL B**
11:00-13:00	**SESSION 5A: Fuel Cells/ Electrolysis and Hydrogen Fuel Combustion-2** Chair: **Yusuf Bicer**	**SESSION 5B: Hydrogen Production-3** Chair: **Inci Eroglu**
11:00-11:15	Peat Based Microbial Fuel Cells and Limiting Parameters **Ahmet Erensoy, Sefa Mulayim, Ayhan Orhan, Nurettin Cek and Namik Ak**	Co Nanoparticle on TiO2 Mesh Support for Sodium Borohydride Hydrolysis to Generate Hydrogen **Valentina Minkina, Cigdem Tuc Altaf and Nurdan Sankir**
11:15-11:30	Experimental Investigation of Hydrogen Enriched Propane in Terms of Emission Values and Flue Gas Temperature **Oguzhan Boztoprak and Murat Tastan**	Design Consideration of an Efficient Oxyhydrogen Generator under Lorentz Force **Hakan Kaplan, Mukerrem Sahin and Gulbahar Bilgic**
11:30-11:45	Development and Analysis of a Hydrogen-Powered Premix Burner **Yagmur Cagli and Mehmet Salih Cellek**	Effect of Catalyst Microstructures on Steam Methanol Reforming Process **Ayse Ece Bedir Sezgin, Samet Sutcu, Nurbanu Cakiryilmaz Sahingoz, Yelda Ciflik, Ayse Deniz Sirkeci, Elif Akbay, İbrahim Pamuk and Bora Timurkutluk**

SCIENTIFIC PROGRAM

11:45-12:00	Evaluation of Hydrogen Evolution Reaction Performance of Ni-Co Coated 3D Printed Electrodes Prepared by Electrochemical Deposition **Bulut Huner, Nesrin Demir and Mehmet Fatih Kaya**	Hydrogen Production from Agricultural Waste **Elif Ece Cagli and Nezihe Ayas**
12:00-12:15	Machine Learning Assisted Analysis of Photoelectrochemical Water Splitting **Burcu Oral, Elif Can and Ramazan Yildirim**	Investigation of Ni/Cu Impregnated Zeolite Catalysts for Hydrogen Production from Methanol Steam Reforming **Ozgecan Caglayan and Nezihe Ayas**
12:15-12:30	Integration of Methane Cracking and Direct Carbon Fuel Cell with CO2 Capture for Hydrogen Carrier Production **Aliya Banu and Yusuf Bicer**	Hydrogen production through dehydrogenation of morpholine borane in the presence of PSSA stabilized Pd-based catalysts **Ceren Yuksel Alpaydin, Mülkiye Kaymaz, Senem Karahan Gulbay and C. Ozgur Colpan**
12:30-12:45	Design of an Optimization Based Adaptive Neural-Fuzzy Inference Systems (ANFIS) for Controlling Output Voltage of Double Chamber Microbial Fuel Cell **Mehmet Hakan Demir and Berkay Eren**	The Usage of Solid State NaBH4 for Hydrogen Production with CoCl2 Catalyst **Asli Boran, Serdar Erkan and Inci Eroglu**
12:45-13:15	**Break**	**Break**
	HALL A	
13:15-15:30	**Keynote Speakers** Chair: **Turan Arat**	
13:15-14:00	**Keynote Speaker - Chao-Jun Li** Combined Solar Energy Harvesting and Reversible Hydrogen Storage with Liquid Aromatics	
14:00-14:45	**Keynote Speaker - Xianguo Li** Degradation Mechanisms and Durability of Automotive PEM Fuel Cells	
14:45-15:30	**Keynote Speaker - Umit B. Demirci** Sodium Borohydride as Hydrogen Carrier, a 'Rough Diamond' That Has Entered into the Age of Prototypes	
	PARALLEL SESSIONS	
	HALL A	**HALL B**
15:30-17:00	**SESSION 6A: PEM Fuel Cells-2** Chair: **Selahattin Çelik**	**SESSION 6B: Hydrogen Production-4** Chair: **Nuri Azbar**
15:30-15:45	The Effects of Anisotropic Electrical Conductivity Depending on Operating Conditions on Gas Diffusion Layers in PEM Fuel Cell **Mert Tas and Gulsah Elden**	Biohydrogen Production from Lignocellulosic Wastes Pretreated by Rumen Microorganisms: An Overview **Gokce Kurt, Bestami Ozkaya and Ahmet Demir**
15:45-16:00	Pt and Pd Based Quaternary Metal Catalysts for the Cathode in PEM Fuel Cell **Cigdem Guldur, Esma Gümüs and Silver Günes**	Comparison of Pure-Hydrogen Production from Sodium Borohydride with Blast Furnace Slag, Fe2O3 and Al Nano Metal Powder Catalysts **Mustafa Kaan Baltacioglu, Feride Cansu Iskenderoglu, Fatih Bekmez and Berat Madenci**
16:00-16:15	Eco-Friendly Production of Graphene Fiber as Metal-Free Electrocatalyst for Hydrogen Evolution Reaction **M. Giray Ersozoglu, Hurmus Gursu, Selin Gumrukcu, A. Sezai Sarac and Yucel Sahin**	Hydrogen Production by Methanol Electrochemical Reforming in the Membrane System **Merve Gordesel Yildiz, Ozgü Yoruk, Duygu Uysal Ziraman, Ozkan Murat Dogan and Bekir Zuhtu Uysal**
16:15-16:30	Development of a High Performance PEM Fuel Cell Stack with Open-Cathode Titanium Bipolar Plate for Unmanned Aerial Vehicles **Ugur Aydin, Omer Erdemir, Mehmed Selim Cogenli, Selahattin Celik, Serkan Toros and Bora Timurkutluk**	Popped Rice Char and Animal Manure Char with Sirnak Asphaltite Char– Characterization of Adsorption Kinetics for H2 in Microfluidic Sorbent Particle Packed Bed Using Biochar by Microwave Radiation **Yildirim Tosun**

SCIENTIFIC PROGRAM

16:30-16:45	Electrical Properties of the Carbon Nanotube (CNT) Reinforced Composite Plates for the PEM Fuel Cell Bipolar Plate Application **Alparslan Topcu, Fatih Daricik, Kadir Aydin and Selahattin Celik**	Ca and Co doped perovskite structures for hydrogen production **Seyfettin Berk Sanlı, Ihsan Emre Yigiter, Berke Piskin, Fatih Piskin and Gülhan Cakmak**
16:45-17:00	Performance Evaluation of the Novel Flow Field for PEM Fuel Cells **Nazım Kurtulmus and Alparslan Topcu**	Fine Tuning the Intrinsic Activity of Layered Iron Nickel Sulphide Nanosheets by Varying Boron Doping to Produce Low Cost and Green Hydrogen **Esaam Jamil, Begum Yarar Kaplan, Selmiye Alkan Gursel and Alp Yurum**
17:00-17:15	**Break**	**Break**
	HALL A	**HALL B**
17:15-18:30	**SESSION 7A: Hydrogen Production-2** Chair: **Murat Ozturk**	**SESSION 7B: Hydrogen Energy Applications-1** Chair: **Kadir Aydin**
17:15-17:30	Effect of Organic Fraction of Municipal Solid Waste Addition to High Rate Activated Sludge System for Hydrogen Production from Carbon Rich Waste Sludge **Dogukan Tunay, Oznur Yildirim, Bestami Ozkaya and Ahmet Demir**	Hydrogen and Ammonia as Fuel for the Decarbonization of Shipping **Omer Berkehan Inal, Burak Zincir and Cengiz Deniz**
17:30-17:45	Investigation and Thermodynamic Analysis of a New Geothermal Energy System for Hydrogen and Other Valuable Outputs **Burak Tekkanat, Yunus Emre Yuksel and Murat Ozturk**	Thermodynamic Optimization of the Scimitar Engine with Fixed Nozzle Geometry **Tayfun Tanbay and Ahmet Durmayaz**
17:45-18:00	A New Multigeneration Plant for Useful Outputs Including Hydrogen **Yunus Emre Yuksel, Murat Ozturk and Ibrahim Dincer**	Energy and exergy analyses of a new geothermal energy-based tri-generation plant **Murat Koc, Yunus Emre Yuksel and Murat Ozturk**
18:00-18:15	Thermodynamic Analysis of a Power and Liquid Hydrogen Production Plant Using Waste Heat **Murat Koc, Yunus Emre Yuksel and Murat Ozturk**	Effect of External Heater Operating Duration on Cold Start Performance of PEM Fuel Cell **Alparslan Topcu, Kadir Aydin and Selahattin Celik**
18:15-18:30	Optimization of Pretreatment of Olive Tree Biomass using Response Surface Methodology for Biological Hydrogen Production **Oznur Yildirim, Dogukan Tunay, Bestami Ozkaya and Ahmet Demir**	Optimum Heating Method for the Assisted Cold Start Technique of PEM Fuel Cell **Alparslan Topcu, Ahmet Ozkan Kocamanoğlu, Kadir Aydin and Selahattin Celik**

SCIENTIFIC PROGRAM

Friday, May 28, 2021		
	PARALLEL SESSIONS	
	HALL A	HALL B
09:00-11:30	**SESSION 8A: Materials for Hydrogen Energy Technologies-2** Chair: **Nezihe Ayas**	**SESSION 8B: Materials for Hydrogen Energy Technologies and Hydrogen Energy Applications-3** Chair: **Nader Javani**
09:00-09:15	Synthesis and Characterization of NiFe2O4-TiO2 Photocatalysts and Their Use for Photocatalytic Hydrogen Production **Irem Firtina-Ertis and Ozge Kerkez-Kuyumcu**	Investigation of Effective Promoters and Iron Precursors in FT Synthesis over TiO2 Supported Iron Catalysts **Utku Burgun, Hadi Rahnmaei Zonouz, Hasan Can Okutan, Husnu Atakul, Selim Senkan, Alper Sarioglan and Gamze Gumuslu Gur**
09:15-09:30	Kinetic Study of Ni-Co/Al2O3 Catalyst Used in Hydrogen Rich Gas Production from Olive Pomace with Thermogravimetric Analysis **Fahriye Dönmez, Vildan Aker and Nezihe Ayas**	The Novel Synthesis Route of BiVO4 and Photocatalitic Activity on Water Splitting **Fatih Tezcan, Meltem Kahya Dudukcu and Gülfeza Kahya Dudukcu**
09:30-09:45	The Influence of Ni/Dolomite Catalyst for Production of Hydrogen from NaBH4 Hydrolysis **Burcu Kiren and Nezihe Ayas**	Synthesis and Characterization of Phase-Pure Perovskite Type Oxides - The Case of BaZr0.80Y0.20O3-δ and SrCe0.95Yb0.05O3-δ **Omer Ozcan and Fatih Piskin**
10:00-10:15	Determination of the Synthesis and Activity of the Sepiolite Supported Catalyst Used in the Production of H2 from Methane **Tugce Basara and Nezihe Ayas**	Analysis and Assessment of a Novel Biomass Gasification Based Integrated System with Hydrogen Generation Process **Mehmet Altinkaynak and Murat Ozturk**
10:15-10:30	Hydrogen from Poppy Seed Gasification over Co-La/Sepiolite Catalyst **Alattin Cakan, Burcu Kiren and Nezihe Ayas**	Thermodynamic Modeling of a Combined Plant for Clean Hydrogen Generation Using High Pressure Air Storage Plant **Mehmet Altinkaynak and Murat Ozturk**
10:30-10:45	H2 Release from NaBH4 with Novel Catalyst **Aybuke Ayse Erturk, Tugba Akkas Boynuegri and Metin Guru**	Energy and Exergy Analyses of a Concentrated Solar Power Generation System Integrated with a Biomass-based Hydrogen Production Process **Mehmet Emre Burulday, Nader Javani and Mehmet Selcuk Mert**
10:45-11:00	**Break**	**Break**
	HALL A	HALL B
11:00-13:00	**SESSION 9A: Solid Oxide Fuel Cells-1** Chair: **Serkan Toros**	**SESSION 9B: Hydrogen Energy Technologies-3** Chair:**Filiz Karaosmanoglu**
11:00-11:15	The stability and corrosion behavior of binary NiPd electrocatlysts in alkaline electrolysis system **Ramazan Solmaz** Pd-modified polyrhodanine thin films as cathode electrocatalysts for water splitting **Ramazan Solmaz and Dursun Öztürk**	Autonomous Hydrogen Production System Design **Feride Cansu İskenderoglu, Mustafa Kaan Baltacıoglu, Caglar Conker and Hasan Huseyin Bilgic**
11:15-11:30	Development of LPG Powered Micro-Tubular Solid Oxide Fuel Cell System for Unmanned Aerial Vehicles **Ugur Aydin, Ibrahim Pamuk, Kerem Talu, Omer Erdemir, Cigdem Timurkutluk, Selahattin Celik and Bora Timurkutluk**	Performance Assessment of Vanadium Chlorine Thermochemical Cycle **Mustafa Balta and Mehmet Keles**

SCIENTIFIC PROGRAM

11:30-11:45	Investigation of Contact Problem in Planar Solid Oxide Fuel Cells **Sezer Onbilgin, Cigdem Timurkutluk, Bora Timurkutluk and Selahattin Celik**	Automatic PEM Water Electrolyzer Control System (PEMECS) Design for Cell Testing **Emre Ozdogan, Ebubekir Tuncay, Ilayda Nur Uzgoren, Murat Kisti, Süleyman Uysal, Bulut Huner, Nesrin Demir and Mehmet Fatih Kaya**
11:45-12:00	Fuzzy- Analytical Hierarchy Process (F-AHP) Based Material Selection for Solid Oxide Fuel Cell Electrolyte **Siamak Alipour, Emrah Sagir and Arash Sadeghi**	A Unique Hydrogen Energy System Developed for Data Centers in Arctic Regions with Heat Recovery **Mert Temiz and Ibrahim Dincer**
12:00-12:15	Development of Ceramic-Fiber Reinforced Sealants for Solid Oxide Fuel Cells **Cigdem Timurkutluk, Gamze Atalmis, Sezer Önbilgin, Furkan Toruntay and Bora Timurkutluk**	A Renewable Energy Based Waste-To-Energy System with Hydrogen Options **Bogachan Gungor and Ibrahim Dincer**
12:15-12:30	Cold Sintering of 8YSZ Electrolytes for Solid Oxide Fuel Cells **Tugce Ucun, Murat Murutoglu, Aligul Buyukaksoy, Yahya Kemal Tur and Huseyin Yilmaz**	Hydrogen Powered Cities: A Perspective on Urban Planning **Munevver Balta and Mustafa Balta**
12:30-12:45	Development of Multi Phase Cathodes for SOFCs via Thermal Plasma Synthesis **Havva Eda Aysal, Gulhan Cakmak and Tayfur Ozturk**	Development of Sustainable Multigeneration System With Recompression SCO2 Brayton Cycle For Hydrogen Production **Serpil Celik Toker, Gamze Soyturk and Onder Kizilkan**
12:45-13:15	**Break**	**Break**
	HALL A	**HALL B**
13:15-15:00	**SESSION 10A: Hydrogen Energy Applications-2** Chair: **Ramazan Solmaz**	**SESSION 10B: Hydrogen Energy Technologies-4** Chair: **Onder Kizilkan**
13:15-13:30	Coolant Selection for the Enhanced Cold Start Capability of PEM Fuel Cell **Alparslan Topcu, Kadir Aydin, Selahattin Celik and Mikail Yagiz**	Machine learning analysis of gas phase photocatalytic CO2 reduction for hydrogen production **Dilara Saadetnejad, Burcu Oral and Ramazan Yildirim**
13:30-13:45	Hydrogen Energy Systems for Underwater Applications **Berna Sezgin, Yılser Devrim, Tayfur Öztürk and Inci Eroglu**	A New Off-Grid Autonomous Energy System Structure and Improved Controller **Süleyman Yildiz, Burak Yildirim and Mahmut Temel Ozdemir**
13:45-14:00	New and Future Approach Technologies on Hydrogen Fuel Cell Applications with Marine Vehicles **Meryem Gizem Surer and Huseyin Turan Arat**	A Novel Chaos Embedded Particle Swarm Optimization Based on Stability Boundary Locus for Delayed Fuel Cell Microgrid with PI Controller **Mahmut Temel Ozdemir and Vedat Celik**
14:00-14:15	Energy, Exergy and Economic Analyses and Multiobjective Optimization of a Novel Solar Multigeneration System for Production of Green Hydrogen and Other Utilities **Mert Colakoglu and Ahmet Durmayaz**	A New Signal Processing-Based Islanding Detection Method for Reliable Grid Integration of Solid Oxide Fuel Cell-Based Distributed Generators **Alper Yilmaz and Gokay Bayrak**
14:15-14:30	Biohydrogen and Bioethanol Production Routes from Pyrolysis Gas **Simge Sertkaya, Gozde Duman, Haris Nalakath Abubackar, Nuri Azbar, Jale Yanik and Tugba Keskin**	Mathematical Modeling of a Solid Oxide Fuel Cell (SOFC) Based Micro-CHP System for Residential Applications **Merve Atilmis and Can Ozgur Colpan**
14:30-14:45	An Experimental Study to Validate Optimum Distance Between Metal Hydride Tanks with Staggered Arrangement for Effective Thermal Management **Ismail Hilali, Ahmet Akbas, Vehbi Balak and Dursun Akaslan**	Automated Classification of Power Quality Disturbances in a SOFC&PV-based Microgrid Using a Hybrid Machine Learning Method with High Noise Immunity **Alper Yilmaz, Ahmet Kucuker and Gokay Bayrak**

SCIENTIFIC PROGRAM

14:45-15:00	A Road Map to Ammonia Deployment as a Green Fuel in the Land Transportation Sector of Qatar **Mohammed Al-Breiki and Yusuf Bicer**	Local Green Hydrogen Production Potentials for Turkey with Solar Energy **Gorkem Kubilay Karayel, Nader Javani and Ibrahim Dincer**
15:00-15:15	**Break**	**Break**
	HALL A	**HALL B**
15:15-16:45	**SESSION 11A: Solid Oxide Fuel Cells-2** Chair: **Bora Timurkutluk**	
15:15-15:30	Effect of Anode Functional Layer Material on the Performance of Anode Supported Micro-tubular SOFCs **Cigdem Timurkutluk, Keremhan Bilgil, Ali Celen, Sezer Onbilgin, Tolga Altan and Ugur Aydin**	
15:30-15:45	Fabrication of Micro-Tubular Solid Oxide Fuel Cells by Tape Casting Method **Tolga Altan, Cigdem Timurkutluk, Bora Timurkutluk and Selahattin Celik**	
15:45-16:00	Effects of Adding Graphene Oxide to Glass Ceramic for Solid Oxide Fuel Cells **Tolga Altan, Mikail Yagiz, Selahattin Celik and Recep Zan**	
16:00-16:15	Effects of Increasing the Electrolyte Surface Area on the Electrochemical Performance **Cigdem Timurkutluk, Tolga Altan, Fuat Yildirim, Sezer Onbilgin, Mikail Yagiz, Bora Timurkutluk and Selahattin Celik**	
16:15-16:30	Modeling of Sheet Hydroforming of Metallic Interconnectors for Solid Oxide Fuel Cells **Habip Gokay Korkmaz, Emre Ucar, Serkan Toros and Bora Timurkutluk**	
16:30-16:45	Cold sintering of GDC electrolyte for SOFCs applications **Murat Murutoglu, Tugce Ucun, Aligul Buyukaksoy, Yahya Kemal Tur and Huseyin Yilmaz**	
16:45-17:00	**Break**	**Break**
	HALL A	
17:00-17:30	**Closing Ceremony**	

KEYNOTE SPEAKERS

KN-01

Recent European Advances in Electrolyzer and Fuel Cell Technologies

Laurent Antoni

CEA-Liten President of Hydrogen Europe Research

In this new era of energy transition, Europe expects profound changes to achieve a climate-neutral Europe by 2050. In addition to the support and development of renewable energies in Europe over the last decades, hydrogen is now recognised as a new player at the service of the environment and the economy. Over the past decades, owing to a continuous European support to research, development and innovation, hydrogen technologies have transitioned from highly specialized applications to commercially available products. This could not have been achieved without a strong commitment from industry, research and the public sector in Europe, in particular within the two FCH and FCH 2 Joint Undertakings. These private-public partnerships have been ensuring coordinated activities based on a common understanding and vision of the European industry represented by Hydrogen Europe (250+ members and 25 national associations), the European research represented by Hydrogen Europe Research (90+ members) and the European Commission with clear, quantified and focused objectives. As a result, Europe is currently leading in several hydrogen technologies as e.g. in electrolysis, and European companies and research institutions can be instrumental in advancing technological developments and industrial scale-up, contributing to cost-competitive renewable and low-carbon hydrogen. Nevertheless, significant additional research and innovation efforts with several research and innovation challenges need to be addressed in the short and medium term by the European research community.

KN-02

Advances in Hydrogen Separation using Palladium-Based Membranes

Wei-Hsin Chen

National Cheng Kung University

Global climate change and fossil fuel depletion have driven the need to shift energy use from the conventional carbon cycle to the hydrogen cycle. One of the prime advantages of consuming hydrogen as a fuel is zero emissions of carbon dioxide and other pollutants. Hydrogen can be produced from fossil fuels, biomass, and hydrocarbons. However, in most conversion processes, hydrogen-rich gases rather than pure hydrogen are produced. There are several ways to separate and purify hydrogen from hydrogen-rich gases such as pressure swing adsorption, cryogenic distillation, and membrane separation. When hydrogen is separated from hydrogen-rich gases using membranes, palladium (Pd) has demonstrated its excellent features of high hydrogen permeability and selectivity. In addition to hydrogen separation and purification, Pd-based membranes can also be thought of as a potential tool to fulfill CO_2 capture. In this talk, the advances in hydrogen separation and purification based on Pd-based membrane systems will be introduced. The important phenomena such as hydrogen permeation, concentration polarization, and membrane permeance measurement will be illustrated. The interfacial and bulk mass transfer behaviors of hydrogen in Pd-based membrane systems will be underlined. The presentation will also show hydrogen permeation in Pd membrane tube systems approached by computational fluid dynamics (CFD) along with artificial intelligence or evolutionary computation, demonstrating the potential of simulations as a powerful tool to aid in membrane system design.

KN-03

A Student Design Project for Hydrogen Fuel Cell Electric-Drive Mining Trucks

John William Sheffield

Purdue University

This multi-semester student design project is an international collaboration between two Peruvian universities, La Universidad de Ingeniería y Tecnología and La Universidad Nacional de Ingeniería and Purdue University in West Lafayette, Indiana (U.S.A.). The goal is to integrate hydrogen fuel cell technologies into a solar photovoltaic microgrid for a hard-rock lithium mining operation in Peru. The current team is challenged with the task of developing a conceptual design for the conversion of the diesel electric-drive to hydrogen fuel cell electric-drive mining haul trucks. The engineering courses are organized as global Vertically Integrated Projects (VIP). The global VIP is a transformative approach to enhancing higher education by engaging undergraduate and graduate students in ambitious, long-term, large-scale, multidisciplinary, international project teams that are led by a group of engineering faculty to give students an opportunity to see results of their learning applied in real applications.

KN-04

Update on Hydrogen and Fuel Cell Activity in Canada

Mark Kirby

Canadian Hydrogen and Fuel Cell Association (CHFCA)

There is a groundswell of interest in hydrogen energy around the world as industry and governments recognize the critical role it will play in achieving net zero 2050. Canada has long been a leader in hydrogen and fuel cell technology. Canada is a leading producer of hydrogen including an increasing amount of clean hydrogen, the cradle of PEM fuel cell technology with leading players such as Ballard Power, and over 100 years of electrolyzer history, including Cummins Canada and its predecessors. With over 90 member companies, the Canadian Hydrogen and Fuel Cell Association is the voice of the sector. Recognizing the importance of hydrogen energy, Canadian federal and provincial governments are working to build our strong base of projects and expertise, to stimulate the deployment of hydrogen energy projects. The paper reviews the status of projects in Canada, new policy and funding initiatives, and the actions that are being taken to support commercialization.

KN-05

Combined Solar Energy Harvesting and Reversible Hydrogen Storage with Liquid Aromatics

Chao-Jun Li
McGill University

Solar energy harvesting and hydrogen economy are the two most important green energy endeavors for the future. However, a critical hurdle to the latter is how to safely and densely store and transfer hydrogen. Herein, we developed a reversible hydrogen storage system based on low-cost liquid organic cyclic hydrocarbons at room temperature and atmospheric pressure. A facile switch of hydrogen addition (> 97% conversion) and release (> 99% conversion) with superior capacity of 7.1 H_2 wt% can be quickly achieved over a rationally optimized platinum catalyst with high electron density, simply regulated by dark/light conditions. Furthermore, the photo-driven dehydrogenation of cyclic alkanes gave an excellent apparent quantum efficiency of 6.0% under visible light illumination (420-600 nm) without any other energy input, which provides an alternative route to artificial photosynthesis for directly harvesting and storing solar energy in the form of chemical fuel.

KN-06

Degradation Mechanisms and Durability of Automotive PEM Fuel Cells

Xianguo Li
University of Waterloo, Canada

PEM fuel cells are playing key role in the post-pandemic economic recovery and climate change action/mitigation plans, with significant commercial activities to decarbonize the transportation sector. However, significant degradation of PEM fuel cell components during operation degrades the fuel cell performance, limits the durability of fuel cells in practical application, and significant cost is associated with the over-design to ensure the durability of the fuel cells. Therefore, understanding the mechanisms of degradation modes for different fuel cell components is of importance to the development of high-performing durable low-cost fuel cells. In this talk, the fundamental mechanisms for the degradation (or aging) of the fuel cell components will be described, and the effect of design and operating conditions will be presented. The degradation rate under steady and unsteady operation will be compared, and the impact of automotive driving conditions such as start/stop, variable load requirement, idling/high electrode potential, and high power demand for hill-climbing and high-speed overpassing will be reviewed. Since the component degradation rate depends on the driving cycles of the vehicle, and the differences in road conditions/designs and traffic conditions/regulations leading to the different “standard” driving cycles in North America, Europe and Japan, etc., complicates the design of PEM fuel cells for vehicles destined to the different markets of the world.

KN-07

Sodium Borohydride as Hydrogen Carrier, a 'Rough Diamond' That Has Entered into the Age of Prototypes

Umit B. Demirci

University of Montpellier, France

Sodium borohydride (SB) as H_2 source is an old compound with new interest. Actually, not so new, for the reason that it has been much investigated since the late 1990s. Going back to the beginning of the history of SB, it was discovered in the 1940s, and at that time, it was found to be an attractive H carrier being able to release H_2 by hydrolysis at ambient conditions. Half a century after, SB as H carrier was re-discovered, but this time for being developed as a technological solution to store H and release, on demand, H_2 at the most favorable operating conditions. More than 20 years have passed since then, and SB is still the 'rough diamond' that it was. We started to work on SB, namely on H_2 release by hydrolysis of SB, about 15 years ago. Like the great majority of the research groups active in the field, we focused on catalysis whereas we overlooked other equally important, or even much more important, aspects. For example, too few prototypes have been developed, and our understanding of the scaled-up H_2 release by hydrolysis of SB is rather limited. That is why, 3 years ago, we initiated works focusing on scaling-up and SB-based prototypes. The main lesson we have learned to date is that there are great differences between the lab-scale hydrolysis of SB and the prototype-scale reaction. Following the online interview that I gave to the Turkish Hydrogen Association in February 2021, the IHTEC 2021 meeting will be a great opportunity to discuss about the technological prospects of SB, a 'rough diamond', especially for Turkey.

PROCEEDINGS

Hydrogen production over Ni-containing MgO supported catalyst: Effect of hydrothermal process duration in catalysts synthesis

Saleh Ahmat Ibrahim, Emine Kaya Ekinci, Birce Karaman, Nuray Oktar[1]*

[1]*Gazi University, Engineering Faculty, Department of Chemical Engineering, 06570, Ankara,Turkey*

* E-mail: nurayoktar@gazi.edu.tr

Abstract

The steam reforming of acetic acid was conducted over different catalysts using optimum reaction parameters (reaction temperature, 750°C; space time of 10.91 s with a feed molar ratio (AA/H_2O) of 1/2.5 mol/mol). Complete acetic acid conversion were achieved over the mono-metallic 5Ni@MgO-24 and the bi-metallic 5Ni-1La@MgO-24 catalysts. Furthermore, relatively high hydrogen selectivity was achieved after Ni impregnation, rising from 6% to 63.3% over 5Ni@MgO-24 catalyst compared to bare MgO-24 support. The addition of La into the 5Ni@MgO-24 catalyst structure played a significant role improving the steam reforming of acetic acid and mitigating the proportion of carbon formed from 17.6% to 12.17%. As expected, La incorporation has increased the agglomeration of basic sites and reinforce the adsorption of carbon dioxide on the catalyst's surfaces. Therefore, the coke deposition was reduced, and the catalyst lifetime was improved.

Keywords: Nickel, magnesium oxide, acetic acid, steam reforming, hydrogen, coke formation.

I. Introduction

Hydrogen's unique properties, as the highest energy content by weight and the capability to be converted, stored, and transported under gaseous and liquid form, make it the best enabler for the decarbonization and energy transition [Collet and Patouillard, 2016]. Until now, hydrogen is generated from fossil resources such as oil, coal, and natural gas [Aika,2006]. However, the fossil fuels used lead to a significant amount of greenhouse gas emissions [Alonso, 2020]. The tendency towards alternative energy sources have become a necessity. As a result, a sustainable energy source such as biomass-derived acetic acid as an alternative feedstock because it has no negative impact to the environment, and it can be used to produce hydrogen without carbon footprint [Basagiannis and Verykios, 2007]. Depending on conditioning, hydrogen produce by the steam reforming of acetic acid can either be used as an energy carrier and as a feedstock for large number of industrial and chemical properties.

II. Experimental Set-up and Procedure

The mesoporous MgO-6 and MgO-24 support materials have been prepared following a new template-free hydrothermal co-precipitation route, which has been discussed elsewhere [Chen, 2014]. The main steps of MgO materials synthesis consist of aqueous solution preparation, hydrothermal processes, filtering, washing and calcination. Figure 1. shows the preparation procedure of the support materials using hydrothermal method.

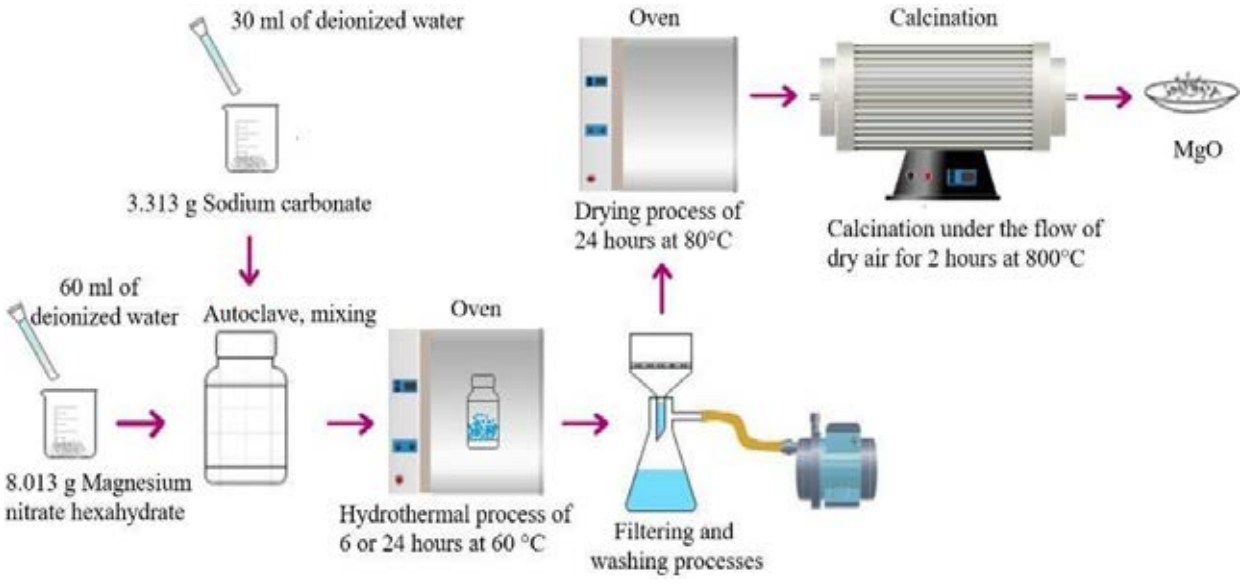


Fig. 1: Experimental procedure of MgO preparation

III. Analysis

In the present study, highly reactive and versatile mesoporous MgO-6 and MgO-24 particles were prepared following a new template-free hydrothermal co-precipitation route. The mono-metallic (5Ni@MgO-6 and 5Ni@MgO-24) and the bi-metallic (5Ni-1La@MgO-24) catalysts were prepared using the simultaneous wet-impregnation method. The synthesized catalysts were characterized by XRD, N_2 adsorption-desorption, SEM/EDS and TGA-DTA and tested for hydrogen production by the steam reforming of acetic acid.

IV. Results and discussions

Fig. 2. depicts the XRD patterns of bare support and Ni-containing catalysts. This result indicates that the MgO material maintains its mesoporosity after the impregnation of nickel without deteriorating the pore structure of the material. The strong and clear XRD spectrum of the catalyst 5Ni@MgO-24 reveals that the synthesized catalyst has a crystalline structure and no characteristic peaks corresponding to the impurities have been observed.

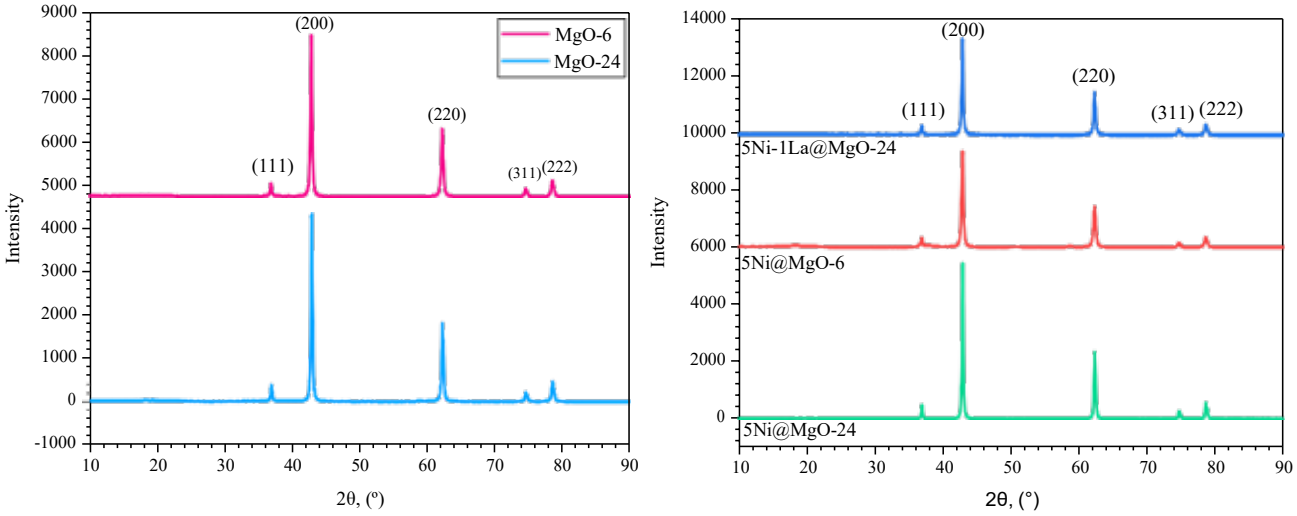


Fig. 2: XRD powder patterns at wide angles of Ni and/or La impregnated MgO-6 and MgO-24 catalysts

The catalytic steam reforming of acetic acid was carried out at 750 °C for a period of 3 hours. Low hydrogen selectivities of 6% and 8% were obtained over the bare supports MgO-24 and MgO-6, respectively. This result indicates a poor performance of the steam reforming of acetic acid. The incorporation of Ni and Ni-La metals in the structure of MgO-24 has remarkably improved the catalytic acivity performance by giving complete conversion of acetic acid consisted with stable hydrogen selectivity values over 5Ni@MgO-24 and 5Ni-1La@MgO-24 catalysts. Moreover, the decrease in the amount of methane from 34.88% to 0.75% in the product distribution proves that Ni is highly active in breaking C-C, C-H and C-O bonds and favoring the steam reforming over the decarboxylation reaction [Pekmezci Karaman,2017].

V. Conclusions

Mesoporous MgO materials were prepared and Ni & Ni-La contents were successfully added into the catalyst supports. The sharp XRD patterns show clearly the well define narrow pores and the mesoporous nature of the catalysts. Over 5Ni@MgO-24 and 5Ni-1La@MgO-24 catalysts, 100% acetic acid conversion and quite stable hydrogen selectivities were achieved. The introduction of La into the mono-metallic catalyst structure, 5Ni@MgO-24, made a noticeable effect in the steam reforming of acetic acid by reducing coke formation from 17.6% to 12.17%.

References

Collet P., Patouillard L. Sensitivity of Technical Choices on the GHG Emissions and Expended Energy of Hydrotreated Renewable Jet Fuel from Microalgae. Oil & Gas Science and Technology–Revue d'IFP Energies nouvelles. 1;71(1):11 (2016).
Aika KI, Baba T, Inazu K, Lefferts L, Seshan K, Takanabe K. Steam reforming of acetic acid as a biomass derived oxygenate: Bifunctional pathway for hydrogen formation over Pt/ZrO2 catalysts. Journal of catalysis. 25;243(2):263-9 (2006).
Alonso CG, de Souza TL, Machado GD, Rodrigues CT. Optimization of bio-oil steam reforming process by thermodynamic analysis. International Journal of Hydrogen Energy. 30;45(53):28350-60 (2020).
Basagiannis AC, Verykios XE. Catalytic steam reforming of acetic acid for hydrogen production. International journal of hydrogen energy. 1;32(15):3343-55 (2007).
Cui, Hongmei, R. I. Boughton, Xiaofeng Wu, Yunfa Chen. "Synthesis and characterization of mesoporous MgO by template-free hydrothermal method." *Materials Research Bulletin* 50: 307-311 (2014).
Arbag H, Cakiryilmaz N, Dogu G, Dogu T, Oktar N, Karaman BP. Performance comparison of mesoporous alumina supported Cu & Ni based catalysts in acetic acid reforming. International Journal of Hydrogen Energy. 19;42(42):26257-69 (2017).

Development of a zero-dimensional dynamic model of a solid oxide electrolyzer in co-electrolysis mode integrated with a PV system

[1*]Alper Can Ince, [2]C. Ozgur Colpan, [1]Mustafa Fazıl Serincan,
[1] 1Gebze Technical University, Faculty of Engineering, Mechanical Engineering Department, Gebze, Kocaeli, 41400, Turkey
[2] Dokuz Eylul University, Faculty of Engineering, Mechanical Engineering Department, Buca, Izmir

* E-mail: a.ince@gtu.edu.tr

Extended Abstract

The global demand for electricity is increasing rapidly owing to the considerable increment in population and industry in the world. The growing awareness of global warming, and thus the aim of decreasing fossil fuels consumption has made renewable energy sources (RES) to be attractive. However, the important limitation of the use of RES is to generate fluctuating power which leads to an increase in temporary surplus electricity and instability in the grid network. In this regard, the use of electricity storage technologies is an important solution to provide a balance between supply and demand in the grid network. For this purpose, the development of different energy storage technologies (e.g., electrical, chemical, mechanical, and electrochemical) has gained attention in recent years. Chemical storage, especially Power to Fuel (P-t-F) brings a potential way to convert surplus electricity into fuel (e.g., methane, methanol) with the capability of storing with a range of large amounts of energy for long periods. In a typical P-t-F system, the hydrogen produced through the water electrolyzer is driven by power generated by renewables. Meanwhile, CO_2 is obtained from different carbon sources (e.g., air, flue gas, and biogas). The combination of CO_2 and H_2 takes place in the chemical reactor for fuel production. In an alternative way, the tailored syngas can be converted into fuel without pure hydrogen production. This way provides to eliminate issues with the hydrogen management (e.g., storage, transportation). A solid oxide cell in co-electrolysis mode (co-SOE) provides a highly efficient way to convert carbon into a tailored synthetic gas with decomposing steam and carbon dioxide simultaneously, as displayed in Figure 1. The synthetic gas generally includes rich hydrogen and carbon monoxide from the cathode side, as well as oxygen from the anode side. In a highly-pressurized system, methane production can also be favoured.

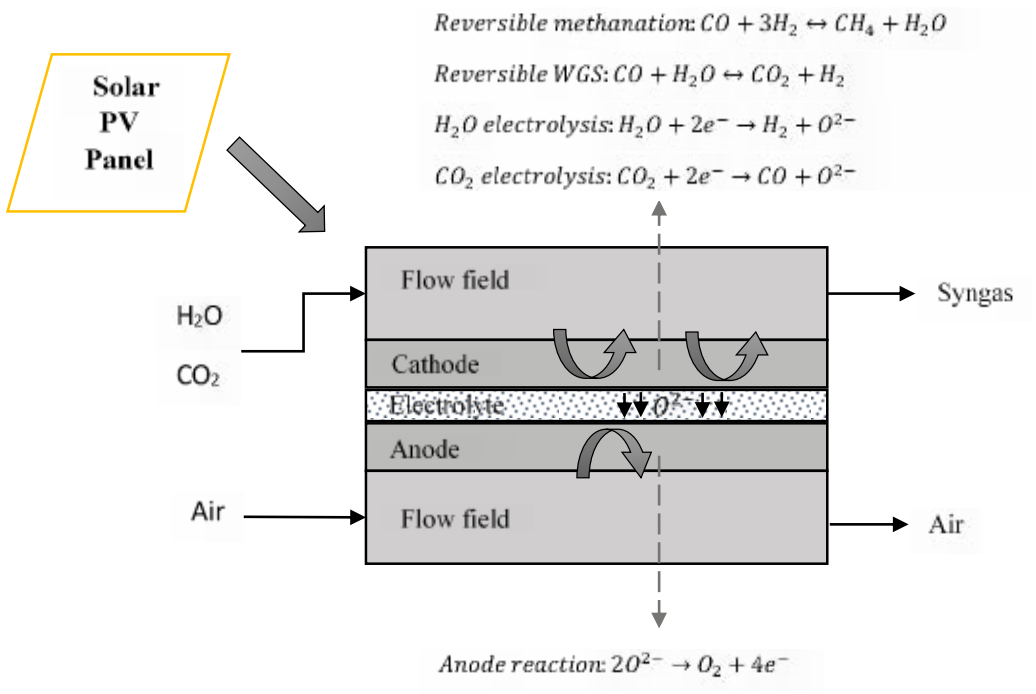


Fig. 1 Working principle of the co-SOE

In the present work, a case study is conducted to assess the feasibility of co-SOE operation for an application in California. In the first step, the duck curve which shows the difference between the electricity demand and the expected produced electricity is obtained. The transient investigation of this system is performed for the potential of grid stabilization. For this purpose, a zero-dimensional (0-D) transient model of the co-SOE integrated with a solar PV is developed under real operating conditions (e.g. shortage, oversupply mitigation, and decreased frequency response). The model, which includes electrochemical and chemical sub-models, is therefore capable of indicating dynamic performance of the co-SOE according to real grid operating conditions. In addition, thermodynamic

analysis of this system is performed using mass and energy balances. Consequently, the system efficiency, syngas production rate, and net power input are found under real operating conditions. In future, the model can be integrated into the methane synthesis system including the balance of plant and other sub-systems (e.g., CO_2 capture process and fuel upgrading system).

Keywords: co-electrolysis, hydrogen, transient response, 0-D modeling, solar PV, grid stability

Hydrogen Production by Solid Fuels with Different Gasification Methods

[1*]Mustafa Tolay, [2]Cemil Koyunoğlu, [3]Andre Waterschoot
[1] Tolay Energy Consulting, 19 Mayıs Street, Halaskargazi Road, Feza Block, No: 192, Floor 8, Sisli, 34360, Istanbul, Turkey
[2] Yalova University, Engineering Faculty, Energy Systems Engineering Department, Cinarcik Road 5th km, Yalova, 77200, Turkey
[3] Verco Renewable Energy Consulting SL, c/Solsona 17, b2, 08173, Sant Cugat del Valies, Barcelona, Spain

* E-mail: drmtolay@libero.it

Abstract
Increasing energy production deficit in the world and of course in our country, Turkey, increasing drought with global warming, price increases put forth by natural gas and oil prices in recent years make it necessary for us to turn to new sources in energy production. Especially in recent years, before the world economic crisis, the barrel of crude oil reaching up to high and the subsequent rise in natural gas prices signal that energy production costs will increase rapidly and energy supply will become difficult soon. The fact that renewable energy sources and nuclear energy are not seen as a solution in energy production in the short term in our country makes the introduction of new primary and secondary energy sources more prominent. On the other hand, the fact that we have recently signed the Kyoto Protocol also limits the misuse of carbon-based fuels in terms of environmental criteria. In terms of carbon-based underground resources, existing solid fuel resources are far from being used except for bad combustion technologies. Coal resources, which have a very important place in energy resources, can be brought to the energy production sector in a short time with coal gasification technologies, high energy production efficiency, and environmentally friendly gasification technologies. The increasing need for clean secondary energy sources such as hydrogen energy is gaining importance.

Keywords: Hydrogen production, solid fuel, gasification, process types

I. Introduction
Today, the cheapest and easiest method available for hydrogen production is the production of syngas by gasification of solid and liquid fuels. In syngas obtained by gasification of solid and liquid fuels and consisting mainly of CO and H_2, it is possible to separate hydrogen with appropriate technologies. The pure hydrogen gas obtained can be used as a secondary energy source in many areas where clean energy is needed, especially in the automotive sector. Syngas produced by gasification systems of solid fuels such as lignite, biomass, and solid waste, especially coal in hydrogen production, can be used both in the production of energy with high efficiency and in the production of chemicals such as hydrogen, methanol, kerosene, and fertilizers. Thus, lignite in Turkey, which is national wealth, which we leave underground without being used idle, and the solid wastes we leave brutally to nature can be brought in both our energy sector and our chemical industry. Developments in the world show that the dominance of fossil fuels such as oil will continue in the next 50 years. On the other hand, considering the issues in which environmental legal regulations for fossil fuel power plants are gradually being tightened and solutions with high efficiency and low CO_2 emissions come to the fore, the 'coal gasification' technique, which was applied on a commercial scale 150 years ago and has become prominent all over the world in recent years, is also is of great importance. In recent years, South Africa, the USA, Canada, Australia, the People's Republic of China, and European Countries have been rapidly investing in the gasification of coal and similar solid fuels to meet energy needs and produce chemicals.
For this study, Turkish lignites (Table-1) were studied for hydrogen production via gasification. After the step of lignite preparing operations, lignites fed into gasifiers. Lignites particle that comes into the gasifier firstly loses its water, dries. Its temperature changes from 250 °C - 400°C. Lignite particular reaches 400°C – 600°C temperatures during its upwards moving in the gasifier and start to pyrolysis and disintegrates to coke, tar, CH_4, and H_2. Oxygen comes in from the bottom or upper parts of gasifiers. When the lignite particulate reaches 1000°C temperature, oxygen and steam react with coke and the formed gas is syngas at 1000-1300°C temperature that generally contains CO, H_2, CO_2, CH_4. Now, lignites particulate is reduced and only its ash remained. Syngas cools down to 600°C while moving upwards. When the syngas reaches 400°C – 600°C by going out from the gasifier, it is pulled to a gas cleaning zone in which ash and dust are collecting special cyclones. Afterward, it comes to gas cleaning and hydrogen separation sections.

II. Gasification of Solid Fuel
The gasification occurs in reactors where solid fuel or solid waste (pet-coke, MSW or RDF, etc.) can contact with air or oxygen, steam, or various mixtures of these substances in the systems called gasifiers. Depending on the solid fuel use, the gasifiers can be classified as a fixed bed, fluid bed, and integrated bed gasifiers. The raw gas type obtained from solid fuels is a chemical process known as combustible gas production, gasification which is called synthesis gas, syngas, air gas, utility gas. With a comprehensive description, gasification is a process of conversion of solid waste with carbon and hydrogen content into a gas product with proper heating value. Gasification includes definitions such as pyrolysis, partial oxidation, reduction, and hydrogenation. Today, the applied technology is partial oxidation and consequently, poor gas or syngas is produced from solid fuel. This gas contains flammable components such as methane, hydrogen, and carbon monoxide and besides oxygen, nitrogen,

and water in different ratios. The gasification process occurs between 800°C and 1300°C. The certain temperature depends particularly on the feeder material preferences like softening and melting points of ash. This case is unconditionally suitable for all fixed bed gasifiers and can be even applied to many fluid beds and moving bed gasifiers and it should be known that the feeder materials here are carbon and hydrogen sources theoretically. In the gasification of solid waste and solid fuels, in large power generation for optimum capacity, fluidized bed and integrated bed gasifiers are generally strong and functional for gasification. The produced syngas is very similar to utility gas and their electrical power and/or chemical substances can be used for fertilizer production. The solid fuel-based electrical generation technology has the most appropriate air emission, solid waste, and wastewater values. The reason for high energy efficiencies in solid fuel gasification is less solid fuel utilization for the same amount of energy production resulting in less carbon dioxide (CO_2) emissions. Gasification is a more environmentally friendly technology compared to incineration technologies and it is more advantageous in terms of CO_2, SO_2, NO_x emissions. Sulfur is mostly available in H_2S form which is easier to be eliminated than SO_2 or pure sulfur form. NO_x, dioxin, and furan problems do not occur during gasification. Syngas composition was as shown in Table-2.

For gasification of treatment solid waste, firstly transforming the substances to proper particle size and then pelletizing are necessary. The solid waste gasification process occurs in several steps. The removal of the water in solid waste is performed during preliminary preparations or the solid waste that is pelletized and containing generally 10-15% water converts its water content into vapor stage in the gasifier. After this drying process, it enters into several reactions such as pyrolysis, reduction, combustion, and similar reactions. Solid waste with more than 35% water content is not suitable for electricity production through thermochemical transformation. For gasification, the moisture ratio between 10-15% is appropriate and the particle size of 3-5 cm is considered ideal. The water in the solid waste is used to produce the water steam necessary for one of the gasification reactions as water steam reaction which is very important. To start the gasification process, the water in the gasifier should be transformed into the vapor phase first, and then should reach the pyrolysis phase, and finally, it should be increased to gasification reaction temperatures by combustion of one part of the carbon element in the solid waste. The reactions occurring in the gasifier can be examined as follows; Drying, Evaporation of Water, Pyrolysis, Reduction (Gasification), Combustion Reactions.

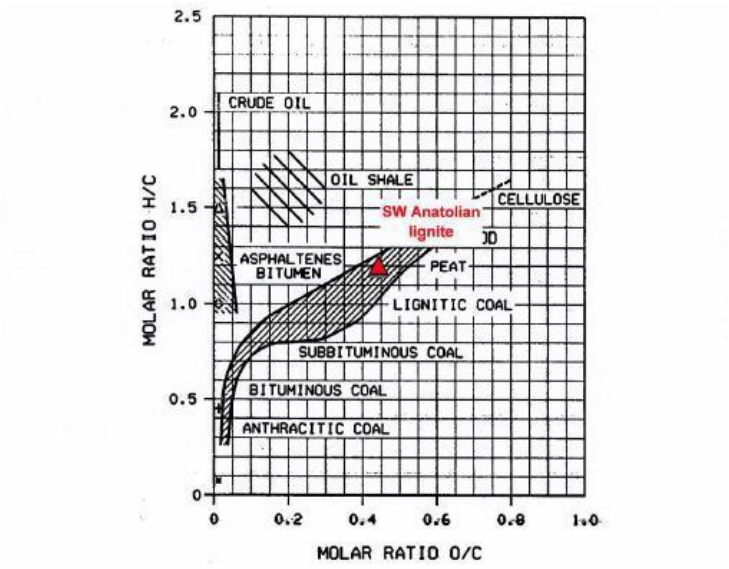


Table 1. Molar ratio H/C and O/C various solid fuels comparing with southwest Anatolian Turkish lignites

Table 2. Calculated syngas composition of gasification for Turkish lignite, Tuncbilek/Kutahya.

CO_2	20.5 % (vol)
CO	40.0 % (vol)
H_2	25.3 % (vol)
CH_4	7.5 % (vol)
C_nH_m	0.5 % (vol)
H_2S + COS	1.3 % (vol)
N_2 + Ar	4.9 % (vol)
Total	100.0 % (vol)
Heating value	11.085 KJ/Nm^3

References

Daradimos, G., Vostan, P., Hirschfelder, H., Yamankaradeniz, H., Tolay, M., “The BGL Gasification Technology for Turkish Lignites”, The ICCI 2008; 14th Energy & Environmental Congress, (2008).

Gray, D., Tomlinson, G., “Hydrogen from Coal”, Mitretek Techn ica l Paper, U.S. DOE, NETL, Contract No: DE-AM26-99FT40465, Nov. 2001, Washington DC, (2001).

Higman, C., Burght, M., "Gasification", GPP, Elsevier, New York, (2003).

Hirschfelder, H., Vostan, P., Tolay, M., “Methanol Production Project for Turkish Lignite Using by The BGL-CTL Gasification Technology”, International Conference on Energy and Automotive Technologies-ICAT 2010 , Istanbul-Turkey.
Johnson, J.L, "Kinetics of Coal Gasification", John Wiley & Sons, New York, (1979).

Okutan, H., Tolay, M., Yamankaradeniz, H., Ekinci, E., “Gasification: The Importance of 150 Years Technology in 21. Century’, Coal and Energy Seminar, General Management of TKİ, Ankara, (2006)

Schellberg, W., ‘‘World’s Largest IGCC Celebrates 10th Anniversary“, Twenty-Fifth Annual International Pittsburgh Coal Conference, September 29 – October 2, 2008, Pittsburgh, PA, USA, (2008).

Schellberg, W., Peña, F.G., Hooper, M., „PRENFLO Gasification; 10 years Operating Experience at ELCOGAS IGCC, Puertollano / Spain“, 1st Energy Efficiency Forum, İstanbul, (2009).

Tolay, M., “Gasification Technologies’, Advanced Workshop on ‘Energy for Future’, ITU, Istanbul, (2006).

Tolay, M., “Clean Energy and Chemical Substance Production by Coal Gasification, ICCI 2007; 13. International Energy, Co-Generation and Environmental Technology Conference, Istanbul, (2007).

Tolay, M. Yamankaradeniz, H., “Solid Fuel Gasification and Gas Cleaning System", Int. Patent Application, No.:PCT/TR2007/05430, Int.App.No.:CT/TR2007/000122, (2007).

Tolay, M., Vostan, P., Waterschoot, A., “ Katı Yakıt Gazlaştırılması ile Hidrojen Üretimi”, IV. Ulusal Hidrojen Kongresi, UHK 2009, 15-16 Kasım 2009, Kocaeli Universitesi, Kocaeli-Turkiye, (2009).

U.S. Department Of Energy, 2004 National Energy Technology Laboratory, Gasifier Technologies, (2004).

Wooten, R., Kerr, C., “South Heart SNG Project”, Gasification Technologies Conference, 5-8 October 2008, Washington DC, (2008).

www.envirotherm.de

www.uhde.eu

www.gasification.org

Characterization of B-site Fe^{3+} and Co^{3+} Substitutied $La_{0.2}Ca_{0.8}Mn_{1-x}B_xO_3$ (x= 0.2) Type Perovskite for Thermochemical Water Splitting

İhsan Emre Yiğiter[1], Seyfettin Berk Şanlı[1], Fatih Pişkin[1], Gülhan Çakmak[1], and Berke Pişkin[1*],
[1] Muğla Sıtkı Koçman University, Faculty of Engineering, Department of Metallurgical and Materials Engineering, Muğla, 48000, Turkey

* E-mail: berkepiskin@mu.edu.tr

Abstract

Hydrogen has an important role as promising technologies for energy related applications. In this context, thermochemical methods take attention in hydrogen production. In two-step thermochemical cycles is one the most important method to obtain pure hydrogen production without the need for any separation process. Thus, the thermodynamics and kinetics of redox reactions are one of the important factors that determine hydrogen production efficiency. This efficiency strongly influenced by the structural properties of active materials used in two-step thermochemical water splitting reactions. For this purpose, in this study we investigated the structural properties of perovskite oxides draws attention to be able to use in TWS reactions due to providing higher structural stability with allowing compositional diversity. This study includes the synthesis and the characterization of $La_{0.2}Ca_{0.8}Mn_{0.8}Fe_{0.2}O_3$ and $La_{0.2}Ca_{0.8}Mn_{0.8}Co_{0.2}O_3$ perovskite oxides to determine their ability to able to use for hydrogen production in TWS.

Keywords: Perovskite oxides, Thermochemical Water Splitting, Hydrogen Production

I. Introduction

The demand for energy is increasing by the day. The use of fossil fuels for energy causes climate change due to their combustion by-products. To mitigate this issue, most research have focused on using renewable energy sources. Molecular hydrogen (H_2) has become prominent as a renewable and carbon-free alternative fuel. In this context, solar based two-step thermochemical water splitting (TWS), using metal oxides as redox materials, allow to produce pure hydrogen at lower temperatures as compared to thermolysis. Nevertheless, the solar-to-fuel efficiency of TWS is still less than other solar-based hydrogen production processes by 10-14% (Abanades, 2019). Under these circumstances, improvement of non-stoichiometric metal oxides has become a crucial factor to obtain high H_2 yield. Non-stoichiometric perovskite oxides with $ABO_{3-\delta}$ chemical formula appear to be the most suitable candidates for TWS application since they are able to accomodate high oxygen vacancy concentration in crystal structure and stable under reduction and oxidation environments. It is known that divalent metal ions like Ca^{2+} doping into the A-site of $LaMnO_3$ based perovskite have relatively much higher redox performance than undoped $LaMnO_3$. Wang et al. have observed that an increase of Ca^{2+} dopant level enhanced more reducibility of $La_xCa_{1-x}Mn_xO_3$ (LCM) However, re-oxidation potential have decreased (Wang *et al.*, 2018). Similarly, the higher redox performance and consequently the extent of oxygen vacancies (δ) can be improved by trivalent metal ions doping into the B-site (Wang *et al.*, 2017). In this context, our purpose is to examine structural properties in terms of morphology and surface area to improve re-oxidation performance by Co^{3+} and Fe^{3+} doping into B-site of $La_{0.2}Ca_{0.8}Mn_{0.8}B_{0.2}O_3$.

II. Experimental Procedure

$La_{0.2}Ca_{0.8}Mn_{0.8}Fe_{0.2}O_3$ (LCMF2882) and $La_{0.2}Ca_{0.8}Mn_{0.8}Co_{0.2}O_3$ (LCMC2882) compounds were synthesized by Pechini method (Pechini, 1967). First, metal nitrate precursors, $La(NO_3)_3{\cdot}6H_2O$, $Ca(NO_3)_2{\cdot}4H_2O$, $Mn(NO_3)_3{\cdot}4H_2O$, $Fe(NO_3)_3{\cdot}9H_2O$ and $Co(NO_3)_2{\cdot}4H_2O$, were dissolved in distilled water. Citric acid, which is used as chelating agent to form metal citrate complex, was then added into the solution and heated up to 70 °C with continuously stirring. The molar ratio of total metal cations and citric acid was 1:1.5. After 1.5 hours, the brownish gel and the pinkish gel were obtained for LCMF2882 and LCMC2882, respectively and kept overnight at 70 °C. The gels were dried at 250 °C for 2 hours in order to remove remaining organics and nitrates which is followed by calcination at 900°C for 6 hours. Crystal structure analysis of synthesized powders was performed by Rigaku SmartLab X-Ray Diffractometer. The diffraction patterns were collected between 2θ= 20° and 90° with a scan rate of 0.02° min^{-1}. Scanning electron microscope (SEM, JEOL JSM-7600F) was used to characterize surface morphology. The surface area was determined by the Brunauer–Emmett–Teller (BET) method.

III. Results and discussions

XRD patterns belonging to LCMF2882 and LCMC2882 are shown in Fig. 1. LCM perovskite structure was identified as orthorhombic in most studies (Markovich *et al.*, 2012). In this study, orthorhombic LCM almost completely transformed into cubic perovskite structure (COD-5910090) by doping Fe^{3+} into the B-site. A small peak appears at 2θ=34° which belongs to orthorhombic structure. On the other hand, both orthorhombic and cubic structure coexists

in LCMC2882. It is a proof that the orthorhombic structure is substantially preserved in Co^{3+} ion substitued LCM. After calcination of LCMF2882 and LCMC2882 at 900°C for 6 hours, the surface morphologies were characterized by SEM, Fig.2. The average particle size of LCMF2882 is below 100 nm whereas LCMC2882 has larger particle size than LCMF2882. It was observed that substituting element does not effect the shape of the particles since bothe LCMC2882 and LCMF2882 have similar spherical morphology.

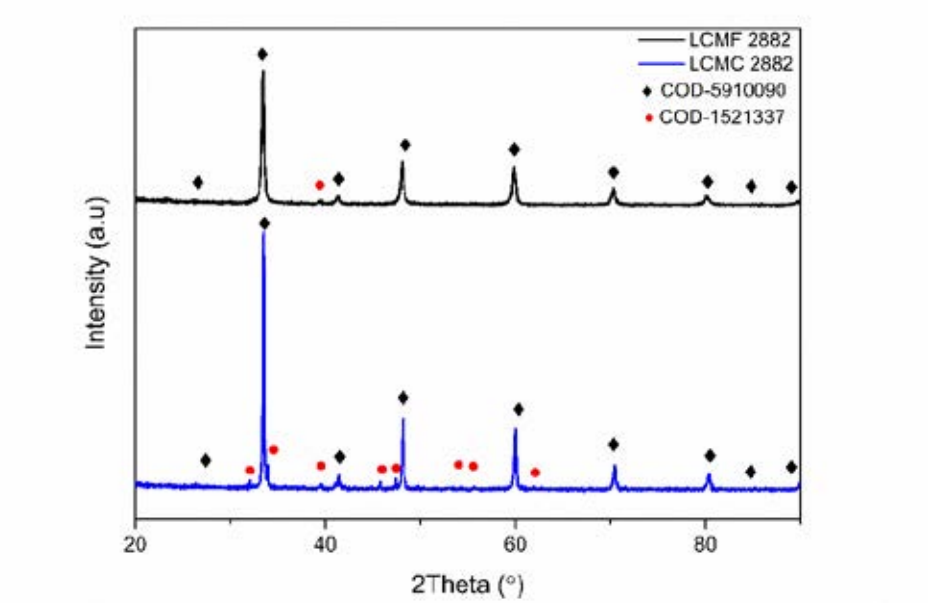


Fig. 1: XRD patterns of LCMF2882 and LCMC2882: (◆) cubic; (·) orthorhombic phase.

High atomic mobility is achieved by high surface area of redox materials, but the small particle size of starting redox materials can be affected by the high atomic mobility which results in rapid sintering and coarsening during calcination (Roeb *et al.*, 2012). LCMC2882 may have suffered from this sintering and coarsening effect which reduce the total surface area. This approach is also verified with the BET results in our studies whereas the surface area of LCMF2882 and LCMC2882 were determined as 15.56 m^2/g and 4.41 m^2/g, respectively.

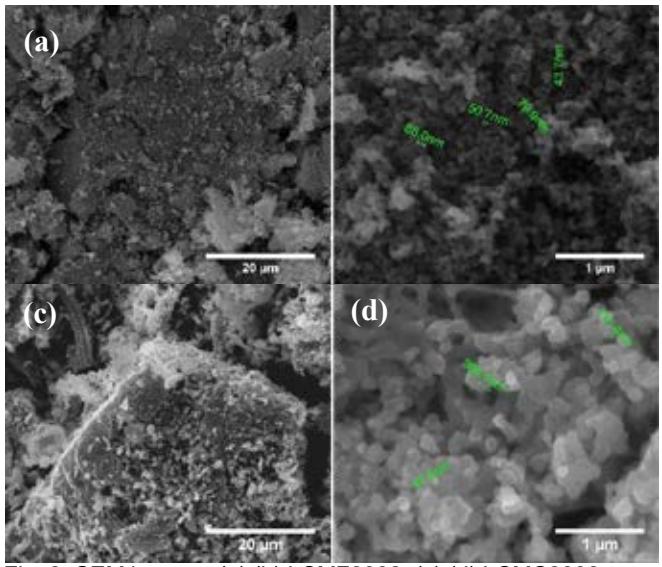


Fig. 2: SEM images; (a),(b) LCMF2882, (c),(d) LCMC2882.

IV. Conclusions

In conclusion, Co^{3+} and Fe^{3+} substitutied $La_{0.2}Ca_{0.8}Mn_{1-x}B_xO_3$ (x=0.2) type perovskites were successfully synthesized and characterized. LCMC2882 has orthorhombic structure and LCMF2882 has cubic structure even both were synthesized under the same conditions. The total surface area of LCMF2882 is higher than LCMC2882 which may be the result of sintering problems of LCMC2882. Therefore, LCMF2882 can be considered as the more suitable candidate for two-step thermochemical water splitting reactions.

Acknowledgements
This research supported by TUBITAK (The Scientific and Technological Research Council of Turkey) with a project number 119M420, which the authors gratefully acknowledge.

References

Abanades, S. (2019) 'Metal Oxides Applied to Thermochemical Water-Splitting for Hydrogen Production Using Concentrated Solar Energy', *ChemEngineering*, 3(3). doi: 10.3390/chemengineering3030063.

Markovich, V. *et al.* (2012) 'Nanometer size effect on structural and magnetic properties of La0.2Ca0.8MnO3.', *Journal of nanoscience and nanotechnology*. United States, 12(11), pp. 8607–8612. doi: 10.1166/jnn.2012.6834.

Pechini, M. P. (1967) 'Method of Preparing Lead and Alkaline Earth Titanates and Niobates and Coating Method Using the Same to Form a Capacitor.'

Roeb, M. *et al.* (2012) 'Materials-Related Aspects of Thermochemical Water and Carbon Dioxide Splitting: A Review.', *Materials*, pp. 2015–2054. doi: 10.3390/ma5112015.

Wang, L. *et al.* (2017) 'Ca2+ and Ga3+ doped LaMnO3 perovskite as a highly efficient and stable catalyst for two-step thermochemical water splitting', *Sustainable Energy Fuels*. The Royal Society of Chemistry, 1(5), pp. 1013–1017. doi: 10.1039/C6SE00097E.

Wang, L. *et al.* (2018) 'Enhanced Thermochemical H2 Production on Ca-Doped Lanthanum Manganite Perovskites Through Optimizing the Dopant Level and Re-oxidation Temperature', *Acta Metallurgica Sinica (English Letters)*, 31(4), pp. 431–439. doi: 10.1007/s40195-018-0715-7.

Planning and analysis of a double flash geothermal plant for purpose of the drying, hydrogen, hot water, and power generation aims.

[1]*Fatih Yılmaz, [1]Murat Ozturk, [2]Resat Selbas
[1]Isparta University of Applied Sciences, Faculty of Technology, Department of Mechatronics Engineering, 32200, Isparta/Turkey
[2]Isparta University of Applied Sciences, Faculty of Technology, Department of Mechanical Engineering, 32200, Isparta/Turkey
E-mails: fatiyilmaz7@gmail.com, muratozturk@isparta.edu.tr , resatselbas@isparta.edu.tr

Abstract:

In the proposed research, a new structure of the double-flash geothermal power plant is proposed and analyzed. The modeled plant generates power, hydrogen, hot water, and dried product with the geothermal water thermal energy. The performance of the single-generation, co-generation, and multi-generation plants is analyzed and compared, based on the energetic and exergetic efficiency perspectives. The energetic performance of the single-generation and co-generation systems are determined as 12.35% and 3019%, respectively. Also, the exergetic efficiencies of these models are computed as 37.95 and 43.12%, respectively. The total electricity and hydrogen generation capacities of this modeled system are about 6.1 MW and 0.01318 kgs^{-1}, respectively. The energetic and exergetic performances of the whole model are 37.95% and 47.95%, respectively.

Keywords: Analysis, energy, exergy, geothermal, hydrogen

I. Introduction

Due to global warming and environmental problems, many countries are planning the utilization of sustainable energy sources as opposed to fossil fuels for a reliable future (Assareh et al. 2021). In this regard, renewable energy springs that can be stated as solar, wind, geothermal, hydropower, and biomass have an importance for the sustainable future and humanity. Geothermal energy is among these sources and it is one of the most hopeful sources that has confirmed to be safe and clean. Moreover, it is a power source that does electricity generation with minimal environmental impact (Barbier, 1997; Fridleifsson, 2001; Komurcu & Akpinar, 2009). Geothermal energy that is the purpose to produce heating, cooling, electricity, drying, clean water, hydrogen, etc. can be used in different designs by integrating them for many useful outputs, and thus their efficiency can be increased. From this point of view, researches on integrated systems called multi-generation systems in the literature have an increasing trend in recent years.

Malik et al. (2015) offered a renewable energy-supported integrated plant that combined biomass and geothermal energy. Their modeled plant has 56.5% energetic performance and 20.3% exergetic performance. Islam and Dincer (2017) modeled a multigeneration system that is including solar and geothermal energy sources. As a result of their work, they claimed that the waste heat recovered through multiple productions could increase the overall system efficiency. For hydrogen and ammonia production, Yüksel et al. (2021) proposed a system designed by a geothermal energy-based multi-generation system. They computed that total energy and exergy performances are 56.68% and 54.73%, respectively. Gnaifaid and Ozcan (2021) examined a plant that products fresh water, power, cooling, and hot water, in terms of thermodynamic analysis and multiobjective optimization approaches. Optimal exergy efficiency is observed as 58% for the modeled plant. By looking at the literature studies, it can be concluded that geothermal energy is used in many areas and it is possible to increase its efficiency with different designs. Besides, these systems can be integrated with cogeneration, trigeneration, and multigeneration systems by applying advanced energy management for different purposes according to the temperature value of the geothermal water coming from the underground well.

The key purpose of this introduced parametric work is to examine and analyze the performance change of this geothermal energy-supported new design system in line with the single-generation, co-generation, and multigeneration purposes. This proposed system comprises of a double flash and is designed for power, hydrogen, hot water, and drying production. In this system, it is intended to rise the system performance by using the thermal energy of the high-temperature geothermal water at the turbine and separator outlet by applying advanced energy management.

II. System Description

A schematic drawing picture of this modeled geothermal system is clearly shown in Figure 1. In short, the geothermal water, which comes out at a temperature of approximately 250°C at state 1, decreases a little in the pressure and temperature in the expansion valve and then enters the Separator called S1. Here, the fluid, which is in the vapor phase, enters Turbine 1 at point 3. The geothermal fluid at the 6 point decreases the pressure and temperature for the second time in the expansion valve and then enters the separator called S2. It provides the thermal energy required for the drying process with the geothermal water heat at state 12 and then returns to the geothermal well at state 13. Electricity is generated in turbine 1 and turbine 2, and some of it goes under PEM electrolysis to generate hydrogen. In this system, hydrogen, drying, and hot water productions have been added to increase energy efficiency.

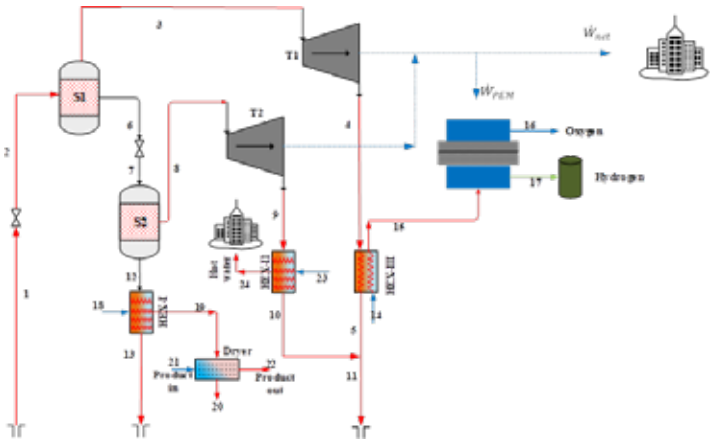


Fig.1 Layout of the modeled geothermal based system

III. Analysis

In the modeled plant, it has been thermodynamically examined using energetic and energy efficiency methods for sustainable hydrogen production. In this context, taking into account the first and second laws of thermodynamics, four fundamental equations of mass, energy, entropy and exergy equilibrium can be given as follows (Cengel & Boles, 2007; Dincer & Rosen, 2012);

$$\dot{m}_i = \dot{m}_e \quad (1)$$

$$\dot{Q}_i + \dot{W}_i + \sum \dot{m}_i h_i = \dot{Q}_e + \dot{W}_e + \sum \dot{m}_e h_e \quad (2)$$

$$\sum \left(\frac{\dot{Q}}{T}\right)_{in} + \sum \dot{m}_i s_i + S_{gen} = \sum \left(\frac{\dot{Q}}{T}\right)_e + \sum \dot{m}_e s_e \quad (3)$$

$$\dot{E}x^{\dot{Q}_{in}} + \dot{E}x^{\dot{W}_{in}} + \sum \dot{m}_i ex_i = \dot{E}x^{\dot{Q}_e} + \dot{E}x^{\dot{W}_e} + \sum \dot{m}_e ex_e + \dot{E}x_{des} \quad (4)$$

Here, the subscripts "i" and "e" describe the streams inlet and exit the components. Also, h and s explain the enthalpy and entropy terms, respectively. The heat and work exergy rates can be defined as:

$$\dot{E}x^{\dot{Q}} = \dot{Q}\left(1 - \frac{T_0}{T_{source}}\right) \quad (5)$$

$$\dot{E}x^{\dot{W}} = \dot{W} \quad (6)$$

After writing the general balance equation, the specific exergy term can be writed as:

$$ex = (h - h_0) - T_0(s - s_0) \quad (7)$$

The above-mentioned equilibrium equations can be applied separately for each component, and then the energy and exergy efficiencies for the single-generation, co-generation, and finally overall plant can be written in general as follows:

$$\eta_{sing} = \frac{\dot{W}_{net}}{(\dot{m}_1 h_1) - (\dot{m}_{13} h_{13} + \dot{m}_{11} h_{11})} \quad (8)$$

$$\psi_{sing} = \frac{\dot{W}_{net}}{(\dot{m}_1 ex_1) - (\dot{m}_{13} ex_{13} + \dot{m}_{11} ex_{11})} \quad (9)$$

$$\eta_{cogeneration} = \frac{\dot{W}_{net} + \dot{Q}_{hotwater}}{(\dot{m}_1 h_1) - (\dot{m}_{13} h_{13} + \dot{m}_{11} h_{11})} \quad (10)$$

$$\psi_{cogeneration} = \frac{\dot{W}_{net} + \dot{E}x^{\dot{Q}}_{hotwater}}{(\dot{m}_1 ex_1) - (\dot{m}_{13} ex_{13} + \dot{m}_{11} ex_{11})} \quad (11)$$

$$\eta_{overall} = \frac{\dot{W}_{net} + \dot{Q}_{hotwater} + (\dot{m}_{20} h_{20}) + (\dot{m}_{H_2} LHV_{H_2})}{(\dot{m}_1 h_1) - (\dot{m}_{13} h_{13} + \dot{m}_{11} h_{11})} \quad (12)$$

$$\psi_{overall} = \frac{\dot{W}_{net} + \dot{E}x^{\dot{Q}}_{hotwater} + (\dot{m}_{20} ex_{20}) + (\dot{m}_{H_2} ex_{H_2})}{(\dot{m}_1 ex_1) - (\dot{m}_{13} ex_{13} + \dot{m}_{11} ex_{11})} \quad (13)$$

IV. Results and Discussion

Detailed performance analysis of the new design model, whose schematic representation is given above, is handled by determining the exergy destruction rates together with the energy and exergy efficiencies. Before moving on to these calculations, the assumptions presented in Table 1 in the system are made and the kinetic and potential energy changes of the whole system are neglected. Besides, the whole plant and components are modeled as a steady-state flow. The results of this parametric study carried out with a package program called EES (Klein, 2020) are illustrated in Table 2 below.

Table .1 Input variables for the designed system

Variable	Unit	Range
Turbine's isentropic efficiency	%	90
Geothermal mass flow rate (state 1)	Kgs^{-1}	100
Geothermal water outlet temperature (state 1)	°C	250
Flash pressure ratio	-	2.5
HEX effectiveness	%	80
Water inlet temperature of PEM	°C	80
PEM efficiency	%	60
Hydrogen low heating value	kJ/kg	119960
Reference point temperature	°C	25
Reference point pressure	kPa	101.325

Table 2. Proposed system analyses results

Variable	Unit	Range
Turbine 1 power production rate	kW	5977
Turbine 2 power production rate	kW	2809
PEM power rate	kW	2636
Net power production rate	kW	6150
Hydrogen generation rate	Kgs^{-1}	0.01318
Hot water production rate	Kgs^{-1}	88.71
Dried production rate	Kgs^{-1}	10.44
$\eta_{singe-gen}$	%	12.35
$\psi_{singe-gen}$	%	37.95
$\eta_{overall}$	%	39.71
$\psi_{overall}$	%	47.97

Figs. 2, 3 and 4 illustrate the influence of the geothermal fluid outlet temperature on the performance of the different design plants and also useful products. As noted from all three figures, with the rise of geothermal water temperature, useful products increase, and also, both the energetic and exergetic performance of single-generation, co-generation, and multi-generation systems increase.

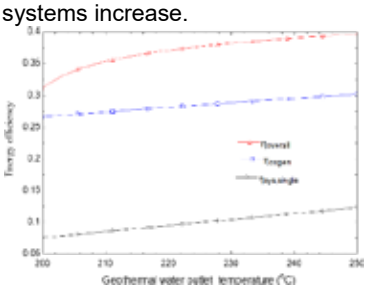


Fig.2. Effect of geothermal water temperature on the Energy efficiency of various system scenarios

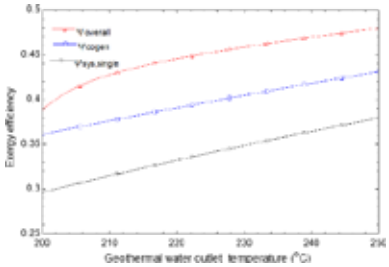


Fig.3. Effect of geothermal water temperature on the exergy efficiency of various system scenarios

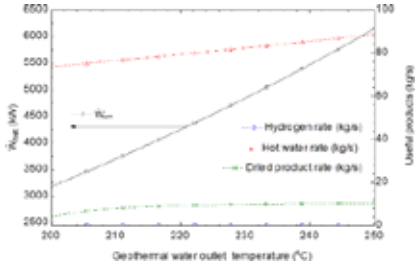


Fig.4. Impact of geothermal water temperature on beneficial productions and net power generation rate

In addition, below, the influence of variation of flash pressure on energy and exergy efficiency for three different systems can be seen in Figure 5. Also, Figure 6 is presented the effect of flash pressure on the net power generation and maximum destruction rate overall model. Finally, in Figure 7, the comparison of performance values of single-production, dual-production, and the whole system under the same conditions is presented.

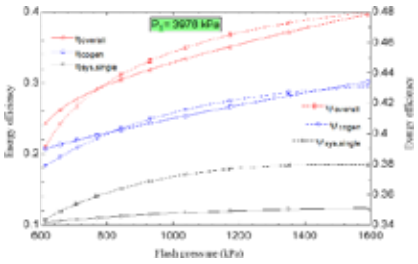


Fig.5. Performance rates of various system scenarios versus different flash pressure

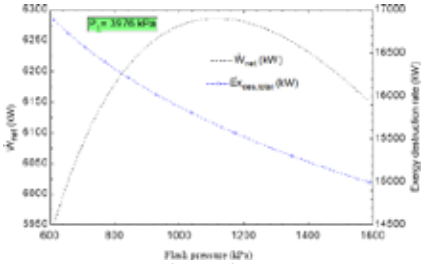


Fig.6. Impact of the flash pressure on the net power production rate and irreversibility

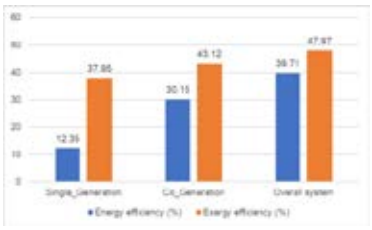


Fig.7. Energetic and exergetic performance of the various model scenarios

V. Conclusion

The new configuration of the double-flash geothermal power plant is proposed and analyzed based on the thermodynamic perspective. The modeled system produces useful products which are power, hydrogen, hot water, and dried product. Calculated and determined of some important results can be briefly summarized as below;

- In terms of energy efficiency, that of a single-generation system is 12.35%, and this value is 39.71% for the entire system. In other words, it can be stated that the efficiency can be increased approximately 3.2 times by adding hydrogen production, drying product, and hot water production to the system.
- Hydrogen generation capacity is 0.01318 kg/s, and also this system capacity is also calculated as approximately 6.1 MW.
- The rise in the temperature of the geothermal water has a positive effect on the system's performance.

Reference

Assareh, E., Alirahmi, S. M., & Ahmadi, P. (2021). A Sustainable model for the integration of solar and geothermal energy boosted with thermoelectric generators (TEGs) for electricity, cooling and desalination purpose. *Geothermics*, *92*, 102042.

Barbier, E. (1997). Nature and technology of geothermal energy: a review. *Renewable and sustainable energy reviews*, *1*(1-2), 1-69.

Cengel, Y. A., & Boles, M. A. (2007). *Thermodynamics: An Engineering Approach 6th Editon (SI Units)*. The McGraw-Hill Companies, Inc., New York.

Dincer, I., & Rosen, M. A. (2012). *Exergy: energy, environment and sustainable development*. Newnes.

Fridleifsson, I. B. (2001). Geothermal energy for the benefit of the people. *Renewable and sustainable energy reviews*, *5*(3), 299-312.

Gnaifaid, H., & Ozcan, H. (2021). Development and multiobjective optimization of an integrated flash-binary geothermal power plant with reverse osmosis desalination and absorption refrigeration for multi-generation. *Geothermics*, *89*, 101949.

Islam, S., & Dincer, I. (2017). Development, analysis and performance assessment of a combined solar and geothermal energy-based integrated system for multigeneration. *Solar Energy*, *147*, 328-343.

Klein, S. A., (2020). EES-engineering equation solver. *F-chart software*. V10.8353

Komurcu, M. I., & Akpinar, A. (2009). Importance of geothermal energy and its environmental effects in Turkey. *Renewable energy*, *34*(6), 1611-1615.

Malik, M., Dincer, I., & Rosen, M. A. (2015). Development and analysis of a new renewable energy-based multi-generation system. *Energy*, *79*, 90-99.

Yuksel, Y. E., Ozturk, M., & Dincer, I. (2021). Evaluation of a new geothermal based multigenerational plant with primary outputs of hydrogen and ammonia. *International Journal of Hydrogen Energy*.

NOx Emission Behaviors of Hydrogen/ Syngas/ Ammonia as Alternative and Clean Fuels

[1*]Mehmet Salih Cellek
[1]Bingol University, Arthitecture and Engineering Faculty, Department of Mechanical Engineering, Bingol, 12000, Turkey

* E-mail: mscellek@bingol.edu.tr

Abstract
Today, it is known that fossil fuels are primary sources of air pollutions. Pollution emissions of fossil fuels such as particular matter, NOx, CO, CO2, and SOx affect atmospheric air quality and cause acid rains and global warming. For this reason, researches on alternative fuels are ongoing. Among others, being carbon-free fuels, hydrogen and ammonia draw attention. On the other hand, syngas fuels have high heating value and low C content, attracting attention. In this study, NOx emission behaviors of hydrogen, syngas, and ammonia have been investigated under lean combustion conditions. The obtained results from the study show that flame temperatures of the hydrogen and syngas fuels are approximately the same and higher than ammonia. Moreover, the flame lengths of these two fuels are longer than that of ammonia. Furthermore, when the levels of OH emissions indirectly affecting NOx formation are examined, it is emitted the highest in hydrogen combustion and the least in ammonia combustion. However, when the NOx emission formations are concerned, it is clear that the ammonia gas release approximately twice and more NOx than the others during its combustion. It can be explained by the fact that after the decomposition of nitrogen, which is bound in ammonia, nitrogen combines with oxygen in the air to form NO and NO_2 through the fuel NOx mechanism. However, the released NOx from the ammonia towards the end of the combustion chamber falls below the other two fuel emission levels.

Keywords: Ammonia, syngas, hidrogen, NOx, NO_2, combustion

I. Introduction

Nowadays, it is known that fossil fuels are the main cause of pollution. Emissions of these fuels are harmful to the environment with their direct (acid rain) and indirect effects (global warming). For this reason, scientists spend time on alternative fuels, and related research is ongoing. At this point, hydrogen attracts attention as an alternative energy source instead of traditional fuels. Recently, intensive research has been carried out to reveal the usability of hydrogen in different areas such as gas turbines, burners, automobiles, etc. Another alternative gas fuel is syngas that is also called synthesis gas. It is produced from biomass, hard and low-quality coal, and waste gasification (Cellek, 2020). Syngas fuel can be used in some applications instead of fossil fuels as a new sustainable source. On the other hand, ammonia as an alternative fuel and hydrogen carrier has received increased attention in recent years (Xiao et al., 2017). Besides, ammonia being carbon-free may allow a hydrogen economy's transition (Hussein et al., 2019). Recently, there have been numerous attempts to use ammonia in internal combustion engines and gas turbines (Erdemir & Dincer, 2021). Furthermore, ammonia can be used as a fuel, but there are several challenges in ammonia combustion, such as low flammability, high NOx emission, and low radiation intensity. Overcoming these challenges requires further research into ammonia flame dynamics and chemistry (Kobayashi et al., 2019). Some of the hydrogen/syngas/ammonia related literature studies is presented in Table 1.

Tab. 1: A brief literature survey on combustion of various fuels

Authors	Studied Fuels
Cellek, M.S., 2020	CH_4/Syngas
Xiao et al.	NH_3/CH_4
Hussein N.A. et al., 2019	NH_3/H_2
Erdemir & Dincer., 2021	NH_3
Kobayashi et al., 2019	NH_3
Li, P., et al. (2014)	CH_4/H_2 blend
Mardani, A. and Mahalegi, H.K.M. (2019)	CH_4/Syngas
Cellek, M.S. (2020)	CH_4/H_2 blend

In this study, non-premixed combustion of hydrogen, syngas, and ammonia have been invesitated at 8.6 kW under lean condition ($\emptyset = 1/\lambda = 0.25$). Flame temperatures, intermediate species, and NO_2, N_2O and NO species, which are named NOx emission, have been compared for each case.

II. Numerical Model and Boundary Conditions

Combustion of hydrogen/syngas/ammonia gas fuels with oxidizer air has been investigated using the Computational Fluid Dynamics (CFD) technique. The non-premixed flamelet combustion model has been utilized for the chemical reaction of hydrogen-air, syngas-air, and ammonia-air by utilizing Gri-mech 2.11 (Bowman et al.,1997) mechanism. The realizable $k - \varepsilon$ model selected for turbulence prediction. The enhanced wall treatment is used for the near-wall model due to boundary layer mesh. The geometrical model and grid generation are presented in Fig. 1. Geometric model of the combustion chamber is based on the reference study published by Brookes and Moss, 1999.

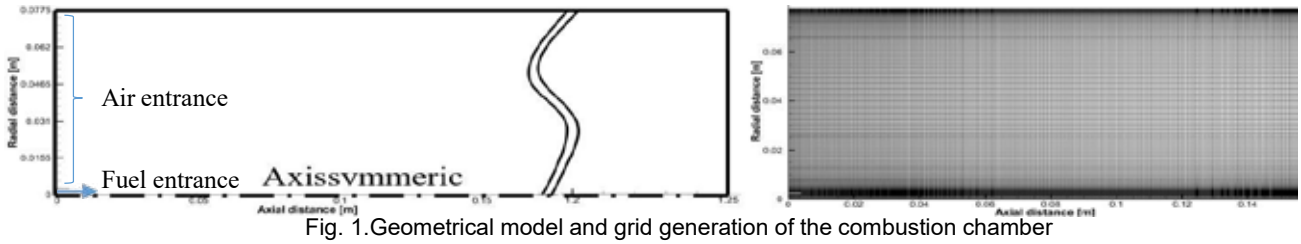


Fig. 1.Geometrical model and grid generation of the combustion chamber

III. Results and discussions

The mass fraction distributions of the H_2 and OH species along the axial distance are shown in Fig.2a-b. The amount of H_2 and OH species is maximum for hydrogen and minimum for ammonia. Besides, these two components turn into other species by joining the reaction chain up to the middle of the combustion chamber. Flame temperatures of the simulated fuels are shown in Fig. 2c. It is clear that the flame peak temperatures of hydrogen and syngas are approximately the same. The flame temperature of ammonia is relatively low. Because the hydrogen flame length is also longer, the flame temperature of hydrogen is more dominant towards the outlet. On the other hand, the variations of the NOx emission released from the simulated fuels on the axial and radial lines are shown in Fig. 2d-f. It is seen from the graphs that the ammonia releases approximately twice and more NOx than the others during its combustion. It results from ammonia decomposing in nitrogen, which tends to combine with oxygen in the air to form NO and NO_2.

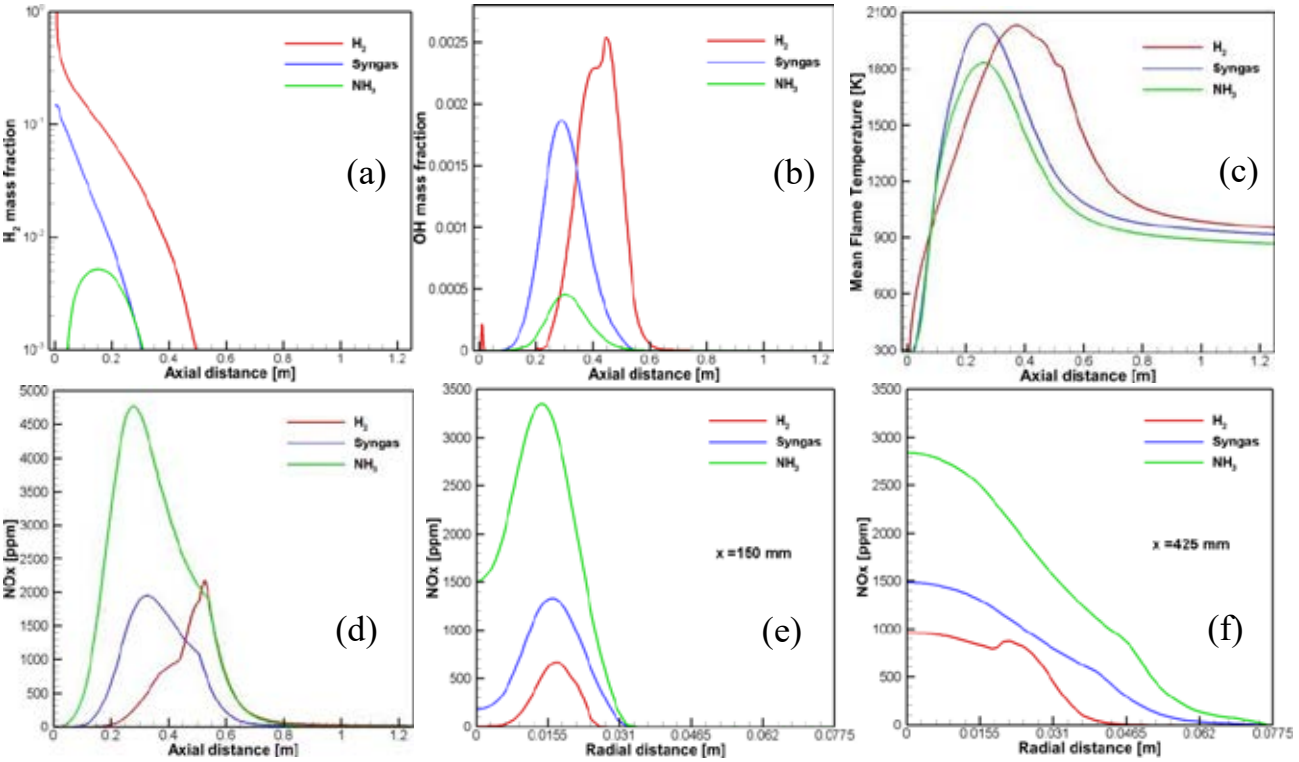


Fig. 2: Reaktant species (H_2), intermediate species (H_2, OH), flame temperature, and NOx emission distribution for each fuel

The adiabatic flame temperature of the hydrogen is maximum as 2370K, while it is minimum for ammonia as 2073 K. The adiabatic flame temperature of syngas is between these two values and closer to hydrogen temperature. Due to operating in lean conditions and heat loss from the combustion walls, the maximum flame temperature obtained in hydrogen combustion is remarkably lower (2040K) than adiabatic flame temperature, as shown in Fig.3-a. The hydrogen flame is thinner at the entrance compared to syngas and ammonia flames but longer than the others. The intermediate species, namely OH, is an effective species that contribute to the prompt NOx and thermal NOx. In hydrogen-fueled combustion, the prominence of OH radicals may contribute to NOx in a manner that is different from combustion fueled by syngas and ammonia, as shown in Fig.3b. Moreover, the region where intermediate product OH is released is also essential in showing approximately the reaction zone's boundary. Another intermediate species, namely H2O2 mass fraction distribution, is shown in Fig.3c. Although the distribution trend of hydrogen peroxide in the combustion chamber is similar to OH radicals, its amount is less than the amount of OH. Although the distribution trends of NO2 and NO released in the combustion chamber are identical, their amounts are very different from each other as shown in Fig. 3d-e. The amounts of NO emission are higher than NO2. In addition, it should be noted that the amount of N2O emission for hydrogen, syngas, and ammonia are 0.27, 0.17, and 31.18 ppm, respectively.

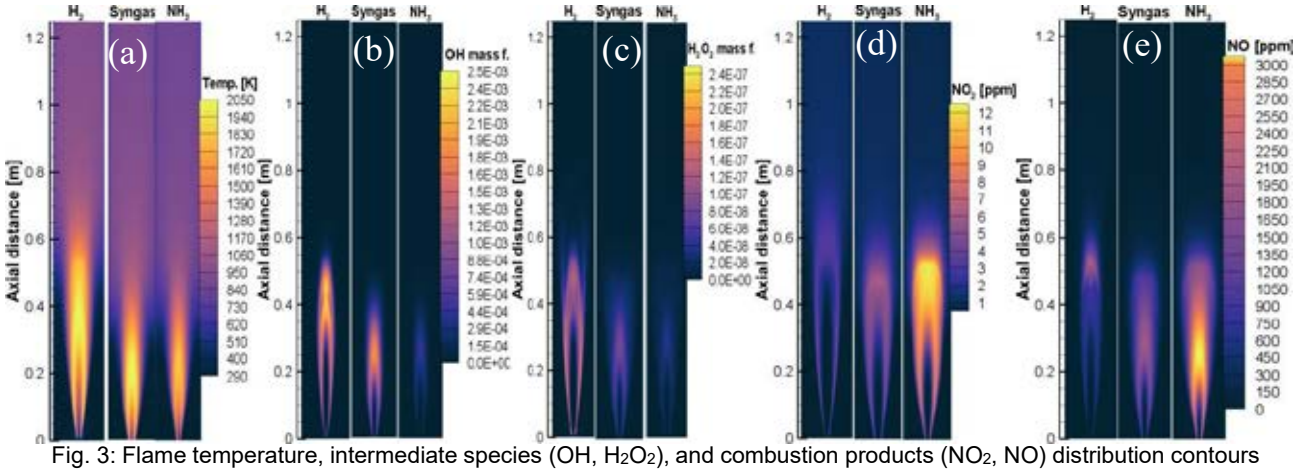


Fig. 3: Flame temperature, intermediate species (OH, H_2O_2), and combustion products (NO_2, NO) distribution contours

IV. Conclusions

Hydrogen, syngas and ammonia gases are the leading fuels that can become widespread as an alternative to conventional fossil-sourced fuels in the future. While hydrogen and ammonia do not contain any carbon species, there is less amount in syngas fuel. This study focussed on non-premixed combustion flame of hydrogen, syngas, and ammonia fuels at the same thermal load under lean condition. The findings can be summarized as follows:

- Maximum flame temperature of hydrogen and syngas fuels are close to each other ($\cong 2040K$). In comparison, ammonia maximum flame temperature is approximately 200 ℃ lower under lean conditions.
- The high amount of OH radicals released during the hydrogen flame increases the NOx emission of hydrogen compared to syngas and ammonia gases.
- Although the flame temperature and the amount of effective intermediate products such as OH are low, a higher proportion of NOx is released during the combustion of ammonia gas. It results from fuel-NOx contribution in ammonia combustion.
- The most effective emission from all three fuels is NO emission. This emission accounts for almost the majority of NOx emissions by more than 70%.
- While the order of the maximum NOx emission levels occurring in the combustion chamber is syngas<hydrogen<ammonia, the order of emission levels measured in the flue gas at the combustion chamber outlet is ammonia< syngas <hidrogen.

Acknowledgements

The author is grateful for the use of the computing resources provided by the National Center for High Performance Computing of Turkey (UHEM, UYBHM) under grant number 1008202020.

References

Bowman C.T. et al., http://www.me.berkeley.edu/gri_mech/.

Brookes SJ., Moss, J B., Measurements of soot production and thermal radiation from confined turbulent jet diffusion flames of methane, Combustion and Flame 116, 49–61, (1999).

Cellek, M. S., Turbulent flames investigation of methane and syngas fuels with the perspective of near-wall treatment models. *Int. J Hydrogen Energy, 45, 32223-35234, (2020).*

Cellek, M.S., Flameless combustion investigation of CH_4/H_2 in the laboratory-scaled furnace, *Int. J Hydrogen Energy* 45 (60), 35208-35222, (2020).

Erdemir, D., & Dincer, I. (2021). A perspective on the use of ammonia as a clean fuel: Challenges and solutions. *International Journal of Energy Research*, *45*(4), 4827–4834, (2021).

Hussein, N. A., Valera-Medina, A., & Alsaegh, A. S., Ammonia- hydrogen combustion in a swirl burner with reduction of NOx emissions. *Energy Procedia*, *158*(2018), 2305–2310, (2019).

Kobayashi, H., Hayakawa, A., Somarathne, K. D. K. A., & Okafor, E. C., Science and technology of ammonia combustion. *Proceedings of the Combustion Institute*, *37*(1), 109–133, (2019).

Li, P., Wang, F. Mi, J., Dally, B.B., Mei, Z., Zhang, J., Parente, A., Mechanisms of NO formation in MILD combustion of CH4/H2 fuel blends. *Int J Hydrogen Energy*, 39, 19187-203, (2014).

Mardani, A. and Mahalegi, H.K.M. Hydrogen enrichment of methane and syngas for MILD combustion. *Int. J Hydrogen Energy*, 44 9423-37, (2019).

Xiao, H., Valera-Medina, A., Marsh, R., & Bowen, P. J., Numerical study assessing various ammonia/methane reaction models for use under gas turbine conditions. *Fuel*, *196*, 344–351, (2017).

Modeling of the Solar Energy-Based Hydrogen and Freshwater Production System

[1]*Fatih Yılmaz, [1]Murat Ozturk, [2]Resat Selbas
[1]Isparta University of Applied Sciences, Faculty of Technology, Department of Mechatronics Engineering, 32200, Isparta/Turkey
[2]Isparta University of Applied Sciences, Faculty of Technology, Department of Mechanical Engineering, 32200, Isparta/Turkey
E-mails: fatiyilmaz7@gmail.com, muratozturk@isparta.edu.tr , resatselbas@isparta.edu.tr

Abstract: The main aim of the modeling system is to generate hydrogen and freshwater with a sustainable method which is solar energy. In this regard, modeling and thermodynamic investigation of the integrated scheme which includes the parabolic through solar collector (PTSC), Rankine cycle, thermal desalination unit, and PEM electrolyzer are investigated by using the energetic and exegetic efficiency approaches. The therminol_72 working oil is selected in the PTSC sub-system due to the high temperature. Also, the influence of some important parameters on system performance and hydrogen production rate are studied. Thermodynamic analysis results show that the overall system has 39.98% and 52.97% energy and energy efficiency.
Keywords: Energy, exergy, hydrogen, freshwater, solar,

I. Introduction

With the increasing the many parameters, for example, human population and industrialization, in parallel to this, the energy demand increases by day by day. As a consequence of this situation, undesirable environmental problems such as global warming, ozone depletion and acid rain emerge, and the future of humanity is endangered. Therefore, the utilization of environmentally friendly technology such as renewable energy sources is a very important topic. In this context, integrating hydrogen production with renewable energy-supported systems is important for sustainability today and in the future. Because, when you look at it, about 95% of hydrogen is still obtained from fossil-based fuels (Kothari et al., 2008) and therefore environmental problems continue to increase.

Many researchers have presented various studies in the literature on multigeneration systems, which are renewable energy supported hydrogen production systems. Gill et al. (2020) presented a solar hydrogen production plant in terms of thermodynamic and economic aspects. The thermal performance of their suggested model is found as 41.08%. Razi and Dincer (2020) examined the identification of potential solar hydrogen production methods for many industries. Yilmaz et al. (2020) modeled a polygeneration system that is solar energy based. They determined that overall energy and exergy performances are 58.43% and 54.18%, respectively. In addition, there are many studies in the literature specifically on solar-assisted hydrogen generation, some of which are presented here as references (Ozturk and Dincer, 2013; Ozlu and Dincer, 2015; Rajeshwar et al., 2008; Saleem et al., 2020; Sorgulu and Dincer, 2018). Above mentioned literature survey indicated that solar energy-based hydrogen generation systems have gained an important role and also many studies presented.

The chief difference of this work is to present the solar energy-supported hydrogen and freshwater generation model. Therminol 72 working fluid is selected in the PSTC sub-cycle. A parametric examination is conducted to investigate the energetic and exergetic efficiency of the designed model. In addition, the change in hydrogen generation rate is investigated according to parameters such as solar radiation, PSTC's length, and width parameters.

II. System Description

The thermal energy needed by the whole plant is met by solar energy, which is PSTC. In short, to describe the operation of the system, Therminol 72 working fluid used in PTSC exits at high temperature at state 3 and enters hot storage tank (HST)and then enters HEX1 at 3 'point. The thermal energy required for the RC system is met here in HEX1 and the system operates. The liquid-vapor mixture emanating from turbine 2 at state 8 transfers the heat to the distillation system, and the distillation system works thermally, distilling the seawater coming from state 11 and producing clean water. Some of the freshwater produced is passed through the water heater and sent to PEM electrolysis for hydrogen production at 80°C, and the system works continuously in this way. the main schematic diagram of the displayed plant is given in Fig. 1.

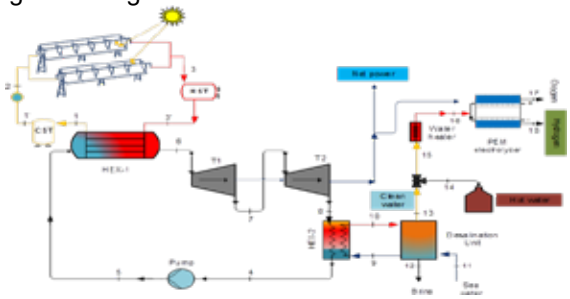


Fig. 1 The diagrammatic layout of the modeled hydrogen production plant

III. Analysis

In the modeled plant, it has been thermodynamically examined using energetic and energy efficiency methods for sustainable hydrogen production. In this context, taking into account the first and second laws of thermodynamics, four fundamental equations of mass, energy, entropy and exergy equilibrium can be specified as (Dincer & Rosen, 2012; Cengel & Boles, 2007):

$$\dot{m}_i = \dot{m}_e \quad : \quad (1)$$

$$\dot{Q}_i + \dot{W}_i + \sum \dot{m}_i h_i = \dot{Q}_e + \dot{W}_e + \sum \dot{m}_e h_e \quad (2)$$

$$\sum \left(\frac{\dot{Q}}{T}\right)_{in} + \sum \dot{m}_i s_i + \dot{S}_{gen} = \sum \left(\frac{\dot{Q}}{T}\right)_e + \sum \dot{m}_e s_e \quad (3)$$

$$\dot{E}x^{Q_{in}} + \dot{E}x^{W_{in}} + \sum \dot{m}_i ex_i = \dot{E}x^{Q_e} + \dot{E}x^{W_e} + \sum \dot{m}_e ex_e + \dot{E}x_{des} \quad (4)$$

Here, the sub-indexes "i" and "e" describe the streams inlet and exit the components. Also, h term defines enthalpy is enthalpy, s term is entropy. Q and W refer to heat transfer rate and power rate. After writing the general balance equation, the heat and work exergy rates should be defined as:

$$\dot{E}x^{\dot{Q}} = \dot{Q}\left(1 - \frac{T_0}{T_{source}}\right) \quad (5)$$

$$\dot{E}x^{\dot{W}} = \dot{W} \quad (6)$$

After writing the general balance equation, the exergy terms can be defined as:

$$ex = (h - h_0) - T_0(s - s_0) \quad (7)$$

Many studies in the literature have been used for PTSC mathematical analysis and can be found here (Almahdi et al.,2016; Ozlu & Dincer, 2015; Ozlu & Dincer, 2016). In this system, the above-mentioned equilibrium equations can be applied separately for each component, and then the energetic and exergetic efficiencies can be written in general as follows:

$$\eta = \frac{\dot{W}_{net} + (\dot{m}_{14} h_{14}) + \dot{m}_{H_2} HHV_{H_2}}{\dot{Q}_{solar}} \quad (8)$$

$$\psi = \frac{\dot{W}_{net} + (\dot{m}_{14} ex_{14}) + \dot{m}_{H_2} ex_{H_2}}{\dot{E}x_3 - \dot{E}x_2} \quad (9)$$

IV. Results and Discussion

The suggested solar energy-based power, freshwater and hydrogen generation system is investigated based on the thermodynamic perspective. In this regard, energetic and exergetic efficiency is also examined for sustainable hydrogen production methods. The system design parameters and thermodynamic analysis results are specified in Table 1. In accordance with the results, the general energy and exergy performance obtained as 39.98% and 52.97%, respectively. Also, the proposed system produces 0.0006739 kgs^{-1} and 1.121 kgs^{-1} hydrogen and freshwater at 800 W/m^2 constant solar flux.

Table 1. Design parameters and thermodynamic analysis results of the modeled system

Design parameters		
PTSC (Modeled from Ozlu and Dincer, 2015)	Width	2 m
	Length	2.5 m
	Receiver efficiency	76 %
	Working fluid	Therminol 72
	Solar radiation	800 W/m^2
	Mass flow rate	2 kgs^{-1}
Rankine Cycle	Pump inlet pressure	75 kPa
	Pump isentropic efficiency	85%
	HEX effectiveness	80%
	Turbine isentropic efficiency	88%
Desalination unit	Sea water temperature	30°C
	Sea water salinity	35000 ppm
	Desalination effect	4
High heating value of H_2	142000 kJ/kg	
Reference temperature	21°C	
Reference pressure	101.325 kPa	
Thermodynamic analysis results		
Energy efficiency of overall plant	39.98 %	
Exergy efficiency of overall plant	52.97 %	
Net power production rate	427 kW	
Hydrogen production rate	0.0006739 kgs^{-1}	
Fresh water production rate	1.121 kgs^{-1}	

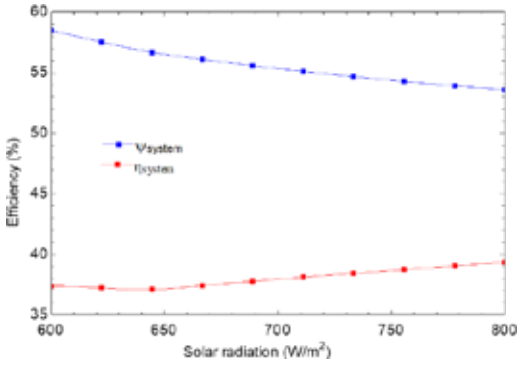


Fig. 2. Impact of solar radiation on efficiency of the total plant

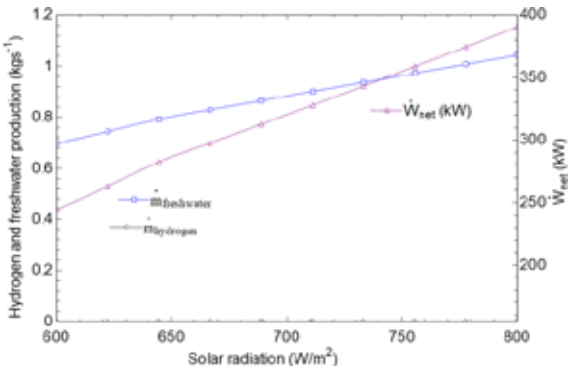


Fig. 3. Impact of solar irradiation on useful products

In Figures 2 and 3, the influence of solar flux changes on plant performance and on the beneficial productivities from the model has been examined and presented. It is found that the rise in the solar flux value caused a rise in energy efficiency and also useful products other than exergy performance. On the contrary hand, the effect of different reference temperatures on system performance and on the beneficial outputs are represented in Figure 4 and 5. With the rise in the dead point temperature, energetic and exergetic efficiency increased.

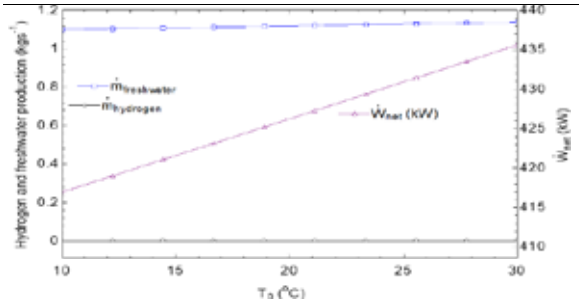


Fig. 4. Effect of reference temperature on the useful products

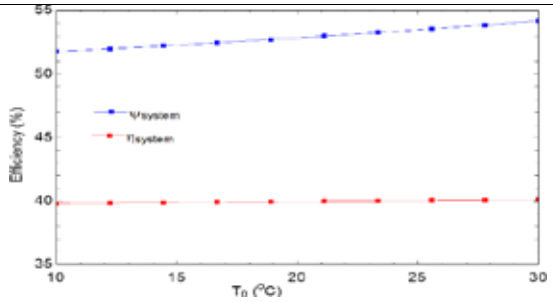


Fig. 5. Effect of dead point temperature on the system efficiency

The last figure that is Fig. 6 presents the influence of seawater temperature on the performance of the distillation unit and freshwater production rate. It can be clearly stated that as the performance of the distillation process advance with the increase of seawater temperature, the production of freshwater also increases.

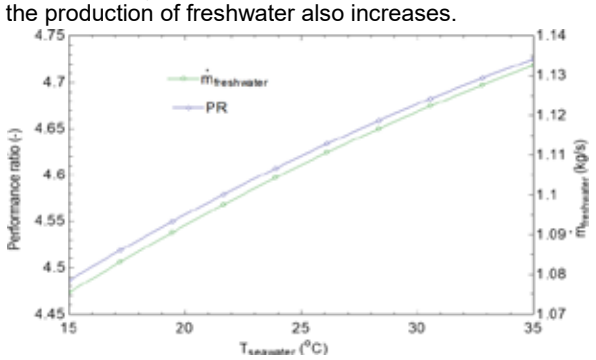


Fig. 6. The impression of seawater temperature on freshwater rate and performance ratio of the distillation unit.

V. Conclusion

The modeled system is investigating hydrogen generation with the sustainable method which is solar energy-based. In this respect, both the energetic and exergetic performance of the whole model and also the amount of hydrogen, power, and freshwater rate are also investigated using the thermodynamic methods. The main results obtained can be summed up as follows:

- The modeled whole system has 39.98% and 52.97% energy and exergy efficiency. In addition, 1.121 kgs^{-1} of freshwater and 0.0006739 kgs^{-1} of hydrogen are produced from this system.
- The unshaded aperture area for a PTSC is calculated as 4.9 m^2.
- Also, System performance increases as the environmental temperature increases.

Reference

Almahdi, M., Dincer, I., & Rosen, M. A. (2016). A new solar based multigeneration system with hot and cold thermal storages and hydrogen production. *Renewable Energy*, *91*, 302-314.

Cengel, Y. A., & Boles, M. A. (2007). *Thermodynamics: An Engineering Approach 6th Editon (SI Units)*. The McGraw-Hill Companies, Inc., New York.

Dincer, I., & Rosen, M. A. (2012). *Exergy: energy, environment and sustainable development*. Newnes.

Gill, E. Z., Ratlamwala, T. A. H., Hussain, G., & Alkahtani, M. (2020). Energy, exergy, exergo-economic and exergo-environmental analyses of solar based hydrogen generation system. *International Journal of Hydrogen Energy*.

Kothari, R., Buddhi, D., & Sawhney, R. L. (2008). Comparison of environmental and economic aspects of various hydrogen production methods. *Renewable and Sustainable Energy Reviews*, *12*(2), 553-563.

Ozlu, S., & Dincer, I. (2015). Development and analysis of a solar and wind energy based multigeneration system. *Solar Energy*, *122*, 1279-1295.

Ozlu, S., & Dincer, I. (2016). Performance assessment of a new solar energy-based multigeneration system. *Energy*, *112*, 164-178.

Ozturk, M., & Dincer, I. (2013). Thermodynamic analysis of a solar-based multi-generation system with hydrogen production. *Applied Thermal Engineering*, *51*(1-2), 1235-1244.

Rajeshwar, K., McConnell, R. D., & Licht, S. (2008). *Solar hydrogen generation* (pp. 41-63). New York: Springer.

Razi, F., & Dincer, I. (2020). A critical evaluation of potential routes of solar hydrogen production for sustainable development. *Journal of Cleaner Production*, 121582.

Saleem, M. S., Abas, N., Kalair, A. R., Rauf, S., Haider, A., Tahir, M. S., & Sagir, M. (2020). Design and optimization of hybrid solar-hydrogen generation system using TRNSYS. *International Journal of Hydrogen Energy*, *45*(32), 15814-15830.

Sorgulu, F., & Dincer, I. (2018). Thermodynamic analyses of a solar-based combined cycle integrated with electrolyzer for hydrogen production. *International Journal of Hydrogen Energy*, *43*(2), 1047-1059.

Yilmaz, F., Ozturk, M., & Selbas, R. (2020). Thermodynamic investigation of a concentrating solar collector based combined plant for poly-generation. *International Journal of Hydrogen Energy*, *45*(49), 26138-26155.

Investigation of Ni-MnxOy Coated SS316 Stainless Steel Mesh as a Gas Diffusion Layer Material for PEM Water Electrolyzer

[1,2]Murat Kıstı, [1,2*]Mehmet Fatih Kaya,
[1] Erciyes University, Engineering Faculty, Energy Systems Engineering Department, Heat Engineering Division, 38039, Kayseri, Turkey
[2] Erciyes University H2FC Hydrogen Energy Research Group, 38039, Kayseri, Turkey

* E-mail: kayamehmetfatih@erciyes.edu.tr

Abstract
Polymer electrolyte membrane water electrolyzers (PEMWE) are highly efficient electrochemical systems used to produce hydrogen cleanly from water. Some of their equipment is still expensive compared to other hydrogen production methods. For more widespread use of these systems, production costs must be reduced. In this study, stainless steel mesh structures are used as an inexpensive alternative for gas diffusion layers in PEMWEs. Commercial SS316 mesh structures in different porosity values (1000, 1200, 1400 and 1600 mesh) are selected as working electrodes. Samples are coated with Ni-MnxOy coatings to increase their corrosion resistance potential and the electrochemical coating method is used as a coating process.
Electrochemical properties of SS316 mesh electrodes have been investigated by Cyclic Voltammetry (CV), Linear Sweep Voltammetry (LSV), Tafel Plot and Electrochemical Impedance Spectroscopy (EIS) techniques. The surface morphologies of stainless-steel electrodes have been characterized by Field Emission Scanning Electron Microscopy (FE-SEM), Energy Dispersive X-Ray Analysis (EDX), and X-Ray Diffractometers (XRD) analysis.

Keywords: Gas diffusion layer, PEM water electrolyzer, Wire mesh

I. Introduction

Energy consumption amount in the world increasing day by day and much of the energy demand is still met from fossil fuels. As a result of huge consumption of fossil fuels, green-house gas emissions are rising significantly. Interest in alternative energy sources is growing in order to prevent environmental pollution and climate change. As a result of the new and clean energy sources research, hydrogen energy attracts a big attention (Chi and Yu 2018). It is necessary to focus on clean hydrogen energy systems. Because, they are easily adapted with alternative energy sources and can be used as an efficient energy carriers (Dawood, Anda et al. 2020).

The electrolysis of water is one of the most environmentally friendly method for hydrogen production. Among the electrolyzer methods, PEMWE is the most promising type of electrolyzer due to its higher energy conversion efficiency. PEMWE is an electrochemical device that operates with high efficiency at relatively low temperatures, allowing high purity hydrogen and oxygen cleanly from the water (Kumar and Himabindu 2019). In addition, there are few disadvantages of these systems, such as high production costs, corrosion, and durability problems of the equipment etc. Production costs must be lowered to provide widespread commercialization of PEMWE systems. In addition, the anode side of the system has a corrosive medium, thus, expensive noble metals and their coatings are (Pt, Ti etc.) used to obtain durable cells (Bessarabov, Wang et al. 2016). To reduce system costs and durability problems, alternative materials must be developed.

Stainless steel materials (SS316, SS304 etc.) are one of the best alternative materials that can be used on the anode side of PEMWE systems because they are easily accessible, easy to form and cost effective materials (Shirvanian and van Berkel 2020). One of the biggest problems of metallic materials is that they are susceptible to acidic corrosion. Corrosion in PEM water electrolyzers causes an increase in contact resistance, which greatly reduces the working efficiency of the electrolyzer (Song, Zhang et al. 2020). In the literature, various coating materials and methods are investigated to avoid corrosive effects for durable GDL electrodes in the anode side (Tawfik, Hung et al. 2007, Wilberforce, Ijaodola et al. 2019). For example, Nickel (Ni) is one of the most used material for water electrolysis due to its low cost and good corrosion resistance (Bhat and Shet 2020, Santos, Corradini et al. 2020). Also, manganese (Mn) has good catalytic activity compared to other non-noble metals (Toulhoat, Raybaud et al. 2018). Mn is generally used in catalyst studies in the literature for PEMWE (Hayashi, Bonnet-Mercier et al. 2019) and it can also be a good coating material with its promising conductivity and oxide phases' corrosion resistance properties (Avgouropoulos, Papavasiliou et al. 2009, Hayashi, Bonnet-Mercier et al. 2019).

In this study, Ni-Mn_xO_y structure is selected as the coating material for SS316L mesh structures in PEMWE anode. Electrochemical properties of SS316 electrodes were measured by CV, LSV and EIS techniques. The surface morphology and physical characterization of the samples are measured by FE-SEM, EDX and XRD analysis.

II. Materials and Methods

In Table 1, the properties of commercial stainless steel mesh structures used in the experiments can be seen.

Tab 1: The properties of the commercial SS316 wire mesh

Sample	Gap (µm)	Diameter (µm)	Thickness (µm)	Porosity
S1	*941*	*443*	*783*	*44%*
S2	*1217*	*452*	*828*	*52%*
S3	*1344*	*468*	*915*	*55%*
S4	*1646*	*512*	*950*	*61%*

In Table 1, the gap term was used to describe the distance between two parallel wires. As seen table 1, S1 sample has approximately 941 microns distance between two wires. S2, S3 and S4 named samples have around 1217, 1344 and 1646 µm gap distance, respectively. Porosity represents the porosity value of the mesh structure for per unit area. As seen in Table 1, S1 has the smallest porosity with 44%, while S4 has the highest porosity by 61%.

Before the coating process, a cleaning procedure was applied to the samples. To remove impurities, samples were placed in an ultrasonic bath for 15 min in distilled water, ethanol, and acetone, respectively. The samples were dried in a vacuum oven at 50°C for 1 hour under N_2 gas atmosphere. Then, samples were molded with epoxy resin. The electrodeposition process was performed using the two-electrode CA method. The coating procedure can be seen schematically in Figure 1.

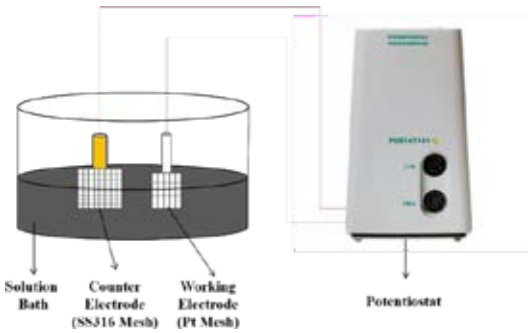


Fig. 1: Electrodeposition process

As seen in Figure 1, wire mesh sample was selected as a cathode electrode and Pt mesh was selected as an anode electrode. The active measurement area of the wire mesh structure was arranged as 25 mm^2. The distance between the electrodes was fixed at 10 mm. For Ni-Mn alloy deposition, $NiCl_2.6H_2O$ (Sigma–Aldrich) and $Cl_2Mn.H_2O$ (Merck) were used as the metal precursors. In the coating process, the solution bath was stirred with a magnetic stirrer at 300 rpm constant speed at room temperature. The electrolyte compositions in different molar volumes are listed in Table 2.

Tab. 2: Composition of the coating baths

Specimens	Ni_1Mn_1	$Ni_1Mn_{1.2}$	$Ni_1Mn_{1.4}$
$NiCl_2.6H_2O$	*100 mM*	*100 mM*	*100 mM*
$Cl_2Mn.H_2O$	*100 mM*	*120 mM*	*140 mM*

After coating process, Mn surface was oxidized to increase the corrosion resistance of the electrode samples. Electrodes were etched in the acid (Aqua Regia) for 3 seconds to oxidize the Mn surface. Then, samples were cleaned with distilled water and dried with N_2 gas.
The electrochemical characterization measurements were carried out using Autolab potentiostat-galvanostat (PGSTAT204) with a three-electrode configuration. Figure 3 shows a three-electrode electrochemical cell configuration for electrochemical analysis.

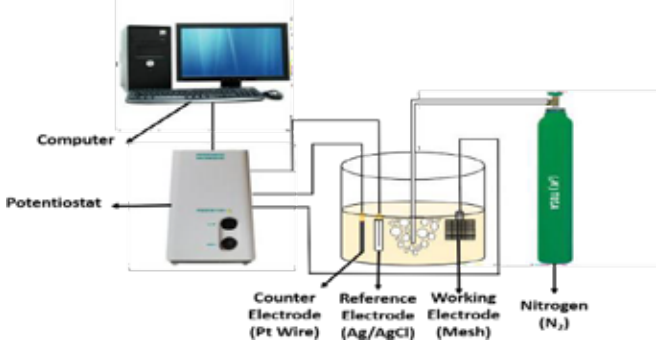


Fig. 2: The three-electrode electrochemical cell configuration

CV, LSV and EIS measurements were conducted in 50 ml, 0.5 M H_2SO_4 solution. In electrochemical measurements, SS316 samples were used as working electrode, Pt wire and Ag/AgCl (3M KCl saturated) were used as a counter electrode and a reference electrode, respectively. CV measurements have been performed at a 100 mV/s scan rate and LSV measurements have been conducted at a 10mV/s scan rate. The EIS measurements were conducted in a frequency range between 10000 Hz to 0.1 Hz at 5mV amplitude.

III. Conclusions

In this study, stainless steel structures are coated with $NiMn_xO_y$ non-noble metals to improve samples' corrosion resistance. It was observed that Ni-Mn_xO_y has better corrosion resistance than non-coated SS316 samples. Moreover, according to LSV measurements 1400 mesh sample's electrochemical performance is observed higher than the other samples at 1.4 V. As a result, Ni-Mn_xO_y coated SS316 can be used as an inexpensive alternative to PEMWE systems.

Acknowledgements

The authors would like to thank The Scientific and Technological Research Council of Turkey (TUBITAK) 1001 Grant number: 120M234 and Scientific Research Projects Unit of Erciyes University for funding and supporting the project under the contract number FKB-2019-9134.

References

Avgouropoulos, G., J. Papavasiliou, M. K. Daletou, J. K. Kallitsis, T. Ioannides and S. Neophytides (2009). "Reforming methanol to electricity in a high temperature PEM fuel cell." Applied Catalysis B: Environmental **90**(3-4): 628-632.

Bessarabov, D., H. Wang, H. Li and N. Zhao (2016). PEM electrolysis for hydrogen production: principles and applications, CRC press.

Bhat, R. S. and V. B. Shet (2020). "Development and characterization of Zn–Ni, Zn–Co and Zn–Ni–Co coatings." Surface Engineering **36**(4): 429-437.

Chi, J. and H. Yu (2018). "Water electrolysis based on renewable energy for hydrogen production." Chinese Journal of Catalysis **39**(3): 390-394.

Dawood, F., M. Anda and G. Shafiullah (2020). "Hydrogen production for energy: An overview." International Journal of Hydrogen Energy **45**(7): 3847-3869.

Hayashi, T., N. Bonnet-Mercier, A. Yamaguchi, K. Suetsugu and R. Nakamura (2019). "Electrochemical characterization of manganese oxides as a water oxidation catalyst in proton exchange membrane electrolysers." Royal Society open science **6**(5): 190122.

Kumar, S. S. and V. Himabindu (2019). "Hydrogen production by PEM water electrolysis–A review." Materials Science for Energy Technologies **2**(3): 442-454.

Santos, H. L., P. G. Corradini, M. Medina, J. A. Dias and L. H. Mascaro (2020). "NiMo–NiCu Inexpensive Composite with High Activity for Hydrogen Evolution Reaction." ACS applied materials & interfaces **12**(15): 17492-17501.

Shirvanian, P. and F. van Berkel (2020). "Novel components in Proton Exchange Membrane (PEM) Water Electrolyzers (PEMWE): Status, challenges and future needs. A mini review." Electrochemistry Communications **114**: 106704.

Song, Y., C. Zhang, C.-Y. Ling, M. Han, R.-Y. Yong, D. Sun and J. Chen (2020). "Review on current research of materials, fabrication and application for bipolar plate in proton exchange membrane fuel cell." International Journal of Hydrogen Energy **45**(54): 29832-29847.

Tawfik, H., Y. Hung and D. Mahajan (2007). "Metal bipolar plates for PEM fuel cell—a review." Journal of power sources **163**(2): 755-767.

Toulhoat, H., P. Raybaud, V. Mendez and E. Puzenat (2018). "A universal relationship predicts optimal catalysts for a given chemical reaction." arXiv preprint arXiv:1812.09531.

Wilberforce, T., O. Ijaodola, E. Ogungbemi, F. Khatib, T. Leslie, Z. El-Hassan, J. Thomposon and A. Olabi (2019). "Technical evaluation of proton exchange membrane (PEM) fuel cell performance–A review of the effects of bipolar plates coating." Renewable and Sustainable Energy Reviews **113**: 109286.

Feasibility Report of 5-6 MW Biomass (Forest and Agricultural waste) Power Generation Facility in Manisa Akhisar Region

[1*]Mustafa Tolay, [2]Cemil Koyunoğlu, [3]Andre Waterschoot
[1] Tolay Energy Consulting, 19 Mayıs Street, Halaskargazi Road, Feza Block, No: 192, Floor 8, Sisli, 34360, Istanbul, Turkey
[2] Yalova University, Engineering Faculty, Energy Systems Engineering Department, Cinarcik Road 5th km, Yalova, 77200, Turkey
[3] Verco Renewable Energy Consulting SL, c/Solsona 17, b2, 08173, Sant Cugat del Valies, Barcelona, Spain

* E-mail: drmtolay@libero.it

Abstract
Biomass is considered as an energy source because it can protect the environment, generate electricity, chemicals, and especially fuel for vehicles. One of the most effective methods of generating energy from biological diaries is combined energy and power generation. Process heat and steam generations for industrial applications can be obtained from combined heat and power generation. Heat generation is needed for processes such as drying in the industrial sector. This can provide resources and generate energy in a short time. In addition, heat energy obtained from small combined heat and power plants can be used in the public space and their heating. energy sources in Turkey lignite, hydro and biomass energy is. After the oil crisis of the 1970s, the focus was on the development of new and renewable energy technologies such as solar power, wind power, hydroelectricity, geothermal energy and biomass. Biomass can be used in energy technology by directly burning or increasing the quality of the fuel with its various types and by obtaining alternative biofuels (easy road, storable and usable fuels) equivalent to existing fuels. Waste biomass (grain residues, forest and forest industry waste, animal droppings, etc.) is traditionally used directly in cooking or heating around the world. They are very suitable and high potential products for biogas, biocarbon and biodiesel production that can be used as a direct biomass source such as animal horses, agricultural waste and fruits.

Keywords: Hydrogen production, solid fuel, gasification, process types

I. Introduction
Today, the cheapest and easiest method available for hydrogen production is the production of syngas by gasification of solid and liquid fuels. In syngas obtained by gasification of solid and liquid fuels and consisting mainly of CO and H_2, it is possible to separate hydrogen with appropriate technologies. The pure hydrogen gas obtained can be used as a secondary energy source in many areas where clean energy is needed, especially in the automotive sector. Syngas produced by gasification systems of solid fuels such as lignite, biomass, and solid waste, especially coal in hydrogen production, can be used both in the production of energy with high efficiency and in the production of chemicals such as hydrogen, methanol, kerosene, and fertilizers. Thus, lignite in Turkey, which is national wealth, which we leave underground without being used idle, and the solid wastes we leave brutally to nature can be brought in both our energy sector and our chemical industry. Developments in the world show that the dominance of fossil fuels such as oil will continue in the next 50 years. On the other hand, considering the issues in which environmental legal regulations for fossil fuel power plants are gradually being tightened and solutions with high efficiency and low CO_2 emissions come to the fore, the 'coal gasification' technique, which was applied on a commercial scale 150 years ago and has become prominent all over the world in recent years, is also is of great importance. In recent years, South Africa, the USA, Canada, Australia, the People's Republic of China, and European Countries have been rapidly investing in the gasification of coal and similar solid fuels to meet energy needs and produce chemicals.
For this study, Turkish lignites (Table-1) were studied for hydrogen production via gasification. After the step of lignite preparing operations, lignites fed into gasifiers. Lignites particule that comes into gasifier firstly loses its water, dries. Its temperature changes from 250 °C - 400°C. Lignite particle reaches 400°C – 600°C temperatures during its upwards moving in the gasifier and start to pyrolysis and disintegrates to coke, tar, CH_4, and H_2. Oxygen comes in from the bottom or upper parts of gasifiers. When the lignite particle reaches 1000°C temperature, oxygen and steam react with coke and the formed gas is syngas at 1000-1300°C temperature that generally contains CO, H_2, CO_2, CH_4. Now, lignites particle is reduced and only its ash remained. Syngas cools down to 600°C while moving upwards. When the syngas reaches 400°C – 600°C by going out from the gasifier, it is pulled to a gas cleaning zone in which there are ash and dust collecting special cyclones. Afterward it comes to gas cleaning and hydrogen separation sections. Gasification reactions were as shown in Table-2.
In this study, especially solid fuel gasification systems, which have proven to be applicable on a commercial scale in hydrogen production, are explained with feasibility examples. Also, we will briefly try to give detailed information about fixed bed gasifiers such as down-draft or up-draft, PRME, BGL, and UHDE Gasifiers, especially with different important examples on a commercial scale, about solid fuel gasification using different gasifiers, specially pressurized fixed bed, syngas production, and hydrogen production. Also, fluidized bed gasifiers will be explained for hydrogen production.

II. The Goal of the Project

It shows the feasibility of the facilities that will allow the utilization of forest wastes (pine, oak) and agricultural wastes (including olive tree, grain and corn) and other solid wastes as energy sources, which are abundant in the Manisa Akhisar region. For this purpose, Tolay Energy has decided to establish a 5.0 MWe energy production facility with gasification method from forest and agricultural wastes in Manisa Akhisar Region. Development of this project; environment (climate change), renewable energy, energy security, waste management, rural employment, etc. It will contribute to the solution of many problems that need to be solved in the fields. Since the developments in rural employment are seen as an important social benefit, the lack of modern facilities producing energy from agricultural wastes in our society-based country increases the importance of this investment in the region. Manisa and spread to other regions in such a plant, Turkey's becoming a center of energy derived from biomass, to experience it performed, to ensure the growth of skilled labor. In addition, such a facility to be established in the region will not only create direct employment, but also indirectly create employment with the technical support of the regional industry to the facilities. As a matter of fact, it is thought that the technology of facilities generating energy from agricultural wastes has become producible in the region.

III. Biomass Fuel

Biomass fuels are organic substances that can be regenerated. The vast majority of biomass fuels used are derived from two classes of biomass: forest and agricultural and animal wastes. Combustion emissions of biomass fuel are lower than the fossil fuels. It produces very little acid rain and smoke compared to fossil fuels. When converted into energy using appropriate technologies and appropriate methods, it has a low impact on the environment, can be quickly reproduced, long-term and safe energy source. The most important feature of biomass that should be taken into consideration in terms of energy production is the moisture in it. The amount of moisture reduces the combustion efficiency. In some fuel production technologies such as gasification or pellet making, it is desirable that the biomass contains a certain amount of moisture. However, no matter how dry, biomass is always less energy-dense than fossil fuels such as oil and natural gas, and as much as domestic coal and lignite.

Due to the low thermal value and the fact that biomass is a waste product, especially when purchasing biomass fuels for a power generation facility, transportation is done by paying unloading fees. The amount of the transportation and unloading fee varies depending on the fuel and the process to be performed. Among biomass fuels, the least unloading fee is paid to woody biomass. Two main factors are considered in the pricing of biomass fuels. These:

- ✓ A competitive market environment that ensures the continuity of the required amount of fuel supply.
- ✓ Biomass fuel collection, processing, transportation costs and by whom these costs will be paid.

IV. Biomass as Forest Waste

Wood is an excellent source of biomass. Wood can be used alone or in combination with coal and other biomass fuels as fuel in heating boilers, power plants and gasification boilers. The technologies of the future enable the production of syngas for use in internal combustion engines, fuel cells or natural gas plants by processing wood waste. In addition, various liquid fuels such as biogasoline and biodiesel can be produced from cellulosic substances found in wood. Wood has a superiority compared to other fuels with its burning in a shorter time and rapid heat release properties. At the end of the combustion, the amount of ash left by the wood is less and it is 8% of its weight. Since some of the heat generated as a result of burning is spent on the evaporation of the water in the wood, the calorie value decreases with the increase in the amount of moisture. Among the tree species, the highest calorie value belongs to yellow pine with 5.274 kcal / kg. In leafy trees, the highest value is eucalyptus with 4.894 kcal / kg, and the lowest value is sycamore with 4.500 kcal / kg.

V. History of Forest Waste Biomass Usage in Turkey

The use of wood and wood products as a source of energy in Turkey is based on very old. Until the early 1800s, virtually almost all the energy used and produced in Turkey was obtained from wood. During the Ottoman Empire period, the country's forests, the need for fuel for the Palace and the timber requirement of the naval shipyards for shipbuilding and repair; No special emphasis was given to the production of weapons in the arsenal or the arsenal, except for certain utilization and utilization purposes, and no records were kept about the production of firewood from forests. It is known that some small sales were carried out in Rumeli Forests between 1857-1868. Between

the years of 1868-1893, forest rights started to be collected from the wood, coal and other forest products that came to the bazaars and bazaars. In 1929, a small system that generates electricity from the scraps of logs was established in the Zingal Lumber Factory operating in Sinop Ayancık.
In operating the electricity produced, log cutting machines and overhead lines; It was used in residential and environmental lighting and generators were used by Ayancık Forest Management until the 1980s.
After the use of oil in the world in the 1900s, petroleum products became cheaper with the increase of technological progress and production techniques. In addition, liquid oil has begun to be preferred in heating systems as it is easier to transport. The high calorie of fossil fuels increased the demand for them enormously, and although wood is an ubiquitous resource, it could not compete with fossil fuels. Due to the cheaper electricity generation from coal and the wider infrastructure of the infrastructure, the use of wood in settlements has decreased significantly. Turkey use coal with the development of the steam engine has started to increase. In addition, the share of wood in consumption of primary energy resources decreased significantly in the 2000s, with the incentives that facilitated the use of solar heating systems in rural areas, and this rate fell to 5% in 2007.

Table 1 As of year's wood production in Turkey

WOOD PRODUCTION	FIREWOOD PRODUCTION	INDUSTRIAL WOOD PRODUCTION	TOTAL WOOD PRODUCTION
Years	m3	m3	m3
1925-1937	11.600.000	6.440.000	18.040.000
1938-1949	38.133.702	6.601.263	44.734.965
1950-1962	103.951.626	19.550.732	123.502.358
1963-1973	127.198.000	46.185.000	173.383.000
1974-1984	44.539.000	25.558.000	70.097.000
1985-1990	38.590.000	75.960.000	114.550.000
1991-1995	25.706.000	34.978.000	60.684.000
1996-2000	22.635.000	35.882.000	58.517.000
2001-2006	30.000.000	49.670.000	79.670.000

References

Cengiz Karaca, H. O. *researchgate*. “Regional Distribution of Agricultural Biomass Potential in Turkey” https://www.researchgate.net/publication/288480914_Regional_Distribution_of_Agricultural_Biomass_Potential_in_Turkey, (2005).

Chioni, M. L. “RDF Gasification in a Circulated Bed Gasifier: Characterization of Syngas and Ashes”, (2002).

Daniela Jölli, S. G. “Unused biomass extraction in agriculture, forestry and fishery”, researchgate, (2005).

Daradimos, G. V. “The BGL Gasification Technology for Turkish Lignites”. ICCI, (2008).

Energy, R. (2002). “Plasma Gasification Process Description Overview”. recoveredenergy, (2002).

Yeast Industry Wastewater Treatment with Microbial Fuel Cells: Effect of Electrode Materials and Reactor Configurations

[1,2]Haris Nalakath Abubackar, [1*]Azize Ayol, [3]İdris Biryol
[1]Dokuz Eylul University, Department of Environmental Engineering, Izmir, Turkey
[2]Chemical Engineering Laboratory, Faculty of Sciences and Centre for Advanced Scientific Research (CICA), University of La Coruña, Rúa da Fraga 10, 15008 – La Coruña, Spain
[3]Dokuz Eylul University, Graduate School of Natural and Applied Sciences, Environmental Engineering, Izmir, Turkey

* E-mail: azize.ayol@deu.edu.tr

Abstract
Simultaneous removal of contaminants and electricity generation using microbial fuel cells is a promising technology that is environmentally friendly and contributes to the circular economy. Several studies have been reported previously by exogenously adding easily degradable sugars for electricity generation in MFCs (Vu and Min, 2019; Zhang etal. 2011). However, in real-world application with wastewater, the process performance varies between sources, microorganisms presented and electrodes used. In this study, simultaneous treatment of yeast industry wastewaters and electricity generation were investigated in different MFCs having the electrodes made up of titanium and graphite. Two-chamber MFC gave better performance provided the presence of active exoelectrogens is enviable for better performance.

Keywords: Microbial fuel cell, wastewater treatment, exoelectrogens, electrodes,

I. Introduction
Bio-electrochemical system technologies have been investigated ranging from harnessing electricity from wastewater with simultaneous pollutant removal by using microbial fuel cell (MFC), electrolysis of water, and generation of hydrogen in microbial electrolysis cells (MEC), CO_2 reduction via biocathode to produce valuable chemicals such as acetate, ethanol, butyrate by a technique called microbial electrosynthesis (MES), to desalination via Microbial desalination cells (MDCs) (Bajracharya etal. 2016). The potential of particular type of microbes (electroactive microbes) to perform bio-electrochemical reaction has been exploited either to produce electric current from chemical energy or vice versa. They are classified into two: exoelectrogens, for those that transfer electrons to the electrodes and electrotrophs that receive electrons from electrodes.
Although the ability of microorganisms to generate electricity has been observed by Potter (1912) with *Escherichia coli* and *Saccharomyces cerevisiae*, it was by the 1980s the improvement effect of electron transfer by exogenously added electron mediators that regained the interest on MFC. Later, in 1999, Kim and colleagues observed for the first time the ability to transfer the electrons to the electrodes without the presence of mediators, marks a new era in the field of bio-electrochemistry (Kim etal. 1999).
Microbial fuel cell can be either a single chamber with no separator or a two-chamber with a separator (ion-permeable membrane) thereby dividing the MFC into two compartments, anode, and cathode. In the anodic compartment, exoelectrogens oxidize the substrates generating electrons and protons. The electrons get accepted at the solid anode transferred through external circuit reaches the cathode where it combines with the oxygen and the protons, which are transferred through the membrane to form water molecules (Bajracharya etal. 2016).
One of the main components that influence greatly the performance of MFC on electricity production and also on the metabolic rate of anaerobic bacteria that is responsible for the degradation of contaminants is the electrode. Properties such as biocompatibility, excellent electrical conductivity and stability are some of the requisite of electrodes. Here in this study, we investigated the influence of electrode materials on yeast industry wastewater treatment and electricity generation using MFCs either single chamber or double chamber by using inoculum from different sources for aerobic and anaerobic reactor compartments.

II. Experimental Set-up and Procedure
Two most commonly studied MFC designs, a single chamber MFC and a H-type double chamber MFC were used in this research for yeast wastewater treatment and electricity generation. These reactors are made of borosilicate glass and a lid made from Delrin®, with several slots for sampling and electrodes. The working volumes of each chamber of MFCs are 300 ml. For double chamber, Nafion 117 (DuPont Co., USA), a proton exchange membrane was used as the separator between anodic and cathodic compartments. More information about the reactors can be found in elsewhere (Ayol etal. 2020). The temperature was maintained constantly at 30^0C and agitated at 100 rpm throughout the experimental run by placing the reactors on a hot plate magnetic stirrer. Four different sets of experiments were performed either in single or double chamber MFC using different types of electrodes as mentioned in table Table 1. For experiments (Single Chamber MFC and Double Chamber MFC 1), 80 ml of anaerobic sludge from wastewater treatment plant (WWTP) of a yeast factory in Izmir, Turkey along with 220 ml of wastewater taken from equalization tank of the yeast factory has been used to reach a working volume of 300 ml in the anodic compartment. For experiments (Double chamber MFC 2 and MFC 3), 60 ml of anaerobic sludge from a municipal wastewater treatment plant in Izmir + 20 ml of inoculum that was used for the previous two studies along

with 220 ml of yeast industry wastewater has been used in the anodic compartment. For cathodic compartments of all the two-chamber experiments were filled with 300 ml of yeast industry wastewater as the catolyte. The dimension of titanium electrodes was cylindrical rod-shaped with the size of 10 x 1 cm and an area of 31.4 cm^2 and that of graphite electrodes were rectangular shaped with the size of 10 x 0.5 x 0.5 cm with an area of 20.5 cm^2 (SGL group,Germany). The electrodes were connected via a copper wire to 1000 ohm resistance and the current generated from MFCs were monitored using 2700/7700 Keithley DMM/Precision Data Acquisition System. Occasionally analyzed parameters to understand the extent of wastewater treatment performance were pH, salinity, electrical conductivity (EC), oxidation-reduction potential (ORP), suspended solids (SS), volatile suspended solids (VSS), and chemical oxygen demand (COD).

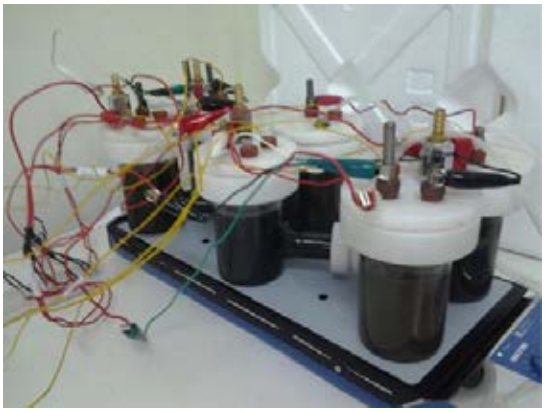


Fig. 1: Experimental setup (two H-type and a single chamber MFCs placed on hot plate magnetic stirrer).

III. Analysis

The performance of MFC on electricity generation was evaluated on basis of power generated. Power and current densities were calculated from the power and current obtained using the Ohm's law taking in to account the external resistance, divided by the surface area of the electrodes, respectively. On the other hand, VSS, VS, and COD were analyzed to understand the treatment performance of yeast industry wastewater in MFCs. All measurements and analysis were done according to Standard Methods (APHA, 2005).

IV. Results and discussions

MFC technology has been exploited for energy generation and pollutant removal with anode has a significant role in the performance of the system. Since anode is in contact with exoelectrogens, electrode material should be rightly chosen that allows enhanced microbial attachment, biocompatible, and with high conductivity improving the electron transfer process. However, the cost, stability, and durability of electrode materials are also needed to consider in addition while commercializing the process. Here, we tested two different types of anode materials: carbon-based (graphite rod) and metal-based (titanium rod); two different inoculum, and two different reactor configurations.

The experiments "Single Chamber MFC" and "Double Chamber MFC1" using titanium rod as electrodes and anaerobic sludge from yeast industry as inoculum were performed in order to check the better reactor configuration that offers higher power. The power density (Table 1) obtained in "Double Chamber MFC1" is five times higher than that obtained in the "Single Chamber MFC". This significant difference in the energy generated between the studied reactor configurations can be attributed to the presence of oxygen in the single-chamber which is detrimental for exoelectrogens. However, a well separation from anodic, which needs to maintain anoxic, from cathodic compartment is possible by the separator such as Nafion membrane. Thus easily available oxidizing agent, oxygen which is required in the cathodic chamber for the reduction reaction can be provided separating from the anodic chamber in dual-chamber configuration.

Tab. 1: Maximum power and current density obtained from the different experimental run

Experiment	Anode	Cathode	Area (cm^2)	Current (µA)	Power (µW)	Current Density (µA/cm^2)	Power density (mW/m^2)
Single Chamber MFC	*Titanium*	*Titanium*	*31.4*	*177.35*	*31.45*	*5.64*	*10.02*
Double Chamber MFC 1	*Titanium*	*Titanium*	*31.4*	*400.24*	*160.19*	*12.74*	*51.02*
Double Chamber MFC 2	*Graphite*	*Titanium*	*20.5*	*223.02*	*49.73*	*10.87*	*24.26*

Double Chamber MFC 3	*Graphite*	*Graphite*	*20.5*	*174.07*	*30.30*	*8.49*	*14.78*

In the next set of experiment “Double Chamber MFC 2” and “Double Chamber MFC 3”, we tested the difference in cathode material on power generation in MFC. For this purpose, we used titanium and graphite rods, respectively. The current obtained in “Double Chamber MFC 2” outperformed “Double Chamber MFC 3” although lower than “Double Chamber MFC 1”, mainly due to the change in inoculum. From these preliminary studies we can conclude that type of cathode material also influence the power generation in MFCs. Achieved power generation is comparable with some of the previous studies (Włodarczyk and Włodarczyk, 2018; Włodarczyk and Włodarczyk, 2020), at the same time, taking into account that there was no pretreatment applied to the sludge and wastewater used in our studies. On other hand, for long-term operation of MFC, the feasibility of using titanium as electrode material might hinders due to corrosion problems (Santoro etal. 2017).
Parameters such as pH, salinity, EC, ORP, DS, VS, SS, VSS, and COD were monitored and recorded in order to understand the extent of wastewater treatment in different MFC experiments (data not shown in the abstract).

V. Conclusions

The Microbial fuel cell is promising technology for pollutant removal and a sustainable way of generating electricity. Electrode types (titanium, graphite), reactor configurations (single and double chamber), and inoculum used were compared in terms of power generation and sludge stabilization extent. The maximum power density of 51.02 mW/m^2 was obtained in the study with titanium electrode in a two-chamber H type reactor using anaerobic sludge from a yeast industry as inoculum. The electrode used in the cathode compartment also shown some influence on the power generation.

Acknowledgements

This study was supported by Dokuz Eylul University, Scientific Research Foundation (DEU-BAP), Turkey under award #2011.KB.FEN.046 “Direct Electricity Generation from Treatment Plant Sludge by using MFCs” research project. HNA thanks the Xunta de Galicia (Spain) for his post-doctoral contracts modalidade A (ED481B-2016/195-0) and modalidade B (ED481D 2019/033) that enabled him to perform the research at DEU, Turkey and UDC, Spain.

References

APHA. In: Eaton A.D., Clesceri L.S., Greenberg A.E., editors. Standard methods for the examination of water and wastewater. 20th ed. [APHA-AWWA-WEF], (2005).

Ayol A., Biryol I., Taskan E., Hasar H., Enhanced sludge stabilization coupled with microbial fuel cells (MFCs), International Journal of Hydrogen Energy, https://doi.org/10.1016/j.ijhydene.2020.10.143 (in press) (2020).

Bajracharya S., Sharma M., Mohanakrishna G., Benneton X. D., Strik D. P., Sarma P. M., Pant, D., An overview on emerging bioelectrochemical systems (BESs): technology for sustainable electricity, waste remediation, resource recovery, chemical production and beyond, Renewable Energy, 98, 153-170 (2016).

Kim B. H., Park D. H., Shin P. K., Chang I. S., Kim H. J., Mediator- less biofuel cell, US Patent 5976719 (1999).

Potter M. C., Electrical effects accompanying the decomposition of organic compounds. Proceedings of Royal Society B Biological Sciences, 84, 260-276 (1911).

Santoro C., Arbizzani C., Erable B., Ieropoulos I., Microbial fuel cells: From fundamentals to applications. A review. Journal of power sources, 356, 225-244 (2017).

Vu, H. T., Min, B., Integration of submersible microbial fuel cell in anaerobic digestion for enhanced production of methane and current at varying glucose levels, International Journal of Hydrogen Energy, 44, 7574-7582 (2019).

Włodarczyk P.P., Włodarczyk B., Microbial Fuel Cell with Ni–Co Cathode Powered with Yeast Wastewater, Energies, 11, 3194 (2018).

Włodarczyk B., Włodarczyk P.P., The Membrane-Less Microbial Fuel Cell (ML-MFC) with Ni-Co and Cu-B Cathode Powered by the Process Wastewater from Yeast Production, Energies,13, 3976 (2020).

Zhang, Y., Min, B., Huang, L., Angelidaki, I., Electricity generation and microbial community response to substrate changes in microbial fuel cell, Bioresource Technology, 102, 1166-1173 (2011).

Effect of Green Synthesized Silver Oxide Nanoparticles on Biological Hydrogen Production

[1*]Oznur Yildirim, [1]Dogukan Tunay, [1]Bestami Ozkaya, [1]Ahmet Demir
[1] Yildiz Technical University, Civil Engineering Faculty, Environmental Engineering Department, Istanbul, Turkey

* E-mail:y.oznur2014@gmail.com

Abstract
This study investigated the effect of silver oxide nanoparticles on bio-hydrogen yield. It is quite popular to support bio-hydrogen production with the use of nanoparticles. The use of nanopariticles produced by supplementing with natural products is important for a sustainable environment. A green synthesis of silver oxide nanoparticles was developed using *Chorella sp.* of microalgae as a reducing agent in this study. SEM, EDX and UV-Visible spectrum analyzes were performed for the characterization of the synthesized nanoparticles. Hydrogen production performance with *Clostridium sp.* was evaluated using different ratios of nanoparticles produced. The effect of addition of nanoparticles on dark fermentative bio-hydrogen production evaluated compared to control set.

Keywords: nanoparticle, bio-hydrogen, silver, clostridium sp., microalgae

I. Introduction

Nowadays, research on the production and use of renewable fuels has intensified due to global warming, climate change, depletion of oil reserves, increased oil prices and greenhouse gas emissions caused by carbon-based fossil fuels. With the population continuing to grow exponentially, it is estimated that not only food but also limited resources in the world will be suppressed. According to the researchs, fossil fuel reserves are decreasing rapidly, and it is stated that oil and natural gas have a life span of about 50 years (Raj and Singh, 2012). Hydrogen production is one of the best options as an energy source because of zero-carbon emission.

Hydrogen production can be carried out by different methods. Biological hydrogen production has three subtitles: fermentative hydrogen production, biophotolysis and photodecomposition (Das and Veziroglu, 2008). The most preferred of these is the fermentative bio-hydrogen production method. Hydrogen production can be achieved by using microorganisms such as *Clostridium* and *Rhodobacteria* species (Lin et al., 2007; Wei et al., 2021).

Nanoparticles (NP) have started to be used intensively in many sectors of Medicine, Aviation, Defense, and Biotechnology (Alsaba et al., 2020; Balogun et al., 2020; McNamara and Tofail, 2017). Due to the small size of the nanoparticles, their surface area increases significantly and provides high yields in many areas of use (Fubini et al., 2010). Researchs are also carried out on the use of nanoparticles in fermentation processes (Kumar et al., 2019). However, it is of great importance to investigate the effect of green nanoparticles, which is an environmentally friendly nanoparticle, on the yield of fermentative bio-hydrogen production.

The aim of this study was to evaluate the green synthesid silver oxide nanoparticles on bio-hydrogen production. *Chlorella sp.* microalgae were grown, and nanoparticle synthesis was carried out with them. The potential of produced nanoparticles to produce dark fermentative bio-hydrogen with *Clostridium sp*. was evaluated.

II. Experimental Set-up and Procedure

Nanoparticle Synhesis

Green microalgae *Chlorella vulgaris* was used for nanoparticle synthesis. *C. vulgaris* was growth in BG-11 medium which includes: 1.5 g/L $NaNO_3$, 0.04 g/L K_2HPO_4, 0.075 g/L $MgSO_4.7H_2O$, 0.036 g/L $CaCl_2.2H_2O$, 0.006 g/L citric acid, 0.006 g/L ferric ammonium citrate, 0.001 g/L EDTA (disodium salt), 0.02 g/L Na_2CO_3 and as trace elements; 2.86 mg/L H_3BO_3, 1.81 mg/L $MnCl_2.4H_2O$, 0.222 mg/L $ZnSO_4.7H_2O$, 0.39 mg/L $NaMoO_4.2H_2O$, 0.079 mg/L $CuSO_4.5H_2O$ and 49,4 µg/L $Co(NO_3)_2.6H_2O$. The microalgae extract filtered through the 0.45 µm membrane filters (mixed cellulose esters, Millipore, Billerica, MA, USA). After that, 20 ml of aqueous extract was added into 180 ml of 1 mM $AgNO_3$ solution ($AgNO_3$ > 99.8%, Sigma-Aldrich). The prepared mixture was heated up to 60°C and stirred for 48 h for reduction of silver ion in dark condition. A control experiment was conducted without microalgae extract. After 48 h reaction, the mixture was centrifuged at 4000 rpm for 30 min. Supernatant was discharged and the NP pellet was washed with distilled water. Finally, NPs were dried at 45°C for 5 h.

Inoculum and Culture Medium

Clostridium sp. was isolated previously (Koroglu et al., 2019) was used for bio-hydrogen production via dark fermentation. The stock culture was precultivated at 35°C an pH 7, in Reinforced Clostridial Medium (RCM) containing meat extract 10 g/L, peptones 5 g/L, yeast extract 3 g/L, D (+) glucose 5 g/L, starch 1 g/L, NaCl 5 g/L, sodium acetate 3 g/L, l-cysteine chloride 0.5 g/L, and agar–agar 1 g/L in distilled water. During precultivation, cells used to inoculate the fermentation reactor were harvested based on optical density of 0.2 at 600 nm (OD_{600}).

Experimental Set-up

Batch experiments were conducted in 120 mL serum bottles with a working volume of 50 mL. The

bio-hydrogen production medium containing 30 g/L glucose, 0.85 g/L KH_2PO_4, 0.75 g/L K_2HPO_4, 0.003 g/L H_3BO_3, 0.2 g/L $MgSO_4 \cdot 7H_2O$, 0.001 g/L $Na_2MoO_4 \cdot 2H_2O$, 0.001 g/L $ZnSO_4 \cdot 7H_2O$, 0.002 g/L $MnSO_4 \cdot 4H_2O$, 0.0001 g/L $Cu(NO_3)2 \cdot 3H_2O$, 0.001 g/L $CaCl_2 \cdot 2H_2O$, 0.002 g/L EDTA, 0.012 g/L $FeSO_4 \cdot 7H_2O$, 0.004 g/L thiamine, 0.003 g/L biotin, 0.005 g/L p-aminobenzoic acid, 0.0065 g/L nicotinamide, 0.420 g/L glutamic acid, 0.001 g/L resazurin. The medium was flushed with oxygen-free nitrogen gas for 5 min. Ag-NP concentration in the range of 5 to 30 µg was applied. The reactors were stirred at 120 rpm and the temperature was maintained at 35°C. The biogas accumulation in the reactors were measured by using a syringes. Experiments were performed in triplicate.

III. Analysis

Characterisation of Green Synthesid Nanoparticle

UV-vis spectrophotometer (WTW PhotoLab 6600 UV–vis Spectrophootometer) was used to determine the wavelength between 300 and 800 nm to track the formation of NPs for certain time intervals. Scanning electron microscopy was used to determine the size and morphology of the NPs. Energy-dispersive X-ray spectroscopy was used for determining the EDX spectrum.

Hydrogen measurement

Produced hydrogen was analyzed in Gas Chramotography (GC) (Shimadzu GC2014, Tokyo, Japan) equipped with a thermal conductivity detector (TCD) and a 2 m length, 1 mm inner diameter packed column (Restek, USA). Argon gas was used as the carrying gas at the flow rate of 10 mL/min. The operating temperatures of the column, detector and injector were 80, 200 and 110 °C, respectively.

IV. Results and discussions

Characterisation of Green Synthesid Nanoparticle

SEM, EDX and UV-Vis analysis results were shown in Fig.1. The silver oxide nanoparticles seem to be distributed with an average size of 90 nm according to SEM analysis. Besides, EDX spectrum verified the presence of the silver nanoparticles.

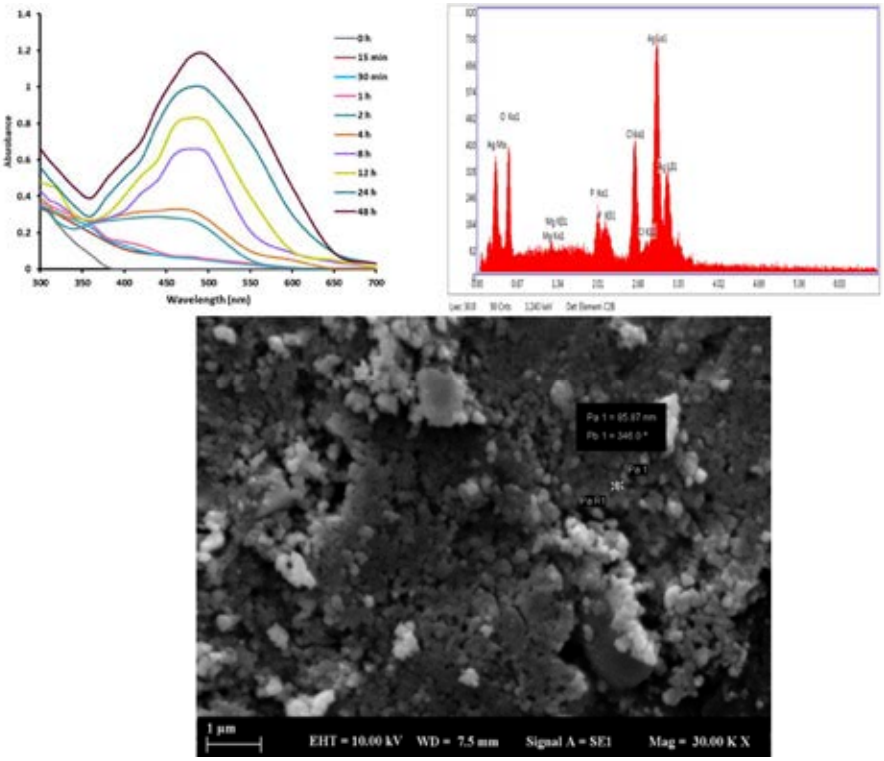


Fig. 1. (a) UV–visible absorption spectra of reaction mixtures at different time intervals. (b) EDX spectra of silver oxide nanoparticles. (c) SEM image of silver oxide nanoparticles.

H_2 Production

The amount of hydrogen obtained by adding different amounts of silver oxide nanoparticles was depicted in Fig. 2. Biological hydrogen production studies are continuing.

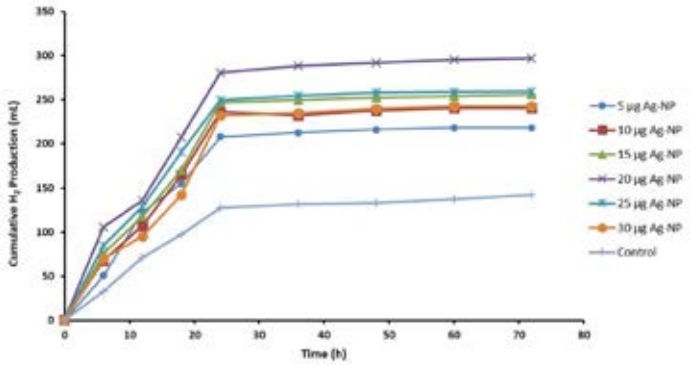


Fig. 2. Cumulative bio-hydrogen production

V. Conclusions

Characterization studies of the nanoparticles produced as a result of the study were carried out. The results showed that the nanoparticles produced had a uniform structure and an average size of 90 nm. This study invastigated that the effect of green synthesized silver oxide NP on the successful improvement of the bio-hydrogen production process via *Clostridium sp*. The addition of even small amounts of NP increased hydrogen production by fermentative microorganisms compared to control.

References

Alsaba, M.T., Al Dushaishi, M.F., Abbas, A.K., 2020. A comprehensive review of nanoparticles applications in the oil and gas industry. J. Pet. Explor. Prod. Technol. 10, 1389–1399.

Balogun, S.W., James, O.O., Sanusi, Y.K., Olayinka, O.H., 2020. Green synthesis and characterization of zinc oxide nanoparticles using bashful (Mimosa pudica), leaf extract: a precursor for organic electronics applications. Sn Appl. Sci. 2, 1–8.

Das, D., Veziroglu, T.N., 2008. Advances in biological hydrogen production processes. Int. J. Hydrogen Energy 33, 6046–6057.

Fubini, B., Ghiazza, M., Fenoglio, I., 2010. Physico-chemical features of engineered nanoparticles relevant to their toxicity. Nanotoxicology 4, 347–363.

Koroglu, E.O., Ozdemir, O.K., Ozkaya, B., Demir, A., 2019. An integrated system development including PEM fuel cell/biogas purification during acidogenic biohydrogen production from dairy wastewater. Int. J. Hydrogen Energy 44, 17297–17303. https://doi.org/10.1016/j.ijhydene.2019.01.291

Kumar, G., Mathimani, T., Rene, E.R., Pugazhendhi, A., 2019. Application of nanotechnology in dark fermentation for enhanced biohydrogen production using inorganic nanoparticles. Int. J. Hydrogen Energy 44, 13106–13113.

Lin, P.-Y., Whang, L.-M., Wu, Y.-R., Ren, W.-J., Hsiao, C.-J., Li, S.-L., Chang, J.-S., 2007. Biological hydrogen production of the genus Clostridium: metabolic study and mathematical model simulation. Int. J. Hydrogen Energy 32, 1728–1735.

McNamara, K., Tofail, S.A.M., 2017. Nanoparticles in biomedical applications. Adv. Phys. X 2, 54–88.

Wei, X., Feng, J., Cao, W., Li, Q., Guo, L., 2021. Photo-biological hydrogen production by a temperature-tolerant mutant of Rhodobacter capsulatus isolated by transposon mutagenesis. Bioresour. Technol. 320, 124286.

Investigation and Modeling of Flow Channels for Direct Borohydride Fuel Cell

[1*]Anıl Can Türkmen, [1]Kürşat Can Ata, [1]Gözde Menteşe [1]Cenk Çelik
[1] Mechanical Eng. Dept., Kocaeli University, Umuttepe Campus, İzmit/Kocaeli
* E-mail: anilcan.turkmen@hotmail.com

Abstract
Bipolar plates, which cover a large part of fuel cells in terms of weight and cost, are an important system element for fuel cells. The selection and optimization of flow field geometries of bipolar plates directly affects fuel cell performance. The pressure drops behavior that occurs in the flow channels has significant effects on fuel cell performance. Within the scope of this study, flow channels of different geometries were created to be used directly in the borohydride fuel cell and pressure drop behavior was investigated by performing experiments at certain flow rates to each flow channel. For this reason, 3 pin type flow channel geometries were created in SOLIDWORKS software, and the CAD data created was processed on a 10cmx10cm polycarbonate plate on a CNC machine. Each of the flow channels processed was tested with certain flow rates (3ml / min, 6ml / min, 9ml / min, 12ml / min and 15ml / min) in the experimental setup created for pressure drop measurement. From the results of the experiment, it has been determined that the pressure drop increases with the increasing flow rate for all 3 types of flow channels. The obtained data were compared with Comsol Multiphysics software and the best flow channel was determined accordingly. However, it was observed that the pressure drop increased with increasing distance between the channels in the pin flow channel.
Keywords: Flow channel, pressure drop, direct borohydride fuel cell, fuel cell

I. Introduction

Fuel cells, which constitute attractive electricity generation technology in the form of direct conversion of chemical energy into electrical energy with high efficiency, are developed for a variety of application ranges from vehicles that require tens of kilowatts to portable and mobile devices that require only a few watts, such as laptops and battery-powered phones. Although there has been a significant improvement in fuel cell technologies over the past two decades, fuel cells have not yet become fully widespread due to cost and a number of technical difficulties.
Fuel cells basically consist of Membrane Electrode Assembly (MEA), flow channels (bipolar plate), current collector plates, compression plates and their connection elements. Bipolar plates used for the distribution of gases for the MEA in fuel cells and collecting the current and water are the most important system elements after MEA. Bipolar plates are one of the most important parts for a good stack performance and uptime, which directly affects fuel cell performance. A reduction in the pumping power consumed for the fuel supply system increases the efficiency of the fuel cell system. Therefore, study of the pressure drop behavior in the flow channel is necessary for the design and optimization of a fuel cell system.
There is quite a limited study in the literature on modeling for direct borohydride fuel cells (DBFC). Especially, this limitation in modeling flow channels has been tried to be overcome by investigating the flow channels made for direct methanol fuel cells (DMFC), which have similar properties with DBFCs. The only experimental study on flow channels in DBFCs was made by Cheng et al. The other components with channel width 2 mm, channel depth 2 mm, channel length 20 mm, distance between channels 2 mm were on bipolar plates with co-parallel and serpentine channel geometry. has been made. In the study, it was determined that the single channel serpentine channel shows 3.5% higher peak power than the parallel channel (Cheng et al., 2006). A number of studies have shown that the geometry of the flow field influences mass transport of methanol to the diffusion layer and DMFC performance (Yang et al., 2005, Wong et al., 2006, Amplett et al., 2001, Arico et al., 2000).

Pressure drop in the anode and cathode flow areas of DMFC, was researched (Argyropoulos et al., 1999). In his work, a complex equation was used to calculate the pressure drop of two-phase flow, which includes the following factors: I) Friction loss at the surface of the flow channel, II) Pressure change due to flow separation at the inlet and flow at the outlet, III) The acceleration of the gas and liquid phases due to the change in density, IV) Gravity, V) Evaporation of water and methanol, VI) Limited solubility of CO_2 in liquid phase. In Argyropoulos's work, it was assumed that the temperature of the reactant stream increased linearly from inlet to outlet.
In the 2D modeling study conducted by Stroman et al., 0.5, 0.75 and 1 mm were used for the canal depth and the decrease in the canal depth in the parametric analysis made increased the power density. In the study conducted by Wang, it was revealed that different types of flow channels were made for DMFCs and that bipolar plates with serpentine channels have a higher power density than bipolar plates with parallel channels. However, it has been stated that the effective power taken from the fuel cell is lower as a result of the high-power consumption of the pump used, since the use of serpentine channels creates higher pressure drops compared to other channel types (Stroman et al, 2014).

II. Experimental Set-up and Procedure

While planning the analyzes, it is focused on choosing the channel type as mentioned before. At this point, drawings of different canal types with constant depth (1 mm) were prepared and their analysis started. Fuel flow rate was determined as a parameter for analysis and 0.5, 1, 5 and 10 ml / min was selected as the value. The duct outlet opens to the atmosphere in room conditions with 1 atm pressure and no external back pressure is applied. The effect of the channel width and the distance between the channels on the pressure drop is a particular consideration.

During the analysis, mainly five different values were determined for the channel width and the distance between the channels. These are 1, 1.5, 2, 2.5, 3 mm. The designs made were made in the combination of these five values. These values can be increased if necessary. In the experiment, 3 different geometries from the pin type flow channel and the design from the parallel type flow channel were created using the SOLIDWORKS program. The CAD designs created were processed in a CNC within the university. The CAD model of pin flow channels is shown in Figure 1. In order to test the prepared flow channels, an experimental setup consisting of a peristaltic pump, a manually prepared pressure measurement equipment, fuel chamber and discharge chamber was created. The water supply to the pump is made from a 500 ml plastic bottle through the suction hose of the pump, and with the outlet hose of the pump, water enters from the lower fuel inlet of the flow channel with the pressure measurement equipment connection first. It then proceeds along the flow channel and leaves the channel at the upper fuel outlet of the flow channel. The water leaving the channel goes through the pressure measuring equipment and into the discharge chamber. During this cycle, the difference in water levels in the pipes of the pressure measuring equipment gives the pressure difference at the inlet and outlet of the flow channel. This test was performed at 5 different flow rates for each 3 geometry of the prepared pin, serpentine and parallel flow channels. Each of the tests was carried out under room conditions, constant temperature and pressure. Flow rates used in the experimental study are 3 ml / min, 6 ml / min, 9 ml / min, 12 ml / min and 15 ml / min, respectively.

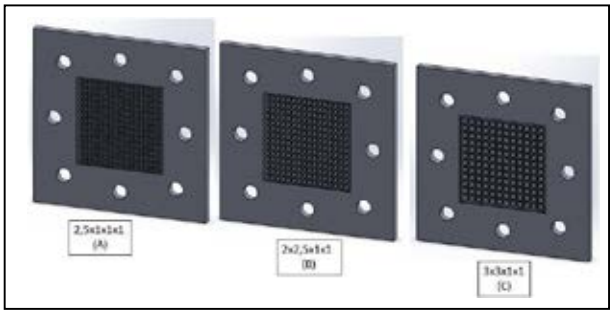


Fig. 1: CAD drawings of pin type flow channels

IV. Results and discussions

When each criterion is evaluated individually based on the results given, it is seen that the highest pressure drop values occur in the serpentine channels. The high pressure drop creates difficulties in terms of both sealing and keeping the pump power low. It can have a positive effect as the increase in the pressure drop in the flow channels can increase the fuel cell performance. Considering the contact area / active area ratios, it is thought that the height of the pin and cascade type flow channels will bring along an increase in performance since the area where the fuel contacts the metallic foam will increase. Although the effect of heat transfer is not observed in the isothermal analysis, it is seen that the height of the contact area / active ratio in pin type channels has an increasing effect on the current density taken from the cell.

Considering the velocity distribution of the fluid in the channels, it is seen that the distribution in the serpentine channels is the highest in the center of the cross-sectional area of the channel, and decreases as it goes towards the channel walls. This behavior continues in the same way in the input-output direction of the channel. In other words, there is a homogeneous flow along the channel and non-homogeneous flow along the channel width. The flow velocity is more homogeneous in pin and cascade types. When looking at the pin type flow channel with the highest current density and limited velocities of 2.5x1x1, it can be easily seen that the average velocities on the horizontal and vertical lines are very close to each other. This has shown once again that the pin type streaming channel is very useful. Pressure drop tests were performed at 3ml / min, 6ml / min, 9ml / min, 12ml / min and 15ml / min flow rates for all 3 geometries of the pin flow channels, respectively. The unit of pressure values read from the pipes of the pressure measurement equipment is cmH_2O, and these values were converted to pascal (Pa). For 2,5x1x1 pin flow channel, test results read from pipes during testing are given in Figure 5. From the test results, it was seen that the pressure drops in the 2.5x1x1 pin flow channel increased with increasing flow rate.

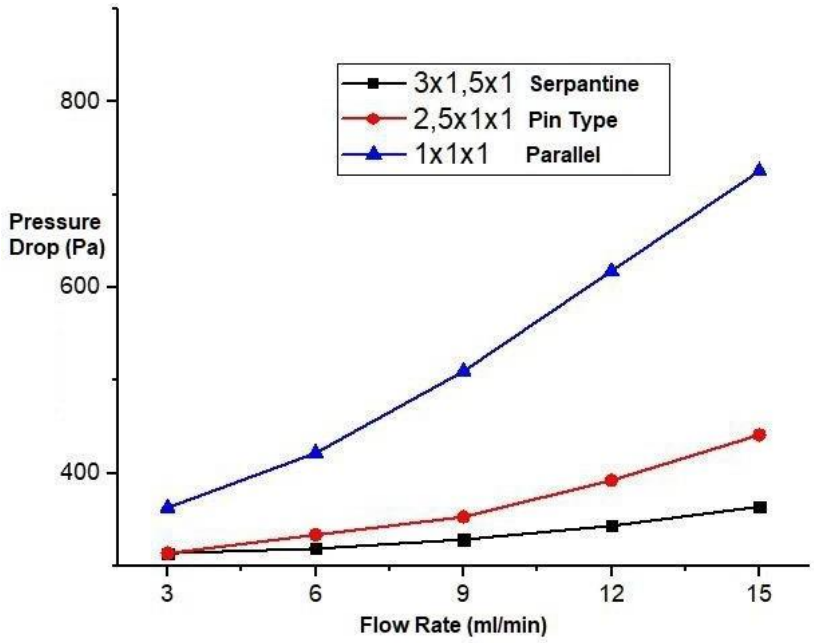


Fig. 2: Collective display of the data obtained

V. Conclusions

In this study, flow channels with different geometries were created for direct borohydride fuel cells and the behavior of pressure drop was investigated by supplying fuel at certain flow rates to the formed flow channels. In the experimental study, 3 pin type flow channels with different geometries were created. The channels created were tested under fixed room conditions at 5 different flow rates: 3 ml / min, 6 ml / min, 9 ml / min, 12 ml / min and 15 ml / min. The results obtained from the experimental study are summarized below. It was observed that the amount of pressure drop decreased with the increasing flow area ratio in the pin type flow channels. Moreover, it was observed that the pressure-drop values in the flow channels with close flow area ratios came close to each other and even at low fuel flows these values could be the same. In addition, it has been determined that the pressure drop increases with increasing fuel flow for all flow channels. The pressure-drop occurring in the flow channels has an optimum value for each fuel cell. The channel geometry can be different in the anode and cathode according to the system used and the need. In addition to choosing the basic geometry, duct dimensions and the flow relationship between ducts must be carefully adjusted. Otherwise, random selections may produce the opposite effect instead of providing the expected cell efficiency and performance increase.

Acknowledgements

This study was supported by the Scientific and Technological Research Council (TUBITAK) of Turkey (Grant id: 215M255) and by Kocaeli University Scientific Research Projects (BAP) Unit (grant id: BAP-2015-038). The support and fundings of these institutions are gratefully acknowledged.

References

Amphlett, J. C., Peppley, B. A., Halliop, E., Sadiq, A., The effect of anode flow characteristics and temperature on the performance of a direct methanol fuel cell, Journal of Power Sources, 96, 204-213 (2001).

Argyropoulos, P., Scott, K., Taama, W.M., Carbon dioxide evolution patterns in direct methanol fuel cells, Electrochim. Acta, 44,3575 – 3584 (1999).

Aricò, A.S., Cretì, P., Baglio, V., Modica, E., Antonucci, V., Influence of flow field design on the performance of a direct methanol fuel cell, Journal of Power Sources 91, 202-209 (2000).

Cheng H., Scott K., Influence of operation conditions on direct borohyride fuel cell performance, Journal of Power Sources, 160, 407-412 (2006).

Stroman R. O., Jackson G., Modeling the performance of an ideal NaBH4-H2O2 direct borohydride fuel cell, Journal of Power Sources, 247, 756-769 (2014).

Wong, C. W., Zhao, T. S., Ye, Q., Liu, J. G., Experimental investigations of the anode flow field of a micro direct methanol fuel cell, Journal of Power Sources, 155, 291-296 (2006).

Yang, H., Zhao, T.S., Effect of anode flow field design on the performance of liquid feed direct methanol fuel cells, Electrochimica Acta 50, 3243-3252 (2005).

Photofermentative Hydrogen Production by Agar Immobilized Co-Cultures of Purple Non-Sulfur Bacteria

[1*]Görkem Baysal, [2]Harun Koku, [2]Inci Eroglu, [1]Meral Yücel
[1] Middle East Technical University, Faculty of Arts and Sciences, Department of Biological Sciences, Ankara, 06800, Turkey
[2] Middle East Technical University, Faculty of Engineering, Department of Chemical Engineering, Ankara, 06800, Turkey

* E-mail:baysal.gorkem@gmail.com

Abstract
Purple non-sulfur (PNS) bacteria have the ability to produce biohydrogen via photofermentation. This study focuses on hydrogen production using co-cultures of immobilized PNS bacteria, investigates the possible synergistic effect of their co-cultures, and the advantages of immobilization. Growth, hydrogen production and substrate utilization of single-cultures and, double and triple co-cultures of *R. capsulatus* hup- (YO3), *Rp. palustris* (DSM 127) and *R. sphaeroides* O.U.001 (DSM 5864) were compared using an artificial hydrogen production medium in 150 mL indoors and outdoors photobioreactors on 40/2 Acetate/Glutamate medium under continuous illumination and anaerobic conditions. Hydrogen yields were found to be within 1.71-3.21 mol H_2/mol acetate and hydrogen productivities were found to be within 0.0447-0.406 mol H_2/(L.h). Additional studies with different temperature, illumination, and substrate concentration parameters need to be carried out for deeper understanding of the mechanism of hydrogen production in immobilized co-cultures in order to further improve and standardize hydrogen yields and productivities.

Keywords: Purple Non-Sulfur Bacteria, Co-cultivation, Biological Hydrogen Production, Photo fermentative Hydrogen Production, Immobilization, Immobilized Co-cultures

I. Introduction

Fossil fuels are still the primary energy source of our times. However, these fuels are non-renewable and cause greenhouse gas emissions implicated in global warming. Hydrogen forms water when combusted, hence is considered an environmentally benign fuel. Additionally, the combustion of 1 kg of hydrogen leads to 142 kJ of energy, which is equivalent to the combustion of 2.1 kg of natural gas or 2.8 kg of gasoline, hence is suitable to be used as the transport fuel of the future (Van Mierlo et.al., 2006). Biological hydrogen production using purple non-sulfur bacteria is a promising field as a clean hydrogen production route, since it is renewable, and bears the possibilities of fuel production from solar energy and waste utilization. Numerous efforts have demonstrated hydrogen production using co-cultures of PNS bacteria and hydrogen production by single cultures of PNS bacteria in an immobilized setting (Basak et.al., 2014, Tiang et.al., 2020). This study focuses on hydrogen production using co-cultures of PNS bacteria in an immobilized setting, and investigates both the synergistic effect of using co-cultures of PNS bacteria, and the potential advantages of utilizing an immobilization system. Immobilization confers numerous benefits to the hydrogen production system (Zhang et.al., 2010, Tsygankov et.al., 2001, Fibler et.al., 1995). High cell concentrations are maintained and cells can be reused without need for re-cultivation, hence, cell recovery and recycling costs are eliminated. Cell wash-out problems are minimized for continuous cultures and high cell concentrations coupled to high flow rates can result in high volumetric productivities. Furthermore, favorable micro-environmental conditions can be provided, genetic stability can be improved, and shear damages due to mixing or aeration of the reactor are eliminated. In addition, if the bacteria are immobilized inside an entrapment medium such as agar, contamination of bacteria and medium toxicity is prevented or mitigated by a physical barrier, therefore this type of hydrogen production is also suitable for waste utilization. This study focuses on indoor and outdoor hydrogen production by agar immobilized single-cultures and, double and triple co-cultures of PNS bacteria, namely, *R. capsulatus* hup- (YO3), *Rp. Palustris* (DSM 127) and *R. sphaeroides* O.U.001 (DSM 5864), and aims to improve hydrogen yield per feedstock, decrease the necessity of resetting the production system by cleaning and re-inoculation with fresh bacterium, due to prevalence of other microorganisms by time, decrease maintenance costs in contrast to non-immobilized systems. The growth and hydrogen production performances of these combinations were investigated on acetate and glutamate as the carbon and nitrogen sources respectively.

II. Experimental Set-up and Procedure

Rp. palustris (DSM 127) and *R. sphaeroides* O.U.001 (DSM 5864) were obtained from Deutsche Sammlung von Mikroorganismen und Zellkulturen GmbH, Braunsweig Germany). *R. capsulatus* hup- (YO3) was obtained during our previous studies (Öztürk et.al., 2006). Following growth until an OD_{660} value of 2.0, cultures were transferred several times by 10% inoculation to fresh media to ensure adequate activity of the bacteria. For bacterial growth and hydrogen production experiments, standard BP media (Biebl et.al., 1981) supplemented with 20 mM acetate and 10 mM glutamate and 40 mM acetate and 2 mM glutamate as carbon and nitrogen sources were used respectively. Anaerobic environment was established by purging the air with argon, and illumination of 2000 lux was provided using tungsten lamps. The temperature was maintained at 30 °C with a cooling incubator. Single cultures and double and triple co-cultures of the strains were immobilized and experiments conducted in 150 mL round reactors on 40 mM/2 mM Acetate/Glutamate medium, indoor and outdoor under anaerobic conditions. For preparation of the production systems, *R. capsulatus* hup- (YO3), *Rp. palustris* (DSM 127) and *R. sphaeroides* O.U.001 (DSM 5864) cultures grown on defined growth medium until OD is 2.00 at 660 nm were concentrated by

centrifugation at 9000 rpm for 20 minutes. Bacterial pellets were collected and resuspended into water to obtain a cell concentration of 10.0 mg DCW/mL. 8% agar was prepared. The agar-bacteria matrix was prepared by mixing hot agar mixture with an equal volume of bacteria-water mixture and pouring into the reactors, solidifying the mixture on the inner lateral surface of the reactor. The final concentration of bacteria was 5 mg/mL dry cell weight gel culture per volume of agar. The single-cultures included 5.0 mg DCW/mL gel culture from either of the three strains, 30 ml each, the double co-cultures included 2.5 mg DCW/mL gel culture each from two of three strains, 15 ml from each, and the triple co-cultures included 5 mg DCW/mL gel culture each from all three strains. Reactors were filled with 120 mL of 40 mM/2 mM Acetate/Glutamate medium and hydrogen production experiments were performed indoors and outdoors. Indoor experiments were conducted under 2000 lux illumination by a tungsten lamp. Temperature for the indoor and outdoor experiments was set to 30ºC. Hydrogen production has continued for 25 days. Gas composition and pH measurements were performed at every 24th hour. The outdoor experiments were performed between October, 17, 2020 and December, 15, 2020.

III. Analysis

OD measurements for dry cell weight calculations were performed at 660 nm by a Shimadzu UV 1800. pH measurements were carried out by a Mettler Toledo 3311 pH meter. Organic acids were detected and quantified by a Shimadzu LC-20A Prominence HPLC system using an Alltech IOA-1000 (300 mm x 7.8 mm) column and an UV-VIS detector (Shimadzu SPD-20AV) at 210 nm wavelength. Gas composition analysis was performed using an Agilent Technologies 6890N GC device utilizing a SupelcoCarboxen 1010 gas column.

IV. Results and discussions

Representative results for the behavior of single and co-cultures are presented in Figure 1, whereas Table 1 summarizes performance comparisons between single cultures and co-cultures.

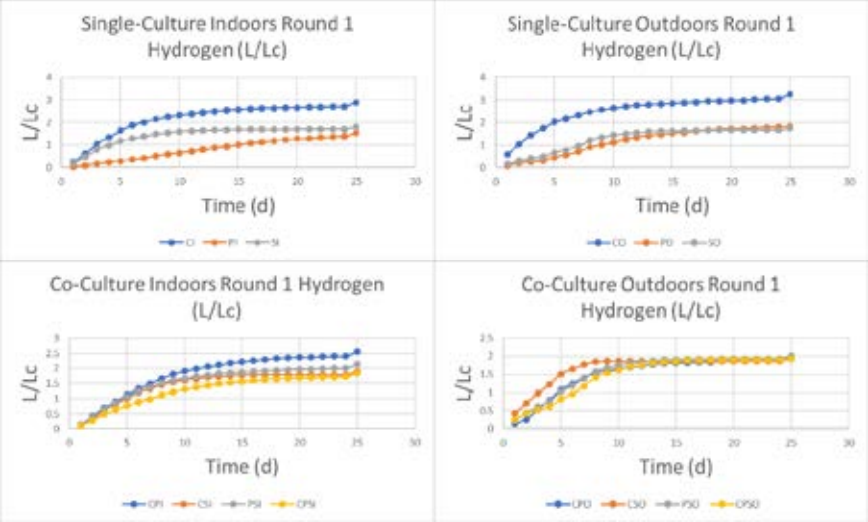


Fig. 1: H_2 Production for single-cultures, double and triple co-cultures of *R. capsulatus* hup- (YO3), *Rp. palustris* (DSM 127) and *R. sphaeroides* O.U.001 (DSM 5864) in an immobilized setting, cultured on hydrogen production media at 30 °C under anaerobic conditions and continuous illumination at 2000 lux for indoor, and under sunlight for outdoor, the first round. C: *R. capsulatus* hup- (YO3) P: *Rp. palustris* (DSM 127) S: *R. sphaeroides* O.U.001 (DSM 5864) I: Indoor, O: Outdoor.

Tab. 1: T.H_2: Total hydrogen production (L/Lc), H_2Y: hydrogen yield (mol H_2/mol Acetate), H_2P: hydrogen productivity (mmol H_2/L.h) and SCE: substrate conversion efficiency (%) comparison single-cultures, and double and triple co- cultures of Immobilized PNS Bacteria, the first round. C: *R. capsulatus* hup- (YO3) P: *Rp. palustris* (DSM 127) S: *R. sphaeroides* O.U.001 (DSM 5864) I: Indoor, O: Outdoor.

	CI	*PI*	*SI*	*CO*	*PO*	*SO*	*CPI*	*CSI*	*PSI*	*CPSI*	*CO*	*PO*	*SO*	*CPSO*
T.H_2	2.88	1.53	1.81	3.27	1.83	1.74	2.56	1.89	2.13	1.83	1.97	1.95	2.00	1.94
H_2Y	3.21	1.71	2.02	3.65	2.04	1.94	2.85	2.11	2.38	2.04	2.20	2.17	2.24	2.17
H_2P	0.357	0.143	0.224	0.406	0.170	0.161	0.238	0.175	0.198	0.170	0.245	0.242	0.249	0.241
SCE	80.4	42.9	50.6	91.3	51.1	48.5	71.4	52.7	59.5	51.0	55.1	54.4	56.0	54.3

Experiments were run in 2 cycles. Although the cultures were prepared at pH 6.3, a pH increase to 7.4-8.0 was observed at the first day of the experiments. pH tended to increase in the following 2-3 days, then tended to decrease. Even though bacterial stress was minimized by keeping the bacteria at suitable temperature for longer periods of time prior to pouring, still the bacterial stress, even though minimized, might be responsible for this initial abnormal pH rise. At the end of the experiments, pH values decreased to 6.6-7.2 interval. Gas chromatography results revealed high hydrogen purity, with an average 81.4 % non-air hydrogen content in

average of all measured samples. From the beginning of the experiments, till the end, high hydrogen content, reaching 99 %, was observed. Total hydrogen production was observed the highest for outdoors and indoors single culture *R. capsulatus* (YO3) with 3.27 and 2.88 (L/Lc), then for Indoor co-culture of *R. capsulatus* (YO3) and *Rp. palustris* with 2.56 (L/Lc), then for Indoor and Outdoor co-culture of *Rp. palustris* and *R. sphaeroides* with 2.13 and 2.00 (L/Lc). A higher production with co-cultivation with respect to single cultures of constituent bacteria was observed only for the *Rp. palustris* and *R. sphaeroides* couple. For other co-cultivated bacterial mixtures, hydrogen production performances between the individual performances of the constituent strains or lower were observed. Hydrogen yields were found between 3.21 and 1.71 mol H_2/mol Acetate and hydrogen productivity values were ranged between 0.406 and 0.0447 (mmol H_2/L.h).

V. Conclusions

In the experiments, *R. capsulatus* (YO3) single culture was found superior to all other groups. The benefits of co-cultivation except for the co-cultures of co-culture of *Rp. palustris* and *R. sphaeroides* were not observed. For single cultures, *R. capsulatus* (YO3) and *Rp. palustris* has performed better in outdoors, whereas *R. sphaeroides* has performed better in indoors. For Co-cultures, *Rp. palustris* has performed better in outdoors. Whereas *R. sphaeroides* has performed better in indoors with *R. capsulatus* (YO3) as couples. *Rp. palustris* and *R. sphaeroides* has performed better in indoors. Whereas *Rp. palustris* and *R. sphaeroides*, together with *R. capsulatus* (YO3), has performed better in outdoors. Hence *R. capsulatus* (YO3) was found to be best producing strain, which is probably inhibited by the presence of other strains in an immobilized setting, *Rp. palustris* and *R. sphaeroides* do benefit from the presence of each other with respect to hydrogen production in an immobilized setting, and *Rp. palustris* and *R. sphaeroides* may dominate *R. capsulatus* (YO3). Suspension culture involves bacteria growing together, dynamically constituting a composition. However, the immobilized setup has a fixed bacterial composition due to arrested growth. This lack of dynamism may be responsible for the inability to observe the concerted benefits of a co-cultivated suspended bacterial culture. However, the immobilized setting has its own advantages, such as avoiding bacterial wash out, hence the ability to utilize wastes, eliminated lag phases, since the cultivation starts with fully grown bacteria and the ability to reuse the bacteria. The new reactor system designed shows benefits in productivity and is promising. Also, even though co-cultivation was not found to yield higher hydrogen production in comparison to single cultures in general, the co-culture of *Rp. palustris* and *R. sphaeroides*, has yielded significantly higher hydrogen production than the single cultures of *Rp. palustris* and *R. sphaeroides* alone. Additional studies with different temperature, illumination, and substrate concentration parameters need to be carried out for deeper understanding of the mechanism of hydrogen production in immobilized co-cultures in order to further improve and standardize hydrogen yields and productivities. Also investigating hydrogen production by immobilized PNS bacteria in a bio-film format would be beneficial, since bio-film type of immobilization may be applied to larger scale production setups and reactors.

References

Basak, N., Jana, A.K., Das, D., Saikia, D., Photofermentative molecular biohydrogen production by purple-non-sulfur (PNS) bacteria in various modes: The present progress and future perspective, International Journal of Hydrogen Energy, Volume 39, Issue 13 6853-6871 (2014).

Biebl, H., Pfennig, N., Isolation of Members of the Family Rhodosprillaceae, M.P. Starr, H. Stolp, H.G. Trüper, A. Balows, H.G. Schlegel (Eds), The prokaryotes 267-273 New York: Springer-Verlag (1981).

Fibler, J., Kohring, G.W., Giffhorn, F., Enhanced hydrogen production from aromatic acids by immobilized cells of Rhodopseudomonas palustris, Appl Microbiol Biotechnol, 44 43-46 (1995).

Öztürk, Y., Yücel, M., Daldal, F., Mandacı, S., Gündüz, U., Türker, L., Eroğlu, İ., Hydrogen production by using Rhodobacter capsulatus mutants with genetically modified electron transfer chains, International Journal of Hydrogen Energy, Volume 31, Issue 11 1545-1552 (2006).

Tiang, M. F., Hanipa, M. A. F., Abdul, P. M., M.d. Jahim, J., Mahmod, S. S., Takriff, M. S., Lay, C., Reungsang, A., Wu, S., Recent advanced biotechnological strategies to enhance photo-fermentative biohydrogen production by purple non-sulphur bacteria: An overview, International Journal of Hydrogen Energy, Volume 45, Issue 24 13211-13230 (2020).

Tsygankov, A., Hydrogen production by purple bacteria: immobilized versus suspension culture, J. Miyake, T. Matsunaga, A.S. Pietro (Eds.), Biohydrogen II, Elsevier Science Ltd, Amsterdam 229-243 (2001).

Van Mierlo, J., & Maggetto, G., Hydrogen as an energy carrier, KVAB (Koninklijke Vlaamse Academie van België voor Wetenschappen en Kunsten) – BACAS (Royal Belgian Academy Council of Applied Sciences) – CAWET (Comité van de Academie voor Wetenschappen en Techniek), 42pgs KVAB (Koninklijke Vlaamse Academie van België voor Wetenschappen en Kunsten) BACAS (Royal Belgian Academy Council of Applied Sciences) CAWET (Comité van de Academie voor Wetenschappen en Techniek), 42pgs (2006).

Zhang, C., Zhu, X., Liao, Q., Wang, Y., Li, J., Ding, Y., Performance of a groove-type photobioreactor for hydrogen production by immobilized photosynthetic bacteria, Int J Hydrogen Energy, 35 5284-5292 (2010).

Low-Cost Membrane-Electrode-Assembly (MEA) Production for Direct Borohydride Fuel Cell

Kürşat Can Ata[1], Ipek Çağlayan[1], Anıl Can Türkmen[1*], Tuncay Kadıoğlu[2], R. Gültekin Akay[2] Cenk Çelik[1]
[1]Mechanical Eng. Dept., Kocaeli University, Umuttepe Campus, İzmit/Kocaeli
[2]Chemical Eng. Dept., Kocaeli University, Umuttepe Campus, /İzmit/Kocaeli
* E-mail: anilcan.turkmen@hotmail.com

Abstract
In this study, the effect of Pd coatings made on Nickel foam on the efficiency was investigated by using SPEEK/PBI blend membranes in DBFC. Single cell tests have been carried out to see the effect of coatings' effectiveness under different conditions on fuel cell performance. As a result of the examination, the best performance in the fuel cell was obtained with a power density value of 120 mW / cm^{-2} applied with 4 V, 1 minute coating time. When looking at polarization and power curves of uncoated commercial Nickel foam and only Pd coated Nickel foam, it was seen that the performance of Pd coated Nickel foam was higher in the fuel cell with laboratory produced SPEEK/PBI blend membranes.

Keywords: Direct Borohydride Fuel Cell, Electrocoating, Metal Foam, SPEEK/PBI Membrane, Hydrogen Energy.

I. Introduction

Fuel Cell research community and the industry both have focused on some specific applications and the available sources for fuel cell technologies especially in the recent decades. For Turkey in particular, technologies utilizing boron containing compounds are important since a vast share of world boron sources are located in the country. Direct Borohydride Fuel Cells (DBFC) is one of the most promising technologies in this sense. Similar to the other classes of fuel cells, membrane is one of the key components to the commercialization of DBFCs. Nafion® is still the first choice and industry standard because of its Teflon like fluorinated backbone and related high chemical-mechanical-thermal stabilities for both PEMFCs and DMFCs. Liu and coworkers used Nafion® in the DBFCs first and almost all of the studies using a CEM related with DBFC development still uses Nafion® (Ma et al, 2001). But Nafion® which is under the CEM class has also well-known drawbacks such as being very expensive (an important barrier for commercialization) and high permeability to reactants because of its well separated channels and the dependence of water. In membranes ion transport occurs according to the principle called “Donnan Exclusion” which states that only the opposite charged ions passes through a membrane with a positive or negative fixed charge (Prakash et al, 2004).

Ata et al. reported that using SPEEK-based blend or composite membranes as CEM for DBFC, have good results. First results showed that SPEEK-Cloisite® 30B composite membrane has given 40 mW/cm^2 power density value which is higher than pure SPEEK membrane (35 mW/cm^2). The proton conductivities of the final composite membranes were close to bare SPEEK membranes which are 0,065 and 0,075 S/cm for SPEEK-Cloisite ® 30B and pristine SPEEK, respectively (Ata et al, 2019). Secondly, Akay et al. investigated SPEEK/PBI blend membranes for DBFC and reported also valuable results. With low blending ratios of 5% and 10% mechanically strong blend membranes were successfully fabricated without sacrificing much of the conductivity. The single cell tests were performed. Despite the decrease in ionic conductivity and increase in fuel crossover with increasing blend ratios the peak power densities were observed to increase (Akay et al, 2018).

Metallic foams, which stand out with their mechanical, conductivity and functional properties in the developing material technology, are increasing in their use in energy generation systems. The use of renewable energy sources in liquid fuel cells is interesting. When the researches are examined, the studies are examined according to different basic metal and usage area.

It was stated by Yang et al. That it showed high catalytic activity and good stabilization in H_2O_2 and KOH strong oxidizing and corrosive solution with electrode prepared by electrocoating of Ni microparticle assembly on Ni foam substrate without three-dimensional carbon and binder. The power density of 19.4 mW/cm^2 is reported directly with peroxide-peroxide fuel cell using Ni / Ni-foam as an anode (Yang et al. 2013).

The background of the use of metal foams in fuel cells lies in the fact that the types of these materials with open-pore structure increase the surface area where the electrochemical reaction process takes place so that the catalyst performs more effectively and as a result, an increase in electrical efficiency. The fact that the effect of different metal foam structures on the process efficiency in the case of technological research has come today is seen as a gap to be filled. Within the scope of the project planned to eliminate the deficiency in the current situation, it is planned to increase the current state in electrical efficiency by revealing the most effective electrochemical reaction situation that can be obtained as a result of the use and tests of metal foams as a fuel cell component.

II. Experimental Set-up and Procedure

PEEK has some thermal and chemical stability problems at high degree of sulfonations (DS). Therefore, an approach to optimize the DS by post-sulfonation of polyetheretherketone (PEEK) and then blending with a polybenzimidazole (PBI) was used to improve its chemical and thermal properties were used. SPEEK was synthesized by post-sulfonation controlling the time and the temperature of the sulfonation reaction to achieve different and optimum degree of sulfonations (DS). Concentrated sulfuric acid was used as the sulfonating agent. All blended membranes were prepared by solvent-casting method by using dimethylacetamide (DMAc). Blending was performed by first dissolving the polymers separately in solvents and then by mixing in pre-determined ratios.

In this study, membranes prepared by different degree of sulfonation processes with same SPEEK/PBI polymer blending (%10, Akay et al.) ratios. The membranes were characterized for their proton conductivity, rate of DS, ion exchange capacity (IEC), water uptake, the reactant permeability tests and single cell tests.
The anode electrode coating process was carried out with the following process steps. With 20 g degreasing chemical and 350 ml degreasing solution prepared with pure water cause the surface of the foam material had to purified from oils and chemicals. The positive end of the DC power supply in the stainless-steel anode, the negative end is connected to the foam material and degreasing is performed by giving 4 V voltage from the power supply for 20 seconds. After the degreasing process, the metal foam is cleaned from the degreasing bath by washing with pure water. Then the metal foam part is dried with the help of heater and compressor and made ready for the next process. Ni foam is removed from the oxide layer on its surface by immersing in 11,2 gr Ammonium bifluoride, 175 ml Nitric acid and 350 ml etching bath prepared with pure water for 20 seconds. After the etching process, the metal foam is washed with pure water and purified from the etching bath. Then the metal foam part is dried with the help of heater and compressor and made ready for the next process. Before proceeding to another stage, the foam material is weighed to determine the weight before coating. The platinum anode immersed in the Pd solution between 50-55 ° C is connected to the positive end of the DC power supply, and the foam material is connected to the negative end of the power supply, and Ni foam is coated at different coating times by applying 4 V voltage from the power supply. After the coating process, the metal foam is cleaned from the coating bath by washing with pure water. The metal foam is then dried with the help of a heater and a compressor and weight measurement are taken after coating.

III. Results and discussions

In single-cell test studies, in the component parts of the fuel cell: 5x5x0.5 cm Pd coated Nickel foam for the anode part, 1mg/cm^2 Pt/C catalyst coated diffusion layer for the cathode part of the fuel cell, fuel cell solution (% wt.) 4% $NaBH_4$ + 12% NaOH was fed membrane as Nafİon 117 and finally 0.3L/min dry oxygen oxidant. Experiments were carried out under a certain conditioning process. The analyzed and discussed a methodology for the estimation of some parameters of the model of the cell's polarization curve and the behavior of the parameters against the basic argument (cell operating temperature). Due to the limited number of test points and especially the experiments only using a MEA, it was not possible to propose general analytical correlations linking parameters and operating temperature, the potential of the analysis method and the ease of the experiments allow it to be applied to a broad MEA typology (Santarelli et al, 2006).

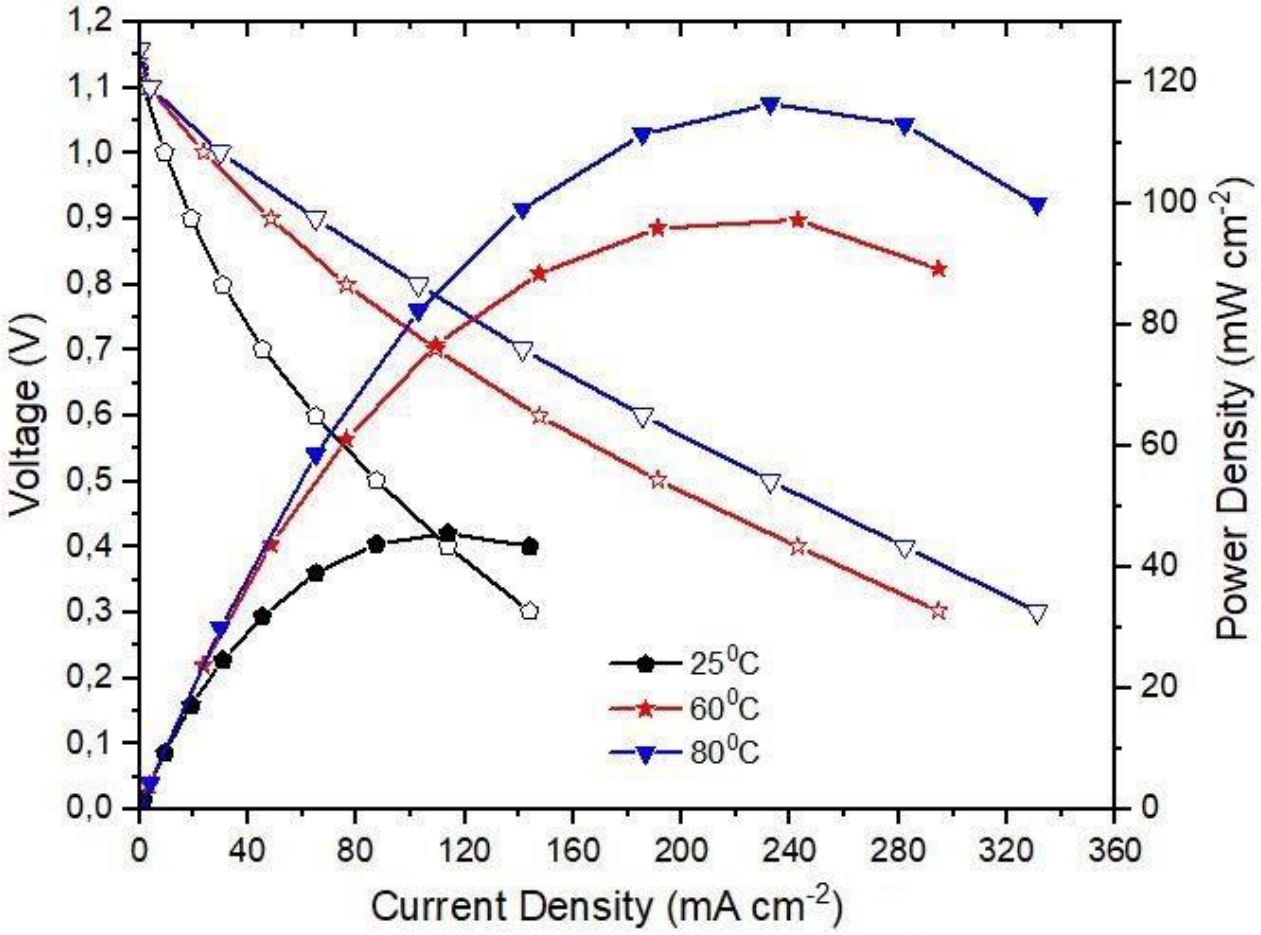


Fig. 1: Single cell results with different operation temperatures.

V. Conclusions

In the study, it was tried to contribute to the studies on the use of metal foam by considering the diffusion layers made for PEMFC and DBFC's in the literature. When the studies were observed, this study was carried out in order to fill the gap in the studies on this subject in the literature on the use of Ni foam. Looking at the polarization curves, it is seen that the current density increases as the temperature increases. The reason for this situation is that the efficiency of the fuel cell increases due to the acceleration of proton conductivity and reduction reactions as the temperature increases. Compared to the others, the SPEEK / PBI membrane fuel cell single cell performance used with the Pd coated nickel foam has shown a positive effect on the performance of the Pd coated nickel foams compared to the single cell tests.

Acknowledgements

This study was supported by the Scientific and Technological Research Council (TUBITAK) of Turkey (Grant id: 215M255) and by Kocaeli University Scientific Research Projects (BAP) Unit (grant id: BAP-2015-038). The support and fundings of these institutions are gratefully acknowledged.

References

Akay RG, Ata KC, Kadıoğlu T, Çelik C, 2018. Evaluation of SPEEK-PBI Blend Membranes for Possible Direct Borohydride Fuel Cell (DBFC) Application. International Journal of Hydrogen Energy 43:18702-11.

Ata KC, Kadıoğlu T, Türkmen AC, Çelik C, Akay RG, 2019. Investigation of the effects of SPEEK and its clay composite membranes on the performance of Direct Borohydride Fuel Cell. International Journal of Hydrogen Energy 45(8), 5430-37.

Ma J, Choudhury, NA, Sahai Y, 2001. A Comprehensive Review of Direct Borohydride Fuel Cells, Renewable and Sustainable Energy Reviews 14:183–199.

Prakash P, Hoskins D, Sengupta AK, 2004. Application of Homogeneous and Heterogeneous Cathion-Exchange Membranes in Coagulant Recovery from Water Treatment Plant Residuals Using Donnan Membrane Process, Journal of Membrane Science, 237:131–144.

Santarelli M. G., Torchio M. F., Cochis P., 2006, Parameters estimation of a PEM fuel cell polarization curve and analysis of their behavior with temperature, Journal of Power Sources, 159, 824–835.

Yang F., Kui Cheng, Xiao Xue, Jinling Yin, Guiling Wang, Dianxue Cao, 2013, Three-dimensional porous Ni film electrodeposited on Ni foam: High performance and low-cost catalytic electrode for H2O2 electrooxidation in KOH solution, Electrochimica Acta 107,194–99.

A two-stage metal hydride compressor based on commercial alloys

[1*]Jussara Barale, [2]Federico Nastro, [1]Paola Rizzi, [2]Carlo Luetto, [1]Marcello Baricco
[1] University of Turin, Department of Chemistry and Inter-departmental Center Nanostructured Interfaces and Surfaces (NIS), INSTM, Via P. Giuria 7, Torino, 10125, Italy
[2] Tecnodelta S.r.l., Via Francesco Parigi 5H, Chivasso (To), 10034, Italy

* E-mail: jussara.barale@unito.it

Abstract
A two-stage metal hydride compressor (MH-C) based on commercial alloys has been realized. The MH-C compresses H_2 from 30 to 250 bar, filling cylinders at 200 bar. Compression occurs between room temperature and 150 °C. Hydrogen is directly supplied to MH-C by an electrolyser (EL). MH-C is inserted in a small hydrogen refuelling station and can be easily integrated with a booster downstream to reach higher pressures for H_2 on site. The compress gas is used for the supply of a hydrogen powered drone.

Keywords: Metal hydride compressor, hydrogen refuelling station, hydrogen powered drone, metal hydride

I. Introduction

Nowadays, drones are used in a wide range of applications, from civil to military. It is therefore of interest to develop systems with increasing performances, in terms of energy efficiency and running time. In this regard, the use of Fuel Cell (FC) is a possible solution, since hydrogen (H_2) has a higher energy density compared to batteries (Belmonte 2018). In the framework of the Clean-DronHy project, supported by Regione Piemonte (Italy), a drone driven by H_2 has been realized. Thanks to compressed H_2, about 70 min of continuous flight is reached, showing the feasibility of FC drones. In addition, a H_2 refuelling station (H2RS) has been developed. Hydrogen is produced by an EL, driven by photovoltaic panels. Afterwards, it is compressed by a two-stage metal hydride compressor (MH-C) and a booster. Finally, it is stored as compressed gas to supply the drone.
The use of metal hydrides (MH) to compress H_2 is an innovative technology (Lototskyy 2014), that exploits the reversible reaction between H_2 and a metal compound (M) to produce a hydride with suitable heat exchanges. The thermodynamics of the equilibrium is characterized by H_2 pressure (p), concentration (c) in the solid phase and temperature (T), which are described in pcT-diagram (Lototskyy 2014). Based on the thermodynamics of the equilibrium, compression occurs since M can absorb H_2 at low pressures and low temperatures (T_{low}), forming MH. Then, MH is heated up at the high temperature (T_{high}) and H_2 is released at significantly higher pressure. Compared to conventional mechanical compressors, MH-C has the advantage to be not noisy and to not require a frequent maintenance. Then, it has the possibility to use waste heat instead of electricity (Lototskyy 2014).
For the building of the MH-C, two commercial intermetallic compounds have been selected and characterized. A (LaCe)Ni_5 alloy is used in the first stage, while the so called Hydralloy-C5 ($TiMn_2$-based alloy) has been apllied in the second one. The Hydralloy is rather sensitive to gas impurities, while the (LaCe)Ni_5 compound is much less, resulting suitable to be supplied directly by the EL, since impurities of oxygen and water are present in the gas stream. After a preliminary study of alloys, the MH-C has been realized and integrated with the EL and the booster. Almost 80 cycles of compression have been perfomed and a preliminary optimization of the process has been reached. The present work shows the results of testing the H2RS, with a focus on MH-C performances.

II. Experimental Set-up and Procedure

II.I Alloys study

The investigation of crystal phases present in the commercial intermetallic compounds an analysis has been performed by Powder X-Ray Driffaction (PXD), using a X'Pert Pro diffractometer equipped with Cu-K source in Debye-Scherrer geometry. For the check of the composition, an elemental mapping has been obtained through the SEM instrument Zeiss EVO 50 XVP-LaB6, with an Oxford Instrument INCA Energy 250 for EDX analysis. Finally, thermodynamic properties have been determined in a volumetric Sievert's type apparatus commercialized by AMC (Pittsburg, USA).

II.II H_2 refuelling station based on the MH-C

Figure 1 shows the H2RS realized, from the electrolyser to the H_2 bottle to be installed in the drone. The EL produces H_2 up to 30 bar, which is directly compressed up to 250 bar by the MH-C. Then, it can directly fill the bottle at 200 bar or it can be further compressed up to 300 bar by the booster. The EL has a H_2 flow of about 250 Nl/h. During the tests, it was supplied by grid current, but it could be also supplied by photovoltaic panels. About 880 g of (LaCe)Ni_5 and 700 g of Hydralloy have been placed inside MH-C reactors. The MH-C works between RT (30 °C) and 150 °C. The *Thermonoil* oil is used as thermal fluid, and it is warmed up thanks to a resistance controlled by a thermostat and cooled by a van. The system is equipped with pressure sensors and thermocouples to follow the evolution of pressure and temperature as a function of time. The drone uses a type IV bottle of 3 l, and, to evaluate the influence of the hydrogen flow on the volume of the cylinder, also 0.5 and 1.1 l bottle have been tested.

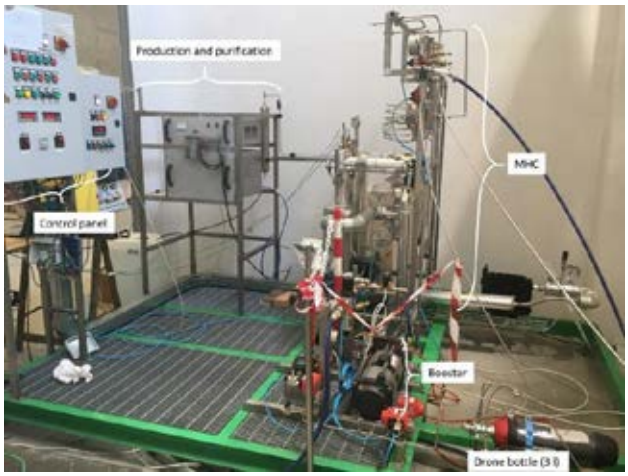


Fig. 1: Integrated Clean-DronHy H2RS

III. Results and discussions

The commercial compositions of the alloys was confirmed and no secondary phases were detected. The study of the alloys resulted in an activation method that can be performed in the same conditions for both alloys, i.e. 6-10 cycles of absorption/desorption at 150 °C with 50 bar of H_2. The thermodynamic study allowed to build a Van't Hoff plot (Figure 2). The enthalpy, ΔH, and entropy, ΔS, of absorption and desorption have been obtained, as reported in Figure 2. Data have been used to predict the operability of the alloy at the defined T_{low} (RT) and T_{high} (150 °C). It was found that H_2 can be compressed from 25 to 200 bar, observing a rather fast absorption kinetics of the $(LaCe)Ni_5$ in plant working conditions (i.e. 25 °C and 23 bar).

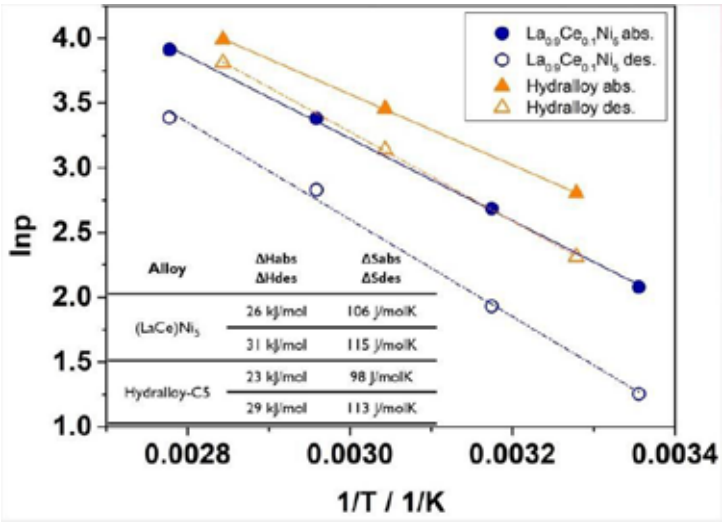


Fig. 2: Van't Hoff plot obtained by the pcT curves registered on $(LaCe)Ni_5$ and Hydralloy used to determine thermodynamic data.

After alloys study, the hydrogen refuelling station has been realized as described in section II.II. The bottle of 3 l was charged at 300 bar, coupling the MH-C and the booster, exploiting an H_2 flow of 151 Nl/h. After a primary optimisation of the MH-C process, an average time for a cycle of compression (i.e. from the absorption in stage 1 to the filling of the cylinder) of 47 min has been obteined. The maximum output flow observed from the MH-C was 164 Nl/h, with an average flow of 85 Nl/h charging the 3 l cylinder at 200 bar. The Hydralloy, is able to release H_2 up to 250 bar, resulting in a final compression ratio (p_{out}/p_{in}) of about 9.

Different bottle volumes (0.5, 1.1 l) have been also filled at 200 bar, to evaluate the influenze on H_2 flow. It was observed that the flow progressively increased with tank volume (Fig. 3).

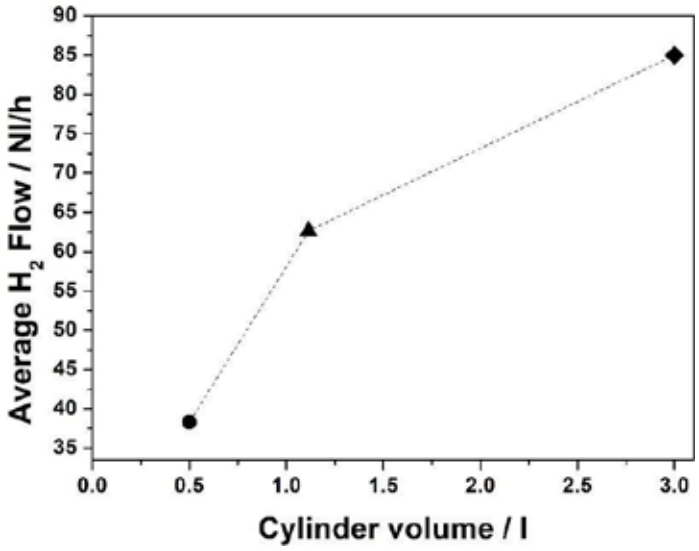


Fig. 3: Average flow of H_2 observed filling a cylinder volume of 0.5, 1.1. and 3.0 l.

Finally, it was estimated a power consumption for the H2RS of about 600 W, with only ≈38 W (depending on the alloy) linked to the reaction of absorption/desorption.

V. Conclusions

A two-stage metal hydride compressor based on commercial alloys has been realized and integrated in a small-scale hydrogen refuelling station. It is supplied directly by an alectrolyser at 25-28 bar, compressing H_2 up to 250 bar between RT and 150 °C. For the filling cylinder at 200 bar, an average flow of 85 Nl/h was observed, while 151 Nl/h have been reached coupling the MH-C with a booster filling hydrogen up to 300 bar. This small-scale prototype has shown the potential of MH-C in H_2 refuelling station, thanks to their low power consumption and easy handle. Future works are related to the cycling of the system and a possible optimization of the process.

Acknowledgements

Authors acknowledge Regione Piemonte for the financial support.

References

N. Belmonte, S. Staulo, S. Fiorot, C. Luetto, P. Rizzi, M. Baricco, “Fuel cell powered octocopter for inspection of mobile cranes: Design, cost analysis and environmental impacts”, Appl. Energy, 215, 2018, 556-565.

M. V. Lototskyy, V. A. Yartys, B. G. Pollet, R.C. Bowman, “Metal hydride hydrogen compressors: A review”, Int. J. Hydrogen Energy, 39, 2014, 5818-5851.

Environmental Effects as a Result of The Use of Fuel Cell and as Hydrogen Alternative Fuel In UAVs

Duran ÇALIŞIR[1*], Selçuk EKİCİ[2] , Adnan MİDİLLİ[3] , Tahir Hikmet KARAKOÇ[1]
[1] Eskişehir Technical University, Faculty of Aeronautics and Astronautics Science, Eskişehir, Turkey
[2] Iğdır University, Department of Aviation, Iğdır, Turkey
[3] Yıldız Technical University, Faculty of Engineering, Mechanical Engineering Department, Istanbul, Turkey

* E-mail: dcalisir@eskisehir.edu.tr

Abstract
The use of UAVs in the aviation industry has been increasing more and more recently. Today, as a result of different climate change, unusual environmental events are increasing. Researches on hydrogen as a clean and alternative fuel in aircraft have been increasing in recent years. In this study, the environmental effects of using Polymer Electrolyte Membrane (PEM) fuel cells in a UAV were investigated. Firstly, a literature search was conducted on the use of fuel cells in UAVs. In the second stage, the environmental effects resulting from the use of the PEM fuel cell in the power plant of an UAV are specified.

Keywords: Aviation, unmanned aerial vehicle (UAV), hydrogen fuel cell, environmental impact.

I. Introduction

It is becoming widespread to use hybrid power systems to increase the flight endurance of IHAs. In order to increase efficiency in hybrid systems. The first use in this direction took place in military UAVs between 1991 and 2001 McConnell (2007). Fuel cells are modelled in a way that the power consumption is optimal for long-time flights Bradley at all (2009). There are applications such as installing photovoltaic panels on the wing surfaces and adding fuel cells in order to increase the flight time by strengthening the power group in UAVs Gadalla and Zafar (2016). In addition to PEM fuel cells that use H2 as fuel to generate the electrical energy required for UAVs Dudek at all (2013); Ozbek al all (2020) DMFC fuel cells that use methanol directly as fuel are also encountered Gonzalez at all (2019). In recent years, there have been studies on fuel cells using NH3 (ammonia) as fuel Siddiqui and Dincer (2018). Another energy source in fuel cells is the H2 fuel obtained from the hydrolysis of NaBrH4 Lapena at all (2017). "Aerostak" shaped PEM-H2 fuel cells play a very useful role in providing uninterrupted energy, especially in the response of lithium polymer batteries under dynamic loads Verstraete at all (2014). During cruise mod flight in UAVs and different temperatures conditions, traditional H2-fueled PEM-FCs can perform better than Lithium-ion, Ni-MH batteries Bayrak at all (2020). Recently developments in PEM fuel cells, it is seen as a suitable power unit in UAVs due to its advantages such as providing direct electrical energy, decreasing their size and weight and it can be easily perform 2-hour flights Kim and Kwon (2012); Depcik at all (2020). The costs and environmental effects of fuel cells and hybrid cell systems of small UAVs, which are used in many areas, have recently been the subject of research Belmonte at all (2018); Baroutaji at all (2018); Sürer at all (2018). Life cycle assessment studies on hydrogen and alternative fuels used in aviation in recent years has started to close the gap in the field. Bicer and Dincer (2017).

II. Goal and Scope

In this study, the environmental impacts coming up during the test flights of the UAV "Hydra", designed by Eskişehir Technical University Anatolia Aero Design Team within the scope of the project numbered 19ADP162, were investigated Yalin (2019) Ozbek at all (2021). Some of the main features of this UAV are given in the table below:

Table 1: Hydra UAV main specification

Characteristics	Description
Wingspan	2.8 meter
Length	1.6 meter
Stall speed	10 m / s
Cruise speed	16 m / s
Maximum flight time	6 hours
Landing Gear	No landing gear, thrown from the hand and land on the body
Maximum take-off weight	6.5 kg

The energy source of this UAV has a hybrid system. In this study, power groups are defined as A and B configurations in analysis and comparisons. These configurations are described as follows:

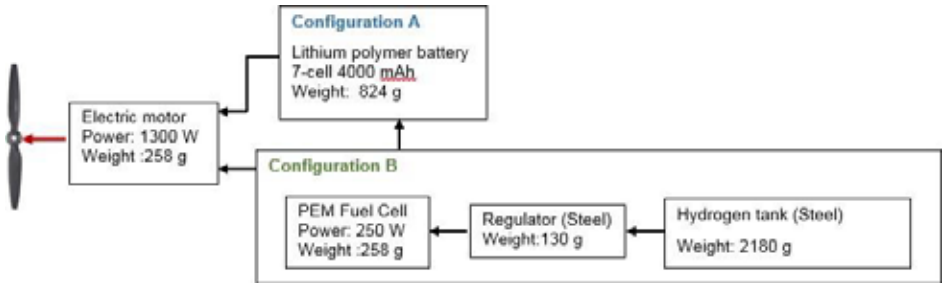


Fig. 1: Hydra UAV power group configurations

A life cycle assessment has been conducted to reveal the environmental impacts of the UAV during the 6-hour test flight. While applying the LCA method, the process from cradle to gate was taken into consideration according to ISO 14040/14044 standards. The cradle-to-gate process covers the stages of raw material procurement, manufacturing and usage. Hydra's test flight area is in the north-north west direction from top of the Bozdağ, which is located in the north with respect to Eskişehir city center. The flight time is 1.5 hours in total. This described flight took place 4 times in the same conditions. The assumptions made according to this scenario are as follows: There is no wind on the route of the entire flight zone and during the entire flight, the air temperature is on average 15 ° C.

III. Analysis

The second and most intensive phase of the LCA method to detect environmental impacts is the inventory analysis phase. The data generated during the raw material procurement, manufacturing and use (test flight) process of the UAV were collected. While collecting data, the inputs and outputs of each process were considered. Inventory analysis of the collected data was made with SimaPro 9.1 software. Ecoinvent 3.6 database was used in inventory analysis. Information about the weight, quantity, component, supply method, energy consumed of all kinds of materials used in the life cycle of the UAV constituted the source of the data in the inventory analysis. After the inventory analysis phase, the impact analysis phase was started. Hot spot analyses were carried out during the processes determined within the scope of the study. Calculations were made according to CML-IA Baseline and ReCiPe method. Ten impact categories has been selected for the CML-IA Baseline method. These are abiotic depletion, abiotic depletion (fossil fuels), global warming (GWP100a), ozone layer depletion (ODP), human toxicity, fresh water aquatic ecotoxicity, terrestrial ecotoxicity, photochemical oxidation, acidification and eutrophication. For the ReCiPe method, 3 impact categories were selected as human health, ecosystems and resources. In order to make a comparison according to impact categories, two different power group options have been considered for the UAV. The first option (configuration A) consists of a Li-Po battery and an electric motor. The second option (configuration B) is the addition of the H2 fuelled PEM fuel cell components in addition to the first option.

IV. Results and discussions

After the impact analysis according to the LCA methodology, the results obtained according to two different power group (configuration A and B) options were compared. Percentage ratio was used to compare the results. The lower percentage impact categories and amounts of configuration A are as follows: Abiotic depletion: 96.88, Abiotic depletion (fossil fuels): 98.24, Ozone layer depletion (ODP): 87.56, Human toxicity: 89.90, Fresh water aquatic ecotox: 96.78.The effect categories and amounts of the B configuration lower in percentage are as follows: Global warming (GWP100a): 93.05, Terrestrial ecotoxicity: 93.65, Photochemical oxidation: 98.77, Acidification: 93.31, Eutrophication: 89.19. When the environmental impacts are compared, the results of environmental impact categories such as Global warming, Terrestrial ecotoxicity, Eutrophication are better in B configuration, where the hybrid system is used according to the A configuration. These results have been obtained because the energy source input of the hybrid system is hydrogen as a clean and environmentally friendly fuel and the main output is H2O. Ozone layer depletion and human toxicity effects in A configuration are remarkably low, especially due to the use of materials such as polystyrene foam (EPS) and epoxy resin during the procurement and manufacturing phase. Especially, Polystyrene foam and the electricity used in its processing have a high effect on the results of hot spot analysis in the production process of the UAV. Although the negative effects of carbon fibre materials are high, the hot spot effect appears to be lower due to the very low amounts used in the manufacturing phase.

V. Conclusions

The use of PEM fuel cells in the power group is becoming widespread for UAVs, whose usage area is

increasing rapidly today, to make them functional by flying longer. This will enable the production of more environmentally friendly UAVs with the LCA approach for improve the environmental impact of the hybrid system. LCA method approach will be applied from cradle to grave, taking into account the entire life cycle of this study UAV in extracting environmental impacts.

Acknowledgements
We would like to thank the Eskişehir Technical University for supporting this research with the 20DRP054 project.

References

Baroutaji, A., Tabbi, W., & Olabi, A. G. (2018). Overview of hydrogen and fuel cell technology in the aviation sector. In 11th Int. Conf. Sustain. Energy Environ. Prot. 8th-11th May.

Bayrak, Z. U., Kaya, U., & Oksuztepe, E. (2020). Investigation of PEMFC performance for cruising hybrid powered fixed-wing electric UAV in different temperatures. International Journal of Hydrogen Energy, 45(11), 7036-7045.

Belmonte, N., Staulo, S., Fiorot, S., Luetto, C., Rizzi, P., & Baricco, M. (2018). Fuel cell powered octocopter for inspection of mobile cranes: Design, cost analysis and environmental impacts. Applied energy, 215, 556-565.

Bicer, Y., & Dincer, I. (2017). Life cycle evaluation of hydrogen and other potential fuels for aircrafts. International Journal of Hydrogen Energy, 42(16), 10722-10738.

Bradley, T. H., Moffitt, B. A., Mavris, D. N., Fuller, T. F., & Parekh, D. E. (2009). Hardware-in-the-loop testing of a fuel cell aircraft powerplant. Journal of Propulsion and Power, 25(6), 1336-1344.

Depcik, C., Cassady, T., Collicott, B., Burugupally, S. P., Li, X., Alam, S. S., ... & Hobeck, J. (2020). Comparison of lithium ion Batteries, hydrogen fueled combustion Engines, and a hydrogen fuel cell in powering a small Unmanned Aerial Vehicle. Energy Conversion and Management, 207, 112514.

Dudek, M., Tomczyk, P., Wygonik, P., Korkosz, M., Bogusz, P., & Lis, B. (2013). Hybrid fuel cell–battery system as a main power unit for small unmanned aerial vehicles (UAV). Int. J. Electrochem. Sci, 8(6), 8442-8463.

Gadalla, M., & Zafar, S. (2016). Analysis of a hydrogen fuel cell-PV power system for small UAV. International Journal of Hydrogen Energy, 41(15), 6422-6432.

Gonzalez-Espasandín, Ó., Leo, T. J., Raso, M. A., & Navarro, E. (2019). Direct methanol fuel cell (DMFC) and H2 proton exchange membrane fuel (PEMFC/H2) cell performance under atmospheric flight conditions of Unmanned Aerial Vehicles. Renewable Energy, 130, 762-773.

Kim, T., & Kwon, S. (2012). Design and development of a fuel cell-powered small unmanned aircraft. International Journal of Hydrogen Energy, 37(1), 615-622.

Lapena-Rey, N., Blanco, J. A., Ferreyra, E., Lemus, J. L., Pereira, S., & Serrot, E. (2017). A fuel cell powered unmanned aerial vehicle for low altitude surveillance missions. International Journal of Hydrogen Energy, 42(10), 6926-6940.

McConnell, V. P. (2007). Military UAVs claiming the skies with fuel cell power. Fuel Cells Bulletin, 2007(12), 12-15.

Özbek, E., Yalin, G., Ekici, S., & Karakoc, T. H. (2020). Evaluation of design methodology, limitations, and iterations of a hydrogen fuelled hybrid fuel cell mini UAV. Energy, 213, 118757.

Ozbek, E., Yalin, G., Karaoglan, M. U., Ekici, S., Colpan, C. O., & Karakoc, T. H. (2021). Architecture design and performance analysis of a hybrid hydrogen fuel cell system for unmanned aerial vehicle. International Journal of Hydrogen Energy.

Siddiqui, O., & Dincer, I. (2018). A review and comparative assessment of direct ammonia fuel cells. Thermal Science and Engineering Progress, 5, 568-578.

Sürer, M. G., & Arat, H. T. (2018). State of art of hydrogen usage as a fuel on aviation. European Mechanical Science, 2(1), 20-30.

Verstraete, D., Lehmkuehler, K., Gong, A., Harvey, J. R., Brian, G., & Palmer, J. L. (2014). Characterisation of a hybrid, fuel-cell-based propulsion system for small unmanned aircraft. Journal of power sources, 250, 204-211.

Yalin, G. (2019). PEM yakit hücresi lityum polimer batarya hibrit sistemiyle tahrikli mini-İHA üretimi ve enerji yönetim sisteminin modellenmesi (Doctoral dissertation, Eskisehir Technical University).

Fundamental hydrogen storage properties of TiFe-alloy with partial substitution of Fe by Ti and Mn

[1,2*]Erika Michela Dematteis, [3]David Dreistadt, [3]Giovanni Capurso, [3]Julian Jepsen, [1]Fermin Cuevas, [1]Michel Latroche, [2]Marcello Baricco
[1] Univ Paris Est Creteil, CNRS, ICMPE, 2 rue Henri Dunant, 94320 Thiais, France
[2] University of Turin, Department of Chemistry, Inter-departmental Center Nanostructured Interfaces and Surfaces (NIS), and INSTM, Via Pietro Giuria 7, 10125 Torino, Italy
[3] Helmholtz-Zentrum Geesthacht, Institute of Materials Research and HydrogenTechnology, Max-Plank-Str. 1, 21502 Geesthacht, Germany

* E-mail:erikamichela.dematteis@unito.it

Abstract
TiFe intermetallic is a low cost material, with good volumetric hydrogen density, and easy tailoring of hydrogenation thermodynamics by elemental substitution, promising for large-scale applications of solid-state hydrogen storage. However, activation and kinetic issues should be amended, and the role of elemental substitution further understood. This work, in the frame of the HyCARE EU project, investigates thermodynamic effects of the variation of Ti content along the homogeneity range of the TiFe phase and of substitution of Mn for Fe, offering a comprehensive picture of hydrogenation properties over an extended Ti and Mn compositional range. Moreover, it demonstrates that Ti-rich TiFe alloys display enhanced reversible storage capacities. Both Mn and Ti substitutions increase the TiFe cell parameter, lowering the plateau pressures and decreasing the hysteresis of the isotherms. A full picture of the dependence of hydrogen storage properties as a function of composition will be discussed, together with observed correlations.

Keywords: hydrogen storage, intermetallic compound, TiFe, substitution, thermodynamics

I. Introduction

Hydrogen as an energy carrier is increasingly coming into focus in politics and industry, as part of the promotion of renewable energies for environmental protection. Among other solutions, metal hydrides are suitable for reversible storing of hydrogen, by chemical uptake and release under appropriate thermodynamic conditions. For industrial applications, the technical efforts and costs required for the integration of such storage systems into energy supply systems are of critical importance. Room-temperature forming hydrides, such as TiFe-type alloys, which can absorb and desorb hydrogen at relatively low temperature (below 100 °C) and gas pressure (below 10 MPa), are suitable for this purpose.

Starting in the 70s, the use of low-temperature metal hydrides in stationary hydrogen storage and the study of the thermodynamic properties of TiFe alloys have been investigated. Since then, extensive research has been carried out on the properties of TiFe compounds with various additional elements. An overview of the properties and investigations of stoichiometric TiFe is given by Sujan *et al.* and the present authors in recent reviews.(Dematteis, Berti, et al., 2021; Sujan et al., 2019)

TiFe exists in a narrow range of composition, which extends from 49.7 to 52.5 at.% Ti at 1000 °C.(Sujan et al., 2019) Non-stoichiometry in TiFe-alloys are accommodated by partial substitution of Ti at Fe site.(Challet et al., 2005) Thus, the lattice parameter is expected to change within the homogeneity domain of TiFe due to the different atomic radius of Ti and Fe: r_{Ti}(1.46 Å) > r_{Fe}(1.24 Å).(Zhang et al., 2014) In addition, activation and hydrogenation properties are affected as well. Indeed, the Ti-rich compound $TiFe_{0.90}$ requires almost no activation process for the first hydrogenation.(Guéguen & Latroche, 2011)

Beside the variation of the Ti:Fe ratio in pure TiFe, elemental substitutions can also change significantly activation processes and hydrogen storage properties.(Bannenberg et al., 2020) Depending on alloy composition and based on Ti-Fe-*M* phase diagrams (where *M* is a substituting element), formation of secondary phase precipitates considerably influences the activation process and hydrogenation properties.(Dematteis, Cuevas, et al., 2021)

Recently, it has been reported that the introduction of Cu in Mn-substituted alloy lowers the first plateau, while moving to higher pressure the second one, hence reducing sensibly the reversible capacity in a narrow pressure range.(Dematteis, Cuevas, et al., 2021)

Enlarging the TiFe cell parameter by elemental substitution appears to be useful for the hydrogenation properties of TiFe, since it generally results in lowering plateau pressure and improving activation in mild conditions, as in the case of Mn. The introduction of Mn, a non-critical raw material for Europe, also preserves good capacity and kinetics. The substitution of Fe by Mn into TiFe was observed to modify the thermodynamic properties and to reduce the activation issues of equiatomic TiFe.(Buchner, 1982; Challet et al., 2005; Fruchart et al., 1980) It was already established that partial substitution of Fe by Mn does not change the crystal structure of TiFe, but expands it owing to the increased atomic size of Mn (r_{Mn} = 1.35 Å) as compared to Fe (r_{Fe} = 1.24 Å).(Fruchart et al., 1980; Zhang et al., 2014) The hydride phase is stabilized due to the increase of the binding energy.(Buchner, 1982) A further important aspect is that the addition of Mn allows activation at a much lower temperature than equiatomic TiFe,(Schlapbach & Riesterer, 1983; Sujan et al., 2019) thereby reducing the technical effort.

II. Experimental Set-up and Procedure

Nine Ti-Fe-Mn samples were synthetized by induction melting of bulk pure elements under argon in a water-cooled copper crucible. Furthermore, to attain thermodynamic equilibrium, the samples were annealed in a resistive furnace at 1000 °C for 1 week and quenched to room temperature into water. The ingots were roughly crushed under air and then finely smashed into fine powder under inert atmosphere. Metallographic examination and elemental analysis by electron probe micro-analysis (EPMA, Cameca SX100) were performed together with the collection of Back-Scattered Electron (BSE) images. Powder X-Ray Diffraction (XRD) patterns were obtained at room temperature on a Bruker D8 Advance Bragg Brentano diffractometer, using Cu-Kα radiation (λ=1.5418 Å), in a 2θ-range of 20–120°, step size 0.02° and time step 7 seconds. All patterns were refined by the Rietveld method. Activation, kinetic studies and Pressure Composition Isotherm (PCI) curves were monitored with a custom-made Sieverts' type apparatus.

III. Analysis

Chemical, structural and morphological characterization of the materials by EPMA analysis show that the Ti-content of the main (matrix) phase ranges between 50.7 at.% and 52.0 at.%, while Fe and Mn contents are close to the alloy nominal compositions. Therefore, this matrix is assigned to the TiFe phase. The compositional balance between Fe and Mn contents suggests that Mn substitutes Fe (site 1*a,* Space group *Pm*-3*m*) in the TiFe structure. In addition, thanks to BSE images, secondary phases could be detected and analysed by EPMA. Secondary phases are defined as $TiFe_2$, β-Ti solid solution, and Ti_4Fe_2O, as corroborated by XRD.

Hydrogenation properties have been determined, all samples have been successfully activated and display a fast absorption rate. The activation of samples with 1:1 Ti:Fe stoichiometry (Ti-poor side of the homogeneity domain) was achieved in harsh conditions: 5 MPa of hydrogen and a heat treatment with a temperature ramp up to 400 °C were necessary for their full activation. In contrast, almost all the Ti-rich alloys could be activated at much milder conditions: room temperature (RT) and 2.5 MPa of H_2.

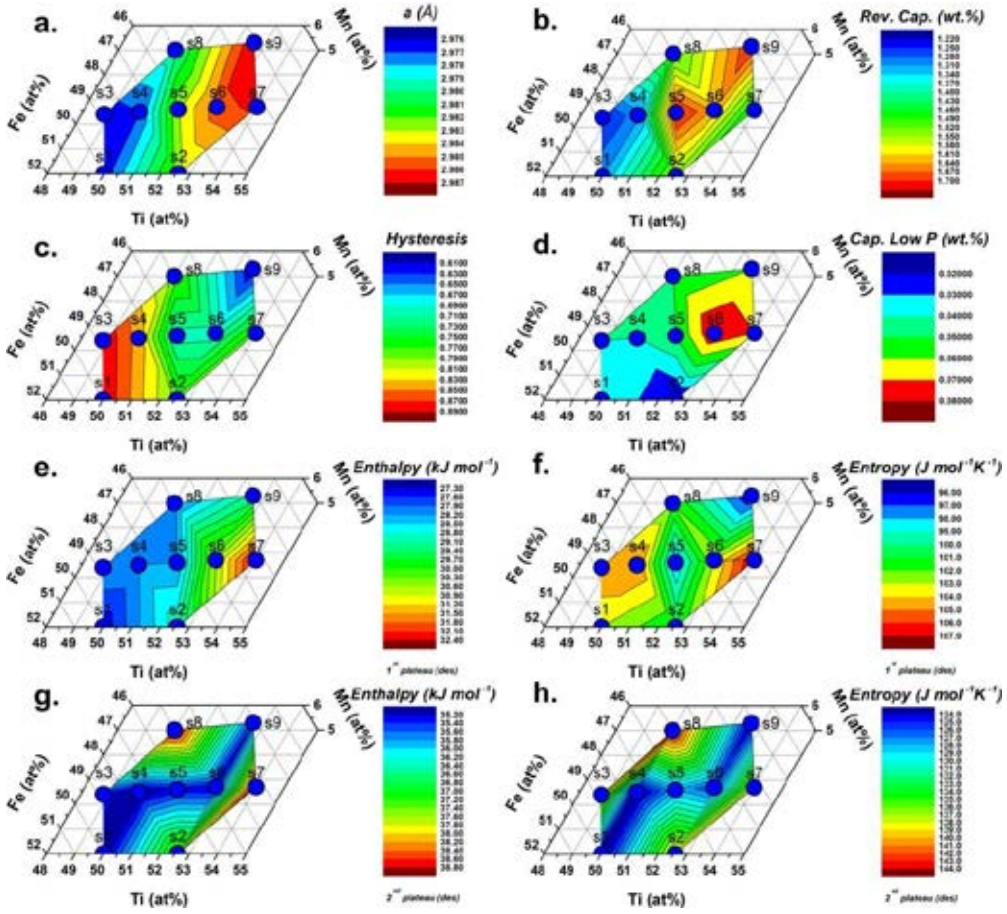


Fig. 1: Compositional counter colour maps maps based on the measured properties (of the cubic TiFe-type phase) for the nine studied samples: a) cubic cell parameter; b) reversible capacity at 25°C between 0.03-2.5 MPa; c) hysteresis of the first plateau; d) hydrogen stored/trapped at low pressure, *i.e.* below the first plateau pressure; first plateau desorption e) enthalpy and f) entropy; and second plateau desorption g) enthalpy and h) entropy.

PCI curves and the thermodynamic parameters (enthalpy ΔH and entropy ΔS of reaction) for nine investigated samples were determined. PCI curves generally consist of a first (low) and second (high) pressure plateau, both in absorption and desorption, though in some cases the double-plateau feature is not resolved due to slope feature or

unachievable pressure required for observing the second plateau.
Absorption enthalpy values of the first plateau range from -28.3 to -24.3 kJ mol^{-1}, while the entropy change ranges between -100 and -95 J mol^{-1} K^{-1}. The second plateau enthalpies and entropies of absorption present higher values compared to the absorption first plateau ones, ranging between $-35.4<\Delta H<-26.2$ kJ mol^{-1} and $-132<\Delta S<-114$ J mol^{-1} K^{-1}. Upon desorption, this trend is maintained. However, higher values are evidenced compared to the absorption ones: $27.4<\Delta H<32.4$ kJ mol^{-1} and $96<\Delta S<107$ J mol^{-1} K^{-1} for the first plateau and $35.2<\Delta H<38.9$ kJ mol^{-1} and $124<\Delta S<144$ J mol^{-1} K^{-1} for the second one.

IV. Results and discussions

Substitution of Ti and Mn in TiFe-type alloy results in enlargement of the cell parameter and volume of the TiFe-phase (Fig.1-a). Thermodynamic investigations were made to examine the influence of the Ti and Mn content on hydrogenation properties. The performed PCI curves allowed a good estimation of the thermodynamic properties of the samples that agree well with the available literature, but further complete the dependency of hydrogenation properties over extended Ti and Mn compositional range, as it can be appreciated in the compositional counter colour maps in Fig.1 from e to h. It can also be seen that the samples at the Ti-rich side of the phase diagram display enhanced storage reversible capacities (Fig.1-b), as limited β-Ti is formed. On the other hand, the formation of secondary phases reactive to hydrogen enhances the activation properties and allows the first hydrogenation of the material in milder conditions, as in the case of Ti and Mn substituted materials. However, high amounts of secondary phases reduce the total and reversible capacity of the material, thus a compromise must be reached. When high amount of β-Ti precipitates is formed, it irreversibly traps hydrogen at very low pressure (Fig.1-d).
Another important result is that the addition of both Ti and Mn increases the cell parameter by substituting Fe (Fig.1-a), thus reducing the equilibrium pressure, diminishing the pressure gap between the first and second plateaus and decreasing the hysteresis of the isotherms (Fig.1-c), linearly depending on the TiFe-phase cell volume.

V. Conclusions

The study presented in this work investigates the role of Ti and Mn substitution in TiFe-type alloy in the range from 48.8 at.% to 54.1 at.% Ti, and from 0 to 5.3 at.% Mn. Within these boundaries, according to the ternary Ti-Fe-Mn phase diagram, the main phase is cubic TiFe, and at the Ti-poor side the formation of $TiFe_2$ can occur, while at the Ti-rich side the formation of β-Ti-type and oxide phase (Ti_4Fe_2O-type) is observed. BSE analyses showed that the induction melting process and subsequent annealing produced alloys formed by a chemically homogeneous TiFe-type phase and minor precipitate phases. Through XRD-analyses and Rietveld's refinement, it is determined that the resulting phases are in good agreement with the expected results based on the ternary phase diagram. In addition, some considerations about hydrogen properties and geometrical consideration have been formulated. The reversible capacity determined at 25 °C between the pressure window of 0.03 and 2.5 MPa is higher in Ti-rich samples, owing to reduced equilibrium pressure and a flatter plateau. In particular, $TiFe_{0.85}Mn_{0.05}$ (s6) sample results to be the best compositional trade-off, as it retains a reversible capacity as high as 1.63 wt.% combined with easy activation process (6 hours incubation time under 2.5 MPa at 25 °C) and fast absorption rate, thanks to its good kinetics, with a time to reach 90% of hydrogenation lower than 2 minutes.

Acknowledgements

Funding from the FCH-JU, EU H2020, and Hydrogen Europe Research, under grant agreement No 826352, HyCARE project are acknowledged.

References

Bannenberg, L. J., Heere, M., Benzidi, H., Montero, J., Dematteis, E. M., Suwarno, S., Jaroń, T., Winny, M., Orłowski, P. A., Wegner, W., Starobrat, A., Fijałkowski, K. J., Grochala, W., Qian, Z., Bonnet, J.-P., Nuta, I., Lohstroh, W., Zlotea, C., Mounkachi, O., … El Kharbachi, A. (2020). Metal (boro-) hydrides for high energy density storage and relevant emerging technologies. *International Journal of Hydrogen Energy*, *45*(58), 33687–33730.

Buchner, H. (1982). *Energiespeicherung in Metallhydriden* (Innovative). Springer Vienna. https://doi.org/10.1007/978-3-7091-8671-8

Challet, S., Latroche, M., & Heurtaux, F. (2005). Hydrogen Storage in TiFe(0.70+x)Mn(0.20-x) (0<x<0.15) and TiFe(0.70)Mn(0.20-y)Ni(y) (0<y<0.08) Metallic Alloys. *Materials Science & Technology*, 13–21.

Dematteis, E. M., Berti, N., Cuevas, F., Latroche, M., & Baricco, M. (2021). Substitutional effects in TiFe for hydrogen storage: a comprehensive review. *Materials Advances*. https://doi.org/10.1039/D1MA00101A

Dematteis, E. M., Cuevas, F., & Latroche, M. (2021). Hydrogen storage properties of Mn and Cu for Fe substitution in TiFe0.9 intermetallic compound. *Journal of Alloys and Compounds*, *851*, 156075.

Fruchart, D., Commandré, M., Sauvage, D., Rouault, A., & Tellgren, R. (1980). Structural and activation process studies of FeTi-like hydride compounds. *Journal of the Less Common Metals*, *74*(1), 55–63.

Guéguen, A., & Latroche, M. (2011). Influence of the addition of vanadium on the hydrogenation properties of the compounds TiFe0.9Vx and TiFe0.8Mn0.1Vx (x=0, 0.05 and 0.1). *Journal of Alloys and Compounds*, *509*(18), 5562–5566.

Schlapbach, L., & Riesterer, T. (1983). The activation of FeTi for hydrogen absorption. *Applied Physics A Solids and Surfaces*, *32*(4), 169–182.

Sujan, G. K., Pan, Z., Li, H., Liang, D., & Alam, N. (2019). An overview on TiFe intermetallic for solid-state hydrogen storage: microstructure, hydrogenation and fabrication processes. *Critical Reviews in Solid State and Materials Sciences*, 1–18.

Zhang, Y., Zuo, T. T., Tang, Z., Gao, M. C., Dahmen, K. A., Liaw, P. K., & Lu, Z. P. (2014). Microstructures and properties of high-entropy alloys. *Progress in Materials Science*, *61*, 1–93.

Electric Taxiing with Fuel Cell Hybrid Power Unit

[1*]Mustafa Keçeci, [2]C. Özgür Çolpan, [1]T. Hikmet Karakoç,
[1] Eskişehir Technical University, Faculty of Aeronautics and Astronautics, Eskişehir, 26555, Turkey
[2] Dokuz Eylül University, Faculty of Engineering, Department of Mechanical Engineering Thermodynamics, İzmir, 35160, Turkey

* E-mail: mustafakececi@anadolu.edu.tr

Abstract

Airport ground operations have a great impact on the environment. Many researchers have proposed innovative systems for taxiing without using the main engines. Their studies have shown that the on board and external electric taxi solutions that have been put forward are not completely carbon-free. The disadvantages of existing solutions can be reduced by using an external fuel cell hybrid power unit to meet the energy required for taxiing that does not put additional weight on the aircraft. Adding this unit results in cleaner and quieter airport operations as well as other operational advantages.

Keywords: Electric taxiing systems, fuel cell hybrid power unit, environment, aviation

I. Introduction

The aviation industry is growing rapidly and this growth will continue at an increasing pace in the future. Although air traffic has decreased significantly since the first quarter of 2020 due to the Covid-19 outbreak, the International Air Transport Association (IATA) estimates that 8.2 billion people will travel by air in 2037, with an annual growth rate of 3.5% (Association, 2017; Iacus, Natale, Santamaria, Spyratos, & Vespe, 2020). As this growth continues, the requirement for more efficient, more reliable and environmentally friendly aviation applications will increase gradually for both airborne and ground operations. The European Commission (EC) drew attention to the problems caused by this growth and in the ―Flight Path 2050 Strategy Plan‖ published in 2011, aimed to reduce the environmental impacts of the air traffic by reducing CO_2 and NO_x emissions 75% and 90% per passenger kilometer compared to 2000 values, respectively. By using sustainable alternative fuels in aviation, zero emissions during taxi operations and minimizing the noise at airports are also aimed in this plan (Krein & Williams, 2012).

Although airplanes consume large amount of the fuel for their flights in the air, they also use a significant amount to taxi on the ground. According to the estimation of Airbus company, up to 30% of the total flight time and 5% to 10% of the fuel used in flights are spent for ground operations and taxiing in flights in Europe (Deonandan & Balakrishnan, 2010). As mentioned above, as a result of the increasing air traffic, airports are expected to expand and increase their capacity further, which means that the taxiing times for aircraft will grow with an increasing trend. Taxi departure times for US domestic flights increased by 21% only between 1995 and 2007, when looking at the period 2003-2007, taxi-out times increased by approximately 11%, while taxi-in times increased by approximately 9% (Goldberg & Chesser, 2008).

Conventionally, aircraft taxi causes approximately 7% of the total thrust force, which is the idle thrust of the jet engines (Khadilkar & Balakrishnan, 2012). This also means that aircraft engines that are optimized for flight work inefficiently (Chakraborty, LeVine, Hassan, & Mavris, 2015; Chen et al., 2016; Enalou, Bozhko, Rashed, & Kulsangcharoen, 2018). Taxi time exceeds 30 minutes at busy and large airports such as the John F. Kennedy (JFK) airport in New York (Balakrishna, Ganesan, Sherry, & Levy, 2008). Considering that the Airbus A 320, which is a narrow body aircraft, consumes approximately 0.1 kg of fuel per second (Hospodka, 2014) for taxiing, it is seen that the aircraft emits a high amount of pollutants at airports.

Electric taxi systems (ETS) have been produced by various companies to solve the problems mentioned above. These systems are structurally divided into two as on-board and external ETS. On-board ETSs are systems that obtain the electrical energy from the auxiliary power unit (APU) (starter generator) already on the aircraft, and provide the necessary traction with appropriate electric motors mounted on the nose or main landing gears of the aircraft (Madonna, Giangrande, & Galea, 2018). However, the APU, which is also used for hotel loads such as lighting and air conditioning is insufficient to provide the necessary power for the aircraft to taxi under the desired conditions. On a taxiway with upslope of 1.5%, an airplane weighing 80 tons with a 1.5% friction coefficient needs to generate approximately 240 kW of power in order to taxi at a speed of 20 knots (37 km / h). However, the nominal capacity of the Boeing B373's APU, which weighs approximately 80 tons, is 90 kVA (Lukic, Giangrande, Hebala, Nuzzo, & Galea, 2019). In addition, although the APU consumes less fuel compared to jet engines, this still does not completely eliminate the emission of pollutants at airports. A power system (fuel cell, battery pack, super capacitors, etc.) that able to provide the necessary power for the aircraft to taxi in the desired conditions can be used on the aircraft, but it will cause the aircraft to fly with extra weight and therefore consume more fuel during the flight. As shown in Fig. 1, this means that the expected decrease in fuel consumption does not occur, especially as the flight range increases.

On the other hand, the external tow truck called TaxiBot ETS produced by the Israeli company, which has advantages such that it does not add any extra weight on the aircraft and does not require any modifications on the aircraft, is actively used at the Frankfurt international airport (Lukic et al., 2019). This tow truck, which enables aircraft to taxi without using jet engines, provides the energy required to tow the aircraft by feeding the electric motors on its wheels from two diesel generators (Hospodka, 2014; Lukic et al., 2019). In addition to their advantages, the disadvantages of these trucks are that they can greatly reduce the autonomy of the aircraft and increase the congestion between gates and runways due to the increase in the number of tow trucks running (Hospodka, 2014). Therefore, changes should be made in the aerodrome infrastructure, such as the addition of new roads for tractor movement after the aircraft takes off. In addition, in this system, although the pilot controls most of the taxiing operations, a driver is still required for push-back operations, to return the vehicle after the aircraft take off, and for a possible emergency. From a carbon footprint perspective, it reduces both fuel consumption and greenhouse gas emissions thanks to the hybrid structure of the traction system. However, despite reducing fuel consumption and emissions, the TaxiBot system does not fully comply with the carbon neutral target (Lukic et al., 2019).

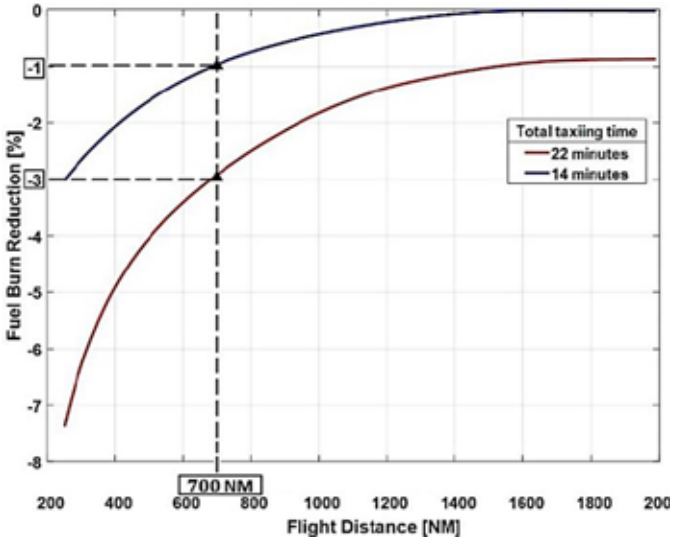


Fig. 1. Fuel reduction based on the flight distance and taxi duration (on board ETS) (Nicolas, 2013)

II. Fuel Cell / Battery Hybrid External Power Unit

Considering the problems mentioned above, as seen in Fig. 1, A hybrid external power unit consisting of a fuel cell and battery pack is designed. In fact, with this system, on board and external systems are also hybridized. As with the use of on board systems, there will be electric motors on the aircraft, but the power unit to feed these engines will not be on the aircraft, so the effect of weight will be reduced during the flight phase. On the other hand, there will be an extra movement on the ground similar to external systems, but since the dimensions will not be as large as the tow trucks, they will be able to leave the track quickly after their operations and will not cause congestion on the runway.

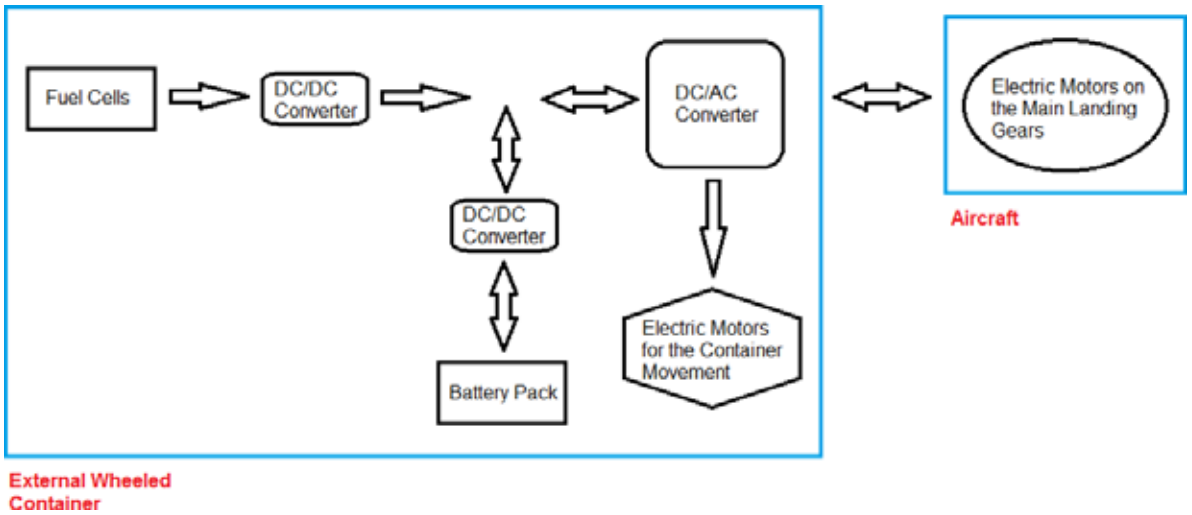


Fig. 2. The architecture of the proposed external power unit

The hybrid external power unit with a fuel cell and battery pack to be designed in this system will be connected to the socket on the fuselage of the aircraft after landing. Thus, the necessary energy to feed the electric motors on the aircraft will be obtained and the aircraft will be able to move on the runway without using jet engines. Similarly, when the aircraft completes ground operations and reaches the runway for take-off, the hybrid external power unit will leave the aircraft and go to the appropriate location at the airport in order to connect to the new aircraft to be landed.

III. Conclusions

With the use of the aforementioned system, the planned emission-free electric taxiing process will take place in the future, and therefore a large amount of CO_2 and other polluting emissions at airports will be eliminated. In addition to eliminating emissions, ground operations can be carried out almost without noise. Moreover, moving the aircraft around the airport without using its engines will reduce the risk of foreign object damage (FOD) and reduce engine maintenance costs. Another benefit of the system is that they will extend the service life of the brakes. In conventional taxi movement, brakes are used extensively to maintain the desired speed, while in ETSs, the speed can be easily controlled and excessive use of the brakes is not required. In addition, since there will be no jet blast near the doors, ground operators will be able to work much safer and healthier. Finally, with the possibility of parallel parking to the terminal building that WheelTug has mentioned, two airport bridges could be allowed to be used for the passenger boarding procedure, which will shorten the boarding time of the passengers (Soepnel & Roling, 2017)

References

Association, I. A. T. (2017). 2036 forecast reveals air passengers will nearly double to 7.8 billion. *International Air Transport Association, 24*.

Balakrishna, P., Ganesan, R., Sherry, L., & Levy, B. S. (2008). *Estimating taxi-out times with a reinforcement learning algorithm.* Paper presented at the 2008 IEEE/AIAA 27th Digital Avionics Systems Conference.

Chakraborty, I., LeVine, M. J., Hassan, M., & Mavris, D. N. (2015). *Assessing taxiing trade spaces from aircraft, airport, and airline perspectives.* Paper presented at the 15th AIAA Aviation Technology, Integration, and Operations Conference.

Chen, J., Weiszer, M., Locatelli, G., Ravizza, S., Atkin, J. A., Stewart, P., & Burke, E. K. (2016). Toward a more realistic, cost-effective, and greener ground movement through active routing: a multiobjective shortest path approach. *IEEE Transactions on Intelligent Transportation Systems, 17*(12), 3524-3540.

Deonandan, I., & Balakrishnan, H. (2010). *Evaluation of strategies for reducing taxi-out emissions at airports.* Paper presented at the 10th AIAA Aviation Technology, Integration, and Operations (ATIO) Conference.

Enalou, H. B., Bozhko, S., Rashed, M., & Kulsangcharoen, P. (2018). *A preliminary study into turbofan performance with LP-HP power exchange.* Paper presented at the Proceedings of Montreal 2018 Global Power and Propulsion Forum.

Goldberg, B., & Chesser, D. (2008). *Sitting on the runway: Current aircraft taxi times now exceed pre-9/11 experience*. Retrieved from

Hospodka, J. (2014). Electric taxiing–Taxibot system. *MAD-Magazine of Aviation Development, 2*(10), 17-20.

Iacus, S. M., Natale, F., Santamaria, C., Spyratos, S., & Vespe, M. (2020). Estimating and projecting air passenger traffic during the COVID-19 coronavirus outbreak and its socio-economic impact. *Safety Science, 129*, 104791.

Khadilkar, H., & Balakrishnan, H. (2012). Estimation of aircraft taxi fuel burn using flight data recorder archives. *Transportation Research Part D: Transport and Environment, 17*(7), 532-537.

Krein, A., & Williams, G. (2012). Flightpath 2050: Europe's vision for aeronautics. *Innovation for Sustainable Aviation in a Global Environment: Proceedings of the Sixth European Aeronautics Days, Madrid, 30*.

Lukic, M., Giangrande, P., Hebala, A., Nuzzo, S., & Galea, M. (2019). Review, challenges, and future developments of electric taxiing systems. *IEEE Transactions on Transportation Electrification, 5*(4), 1441-1457.

Madonna, V., Giangrande, P., & Galea, M. (2018). Electrical power generation in aircraft: Review, challenges, and opportunities. *IEEE Transactions on Transportation Electrification, 4*(3), 646-659.

Nicolas, Y. (2013). eTaxi—Taxiing Aircraft with Engines Stopped. *Flight Airworthiness Support Technology (FAST), 51*, 2-10.

Soepnel, S., & Roling, P. C. (2017). *Impact of electric taxi systems on airport apron operations and gate congestion.* Paper presented at the 17th AIAA Aviation Technology, Integration, and Operations Conference.

Onboard Hydrogen Storage for Ships: An Overview

[1]*Omer Berkehan Inal, [1]Caglar Dere, [1]Cengiz Deniz

[1]Istanbul Technical University, Maritime Faculty, Marine Engineering Department, Istanbul, Turkey

*E-mail: inalo@itu.edu.tr, derec@itu.edu.tr, denizc@itu.edu.tr

Abstract

Maritime transportation is under the pressure of reducing greenhouse gas emissions from ships. The rule-maker of the maritime industry, International Maritime Organization tightens the bond around ships to eliminate harmful exhaust emissions due to environmental concerns. Considering chemical properties, the use of hydrogen in ships may be a solution through zero-emission shipping. In this study, onboard hydrogen storage methods are reviewed and compared for ships. Obstacles in front of the industry are revealed and required changes are highlighted. Bunkering and storage infrastructure, global availability of hydrogen fuel, and safety issues for reliable operations seem like the biggest challenges at the first step of the industry.

Keywords: Hydrogen, Maritime Transportation, Zero-Emission Shipping, Hydrogen Fuel Cells

I. Introduction

Generating energy from clean sources instead of fossil fuels is an increasing trend for the shipping industry. The main motivation is to minimize ship-sourced greenhouse gas (GHG) emissions by forcing the industry with incoming emission regulations (Zincir & Deniz, 2018). International Convention for the Prevention of Pollution from Ships (MARPOL), Annex VI Regulations for the Prevention of Air Pollution from Ships is the main strategy for controlling the ship sourced emission in global shipping (Ling-Chin & Roskilly, 2016). The amount of greenhouse gas (GHG) emissions of international maritime transportation is comparable to the GHG emissions of Germany (Olmer et al., 2017). The maritime transportation GHG emissions, CO_2, methane (CH_4), and nitrous oxide (N_2O), have arisen from 977 million tons to 1,076 million tons and CO_2 emissions increased from 962 million tons to 1,056 million tons from 2012 to 2018 (IMO, 2020). It can be seen that CO_2 emissions are the major GHG emissions from maritime transportation.

There are various emission mitigation methods for ships and using hydrogen as an alternative fuel is one of the options (Deniz & Zincir, 2016). Hydrogen may play a key role in the transition to zero-emission shipping with its carbon-free structure (Inal & Deniz, 2018). Thus, storage of the hydrogen gain importance and receive attention specifically for the transportation sector which is on the way of reducing fossil fuel dependence, hence maritime transportation is one the most important branches of this sector. Firstly, it is necessary to specify the storage chain of the hydrogen as in the vehicles, in refueling stations, and connection of hydrogen production and distributions (Andersson & Grönkvist, 2019). The scope of this paper is limited to the onboard storage options of the hydrogen for ships therefore the following sections are shaped within this framework. The hydrogen storage researches in transportation are mainly focused on fuel cell vehicles (FCVs) (Hwang & Varma, 2014) and the proton exchange membrane (PEM) fuel cell is the leading type among different types of fuel cells with its technological maturity (Inal & Deniz, 2021).

II. On-Board Hydrogen Storage

In this section hydrogen storage techniques for the onboard ship are reviewed. The four main storage technologies compressed, liquid, solid-state, and alternative carriers are elaborated, respectively and shown in figure 1. Additionally, alternative carriers are separated into three subtitles as N_2 based, CO_2 based, and organic liquids. This section provides general knowledge about the technologies with their pros and cons for comparison in the next section.

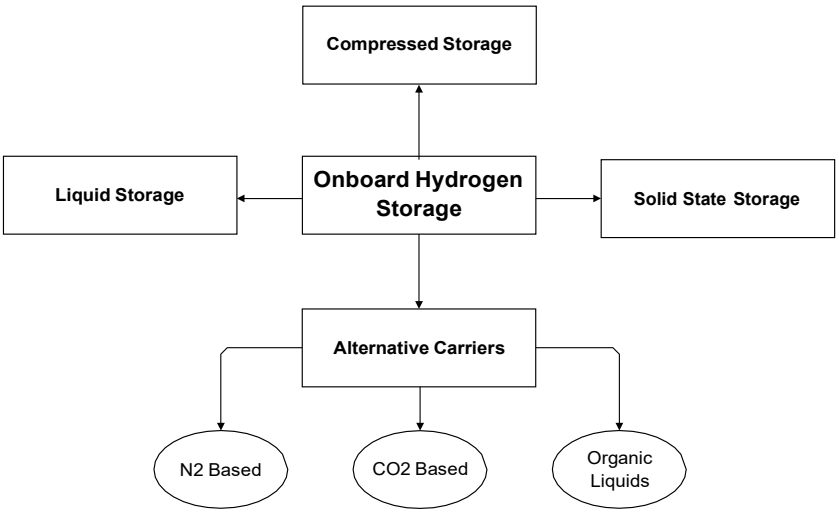


Figure 1: Onboard Hydrogen Storage Techniques.

II.I. Compressed Hydrogen Storage

The compressed hydrogen storage is the most developed and well-experienced method among different technologies. The hydrogen is kept under very high pressures around 350-700 bar which give a density of 23.3 kg/m^3 and 39.3 kg/m^3, respectively (Raucci et al., 2015). The storage phenomena of compressed hydrogen have two main components; storage tanks, and compressors. Table 1 shows the four different tank types with the material, typical pressure, and approximate cost.

Table 1: Storage Tank Types (Rivard et al., 2019).

Type	Material	Typical Pressure (bar)	Cost ($/kg)
I	All-metal construction	300	83
II	Mostly metal, composite overwrap in the hoop direction	200	86
III	Metal liner, full composite overwrap	700	700
IV	All-composite construction	700	633

II.II. Liquid Hydrogen Storage

The fundamental of storing hydrogen in liquid form is to reduce temperature to -253 °C which is its boiling temperature. The advantage of liquefaction is the ability to reach high hydrogen densities at atmospheric pressures, which is 70 kg/m^3 and 775 times higher than the gaseous form (Van Hoecke et al., 2021).

II.III. Solid-State Hydrogen Storage

There are various methods to store hydrogen in solid materials but the promising ones; metal hydride and boron-based storage will be reviewed in this paper. Firstly, metal hydrides will be elaborated under two different titles as magnesium hydrides and aluminum hydrides. Secondly, the two most common boron-based storage materials $NaBH_4$ and NH_3BH_3 will be summarized.

II.IV. Alternative Hydrogen Carriers

II.IV.I N_2 Based

Ammonia is the key chemical in fertilizer production by combining hydrogen with nitrogen from air. Ammonia based storage of the hydrogen is a good option too for ships. Ammonia based storage and use of ammonia is elaborated in this section.

II.IV.II CO_2 Based

Methanol, formic acid, S-LNG and FTS-diesel are seen in this section as an alternative hydrogen carriers for shipping industry.

II.IV.III Organic Liquids

Liquid organic hydrogen carriers are based on the concept of hydrogenation and dehydrogenation of the compounds to store hydrogen (Hu et al., 2015). The advantage of this method is easy handling compared to compression.

III. Discussions

The current state of hydrogen in the maritime sector, hydrogen fuel cells for shipping have been reviewed. Bunkering and safety will be evaluated for ships as the main criteria in a comparison table according to different types of storage techniques which are given in previous sections.

IV. Conclusion

The results of the study will be explained by giving an insight on the possible future studies.

References

Andersson, J., & Grönkvist, S. (2019). Large-scale storage of hydrogen. *International Journal of Hydrogen Energy*, *44*(23), 11901–11919. https://doi.org/10.1016/j.ijhydene.2019.03.063

Deniz, C., & Zincir, B. (2016). Environmental and economical assessment of alternative marine fuels. *Journal of Cleaner Production*, *113*(X), 438–449. https://doi.org/10.1016/j.jclepro.2015.11.089

Hu, P., Fogler, E., Diskin-Posner, Y., Iron, M. A., & Milstein, D. (2015). A novel liquid organic hydrogen carrier system based on catalytic peptide formation and hydrogenation. *Nature Communications*, *6*. https://doi.org/10.1038/ncomms7859

Hwang, H. T., & Varma, A. (2014). Hydrogen storage for fuel cell vehicles. In *Current Opinion in Chemical Engineering* (Vol. 5, pp. 42–48). Elsevier Ltd. https://doi.org/10.1016/j.coche.2014.04.004

Inal, O. B., & Deniz, C. (2021). Emission Analysis of LNG Fuelled Molten Carbonate Fuel Cell System for a Chemical Tanker Ship: A Case Study. *Marine Science and Technology Bulletin*, *10*, 118–133. https://doi.org/10.33714/masteb.827195

Inal, O. B., & Deniz, C. (2018). Fuel Cell Availability for Merchant Ships. *3rd International Naval Architecture and Maritime Symposium*, 907–916.

Ling-Chin, J., & Roskilly, A. P. (2016). Investigating a conventional and retrofit power plant on-board a Roll-on/Roll-off cargo ship from a sustainability perspective - A life cycle assessment case study. *Energy Conversion and Management*, *117*. https://doi.org/10.1016/j.enconman.2016.03.032

Olmer, N., Comer, B., Roy, B., Mao, X., & Rutherford, D. (2017). Greenhouse Gas Emissions From Global Shipping, 2013-2015. *The International Council on Clean Transportation*, *October*, 1–38. https://www.theicct.org/sites/default/files/publications/Global-shipping-GHG-emissions-2013-2015_ICCT-Report_17102017_vF.pdf

Raucci, C., Calleya, J., Suarez de la Fuente, S., & Pawling, R. (2015). Hydrogen on board ship: A first analysis of key parameters and implications. *International Conference on Shipping in Changing Climates*, 12.

Rivard, E., Trudeau, M., & Zaghib, K. (2019). Hydrogen storage for mobility: A review. *Materials*, *12*(12). https://doi.org/10.3390/ma12121973

Van Hoecke, L., Laffineur, L., Campe, R., Perreault, P., Verbruggen, S. W., & Lenaerts, S. (2021). Challenges in the use of hydrogen for maritime applications. *Energy & Environmental Science*, *x*. https://doi.org/10.1039/d0ee01545h

Zincir, B., & Deniz, C. (2018). Maritime Industry Developments Related to Alternative Fuels. *3rd International Naval Architecture and Maritime Symposium*, *April*, 893–904.

Fuel Cell Systems for Submarines

[1*] Ibrahim Pamuk, [1] Ugur Aydin [2,3] Selahattin Celik, [2,3] Bora Timurkutluk, [2,3] Serkan Toros, [2,3] Yuksel Kaplan
[1] Vestel Defense Industry, Titanium Block 17/B, ODTU, Teknokent, 06800 Ankara, Turkey
[2] Nigde Omer Halisdemir University, Engineering Faculty, Mechanical Engineering Department, Nigde, 51245, Turkey
[3] Nigde Omer Halisdemir University, Prof. Dr. T. Nejat Veziroglu Clean Energy Research Center, Nigde, 51245, Turkey
* E-mail: ibrahim.pamuk@vestel.com.tr

Abstract

The high seas have long avoided air emission regulations, while fuel cell cars promise reduced emissions on land as well as reduced foreign dependency on fuel. There is no effective way to regulate pollution emissions from ships, but the fuel cell has a significant future for underwater as the best alternative to nuclear power. The fuel cell has many advantages for submarines, while the most attractive one is that it provides completely silent and air independent operation and can stay underwater for a long time without snorkel compared to that of the battery. Unlike other non-nuclear submarine variants such as gas turbines and diesel engines, fuel cells, while costly in themselves, can also be deployed on a ship for greater design flexibility, which can reduce shipbuilding costs.
Keywords: Fuel cells; Submarine; Air independent propulsion; AIP; Methanol.

I. Introduction

Submarines are classified as nuclear powered or conventionally powered vessels, depending on the propulsion type. Conventional submarines are equipped with a diesel-electric propulsion system and divided three categories (Lu et al., 2001):

- Category "A" - classic submarine with diesel-electric propulsion system
- Category "B" - classic submarine with diesel-electric propulsion system additionally supplied with air independent propulsion (AIP) system "hybrid propulsion system"
- Category "C" - submarine equipped only with air independent propulsion system

The energy generated by Category "A" is loaded into the batteries and the submarine diving operation is provided. The submersible underwater time is limited by the capacity of the batteries and the batteries are recharged with a diesel generator during snorkel. While the submarine is in the surface period, the risk of being detected by the enemy is quite high. Therefore, it has been investigated that submarine systems are equipped with a propulsion system closed to the atmosphere before entering the surface period and by this way they are submerged for relatively long times. In order to achieve this goal, propulsion systems such as closed-circuit diesel engine, Stirling engine, closed cycle gas-steam turbines and fuel cells have been developed. However, fuel cells are more preferred than other energy systems due to their specific advantages as follows:

- Operation for long periods without rising to the surface of the water
- Low noise level while working due to low magnetic properties
- Small amount of heat transfer to sea water

In 1980, for the first time in Germany, a company association was formed by Howaltswerke-Deutsch Werft AG (HDW), Ingenieurkontrol Lubeck (IKL) and Ferrostaal for the application of fuel cells to submarines. In early research, great progress has been made regarding the application of polymer electrolyte fuel cells to submarine systems. Later, 6.2 kW fuel cells consisting of 16 modules were developed by Siemens. Fuel cells with a total power of 300 kW were used in submarines named 212 Type, produced by HDW. In order for the system to operate in a safe environment, all hydrogen tanks are kept in pressure-resistant compartments. Fuel cells produced as standard for 212 Type submarines consist of 30–50kW modules, later modules with a power of up to 120 kW were also developed by Siemens.

Fuel cells, one of the leading AIP candidates, are electrochemical energy conversion devices that convert the chemical energy of a stored fuel into directly to electricity with an oxidant. There are various types of fuel cells and are generally classified according to electrolyte and operating temperature. PEM type fuel cells are the most suitable for submarines as they provide high performance at low operating temperatures. The only disadvantage is that it has limited tolerance to fuel impurities. For this reason, they need high purity hydrogen and oxygen. Therefore, liquid oxygen tank (LOX) is used as a cathode oxidizer in fuel cell submarines and pure oxygen can be easily supplied to the fuel cell. The situation is more complicated on the side of supplying fuel to the fuel cell anode. It is very difficult to store hydrogen as easily as oxygen especially for a long time. Therefore, there are different ways of supplying hydrogen to the fuel cell. The first of these is that pure hydrogen is stored in metal hydride tanks and supplied to the fuel cell system, as HDW does. Although this method makes the submarine heavier, it was preferred because of its high volumetric energy density and less risk than compressed hydrogen (Krummrich et al., 2015). However, this method needs to be improved due to the long hydrogen filling time and the limited number of mass hydrogen tanks allowed for small submarine systems. This potential problem is solved if hydrogen is produced on board rather than stored in metal hydride form. Efforts are underway to produce hydrogen from liquid form fuels in submarine systems. The most popular one is to obtain hydrogen by separating diesel and methanol. Naval Group has reported that generated electricity continuously for 18 days in representative submarine patrol operational conditions. A methanol reforming technology development can be applied to obtain hydrogen for the fuel cell to power the submarine. However, the liquid hydrogen and methanol reforming methods are both volume limited and the plug displacement is much greater than the system mass (Brighton et al., 1994). Therefore, it needs to be

developed to be more compact. A development collaboration agreement between ThyssenKrupp Marine Systems and SENER was signed to develop this process in 1995. The first full-size methanol reformer in ThyssenKrupp Marine Systems has been tested since 2008. It was successfully operated with the SIEMENS fuel cell (2010) and the SENER (2013) exhaust gas dissolution system. The hydrogen produced by the reformer fulfilled the high purity requirements of the fuel cell, with no difference observed when compared to the treatment on pure hydrogen from liquid hydrogen storage. Moreover, the reformer exhaust gas was completely dissolved in seawater and no bubbles were reported even under more restrictive environmental conditions. The schematic of fuel cell system for submarine AIP is shown in Figure 1.

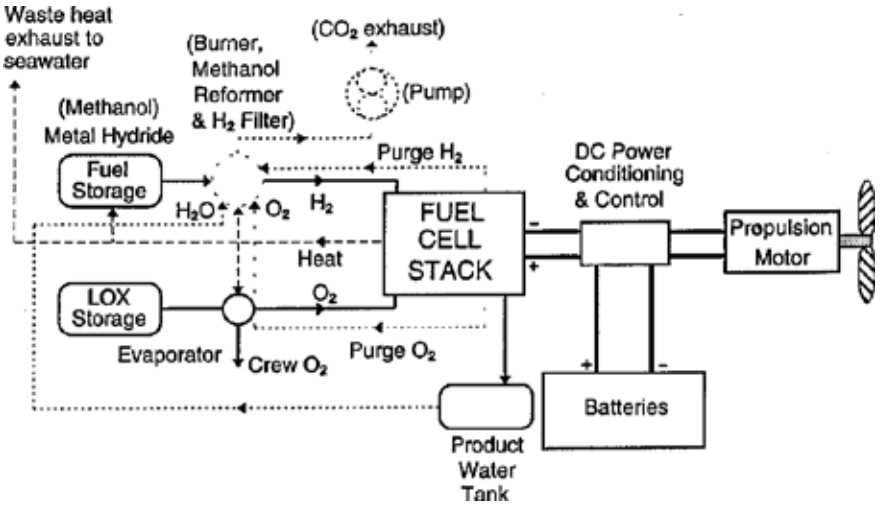


Fig. 1: Schematic of Fuel Cell System for Submarine AIP (Mart et al., 1995)

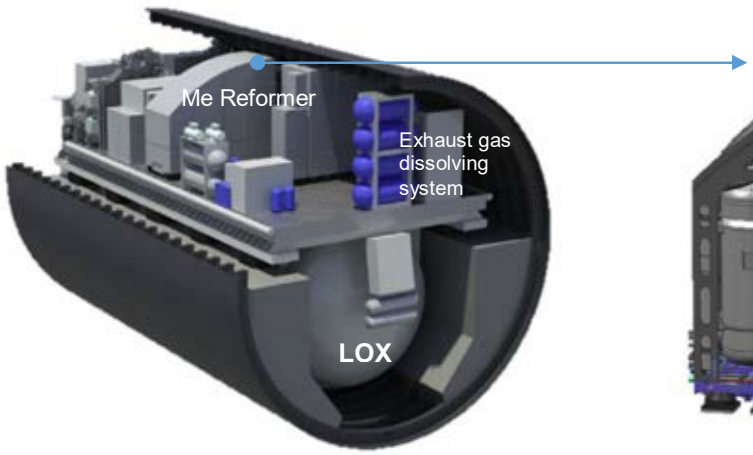


Fig. 2: AIP integration on the submarine (Krummrich et al., 2015)



Fig. 3: Details of metanol reformer section

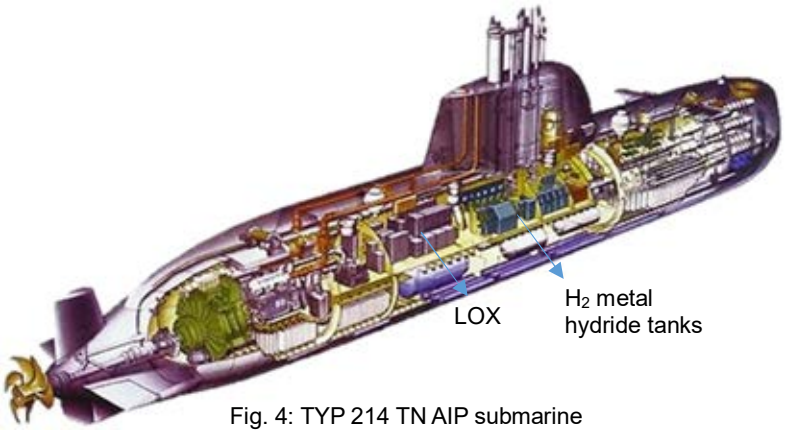


Fig. 4: TYP 214 TN AIP submarine

Figure 2 and Figure 3 show the submarine integration of AIP and details of the methanol reformer, respectively. As can be seen from the figures, it is understood that volumetric restrictions have been developed. The use of volumetric limitations in liquid hydrogen storage has been tested by adjusting the evaporation rate of hydrogen in unmanned aerial vehicles according to fuel cell consumption, and positive results have been obtained. However, in these liquid hydrogen tanks that are not cryogenically cooled, the excess hydrogen evaporated must be evacuated. In addition, the logistics of liquid hydrogen to the submarine is more difficult than that of methanol. Therefore, the use of liquid hydrogen in submarine systems has limitations that need to be improved. As a result, hydrogen production onboard with methanol reforming will take place in the world market commercially in a more viable structure in the future.
Figure 4 shows the TYP 214 TN submarine, which was manufactured jointly by the Turkish Naval Forces and expected to be commissioned in 2022. The submarine is operated by the fuel cells using hydrogen stored in metal hydride tanks (Sunnetci, 2020). Naval Group has announced generated electricity continuously for 18 days in representative submarine patrol operational conditions, thanks to a fuel cell powered by a diesel reforming hydrogen production system developed in partnership with IFPEN (Ifp energies, 2015).

II. Numerical Set-Up and Procedure

VESTEL Defence Industry has gained significant knowledge in Solid Oxide Fuel Cell (SOFC), diesel reformer and stack development and has created national and international publications in SOFC membrane production, SOFC cell and stack design/fabrication, sodium boron hydride (SBH) hydrogen production, PEM fuel cells for UAV's areas as well as many patents and utility models. Recently, experimental studies have been conducted on PEM fuel cells using H_2 / O_2. An innovative cell design has been developed for use in all types of marine systems. During the design development process, mechanical, flow and electrochemical simulations related to cell manufacturing were performed and performance tests were carried out at the end of manufacturing.

III. Results and discussions

Performance results of the open-cathode PEM fuel cell are shown in Figure 5. The maximum power density of about 900 mW/cm^2 has been reached in optimum operating conditions (80 °C, %80 humidity).

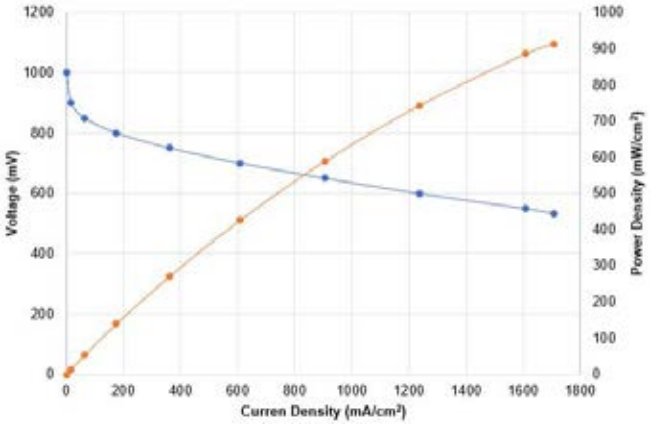


Fig. 5: Performance tests results

IV. Conclusions

PEM fuel cells and metal hydride hydrogen storage combination for submarine systems are accepted as air-independent propulsion systems. It is anticipated that in the future, methanol reforming systems, where hydrogen fuel is produced in the submarine will be used. Similarly, if the diesel reforming - solid oxide fuel cell combination passes some tests successfully, it will be an alternative to methanol reforming. According to the results of the experimental study, high power density values are obtained from the newly developed fuel cell design. In the next step, a high performance fuel cell stack will be designed and tested in accordance with the air independent propulsion system. High performance separation will be achieved by developing a new type of catalyst for reforming methanol. It is aimed to provide high performance separation by developing a new type of catalyst for methanol reforming. In addition, more work is needed to purify the hydrogen-rich gas formed as a result of the reaction and release carbon dioxide from the submarine without leaving a trace.

References

Brighton D.R., Mart P.L., Clark G.A., Rowan M.J.M., The use of fuel cells to enhance the underwater performance of conventional diesel electric submarines, Journal of Power Sources, 51, 3, 375-389, (1994).

Mart P., Margeridis J., Fuel Cell Air Independent Propulsion of Submarines, Engineering (1995)

Lus T., Submarine Hybrid Propulsion Systems, Journal of Kones. Combustion Engines, 8, 1-2, (2001).

Krummrich S., Llabres J., Methanol reformer -The next milestone for fuel cell powered submarines, International journal of hydrogen energy, 40, 5482-5486, (2015)

Ifp energies nouvelles, https://www.ifpenergiesnouvelles.com/article/onboard-hydrogen-production-submarines

Sunnetci İ., "Type 214TN REIS Class & Submarine Capabilities in the Eastern Mediterranean", Defence Turkey, 14, 98, 82-89, (2020)

The Optimal Isosteric Heat of H_2 Adsorption on Co(II)- and Ni(II)- exchanged ZSM-5 and US-Y

[1]Nurkan Sarohan, [1]*Bahar Ipek
[1]Middle East Technical University, Faculty of Engineering, Chemical Engineering Department, Dumlupinar Bulvari No 1, Ankara, 06800, Turkey

* E-mail: bipek@metu.edu.tr

Abstract
The most crucial problem encountered in hydrogen storage applications is the target level of 5.5 wt.%, which cannot be reached using existing technologies at room temperature and low pressures (<100 bar). In this project, Co(II)- and Ni(II)-exchanged mesoporous ZSM-5 and zeolite Y were prepared and tested for H_2 adsorption at room temperature and up to pressures of 50 bar. A mesopore volume of 0.18 cm^3/g was obtained on ZSM-5 using desilication method. Following the ion-exchange in aqueous medium, M^{+2}/Al ratios as high as 0.20-0.25 were obtained. According to the H_2 adsorption tests, Ni(II)-ZSM-5 and Ni(II)-US-Y showed 0.55 wt.% H_2 capacity at 50 bar and 298 K, which is higher than the capacity obtained on a Ni_2(m-dobdc) MOF sample at similar conditions. The isosteric heat of adsorption values calculated using Clausius-Clapeyron equation were found between 18 and 45 kJ/mol on Co(II) and Ni(II)-exchanged zeolites.

Keywords: H_2 storage, zeolite, cobalt, nickel, isosteric heat

I. Introduction

Reduced resources and concerns about the negative environmental impacts of burning fossil fuels motivated search for alternative and sustainable energy sources for transport applications. In this regard, hydrogen becomes an attractive option to replace existing hydrocarbon-based systems with high energy storage capacity (1 kg hydrogen supplies 120 MJ energy). The disincentive concern in front of the use of hydrogen as an alternative fuel is the inefficiency of the storage technologies. In practice, the 2025 targets decided by the US DOE (Department of Energy) are: gravimetric capacity of 5.5 wt % and volumetric capacity of 40 g/L at an operating temperature of 233 K to 333 K under a maximum delivery pressure of 12 bar. Specific to material-based adsorption systems, hydrogen can be stored either chemically or physically. Chemical adsorption involves strong chemical interaction in complex hydrides or metal hydrides (Bellosta von Colbe et al., 2019), which can reach DOE targets with $Mg(BH_4)_2$ (14.9 wt %) and $LiBH_4$ (18.5 wt %,120 g/L) (Orimo et al., 2007) with a high adsorption energy (110 kJ/mol–230 kJ/mol) that requires temperatures above 573 K for desorption. In comparison to chemisorption, physisorption with porous materials (carbon based materials, metal organic frameworks (MOF), covalent organic framework (COF), and zeolites) shows reversible and fast hydrogen uptake. Many of porous materials show moderately high hydrogen storage capacities at cryogenic temperatures (77 K) and high pressures. However, their capacities drop below 1 wt.% at ambient temperature and pressure in the range 50-100 bar (Broom et al., 2016) due to their low heat of adsorption values. To illustrate, Ni_2 (m-dobdc) and Co_2 (m-dobdc) MOFs shows the highest adsorption values of 11 g H_2/L by volume or 0.9% by weight (298 K, 100 bar) at ambient temperature (Kapelewski et al., 2018) with reported heat of H_2 adsorption values of ~12kJ/mole (Kapelewski et al., 2014). According to theoretical calculations, the optimum adsorption enthalpy of porous materials at ambient temperature should be between 15–25 kJ/mole to have maximum H_2 delivery amounts between the designated adsorption and desorption pressure values. (Bae & Snurr, 2010; Garrone et al., 2008a). H_2 storage capacities of zeolites containing protons or alkali metal cations are reported between 1 and 2 percent by weight (77 K at 1 atm) mainly due to the low heat of adsorption values besides limited pore volumes (maximum 0.33 cm^3/g) (Vitillo et al., 2005). In order to overcome pore restriction problem, as well as low heat of adsorption values, we prepared transition metal (Co(II) and Ni(II)) exchanged zeolites with mesopore additions. For mesopore additions, a top-down method (desilication) is applied to ZSM-5. Then, prepared zeolites were tested for H_2 storage at 298 K and 50 bar. The isosteric heat of adsorption values were also calculated for temperatures between 293 K and 333 K at pressures up to 10 bar.

II. Experimental Set-up and Procedure

ZSM-5 was synthesized using a procedure ($100SiO_2$:$2Al_2O_3$:40TPA:$8Na_2O$:$150H_2O$) reported elsewhere (Kustova et al., 2006). In order to increase mesopores in ZSM-5, desilication was applied with NaOH (J.T.Baker,95%) in 200 ml of 0.2 M at 353 K for 30 min (Groen et al., 2004) and NH_4^+-US-Y (Alpha Aesar, Si/Al=6, CAS:1318-02-0.1) was obtained commercially. NH_4^+-ZSM-5 were exchanged three times with cobalt (II) nitrate hexahydrate (Merck, 98%) in 150 ml of 0.1 M at 353 K for 9 h and two times with cobalt-(II)-sulfate heptahydrate (Merck, 97%) in 75 ml of 0.5 M at ambient temperature for 24 h to obtain Co(II)-ZSM-5. NH_4^+-ZSM-5 were exchanged three times with nickel-(II)-nitrate hexahydrate (Merck, 99%) in 150 ml of 0.2 M at 353 K for 9 h and one time at ambient temperature for 24 h to obtain Ni(II)-ZSM-5. NH_4^+-US-Y were exchanged with cobalt (II) nitrate hexahydrate (Merck, 98%) in 150 ml of 0.03 M at ambient temperature for 12 h and 0.1 M at ambient temperature for 24h to obtain Co(II)-US-Y. NH_4^+-US-Y were exchanged two times with nickel-(II) nitrate hexahydrate (Merck, 98%) in 75 ml of 0.5 M at ambient temperature for 24 h to obtain Ni(II)-US-Y.

High pressure (up to 50 bar) experiments were conducted using a Micrometric High Pressure Volumetric Analyzer. Before the experiment, degas was applied for 4 hours at 623 K and hydrogen was adsorbed up to 50 bar at 298 K. In order to determine isosteric heat values, hydrogen adsorption experiments were also carried out with a home-

made and high pressure volumetric adsorption system. This system consists of high pressure resistant steel pipes and connections. In addition, there is an explosion-proof digital pressure manometer (Keller, ECO2-Ei / -1 30bar / 81201.1) and a 7 micron filter (Swagelok Filter, 0002454293). Primarily, zeolites were degassed under vacuum for 1 hour at 653 K using a scroll vacuum pump (Agilent Technologies, Model IDP3). The free volume was calculated at room temperature using Helium (Hatgaz, 99.999%). After free volume measurements, the system was evacuated for 1 h at 653 K. For the H_2 adsorption experiments carried out at room temperature, hydrogen (Hatgaz, 99.999%) was dosed incrementally up to 10 bar using 0.5 bar increments. At each gas dosing, an average of 10 minutes was waited for equilibrium. In order to calculate the isosteric heat, H_2 adsorption was repeated at three different temperatures and coverage dependent heat values were calculated using Clasius-Clapeyron (Equation.1).

$$\ln \frac{P_1}{P_2} = -\frac{Q_{st}}{R}\left(\frac{1}{T_1} - \frac{1}{T_2}\right) \quad \text{(Equation.1)}$$

The crystallinity of prepared zeolites were tested in METU Central Laboratory using Rigaku Ultima-IV X-Ray Diffraction Device (Cu Kα source, λ = 1.54 Å) with a scanning speed of 1°/min between 2–50 2θ degrees. Scanning electron microscope pictures of zeolites were obtained with QUANTA 400F Field Emission electron microscope. 20-30 kV voltage is used. The elementary analysis was performed using both energy dispersive X-ray analysis (EDX) and inductively coupled plasma-optical emission spectrometer (Perkin Elmer Optime 4300DV). Surface area and pore volumes of zeolites were calculated using N_2 adsorption experiments conducted at 77 K by Micromeritics Tristar II 3020. Prior to N_2 (Oksan, 99.999%) adsorption tests, the samples were degassed under 150 mbar vacuum at 573 K for 6 hours. Statistical thickness method, t-plot method, was used for micropore volumes, BJH method was used for pore size distribution.

IV. Results and Discussions

The highest H_2 adsorption amount was observed on both Ni(II)-ZSM-5 and Ni(II)-US-Y with a storage value of 0.55 wt.% at 50 bar and 298 K (see Figure 1). Co(II)-US-Y and Co(II)-ZSM-5 followed the nickel exchanged zeolites with 0.44 wt.% and 0.35 wt.% storage capacity values respectively. Considering the higher Ni-concentration in US-Y when compared to Ni-ZSM-5 (3.8 mmol/g in Ni-USY vs. 1.9 mmol/g in Ni-ZSM-5, see Table 1), the H_2 adsorption per Ni(II) cation is higher in ZSM-5, indicating a stronger Ni(II)-H_2 interaction. The H_2/metal ratios obtained from Figure 1 follows an order of Ni(II)-ZSM-5, Co(II)-USY, Co(II)-ZSM-5 and Ni(II)-USY, which is the same order when the initial heat of adsorption values are considered (see Figure 2). This indicates a strong influence of heat of adsorption values on H_2 storage capacity values even at 50 bar. For example, Ni(II)-ZSM-5 shows higher adsorbed hydrogen than Co(II)-ZSM-5 in both per gram and per metal basis (0.35 wt.% and 7.2 H_2/Co vs. 0.55 wt.% and 14 H_2/Ni) indicating that nickel ions make stronger bonds with hydrogen. When isosteric heats are considered in the Figure 2, Ni(II)-ZSM-5 show an initial heat of adsorption value of 45 kJ/mol, while Co(II)-ZSM-5 show a value of 18 kJ/mol.

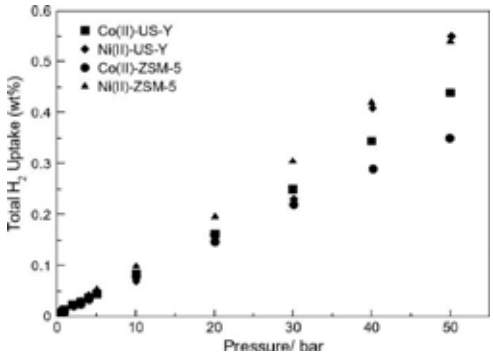


Fig. 2:H_2 adsorption isotherm in terms of gravimetric capacity

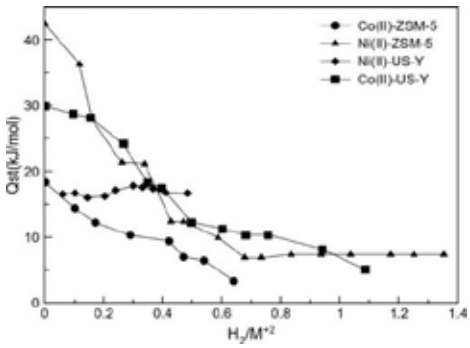


Fig. 1:Isosteric heats with respect to per metal adsorbed hydrogen

However, H_2/M^{+2} ratios exceeding 10 at 50 bar also indicates that not all H_2 molecules are bonded to cations. After the cations in the structure are saturated with approximately two H_2 molecules, hydrogen begins to be adsorbed on the pore walls. For adsorption on pore walls, both surface area and the pore size of the adsorbents become important. In particular, the smaller pore opening (~ 0.5 nm) of the ZSM-5 frame may have caused high H_2 adsorption due to increased Van der Waals interactions, although they have lower total pore volume and surface area when compared to Y zeolite that has larger pore sizes (> 1 nm) (Jordá-Beneyto et al., 2007). However, since adsorption on walls becomes important, the higher surface area of US-Y zeolites (reaching ~1000 m^2/g) is useful especially at higher pressures.

It has been emphasized in the theoretical studies conducted so far that 15–25 kJ/mol energy should be targeted for low chemical adsorption and strong physical adsorption (Garrone et al., 2008b). When our coverage dependent heat of adsorption results are examined, it can be said that the average heat of adsorption values, Q_{st}, are close to the optimal range. In previous studies performed with different metals, especially with the MOFs, the hydrogen holding enthalpy ranges between 8–12 kJ / mol (Gygi et al., 2016). Therefore, addition of transition metal cations; Ni(II) and Co(II), to zeolites favors H_2 adsorption at room temperature due to close to optimal heat of adsorption values as well as favored pore sizes.

Table 1:Elemental analysis (EDX) and micropore (t-plot) /mesopore volumes (V_{total}-V_{micro}) of Ni(II)-ZSM-5,Co(II)-ZSM-5, Ni(II)-US-Y and Co(II)-ZSM-5

	Co(II)-ZSM-5	Ni(II)-ZSM-5	Co(II)-US-Y	Ni(II)-US-Y
Si/Al	16±2	18±2	5	5±0.5
M^{+2}/Al	0.25±0.06	0.22±0.05	0.1	0.21±0.06
mmol M^{+2}/g	1.4	1.9	1.6	3.8
$A_{Langmuir}$ (m^2/g)	343	354	968	1006
V_{total} (cm^3/g)	0.27	0.25	0.46	0.49
t-plot V_{micro} (cm^3/g)	0.10	0.09	0.28	0.29
V_{meso} (cm^3/g)	0.18	0.16	0.18	0.20

V. Conclusions

H_2 adsorption capacity and isosteric heat of H_2 adsorption values were investigated on Ni (II)-ZSM-5, Co(II)-ZSM-5, Ni(II)-US-Y and Co(II)-US-Y at 298 K and up to 50 bar pressure. Mesoporous Ni(II)-ZSM-5 and Ni(II)-US-Y show promising gravimetric storage capacity with a value of 0.55 wt%(g/g). H_2 storage capacity of Ni(II)-ZSM-5 at 298 K and 50 bar is found to be higher than the highest H_2 storage capacity reported on physical adsorbents in literature (0.54 wt.% at 298 K and 50 bar, (Kapelewski et al., 2018)) Ni(II)-ZSM-5 showed the highest initial heat value with 45 kJ/mol. This zeolite was followed by Co(II)-USY (30 kJ/mol), Co(II)-ZSM-5 (18 kJ/mol), and Ni(II)-USY (17 kJ/mol) respectively. The calculated isosteric heats were found to be an important factor in determination of the H_2 storage capacity values at 298 K. However, as the H_2/M^{+2} values increased, the heat of adsorption values decreased as expected (up to ~ 8 kJ / mol values), indicating adsorption on zeolite walls. The average heat of adsorption values in the 1–10 bar range were found to be close to the reported optimal 25 kJ/mol value indicating potential for Co(II) and Ni(II)-exchanged zeolites.

Acknowledgements

This research was supported by Middle East Technical University BAP project number GAP-304-2020-10275. We also acknowledge Koç University TÜPRAŞ Enerji Merkezi (KUTEM) for high pressure H_2 adsorption experiments.

References

Bae, Y. S., & Snurr, R. Q. (2010). Optimal isosteric heat of adsorption for hydrogen storage and delivery using metal-organic frameworks. *Microporous and Mesoporous Materials*, *132*(1–2), 300–303. https://doi.org/10.1016/j.micromeso.2010.02.023

Bellosta von Colbe, J., Ares, J. R., Barale, J., Baricco, M., Buckley, C., Capurso, G., Gallandat, N., Grant, D. M., Guzik, M. N., Jacob, I., Jensen, E. H., Jensen, T., Jepsen, J., Klassen, T., Lototskyy, M. V., Manickam, K., Montone, A., Puszkiel, J., Sartori, S., … Dornheim, M. (2019). Application of hydrides in hydrogen storage and compression: Achievements, outlook and perspectives. *International Journal of Hydrogen Energy*, *44*(15), 7780–7808. https://doi.org/10.1016/j.ijhydene.2019.01.104

Broom, D. P., Webb, C. J., Hurst, K. E., Parilla, P. A., Gennett, T., Brown, C. M., Zacharia, R., Tylianakis, E., Klontzas, E., Froudakis, G. E., Steriotis, T. A., Trikalitis, P. N., Anton, D. L., Hardy, B., Tamburello, D., Corgnale, C., van Hassel, B. A., Cossement, D., Chahine, R., & Hirscher, M. (2016). Outlook and challenges for hydrogen storage in nanoporous materials. *Applied Physics A: Materials Science and Processing*, *122*(3), 1–21. https://doi.org/10.1007/s00339-016-9651-4

Garrone, E., Bonelli, B., & Otero Areán, C. (2008a). Enthalpy-entropy correlation for hydrogen adsorption on zeolites. *Chemical Physics Letters*, *456*(1–3), 68–70. https://doi.org/10.1016/j.cplett.2008.03.014

Garrone, E., Bonelli, B., & Otero Areán, C. (2008b). Enthalpy-entropy correlation for hydrogen adsorption on zeolites. *Chemical Physics Letters*, *456*(1–3), 68–70. https://doi.org/10.1016/j.cplett.2008.03.014

Gygi, D., Bloch, E. D., Mason, J. A., Hudson, M. R., Gonzalez, M. I., Siegelman, R. L., Darwish, T. A., Queen, W. L., Brown, C. M., & Long, J. R. (2016). Hydrogen Storage in the Expanded Pore Metal-Organic Frameworks M2(dobpdc) (M = Mg, Mn, Fe, Co, Ni, Zn). *Chemistry of Materials*, *28*(4), 1128–1138. https://doi.org/10.1021/acs.chemmater.5b04538

Jordá-Beneyto, M., Suárez-García, F., Lozano-Castelló, D., Cazorla-Amorós, D., & Linares-Solano, A. (2007). Hydrogen storage on chemically activated carbons and carbon nanomaterials at high pressures. *Carbon*, *45*(2), 293–303. https://doi.org/10.1016/j.carbon.2006.09.022

Kapelewski, M. T., Geier, S. J., Hudson, M. R., Stück, D., Mason, J. A., Nelson, J. N., Xiao, D. J., Hulvey, Z., Gilmour, E., Fitzgerald, S. A., Head-Gordon, M., Brown, C. M., & Long, J. R. (2014). M2(m-dobdc) (M = Mg, Mn, Fe, Co, Ni) metal-organic frameworks exhibiting increased charge density and enhanced H2 binding at the open metal sites. *Journal of the American Chemical Society*, *136*(34), 12119–12129. https://doi.org/10.1021/ja506230r

Kapelewski, M. T., Runčevski, T., Tarver, J. D., Jiang, H. Z. H., Hurst, K. E., Parilla, P. A., Ayala, A., Gennett, T., Fitzgerald, S. A., Brown, C. M., & Long, J. R. (2018). Record High Hydrogen Storage Capacity in the Metal-Organic Framework Ni2(m-dobdc) at Near-Ambient Temperatures. *Chemistry of Materials*, *30*(22), 8179–8189. https://doi.org/10.1021/acs.chemmater.8b03276

Orimo, S. I., Nakamori, Y., Eliseo, J. R., Züttel, A., & Jensen, C. M. (2007). Complex hydrides for hydrogen storage. *Chemical Reviews*, *107*(10), 4111–4132. https://doi.org/10.1021/cr0501846

Vitillo, J. G., Ricchiardi, G., Spoto, G., & Zecchina, A. (2005). Theoretical maximal storage of hydrogen in zeolitic frameworks. *Physical Chemistry Chemical Physics*, *7*(23), 3948–3954. https://doi.org/10.1039/b510989b

Comparison of PEM Fuel Cell vs. Lithium-Sulfur Battery Systems for Unmanned Aerial Vehicles

[1,2*]Nisa Erisen, [3]Damla Eroglu, [1]Harun Koku, [1]İnci Eroglu
[1] Middle East Technical University, Department of Chemical Engineering, 06800, Ankara, Turkey
[2] Roketsan Missiles Inc. Ankara, Turkey
[3] Boğaziçi University, Department of Chemical Engineering, 34342, İstanbul, Turkey

* E-mail: erisen.nisa@metu.edu.tr

Abstract
Electrically powered unmanned aerial vehicles (UAVs) are gaining attention and attempts are underway to improve their performance in terms of weight, vibration, noise, emission and reliability. Fuel cells or batteries are commonly used systems in these UAVs. In this study, the energy storage comparison between the Proton Exchange Membrane (PEM) fuel cell and the Lithium-Sulfur (Li-S) battery is performed for a 500W UAV to determine the appropriate design. While a commercial product is used for the mass predictions of the PEMFC case, the developed system-level performance model is used for the Li-S battery. It is observed that the PEM fuel cell case is favorable for all of the flight times investigated here and there is a need for an analysis beyond the boundaries of the designated case study to observe the conditions in which the use of Li-S battery is more advantageous.

Keywords: Hydrogen Energy, PEM Fuel Cell, Li-S Battery, Unmanned Aerial Vehicles

I. Introduction

UAVs are autonomously or remotely controlled flying robots, used for applications in diverse fields such as meteorology, monitoring, agriculture and delivery. Their propulsion systems are based on batteries, fuel cells, micro-diesels and micro gas turbines. Having an electric-based powertrain in unmanned aerial vehicles is the most convenient option when the weight, vibration, noise, emission and reliability are considered (Pan et al., 2019). Among electrically powered UAVs, Proton Exchange Membrane (PEM) fuel cells, Lithium-ion (Li-ion) and Lithium-Polimer (Li-Po) batteries are widely used power sources (Wang et al., 2020). Fuel cells are advantageous in terms of high energy density and quick refueling, but they have drawbacks related with hydrogen storage and slow response. In contrast, batteries are advantageous in terms of power density and fast response, however their recharging is slow.

Increasing the endurance and the flight range at reasonable weight and volume is crucial. To achieve an extension in endurance, while the battery-based case requires a multiplication of batteries, the fuel cell-based case requires an increased amount of hydrogen stored only, without a change in the fuel cell stack weight. Thus, the increase in the weight of the battery pack is significant compared to fuel cell system for longer flight times. To overcome this endurance limitation, current Li-ion and Li-Po batteries can be replaced by high energy density equivalents since their technology have become saturated. As a result, there is a need for investigation beyond Li-ion batteries, such as Lithium-Sulfur (Li-S) batteries in those application areas.

Li-S batteries are becoming promising energy storage systems alternative in rechargeable battery technologies due to their high theoretical specific energy (2567 Wh/kg) and sulfur's natural abundancy, non-toxicity and low cost (Emerce and Eroglu, 2019). The overall reaction for the Li-S battery with a standard potential of U_0=2.2 V (vs Li/Li+) is shown in Equation 1.

$$16Li + S_8 \rightarrow 8Li_2S \quad (1)$$

In the literature, there are examples of UAVs based on a hybrid powertrain of Li-S batteries with solar cells (Rapinett, 2009) and with combined solar cell and fuel cell (Lee, 2020), with the former having an energy density of 350 Wh/kg and the latter 410 Wh/kg. (Dörfler et al., 2021). Both cases exhibit a higher energy density with respect to commercial Lithium-based battery equivalents.

Thus, it is worthwhile to discuss whether which case, fuel cell or battery, is reasonable for the specifically designed UAVs. In this study, a comparison of the UAV powertrains of PEM Fuel Cell-based and Li-S battery-based has been conducted to analyze the weight increase in both systems as the UAV energy requirement increases. Based on this analysis, a conceptual design of the UAV can be proposed.

II. Modeling

The modelling basis was developed according to a study of Ustolin et al. (2018) and a design for a UAV was proposed according to the parameters in Table 1. Thus, both the PEM fuel cell and the Li-S battery system were designed accordingly. The PEM fuel cell system consists of a fuel cell stack, a hydrogen tank, a pressure regulator, a DC/DC converter, a stack controller and a purge valve (Ustolin et al., 2018). The Li-S battery system is composed of a battery pack, Battery Management System (BMS), Thermal Management System (TMS) and a DC/DC converter. For the Li-S battery system design, the methodology developed by Eroglu et al. (2015) and Emerce and Eroglu (2019) was followed.

Tab. 1: The parameters used in the model

	Parameter	Value
UAV Design Parameters	**Power, [W] [a]**	500
	Voltage, [V] [a]	*35*
	Endurance time, [hr]	*1 to 5*
PEM Fuel Cell Parameters	**Number of cells [a]**	*45*
	Stoichiometric ratio of H_2	*1.2*
Li-S Battery Parameters [b]	**The capacity usage, %**	*85*
	Cathode active material/carbon/binder weight percentage	*70/20/10*
	Electrolyte volume percentage	*50*

[a] The values are taken from commercially available Aerostack A-500 PEM Fuel Cell.
[b] The detailed modelling parameters are available in the study of Eroglu et al. (2015) and Emerce and Eroglu (2019).

III. Analysis

For the PEM fuel cell analysis, after the selection of the off-the-shelf stack, the hydrogen requirement is calculated by using Equation 2.

$$m_{H_2} = S_{H_2} * \frac{I}{2F} * M_{H_2} \quad (2)$$

Where $\dot{m}_{H_2}$ defines the hydrogen flow rate (g.s-1); S_{H_2} defines the stoichiometric ratio of hydrogen; I defines the stack current (A); F defines the Faraday's constant (C.mol-1) and M_{H_2} defines the molecular weight of hydrogen.

After the stored hydrogen amount for the specified flight times is determined, it is assumed to be stored at 300 bar gas cylinders. The hydrogen tanks to fulfill that mission is selected according to the products given by Luxfer Gas Cylinders. Finally, mass of the whole system is found by multiplication of the total mass of FC stack, hydrogen and hydrogen tank by the BOP coefficient as there is no detailed information available in the study of Ustolin et al. (2018). The weight increase at extending flight times is taken into account in the model by changing the amount of hydrogen stored and keeping the fuel cell stack mass constant.

For the Li-S battery analysis, a system-level performance model, which predicts the weight of the Li-S battery, is proposed by modifiying the publicly available Battery Performance and Cost (BatPaC) model (Nelson et al., 2012). First, the designated power, energy and voltage values are fed to the model. The Li-S cell is designed accordingly by considering the critical cell design parameters. The proposed system-level performance model uses an electrochemical model to predict the electrochemical performance and couple it with the cell- and system-level design, whose detailed explanation is given in the study Emerce and Eroglu (2019). Here, the total overpotential is calculated via the electrochemical model for the cell composed of the porous sulfur-carbon composite cathode, porous separator, Li-metal anode and the current collectors. Then, the cell area is determined by the power requirements, the cell capacity and thickness are defined by the energy necessities and the number of cells are calculated based on the pack voltage specifications. Finally, the cell- and system-level energy density and specific energy of the Li-S battery are predicted by the model. For all of the flight times, the energy storage is calculated by multiplying the power and the endurance and the design for the Li-S battery-based UAV is conducted accordingly.

IV. Results and discussions

For the designed 500 W UAV, the effect of energy storage from 500 Wh to 2500 Wh on the fuel cell and Li-S battery system mass is given in Figure 1.

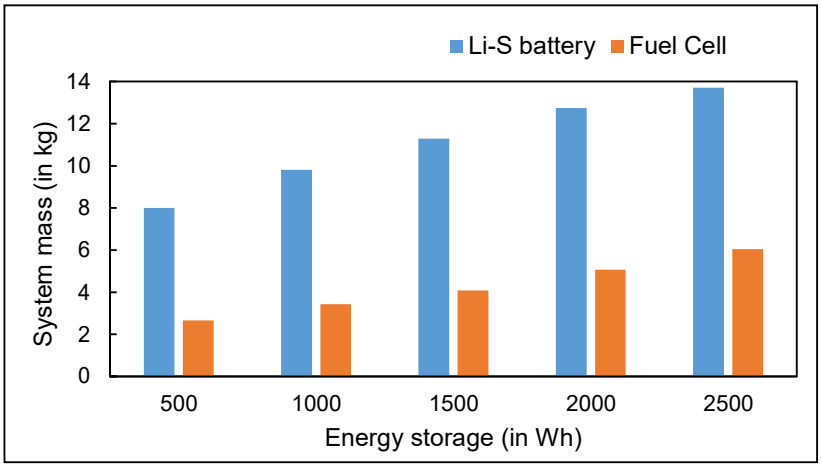


Fig. 1: The change in the energy storage of the 500 W PEM fuel cell system mass vs. Li-S battery mass

For all the energy storage values studied here, the UAV having a Li-S battery is much heavier than the one with a fuel cell and it is concluded that for the designed UAV spesifications, fuel cell case is more advantageous. In the study of Ustolin et al. (2018), the battery is lighter than the fuel cell at low energy storage values, whereas as the energy storage increases, the fuel cell case becomes more favorable. In our study, we do not observe such a trend, which may arise from the balance-of-plant (BOP) components of the Li-S battery. As a future work, there is a need for extending the lower and upper boundaries of the energy and power requirements to observe the change in the system mass. Morever, the effect of critical design parameters in a Li-S battery, such as the sulfur loading and the electrolyte-to-sulfur ratio in the cathode, on the system mass will be analyzed.

V. Conclusions

The UAVs are dominantly used in many application areas and there is a demand for higher endurances in the advantageous electrically powered ones. In this study, system mass comparison of PEM fuel cell- vs. Li-S battery-powered 500 W UAV is performed for 1 to 5 hr flight endurance. For the fuel cell case, a commercial PEMFC stack is selected and the required hydrogen mass is calculated. For the Li-S battery case, an electrochemical model coupled with a system-level performance model for the battery pack is used. According to the case study analysis, fuel cell-based UAV is lighter than the Li-S battery-based UAV. There is a need for further investigation to determine the power and the energy requirements where the Li-S battery case is more beneficial. A sensitivity analysis will be performed on the critical design parameters of the Li-S battery for the mass predictions for the UAV.

References

Dörfler S., Walus S., Locke J., Fotouhi A., Auger D. J., Shateri N., Abendroth T., Härtel P., Althues, H. and Kaskel, S., Recent Progress and Emerging Application Areas for Lithium–Sulfur Battery Technology. Energy Technology, 9(1), 2000694, (2021).

Emerce N. B., & Eroglu D., Effect of electrolyte-to-sulfur ratio in the cell on the Li-S battery performance. Journal of The Electrochemical Society, 166(8), A1490, (2019).

Eroglu D., Zavadil K. R., & Gallagher K. G., Critical link between materials chemistry and cell-level design for high energy density and low cost lithium-sulfur transportation battery. Journal of The Electrochemical Society, 162(6), A982, (2015).

HES. Aerostacks A-series. 2021 [Online]. Available: https://www.hes.sg/aerostak [Accessed 10 March 2021].

Lee S., LG Chem tests drone with lithium-sulfur battery. Production to begin in 2025, http://www.thelec.net/news/articleView.html?idxno=1525 (accessed: March 2021)

Luxfer Gas Cylinders [Online]. https://www.luxfercylinders.com/products/ [Accessed 23 March 2021].

Nelson P. A., Gallagher K. G., Bloom I. D., & Dees D. W., Modeling the performance and cost of lithium-ion batteries for electric-drive vehicles (No. ANL-12/55). Argonne National Lab.(ANL), Argonne, IL (United States), (2012).

Rapinett A., Zephyr: a high altitude long endurance unmanned air vehicle. Doctor, Department of Physics, University of Surrey, (2009).

Ustolin F., Taccani R., Fuel cells for airborne usage: Energy storage comparison. International Journal of Hydrogen Energy, 43(26), 11853-11861, (2018).

Wang B., Zhao D., Li W., Wang Z., Huang Y., You Y., & Becker S., Current technologies and challenges of applying fuel cell hybrid propulsion systems in unmanned aerial vehicles. Progress in Aerospace Sciences, 116, 100620,

Development of Cost-effective Dense Metallic Membranes for Hydrogen Separation

[1,2]Fatih Piskin and [2,3]Tayfur Öztürk

[1] Dept. of Metallurgical and Materials Engineering, Muğla Sıtkı Koçman University, Muğla, TURKEY
[2] ENDAM, Center for Energy Storage Materials and Devices, Middle East Technical University, Ankara, TURKEY
[3]Dept. of Metallurgical and Materials Engineering, Middle East Technical University, Ankara, TURKEY

* E-mail: ozturk@metu.edu.tr

Abstract
The need for hydrogen separation membranes has augmented over the years and it appears that it will continue augmenting further in coming decades. Instead of classical approach of addressing the need for hydrogen separation in centralized syngas facilities, it appears that there will be widespread need of relatively small scale installments either for feeding the hydrogen into storage system or taking the hydrogen from it wherever it is needed. The storage system in question could cover a number of alternatives, the most important is the network of natural gas pipeline which appears to be the emerging storage medium for hydrogen. It is thus timely to have a look at cost reduction strategies that can be employed in fabrication of separation membranes. The basis is commonly used separation membrane with composition of Pd-23%Ag. Two strategies may be employed; one to follow the basic strategy reflected by Pd- 23 %Ag, i.e. f.c.c. membranes that are ductile and can be processed metallurgically into capillary tube or foil so that useful separation devices can be fabricated. Here there are two issues to be addressed; one how to reduce Pd content in order to make it cost effective, the second how to reduce the operating temperature which are traditionally targeted to syngas generation down to the much lower temperatures needed for the present or future needs. The second strategy would address the same but not via metallurgical processing of selected alloys but to direct fabrication of separation membranes via thin film deposition. In this paper, we investigate cost effective membranes in ternary alloys based on Pd-Ag-Ti, Pd-Ag-Ni, Pd-Ag-Mn and Pd-Nb-Ti using an efficient search methodology based on combinatorial material chemistry.

Keywords: Hydrogen separation membranes, Thin film membranes, Capillary tube,

Energy and environmental assessment of transition to hydrogen vehicles

[1]Merve Nur Dinç, [1]Murat Kıstı, [1,2*]Saltuk Buğra Selçuklu, [1]Mehmet Fatih Kaya
[1] Erciyes University, Engineering Faculty, Energy Systems Engineering Department, Kayseri, Turkey
[2] Erciyes University, Energy Conversion Research and Application Center, Kayseri, Turkey

* E-mail: sbselcuklu@erciyes.edu.tr

Abstract
Technological and economic developments both in our country and in the world cause an increase in CO_2 emissions along with energy consumption and a rapid decrease in fossil-based resources. Increasing prices and environmental problems with the decrease in fossil fuel reserves encourage people to use alternative fuel vehicles. About one-quarter of total energy consumption in Turkey originated from the transportation sector. The use of hydrogen as a domestic fuel in the transportation sector and the widespread use of hydrogen vehicles can greatly reduce harmful emissions and dependence on fossil fuels. In this study, a system dynamics vehicle inventory turnover model is built to assess the impact on CO_2 emissions and energy usage of various municipal vehicles in Turkey. Preliminary results show that switching to hydrogen vehicles can greatly contribute to reducing CO_2 emissions.

Keywords: hydrogen vehicles, fleet transition, system dynamics

I. Introduction

Today, 26% of the energy consumption in the world originates from the transportation sector. With the increasing population and developing technology, the number of vehicles used in the transportation sector is increasing rapidly. The world faces environmental and economic problems associated with fossil fuel depletion and global warming, as well as various air pollution problems such as chemical smog, acid rain and particulate matter (Lee, Cha et al. 2011). The current transportation system, which is mostly based on fossil energy sources, is not sustainable, and the gradual increase in greenhouse gas emissions from the transport sector is an important topic of discussion all over the world, especially in Europe (Ajanovic and Haas 2020). Targeting the year 2020, the European Union wanted to reduce all greenhouse gas emissions by at least 20% compared to the greenhouse gas emission values of 1990. In order to achieve this goal, the European Union has reduced the amount of CO_2 emitted into the atmosphere from 130 grams per kilometer to below the 120-gram limit, with various studies since 2012. For 2020, it was aimed to reduce the amount of CO_2 emitted by internal combustion engines to the atmosphere to 95 grams per kilometer (Gürbüz and KULAKSIZ 2016). However, this value indicates that high amounts of greenhouse gas emissions will continue to be released into the atmosphere. (Wang, Zamel et al. 2013) Studies in this area are also carried out in our country. According to data from 2015, 25% of Turkey's total energy consumption is from transportation sector, 91.6% of which arises from road transport. While many alternative fuels and vehicle technologies are offered to make the transportation system cleaner, hydrogen may be the preferred option by many. For mass adoption of hydrogen, many challenges must be overcome, including proper refueling, infrastructure supply transitions, consumer vehicle buying behavior, and fuel costs. On the other hand, changing the vehicle fleet at an early stage is a recommended strategy to increase the use of hydrogen in the transport sector (Langford and Cherry 2012). Therefore, it is important that governmental bodies, such as municipalities, lead the way for a transition.

Most of the hydrogen fueled vehicle research conducted so far, with some exceptions, are carried out by developed countries. However, developing countries rely heavily on alternative transport because developing economies are more dependent on public transport and face energy security and air pollution problems. One of the important technologies that meet the dependence of developing countries on imported energy and the demands of reducing greenhouse gas emissions is hydrogen-fueled vehicle technology (Nalbant 2019). As most new vehicle sales are net growth purchases compared to developed countries, the rate of diffusion of new automotive technologies in developing countries is higher. In this sense, the introduction of fuel-saving technologies in developing countries will have the fastest effect in reducing the average fuel consumption (Schafer, Heywood et al. 2009). In a study by Palencia et al. (2016), an approach that reduces the increased capital cost of electric vehicles through vehicle size reduction is proposed. The approach focuses on reducing the vehicle size by considering the transition from normal and compact vehicles in new vehicle sales to mini-size vehicles.

Inclusion of hydrogen vehicles in public transport is a key step towards minimizing emissions from transport globally (Smaragdakis, Kamenopoulos et al. 2020). (Hua, Ahluwalia et al. 2014) Several fuel cell-powered bus prototypes have been implemented in recent years. However, very little information has been published in the literature on this subject. (Wimmer 1997) Fuel cell buses are currently costly and have difficulty installing and operating the required hydrogen fuel infrastructure. However, with steady progress in fuel cell and hydrogen storage technology and projected cost reductions, fuel cell buses are becoming more affordable every year (James, Kalinoski et al. 2010)(James, Kalinoski et al. 2010, Paster, Ahluwalia et al. 2011). The commercialization of fuel cell buses is seen as one of the most viable ways to transition to the hydrogen economy (Nalbant 2019). Fuel cell buses are projected to match the cost of diesel buses by 2030 (Zaetta and Madden 2011). Although such tools have already started to be introduced globally in some countries, there are limited publications on their operation and maintenance (Smaragdakis, Kamenopoulos et al. 2020).

Heavy haulage transport is another major emitter of CO_2 and its share in emissions is increasing worldwide (Calvo

Ambel). Hydrogen vehicles are also promising in this area because they provide the ability to increase power while minimizing weight compared to other zero emission vehicles. However, (Kast, Vijayagopal et al. 2017) there is a gap in literature on the CO_2 reduction potential of a fuel cell truck fleet (Çabukoglu, Georges et al. 2019). There is only one study that examines the electrification of road freight transport using battery electric vehicles (BEV) and fuel cell electric vehicles (FCEV) and determines which share of the truck fleet should be converted to electric trucks to achieve CO_2 reduction targets (Talebian, Herrera et al. 2018). However, there are no studies analyzing the CO_2 reduction potential of an entire truck fleet using hydrogen power (Çabukoglu, Georges et al. 2019). Fuel cell electric trucks (FCET) are often in their infancy, so a limited number of real vehicles and data are available (Lee, Elgowainy et al. 2018). The transport sector will contribute to the economy as it supports all other sectors. The transition to hydrogen technology has accelerated in the world and investments made in this energy have increased. If Turkey does not want to be a late party in this transition and if we want to reduce CO_2 emissions and contribute to sustainable growth as well as clean and green transportation, we must accelerate the transition to hydrogen as a country. In this study, a system dynamics vehicle inventory turnover model is developed for a selected region in Turkey to simulate the transition to hydrogen vehicles. The model is a regional bottom-up dynamic accounting model to assess the diffusion of hydrogen vehicles and the impact on energy consumption, CO_2 emissions and costs.

II. Methodology

This research evaluates the impact of hydrogen vehicle diffusion various vehicle types on the CO_2 emissions and costs considering the vehicle stock turnover dynamics. Figure 1 shows the flowchart of the model. General body of the model is modified from Palencia et al. (2016) and converted to a system dynamics model for application to a municipality in Turkey.

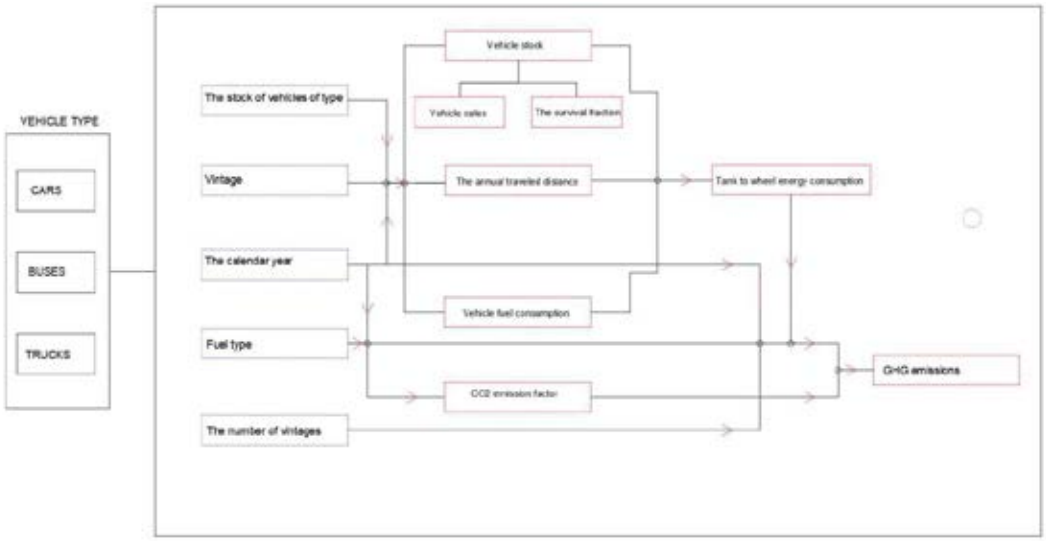


Fig. 1: Flowchart of the model

Tank to wheel energy consumption, *ETTW*, is the energy consumed by the stock of vehicles of type *t* and vintage *v* in the calendar year *y* and it is calculated as the product of the vehicle stock *N*, the annual traveled distance *M* and the vehicle fuel consumption *R* using Eq. (1).

$$ETTW_{t,y,v} = N_{t,y,v}\, M_{t,y,v}\, R_{t,y,v} \quad (1)$$

The annual traveled distance and the vehicle fuel consumption are exogenous parameters. The stock of vehicles of type *t* and vintage *v* in the calendar year *y* is estimated as the product of the new vehicles *S* and the survival fraction *F* as indicated in Eq. (2).

$$N_{t,y,v} = S_{t,v}\, F_{y\ v} \quad (2)$$

It should be noted that for any given year, the new vehicle sales correspond only to new vehicles. CO_2 emissions G_{TTW} is estimated as the product of the energy consumption and the CO_2 emission factor *EF*, as indicated by the Eq. (3)

$$GTTW_{y,z} = ETTW_{t,y,v}\, EF_{y,z} \quad (3)$$

where *z* is the fuel type.

IV. Results and discussions

New vehicle additions to the fleet are expected to increase in medium term in Turkey. The use of hydrogen as a domestic fuel in the transportation sector can reduce the dependence on fossil fuels and will contribute to the reduction of CO_2 emissions. Nowadays, energy efficiency and environmental effects are at the forefront and hydrogen vehicles are expected to have a promising future due to their high efficiency capabilities and environmentally friendly features. Fuel cells, which do not contain moving parts, greatly reduce the noise pollution of the vehicle in which they are used, thanks to these features. In the future vehicle technology, hydrogen vehicles are expected to occupy a large place, taking their mobility from electric motors.
Table 1 shows CO_2 emissions between 1990 and 2019 in Turkey that is originated from the transportation sector. Our preliminary results show that the increasing trend can be reversed by a transition to hydrogen vehicles. Governmental bodies, such as municipalities, can have a great impact on leading the transition.

Tab. 1: CO_2 Emission Statistics, 1990-2019 (thousand tonnes)

1990	**1995**	**2000**	**2005**	**2010**	**2011**	**2012**
26 250.8	33 180.0	35 490.2	41 043.8	44 382.6	46 366.8	61 248.5
2013	**2014**	**2015**	**2016**	**2017**	**2018**	**2019**
67 478.1	72 084.3	74 271.6	80 207.8	82 953.4	82 787.8	80 745.0

V. Conclusions

A bottom-up system dynamics accounting model is used to examine the impact of hydrogen vehicle diffusion on energy consumption, CO2 emissions and cost. Main conclusions are presented below:

- 3 vehicle types were discussed in the study. The car fleet has less impact on energy consumption and CO2 emissions.
- Fuel cell electric buses and trucks provide a significant reduction in noise and CO_2 emissions without some of the performance and range issues seen in other zero emission technologies.

References

Ajanovic, A. and R. Haas (2020). "Prospects and impediments for hydrogen and fuel cell vehicles in the transport sector." International Journal of Hydrogen Energy.

Gürbüz, Y. and A. A. KULAKSIZ (2016). "Elektrikli araçlar ile klasik içten yanmalı motorlu araçların çeşitli yönlerden karşılaştırılması." Gümüşhane Üniversitesi Fen Bilimleri Enstitüsü Dergisi 6(2): 117-125.

James, B. D., J. A. Kalinoski and K. N. Baum (2010). Mass Production Cost Estimation For Direct H2 PEM Fuel Cell Systesm for Automotive Applications. 2010 Update, Directed Technologies, Arlington, VA (United States).

Lee, J.-Y., K.-H. Cha, T.-W. Lim and T. Hur (2011). "Eco-efficiency of H2 and fuel cell buses." International journal of hydrogen energy 36(2): 1754-1765.

Nalbant, M. K. (2019). Hidrojen ekonomisinin otomotiv sektöründe önemi: Türkiye örneği, Marmara Universitesi (Turkey).

Palencia, J. C. G., M. Araki and S. Shiga (2016). "Energy, environmental and economic impact of mini-sized and zero-emission vehicle diffusion on a light-duty vehicle fleet." Applied Energy 181: 96-109.

Schafer, A., J. B. Heywood, H. D. Jacoby and I. A. Waitz (2009). Transportation in a climate-constrained world, MIT press.

Smaragdakis, A., S. Kamenopoulos and T. Tsoutsos (2020). "How risky is the introduction of fuel cell electric vehicles in a Mediterranean town?" International Journal of Hydrogen Energy 45(35): 18075-18088.

Talebian, H., O. E. Herrera, M. Tran and W. Mérida (2018). "Electrification of road freight transport: Policy implications in British Columbia." Energy policy 115: 109-118.

Zaetta, R. and B. Madden (2011). "Hydrogen fuel cell bus technology state of the art review." Project EC FCH-JU-2008-1 Grant Agreement Number 245133, Report Version 3.

High Temperature Electrochemical Hydrogen Purification Using Polybenzimidazole Membrane

[1]Gizem Nur Bulanık Durmuş, [2]C. Ozgur Colpan, [1]Yılser Devrim*
[1]Atılım University, School of Engineering, Energy Systems Engineering, Kizilcasar Mahallesi, Incek Golbasi Ankara, 06830, Turkey
[2] Department of Mechanical Engineering, Dokuz Eylul University, Buca, Izmir, Turkey

*E-mail: yilser.devrim@atilim.edu.tr

Abstract
Clean and sustainable energy with positive environmental impacts and no carbon footprint pave the way for promising innovative technologies for the coming decades. Notwithstanding fuel cell applications are promising with a wide range of uses from defense industry to domestic use, there are some factors such as economic and logistics in the commercialization of these systems. The pure hydrogen demand causes the procurement cost to increase. In this study, it is aimed to introduce the electrochemical hydrogen compressor (ECHC) and its unique components, which can separate hydrogen from the reformate gas mixture and reach high purities, in contrast to conventional systems. As it is known, purification by separating hydrogen from reformate gases containing impurities such as CO and CO_2 give better results at high temperatures due to high temperatures have higher CO tolerance. In this direction Poly[2,2-(m-phenylene)-5,5-bibenzimidazole] (PBI) membranes are used for hydrogen purification in ECHC system.

Keywords: Electrochemical hydrogen compressors, electrochemical hydrogen pumps, hydrogen purification

I. Introduction

Electrochemical hydrogen compressors (ECHC) provide both purification and pressurization of hydrogen by separating it from a gas mixture containing H_2. In spite of the fact that this technology has been known for years, it has become possible to reach high yields in recent years by remarkable developments in material technology (Rohland et al., 1998). Hydrogen does not exist alone in nature and must be produced. Today, most of the hydrogen production still comes from fossil fuels and besides hydrogen contains impurities such as CO, CO_2, CH_4, N_2, H_2O and some light hydrocarbons. Even though hydrogen seems as an attractive energy carrier for innovative applications, high efficiencies can only be achieved with high purity hydrogen. In the light of this information, it can be said that purification of the produced hydrogen is of great importance.

The main methods used in hydrogen purification can be listed as pressure swing adsorption (PSA), cryogenic separation method, membranes, and metal hydride alloys. ECHC systems, which are competitively close to the most widely used PSA method, stand out with their material studies and high CO poisoning tolerances at high temperatures.

Most of the studies on ECHC in the literature consist of studies conducted at low temperatures. Nordio et al. (2019) consider both numerical and experimental study by nitrogen, methane, helium, and hydrogen gas mixture at 28°C. According to their results 100% hydrogen purification was achieved in a mixture of nitrogen and methane, and over 98% purification was performed in helium experiments. They also observed the positive effects of temperature on ECHC in their study, they explained increasing temperature, increases the membrane conductivity and decreases ohmic losses. Another promising study was conducted by Lee et al. (2004) at 30°C, 50°C, and 70°C, using hydrogen, nitrogen, carbon dioxide gases. Again, in this low temperature study, 97.39% hydrogen purity was reached. According to Lee et al., these pioneering studies are promising for further purification processes and seem more advantageous than conventional membrane purification methods.

II. Experimental Set-up and Procedure

ECHC provides the purification of hydrogen by a simple mechanism: The hydrogen containing gas mixture is fed to the anode, hydrogen is first separated into protons and electrons by hydrogen oxidation reaction (HOR) (Eq. 1). Since only protons pass through the membrane, impurities such as CO and CO_2 leave the system again from the anode side and only protons reach the cathode through the membrane. Here, protons combine with electrons from the outer circuit to form the hydrogen by hydrogen evolution reaction (HER) (Eq.2) .

Hydrogen oxidation reaction (HOR) at anode side: $H_2(LP) \rightarrow 2H^+ + 2e^-$ (1)
Hydrogen evolution reaction (HER) at cathode side: $2H^+ + 2e^- \rightarrow H_2\ (HP)$ (2)
Overall cell reaction: $H_2\ (LP) \rightarrow H_2\ (HP)$ (3)

This study covers the production of a high temperature ECHC membrane, its characterization, and MEA development aims to obtain high purity hydrogen from the reformate gas mixture by using the ECHC system. H_2, CO, and CO_2 flow rates were set to achieve a desired composition, mixed in a T-junction, and sent to the cell. Different reformate gas mixtures with various concentrations of H_2, CO, and CO_2 gases were fed to the anode part of the ECHC, and purification was made according to different concentrations. The gas coming out of the cathode was sent to the gas chromatography device and the analysis of the impurities in the gas was observed.

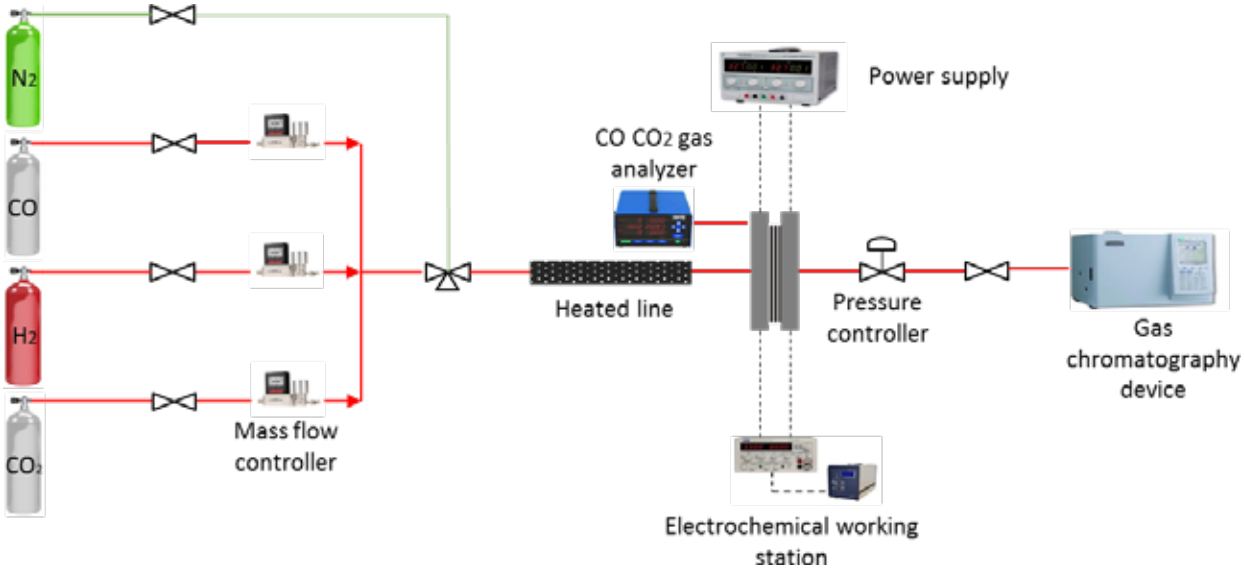


Fig. 1: Experimental set-up for hydrogen purification tests

III. Analysis

In this study, experiments were carried out with PBI membranes at 160°C temperature. PBI membranes can operate at high temperatures, besides, these membranes show high mechanical strength, high proton conductivity, and acid retention. The Thermogravimetric Analysis System (TGA) has been used to determine the thermal behavior of PBI membranes. XRD studies, X-ray diffractometry were used to study the crystal properties of membranes. Scanning Electron Microscope (SEM) Analysis was performed to examine the surface morphology of the PBI membranes. The acid loading degrees of the membranes were determined gravimetrically. The prepared membranes were kept in phosphoric acid solution for a certain period of time. The degree of acid loading of the membranes that were cleaned from the acid and weighed at the end of the period was determined from the % mass difference between before and after acid loading. Determining the proton conductivity of membranes is important for predicting ECHC performances. The through-plane proton conductivities of PBI membranes were measured using an electrochemical instrument. A four-probe impedance spectroscopy method was used in this study. Finally, in order to measure the mechanical properties of the membranes, the mechanical tests of phosphoric acid loaded and unloaded membranes were performed using a universal mechanical tester.

To evaluate the gas permeation property, a differential pressure method was examined. In this method, permeation and diffusion coefficients and were determined based on the permeation behavior of the gas penetrates through the specimen set between a high-pressure cell and a low-pressure cell.

After a detailed analysis of the membranes, MEA was prepared. Considering previous studies, MEAs were prepared by the ultrasonic coating method (Devrim et al., 2012), which provides minimum catalyst loss and homogeneous coating. Gas diffusion electrodes were prepared first and then the prepared electrodes were attached to both surfaces of the PBI membrane by hot pressing. In this study, electrodes with <0.5 mg/cm^2 catalyst load were prepared by ultrasonic coating on the fabric gas diffusion layer with commercial Pt/C catalysts. Electrodes were first prepared using catalyst solution commercial catalyst, binder, and isopropanol as solvent. Considering the previous studies, PVDF and PTFE binders preferred in PBI studies were used as binders (Nalbant et al., 2018). The prepared catalyst mixture was mixed in an ultrasonic bath for 30 minutes and then coated on commercial carbon paper using an ultrasonic coating at 80°C (120 kHz). Finally, MEAs were prepared by hot pressing at 150°C and 172 N/cm^2 for 10 minutes on both surfaces of the prepared phosphoric acid doped PBI membranes.

IV. Results and discussions

The gas permeability of the PBI membrane was determined as <30 barrers at 160°C. ECHC tests were performed on a 25 cm^2 single-cell hardware and H_2 purification test station. Before ECHC testing, a break-in of at least 12 h was done by operating the cell at 160 °C and a 0.2 A/cm^2 current density with pure H_2 on the anode and no sweep gas on the cathode. Polarization curves were recorded at 160-200 °C with various reformate gas streams, including pure H_2 and premixed reformate test gas. The purity was determined by an Schimadzu gas chromatograph with TCD detector (argon as carrier gases). PBI membrane showed improved EHS operation as the temperature increased gradually from 160-200 °C. Increasing the ECHC operating temperature resulted in an increased Pt catalyst tolerance to CO_2 and CO, leading to the reduction of voltage requirements and thus an increase in power efficiency. The ECHC based on PBI membranes can be operated using dilute hydrogen feed streams with large amounts of CO_2 and CO (24 %, 1%), producing pure hydrogen products (>99.6%) with high-power efficiencies.

V. Conclusions

The meta-PBI membrane was synthesized and characterized as the membrane for electrochemical H_2 purification. High-temperature ECHC based on PBI membrane was used to demonstrate the electrochemical hydrogen separation from various feed gases, which included pure H_2 and reformate stream containing H_2, CO_2, and CO. The final output H_2 purity was dependent upon the applied current and typically found to be >99.6% with ppm levels of CO and CO_2.

Acknowledgments
This study was supported by The Scientific and Technological Research Council of Turkey (TUBITAK) 1001 (Grant number: 219M333) Project.

References

Devrim, Y., Erkan, S., Baç, N., & Eroglu, I. (2012). Improvement of PEMFC performance with Nafion/inorganic nanocomposite membrane electrode assembly prepared by ultrasonic coating technique. *International Journal of Hydrogen Energy*, *37*(21), 16748–16758. https://doi.org/10.1016/j.ijhydene.2012.02.148

Lee, H. K., Choi, H. Y., Choi, K. H., Park, J. H., & Lee, T. H. (2004). Hydrogen separation using electrochemical method. *Journal of Power Sources*, *132*(1–2), 92–98. https://doi.org/10.1016/j.jpowsour.2003.12.056

Nalbant, Y., Colpan, C. O., & Devrim, Y. (2018). Development of a one-dimensional and semi-empirical model for a high temperature proton exchange membrane fuel cell. *International Journal of Hydrogen Energy*, *43*(11), 5939–5950. https://doi.org/10.1016/j.ijhydene.2017.10.148

Nordio, M., Rizzi, F., Manzolini, G., Mulder, M., Raymakers, L., Van Sint Annaland, M., & Gallucci, F. (2019). Experimental and modelling study of an electrochemical hydrogen compressor. *Chemical Engineering Journal*, *369*, 432–442. https://doi.org/10.1016/J.CEJ.2019.03.106

Rohland, B., Eberle, K., Ströbel, R., Scholta, J., & Garche, J. (1998). Electrochemical hydrogen compressor. *Electrochimica Acta*, *43*(24), 3841–3846. https://doi.org/10.1016/S0013-4686(98)00144-3

Modeling of Hydrogen and Electric Powered Vehicle Filling Stations Using a Floating Photovoltaic System

[1]Seyfi Bulduk, [2,3 *] Mehmet Fatih Kaya
[1] Erciyes University, Engineering Faculty, Energy Systems Engineering Department, 38039, Kayseri, Turkey
[2] Erciyes University, Engineering Faculty, Energy Systems Engineering Department, Heat Engineering Division, 38039, Kayseri, Turkey
[3] Erciyes University H2FC Hydrogen Energy Research Group, 38039, Kayseri, Turkey

* E-mail: kayamehmetfatih@erciyes.edu.tr

Abstract
In this study, a floating photovoltaic (FPV) system and a hybrid system that generates electricity and hydrogen for use in electric and hydrogen energy vehicles has been investigated. Firstly, a geographical region with high solar radiation values is selected. The ponds and dams required to establish a FPV system on this region are examined and Çayboğazı Dam is determined as the area where the study will be carried out. For this hybrid system, the charging station and hydrogen filling station are modeled with PVsyst software. Then, on this modeled micro system HOMER program, both the DC electricity storage and the storage of the generated energy as hydrogen are taken into consideration, and cost and efficiency analyzes are made for both systems. Considering the intermittent operation of the FPV, different scenarios are created on the system and examined separately for each case. Storing the energy generated from FPV as hydrogen provided great advantages for electric vehicle (EV) charging stations.

Keywords: Hydrogen Production, Electricity Production, Electric Vehicle, Hydrogen fuel cell vehicles, Floating Photovoltaic System, Hybrid system

I. Introduction

The depletion of fossil resources, the energy dependence of internal combustion engine vehicles (ICEVs), the increase in fuel costs and environmental concerns, developments in battery technology and their manufacturing processes have encouraged the transition to battery electric vehicles (BEVs). Today, approximately 20% of the total CO_2 emissions in the world originate from the transportation sector, while 71% of the transportation sector originates from road transport (Gönül, Duman et al. 2021). This means that the use of electric vehicles will both reduce the damage to the environment and reduce our need for fossil fuels.

Turkey has a significant solar energy potential by 2741 hours of sunshine duration per year and total solar energy values of 1527 kWh / m^2 per year (YOLCAN and Ramazan) . Therefore, it would be the right choice to meet energy needs by using solar energy. The most common form of solar energy application is photovoltaic (PV) systems that absorb sunlight to generate electricity (Kumari and Geethanjali 2018). However, the increase in the temperature of the PV panels negatively affects the efficiency of the solar panels (Akbarzadeh and Wadowski 1996, Ratlamwala, Gadalla et al. 2011). One of the promising applications of PV modules is FPV systems, which have higher efficiency and can also reduce the evaporation of water reservoirs. Due to its high electricity generation potential, the application of renewable energy technologies in floating forms is developed rapidly (Ranjbaran, Yousefi et al. 2019). In addition, there are few studies examining hydrogen production with solar energy in FPV applications (Zahedi and Gharehpetian 2019, Temiz and Javani 2020). The production and storage of hydrogen, which is seen as the energy of the future, by the FPV system provides positive advantages.

Hydrogen fuel cell vehicles (FCEVs) are classified as hydrogen powered electric vehicles because they are powered by an electric motor and a fuel cell. Another important advantage of EVs is that the energy required for the system can be used as a hybrid system by conversion of the stored hydrogen into electrical energy by the help of fuel cells in high efficiency. The use of hydrogen by converting into electricity by the fuel cell also eliminates the problems of high charging times and low range, which are one of the biggest problems for commercial EVs. The use of hydrogen produced from the hybrid system in EV charging stations will be both an environmentally friendly, clean and sustainable approach (Veziroğlu). By the spread of EV, it is a definite result that not only the number of EV charging stations but also the number of hydrogen filling stations will increase and become widespread.

II. Methodology

In this study, FPV system was modeled using PvSyst and Homer softwares. PvSyst software was used to determine possible efficiency losses of the FPV system. Firstly, the regions with high irradiation values were examined by taking the solar energy atlas into consideration, and the performance values of the 21 KWp FPV system were created separately for each region in the PVsyst software. Calculated power values are listed in Table 1. In Table 1, Karacaören Dam and Karataş Lake were not taken into consideration because they are naturally protected areas and it is not allowed to build a FPV system. Çayboğazı Dam is located at 36.53 ° N latitude 26.68 ° D longitude coordinates. These coordinates were chosen as the study area for this model. As stated by Kalogirou et al. (Kalogirou and Tripanagnostopoulos 2006) in PVsyst software, 1 °C increase in the temperature, efficiency of

monocrystalline silicon solar panels reduces the approximately by 0.45%.

Table. 1: Power performance values of FPV systems obtained from different dams and lakes on PVsyst Software

PVsyst efficient results of the possible locations with the highest solar radiation values according to Turkey's annual global solar radiation map					Location values		System	
SN	Output Power (MW/year)	PV System (kW/h)	Performans values	Location	Area (km^2)	Height (m)	Total Power (kW/h)	Total power (MW/year)
1	39,8	21	1,895048	Girdev Lake	3,5	1733	273,23	517,79
3	39,4	21	1,87619	Çayboğazi Dam	2,25	1275	175,65	329,55
4	39,2	21	1,866667	Karagöl	dried	1029		
5	38,2	21	1,819048	Avlan Lake	8,5	1030	663,57	1207,06
6	38	21	1,809524	Karacaören Dam	46	253	3591,08	6498,14
7	37,9	21	1,804762	Yazir Lake	2,11/13,44	1480	164,72	297,28
8	37,4	21	1,780952	Korkuteli Dam	2,2	1050	171,75	305,87
9	36,9	21	1,757143	Karataş Lake	8	1050	624,54	1097,4
10	36,8	21	1,752381	Boranda Pond	0,5	1521	39,03	68,4
11	36,7	21	1,747619	Ermenek Dam Lake	58,74	540	4585,65	8013,97
12	36,62	21	1,743905	Yaprakli Dam	6,5	1065	507,43	884,92
13	25,31	14,56	1,738324	Mumcular Dam 1	1,42	32	76,86	133,61
14	36,5	21	1,738095	Manavgat Dam	8,6	30	671,38	1166,91
15	36,44	21	1,735238	Mumcular Dam 2	1,42	32	110,86	192,36
16	25,02	14,56	1,718407	Korkuteli Dam	2,2	1055	119,08	204,62
17	35,9	21	1,709524	Alakir Dam	4,28	113	334,13	571,2
18	35,71	21	1,700238	Sülüngür Lake	2	8	156,13	265,46
19	35,7	21	1,7	Atatürk Dam	817	521	63780,67	108427,1
20	24,56	14,56	1,686813	Ula Lake	0,35	648	18,94	31,96
21	24,52	14,56	1,684066	Sarimsakli Dam	2,44	1196	132,07	222,41
22	24,52	14,56	1,684066	Kocagöl	3	7	162,38	273,46

In all systems, to minimize the shadows dropped by FPV panels on each other and to minimize the area to be covered by the panels, the pitch distance between the panel groups was calculated as 6 m, tilt angle and azimuth angle is arranged as 34 ° and 0 °, respectively. In this case, the total solar panel area of the system was calculated as 269 m^2. FPV system was build by connecting the 60 PV solar panels in 10 serials and 6 parallel configurations. In figure 1, construction of FPV system can be seen in the 3D.

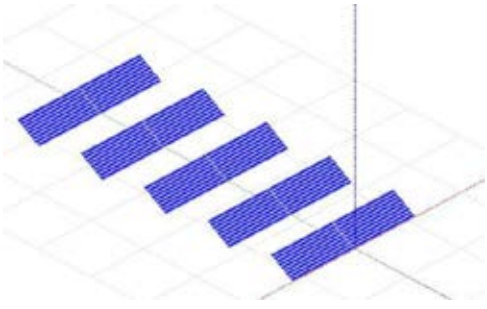


Fig. 1. 3D construction for the shading simulation in PvSyst

Illustrated FPV system was transferred to HOMER Program to calculate maximum DC battery storage and hydrogen storage capacity. The necessary equipments for the system installation was created as shown in Figure 2. In Homer Software the costs of both DC electricity storage and hydrogen energy storage systems were calculated, respectively. System sizing was prepared by considering two different scenarios. In Scenario 1, hydrogen gas storage system for FCEV was discussed. The biggest advantage of this system was faster storage of the hydrogen energy from gas cylinders. In Scenario 2, the system cost was calculated by for BEVs' storage system. It was needed longer times to fully charge the vehicle as a disadvantage for this system. The components used in the hybrid system are shown in Figure 2. This configuration was changed for different scenarios and situations.

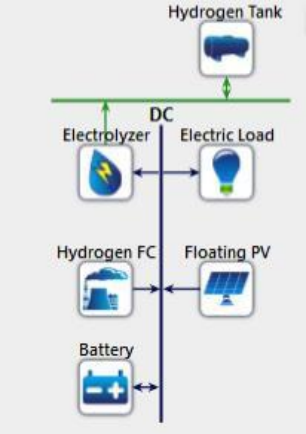


Fig. 2. System Components

As can be seen in Figure 2, the FPV System equipment is designed for DC current configuration. In this context, the feasibility analysis was performed to determine the most appropriate component properties and dimensions of the FPV, hydrogen fuel cell, battery, electrolyser, and hydrogen tank.

III. Conclusions

As a conclusion, installed FPV system has more efficiency values than land-based PV power plants, resulting in more energy outputs. In addition, by covering the water surface with FPV systen, evaporation of water is decreased, and zero CO_2 emission is obtained in the established system. It has been observed that hydrogen storage for FCEVs has lower storage efficiency than DC battery electrical storage system. However, this disadvantage may be eliminated by low cost electrolyzer and fuel cell technologies. Because FCEVs' faster storage option of hydrogen and its range extender properties by using fuel cells will cause big demand in the transportation for the future.

References

Akbarzadeh, A. and T. Wadowski (1996). "Heat pipe-based cooling systems for photovoltaic cells under concentrated solar radiation." Applied Thermal Engineering **16**(1): 81-87.

Gönül, Ö., A. C. Duman and Ö. Güler (2021). "Electric vehicles and charging infrastructure in Turkey: An overview." Renewable and Sustainable Energy Reviews **143**: 110913.

Kalogirou, S. A. and Y. Tripanagnostopoulos (2006). "Hybrid PV/T solar systems for domestic hot water and electricity production." Energy Conversion and Management **47**(18): 3368-3382.

Kumari, P. A. and P. Geethanjali (2018). "Parameter estimation for photovoltaic system under normal and partial shading conditions: A survey." Renewable and Sustainable Energy Reviews **84**: 1-11.

Ranjbaran, P., H. Yousefi, G. B. Gharehpetian and F. R. Astaraei (2019). "A review on floating photovoltaic (FPV) power generation units." Renewable and Sustainable Energy Reviews **110**: 332-347.

Ratlamwala, T. A. H., M. A. Gadalla and I. Dincer (2011). "Performance assessment of an integrated PV/T and triple effect cooling system for hydrogen and cooling production." International Journal of Hydrogen Energy **36**(17): 11282-11291.

Temiz, M. and N. Javani (2020). "Design and analysis of a combined floating photovoltaic system for electricity and hydrogen production." International Journal of Hydrogen Energy **45**(5): 3457-3469.

Veziroğlu, A. "Hidrojen neden potansiyel bir ulaşım yakıtı olarak seçilmelidir?" Niğde Ömer Halisdemir Üniversitesi Mühendislik Bilimleri Dergisi **10**(1): 404-411.

YOLCAN, O. O. and K. Ramazan "TÜRKİYE'NİN GÜNEŞ ENERJİSİ DURUMU VE GÜNEŞ ENERJİSİ SANTRALİ KURULUMUNDA ÖNEMLİ PARAMETRELER." Kırklareli Üniversitesi Mühendislik ve Fen Bilimleri Dergisi **6**(2): 196-215.

Zahedi, R. and G. B. Gharehpetian (2019). Optimal Sizing of Floating Photovoltaic System Equipped with Hydrogen Tank and Battery ESS. 2019 Smart Grid Conference (SGC).

A Numerical Study on Cooling Performance of Vairous Flow Field Designs of Cooling Plates

[1*]Mahmut Caner Acar, [1]Bahadir Erman Yuce,
[1] Bitlis Eren University, Faculty of Engineering and Architecture, Mechanical Engineering Department, Rahva Yerleşkesi Beş Minare Mahallesi Ahmet Eren Bulvarı, BİTLİS, 13000, Turkey

* E-mail: mcacar@beu.edu.tr

Abstract
Almost half of the chemical energy of hydrogen is lost as heat during the operation of polymer electrolyte membrane (PEM) fuel cells. Therefore, temperature of PEM fuel cells continuously increases as a result of electrochemical reactions occurring in each cell. This temperature rise can cause overheating of the fuel cell, which results in a performance degradation. Thus, thermal management is essential for the efficient operation of PEM fuel cells. In this study, a three dimensional numerical study is presented for two different cooling plates having serpentine and parallel type flow field designs. Based on the computational fluid dynamics (CFD) simulations, the performances of two different coolant flow field designs are assessed in terms of the maximum temperature, temperature uniformity index (U_T) and pressure drop characteristics. Results show that the serpentine type flow field design provides more uniform temperature distribution than that of parallel type.

Keywords: PEM fuel cell, cooling, flow field, CFD.

I. Introduction

Heat is generated as a result of electrochemical reactions occurring inside the PEM fuel cells. The amount of this heat is almost equal to the output power of PEM fuel cell stack [1], and this heat causes an increase in the temperature and affects the performance of stack. Especially, non-uniform temperature distribution can cause a degradation in the performance and also hot spot points can damage the polymer electrolyte membrane [2,3]. Therefore, choosing of an appropriate cooling strategy is essential for the performance, durability and reliability of PEM fuel cells. Depending on the output power capacity, PEM fuel cells are generally cooled by air or liquids (especially water) along the flow channels formed on bipolar plates or cooling plates [4]. Due to the lower specific heat of air, it is preferred in small-scale fuel cell applications. On the contrary, as liquid water has a higher specific heat, it is often used in large-scale applications. In addition to air and water, nano fluids can also be used as a coolant fluid [5–7]. Using air instead of liquid water as a coolant fluid increases the stack cost, and also requires more pumping power. However, if liquid water is used, more equipment is needed and the system becomes more complex. In order to remove excess heat from the fuel cell, coolant fluids are circulated through the flow fields which are formed on cooling or bipolar plates. There are different types of flow field designs such as serpentine, parallel, parallel-serpentine, radial, spiral, pin-type etc. [8,9]. Among them serpentine and spiral type flow field designs are superior from the point of uniform temperature distribution and cooling performance [10]. In this study, a three dimensional numerical simulation is performed by using Ansys Fluent to investigate the effects of various flow field designs on thermal performance of cooling plates. In this context, serpentine and parallel type flow field designs formed on a cooling plate with 7.1 x 7.1 cm^2 surface area are evaluated according to the maximum temperature, temperature uniformity and pressure drop characteristics.

II. Numerical Procedure

Model validation:

A model validation study is carried out to confirm the considered numerical model. Fig. 1 shows the geometry used in the validation process. The surface area and thickness of cooling plate are 11 x 11 cm^2 and 2 mm, respectively, and it has 27 parallel channels. The width and height of each parallel channel are 2 mm and 1 mm, respectively. Liquid water is used as the coolant fluid and enters the channels at 40 °C with a volume flow rate of 1.8 x 10^{-6} m^3s^{-1}. The value of heat flux exposed from the bottom surface is 5000 Wm^{-2}. A symmetry boundary condition is imposed on the top surface of cooling plate. Since the thermo-physical properties of water (density, thermal conductivity, dynamic viscosity and specific heat) change with temperature, these properties are determined by the defined polynomial functions. A constant heat flux boundary condition and a symmetry boundary condition are applied on the bottom and top surfaces of the cooling plate, respectively.

Numerically computed value of f.Re (f: Darcy friction factor) along the straight channel are illustrated in Fig. 2(a). The entrance length is analytically determined as 0.89 cm by using the $x_{fd}/D_h = 0.05Re$ (Re=135, D_h=1.33mm) equation [Incropera] while it is numerically determined as 0.96 cm. This result shows that the computed value is in good agreement with the calculated one. After this point, a fully developed flow condition occurs and the value of f.Re remains nearly constant as 54.16. This figure is also comparable with the value of 62 which is a reference value for laminar and fully developed flow [Incropera]. The validation of the model is also done thermally in terms of thermal entrance length and Nusselt number as shown in Fig. 2 (b). The calculated value of thermal entrance length is 3.9 cm (from $x_{fd,t}/D_h = 0.05RePr$), while computed value is 3.81, which is in good agreement with the analytically calculated value. Nusselt number is constant and takes the value of 2.93 after the thermal entrance length which is also in relatively good agreement with 4.12 which is a reference value [Incropera] for laminar and thermally fully developed flow through a rectangular flow channel having an aspect ratio of 2.

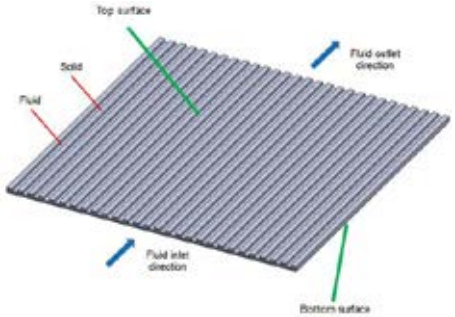


Fig. 1: Cooling plate and flow channels used in model validation.

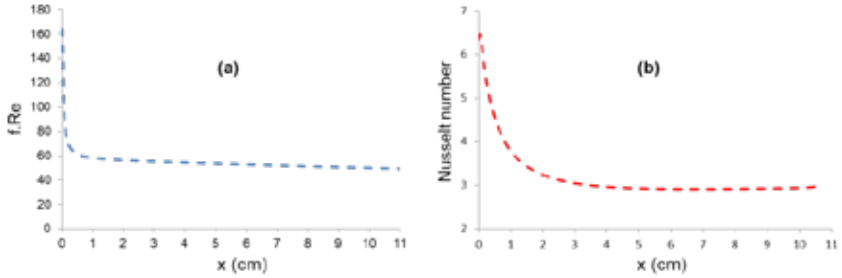


Fig. 2: Evolution of friction factor and Nusselt number along the channel.

Geometric model and grid independency:

The model geometry of cooling plates with parallel and serpentine type flow fields are shown in Fig. 3. Both plates have 7.1 x 7.1 cm^2 square area and 2 mm thick. The values of channel depth, channel width and rib width are equal and 1 mm. Parallel type cooling plate has 35 inlets and 35 outlets, while serpentine type has one inlet and one outlet. A grid independency study is performed to show the accuracy of results obtained from the numerical model. For this purpose, four different grid sizes having 483,936, 1,008,200, 3,871,488 and 4,440,592 elements are tested for both flow field types in terms of pressure drop (between inlet and outlet) and average temperature of bottom surface. A little difference is seen in pressure drop and average temperature for both flow field designs when the element size exceeds 3,871,488, thus, this grid structure is used in the model.

Numerical procedure:

Partial differential equations representing the conservation equations (continuity, momentum and energy) are discretized based on the finite volume method. A coupled algorithm is used for the velocity-pressure coupling of the continuity and momentum equations. The numerical result is assumed to converge when the residual for the equations of continuity and momentum become smaller than 1 x 10^{-5} and for the equation of energy smaller than 1 x 10^{-6}.

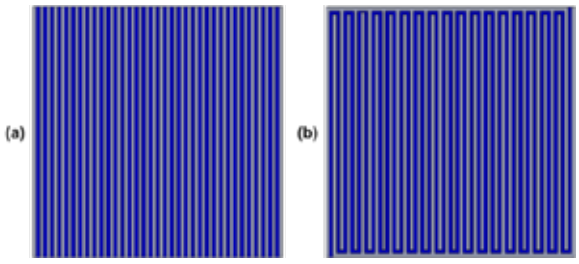


Fig 3: Model geometry; (a) parallel flow field, (b) serpentine flow field.

III. Results and discussions

The simulation results obtained with the parallel and serpentine type flow field designs are evaluated and compared. The inlet temperature and volume flow rate of the liquid water are 40 °C and 3.5 x 10^{-7} m^3s^{-1}, respectively. The heat flux applied on the bottom surface is 5000 Wm^{-2}. A symmetry boundary condition and an adiabatic boundary condition are imposed on the top surface and edges of cooling plate, respectively. The temperature distribution on the top surface and pressure distribution along the flow channels of cooling plates for parallel and serpentine flow fields are shown in Fig. 4. Due to the absorbing of heat by the liquid water along the channels, the temperature is low near the inlet and high near the outlet of the cooling plate. The pressure drop in serpentine flow field design is higher, indicating more pumping power requirement.

The temperature uniformity index is utilized to determine the cooling performance of any design and can be calculated by the following equation;

$$U_T = \frac{\int |T - T_{avg}| dA}{\int dA} \text{ and } T_{avg} = \frac{\int T dA}{dA} \quad (1)$$

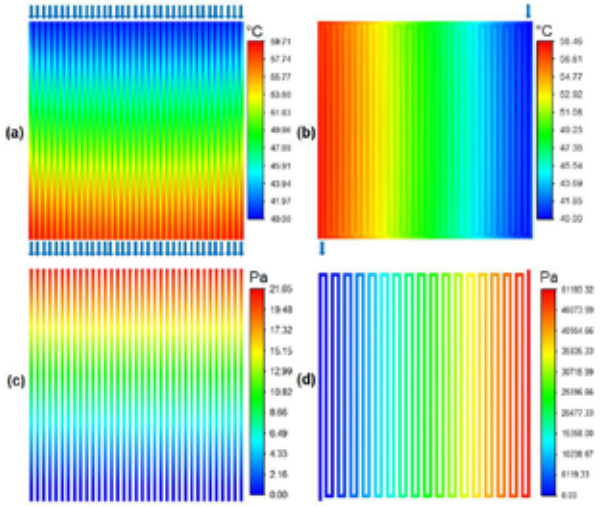


Fig 4: Temperature distribution; (a) parallel flow field, (b) serpentine flow field, pressure distribution; (c) parallel flow field, (d) serpentine flow field.

where T_{avg} is the average surface temperature, T is the surface temperature and A is the surface area. Table 1 shows the maximum temperature and temperature uniformity index on the bottom surface of the cooling plate, and pressure drop between inlet and outlet of the channels. The difference in maximum bottom surface temperatures of parallel and serpentine flow fields is 1.26 °C. In addition, both designs have almost the same temperature uniformity index value. However, a huge difference is seen in pressure drop between inlet and outlet of the channels. Therefore, more pumping power will be needed when the serpentine flow field design is preferred instead of parallel design.

Table 1: Simulation results for maximum temperature, temperature uniformity index and pressure drop.

Type	T_{max} (°C)	U_T (°C)	ΔP (Pa)
Parallel	59.70	4.29	21.28
Serpentine	58.44	4.26	51,184.73

IV. Conclusions

In this study, a three dimensional CFD study is performed for two different cooling plate designs having various flow fields; parallel and serpentine. For this purpose, the effects of flow field types on the thermal performance of cooling plate are investigated according to the temperature and pressure distributions on the symmetry surface, maximum temperature and temperature uniformity index on the bottom surface, and pressure drops along the channels. Almost the same temperature uniformity index values are obtained for both parallel and serpentine flow field designs. The maximum temperatures on the bottom surface for parallel and serpentine designs are 59.70 °C and 58.44 °C, respectively, and the difference is 1.26 °C. A big difference is observed in pressure drop as 51 kPa between these two designs. According to the results, the serpentine flow field is superior in terms of thermal performance of cooling plate. However, the pumping power requirement to circulate the coolant fluid inside the channels increases when serpentine flow field is used.

Acknowledgements

Computing resources used in this work were provided by the National Center for High Performance Computing of Turkey (UHeM) under grant number <1009302021>.

References

[1] S.M. Baek, S.H. Yu, J.H. Nam, C.J. Kim, A numerical study on uniform cooling of large-scale PEMFCs with different coolant flow field designs, Appl. Therm. Eng. 31 (2011) 1427–1434. https://doi.org/10.1016/j.applthermaleng.2011.01.009.

[2] A. Faghri, Z. Guo, Challenges and opportunities of thermal management issues related to fuel cell technology and modeling, Int. J. Heat Mass Transf. 48 (2005) 3891–3920. https://doi.org/10.1016/j.ijheatmasstransfer.2005.04.014.

[3] S.G. Kandlikar, Z. Lu, Thermal management issues in a PEMFC stack - A brief review of current status, Appl. Therm. Eng. 29 (2009) 1276–1280. https://doi.org/10.1016/j.applthermaleng.2008.05.009.

[4] X. Li, I. Sabir, Review of bipolar plates in PEM fuel cells: Flow-field designs, Int. J. Hydrogen Energy. 30 (2005) 359–371. https://doi.org/10.1016/j.ijhydene.2004.09.019.

[5] M.R. Islam, B. Shabani, G. Rosengarten, Nanofluids to improve the performance of PEM fuel cell cooling systems: A theoretical approach, Appl. Energy. 178 (2016) 660–671. https://doi.org/10.1016/j.apenergy.2016.06.090.

[6] R. Islam, B. Shabani, J. Andrews, G. Rosengarten, Experimental investigation of using ZnO nanofluids as coolants in a PEM fuel cell, Int. J. Hydrogen Energy. 42 (2017) 19272–19286. https://doi.org/10.1016/j.ijhydene.2017.06.087.

[7] I. Zakaria, W.H. Azmi, A.M.I. Mamat, R. Mamat, R. Saidur, S.F. Abu Talib, W.A.N.W. Mohamed, Thermal analysis of Al2O3-water ethylene glycol mixture nanofluid for single PEM fuel cell cooling plate: An experimental study, Int. J. Hydrogen Energy. 41 (2016) 5096–5112. https://doi.org/10.1016/j.ijhydene.2016.01.041.

[8] S. Asghari, H. Akhgar, B.F. Imani, Design of thermal management subsystem for a 5 kW polymer electrolyte membrane fuel cell system, J. Power Sources. 196 (2011) 3141–3148. https://doi.org/10.1016/j.jpowsour.2010.11.077.

[9] D.L. Wood, J.S. Yi, T. V. Nguyen, Effect of direct liquid water injection and interdigitated flow field on the performance of proton exchange membrane fuel cells, Electrochim. Acta. 43 (1998) 3795–3809. https://doi.org/10.1016/S0013-4686(98)00139-X.

Hydrogen Adsorption on Metal (Na, K, Mg, Ca) Porphyrin Complexes: A DFT Study

[1]Ahmet Köse, [1]Numan Yüksel, [1*]Mehmet Ferdi Fellah
[1] Bursa Technical University, Faculty of Engineering and Natural Sciences, Department of Chemical Engineering, Mimar Sinan Campus, 16310, Bursa, Turkey

* E-mail: mferdi.fellah@btu.edu.tr

Abstract
In this study, it has been investigated the hydrogen adsorption on metal (N, K, Mg, Ca) porphyrin complex structures at room temperature. WB97XD method with 6-31G(d,p) basis set have been used. The electronegativity, HOMO and LUMO energy, chemical hardness, chemical potential, charge transfer, adsorption enthalpy and adsorption energy values have been calculated. The lowest hydrogen adsorption enthalpy value was calculated as -21.9 kJ/mol for Na-Porphyrin. Then, hydrogen storage capacity studies were carried out for this complex and it was determined as 5.5 wt%. As a result, Na-porphyrin complexes have been shown to be potential cryo-adsorbents for hydrogen storage at room temperature.

Keywords: Hydrogen, Adsorption, Porphyrin, DFT, Metal complex

I. Introduction
Since limited hydrocarbon resources, the use of hydrogen as the energy carrier in the future has been important over the past three decades (Strub and Imarisio, 1980). However, it will be necessary to develop a safe and efficient method for using hydrogen as an energy carrier and for storing it (Fellah, 2017). The US Department of Energy's (DOE) target for hydrogen storage capacity for 2025 is 5.5 wt%. (Boateng and Chen, 2020). MOFs are highly porous crystal structures with a large surface area that have the potential to capture huge amounts of gas molecules in their cavities. With the addition of heat or pressure, the hydrogen adsorbed by the weekly van der Waals force on the pores of the MOFs can be rapidly desorbed (Shet et al., 2021). Porphyrin, a member of the macrocyclic class, is a MOF that can complex with metal atoms and is effective in gas studies (Xu et al., 2020; Saeidipoor et al., 2021).

II. Model and Method
In this work, the theoretical calculations were utilized in order to obtain electrical characteristics and geometry optimizations based on density functional theory (DFT) (Kohn and Shamn, 1965). DFT calculations were made through Gaussian 09 software (Frisch et al., 2013). The applied method was the WB97XD (including dispersion) hybrid formalism method in present work. The basis set of 6-31G(d, p) was utilized for all atoms. The complex formations were realized by replacing one metal atom with two hydrogen molecules at the center of the porphyrin structure. Geometry optimizations were firstly made for metal-porphyrin complexes. Then, in order to obtain the adsorption Equilibrium Geometries (EGs), hydrogen molecules were added to the complexes and optimization calculations were made. All atoms have been kept relaxed during calculations.

III. Analysis
These energy values for hydrogen adsorption were computed as follows:

$$E = E_{Electronic} + ZPE + E_{Vibrational} + E_{Rotational} + E_{Translational} \quad (1)$$

$$H = E + RT \quad (2)$$

where E is the sum of the electronic and zero-point energies and thermal energies, H is the sum of the electronic and thermal enthalpies, T is the temperature used for the vibrational frequency calculations. The HOMO and LUMO energy values, charge transfer (Mulliken charge distribution analysis), chemical hardness, electronegativity and chemical potential were obtained to have information about the activity of structure. These values are obtained based on the Koopman's approach (Pearson, 2005). The hydrogen storage capacity was computed by following equation:

$$H_2\ wt\% = [\frac{M_{H_2}}{M_{H_2}+M_{Host}}]\ x100 \quad (3)$$

IV. Results and discussions
The obtained adsorption energy values for hydrogen adsorption on metal-porphyrin complexes were listed in Table 1. The Na-Porphyrin (Na-P) complex has been identified as having the lowest hydrogen adsorption energy. Hydrogen storage studies have been carried out for this complex. Hydrogen storage capacity was calculated as 5.5 wt%. Optimized geometries of Na-P structure and nine H_2 molecules adsorbed Na-P structure were represented Fig. 1.

Tab. 1: Adsorption energy values, HOMO and LUMO energy, chemical hardness, chemical potential, electronegativity, Mulliken charges and HLG values for the optimized metal-porphyrin structures and the optimized H_2 adsorbed on metal-porphyrin structures (Energy values are in units of kJ/mol).

Properties		**Na-P**	**H_2 adsorbed on Na-P**	**K-P**	**H_2 adsorbed on K-P**	**Mg-P**	**H_2 adsorbed on Mg-P**	**Ca-P**	**H_2 adsorbed on Mg-P**
Mulliken Charges, e	Metal atom	+0.659	+0.615	+0.717	+0.697	+0.911	+0.900	+1.301	+1.271
	H_2 molecule	0	+0.013	0	+0.008	0	+0.027	0	+0.019
Adsorption Energy	ΔE	-	-19.5	-	-1.9	-	-4.4	-	-6.5
Adsorption Entalphy	ΔH	-	-21.9	-	-4.4	-	-6.9	-	-9.0
HOMO	α MOs	-612.8	-602.9	-584.4	-586.7	-639.9	-637.3	-610.5	-610.9
	β MOs	-663.7	-666.2	-647.6	-649.6				
LUMO	α MOs	-98.3	-85.5	-65.2	-67.4	-78.7	-77.5	-55.5	-56.2
	β MOs	-213.4	-206.8	-185.1	-186.5				
HLG	α MOs	514.5	517.4	519.2	519.3	560.2	559.8	555.1	554.7
	β MOs	450.3	459.3	462.6	463.1				
Chemical Hardness	α MOs	257.2	258.7	259.6	259.6	280.1	279.9	277.5	277.4
	β MOs	225.1	229.7	231.3	231.5				
Chemical Potential	α MOs	-355.6	-344.2	-324.8	-327.1	-358.8	-357.4	-333.0	-333.5
	β MOs	-438.6	-436.5	-416.3	-418.1				
Electronegativity	α MOs	355.6	344.2	324.8	327.1	358.8	357.4	333.0	333.5
	β MOs	438.6	436.5	416.3	418.1				

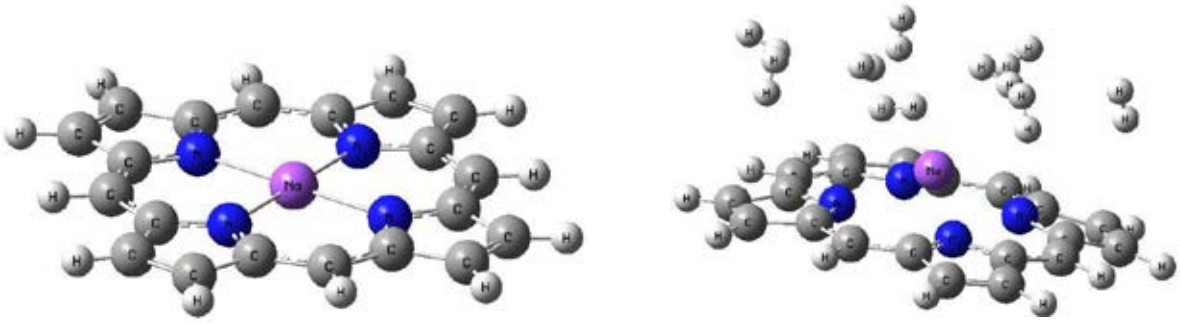


Fig. 1. Optimized structures of the Na-P (left) and the nine H_2 molecules adsorbed on Na-P (right)

The HOMO and LUMO representations for both α and β molecular orbitals (spin up and spin down respectively) of Na-P structure and H_2 adsorbed on Na-P structure are represented in Fig. 2. Mulliken population analysis have been utilized to obtain charge distributions before and after adsorption of H_2 molecule on metal-porphyrin complexes. These results indicate that small charge transfer has occurred from the adsorbed hydrogen molecule to the metal-porphyrin complexes.

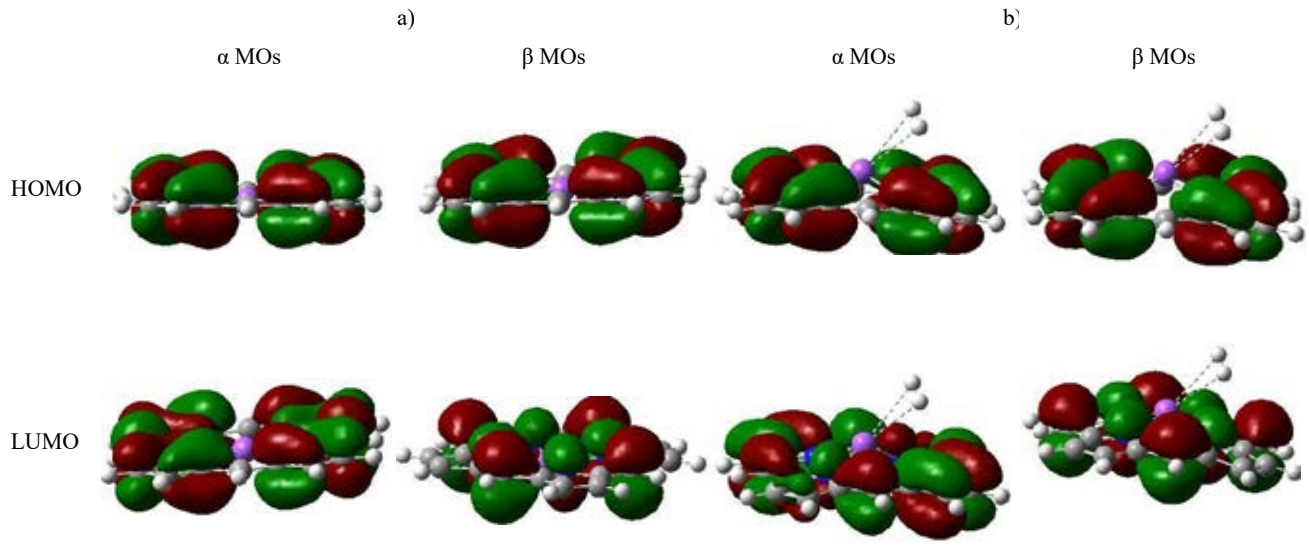


Fig. 2. HOMO and LUMO representations of α and β MOs a) for the optimized structure of Na-P b) for the optimized structure of the adsorbed nine H_2 on Na-P

V. Conclusions

In the present study, DFT calculations with WB97XD hybrid formalism method have been utilized fhydrogen adsorption on the metal-porphyrin complexes. The adsorption enthalpy values on the complexes are greater than the liquefaction enthalpy (0.9 kJ/mol) of the hydrogen molecule. The lowest hydrogen adsorption enthalpy value was calculated as -21.9 kJ/mol for Na-Porphyrin. Then, hydrogen storage capacity was determined as 5.5 wt% for Na-P complex. As a result, Na-porphyrin complexes have been shown to be a potential cryo-adsorbent for storage of the H_2 molecule at room temperature.

Acknowledgements

The numerical calculations reported in this paper were in part completed at TUBITAK/ULAKBIM, HighPerformance and Grid Computing Center (TRUBA resources).

References

Boateng E., Chen A., Recent advances in nanomaterial-based solid-state hydrogen storage, Materials Today Advances, 6, 100022, (2020).

Fellah MF., A DFT study of hydrogen adsorption on Be, Mg and Ca frameworks in erionite zeolite, Applied Surface Science, 394, 9-15, (2017).

Frisch et al., Gaussian 09 Revision D.01, Gaussian Inc., Wallingford CT, (2013).

Kohn W., Shamn L., Self-consistent equations including exchange and correlation effects, Journal of Physical Review, 140, A1133-A1138, (1965).

Pearson RG., Chemical hardness and density functional theory, Journal of Chemical Sciences, 117, 369-377, (2005).

Saeidipoor A., Arshadi S., Benam MR., The Titano-Porphyrin doped pillared graphene as a novel “turn-off” fluorescent sensor for CO gas: Theoretical study, Physica E: Low-dimensional Systems and Nanoclusters, 127, 114554, (2021).

Shet SP., Priya SS., Sudhakar K., Tahir M., A review on current trends in potential use of metal-organic framework for hydrogen storage, International Journal of Hydrogen Energy, 46, 11782-803, (2021).

Strub AA., Imarisio G., Hydrogen as an energy vector, Springer, Dordrecht, (1980).

Xu J., Liu X., Zhou Z., Xu ., Photocatalytic CO_2 reduction catalyzed by metalloporphyrin: Understanding of cobalt and nickel sites in activity and adsorption, Applied Surface Science, 513, 145801, (2020).

Preparation of polybenzimidazole-MOF composite membranes with enhanced proton conductivity

[1] *Enis Oğuzhan Eren, Necati Özkan[1], Yilser Devrim[2]*,*
[1] Middle East Technical University, Polymer Science & Technology, 06800, Ankara, Turkey
[2] Atilim University, Energy Systems Engineering, Ankara, 06836, Turkey

*E-mail: yilser.devrim@atilim.edu.tr

Abstract We fabricate composite membranes consisting of polybenzimidazole polymer as a matrix and ZIF-8 and UIO-66 metal-organic-frameworks as fillers to enhance the proton conductivity of pure PBI membranes, which is still the leading material for high-temperature electrochemical hydrogen compressors. Conductivity measurements at the 140°C and 160°C reveal that the PBI-MOF composite membranes exhibit between 27 and 60% improvements, depending on the filler type and amount.

Keywords: Polybenzimidazole, metal-organic-framework, composite, membrane, conductivity

1. Introduction

An electrochemical hydrogen compressor is a device where hydrogen can be supplied to the anode and collected from the cathode with high pressure, resulting in improvements for hydrogen storage and purification processes.[i] Acid doped PBI (Polybenzimidazole) is the critical polymer for high-temperature electrochemical hydrogen compressors because of the good thermal and chemical stability over 120°C. Recently it is noted that the acid-doping capacity and proton conductivity of the PBI membrane can be further increased by using the metal-organic-frameworks as a filler to fabricate PBI-based composite membranes.[ii,iii]Based on this phenomenon, we prepare several PBI-MOF composite membranes consisting of ZIF-8 and UIO-66 MOFs with different compositions. Furthermore, we successfully characterize their physical and chemical states and report significant improvements in the proton conductivity.

2. Experimental

Synthesis of Zn-MOF (ZIF-8) and Zr-MOF (UIO-66) by the solvothermal method is achieved accordingly. For the synthesis of ZIF-8, a certain amount $Zn(NO_3)_2{\cdot}6H_2O$ and 2-methylimidazole were ultrasonically dissolved in DMF for about 30 mins. The vial heated at a rate of 5°C·min^{-1} to 135°C in a programmable oven and held at this temperature for 24 h, then cooled to room temperature. The product was collected by centrifugation at 5000 rpm for 20 min. The obtained yellowish product is washed with DI water three times and dried overnight at 60°C. For the UIO-66, a certain amount of terephthalic acid and $ZrCl_4$ were ultrasonically dissolved in two separate DMF solvents. Then, two solutions were mixed and stirred for about 15 mins. The vial heated at a rate of 5°C·min^{-1} to 135°C in a programmable oven and held at this temperature for 24 h, then cooled to room temperature. The product was collected by centrifugation at 5000 rpm for 20 min. The obtained whitish product is washed with DI water three times and dried overnight at 60°C.

For fabrication of PBI-MOF composite membranes, a certain amount of PBI powder was dissolved in 10 mL DMAc under a magnetic stirrer at 75°C. Then, MOF powder was added to the solution and mixed for about 15 mins. In order to provide uniform dispersion, the as-prepared solution was ultrasonicated for about 10 mins. As-prepared membrane solution was cast onto the mold. Finally, to remove the excessive DMAc, membranes were dried overnight at 100°C. A total of four samples were prepared for each MOF material (2.5, 5.0, 7.5, and 10% wt.).

The crystallinity of the metal-organic-frameworks was determined by X-ray diffraction (XRD) using Rigaku Ultima-IV (Cu Kα radiation, 1.54056 Å). Thermal gravimetric analysis (TGA) was conducted using Perkin Elmer Pyris 1 under N_2 at a heating rate of 5 °C·min^{-1}. Autosorp-6B was used for obtaining nitrogen adsorption/desorption isotherms at 273 K. Quanta 400F was used as a field-emission scanning electron microscopy (FE-SEM). JEOL JEM 2100F with an accelerated voltage of 200 kV was used as a high-resolution transmission electron microscope (HR-TEM). Electrochemical workstation Wonatech Zive SP-2 is used for the potentiostatic EIS analysis (4 probes).

3. Results and discussion

The corresponding X-ray diffraction (XRD) patterns of the ZIF-8 and UIO-66 are shown in Figures 1a and 1b, respectively. In Figure 1a, corresponding characteristic peaks at 2θ = 7.3, 10.3, 12.7, 14.8, 16.4, and 18.0 are directly related to the planes (100), (200), (211), (220), (311), and (222) of ZIF-8, respectively, indicating that the ZIF-8 has very high crystallinity.[iv] However, a sharp peak at 2θ = 29.6 corresponds to the (044) plane[v], meaning that excessive crystal growth related to that plane is very likely. The average crystallite size is calculated around 100 nm for the ZIF-8 using the modified Scherer equation (Williamson-Hall plot), considering the generation of possible lattice strains. In Figure 1b, characteristic peaks positioned at 2θ = 7.4, 8.5, 12.0, 14.7, 17.0, 22.1, and 25.6 are also related to the planes (111), (002), (222), (044), and (006) of UIO-66, respectively, and confirmed that the successful synthesis of the metal-organic-framework.[vi] The average crystallite size for the UIO-66 is calculated as around 70 nm using the modified Scherer equation.

Nitrogen adsorption/desorption isotherms (Type I) at 0°C indicating a structure with micropores are shown in Figure

1d and summarized in Table 1. BET surface area and micropore volume of ZIF-8 are found as 878 $m^2 \cdot g^{-1}$ and 0.413 $cm^3 \cdot g^{-1}$, respectively, meaning that the synthesized ZIF-8 has a comparable or slightly lower surface area than reported in the literature (e.g., 700-1500).[vii] However, it must be noted that the excessive growth along the plane (044) might create a malformation on the usual dodecahedron shape. Hence, higher specific surface areas cannot be achieved even if within the presence of a higher micropore volume. Cumulative and BET surface area of UIO-66 is found as 476 and 350 $m^2 \cdot g^{-1}$, respectively. The reason for such a low surface area can be attributed to the small micropore volume, which we already know from previous studies.[viii] However, it must be noted that there is not a strict correlation between conductivity and the BET surface area of the fillers. In fact, some studies[ix] reveal that the conductivity may even decrease with an increase in BET surface area due to the decrease in intermolecular interactions.

Table 1. Physical properties of as-synthesized MOF powders.

MOF	$S_{cumulative}$ ($m^2 \cdot g^{-1}$)	S_{BET} ($m^2 \cdot g^{-1}$)	V_{pore} ($cm^3 \cdot g^{-1}$)	d_{pore} (nm)
UIO-66	467	350	0.16	0.16 - 0.47
ZIF-8	1165	878	0.41	0.35 - 0.70

TGA curves (Figure 1e) of the MOFs are parallel to the literature showing an initial minor weight loss, which is attributed to the removal of residual solvents and guest molecules. The sharp weight losses of ZIF-8 between 400-600 are related to the decomposition of the organic imidazolate species. Further weight loss is associated with the steady collapse of the ZIF-8 structure.[x] Also, the sharp weight loss of UIO-66 between 500-600 is related to the collapse of the structure. Standalone MOFs and PBI-MOF composite membranes are further characterized with FE-SEM (figure 1c and 1f).

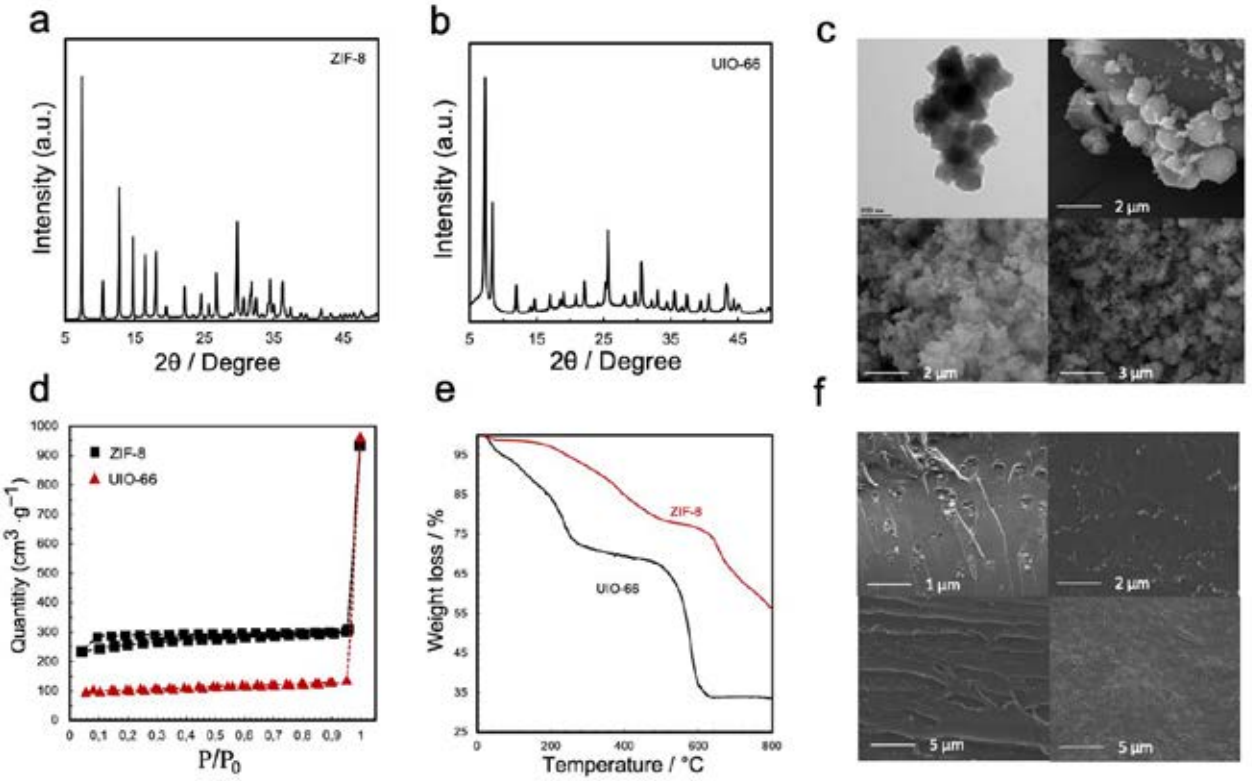


Figure 1. Corresponding XRD patterns showing characteristic peaks for synthesized metal-organic-frameworks (a) ZIF-8 and (b) UIO-66. (c) HR-TEM and FE-SEM images of the as-synthesized ZIF-8 and UIO-66 MOF particles. (d) Nitrogen adsorption/desorption isotherms of ZIF-8 and UIO-66 at 273 K. (e) TGA curves of ZIF-8 and UIO-66 under N_2 at a heating rate of 5ºC·min^{-1}.(f) FE-SEM images of the PBI-MOF composites with different magnifications.

Before the acid-doping level measurements, membranes are immersed in the phosphoric acid for about seven days. The acid-doping capacity of the composite membranes is slightly increased compared to the pure PBI membrane. However, the most striking data comes from their proton conductivity capability. As seen in Table 2 and Figure 2, improvement in proton conductivity of the composite membranes ranges from 27% to 60%, depending on the composition and the type of the fillers.

Table 2. Summary of the improvements in phorphoric acid-doping level and the proton conductivity.

Membrane	PA doping level	Conductivity 140°C ($S \cdot cm^{-1}$)	Conductivity 160°C ($S \cdot cm^{-1}$)	Increase in conductivity w.r. to pure PBI (%, avg. for 140°C and 160°C)
Pure PBI	10.8	0.0375	0.0397	-

PBI-ZIF8 (2.5 wt%)	11	0.0450	0.0529	27
PBI-ZIF8 (5.0 wt%)	11.3	0.0475	0.0554	33
PBI-ZIF8 (7.5 wt%)	11.3	0.0503	0.0612	44
PBI-ZIF8 (10.0 wt%)	11.5	0.0508	0.0622	46
PBI-UIO66 (2.5 wt%)	11.5	0.0563	0.0611	52
PBI-UIO66 (5.0 wt%)	12.5	0.0573	0.0614	54
PBI-UIO66 (7.5 wt%)	11.3	0.0568	0.0629	55
PBI-UIO66 (10.0 wt%)	11	0.0602	0.0633	60

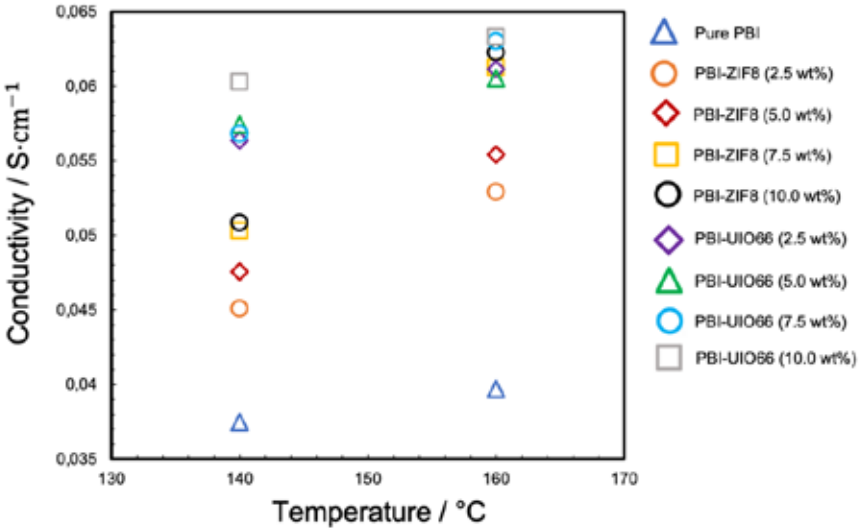


Figure 2. Comparison of proton conductivities at 140°C and 160°C.

4. Conclusions

In summary, the fabrication of MOF crystals and PBI-MOF composite membranes are successfully characterized by the XRD, TEM, TGA, BET, HR-TEM, FE-SEM analysis. Studies reveal that the effect of the MOFs on the conductivity is enormous; also, MOF fillers provide a slight increase in acid-doping capacity of the membrane, which can be very supportive especially working at elevated temperatures. Among the MOF materials, UIO-66 exhibits the best performance with an increase of over 50% with respect to the baseline pure PBI.

Acknowledgements

This study is supported by The Scientific and Technological Research Council of Turkey under grant no of 219M333.

References

[i] Zou, J., Han, N., Yan, J., Feng, Q., Wang, Y., Zhao, Z., Fan, J., Zeng, L., Li, H., & Wang, H. (2020). Electrochemical Compression Technologies for High-Pressure Hydrogen: Current Status, Challenges and Perspective. *Electrochemical Energy Reviews*, *3*(4), 690–729.

[ii] Escorihuela, J., Olvera-Mancilla, J., Alexandrova, L., del Castillo, L. F., & Compañ, V. (2020). Recent Progress in the Development of Composite Membranes Based on Polybenzimidazole for High Temperature Proton Exchange Membrane (PEM) Fuel Cell Applications. *Polymers*, *12*(9).

[iii] Mukhopadhyay, S., Das, A., Jana, T., & Das, S. K. (2020). Fabricating a MOF Material with Polybenzimidazole into an Efficient Proton Exchange Membrane. *ACS Applied Energy Materials*, *3*(8), 7964–7977.

[iv] Nordin, N. A. H. M., Ismail, A. F., Misdan, N., & Nazri, N. A. M. (2017). Modified ZIF-8 mixed matrix membrane for CO2/CH4 separation. *AIP Conference Proceedings*, *1891*(1), 20091.

[v] Pillai, P., Dharaskar, S., Sasikumar, S., & Khalid, M. (2019). Zeolitic imidazolate framework-8 nanoparticle: a promising adsorbent for effective fluoride removal from aqueous solution. *Applied Water Science*, *9*(7), 150.

[vi] Wu, R., Qian, X., Zhou, K., Liu, H., Yadian, B., Wei, J., Huang, Y. (2013). Highly dispersed Au nanoparticles immobilized on Zr-based metal–organic frameworks as heterostructured catalyst for CO oxidation. *J. Mater. Chem. A*, *1*(45), 14294–14299.

[vii] Lee, Y.-R., Jang, M.-S., Cho, H.-Y., Kwon, H.-J., Kim, S., & Ahn, W.-S. (2015). ZIF-8: A comparison of synthesis methods. *Chemical Engineering Journal*, *271*, 276–280.

[viii] Su, Z., Miao, Y.-R., Zhang, G., Miller, J. T., & Suslick, K. S. (2017). Bond breakage under pressure in a metal organic framework. *Chem. Sci.*, *8*(12), 8004–8011.

[ix] Shanahan, J., Kissel, D. S., & Sullivan, E. (2020). PANI@UiO-66 and PANI@UiO-66-NH2 Polymer-MOF Hybrid Composites as Tunable Semiconducting Materials. *ACS Omega*, *5*(12), 6395–6404.

[x] Chu, F., Zheng, Y., Wen, B., Zhou, L., Yan, J., & Chen, Y. (2018). Adsorption of toluene with water on zeolitic imidazolate framework-8/graphene oxide hybrid nanocomposites in a humid atmosphere. *RSC Adv.*, *8*(5), 2426–2432.

A Density Functional Theory Study of Hydrogen Adsorption on Ni Doped Carbon Nanocone

[1] *Ahmet Köse*, [1] *Numan Yüksel*, [1*] *Mehmet Ferdi Fellah*
[1]Bursa Technical University, Faculty of Engineering and Natural Sciences, Department of Chemical Engineering, Mimar Sinan Campus 16310, Bursa, Turkey

*Corresponding author e-mail: mferdi.fellah@btu.edu.tr

Abstract

Hydrogen molecule adsorption was investigated on Ni doped Carbon Nanocone (CNC) by Density Functional Theory (DFT). The electronegativity, HOMO and LUMO energy, chemical hardness, chemical potential, adsorption enthalpy and adsorption energy values have been calculated on Ni doped CNC 180º cluster model. The hydrogen adsorption enthalpy value was calculated as -27.8 kJ / mol. This value is greater than the liquefaction enthalpy value of the hydrogen molecule, which indicates that Ni doped CNC 180º structure appears to be an incentive candidate for hydrogen storage as a cryoadsorbent at room temperature.

Keywords: Adsorption, hydrogen, DFT, nanocone, Ni atom

I. Introduction

The idea that hydrogen can be used as the main energy carrier has attracted considerable attention in the last 30 years. However, it will be necessary to develop a safe and efficient method for using hydrogen as an energy carrier and for storing it (Fellah, 2017; Strub and Imarisio, 1980). Hydrogen storage in carbon nanotubes is notable for their light mass densities and high reactivity between carbon and hydrogen. The curvature of carbon nanotubes (CNT) is known to increase hydrogen storage capacity, but the interaction between hydrogen and the nanotube surface is due to weak Van der Waals forces. In this case, it leads a decrease in the storage capacity under ambient conditions. On the other hand, it has been observed that there is a stronger interaction between the adsorbed hydrogen atoms and the conical parts of the CNTs than the tube parts. For this reason, it is thought that CNC (carbon nanocone) can show better performance in hydrogen storage compared to CNTs (Barbary, 2019). There is no study concerning adsorption of hydrogen on Ni doped CNC 180º in either theoretical or experimental open literature. The aim of this study is to examine the activity of Ni doped CNC for the hydrogen adsorption.

II. Computational Method

The theoretical calculations performed in the present work were based on DFT (Kohn and Shamn, 1965). The Gaussian 09 software (Frisch et al., 2013) was used to carry out the calculations, and the method implemented was the WB97XD hybrid formalism. The WB97XD method is a very recent hybrid method using a version of Grimme's D2 dispersion model. The basis sets 6-31G(d,p) (for carbon and hydrogen atoms) and LANL2DZ (for nickel atom) were utilized in the calculations. There are CNCs synthesized at 5 different inclination angles in the literature. In this study, CNC with an angle of inclination of 180 was used. CNC structure which consists of 102 carbon atoms was used in this study for hydrogen adsorption study. Hydrogen (H) atoms were inserted to end parts of CNC free carbon atoms' bonds for the purpose of neutral charge on the cluster. One of the carbon atoms at the tip of the CNC has been replaced by the Ni atom. Geometries have been optimized by Equilibrium Geometry (EG) calculations. All atoms have been kept relxed during theoretical calculations.

III. Analysis

In this study, values of energy difference consist of the zero-point energy (ZPE) corrections which have been calculated by using vibrational frequency calculations through Single Point Energy (SPE) calculations. Additionally, the thermal energy and thermal enthalpy were computed by frequency calculations at room temperature because either theoretical or experimental literature has no thermochemistry data for hydrogen adsorption on Ni-CNC. These energy values have been computed by following equations:

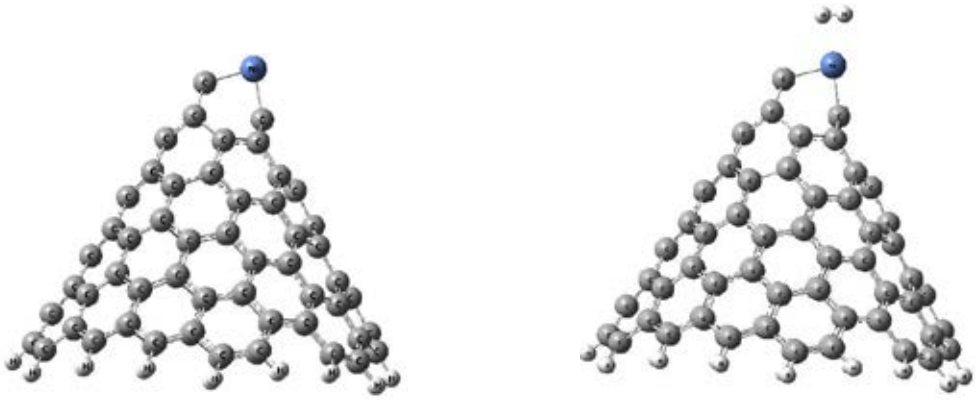
$$E = E_{Electronic} + \mathrm{ZPE} + E_{Vibrational} + E_{Rotational} + E_{Translational} \quad (1)$$

$$\mathrm{H} = \mathrm{E} + \mathrm{RT} \quad (2)$$

The chemical potential, electronegativity and chemical hardness values were calculated by using HOMO and LUMO energies. Energy of the highest occupied molecular orbital and energy of the lowest unoccupied molecular orbital have been utilized by based on the approximation of Koopmans approach (Pearson, 2005). Mulliken population analysis was utilized to obtain Mulliken atomic charges of atoms.

IV. Results and discussions

Initially, Ni-doped CNC cluster optimization was performed by EG calculation with a neutral charge and doublet spin multiplicity (SM). Moreover, doublet SM was established for the cluster-hydrogen molecule system. After optimization of the cluster and hydrogen, adsorption of hydrogen was performed on Ni-doped CNC structure. Optimized geometry of Ni-doped CNC and the optimized geometry of hydrogen adsorbed on the Ni-doped CNC are shown in Fig. 1.



a) b)

Fig. 1: a) Optimized geometry of Ni-doped CNC 180º cluster b) Optimized geometry of Ni-doped CNC 180º cluster with adsorbed H_2

Structural parameters, the HOMO and LUMO energy values, chemical potential (μ), chemical hardness (η) and electronegativity (χ) values and the adsorption energy values (ΔE and ΔH) for hydrogen adsorption on Ni-doped CNC clusters have been showed in Table 1.

Tab. 1: Structural parameters, energy values, HOMO and LUMO energy, chemical hardness, chemical potential and electronegativity values for the optimized Ni doped CNC cluster and the optimized hydrogen adsorbed on Ni doped CNC

Properties		**Ni doped CNC**	**H_2 adsorbed on Ni doped CNC**
Distance, Å	Ni-Cs (bonded with C atoms)	1.914 1.914 1.811	1.948 1.954 1.817
	Ni-H	-	1.834
Mulliken Charges, e	Ni atom	0.232	0.083
	H_2 molecule	0	0.116
Adsorption energies, (kj/mol)	ΔE	-	-25.3
	ΔH	-	-27.8
α MOs, (kj/mol)	HOMO Energy	-535.7	-536.1
	LUMO Energy	-144.9	-136.4
	HLG	390.7	399.7
	Chemical Hardness (η)	195.3	199.8
	Chemical Potential (μ)	-340.3	-336.3
	Electronegativity (χ)	340.3	336.3
β MOs, (kj/mol)	HOMO	-568.1	-566.8
	LUMO	-220.5	-219.7
	HLG	347.6	347.1
	Chemical Hardness (η)	173.8	173.5
	Chemical Potential (μ)	-394.3	-393.2
	Electronegativity (χ)	394.3	393.2

When the Mulliken charges are examined, the total charge of hydrogen adsorbed on the cluster is +0.116e. This result shows that the charge transfer is from adsorbed hydrogen to the cluster. In this study, the adsorption enthalpy of hydrogen was calculated as -27.8 kj/mol. This value is higher than the liquefaction enthalpy value of hydrogen molecule that is 0.9 kj/mol. According to the results, HOMO-LUMO gap (HLG) values increased for alpha molecular orbital and slightly decreased for beta molecular orbital. This result indicates that the electrical conductivity is weak. α and β HOMO-LUMO representations for Ni-doped CNC and adsorbed hydrogen Ni-doped CNC are shown in the Fig. 2. Besides, the distribution of electrostatic potential (ESP) for Ni-doped (4,0) CNC cluster and hydrogen adsorbed Ni-doped CNC cluster have been represented in Fig. 3. The positive and negative regions of the van der Waals surface have been characterized by the blue and red colors on the ESP map (Sjoberg and Politzer, 1990).

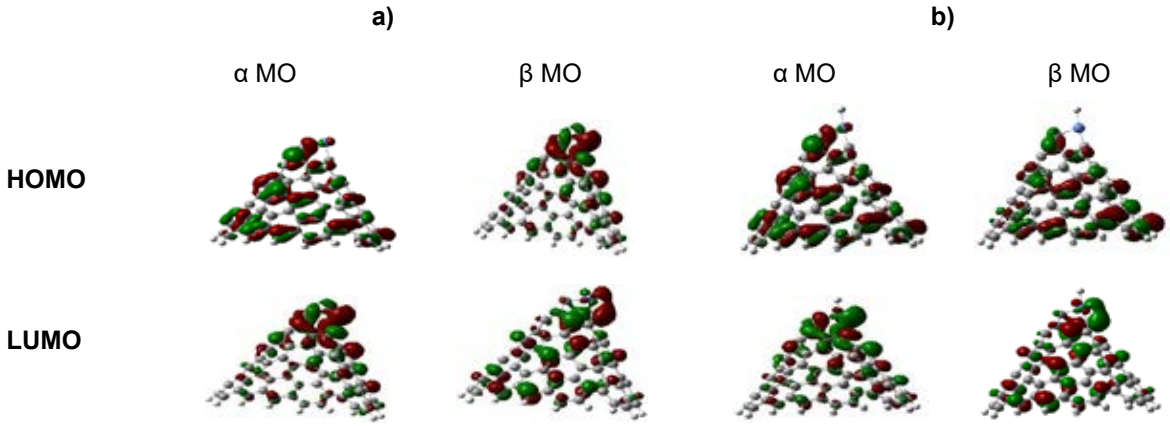
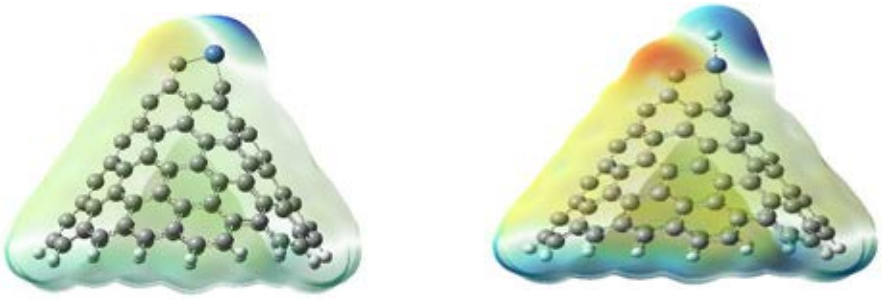


Fig. 2: HOMO-LUMO representations of α and β MOs a) for the optimized structure of Ni-doped CNC b) for the optimized structure of the adsorbed hydrogen on Ni-doped CNC



a) b)

Fig. 3: ESP distribution maps a) for the optimized structure of Ni-doped CNC b) for the optimized structure of the adsorbed hydrogen on Ni-doped CNC

V. Conclusions

In this study, DFT calculations with WB97XD method have been used for hydrogen adsorption on Ni-doped CNC. Adsorption enthalpy value of hydrogen is -27.8 kj/mol which is higher than liquefaction enthalpy value of hydrogen molecule. This result designates that Ni-doped CNC may be used as a potential cryoadsorbent for hydrogen storage at room temperature.

Acknowledgements

The numerical-calculations reported in this paper were partially performed at TUBITAK ULAKBIM, High-Performance and Grid-Computing-Center-(TRUBA resources).

References

El-Barbary, A.A., Hydrogen storage on cross stacking nanocones, International Journal of Hydrogen Energy, 44, 20099—20109, (2019).

Fellah MF., A density functional theory study of hydrogen adsorption on Be-, Mg-, and Ca-exchanged LTL zeolite clusters, Journal of Molecular Modeling, 23, 184, (2017).

Frisch et al., Gaussian 09 Revision D.01, Gaussian Inc., Wallingford CT, (2013).

Kohn W., and Shamn L., Self-consistent equations including exchange and correlation effects, Journal of Physical Review, 140, A1133-A1138, (1965).

Pearson R.G., Chemical hardness and density functional theory, Journal of Chemical Sciences, 117, 369-377, (2005).

Sjoberg P., Politzer P., Use of the electrostatic potential at the molecular surface to interpret and predict nucleophilic processes, Journal of Physical Chemistry 94, 3959–3961, (1990).

Strub AA., Imarisio G., Hydrogen as an energy vector, Springer, Dordrecht, (1980)

Chemically and Thermally Reduced Graphene Oxide Supported Pt Catalysts Prepared by Supercritical Deposition

[1*]Meryem Samancı, [1,2]Ayşe Bayrakçeken Yurtcan
[1] Atatürk University, Faculty of Engineering, Department of Chemical Engineering, Erzurum, 25240, Turkey
[2] Atatürk University, Department of Nanoscience and Nanoengineering, Erzurum, 25240, Turkey

* E-mail: meryemsamanci@gmail.com

Abstract
In this study, the synthesis of reduced graphene oxide was carried out by thermal and chemical reduction processes. Two different catalysts were synthesized using 1,5-dimethyl platinum cyclooctadiene as the Pt precursor on the reduced graphene oxide supports. Supercritical carbon dioxide deposition technique was used in the catalyst synthesis. Electrochemical and physicochemical analyzes were performed on the synthesized materials.

Keywords: Reduced graphene oxide, Chemical reduction, Thermal reduction, $ScCO_2$ deposition

I. Introduction

Graphene-based materials are widely used electrode support materials for PEM fuel cells. One of the most important type of these support materials is reduced graphene oxide. Reduced graphene oxide (rGO) is very similar to the original graphene and reduction of graphene oxide is the most important process during the synthesis. The reduction can be done by thermally (annealing, microwave, light), chemically (a reducing agent, photocatalyst, electrochemistry, hydrothermal reaction) or a combination of these methods. Among these methods, chemical and thermal reduction methods are often preferred. In this study, the synthesis of reduced graphene oxide was achieved by chemical and thermal reduction of graphite oxide. PEM fuel cell catalysts were synthesized by loading Pt to the synthesized support materials under supercritical conditions. It is aimed to improve fuel cell performance with the synthesized supports.

II. Experimental Set-up and Procedure

Graphene oxide synthesized by the Hummer method was used as the precursor material in the synthesis of reduced graphene oxide (Hummers and Offeman, 1958). In the synthesis of chemically reduced graphene oxide, hydrazine monohydrate ($NH_2NH_2.H_2O$) as reductant, methanol and purified water were used in the washing process. Thermally reduced graphene oxide synthesis was carried out in argon (Ar) atmosphere. In the synthesis of Pt electrocatalyst, 1,5-dimethyl platinum cyclooctadiene $Pt(COD)Me_2$ compound was used as the Pt precursor. Adsorption process was performed using supercritical CO_2 under supercritical conditions and then thermal reduction of the precursor was achieved at high temperature in N_2 environment.

Chemically reduced graphene oxide synthesis (C-RGO):

In chemically reduced graphene oxide synthesis, hydrazine monohydrate was used as the chemical reductant. The chemical reduction process was carried out using the reflux system. GO was added to pure water and mixed well. Later, hydrazine monohydrate was added to this solution and mixed for a while at 100 °C in reflux system. The mixture was stirred for a while at its own temperature. By filtering, washing was done with methanol in the centrifuge. It was kept in the oven at 80 °C overnight and finally C-RGO was obtained.

Thermally reduced graphene oxide synthesis (T-RGO):

In the synthesis of thermally reduced graphene oxide, the specified amount of GO was placed in a tubular furnace and kept in an argon atmosphere at 500 °C for 2 hours. The heating rate of the oven is set at 10 °C/min. T-RGO material was synthesized at the end of this thermal process.

Preparation of Pt Catalyst by $SCCO_2$ deposition method:

Catalyst synthesis consists of two stages. The first stage is adsorption and the second stage is thermal reduction. First of all, the support material and the Pt precursor are mixed in a certain ratio and placed in the reactor. The reactor temperature was provided to be 80 °C. The reactor pressure was adjusted to 3500 psi and CO_2 was introduced into the system. Under these conditions, it was kept for a while in order for the Pt precursor to dissolve well and adsorb to the support surface. After adsorption process, the sample removed from the reactor, weighed and thermally reduced in N_2 environment at 500 °C for 3 hours.

III. Analysis

Characterization of Support Materials:

The following characterization methods are used for the characterization of synthesized support materials. Morphological structure (such as surface area, pore diameters, pore size distribution) of synthesized samples are determined by nitrogen adsorption/desorption isotherm analysis by Brunauer, Emmett and Teller (BET) method. Micromeritics 3Flex 3-port BET surface area device will be used in surface area analysis. Determination of surface groups in the synthesized materials with FTIR device is made. IR spectra of the synthesized materials were taken using Fourier Transform Infrared Spectrometer (Perkin Elmer Spectrum One). Spectra were obtained in the range 4000-400 cm^{-1} at room temperature. Crystal structures of the synthesized materials are carried out in the range of $10° \leq 2\theta \leq 90°$ using X-ray diffractometer (PANalytcal Empyrean X-Ray Diffractometer). Raman spectroscopy (WITech alpha 300R) is used to obtain information about the bonds.

Electrochemical characterizations of the synthesized materials were made by cyclic voltammetry (CV) method, which was obtained from Pine Instrument, combined with Versastat 3 potentiostat and rotating disk electrode system. CV analyzes were performed with a standard three-electrode electrochemical cell system consisting of the working (glassy carbon; GC), reference (Ag/AgCl) and counter (Pt wire) electrodes. Experiments were performed in Perchloric acid, $HClO_4$ (0.1 M) electrolyte.

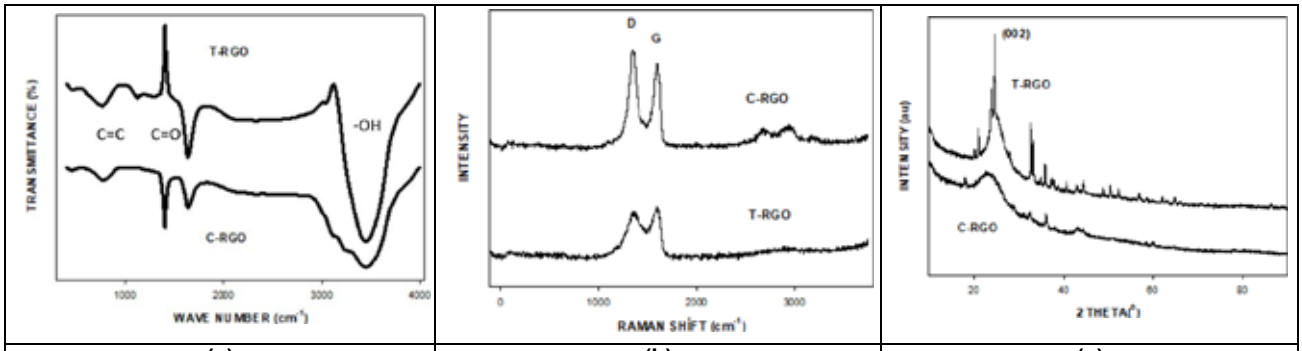
IV. Results and discussions

The multi-point BET surface area and BJH pore volume data of T-RGO and C-RGO supports are summarized in Table 1. According to the results of the BET analysis, specific surface areas of T-RGO and C-RGO were found as 213.37 m^2/g and 166.92 m^2/g, respectively.

Tab. 1: BET analysis data of graphene support material

Material	BET surface area (m^2/g)	Average pore diameter (nm)	Langmuir surface area (m^2/g)	t-Plot Micro pore area (m^2/g)	Average particle size (nm)	BJH surface area (m^2/g)	D-H surface area (m^2/g)	BJH pore volume (cm^3/g)	D-H pore volume (cm^3/g)
C-RGO	*166,92*	*4,27*	*1413,52*	-	*35,95*	*149,82*	*202,41*	*0,205*	*0,259*
T-RGO	*213,37*	*13,28*	*1783,16*	-	*28,12*	*416,33*	*471*	*1,287*	*1,411*

FTIR spectra of T-RGO and C-RGO are given in Figure 1 (a). Peaks at 3440 cm^{-1} and 1635 cm^{-1} of T-RGO and C-RGO correspond to -OH stress vibrations. The absorption peaks in between 760-790 cm^{-1} belong to the aromatic C-H deformation. Peaks at 1120-1135 cm^{-1} provide information on the C-O-C stretch of alkoxy groups (Kaniyoor etal., 2010; Surekha etal., 2020).



(a) (b) (c)

Fig. 1: (a) FTIR, (b) RAMAN and (c) XRD spectra of T-RGO and C-RGO materials

In Raman spectrum Figure 1 (b), G band gives information about sp^2 hybridization by showing the degree of graphitization. The D band represents the irregular carbon structure in the lattice of sp^3 hybridized carbon atoms. For this reason, D-peak intensity is often used as a measure of the degree of disorder. Ratio between D band and G band (ID/IG) is used to determine the degree of irregularity in the graphene's lattice structure (Dresselhaus etal., 2010). Table 2 shows Raman shear values and D and G peak intensities in D and G band of C-RGO and C-RGO. In the light of these data, the defects in the structure were examined by calculating the ID/IG values. Accordingly, C-RGO was found to have the highest cage and structural distortion defects.

Tab. 2: Results of raman spectra of T-RGO and C-RGO

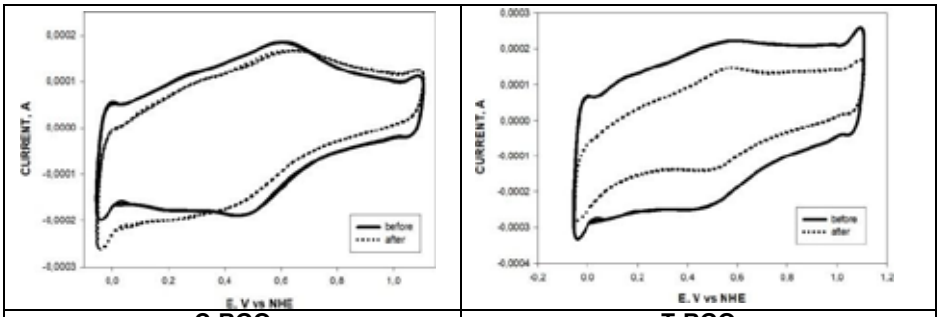
Material	Raman shift (cm^{-1})		D peak intensity (au)	G peak intensity (au)	ID/IG
	D band	G band			
T-RGO	*1371,65*	*1587,14*	*424*	*440,5*	*0,96*
C-RGO	*1351,41*	*1598,94*	*889*	*750,5*	*1,184*

XRD graph of T-RGO and C-RGO is also given in Figure 1 (c). A pronounced peak (002) was seen at 2θ = 24.7° for T-RGO and at 2θ = 22.9° for C-RGO. The results of the peak analysis based on the XRD spectra are summarized in Table 3. The presence of the large (002) peak within the crystal phase of RGOs indicates that the graphene sheets are arranged randomly. The resulting graphene nanosheets have a structure between crystalline and amorphous structures (Hidayah etal., 2017).

Tab. 3: Analysis of XRD peaks of T-RGO and C-RGO

Material	Peak (2θ)	d (Å)	Crystal size D (Å)	Number of layers N
T-RGO	*24,7˚*	*3,6*	*16,2*	*4,5*
C-RGO	*22,9˚*	*3,9*	*18,1*	*4,6*

CV tests were carried out to determine the resistance of synthesized T-RGO and C-RGO materials against carbon corrosion in PEM fuel cell under harsh conditions. CV curves of T-RGO and C-RGO are given in Figure 2. When we look at the current-voltage curves taken for before and after corrosion, we see that the corrosion resistance of C-RGO is better than T-RGO.



C-RGO **T-RGO**

Fig. 2: CV results of T-RGO and C-RGO support materials

V. Conclusions

The development of the support material used in PEM fuel cells increases the efficiency of the Pt catalyst which reduces the cost of the fuel cell production. In this study, two different methods were used to synthesize reduced graphene oxide. Later, these supports were loaded with Pt with the supercritical CO_2 deposition technique. It is aimed to improve fuel cell performance with the synthesized support materials.

Acknowledgements

This work is supported by the Scientific Research Projects (BAP) Coordination Unit of Atatürk University with FDK-2020-8560 project number. Thank you to BAP for their support.

References

Hummers, W. S., Offeman, R. E., Preparation of Graphitic Oxide. Journal of the American Chemical Society, 80(6), 1339–1339, (1958).

Kaniyoor, A., Baby, T. T., Ramaprabhu, S., Graphene synthesis via hydrogen induced low temperature exfoliation of graphite oxide. Journal of Materials Chemistry, 20(39), 8467-8469, (2010).

Surekha, G., Krishnaiah, K. V., Ravi, N., Padma Suvarna, R., FTIR, Raman and XRD analysis of graphene oxide films prepared by modified Hummers method. Journal of Physics: Conference Series, 1495, 012012, (2020).

Dresselhaus, M., Jorio, A., & Saito, R., Characterizing graphene, graphite, and carbon nanotubes by Raman spectroscopy. Annu. Rev. Condens. Matter Phys., 1(1), 89-108, (2010).

Hidayah, N. M. S., Liu, W.-W., Lai, C.-W., Noriman, N. Z., Khe, C.-S., Hashim, U., & Lee, H. C., *Comparison on graphite, graphene oxide and reduced graphene oxide: Synthesis and characterization.* AIP Conference Proceedings 1892, (2017).

Catalyst Development for Viability of Electrochemical Hydrogen Purifier and Compressor Technology

[1*]Yasemin Aykut, [2]Ayşe Bayrakçeken Yurtcan
[1] Atatürk University, Engineering Faculty, Chemical Engineering, Erzurum, 25240, Turkey
[2] Atatürk University, Engineering Faculty, Chemical Engineering, Erzurum, 25240, Turkey

* E-mail: yaseminn.aykut@gmail.com, abayrakceken@atauni.edu.tr

Abstract
It becomes important to develop methods for the purification and storage of hydrogen with the development of hydrogen technology. It is thought that the development of electrochemical hydrogen purifier and compressor (EHPC) system will make a great contribution to this field. This study covers the introduction of the EHPC system and the development of the catalyst which is one of the main components of the system. In this work, the preparation of PtPd-based catalysts and the results of the characterization of the prepared catalysts by ICP-MS, XRD, SEM-EDS and cyclic voltammetry (CV) are given.

Keywords: compression, electrocatalyst, hydrogen, purification

I. Introduction

Today, the increase in environmental pollution and global warming with the increasing energy demand and the decrease in fossil fuels pose a great concern. This situation raises awareness of alternative energy sources in the world and the issue of transition to 100% renewable energy by 2050 for a solution is constantly being voiced in the world press. Especially, it is aimed to define this issue in all details in research and development studies and to highlight the studies in which energy consumption is low and renewable energy resources are used in new technological designs to be developed (Gielen et al., 2019). Although different alternatives were offered to replace fossil fuels, which are the primary energy sources, a consensus is reached that the ideal solution could be hydrogen, due to its superior properties. In particular, the development of fuel cell technologies in transportation is one of the most important factors in the development of hydrogen technologies (Peschel, A., 2020). Besides the abundance of hydrogen in the universe, it is renewable and its ability to be produced from sustainable sources offers an environmentally friendly solution to meet the increasing energy demand. However, some problems encountered should be solved for the continuity of this technology. The most important of these problems is the development of appropriate methods that will enable the hydrogen obtained by different methods to be purified and compressed for safe storage in terms of availability (Zou et al., 2020). When the properties of the existing methods are examined, it is important to supply the separation of hydrogen from various gas mixtures at high purities and develop low-cost, high efficiency compressor systems. In the light of this information, the development of an electrochemical hydrogen purifier and compressor (EHPC) system that can purify and compress hydrogen in mixed form will greatly contribute to studies in the field of hydrogen technologies (Rhandi et al., 2020). The EHPC system is similar to electrochemical hydrogen compressors and consist of an anode, cathode electrode and polymer-based membrane (Figure 1). In the working principle of this system, firstly hydrogen in the form of a mixture is fed to the anode at low pressure, where hydrogen is oxidized to form protons. The formed protons reach the cathode part by passing through the membrane and hydrogen is formed at high pressure after reduction at the cathode (Jackson et al., 2020).

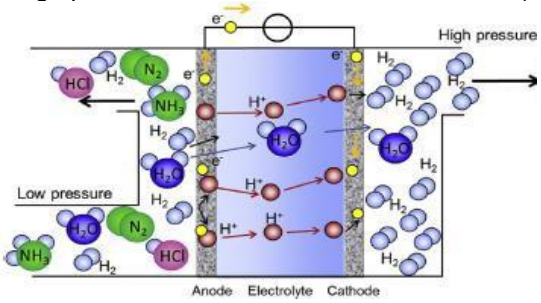


Fig. 1: Working principle of electrochemical hydrogen compressor (Jackson et al., 2020).

In this study, it is aimed to prepare the hydrogen oxidation and formation catalyst that can be used in EHPC system. PtPd (1:1) bimetallic catalyst by weight was made by using microwave heating method (MWI). The structure of the prepared catalysts were examined by physical and electrochemical characterizations.

II. Experimental Set-up and Procedure

In the study, H_2PtCl_6 (Alpha Easer) and $PdCl_2$ (Aldrich) were used as metal precursors and Vulcan XC-72 (Cabot) as carbon support. Solutions of Pt, Pd nanaparticles were prepared by dissolving H_2PtCl_6 salt in water and $PdCl_2$ salt in HCl. It was added to the ethylene glycol (EG) used as reducing agent by taking the determined mass proportions from the prepared solution. After this solution was mixed in the magnetic stirrer for 20 minutes, the pH was adjusted to 12 using 1M KOH, since the reduction was better in the basic environment, and the magnetic stirrer

application was continued. 100 mg of Vulcan XC-72 was added to the prepared solution and it was mixed in magnetic stirrer for 60 minute to make the solution homogeneous. This solution prepared in the beaker was exposed to microwave energy of 800 W for 1 minute and the reduction process was carried out. After the microwave treatment, the solution in the beaker was cooled suddenly. After this process, EG was removed from the solution by centrifugation. In order to remove the impurities in the solution, washing with acetone and pure water was carried out and centrifuged again. After these processes, the tubes were kept in the oven at 100°C for 12 hours (Figure 2). The prepared catalyst was characterized with ICP-MS, SEM-EDS, XRD and cyclic voltammetry (CV).

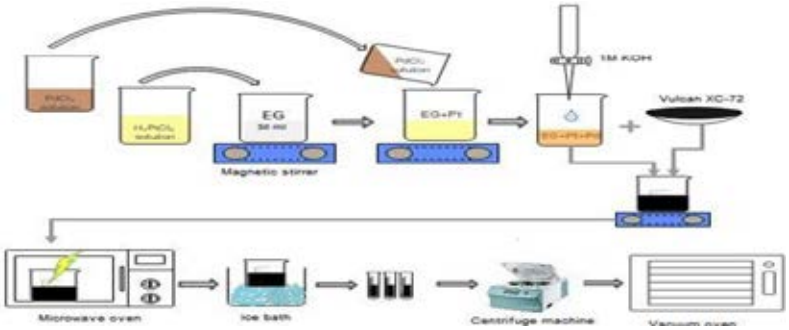


Fig. 2: PtPd/C catalyst synthesis procedure

III. Analysis

Qualitative analysis of the elemental composition via ICP-MS (Agilent 7800), SEM (Scanning Electron Microscope) for surface morphology and EDS (Energy Dispersion Spectroscopy) analysis for elemental composition (FEI, Inspect s50), to examine the crystallite size, X-ray diffraction analysis (Rigaku Miniflex) measurements were carried out by using Cu Kα (λ = 1.54 Å), in the range of 10-90°(2Θ).

IV. Results and discussions

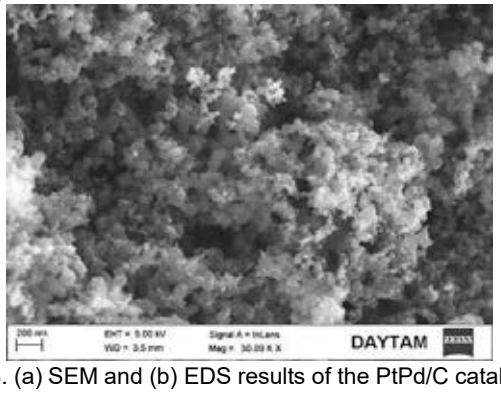
ICP-MS result of the prepared PtPd/C (20%) catalyst is given in Table-1. Table-1 showed that the Pt and Pd loadings are very close to the nominal value of 20 wt%.

Table 1. ICP-MS result of PtPd/C catalyst

Synthesized Catalyst	Mass (%)	
	Pt	Pd
PtPd /C	10.5	7.8

The SEM image and the EDS result of the synthesized PtPd/C catalyst is shown in Figure 3. SEM image only showed the morphological structure of the support material, and information about metals was not obtained.

a) **b)**



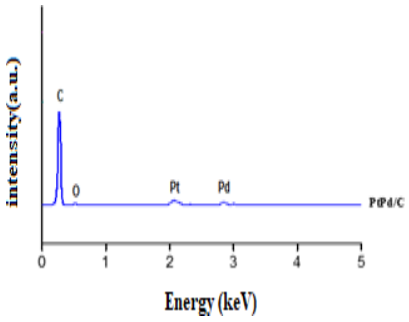


Figure 3. (a) SEM and (b) EDS results of the PtPd/C catalyst

As seen in the EDS result of the synthesized catalyst, the structure contains Pt, Pd, C elements. According to the EDS result, the atomic percent and weight ratios of these elements are summarized in Table 2.

Table 2. Atomic and weight percentages of PtPd/C catalyst from EDS result

Synthesized Catalyst	Atomic (%)			Mass (%)		
	Pt	Pd	C	Pt	Pd	C
PtPd/C	0.9	1.2	97.9	12.2	8.3	79.5

It is seen that the ratio values by weight are generally close to the targeted values when the data in Table 2 are examined. EDS analysis results was consistent with the ICP-MS results of the same catalyst, it was seen that the catalyst can be synthesized close to the targeted metal loading value.

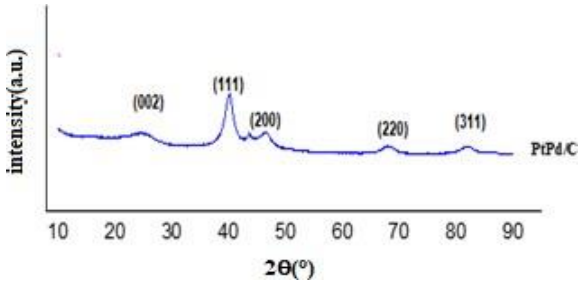


Figure 4. XRD result of PtPd/C catalyst

XRD result of the catalyst is given in Figure 4. It is seen that the peak corresponding to support material is seen at the diffraction value of 2θ <30°. Since the atomic sizes of Pt and Pd are similar, the crystal structures are the same and the maximum diffraction peaks are located at the same angle. Pt-Pd peaks are defined as (111), (200), (220), (311) of the crystalline structure with face-centered cubic (fcc) in diffraction patterns.

The electrochemical activity of the prepared PtPd/C catalyst was determined using CV. CV profiles of PtPd/C was recorded in between -0.28 - 1V in 0.1 M $HClO_4$ which was saturated with Ar. Figure 5 shows the representative CV curves of the PtPd/C catalyst at various scan rates ranging from 10 to 100 mV/s. All CV curves are given with respect to reversible hydrogen electrode (RHE).

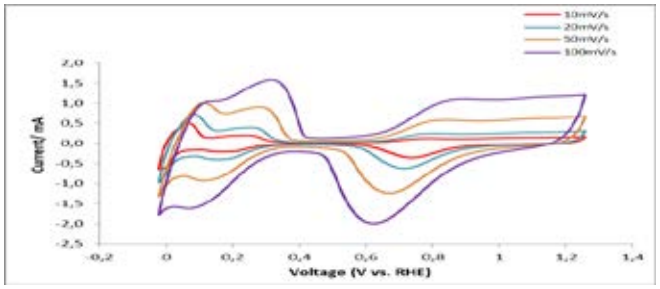


Fig. 5: CV curves of PtPd/C catalyst at different scan rates.

It can be seen that the peak current increases as the scan rate is increased. The peaks observed for the PtPd/C catalyst are the combination of the peaks formed by both metals.

V. Conclusions

In this study, the microwave irradiation method was used to prepare the PtPd/C catalyst, which is one of the most important components of EHPC systems. In this method, the supported bimetallic catalyst was successfully synthesized by combining two metals. Physical and electrochemical characterization analyzes of the synthesized catalyst was used to enlighten their structure. Within the scope of this study, our research and development studies for the development of the new catalysts will continue.

Acknowledgements

This research is supported by TUBITAK-1003 programme, thank you to TUBITAK for this support. (Project number: 218M815).

References

Gielen,D., Boshella, F., Saygin, D., Bazilian, M. D.,Wagner,N., Gorinia, R.,The role of renewable energy in the global energy transformation" Energy Strategy Reviews, 24, 38-50, (2019)

Jackson, C., Raymakers, L.F.J.M., Mulder, M.J.J., Kucernaka, A.R.J., Poison mitigation strategies for the use of impure hydrogen in electrochemical hydrogen pumps and fuel cells, Journal of Power Sources, 472, 228476, (2020)

Peschel, A., Industrial perspective on hydrogen purification, compression, storage, and distribution, Fuel Cells, 20(4), 385-393, (2020)

Rhandi, M., Tregaro,M., Druart, F.,Deseure, J.,Chatenet, M., Electrochemical hydrogen compression and purification versus competing technologies: Part II. Challenges in electrocatalysis, Chinese Journal of Catalysis, 41, 770-782, (2020)

Zou,J., Han,N., Yan, J., Feng,Q., Wang,Y., Zhao,Z., Fan,J., Zeng, L., Li, H., Wang,H.,Electrochemical compression technologies for high-pressure hydrogen: current status, challenges and perspective, Electrochemical Energy Reviews,3, 690-729,(2020)

High Performance Sulfonated Silica-Based Electrospun Membrane-Electrode-Assemblies (MEAs) for PEM Fuel Cells

[1*]Begüm Yarar Kaplan, [2]Naeimeh Rajabalizadeh Mojarrad, [2]Bilal İskandarani, [1]Alp Yürüm, [1,2]Selmiye Alkan Gürsel

[1] Sabancı University Nanotechnology Research and Application Center (SUNUM), 34956, Istanbul, Turkey
[2] Sabancı University, Faculty of Engineering and Natural Sciences, 34956, Istanbul, Turkey

* E-mail: begumyarar@sabanciuniv.edu

Abstract

In the present study, sulfonated silica (S-SiO_2) nanoparticles (NPs) which are cheap and stable at low humidity are synthesized and employed in both membrane and electrode structure of PEM fuel cells. Here, electrospinning is utilized to prepare hybrid nanofiber based PEM fuel cell membranes containing S-SiO_2 NPs, poly(vinylidene fluoride) (PVDF), poly(vinylidene fluoride-co-trifluoroethylene) (PVDF-TrFE) binders (carrier polymers); and electrodes containing commercial Pt/C catalyst, S-SiO_2 NPs, and PVDF and PVDF-TrFE carrier polymers. Firstly, the morphology of both electrospun membranes and electrodes have been investigated by scanning electron microscopy (SEM) to determine optimum electrospinning conditions to achieve a uniform nanoparticle distribution along the carrier polymer. In order to prepare hybrid membranes, fiber mats were transformed into dense membranes by hot-pressing and Nafion® impregnation steps. After obtaining compact membrane, ionic conductivity, water uptake and mechanical strength of the hybrid membranes have also examined. Electrospun electrodes also are characterized by transmission electron microscopy (TEM) to investigate catalyst (Pt/C) distribution along the nanofibers. Additionally, porosity of electrospun electrodes have been investigated by mercury porosimetry. After obtaining nanofiber-based hybrid membrane and electrodes, membrane electrode assemblies (MEA) are fabricated, and fuel cell tests are performed with using H_2/air at different humidity levels. These novel electrospun hybrid membranes and electrodes possess a superior PEM fuel cell performance especially at low humidity conditions compared to Nafion® based membranes and electrodes.

Keywords: PEM fuel cells, sulfonated silica, electrospinning, membrane-electrode-assembly

I. Introduction

Polymer electrolyte membrane (PEM) fuel cells draw great attention due to their clean operation, high power density and efficiency, compactness and fast start-up and response times (Sopian and Wan Daud (2006)). Membrane electrode assembly (MEA) is the heart of the PEM fuel cells. Therefore, development of MEA design and materials is one of the most important research areas. The two main problems of MEA are: i) commonly used perfluorosulfonic acid-based membrane/ionomer (commercial Nafion® membrane/ionomer) is very expensive, its ionic conductivity is strongly based on humidity of environment, degrades easily under low humidity conditions; ii) platinum (Pt) which is used as a catalyst in electrode structure is very expensive and its reserves are limited. For that reasons, there are barriers to commercialization of PEM fuel cells. Therefore, development of electrodes with low-Pt loading, non-Pt group metal (non-PGM) catalysts, and alternative hydrocarbon-based/inorganic ionomers has gained growing attention in the past few decades (Paddison and Gasteiger (2012), Easton etal. (2019)). Compared to other inorganic ionomers, sulfonated silica provides higher surface area, water retention and proton conductivity, even if used very little in the electrode structure (Eastcott and Easton (2015)).

In recent years, electrospinning is frequently used technique to produce nanomaterials especially in the field of energy (for examples; solar cells, fuel cells, Li-ion and Li-S batteries, supercapacitors) (Santangelo (2019)). Electrospinning is also a promising technique for creating nanostructured fuel cell electrodes with superior catalyst utilization and long-term durability (Zhang and Pintauro (2011), Brodt (2016)). This technique provides an enhancement of the triple phase interface where electrochemical reactions occurred at active catalyst site. Additionally, hybrid membrane fabrication with organic and inorganic constituents via electrospinning technique is considerably attactive due to long-range organisation of hydrophilic and hydrophobic parts in the nanoscale (Sood etal. (2016)). Compared to other hybrid or composite membranes, silica based PEMFC membranes offer various advantages such as low cost, high water retention capacity, and relatively high ionic conductivity (Ying etal. (2018)).

Herein, we report novel electrospun hybrid PEM fuel cell membranes and electrodes to provide better water retention properties, conductivity, and mechanical strength by means of integration of sulfonated silica and electrospinning. Our experiments focused on determining the effects of electrospinning ink composition, carrier polymer, and nanofiber diameter on conductivity, catalytic activity and fuel cell power output.

II. Experimental Set-up and Procedure

The electrospinning solutions of membranes and inks of electrodes prepared by using DMAc/acetone solvent

mixture. First, S-SiO_2 prob sonicated, and mechanically stirred overnight with the previously prepared carrier polymer. Tab.1 shows membrane composition, and summary of ink and electrode composition in Tab.2. After preparation of electrospinning solutions, it was loaded into a 5 mL syringe and was electrospun onto the collecting drum collector. Fig.1 shows schematic of electrospinning setup used in experiments. The obtained fiber mats were then pealed for further morphological and electrochemical analysis.
MEAs were fabricated using elecrtospun hybrid membranes and electrodes. Here, 5 cm^2 electrospun electrodes used as a cathode, and sprayed electrodes as an anode (0.1 and 0.2 mg_{pt}/cm^2 loading). Electrospun hybrid membrane was located these two electrodes and hot pressed 5 min. hot pressed at 133 °C.

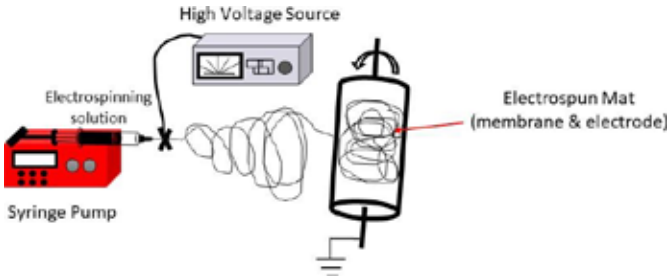


Fig. 1: Schematic diagram of electrospinning set-up and electrospun hybrid membrane and electrode preparation

Tab. 1: Summary of ink and electrospun hybrid membrane composition

Sample	P/S-SiO_2-50	P/S-SiO_2-60	P/S-SiO_2-70	T/S-SiO_2-50	T/S-SiO_2-60	T/S-SiO_2-70
Carrier Polymer	*PVDF*	*PVDF*	*PVDF*	*P(VDF-TrFE)*	*P(VDF-TrFE)*	*P(VDF-TrFE)*
Polymer/S-SiO_2 (wt:wt %)	*50:50*	*40:60*	*30:70*	*50:50*	*40:60*	*30:70*

* **PVDF:P, P(VDF-TrFE):T**

Tab. 2: Summary of ink and electrospun electrode composition

Ink	Binder	Electrode Composition wt. %
1	*PVDF*	*65 Catalyst, 20 PVDF, 15 S-SiO_2*
2	*PVDF*	*65 Catalyst, 17 PVDF, 18 S-SiO_2*
3	*P(VDF-TrFE)*	*65 Catalyst, 20 PVDF-TrFE, 15 S-SiO_2*
4	*P(VDF-TrFE)*	*65 Catalyst, 17PVDF-TrFE, 18 S-SiO_2*

III. Results and discussions

SEM micrographs and fiber diameter distribution histograms of prepared PVDF/S-SiO_2 and P(VDF-TrFE)/S-SiO_2 membranes were shown in Fig. 2. A uniform nano-sized fiber diameter distribution as well as high extent of fibers coverage with S-SiO_2 NPs was proved. Comparing the fiber distribution diameter histograms showed a narrow fiber diameter rang with average value of 0.6 µm and 0.2 µm for PVDF and P(VDF-TrFE)/S-SiO_2 respectively. In case of PVDF polymer the diameter of obtained fibers is about three-fold that of P(VDF-TrFE)/S-SiO_2

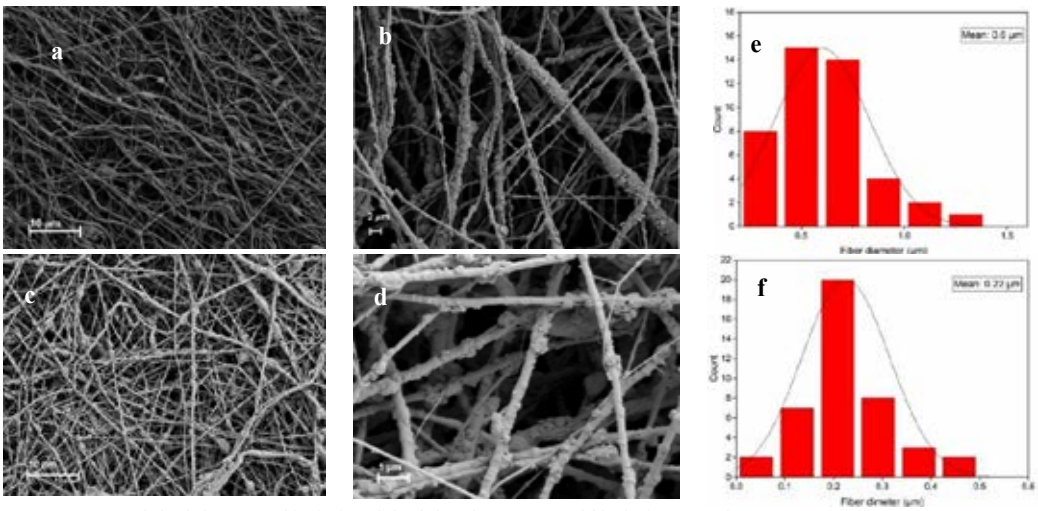


Fig. 2: SEM micrographs (a), (b) PVDF/S-SiO_2, (c), (d) P(VDF-TrFE)/S-SiO_2 nanofibers, and fiber diameter histograms of (e) PVDF/S-SiO_2, (f) P(VDF-TrFE)/S-SiO_2 nanofibers

Morphology of electrospun electrodes was investigated by SEM. Fig. 3.a shows the SEM image of 65Pt/C/20PVDF/15S-SiO_2 (Ink 1) electropun electrode, and Fig. 3.b. 65Pt/C/20PVDF-TrFE/15S-SiO_2 (Ink 3). It can be depicted that Pt/C and S-SiO_2 NPs well distributed along the PVDF and PVDF-TrFE carrier. The average fiber diameter is 510 nm for PVDF and 520 nm for PVDF-TrFE carrier.

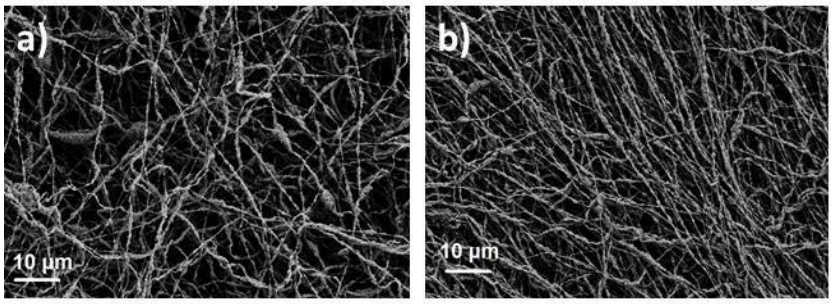


Fig. 3: SEM images of electrospun a) Pt/C/S-SiO_2/PVDF, and b) Pt/C/S-SiO_2/PVDF-TrFE electrodes

IV. Conclusions

In the present study, sulfonated silica and P(VDF-TrFE) nanofiber-based hybrid membranes and electrodes were successfully fabricated via the electrospinning technique for the first time in literature. In conclusion, electrospun Pt/C/S-SiO_2/PVDF, and Pt/C/S-SiO_2/PVDF-TrFE electrodes, and PVDF/S-SiO_2 and PVDF-TrFE/S-SiO_2 were fabricated, characterized, and tested in PEM fuel cell. Electrospinning is a powerful, robust, and effective technique to fabricate S-SiO_2 based MEAs for PEM fuel cells. Herein we shown that electrospun hybrid membranes showed a superior proton conductivity, and promising mechanical strength. Moreover, utilization of S-SiO_2 as an ionomer/functional additive, provides better performance at lower humidity during fuel cell testing. The outstanding performance of electrospun electrodes arise from uniform distribution of Pt/C catalyst, high catalytic activity, and better proton and reactant gas transport to the catalysts during fuel cell operation.

Acknowledgements

The authors gratefully acknowledge the financial support of The Scientific and Technological Research Council of Turkey (TÜBİTAK) (Grant Number: 217M639)

References

Brodt M., Wycisk R., Dale N., Pintauro, P., Power output and durability of electrospun fuel cell fiber cathodes with PVDF and nafion/PVDF binders, Journal of The Electrochemical Society, 163(5): 401-410 (2016).

Eastcott J.I. and Easton E.B., Investigation of transport mechanisms for sulfonated silica-based fuel cell electrode structures, Journal of The Electrochemical Society, 162(7):764-771 (2015).

Easton E.B., Acheampong R., Esfahani R.A.M., Cavallari V.J., Moghaddam R.B., Fruehwald H.M., Afsahi F., Recent Advances with Sulfonated Silica Ceramic Carbon Electrodes for Fuel Cells, ECS Transactions, 92(8):559 (2019).

Paddison S.J. and Gasteiger H.A., PEM Fuel Cells: Materials and Design Development Challenges. In: Lipman T., Weber A. (eds) Fuel Cells and Hydrogen Production, Encyclopedia of Sustainability Science and Technology Series, Springer, New York, NY (2012).

Santangelo S., Electrospun Nanomaterials for Energy Applications: Recent Advances. Applied Sciences 9(6): 1049 (2019).

Sood R., Cavaliere S., Jones D. J., Rozière J., Electrospun nanofibre composite polymer electrolyte fuel cell and electrolysis membranes, Nano Energy, 26, 729-745 (2016).

Sopian K. and Wan Daud W.R., Challenges and future developments in proton exchange membrane fuel cells, Renewable Energy, 31:719-727 (2006).

Ying Y.P., Kamarudin S.K., Masdar M.S., Silica-related membranes in fuel cell applications: An overview, International Journal of Hydrogen Energy, 43(33), 16068-16084 (2018).

Zhang W. and Pintauro, P. N., High Performance Nanofiber Fuel Cell Electrodes, ChemSusChem, 4(12):1753-1757 (2011).

Surface Modification of 316L by Electrochemical Dealloying

[1]Ömer Özcan, [1*]Fatih Pişkin
[1] Muğla Sıtkı Koçman University, Dept. of Metallurgical and Materials Engineering, Muğla, 48000, Turkey

* E-mail: fatihpiskin@mu.edu.tr

Abstract
The current study concentrates on the surface modification of 316L foil by sequential electroplating and electrochemical dealloying processes in order to create a nanoporous surface layer. The 316L foils were initially electroplated by Ni-Cu alloys using plating solutions with different Ni:Cu ratios. Ni_xCu_{1-x} alloys electroplated on 316L foils were then subjected to an electrochemical dealloying process in order to dissolve Cu back into the plating solution and remain a nano-porous Ni surface layer. Several Ni_xCu_{1-x} alloy compositions were employed in the study in order to determine an alloy composition that offers a pore size less than 100nm at the Ni surface layer.

Keywords: Nano-porous Ni, electrochemical dealloying, electroplating.

I. Introduction

316L porous stainless steel (PSS) is a suitable support material for thin-film Pd-based membranes due to its high thermal, oxidation resistance and having a similar thermal expansion coefficient with Pd (Alique *et al.*, 2016; Nayebossadri *et al.*, 2016). However, commercially available PSS have often very large surface pores (>20μm) that affect the final thickness of the membrane deposited on it (Mardilovich *et al.*, 1998). That's why the membrane thickness deposited on the PSS can reach several tens of microns in order to create a porous-free membrane.

There are several studies that focus on applying an interlayer between PSS and thin-film membrane so as to reduce the size of pores at the PSS surface (Su *et al.*, 2005; Wei *et al.*, 2014) and thus reduce the thickness of the membrane. However, it is often not easy to control the size of surface pores and keep their size under a threshold. Any remaining large pore at the surface of support material causes the formation of pin-holes in the membrane and this might result in a reduction in hydrogen selectivity. That's why modification of PSS surface has to be employed in a controlled manner and should be reproducible.

The current study concentrates on surface modification of PSS as a support material in order to enable thin-film membrane (<1μm) deposition on PSS. In this respect, 316L foil was used as a model system to determine the application parameters for the formation of a nanoporous Ni surface layer on the PSS. 316L foils were initially electroplated by Ni-Cu alloys using plating solutions with different Ni:Cu ratios. Subsequently, the Ni-Cu surface layers on 316L foils were subjected to an electrochemical dealloying process in order to dissolve Cu back into the plating solution and remain a nanoporous Ni layer.

II. Experimental Set-up and Procedure

Electroplating and electrochemical dealloying processes were performed under ambient conditions in a three-electrode cell, Fig. 1. Ni_xCu_{1-x} alloys were electroplated on 50μm 316L foils. Electroplating of Ni_xCu_{1-x} alloys was performed at -1.0V potential in plating solutions composed of $NiSO_4.7H_2O$ and $CuSO_4.5H_2O$ for up to 30min. The concentration of $NiSO_4.7H_2O$ was kept constant at 0.8M, while $CuSO_4.5H_2O$ ranged from 0.01M to 0.1M in the plating solutions in order to obtain different $NiSO_4.7H_2O$-$CuSO_4.5H_2O$ ratios, so the different Ni_xCu_{1-x} alloys. The alloys were then subjected to electrochemical dealloying in the same plating solutions at +0.5V up to 15min.



Fig. 1: A view from electroplating of Ni_xCu_{1-x} alloy on 316L foil.

III. Analysis

Morphology of the Ni_xCu_{1-x} alloys electroplated and the remaining porous Ni surface layer on 316L foils after the dealloying process was investigated by a JEOL JSM-7600F scanning electron microscope (SEM). During the course of the SEM studies, secondary electron imaging mode was performed at an accelerating voltage ranging between 10-20kV. The compositions of the alloys were analyzed by an auxiliary energy-dispersive X-ray spectroscopy (EDX) detector integrated into the SEM.

X-ray diffraction (XRD) measurements were carried out with a Rigaku SmartLab spectrometer using Cu-Kα radiation at 40kV and 30mA in Bragg-Brentano geometry.

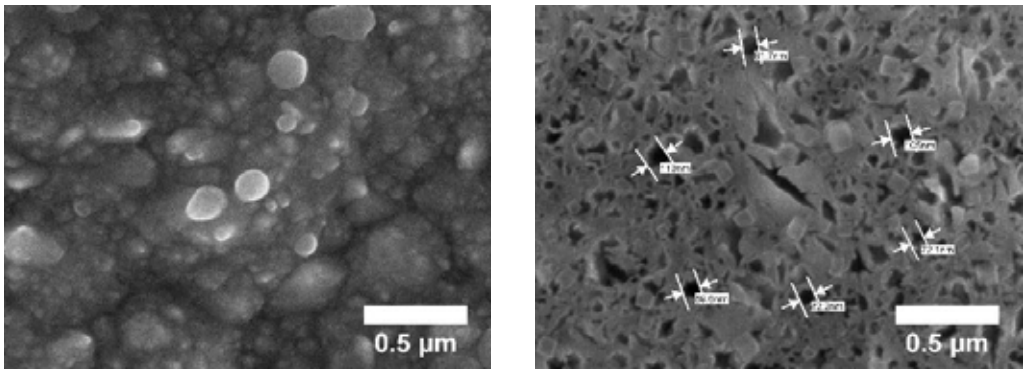
IV. Results and discussions

Ni_xCu_{1-x} electroplating with the methodology described above resulted in different alloy compositions. Alloy compositions obtained using plating solutions having different Ni:Cu concentrations are summarized in Tab. 1.

Tab. 1: Ni_xCu_{1-x} alloy compositions electroplated at -1.0V on 316L foils using plating solutions having different Ni:Cu concentrations for 30min.

Plating Solutions	Ni (at.%)	Cu (at.%)	Composition
0.8M $NiSO_4.7H_2O$ - 0.010M $CuSO_4.5H_2O$	86.73	13.27	Ni87Cu13
0.8M $NiSO_4.7H_2O$ - 0.050M $CuSO_4.5H_2O$	73.39	26.61	Ni73Cu27
0.8M $NiSO_4.7H_2O$ - 0.075M $CuSO_4.5H_2O$	53.26	46.74	Ni53Cu47
0.8M $NiSO_4.7H_2O$ - 0.100M $CuSO_4.5H_2O$	31.59	68.41	Ni32Cu68

Ni53Cu47 alloy electroplated on 316L foil was investigated before and after the electrochemical dealloying process by SEM. The morphology of the alloy at each stage is given in Fig. 2. It has been observed that a porous surface layer having pores less than 100nm was obtained with the sequential electroplating and dealloying processes.



(a) (b)

Fig. 2: (a) Ni53Cu47 alloy electroplated on 316L foil using 0.8M Ni(II)-0.075M Cu(II) plating solution at -1.0V for 30min. (b) The porous structure obtained after the electrochemical dealloying process at +0.5V for 15min.

V. Conclusions

In the current work, a sequential Ni-Cu electroplating and electrochemical dealloying process were applied to obtain a nanoporous Ni surface layer on 316L foil. In this respect, several plating solutions with different Ni:Cu concentrations were prepared. The electrochemical dealloying of Cu was performed on each Ni-Cu alloy deposited by different plating solutions and the ideal conditions were identified so as to obtain a porous Ni surface layer having pores less than 100nm in diameter on 316L foil.

Acknowledgements

The authors gratefully acknowledge the financial support of this research from the Scientific and Technological Research Council of Turkey (TUBITAK) with project number 119M636. Ömer Özcan is also supported by TUBITAK with a scholarship under 2210-C Domestic Priority Graduate Scholarship Program, No: 1649B022000693.

References

Nayebossadri S., Fletcher S., Speight J.D., Book D., Hydrogen permeation through porous stainless steel for palladium-based composite porous membranes, Journal of Membrane Science, 515, 22-28, (2016).

Alique D., Martinez-Diaz D., Sanz R., Calles J.A., Review of supported Pd-based membranes preparation by electroless plating for ultra-pure hydrogen production, Membranes, 8, 1-39, (2018).

Mardilovich P.P., She Y., Ma Y.H., Rei M.H., Defect-free palladium membranes on porous stainless-steel support, AIChE Journal, 44, 310-322, (1998).

Wei L., Hu X.,Yu J., Huang Y., Aluminizing and oxidation treatments on the porous stainless steel substrate for preparation of H2-permeable composite palladium membranes, International Journal of Hydrogen Energy, 39, 18618-18624, (2014).

Su C., Jin T., Kuraoka K., Matsumura Y., Yazawa T., Thin Palladium Film Supported on SiO_2-Modified Porous Stainless Steel for a High-Hydrogen-Flux Membrane, Industrial & Engineering Chemistry Research, 44, 3053-3058, (2005).

Enhanced Fuel Cell Performance and Durability of PVDF-based Sulfonated Silica-loaded Fibrous Electrodes

[1]Bilal Iskandarani, [1]Selmiye Alkan Gürsel ,[2]Begüm Yarar Kaplan,
[1] Sabancı University, Faculty of Natural Science and Engineering, Material Science, Istanbul, 34956, Turkey
[2] Sabancı University Nanotechnology Research and Application Center (SUNUM), Istanbul, 34956, Turkey

* E-mail: Bilal@sabanciuniv.edu

Abstract
The durability of sulfonated silica (S-SiO_2) fibrous based electrodes with a hydrophobic carrier polymer (PVDF) was tested. PVDF-based fiber electrodes showed an increase in maximum power output (by 6.4%) after 100 hours for low S-SiO_2 loadings. However, the maximum power output declines (by 19.7%) as the S-SiO_2 loading increases. Increasing the S-SiO_2 caused an enhancement in performance in the activation region. Conversely, mass transport was supressed by the action of water flooding.

Keywords: PEMFC, electrode-sulfonated silica, nanofibers, electrospinning, durability

I. Introduction

Polymer Electrolyte Fuel cells (PEMFC) are attracting much attention nowadays putting them among the most highly invested devices in the energy conversion sector. The emergence of PEMFCs and similar alternative came as a consequence of fossil fuel reserve decline and the need for a cleaner energy source. In this sense, PEMFCs are attributed with high energy density due to the usage of the relatively light hydrogen gas input and its high efficiency exceeding that of internal combustion engines (ICE). Furthermore, PEMFCs are considered as clean energy source as the it generates only heat and water vapor exhaust only besides electrical energy. The aforementioned factors all together made PEMFCs a promising candidate for stationary and mobile applications. However, several drawbacks hinder the wide commercialization of PEMFCs. Among those is the poor durability in conventional PEMFCs (Sopian,2006).

The membrane electrolyte assembly (MEA) is considered as the beating heart of PEMFCs.MEAs are in turn composed of two electrodes (an anode and a cathode) sandwiching a polymer-based electrolyte. For an electrode to perform optimally, the water content needs to be on a moderate level. In other words, excessive water content plugs the flow channels and leads to reactant starvation while drying the electrode out reduces its activity. Therefore, the loss in cell performance over time can be related to the content and architecture of the electrode (Schmittinger,2008). In terms of architecture, Electrospinning have shown to be a vital yet facile technique to generate fiber-based electrodes. This particular architecture provides additional reactant pathways through the porosities formed between the fibers and within the fibers themselves. Therefore, electrospun material have shown to be very effective in boosting both the performance and durability of the electrode (Waldrop,2020). While in terms of content, employing a hydrophobic carrier polymer is expected to reduce the accumulation of water withn the electrode (Brodt,2016) (Slack,2020). Furthermore, a hydrophilic and hygroscopic ionomer can be used to balance the water level within the electrode to avoid any potential draught. Furthermore, replacing the Nafion as a cheaper alternative with a potential performance and effect on the electrode durability. In this study, the durability of fiber-based electrodes using a hydrophobic polymer (PVDF) loaded with S-SiO_2 ionomer was put into test. The result has shown a reasonable performance retention for the aforementioned electrodes exceeding that of conventional sprayed electrodes. Furthermore, the durability was found to be highly dependent on the ionomer loading and the type of polymer used.

II. Experimental Set-up and Procedure

Fuel cell performance, accelerated durability, electrochemical impendance spectroscopy (EIS) and Cyclic voltammetry (CV) measurments were all performed via a Scribner Series 850e test station. In the process, a 5 cm^2 MEA was assembled composed of the fibe-based electrode as the cathode with platinum loading in the range 0.1-015 mg/cm^2 facing a conventionally sprayed anode with a 0.3 mg/cm^2 platinum loading sandwiching a 212 Nafion membrane.

Accelerated durability test was for a span of 100 hours at a fixed potential of 0.6V. The cell voltage was fixed at 80^{o}C where fully humidified 0.5 L/min air and 0.125 L/min hydrogen gas were fed to the cathode and the anode respectively with a 14psi backpressure. Beginning of life (BOL) and end of life (EOL) polarization curves were recorded separately at the same temperature and feed conditions but at 25psi backpressure.

Electrochemical Impedance spectroscopy measurements were collected within a frequnce range of 0.1-10000hz and at a bias potential of 0.425V. Fully humidified Oxygen and Hydrogen gasses were fed at an equal flowrate of 0.125 L/min to the cathode and the anode respectively with no backpressure. The Nyquist plots at BOL and EOL were collected then analyzed and fitted using Zview in accordance to the equivalent circuit (Fig.1). in which R_e is the bulk resistance, $R_{ch,t}$ is the charge transfer resistance and $R_{M,t}$ is the mass transfer resistance.

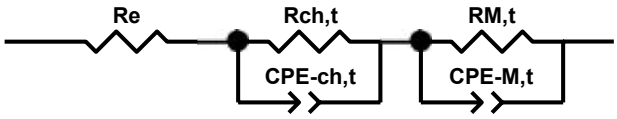


Fig. 1:Equivalent circuit used for electrochemical impedance spectroscopy (EIS) analysis

Cyclic voltammograms were collected at BOL and EOL at 30°C cell temperature and feed temperature. 0.1 L/min hydrogen gas was fed to the anode while no gas was fed into the cathode with no backpressure applied. Measurements were taken with a potential window of 0.04-0.9V with a scan rate of 40 mV/sec for 30 cycles. The area under the hydrogen oxidation peak was graphically measured to calculate the electrochemical surface area ECSA using the following equation:

III. Results and discussions

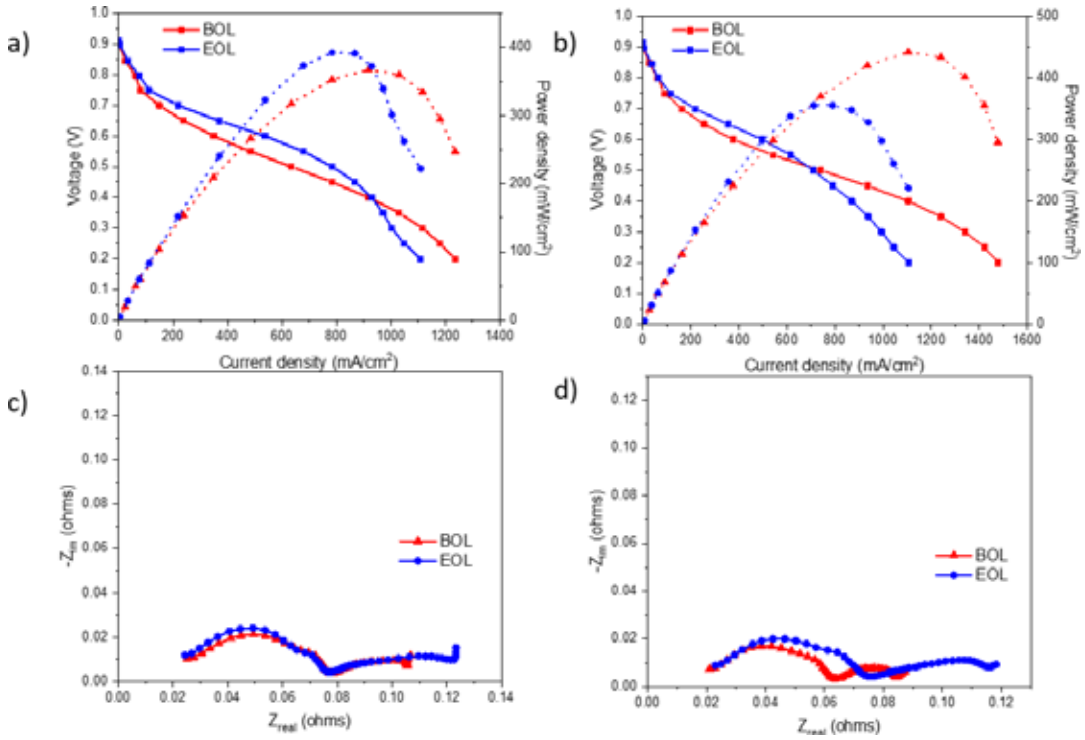


Fig. 2: Performance polarization curves collected at begginning of life (BOL) and end of life (EOL) of a) 65%Pt/C,20%S-SiO_2, and 15% PVDF and b) 65%Pt/C,22%S-SiO_2, and 13% PVDF containing MEAs. Nyquist plot of the electrochemical Impedance spectroscopy (EIS) measurements taken at begginning of life (BOL) and end of life at 0.425V bias potential and fully humidified conditions of c) 65%Pt/C,20%S-SiO_2, and 15% PVDF and d) 65%Pt/C,22%S-SiO_2, and 13% PVDF containing MEAs

The performance of the electrodes at BOL and EOL have shown an abrupt change upon changing the S-SiO_2 loading from 20% into 22%. The electrodes have shown a dramatic drop in voltage at high current densities (> 700mA/cm^2). However, the 22% loaded S-SiO_2 based electrode have shown an even more severe loss in voltage at high power densities. The drop in voltage at high current densities can be directly related to water flooding. The decomposition of PVDF with time partially eliminates the hydrophobic factor of the electrode which triggers more water retention within. Therefore, increasing the hydrophilic ionomer not only does it favor the decomposition of the electrode components but also water accumulation within the electrode. The aforementioned result can be further illustrated using electrochical impedance spectroscopy (EIS) (Fig.2 and Tab.1). Both S-SiO_2 loadings have shown a significant increase in the mass transfer resistance $R_{M,t}$. 20% S-SiO_2-loaded electrode showed only a 17.19% increase in $R_{M,t}$ accompanied with a decrease in the bulk resistance R_e compensating for the former leading in turn to a slight increase in performance (367 mW/cm^2 into 392 mW/cm^2).However, S-SiO_2-loaded electrode showed a 42.% increase in $R_{M,t}$ which explains in turn the significant drop in performance (442 mW/cm^2 into 356 mW/cm^2) .

Tab. 1: electrochemical Impedance spectroscopy fitting results and the maximum power density reported for both electrodes with 20% S-SiO_2 and 22% S-SiO_2 loadings respectively

Electrode	stage	R_e (ohm)	$R_{ch,f}$(ohm)	$R_{M,f}$(ohm)	Maximum Power density (mW/cm^2)
65% cat, 20% S-SiO_2, 15% PVDF	BOL	0.024	0.046	0.053	367
	EOL	0.021	0.053	0.064	392
65% cat, 22% S-SiO_2, 13% PVDF	BOL	0.021	0.038	0.033	442
	EOL	0.022	0.048	0.057	356

IV. Conclusions

PVDF-based S-SiO_2-loaded fiber electrodes have shown different performances before and after cycling for 100 hours. The durability of the fiber-based electrodes have shown to mitigate performance losses with time well know for the conventional PEM fuel cells. Furthermore, the content of the electrode have shown to have a significant result on its durability. Increasing the S-SiO_2 loading serves in increasing water accumulation within the electrode and therefore increases the risk of water flooding. Therefore, the performance of the 22% S-SiO_2 loaded electrodes dropped 19.5% compared to a slight increase in performance of 7% for 20% S-SiO_2-loaded electrodes.

Acknowledgements

This research has received funding from The Scientific andTechnological Research Council of Turkey (TUBITAK) (Project Number: 217M639).

References

Kamaruzzaman Sopian, Wan Ramli, and Wan Daud, Challenges and future developments in proton exchange membrane fuel cells, Renewable Energy 31 719–727(2006)

Brodt M., Wycisk R., Dale N., and Pintauro P., Power Output and Durability of Electrospun Fuel Cell Fiber Cathodes with PVDF and Nafion/PVDF Binders, Journal ofThe Electrochemical Society, 163 (5) F401-F410 (2016).
Schmittinger W., Vahidi A., A review of the main parameters influencing long-term performance and durability of PEM fuel cells, Journal of Power Sources 180 1–14(2008).

Slack J.J., Brodt M., Cullen D.A., Reeves K. S., More K.L., and Pintauro P.N., Impact of Polyvinylidene Fluoride on Nanofiber Cathode Structure and Durability in Proton Exchange Membrane Fuel Cells, Journal of The Electrochemical Society, 167 054517, (2020).

Krysta Waldrop, Ryszard WyciskPeter, and N. Pintauro Application of electrospinning for the fabrication ofproton-exchange membrane fuel cell electrodes, Current Opinion in Electrochemistry,21:257–264 (2020)

Proposal of an Ocean Thermal Energy Conversion Based Subcritical Co_2 Power Cycle for Clean Hydrogen Production

[1*]Gamze Soyturk, [1]Serpil Celik Toker, [1]Onder Kizilkan
[1] Isparta University of Applied Sciences, Technology Faculty, Department of Mechanical Engineering, Isparta, 32000, Turkey

* E-mail: gamzeyildirim@isparta.edu.tr

Abstract
In the proposed study, the thermodynamic performance of ocean thermal energy conversion (OTEC) and solar energy-driven hydrogen generation systems is investigated. This system consists of the heat exchangers, turbine, condenser, evaporator, pumps, solar collector system, and proton exchange membrane (PEM) electrolyzer. EES software program is utilized to perform the performance assessment of the system. The analyses are performed applying the first and second laws of thermodynamics. In addition to that, the impacts of seawater temperature on hydrogen production and net power generation and reference ambient temperature on the exergetic performance of the OTEC-based hydrogen production system are analyzed. The results of the thermodynamic analysis show that the energetic and exergetic efficiencies of the integrated system are founded as 6.9% and 27.5%, respectively.

Keywords: Solar collector, hydrogen production, OTEC, PEM electrolyzer.

I. Introduction

Energy production and consumption are accepted as an exceedingly critical issue in the last years because they are linked to such as economic, social, environmental conditions of countries. While energy demand increases together with population growth and demands for better living standards, climate change raises deeper concerns related to fossil-fuel-based energy use. Because as a large proportion of energy production is still derived from fossil fuels, environmental problems continue to increase, such as global warming, resource depletion, and environmental damage, etc. In addition, in the coming years, the use of alternative fuels will be inevitable because of the limited fossil fuels. In this context, the free carbon sources (hydrogen) and renewable energy sources will become promising for energy consumption sectors.

Hydrogen as an energy carrier is facilitating sustainable energy systems. The development of sustainable, carbon-neutral energy sources is increasingly significant in the world today. Hydrogen is produced from various energy sources using methods like biomass conversion, steam methane reforming, and water splitting. Hydrogen is produced in a relatively environmentally benign manner (depending on the source of the input energy) via splitting water by photocatalysis, thermochemical cycles, and electrolysis. Currently, both thermochemical and photocatalysis hydrogen production are not economically competitive, but water electrolysis is a mature technology for large-scale hydrogen production. Hydrogen production by PEM electrolysis has numerous advantages, such as low environmental impact and easy maintenance (Ahmadi et al.,2012).

A large amount of solar energy is stored as heat in the surface waters of the world's oceans, providing a source of renewable energy. OTEC is a technology that utilizes the concept of the temperature difference between hot surface seawater and cold deep seawater to generate electricity. OTEC usually incorporates a low-temperature Rankine cycle engine which boils a working fluid such as ammonia to generate a vapor which turns the turbine to generate electricity and then is condensed back into a liquid in a continuous process. Due to the small temperature difference, the main technical challenge faced by OTEC is the low energy conversion efficiency. The temperature difference between hot surface seawater and cold deep seawater, even in the tropical area, is only 20-25°C. Although OTEC required abundant seawater flow rates, the best thermodynamic efficiency achieved lies in the range of 3-5% (Aydin etal.2014). In a typical OTEC plant, the net power efficiency is between 50-80% of the system. There are some studies about the OTEC system in recent years for clean and sustainable power production in the literature. Ahmadi et al. (2015) have investigated an ocean thermal energy-based multigeneration system for hydrogen production. They have studied the multiobjective optimization of the OTEC system. According to the results of their work, the performance of the system is remarkably affected as a result of the variation in solar irradiation, mass flow rate of ocean surface water, condenser temperature, and evaporator pinch point temperatures. Yilmaz et al. (2018) have performed thermodynamic analyses of OTEC-assisted hydrogen generation plants. Their study consists of an OTEC system, hydrogen generation, and liquefaction subsystem with a PEM electrolyzer and a solar collector. The whole energy and exergy efficiency of the plant is determined as 43.49% and 36.49%, respectively.

The main purpose of this paper is to investigate the thermodynamic performance of OTEC and solar energy-based integrated hydrogen generation systems. This integrated process consists of the heat exchangers, turbine, condenser, pumps, solar collector system, and PEM electrolyzer. The thermodynamic performance assessment of subsystems and the whole process is performed by using the energetic and exergetic analysis methods.

II. System Description

Fig. 1 shows a schematic diagram of an integrated OTEC system equipped with evacuated U-tube solar collectors and a PEM electrolyzer. For thermodynamic modeling purposes, the integrated OTEC system for hydrogen production considered here is divided into three parts: evacuated U-tube solar collector, OTEC unit, and

PEM electrolyzer. The OTEC cycle and solar collector system are used in the integrated system to generate useful heat and power for the PEM electrolyzer to produce hydrogen. This integrated system uses hot surface seawater to vaporize the CO_2 working fluid. Evaporating CO_2 drives a turbine to generate electricity, which is used to drive a PEM electrolyzer to generate hydrogen. After passing through the turbine, CO_2 is condensed in a condenser that is cooled by cold deep seawater. The working fluid is pumped back into the evaporator, and the cycle is repeated continuously. In addition to that, the working fluid in evacuated U-tube collectors gives its heat energy to the electrolysis water before entering the PEM electrolyzer.

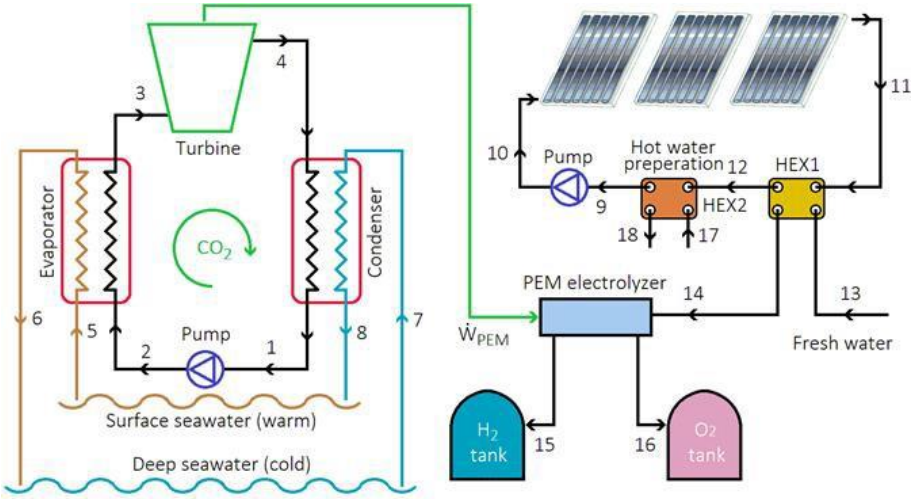


Fig. 1. Schematic illustration of OTEC and solar energy-based hydrogen production

General mass balance, energy balance, entropy balance and exergy balance equations used for thermodynamic analysis can be written as follows equations (Çengel, 2015; Bejan, 1996; Dincer, 2013).

$$\sum \dot{m}_{in} = \sum \dot{m}_{out} \quad (1)$$

$$\sum \dot{m}_{in}\left(h + \frac{v^2}{2} + gz\right)_{in} + \sum \dot{Q}_{in} + \sum \dot{W}_{in} = \sum \dot{m}_{out}\left(h + \frac{v^2}{2} + gz\right)_{out} + \sum \dot{Q}_{out} + \sum \dot{W}_{out} \quad (2)$$

$$\sum \dot{m}_{in} s_{in} + \sum \frac{\dot{Q}}{T}_{in} + \dot{S}_{gen} = \sum \dot{m}_{out} s_{out} \quad (3)$$

$$\sum \dot{m}_{in} e\dot{x}_{flow} + \sum E\dot{x}^{Q}_{in} + \sum E\dot{x}^{W}_{in} = \sum \dot{m}_{out} e\dot{x}_{flow} + \sum E\dot{x}^{Q}_{out} + \sum E\dot{x}^{W}_{out} + E\dot{x}_{dest} \quad (4)$$

where, $\dot{m}$ is the mass flow rate, $\dot{Q}$ is the heat energy transfer rate, $\dot{W}$ is the power transfer rate, h is the specific enthalpy, v is the velocity, z is the high, g is the gravitational acceleration, s is the specific entropy, $\dot{S}_{gen}$ is entropy generation rate, $e\dot{x}_{flow}$ is the flow exergy, $E\dot{x}^{Q}$ is the exergy associated with heat flow across the control volume of the process, $E\dot{x}^{W}$ is the exergy associated with work and $E\dot{x}_{dest}$ is the exergy destruction.

The amount of hydrogen produced by the electrolyzer can be obtained using the following equation:

$$\dot{m}_{H_2} = \eta_{elec} \, x \, \frac{\dot{W}_{elec}}{HHV_{H_2}} \quad (5)$$

IV. Results and discussions

The engineering equation solver (EES) software program has been used in the modeling of OTEC and solar energy-based integrated processes for more efficiently integrated system design. The reference temperature and pressure are taken as 25 ℃ and 101.3 kPa, respectively.

Fig. 2 explained that the impact of reference temperature on the exergetic performance of the whole system. As from this Figure, as the changes of reference temperature from 15 ℃ to 25 ℃, the exergetic performance of the whole system rises. The total exergy efficiency of the examined cycle is found as 0.30 at 20 ℃ reference temperature.

In the study, another important parameter is the seawater temperature. Fig. 3 demonstrated that the impact of seawater temperature on hydrogen production rate. It seen that, the hydrogen production rate, one of the system outputs increases about from 0.11 kg/h to 0.43 kg/h with sea warm temperature changes from 25 ℃ to 35 ℃. Fig. 4 showed the effect of seawater temperature on the net power generated from the integrated system. As can be seen from the figure, as the sea water increases, the net power produced from the integrated system increases linearly. Fig. 5 displays the exergy destruction rates of the components of examined multigeneration system. As seen from the figure, the highest exergy destruction rate is found to be in the solar dish, with almost 65% of the total irreversibility.

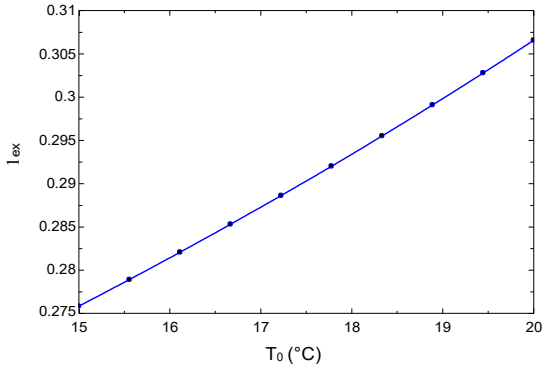


Fig. 2. The effect of seawater temperature on hydrogen generation

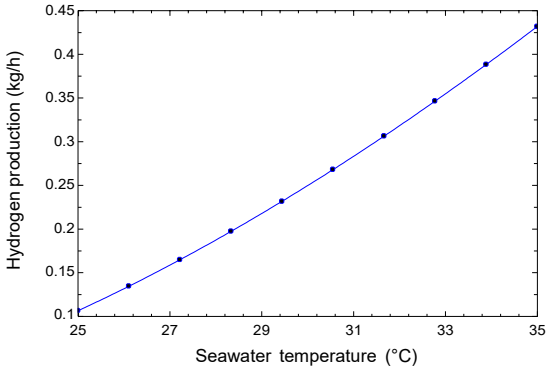


Fig. 3. The effect of seawater temperature on hydrogen production

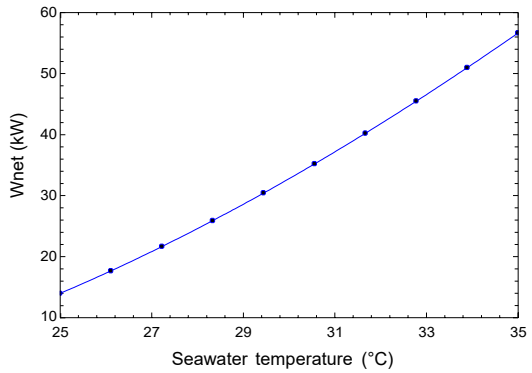


Fig. 4. The effect of seawater temperature on net power generation

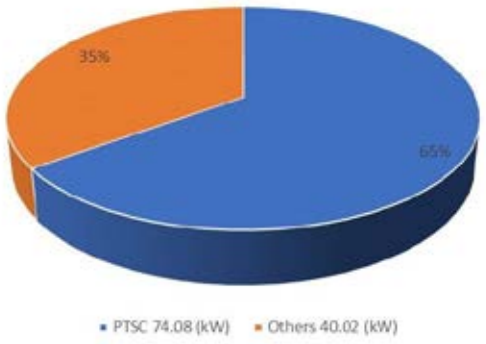


Fig. 5. The effect of seawater temperature on net power production

V. Conclusions

In this study, the thermodynamic performance assessments of OTEC and solar energy driven hydrogen generation system is investigated. Parametric studies were conducted to examine the effects of the seawater temperature on hydrogen generation and net power generation and the effects of the reference ambient temperature on the exergetic performance of the OTEC based hydrogen generation system. Parametric studies have shown that as the reference ambient temperature increases, exergy efficiency increases, and as the seawater temperature increases, hydrogen production and net power generation increase. Also, for the base conditions, the system is produced hydrogen 0.23 kg/h. Thermodynamic analysis shows that the energetic and exergetic efficiencies of the integrated system are founded as 6.9% and 27.5%, respectively. Besides, the highest exergy destruction rate is found to be in the solar dish, with almost 65% of the total irreversibility.

References

Ahmadi P., Dincer I., Rosen MA., Energy and exergy analyses of hydrogen production via solar-boosted ocean thermal energy conversion and PEM electrolysis, International Journal Hydrogen Energy, 38,1795-1805, (2012).

Ahmadi P., Dincer I., Rosen MA., Multiobjective optimization of an ocean thermal energy conversion system for hydrogen production, International Journal Hydrogen Energy, 40,7601-7608, (2015).

Aydin H., Lee HS., Kim HY., Shin SK., Park K., Off-Design Performance Analysis of a Closed-cycle Ocean Thermal Energy Conversion System with Solar Thermal Preheating and Superheating. Renewable Energy, 72, 154-163, (2014).

Bejan A., Moran MJ., Thermal design and optimization, New York: John Wiley & Sons, (1996).

Cengel YA., Boles MA., Thermodynamics: An Engineering Approach 8th Edition, (2015).

Dincer I., Rosen MA., Exergy: energy, Environment Sustainable Development, (2013).

Yilmaz F., Ozturk M., Selbas R., Thermodynamic performance assessment of ocean thermal energy conversion based on hydrogen production and liquefaction process, International Journal Hydrogen Energy, 43,10626-10636, (2018).

Radiation-Grafted PVDF based Dual-Electrospun Membranes forAnion Exchange Membrane Fuel Cells

[1*] Ahmet Can Kırlıoğlu, [1] Naeimeh Rajabalizadeh, [1,2] Selmiye Alkan Gürsel and [2]Begüm Yarar Kaplan
[1]Sabancı University, Faculty of Engineering and Natural Sciences, 34956, Istanbul, Turkey
[2]Sabancı University Nanotechnology Research and Application Center(SUNUM), 34956, Istanbul, Turkey

*E-mail: kirlioglu@sabanciuniv.edu

Abstract

Anion exchange membrane fuel cells (AEMFC) have the potential to become the prevalent energy conversion device with its rather cheaper components than its competitor proton exchange membrane fuel cells (PEMFC). However, there is still a need for a durable and good ion-conductive membrane to be able to compete. In order to fine-tune to mechanical and conductive properties of the membrane, we prepared anion conducting membranes for AEM fuel cells by a dual-electrospinning technique using inert poly(vinylidene fluoride) (PVDF) powders and radiation-induced grafted PVDF with vinylbenzyl chloride (VBC). Dual-spinning provided us a way to control the mechanical properties without sacrificing ionic conductivity. The electrospun fibers, that are prepared by this dual spinning technique, are hot-pressed into mats and then aminated with triethylamine for gaining ion exchange capabilities. We have investigated the grafting levels of the PVDF powder with VBC, morphologies of the e-spun fibers as well as the ion exchange capacities, mechanical properties and ion conductivity of the fabricated dual-fiber-based anion exchange membranes.

Keywords: Electrospinning, Radiation-induced grafting, Anion Exchange Membrane, Fuel cells

I. Introduction

In order to extend the use of fuel cells, which are more environmentally friendly than traditional fossil fuel engines, the problem regarding the high cost of rare-earth catalysts is needed to be solved. Anion exchange membrane fuel cells can be the solution of it by the fact that high pH conditions open up the opportunities to use a wider range of catalyst materials such as non-precious metals which makes the system cheaper and more suitable for better commercialization (He and Cairns (2015)). However, there is a lack of membrane technology for AEMFCs that is comparable to the performance of the Nafion® membrane for the PEMFCs. To provide similar performance, the problems that are needed to be solved, are:

i) low ion conductivity due to difficulty of OH^- ions transport compared to H^+ ions;

ii) low mechanical and chemical stability of membranes;

iii) low fuel cell performance due to high resistance of membrane;

iv) high water absorption and swelling.

Overcoming these barriers may lead to more applicability and commercialization of AEM fuel cells.

In order to solve the problems mentioned above, first, we performed radiation-induced grafting of the PVDF powders in an optimized reaction with VBC to control the ion exchange capacity and the ion conductivity of the final membrane, however, radiation-grafting usually decreases the mechanical robustness of the membranes because of the chain scissions of the backbone polymer (Bürger et al. (1993)). Hence, we used the electrospinning technique and fabricated dual-fiber-based electrospun mats which include the inert and grafted PVDF powders to control the mechanical properties of the final membrane by adjusting the ratio without a dramatic decrease in ion conductivities. Firstly, characterizations of the radiation grafted PVDF-*g*-VBC to determine the grafting levels of the PVDF powder with VBC using NMR, FT-IR, FT-Raman; SEM and EDS to investigate morphologies and elemental analysis of the electrospun fibers as well as the ion exchange capacities and ion conductivity of the aminated mats were carried out as well in this work.

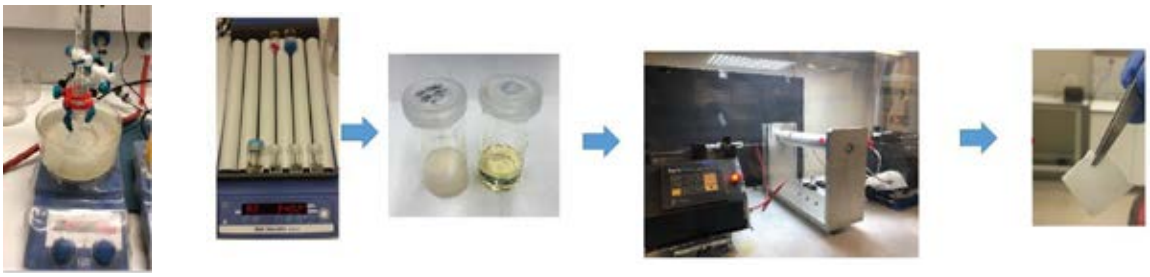


Figure 1. Schematic of dual-spun mat production setup

II. Experimental Set-up and Procedure

Figure 1 shows the experimental procedure steps. First, the commercial PVDF powders are irradiated with 50 kGy gamma rays and grafted with VBC to prepare PVDF-*g*-VBC powders while changing the parameters such as temperature, reaction duration, mixing rate to optimize the grafting levels which were calculated by before-after weight change of the powders. Using these powders and inert commercial PVDF, two different solutions were prepared and used at the dual-spin setup which can be seen in the 4th inset of Figure 1. These e-spun fibers were hot-pressed to the thickness of 50 µm and aminated with trimethylamine solution for one day, and finally alkylated with potassium hydroxide.

Nuclear Magnetic Resonance spectroscopy (NMR), Fourier-Transform Infrared spectroscopy (FT-IR), and Fourier-Transform Raman spectroscopy were employed for characterization of the molecular structure of the PVDF-g-VBC and its grafting levels.

Additionally, Scanning Electron Microscopy (SEM), Energy dispersive spectroscopy (EDS) were conducted with e-spun mats to investigate the morphology and elemental mapping of the fibers. The mechanical tensile test, ion exchange, and ion conductivity tests were done for the mats after the hot-pressing and amination, and alkalization steps.

III. Results and discussions

Figure 2 shows the successful grafting of the VBC into the PVDF backbones with 2 graphs; FT-Raman results on the left and NMR results on the right. FT-Raman peaks at the 1450 cm^{-1} show the CH_2 scissor mode of vibration for the inert PVDF powder. The VBC grafted powders were showing additional peaks at 1001 cm^{-1} and 1611 cm^{-1} which were due to aromatic peaks of VBC. Additionally, the peak at the 1266 cm^{-1} the broad peaks between 600-800 cm^{-1} are showing the C-Cl bonds. The pointed emerging peaks corresponding to the emerging bonds after the grafting which is also in parallel with the H1 NMR peaks with their corresponding hydrogens shown in the inset on the right as PVDF-g-VBC molecular structure. The peaks named “a” correspond to the backbone hydrogens while the peak named “b” were showing hydrogen at the grafted branch. These results indicate the successful grafting of VBC into the PVDF backbone with active sites because of irradiation.

In figure 3 the SEM micrographs of the e-spun fibers are given at the 5000X magnification as well as their elemental analysis is shown with the spectrums that are obtained from the single points on top of the two fibers with different morphologies. The images indicate a good fibrous structure without any beads and homogenous distribution of the dual-fibers which were confirmed by the elemental analysis of the fibers with EDS.

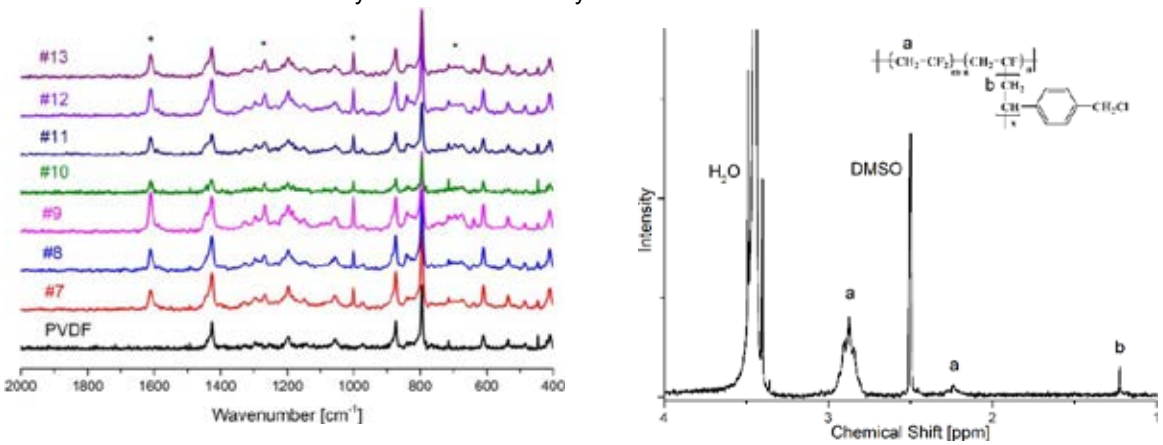


Figure 2. FT-Raman and NMR results of the PVDF-g-VBC

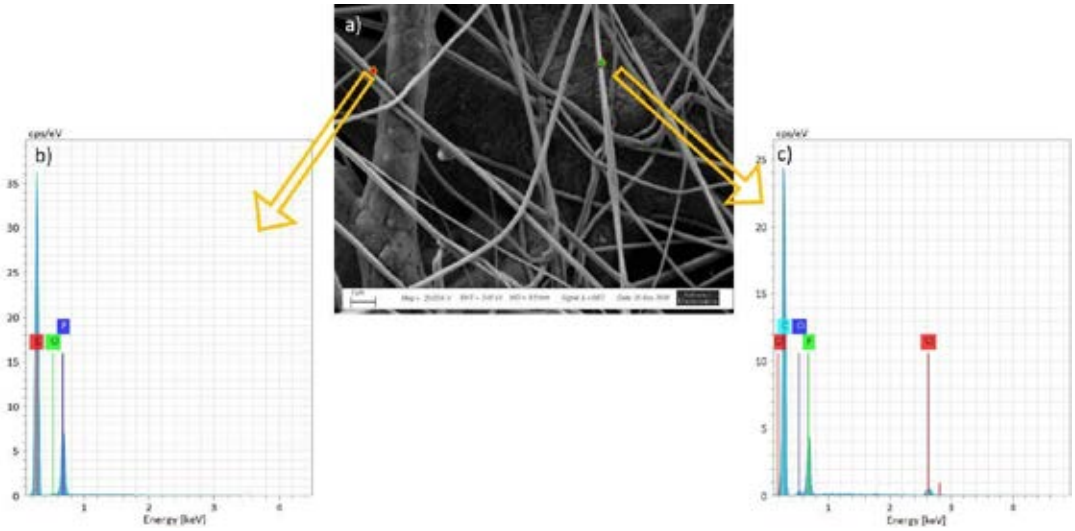


Figure 3. SEM micrographs of the two different fiber structures and their corresponding EDS results

V. Conclusion

In this study, radiation-induced grafting and electrospinning techniques are have utilized to fabricate dual fiber-based electrospun anion exchange membranes, and both ex-situ characterization and in-situ characterization in single fuel cells have demonstrated for the first time in literature. A two-step procedure was developed to achieve anion exchange membranes with promising ionic conductivity and mechanic strength, First, VBC monomers were grafted into irradiated PVDF powders. Then, the grafted and inert PVDF powders were solved and electrospun into dual-fiber mats which were later aminated and alkalized into the anion exchange membrane forms. The radiation grafting steps have proven to be successful employing NMR, FT-Raman and FT-IR. Moreover, a homogenous structure and morphology with well-distributed dual-fiber structures of the membranes have been shown by SEM-EDS spectroscopy analysis. After the amination and alkalization steps, it was found that resultant dual-fiber-based electrospun anion exchange membranes exhibited promising ionic conductivity and the ion exchange capacity showed promising results.

Acknowledgments

The authors gratefully acknowledge the financial support of The Scientific and Technological Research Council of Turkey (TÜBİTAK) (Grant Number: 119M059)

References

Bürger, W., Lunkwitz, K., Pompe, G., Petr, A., Jehnichen, D., Radiation degradation of fluoropolymers: Carboxylated fluoropolymers from radiation degradation in presence of air, Journal of applied polymer science, 48(11), 1973-1985, (1993).

He, Q., and Cairns, E. J., Recent progress in electrocatalysts for oxygen reduction suitable for alkaline anion exchange membrane fuel cells, Journal of The Electrochemical Society, 162(14), F1504, (2015).

Techno-Economic Analysis of a Solar Hydrogen Production Plant Using Textile Wastewater

*[1,2]Murat Emre Demir, [1,3]Ibrahim Dincer
[1]Clean Energy Research Laboratory, University of Ontario Institute of Technology, Faculty of Engineering and Applied Science, 2000 Simcoe Street North, Oshawa, Ontario L1H 7K4, Canada
[2] Faculty of Naval Architecture and Ocean Engineering, Istanbul Technical University, Maslak-Sariyer, Istanbul, 34469, Turkey
[3] Yildiz Technical University, Faculty of Mechanical Engineering, Istanbul, 34349 Turkey
*E-mail: medemir@itu.edu.tr

Abstract
In this study, a cost analysis study is carried out for a commercial-scale hydrogen production and wastewater treatment plant that produces 1000 kg of hydrogen and treats 222 m^3 of wastewater per day. The cost-analysis model investigates the technical and financial aspects of central and forecourt hydrogen production technologies. A photoelectrochemical solar concentrator system with heliostats/concentrators is used in the model to focus solar irradiance at a 10:1 intensity ratio onto multi-junction PV/PEC cell receivers immersed in an electrolyte reservoir and pressurized to 300 psi. The PV cells are in electrical contact with an electrolyte reservoir and, on the anode side, treat wastewater via Fenton-like reactions while producing hydrogen gas on the cathode side. In the scale-up analyses, the concentrated light-based PEC hydrogen production plant with a 1,053 kg/day design capacity is considered. The cost of hydrogen is calculated to be $5.75/kg, respectively.

Keywords: Cost analysis, hydrogen production, photovoltaics, solar energy, waste water treatment.

1. Introduction

Today, there is a substantial demand for sustainable development in response to meet growing global needs for both energy and clean water. Reactors that generate hydrogen as an energy carrier while concurrently treating wastewater have gained popularity. Simultaneous hydrogen production and wastewater treatment reactors can be constructed using biological, electrochemical, photochemical, or hybrid technologies (combining one or more of these processes). Electrochemical processes are capable of producing extremely pure hydrogen. These reactions, however, need a relatively high electrical potential, which increases the cost of hydrogen production. One way to reduce the amount of energy used in the electrolyzer is to replace the anodic reaction used to generate O_2 with a less energy-consuming reaction. It could be accomplished by electrochemical anodic oxidation of iron (Navarro-Solís, Villalba-Almendra, and Alvarez-Gallegos 2010). Fenton reaction in an electrolyzer had been examined in the literature (Demir et al. 2019) and showed promising results. However, prior to being commercialized, a design is needed to have an extensive feasibility analysis that also considers economics. In this study, A cost evaluation is performed in a case study, which includes the stages of simultaneous solar hydrogen production from textile wastewater and textile wastewater treatment processes. An economic study is performed for a commercial-scale hydrogen production and wastewater treatment plant that produces 1000 kg of hydrogen per day and handles 222 m^3 of wastewater per day.

2. System Description

A cost analysis is carried out for a commercial-scale hydrogen production and wastewater treatment plant that generates 1000 kg of hydrogen and treats 222 m^3 of wastewater daily. Since the mass production of goods costs less, scale-up research may produce more practical results that demonstrate the feasibility of the lab-scale cost analysis. The cost analysis is performed with the model developed by the U.S. Department of Energy, "Hydrogen & Fuel Cells Program, Future Central Hydrogen Production from Photoelectrochemical Process" (James 2012). The corresponding model investigates the technological and financial aspects of central and forecourt hydrogen production technologies. A photoelectrochemical solar concentrator system with heliostats/concentrators is used in the model to concentrate solar irradiance at a 10:1 intensity ratio onto multi-junction PV/PEC cell receivers submerged in an electrolyte reservoir and pressurized to 300 psi. The PV cells are in electrical contact with an electrolyte reservoir and, on the anode side, process wastewater while producing hydrogen gas on the cathode side.

The minimum levelized cost of the generated H_2 is calculated using a conventional discounted cash flow rate of return methodology. The cost of hydrogen is estimated with an after-tax internal rate of return from the manufacturing technology. Other major financial parameters that influence the cost rate include capital costs, operational and maintenance costs, and capacity factors are also taken into account. Fig. 1 depicts the configuration of the integrated system. For a textile factory, an integrated commercial system is considered. The textile wastewater is initially sent to the PEC reactor, where the decolorization and chemical oxygen demand reduction processes take place simultaneously with the hydrogen production. After the reactor, the decolorized water is directed to the electrolysis plant for desalination purposes.

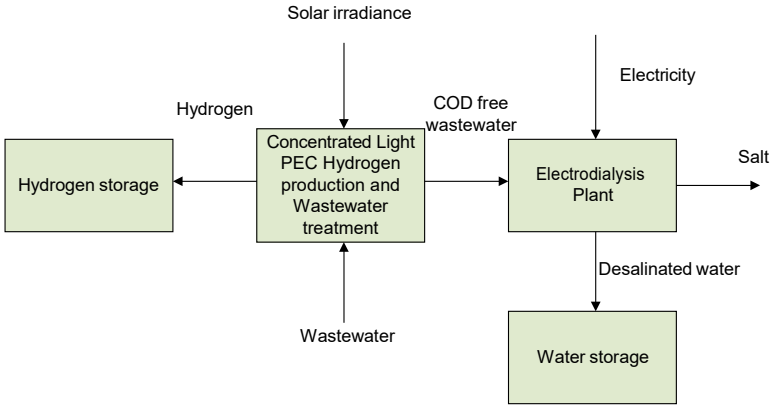


Fig. 1 The layout of the scale-up system

3. Results and Closing Points

Tab. 1 summarizes the plant's main costs. The model accounts for all capital, decommissioning, salvage, and operation and maintenance costs. The prices are given in US dollars. The plant's capital cost for hydrogen production and wastewater treatment is estimated to be $7,714,878. Only about 2% of the capital cost is related to non-depreciable system costs.

Tab. 1: The costs of PEC plant

Plant Costs*	2010$
Depreciable portion	*7,541,620*
Non-Depreciable portion	*173,258*
Total investment	*7,714,878*
Cost of decommissioning	*754,162*
Plant salvage value	*771,488*
Annual fixed operating costs in $/year	*280,028*

* Inflated to start-up,** Not including tax credits and incentives

Tab. 2: Fixed operating costs of the plant.

Fixed Operating Costs	2010$
Plant staff presented as # of FTEs employed by the plant	*0.36318*
Burdened labor cost, with overhead $/man-h	*53.56*
Labor cost in $/year	*40,459*
G&A in $/year	*8,092*
Permits, fees and licensing costs in $/year	*1,176.42*
Insurance and property taxes in $/year	*127,825*
Production repairs and maintenance in $/year	*24,929.20*
Hydrogen peroxide cost in $/year	*29,502.90*
Summation	*231,985*

The model also considers indirect depreciable expenses such as site preparation, engineering, design processes, upfront permitting, and project contingency costs. Tab. 2 represents the plant's fixed cost of operation. The total annual operating cost is expected to be $231,985. The property tax and insurance contribute the most to these expenses, making $127,825 per year.

The direct capital cost of system elements such as the PEC cell body, concentrating and containment system, electrodes and condensers, sensors, and monitoring systems is also considered in this study. The concentrating Plexiglas and containment system's cost is estimated to be $3,778,491, making it the most expensive component of the system. This is followed by the PEC electrode's costs ($576,447) and the reactor foundation and erection ($352,926). At maximum capacity, the required PEC electrode area to produce 1,053 kg of hydrogen and 233 m^3 of treated water is calculated to be 22,667 m^2. The costs of reactor feed installation, pump for make-up water, collection piping, wiring-related instrument, and power are the lowest.

The cost of directly extracting water from the ground and surface is also reviewed in the scope of the study. Based on the literature review (Demir 2018) the cost can vary from $0.40 to $0.75 per m^3 in different regions. Furthermore, the desalination process can cost from $0.44 up to $11.29 per m^3. In contrast to conventional hydrogen production plants, the proposed system produces treated water as a by-product and directs the treated wastewater to an electrodialysis plant for desalination. The annual benefit from wastewater treatment is estimated to be $81,030 based on a revenue per cubic meter of treated wastewater of 1.0 $/$m^3$.

Some closing points are (i) the capital cost of the plant for hydrogen production and wastewater treatment is $7,714,878. (ii) The cost of hydrogen is 5,75 $/kg. (iii)The total yearly operating cost is $231,985. (iv) The yearly benefit from wastewater is $81,030.

References

Demir, M. E., Ghassan Chehade, Ibrahim Dincer, Burak Yuzer, and Huseyin Selcuk. 2019. "Design and Analysis of a New System for Photoelectrochemical Hydrogen Production from Wastewater." *Energy Conversion and Management* 199:111903. doi: 10.1016/j.enconman.2019.111903.

Demir, Murat Emre. 2018. "Experimental Investigation of an Integrated Solar Driven Wastewater Treatment System for Trigeneration Applications." University of Ontario Institute of Technology.

James, Brian D. 2012. "DOE H2A Production Analysis. H2A Cent. Hydrog. Prod. Model."

Navarro-Solís, Isabel, Lilia Villalba-Almendra, and Alberto Alvarez-Gallegos. 2010. "H2 Production by PEM Electrolysis, Assisted by Textile Effluent Treatment and a Solar Photovoltaic Cell." *International Journal of Hydrogen Energy* 35(20):10833–41.

Investigating the Hydrogen Bake-out Operation of Armor Steels conforming to MIL-DTL-12560 Class 4a and MIL-DTL-46100 Military Standards

[1*]Ferdi Caner Bayram, [1]Burak Bal, [2]Baris Cetin

[1]Abdullah Gul University, Department of Mechanical Engineering, Kayseri, 38080, Turkey
[2]FNSS Defense Systems Co. Inc., R&D Center, Ankara, 06830, Turkey

E-mail: ferdicaner.bayram@agu.edu.tr, burak.bal@agu.edu.tr, cetin.baris@fnss.com.tr

Abstract
Hydrogen embrittlement (HE) is a complex phenomenon which degrades the mechanical properties of certain metallic materials (i.e., high strength steels, titanium alloys, aluminum alloys and high-Mn steels) and leads to catastrophic brittle failures of structural components during service. In general hydrogen baking is a widely-used solution to overcome HE in metallic materials. In this study, hydrogen bake-out operations were performed in order to drive diffused and trapped hydrogen atoms out of the material's lattice defects such as interstitial sites, grain boundaries, dislocations and vacancies. To specify the effectiveness of this operation, Charpy V-notch impact tests of two different armor steels which satisfy MIL-DTL-12560 Class-4a and MIL-DTL-46100 were conducted with as-received, hydrogen-charged and hydrogen-charged + baked specimens, respectively. During the bake-out operations, different duration and temperature values were utilized in order to optimize these process parameters. The impact toughness results exhibited that bake-out operation was almost completely diffuse the hydrogen atoms out from the microstructure and finally the process parameters were also successfully optimized.

Keywords: Hydrogen embrittlement, hydrogen bake-out, armor steels,

I. Introduction

The ingress and distribution of hydrogen atoms across various defects and microstructures have ever been proven to be technically detrimental especially for certain alloys and steels including titanium alloys, armor steels and class of high strength steels which have an ultimate tensile strength of more than 1000 MPa (Das et al. 2020). This phenomenon is called as "hydrogen embrittlement". It is a serious matter which mechanically degrades a wide range of different structural materials. The diffusion and presence of hydrogen within microstructure could happen before and/or during in-service when exposed to hydrogen-rich environment. Figure 1 clearly shows that the solubility of hydrogen in pure iron increases as temperature increases and reaches maximum point in liquid phase.

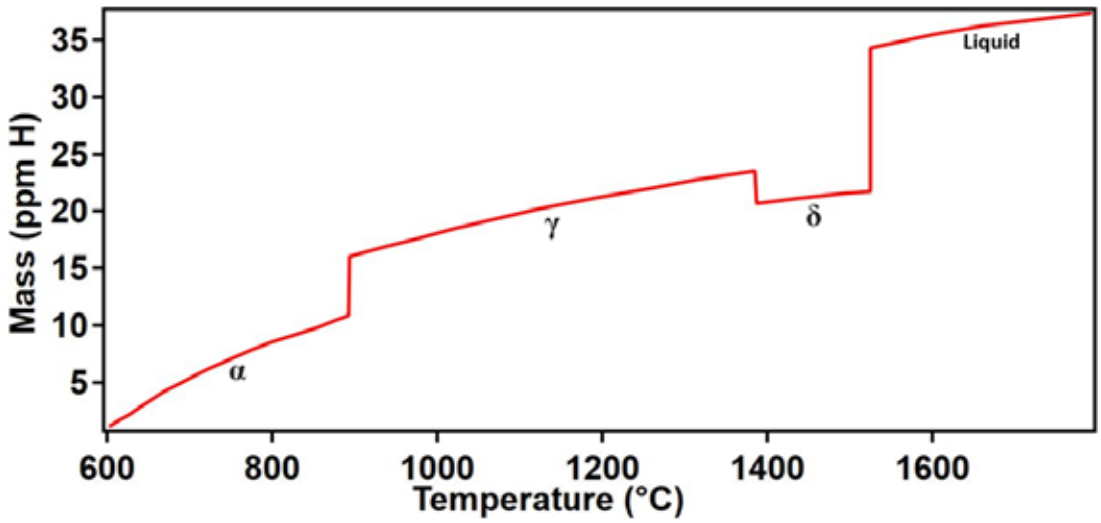


Fig. 1: Hydrogen solubility in pure iron at 1 atm pressure of H_2 (Data recompiled from Vrbek et al. 2015)

During the solidification process, most of the hydrogen is diffused out of the crystal lattices but sometimes hydrogen is trapped in lattice defects and unable to drive out of microstructure. Even a small amount of hydrogen atoms (only a few ppm) in steel-making process could later have an adverse effect to mechanical properties of certain materials. On the other hand, the introduction of hydrogen though the metals could take place during their service life either. Structural materials usually expose to hydrogen-rich environments such as corrosion of steel by H_2S, abundant molecular hydrogen in air or to contact with water. It occurs by the adsorption, absorption and diffusion of hydrogen atoms throughout hydrostatic stress zone. Figure 2 demonstrates the travelling of hydrogen atoms from liquid and gaseous phases to hydrogen accumulation zone which usually occurs at the tip of a crack.

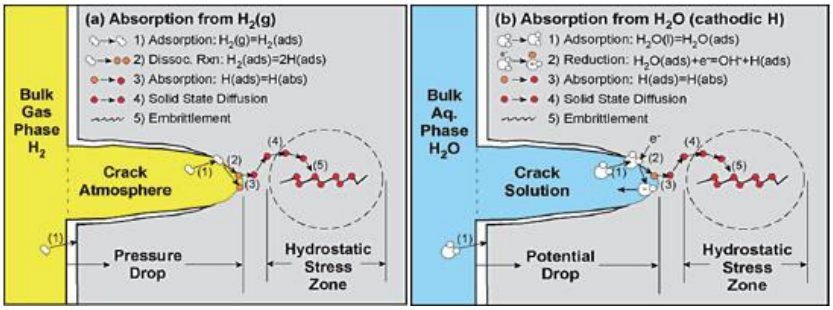


Fig. 2: The ingress of hydrogen into metals from gaseous and liquid phase [adapted from http://www.heat-treat-doctor.com/]

Once hydrogen content reaches a critical level (only a few ppm) within microstructure, it increases local stresses at the crack tips and micro and nano-scale cracks are initiated by way of applied stress, pressure and/or temperature. The time required for hydrogen embrittlement phenomenon to occur highly depends on the hydrogen content, type of material, applied stress and exposure to hydrogen. Researchers have been working on to solve hydrogen embrittlement for nearly 150 years but the exact nature of it still remains unknown and difficult to predict. Therefore, the embrittlement of most important metals, steels and alloy systems can be prevented by several methods, in which all of them are relying on to minimize contact between hydrogen and metals. Luckily, hydrogen embrittlement can totally be reversible by removing the hydrogen source within the crystal lattices and triggering hydrogen atoms to diffuse out of microstructure by applying heat treatment process. The hydrogen bake-out process is one of the methods to prevent the embrittlement of structural materials due to hydrogen. It basically involves the heating of related material to an elevated temperature and keeping the material for a length of time at that temperature. By doing so, hydrogen atoms which were diffused or trapped within interstitial sites or metal lattice defects are driven out of the microstructure and finally the embrittlement due to hydrogen is prohibited. The effectiveness and success have been proven by several researches. In our study, we have applied a bake-out process to regain the lost mechanical properties of armor steels due to electrochemical hydrogen charging operation. The results show that hydrogen is almost completely removed from microstructure by optimizing bake-out parameters (temperature and duration).

II. Experimental Set-up and Procedure

In order to perform hydrogen bake-out process, armor steels which conform to MIL-DTL-12560 Class 4a and MIL-DTL-46100 were pre-charged with hydrogen using an electrochemical hydrogen charging method. Detailed illustration of this hydrogen charging operation is given in Figure 3.

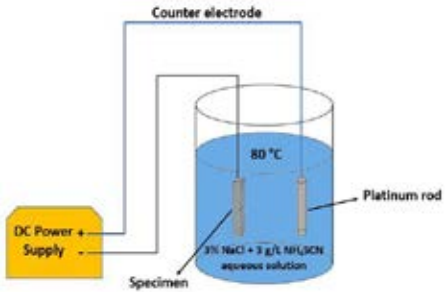


Fig. 3: Schematic representation of the hydrogen charging setup (Bal et al. 2020)


Fig. 4: AIT-300 EN and Protherm PC442T

Specimens were subjected to hydrogen-rich chemical aqueous solution with 3% (mass %) NaCl consisting of 3 g/L ammonium thiocyanate (NH4SCN) for 72 hours at a current density of 100 A/m^2. To perform Charpy V-notched impact tests and bake-out operations, AIT-300 EN and Protherm PC442T given in Figure 4 were used, respectively.
The experimental procedure for hydrogen bake-out operation is given in Table 1.

Table 1: Experimental procedure for impact tests and bake-out operations

	Trials	Baking Temp.	Baking Hours		Trials	Baking Temp.	Baking Hours
MIL-DTL-12560 Class 4a	As received	-	-	**MIL-DTL-46100**	As received	-	-
	Charged	-	-		Charged	-	-
	Trial 1	190 ºC	16 h		Trial 1	210 ºC	20 h
	Trial 2	210 ºC	16 h		Trial 2	210 ºC	28 h
	Trial 3	210 ºC	20 h				
	Trial 4	210 ºC	28 h				

All impact tests at the begining were performed three times to ensure the consistency of the results. The geometric dimesions of Charpy specimens were 7.5 mm x 10 mm x 55 mm with R0.25 notch radius and 2 mm notch height.

III. Results and discussions

First of all, impact tests were conducted three times with as recieved and hydrogen-charged specimens prior to bake-out operation. The upper and lower toughness values were determined. For the armor steel which satisfies MIL-DTL-12560 Class-4a, the average impact values of as received and hydrogen-charged specimens were 41 Joule (J) and 30 J, respectively. Pre-charging of armor steels with hydrogen remarkablely reduced load-bearing capacity, since they were subjected to hydrogen-rich chemical aqueous solution at 353K for 72 hours. Later on, third set which was consisted of three Charpy specimens were charged with hydrogen and baking operation were performed prior to Charpy test. ASTM B850–98 standard was used to determine temperature and duration parameters as well as impact test temperature which is -40 ºC. Baking temperature and duration parameters for both armor steel standards were given in Table 1 and the results of impact tests of all experimenters are provided in Table 2.

Table 2: Experimental results of Charpy V-notch impact tests

	Trials	**Toughness (J) (-40 ºC)**		**Trials**	**Toughness(J) (-40 ºC)**
MIL-DTL-12560 Class 4a	As received	41	**MIL-DTL-46100**	As received	27
	Charged	30		Charged	19.5
	Trial 1	32		Trial 1	25
	Trial 2	33.5		Trial 2	26.5
	Trial 3	36.5			
	Trial 4	40			

Table 2 clearly shows the effectiveness of hydrogen bake-out operation to drive hydrogen out of microstructure. The more hydrogen diffuses out of lattice defects, the less susceptible materials become to hydrogen embrittlement (Kim et al. 2019). Temperature and duration parameters were tried to optimize through the obtained toughness results. Temperature parameter were kept between 190 ºC - 210 ºC as it is suggested in ASTM B850–98 standard. Yet, minimum duration parameter has increased gradually from 16 hours to 28 hours. According to this standard, parameters were determined by ultimate tensile strength values of materials. Considering different type of microstructures, hydrogen solubility and diffusion which significantly changes by material itself, suggesting baking durations would not be satisfactory for each material. Therefore, baking time is carefully optimized.

IV. Conclusions

Hydrogen bake-out operation was applied for two armor steels which conform to MIL-DTL-12560 Class 4a and MIL-DTL-46100 military standards. Charpy V-notch impact tests were performed with as received, charged and charged + baked specimens, respectively. Hydrogen charging operation was performed electrochemically. The results revealed that hydrogen is almost removed out of microstructure after bake-out operation and hydrogen embrittlement is proven to be completely revesible process for this specific armor steels. Baking parameters were also optimized by conducting various experiments with different duuration and temperature values. In addition, regarding the studied armor steels, some differences were observed between the experimenatal findings and recommendastions of ASTM B850–98 standard.

Acknowledgements
The authors sincerely acknowledge the financial support of Presidency of Defense Industries Turkey and FNSS Defense Systems Co. Inc.

References

Bal, Burak, Bilge Okdem, Ferdi Caner Bayram, and Murat Aydin. 2020. “A Detailed Investigation of the Effect of Hydrogen on the Mechanical Response and Microstructure of Al 7075 Alloy under Medium Strain Rate Impact Loading.” *International Journal of Hydrogen Energy* 45(46):25509–22.

Das, Tuhin, Esaie Legrand, Salim V Brahimi, Jun Song, and Stephen Yue. 2020. “Evaluation of Material Susceptibility to Hydrogen Embrittlement (HE): An Approach Based on Experimental and Finite Element (FE) Analyses.” *Engineering Fracture Mechanics* 224(February 2019):106714.

Kim, Hye-jin, Hyeong-kwon Park, Chang-wook Lee, Byung-gil Yoo, and Hyun-yeong Jung. 2019. “Baking Effect on Desorption of Diffusible Hydrogen and Hydrogen Embrittlement on Hot-Stamped Boron.” *Metals* 9(6):636.

Vrbek, K., Lamut, J., Marolt, M., & Knap, M. 2015. “Changes in Hydrogen Content During Steelmaking.” *Archives of Metallurgy and Materials* 60(1):295–299.

Hydrogen as A Renewable Energy Source

[1*]Sibel Demiroğlu Mustafov
[1]Department of Metallurgical and Materials Engineering, Dokuz Eylul University, Izmir, Turkey

E-mail: sbldemiroglu@gmail.com

Abstract
Recently, there has been an increment in the quantity of energy consumed with the population growth, and especially the fuel need in the sector of transportation is mostly obtained from fossil fuels. Every year, the fossil fuels' reserve life utilized decreases with this increase. In the near future, continuously increasing environmental pollution, CO_2 emissions, and increasing fossil fuel prices make it unavoidable to seek different energy sources. For this aim, a clean, non-toxic energy carrier such as hydrogen, which is abundant in the universe, is required to utilize renewable energy sources. In energy systems where hydrogen can be used as fuel, the product released into the atmosphere is only water or water vapor. Hydrogen is an efficient, renewable, and comprehensive source of energy and tends to replace non-renewable materials such as hydrocarbons.

Keywords: Energy source, fuel, hydrogen**,** renewable

I. Introduction

The rapidly increasing need for energy has encouraged scientists to develop renewable and green energy sources to substitute fossil fuels. For this reason, hydrogen has been regarded as a future-proof green fuel, a non-carbon-based energy source capable of replacing fossil fuels, and since the product of the reaction is water, it has also attracted attention due to the lack of CO_2 emissions.

Hydrogen production using solar energy has many benefits in terms of both the climate and the economy. Given the fact that fossil fuels will be depleted in the near future, studies have focused on the solar-hydrogen system in recent years. The solar-hydrogen system is an extremely clean and safe way of generating energy. Numerous methods for obtaining hydrogen using solar energy have been proposed, and studies in this area are still ongoing. Hydrogen production from solar energy can be classified into four categories; 1) Photovoltaic (PV) 2) Photoelectrochemical 3) Photobiological and 4) Solar thermal energy by Yilanci et al. (2008).

Photoelectrochemical water separation method working with solar energy for hydrogen production is an important research subject among scientists because solar energy is almost inexhaustible and hydrogen is stable and storable by Yoo et al. (2020). In 1972, the photocatalytic decomposition of H_2O into hydrogen and oxygen in photostimulated TiO_2 and Pt counter electrodes is considered an important discovery by Fujishima and Honda, who provided an encouraging clean, low-cost pathway with solar energy for environmentally friendly and renewable hydrogen production by Fujishima (1972). However, energy conversion efficiency, durability, and cost of materials are insufficient for conversion from high-performance solar energy to fuel. To resolve these obstacles, researchers have been worked hard in recently to develop an extremely active photocatalyst by Ni et al. (2007).

The decomposition reaction of water in hydrogen and oxygen gases with the help of heat energy is observed with a large Gibbs free energy exchange. Photocatalytic hydrogen production is of great importance for renewable hydrogen production and environmentally friendly energy production. Photocatalytic production is very similar to photosynthesis performed by green plants and chlorophyll-bearing creatures. In this context, hydrogen production by decomposition of water can be defined as artificial photosynthesis. For the production of hydrogen in the artificial photosynthesis process, a catalyst or photocatalyst is needed because the positive Gibbs free energy cannot react alone by Carrasco et al. (2019).

When semiconductor catalysts are used in the production of photoelectrochemical and photocatalytic hydrogen, the process takes place in three main steps. Fig.1 shows the decomposition of water by the photocatalytic method.

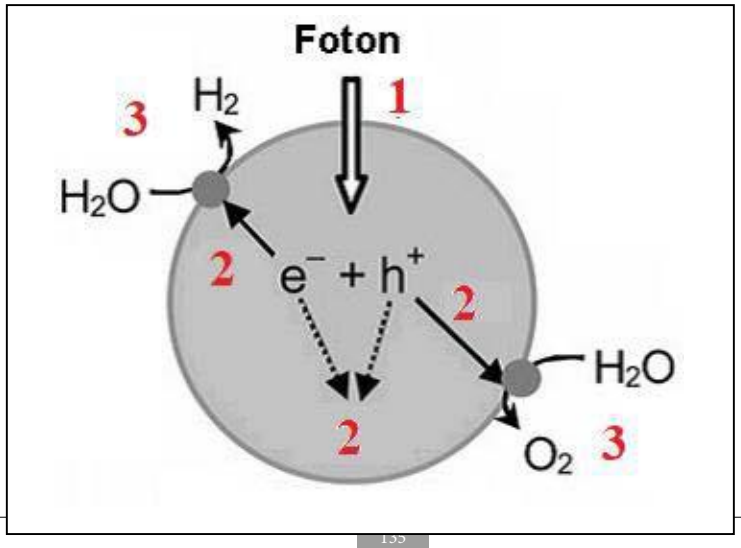


Fig. 1: H_2 and O_2 decomposition of water by the photocatalytic method by Aslan (2014).

In the 1st stage of the decomposition of water by the photocatalytic method shown in Fig.1, the photons transmitted on the semiconductor photocatalyst are absorbed and the electron gap pair are separated from each other. In the second phase, the separated loads are transferred to the area where the reaction will take place. In the third stage, H_2 production occurs by the electron excited in the active parts of the surface by reducing the water and O_2 production occurs by increasing the space in the water. For the photocatalytic reaction to complete, the energy of the transmitted photon must be higher than the semiconductor photocatalyst bandgap. The charges are separated from each other by the transmission of the high-energy photon onto the photocatalyst. The orbital gap is formed during the migration of the separated electron. The difficulty of this method is that the oxygen gas formed in the environment dissolves in aqueous solutions and causes disruption in hydrogen production. Photoelectrochemical systems are commonly used methods for complete water separation. In this method, oxygen and hydrogen gases are formed at the anode and cathode that are physically separated from each other. These limitations of the method are overcome by producing photocatalytic hydrogen using electron donor solutions. Photocatalytic oxygen production occurs in electron acceptor solutions by Lee et al. (2019).

II. Conclusions

Due to the CO_2 emission caused by the use of fossil fuels, research has focused on renewable energy sources, which include wind, solar, and biomass energy. The use of hydrogen plays a significant role in the storage and transportation of renewable energy resources. The availability of renewable hydrogen depends on the use of renewable energy. It is thought that an even stronger renewable energy implantation will be required to meet both electricity and hydrogen production in the future. In this way, hydrogen will be able to be used in every phase of the energy market in the near future and will be produced entirely from renewable energy sources with the researches in this field. One of the most important reasons why hydrogen use is not common at the moment is that the installation cost of renewable energy sources is high. For this reason, new technologies are needed to create hydrogen economies.

Acknowledgments

This research was funded by TUBITAK BIDEB's "2218-National Postdoctoral Research Fellowship Programme".

References

Aslan E., Nanoparticle-Based Hydrogen Production, Master Thesis, Selcuk University, Turkey (2014).

Carrasco-Jaima O.A., Hernandez J.M.M., Torres-Martínez L.M.T., Moctezuma E., A comparative study on the photocatalytic hydrogen production of $ATiO_3$ (A = Zn, Cd and Pb) perovskites and their photoelectrochemical properties, Journal of Photochemistry and Photobiology A: Chemistry, 371, 98-108, (2019).

Fujishima A., Honda K., Electrochemical Photolysis of Water at a Semiconductor Electrode, Nature, 238, 37-38, (1972).

Lee G.J., Chen H.C., Wu J.J., (In, Cu) Co-doped ZnS nanoparticles for photoelectrochemical hydrogen production, International Journal of Hydrogen Energy, 44(1), 110-117, (2019).

Ni M., Leung M.K.H., Leung D.Y.C., A review and recent developments in photocatalytic water-splitting using TiO_2 for hydrogen production, Renew. and Sust. Ener. Rev., 11, 401-425, (2007).

Yilanci A., Dincer I., Ozturk H.K., A review on solar-hydrogen/fuel cell hybrid energy systems for stationary applications, Progress in Energy and Combustion Science, 3, 231–244, (2008).

Yoo J., Kwak I. H., Kwon I. S., Park K., Doyeon K., Lee J. H., Lim S. A., Cha E. H., Park J., Nickel sulfide nanocrystals for electrochemical and photoelectrochemical hydrogen generation, Mater. Chem. C, 8, 3240-3247, (2020).

B-site Al Dopant Effect on The Structural Properties of $La_{0.4}Sr_{0.6}Mn_{1-x}Al_x$ (x=0.4,0.5 and 0.6) Perovskite Oxides

Seyfettin Berk Şanlı[1], İhsan Emre Yiğiter[1], Fatih Pişkin[1], Gülhan Çakmak[1], and Berke Pişkin[1*],
[1] Muğla Sıtkı Koçman University, Faculty of Engineering, Department of Metallurgical and Materials Engineering, Muğla, 48000, Turkey

* E-mail: berkepiskin@mu.edu.tr

Abstract
Perovskite oxides are one of the material groups that have attracted a lot of attention in many fields related to energy production. Thermochemical water splitting is one of the most important method which uses perovskite oxides as active material during redox reactions for hydrogen production. Amount of hydrogen production strongly depends on the properties of active materials undergoes these reactions. Many doping studies have been carried out to improve ionic and electrical conductivity, thermal and structural stability, and oxygen non-stoichiometry affecting redox characteristics. In this work, we investigated the B-site Al dopant effect on the structural properties of $La_{0.4}Sr_{0.6}Mn_{1-x}Al_x$ perovskite oxides in terms of morphology and surface area. For this purpose, $La_{0.4}Sr_{0.6}Mn_{1-x}Al_x$ were synthesized via Pechini Method. XRD, SEM, EDS, and BET techniques were performed to examine structural and chemical properties of powders synthesized.

Keywords: Perovskite oxide, Pechini Method, Thermochemical water splitting.

I. Introduction

The most promising material group is perovskite oxides for hydrogen production. Perovskite oxides have the chemical formula of ABO_3 and their ideal crystal structures are cubic (Gokon et al. 2019). The A site cation is generally composed of lanthanides or alkaline earth metals, while the B earth cation consists of transition metals that can take different valence (Sunarso et al. 2008). Perovskite oxide materials have a variety of superior properties such as high structural stability, flexible doping / alloying, non-stoichiometric oxygen vacancy formation, composition variety, and low cost. (McDaniel, Ambrosini, et al. 2013; McDaniel, Miller, et al. 2013; Scheffe, Weibel, and Steinfeld 2013). Due to these features, many perovskite families have been investigated as redox material for thermochemical water splitting. In addition to the superior properties of perovskite materials as redox material, factors such as surface area and crystal structure are important for redox reaction. At this point, having cubic crystal structure, high surface area and purity of active material increase the efficiency of the reactions.

The LaSrMnO3 perovskite family, especially the studies with Al doping have drawn increasing attention. It was emphasized that the Al B-site doped increases the structural stability (Sastre et al. 2017). Therefore, the aim of this study is to invastigate the structural effect of B site Al dopant amount (x = 0.4, 0.5 and 0.6) on $La_{0.4}Sr_{0.6}Mn_{1-x}Al_x$ (LSMA) perovskite oxides.

II. Experimental Procedure

Perovskite oxides were prepared via Pechini Method (Pechini 1967). The desired stoichiometric amount of nitrates salt of the elements was dissolved in deionized water. $La(NO_3)_3 \cdot 6H_2O$, $Sr(NO_3)_2$, $Mn(NO_3)_2 \cdot 4H_2O$, and $Al(NO_3)_3 \cdot 9H_2O$ were used as precursors to synthesize LSMA perovskite oxides. Citric acid was added with a molar ratio of 1.5:1 respect to the total metal cation. Solutions prepared were heated to 70 °C and pH was adjusted as 8 by the addition of ammonium solution (25%) with continuous stirring the solution at 300 rpm until gel-like structure formation. After the gelation, it was kept at 70 °C for till the water was completely removed. The drying process was completed by keeping them at 250 ° C for 2 hours to remove residual organic components and salts. Subsequently, synthesized powders were calcined at 900 °C for 6 hours in order to obtain a crystalline perovskite structure.

For the phase identification of sythesized powders, Rigaku SmartLab X-ray diffractometer was used with Cu-Kα wavelength (1.5406 Å) with the angle from 10 to 100° with a scan rate of $0.02^{o}\ min^{-1}$ in Bragg-Brentano geometry. Chemical analysis of samples was examined by energy dispersive spectrometer (EDS). Scanning electron microscope (SEM), JEOL JSM-7600F, was used to analyze the particle shape and size of the powders synthesized where Brunauer-Emmett-Teller (BET), (Quantachrome brand Autosorb 1C-MS) was used to confirm the surface area of the active materials.

III. Results and discussions

The XRD patterns of the sythesized $La_{0.4}Sr_{0.6}Mn_{0.6}Al_{0.4}$ (LSMA4664), $La_{0.4}Sr_{0.6}Mn_{0.5}Al_{0.5}$ (LSMA4655) and $La_{0.4}Sr_{0.6}Mn_{0.4}Al_{0.6}$ (LSMA4646) perovskites are shown in Fig.1.

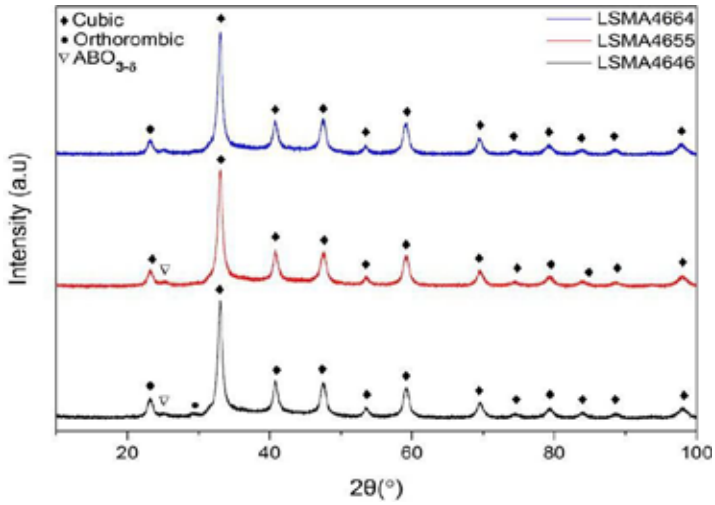


Fig. 1: XRD patterns of synthesized perovskite oxides

As seen in Fig.1, LSMA4664 has the major peaks which are belongs to the perovskite oxide structure and no impurity phases were detected. All the peaks of LSMA4664belongs to typical cubic structure. However, when the B-site doping of Al content was further increased to 0.5 and 0.6, oxygen deficient phase was detected, which may affect redox behaviour of active materials in TWS, in the XRD patterns for both LSMA4655 and LSMA4646 perovskites. Moreover, in the XRD pattern of LSMA4646 contain the diffraction peak at 28˚ belongs to characteristic of orthorombic structure. No undesirable secondary phase was detected except oxygen deficient phases for all synthesized LSMA perovskite oxides. EDS results represent the average of three analysis results in Tab. 1. It is seen that the composition values aimed to be synthesized have been successfully obtained.

Tab. 1: EDS results of Perovskite oxides

Samples	Atomic Percentages (at.%)			
	La	Sr	Mn	Al
LSMA4664	20.55	29.45	29.67	20.33
LSMA4655	19.09	30.96	24.12	25.83
LSMA4646	20.44	30.43	19.58	29.55

SEM images, Fig.2., show that all perovskite oxides have similar equiaxed and fine grain structure. In addtiton to that, primary particle size of the synthesized powders is <100 nm. BET analysis also confirmed SEM results shown in Tab. 2. High surface area was obtained for all compositions.

Tab. 2: BET analysis results of synthesized samples

Sample	Surface area (m^2/g)
LSMA4664	33.52
LSMA4655	28.40
LSMA4646	34.74

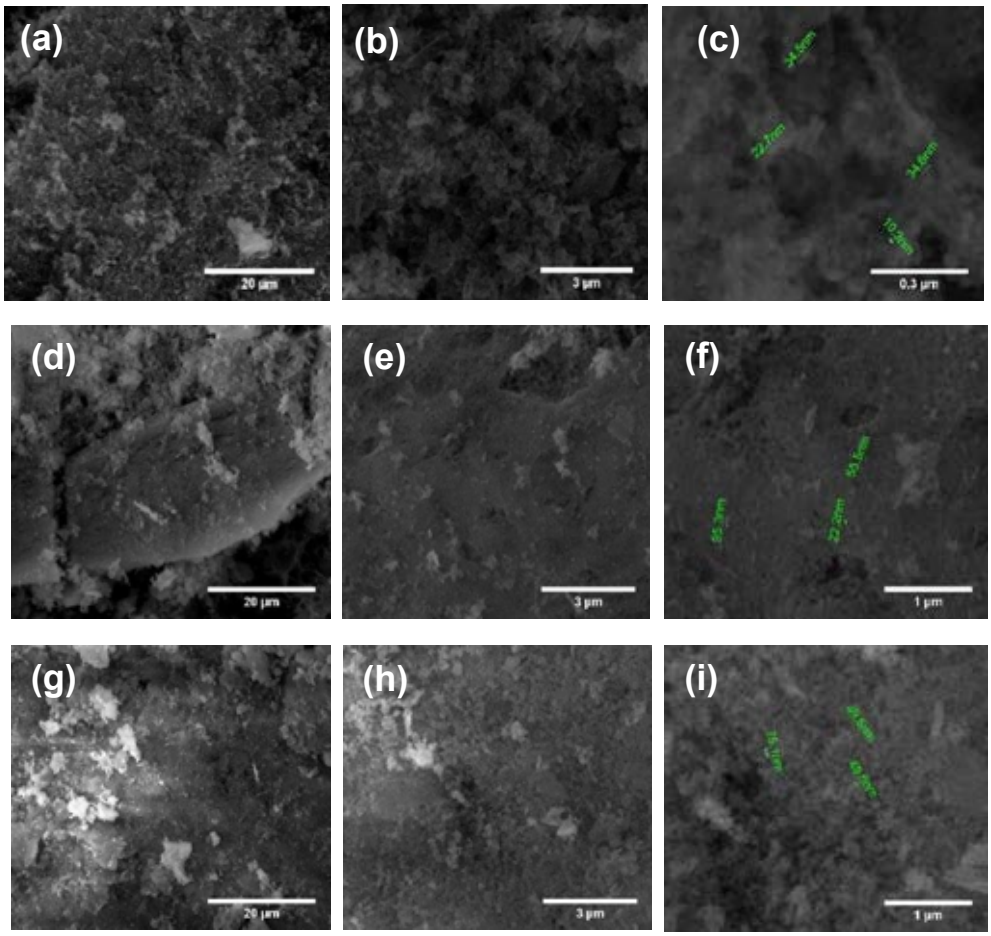


Fig. 2: SEM images of LSMA4664(a, b, c), LSMA4655(d, e, f) and LSMA4646(g, h, I)

IV. Conclusions

In this study, $La_{0.4}Sr_{0.6}Mn_{1-x}Al_x$ perovskites were synthesized by Pechini method. To understand structural effect of Al dopant, different ratio of Al has been substituted on $La_{0.4}Sr_{0.6}Mn_{1-x}Al_xO_3$. It was found that oxygen deficient phase was observed with the increase of Al amount >0.4 even all perovskite oxides have similar morphology. It can be commented on that the morphology of perovskite was not affected by amount of Al dopant. Consequently, LSMA4664 can be a promising candidate to be able to use in TWS redox reactions due to its cubic structure with higher surface area.

Acknowledgements

This research supported by TUBITAK (The Scientific and Technological Research Council of Turkey) with a project number 119M420, which the authors gratefully acknowledge.

References

Gokon, N. *et al.* (2019) “Thermochemical two-step water splitting cycle using perovskite oxides based on LaSrMnO3 redox system for solar H2 production,” *Thermochimica Acta*, 680, p. 178374.

McDaniel, A. H., Ambrosini, A., *et al.* (2013) “Nonstoichiometric perovskite oxides for solar thermochemical H2and CO production,” in *Energy Procedia*.

McDaniel, A. H., Miller, E. C., *et al.* (2013) “Sr- and Mn-doped LaAlO3−δ for solar thermochemical H2 and CO production,” *Energy & Environmental Science*, 6(8), p. 2424.

Pechini MP. Method of preparing lead and alkaline earth titanates and niobates and coating method using the same to form a capacitor. 3,330,697, 1967.

Sastre, D. *et al.* (2017) “Exploring the Redox Behavior of La0.6Sr0.4Mn1−xAlxO3 Perovskites for CO2-Splitting in Thermochemical Cycles,” *Topics in Catalysis*, 60(15–16), pp. 1108–1118.

Scheffe, J. R., Weibel, D. and Steinfeld, A. (2013) “Lanthanum-strontium-manganese perovskites as redox materials for solar thermochemical splitting of H2O and CO2,” in *Energy and Fuels*.

Sunarso, J. *et al.* (2008) “Mixed ionic–electronic conducting (MIEC) ceramic-based membranes for oxygen separation,” *Journal of Membrane Science*, 320(1–2), pp. 13–41.

Turkey's Offshore Hybrid Energy Potential and Techno-Economic Analysis in the Eastern Mediterranean

[1*]Soner ÇELİKDEMİR, [2]Mahmut Temel ÖZDEMİR
[1] Bitlis Eren University, Adilcevaz Vocational School, Electric and Energy, Bitlis, 13000, Turkey
[2] Firat University, Engineering Faculty, Electrical and Electronics Engineering, Elazig, 23000, Turkey
* E-mail: celikdemirsoner@gmail.com

Abstract

The Eastern Mediterranean region, which has been declared an Exclusive Economic Zone (EEZ) by Turkey, has also been deferred by international agreements.Turkey's ongoing hydrocarbon resource exploration in this region continues. As a result of these studies, it is highly possible to find hydrocarbon resources and to establish platforms for their extraction. In support of these studies, the focus has been on determining the renewable energy resource (RES) potential of the region and techno-economic analysis. The study was carried out in two stages for this purpose. First of all, the RES potential of the determined region was examined. In the second stage, scenarios for the storage of excess energy that may be used to meet the energy needs of these platforms are discussed.

Keywords: Offshore Wind Energy, Wave Energy, Solar Energy, Hydrogen Production

I. Introduction

In today's world, energy sources of fossil origin are decreasing over time. This situation requires both the search for new resources and the more efficient use of existing resources. The importance of RESs increases when the irreversible effects of fossil origin energy sources on the environment are taken into account. The main ones of RES are; It can be listed as wind, wave, geothermal, biomass and solar energy. These energy sources vary according to geographical and geological characteristics. Likewise, hydrogen energy, which is among the RESs, has an increasing interest day by day due to its positive characteristics as an energy carrier (İbrahim Dinçer, İnci Eroğlu 2021). In this context, it is normal for countries to diversify their energy sources in order to increase their energy security.

Turkey's, which has a developing economy, the need for energy is also increasing. Turkey is going through a process to develop its own energy resources. A process for this is carried out in the Eastern Mediterranean. The process, which began in 2011 with an agreement with the Turkish Republic of Northern Cyprus, was developed through bilateral agreements with the Libyan Governments. With these countries, the continental shelf was finally determined some of the borders of the economic exclusive zone were finalized. With these agreements, Turkey will have many advantages economically and strategically in the short and long term (Yayci 2011). The Eastern Mediterranean EEZ is very important in terms of its potential. Currently, efforts for hydrocarbon exploration continue in the Eastern Mediterranean. As a result of the findings of Barbaros Hayreddin Paşa and Oruç Reis Seismic Research vessels, Yavuz and Fatih Drilling vessels operating in the region, oil and/or gas platforms will probably be established in the region.

Offshore Oil and Gas platforms have intense power demands ranging from 10 MW to several hundred MW, depending on various variables such as the size, field conditions and characteristics of the platform (He et al. 2013). These power demands are met by independent electrical systems that use multiple redundant gas turbines, as natural gas is generally present in research sites. This structure leads to greater fuel use and lower efficiency (about 30%), which negatively affects carbon footprints (Haces-Fernandez, Li, and Ramirez 2018).

Extracting offshore hydrocarbon resources and meeting the energy needs of refining processes with RES s is an issue addressed by researchers. Despite this, the determination of the RES potential of the EEZ has not been investigated before. With this study, it is aimed to fill this gap in the literature. In the study, information about the state of the region was given first. Then wind energy, wave energy and solar energy potential were determined for certain points. With these potential types, it has been designed to provide the energy of the platform. Hydrogen production status is discussed with excess energy to be produced from the system. As a result, it has been shown that the energy required by the platforms can be provided with RES, regardless of its power.

II. Turkey Eastern Mediterranean Continental Shelf

There are oil and gas reserves in the Middle East and Caucasus in the geography of Turkey. In recent years, natural gas reserves discovered in the Eastern Mediterranean basin have further increased the geopolitical and geostrategic position of the region. These reserves will deepen the political problems between the countries in the Eastern Mediterranean, one of the most politically problematic regions in the world. Today, the importance of the Eastern Mediterranean in particular continues to increase day by day. In other words, 30% of the world's sea trade is carried out in the Mediterranean, which covers approximately 0.7% of the world's seas. Again, approximately 370 million tons of oil are transported annually in this region by tankers. Approximately 220,000 ships are in operation in the Mediterranean annually. The fact that countries bordering the Eastern Mediterranean (Turkey, Syria, Lebanon, Israel, Egypt, Palestine, Cyprus and the TRNC) claim oil and gas deposits in the region and there is no complete agreement on its sharing makes the issue even more unsolved.

In recent history, the first sea-sharing struggle in the Eastern Mediterranean began with the agreement of the Greek Cypriot Administration of Southern Cyprus with Egypt. Then the same country tried to establish status by

agreeing with Lebanon in 2007 and Israel in 2010. Turkey took its first step towards the delimitation of maritime jurisdiction areas in the Eastern Mediterranean by agreeing with the KKTC in New York on September 21, 2011. In 2013, it was announced that the note given to the AB and the BM would determine the continental shelf according to the common line between the Egyptian-Turkish coast. This line was confirmed by the BM in 2019 (Paralı 2020). As a result, on November 27, 2019, the Government of the Republic of Turkey and the Government of the State of Libya signed the memorandum of understanding on the limitation of maritime jurisdictions areas in the Mediterranean sea in Istanbul (Tuna 2020). According to these developments, Turkey has a continental shelf with an area of 145,000 km^2. The selected region; RES potential as wind, wave, and solar energy will be examined.

III. Eastern Mediterranean Turkish EEZ Region RES Potential

Wind speed data of the region for the years 2010-2017 are given in Figure 1-a). According to these values, it is seen that the average wind speed value at a height of 10 meters reaches 7 m/sec in some regions. This value is above 10 m/s if it is at a height of 100 meters. However, wind speed value increases especially in the eastern and western regions of Crete Island. According to these values, the wind energy potential of the region is over 1140 W/m^2. It is seen that the eastern region of Crete Island, which is located within the EEZ, appears to have a significant wind energy potential that can be evaluated.

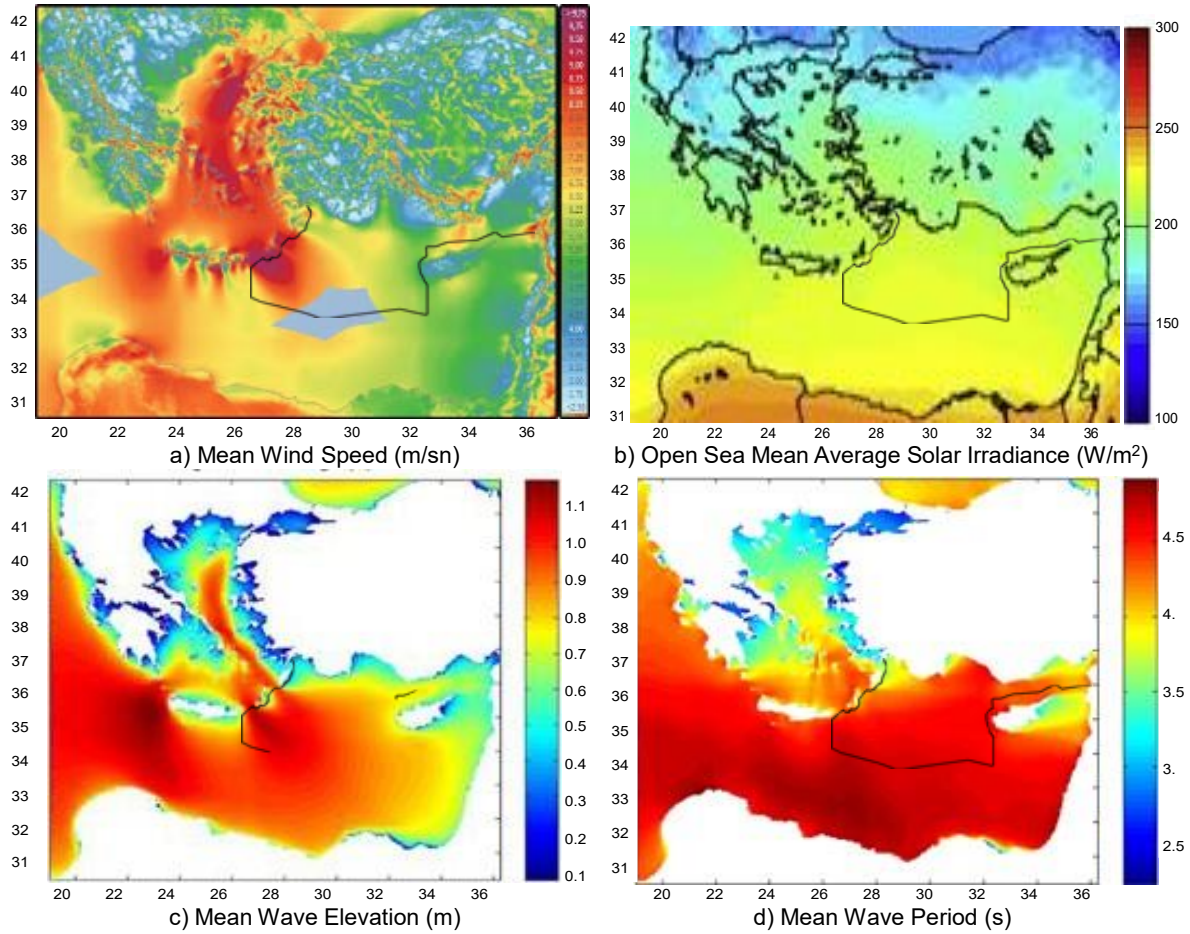


Fig. 1. Potential maps of Turkish EEZ

Solar energy, which is the source of many RESs, is the radiation energy released as a result of fusion occurring in the core of the sun. The surface solar radiation values of the EEZ examined in the study are given in Figure 2-b (Alexandri et al. 2017). Accordingly, the solar energy potential of the region has been calculated as 1990 kWh/m^2. According to these values, it is seen that the region has an assessable potential in terms of solar energy.

Wave energy is an energy source created by wind, sea floor movements, gravitational forces of the sun and moon, human activities and different mass movements on the water surface. There are two important components that make up the wave energy (Nikolaidis et al. 2019). These are wave height value and wave period value. When examining the wave energy potential of a region, these two components should be taken into account.

The graph containing wave height data is given in Figure 2-c) (Nikolaidis et al. 2019). Accordingly, the highest average value is seen off the eastern and western offshore of the Island of Crete. This value is more than 1,1 meters for the EEZ in question. Likewise, the graph containing the wave period value is given in Figure 2-d (Nikolaidis et al. 2019). Accordingly, the lowest wave period value is on the shores of Turkey. However, on the coast of Africa, this value is at maximum value. When meb is taken into account, it is seen that the wave period value varies between 4-4,5 seconds in the southern region of crete island. Considering the wave height and wave period value for the wave energy potential, it is seen that the region in question has an evaluable potential.

IV. Results and discussions

In the Eastern Mediterranean EEZ, the result of renewable energy potential being evaluated economically is seen. In this way, the energy needs of the said platforms will be met with the hybrid power plant to be established in the region. The excess energy produced will be used in hydrogen production. Installed power and cost values of such a hybrid power plant are given in Table 1.

Tab. 1. Installed Power and Costs of RES

RES	Power (MW)	Cost (milyon $)	Energy (GWh)	References
Wind Energy	80	377,956	7000	(Mattar and Guzmán-Ibarra 2017)
	160	*600,803*	*14000*	
	240	*861,196*	*21000*	
Wave Energy	0,25	7,378	0,96	(O'Connor, Lewis, and Dalton 2013)
	0,5	*5,902*	*1,92*	
	1	*4,427*	*3,84*	
Solar Energy	*2,5*	*18,433*	*3810*	(Chandel et al. 2014)

In EEZ; approximately 10813,84 GWh of energy will be generated annually with hybrid power plants consisting of 80 MW wind energy, 1 MW wave energy and 2,5 MW solar power plant. 50% of this energy can be used in the platforms to be established and 50% in hydrogen production. In this case, if 5406,92 GWh energy is used in the production of hydrogen, $138{,}163 \times 10^6$ Kg of hydrogen are produced with 75% efficiency and 39 kWh/kg. Then, with the existing hydrogen energy source 35,6 kWh / kg, 4935,54 GWh of energy generates with an energy conversion rate. The amount of loss between conversions calculates as 471,38 GWh. Also different scenarios for storing increased energy from existing platforms are discussed. These scenarios include the transportation of the produced hydrogen by natural gas if there are pipelines, freighters and finally natural gas reserves in the region. In this case, the cost is 1444,17 $/km if the increased energy is transported by freighters. Likewise, if transported by hydrogen pipelines, the cost is $3536,46 $/km.

V. Conclusions

For the Turkish exclusive economic zone, YEP has been shown to be at a assessable level. In addition, hybrid studies have gained importance in order to make energy investments more economical today. For this purpose, a hybrid model has been proposed to meet the energy needs of the oil and gas platform to be established in the region. The cost of the hybrid power plant with 83,5 MW installed power in the region was estimated at approximately 400,816 million $. After the energy demand of the platform was met, excess energy was used for hydrogen production. Costs for different scenarios for transporting the produced hydrogen were examined. As a result, the most affordable cost was calculated as 1444,17 $/km for transportation using freighters.

References

Alexandri, G., A. K. Georgoulias, C. Meleti, D. Balis, K. A. Kourtidis, A. Sanchez-Lorenzo, J. Trentmann, and P. Zanis. 2017. "A High Resolution Satellite View of Surface Solar Radiation over the Climatically Sensitive Region of Eastern Mediterranean." *Atmospheric Research*. https://doi.org/10.1016/j.atmosres.2016.12.015.

Chandel, Mevin, G. D. Agrawal, Sanjay Mathur, and Anuj Mathur. 2014. "Techno-Economic Analysis of Solar Photovoltaic Power Plant for Garment Zone of Jaipur City." *Case Studies in Thermal Engineering*. https://doi.org/10.1016/j.csite.2013.10.002.

Haces-Fernandez, Francisco, Hua Li, and David Ramirez. 2018. "Assessment of the Potential of Energy Extracted from Waves and Wind to Supply Offshore Oil Platforms Operating in the Gulf of Mexico." *Energies*. https://doi.org/10.3390/en11051084.

He, Wei, Kjetil Uhlen, Mahesh Hadiya, Zhe Chen, Gang Shi, and Emilio del Rio. 2013. "Case Study of Integrating an Offshore Wind Farm with Offshore Oil and Gas Platforms and with an Onshore Electrical Grid." *Journal of Renewable Energy*. https://doi.org/10.1155/2013/607165.

İbrahim Dinçer, İnci Eroğlu, Merve Öztürk. 2021. "Türkiye İçin Hidrojen Teknolojileri Yol Haritası." https://doi.org/ISBN: 978-605-66381-9-0.

Mattar, Cristian, and María Cristina Guzmán-Ibarra. 2017. "A Techno-Economic Assessment of Offshore Wind Energy in Chile." *Energy*. https://doi.org/10.1016/j.energy.2017.05.099.

Nikolaidis, Georgios, Andria Karaolia, Anastasios Matsikaris, Andreas Nikolaidis, Marios Nicolaides, and Georgios C. Georgiou. 2019. "Blue Energy Potential Analysis in the Mediterranean." *Frontiers in Energy Research*. https://doi.org/10.3389/fenrg.2019.00062.

O'Connor, M., T. Lewis, and G. Dalton. 2013. "Techno-Economic Performance of the Pelamis P1 and Wavestar at Different Ratings and Various Locations in Europe." *Renewable Energy*. https://doi.org/10.1016/j.renene.2012.08.009.

Paralı, Z. 2020. "Türkiye Cumhuriyeti İle Libya Devleti Ulusal Mutabakat Hükümeti Arasında İmzalanan Akdeniz'de Deniz Yetki Alanlarının Sınırlandırılmasına İlişkin Mutabakat Muhtırasının Uluslararası Politikaya Etkileri." *Nazilli İktisadi ve İdari Bilimler Fakültesi Dergisi* 1 (1): 49–64.

Tuna, Fatih. 2020. "Türk Dış Politikasında Realist Yaklaşım: Türkiye'nin Doğu Akdeniz ve Libya Politikası." *Uluslararası Hukuk ve Sosyal Bilim Araştırmaları Dergisi*.

Yayci, C. 2011. "Doğu Akdeniz'de Deniz Yetki Alanlarının Sınırlandırılmasında Libya'nın Rolü ve Etkisi." *Güvenlik Stratejileri Dergisi*, no. 14: 17–41.

Hydrogen Evolving Studies over Pellet Type Catalyst for Decomposition of Ammonia Borane Solutions

[1]Bilge Coşkuner Filiz, [2]Aysel Kantürk Figen
[1] Yıldız Technical University, Chemistry-Metallurgy Faculty, Department of Metalluryg and Materials Engineering, Istanbul, 34210, Turkey
[2] Yıldız Technical University, Chemistry-Metallurgy Faculty, Department of Chemical Engineering, Istanbul, 34210, Turkey

E-mail: bilgecoskuner@gmail.com; ayselkanturk@gmail.com

Abstract
In this study, the aqueous solutions of ammonia borane (NH_3BH_3) were catalytically decomposed to evolve hydrogen in presence of supported $Co(OH)_2$ catalysts. Two different size active carbon pellets (ACP) were preferred to prepare catalysts. The pellet type catalysts were prepared via vacuum impregnation-reduction method to get catalytic properties by loaiding of Co species on active carbon structures. The catalysts morphological and surface properties were characterized via SEM technique. The hydrogen evolving experiments were performed at various temperature changing between 20ºC to 80ºC to evaluate the temperature effect and got kinetic data. This study was supported by by Yildiz Technical University Scientific Research Projects Coordinator's project numbered FBA-2019-3476.

Keywords: Pellet, Catalysts, Hydrogen, Ammonia Borane

I. Introduction

Growing interest for the renewable energy sources due to concenrs about climate exchanges and restrictions from goverments such as Green Deal, eco-friendly energy applications gain importance. Sustainable energy sources provide nature, abundance and high energy density. Hydrogen as an energy carrier is one of the good options towards alternative sources.

The most effective and safest way of storing hydrogen is to use solid media such as metal hydrides, boron based materials, MOFs and carbon based materials. Beyon the classical ways of hydrogen gas stogage, this materials provided safety and practical way of storage and transfer. According to the U.S.A. Deperatment of Energy, certain calss of hydires meet hydrogen energy systems requirments. Ammonia borane is the one with the highest hydrogen storage density. 19.3 wt. of its molecular is hydrogen gas. This material is an inert under atmospheric conditions and its aqueous solutions shows also stability. There is no need extra specific handiling, transport or storage conditions (Demirci, 2017). This stability required to use of active catalyst to production of hydrogen which enables decomposition of stable structre. Noble metals shows pretty good activity for hydrolysis, thermolysis and hydrothermolysis type of hydrogen production reactions from ammonia borane. Besides their good activity, their high price made the process expensive to use in practical applications. Non-noble metals such as cobalt, nickel, copper are the good alternatives, which shows high activity. Their oxide, hydride, multi metallic forms provided different activity. Also the support effect hydrogen production tendency of catalytic procedure.

The hydrogen evolving from the ammonia borane could be performed in three ways as hydrolysis, hydrothermolysis and thermolysis reactions. The hydrolysis reaction enable 3 moles of hydrogen evolution by decomposition of B-H and N-H bounds. Water and ammonia borane do not have interaction that resulted with hydrogen gas production. The high stability of aqueous solutions of ammonia borane under ambient conditions makes this reaction favorable compared to the other two (Huang, et all, 2012; Baumann, 2005, Liu, 2021). This stability of the solutions required a catalytic material to hydrogen generation. Several noble and non-noble metals in the form of metal, metal oxide, alloy, multi metallic compounds, powder, solid material, supported and unsupported have been investigated to enhance and control the hydrogen generation to reach energy systems target. Along the several option, cobalt based materials have really good acitivity to breake bounds to get hydrogen gas, which have ben proffed via several scientists. Moreover this, high interaction area of catalytic materials improved reaction and provide fast conversion of reactants to products. Active carbon is the one of the material which has highest surface areas. Besides, the powder form of catalysts enable better interaction, the obstacles in the removal of them from the reaction mixture is a important problem. During the separation process, lose of catalyst and impurites due to catalysts in product or by-products are important problems that want to avoid. The solid form of catalysts is one of the solution with the easy separation of catalysts (Geniş et all, 2020; Kinsiz et all, 2021).

In this study, we prepared pellet type catalysts for decomposition of ammonia borane solutions. Carbon pelletts in two different size used as catalysts supporting material for providing larger deposition area of Co species and ealy recovery of catalystic material. Vacuum impregnation modified reduction method was preferred for loading active Co phase on the active carbon pellets. The prepared catalysts were tested for hydrogen evolving studies via decompositiom of ammonia borane solutions. The pellet type catalysts's hydrogen evolving tendencies were evaluated at the temperature range of 20ºC-80 ºC.

II. Experimental Set-up and Procedure

In the experimental study, two different types of activated carbon pellets were used as an catalysts support as given in Figure 1. The catalysts were prepared via vacuum impregnation modified in-situ reduction method. Each activated carbon pellets were loaded with 20% by weight of cobalt. In the first stage of loading, cobalt chloride (3.97 g, $CoCl_2.6H_2O$, Merck, purity> 97%) was dissolved in 50 mL of distilled water in a beaker with the help of a magnetic stirrer, 5 g of activated carbon pellets were added to the resulting solution and stirring was continued. After the mixing process, the mixture obtained in the impregnation process was continued in the vacuum oven at 60 °C and under vacuum, until the liquid phase of the mixture was fully evaporated. Then the drying process was completed in the oven at 120 °C. As the second step, the reduction process was applied. For this purpose, sodium boron hydride ($NaBH_4$, Merck,> 99) was dissolved in 75 mL of pure water with the help of a magnetic fish in a temperature controlled magnetic stirrer. The catalyst reduction process was carried out in the ice bath at 0 °C, and when the reduction process was completed, when the gas output stopped. Each catalyst with complete reduction was washed with distilled water. And directly used in hydrolysis reactions.

The morphological and surface properties of catalysts were characterized via methods explained in detail. The morphology and particle size of active carbon pellet supported catalysts were characterized by scanning electron microcopy studies that performed on ZEISS EVO LS10 SEM operated at 7 kV. Carbon support film coated aluminium SEM sample holders were used.



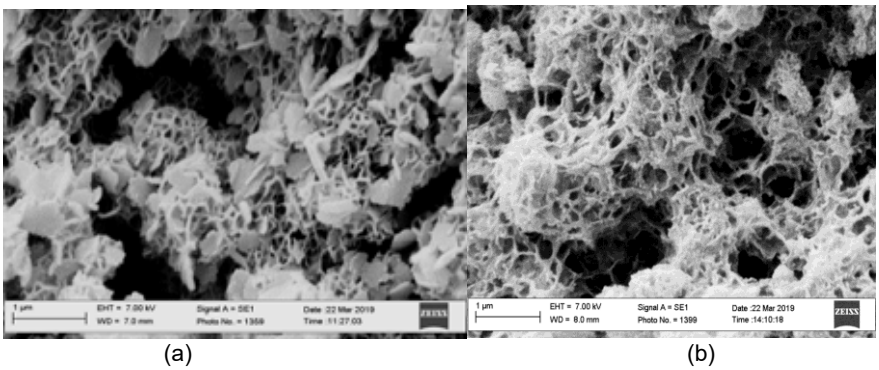
(a) (b)

Fig. 1: Active carbon pellets used in catalysts preparation: (a) $Co(OH)_2$@ACPB and (b) $Co(OH)_2$@ACPS

Hydrogen production was investigated by hydrolysis reactions in presence of two various size $Co(OH)_2$@AC. 0.2 M solution was prepared by adding 0.001 mol of AB derivative compound and 5 ml of deionized water. The cobalt-containing activated carbon supported catalysts prepared afterwards were weighed in the same amount (0.1 g) in grams and the reaction temperature controlled (20 °C-80 °C) magnetic stirrer (200 rpm). The volumes of evaluated hydrogen were read by replacing the H_2 gas with water in the cylinder with the help of the stopwatch. In the hydrolysis experiments, it was waited until the H_2 gas output was completed and the produced H_2 gas volume was plotted against time and the production rate profiles were examined. The effects of production rate profiles, changing temperature conditions of the reactions and the catalysts size effect were investigated.

IV. Results and discussions

The morphology of $Co(OH)_2$@ACPB and $Co(OH)_2$@ACPS catalysts were characterized via SEM analysis. The nano-size particles in the form of web. The morphology of the both catalysts were almost same. The porous structure and small size of flakes related with Co spiecies were also recorded as seen from Fig.2.



(a) (b)

Fig. 2: SEM images of (a) $Co(OH)_2$@ACPB and (b) $Co(OH)_2$@ACPS catalysts

The ammonia borane solutions (0.12 M) were tested for hydrogen evolving over pellet types catalysts. Fig.2 shows the volume of hydrogen evolved respect to time at different reaction temperatures in presence of $Co(OH)_2$@ACPB. The temperature strongly affect the evolved hydrogen quatity per unite time.

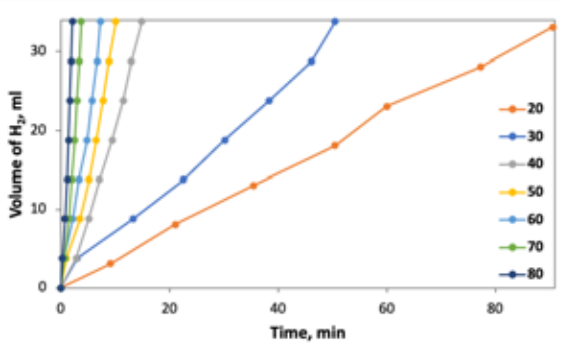


Fig. 2: Hydrogen evolving studies over $Co(OH)_2$@ACPB for decomposition of AB solutions

The hydrogen generation properties of pellet type catalysts were evaluated by comparasion of hydrogen evolving rates. The size of catalysts support changed the HGR. Bigger size $Co(OH)_2$@ACPB catalyzed the decomposition of AB solutions faster than the $Co(OH)_2$@ACPS. Besides the surface area of $Co(OH)_2$@ACPS, $Co(OH)_2$@ACPB catalysts showed better activity.

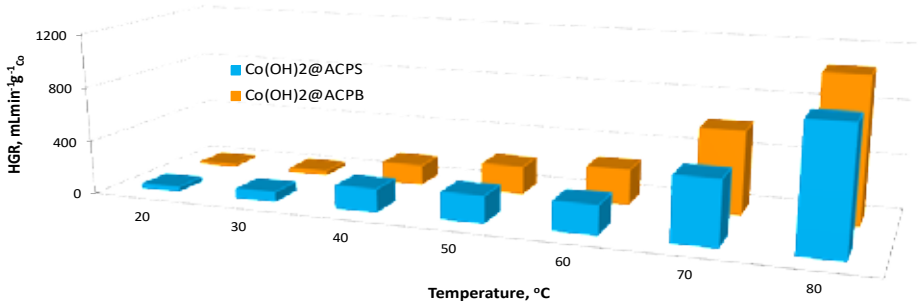


Fig. 3: The comparsion of hydrogen evolving rates of pellet type catalysts.

V. Conclusions

Our study was focused on the evaluation of different sized pellet type catalysts for decomposition of aquesous ammonia borane solutions. The vacuum impregnation- insitu reduction method was used to prepare $Co(OH)_2$@AC pellet catalsysts. The results indicated that size of pellet has an significant effect due to the amount of active size was depend on the AC size. The direct proportion was found between temperature and HGR as expected. Usage of this type of catalysts made easier removal of catalysts after reaction.

Acknowledgements

This study was supported by by Yildiz Technical University Scientific Research Projects Coordinator's project numbered FBA-2019-3476.

References

Demirci, U.B. Ammonia borane, a material with exceptional properties for chemical hydrogen storage, International Journal of Hydrogen Energy, 42, 15, 9978-100013.

Kinsiz, B.N., Coşkuner Filiz, B., Kılıç Depren, S., Kantürk Figen, A. Nano-casting procedure for catalytic cobalt oxide bead preparation from calcium-alginate capsules: Activity in ammonia borane hydrolysis reaction, Applied Materials Today, 22, 100952.

Geniş, D., Coşkuner Filiz, B., Kılıç Depren, S., Kantürk Figen, A. Reusable hybrid foam catalyst for hydrolytic dehydrogenation of amine adducts of borane: Porous PVA-Immobilized Co–Ru nanoparticles, Microporous and Mesoporous Materials 305, 110363

Li, Y., Hao, J., Liu, H., Lu, S., John, S.T. High-energy density and superhard nitrogen-rich BN compounds. Physical review letters, 115(10), 105502

Huang, Z., Autrey, T. Boron–nitrogen–hydrogen (BNH) compounds: recent developments in hydrogen storage, applications in hydrogenation and catalysis, and new syntheses. Energy & Environmental Science, 5(11), 9257-9268.

Baumann, J., Baitalow, F., Wolf, G. Thermal decomposition of polymeric aminoborane (H2BNH2) x under hydrogen release. Thermochimica acta, 430(1-2), 9-14.

Liu, H., Liu, C., Li, Q., Ma, Y., Chen, C. Pressure-Induced Evolution of Crystal and Electronic Structure of Ammonia Borane. *The Journal of Physical Chemistry Letters*, *12*, 2036-2043.

The importance of hydrogen in terms of energy diversity for Turkey's energy projection

[1]Cengiz Amil, [1*]M. Zeki Yılmazoğlu
[1]Gazi University Faculty of Engineering Department of Mechanical Engineering, Maltepe, Ankara, 06570, Turkey

[*]E-mail: zekiyilmazoglu@gazi.edu.tr

Abstract
Hydrogen and hydrogen-related technologies will have an important role in world energy projection in the near future. Interest in hydrogen technologies will also increase, especially due to the smart cities concept and the increase in renewable energy supply. In addition to being a clean energy source, the tendency of hydrogen to 100% renewable energy supply makes it ahead of other alternative fuels. The share of hydrogen and related energy technologies in reducing global warming and emissions will continue to increase day by day. For this reason, projections and investment opportunities should be determined for the coming years. In energy projections, the evaluation of hydrogen in terms of energy diversity until 2030 was carried out with EnergyPlan software. Accordingly, the reduction in the amount of emissions and costs were determined by mixing hydrogen into the natural gas pipelines by 5-10, and 20% by volume by producing electrolyzers with photovoltaic systems and according to the number of vehicles with fuel cells in the transportation sector until 2030.

Keywords: energy projection, 2030, hydrogen, smart cities, fuel cells, hydrogen technologies, mixing hydrogen with natural gas

I. Introduction

By the end of 2019, Turkey's installed capacity has reached to 91267 MW. Distribution of installed power according to resources; 31.2% hydraulic energy, 28.4% natural gas, 22.2% coal, 8.3% wind, 6.6% solar, 1.7% geothermal, and 1.6% is in the form of other sources. For hydrogen, it is currently 1.6% mainly used in the industrial sectors to produce ammonia or other processes. Although hydrogen does not contribute directly into the energy generation, it is used as an input raw material in the industry. The pilot hydrogen facility established in Haliç produces up to 65 kg of hydrogen per day with an electrolyzer powered by the grid and can be stored up to 100 kg. Hydrogen refueling of both land and sea vehicles can be made, and for a 3.25 kg tank, 20 vehicles with a range of 390 km can simultaneously refuel. Hydrogen production with electrolysis is included as a pilot project by using wind energy to meet the electricity needs of the district governorship and health center established in Bozcaada. Currently, no data is available for a vehicle with hydrogen fuel in Turkey other than two vehicles built under the leadership of TÜBİTAK [1]. Likewise, the absence of a law on hydrogen currently stands as an obstacle to the development of this technology.

II. 2030 Turkey Energy Projection

It is predicted that the hydraulic resource capacity, which currently ranks first among the energy resources of Turkey, will have an installed power of 35,000 MW by 2030. In particular, the fact that the rivers in Turkey have not reached their full potential in terms of energy and that energy is obtained by natural and clean ways is also important in terms of being cleaner than fossil energy types that will increase carbon emissions. It is anticipated that the capacity of the natural gas cycle power plants, which was 25,612 MW as of August 2020, will decrease year by year. Although a large natural gas reserve has been found for Blacksea and Mediterranian sea, the time until the extraction of this resource and the production of approximately 15 billion cubic meters per year cannot fully save us from natural gas imports. Ensuring energy security with an imported product will also have negative consequences for both strategic and national economy. Natural gas should be used in sectors suitable for the heat capacity required by the thermal process. For the coal-based power plant capacity and production, it is seen that the amount of electricity obtained is lower, although the installed power is higher due to the lower calorific value of domestic lignite coal compared to imported coal. When energy production from coal is the case, the focus should be on clean coal technologies, which is to obtain coal by gasification, as used in countries such as the USA and Russia instead of traditional methods. Although it is not in 2030, it is thought that we will be able to benefit from this technology until 2050. It is predicted that our coal-fired power plant capacity will not exceed 25,000 MW in total in 2030. When the Mersin Akkuyu nuclear power plant, which is projected to be completed by 2030 and will be the first nuclear facility of Turkey, will consist of 4 units, each with an installed power of 1,200 MW, the total installed power of the plant will

be 4,800 MW. It is planned to generate 35,000 GWh of electricity at full capacity annually from this power plant. By 2030, the number of wind and solar power plants is expected to increase. Investments in solar energy will be folded, especially when daylight times are taken into consideration. With the power plants planned to be established, it is predicted that the installed power of wind power plants will be 22,000 MW and the installed power of solar power plants will be 25,000 MW. Waste facilities will also be very important in terms of utilizing the waste potential. The resource installed power released as biogas is expected to increase five times in 2030 and reach 6,000 MW. In geothermal energy, electricity is currently produced in most of the Aegean region in 54 power plants with a total installed power of 1515 MW [1-2]. The capacity of the geothermal power plants, which will reach 2,197 MW during the project phase and with the ongoing construction, will be at the level of 3,500 MW with the addition of new projects that do not exist until 2030. The hydrogen fueled vehicle target numbers of some countries in the world for 2030 are given below [2]:

• The Netherlands, which has 241 vehicles in 2019, plans its 2030 target as 300,000 vehicles.

• The USA, with 8,039 vehicles in 2019, is the country with the most hydrogen-fueled vehicles.

• Japan, which has 3,633 vehicles in 2019, plans its 2030 target as 811,200 vehicles.

• France has set its target for 2028 as 52,000 vehicles.

• Korea has planned 81,000 vehicles to be actively used in the market by the end of 2022.

Until the year 2030 1.000 total hydrogen-fueled vehicle market is estimated to be used in Turkey.

Scenarios

The simulations were carried out in EnergyPlan code (Fig.1). Four scenarios were considered in addition to the hydrogen cases. The first scenario is the 'Technical Turkey' for 2030. In the subtasks of this scenario, the heat and electricity demand balancing strategy was chosen. The heat pump simulation was considered to support only critical overproduction. The transport regulation was decided to balance the critical surplus generation and power plant. In the second scenario projections for 2030 Turkey 'Economic Market' simulation was selected. In the subtasks of this scenario, no limit option was selected for electric vehicles fed from the grid. The effect of transmission capacity on the system was neglected and the effect of renewable energy systems on electricity prices was selected as negative.

In the next scenario, 20% low installed power is considered. According to the scenario, the installed powers projected for 2030 and expected to increase compared to 2019 are 20% lower than the first scenario. In the fourth scenario, 20% high capacity is considered. In the results obtained from the scenarios, the effect of hydrogen was not considered. The effect of hydrogen was also considered in the fifth scenario, and simulations of mixing 5%, 10% and 20% hydrogen gas with natural gas by volume were performed on the pipelines. By keeping the demands met by the existing total natural gas constant, the amount of natural gas in equivalent energy equal to the amount to which hydrogen is added was reduced.

III. Results

The number of vehicles used for transportation was taken as 1.000 and Toyota Mirai values were taken for vehicle power consumption [3]. Energy coming from wind and solar energy systems will be used in the electrolyzer in obtaining hydrogen, and the use of hydrogen gas obtained from here is planned. There is a demand of 0.16 TWh per year for 1,000 vehicles. The energy equivalent of hydrogen mixed with 20% of natural gas is included in the calculation as 68 TWh / year. The reduction in CO_2 emissions is 4% from 316.93 Mt to 304.21 Mt. The reduction in CO_2 emissions is 4% from 316.93 Mt to 304.21 Mt. CO_2 emission unit price is taken as 90₺/t. According to the results, the economic value of 12.72 Mt CO_2 emission reduction is 1.144.800.000 ₺. When 5% hydrogen is mixed to natural gas, the amount of CO_2 from 309.49 to 307.26 Mt decreases from 309.49 to 2.23 Mt of CO_2. Its economic value is 200.700.000₺. When 10% hydrogen is mixed to natural gas, the amount of CO_2 decreases from 309.49 to 305.19 Mt by 4.3 Mt and its economic value is 387.000.000 ₺.

The hydrogen energy performance that Turkey will demonstrate by 2030 will show whether we can play a role in the future of this technology. Until 2030, if 1,000 hydrogen fuel cell vehicles and 5% natural gas are mixed, 200.700.000 ₺ will be saved from only CO_2 reduction and it means approximately 1.6 billion m^3 or 2.6 billion ₺ of natural gas savings. In the case of mixing with natural gas at a rate of 20%, 1.144.800.000 ₺ will be saved from the reduction of CO_2 emission amount alone and it means a natural gas saving of 6.39 billion m^3 or 10.4 billion ₺.

References

Bjelić I.B., Rajaković N., Simulation-based optimization of sustainable national energy systems, Energy, Volume 91, 2015, Pages 1087-1098, ISSN 0360-5442,https://doi.org/10.1016/j.energy.2015.09.006. (https://www.sciencedirect.com/science/article/pii/S0360544215011986)
Bonati A., G. De Luca, S. Fabozzi, N. Massarotti, L. Vanoli, The integration of exergy criterion in energy planning analysis for 100% renewable system, Energy, Volume 174, 2019, Pages 749-767, ISSN 0360-5442, https://doi.org/10.1016/j.energy.2019.02.089. (https://www.sciencedirect.com/science/article/pii/S0360544219302841)
Dorotić H., Doračić B., Dobravec V., Pukšec T., Krajačić G., Duić N., Integration of transport and energy sectors in island communities with 100% intermittent renewable energy sources, Renewable and Sustainable Energy Reviews, Volume 99, 2019, Pages 109-124, ISSN 1364-0321, https://doi.org/10.1016/j.rser.2018.09.033. (https://www.sciencedirect.com/science/article/pii/S1364032118306816)
Dranka G.G., Ferreira P., Planning for a renewable future in the Brazilian power system, Energy, Volume 164, 2018, Pages 496-511, ISSN 0360-5442, https://doi.org/10.1016/j.energy.2018.08.164. (https://www.sciencedirect.com/science/article/pii/S0360544218317006)
Fanni S., Modelling the Hungarian energy system – The first step towards sustainable energy planning, Energy, Volume 69, 2014, Pages 58-66, ISSN 0360-5442,https://doi.org/10.1016/j.energy.2014.02.067. (https://www.sciencedirect.com/science/article/pii/S0360544214002011)
Internet, https://cms.law/en/int/expert-guides/cms-expert-guide-to-hydrogen/turkey
Internet, https://www.iea.org/reports/hydrogen
Internet, https://en.wikipedia.org/wiki/Toyota_Mirai
Lund H., Kempton W., Integration of renewable energy into the transport and electricity sectors through V2G, Energy Policy, Volume 36, Issue 9, 2008, Pages 3578-3587, ISSN 0301-4215, https://doi.org/10.1016/j.enpol.2008.06.007. (https://www.sciencedirect.com/science/article/pii/S0301421508002838)
Meiere I., Bažbauers, G. Sustainability Analysis of Innovative Transport System. Environmental and Climate Technologies. Vol.6, 2011, pp.63-68. ISSN 1691-5208.
Pupo-Roncallo O., Campillo J., Ingham D., Hughes K., Pourkashanian M., Large scale integration of renewable energy sources (RES) in the future Colombian energy system, Energy, Volume 186, 2019, 115805, ISSN 0360-5442,https://doi.org/10.1016/j.energy.2019.07.135. (https://www.sciencedirect.com/science/article/pii/S036054421931477X)
Wang K., Chen S., Liu L., Zhu T., Gan Z., Enhancement of renewable energy penetration through energy storage technologies in a KIGS-based energy system for Chongming, China, Energy, Volume 162, 2018, Pages 988-1002, ISSN0360-5442,https://doi.org/10.1016/j.energy.2018.08.037. (https://www.sciencedirect.com/science/article/pii/S0360544218315573

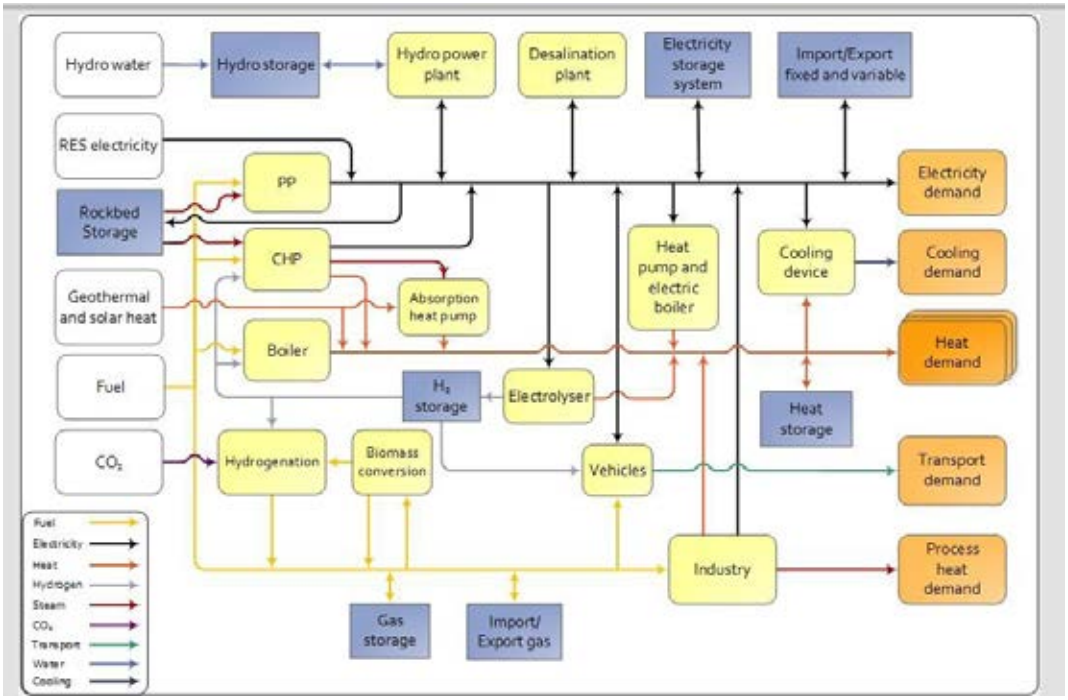


Fig. 1. EnergyPlan Model

Increasing Activation of Aluminum by Alloying with Zn and Sn for Hydrogen Generation

[1*]Sevgin Köymen, [2]Sevim Yolcular, [3]Serdar Karaoğlu
[1] Ege University, Graduate School of Natural and Applied Science, Materials Science and Engineering Department, Bornova, İzmir
[2] Ege University, Engineering Faculty, Chemical Engineering Department, Bornova, İzmir
[3] Ege University, Engineering Faculty, Mechanical Engineering Department, Bornova, İzmir

* E-mail: sevginkoymen@gmail.com

Abstract

There is an increasing need for renewable, clean fuels due to the depletion of fossil fuels and air pollution. Hydrogen, has attracted a lot of attention because it has a high calorific value and is environmentally friendly. Interest in hydrogen production through the aluminum-water reaction has increased in recent years. In many studies, aluminum alloys have been prepared by mechanical ball milling for hydrogen production. In these studies, the effects of alloy composition and preparation process on hydrogen production has been investigated. Prepared alloys show different morphologies due to their different composition and grinding times. Reaction temperature and alkaline solution concentration used are also very important in hydrogen production experiments. Because of their effective hydrogen production capacity, these alloys are expected to become an energy source for future hydrogen supply. This article has been prepared to give information about aluminum (Zn and Sn) alloys and hydrogen production with these alloys.

Keywords: Hydrogen generation, aluminium alloys, Al - Zn and Sn alloys, ball milling.

I. Introduction

Due to the depletion of fossil fuels and with the increasing concern about CO_2 emissions, there is a need for new and sustainable energy sources. Hydrogen has proven to be a promising alternative fuel source due to its high heating value and regeneration capacity by Wang et al. (2009), Preez and Bessarabov (2017). Hydrogen production should be well developed first then the technology can be used in a sustainable, clean, and economical manner.

In recent years aluminum and its alloys are approved to be one of the most suitable metals applicable for future hydrogen production. The metal usage is recognized to be an efficient, user-friendly, and safe approach for hydrogen production by Wang et al. (2009), Preez and Bessarabov (2017).

The biggest problem encountered during this corrosion reaction is the passive oxide or hydroxide layer formed on the Al surface. This passivation can be reduced by controlling several experimental parameters such as temperature, alkali concentration, aluminum morphology and the aluminum raw material used. The use of Al-based alloys also very effective for this purpose.

The selected elements are added to the Al to provide alloys. In the preparation of Al-based alloys some elements such as Zn, Ca, Ga, Bi, Mg, In, Ni, Co, Fe and Sn etc. have been used by by Preez and Bessarabov (2017). These alloys increase the hydrolysis reaction by the formation of nanogalvanic cells and also promote pitting corrosion.

The objective of this work is the production of hydrogen via aluminium alloys (Zn and Sn) and water reaction. This paper aims to give a viewpoint on the existing methods for producing hydrogen using aluminum (Zn and Sn) alloys. Also gives information about the increase in the activity of Al by alloying Zn and Sn.

II. Hydrogen Production

Although hydrogen is abundant on earth as an element, it is almost always present as part of another compound and must be separated into pure H_2 for use in different purposes. Hydrogen can be produced from fossil fuels by steam reforming of natural gas, partial oxidation of methane, and coal gasification. Other methods of hydrogen production include renewable energy sources, such as biomass, wind, solar, geothermal, and hydro-electric power by using a wide range of processes by Wikipedia (2021). In recent years, hydrogen storage by use of chemical hydrides has received much attention and it offers a safe solid-state storage for hydrogen. The physisorption of hydrogen in porous structures, are also investigated. Recently, the use of metals in hydrogen production has been a very interesting subject. In particular metal reactions, hydrogen release can be produced after the contact between reactants also under mild conditions by Wang et al. (2009). Between the different metals, aluminum is the most promising candidate for the purpose of hydrogen production.

III. Al-based Alloys for Hydrogen Production

Al alloys have attracted a lot of attention in recent years. Al has a high energy density of 29 MJ / kg, allowing it to be used as a hydrogen storage material. With low density of aluminum as 2700 kg / m^3, It is the lightest metal among all other used metals. The density of its different alloys is in the range of 2600–2800 kg/m^3. Because of these properties Al alloys have been preferred for hydrogen production. This property helps to the reduction in the total weight of a system. In recent years, studies have increased in terms of aluminum corrosion reactions and hydrogen production. Aluminium and its alloys are usually well protected by a dense oxide layer on their surface. In fact, aluminum-based materials are considered to have good resistance to corrosion. This corrosion resistance can

be a significant advantage for aluminum used as building materials. But this corrosion resistance is the biggest obstacle to realizing continuous hydrogen production through aluminum corrosion. Corrosion processes of aluminium are CO_2 free and environmentally friendly. The by-products of Al corrosion reactions are aluminum oxide $Al2O_3$ and aluminum hydroxide $Al(OH)_3$. They can be used in water treatment, paper making, and fire inhibition. Also, aluminum can be recovered from Al_2O_3 through the Hall–He´roult process. Many different Al-alloys have been prepared and studies have been carried out. Some elements such as Zn, Ca, Ga, Bi, Mg, In, Ni, Co, Fe and Sn etc. have been added to Al in order to prepare Al-alloys by Preez and Bessarabov (2017), Hernández-Torres et al. (2020). In order to satisfy continuous hydrogen generation, metal particles can be used with small sizes. This increases the surface area of metals and then provides continuous hydrogen generation. One of the methods is ball milling. Mechanical properties of metals affect the size reduction formed by ball milling. Milling time is very important in the processes. Prolonged milling can cause decreases in the powder surface area and the oxidation of powders. As a result, with prolonged milling times corrosion resistance of metals increases and inhibits the reaction of metal with water. Hydroxide ions (OH^-) in strongly alkaline solutions are able to destroy the protective oxide layer on the aluminum surface forming AlO_2^-. Aluminum and its alloys are readily dissolved in the alkaline environment even at room temperature, resulting in hydrogen production by Wang et al. (2009). Hydrogen generation performances were investiged with different hydroxides, such as NaOH, KOH, $Ca(OH)_2$ etc. by Porciúncula et al. (2012), Soler et al. (2007).

Al-water reaction with assistance of alkalis:

$$2Al + 6H_2O + 2NaOH \rightarrow 2NaAl(OH)_4 + 3H_2 \quad (1)$$
$$2NaAl(OH)_4 \rightarrow NaOH + Al(OH)_3 \quad (2)$$
$$2Al + 6H_2O \rightarrow 2Al(OH)_3 + 3H_2 \quad (3)$$

The kinetics of the aluminum–water reaction with the addition of NaOH has been extensively studied by different researchers. Reported activation energy for this reaction is in the range of 42.5–68.4 kJ/mol by Porciúncula et al. (2012), Wang et al. (2009).

Zn has a low melting point and highly reacts when alloyed with Al, especially in alkaline solutions. Zn also increases the pitting corrosion of Al alloys. Thus, hydrogen generation rate increases, by Zhang et al. (2018). In their study, the sample with 30 % Sn addition to Al gives the highest hydrogen generation. But, as the Sn content increased to 50 % hydrogen generation speed decreased. In their study, Zn enhances hydrogen generation rate when compared to Fe, Ni, Cu, Mg, and Si. They concluded that, Sn enhances the hydrogen generation by formation of nano galvanic cells. The replacement of Sn with Zn can not enhance the effect of nanogalvanic cells because Zn has lower electrode potential than Sn. The standard potentials of Sn and Zn are -1.36 V and -0.76 V, respectively. The changes in the amounts of Sn and Zn changed the hydrogen generation behaviour. The best reaction rate and yield were achieved in their study for the Al-30wt %Sn-10wt %Zn alloy. Kireche et al. (2014) studied the addition of Zn to Al, and this addition shifted the reaction of pitting corrosion to more electronegative values.

IV. Results and discussions

Aluminum and Al-based alloys can be used in various studies, such as construction, metallurgy, mechanical engineering, transport vehicle industry and in food production of the packaging material industry, etc. Al and Al alloys recently have been used for hydrogen generation.

Al corrosion reaction generates the formation of Al_2O_3 passive film. The Al_2O_3 film is not stable in water, and it become $Al(OH)_3$ by hydration. As a result, the accumulation of the oxide or hydroxide film on the aluminum surface slows the Al corrosion. Then, H_2 evolution also slows and stops by blocking active sites by these films.

There are some methods to remove the protective oxide film. One of them is use of alkaline solutions, NaOH is the much preferred alkaline. Because (OH^-) ions help to remove the protective oxide film. The other is use of salt or salt solutions, NaCl solutions preferred for this purpose. Chloride ions (Cl^-) cause the pitting corrosion of aluminium in aqueous solutions by removing the surface oxide film. Another method is ball milling, which activates the alloy powders to remove this film during the reaction. Alloying of Al is also used for activation purposes to remove this oxide film. Alloying with ball milling gives very good results for hydrogen generation.

Alloying elements make aluminium more active. Cu, Ga, Sn, Zn, Si, Mg, Hg, In, Mn etc. can be added to Al. By the addition of these alloying elements which are less active than Al, corrosion potential of alloy increases. Si, Cu and Mn are nobler than aluminum, by the addition of them corrosion potential increases. Zn and Mg are more active than aluminum and by the addition of them the corrosion potential of the aluminium alloys decreases.

With the addition of elements such as, Hg, In, Ti, Ga, Zn or Sn, the pitting potential of Al is shifted to more negative values which allows a us of the alloy, as anode materials in batteries or cathodic protection systems for underwater installations. Since if there is no activator, the corrosion potential would be – 75 mV which is inadequate to ensure cathodic protection. These elements are added to create more electronegative potential of the anode and improve its performance. Then they remove the passivation layer from the surface of the aluminum by Kireche et al. (2014).

With the addition of Zn and Sn they are present at the grain boundaries and this cause the intergranular corrosion. Passive behavior is observed with pure Al and Al–Zn alloys, however Al–Zn–Sn alloys exhibit no passive region. The addition of Zn and Sn produces a significant activation of aluminum. This activation caused by the shift of the corrosion and pitting potentials to more electronegative values. The degree of activation depends on the

element and its proportion in the alloy. It increases by increasing amounts of Sn addition to Al-5Zn alloy by Kireche et al. (2014).

In the study of Munoz et al. (2002), they found that the presence of Zn facilitates a surface In enrichment by a displacement reaction. This, facilitates Cl^- adsorption and its surface enrichment at potentials more positive than -1.1 V. This surface condition promotes and maintains the activation of Al. This assures an accumulation of adsorbed Cl^- which maintains an active state of the Al matrix. The presence of In at the bare Al surface favours chloride adsorption, so avoiding repassivation.

In the study of Shayeb et al. (1999), Al-Sn alloy exhibits an active behaviour compared to that of pure Al. The pitting potential takes more negative value than pure Al and a recognizable reduction of the passive region is observed. This behaviour is attributed to the presence of Sn as an alloying element leading to an electrochemical activity of the alloy. They concluded that the mechanisms of film breakdown of pure Al, Al-Zn, and Al-Zn-Sn alloys are similar. Defect centers affect the initiation step by deposition of In at these defect centers which cause the adsorption of Cl^- at more negative potentials.

V. Conclusions

Hydrogen production with Al-based alloys has gained importance in recent years. Various studies have been carried out with many different alloying elements. Each element has been shown to have different effects. In this study, the effects of Zn and Sn elements were investigated. The addition of alloying elements such as Zn and Sn brings more defects and prevents the formation of a protective oxide film on the alloy surface. This ensures uniform dissolution of the anode, prevents passivation and improves its performance. Aluminum corrosion occurs through pitting corrosion, and it is well known that pitting corrosion occurs due to the transition of ions through the passive oxide film in regions of microstructural defects. The addition of Zn and Sn increases the activation of aluminium. This activation occurs because the corrosion and pitting potentials shift to more electronegative values. The degree of activation depends on the element added and the proportion of element in the alloy. The addition of Sn leads to an electrochemical activity of the Al-Sn alloy and this leads to active dissolution of Al due to the change in the chemistry of the film. Pitting potential gets more negative value than pure Al and passive region decreases. Consequently, Al-based alloys with Zn and Sn show a high activity compared to pure Al. Hydrogen production of Al alloys can be improved not only by lattice strain and lattice defects, but also by selection of suitable alloy additives.

Acknowledgements

This research was supported by GKE Energy. These supports are gratefully acknowledged.

References

Wang H.Z., Leung D.Y.C., Leung M.K.H., Ni M., A review on hydrogen production using aluminum and aluminum alloys, Renewable and Sustainable Energy Reviews, 13, 845–853, (2009).

Porciúncula C. B., Marcilio N. R., Tessaro I. C. and Gerchmann M., Production of hydrogen in the reaction between aluminum and water in the presence of NaOH and KOH, Brazilian Journal of Chemical Engineering, 29 (02), 337 – 348, (2012).

Soler L., Macanás J., Muñoz M., Casado J., Aluminum and aluminum alloys as sources of hydrogen for fuel cell applications. J. Power Sources, 169, 144-149, (2007).

Preez S.P. du, Bessarabov D.G., Hydrogen generation of mechanochemically activated Al-Bi-In composites, International Journal of Hydrogen Energy, 42, 16589-16602, (2017).

Hernández-Torres A. G., López-Miranda J.L., Santos-Ramos I., Rosas G., Hydrogen generation performance of Al–20at%Ca alloy synthesized by mechanical alloying, AIMS Materials Science, 7(2): 144–156, (2020).

Zhang F., Edalati K., Arita M., Horita Z., Hydrolytic hydrogen production on Al-Sn-Zn alloys processed by high-pressure torsion. Materials, 11, 1209- 1226, (2018).

Khireche S.; Boughrara D.; Kadri A.; Hamadou L.; Benbrahim N., Corrosion mechanism of Al, Al-Zn and Al-Zn-Sn alloys in 3 wt. % NaCl solution. Corros. Sci., 87, 504–516, (2014).

Munoz A.G., Saidman S.B., Bessone J.B., Corrosion of an Al–Zn–In alloy in chloride media, Corrosion Science, 44 2171–2182 (2002).

El Shayeb H. A., Abd El Wahab F. M. and Zein El Abedin S., Electrochemical behaviour of Al, Al-Sn, Al-Zn and Al-Zn-Sn alloys in chloride solutions containing indium ions, Journal of Applied Electrochemistry 29, 473-480, (1999).

Wikipedia, Hydrogen production, https://en.wikipedia.org/wiki/Hydrogen_production, received: April 1, 2021.

Hydrogen Economy In The Light Of Europe's Green Deal Plan And Green Jobs Opportunities

[1*]Erhan Atay, [2]Sudi Apak

[1]Trakya University, Economics Dept, 22800, Edirne/Türkiye
[2]Istanbul Esenyurt University, Ind. Eng. Dept,34500 Istanbul/Türkiye

* E-mail: erhanatay@trakya.edu.tr, sudiapak @esenyurt.edu.tr

Abstract

Nowadays, hydrogen is an environmental friendly energy but it is expensive to produce .According totheEuropean Green Deal ,EU aims zero greenhouse gas emissions by 2050. In addition, new business areas will emerge with the green economy, which is the fundamental building block and strategy of sustainable development.
Therefore, green jobs and skills will be attractive in the worldwide. In a sense, this means closing the "blue collar" era and opening the "green collar" era in the 21th century. Because the "green economy" will open new business initiative and breakthrough doors to young people.
Paper aims to show the importance of some professions will come to the the green economy for the innovative employment as well as renewable industries especially hydrogen economy for the future generations.

Keywords:" Green job and skills,hydrogen economy,European Green Deal,renewable energy."

I.Introduction

The demand for energy increases as the quality of human life evolves and is essential for daily life.On the other hand, unfortunately as of today sea levels are likely to rise drastically due to climate change.
As the new USA administration develops both a renewable energy perspective and final social cost of carbon estimate, what factors will be most important to consider? Steel companies are committing to deep decarbonization. Can hydrogen-based technologies help them ?
We can answer this question that the largest steel manufacturers in the world such as , China's Baowu, and Japan's Nippon Steel all have committed in recent months to achieve net-zero emissions by 2050. Details about how these companies will decarbonize the notoriously emissions-intensive steel industry remain sparse for now, but steelmakers have increasingly looked to decarbonized hydrogen as a promising alternative.
In this regard, the USA aims to decarbonize the power sector by 2035, an ambitious goal that has been made easier by the long-term decline of coal. There's a big opportunity for the new administration just because the electricity sector is getting cleaner on its own.
The outline of the paper is as follows. Section 2 sets up Hydrogen economy and European Green Deal Plan while section 3 deal with green jobs and skills .Finally last section is conclusion.

II. Hydrogen Economy and European Green Deal Plan

For sustainable development, hydrogen can be an intrinsic energy carrier to an energy system that uses renewable resources, thereby enabling a complete replacement of the fossil fuels systems.
Accordingly,our planet has gone through quite frequent warming and cooling cycles. Today, it is a very common attitude to explain almost everything with climate change, but in fact, the todays climate is in situation of revolution as it has never remained impatient, so every event in history has occurred at the same time as a climate change. Harari (2015)
The economies that emerge will depend on hydrogen and will be called hydrogen economies.Concerns about the health costs associated with air, water, soil pollutions, and global climate change and the desire to achieve sustainable development have created interest in as a fuel.Pahwa (2014). On the other hand, instead of focusing on CO2, we should focus our attention on the incredible amount of water vapor released into the atmosphere from the cooling towers of power plants and the burning of hydrocarbons such as coal, natural gas and oil. Moreover, we must be wary of the fact that a hydrogen-based economy that will release significant amounts of water vapor into the atmosphere will further heat our planet. Sinn (2016).
EU 's Renewable Energy and European Green Deal Plan :
Renewables accounted for a larger share of electricity than fossil fuels in Europe for the first time ever last year, due in no small part to the EU's Renewable Energy Directive, which required member states to supply at least 20 percent of energy from renewable sources by 2020. But the directive has been a source of contention among some environmentalists due to its classification of forest bioenergy as carbon neutral.

The EU's regulations to combat climate change, the incentives it provides and the steps it wants to take continue with the European Green Deal after the Paris Agreement. Its aims to transform EU countries and citizens in a fair and competitive environment with zero greenhouse gas emissions by 2050.
The basic EU regulations on the subject can be listed as follows:
1. EU emissions trading system **2**.Member states' targets for non-emission trade sectors
3. Contribution of forests and lands to combating climate change
4. Reducing greenhouse gas emissions in transport
5.Energy efficiency and renewable energy investments
6.Supporting low carbon technologies
7. Stage reduction of fluorinated greenhouse gases
8. Protection of the ozone layer
9. Preparing for the effects of climate change
10. Climate change investments **;** EU Com **(**2019**).**

III. Green Jobs and Skills: Towards Low Carbon Economy
Defining the economy as "an economy that reduces environmental risks and ecological scarcity and aims at sustainable development without destroying the environment". The idea of limiting the use of fossil fuels (coal, oil, natural gas) and focusing on renewable energy hydrogen (wind, water, geothermal, biomass and solar energy) sources lies behind the green economy idea that suggests low carbon use.
According to the economists R. Gordon, the growth rhythm in production per capita is doomed to slow down gradually in the most developed countries, especially in the US, and is likely to hover below 0.5% per year between 2050 and 2100. It is impossible for a 1.2% increase unless new energy sources are used instead of rapidly depleting hydrocarbon energy resources. Piketti (2015).
Green economy can be implemented in key sectors of the economy such as renewable energy, research-development, construction, transportation, industry, agriculture and forestry. In low-carbon and sustainable economies, jobs such as the installation of solar panels, bio-fuel and hybrid vehicle production, organic agriculture, insulation, and the construction of giant wind turbines, which provide protection from the environmental quality and protection of the eco-system, are also called green jobs. It is estimated that roughly 2.3 million people have been employed in green jobs in recent years worldwide.
In this context , training, planning and training of competent personnel in environmentally sensitive, future-oriented areas defined as "green jobs" is also a serious investment and development area. From now on we will talk more about "green collar".
We are sure that we will hear new professions we have not heard of such as solar panel and wind turbine assembly technician, drone and electric vehicle engineer, operator in renewable energy facility, sustainability officer, recycling plant technician, environmental scientist, nature observer, smart network manager etc.
Some existing professions will evolve and turn green. In this sense, there will be changes in the course and curriculum at the higher education level. We hope that investing in a greener, more inclusive recovery can also be a strategy for tackling the unemployment crisis as a result of the todays pandemic.

IV. Conclusions
We have to act now to save our planet from climate change hazard. We are not ready to solve the clime change problem immediately. Climate literacy is essential for the modern oil and gas industry. Companies need to immediately share aspirations with the public for a decarbonizing energy future.
Today,conventional technologies does not automatically equate to a leading position for hydrogen technologies in the future. For example, if a country has the current manufacturing capacity to construct conventional internal combustion engines, this does not necessarily mean that it will also have a relevant industry for stack production in the future, owing to the technological differences between the technologies.
In this context, there are two alternative scenarios were developed to take this into account. The ‘pessimistic scenario’ shows what could happen if other regions of the world assume the leading position and Europe has to import hydrogen vehicles. In this scenario, it was assumed that all hydrogen-vehicle technology will be imported.In contrast, the ‘optimistic scenario’ assumes that major efforts will be undertaken,which result in increased EU exports in hydrogen vehicles and technologies. Indeed, it is supposed that hydrogen vehicles, as well as stacks and hydrogen production technology, could be exported even more than conventional technology.See.Wietschel,& Ball. (2009).
In this regard ,we can offer “energy communities” in environmental remediation efforts, which could offer support to oil and gas workers who are struggling amid a transition to clean energy.At the same time, fossil fuel companies should rethink their opposition to the administration’s efforts to boost clean energy such as hydrogen. Rather than continue to opp ose the inevitable, they should ride the wave of green innovation that will be the hallmark of the twenty-first century.
Finally, governments must stimulate the necessary courses with public sector jobs and subsidised green jobs in the private sector, through tax incentives, with the best minds attracted to a green transformation.

References

European. Commission (2019). (Accession date: 22 Oct. 2020) ,(2019).
Harari,YN . Sapiens:A Brief History of Humankind, (2015).
Pahwa, P. K., and G. K. Pahwa Hydrogen Economy. The Energy and Resources Institute,.(2014) Piketty,T Capital in the 21 th century, (2015).
Sinn, WH .Green Paradox: Supply side approach to the global warming, (2016).
Wietschel, M; Ball, M.The Hydrogen Economy Opportunities and Challenges Cambridge, UK : Cambridge University Press, (2009).

Design and Economic Optimization of PV/Wind/Hydrogen Hybrid Power System

[1]Duygu Kemeriz Özkök, [1]Yağmur Budak, [2]Serkan Eryılmaz, [3*]Yılser Devrim
[1] Atılım University, Faculty of Engineering, Mechanical Engineering, Kizilcasar Mahallesi, Incek Golbasi Ankara, 06836, Turkey
[1] Atılım University, Faculty of Engineering, Industrial Engineering, Kizilcasar Mahallesi, Incek Golbasi Ankara, 06836, Turkey

* E-mail: yilser.devrim@atilim.edu.tr

Abstract
In this study, design and optimization of a Photovoltaic/WindTurbine/Electrolyzer/Proton Exchange Membrane Fuel Cell (PV/WT/Electrolyzer/PEMFC) hybrid power system was examined to supply continuously electrical load demand. The proposed hybrid system with PEMFC was preferred to supply continuous production of electric energy throughout the year. The Transient System Simulation Program (TRNSYS) and MATLAB were combined to design and optimization of proposed hybrid system. The obtained results show the proposed hybrid power system provides an applicable option for powering stand-alone application in a self-sustainable expedient.

Keywords: Photovoltaic, Hybrid energy systems, Techno-economic analysis, Wind energy, Fuel cell

I. Introduction

Renewable energy sources become important as global warming increases and fossil fuel resources are exhausted (Fay & Golomb, n.d.). Clean energy sources such as sunlight, wind, geothermal energies and hydro energy are renewable energy sources. The endless source of sun and wind makes renewable energy more important day by day. In addition, the reduction in foreign dependency also increases the importance of renewable energy sources. Our country has a very efficient position in terms of both solar radiation and wind potential. This makes electricity production from solar energy and wind energy more important. However, low energy conversion efficiencies reduce the availability of renewable energy. Failure to produce electricity from solar energy in the evening also causes interruptions. Therefore, solar and wind energy systems integration are used as complementary systems. Rather than using a single renewable energy source, the use of the hybrid system is both more advantageous in terms of cost and more advantageous in terms of efficiency (Karabanov et al., 2010). Another problem that can be encountered in renewable energy sources is storage. As known, the batteries used in solar energy do not make seasonal storage. This indicates that over-produced electricity cannot be used. Therefore, hydrogen energy is activated as an alternative energy source. Storing energy in the form of hydrogen creates solutions for both daily and seasonal storage. Fuel cells are also a source that converts the chemical energy generated by hydrogen into electrical energy in this system. Fuel cells integrated into the solar-wind system are also an alternative solution to increase energy conversion. There are six types of fuel cells. Of these, the proton exchange membrane fuel cell is the most attractive due to its quiet operation and lower corrosion, high power density, low local emissions, low operating temperatures, so they can be operated with PEM fuel cell for hybrid systems with photovoltaic panels and wind turbines (Devrim & Bilir, 2016).The main novelty of this study is the preparation of MATLAB models of the PEM electrolyzer and PEMFC according to experimental data and then integrate into TRNSYS to examine the transient behavior of the proposed hybrid system over a year.

II. Experimental Set-Up and Procedure

The system was simulated according to the weather data obtained from Atilim University. Weather data were transferred to photovoltaic panels and wind turbine using Type 16c. PEM electrolyzer and PEMFC were designed via MATLAB according to previous study (Budak & Devrim, 2019). The design code, which is written in MATLAB has been integrated to TRNSYS. Thanks to the electricity generated from the panels and the turbine, the electricity requirement of the designed electrolyzer was met. The water separated as hydrogen and oxygen was stored in tanks by increasing its pressure by means of compressors. The PEMFC, designed with the specified parameters through MATLAB, was used when

needed by converting chemical energy into electrical energy. The proposed system design is given in Figure 1.

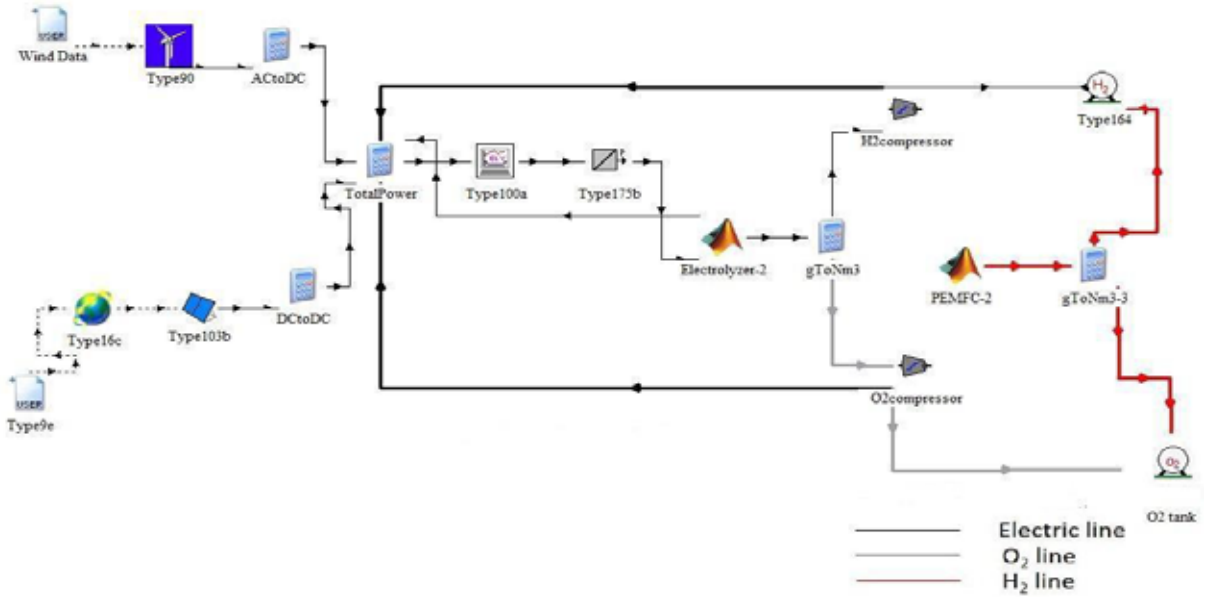


Fig. 1: Simplified hybrid system design at TRNSYS Software

III. Analysis

Weather data were measured according to the location of Atilim University. These data were transferred to TRNSYS. Radiation and wind graphs according to the data transferred are shown in Figure 2.

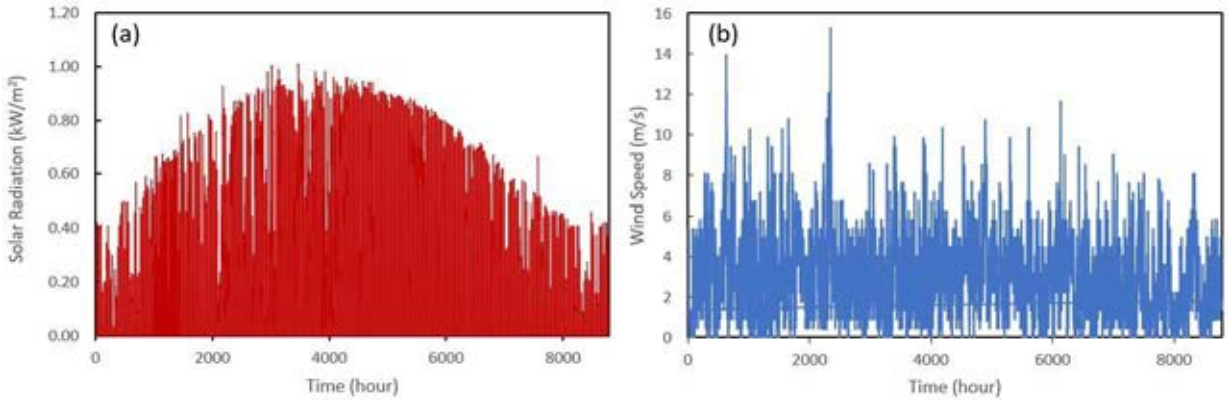


Fig. 2: a) Hourly global horizontal solar radiation and b) Hourly wind speed data for Atilim University

IV. Result and discussions

To obtain long term interrupted energy storage, a part of the produced excess energy can be converted using the PEM electrolyzer to H_2. In the designed hybrid system, there must be sufficient H_2 gas tank for PEMFC. In the initial designs, the uninterrupted operation of the hybrid system throughout the year was investigated using PV, WT and PV/WT when the gas tanks were initially almost empty (~1 m^3). As a result of the analysis, it was determined that a numerously PV and WT are required to ensure sufficient H_2 production from electrolyzer, especially in months when solar and wind data are low. Results show that the fluctuating nature of both solar radiation and wind speed affects the output of the simulation. Table 3 shows the optimum value chosen for uninterrupted power supply. The power values produced PV and WT and store H_2 throughout the year taken from TRNSYS software are given in Figure 3 and Figure 4, respectively.

Tab. 3:Simulation of hybrid system for 25 kWh PEMFC power output

Case	Number of WT	Number of PV	Initial H_2 tank level(m^3)	Initial O_2 tank level(m^3)	Total Generated Energy(MWh)
1	1	85	15	12	40.7

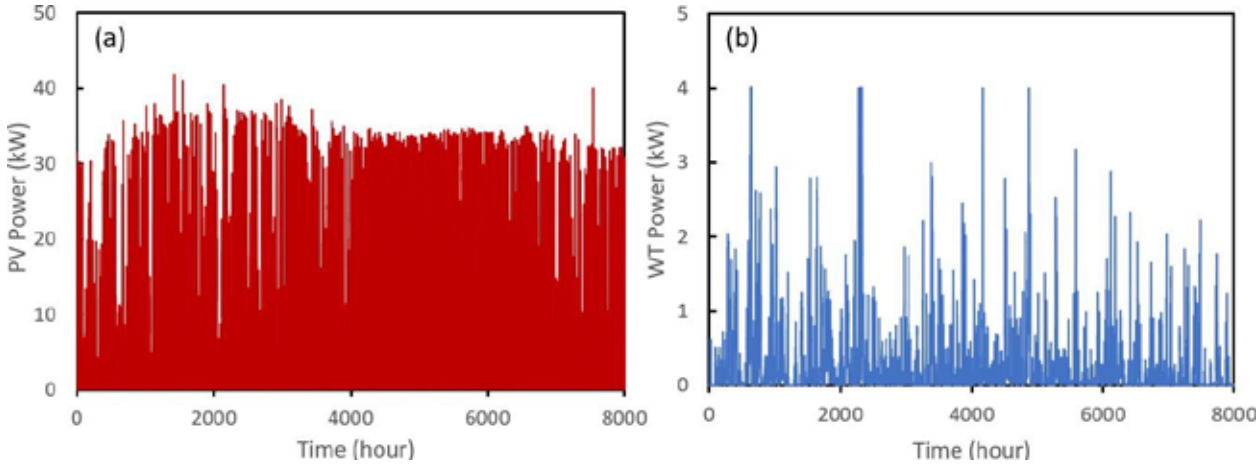


Fig. 3: TRNSYS Simulations results a) generated power from PV b) generated power from WT throughout the year.

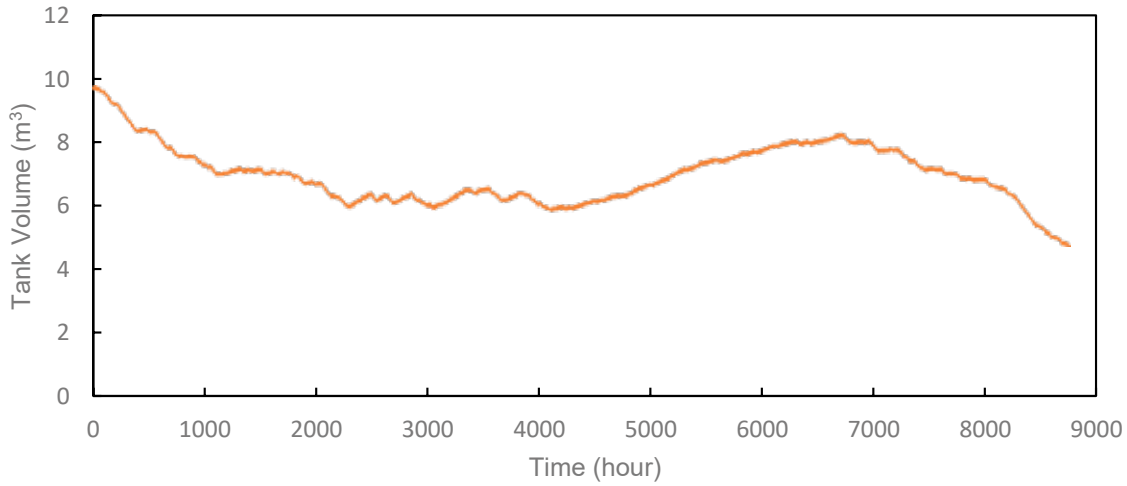


Fig. 4: TRNSYS Simulations results of store H_2 throughout the year.

V. Conclusions

In this study, H_2 production from PV/WT/Electrolyzer/PEMFC hybrid power system and optimum design of a system based on PEMFC has been investigated. In order to meet the energy needs of Atilim University without interruption, 12-month system simulations were carried out in different scenarios considering the LCOE value.

V. Acknowledgements

This work was supported by The Scientific and Technological Research Council of Turkey (TUBITAK) under project TUBITAK 1001-119F182.

References

Budak, Y., & Devrim, Y. (2019). Comparative study of PV/PEM fuel cell hybrid energy system based on methanol and water electrolysis. Energy Conversion and Management, 179(August 2018), 46–57. https://doi.org/10.1016/j.enconman.2018.10.053

Devrim, Y., & Bilir, L. (2016). Performance investigation of a wind turbine–solar photovoltaic panels–fuel cell hybrid system installed at İncek region – Ankara, Turkey. Energy Conversion and Management, 126, 759–766. https://doi.org/10.1016/j.enconman.2016.08.062

Fay, J. A., & Golomb, D. S. (n.d.). Energy and the Environment.

Karabanov, S., Kukhmistrov, Y., Miedzinski, B., & Okraszewski, Z. (2010). Photovoltaic systems. In Proceedings - International Symposium: Modern Electric Power Systems, MEPS'10. https://doi.org/10.1016/b978-0-12-397270-5.00009-1

Ozgirgin, E., & Albostan, A. (2015). ScienceDirect Modeling and simulation of a hybrid photovoltaic (PV) module-electrolyzer-PEM fuel cell system for micro-cogeneration applications. 0, 2–8. https://doi.org/10.1016/j.ijhydene.2015.06.122

Peat Based Microbial Fuel Cells and Limiting Parameters

[1*]Ahmet Erensoy, [2]Sefa Mulayim, [3]Ayhan Orhan, [4]Nurettin Çek, [5]Namık Ak
[1] Fırat University, Faculty of Medicine, Department of Parasitology, Elazıg, 23119, Turkey
[2] Fırat University, Faculty of Medicine, Department of Parasitology, Elazıg, 23119, Turkey
[3] Fırat University, Faculty of Technology, Department of Metallurgical and Materials Enginering, Elazıg, 23119, Turkey
[4] Mersin University, Institute of Science, Department of Metallurgical and Materials Engineering, Mersin, 33343, Turkey
[5] Karamanoğlu Mehmetbey University, Faculty of Engineering, Department of Energy Systems Engineering, Karaman, 70200, Turkey

* E-mail: aerensoy@firat.edu.tr

Abstract

The production and work of microbial fuel cells highlight a multidisciplinary field including various engineering, materials sciences, and microbiology. The use of the microbial fuel cell as an alternative source for bioenergy production is considered a renewable, non-toxic, reliable, clean and efficient process. Microbial fuel cell provides numerous opportunity to improve sustainable applications in varied sites, ranging from industrial to home. The low power output of microbial fuel cells is one of the important factors that hinder their commercialization. Therefore, power outputs must be improved to contribute to the commercialization of microbial fuel cells. In this study, organic peat material was used as a substrate for a double chamber MFC. In addition, since it was seen that *Clostridium* bacteria were present in the structure of organic peat material, no additional bacterial strain was used. In this MFC application where graphite is used as both anode and cathode electrodes, 1 mol/L NaOH solution was used as the cathode chamber solution. This peat-based MFC provided the highest electrical power density of 438.116 mW/m^2. The most important limiting factor of the peat-based MFC was the spreading of the NaOH solution throughout the cell due to the rupture of the proton exchange membrane after 9 hours of operation.

Keywords: Peat, Microbial fuel cell, Bioelectricity, Microorganism

I. Introduction

The renewable and sustainable energy production process contains studies on protecting nature and also keeping nature alive for longer. In particular biomass energy, which generated from living things and their residues, is a renewable and sustainable energy source that allows it to be recycled to nature (Çek (2016); Kumar and Senthilkumar (2020)). The Microbial fuel cell (MFC) is one of the most recently developed bio-electrochemical devices that convert biomass-based resources into electrical power. Currently, the commercialization of microbial fuel cells is still not considered reliable due to their low power density, short durability, and high cost (Liew et al. (2020)).

MFCs; it is described as environmentally friendly, renewable, bio and green energy production tools that convert the bio-electrochemical energy of organic materials with different structures such as glucose, acetate, butyrate, lactate, ethanol, compost, sediment into electrical energy directly through the catalysis reactions of bacteria (Tee et al. (2018); Çek and Erensoy (2020)). Considerable efforts have been made to optimize various operational factors such as electrode type, catalyst material, wastewater conditions, bacterial cultures, and substrate concentration to improve the performance of MFCs (Choi et al. (2020); Çek and Erensoy (2020)). Various alternative organic materials are being investigated to increase the electrical power output of MFCs. In recent studies, organic biomass-based materials such as poplar wood, sediment, and compost have been investigated as a suitable substrate for MFCs (Çek (2017); Erensoy and Çek (2018); Çek and Erensoy (2019)). However, since these materials are not widely used commercially, they are difficult to obtain and have a low cost.

Organic materials called peat are anaerobic environments formed by the accumulation of organic materials as a result of the decomposition of plants due to excess water (Tolunay (2007)). Peat, which has both good organic matter content and high bacterial count, is one of the most used plant growing and soil regulators in the world and its use is constantly increasing (Tolunay (2007); Kadıoğlu and Canbolat (2019)). Therefore, we thought peat would be a suitable substrate for the commercialization of MFC. In this study, a double-chamber MFC was manufactured and peat-based MFC was manufactured using peat as substrate in the anode chamber, sodium hydroxide (NaOH) in the cathode chamber, and graphite as the electrode. The working principle of this MFC and the limiting factors of this MFC has been demonstrated by experimental works.

II. Experimental Set-up and Procedure

The plastic container (288 mL) was used as MFC reactor, and it separated from the middle as an anode chamber and cathode chamber with the proton exchange membrane (PEM). A graphite cylinder rod was used as both anode electrode and cathode electrode. The peat material with a rich organic material content was placed in the anode chamber, the peat served as the substrate. Biochemical reactions were initiated by adding water to the peat. Since there were *Clostridium* bacteria in the structure of the peat thus extra other bacteria were not used. In previous studies, it has been reported that the high pH values of the solution in the cathode chamber increase the electrochemical performance of MFCs (Gajda et al. (2015); Zhang et al. (2019)). Therefore, 1 mol/L sodium hydroxide (NaOH) was used as the cathode chamber solution in this study as described in previous studies (). In order to meet the oxygen demand of the graphite cathode electrode, a 5 mm hole was opened in the cathode

chamber and it was contacted with air. All processes were completed step by step and the peat-based MFC was manufactured. The schematic diagram and working principle of this peat-based MFC is given in Fig. 1.

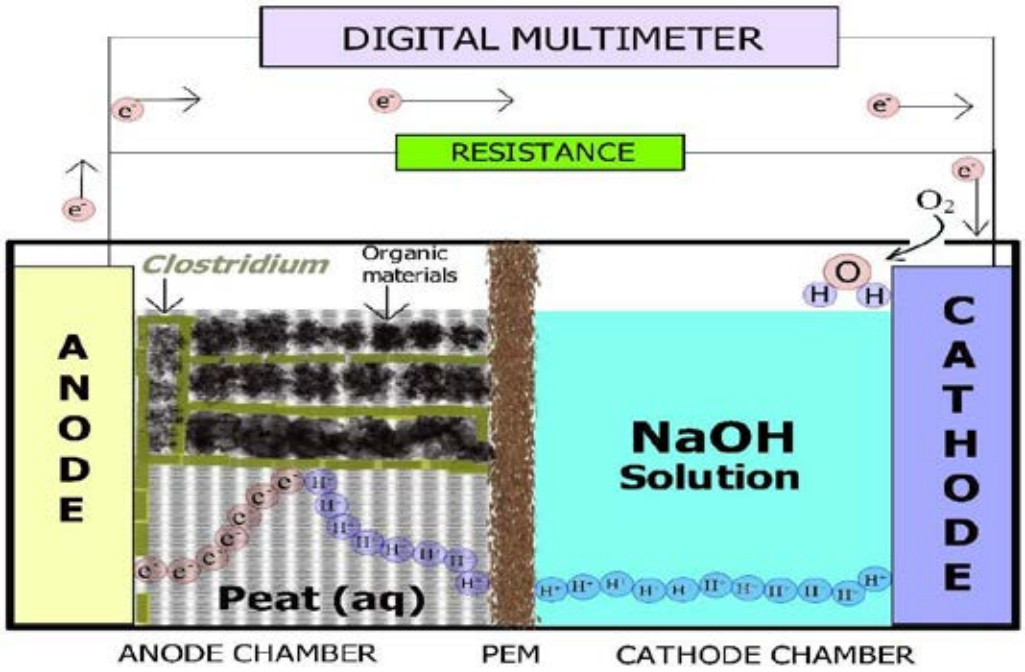


Fig. 1: Schematic presentation of experimental installation

III. Analysis

After the peat based MFC was installed, the open circuit voltage (OCV) value was measured hourly with a multimeter device. During the time period when the OCV value was constant, measurements were made with a multimeter as in previous studies, the current was calculated based on the voltage (voltage (V)) on the external resistor and recorded using a computer-based data acquisition system. Current density (i), power and power density (Pd); the voltage was expressed using equation (1), equation (2) and equation (3), respectively, based on the active surface area (A) of the cathode and the external resistance (R).

$$i=\frac{V}{R.A} \quad (1)$$

$$P=i.V \quad (2)$$

$$Pd=\frac{P}{A} \quad (3)$$

The internal resistance (R_{int}) was calculated using equation (4).

$$R=\sqrt{\frac{(OCV)^2 xRext}{Pdmax}}-Rext \quad (4)$$

The peat material was watered and kept in a closed container for 6 hours, and then examined with an optic microscope.

IV. Results and discussions

While the OCV value provided by the peat-based microbial fuel cell was 280 mV at the beginning, it fell sharply to 110 mV in the first 2 hours. The decrease in the OCV value continued at the 3rd hour and fell to its lowest value with 53.2 mV at the end of 4 hours. By 6 hours the OCV value started to rise again and remained constant until the end of 9 hours, providing a constant OCV of 92 mV from 7 hours. Polarization and power curves of peat-based microbial fuel cells were formed during the time period when constant OCV value was achieved. While creating the polarization curves, external resistors between 0-1000000 Ω were connected on the outer circuit and the voltage measurement on each resistor was made using a multimeter device with 10 minutes intervals. The power and power density of the MFC was calculated by applying equation (2) and equation (3) to the voltage and current values that form the polarization curves. The maximum power density of the peat-based MFC was 438,116 mW/m^2. The internal resistance of the peat-based microbial fuel cell was calculated as 1001.13 ohm. By decreasing this internal resistance value, the electrical power output of peat-based MFCs can be increased. The peat material in this study contains *Clostridium* bacteria in its structure. *Clostridium* bacteria show in Fig.2 were examined using a light microscope at 40X and 100X magnification. Thanks to the microscope, properties such as length, width, and diameter of bacteria can be measured at 40X magnification. As stated in previous studies, *Clostridium* bacteria in

this study are 1.6-20 µm long, 0.5-2 µm wide and survive in anaerobic (oxygen-free) environments (Orhan et al. (2020)). As a result of the puncture of the PEM in the peat-based MFC, the mixing of the NaOH solution in the cathode chamber with the anode chamber, it was clearly understood that the electrochemical performance of *Clostridium* bacteria decreased and the growth of bacteria was limited.

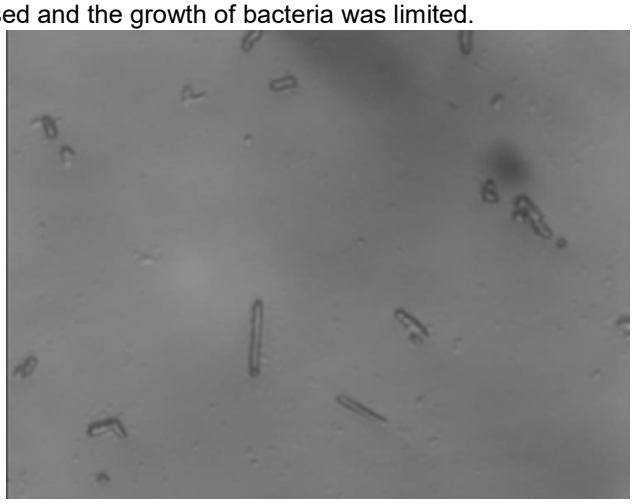


Fig. 2: Microscope images of *Clostridium* bacteria in peat structure

V. Conclusions

The biggest limiting factor for the peat-based microbial fuel cell was PEM. Because PEM was pierced at the end of 9 hours of operation. This study provided the infrastructure to determine the properties of the tested peat-based microbial fuel cell and to switch the microbial fuel cell to commercial applications. The increase in power output compared to the peat-based microbial fuel cell and microbial fuel cells that use other organic materials as substrate is an important step in the commercialization of microbial fuel cells. Because peat is an organic material that can be obtained easily and is now used commercially in various applications.

Acknowledgements

We would like to thank Koç Holding, Arçelik, and Tüpraş for the help of experimental instruments.

References

Choi, Y. J., Mohamed, H. O., Park, S-G., Al Mayyahi, R., Al-Dhaifallah, M., Rezk, H., Ren, X., Yu, H., Chae, K-J. Electrophoretically fabricated nickel/nickel oxides as cost effective nanocatalysts for the oxygen reduction reaction in air-cathode microbial fuel cell, International Journal of Hydrogen Energy, 45, 5960-5970, (2020).

Çek, N. Parçacıklar ve Enerji Kaynakları, Lambert Academic Publishing, Germany (2016).

Çek, N. Examination of Zinc Electrode Performance in Microbial Fuel Cells, Gazi University Journal of Science, 30, 395-402, (2017).

Çek, N. Erensoy, A. Kompost Mikrobiyal Yakıt Hücreleri İçin Titanyum Elektrot Performansının İncelenmesi, European Journal of Science and Technology, 17, 909-915, (2019).

Çek, N. and Erensoy, A. Yakıt Hücresi Teknolojilerinde Gelişmeler, Nobel Academic Publishing, Turkey (2020).

Erensoy, A. and Çek, N. Alternative Biofuel Materials for Microbial Fuel Cells from Poplar Wood, ChemistrySelect, 3, 11251-11257, (2018).

Gajda, I., Greenman, J., Melhuish, C., Santoro, C., Li, B., Cristiani, P., Ieropoulos, I. Electro-osmotic-based catholyte production by Microbial Fuel Cells for carbon capture, Water Research, 86, 108-115, (2015).

Kadıoğlu, B., Canbolat, M. Y. Farklı yetiştirme ortamlarında bazı bakterilerin buğday ve mısır gelişimi üzerine etkisi, Toprak Bilimi ve Bitki Besleme Dergisi, 7, 139-148, (2019).

Kumar, M. N., Senthilkumar K. Captivating Technology for Generation of Bioenergy from Industrial Waste: Microbial Fuel Cell, Biomass Valorization to Bioenergy. Energy, Environment, and Sustainability, pp-85-96. Eds: R. Praveen Kumar, B. Bharathiraja, R. Kataki, V. Moholkar, Springer, Singapore (2020).

Liew, K. B., Leong, J. X., Daud, W. R. W., Ahmad, A., Hwang, J. J., Wu, W. Incorporation of silver graphene oxide and graphene oxide nanoparticles in sulfonated polyether ether ketone membrane for power generation in microbial fuel cell, Journal of Power Sources, 449, 1-10, (2020).

Orhan, A., Ak, N., Erensoy, A., Çek, N. Betonda Bazalt Agreganın Kullanımı ve Özellikleri, European Journal of Science and Technology, 19, 524-532, (2020).

Tee, P. F., Abdullah, M. O., Tan, I. A. W., Amin, M. A. M., Nolasco-Hipolito, C., Bujang, K. Bio-energy generation in an affordable, single-chamber microbial fuel cell integrated with adsorption hybrid system: effects of temperature and comparison study, Environmental Technology, 39, 1081-1088, (2018).

Tolunay, D. Peyzaj Uygulamalarında Torf Kullanımı ve Torfların Genel Özellikleri, Bitki Üretiminde Kullanılan Ortam (Toprak) Materyalleri, İstanbul Ağaç ve Peyzaj A. Ş. Yayını, pp. 103-120, İstanbul, (2007).

Zhang, Y., Zhao, Y-G., Guo, L., Gao, M. Two-stage pretreatment of excess sludge for electricity generation in microbial fuel cell, Environmental Technology, 40, 1349-1358, (2019).

Co nanoparticle on TiO_2 mesh support for sodium borohydride hydrolysis to generate hydrogen

[1*]V.G. Minkina, [1]S.I. Shabunya, [1]V.I. Kalinin, [2]C.Tuc Altaf,[2**]N. Demirci Sankir
[1] A.V. Luikov Heat and Mass Transfer Institute of the National Academy of Sciences of Belarus,
P. Brovka, 15. Minsk, 220072 Republic of Belarus
[2] TOBB University of Economics and Technology, Department of Materials Science and Nanotechnology Engineering,
Sogutozu C No 4306560 Sogutozu, Ankara, Turkey

* E-mail: minkina@dnp.itmo.by ** E-mail: nsankir@etu.edu.tr

Abstract
In this work, isothermal and nonisothermal hydrolysis reaction of sodium borohydride ($NaBH_4$) has been investigated in the presence of Co nanoparticle on TiO_2 (325 mesh) support as a catalyst which was proven to be good reproducibility upon repeated use. The volume of H_2 generation has been detected as 3500 ml from $NaBH_4$ hydrolysis in the thermostat at room temperature.

Keywords: Co-TiO_2 catalysts; sodium borohydride; hydrolysis; hydrogen

I. Introduction

Metal hydrides such as $NaBH_4$ are considered as one of the most promising sources for hydrogen production (Minkina, 2016). In the hydrolysis of $NaBH_4$, which is the most popular candidate in metal hydride derivatives with a hydrogen content of ~10.8 wt. %, hydrogen and sodium metaborate (water-soluble side product) are generated as products. This hydrolytic reaction requires a suitable catalyst to proceed at a practical rate. Although the noble metal catalysts (Ru, Rh, Pt) have been proven to be highly effective in $NaBH_4$ hydrolysis (Semiz, 2018), the high expense and scarcity limit their usage in large-scale applications. Consequently, seeking efficient non-noble-based catalysts for $NaBH_4$ hydrolysis process is of great research interest in the sustainable energy field. Among the researches based on the earth-abundant metal catalysts for $NaBH_4$ hydrolysis, Co-based catalysts have shown promising performance and proven to be an alternative to replace noble metal catalysts as being reactive and much economic (Wu, 2018). Additionally, Co nanoparticles (NPs) have also been reported to be effective in catalytic hydrogen generation. The catalysts have been deposited initially as Co^{+2} ions on a support material and then chemically reduced to Co(0) nanoparticles.
However, the major drawback of using non-noble metals is the agglomeration owing to the high surface energy leading to a significant loss in the catalytic activity. The common strategy to unravel this issue is finding an appropriate supporting material to provide a large specific surface area along with the chance of better dispersion of the active phases (Xiang, 2015). TiO_2 has been extensively used in the energy research field, especially in catalytic/photocatalytic applications, owing to its unique chemical and physical features, stability, low cost, and nontoxicity. Thus, in this study, we aimed to investigate the activity of Co nanoparticles on TiO_2 mesh support.

II. Experimental Set-up and Procedure

Catalyst Preparation. Co NPs synthesis has been adapted from the previously reported procedure (Delgado, 2016). As a support material, TiO_2 micron powder (325 mesh, purity of 99.99%) has been obtained from Nanography Nano Technology.

Hydrogen Generation Measurement

Design of the catalytic unit: A thermally insulated reactor and batch reactor are manufactured to observe the thermal catalytic effects of the $NaBH_4$ hydrolysis. The reactor' temperature is measured with a type K thermocouple and the hydrogen gas pressure - by a Keller PA-21SR/80520.3 pressure sensor (Fig. 1a). Fig. 1b shows the diagram of an experimental stand including a catalytic hydrolysis reactor and a water thermostat.

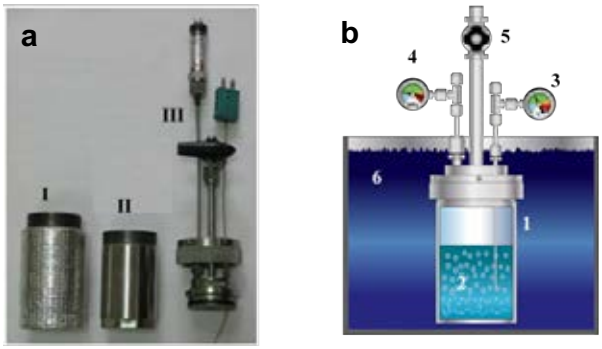


Fig. 1. (**a**) Experimental setup components: I - Thermally insulated reactor, II - Batch reactor and III - The top part of the reactor with a pressure sensor and a thermocouple, (**b**) Diagram of an experimental stand containing; 1 - Batch reactor, 2 -

Reacting composition, 3 - Thermocouple, 4 - Pressure sensor, 5 - Pressure release valve, 6 - Water thermostat

III. Analysis

Isothermal experiments are conducted in a thermostat, while nonisothermal experiments are carried out without a thermostat.

IV. Results and discussions

XRD analysis given in Fig. 2a exhibited the well-resolved signals corresponding to 101, 004, 200, 105, and 211 diffraction planes, which are assigned to the anatase phase of TiO_2 (PDF# 21-1272). However, Co nanoparticle incorporation on the TiO_2 support could not be detected via XRD which is probably owing to the low concentration. The surface composition and chemical states of the catalyst have been investigated via XPS spectroscopy analysis. The survey spectrum exhibits intense Ti 2p, O 1s peaks at 459.1 and 531.1, respectively along with Ti 3s and Ti 3p peaks at low and Co 2p and Ti 2s at higher binding energy regions (Fig. 2b). ESEM image of Co-loaded TiO_2 nanoparticles depicted in Fig. 2C shows that the nanoparticles are agglomerated. BET surface area of the prepared Co/TiO_2 catalyst was 78.56 m^2/g and the micropore area was 109.3 m^2/g. Besides, pore volume and diameter have been observed as 0.03894 cm^3/g and 3.243 nm, respectively.

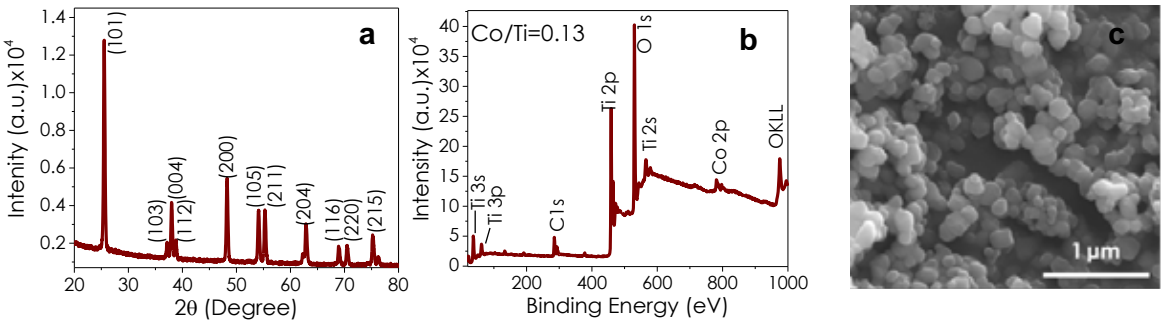


Fig. 2. (**a**) XRD pattern, (**b**) survey spectra; (**c**) ESEM image of Co-TiO_2 NPs.

$NaBH_4$ hydrolysis process consists of two types of data. The data of experiments in a reactor placed in a thermostat is considered to be “almost” isothermal. The word “almost” is used because although the temperature in the thermostat is constant, the temperature of the solution in the reactor is fundamentally slightly higher, since it is necessary to remove the heat generated by hydrolysis from the reactor. The temperature difference depends on the rate of H_2 production, which is proportional to the amount of catalyst and exponentially dependent on the absolute temperature of the solution. According to the nature of the decomposition curves of $NaBH_4$ (Fig. 3a), one can be assumed that after the first use of the catalyst, it is activated from cycle to cycle and, after the fourth cycle, its activity is stabilized. After the first cycle, self-heating of the solution occurs (Fig. 3b). Thus, the catalyst obtained by the present method shows good reproducibility upon repeated use.

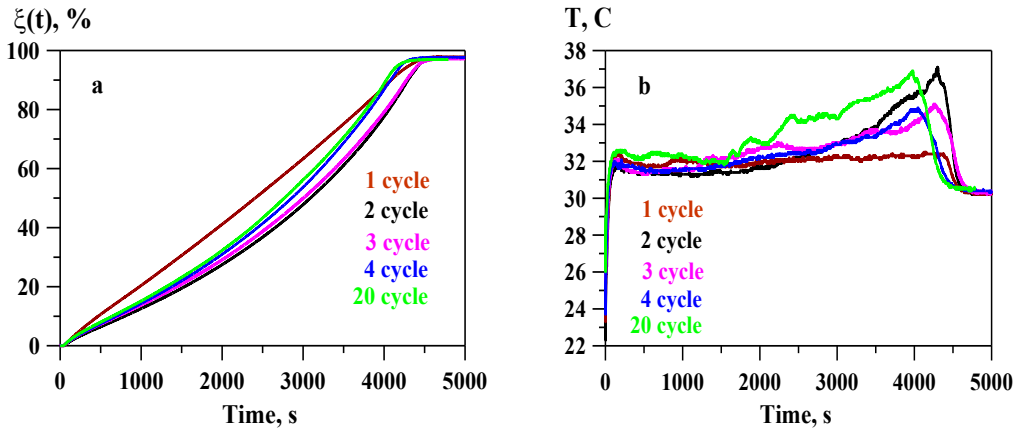


Fig. 3. Profiles of the degree of $NaBH_4$ decomposition (**a**) and temperature, (**b**) on time with repeated use of Co/TiO_2 catalyst. $H_2O/NaBH_4$ = 13.4; the temperature in a thermostat is 30 °C.

As mentioned above, our experiments conducted in a thermostat cannot be considered isothermal. The measurements by a thermocouple placed in a solution in five experiments with a thermostat temperature of 20, 30, 40, 60, and 80 °C are shown in Fig. 4a. In the first two experiments, the heating of the working solution is small, and they could be considered isothermal, however, these data are insufficient to find temperature dependence of the reaction rate constant. In the last three experiments, the temperature changes are very large. Fig. 4b presents the volume of generated H_2 gas at 20-80 °C intervals. Processing such data requires a technique different from the standard technique for isothermal experiments.

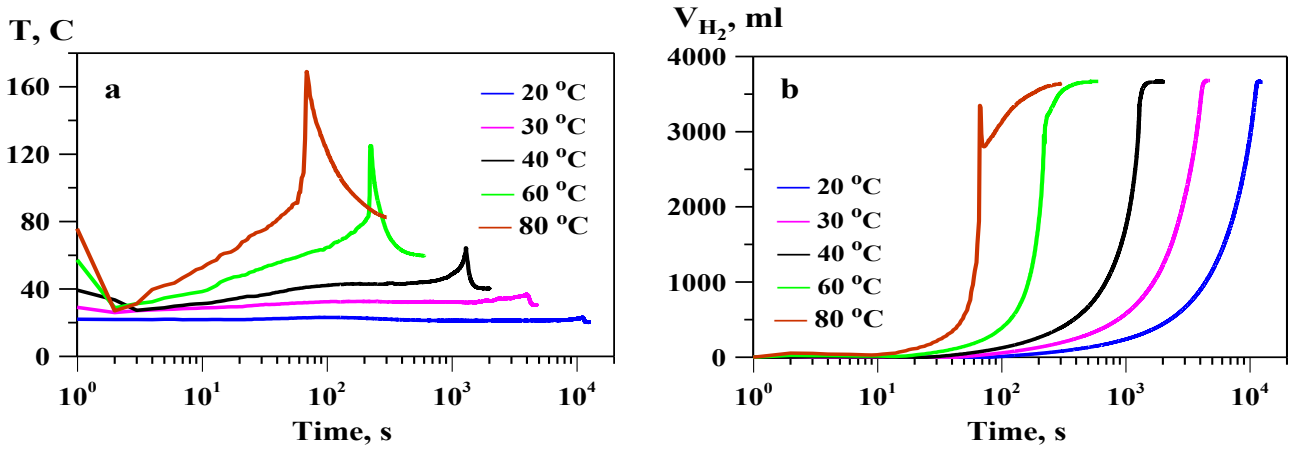


Fig. 4. Profiles of temperature (**a**) and degree of $NaBH_4$ decomposition (**b**) on time in a thermostat. $H_2O/NaBH_4$=13.4(13.8 wt. %); 0.4 g Co/TiO_2

The experiments of the second group were carried out without a thermostat in a reactor modified for hydrolysis under conditions close to adiabatic. The modified version of the experimental reactor has a Teflon cup placed inside the reactor, to reduce the heat transfer of the solution to the reactor vessel. demonstrate the effect of initial $NaBH_4$ concentration on the rate of the generated hydrogen volume (within the range from 5.0 to 19.4 wt.%) during the hydrolysis process. From the analysis of experimental data with a fixed amount of $NaBH_4$ (2.1 g), it follows that the rate of hydrogen generation decreases with the increasing volume of $NaBH_4$ solution (Fig. 5a) since part of the generated heat goes to its heating, which follows from temperature profiles (Fig. 5b). An important characteristic is the amount of catalyst that determines the time of the hydrolysis process. The degree of $NaBH_4$ decomposition versus time with different amounts of catalyst in concentrated aqueous solutions characterized by $H_2O/NaBH_4$ = 8.9 (dashed line) and 13.4 (solid line) as shown in Fig. 5c. The time of complete hydrolysis grows with increasing concentration of $NaBH_4$ solution at the fixed amount of catalyst.

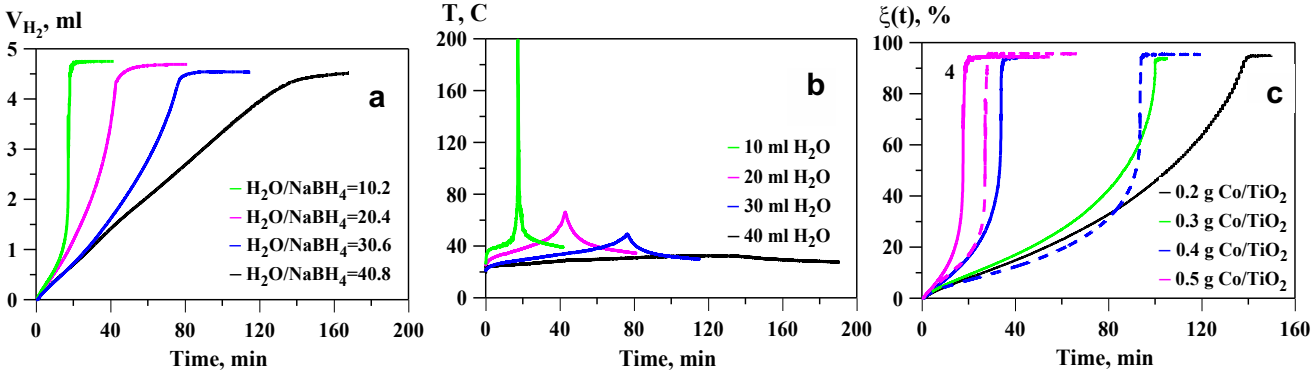


Fig. 5. Profiles of the degree of $NaBH_4$ decomposition (**a**) volume of H_2 generation with time, (**b**) temperature-time, (**c**) Dependence of the degree of $NaBH_4$ decomposition versus time in a thermally insulated reactor. The solid and dashed lines correspond to the molar ratio $H_2O/NaBH_4$ equal to 13.4 and 8.9 respectively.

V. Conclusions

Self-heating of concentrated $NaBH_4$ solutions with the Co-loaded TiO_2 nanoparticle catalyst allows the catalytic hydrolysis process to be carried out at RT, and the weight ratio of $NaBH_4$/catalyst controls the rate of hydrolysis. Achieving good thermal insulation of the reactor, it is possible to choose the optimal value of $NaBH_4$/ catalyst weight ratio from the point of view of the hydrolysis process, depending on the application.

Acknowledgments

This study was financially supported by The Scientific and Technological Research Council of Turkey (TUBITAK) under the research grants 119M030 and Belarusian Republican Foundation for Fundamental Research (BRFFR) under the grant number T19TUB–004.

References

Delgado, J. A.; Claver, C.; Castillón, S.; Curulla-Ferré, D.; Ordomsky, V. V.; Godard, C. Fischer-Tropsch Synthesis Catalysed by Small TiO2 Supported Cobalt Nanoparticles Prepared by Sodium Borohydride Reduction. Applied Catalysis A General, 513, 39–46, (2016).

Minkina V.G.; Shabunya, S.I.; Kalinin, V.I.; Smirnova, A., Hydrogen generation from sodium borohydride solutions for stationary applications, International Journal of Hydrogen Energy, 41, 9227-9233, (2016).

Semiz, L; Abdullayeva, N.; Sankir, M., Nanoporous Pt and Ru catalysts by chemical dealloying of Pt-Al and Ru-Al alloys for ultrafast hydrogen generation, Journal of Alloys and Compounds, 744,110-115, (2018).

Wu, X.; Zhang, X.; Han, G.; Liu, Y.; Liu, B.; Gao, J.; Fan, Y.; Li, B. Reaction of Co_3O_4 Nanocrystals on Graphene Sheets to Fabricate Excellent Catalysts for Hydrogen Generation. ACS Sustainable Chemistry and Engineering, 6 (7), 8427–8436 (2018).

Xiang, C.; Jiang, D.; She, Z.; Zou, Y.; Chu, H.; Qiu, S.; Zhang, H.; Xu, F.; Tang, C.; Sun, L. Hydrogen Generation by Hydrolysis of Alkaline Sodium Borohydride Using a Cobalt-Zinc-Boron/Graphene Nanocomposite Treated with Sodium Hydroxide. Interntional Journal of Hydrogen Energy, 40 (11), 4111–4118, (2015).

Experimental investigation of hydrogen enriched propane in terms of emission values and flue gas temperature

[1*]Oğuzhan Boztoprak, [2*]Murat Taştan

[1]Erciyes University, Institute of Natural and Applied Science, Department of Civil Aviation, Kayseri, 38039, Turkey

[2]Erciyes University, Aviation and Space Sciences Faculty, Department of Aircraft Airframe and Powerplant, Kayseri, 38039, Turkey,

E-mail: oboztoprak@hotmail.com, mrt@erciyes.edu.tr

Abstract
Hydrogen is very famous among alternate fuel researchers because of its relatively clean emission features. Various hydrogen-hydrocarbon mixtures are investigated by researchers. In this experimental investigation hydrogen enriched propane is used in order to investigate and determine emission values and flue gas values of the mixtures. Mixture examined at premixed combustion chamber, constant equivalence ratio (1.2), swirl number (1) and 7kw thermal energy. Starting with determining mixture's hydrogen ratio. The mixtures that consist of %10,%20 and %30 hydrogen investigated.

Keywords:" Flue gas temperature, propane, hydrogen enrichment, combustion."

I. Introduction

Internal combustion engines emit various amounts of harmful emissions due to many parameters such as fuel's chemical features, combustion itself, combustion stability, combustion chamber design, engine performance [1], etc. One of the most important is fuel's composition and characteristic features and this subject is very attractive for researchers [2]. Nowadays generally jet a1 is used in aviation industry. Because of its high pollutant emissions and produced from crude oil which is going to be consumed away [3], it is estimated that within 5-10 years it will be switched with a more efficient fuel with low emission values. Propane, which is fundamental part of liquid petroleum gas, has a lot of opportunities such as promising simplicity of mixing, because of fluidization easiness it is convenience to store and has relatively low emission values [4]. Although there are some obstacles in storage and production of hydrogen, it still takes attention from researchers because of its clean emission values, promising efficiency of fuel cells, the richest source by comparison with fossil fuels, high flame speed and, good flammability length [5,6]. Hongyu Huang et al did experimental and numerical examine on h2-air mixtures combustion and heat release characteristics on a micro-jet array burner. They find out OH distribution and heat release can be arranged by equivalence ratio and thermal power selection. At 0.5 equivalence ratio and 0.1kw thermal power concentrated heat release rate was obtained [7]. M.Ilbas et al. did an experimental study on laminar-burning velocities of hydrogen–air and hydrogen–methane–air mixtures and at the experiment ignition and combustion of hydrogen-air mixture can occur at up to 3.2 equivalence ratio. Experimental results show that when the hydrogen value increased in methane-hydrogen mixture, flame speed and burning velocities increased [8]. B. Alabas¸ et al. studied on experimental investigation of methane enrichment with oxygen and hydrogen in different volumes and acoustic enforcement effects on mixtures. The results show that hydrogen additive on different fuel mixtures increases combustion stability under burning with air in addition to NOx decrease on emission values [9].

II. Experimental Set-up and Procedure

Erciyes University Combustion Research Laboratory was used for this experimental investigation. The experiment performed under constant equivalence ratio 1.2, swirl number 1 ,7kw thermal energy, 20 mbar pressure and a premixed combustion chamber has been chosen. When past propane-hydrogen flame studies evaluated, 1.2 equivalence ratio was decided [6]. The length and the inner diameter of the combustion chamber is 165cm and 32cm respectively.

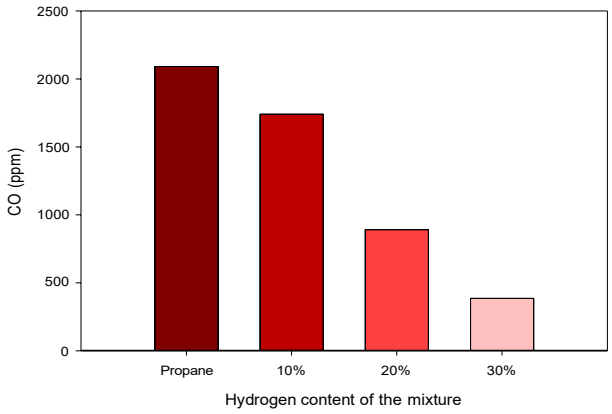
Table 1 Experiment Matrix.

Experiment no	*C3H8%*	*H2%*
Exp. No 1	100	0
Exp. No 2	90	10
Exp. No 3	80	20
Exp. No 4	70	30

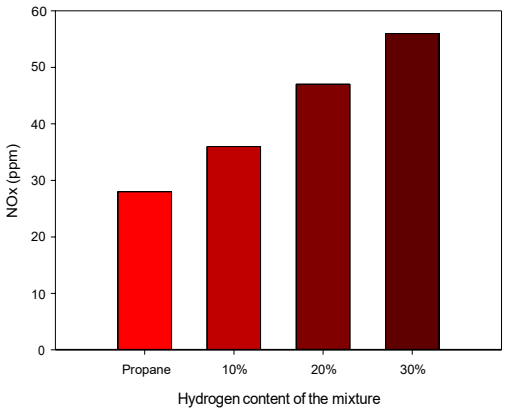
Firstly propane's blowout and flashback limits tested and determined as 0.8, 1.9 respectively. After that started with experiment no 1 and continued respectively to the end. To control the mass flow of gases mass flow controllers and vacuum system controller station was used. To supply constant air ,air compressor and external air tank was used. To collect data from system thermocouples, pressure transducers, photodiodes and data loaders was used. To get emission values there is a hole on the exhaust pipe and to collect emission data MRU Nova Plus emission device was used. To establish mixing fuel-air premixer and a gas collector was used. Propane and hydrogen supplied from tanks.

III. Analysis

IV. Results and discussions



Graph 1

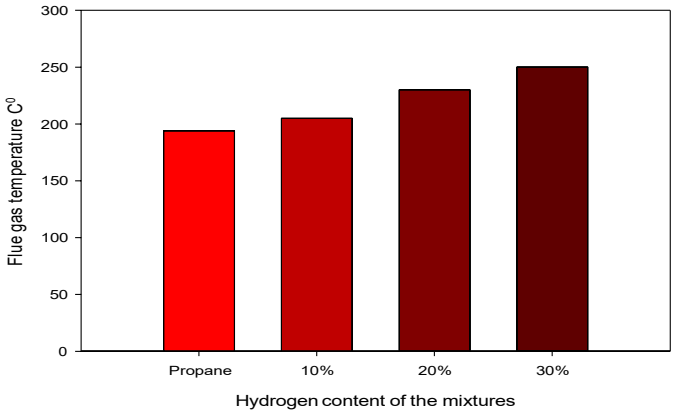


Graph 2

The graph 1 shows CO (ppm) values of the mixtures' s combustions. While experimental investigation the CO (ppm) value decreased mixture as 2092, 1740, 890, 385 ppm respectively with increasing hydrogen rate. Hydrogens heating value and burning velocity has a big effect on this fall. Because of hydrogen does not contain carbon, it has increased the combustion efficiency. Thus, as a result similar to the studies in the literature, the amount of CO decreased with the increase of hydrogen content.

The graph 2 shows NOx (ppm) values of the mixtures' s combustions. The NOx values increased as 28, 36, 47, 56 ppm respectively with increasing hydrogen rate. As seen in graph 2, NOx emission increased with hydrogen enrichment. As it is known, there are three different mechanisms of NOx formation. NOx formed during the experiment is in the form of thermal and rapid NOx formation. With the addition of hydrogen, the temperature increased, which increased the formation of NOx.

The graph 3 shows flue gas temperature (C^0) values of the mixtures' s combustions. The temperatures raised as 194 205 230 250 C^0 respectively with increasing hydrogen rate. Hydrogen has a high heating value that approximately three times that of propane. With the increase in the hydrogen ratio in the mixtures, the combustion temperature increased and accordingly the flue gas temperature increased relatively.



Graph 3

V. Conclusions

Comments on temperature and emission values of hydrogen enriched propane combustion can be summarized as follows.

- Compared to burning pure propane with air, it has been observed that the combustion calorific values of hydrogen enriched mixtures are increased.
- With the increase in the amount of hydrogen in the mixture, the amount of CO decreased by approximately 80 percent.
- NOx emissions increased with the increase in the amount of hydrogen in the mixtures due to the heating value of hydrogen.
- It has been observed that the temperature values taken from the centre of the chimney at the exit of the combustion chamber increase with the amount of hydrogen in the mixtures.

Acknowledgements

The authors wish to thank by The Scientific and Technological Research Council of Turkey (TUBITAK) for supporting this study with project number: MAG-215 M821 project and Erciyes University Research Foundation (Project No. FYL-2020-10631) for its financial support.

References

[1] A. DSpelheuer., M. Lecht., Influence of engine performance on emission characteristics, RTO AVT symposium, 20, (1998).

[2] A. Kakaee, A.Paykani, M.Ghajar, The influence of fuel composition on the combustion and emission characteristics of natural gas fueled engines, Renewable and Sustainable Energy Reviews, 38, 64-78, (2014).

[3] E.Nygren, K. Aleklett, M.Höök, Aviation fuel and future oil production scenarios, Energy Policy, 37, 4003–4010, (2009).

[4] D. Yap, J. Karlovsky, A. Megaritis, M.L. Wyszynski, H. Xu, An investigation into propane homogeneous charge compression ignition (HCCI) engine operation with residual gas trapping, Fuel, 84, 2372–2379, (2005).

[5] G.W. Crabtree, M.S. Dresselhaus, The Hydrogen Fuel Alternative, MRS Bulletin, 33, 421-428, (2008).

[6] C. Tang, Z. Huang, C. Jin, J. He, J. Wang, X. Wang, H. Miao, Laminar burning velocities and combustion characteristics of propane–hydrogen–air premixed flames, International Journal of Hydrogen Energy, 33, 4906-4914, (2008).

[7] J. Li, H. Huang, Y. Bai, S. Li, N. Kobayashi, Combustion and heat release characteristics of hydrogen/air diffusion flame on a micro-jet array burner, International Journal of Hydrogen Energy, 43, 13563-13574, (2018).

[8] M. Ilbasa, A.P. Crayfordb, I. Yılmaza, P.J. Bowenb, N. Syredb, Laminar-burning velocities of hydrogen–air and hydrogen–methane–air mixtures: An experimental study, International Journal of Hydrogen Energy, 31, 1768 – 1779, (2006).

[9] B. Alabaş, G. Tunç, M. Taştan, I. Yilmaz, Experimental investigation of the emission behaviour and flame stability of the oxygen and hydrogen enriched methane under acoustic enforcement, Fuel, 290, 120047, (2021).

Design Consideration of an Efficient Oxyhydrogen Generator under Lorentz Force

[1*]Hakan Kaplan, [1]Mükerrem Şahin, [1]Gülbahar Bilgiç
[1]Ankara Yildirim Beyazit University, Department of Energy Systems Engineering, Kecioren, Ankara, 06010, Turkey

* E-mail: hakankaplan89@gmail.com

Abstract
Hydrogen is known as good energy carrier for sustainability. There are many different methods in industry to obtain the hydrogen such as electrolysis, steam methane reforming, PV electrolysis, biological methods etc. Water electrolysis is one of the energy system technologies used for hydrogen production. With this system, water is separated into molecules by applying electric current. The gas, which is a mixture of hydrogen and oxygen gases released by the operation of the cell, is called oxyhydorgne generator. The generator is evaluated by value of drawn current and amount of produced gas. To achieve more efficient for the hydrogen production, the magnetic field is applied to the electrolysis cells. In this study, magnetic field lines were degined effectivelly by field simulation software before deciding shape and size of the generator. It has advantageous in terms of gas flow rate.

Keywords: Oxyhydrogen, hydrogen, magnetic field, Lorentz Force, efficiency

I. Introduction

Alternative energy systems containing hydrogen are a promising candidate for solving global environmental problems and meeting the increasing energy needs. Hydrogen energy conversion technologies play an important role in the green energy development to overcome environmental problems (Zhou, 2016). The electrolysis of water is an important technology for high purity hydrogen and oxygen gas production. Hydrogen is considered as a potential energy carrier because there is no greenhouse polluting gas (such as carbon dioxide) generated during the energy releasing process (Sadurmanta et al, 2016). Among methods of hydrogen production, water electrolysis is the most common way because the produced hydrogen has a high purity (Dincer, 2012). Therefore, how to increase the water electrolysis efficiency is one of the topics worth being studied further.

With the oxyhydrogen (HHO) dry cell design, they are outside of the water/catalyst solution which is stored in a separate reservoir and recirculated by the HHO dry cell, this help in producing more HHO gas and less heat (steam) At 570°C, it burns itself under normal pressure value. Because of renewable energy property, it is widely used in the industry especially in the automotive industry. (also welding and material processing). HHO dry cell is defined as converting water to the hydroxy gases. Mainly, HHO is that water molecule is splitted into its molecules by applying electrical current (Sadurmanta et al, 2016). The voltage that is applied in the system must be DC. Otherwise an AC-DC inverter should be preferred. HHO can be used in high flame application because it has quite high flame threshold (Nikolaidis and Poullikkas, 2017).

Lorentz force is a force applied on a charged particle moving in an electromagnetic field. In previous studies in literature, the reason for adding a magnetic field to HHO system for hydrogen production is to increase the electrolysis rate (Iida et al, 2007 and Lasia, 2003). The charged particles will be forced in the direction perpendicular to the magnetic lines as the magnetic field and electric field lines are perpendicular to each other. Thus, the charged particles will be affected by the Lorentz force and the direction of movement of the particles will change. The Lorentz force also effects on movement of hydrogen bubble on electrode surface. Separation of the bubbles from the surface means that more hydrogen is generated (Lin et al, 2016). Therefore, an appropriate design of the magnetic field will provide a uniform flow area and an appropriate ion distribution between the electrodes which provides increasing in electrolysis rate and efficiency (Elias and Hegde, 2017).

II. Experimental Set-up and Procedure

Plexiglass material is used for end plates (two pieces) the size is 160mm*120mm and 10mm thickness that white color was preferred. There is one through hole on each plate that one is for inlet and other is for an outlet. In our setup, we have used 3 types of stainless-steel plates. Negative, positive, and neutral plates are essential for HHO generator. The number of six plates is chosen for neutral which has rectangular shape as 120mm*80mm and 0.5mm thickness. The number of positive and negative plates is one respectively, moreover the shape of it is same as neutral plates, however they have 2mm thickness and a tail on the corner because of conduction (electrical connection) for anode and cathode. All these plates were manufactured by Yb doped continuous wave fiber laser. We implemented two types of bolts. 14 of them is used for compression of end plates, while 2 of them is used for anode and cathode connection. The number of 32 washers and 20 pieces of nuts is essential for mechanical compression. Before compression the plates, number of 9 rubber gasket is also placed between them to protect water isolation.

After complete setup, electrical connection was coupled. Constant DC voltage is implemented between cathode and anode as positive and negative respectively. There is a water tank that contains solution with KOH and water. It is connected to input hole through pneumatic hose on the plexiglass. The output hole on the other plexiglass should be connected to the water tank. At that point, we can see a mixture of hydrogen and oxygen gasses. During hydrogen gas production, change in current and flow of gas has been noted. After a while, there will be saturation. At that time, the system should be shut down otherwise it will be warming up.

System design is drawn in a CAD software. After the final design, we started to manufacture parts. Neutral plates, electrodes and rubber gaskets as black color are sandwiched tightly between delrin plates (seen as green) as in shown in Fig. 1(a). In our setup, there are 7 water compartments. According to literature, voltage between two successive plates can be almost 2 volts due to overpotential effect. So, we may apply nearly 14 volts between two electrodes. In addition to the dry cell, DC power supply, water tank (for %3.5 KOH solution), HHO tank (to collect HHO gas) and blue pneumatic hose as shown in Fig. 2(a) Moreover, the assembled dry cell is illustrated in Fig. 2(b) When switch on the power supply, the cell immediately generates HHO gas. During the experiment, the applied voltage is constant. Whereas current starts to increase. It means that HHO production is going on. After a while, the system begins to warm and HHO production efficiency decreases.

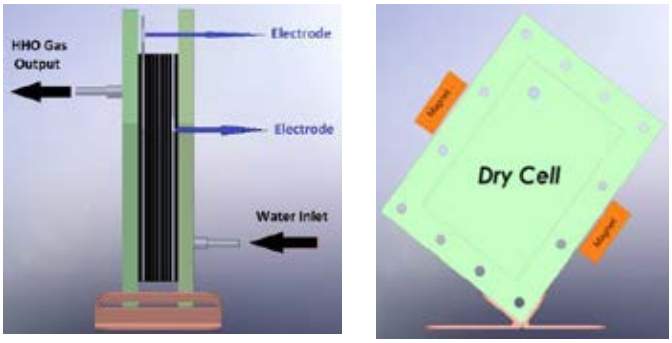


Fig. 1 – (a) CAD design of the cell; (b) with magnet (orange color).

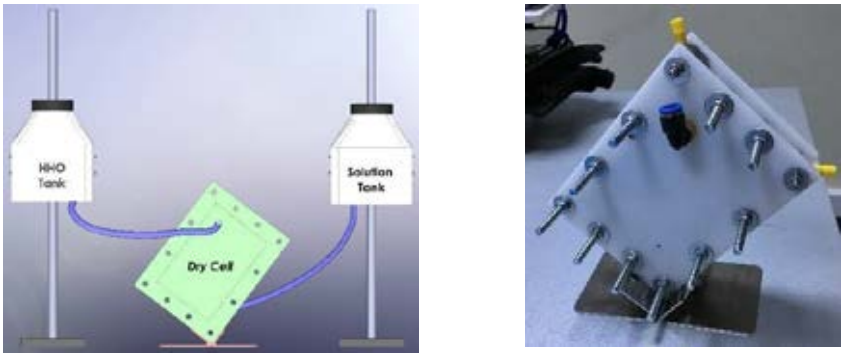


Fig. 2 - (a) Experimental Setup; (b) manufactured dry cell (right side).

III. Results and discussions

In HHO generator design, mechanical parts are designed by regarding magnetic field distrubution. Effectively using magnetic field lines are quite critical for efficiency of the system. We have designed the lines using simulation software. Permanent magnets were chosen for creating the lines. We implemeted NdFeB type magnets to the simulation. It has deimension of 50mm (length), 20mmn (width) amd 10mm (height). The simulation results give us information about size of the dry cell. The software output is magnetic field intensity and flux density in terms of Tesla (or Gauss). In Fig.3(a), result of two magnets is shown with respect to Tesla. Whereas, values of magnetic field intesity result is illustrated in Fig. 3(b). According to results, cell dimesion can be below 120mm as in direction of magnetic field. So, our cell has size of 80mm as length.

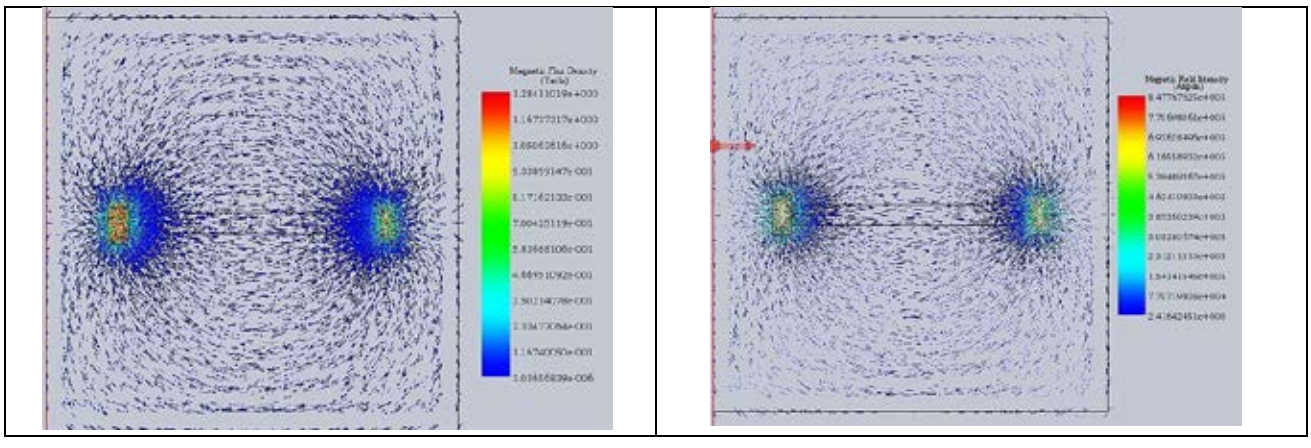


Fig. 3- Simulation results of two magnet (a) in terms of flux; (b) in terms of intensity

The aim of this study is to design of a new dry cell system for industrial applications. Water electrolysis was performed for hydrogen evolution reaction that is done by the dry cell. We studied parameter optimization to enhance the efficiency of the cell. Certain important parameters are material selection (resist to corrosion), electrode selection (in terms of shape, size, and thickness), supplied voltage, controlling heating problem and solution (type and percentage). We will choose to apply of magnetic field to increase the efficiency of the system, although there are many methods to enhance the efficiency of hydrogen production. Because there is no needed additional energy, just use magnets. This is the main advantage to use it. Magnets are placed side of our setup as shown in Fig. 1(b) It is illustrated as a figure in Fig. 4 that includes flow rate of HHO production versus output current at constant applied voltage as 13.8V. Results demonstrates that, voltage is applied as constant so current is increasing as well as flow rate is increasing. Flow rate is measured in manual as how many minutes is necessary for 1lt water is spilled inside bottle.

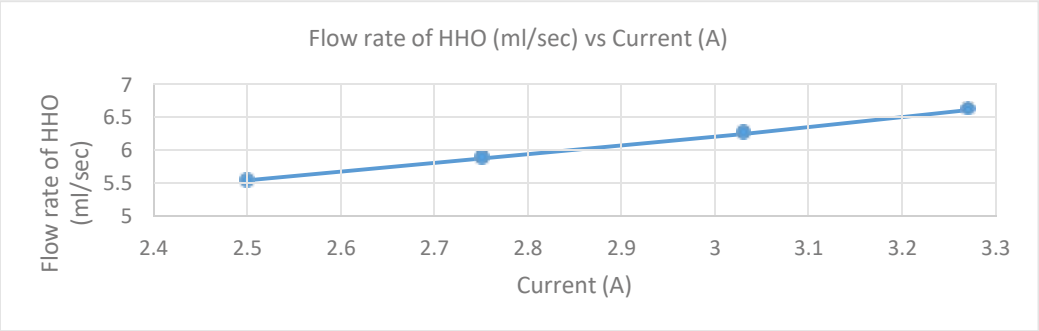


Fig. 4 - Produced HHO gas in terms of output current at constant voltage.

IV. Conclusions

In the study, hydrogen generator is investigated due to having some unique properties especially for the industry. Our system has cost effective, efficient, maintenance is easy and flexible. Nowadays dry cells are widely used in automobiles. It supplies fuel saving for them. According our study, we use magnets to increase production efficiency. Of course, other ways can increase the efficiency of the dry cell. However, magnets work without any energy consuming. Design of the cell is proved by using magnetics simulation software. The software helps us as foresight before completing mechanical design. Applying the magnetic field to the cell will help transport hydrogen bubbles from cathode surface. Thus, bubbles are not collected on the cathode surface and more bubbles can be generated. This means flow rate increases. In future studies, we will try to find optimized values in terms of electrode thickness, electrode surface area, shape and numbers of the electrode, percentage of the solution, space between two consecutive electrodes and strength of applied magnetic field in terms of Tesla. We will have more efficient new electrolysis cell design and more portable for industry.

References

Zhou W, Jia J, Lu J, Yang L, Hou D, Li g and Chen S. Recent developments of carbon-based electrocatalysts for hydrogen evolution reaction. Nano Energy 2016;28:29-43. https://doi.org/10.1016/j.nanoen.2016.08.027.

Sadurmanta B, Darsopuspito S and Sungkono D. Application of dry cell hho gas generator with pulse width modulation on sinjai spark ignition engine performance. International Journal of Research in Engineering & Technology [IJRET] 2016;05:105-112.

Dincer I. Green methods for hydrogen production. International Journal of Hydrogen Energy 2012;37:1954-1971. https://doi.org/10.1016/j.ijhydene.2011.03.173.

Nikolaidis P and Poullikkas A. A comparative overview of hydrogen production processes. Renewable and Sustainable Energy Reviews 2017;67:597-611. https://doi.org/10.1016/j.rser.2016.09.044.

Lasia A. Hydrogen evolution reaction. Chichester, John Wiley & Sons, Ltd 2003. https://doi.org/10.1002/9780470974001.f204033.

Iida T, Matsushima H and Fukunaka Y. Water Electrolysis under a Magnetic Field. Journal of The Electrochemical Society 2007;154: E112-E115. https://doi.org/10.1149/1.2742807.

Lin MY, Hsu WN, Hourng LW, Shih TS and Hung CM. Effect of Lorentz force on hydrogen production in water electrolysis employing multielectrodes. Journal of Marine Science and Technology 2016;24:511-518. http://dx.doi.org/10.6119%2fJMST-015-1026-1.

Elias L. and Hegde A. C. Effect of Magnetic Field on HER of Water Electrolysis on Ni–W Alloy. Electrocatalysis. 2017;**8:375**–382. https://doi.org/10.1007/s12678-017-0382-x.

Development and Analysis of a Hydrogen-Powered Premix Burner

Yagmur Cagli[1], Mehmet Salih Cellek[2]*
[1]Bingol University, Arthitecture and Engineering Faculty, Renewable Energy Systems, Master Student
[2]Bingol University, Arthitecture and Engineering Faculty, Department of Mechanical Engineering, Bingol, 12000, Turkey

*E-mail: mscellek@bingol.edu.tr

Abstract

Nowadays, existing fossil fuels emit poisonous emission gases in many respects. On the other hand, there is a shortage of alternative energy sources. Besides, high flame temperatures in conventional non-premix burner technologies cause an increase in emissions such as NOx. Although different methods have been developed to reduce the flame temperature, it is not easy to reduce the emissions to the desired levels. Thus, researchers have focused on new technologies for the best and economic ones. In this study, after developing a hydrogen-powered premix burner, premix combustion of hydrogen-air has carried out by CFD simulation. According to the numerical results, a hydrogen-powered premixed burner design without flame flashback has thrived.

Keywords: Hydrogen, premix burner, hydrogen premix combustion, flame flashback

I. Introduction

In premixed combustion, fuel and oxidizer air, known as reactants, mixed at molecular level before ignition. After that, combustion take place as a flame front propagating into the unburnt species. Moreover, Premixed combustion is generally arised as a thin, enlarged flame that controlled by the turbulence (ANSYS Inc, 2021). Compared to non-premixed combustion, premixed combustion has some difficulties in modeling as it is constrained only for turbulent, subsonic flows that do not involve modeling pollutant emissions. Even so, the turbulent premixed combustion is modeled based on the studies by Zimont et al. (Zimont, 2000, Zimont et al., 1998, and Zimont and Lipatnikov, 1995) concerning the solution of a transport equation for the reaction progress variable.

Several studies have been conducted regarding of premix combustion for alternative fuels (Suprianto et al., 2016, Karyayen and İlbas, 2018). Hydrogen fuel have a higher flame temperature as well as higher laminar flame speed than hydrocarbon fuels such as methane, ethane and propane. Laminar flame speed is an important parameter of a combustible mixture as it contains fundamental information on reactivity, diffusivity, and exothermicity. The value of the flame speed has important impacts upon the propensity of a flame to flashback and blowoff and controls other key combustion characteristics, such as the flame's spatial distribution (Dong et al, 2010). Flame instability is one of the recent major issues in premixed combustion. Mixing of air with fuel under lean conditions with the aid of hydrogen enrichment enhance flame stability. This technique will favour flame stability and reduction in NOx emissions. But, hydrogen enrichment causes its own challenges in terms of flashback phenomenon, due to its higher flame temperature that bring about overheating of the components. (Rashwan et al., 2016, Gazzani et al, 2000, Sheu and Ghoniem, 2014). As a solution of flame flashback, using a flashback arrestor would prevent the resulting danger. However, this can result in a significant drop in pressure, lowering throughput capacity. The aim of the study is to develop and simulate a premixed burner for the operation with 100% hydrogen gas.

II. Design of Hyrogen-Powered Premix Burner and Operation Conditions For Simulation

The burners are the devices utilizing to combust the fuel with an oxidizer to alter the chemical energy available in the fuel into thermal energy (Baukal et al, 2001). Since fuel and oxidizer are best mixed within the burner, premixed combustion is a promising combustion state. (Karyayen and İlbas, 2018). To the development of a flashback-proof burner, the diameters of the fuel and air pipe should be selected carefully considering mass flow rates and pressures in each pipe. Moreover, the fuel pipe nozzle should located in a specific and strategic point where air intake is not technically possible. In this study, the venturi flowmeter design strategy considered for flame flashback prevention. Thus, it is predicted that combustion of the air-fuel mixture could be prevented from advancing in the direction of arrival of the fuel. The operation conditions for the numerical premix combustion are presented in the Table 1.

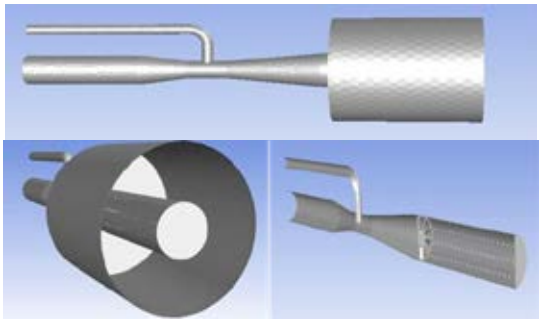


Fig. 1. Premixed burner design

Tab. 1: Premix mixture properties and operation conditions

Authors	Units	Studied Fuels
Mass of air	kg/kgmol	0.5x(32+3.76x28)/0.77=89.14
Mass of 1 mole of fuel	kg/kgmol	2.01
Mass fraction of fuel	-	0.0226
Heat of combustion	Mj/kg	120.90
Adiabatic Temperature	K	2370
Laminar Flame Speed ($\emptyset = 0.77$)	m/s	1.75
Velocity of fuel	m/s	11.61
Velocity of air	m/s	44.65
Equivalance ratio	-	0.77
Power	kW	50

In this numerical study, hydrogen-powered premixed combustion in a premix burner has investigated at 50 kW under lean condition using the Computational Fluid Dynamics (CFD) technique. The realizable $k - \varepsilon$ model selected for turbulence prediction. Zimont model is selected for flame speed model with default model coefficinent.

III. Premix Combustion

Combustion efficiency of premixed flames are higher than non-premixed flames, as almost all of the fuel burned with air. The volume of fuel injected into fresh gases can effectively regulate the temperature of the burnt gases. Thus, pollutant emissions can be controlled to some extent. Potential safety issues can arise in premixed combustion applications due to the fire that occurs as soon as fuel and air are mixed. (Poinsot and Veynante, 2004). Diffusion/reaction processes spread premixed flames against the fresh fuels. The reaction's heat preheats the reactants by diffusion before the reaction begins. The laminar flame speed (s_l) varies based on the reactants, the temperature of the fresh gas, and the pressure. Fresh gases are faster in turbulent premix flame, called turbulent flame speed (s_T). It depends on such parameters as chemistry characteristics, flow geometry and larger than laminar flame speed. The relation between laminar and turbulent speeds are as follows (Poinsot and Veynante, 2004).

$$\frac{s_T}{s_l} = 1 + \alpha \left(\frac{u'}{s_l}\right)^n \quad (1)$$

Where α and n are two model parameters of the order of unity, u' is the turbulent intensity of the incoming flow.. (Poinsot and Veynante, 2004). In the ANSYS FLUENT, the flame front propagation is modeled by solving a transport equation for the density-weighted mean reaction progress variable, denoted by c. The progress variable is defined as a normalized sum of the product species. The value of c is defined as a boundary condition at all flow inlets. It is usually specified as either 0 (unburnt) or 1 (burnt) (ANSYS Inc, 2021):

$$\frac{\partial(\rho c)}{\partial t} + \nabla \cdot (\rho \bar{v} c) = \nabla \cdot \left(\frac{\mu_t}{Sc_t} \nabla c\right) + \rho . Sc \quad (2)$$

$$c = \frac{\sum_{i=1}^{n} Y_i}{\sum_{i=1}^{n} Y_{i,eq}} \quad (3)$$

where c is the mean reaction progress variable, Sc_t is the turbulent Schmidt number, and Sc is the reaction progress source term, n is the number of products, Y_i mass fraction of product species, equilibrium mass fraction of product species. The mean reaction rate in Equation (1) is modeled as (Zimont et al. 1998)

$$\rho . Sc = \rho_u s_T |\nabla c| \quad (4)$$

where ρ_u density of unburnt mixture (ANSYS Inc, 2021).

IV. Results and discussions

Hydrogen-air premix combustion under the lean conditions have been simulated with ANSYS Fluent 18.2 in a fully premixed burner. The pressure and velocity distributions on the center plane in the premix burner are shown in Fig.2 a-b. It is shown from the figures that pressure decreases towards the pipes inside the burner. The lowest pressure zones have been obtained in the Venturi throat and in the region where the combustion takes place. On the other hand, the velocities of the flow are relatively high in these region. The variation of the mean reaction progress variable in the burner can be seen in the Fig.2c. It is clear that the mean reaction progress variable is 0 where the mixture is unburnt, whereas it is 1 where mixture is burnt. It has also been observed that the mean reaction progress variable value varies between 0-1 in regions where the combustion has not yet been completed. Finally, flame temperature of the premix combustion on the center plane is shown in Fig. 2d. The flame temperature level is high where the mean reaction progress variable value is about 1. The temperature level is minimal for unburnt mixture where c is 0. On the other hand, flame temperature is relatively lower for 0<c<1. This result shows that those regions are transition zones and the combustion has not completed, yet.

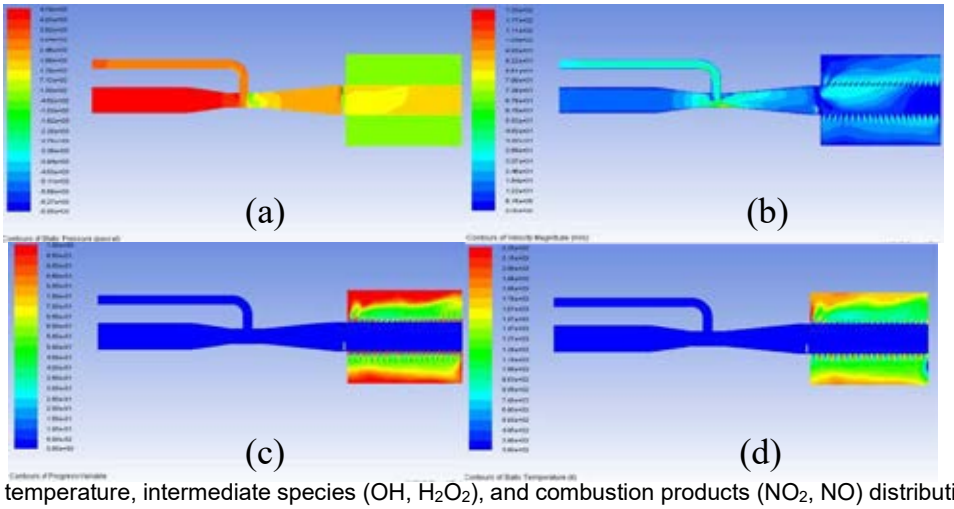


Fig. 2: Flame temperature, intermediate species (OH, H_2O_2), and combustion products (NO_2, NO) distribution contours

IV. Conclusions

Hydrogen gas has emerged as an alternative fuel in order to get rid of some harmful side effects of fossil fuels, and has recently attracted attention to become the fuel of the future. This study is concentrated on premixed combustion flame of hydrogen under lean condition. The findings can be summarized as follows:

- Prevention of flame backflow is of great importance in the design of premixed hydrogen fuel burner. This is one of the most important issues in premixed burner design. Pipe diameters and mixture shape are important in order to prevent flame flashback. The Venturi design shape can be useful in this respect.
- The increasing popularity of hydrogen, emission limitations and increased competition in combustion systems could set a new trend towards hydrogen-fueled premix burner design.
- CFD design and analysis offers excellent ideas and insights before manufacturing.

Acknowledgements

The author is grateful for the use of the computing resources provided by the National Center for High Performance Computing of Turkey (UHEM, UYBHM) under grant number 1008202020.

References

ANSYS INC., ANSYS Fluent 12.0/12.1 Documentation, (2021).

Baukal C.E., Schwartz R.E., John Zink Company, Boca Raton, FL. CRC Press, (2001).

Dong C., Zhou Q, Zhang X, Zhao Q, Xu T, Hui S., Experimental study on the laminar flame speed of hydrogen/natural gas/air mixtures, Front. Chem. Eng. China, 4(4): 417– 422, 2010.

Gazzani, M., Chiesa, P., Martelli, E., Sigali, S., Brunetti, I. Using Hydrogen as Gas Turbine Fuel: Premixed Versus Diffusive Flame Combustors, J. Eng. Gas Turbines Power 136(5), (2014).

Karyeyen S., Ilbas M., Experimental and numerical analysis of turbulent premixed combustion of low calorific value coal gases in a generated premixed burner, Fuel 220, 586–598, (2018).

Suprianto F.D., Anggono W, Tanoto M.S.C., Effect of Carbon Dioxide on Flame Characteristics in Biogas External Premix Combustion, International Journal of Applied Engineering Research, 11:4, 2240-2243, (2016).

Poinsot T. J., Veynante, D.P., Combustion, Encyclopedia of Computational Mechanics. Edited by Erwin Stein, Ren´e de Borst and Thomas J.R. Hughes. John Wiley & Sons, Ltd., (2004).

Rashwan S.S., Nemitallah,M.A., Habib M.A, Review on Premixed Combustion Technology: Stability, Emission Control, Applications, and Numerical Case Study, Energy Fuels, 30:12, 9981–10014, (2016).

Sheu, E. J. Ghoniem, A. F. Redox reforming based, integrated solar-natural gas plants: Reforming and thermodynamic cycle efficiency, Int. J. Hydrogen Energy 39:27,14817-14833, (2014).

Sreenivasan, K.R., Raghu S. The Control of Combustion Instability: A Perspective. *Current Sci.*, vol. 79:6, 867–883, (2000).

Wang Z., Tang Q., Yang Z., He P., Experimental study on premixed flame combustion of annular burner with CO_2 dilution based on OH-PLIF technology, Cogent Engineering 6:1593074, (2019).

Zimont V., Gas Premixed Combustion at High Turbulence. Turbulent Flame Closure Model Combustion Model. Experimental Thermal and Fluid Science, 21:179-186, (2000).

Zimont V.L, Polifke W., Bettelini M., and Weisenstein W. An Efficient Computational Model for Premixed Turbulent Combustion at High Reynolds Numbers Based on a Turbulent Flame Speed Closure. J. of Gas Turbines Power, 120:526-532, (1998).

Zimont V.L, Lipatnikov A.N., A Numerical Model of Premixed Turbulent Combustion of Gases. Chem. Phys. Report, 14(7):993-1025, (1995).

Effect of catalyst microstructures on steam methanol reforming process

[1,2*]Ayse Ece Bedir Sezgin, [1]Samet Sutcu, [1]Nurbanu Cakiryilmaz Sahingoz, [1]Ayse Deniz Sirkeci, [1]Yelda Ciflik, [2]Elif Akbay, [1]İbrahim Pamuk, [3,4]Bora Timurkutluk
[1] Vestel Defense Industry, Titanium Block 17/B, ODTU, Teknokent, 06800 Ankara, Turkey
[2] Eskişehir Technical University, Engineering Faculty, Chemical Engineering Department, Eskişehir, 26480, Turkey
[3] Nigde Omer Halisdemir University, Engineering Faculty, Mechanical Engineering Department, Nigde, 51245, Turkey
[4] Nigde Omer Halisdemir University, Prof. Dr. T. Nejat Veziroglu Clean Energy Research Center, Nigde, 51245, Turkey
* E-mail: ece.bedir@vestel.com.tr

Abstract
Steam methanol reforming (SMR) is based on the reaction of methanol and steam with the help of catalyst and releases hydrogen and carbon dioxide. The catalyst activity and selectivity are the properties, which can be enhanced by engineering the microstructure of the catalyst. In this study, to get improved catalytic behavior of the catalyst, which exhibits high specific surface area, high dispersion and higher activity towards H_2 production, the effects of the catalyst preparation method on the microstructure and catalytic behavior of $Cu/ZnO/Al_2O_3$ are investigated. Sequential co-precipitation and conventional co-precipitation procedures are followed. The results show that the catalysts obtained by sequential co-precipitation have a high specific surface area and dispersion giving a higher activity which promotes the superior catalytic performance depending on the formation of the active copper material with higher specific surface area and a stronger Cu–Zn synergy due to the proper incorporation of zinc species into the precursors.

Keywords: Methanol steam reforming; hydrogen production; $Cu/ZnO/Al_2O_3$ catalyst.

I. Introduction

In the recent years, hydrogen has gained a considerable interest as an energy carrier in many applications and particularly, for polymer electrolyte membrane fuel cells (PEMFCs). The improvement of PEM fuel cell systems including fuel reformer has attracted significant attention worldwide due to their higher productivity, ecological benefits and possible market. There are various types of hydrogen generation technologies for PEMFCs and the most common types among them are given in detail by Holladay et al. 2009. However, very high purity hydrogen is essential for PEMFCs. This restriction also brings about some limitations regarding the storage and transportation of the pure hydrogen fuel. Therefore, hydrogen generation from both alcohols and hydrocarbons by steam reforming reaction is generally preferred. Most researches on the hydrogen production for fuel cells focus on two sorts of carbon compounds: one is oxygen-containing compound like alcohols (methanol, ethanol etc.) or dimethyl ether, the other includes hydrocarbons like natural gas, diesel etc. (Azizan et al. 2020), (Shen and Song 2002). Although steam reforming of hydrocarbons having high energy density has been studied in a number of researches, they are suffering from difficulties in the technical processes, i.e. conversion efficiency of fuel, desulfurization step, high pressure and temperature requirement (Lakeman and Browning 2004). Furthermore, gas purification is more complex. Another promising option for the hydrogen production for PEMFCs is the methanol steam reforming (Zhang et al. 2005). The production of hydrogen from methanol steam reforming has key advantages over hydrocarbons reforming processes such as good gravimetric and volumetric energy density, no sulfur production which means that there are no requirements for desulfurization, relatively high H/C ratio and low reforming temperature (200-300 °C) since reaction conditions are mild because of low ΔH (Shen and Song 2002). Hydrocarbon fuels have extensive distribution infrastructure, but it is not a drawback for methanol as well. In the methanol reforming process, the most common catalysts are copper containing ones, especially CuO/ZnO and $Cu/ZnO/Al_2O_3$ due to their high selectivity and activity (Zhang et al. 2005). Dispersion, metal surface area and particle size are important parameters for the catalyst and the conversion mainly relies on the status of copper. It is also stated in the literature that catalyst with high copper dispersion shows better performance in methanol steam reforming. Since all these parameters are directly affected by the microstructure of the catalyst, the effect of the preparation method on the microstructure and catalytic behavior of the $Cu/ZnO/Al_2O_3$ catalysts with respect to methanol conversion, H_2 production and CO concentration are significant and needs a detailed investigation. There are several methods such as impregnation, co-precipitation and oxalate gel–coprecipitation comparatively examined as the preparation of catalysts for the production of hydrogen by methanol steam reforming. Regarding the synthesis of $Cu/ZnO/Al_2O_3$ catalyst with high content of Cu, the preparation method of co-precipitation is chosen in this study. This process has some difficulties, such as multistep processing and the need for sensitive pH and temperature control, alkaline metal contamination (Zhang et al.2005). Co-precipitation procedure comprises the mixing of metal nitrates and sodium carbonate solutions at a controlled pH and temperature. Initially formed precipitate structure is amorphous. When it is aged, the formation of crystalline precursors is obtained. This ageing step is considered as necessary to generate optimum crystalline hydroxycarbonate precursors from an amorphous phase resulting in the desired highly active catalyst characteristics (Zhang et al. 2005, Smith et al. 2017). In this study, both the amorphous georgeite and crystalline malachite hydroxycarbonate precursors are synthesized. In the preparation steps of malachite, initially georgeite is formed as a transient phase and then rapidly transforms into malachite. Zn is incorporated into georgeite to form zincian georgeite and zincian malachite. While zincian

malachite is obtained by both conventional co-precipitaion and sequential co-precipitation method, zincian georgeite is prepared by procedure modified sequential co-precipitation to inhibit crystalline malachite phase formation.

II. Experimental Set-up and Procedure

Zincian georgeite, an amorphous copper-zinc hydroxycarbonate, and Zincian malachite, a crystalline copper-zinc hydroxycarbonate, were prepared by sequential coprecipitation using the corresponding nitrate salts. Also one more sample was prepared with conventional co-precipitation procedure for comparison. Incorporation of zinc into the georgeite phase and mild ageing conditions inhibit crystallization into zincian malachite or aurichalcite. Sensitive temperature and pH control, ageing time and the exclusion of alkali metals acting as catalyst poisons from the synthesis procedure are the key points which should be considered for the enhanced catalytic performance.

The first catalyst sample of Copper–zinc hydroxycarbonates was prepared by sequential co-precipitation procedure. For this purpose, first $Al_2(NO_3)_3.xH_2O$ solution (1 M) and Na_2CO_3 (1 M) solution was prepared using deionized water and heated up to 40 °C. These two solutions were first precipitated at constant temperature of 40 °C and left stirring for 15 min. Meanwhile a mixed $Cu(NO_3).xH_2O$ and $Zn(NO_3).xH_2O$ solutions (each of 1 M) were prepared using deionized water to give CuO : ZnO : Al_2O_3 mass ratio of 55/33/12. These two solutions were pre-heated along with a separate aqueous solution of Na_2CO_3 (1 M). The hydroxycarbonates were precipitated by combining these two solutions simultaneously at 40 °C, keeping the pH constant at around 6.5–7.0 into the first prepared $Al_2(NO_3)_3$ containing solution. The precipitates were aged for 15 minutes at a constant temperature around 40°C. During this process the solution retained its blue color. Ageing process was then followed by the filtration to collect the precipitates and then these were washed with deionized water (25 °C) in order to minimize their sodium content. A conductivity meter was used to make sure that there was no further change in the sodium content within the solution and then it was dried at 40 °C for 12 h in a muffle furnace. The second copper–zinc hydroxycarbonates sample was prepared in the same precipitation sequence but this time temperature was kept 80 °C and ageing duration was chosen as 3 h. At this time, solution color changed from blue to green. Also drying of precipitates was carried out at 110 °C for 12 h. Third sample of copper–zinc hydroxycarbonates were also synthesized by the conventional co-precipitation procedure by mixing $Cu(NO_3).x\ xH_2O$, $Zn(NO_3).\ xH_2O$ and $Al_2(NO_3)_3.xH_2O$ solution (each of 1 M) with using deionized water to give same CuO : ZnO : Al_2O_3 mass ratio of 55/33/12 for comparative purposes. This solution was pre-heated along with a separate aqueous solution of Na_2CO_3 (1 M). The hydroxycarbonates were precipitated by combining these two solutions simultaneously at 65 °C, keeping the pH constant at around 7.0-8.0. The precipitates were aged for 2 hours by keeping the temperature constant and the same color change was also observed. The filtration and washing procedures were then applied similarly and it was then dried at 110 °C for 12h in a muffle furnace again. After all, all precursors were calcinated at 350 °C to obtain oxide forms. Catalyst powders were then pelletized and then reduced by hydrogen at 300 °C for 3h with a heating rate of 5°C/min.

III. Results and discussions

$Cu/ZnO/Al_2O_3$ catalysts were prepared by different coprecipitation procedures and characterized by XRD and BET analysis. The catalytic performances of these catalysts for the steam reforming of methanol were evaluated in a laboratory-scale tubular plug flow reactor at a temperature of 280 °C. 16 grams of each sample were used in SMR experiments. SMR rate expression was fitted to the experimental data in order to predict the rates of CO_2 and H_2 formation. CO formation was not observed in the reforming process. Catalytic performance of sequential co-precipitated georgeite catalyst regarding the methanol conversion is calculated as 94.66% at the end of the 6 hours of the experimental period. The results show that the catalytic activity depends strongly on the catalyst precursor structure and the specific surface area of Cu. BET analysis of the synthesized catalysts within the scope of characterization studies was also performed. Before the reforming experiments, the analyzes of zinc georgeite, which is an amorphous copper-zinc hydroxycarbonate, and zinc malachite in crystalline form were carried out.

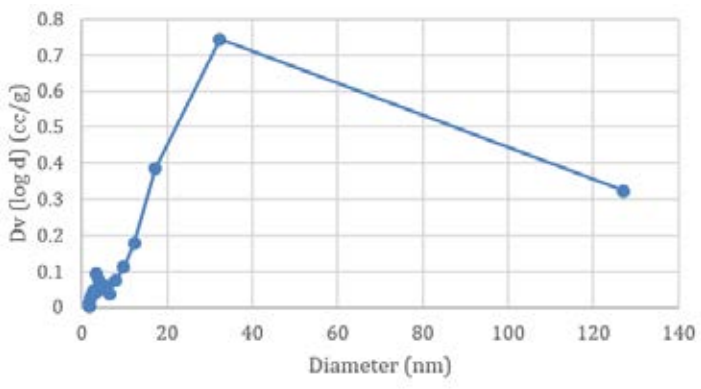


Fig. 1: Pore diameter distribution of zinc malachite

As can be seen from Fig.1., the average pore diameter of the zinc malachite catalyst is around of 3.838 nm. BET surface areas of the prepared catalysts were measured by conventional liquid nitrogen adsorption. The outputs of the device according to the BJH method are taken into account. The surface area and pore volume values of the catalyst are approximately 83.53 m^2/g and 0.5934 cc/g, respectively.

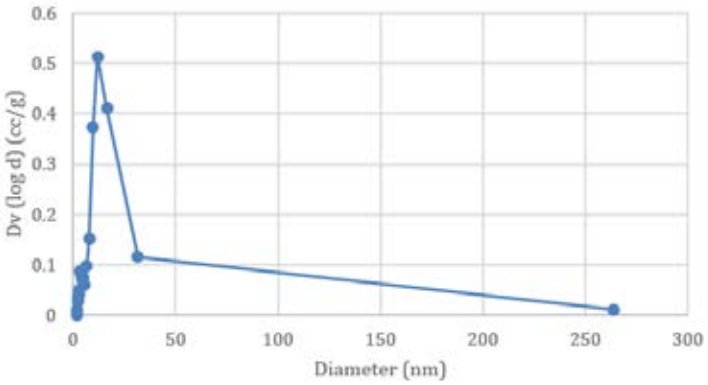


Fig. 2: Pore diameter distribution of zinc georgeite

The average pore diameter of the zinc malachite catalyst, on the other hand, is found to be around of 3.08 nm as given in Fig.2. The surface area and pore volume values of the catalyst are approximately 70.75 m^2/g and 0.2479 cc/g, respectively. BET results of Hifuel R-120 commercial methanol reforming catalyst from Johnson Matthey are also obtained for comparison. It is found that the average pore diameter, surface area and pore volume values of the commercial catalyst are 2.47 nm, 77.28 m^2/g and 0.207 cc/g, respectively. XRD analysis is also carried out to determine the crystallographic properties of the catalysts and the phases.

IV. Conclusions

In this study, different coprecipitation procedures are studied to prepare $Cu/ZnO/Al_2O_3$ catalyst. XRD and BET analysis were performed for characterization. The catalysts obtained by sequentially co-precipitation show superior catalytic performance with high methanol conversion rate and low CO formation comparing to those of the catalysts prepared by different method. It can be concluded that the catalytic activity depends greatly on the catalyst precursor structure, dispersion and the specific surface area of Cu which promotes the higher activity as well as the long term stability. The surface area and pore volume values of the malachite form catalyst are approximately 83.53 m^2/g and 0.5934 cc/g, respectively, while georgeite form has a specific surface area and pore volume as approximately 70.75 m^2/g and 0.2479 cc/g, respectively. The catalytic performance of georgeite catalyst considering the methanol conversion is found to be 94.66%.

Acknowledgements

This research was supported by Vestel Defence Industry, Turkey.

References

Azizan M. T., Aqsha A., Ameen M., Syuhada A., Klaus H., Abidin S. Z., Sher F., Catalytic Reforming of Oxygenated Hydrocarbons for the Hydrogen Production: An Outlook, Biomass Conversion and Biorefinery, 1–24, (2020).

Lakeman, J. B., Browning D., The Role of Fuel Cells in the Supply of Silent Power for Operations in Littoral Waters, (2004).

Shen J. P., Song C., Influence of Preparation Method on Performance of Cu/Zn-Based Catalysts for Low-Temperature Steam Reforming and Oxidative Steam Reforming of Methanol for H2 Production for Fuel Cells, In Catalysis Today, Elsevier, 89–98 (2002).

Smith P., Kondrat S., Chater P., A New Class of Cu/ZnO Catalysts Derived from Zincian Georgeite Precursors Prepared by Co-Precipitation, Chemical Science 8, 2436–47 (2017)

Zhang X., Wang C., A Highly Efficient Cu/ZnO/Al2O3 Catalyst via Gel-Coprecipitation of Oxalate Precursors for Low-Temperature Steam Reforming of Methanol, Catalysis Letters, 102, 183-190 (2005)

Evaluation of Hydrogen Evolution Reaction Performance of Ni-Co Coated 3D Printed Electrodes Prepared by Electrochemical Deposition

[1,2]Bulut Hüner, [1,2,*]Nesrin Demir, [1,2]Mehmet Fatih Kaya,
[1] Erciyes University, Engineering Faculty, Department, Heat Engineering Division, Kayseri, 38039, Turkey
[2]Erciyes University H2FC Hydrogen Energy Research Group, Kayseri, 38039, Turkey

* E-mail: nkayatas@erciyes.edu.tr

Abstract
For sustainable hydrogen generation systems, energy consumption during the electrolysis of water must be lowered. Therefore, it has become important to reduce energy consumption and increase electrical conductivity of the components by developing novel electrode materials. In particular, the electrodes used for hydrogen evolution reaction (HER) have an important place in electrochemical applications. In this study, the electrodes are prepared by the 3D printing method using a conductive polylactic acid (PLA) filament. Then, electrodes are electrochemically coated with Ni and Co in a solution bath with a different molar ratio. Electrochemical properties of the electrode samples are measured using Cycling Voltammetry (CV), Linear Sweep Voltammetry (LSV), Electrochemical Impedance Spectroscopy (EIS), and Chronoamperometry (CA) techniques. The surfaces of electrodes are characterized by Field Emission Scanning Electron Microscopy (FE-SEM) and X-Ray Powder Diffraction (XRD) analysis.

Keywords: Hydrogen evolution reaction, 3D printed electrode, Binary coating, Additive manufacturing

I. Introduction

Fossil fuels that meet most of the energy need in the world are decreasing day by day and cause environmental and air pollution. Hydrogen which is known as an energy carrier has emerged as an important potential to overcome these problems. Hydrogen is not a natural fuel, and it can be obtained by using primary energy sources. Among the hydrogen production methods, the simplest method is the electrolysis of water. In water electrolysis method, hydrogen and oxygen is produced by DC current (Wang et al., 2014). However, electrical energy consumption during the water electrolysis and the overpotentials due to the degredation in the electrodes are disadvantages for this method. For this reason, researchers have been focused on the development of novel electrode and coating materials. An ideal electrode for electrolysis of water must have properties such as a large active surface area, electrochemical stability, good electrical conductivity, low overpotential, low-cost, and ease of use. Therefore, electrode and electrolyte material selection are extremely important for high performance cell structures. Recently, the development of cheaper electrode materials with high kinetic activity for HER has an important place in the electrochemical applications (Santos et al., 2020, Lotfi et al., 2019). 3D printing or additive manufacturing (AM) has attracted the attention of many researchers for the production of electrodes in electrochemical applications due to its advantage of rapid prototyping (BrowneRedondo and Pumera, 2020, Liu et al., 2020). Thermoplastic filaments like PLA, ABS, polyethylene, and polystyrene are utilized in 3D printing technologies. The use of graphene and conductive filaments in the 3D printing method in energy conversion applications has increased recently (Browne and Pumera, 2019, Manzanares Palenzuela et al., 2018, Gusmão et al., 2019). However, the surface of 3D printed electrodes prepared by using conductive PLA filament has poor kinetic and electrical properties. Therefore, to improve these properties of electrodes, an electrochemical coating process can be applied. The electrochemical coating is a process by which metal coating is made on the material by the aid of a direct electric current. This process has many advantages such as wide application areas, low cost, and coating thickness control. To increase the kinetic activity and corrosion resistance of the electrodes, binary or ternary alloy coatings can be required (Bhat and Manjunatha, 2020). Noble metals such as platinum (Pt), palladium (Pd), and ruthenium (Ru) have high kinetic activity for the hydrogen evolution reaction (HER). However, these noble metals are scarce in the world and their prices are very high (Papaderakis et al., 2014).The combining two or more metals instead of these expensive noble metals, HER performance can be increased. Because electrodes prepared by the co-deposition of noble metals and transition metals provide a good kinetic activity for HER in the alkaline medium. In particular, the nickel (Ni) and its alloys have widely used for HER due to their high kinetic activity and excellent corrosion resistance in an alkaline medium. Similarly, cobalt (Co) and its alloys have also relatively low overpotential and good stability for HER. Among Ni-based alloys, Ni-Co alloys have high kinetic activity potential and low cost compared to other transition metals for HER in an alkaline medium (Bhat and Shet, 2020, Zhang et al., 2020).

In this study, 3D printed electrodes were fabricated by Fused Deposition Modelling (FDM) using a commercial conductive PLA filament (diameter 1.75 mm). Then, they were electrochemically coated with nickel and cobalt at different molar ratios under a constant voltage at 10V. Electrochemical properties of electrodes were analyzed by CV, LSV, EIS, and CA techniques. The morphological and structural characteristics of electrodes were measured by FE-SEM and XRD analysis.

II. Experimental Procedure

Fabrication of the electrodes was carried by Ultimaker^{2+} 3D printer using the FDM method. Electrodes were designed in 5 mm width and 50 mm length. The active surface area of the samples was set to 25 mm^2. The remained surfaces of the electrodes were insulated with Teflon tape. A schematic view of the 3D printed electrode can be seen in Figure 1.

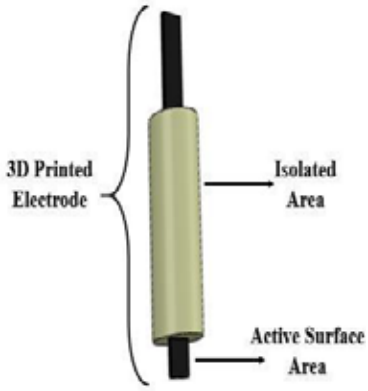


Fig. 1: 3D printed electrode used in the coating process.

The 3D printed electrodes were kept in an ultrasonic bath in ethanol for 15 minutes and then cleaned with deionized water before the electrochemical deposition to remove the impurities on the surface. Electrochemical deposition process was carried out under a constant voltage at 10V using a direct current (DC) power source (AATECH-APS3303DD). printed electrode and Pt sheet were used as cathode (negative electrode) and anode (positive electrode), respectively. Prior to electrochemical deposition, all electrolytes were purged with N_2 gas for 30 minutes to remove dissolved oxygen. Electrode samples and the electrolyte configurations in different molar ratio are given in Table 1.

Tab. 1: Composition of the coating baths in different molar ratios

Specimens	NixCox	NixCo3x	NixCo5x	Reference
$NiSO_4.6H_2O$	*0.5M*	*0.5M*	*0.5M*	*(Tebbakh et al., 2013)*
$CoSO_4.7H_2O$	*0.1M*	*0.3M*	*0.5M*	
H_3BO_3	*0.5M*	*0.5M*	*0.5M*	

Electrochemical measurements were conducted at 25^{o}C temperature using a potentiostat-galvanostat device controlled by a desktop PC and three electrodes configuration is selected for the electrochemical measurement. 3D printed electrode was used as the working electrode. Ag/AgCl (3M KCl saturated) and Pt wire were used as reference and counter electrodes, respectively. The CV, LSV, EIS, and CA measurements were measured in 1M KOH solution. CV and LSV measurements were performed at a scanning speed of 100 mV/s and 10 mV/s respectively. EIS measurements were measured at an amplitude of 10 mV and a frequency range from 1kHz to 0.1Hz.

III. Conclusions

Electrochemical coating processes play an important role in the preparation of electrodes. Ni, Cu, Co, and their alloys are widely used in coating applications due to their excellent properties. Ni and its alloys are one of the most studied electrode materials in an alkaline medium. Therefore, it has been stated that Ni-Co coated electrodes containing different Co ratios have higher kinetic activity properties for HER.

Acknowledgements

The authors would like to thank TUBITAK 1001 (grant number 120M324), and Erciyes University BAP (FDK-2020-10548) for their financial support. The first named author Bulut HÜNER thanks TUBITAK 2211-C (grant number 1649B032000098) and YÖK 100/2000 Ph.D. Scholarship Program.

References

Bhat, R. S. & K. Manjunatha, Corrosion performance of Zinc Based Binary and Ternary Alloy Coatings, Chemical Data Collections**,** 100440, (2020).

Bhat, R. S. & V. B. Shet, Development and characterization of Zn–Ni, Zn–Co and Zn–Ni–Co coatings, Surface Engineering, 36**,** 429-437, (2020).

Browne, M. P. & M. Pumera, Impurities in Graphene/PLA 3D-Printing Filaments Dramatically Influence The Electrochemical Properties of The Devices, Chemical Communications, 55**,** 8374-8377, (2019).

Browne, M. P., E. Redondo & M. Pumera, 3D printing for electrochemical energy applications, Chemical Reviews, 120**,** 2783-2810, (2020).

Gusmão, R., M. P. Browne, Z. Sofer & M. Pumera, The Capacitance and Electron Transfer of 3D-Printed Graphene Electrodes are Dramatically Influenced by The Type of Solvent Used for Pre-Treatment, Electrochemistry Communications, 102**,** 83-88, (2019).

Liu, S., R. Liu, D. Gao, I. Trentin & C. Streb, A 3d-printed composite electrode for sustained electrocatalytic oxygen evolution, Chemical Communications, 56**,** 8476-8479, (2020).

Lotfi, N., T. Shahrabi, Y. Yaghoubinezhad & G. B. Darband, Surface modification of Ni foam by the dendrite Ni-Cu electrode for hydrogen evolution reaction in an alkaline solution, Journal of Electroanalytical Chemistry, 848**,** 113350, (2019).

Manzanares Palenzuela, C. L., F. Novotný, P. Krupička, Z. k. Sofer & M. Pumera, 3D-Printed Graphene/Polylactic Acid Electrodes Promise High Sensitivity in Electroanalysis, Analytical Chemistry, 90**,** 5753-5757, (2018).

Papaderakis, A., N. Pliatsikas, C. Prochaska, K. M. Papazisi, S. P. Balomenou, D. Tsiplakides, P. Patsalas & S. Sotiropoulos, Ternary Pt-Ru-Ni catalytic layers for methanol electrooxidation prepared by electrodeposition and galvanic replacement, Frontiers in chemistry, 2**,** 29, (2014).

Santos, H. L., P. G. Corradini, M. Medina, J. A. Dias & L. H. Mascaro, NiMo–NiCu Inexpensive Composite with High Activity for Hydrogen Evolution Reaction, ACS applied materials & interfaces, 12**,** 17492-17501, (2020).

Tebbakh, S., A. Beniaiche, N. Fenineche, A. Azizi, G. Schmerber & A. Dinia, Electrochemical nucleation behaviours and properties of electrodeposited Co–Ni alloy thin films, Transactions of the IMF, 91**,** 17-23, (2013).

Wang, M., Z. Wang, X. Gong & Z. Guo, The intensification technologies to water electrolysis for hydrogen production–A review, Renewable and Sustainable Energy Reviews, 29**,** 573-588, (2014).

Zhang, F., Z. Yao, O. Moliar, Z. Zhang & X. Tao, Ultra-low-power preparation of multilayer nanocrystalline NiCo binary alloy coating by electrochemical additive manufacturing, Surface and Coatings Technology, 403**,** 126404, (2020).

Hydrogen Production from Agricultural Waste

[1]Elif Ece Çağlı, [1*] Nezihe Ayas
[1]Eskisehir Technical University, Engineering Faculty, Department of Chemical Engineering, Eskişehir, 26555, Turkey

* E-mail: nazcan@eskisehir.edu.tr

Abstract
This work presents an investigation on gasification of biomass using catalysts that were loaded various amounts of Ni metal on kaolin in order to evaluate agricultural waste for producing hydrogen-rich gas. For this purpose, the oil extracted sunflower seeds (pulp), tea, and tobacco waste were mixed in equal proportions and subjected to the gasification process. The experiments were performed in an updraft fixed bed gasifier using air as the gasification agent, at various reaction temperatures (650-850 °C) and reaction times (15-30 min). The Ni/Kaolin catalysts were synthesized by the impregnation method and then characterized by X-ray diffraction (XRD), and X-ray fluorescence (XRF). The highest hydrogen yield was obtained as 6.08 mol/kg biomass at 650 °C, 15 min reaction time in the presence of 20 wt.% of 30Ni/Kaolin.

Keywords: Kaolin, catalyst, biomass, gasification, hydrogen

I. Introduction

Nowadays, energy consumption is increasing with the rapid growth of the world population and industries nevertheless the energy demand is met from conventional fossil-based energy sources such as coal, petroleum, and natural gas. Biomass is one of the most suitable renewable energy sources which is carbon-neutral, limitless, and can be obtained easily from nature and it can be used instead of using fossil-based sources in order to reduce greenhouse gas emissions (Cao etal., 2020).

Hydrogen is a promising and clean energy carrier and has a high energy density (143 MJ/kg) compared to other fossil-based fuels. The use of biomass as a renewable energy source for producing hydrogen can be classified into two main conversion processes; thermochemical process (combustion, pyrolysis, and gasification) and biological process (fermentation and photolysis) (Mazloomi and Gomes, 2012). The principle of the gasification process represents the partial oxidation of the organic compound in the presence of gasification agent (i.e. air, steam, oxygen, and air/steam) and catalyst. Gaseous, liquid, and solid products (syngas, tar, and char) are obtained as a result of gasification. The main purpose here is to achieve high gas product yield at lower temperatures. The gas product consists of H_2 (hydrogen), CH_4 (methane), CO (carbon monoxide), CO_2 (carbon dioxide), light and heavier hydrocarbons (Molino etal., 2016).

The major problem of the gasification process is tar formation which causes cocking, plugging, clogging, and other problems. The various catalysts have been used in order to improve the removal of tar and the hydrogen yield. Clay-based catalysts are widely used which are dolomite, olivine, and lime, etc., and that are cheaper, natural, and easily accessible according to commercial catalysts (Islam, 2020). A single study has been found in which kaolin, one of the clay types, was used as a catalyst in the gasification of coal (Kosminski etal., 2006). However, there are a few studies that are used for different purposes such as bed material (Zhou etal., 2016) in fluidized bed gasifiers and to reduce the alkali metal concentration (Oliviera etal., 2015). There is no detailed study in the literature on the biomass gasification by using Ni loaded on Kaolin catalyst.

In this study, kaolin was used as a support material and different amount of Ni was loaded by impregnation method. Agricultural waste was gasified in an updraft tubular reactor by using air as the gasification agent and synthesized catalyst in order to obtain hydrogen-rich gas. The influence of reaction time, reaction temperature, and amount of Ni loading on kaolin were investigated on the composition gas yield.

II. Experimental Set-up and Procedure

Sunflower seed pulp obtained from a factory producing vegetable oil and unprocessed tobacco and tea wastes were provided from the factory in the Black Sea region in Turkey. $Ni(NO_3)_2.6H_2O$ was purchased from Sigma-Aldrich.

Ni/Kaolin catalysts were prepared by the impregnation method using an aqueous solution of $Ni(NO_3)_2.6H_2O$ and kaolin at 70 °C. The Ni loading amount was varied from 10, 20, 30 wt.%. After loading, it was aged for 24 h at room temperature and dried for 24 h at 105 °C. The samples were calcined for 2 h at 400°C and then particle size of the catalysts were reduced by grinding. The catalysts were reduced at 800 °C for 0.5 h by a H_2/N_2 (20 (v/v) % of H_2) mixture and used in the gasification process.

The chemical compositions of kaolin and synthesized catalysts were determined with X-ray fluorescence (Rigaku ZSX) (Tab.1). To determine the kaolin components and the crystalline structure, the catalysts were analyzed by X-ray diffraction (Rigaku, Rint 2200) using Cu-Kα radiation in the 2θ range of 5 ° -85 ° at a scanning speed of 2 °/min and working at 40 kV and 15mA.

The activity of the synthesized catalysts was tested in the gasification of the agricultural waste mixture. The experimental system consists of an updraft tubular reactor (316SS, 90 x 1 cm reactor), located in a ceramic insulator, and followed by a gas-liquid separator and particle-moisture traps, respectively. Firstly, 3 grams of ground waste mixture and 20 wt.% catalyst were mixed uniformly and then put into the reactor. High purity air was introduced to

the reactor at a 3L/h flow rate. Gasification studies were carried out in the presence of a catalyst at different reaction temperatures (650-850 °C), and times (15-30 min). The existing gas product was collected in a gas sampling bag and analyzed by using a μ-GC (Micro gas chromatography) equipment.

III. Results and discussions

The chemical compositions of kaolin and Ni/kaolin catalysts are given in Table 1.

Tab. 1: XRF analysis of kaolin and Ni/Kaolin catalysts

	Chemical Components (Weight (%))											
	NiO	**Na_2O**	**MgO**	**Al_2O_3**	**SiO_2**	**P_2O_5**	**SO_3**	**K_2O**	**CaO**	**TiO_2**	**Fe_2O_3**	**LOI***
Kaolin	-	*0.15*	*2.16*	*12.64*	*64.92*	*0.10*	*3.31*	*1.25*	*3.20*	*0.28*	*0.49*	*11.04*
10Ni/Kaolin	*12.02*	*0.10*	*1.05*	*11.26*	*57.23*	*0.08*	*3.12*	*1.15*	*2.61*	*0.25*	*0.35*	*10.78*
20Ni/Kaolin	*23.77*	*0.08*	*1.03*	*10.50*	*47.29*	*0.07*	*2.63*	*0.89*	*2.54*	*0.24*	*0.29*	*10.67*
30Ni/Kaolin	*34.87*	*0.06*	*0.89*	*7.78*	*41.16*	*0.07*	*1.97*	*0.83*	*2.14*	*0.17*	*0.29*	*9.87*

*LOI= Loss on ignition

The major components of kaolin are silica oxide and alumina which are commonly used as a catalyst support materials therefore kaolin has a high potential to be used. As it can be seen in Tab. 1, the amount of Ni is higher than the expected amount loading since nickel oxide form is presented in the catalyst.

The structural variations of kaolin and subsequent incorporation of Ni precursors were investigated with XRD analysis (Fig 1.).

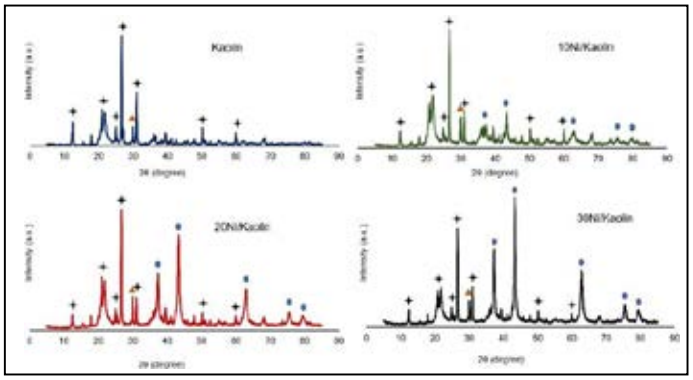


Fig. 1: XRD patterns for kaolin and Ni/kaolin catalysts (NiO: , Kaolinite: , Quartz:)

The main minerals in kaolin are kaolinite and quartz. The peaks of kaolinite with varying intensities are shown at 2θ=12.5°, 20°-25°, 34.8°-40°, 45.8°, 55.5°-60° (Ayoldele and Abdullah, 2019). The intensities of NiO peaks proportionally enhanced at 37.3°, 43.4°, 62.9° while the increase of nickel-metal loadings. The intensities of kaolinite peaks decreased after Ni metal loading.

Fig. 2 and Fig. 3 show the distribution of gas composition yields versus reaction temperature and reaction time, respectively. First of all, in order to determine suitable reaction temperature and time, experiments were carried out at 700, 750, 800, and 850 °C and reaction time of 15 and 30 min without using a catalyst.

As shown in Fig 2, when the temperature is increased from 700 °C to 850 °C, the hydrogen yield increases from 4.53 mol H_2/kg biomass to 5.26 mol H_2 /kg biomass. As the water-gas and methane reforming reactions are endothermic, the reaction shifts to forward direction as the temperature increases. Consequently, hydrogen yield increases (Jeong etal., 2019).

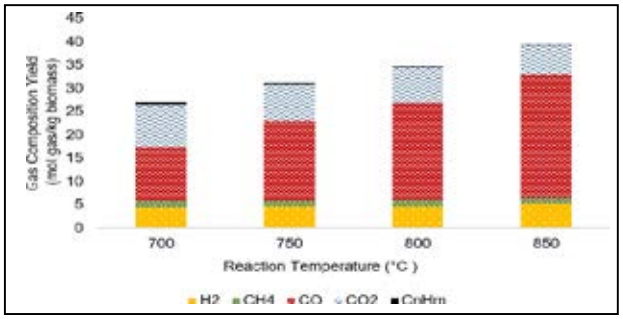


Fig. 2: Effect of reaction temperature on gas product distribution at 15 min, 3L/h air and non-catalytic conditions

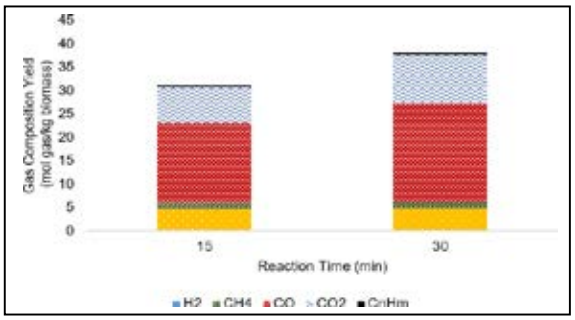


Fig. 3: Effect of reaction time on gas product distribution at 750 °C, 3L/h air and non-catalytic conditions

According to Fig 3, as a result of the increase in reaction time, hydrogen gas yield improves with time. The increase

of hydrogen yield by increasing reaction time could be explained by the thermal cracking of heavier hydrocarbon gases (Jeong etal., 2019). There is no considerable difference in hydrogen yield compared to 15 min and 30 min therefore reaction time kept as 15 min.

The effect of nickel amount of loaded on gas composition yield was investigated at 650 °C, for 15 min and in the presence of 20 wt.% catalyst. The distribution of gas composition yield is presented in Fig. 4.

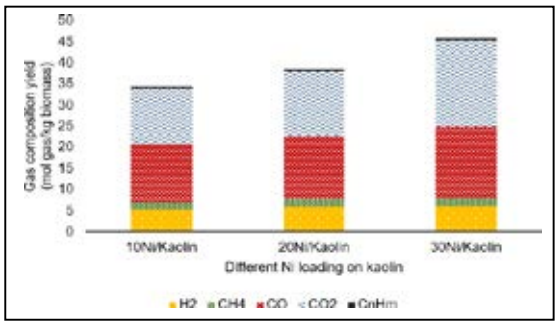


Fig. 4: Effect of different nickel loading on kaolin on gaseous product distribution at 650 °C, 15 min, and 20 wt.% catalyst

From Fig 4., it can be seen that hydrogen yield enhances by increasing the amount of Ni content of the catalyst. The hydrogen yield increases from 5.25 to 6.08 mol H_2/kg biomass by increasing the Ni content from 10 to 30 wt.%. The increasing amount of Ni is provided to shift the water-gas shift reaction to forward direction, thus the hydrogen yield improved (Chan and Tanksale, 2014).

IV. Conclusions

As a conclusion, Ni/Kaolin catalysts were synthesized and characterized by XRF and XRD. Activity studies were performed by the gasification of agricultural waste (sunflower seed pulp, tea, and tobacco). The effects of reaction temperature, time, and amount of Ni loading have been studied in an updraft tubular reactor. The highest hydrogen yield was obtained as 6.08 mol H_2/kg biomass at 650 °C reaction temperature, 15 min reaction time and in the presence of 20 wt.% of 30Ni/Kaolin catalyst. Besides, the similar hydrogen yields were obtained by using 20 wt.% of 10Ni/Kaolin at 650°C and without using catalyst at 850 °C. It was observed that increasing the amount of Ni increased the hydrogen yield. The effect of pre-treated support material is ongoing researches in addition to this study as well.

Acknowledgements

This work has been supported by TAGEM, UNIDO, and GEF. We would like to thank for supporting this research.

References

Ayoldele O. B., Abdullah A. Z., Exploring kaolinite as dry methane reforming catalyst support: Influences of chemical activation, organic ligand functionalization and calcination temperature, Applied Catalysis A: General, 576, 20-31 (2019).

Cao L., Yu I.K.M., Xiong X., Tsang D.C.W., Zhang S., Clark J.H., Hu C., Ng Y.H., Shang J., Ok Y.S., Biorenewable hydrogen production through biomass gasification: A review and future prospects, 186, 109547, (2020).

Chan F. L., Tanksale A., Review of recent developments in Ni-based catalysts for biomass gasification, Renewable and Sustainable Energy Reviews, 38, 428-438, (2014).

Islam M.W., A review of dolomite catalyst for biomass gasification tar removal, Fuel, 267, 117095, (2020).

Jeong Y., Choi Y., Park K., Kim J.S., Air co-gasification of coal and dried sewage sludge in a two-stage gasifier: Effect of blending ratio on the producer gas composition and tar removal, Energy, 185, 708-716, (2019).

Kosminski A., Ross D. P., Agnew J. B., Reactions between sodium and kaolin during gasification of a low-rank coal, Fuel Processing Technology, 87, 1037-1049, (2006).

Mazloomi K., Gomes C., Hydrogen as an energy carrier: Prospects and challenges, Renewable and Sustainable Energy Reviews, 16, 3024-3033 (2012).

Molino A., Chianese S., Musmarra D., Biomass gasification technology: The state of the art overview, Journal of Energy Chemistry, 25, 10-25, (2016).

Oliveira L.C.C.D., Oliveira J.F.G.D., Melo F.L.G.D., Moreno J.D.L., Melo C.D. A.F., Torres A.E.B., Bastos N.M. A., Azevedo C.S.D., Mineral sorbents for downstream sodium capture in biomass gasifiers, Fuel Processing Technology, 138, 629-636, (2015).

Zhou C., Rosén C., Engvall K., Biomass oxygen/steam gasification in a pressurized bubbling fluidized bed: Agglomeration behavior, Applied Energy, 172, 230-250, (2016).

Machine Learning Assisted Analysis of Photoelectrochemical Water Splitting

[1]Burcu Oral, [1]Elif Can, [1*]Ramazan Yıldırım
[1]Boğaziçi University, Engineering Faculty, Department of Chemical Engineering, Istanbul, 34342, Turkey

* E-mail: yildirra@boun.edu.tr

Abstract

In this study a database containing 180 articles (584 instances) for photoelectrochemical water splitting was analyzed using machine learning techniques. Band gap energies of semiconductors and photocurrent density were predicted by random forest and decision tree algorithms by using 33 descriptors including electrode material properties, synthesis methods and factor related to the photoelectrochemical cell used. A descriptive analysis of the database was performed first using simple statistical tools to understand the basic trends in materials, synthesis methods and photoelectrochemical cell setup. Then, association rule mining algorithm was used to identify the effective variables on the band gap of the semiconductors and high photocurrent density; the predictive models for for band gap and current density were also developed.
Keywords: Photoelectrochemical water splitting, machine learning, association rule mining, band gap prediction

I. Introduction

Solar energy is considered to be one of the major energy source for renewable energy in the future while the hydrogen is a potential energy carrier due to its high gravimetric energy density (Prakash etal.,2020). Since the pioneer work by Honda and Fujishima, photoelectrochemical water splitting (PECWS) has been widely studied for hydrogen production from water using solar energy (Momeni etal., 2020). Theoretically, 1.23 eV is needed to split water into hydrogen and oxygen but due to energy losses in practical applications, ~1.8 eV energy is required (Choudhary etal., 2012). For an efficient PECWS, it is important to optimize the photoelectrochemical cell components (i.e photo electrodes and electrolyte), so that energy from sun is efficiently used. The technology is still its infancy; hence large number of studies have been performed to find a way to overcome the problems that limits its performance. Machine learning, which is a practical tool to analyze and deduce trends in large datasets, can be used to analyze PECWS systems as our group had done for photocatalytic hydrogen production over perovskites in a previous work (Can and Yildirim, 2019). In this work a database for photoelectrochemical water splitting is constructed and analyzed by machine learning tools.

II. Method

A comprehensive database was constructed by scanning hundreds of scientific papers on photoelectrochemical water splitting published between 2007 and 2020 at 13 different online sources. After a detailed review (top hits in relevance sorting), 584 experiments from 180 experimental articles were included in the database. The materials used for the electrodes and their preparation processes, as well as the factors related to electrochemical cell (such as reaction medium and light source), were chosen as input variables (descriptors) while band gap (eV) of the working electrode and photocurrent density obtained (mA/cm^2) were defined as the output variables. For classification approach, the data divived into 3 equal parts and named as high, medium and low class. For the band gap classification, the limits for medium class were 2.45 eV and 3 eV whlile they were 0.15 mA/cm^2 and 0.64 mA/cm^2 for photo current density classification; the lower and higher values from these ranges were labeled as low and high classes respectively.
Association rule mining (ARM) was used to identify the effective input variables on the band gap of working electrode and leading high photocurrent density. The *arules* (CRAN “arules”, 2021) and *arulesviz* (CRAN “arulesviz”, 2021) packages of R were chosen for ARM application and visualization, respectively. Random forest (RF) was used in prediction of band gap values and classification of photocurrent density. The *randomForest* (CRAN “randomForest”, 2021) package of R was used for RF application. In the prediction process, 5-fold cross validation (5-fold CV) was applied and the instances with unknown band gap values excluded from the procedure. Then the optimum model, which was determined from the results of 5-fold CV procedure, was tested with *unseen* (25% of overall) data. The evaluation criteria for RF algorithm were selected as the mean absolute error, root mean squared error (RMSE) and R^2. A wide range of the parameters of *ntree* (number of trees in forest) and *nodesize* (number of instances in a terminal node of a tree) were scanned and the results were evaluated to find the model with minimum complexity and highest prediction accuracy. In the last step, the decision tree (DT) analysis was applied to extract heuristic rules leading to the input variables for band gap class and high photocurrent density. This analysis was performed using *rpart* (CRAN “rpart”, 2021) and *rattle* (CRAN “rattle”, 2021) packages for modelling and visualization, respectively. The *complexity parameter* was chosen as the optimization criteria in DT algorithm; and again 5-fold CV was applied to obtain optimum tree model. All models created using R was developed in RStudio.

III. Analysis

The dataset consists of two main parts; material details and photoelectrochemical cell setup. In first part electrode (anode) materials type and propertes, their synthesis methods and treatments are given. In second part, the details about electrolyte and light type are provided. In our dataset, the most studied semiconductor is TiO_2 followed by Fe_2O_3, WO_3, ZnO and $BiVO_4$. Co-catalyst loading and doping are extensively investigated to increase the performance. Hydrothermal method is the most commonly used semiconductor preparation method followed by anodization, electrodeposition and sol-gel synthesis. Xe lamp was used as the light source in 73% of data. NaOH is the most common electrolyte followed by Na_2SO_4 and then KOH; others have less than 5% share in entire dataset.

IV. Results and discussions

The instances with missing band gap values (78 out of 479) were eliminated before RF application. The 401 instances divided into three subsets and labelled as training (4/5 of 301 at each turn), validation (1/5 of 301 at each turn), and testing (100 out of 401); 5-fold cross validation procedure was applied to find the optimum model parameters (ntree=20, nodesize=5). Then, the RF model was tested on testing subset; Figure 1 shows the predicted versus real band gap for testing; the testing error, RMSE, and R^2 were evaluated as 0.12, 0.17, and 0.87, respectively.

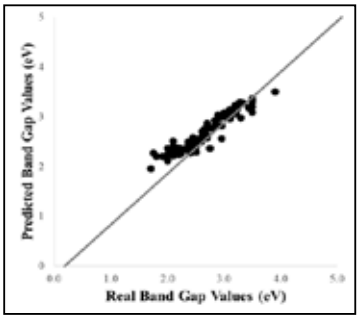


Fig. 1: Predicted versus actual band gap values by using random forest model for testing subset

Association rule mining (ARM) helps to reveal the frequently occuring if-then relations between input and output variables within a large dataset. For example, two variables may be chosen to observe their previously unknown relation as in Figure 2, which shows the relation between the preparation method used for the bottom layer of electrode and the band gap. The x-axis represents bottom layer preparation method while y-axis stands for the band gap classes, which is also labeled with color (low=red, yellow=medium and purple=high); the bubble sizes indicate the probability of apparence. For example, if the bottom layer of electrode is prepared by chemGro (chemical growth) method, the semiconductor tends to have a band gap value smaller than 2.45 eV (low class) because the size of red bubble is bigger than the others. Similarly, the etching mostly produces low bandgap semiconductors when the cases in our dataset are taking into account.

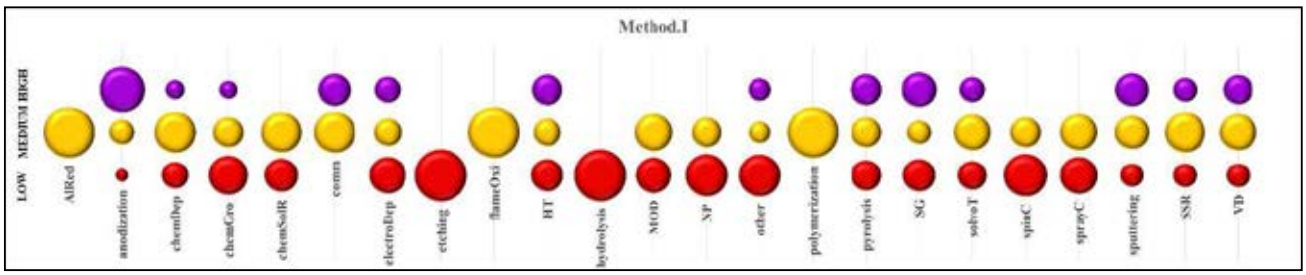


Fig. 2: The effect of bottom layer preparation method on the band gap value of that semiconductor

In Table 1, the confusion matrix for decision tree model of photocurrent density is given. When recall and precision values are analyzed, it is seen that model fails to predict medium class (B) correctly, which is usually the case due to the leaks from both sides, but the prediction of high and low classes (A and C respectively) are reasonably well.

Tab. 1 Confusion matrix for classification model of photocurrent density

Confusion Matrix	**Overall Accuracy**	**Real Class**	**Total number**	**Predicted Class**			**Class Accuracy (Recall)**
				A	**B**	**C**	
Train	0.61	**A**	2671	1977	438	256	0.74
		B	2623	908	1063	652	0.40
		C	2622	326	469	1827	0.70
			Precision	0.62	0.54	0.67	
Test	0.54	**A**	865	543	187	135	0.63
		B	909	276	348	285	0.38
		C	869	129	222	518	0.60
			Precision	0.57	0.46	0.55	

In Figure 3, the optimum decision tree model is given. When the rules are read from top node to the bottom, some general trends can be observed for the high performence (if the number of data and purity of the node are high). For example, it can be said that if the applied bias is less than 0.99 V and the molarity of the electrolyte is greater than 4 M, the tree results in class A (representing high class) with 0.92 purity suggesting that these combinations can be considered as a reliable rule to follow.

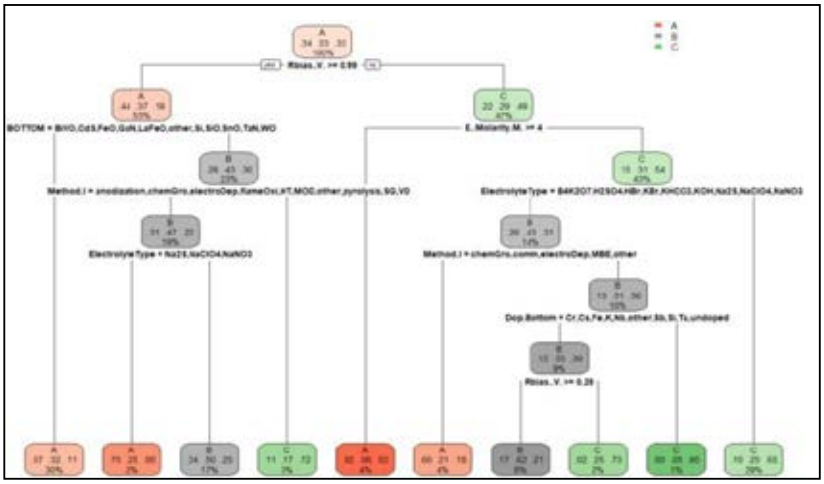


Fig. 3: Decision Tree model for photocurrent density prediction

V. Conclusions

In this work, a comprehensive database for PECWS is constructed with 180 scientific articles and then analyzed by using association rule mining, random forest, and decision tree algorithms aiming to predict band gap and to determine the relation between input and output variables (band gap or photocurrent density). The band gap was predicted successfully with the testing error, RMSE, and R^2 values of 0.12, 0.17, and 0.87, respectively. The association rules revealed the effect of material, preparation method and post-treatment conditions on the band gap of the electrode produced. Although the RF algorithm failed to predict the current density, the decision tree developed for that, provided some heuristic rules with higher than 70% accuracy. The results of band gap prediction can be a guide to researchers to foresee the possible band gap of photoanode to be produced. Similarly, ARM and DT algorithms may be helpful to determine optimum photoanode specifications and reaction conditions to reach the band gap value (in intended interval) and high photocurrent density.

References

Can E., Yildirim R., Data mining in photocatalytic water splitting over perovskites literature for higher hydrogen production, Applied Catalysis B: Environmental 242, 267–283 (2019).

Choudhary, S., Upadhyay, S., Kumar, P., Singh, N., Satsangi, V. R., Shrivastav, R., Dass, S., Nanostructured bilayered thin films in photoelectrochemical water splitting - A review. International Journal of Hydrogen Energy, *37*(24), 18713–18730 (2012).

CRAN, arules: Mining Association Rules and Frequent Itemsets, https://cran.r-project.org/web/packages/arules/index.html, (accessed April 2021)

CRAN, arulesViz: Visualizing Association Rules and Frequent Itemsets, https://cran.r-project.org/web/packages/arulesViz/index.html, (accessed April 2021).

CRAN, randomForest: Classification and Regression Based on a Forest of Trees Using Random Inputs, https://cran.r-project.org/web/packages/randomForest/randomForest.pdf, (accessed April 2021).
CRAN, rattle: Graphical User Interface for Data Science in R, https://cran.r-project.org/web/packages/rattle/rattle.pdf, (accessed April 2021).

CRAN, rpart: Recursive Partitioning and Regression Trees, https://cran.r-project.org/web/packages/rpart/rpart.pdf, (accessed April 2021).

Momeni M.M., Ghayeb Y., Ezati F., Investigation of the morphology, structural, optical, and photoelectrochemical properties of WO3–Fe2O3/CrTiO2 thin-film photoanodes for water splitting, Applied Physics A, 126, 303 (2020).

Prakash J., Prasad U., Shi X., Peng X., Azeredo B., Kannan A.M., Photoelectrochemical water splitting using lithium doped bismuth vanadate photoanode with near-complete bulk charge separation, Journal of Power Sources 448, 227418(2020).

Investigation of Ni/Cu Impregnated Zeolite Catalysts for Hydrogen Production from Methanol Steam Reforming

[1]Özgecan Çağlayan, [1*]Nezihe Ayas,
[1]Eskişehir Technical University, Engineering Faculty, Department of Chemical Engineering, 2 Eylul Campus,Eskişehir, 26555, Turkey

* E-mail: nazcan@eskisehir.edu.tr

Abstract
Hydrogen, in addition to being a renewable, is a sustainable and clean energy carrier. Using pure hydrogen as a fuel has some problems about storage and transportation. Methanol is an attractive hydrogen source since it is liquid at room temperature and has a high hydrogen ratio. The impregnation method was used in this study to synthesize Ni/Zeolite and Ni-Cu/Zeolite catalysts, which were then characterized using XRF, XRD, and FT-IR and their activities in methanol steam reforming were examined. The catalytic activities of zeolite supported catalysts for methanol steam reforming were investigated at various temperatures (200-800°C) using a constant steam:carbon (3:1) molar ratio, liquid hourly space velocity (LHSV=0.012L/h.gcat) and a constant 0.02mL/min. flow rate. The highest hydrogen yield (34.96 mole H_2 prod./mole methanol feed) was reached at 600 ° C with a 6% Ni-24% Cu/Zeolite catalyst.

Keywords: Hydrogen, Methanol, Steam Reforming, Zeolite, Catalyst, Impregnation.

I. Introduction

Over the past several years, there has been an increasing demand for new clean energy sources. Hydrogen is a clean energy source that is both environmentally friendly and efficient, with the additional benefit of releasing only water and energy when burned. Because of the transportation and storage problems of pure hydrogen, the focus has shifted to alternative hydrogen carriers (Iulianelli et al.,2014).

Methanol is a beneficial fuel in several aspects, which explains why it is so effective as a hydrogen carrier including the ability to be produced from renewable sources. Methanol has a high H/C ratio (4:1) with no carbon-carbon bonds that need to be broken. In contrast to methane reforming, which occurs at 800-1000°C, the methanol steam reforming reaction occurs at comparatively low temperatures (150-350°C). The Methanol Steam Reforming process has been regarded as a very appealing method for hydrogen production (Paulo et al.,2007 and Iulianelli et al.,2014). The following chemical reactions can be used to describe it (Iulianelli et al.,2014):

$CH_3OH + H_2O \leftrightarrow CO_2 + 3H_2$	$\Delta H^0_{298K} = +49.7$ kJmol^{-1}	(I)
$CO + H_2O \leftrightarrow CO_2 + H_2$	$\Delta H^0_{298K} = -41.2$ kJmol^{-1}	(II)
$CH_3OH \leftrightarrow CO + 2H_2$	$\Delta H^0_{298K} = +90.7$ kJmol^{-1}	(III)

The Methanol Steam Reforming is defined by reaction (I), the water gas shift reaction is embodied by reaction (II), and the decomposition of methanol reaction is represented by reaction (III). Only the water gas shift reaction is exothermic and occurs without a change in the number of moles. The Methanol Steam Reforming reaction is endothermic, and it involves an increase in the number of moles. (Iulianelli et al.,2014).

For the syntesis of hydrogen-rich syngas, various catalysts have been researched. Copper-based catalysts have a higher hydrogen selectivity than nickel-based catalysts for methanol steam reforming. The addition of copper to nickel catalysts has been shown to enhance their activity and selectivity. (Lytkina et al., 2015). The mechanism of methanol molecules adsorption on the catalyst surface has changed, which is why the properties of catalysts depending on the dominant metal have changed. It lowers CO yield since high copper content catalysts have a greater proclivity for single-center alcohol adsorption. (Iulianelli et al.,2014). The activity of the catalyst in the reactions is also dependent on catalyst support. Currently, zeolites have promising advantages in the area of hydrogen production. Zeolite catalysts are crystalline alumina-silicates with a microporous structure and an open structure of tetrahedral crystals with a defined pore size (Yao et al.,2018). Zeolites can be used as a porous support material for nickel and other metals such as copper to assist metal dispersion and improve catalytic activity in order to produce hydrogen-rich syngas.

In the literature research, it was found that catalysts synthesized with different support materials were used in methanol steam reforming and zeolite supported catalysts were used in steam reforming of other chemicals such as dimethyl ether and methane. However, there are no studies in which zeolite supported catalysts are used in methanol steam reforming.

In this study, the production of hydrogen was investigated as a function of temperature using methanol steam reforming with the help of zeolite catalysts. By keeping the metal loading weight of the catalysts constant at 15% and 30%, the percentages of Ni and Cu were changed. Ni/Zeolite and Ni-Cu/Zeolite catalysts, which were used in this work were made by impregnation method and characterized using X-ray diffraction (XRD), X-ray fluorescence (XRF) and Fourier transform infrared spectroscopy (FT-IR).

II. Experimental Set-up and Procedure

99% purity of Nickel(II)nitratehexahydrate [$Ni(NO_3)_2.6H_2O$], Copper(II)nitratetrihydrate [Cu(NO3)2.3H2O and methanol were used for catalyst synthesis and steam reforming without further purification. Zeolite was provided by a private company from Balıkesir/Turkey.

The impregnation method was used to synthesize Ni/Zeolite and Ni-Cu/Zeolite catalysts at various Ni and Cu weight ratios (15-30 wt./wt.%). Before the impregnation process, the zeolite was ground in the Vibrating Cup Mill for 45 seconds until it reached a particle size of 50-60 microns. Then the nitrate salts were dissolved in pure water, then stirred for 3 hours at 70°C with the addition of zeolite as a support material. The samples were aged for a day at room temperature before drying for 24 hours at 105°C. The Ni-based catalyst was calcined in a tubular furnace at 600°C for 3 hours at a heating rate of 3°C/min and the flow rate of air is 0.3 L/min. Catalysts containing Cu were calcined in a tubular furnace at 550°C for 3 hours at a heating rate of 3°C/min at an air flow rate of 0.3 L/min. Before being used in methanol steam reforming experiments, catalysts were reduced at 800°C under a flow rate of 0.4 L/min, H_2 for 45 min.

Synthesised catalyst were characterised using several techniques. Those are Rigaku ZSX model XRF instrument was used to determine the mass composition of the catalysts. The catalysts' crystal structures were investigated using a Rigaku Rint 2200 brand XRD device set to 40 kV voltage and 15 mA current with Cu-K as the X-ray source, with a scanning angle of 0.02°, a scanning speed of 4°/min, and a range of 2θ = 3-85°. The functional groups of the catalysts were determined using an FT-IR system from Thermo Science Nicolet IS10 brand. Analyses were carried out at 64 scan speeds and 4 cm^{-1} resolution, with a scanning range of 525-4000 cm^{-1} at room temperature.

The catalysts' activities were tested by steam reforming of methanol at atmospheric pressure in a fixed bed continuous flow quartz reactor (PID Eng & Tech Micro Efficiency). In the experiments, the reaction volume was formed by mixing 0.2 g of catalyst with SiC. Experimental studies were carried out at different temperature range of 200-800 °C at constant steam:carbon ratio (3:1) and LHSV value (0.12L/h.gcat). Water and methanol were fed into the system via HPLC pumps at a flow rate of 0.02 mL/min. The composition of the gas product mixture was determined online by An Agilent 490 Micro Gas Chromatograph (µGC) calibrated with a standard gas mixture.

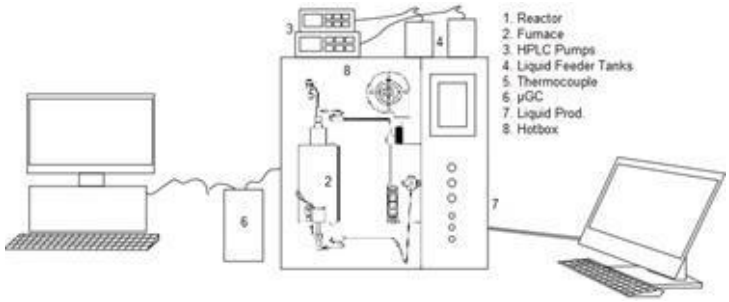


Fig.1: Catalytic activity test system.

III. Results and discussions

The mass composition of the zeolite used as support material and the synthesized catalysts were determined by XRF analysis and are given in Tab.1 and Tab.2 respectively. As seen in Tab.1, the main components of the zeolite consist of 72.85% SiO_2, 11.36% Al_2O_3 and 4.14% CaO, while the remaining part contains K_2O, MgO, Fe_2O_3 and TiO_2. The XRF results are higher than the desired value because they are in oxide form, and calculations are based on metallic Ni and Cu.

Tab. 1: XRF Results of Zeolite

Support	SiO_2	Al_2O_3	CaO	K_2O	MgO	Fe_2O_3	TiO_2	LOI
Zeolite	72.85	11.36	4.14	3.67	1.20	0.79	0.11	5.88

LOI: Loss on Ignition

Tab.2: XRF Results of Catalysts

Catalysts	NiO	CuO
15% Ni / Zeolite	18.22	-
10% Ni - 5% Cu / Zeo.	11.84	5.43
5% Ni - 10% Cu / Zeo.	5.51	11.51
7.5% Ni - 7.5% Cu / Zeo.	9.64	8.70
24% Ni - 6% Cu / Zeo.	29.93	6.48
6% Ni - 24% Cu / Zeo.	8.73	25.22

The FT-IR results of the catalysts are represented in the Fig.2. The stretching vibrations of the Ni-O bond are defined as 1050 cm^{-1} in the characteristic Ni bands. The vibrational modes greater than 1100 cm^{-1} correspond to the M-OH. The lack of other band in the spectrum means that the catalyst surface is free of contamination. It shows the presence of incoming peak CO_2 at a wavelength of 2350 cm^{-1}.

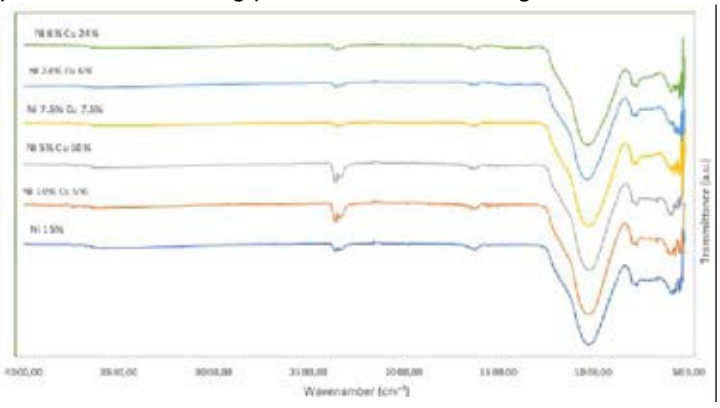


Fig.2. FT-IR Results of Catalysts

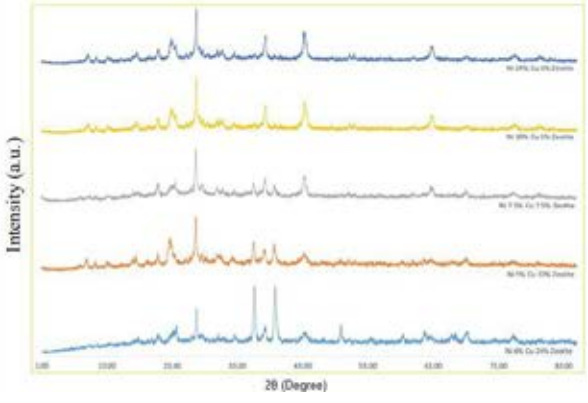


Fig.3. XRD Results of Catalysts

Fig.3 shows that the catalysts have NiO characteristic peaks at 2θ=37.18°, 43.12°, 63.08°, 64.32° and 79.74°, CuO characteristic peaks at 2θ=16.72°, 32.5°, 48.94°, 56.82°.

Catalyst activities were determined in the methanol steam reforming and the effect of catalyst loading ratios and temperature on hydrogen yield is given in Figure 4.

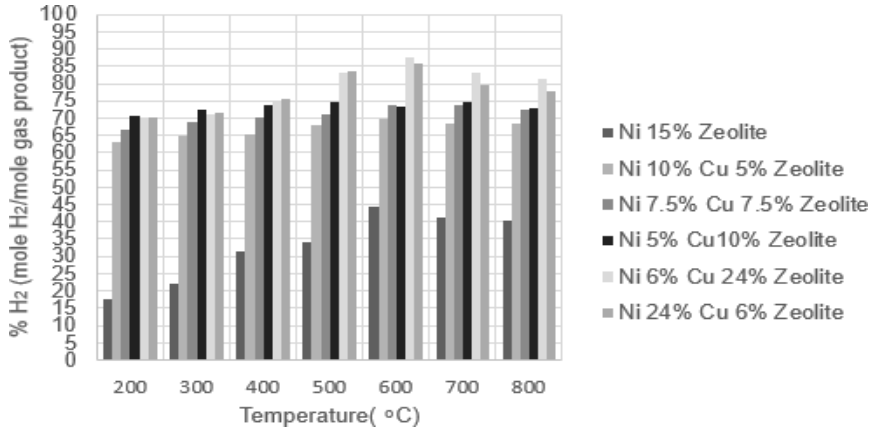


Fig.4. Effects of the catalyst and temperature on the moles of hydrogen in gas product (LHSV=0.012L/h.gcat. / S:C=3:1)

According to Fig.4 keeping the S:C ratio, LHSV value, and catalyst amount constant, the effect of catalyst and temperature on hydrogen production was examined in this work. While the conversions were 94.92% at low temperatures, 100% methanol conversion was achieved in all catalysts at high temperatures. All catalysts had the highest hydrogen molar content at 600°C. Since the highest hydrogen content was reached at 600°C, hydrogen selectivity and yield were calculated at this temperature.

Catalysts' selectivity and yield were specified in Tab. 3 at constant reaction conditions of at 600°C, LHSV=0.012L/h.gcat. / S:C=3:1.

Tab.3: Catalysts' selectivity and hydrogen yield

Catalysts	Selectivity % (mole H_2 prod. / total moles of H_2 in the gas prod.)	Yield % (mole H_2 prod. / mole methanol feed)
15% Ni / Zeo.	77.94	17.80
10%Ni - 5%Cu / Zeo.	94.44	27.92
7.5% Ni - 7.5% Cu / Zeo.	93.06	29.54
5%Ni - 10%Cu / Zeo.	86.92	29.30
6%Ni - 24%Cu / Zeo.	91.04	34.96
24%Ni - 6%Cu / Zeo.	92.62	34.38

As seen in Tab.3, the highest hydrogen selectivity (94.44% mole H_2 prod./total moles of H_2 in the gas prod.) was achieved with 10%Ni - 5%Cu/Zeolite catalyst, while the highest hydrogen yield (34.96% mole H_2 prod./mole methanol feed) was obtained with 6% Ni - 24% Cu/Zeolite catalyst.

IV. Conclusions

The purpose of this research the investigation of zeolite supported catalysts for the methanol steam reforming. It has been observed that zeolite supported catalysts are effective in hydrogen production from Methanol steam reforming. Due to the composition, acidity and crystal structure of the zeolite, it has been determined that it is a suitable support material for the catalyst to be used in methanol steam reforming. It was determined that Cu among the metals loaded on the support material increased the yield while nickel increased the hydrogen selectivity. As a result, Ni-Cu / Zeolite catalysts have been discovered to be effective in the methanol steam reforming. As a result, Ni-Cu/Zeolite catalysts have been discovered to be effective in methanol steam reforming.

References

Inaba, M., Murata, K., Saito, M., & Takahara, I. Hydrogen Production by Gasification of Cellulose over Ni Catalysts Supported on Zeolites. Energy & Fuels, 20(2), 432–438, (2006).

Iulianelli A., Ribeirinha P., Mendes A., Basile A., Methanol steam reforming for hydrogen generation via conventional and membrane reactors: A review, Renewable and Sustainable Energy Reviews, Vol 29, Pages 355-368, (2014).

Lytkina, A. A., Zhilyaeva, N. A., Ermilova, M. M., Orekhova, N. V., & Yaroslavtsev, A. B., Influence of the support structure and composition of Ni–Cu-based catalysts on hydrogen production by methanol steam reforming. International Journal of Hydrogen Energy, 40(31), 9677–9684, (2015).

Palo D.R., Dagle R.A., Holladay J.D., Methanol Steam Reforming for Hydrogen Production, Chem. Rev., 107, 3992−4021, (2007).

Yao D., Yang H., Chen H., Williams P.T., Investigation of nickel-impregnated zeolite catalysts for hydrogen/syngas production from the catalytic reforming of waste polyethylene, Applied Catalysis B: Environmental, Vol 227, 477-487, (2018).

Integration of methane cracking and direct carbon fuel cell with CO_2 capture for hydrogen carrier production

[1*]Aliya Banu, [1]Yusuf Bicer
[1] Division of Sustainable Development, College of Science and Engineering, Hamad Bin Khalifa University, Doha, Qatar

* E-mail: alba34159@hbku.edu.qa

Abstract
Hydrogen fuel production from methane cracking is a sustainable process compared to the steam methane reforming currently in practice, due to minimal/zero greenhouse gas emissions. Also, carbon black that is co-produced is valuable and can be marketed to other industries. As this is a high-temperature process, using solar energy can further improve its sustainability. An integrated solar methane cracking system is proposed where hydrogen and carbon products are sent to fuel cells to generate electricity. The CO_2 exhaust streamfrom the carbon fuel cell can be captured and reacted with hydrogen in the CO_2 hydrogenation unit to produce liquid fuels such as methanol and dimethyl ether. In this study, the process is simulated in Aspen Plus™ to obtain the thermodynamic properties and its energy and exergy efficiencies are evaluated by carrying out a detailed thermodynamic analysis.

Keywords: Direct Carbon Fuel Cell, Proton Exchange Membrane Fuel Cell, Carbon dioxide Hydrogenation, Methanol Production, DME Production.

I. Introduction

Industrially hydrogen is produced using steam methane reforming (SMR) and coal gasification (Saxena et al., 2008). These processes lead to a high amounts of CO_2 emissions. Methane cracking, on the other hand, is a cleaner process and produces solid carbon. Carbon by-product can be used in other industries (Muradov et al., 2005). This process takes place at temperatures above 1200 ℃. Utilizing concentrated solar energy as the heating source can provide the required temperatures without a catalyst. This route allows for cleaner production of hydrogen fuel.

Hydrogen, due to its low energy density by volume, is difficult to transport and store. It is also flammable and explosive (Goeppert et al., 2014). It requires a significant amount of energy for either liquefaction or compression to make transportation feasible. Therefore, hydrogen's conversion into another hydrogen carrier is suggested as a possible route towards a hydrogen economy. Chemical fuels such as methanol and dimethyl ether (DME) are safer to transport and can be stored as liquids at room temperatures. They can be later converted to hydrogen at the point of use or utilized directly as fuel.

The CO_2 needed for methanol, and DME synthesis can be obtained through methane cracking by adding a direct carbon fuel cell (DCFC). Carbon black from methane cracking can be supplied to the DCFC to produce electricity and CO_2. It was shown that molten carbon anode fuel cells produce exhaust stream rich in CO_2, making them more suitable for carbon capture (Campanari et al., 2013).

This paper reports an integrated energy system consisting of solar methane cracking for hydrogen production, followed by its conversion to methanol and DME. A thermodynamic analysis will be conducted for the system's components to calculate the integrated system's energy and exergy efficiencies.

II. System Description

The study proposes an integrated system that consists of a methane cracking unit using solar energy for methanol and DME production. The methane cracking system products: hydrogen and carbon are sent to the hydrogen fuel cell system and a DCFC to produce electricity. The CO_2 from the DCFC product stream is reacted with hydrogen to produce methanol and further dehydrated to synthesize DME. This system allows the production of green hydrogen using solar energy, converted to liquid hydrogen energy carriers using CO_2 captured from within the system. The sources, systems and services of the system are depicted in Fig. 1. The process flow diagram of the proposed overall integrated process is presented in Fig. 2.

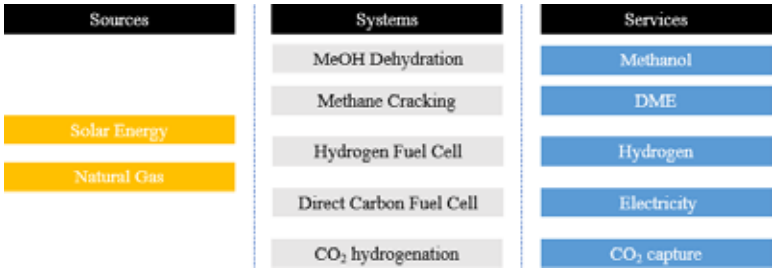


Fig. 1: The sources, included subsystems and the services provided by the proposed integrated system.

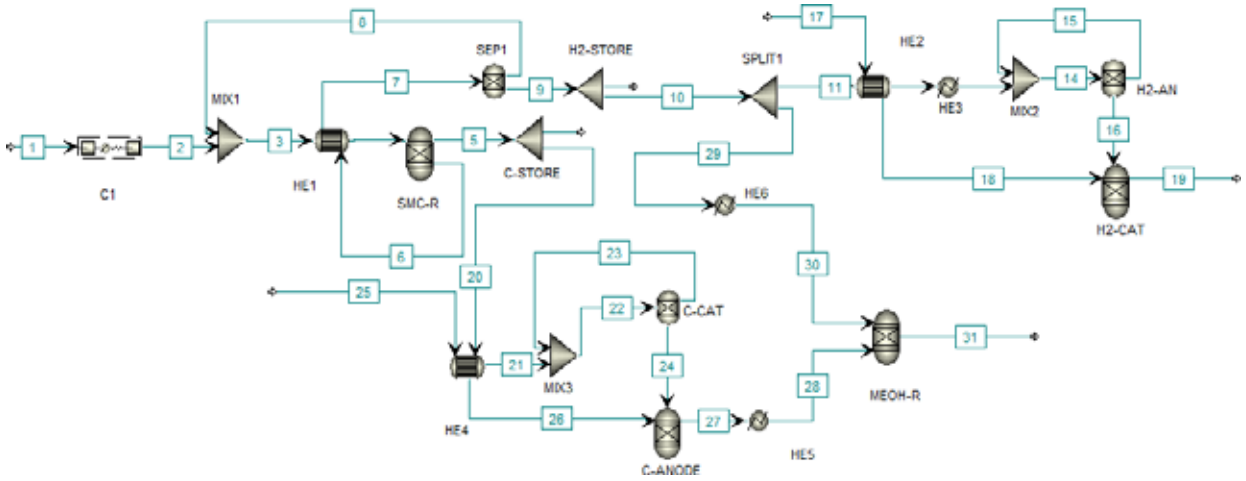


Fig 2: Process flow diagram of the proposed system

III. Thermodynamic Analysis

A detailed thermodynamic assessment is conducted for the proposed integrated system. The system is modelled and simulated on Aspen Plus™. Balances are performed over the system's components using the obtained thermodynamic properties of the streams. Energy and exergy efficiencies are calculated over the components and the overall system to assess its performance. The mass, energy, entropy, and exergy balances are carried out by using eq. 1,2,3,and 4 respectively.

$$\sum_{in} \dot{m}_i = \sum_{out} \dot{m}_i \quad (1)$$

$$\dot{Q}_{in} + \dot{W}_{in} + \sum_{in} \dot{m}_i h_i = \dot{Q}_{out} + \dot{W}_{out} + \sum_{out} \dot{m}_i h_i \quad (2)$$

$$\frac{\dot{Q}_{in}}{T_s} + S_{gen} + \sum_{in} \dot{m}_i s_i = \frac{\dot{Q}_{out}}{T_s} + \sum_{out} \dot{m}_i s_i \quad (3)$$

$$\dot{E}x_{Q_{in}} + \dot{E}x_{W_{in}} + \sum_{in} \dot{m}_i ex_i = \dot{E}x_{Q_{out}} + \dot{E}x_{W_{out}} + \sum_{out} \dot{m}_i ex_i + \dot{E}x_D \quad (4)$$

where, $\dot{S}_{gen}$ is the rate of energy generation from the components (kW.K-1) and $\dot{E}x_D$ Is the rate of exergy destruction from the component (kW). The below equations calculate the energy and exergy of the subsystems and overall system:

$$\eta_{en} = \frac{\sum E_{useful}}{\sum E_{input}} \quad (5)$$

$$\eta_{ex} = \frac{\sum Ex_{useful}}{\sum Ex_{input}} \quad (6)$$

In the thermodynamic modelling of the system, the following assumptions were used:

- The system operates as a steady-state process
- All compressors have an isentropic efficiency of 80%
- Pressure drops are neglected
- Reference conditions of 25° C and 101.325 KPa
- The potential and kinetic are neglected in the energy and exergy balances

The integrated system is simulated in Aspen Plus™ using the Peng-Robinson equation of state to calculate the thermodynamic properties. Due to the presence of solid carbon in the system, a stream class of MIXCIPSD was used. The methane cracking reactor is simulated using Gibbs free energy minimization with phase equilibrium calculations using the built-in RGibbs block operating at 1200 ℃ and 10 atm. A separator is used to model the hydrogen membrane separator, which has a hydrogen separation rate of 90%. The unreacted methane is recycled into the cracking reactor.

For the H_2 , a proton exchange membrane fuel cell (PEMFC) is used, the anode is modelled using a separator where heated steam is split and sent to the cathode, simulated using an RGibbs block where the cell reaction takes places. Air heated to the cell's operating temperature enters the cathode, where the oxygen reacts with the hydrogen from the anode, and steam exits from the cathode. The DCFC is modelled in a similar manner where the anode is modelled using the RGibbs reactor operating at 600 ℃ and 1 bar.

IV. Results and discussions

Pure methane at atmospheric pressure and 25 C is used as the feed to the process. The feed is heated and compressed before entering the solar reactor which operates at 1200 ℃ and 10 atm, these conditions give a methane conversion rate of 95%. The results of the Aspen simulation of the methane cracking unit is shown in Table 1. A methane feed flowrate of 0.5 kg/s produces 0.37 kg/s carbon black and 0.13 kg/s hydrogen. The carbon is stored and used in a direct carbon fuel cell. While part of the hydrogen produced is used for in a PEMFC to generate electricity. The net electrical output from the cells is 4.18 MW. The calculated energy and exergy efficiency of the subsystems are shown in Fig. 3.

Tab. 1: Results of the thermodynamic properties obtained from Aspen Plus™ for the methane cracking subsystem

Property	Unit	1	2	3	4	5	6	7	8	9
Temperature	*C*	*25*	*200*	*249.3695*	*917.972*	*1200*	*1200*	*500*	*500*	*500*
Pressure	*kPa*	*101.325*	*1013.25*	*1013.25*	*1013.25*	*1013.25*	*1013.25*	*1013.25*	*1013.25*	*1013.25*
Mass Enthalpy	*kJ/kg*	*-4646.2*	*-4213.8*	*-3879.4*	*-958.8*	*2711.7*	*14971.4*	*5391.7*	*458.3*	*6904.9*
Mass Entropy	*kJ/kg-K*	*-5.026*	*-5.085*	*-4.423*	*-0.936*	*3.033*	*12.306*	*3.531*	*0.225*	*4.321*
Mass exergy	*kJ/kg*	*51820.4*	*52270.4*	*54111.9*	*55992.8*	*35963.1*	*119516.1*	*112552.6*	*78252.3*	*123073.6*
Mass Flows	*kg/s*	*0.5*	*0.5*	*0.538541*	*0.538541*	*0.374343*	*0.164192*	*0.164192*	*0.038541*	*0.125651*

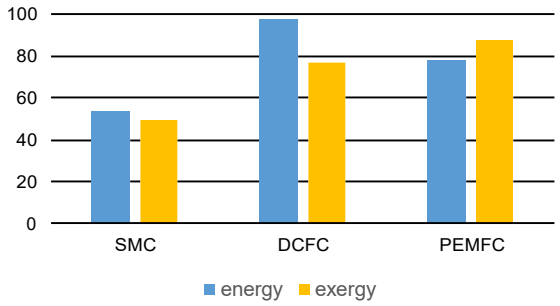


Fig. 3: Energy and Exergy efficiency of the solar methane cracking (SMC), DCFC and PEMFC subsystems.

V. Conclusions

The proposed integrated system is evaluated thermodynamically but simulating the system in Aspen. Mass, energy, entropy, and exergy balances are performed over the units of the subsystem and the efficiencies are calculated. The solar methane cracking subsystem has energy and exergy efficiencies of 53% and 49%, respectively.

Future work consists of modelling of the CO_2 hydrogenation section, where pure CO_2 stream and hydrogen from the methane cracker will be reacted to synthesize methanol. After separation of the methanol from the steam by-product, it will be dehydrated in another reactor to produce DME. The energy and exergy analyses of the CO_2 hydrogenation section and the overall integrated system will be studied.

Acknowledgements

This report was made possible by an Award (GSRA7-2-0427-20025) from the Qatar National Research Fund.

References

Campanari S., Gazzani M., Romano MC., Analysis of direct carbon fuel cell based coal fired power cycles with CO_2 capture, J Eng Gas Turbines Power, (2013).

Goeppert A., Czaun M., Jones JP., Surya Prakash GK, Olah GA., Recycling of carbon dioxide to methanol and derived products-closing the loop, Chem Soc Rev, (2014).

Muradov N., Smith F., T-Raissi A., Catalytic activity of carbons for methane decomposition reaction, Catalysis Today, (2005).

Saxena SK, Drozd V, Durygin A. A fossil-fuel based recipe for clean energy. International Journal of Hydrogen Energy, (2008).

Hydrogen production through dehydrogenation of morpholine borane in the presence of PSSA stabilized Pd-based catalysts

[1*]Ceren Yuksel Alpaydin, [2]Mülkiye Kaymaz, [3]Senem Karahan Gülbay, [4]C.Ozgur Colpan
[1]Dokuz Eylul University, The Graduate School of Natural and Applied Sciences, Department of Mechanical Engineering, Izmir, Turkey
[2]Dokuz Eylul University, The Graduate School of Natural and Applied Sciences, Department of Chemistry, Izmir, Turkey
[3]Dokuz Eylul University, Department of Chemistry, Izmir, Turkey
[4]Dokuz Eylul University, Department of Mechanical Engineering, Izmir, Turkey
* E-mail: yukselceren@yandex.com

Abstract
Catalytic hydrolysis of boron compounds is a safe and clean method for hydrogen production. In this study, PSSA stabilized Pd catalysts were investigated for the dehydrogenation reaction of morpholine borane. PSSA stabilized Pd, PdNi, PdAg and PdCo catalysts were synthesized in situ and equal proportions of PSSA (metal/PSSA=1) were used for each. Dehydrogenation experiments were carried out in a laboratory scale test setup containing a schlenk flask, hot water circulator and burette, and the amount of hydrogen produced was measured by the water displacement method. It was concluded that the PdAg catalyst is the most active catalyst for the hydrolysis of morpholine borane at room temperature, and all bimetallic catalysts studied are more active than the monometallic Pd catalyst. In addition, optimization of the ratio of PSSA and metals for PdAg catalyst and reaction kinetics for 15, 20, 25, and 30°C were investigated. The results showed that morpholine borane is a suitable candidate for hydrogen production.

Keywords: Hydrogen production, boron compounds, stabilized catalysts, hydrolysis reaction

I. Introduction

The necessity to find environmentally friendly and efficient solutions that can overcome the energy problem has been the source of motivation for many scientific studies today. Clean energy sources such as solar and wind energy have been studied extensively in this context, but hydrogen energy stands out in this area because it is not dependent on the climate and the environment. Since hydrogen is not found in nature as pure, it is necessary to produce hydrogen using environmentally friendly technologies. Boron compounds are easily hydrolyzed at room temperature, produce hydrogen and some non-toxic by-products as a result of hydrolysis reaction (Lai et.al, 2015). Sodium borohydride ($NaBH_4$), ammonia borane (NH_3BH_3), dimethylamine borane (C_2H_7BN) and hydrazine borane ($N_2H_4BH_3$) are the most researched materials so far. Morpholine borane is recommended as an alternative material to these materials (Can and Metin, 2019).

In this study, four different catalysts, PSSA stabilized Pd, PdNi, PdCo, and PdAg, were investigated for hydrogen production from morpholine borane. PSSA stabilized PdAg was the highest performing catalyst among these catalysts. The optimum amount of PSSA and metals for the PdAg catalyst were determined. Finally, hydrogen production performances were investigated for four different temperatures: 15, 20, 25, and 30°C.

II. Experimental Set-up and Procedure

Poly(4-styrenesulfonic acid-co-maleic acid) sodium salt (PSSA, MW 20000), palladium(II) nitrate dihydride %40 Pd basis, silver nitrate (≥99%), nickel(II) chloride hexahydride (99.99%), cobalt(II) chloride hexahydrate (98%), borane morpholine complex (95%) were purchased from Sigma-Aldrich. Distiled water was used in all experiments.

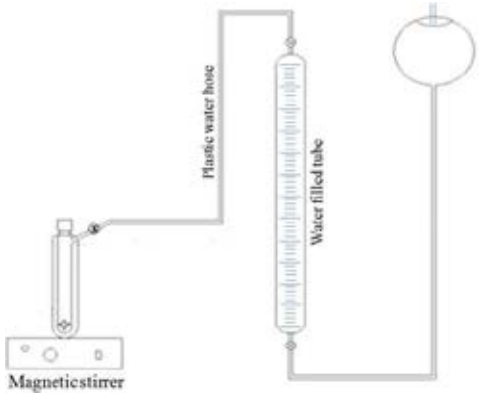


Fig. 1: Experimental set-up

Hydrolysis experiments of $C_4H_{12}BNO$ were carried out in the jacketed Schlenk shown in Figure 1. First, appropriate amounts of PSSA were added to the reactor. Then, metal precursors dissolved in 7 mL of water were

added and the catalyst solution and PSSA were mixed with a magnetic stirrer at the desired temperature with the help of a temperature-controlled circulator for 15 minutes. Finally, $C_4H_{12}BNO$ dissolved in 3 mL of water was added to the reactor and the catalytic hydrolysis reaction was initiated. The connection of Schlenk to the water-filled column was provided with a plastic hose and the change of the water level in the water-filled column and the hydrogen gas output was observed volumetrically.

III. Results and Discussions

In order to determine the catalyst with the highest catalytic activity, 2 mM Pd, 2 mM PdNi, 2 mM PdCo and 2 mM PdAg catalysts were synthesized in situ with 2 mM PSSA (metal/PSSA = 1) and 100 mM $C_4H_{12}BNO$. The reaction was carried out at 25°C and it was concluded that all bimetallic catalysts had higher performance than monometallic Pd catalysts.

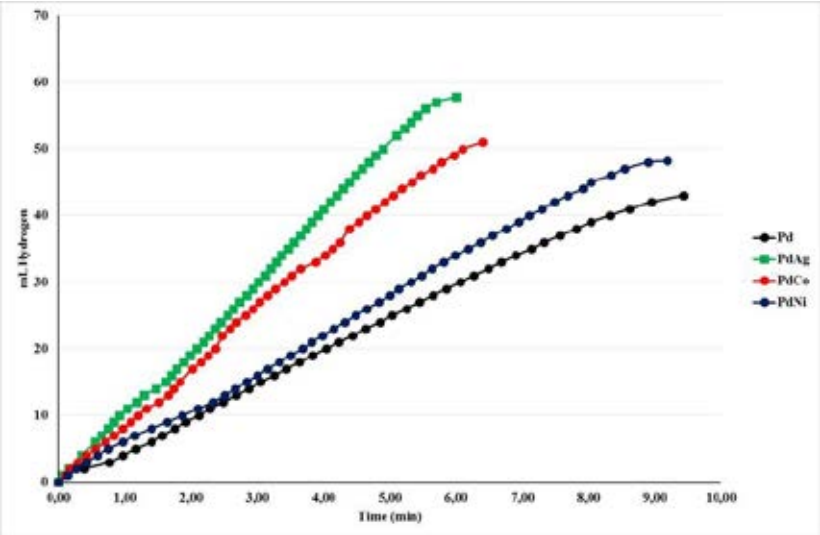


Fig. 2: Hydrogen production performance of different Pd-based cataysts

The catalytic activity order of the synthesized catalysts is Pd<PdNi<PdCo<PdAg. 58 mL of hydrogen was produced in approximately 6 minutes with the PdAg catalyst. In the optimization studies of the amount of PSSA for the 2 mM PdAg catalyst, 7 different ratios of metal/PSSA=1/0.25, 1/0.5, 1/1, 1/2, 1/4, 1/8 and 1/16 were studied and the optimum PSSA amount was 1/4 (2 mM PdAg 8 mM PSSA) (Figure 3).

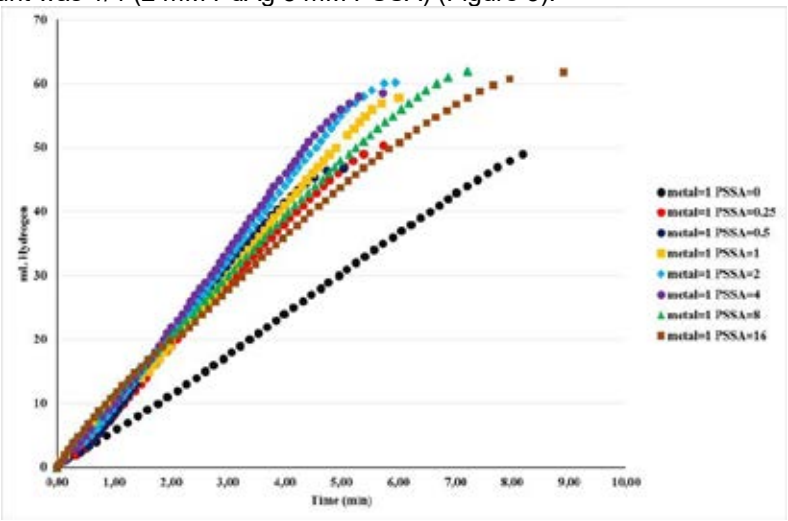


Fig. 3: Hydrogen production performance of PdAg catalyst with different PSSA ratios

For the optimization studies of metal amounts, 3 different metal ratios were taken into consideration: 2 mM $Pd_{0.75}Ag_{0.25}$, 2 mM $Pd_{0.50}Ag_{0.50}$, and 2 mM $Pd_{0.25}Ag_{0.75}$. In Figure 4, the results for the optimization experiments of the metal amounts is given. According to the Figure 4, optimum metal ratio was obtained with $Pd_{0.50}Ag_{0.50}$ catalyst.

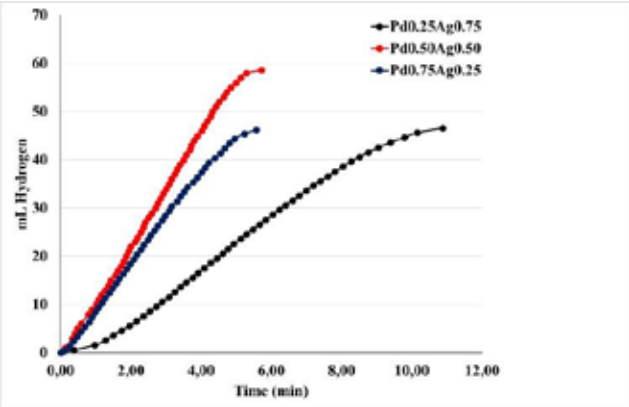


Fig. 4: Optimization of metal ratios

Hydrogen production performance of $Pd_{0.50}Ag_{0.50}$ catalyst at 15, 20, 25 and 30°C is given in Figure 5. The hydrogen production performance of the catalyst increases depending on the temperature.

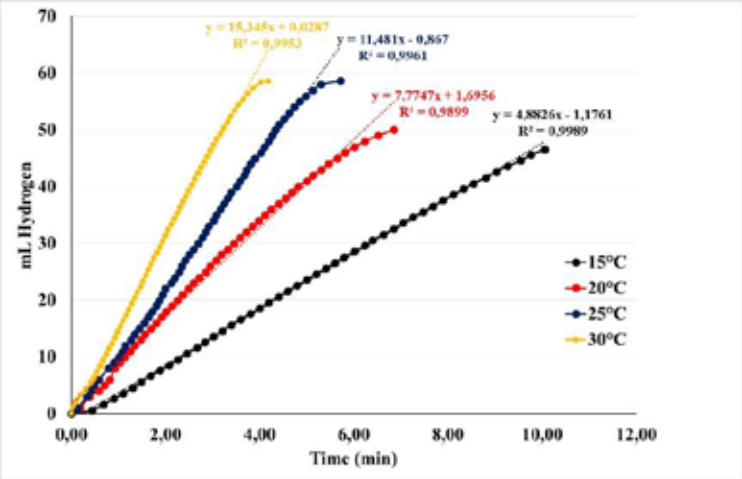
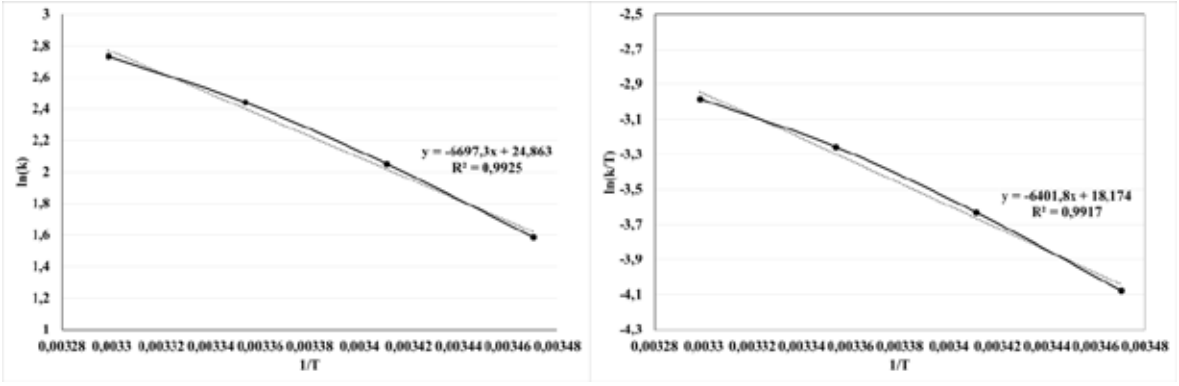


Fig. 5: Hydrogen production performance of $Pd_{0.50}Ag_{0.50}$ at different temperatures

Arrhenius and Eyring plots are given in Figure 6. According to these graphs, the activation energy of the reaction was calculated as 55.681 kJ/mol and the enthalpy as 53.225 kJ/mol.



a b

Fig. 6: a)Arrhenius b)Eyring plots

IV. Conclusions

PSSA stabilized PdAg catalyst was examined for the hydrolysis reaction of morpholine borane. The optimum PSSA ratio was 1/4, optimum metal ratios $Pd_{0.50}Ag_{0.50}$, the activation energy of the reaction (55.681 kJ/mol) and the enthalpy of the reaction (53.225 kJ/mol) were determined.

References

Lai, Qiwen, et al. "Hydrogen storage materials for mobile and stationary applications: current state of the art." ChemSusChem 8.17: 2789-2825 (2015).
Can, Hasan, and Önder Metin. "Hydrogen generation via the catalytic hydrolysis of morpholine-borane: A new, efficient and cost-effective hydrogen storage medium." International Journal of Hydrogen Energy 44.47: 25642-25651 (2019).

Design of an optimization based Adaptive Neural-Fuzzy Inference Systems (ANFIS) for controlling output voltage of double chamber microbial fuel cell

[1*]Mehmet Hakan Demir, [1]Berkay Eren
[1] Iskenderun Technical University, Faculty of Engineering and Natural Science, Department of Mechatronics Engineering, Hatay,31200, Turkey

* E-mail: mhakan.demir@iste.edu.tr

Abstract
Microbial fuel cells (MFCs) are complex bioelectrochemical systems and many factors such as environmental temperature, substrate concentration, biological environment, and load degradation will have a significant impact on its performance. For improving the performance of MFC, an optimized based Adaptive Neural-Fuzzy Inference Systems (ANFIS) controller is designed to adjust the output voltage of the two chamber MFC by using a model in which biochemical reactions, Butler–Volmer expressions, and mass/charge balances are included. This study extends the previous studies by using Particle Swarm Optimization (PSO) to adjust ANFIS parameters. The designed provide more efficient and successful performances for tracking the reference voltage pattern quickly and robustly against the variations in the external load, disturbances, and parameter uncertainties. This means that the MFC will more consistently provide the energy required for the external load.

Keywords: Microbial, fuel cell, control, optimization, PSO, Neuro-Fuzzy

I. Introduction

Microbial fuel cells are structures that transform biochemical energy into electrical energy and enable direct electricity, unlike other biomass-based electrical energy generation techniques. MFCs, simple carbohydrates such as glucose, acetate and butyrate, and complex organic compounds such as pig wastewater, domestic wastewater and manure sludge, transform the biochemical energy generated by breaking down countless organic substances into electrical energy through the catalytic reactions of microorganisms, and the use of these various raw materials compared to traditional chemical fuel cell. They have many advantages such as light reaction conditions, environmental friendliness and high efficiency. There are two compartments in MFC as anode and cathode. In the anode compartment, electrons and hydrogen are produced by oxidizing organic materials by microorganisms and transferred to the surface of the anode electrode made of a conductive material (carbon). Electrons are transmitted through an external resistor to the other electrode used as a cathode. On the other hand, hydrogen passes through the proton exchanger membrane and reaches the cathode chamber where it combines with the final electron acceptor (e.g. O2) and turns into water. In short, the organic destruction in the anode region in the MFC is completed with the oxygen in the cathode region becoming an electron acceptor, causing a voltage to occur.

One of the first MFC models was proposed by (Zhang and Halme, 1995) to simulate a suspended cell with an external mediator. In this study, in which and one dimensional, dynamic conduction-based and anode-based model is developed, they focused on the power generated in relation to the substrate concentration and the cathodic chamber mediator. Another one-dimensional anode-based model was developed by (Marcus et. al., 2007) and the previous work expanded the properties of biofilms and multispices, in which electrons are transferred directly from the substrate to the anode by the biofilm under the influence of electroactive microorganisms. This model demonstrates that the conductivity of the biofilm is one of the most important limiting factors of the system, and since this factor is directly related to the energy output, it provides a clearer understanding of the electron transfer mechanism that occurs when generating a power at the MFC output. On the other hand, (Picioreanu et al., 2010) handled the problem in two dimensions and analyzed some process parameters through a model with micro and macro perspective. Taking into account the mass transport by convection, a more realistic approach has been made in the model, and they determined that PH value has a key role on the process. They found that the PH value can also be seen as a key factor predicted by the cell geometry and considered the limiting factor (acidification) of the system. The models in which the working principles of the MFC and the effects of some of its parameters on this process are summarized by (Ortiz-Martínez et al.,2015) and (Xia et al.,2018).

The complexity of a microbial fuel cell makes it difficult to improve its performance. So far, almost all research on microbial fuel cells has focused on the structure or material options of the microbial fuel cell, with performance optimization through control rarely taken into account. Advanced control technology is an alternative solution to optimize the performance of the microbial fuel cell. The studies on the control of the MFC in the literature show that the stability and performance of the MFC is preserved in the presence of parametric uncertainties and external disturbances. (Boghani et al., 2018) implements a strategy based on the gain programming control strategy for the output voltage control of the MFC, and for the non-parametric MFC model, it can be successfully used with a simple continuous time proportional + integral (PI) applied to the output voltage against disturbances in temperature, loading rate and other undefined irregularities. PID control is often preferred in applications due to its simple and successful performance and was applied by (Racio-Garrido et al., 2016) for waste quality control in two-stage MFCs. (Yan and Fan, 2013) have designed a Fuzzy PID controller with a stronger performance than a PID controller in order to obtain a constant voltage output at the output of a two-stage MFC and the controller has a fast and good steady-state behavior against parameter changes and disturbances. An adaptive fuzzy control scheme has been proposed for the MFC to obtain constant voltage output under different loads in (Fan et al., 2014). Main fuzzy

controller is used to monitor the reference voltage and an auxiliary fuzzy logic controller is used to adjust the variables of the main fuzzy controller. In this study, an optimization based ANFIS controller has been developed for a MFC to follow the reference voltage input quickly and smoothly at the output. The previous studies are extended by applying optimization based Fuzzy-PID controller to the MFC for improving its performance.

II. Modeling

In this study, the control of the voltage generated at the output of the two-chamber MFC, whose schematic diagram is given in Figure 1, is emphasized. Before explaining the two-chamber MFC model, it is necessary to mention the working logic of the two-chamber MFC given in the diagram.

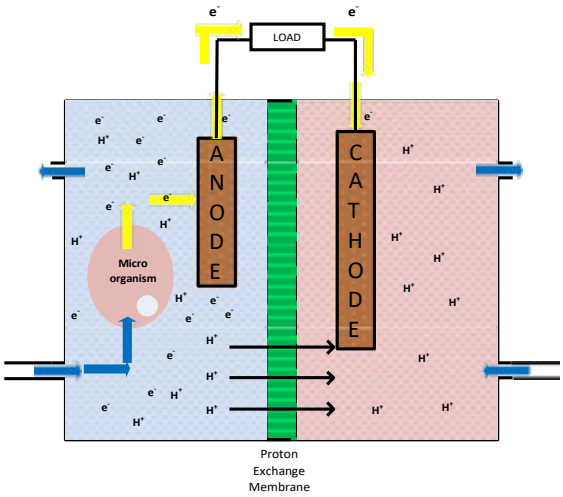


Fig. 1:Schematic diagram of the two chamber MFC

The most advanced model in which anode and cathode chambers are included together is the mechanic-based model developed by Zeng [11] in which the effects of biochemical reaction, Butler-Volmer equation, material and charge balance are taken into account. In this study, this model is used to control the output voltage of the two-chamber MFC. In this model, electrochemical reactions at the anode and cathode chambers are given in Eq. (1).

$$(CH_2O)_2 + 2H_2O = 2CO_2 + 8H^+ + 8e^-$$
$$O_2 + 4e^- + 2H_2O = 4OH^- \quad (1)$$

Due to these chemical reactions taking place at the anode and cathode, it is necessary to examine the dynamic structure of the MFC in order to obtain the voltage and power produced by the MFC at its output, despite the change in the flow rates of the fuel acetate fed to the anode chamber, which is the inputs of an MFC, and the water fed to the cathode chamber. This dynamic structure can be seen in Figure 2.

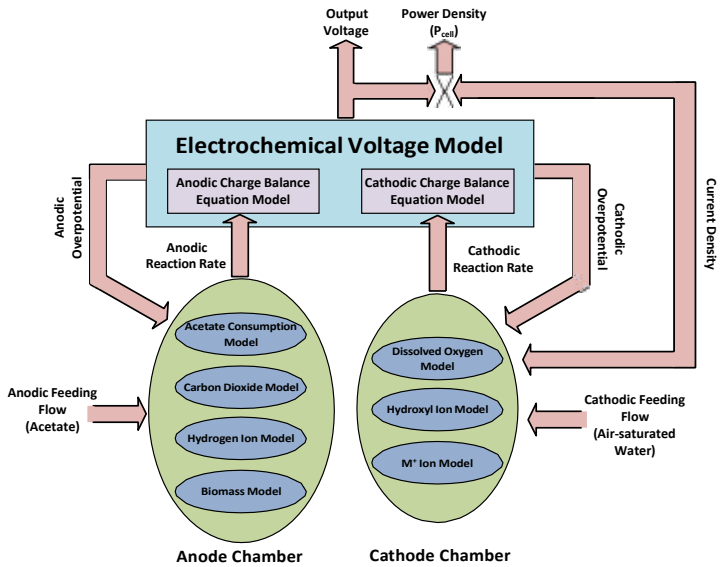


Fig. 2: Dynamic model block diagram of MFC

III. The Control Strategy

In this study, optimized ANFIS controllers, which is one of the most preferred methods of artificial intelligence techniques, will be designed to ensure that the output voltage of the MFC follows the desired reference quickly and

robustly. Neuro-Fuzzy based controllers have many advantages such as bringing simple solutions to the control of uncertain, time-varying, complex and nonlinear systems, and being able to produce realistic results for ill-defined systems with unclear situations. However, the most important disadvantage of this type of controllers is that these types controllers have quite a lot of parameters that need to be adjusted during the design phase. The adjustment of these parameters is usually done by experts and trial-error method is used. However, since this process is quite time consuming, requires attention and knowledge, the mentioned parameters are adjusted by using optimization techniques in applications. Creating more efficient control systems by combining the ANFIS method with other artificial intelligence methods gives successful and sufficient results in the control of many systems.

IV. Results and Discussion

Figure 3 presents the voltage output of the MFC system, whose membership functions are adjusted on two different voltage settings as 0.4 and 0.6 V with the PSO algorithm, and also obtained by using three different fitness functions. When the simulation results are examined, it is seen that FPID can provide a controlling effect for all fitness functions, but the response of the system creates small differences.

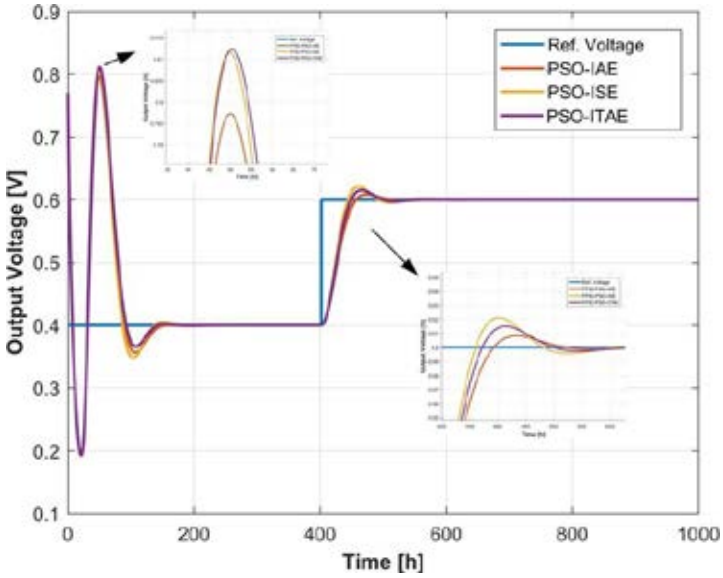


Fig. 3: Voltage-tracking performances of PSO based ANFIS with different fitness functions

V. Conclusions

An optimization based Neuro Fuzzy Inference controller is designed to adjust the output voltage of the two chamber MFC by using a model with biochemical reactions, Butler–Volmer expressions and mass/charge balances. The optimization algorithm, such as Particle Swarm Optimization (PSO), adjust the parameters of Neuro-Fuzzy Inference structure. In this study, it is applied to different scenarios, in which the reference voltage and the load connected to the MFC are changed, to test the performance of the controllers. The results show that the designed optimized intelegent controllers provide that the output voltage tracks the reference voltage pattern quickly and robustly against the variation in the external load, external disturbances and parameter uncertainties.

References

Boghani HC, Michie I, Dinsdale RM, Guwy AJ, Premier GC. Control of microbial fuel cell voltage using a gain scheduling control strategy. J Power Sources 2016;322:106–15.

Fan L, Li C, Boshnakov K. Performance improvement of a Microbial fuel cell based on adaptive fuzzy control. Pak J Pharm Sci 2014;27:685–90.

Marcus AK, Torres CI, Rittmann BE. Conduction-Based Modeling of the Biofilm Anode of a Microbial Fuel Cell. Biotechnol Bioeng 2007;98:1171–82

Ortiz-Martínez VM, Salar-García MJ, de los Ríos AP, Hernández-Fernández FJ, Egea JA, Lozano LJ. Developments in microbial fuel cell modeling. Chem Eng J 2015;271:50–60.

Picioreanu C, van Loosdrecht MCM, Curtis TP, Scott K. Model based evaluation of the effect of pH and electrode geometry on microbial fuel cell performance. Bioelectrochemistry 2010;78:8–24.

Xia C, Zhang D, Pedrycz W, Zhu Y, Guo Y. Models for Microbial Fuel Cells: A critical review. J Power Sources 2018;373:119–31.

Yan M, Fan L. Constant voltage output in two-chamber microbial fuel cell under fuzzy pid control. Int J Electrochem Sci 2013;8:3321–32.

Zhang X, Halme A. MODELLING OF A MICROBIAL FUEL CELL PROCESS Xia-Chang Zhang and Aarne Halme Automation Technology Laboratory, Helsinki University of Technology, 02150 ESPOO, FINLAND. Biotechnol Lett 1995;17:809–14.

The Usage of Solid State $NaBH_4$ For Hydrogen Production With COCL2 Catalyst

[1*] Asli Boran, [2] Serdar Erkan, [3] Inci Eroğlu
[1,3] Middle East Technical University, Department of Chemical Engineering, Ankara, Turkey
[2] Erdes Teknoloji Kimya Endüstriyel Tasarım Kontrol ve Dış Ticaret Ltd. Şti., Büyükesat Mahallesi Seyyah Sok. 9/6 G.O.P., Ankara, 06680, Turkey

*E-mail: yurdakulasli@gmail.com

ABSTRACT

Hydrogen storage is one of the most crucial technical barriers in front of the commercialization of hydrogen-based energy systems. This study aims to be a solution of hydrogen storage using solid state $NaBH_4$ for hydrogen production with $CoCl_2$ catalyst. In this study $CoCl_2$ was added by following two methodologies: In the Case 1, solid $CoCl_2$ was placed in a glass reactor with solid $NaBH_4$ and water added to initiate the hydrolysis reaction. The maximum efficiency was obtained for Case 1 is 62.52% with a maximum hydrogen generation rate of 2.1 L/min when 5g of $NaBH_4$, 0.15 g $CoCl_2$ and 33.30g water was used. In Case 2, solid $NaBH_4$ was placed in a glass reactor. Solid $CoCl_2$ was dissolved in desired amount of water to obtain catalyst solution. This catalyst solution was added into the reactor to generate hydrogen. The maximum efficiency was obtained for Case 2 is 56.55% when 5g $NaBH_4$, 0.15g $CoCl_2$ was dissolved in 52.33g water with a maximum hydrogen generation rate of 1.9 L/min. The water amount is found to be a critical parameter that should be optimized. This system is promising for integration with PEM fuel cells.

Keywords: Hydrogen Production, Hydrolysis Reactor, Sodium Borohydride

INTRODUCTION

Fossil fuels era is soon come to an end and hydrogen is one of the most promising candidates to replace them. Hydrogen storage is one of the main obstacles that must overcome before the 'hydrogen economy' commercialization. Sodium borohydride, $NaBH_4$, is a good alternative material for hydrogen storage. In the presence of water, $NaBH_4$ gives its H_2 by hydrolysis reaction as shown in Eq. (1).

$$NaBH_4 + 2H_2O \longrightarrow NaBO_2 + 4H_2 + heat \quad (1)$$

The reaction is highly exothermic with a heat of reaction of -217kJ/mol. The reaction rate is strongly dependent on initial $NaBH_4$ concentration (Ferreira et al 2012).
If water is in excess, the reaction is expressed as in Eq. (2).

$$NaBH_4 + (2+x)H_2O \xrightarrow{catalyst} NaBO_2.xH_2O + 4H_2 + heat \quad (2)$$

where, x is called "*hydration factor*".

In literature, generally $NaBH_4$ is introduced to the hydrolysis reactor system as in aqueous form that is stabilized with NaOH. In this study we focus on solid state $NaBH_4$. So, NaOH is not used in this study.
Using solid sodium borohydride instead of stabilized aqueous solution, has several advantages. First, it increases the gravimetric hydrogen storage capacity of sodium borohydride by using limited amount of water and decreases system weight. Also, it increases shelf life of $NaBH_4$.
The aim of this work is to investigate $CoCl_2$ catalyst for $NaBH_4$ hydrolysis reaction. The hydrolysis reaction initiation methodology is also discussed in present paper.

MATERIALS AND METHODS

Cobalt (II) chloride hexahydrate ($CoCl_2$) were supplied from Carlo Erba Reagents® batch number of V5E550316H and solid-state sodium borohydride ($NaBH_4$) (was supplied from Turkish National Institute of Boron with a purity of ≥96) was used in experiments. Spring water is used as reactant.
Hydrogen generation reactor with and internal volume of 290mL and cover diameter of 7.5cm, which was made from tempered glass (WECK glass) was used. For hydrogen generation from solid state $NaBH_4$ hydrolysis an experimental setup composed of 4 main parts which are; hydrolysis reactor, gas-liquid separator, mist eliminator in order to prevent the liquid drops coming from reactor and finally mass flow meter (Bürkert®, Model No: 8705) that has maximum hydrogen flow rate of 3 L/min was constructed. Mass flow meter was connected to the computer with RS485.So, H_2 generation flow rate was directly measured and monitored online by using Reliance 5.0 program. H_2 generation rate was recorded in every 1 second. Fig. 1 shows the picture of the experimental setup.

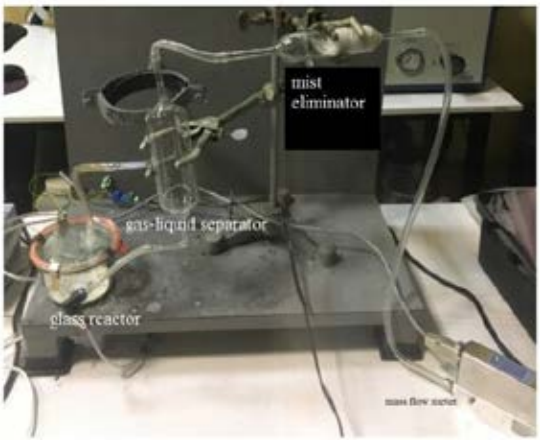


Fig. 1 Picture of experimental setup for hydrolysis of $NaBH_4$

Two different procedures were applied for start-up of hydrogen generation from hydrolysis of NaBH4 experiments. In the first case, Case 1, desired amount of solid $NaBH_4$ and solid catalyst were placed in the reactor. Required quantity of water at room temperature was injected directly into the reactor with a syringe that has a volume of 100mL in order to initiate the hydrolysis reaction. H_2 generation rate was monitored after the injection of water. In the second case, Case 2, only the desired amount of solid $NaBH_4$ was placed in the reactor. The solid catalyst was dissolved in the desired amount of water and catalyst solution was obtained. This catalyst solution at room temperature was injected with a syringe(100mL) into the reactor which contains only solid $NaBH_4$. H_2 generation rate was monitored starting with the injection of catalyst solution.

RESULTS AND DISCUSSION

Effect of hydration factor on H_2 generation rate was investigated on solid $CoCl_2$ catalyst. For these experiments, for start-up, Case 1 and Case 2 are compared. For both cases 5g of $NaBH_4$ and 0.15g of solid $CoCl_2$ were used.

"H_2 Generation Yield" was defined as liter of H_2 produced per grams of $NaBH_4$ according to the Eq. (3).

$$Yield = \frac{Total\ H_2\ produced(L)}{Amount\ \text{of}\ NaBH_4(g)} \tag{3}$$

"Efficiency %" was defined according to Eq. (4).

$$Efficiency(\%) = \frac{Total\ H_2\ \text{Generated}(L)}{Theoretical\ H_2\ \text{Generated}(L)} \times 100 \tag{4}$$

Table 1 summarizes the experiments conducted with different hydration factors for $CoCl_2$ catalyst for Case 1 and Case 2.

Table 1. Summary of results of experiments with $CoCl_2$ catalyst for the two cases

Case Number	H_2O amount	Total H_2 generated (L)	Duration (min)	Mean H_2 generation rate (L/min)	Yield (L H_2/g $NaBH_4$)	Efficiency %
Case 1	23.8g, x=8	7.90	20.43	0.38	1.58	61.11
Case 1	33.3g, x=12	8.08	16.17	0.48	1.62	62.52
Case 1	42.8g, x=16	7.29	17.22	0.42	1.46	56.39
Case 1	52.3g, x=20	7.75	22.57	0.34	1.55	59.95
Case 2	33.3g, x=12	6.95	31.82	0.22	1.39	53.76
Case 2	42.8g, x=16	6.6	44.57	0.15	1.32	51.06
Case 2	52.3g, x=20	7.31	43.67	0.17	1.46	56.55

It was found that hydrolysis mechanisms are different for Case 1 and Case 2. The common fact for both cases is that the catalyst colour turned purple to black as soon as the reaction initiates. After the dissolution of $CoCl_2$ catalyst in water, Co^{+2} undergoes a reduction and converts to Co^{+}. This may cause a change in color of catalyst. [2,3]

Although, in Case 2 the reaction durations are high, the reaction immediately stops after giving the maximum H_2 generation rate. This behavior is decided to be not suitable for PEMFC applications because of the risk of sudden increase in hydrogen generation rate and thus increase in the solution volume suddenly which may damage the pipelines of reactor. Moreover, for Case 1, the yield and efficiency values are higher than Case 2. So, Case 1 is selected to be a more appropriate method for initiation of hydrolysis reaction. When hydration factor is equal to 12, the hydrolysis reaction gave its optimum conditions.

CONCLUSIONS

Using solid sodium borohydride instead of introducing it as an aqueous solution stabilized with NaOH to the system promotes 3 main advantages listed as follows:

i. Increases the gravimetric hydrogen storage capacity of sodium borohydride by using limited amount of water.

ii. Decreases the system weight.

iii. There is no need to use a separate storage fuel tank for storing the aqueous $NaBH_4$ solution. So, the number of equipment that is necessary for system design is reduced. [Boran et al 2019.]

Hydration factor, x is most critical parameter for solid state $NaBH_4$ hydrolysis reaction. Two different cases for initiation of hydrolysis reaction is proposed. In Case 1, $NaBH_4$ and catalyst are stored in the reactor in solid state. Water is injected to the reactor in order to start hydrogen production. In Case 2, only $NaBH_4$ is stored in the reactor in solid state. Catalyst is dissolved in certain amount of water. This catalyst solution is injected to the reactor to initiate the H2 production. For both cases effect of hydration factor is investigated. Case 1 is selected to be an appropriate method for integration to PEM fuel cell. The optimum condition in Case 1 is found as 5g $NaBH_4$ and 0.15g $CoCl_2$ were used with hydration factor of 12. This system is promising for portable PEM fuel cell applications.

REFERENCES

1. Ferreira MJF, Rangel CM, Pinto AMFR. 2012. Water handling challenge on hydrolysis of sodium borohydride in batch reactors. International Journal of Hydrogen Energy 37:6985-6994.
2. Glavee GN, Klabunde KJ, Sorensen CM, Hadjapanayis GC. 1993. Borohydride reduction of cobalt ions in water: Chemistry leading to nanoscale metal, boride or borate particles. Langmuir 9:162–169.
3. Krishnan P, Advani S., Prasad AK. 2008. Cobalt oxides as Co_2B catalyst precursors for the hydrolysis of sodium borohydride solutions to generate hydrogen for PEM fuel cells. International Journal of Hydrogen Energy 33:7095-7102.
4. Boran A, Erkan S, Eroglu I. 2019. Hydrogen generation from solid state $NaBH_4$ by using $FeCl_3$ catalyst for portable proton exchange membrane fuel cell applications. International Journal of Hydrogen Energy 44: 18915-18926.

The Effects of Anisotropic Electrical Conductivity Depending on Operating Conditions on Gas Diffusion Layers in Pem Fuel Cell

[1]Mert TAŞ, [1,2*]Gülşah ELDEN
[1] Erciyes University, Engineering Faculty, Energy Systems Engineering, Kayseri, 38039, TURKEY
[2] Erciyes University, Energy Conversions Research and Application Center, Melikgazi, Kayseri, 38039, Turkey

* E-mail: gulsah@erciyes.edu.tr

Abstract
The electrical conductivity of the carbon-fiber layer forming the porous structure is affected by fuel cell operation conditions such as temperature, relative humidity and clamping pressure. In order to bring out that these effects, two separate three-dimensional Polymer Electrolyte Membrane (PEM) fuel cell models which containing gas diffusion layer (GDL) and gas diffusion layer coated micro porous layer (MPL) are prepared by Comsol software. Electrical conductivities of gas diffusion layers which experimentally obtained depending on operating conditions are integrated numerical model. The effects of these electrical conductivities on electrochemical reaction phenomena in PEM fuel cell are investigated. The current density increases in both models as the cell temperature rises from 50°C to 80°C at constant relative humidity and clamping pressure. Furthermore, the cell performance of second model slightly is higher than first model.

Keywords: Gas diffusion layer, Anisotropic electrical conductivity, Computational model, PEM fuel cell

I. Introduction

The properties of GDL such as permeability, thermal, ionic and electrical conductivity affect the losses in polymer electrolyte membrane (PEM) fuel cells. Due to the carbon-fiber structure and differences in production methods, the fibers have different densities in different directions. Since the fiber density changes the electrical conductivity of GDL, it is important to determine anisotropic electrical conductivity. Until recently, some experimental studies have been conducted about the measurement of anisotropic electrical conductivity Mason et al. (2012), Nitta et al. (2007), Vikram et al. (2016) and Todd et al. (2016). The effects of anisotropic electrical conductivities on 3D PEM fuel cell model by the parametric method are analysed by Zhou and Liu (2006). The increase in through-plane conductivity increases the performance at constant in-plane conductivity (300 Sm^{-1}). The effects of electrical conductivities on fuel cell performance are analyzed using 3D PEM fuel cell model by Ismail etal (2012). Anisotropic electrical resistance effects on current density distribution are investigated in a two-dimensional model by Bapat and Thynell (2008). Numerical modeling studies related to anisotropic modeling are limited in the literature. Some model studies are parametric, while others are examined only one of the operation conditions. Effects of anisotropic electrical conductivity in PEM fuel cell are numerically examined with case study Elden and Taş (2018). The aim of this study is to investigate the effects of electrical conductivities obtained under different operating conditions (temperature, clamping pressure and relative humidity) on PEM fuel cell electrochemical phenomena.

II. Numerical Methods

Two different PEM fuel cell model are prepared for using GDL and MPL coated GDL. The geometric model of PEM cell consisting of seven components is given in Figure 1. These components are anode flow channel (AC), anode gas diffusion layer (Anode GDL), anode catalyst layer (Anode CL), membrane, cathode catalyst layer (Cathode CL), cathode gas diffusion layer (Cathode GDL) and cathode flow channel (CC). In the second model, MPL is placed between cathode GDL and cathode CL, unlike the first model. Electrical conductivities of both gas diffusion layers which experimentally obtained depending on operating conditions are integrated numerical models Taş and Elden (2020). In order to simplify the model, following assumptions are made: steady-state, laminar flow, single phase (gas) flow, ideal gas and none-gas permeability of the membrane. Table 1 indicates the model parameters.

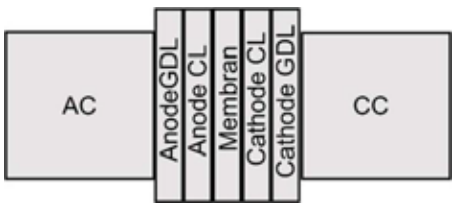


Fig. 1. PEM Fuel Cell model components

Tab. 1. Model parameters

Parameters	Symbols	Values
Channel depth	*L*	*$2 \cdot 10^{-2}$ [m]*
Channel height	*H_ch*	*$1 \cdot 10^{-3}$ [m]*
Channel witdh	*W_ch*	*$0.78 \cdot 10^{-3}$ [m]*
Rib width	*W_rib*	*$0.90 \cdot 10^{-3}$ [m]*
GDL width	*H_gdl*	*$380 \cdot 10^{-6}$ [m]*
Catalst layer thickness	*H_electrode*	*$50 \cdot 10^{-6}$ [m]*
Membrane thickness	*H_membrane*	*$100 \cdot 10^{-6}$ [m]*
GDL porosity, MGDL porosity	*eps_gdl, eps_mpl*	*0.83, 0.75*
GDL permeability	*kappa_gdl*	*$4 \cdot 10^{-12}$ [m^2]*
MGDL permeability	*kappa_mpl*	*$2.3 \cdot 10^{-12}$ [m^2]*
Catalyst layer porosity	*eps_cl*	*0.4*
Catalyst layer permeability	*kappa_cl*	*$8 \cdot 10^{-13}$ [m^2]*
Inlet H_2 mass fraction (anode)	*wH2_in*	*0.743*
Inlet H_2O mass fraction (cathode)	*wH2O_in*	*0.023*
Inlet oxygen mass fraction (cathode)	*wO2_in*	*0.228*
Anode inlet flow velocity	*U_in_anode*	*0.2 [m/s]*
Cathode inlet flow velocity	*U_in_cathode*	*0.5 [m/s]*
Anode viscocity	*mu_anode*	*$1.19 \cdot 10^{-5}$ [Pa*s]*
Cathode viscocity	*mu_cathode*	*$2.46 \cdot 10^{-5}$ [Pa*s]*
H_2-H_2O diffusion coefficient	*D_H2_H2O*	*$9.15 \cdot 10^{-5} \cdot (T/307.1[K])^{1.75}$ [m^2/s]*
N_2-H_2O diffusion coefficient	*D_N2_H2O*	*$2.56 \cdot 10^{-5} \cdot (T/307.15[K])^{1.75}$ [m^2/s]*
O_2-N_2 diffuzyon coefficient	*D_O2_N2*	*$2.2 \cdot 10^{-5} \cdot (T/293.2[K])^{1.75}$ [m^2/s]*
O_2-H_2O diffusion coefficient	*D_O2_H2O*	*$2.82 \cdot 10^{-5} \cdot (T/308.1[K])^{1.75}$ [m^2/s]*
Reference pressure	*p_ref*	*$101 \cdot 10^3$ [Pa]*
O_2 and H_2 reference concentration	*cO2_ref, cH2_ref*	*40.88 [mol/m^3]*

III. Analysis

Three-dimensional numerical models are prepared with the multiple computational area approach using the following equations. These equations are Continuity, Navier-Stokes, Darcy, Stephan-Maxwell and Charge conservation equations, respectively.

$$\nabla(\rho u) = 0 \tag{1}$$

$$\nabla(\rho \bar{u}\bar{u}) = -\rho(\nabla P) + \nabla(\mu^{eff}\nabla) \tag{2}$$

$$u = \frac{k_p}{\mu} \tag{3}$$

$$\rho \bar{u} \nabla m_i = \nabla\left[\rho m_i \sum_{j_=1}^{N} D_{ij}\left\{\frac{M}{M_i}\left(\nabla m_i + m_i \frac{\nabla M}{M_i}\right)\right\}\right] \tag{4}$$

$$\nabla(\sigma_i \nabla \phi) = 0 \tag{5}$$

IV. Results and discussions

The polarization curve of a PEM fuel cell based Nafion membrane is obtained at 80°C operating temperature and 100% relative humidity conditions. The same operating conditions are applied to the numerical model and the polarization curve is generated. As is shown in Fig. 2.a. the numerical model is compatible with the experimental data. The effect of temperature on fuel cell performance is exhibited in Fig 2.b. and Fig.2.c for both numerical models,

separately. The current density increases in both models as the cell temperature rises from 50°C to 80°C at constant relative humidity and clamping pressure. Furthermore, the cell performance of second model slightly is higher than first model.

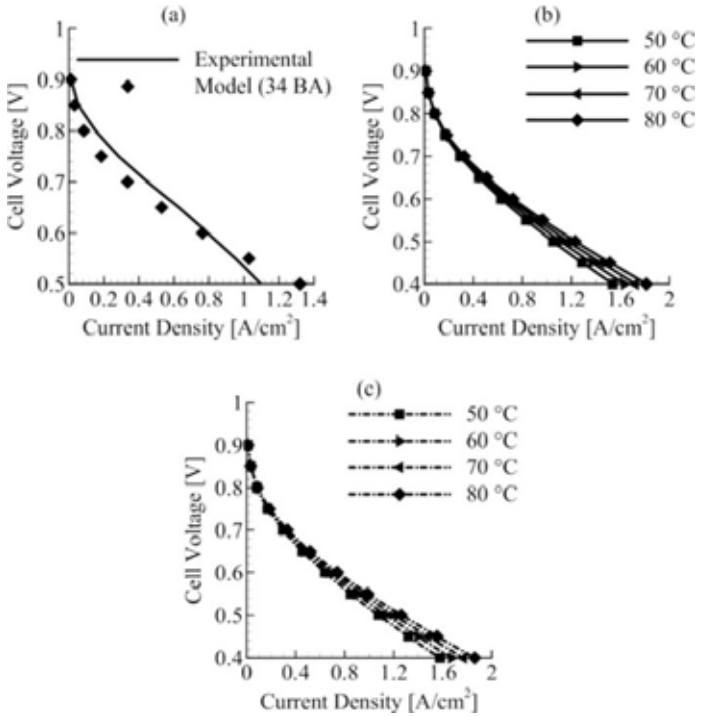


Fig. 2. Model results; a) Validation of the model with experimental data, (b) The variation of performance depending on temperature for the first model, (c) The variation of performance depending on temperature for the second model

V. Conclusions

Experimentally obtained electrical conductivities are integrated into the PEM fuel cell models. As a result of the analysis, it is revealed that the performance of PEM fuel cell is positively affected by increasing temperature at constant relative humidity and clamping pressure.

Acknowledgements

The authors would like to thank the Scientific Research Projects Unit of Erciyes University for funding and supporting the projects under the contract no: FYL-2017-7235.

References

Bapat C. J., Thynell S. T., Effect of anisotropic electrical resistivity of gas diffusion layers (GDLs) on current density and temperature distribution in a Polymer Electrolyte Membrane (PEM) fuel cell, Journal of Power Sources 185(1), 428–432, (2008).

Elden G., Taş M., Numerical investigation of anisotropic electrical conductivity effects in Proton Exchange Membrane Fuel Cell, European Journal of Science and Technology, Special Issue, 2-6, (2018).

Ismail M.S., Hughes K.J., Ingham D.B., Ma L., Pourkashanian M., Effects of anisotropic permeability and electrical conductivity of gas diffusion layers on the performance of proton exchange membrane fuel cells, Applied Energy, 95, 50–63, (2012).

Mason T.J., Millichamp J., Neville T.P., El-Kharouf A., Pollet B. G., Brett D. J. L., Effect of clamping pressure on ohmic resistance and compression of gas diffusion layers for polymer electrolyte fuel cells, Journal of Power Sources, 219, 52–59, (2012).

Nitta I., Hottinen T., Himanen O., Mikkola M., Inhomogeneous compression of PEMFC gas diffusion layer Part I: Experimental, Journal of Power Sources, 171, 26–36, (2007).

Taş M., Elden E., An experimental investigation of the effects of operating conditions on anisotropic electrical conductivity in a PEM fuel cell, Fuel Cells, 20(5), 531-539, (2020).

Todd D., Bennett S., Merida W., Anisotropic electrical resistance of proton exchange membrane fuel cell transport layers as a function of cyclic strain, International Journal of Hydrogen Energy, 41(14), 6029–6035, (2016).

Vikram A., Chowdhury P. R., Phillips R.K., Hoorfar M., Measurement of effective bulk and contact resistance of gas diffusion layer under inhomogeneous compression Part I: Electrical conductivity, Journal of Power Sources, 320, 274–285, (2016).

Zhou T., Liu H., Effects of the electrical resistances of the GDL in a PEM fuel cell, Journal of Power Sources, 161(1), 444–453, (2006).

Biohydrogen Production from Lignocellulosic Wastes Pretreated by Rumen Microorganisms: An Overview

[1*]Gökce Kurt, [1]Bestami Özkaya, [1]Ahmet Demir,
[1] Yildiz Technical University, Faculty of Civil Engineering, Environmental Engineering Department, Davutpasa, Istanbul, 34220, Turkey

* E-mail:gokcek@yildiz.edu.tr

Abstract
The agricultural sector has an important place in the economy of our country. Therefore, formation of agricultural wastes is observed to a large extent. Agricultural wastes have a great energy potential. However, these wastes have a complex lignocellulosic structure containing cellulose, hemicellulose and lignin, which are obstructing bioenergy production from lignocellulosic biomass. Therefore, a pretreatment is required to ensure lignocellulose hydrolysis prior to bioenergy production. Biological pretreatment methods distinguish due to its environmentally friendly and economical nature. Rumen microorganisms found in the stomachs of ruminant animals contain microbial consortiums that can hydrolyze lignocellulose biologically. In this literature review, biohydrogen productions from various lignocellulosic wastes pretreated with different methods were reviewed. Rumen microorganisms were suggested as an alternative pretreatment method for biohydrogen production. Optimization of biological pretreatment conditions for the best lignocellulose hydrolysis and hydrogen yield should be done.

Keywords: Biohydrogen, lignocellulose, rumen pretreatment

I. Introduction

Biomass is a material of plant or animal origin, and contains organic substances with a large amount of carbon, oxygen and hydrogen. Food industry, forestry, agricultural, animal and municipal wastes and all plants are examples of biomass. Mismanagement of these biomass-sourced wastes causes environmental pollution. Biomass is a renewable energy source and can reduce the demand for fossil fuels in energy. Energy produced from biomass is clean; thus, as Gokcol et al. (2009) stated, has the potential to improve the environment, economy and energy security. Biomass is a great source for hydrogen production since it contains large amounts of hydrogen elements. Hydrogen energy is among the cleanest alternative energy sources. In contrast to hydrogen production methods such as water electrolysis, methane steam reforming and steam catalytic conversion (Chen et al., 2018), hydrogen production from biomass is an efficient, energy-saving and environmentally friendly way of producing hydrogen. The production of hydrogen gas by fermentation is carried out from carbohydrate-rich substrates using anaerobic bacteria. H_2 and CO_2 gas are primarily produced in these reactions, and CH_4, CO and some hydrogen sulfides in low amounts are also produced. Therefore, separation of these gasses is required to increase the hydrogen purity (Senturk and Buyukgungor, 2010).

Lignocellulosic Biomass

Lignocellulosic waste is a type of biomass mostly produced in agriculture and food industries. Lignocellulose is found in plant cell walls and consists of cellulose and hemicellulose, surrounded by lignin matrix. Celluloses are made up of glucose, hemicelluloses are xylose, arabinose, galactose and mannose, and lignins are made up of different phenolic polymeric units (Yu et al., 2016). Since celluloses and hemicelluloses in lignocellulosic biomass are fermentable sugars, they can be converted into biofuels through biological transformation. However, the breakdown and hydrolysis of lignocellulosic biomass becomes a rate-limiting step during anaerobic digestion. Due to its complex structure, lignin is resistant to biodegradation. In addition, according to Kumar et al. (2020), the crystalline structure of cellulose embedded in hemicellulose and lignin matrix also causes difficult decomposition.Therefore, pretreatment of lignocellulose is required. According to Islam et al. (2020), the breakdown of biomass ensures that substrate accessibility is maximized and increases the yield of sugar and biogas.

Pretreatment of Lignocellulosic Biomass

The purpose of the pretreatment is to facilitate the degradation of lignocellulosic polymers, to change the lignocellulose structure, to enlarge the surface area of the materials and to reduce the crystallization in order to provide sufficient contact area in the enzymatic hydrolysis or sugaring stage. According to Abbasi and Abbasi (2010), pretreated biomass can increase biohydrogen production during the fermentation process and reduce the formation of by-products. The 3 basic techniques for pretreatment of lignocellulosic biomass are subdivided into physical, chemical, physicochemical and biological methods.

Physical pretreatment

The purpose of physical pretreatment is to reduce the biomass' size, water amount and crystallinity by mechanical methods such as drying, crushing, milling, cutting, rolling, freezing, microwaving and shredding (Kumari and Singh, 2018). However, a single physical pretreatment of lignocellulose is not sufficient for an effective enzymatic degradation. Physical pretreatment may be sufficient to advance biofuel production, but this

method must be done before or combined with chemical pretreatments. Factors such as high operating and operational costs and tool corrosion are some of the disadvantages of this pretreatment method (Harmsen et al., 2010).

Chemical pretreatment

Chemical pretreatment is carried out using different chemicals such as acids, bases organic solvents and oxidizing agents (Kumari and Singh, 2018). The purpose of this pretreatment is to increase the digestibility of sugar substrates by dissolving hemicellulose, precipitating lignin, and making cellulose more accessible to microorganisms. Sulfuric acid and hydrochloric acid are the two most commonly used acids for the hydrolysis process. However, concentrated acids can damage lignin structure and form toxic compounds. The alkali pretreatment of lignocellulose involves the dissolution and saponification reaction during hydrolysis. According to Liu et al. (2003), this process helps to increase the swelling of the biomass structure, reduce crystallinity, and increase the accessibility of enzymes and bacteria.

Biological pretreatment

Degradation of lignocellulose by biological pretreatment can be carried out by fungi, microbial consortiums and enzymes capable of breaking down lignin and hemicellulose. Wood decomposing fungi produce enzymes that can depolymerize or break down lignin, cellulose, and hemicellulose. In fungal pretreatment, white rot fungi have been preferred more than other fungi species due to their efficiency in breaking down lignin (Lundquist et al., 1977). Biological pretreatment with pure ligninolytic enzymes such as manganese peroxidase, lignin peroxidase, versatile peroxidase and laccase can be used, instead of using fungi as a pretreatment method (Millati et al., 2020). In addition to fungi and enzymes, microbial consortiums can be used in biological pretreatment. Unlike fungal pretreatment, which can selectively break down lignin, the microbial consortium contains hydrolytic microorganisms capable of breaking down cellulose and hemicellulose. Since the microbial consortium includes several types of microorganisms, there is competition where hydrolytic and fermentative microorganisms work simultaneously in producing and consuming soluble materials to be used in fermentation. Therefore, pretreatment time becomes critical (Yuan et al., 2016).

Rumen microorganisms, an example of a microbial consortium, can be used in biological pretreatment. They can biodegrade lignocellulosic biomass in a known natural cycle. Lignocellulose hydrolysis occurs naturally in the rumen of ruminant animals such as sheep and cows. Rumen fluid contains a complex anaerobic microbial ecosystem that includes bacteria, fungi, and protozoa. These microorganisms can separate the bonds that hold cellulose, hemicellulose and lignin together. In a study conducted by Baba et al. (2013), lignocellulose degradation was carried out with rumen before the methane production phase. At the end of the study, it was observed that 2 to 6 times more methane was produced with the waste pretreated with rumen compared to the non pretreated. For this reason, the use of rumen microorganisms in bioenergy production from lignocellulosic biomass as a biological pretreatment method is becoming a preferred method due to its positive effect on bioenergy production in addition to being a natural process.

II. Results and discussions

The biohydrogen production from lignocellulosic wastes has varied with both the types of lignocellulosic wastes and the pretreatment method used. Nevertheless, the hydrogen outcome has obtained with better yields in pretreated substrates than the non pretreated substrates. The results obtained by Antonopoulou et al. (2016) showed that biohydrogen obtained from NaOH pretreated sunflower straw wastes was 52.5-fold of the non pretreated corn stalk wastes. However, pretreatment with alkali solutions may result in denser and more stable cellulose than its natural state, and lowering the hydrolysis (Hendriks and Zeeman, 2009). One of the few studies on rumen pretreatment for biohydrogen production is conducted by Chang et al. (2010), and they found out the pretreatment hydrolyzed 27% of hemicellulose and 2% of cellulose including in napier grass. This resulted in an increase in biohydrogen production. The studies using various pretreated lignocellulosic wastes for hydrogen production are given in Table 1.

Tab. 1: Examples of hydrogen production with pretreated lignocellulosic wastes

Lignocellulosic Waste	Pretreatment	H_2 Production ($mL\ H_2/g_{substrate}$)	Reference
Sunflower straw	Alkali	155.3	Antonopoulou et al. (2016)
Sake brewery waste	Hot compressed water	112.07	Choiron et al. (2020)
Corn stalk	Fungal	89.3	Zhao et al. (2013)
Napier grass	Rumen bacteria	55	Chang et al. (2010)
Corn stover	Steam	51.9	Zhang et al. (2016)

III. Conclusions

Hydrogen productions from pretreated lignocellulosic wastes were investigated. Although chemical pretreatment methods yielded higher amounts of hydrogen, these methods may damage both the substrate structure and the environment. On the other hand, biological pretreatment methods are safe alternatives since they are environmentally-friendly. Rumen fluid from ruminant animals can be an alternative biological pretreatment

method instead of using fungi and enzymes. Despite there are some studies on biomethane production from rumen pretreated lignocellulosic wastes in literature, this method has been used rarely for biohydrogen production.

Energy from hydrogen gas is cleaner than the methane gas, which is a greenhouse gas. Therefore, comparative studies should be done on both biomethane and biohydrogen productions from rumen pretreated lignocellulosic biomass. In addition, optimization studies should be performed to increase productivity of biohydrogen.

Acknowledgements
This research was supported by Yildiz Technical University, Civil Engineering Faculty, Environmental Engineering Department. This study is a part of the Master thesis of the corresponding author.

References

Abbasi T., Abbasi S., Biomass energy and the environmental impacts associated with its production and utilization, Renew. Sustain. Energy Rev., 14 (3), 919-937, (2010).

Antonopoulou G., Vayenas D., Lyberatos G., Ethanol and hydrogen production from sunflower straw: The effect of pretreatment on the whole slurry fermentation. Biochemical Engineering Journal, 116, 65-74, (2016).

Baba Y., Tada C., Fukuda Y., Nakai Y., Improvement of methane production from waste paper by pretreatment with rumen fluid, Bioresour. Technol., 128, 94-99, (2013).

Chang J.J., Lin J.J., Ho C.Y. et al., Establishment of rumen-mimic bacterial consortia: a functional union for bio-hydrogen production from cellulosic bioresource, Int. J. Hydrog. Energy, 35, 3399-13406, (2010).

Chen J., Liu B., Gao X., Xu D., Production of hydrogen by methane steam reforming coupled with catalytic combustion in integrated microchannel reactors, Energies 2018, 11 , 2045," Energies, MDPI, Open Access Journal, 12(14), 1-1, (2018).

Choiron M., Tojo S., Chosa T., Biohydrogen production improvement using hot compressed water pretreatment on sake brewery waste. International Journal of Hydrogen Energy, 45(35), 17220-17232, (2020).

Gokcol C., Dursun B., Alboyaci B., Sunan E., Importance of biomass energy as alternative to other sources in Turkey, Energy Policy, 37 (2), 424-431, (2009).

Senturk G.I., Buyukgungor H., Biyohidrojen üretim yöntemleri ve kullanilan farkli atik materyallerin incelenmesi, Journal of Engineering and Natural Sciences Mühendislik ve Fen Bilimleri Dergisi. Sigma 28, 369-395, (2010).

Harmsen P. et al., Literature review of physical and chemical pretreatment processes for lignocellulosic biomass, Wageningen UR-Food & Biobased Research, (2010).

Hendriks A.T.W.M., Zeeman G., Pretreatments to enhance the digestibility of lignocellulosic biomass. Bioresource Technology, 100(1), 10-18, (2009).

Islam M.K., Wang H., Rehman S. et al., Sustainability metrics of pretreatment processes in a waste derived lignocellulosic biomass biorefinery, Bioresource Technology, 298, (2020).

Kumar A., Rapoport A., Kunze G. et al., Multifarious pretreatment strategies for the lignocellulosic substrates for the generation of renewable and sustainable biofuels: A review, Renewable Energy, 160, 1228-1252, (2020).

Kumari D., Singh R., Pretreatment of lignocellulosic wastes for biofuel production: A critical review, Renewable and Sustainable Energy Reviews, 90, 877-891, (2018).

Liu H., Zhang T., Fang H.H., Thermophilic H_2 production from a cellulose-containing wastewater, Biotechnol. Lett., 25 (4), 365-369, (2003).

Lundquist K., Kirk T.K., Connors W.J., Fungal degradation of kraft lignin and lignin sulfonates prepared from synthetic 14C-lignins, Arch. Microbiol., 112, 291-296, (1977).

Millati R., Wikandari R., Ariyanto T. et al., Pretreatment technologies for anaerobic digestion of lignocelluloses and toxic feedstocks, Bioresource Technology, 304, (2020).

Yu Q., Zhuang X., Wang W. et al., Hemicellulose and lignin removal to improve the enzymatic digestibility and ethanol production, Biomass and Bioenergy, 94, 105-109, (2016).

Yuan X., Ma L., Wen B. et al., Enhancing anaerobic digestion of cotton stalk by pretreatment with a microbial consortium (MC1), Bioresour. Technol., 207, 293-301, (2016).

Zhang S.C., Lai Q.H., Lu Y. et al., Enhanced biohydrogen production from corn stover by the combination of Clostridium cellulolyticum and hydrogen fermentation bacteria. Journal of Bioscience and Bioengineering, *122*(4), 482-487, (2016).

Zhao L., Cao G.L., Wang A.J. et al., Simultaneous saccharification and fermentation of fungal pretreated cornstalk for hydrogen production using Thermoanaerobacterium thermosaccharolyticum W16. Bioresource technology, 145, 103-107, (2013).

Pt and Pd based quaternary metal catalysts for the cathode in PEM fuel cell

[1*]Çiğdem Güldür, [1]Esma Gümüş, [3]Silver Güneş
[1] Gazi University, Engineering Faculty, Chemical Engineering Department, Maltepe, 06570, Ankara, Turkey
[2] Gazi University, Engineering Faculty, Chemical Engineering Department, Maltepe, 06570, Ankara, Turkey
[3] Gazi University, Graduate School of Natural and Applied Sciences, Beşevler, 06500, Ankara, Turkey

* E-mail: cguldur@gazi.edu.tr

Abstract
The commercialization of PEM fuel cells is hindered by the high cost of the Pt and other noble metals used for the catalysis of oxygen reduction reaction at the cathode. Using multi-metallic catalysts is a prominent approach for reducing the Pt amount at the cathode. In this study, Pt and Pd containing quaternary catalysts were synthesized and investigated as potential catalysts for PEM cathode. Furthermore, ordered mesoporous carbon synthesized by organic-inorganic self assembly technique was used as catalyst support. Nitrogen adsorption analysis revealed that the catalyst surface areas varied between 458 and 486 cm^2/g, pore sizes varied between 4 and 4,65 nm, while the mesopore texture has been largely preserved after the metal loading process. It has been found that the electrochemically active surface areas of the catalysts varied between 485 and 862 cm^2/mg, and Mn containing catalyst had relatively higher active surface areas.

Keywords: PEM, Fuel Cell, Platinum, Palladium, Quaternary Catalyst

I. Introduction
In todays world, fossil fuels form the backbone of the energy sector and it is estimated that by year 2050, 75% of energy production will be still met by fossil fuels [Manoharan, 2019]. One of proposed solution is the fuel cell technology, which works by converting the chemical energy directly to electrical energy without any significant harm to environment. PEM (Polymer electrolyte membrane) fuel cells are the most promising fuel cell type among different cell types. The key factor in the feasibility of PEM fuel cell is improving the cathode half reaction rate, which can be achieved by use of active catalysts.The recent trend in the literature focuses on solutions based on multimetallic platinum alloys, in hope for reducing the Pt cost in the catalyst [Antolini, 2007; Li, 2013; Güldür, 2011].

Here in this study, Pt/Pd multimetallic catalysts were developed, characterized and their electrocatalytical properties measured against oxygen reduction reaction. Ordered mesoporous carbon (OMC) was used as catalyst support. OMC was synthesized by employing an organic-inorganic self assembly technique. Then, four-metallic catalysts, namely PtAgFeMn/OMC, PtAgFeNi/OMC, PdAgFeMn/OMC and PdAgFeNi/OMC were prepared and loaded on the mesoporous support by wet impregnation reduction method.

II. Experimental Set-up and Procedure
The synthesis procedure of ordered mesoporous carbon (OMC) briefly consists of the following steps. 1.25 g resorcinol and triblock copolymer F127 were dissolved in ethanol/water solution so as the carbon/surfactant ratio will be 2:1. Hydrochloric acid (0.44 M) was added as the polymerization catalyst. This was followed by addition of tetraethyl orthosilicate and formaldehyde (Resrocinol/formaldehyde = 1:1). The resultant polymer was carbonized at 700 °C in a tube furnace with a controlled gas atmosphere consisting of argon. The carbonized material was soaked in 15% HF solution in order to etch the remaining silicates in the composite structure. The resultant OMC samples were treated with 2 M nitric acid to create oxygen rich functional groups on the carbon surface.

The Pt and Pd containing four-metallic catalysts were loaded on the OMC support by using wet-impregnation method. In all catalysts the metal atomic ratios were equal and the metal to carbon ratio was set to 20% metal by weight. Metal salt precursors were reduced to metallic form by addition of 1% (w/w) sodium borohydride solution. Finally the catalysts were filtered and dried overnight. The structural properties of the OMC and OMC supported catalysts were analysed by nitrogen adsorption method. Cyclic voltammetry measurements were carried out to measure the electrochemically active surface areas and the ORR activities of the catalysts. Tests were performed in 0.5 M H_2SO_4 electrolyte solution in the potential range of -0.2V and 1V.

III. Results and Discussion
According to the nitrogen adsorption analysis, the blank OMC sample was found to have a surface area of 711 cm^2/g, which is significantly greater than that of commercial carbon black support (around 250 m^2/g) [Liang, 2018]. The mean pore size was measured as 5.6 nm. The shape of adsorption-desorption isotherms matched with a type 4 isotherm behaviour which was indicative of a mesoporous structure. The nitrogen adsorption analysis was applied to the catalyst loaded samples, namely, PtAgFeMn/OMC, PtAgFeNi/OMC, PdAgFeMn/OMC and PdAgFeNi/OMC. The adsorption-desorption isotherms were mostly similar to that of OMC and showed that the mesoporous structure was well preserved after metal loading. The surface areas of the Pt and Pd based catalysts varied between 436 and 486 cm^2/g, which were still higher than carbon black. The highest surface area was obtained from the PtAgFeNi/OMC with 486 cm^2/g. The pore sizes of the catalysts varied between 4 and 4.64 nm. The expected reduction in pore sizes have been caused by the decrease in the pore volume due to incorporation of the metal particles in pores (Table 1).

Tab. 1. Surface properties of the catalysts

Catalyst	S_{BET}, cm^2/g	S_{BJH}, cm^2/g	Dpore, BJH, nm	Vpore, BJH, cm^3/g	Vmicro, BJH, cm^3/g
PtAgFeMn/OMC	469.4	344.9	4.01	0.553	0.239
PtAgFeNi/OMC	486.4	356.9	4.64	0.556	0.247
PdAgFeMn/OMC	436.9	330.6	4.65	0.543	0.239
PdAgFeNi/OMC	458.2	342.3	4.64	0.552	0.234

The electrochemically active surface areas (EAS) of the catalysts were measured by cyclic voltammetry (Figure 1). The EAS values were determined on the basis of the hydrogen desorption current in the positive scan. By integration of the area under the hydrogen desorption region, the current due to desorption of a monolayer of hydrogen atoms was calculated.

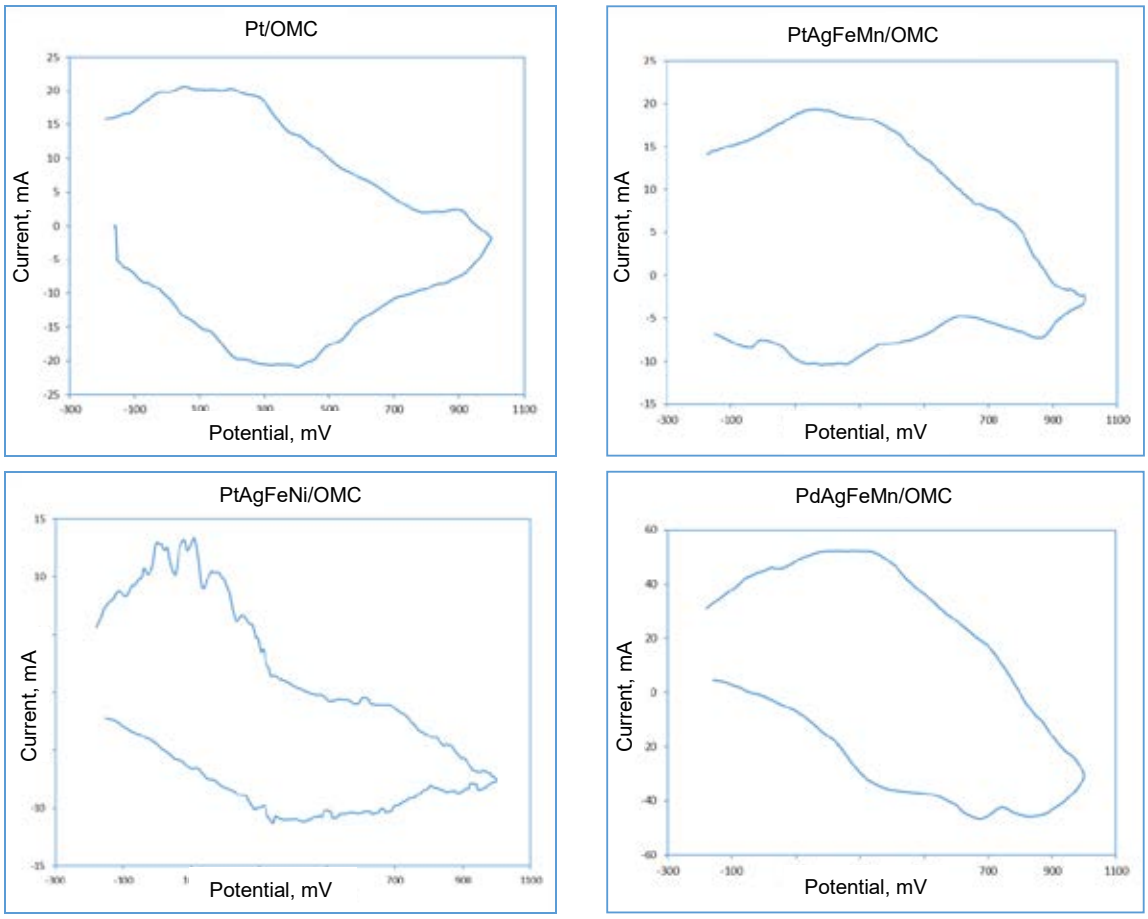


Fig. 1. Cyclic voltammograms of the quaternary catalysts compared with Pt/OMC a) Pt/OMC b) PtAgFeMn/OMC c) PtAgFeNi/OMC and d) PdAgFeMn/OMC

Electrochemically active surface areas of the catalysts were compared in Table 2. The EAS values of the quaternary catalysts were lower than that of pure Pt catalyst. However, these values are still comparable to pure Pt considering the significantly lower Pt amount used in those catalysts. Especially, PtAgFeMn/OMC and PdAgFeMn/OMC had close EAS values to Pt/OMC. In general, it was observed that the choice between Mn and Ni has a greater effect on EAS than the choice of Pt or Pd, as Mn containing catalysts showed higher EAS values.

Tab. 2. Comparison of the EAS values of the catalysts

Catalyst	Qh, mC	EAS, cm^2/mg
Pt/OMC	10.65	905
PtAgFeMn/OMC	2.53	862
PtAgFeNi/OMC	1.43	485
PdAgFeMn/OMC	2.52	856
PdAgFeNi/OMC	1.79	609

IV. Conclusions

In this study, Pt and Pd based, Ag, Fe and Mn/Ni containing four-metallic catalysts were prepared. Ordered mesoporous carbon was synthesized by organic-inorganic self assembly method and used as the metal support. Nitrogen adsorption studies showed that the mesoporous structure was largely preserved after the metal loading, with some reduction in surface areas and pore sizes between 34-36% and 17-18%, respectively. The electrochemically active surface areas were measured between 485 and 862 cm^2/mg. Mn containing catalysts had higher EAS values compared to those containing nickel. It can be concluded that, PtAgFeMn/OMC and PdAgFeMn/OMC catalysts can be used as alternative catalysts instead of pure Pt without significant loss of performance, especially in cases where availability of Pt is limited.

Acknowledgements

This study was financially supported by Gazi University Scientific Research Projects Unit (BAP) through project number 06/2018-24.

References

1. Manoharan Y., Hosseini S. E., Butler B., Alzhahrani H., Senior B. T. F., Ashuri T., and Krohn J., Hydrogen fuel cell vehicles; current status and future prospect. Applied Sciences, 9, 1-2, (2019).

2. Antolini E., Salgado J.R.C., da Silva R.M., Gonzales E.R. Preparation of carbon supported binary Pt–M alloy catalysts (M = first row transition metals) by low/medium temperature methods, Materials Chemistry and Physics, 101, 395–403, (2007).

3. Li B., Chan S., PtFeNi tri-metallic alloy nanoparticles as electrocatalyst for oxygen reduction reaction in proton exchange membrane fuel cells with ultra-low Pt loading, International Journal of Hydrogen Energy, 38, 3338-3345, (2013).

4. Güldür Ç., Güneş S., Carbon supported Pt-based ternary catalysts for oxygen reduction in PEM fuel cells. Catalysis Communications, 12, 707-711, (2011).

5. Liang J. Z., Yang Q. Q., Effects of carbon black content and size on conductive properties of filled high-density polyethylene compositesi Advances in Polymer Technology, 37, 2238–2245, (2018).

Comparison of Pure-Hydrogen Production from Sodium Borohydride with Blast Furnace Slag, Fe_2O_3 and Al Nano Metal Powder Catalysts

[1]Mustafa Kaan Baltacıoğlu [2*]Feride Cansu İskenderoğlu, [2]Fatih Bekmez, [2]Berat Madenci
[1] İskenderun Technical University, Faculty of Engineering and Natural Science, Mechatronics Engineering Department, Hatay,31200, Turkey
[2] İskenderun Technical University, Faculty of Engineering and Natural Science, Mechanical Engineering Department, Hatay, 31200, Turkey
* E-mail: fiskenderoglu.mfbe18@iste.edu.tr

Abstract
Opportunities of rapid technological change such as renewable energy sources, which are more environmentally friendly and more efficient, will come into play for energy production in a sustainable future. One of these sources is hydrogen, which can be using as an energy raw material in today and the future. A popular way to obtain hydrogen is using sodium boron hydride (NaBH4) which is a purposive hydrogen carrier. In this study, metal powders which are ingredients of slag, and slag are using as catalysts for the hydrolysis reaction under appropriate pressure and temperature. Moreover, some metal powders, that are in ingredients of slag, such as Al and Fe_2O_3 can produce hydrogen with only water under optimal conditions. As obtained results of experiments, it was observed that metal powders and the mix of the blast furnace slag/metal powder were more efficient compared to the blast furnace slag.
Keywords: Metal powders, NaBH4, Hydrogen production, Nano Material, Blast Furnace Slag.

I. Introduction

Humankind has needed the energy to survive for centuries. Most of our energy needs are provided by fossil fuels. Fossil fuel sources are limited as they are non-renewable energy sources, also, are rapidly being depleted with the increase in industrialization. Although fossil fuels seem useful to meet energy needs, serious damage is caused to the environment during the extraction and transportation process, thus, create very harmful environmental effects of the fossil fuel resources. Since the main component of fossil fuels is carbon, they emit greenhouse gases (CO_2, CH_4, N_2O) that are harmful to the atmosphere when they are combusted. Due to this, air pollution problems arise (Barbır,1990). Due to the decrease in the reserves of fossil energy resources and the damage they cause to the environment, a search for new energy resources has been started. As a result of this search, renewable energy resources have been increased interest to them. These resources are the most ideal energy sources for continuous energy needs and clean energy (Panwar, 2011). As one of the renewable energy sources, hydrogen is a great hope to reduce the ever-growing energy need and environmental pollution. Although hydrogen gas has many advantages, its biggest disadvantage is storage difficulty. Due to its low density, it must be stored in high pressure tanks to provide sufficient fuel to the systems, thus increasing the storage cost (Yang, 2018). Hydrides have been preferred in recent years due to their high hydrogen volume and reliability. Many types of hydrides such as metal hydrides and chemical hydrides are used in obtaining hydrogen. Examples of the most popular chemical hydrides are sodium boronhydride ($NaBH_4$), NH_3 and MgH_2. Boronhydrides such as $NaBH_4$ are preferred due to their environmental friendliness, non-flammability and stability in alkaline solutions (Nabid, 2019). Among the chemical hydrides, $NaBH_4$ is the most studied and researched (Balbay, 2021). Some of the main advantages $NaBH_4$ can be listed as; i) High ability to produce hydrogen at room temperature, ii) It is a hydrogen reservoir and has a high hydrogen density (About 10%), iii) It has a high reduction, iv) It has easy storage and transportation features.

As a result of the study done by Schlesinger in 1950, it was observed that $NaBH_4$ hydrolysis was slow at room temperature. Adding catalysts to the hydrolysis reaction increases hydrogen production by reducing the activation effect (Balbay,2021; Lee,2019). Most of the $NaBH_4$ hydrolysis studies are based on more efficient and faster hydrogen gas generation than the hydrolysis reaction. With the various chemicals used during hydrolysis reactions, it is aimed to produce hydrogen gas in a faster and more sustainable manner. In the literature, the effect of the catalyst used in the hydrolysis of $NaBH_4$ depends on the large area of the surface, high conductivity or high degree of graphitization, a suitable pore structure to ensure mass transport and the amount of metal particles. Metal-containing catalysts used as catalysts in hydrogen production reactions from $NaBH_4$ have high catalytic activity. Noble metal based catalysts such as Ru, Pd and Pt are used in the hydrolysis reaction of $NaBH_4$ (Lee,2019; Wei,2018; Baydaroğlu,2013). These catalysts have been observed to greatly increase the catalytic activity of the reaction, but their use is limited due to their rare and costly properties in the industrial field. In studies where transition metals such as Co, Ni, Fe, Cu are used, it is expected that these metal catalysts will be used as high efficiency catalysts, considering the high catalytic activity of Ni and Co metal catalysts and because they are less costly than noble metals. In this study, the effect of Fe_2O_3 Nano and Al Nano metal powders that are ingredients of slag, which were not used before in the literature, on hydrogen production from $NaBH_4$ was investigated. The effect of Fe_2O_3 and Al metal powders used in different amounts has been demonstrated in a series of experiments. In addition to these experiments, the effects of slag by-product and HCl acid obtained from iron and steel factories in our region as supporting materials in these experiments were also investigated. As a result, it is aimed to produce an efficient hydrogen gas by using a more environmentally friendly catalyst material, which is cheaper than other catalysts and in terms of zero waste usage.

II. Experimental Set-up and Procedure

98.5% pure NaBH4 that contains 0.05% Si and 0.005% Fe was supplied from a commercial company. Fe2O3 was also obtained from a commercial company. Nano size Fe2O3 has 99.55% purety and contains 0.003% Ca, 0.015% Cr, 0.14% Mn, 0.05% Al and 0.091% SiO2. Slag was supplied from Iskenderun Iron and Steel factory.

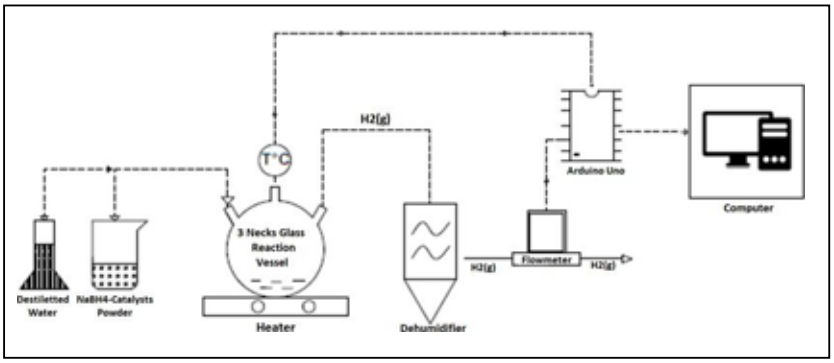


Fig. 1: Experimental installation

It consists of a 3-port reactor, heater, moisture trap, Alicat Scientific brand flow meter, DS18B20 temperature sensor, MTOPS MS300HS brand heater and Arduino Uno. The amount of $NaBH_4$ was kept constant as 2 g for all experiments. Then, in the hydrolysis reaction of $NaBH_4$, Fe_2O_3 Nano, Al Nano and slag powders together with distilled water were weighed one by one on an analytical balance as 0.2 g, 0.5 g, 1 g and 2 g and used in the experiments. The performances of these metal powders in the hydrolysis reaction of $NaBH_4$ were investigated using the experimental setup in Figure 1. The port into which catalyst and water are added, the port where the temperature meter enters and the port where the gas outlet takes place were wrapped with gas teflon tape against gas leakage, thus providing a high sealing environment. The preparing catalyst mixtures and 20 ml distilled water were transferred from the water and catalyst inlet port into the reactor vessel. The heating plate has been heated up to 50 ° C. The reaction temperature is measured with a DS18B20 thermometer connected to the Arduino Uno. The water vapor in the hydrogen gas produced in the reaction is separated by using a moisture scavenger. The volumetric flow rate (liter per minute) of released hydrogen gas is measured by a high precision flowmeter. The measured manual data are simultaneously transferred to the digital signals via Arduino Uno and transferred to the host computer.

III. Results and discussions

In all experiments, hydrolysis reactions were carried out by using 20 ml of distilled water and 2 g of $NaBH_4$ and the reaction vessel was preheated to 50 ° C. Al and Fe_2O_3 Nano metal powders catalyst were used in 3 different amounts as 0.2 g - 0.5 g - 1 g. During the experiments with 0.2 g, 0.5 g and 1g of Fe_2O_3 catalyst, the total flow rates were 339.07 L, 372.5 L and 358.97 L, respectively. On the other hand, the total flow rate results of Al catalyst for 0.2 g, 0.5 g and 1g usages were 184.05 L, 316.11 L and 366.81 L, respectively.

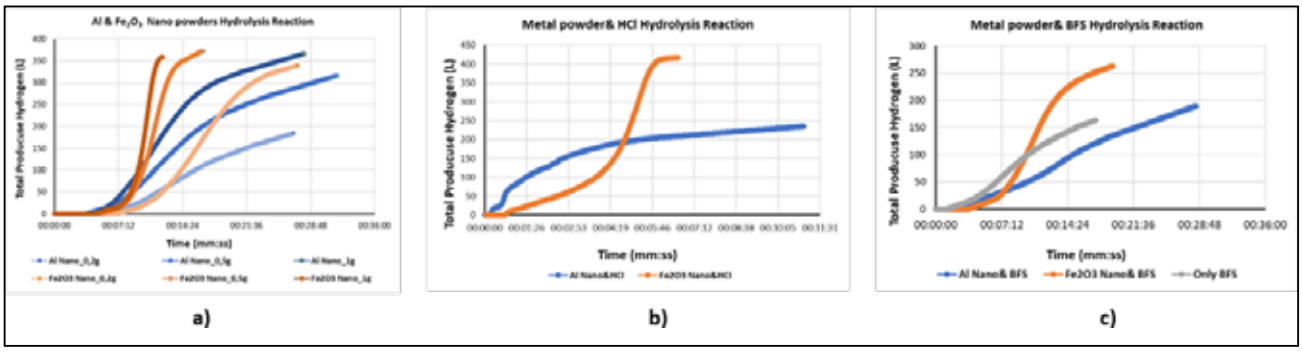


Fig. 2.a) Al and Fe_2O_3 (Nano), 2.b) Al and Fe_2O_3 (Nano) with HCl acid, 2.c) Al and Fe_2O_3 (Nano) with BFS

In this study, it has been proved by experiments that Fe_2O_3 catalysts can be used as efficient catalysts in $NaBH_4$ hydrolysis reaction. In these experiments, the catalyst samples were made suitable for the $NaBH_4$ hydrolysis reaction by various experiments in different amounts, slag by-product and HCl acid effect. In this study, the analysis of the hydrogen production reaction carried out under 5 different conditions with the Al and Fe_2O_3 catalysts was made. During the study, 10 different experiments were repeated 3 times, a total of 22.5 hours were carried out in the experimental setup established in the ISTE Machanical Engineering Laboratory and the results were recorded digitally with the aid of computer softwares. It has been shown that both type of catalysts can be used efficiently in hydrolysis reactions when the experimental results of these metal powder catalysts are compared. According to the results of these optimization experiments, more effective test results are obtained by using different parameters and

combinations.

In the hydrolysis experiment in which Fe_2O_3 metal powder was used together with slag, approximately 45% more hydrogen production was observed compared to the experiment using only slag. In the Al Nano experiment with the addition of slag, approximately 30% more hydrogen production was observed compared to the experiment using only slag. However, the use of slag does not increase the yield in hydrolysis reactions where only Al and Fe_2O_3 metal powders are used as catalysts. In hydrolysis reactions using HCl acid, total hydrogen production increased by 13% in the experiment where Fe_2O_3 Nano and HCl acid were used together, while the total amount of hydrogen produced increased by 20% in the experiment where Al Nano and HCl acid were used together. It has been observed that adding HCl acid gives efficient results in the reaction. Therefore, it can be recommended to use HCl acid solutions with different molarities in reactions.

IV. Conclusions

In this study, the yields of Fe_2O_3 and Al catalysts were compared with the experiments conducted for hydrogen production from the catalytic hydrolysis of $NaBH_4$ supported with Slag by-product and HCl acid. As a result of the obtained data, it was determined that Fe_2O_3 and Al catalysts have advantages over hydrogen production rate and fuel conversion. In line with the results obtained from the experiments, the Fe_2O_3 catalyst and the Fe_2O_3 catalyst & HCl acid experiments show a very high success in different parameters, and also Fe_2O_3 catalysts create promising effects in the hydrolysis reactions of $NaBH_4$. Among the catalyst samples, the highest efficiency performances are achieved with Fe_2O_3 Nano catalyst samples at 50 ° C preheat with an instantaneous hydrogen generation rate of approximately 29.91 L / min for 12 minutes. There is no study in the literature with Fe_2O_3 catalysts in $NaBH_4$ hydrolysis reactions. In addition, other metal catalysts used in these reactions are quite expensive and inefficient compared to Fe_2O_3 catalysts. The use of Fe_2O_3 catalysts as cheap and efficient catalysts in hydrolysis reactions has made a great contribution to literature studies.

Acknowledgements

This research was supported by TUBITAK and Prof. Dr. Ertuğrul Baltacıoğlu.The slag was provided by the İSTE Civil Engineering Department.

References

Balbay, A., Selvitepe, N., Saka, C., Fe doped-CoB catalysts with phosphoric acid-activated montmorillonite as support for efficient hydrogen production via NaBH4 hydrolysis, International Journal of Hydrogen Energy, 46(1), 425-438, (2021).

Barbır F., Vezıroglu T. N., Plass H. J., Environmental damage due to fossil fuels use. United Kingdom., International Journal of Hydrogen Energy, (1990).

Baydaroğlu F. O., Sodyum Borhidrürün Hidrolizinden Hidrojen Eldesi İçin Etkin Katalizörlerin Geliştirilmesi, Master Thesis, Gebze Technical University, Gebze, Turkey (2013).

Öztürk E., Synthesis of metallic catalysts with various support materials for hydrogen generation from sodium borohydride, Ondokuz Mayıs University, Samsun, Turkey (2019)

Lee, J., Shin, H., Choi, K. S., Lee, J., Choi, J. Y., Yu, H. K. (2019). Carbon layer supported nickel catalyst for sodium borohydride (NaBH4) dehydrogenation,. International Journal of Hydrogen Energy, 44(5), 2943-2950.

Nabid, M. R., Bide, Y., & Kamali, B., Hydrogen release from sodium borohydride by Fe2O3@ nitrogen-doped carbon core-shell nanosheets as reasonable heterogeneous catalyst, International Journal of Hydrogen Energy, 44(47), 25662-25670, (2019).

Panwar, N. L., Kaushik S. C., Kothari S., Role of renewable energy sources in environmental protection: A review., Renewable and sustainable energy reviews 15(3) 1513-1524, (2011).

Yang, H., Lombardo, L., Luo, W., Kim, W., Züttel, A., Hydrogen storage properties of various carbon supported NaBH4 prepared via metathesis. International Journal of Hydrogen Energy, 43(14), 7108-7116, (2018).

Wei, Y., Wang, Y., Wei, L., Zhao, X., Zhou, X., Liu, H., Highly efficient and reactivated electrocatalyst of ruthenium electrodeposited on nickel foam for hydrogen evolution from NaBH4 alkaline solution, International Journal of Hydrogen Energy, 43(2), 592-600, (2018).

ECO-FRIENDLY PRODUCTION OF GRAPHENE FIBER AS METAL-FREE ELECTROCATALYST FOR HYDROGEN EVOLUTION REACTION

M. Giray Ersozoglu[1], Hurmus Gursu[2], Selin Gumrukcu[3], A. Sezai Sarac[1,4], Yucel Sahin[2*]
[1]Polymer Science and Technology, Istanbul Technical University, Istanbul 34469, Turkey
[2]Faculty of Arts and Science, Department of Chemistry, Yildiz Technical University, 34220 Istanbul, Turkey
[3]Faculty of Arts and Science, Department of Chemistry, Istanbul Technical University, Istanbul 34469, Turkey
[4]Nanoscience and Nanoengineering, Istanbul Technical University, Istanbul 34469, Turkey
E-mail: yucelsahin06@gmail.com

Abstract
The hydrogen economy is growing, and hydrogen production with low-cost and eco-friendly catalysts has become more critical.
Here, commercial carbon fibers were modified via green, cost-effective, and scalable electrochemical technics for hydrogen evolution. The intercalation and semi-exfoliation are observed on carbon fibers surface. Moreover, according to morphologic and spectroscopic analysis, graphene skin and sulfur doping are confirmed on the flexible fiber surface. The graphene fibers are tested in acidic media via linear sweep voltammetry to investigate hydrogen evolution reaction kinetics. Tafel slope of S-GrF1 (165 mV/dec) and S-GrOF1 (163 mV/dec) is significantly smaller compared to bare carbon fiber (345 mV/dec). Therefore, graphene fibers can be seen as a good option for hydrogen evolution catalysts.

Keywords: Graphene fiber, metal-free catalyst, hydrogen evolution, electrochemical method, cyclic voltammetry

I. Introduction

Sustainable and clean solutions are needed to replace existing energy production systems that use fossil fuels or nuclear power. One prominent solution is hydrogen energy that is environmentally friendly, safe, and easily scalable. Hydrogen systems have many significant energy conversion application potentials: supplying cleaner energy sources via fuel cells to vehicles, residences, renewable integrated systems with intermittent nature, fuel to internal combustion engines, and heating/cooling sources. However, only if the hydrogen production method and materials, in other words, "technology," are appropriately selected, hydrogen energy gives optimum outcomes. Hydrogen production methods classification can be considered primary energy-based: electrochemical, photochemical, photo-electrochemical, photonic, biological, thermal, and thermochemical (Ahmed and Dincer 2019; X. Zou and Zhang 2015). Among these technologies, electrochemical water splitting is superior technology due to its low set-up and maintenance cost, ease of scalable and accessibility, and environmentally friendly properties. (Nivetha et al. 2018). Nowadays, carbon-based metal-free electrodes have excellent attention for HER due to their cost effectiveness, durability at long cycles in acidic and alkaline media, and feasible mass production. Nevertheless, pristine carbon materials suffer from insufficient catalytic activity since symmetric dispersion of valence and conduction band; thus, defect-rich structures by heteroatom doping into carbon lattice have been intensely reported to increase activity (Wu et al. 2020).
Among the carbon-based materials (fiber-based, graphene, carbon nanotubes, carbon black), carbon fibers (CF) have become prominent due to their excellent mechanical strength, high surface area, and flexibility with high carbon content (approx. %99), good electrical conductivity, high chemical, and mechanical stability. However, CF's compact crystal structure leads to low-ion diffusion and insufficient electrochemical active sites. Thus, commercial CF, in particular, needs activation via creating defects and doping (Chen, Qiu, and Cheng 2020).
Herein, we report an innovative strategy to fabricate electrochemically enhanced, self-standing S-doped graphene fiber (S-GrF) from commercial CF. The binder-free S-GrF was obtained by cyclic voltammetry, which is also called Yucel's method (Gürsu et al. 2020), a green and versatile method of graphene production from graphite. The S-GrFs are performed as HER catalyst, and their catalytic efficiency is boosted significantly in contrast with unmodified commercial CF.
The production method is also a cost-effective and controllable way to fabricate graphene-skinned CF for catalyst and energy storage applications.

II. Experimental Set-up and Procedure

Sulfur-doped graphene fibers (S-GrFs) and sulfur-doped graphene oxide fibers (S-GrOFs) were prepared in one step directly from commercial carbon fiber via Yucel's method (Gürsu, Gençten, and Şahin 2018) and chronoamperometric method (Ersozoglu et al. 2021), respectively. The PAN-based carbon fiber, Ag wire, and Pt wire were used as a working, reference, and auxiliary electrode, respectively, in a conventional electrochemical cell containing a three-electrode system. All electrodes were rinsed thoroughly with water, acetonitrile and dried at 50°C before all treatments. PAN-based carbon fibers (CFs) were treated electrochemically in various sulfuric acid solutions in a specific potential range at room temperature with 50 voltammetric cycles. The electrodes prepared in 1.0 M, 3.0 M, and 5.0 M sulfuric acid solutions were S-GrF1, S-GrF2, and S-GrF3. Afterward, PAN-based carbon fibers (CFs) were electrochemically treated in 1.0 M, 3.0 M, and 5.0 M sulfuric acid solutions at a constant potential for 5.0 minutes named S-GrOF1, respectively. After each electrochemical treatment, the obtained electrodes were washed with deionized water to remove impurities and acidity.

III. Analysis

Raman analysis was done by using of 785-nm laser with the equipment of Kaiser Optical Raman. X-ray photoelectron spectroscopy (XPS), Thermo Scientific K-Alpha model, Al anode Kα = 1468.3 eV, Avantage 5.934 software, was utilized to determine the chemical composition. Morphological characterizations of sulfur-doped graphene-based fiber electrodes were elucidated Carl Zeiss EVO LS model scanning electron microscope (SEM). PGSTAT302N and GAMRY3000 potentiostat/galvanostat were used for all electrochemical analysis.

IV. Results and discussions

Sulfur-doped graphene fibers (S-GrFs) were prepared via Yucel's method based on cyclic voltammetry in increasing H_2SO_4 concentration in an aqueous solution. The intercalation of sulfate ion, hydroxyl ion result from water reduction and H^+ at anodic and cathodic scanning leads to graphite layer expansion on the carbon fiber surface. Besides the color change, yellow and light brown corresponds with semi-exfoliated graphene layers in an electrolyte solution. (Dou et al. 2019; Y. Zou and Wang 2015).

SEM presents the morphology change in Fig1. In this case, changing acid concentration brings about entirely different morphologies. While S-GrF1 illustrates porous structure with semi-exfoliated graphene nanofibers, S-GrF2 and S-GrF3 have blistered outer layer conformation, and S-GrOF has nano-rods on fiber skin.

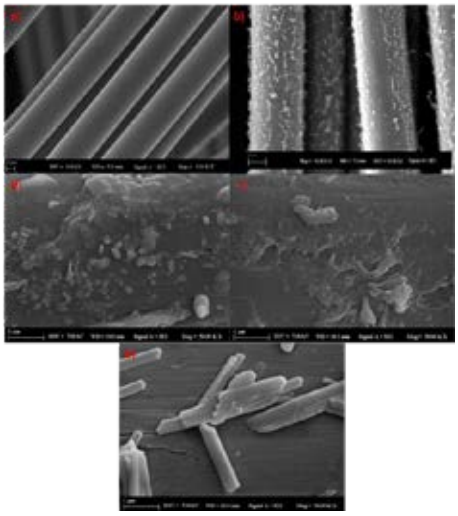


Fig.1 SEM images of a) Unmodified CF, b) S-GrF1, c) S-GrF2, d) S-GrF3, e) S-GrOF

The Raman spectra of S-GrFs and S-GrOF (Fig. 2) have two essential bands have underlined, located around 2650 cm^{-1} (2D band) and 2900 cm^{-1} (D+G band). In general D+G band is associated with characteristic graphene peak; however, there is no peak for unmodified carbon fiber in this region.

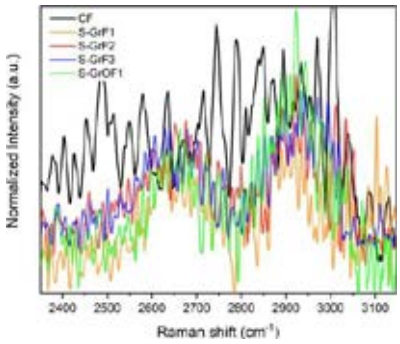


Fig.2 Raman spectra 2D bands of unmodified, S-GrFs and S-GrOF

The chemical composition of all sulfur-doped graphene-based fiber electrodes was analyzed by XPS analysis. C1s and S2p, XPS spectrums were measured for all sulfur-doped graphene fiber-based electrodes (Fig. 3). C1s spectra are fitted into three peaks, which are associated with sp2 hybridized (C=C) carbon (284.3 eV), C-C sp3 hybridization (286 eV), and -C=O/O-C-O (288.3 eV). Moreover, S2p spectra fitting illustrates the formation of three binding energies of 163.8, 165, and 168.8 eV, which correspond to C-S-C, C=S, and C-SOx, respectively. It indicates successful doping of sulfur group to the carbon fiber surface.

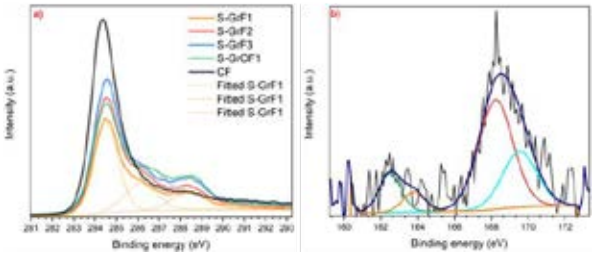


Fig.3 XPS results of a) All treated and unmodified fibers C1s spectra, b) S2p spectra of S-GrF1

HER kinetics of graphene fibers is measured with linear sweep voltammetry at a scan rate 5 mV.s^{-1} in acidic media at room temperature and derived Tafel plots showed in Fig.4. LSV and Tafel plot is presented with reversible hydrogen electrode (RHE) potential for comparison. Tafel slope is a universal indicator for investigation on HER reaction kinetic, and a smaller Tafel slope corresponds fast reaction rate. Therefore, S-GrF1 and S-GrFO1 indicate the best catalyst performance with 165 mV/dec and 163 mV/dec compared to S-GrF2 (216 mV/dev) and S-GrF3 (250 mV/dec). Besides, the unmodified CF has a slow reaction rate due to its insufficient electrochemical activity. The stability of S-GrF1 also showed that the graphene fibers have reasonable durability for hydrogen production operations.

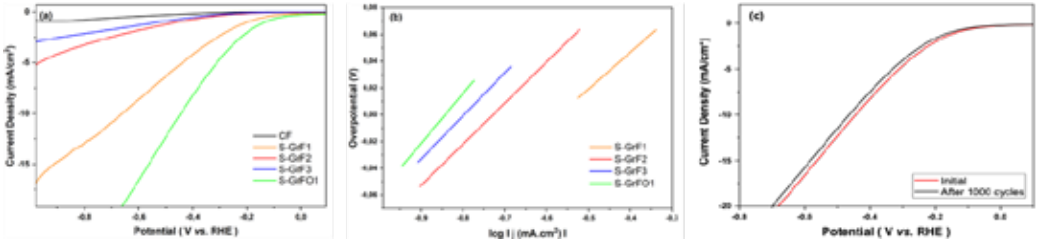


Fig.4 HER performance in 0.5 M H_2SO_4. (a) HER polarization curves with a scan rate of 5mV s^{-1}, and (b) corresponding Tafel slopes of the series of flexible graphene and graphene oxide fibers. (c) HER polarization curves of S-GrF1 initial and after 1000 CV cycles.

V. Conclusions

S-doped graphene fibers were manufactured via cyclic voltammetry and exhibit good catalyst perfomance compared to bare carbon fiber for HER. The graphene fibers can be considered as a cost-efficient option against metal catalyst, particularly noble metals. In addition, S-GrF1 is a promising catalyst for flexible, long life and low-priced hydrogen production systems.

Acknowledgements

We thank Dr. Baris Yagci at KUYTAM, Koc University, for his help with XPS measurements and SARGEM, Sakarya University's academic staff, for their help for spectroscopic and morphological tests.

References

Ahmed, Mahmoud, and Ibrahim Dincer. 2019. "A Review on Photoelectrochemical Hydrogen Production Systems: Challenges and Future Directions." *International Journal of Hydrogen Energy* 44(5): 2474–2507. https://doi.org/10.1016/j.ijhydene.2018.12.037.

Chen, Shaohua, Ling Qiu, and Hui Ming Cheng. 2020. "Carbon-Based Fibers for Advanced Electrochemical Energy Storage Devices." *Chemical Reviews* 120(5): 2811–78.

Dou, Zhenjun et al. 2019. "High–Performance Flexible Supercapacitor Based on Carbon Cloth through in–Situ Electrochemical Exfoliation and Re–Deposition in Neutral Electrolyte." *Carbon* 153: 617–24. https://doi.org/10.1016/j.carbon.2019.07.073.

Ersozoglu, M. Giray et al. 2021. "A Green Approach to Fabricate Binder-Free S-Doped Graphene Oxide Electrodes for Vanadium Redox Battery." *International Journal of Energy Research* 45(2): 2126–37. https://onlinelibrary.wiley.com/doi/10.1002/er.5906 (January 29, 2021).

Gürsu, Hürmüs et al. 2020. "A Novel Green and One-Step Electrochemical Method for Production of Sulfur-Doped Graphene Powders and Their Performance as an Anode in Li-Ion Battery." *Ionics* 26(10): 4909–19.

Gürsu, Hürmüs, Metin Gençten, and Yücel Şahin. 2018. "Cyclic Voltammetric Preparation of Graphene-Coated Electrodes for Positive Electrode Materials of Vanadium Redox Flow Battery." *Ionics* 24(11): 3641–54.

Nivetha, Ravi et al. 2018. "Cobalt and Nickel Ferrites Based Graphene Nanocomposites for Electrochemical Hydrogen Evolution." *Journal of Magnetism and Magnetic Materials* 448: 165–71. https://doi.org/10.1016/j.jmmm.2017.05.083.

Sathe, Bhaskar R., Xiaoxin Zou, and Tewodros Asefa. 2014. "Metal-Free B-Doped Graphene with Efficient Electrocatalytic Activity for Hydrogen Evolution Reaction." *Catalysis Science and Technology* 4(7): 2023–30.

Wu, Mingguang et al. 2020. "2020 Roadmap on Carbon Materials for Energy Storage and Conversion." *Chemistry - An Asian Journal* 15(7): 995–1013.

Zou, Xiaoxin, and Yu Zhang. 2015. "Noble Metal-Free Hydrogen Evolution Catalysts for Water Splitting." *Chemical Society Reviews* 44(15): 5148–80.

Zou, Yuqin, and Shuangyin Wang. 2015. "Interconnecting Carbon Fibers with the In-Situ Electrochemically Exfoliated Graphene as Advanced Binder-Free Electrode Materials for Flexible Supercapacitor." *Scientific Reports* 5(June): 1–7. http://dx.doi.org/10.1038/srep11792.

Hydrogen Production by Methanol Electrochemical Reforming in the Membrane System

[1*] Merve Gördesel Yıldız, [2] Özgü Yörük, [3] Duygu Uysal Zıraman, [4] Özkan Murat Doğan, [5] Bekir Zühtü Uysal
Gazi University, Faculty of Engineering, Department of Chemicel Engineering, Ankara, 06570, Turkey

* E-mail: mervegordesel@gazi.edu.tr

Abstract
In this study, hydrogen production by electrochemical reforming of methanol was investigated. Within this scope, the effects of membrane type and the pre-treatment applied to the membrane on current density and hydrogen production were investigated. According to the results obtained from the polarization curves, use of pretreated Nafion XL membrane, at 70°C temperature with Pd/Pt electrode pair in the presence of 6 M methanol and 0.04 M H_2SO_4 at the anode compartment and 0.04 M H_2SO_4 at the cathode compartment provided the most suitable operation conditions. Thus, pure hydrogen was obtained in the cathode compartment by electrochemical reforming of methanol in the two-compartment membrane electrolysis cell.
Keywords: Methanol, electrochemical reforming, hydrogen, membrane

I. Introduction

Hydrogen stands out as a clean and ideal fuel for all energy systems with its features such as high energy density and zero emission. Hydrogen is expected to play an important role in future energy systems with the effect of its energy density per unit mass, being considerably higher than natural gas and oil. Today, 95% of hydrogen production is provided by fossil fuels. For this reason, in hydrogen production, it is necessary to lean into technologies that are less harmful to the environment, based on sustainable and innovative resources.

Methanol is an inexpensive and easily obtainable chemical used in hydrogen production. In addition, the high energy of methanol fulfills most of the external energy need for electrochemical reforming. Thus, the amount of energy required for hydrogen production decreases. In this way, hydrogen production occurs at low cost. The reactions taking place in hydrogen production by electrochemical reforming from methanol are given below (Take et al., 2007, Cloutier et al., 2010).

Anode : $CH_3OH + H_2O \rightarrow CO_2 + 6H^+ + 6e^-$
Katode : $6H^+ + 6e^- \rightarrow 3H_2$
Overall : $CH_3OH + H_2O \rightarrow CO_2 + 3H_2$

The theoretical cell voltage required for the overall reaction is 0.02 V. This value is 1.23 V for water. Compared to energy consumption, it is 55 kWh/kg-H_2 for water and 0.6 kWh/kg-H_2 for methanol (Chen et al., 2014). The need for less energy compared to the electrolysis of water, will also solve the cost problem that prevents the spread of hydrogen technology, and significant contributions will be made to hydrogen economy. The electrochemical reforming of methanol is a promising option for the future to commercialize hydrogen production with innovative methods from alternative sources in terms of selectivity, efficiency, operating conditions and cost.

II. Experimental Set-up and Procedure

Pure hydrogen production and its separation was carried out in a single step. With this method, thermal energy is not needed since hydrogen production occurs under atmospheric conditions at low temperatures, only electrical energy consumption is a matter of importance. Pure hydrogen production with the electrochemical reforming method occurs at a lower temperature compared to other systems, in a controlled, fast, simple and economic way.

In the method used, an electrical potential is applied between two electrodes in the cell whose compartments are separated by a membrane. Electrooxidation reaction occurs at the anode electrode. The protons formed at the anode pass through the selectively permeable membrane to the cathode compartment. Here, hydrogen is formed by combining with the electrons coming from the outer circuit. Thus, pure hydrogen is obtained instantly without the need for any separation and purification processes.

The two-compartment electrolysis cell used in the experiments is shown in Figure 1. Experiments in a two-compartment electrolysis cell with a membrane were carried out with a Pd/Pt electrode pair at room temperature and 70°C, at 240 RPM mixing speed, in the presence of 6 M methanol and 0.04 M H_2SO_4 at the anode side, and 0.04 M H_2SO_4 at the cathode side.

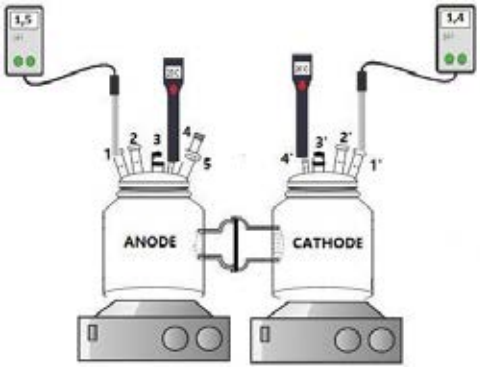


Fig. 1: Two-compartment electrolysis cell (1/1 ': pH meter input, 2/2': electrode input, 3/3 ': gas outlet, 4/4': thermometer input, 5: reference electrode input)

Nafion membranes (Ion Power brand) were used in the system. Nafion membranes are cation exchange membranes that contain negatively charged active sites. For this reason, they play an important role in the transmission of H^+ ions that have opposite charges with them. Depending on the pressure that will affect the membrane, the physical constraints of the system, and the working life, membranes of different thicknesses suitable for the system can be selected. As the thickness of the membranes decreases, the resistance and ohmic losses in the system decrease while the ion permeability increases (Liu et al., 2018, Lin et al., 2019). However, as the thickness decreases, the durability decreases (Yuan et al., 2010). In addition, high ion exchange capacity and low resistance feature are required in membranes. In this study, Nafion XL (27.5 µm) and Nafion 117 (183 µm) membranes were compared to determine the effects of such properties on the system.

The membranes used in the experimental system were activated with different pre-treatment procedures; hence the amount of water molecules bound to the sulfonic acid group in the membrane structure was increased. The water molecules in the Nafion membrane create weak bonds with the proton, allowing the hydrogen ion to move from the anode compartment to the cathode compartment. For this reason, ion exchange over the membrane occured more effectively with the pre-treatment. The pre-treatments used in the study, called procedure-1 and procedure-2, are given below.

Procedure-1 (Cloutier et al., 2010)
1. Kept in a 3% by mass H_2O_2 solution at 80°C for 30 min.,
2. Washed with deionized water,
3. Kept in deionized water at 80°C for 30 min.,
4. Washed with deionized water,
5. Kept in 0.5 M H_2SO_4 solution at 80°C for 30 min.

Procedure-2 (Kuwertz et al., 2016)
1. Kept in 2 M H_2SO_4 solution for 24 hours,
2. Kept in deionized water for 24 hours.

III. Results and discussions

Nafion XL and Nafion 117 membranes were used in methanol electrochemical reforming experiments performed at room temperature in a two-compartment electrolysis cell. The polarization curves obtained are comparatively given in Figure 2.

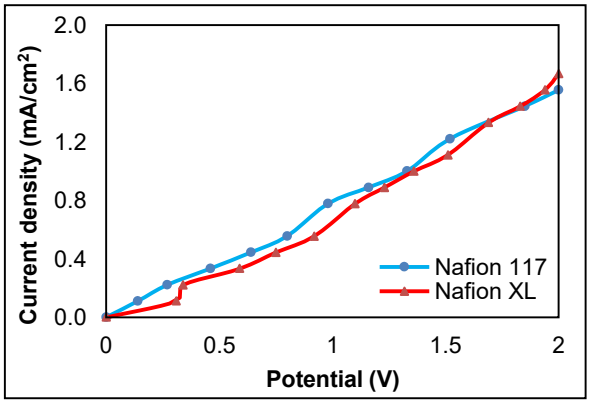


Fig. 2: Comparison of polarization curves for Nafion 117 and Nafion XL membrane at room temperature

There is about 6 times the difference between the thicknesses of Nafion XL and Nafion 117 membranes. Nafion 117 membrane is a highly preferred type of membrane in electrochemical processes. Nafion XL membrane is also very convenient to use in electrolysis systems due to its thin structure and high ion exchange capacity. According to Figure 2, the current density values obtained for both membrane types are close to each other. However, especially at high temperature values, due to the limitations caused by the present system, it has become difficult to ensure the sealing of the system by using a thick membrane. For this reason, Nafion XL membrane was preferred for activation with pre-treatments. Polarization curves obtained by using pre-treated membranes are given in Figure 3.

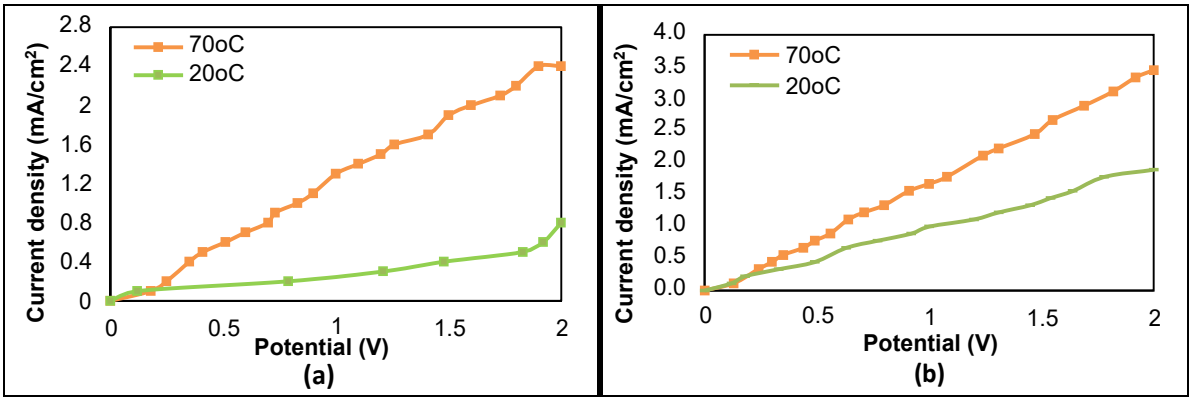


Fig. 3: Polarization curves obtained in methanol electrochemical reforming using Nafion XL membranes pretreated according to procedure-1 (a) and procedure-2 (b)

Among the pre-treatments applied to the Nafion XL membrane, procedure-2 is more effective at both operating temperatures than procedure-1. This is propabaly because of longer membrane-solution contact time in procedure-2 than procedure-1.

Also, gas samples were collected from the anode and cathode compartments during the 6-hour experiments. The gases were analyzed by gas chromatography and pure hydrogen formation in the cathode compartment was determined in all experiments.

IV. Conclusions

In this work, 28% higher current density values were obtained using a pre-treated membrane according to procedure-2 at a temperature of 70°C compared to pretreatment with procedure-1. Optimum yield for methanol electrochemical reforming under the operating conditions examined in the current system was obtained at 70°C with the Pd/Pt electrode pair in the presence of 6 M methanol and 0.04 M H_2SO_4 at the anode side, 0.04 M H_2SO_4 at the cathode side and with Nafion XL pretreated according to procedure-2.

Acknowledgements

This research was supported by Gazi University Projects of Scientific Investigation Unit (Project No: 06/2019-03). We would like to thank Gazi University Projects of Scientific Investigation Unit.

References

Chen, Y.X., Lavacchi, A., Miller, H.A., Bevilacqua, M., Filippi, J., Innicenti, M., Marchionni, A., Oberhauser, W., Wang, L., Vizza, F. “Nanotechnology makes biomass electrolysis more energy efficient than water electrolysis”, Nat. Commun. 5, 4036, 2014.

Cloutier, C. R., Wilkinson P. D., “Electolytic production of hydrogen from aqueous acidic methanol solution”, International Journal of Hydrogen Energy, 35, 3967-3984, 2010.

Kuwertz, R., Kirstein, C., Turek, T., Kunz, U. “Influence of acid pretreatment on ionic conductivity of Nafion® membranes”, Journal of Membrane Science, 500, 225-235, 2016.

Lin, Q., Sun, X., Chen, X., Shi, S. “Effect of Pretreatment on Microstructure and Mechanical Properties of Nafion™ XL Composite Membrane”, Fuel Cells, 19(5), 530-538, 2019.

Liu, Y., Wang, H., Xiang, Y., & Lu, S. 2018. “The effect of nafion membrane thickness on performance of all tungsten-cobalt heteropoly acid redox flow battery”, Journal of Power Sources, 392, 260-264, 2018.

Take, T., Tsurutani, K., Umedab, M., “Hydrogen production by methanol–water solution electrolysis”, Journal of Power Sources, 164, 9–16, 2007.

Yuan, X.-Z. Zhang, S. Wang, H. Wu, J. Sun, J. C. Hiesgen, R. Friedrich, K. A. Schulze, Haug, M. A. J. Power Sources 195, 7594, 2010.

Development of a High Performance PEM Fuel Cell Stack with Open-Cathode Titanium Bipolar Plate for Unmanned Aerial Vehicles

[1*]Uğur Aydın, [1] Ömer Erdemir, [1] Mehmed Selim Çögenli, [2,3]Selahattin Çelik, [2,3] Bora Timurkutluk, [2,3] Serkan Toros, [2,3] Kıvanç Karacan
[1] Vestel Defense Industry, Titanium Block 17/B, ODTU, Teknokent, 06800 Ankara, Turkey
[2] Nigde Omer Halisdemir University, Engineering Faculty, Mechanical Engineering Department, Nigde, 51245, Turkey
[3] Nigde Omer Halisdemir University, Prof. Dr. T. Nejat Veziroglu Clean Energy Research Center, Nigde, 51245, Turkey
* E-mail: uguraydin@vestel.com.tr

Abstract

Unmanned Vehicles are one of the most important milestones of the military operation. Due to their operational cost, numerous unmanned air, ground, and sea vehicles are in service and deployed around the world. VESTEL Karayel, TUSAŞ Anka, TUSAŞ Anka-Aksungur, Baykar Bayraktar TB-2, Baykar Bayraktar Akıncı are most important unmanned air vehicles (UAV) which are developed in Turkey. To use UAVs widely, developers are needed for a more efficient, powerful, lightweight, reliable, and logistically supportable power module for propulsion. Fuel cells present a solution for small size UAV due to higher efficiency and low fuel consumption compared to the internal combustion engine and Lipo batteries. In this study, an open cathode (air-breathing) 250Wel fuel cell is designed and some simulations are performed. The design and stamping processes, the simulation of the fuel cell are carried out using Catia, Comsol Multiphysics, Eta-Dynaform, and Ansys/Fluent, respectively. The preliminary preparation is obtained for the production phase with these analyses.

Keywords: PEM fuel cell, open cathode (air-breathing), light-weight stack, formability,

I. Introduction

Fuel cells are frequently used in unmanned aerial vehicles through their advantages such as high efficiency, low acoustic signature, easy maintenance, reduced life-cycle cost, emission-free exhaust, and increased reliability versus internal combustion engine. Open cathode fuel cells can maximize power density thanks to their simple structure. Ambient air is directly used to provide both oxidant and cooling. It is also used to prevent flooding behaviour. Cathode side fin dimensions, hole size, and fan rotation speed are the main factors to control fuel cell performance. A large amount of the generated heat transfer via conduction. The thickness of the fin material affects high heat transfer, and also stamping force of the fin is a function of the thickness (Kim et al., 2016).

The weight of the power module is one of the important parameters for design. The center of gravity affects flight performance. According to the preliminary investigation of this project, 40% of the single-cell weight is derived from the corrugated sheet. Therefore, material selection is very important due to heat transfer, surface oxidation, density, high strength, and formability. The past studies demonstrate that grade 2 titanium sheets fit best for UAV application of open cathode PEM fuel cells due to the weight advantages (Herwerth et al., 2007).

The Anode side of the PEM fuel cells includes three main parts such as catalyst layer, gas diffusion layer, and flow field. On the other hand, open cathode PEM fuel cells use dry hydrogen as fuel. Hydrogen can easily diffuse inside the gas diffusion layer. Thin cuts with a width of 1 mm on a high PTFE included gas diffusion layer are used as an anodic flow field. Hence, weight saving, simplicity, and cost reduction are obtained. High PTFE content is necessary to maintain humidity balance by increasing hydrophobicity. (Kim et al., 2009) To investigate the effect of thin cut shape, Comsol Multiphysics flow simulation and Ansys/Fluent analysis are carried out. A dual mustacle shape with a 25mm length flow field is developed and the details of the designed anode flow field are given in Figure 1.

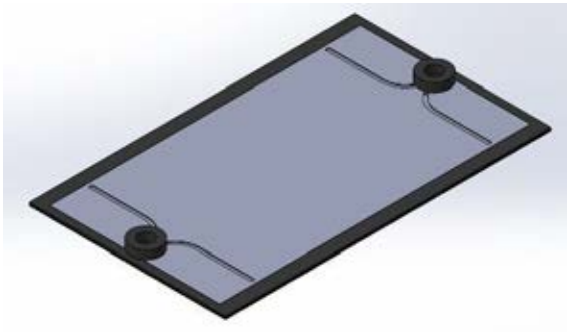


Fig. 1: Anode Flow Channel

There are several mechanisms for water transport across a polymer membrane. Electroosmotic drag and back diffusion are responsible to control the humidity of the membrane (F. Barbir,2005). A thin membrane is selected since the high current density and sufficient to counteract the anode-drying effect. Furthermore, the diameter and

number of cathode holes are related to the humidity of the membrane. The fluent analyses show that a 0.3 mm diameter hole with 1 mm space provides optimum humidity level on the membrane. The details of the designed corrugated cathode fin and cathode side hole plate are given in Figures 2 and 3, respectively.



Fig. 2: Corrugated Fins

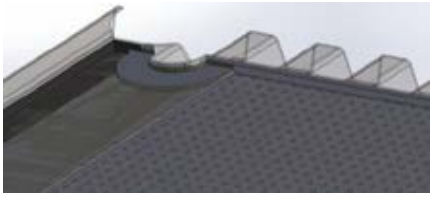


Fig. 3: Cathode Holes

In this study; design, simulation, and single-cell test of an open cathode PEM fuel cell are performed and the designed open cathode PEM fuel cell is given in Figure 4 as follows.



Fig. 4: Cross Section view of open cathode PEM fuel cell single cell

II. Numerical Set-Up and Procedure

In the study, design and some preliminary analyses are carried out via the Comsol Multiphysics and flow simulation add-in application. The software gives the volume flow result according to inlet and outlet boundary conditions. The outlet boundary conditions are selected according to the known fuel cell blower.

Solid model design results belong to the corrugated sheet were transferred to the Eta-Dynaform simulation software. Deformation zones were examined in EtaPostProcessor software. According to the forming limit diagrams, it was decided whether to make a design change. The design and forming simulation cycle was repeated, until getting a safe forming limit diagram.

After a safe forming limit diagram is obtained, one repeated section is transferred to Ansys/Fluent software to find a suitable cathode side hole size. Ansys/Fluent boundary condition parameters are selected to provide 50 cm^2 single-cell real performance.

III. Results and discussions

The 2d rubber pad formability characteristics of the grade 2 titanium with 0.1 mm thickness were carried out with Dynaform, LS-PrePost, and LSDyna solver. LS-PrePost is used for changing the material properties of the rubber part. By doing time saver 2d simulation maximum depth for the blank part was calculated. The orientation of the simulation can be seen in Figure 5.

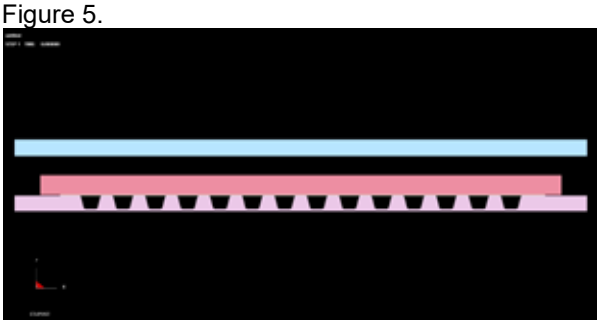


Fig. 5: Orientation view of 2d rubber pad forming simulation

The 3d formability characteristics of titanium can be seen in Figure 6. Figure 6 was belong to 2mm depth with 0.1mm radius and crack formation has been observed. To prevent crack formation, channel depth and radius were reduced.

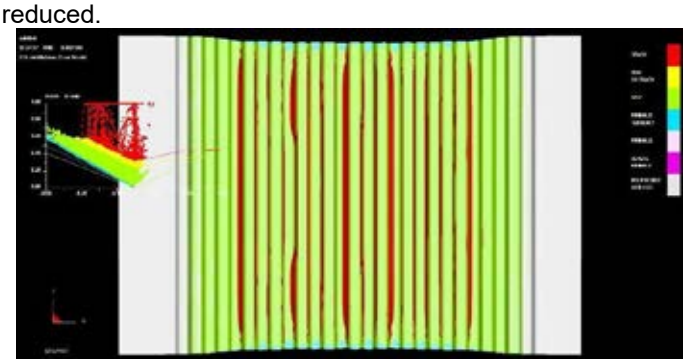


Fig. 6: Crack included Eta-Dynaform simulation

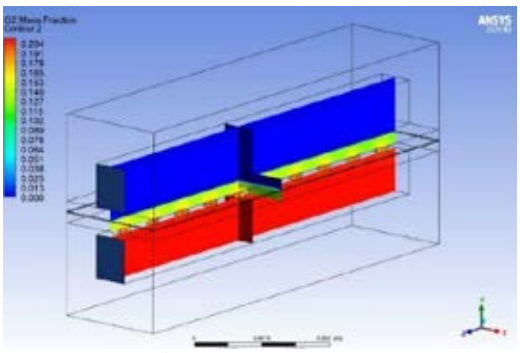


Fig. 7: One repeated cell analysis

To find a suitable hole size some analysis was carried out. Figure 7 belonged to 0.1 mm hole size with 1mm space. It is noticed that the distance of repetitive hole and diameter was sufficient to get the optimum performance and enough oxygen mass fraction from the fuel cell. Performance results of the open-cathode PEM fuel cell are shown in Figure 8. The maximum power density of about 650 mW/cm^2 has been reached in optimum operating conditions.

IV. Conclusions

In the study, design, simulation, and single-cell performance tests were evaluated to meet the power module of a small-scale tactical UAV. As a result, 0.1 mm thick, 1.8 mm depth with 0.2 mm radius corrugated fins shows better formability and cooling performance, and hole size 0.3 mm diameter at a distance of 1 mm from each other shows better humidity effect on the membrane. Furthermore, compact, light, and easy produce cells were obtained with a second gas diffusion layer with 1 mm width and 25 mm length thin cut shown in Figure 1.

Acknowledgments

The equipment and materials support of this research by TUBITAK under a project number of 3180578 is gratefully acknowledged.

References

F. Barbir, PEM Fuel Cells: Theory and Practice, Elsevier Academic Press, New York, (2005).

Qiu, Diankai, et al. "Numerical analysis of air-cooled proton exchange membrane fuel cells with various cathode flow channels." Energy 198, 117334, (2020).

Kim, Minkook. Development of the anode bipolar plate/membrane assembly unit for air-breathing PEMFC stack using silicone adhesive bonding. Journal of Power Sources, 315, 86-95, (2016).

Kim, Sung Han, et al. Air-breathing miniature planar stack using the flexible printed circuit board as a current collector. International journal of hydrogen energy, 34.1, 459-466, (2009).

Herwerth, Christopher, et al. Development of a small long endurance hybrid PEM fuel cell powered UAV. No. 2007-01-3930. SAE Technical Paper, (2007).

SSM. Türkiye insansız hava aracı sistemleri yol haritası (2011-2030), Ankara (2011)

Electrical Properties of the Carbon Nanotube (CNT) Reinforced Composite Plates for the PEM Fuel Cell Bipolar Plate Application

[1*] Alparslan Topcu, [1] Fatih Darıcık, [2]Kadir Aydın, [3]Selahattin Çelik
[1] Alanya Alaaddin Keykubat University, Rafet Kayış Faculty of Engineering, Department of Mechanical Engineering, Alanya, Antalya, 07425, Turkey
[2] Çukurova University, Faculty of Engineering, Department of Mechanical Engineering, Adana, 01330, Turkey
[3] Niğde Ömer Halisdemir University, Faculty of Engineering, Department of Mechanical Engineering, Niğde, 51240, Turkey

* E-mail: alparslan.topcu@alanya.edu.tr, fatih.daricik@alanya.edu.tr, kdraydin@gmail.com, scelik@ohu.edu.tr

Abstract
In this study, the effect of carbon nanotube (CNT) additive on the electrical properties of the carbon fiber-based composite materials was investigated. Initially, unmodified and CNT-modified carbon/epoxy composite laminates were manufactured by the hot pressing technique. CNT particles were added into the epoxy matrix of the carbon fiber/epoxy laminate with a mass ratio of 0.25, 0.5, 0.75, and 1%. Composite plates produced in ~1 mm thickness were cut in 20x30 mm^2 dimensions by a CNC water jet cutting machine. The four-point probe method was used to determine the electrical resistance of the CNT-modified carbon/epoxy laminates. Normally, carbon fiber/epoxy laminated composite plates have poor electrical properties. However, conductivity values are increased with the CNT reinforcement. In the light of specified electrical magnitudes, CNT-reinforced composite plates can use as bipolar plates (BP) for PEM fuel cells. Also, the stack weight was decimated with the fabrication of the lightweight composite BPs.
Keywords: PEM fuel cell, composite, bipolar plate, CNT.

I. Introduction

Fuel cells are one of the most promising alternative energy conversion technologies owing to their features such as high power density, silence operation, quick start-up, and zero-emission (Hao et al., 2019; Liao et al. 2010). Among fuel cell types, PEM (proton exchange membrane or polymer electrolyte) fuel cell come forward as the most developed fuel cell type and it is presently used in automotive and aviation applications. PEM fuel cells operating at 60-70 °C silently and bipolar plate (BP) is one of the most critical components of the PEMFC stack (Antunes et al., 2011). BPs responsible for separating oxidant and reactant gases owing to their channel system, and collecting of generated electricity occurred in the active area of the membrane. BPs should have high electrical conductivity, high mechanical strength, high corrosion resistance, low gas permeability, and low cost (Song et al., 2019). In addition, BPs composed ~80% of PEMFC stack weight and ~40% of stack cost (Silva et al., 2006). Department of Energy (DOE) shares technical targets for BPs and other components of the PEMFC stack, periodically. DOE requirements for composite BPs were presented in Tab. 1 (DOE, 2017).

Tab. 1: DOE 2020 technical targets for bipolar plates (DOE, 2017)

Property	Unit	Value
Plate Weight	$kg.kW^{-1}$	*< 0.4*
Flexural Strength	*MPa*	*> 25*
Electrical Conductivity	$S.cm^{-1}$	*> 100*
Area Specific Resistance	$ohm.cm^2$	*< 0.01*
Cost	$\$.\ kW^{-1}$	*3*
Forming Elongation	*%*	*40*
Corrosion Resistance	$\mu A.cm^{-2}$	*< 1*

Graphite materials were used as BPs due to their superior electrical conductivity (10^4 S/cm at room temperature). Besides their good electrical conductivity, graphite BPs have some disadvantages such as brittleness, high weight, and high cost. Metallic BPs also present good performance with their robust structure and good conductivity. But humid nature of the fuel cell stacks causes easy corrosion and deterioration of the metallic BPs. For this reason, different materials try and use as an alternative to graphite materials for many years. Composite materials, stainless steel materials, and alloys are the most considered materials for BP application. Composite materials have high mechanical strength as well as lightweight. On the other hand, these material groups have poor electrical conductivity, normally. Therefore, some additive materials use to increase conductivity such as carbon black, graphene, carbon fiber, carbon nanotube (CNT) (Taherian, 2014). Hence, lightweight BPs can manufacture with composite materials as well as high electrical conductivity. Lim et al., (2012) developed gasketless BPs using a carbon fiber/epoxy-based composite materials. They calculated the area-specific resistance (ASR) value of produced BP as 36 $m\Omega.cm^2$ under 1 MPa pressure and indicated that with the increase of pressure, decrease the ASR value. A theoretical analysis was performed by Darıcık and Topcu (2020), and they investigated the electrical, thermal, and mechanical properties of the MWCNT-modified fiber-reinforced composite plates. It was stated that the MWCNT modification increased the electrical conductivity. On the other hand, mechanical properties were not influenced prominently by the MWCNT additive. Yu et al., (2012) developed a

plasma treatment process to reduce the contact resistance between BP and gas diffusion layer (GDL). They used carbon fiber/epoxy-based composite material with the [0/45/-45/45/0] stacking sequence as BP. Bairan et al., (2016) manufactured carbon black-polypropylene-graphite-CNT modified composite BP and investigated the effects of additives on the mechanical and electrical properties.

CNT particles have very high electrical conductivity values and use in BP made as understand from the literature. In this study, multiwalled CNT-reinforced (MWCNT) carbon fiber/epoxy composite BPs were manufactured with different concentrations in weight. Then, specifications of MWCNT-reinforced composite plates were checked whether or not appropriate as the BP application for PEMFCs.

II. Experimental

Firstly, carbon fiber/epoxy-based and MWCNT-reinforced carbon fiber/epoxy-based composite plate manufacturing processes were studied. Unidirectional carbon fiber materials were used which has 300 gr/cm^2 weight in the composite plate manufacturing. Hexion bisphenol A type MGS L160 epoxy and H160 type epoxy hardener materials were used as matrix elements. Epoxy and epoxy hardener were mixed 100:30 by volume and resin were obtained. Specifications of the MWCNT material used in the study were presented in Tab. 2.

Tab. 2: Specifications of MWCNT particles

Technical Specification	Unit	Value
Outer Diameter	*nm*	*10 - 20*
Inner Diameter	*nm*	*5 - 10*
Length	*μm*	*10 - 30*
Purity	*%*	*> 95*
Specific Surface Area	*m^2/g*	*> 200*
Reel Density	*g/cm^3*	*~ 2,1*
Bulk Density	*g/cm^3*	*0,22*

Composite plates were produced by the hot pressing technique. Composite plate manufacture steps were illustrated in Fig. 1. In this approach, firstly CNT material was added on resin 0.25, 0.5, 0.75, and 1% by weight, and the slurry was obtained. Then, the slurry was mixed in a magnetic mixer and ultrasonic mixer, respectively for homogeneous CNT distribution and penetration. CNT slurry was impregnated on each surface of the fabrics with pouring. Carbon fiber/epoxy laminates were manufactured by hand lay-up and hot press with a unidirectional stacking sequence of [0_4]. The layers were cured under 6 bar pressure at 100 °C for 2 hours. The final thickness of the laminate was ~1 mm. A water jet cutting machine was used to obtain test specimens for the electrical tests, and specimens were cut into 20x30 mm^2 dimensions.

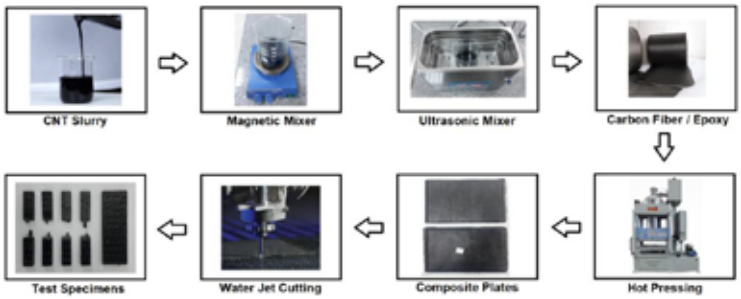


Fig. 1: Composite plate production steps

Electrical conductivity values were obtained using resistivity measurements of specimens. Firstly, the resistances of specimens were measured by the four-point probe method (Jandel CYL-RM3000 Four Point Probe System). Then, conductivity was calculated using sample thickness, and resistance values. The application f the four-point probe electrical conductivity measurement technique is illustrated in Fig. 2. The resistivity values were recorded in Ω/sq unit. Therefore, the conductivity magnitudes of the CNT reinforced composite plates were calculated with the help of Eq. 1, where the R is the resistivity of the sample, t is the thickness in cm unit.

$$Conductivity\ [S/cm] = \frac{1}{Rt} \quad (1)$$

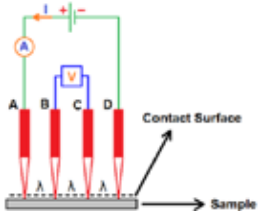


Fig. 2: Four-point probe electrical conductivity measurement approach

III. Results and discussions

The resistivity and the calculated electrical conductivity magnitudes of the CNT-reinforced composite plates were presented in Tab. 3. Normally, carbon fiber/epoxy laminated composite plates have poor conductivity. But, the electrical conductivity values increased with the increase of the CNT reinforcement as seen in Tab. 3. 94.58 S/cm conductivity was measured with the 1% CNT-reinforced plate, and this value is pretty close with the technical target of the DOE (> 100 S/cm).

Tab. 3: Electrical resistivity and determined conductivity properties of the CNT-reinforced composite plates

CNT Reinforcement (% in wt.)	Thickness (cm)	Resistivity (Ω/sq)	Conductivity (S/cm)
0.25	*0.105*	*0.193*	*49.35*
0.5	*0.109*	*0.163*	*56.28*
0.75	*0.103*	*0.151*	*64.3*
1	*0.097*	*0.109*	*94.58*

IV. Conclusions

MWCNT-reinforced carbon fiber/epoxy composite plates were manufactured and controlled whether or not for the BP application in PEMFCs in terms of electrical properties. Thus, electrical characterization tests were performed, and the CNT-reinforcement process increased the electrical conductivity of the carbon fiber/epoxy composite plate. As an overall conclusion, electrical properties of the 1% CNT-reinforced carbon fiber/epoxy composite plates were determined pretty close with the targets of DOE. Therefore, it was predicted from the results that the electrical conductivity values will be increased with the CNT reinforcement above 1%. In addition, the stack weight was decimated with the fabrication of the lightweight composite BPs.

References

Antunes RA., de Oliviera MCL., Ett G., Ett V., Carbon materials in composite bipolar plates for polymer electrolyte membrane fuel cells: A review of the main challenges to improve electrical performance, Journal of Power Sources, 196, 2945-2961, (2011).

Bairan A., Selamat MZ., Sahadan SN., Malingam SD., Mohamad N., Effect of carbon nanotubes loading in multifiller polymer composite as bipolar plate for PEM fuel cell, Procedia Chemistry, 19, 91-97, (2016).

Darıcık F., Topcu A., Theoretical analysis on the thermal and electrical properties of fiber reinforced laminates modified with CNTs, Çukurova University Journal of the Faculty of Engineering and Architecture, 2020, 35(4), 925-936.

DOE technical targets: Bipolar plates for transportation applications, https://www.energy.gov/sites/default/files/2017/05/f34/fcto_myrdd_fuel_cells.pdf, [Accessed on 04.02.2021].

Hao W., Ma H., Sun G., Li Z., Developing high performance magnesium phosphate cement composite bipolar plates for fuel cells, Energy Procedia, 158, 1980-1985, (2019).

Liao S-H., Weng C-C., Yen C-Y., Hsiao M-C., Ma C-CM., Tsai M-C., Su A., Yen M-Y., Lin Y-F., Liu P-L., Preparation and properties of functionalized multiwalled carbon nanotubes/polypropylene nanocomposite bipolar plates for polymer electrolyte membrane fuel cells, Journal of Power Sources, 195, 263-270, (2010).

Lim JW., Kim M., Kim KH., Lee DG, Innovative gasketless carbon composite bipolar plates for PEM fuel cells, International Journal of Hydrogen Energy, 37, 19018-19026, (2012).

Silva RF., Franchi D., Leone A., Pilloni L., Masci A., Pozio A., Surface conductivity and stability of metallic bipolar plate materials for polymer electrolyte fuel cells, Electrochimica Acta, 51, 3592-3598, (2006).

Song Y., Zhang C., Ling C-Y., Han M., Yong R-Y., Sun D., Chen J., Review on current research of materials, fabrication and application for bipolar plate in proton exchange membrane fuel cell, International Journal of Hydrogen Energy, 45(54), 29832-29847, (2019).

Taherian R., A review of composite and metallic bipolar plates in proton exchange membrane fuel cell: Materials, fabrication, and material selection, Journal of Power Sources, 265, 370-390, (2014).

Yu HN., Lim JW., Kim MK., Lee DG., Plasma treatment of the carbon fiber bipolar plate for PEM fuel cells, Composite Structures, 94, 1911-1918, (2012).

Ca and Co doped perovskite structures for hydrogen production

[1]Seyfettin Berk Şanlı , [1]İhsan Emre Yiğiter , [1]Berke Pişkin , [1]Fatih Pişkin and [1]Gülhan Çakmak*
[1]Mugla Sıtkı Kocman University, Engineering Faculty, Metallurgical and Materials Engineering Department, Mugla, Turkey
* E-mail:gulhancakmak@mu.edu.tr

Abstract
Perovskite phases are attracting significant interest because of their unique potential for many applications requiring mixed ionic and electronic conductivity. Two-step, solar thermochemical splitting of water using n redox-active metal oxides has emerged for large-scale hydrogen production. Perovskites have been proposed as alternatives to $CeO_{2-\delta}$ because of their potential for lowering reduction temperature while maintaining high fuel productivity. In the present study, the perovskite series $La_{1-x}Ca_xMn_{1-y}Al_yO_3$ (x, y = 0.2, 0.4, 0.6, or 0.8) was fabricated using a modified Pechini method and comprehensively investigated to determine the applicability of these materials to solar H_2 production via two-step thermochemical water splitting
Keywords: hydrogen production, thermochemical water splitting, hydrogen energy,

I. Introduction

Increasing interest in sustainable energy sources and climate change has encouraged researchers to produce H_2 from H2O. One of the significant methods being explored for the generation of H2 is the thermochemical water splitting of H2O by using oxide materials (Orfila,2016).
Perovskite oxides have been suggested as promising substances for the solar thermochemical splitting of H_2O and have been widely studied recently (Wang,2018). We have carried out a systematic experimental study of Ca and Co-doped $LaMnO_3$ perovskites within the composition range of $La_{1-x}Ca_xMn_{1-y}Al_yO_3$ (Ca=0.4-0.8, Co=0.2-0.6).

II. Experimental Procedure

LCMC($La_{1-x}Ca_xMn_{1-y}Al_yO_3$) perovskite oxides were synthesized by a solution-based method (Pechini,1967). For this purpose, nitrate salts of the La, Ca, Mn, and Co at appropriate proportions were used. Deionized water was used as a solvent, and citric acid was added to the system. The solution was stirred by heating at 120 ° C with ethylene glycol addition. After gelation, the system was dried, and the obtained powders were ground.
Powders were calcined at 1300 °C for 6 hours. The phase analysis of the powders was performed by using X-ray diffractometer (Rigaku SmartLab X) using Cu-Kα radiation at 40 kV and 200 mA. The structures are refined using Maud program to identify their crystal structure. BET surface area was evaluated by N_2 adsorption at 77 K in a constant volume adsorption apparatus (Quantachrome Autosorb 1C-MS). The Powders obtained were examined morphologically using SEM (JEOL JSM-7600F). The effect of the production parameters and calcination temperatures on the surface area and particle size was investigated.

III. Results and discussion

"The studies started by determining the synthesis parameters for LCMC composition. For this purpose, LCMC4664($La_4Ca_6Mn_6Co_4O_3$) composition was selected and synthesized under four different conditions (1. citric acid addition, 2. citric acid addition and keeping pH ~8, 3. Citric acid and ethylene glycol addition, 4. Citric acid and ethylene glycol addition and keeping pH ~8). X-ray diffraction pattern of the resulted powders is given in Figure 1. These patterns revealed that cubic and orthorhombic crystal structure of perovskite are formed for all synthesis conditions. This has been confirmed with the Rietveld analysis.

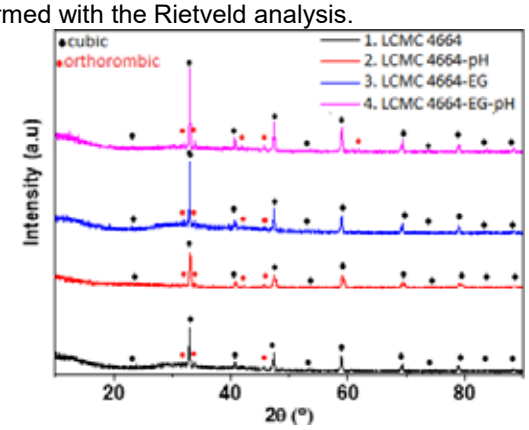


Fig. 1 XRD pattern of LCMC4664 powders synthesized at four different conditions and calcined at 1300 ° C.

SEM, EDS and BET methods were used to compare other properties such as grain structure, morphology, chemical composition and surface area formed in LCMC4664 compositions synthesized with different parameters. The values obtained from the EDS analysis are summarized in Table 1. In the analysis, it is seen that the composition distribution is at the desired level for all synthesis parameters.

Tab. 1:EDS analysis results of LCMC4664 powders synthesized under different conditions and calcined at 1300 ° C for 6 hours
.

sample	La	Ca	Mn	Co
Atomic percentages (at %)				
LCMC4664 (1)	20,84	29,61	29,78	19,77
LCMC4664-pH (2)	21,06	29,45	29,57	19,92
LCMC4664-EG (3)	20,19	30,87	29,76	19,18
LCMC4664-EG-pH(4)	21,01	29,94	29,33	19,72

Among the powders TM:CA:EG 1:1.5:1.5 pH = 8.00 have the lowest surface area. The highest surface area is achieved for the synthesis condition of TM:CA1:1.5 pH≤1.00 (0.66m2/g). These observations are also confirmed with SEM analysis.
The study continues in the direction of determining the thermochemical water splitting properties of the powders produced.

IV. Conclusions
The study includes the solution based production of LaMnO3 perovskite powders with Ca and Co addition for thermochemical water splitting. For this purpose, powders have been successfully synthesized using different production parameters, and their hydrogen production properties are under investigation.

Acknowledgements
This work was supported by TÜBITAK (The Scientific and Technological Research Council of Turkey) (Project Number 119M420), which the authors gratefully acknowledge.

References

Orfila M. ,M. Linares, R. Molina, Perovskite materials for hydrogen production by thermochemical water splitting, Int. J. Hydrogen Energy, 49(9), 19329 (2016)

Pechini MP., Method of preparing lead and alkaline earth titanates and niobates and coating method using the same to form a capacitor. 3,330,697, (1967)

Wang L, Al-Mamun M, Liu P, Wang Y, Yang HG, Zhao H. , Notable hydrogen production on LaxCa1−xCoO3 perovskites via two-step thermochemical water splitting. J Mater Sci 53:6796–806(2018)

Investigation of Ni/Cu Impregnated Zeolite Catalysts for Hydrogen Production from Methanol Steam Reforming

[1]Özgecan Çağlayan, [1*]Nezihe Ayas,
[1]Eskişehir Technical University, Engineering Faculty, Department of Chemical Engineering, 2 Eylul Campus,Eskişehir, 26555, Turkey

* E-mail: nazcan@eskisehir.edu.tr

Abstract
Hydrogen, in addition to being a renewable, is a sustainable and clean energy carrier. Using pure hydrogen as a fuel has some problems about storage and transportation. Methanol is an attractive hydrogen source since it is liquid at room temperature and has a high hydrogen ratio. The impregnation method was used in this study to synthesize Ni/Zeolite and Ni-Cu/Zeolite catalysts, which were then characterized using XRF, XRD, and FT-IR and their activities in methanol steam reforming were examined. The catalytic activities of zeolite supported catalysts for methanol steam reforming were investigated at various temperatures (200-800°C) using a constant steam:carbon (3:1) molar ratio, liquid hourly space velocity (LHSV=0.012L/h.gcat) and a constant 0.02mL/min. flow rate. The highest hydrogen yield (34.96 mole H_2 prod./mole methanol feed) was reached at 600 ° C with a 6% Ni-24% Cu/Zeolite catalyst.

Keywords: Hydrogen, Methanol, Steam Reforming, Zeolite, Catalyst, Impregnation.

I. Introduction

Over the past several years, there has been an increasing demand for new clean energy sources. Hydrogen is a clean energy source that is both environmentally friendly and efficient, with the additional benefit of releasing only water and energy when burned. Because of the transportation and storage problems of pure hydrogen, the focus has shifted to alternative hydrogen carriers (Iulianelli et al.,2014).

Methanol is a beneficial fuel in several aspects, which explains why it is so effective as a hydrogen carrier including the ability to be produced from renewable sources. Methanol has a high H/C ratio (4:1) with no carbon-carbon bonds that need to be broken. In contrast to methane reforming, which occurs at 800-1000°C, the methanol steam reforming reaction occurs at comparatively low temperatures (150-350°C). The Methanol Steam Reforming process has been regarded as a very appealing method for hydrogen production (Paulo et al.,2007 and Iulianelli et al.,2014). The following chemical reactions can be used to describe it (Iulianelli et al.,2014):

$$CH_3OH + H_2O \leftrightarrow CO_2 + 3H_2 \qquad \Delta H^0_{298K} = +49.7\ kJmol^{-1} \qquad (I)$$
$$CO + H_2O \leftrightarrow CO_2 + H_2 \qquad \Delta H^0_{298K} = -41.2\ kJmol^{-1} \qquad (II)$$
$$CH_3OH \leftrightarrow CO + 2H_2 \qquad \Delta H^0_{298K} = +90.7\ kJmol^{-1} \qquad (III)$$

The Methanol Steam Reforming is defined by reaction (I), the water gas shift reaction is embodied by reaction (II), and the decomposition of methanol reaction is represented by reaction (III). Only the water gas shift reaction is exothermic and occurs without a change in the number of moles. The Methanol Steam Reforming reaction is endothermic, and it involves an increase in the number of moles. (Iulianelli et al.,2014).

For the syntesis of hydrogen-rich syngas, various catalysts have been researched. Copper-based catalysts have a higher hydrogen selectivity than nickel-based catalysts for methanol steam reforming. The addition of copper to nickel catalysts has been shown to enhance their activity and selectivity. (Lytkina et al., 2015). The mechanism of methanol molecules adsorption on the catalyst surface has changed, which is why the properties of catalysts depending on the dominant metal have changed. It lowers CO yield since high copper content catalysts have a greater proclivity for single-center alcohol adsorption. (Iulianelli et al.,2014). The activity of the catalyst in the reactions is also dependent on catalyst support. Currently, zeolites have promising advantages in the area of hydrogen production. Zeolite catalysts are crystalline alumina-silicates with a microporous structure and an open structure of tetrahedral crystals with a defined pore size (Yao et al.,2018). Zeolites can be used as a porous support material for nickel and other metals such as copper to assist metal dispersion and improve catalytic activity in order to produce hydrogen-rich syngas.

In the literature research, it was found that catalysts synthesized with different support materials were used in methanol steam reforming and zeolite supported catalysts were used in steam reforming of other chemicals such as dimethyl ether and methane. However, there are no studies in which zeolite supported catalysts are used in methanol steam reforming.

In this study, the production of hydrogen was investigated as a function of temperature using methanol steam reforming with the help of zeolite catalysts. By keeping the metal loading weight of the catalysts constant at 15% and 30%, the percentages of Ni and Cu were changed. Ni/Zeolite and Ni-Cu/Zeolite catalysts, which were used in this work were made by impregnation method and characterized using X-ray diffraction (XRD), X-ray fluorescence (XRF) and Fourier transform infrared spectroscopy (FT-IR).

II. Experimental Set-up and Procedure

99% purity of Nickel(II)nitratehexahydrate [$Ni(NO_3)_2.6H_2O$], Copper(II)nitratetrihydrate [Cu(NO3)2.3H2O and methanol were used for catalyst synthesis and steam reforming without further purification. Zeolite was provided by a private company from Balıkesir/Turkey.

The impregnation method was used to synthesize Ni/Zeolite and Ni-Cu/Zeolite catalysts at various Ni and Cu weight ratios (15-30 wt./wt.%). Before the impregnation process, the zeolite was ground in the Vibrating Cup Mill for 45 seconds until it reached a particle size of 50-60 microns. Then the nitrate salts were dissolved in pure water, then stirred for 3 hours at 70°C with the addition of zeolite as a support material. The samples were aged for a day at room temperature before drying for 24 hours at 105°C. The Ni-based catalyst was calcined in a tubular furnace at 600°C for 3 hours at a heating rate of 3°C/min and the flow rate of air is 0.3 L/min. Catalysts containing Cu were calcined in a tubular furnace at 550°C for 3 hours at a heating rate of 3°C/min at an air flow rate of 0.3 L/min. Before being used in methanol steam reforming experiments, catalysts were reduced at 800°C under a flow rate of 0.4 L/min, H_2 for 45 min.

Synthesised catalyst were characterised using several techniques. Those are Rigaku ZSX model XRF instrument was used to determine the mass composition of the catalysts. The catalysts' crystal structures were investigated using a Rigaku Rint 2200 brand XRD device set to 40 kV voltage and 15 mA current with Cu-K as the X-ray source, with a scanning angle of 0.02°, a scanning speed of 4°/min, and a range of 2θ = 3-85°. The functional groups of the catalysts were determined using an FT-IR system from Thermo Science Nicolet IS10 brand. Analyses were carried out at 64 scan speeds and 4 cm^{-1} resolution, with a scanning range of 525-4000 cm^{-1} at room temperature.

The catalysts' activities were tested by steam reforming of methanol at atmospheric pressure in a fixed bed continuous flow quartz reactor (PID Eng & Tech Micro Efficiency). In the experiments, the reaction volume was formed by mixing 0.2 g of catalyst with SiC. Experimental studies were carried out at different temperature range of 200-800 °C at constant steam:carbon ratio (3:1) and LHSV value (0.12L/h.gcat). Water and methanol were fed into the system via HPLC pumps at a flow rate of 0.02 mL/min. The composition of the gas product mixture was determined online by An Agilent 490 Micro Gas Chromatograph (µGC) calibrated with a standard gas mixture.

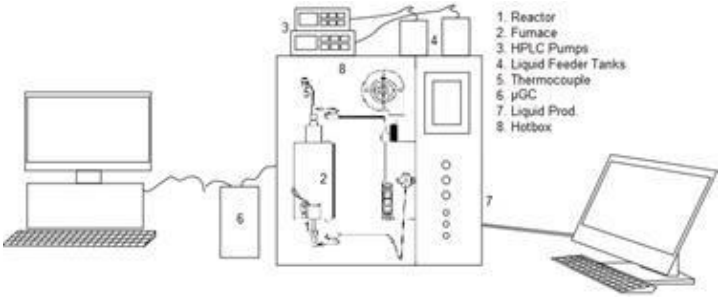


Fig.1: Catalytic activity test system.

III. Results and discussions

The mass composition of the zeolite used as support material and the synthesized catalysts were determined by XRF analysis and are given in Tab.1 and Tab.2 respectively. As seen in Tab.1, the main components of the zeolite consist of 72.85% SiO_2, 11.36% Al_2O_3 and 4.14% CaO, while the remaining part contains K_2O, MgO, Fe_2O_3 and TiO_2. The XRF results are higher than the desired value because they are in oxide form, and calculations are based on metallic Ni and Cu.

Tab. 1: XRF Results of Zeolite

Support	SiO_2	Al_2O_3	CaO	K_2O	MgO	Fe_2O_3	TiO_2	LOI
Zeolite	72.85	11.36	4.14	3.67	1.20	0.79	0.11	5.88

LOI: Loss on Ignition

Tab.2: XRF Results of Catalysts

Catalysts	NiO	CuO
15% Ni / Zeolite	18.22	-
10% Ni - 5% Cu / Zeo.	11.84	5.43
5% Ni - 10% Cu / Zeo.	5.51	11.51
7.5% Ni - 7.5% Cu / Zeo.	9.64	8.70
24% Ni - 6% Cu / Zeo.	29.93	6.48
6% Ni - 24% Cu / Zeo.	8.73	25.22

The FT-IR results of the catalysts are represented in the Fig.2. The stretching vibrations of the Ni-O bond are defined as 1050 cm^{-1} in the characteristic Ni bands. The vibrational modes greater than 1100 cm^{-1} correspond to the M-OH. The lack of other band in the spectrum means that the catalyst surface is free of contamination. It shows the presence of incoming peak CO_2 at a wavelength of 2350 cm^{-1}.

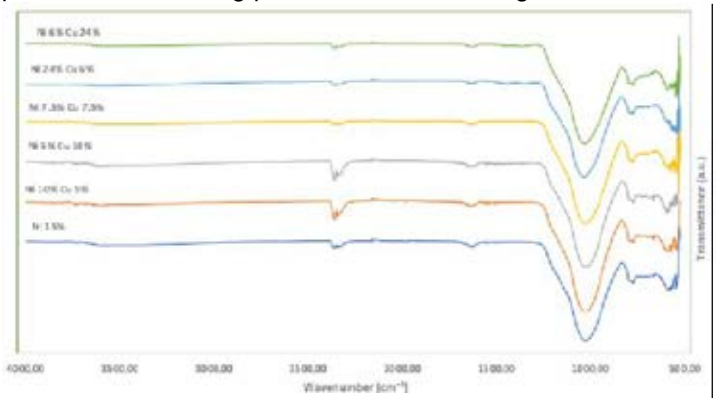


Fig.2. FT-IR Results of Catalysts

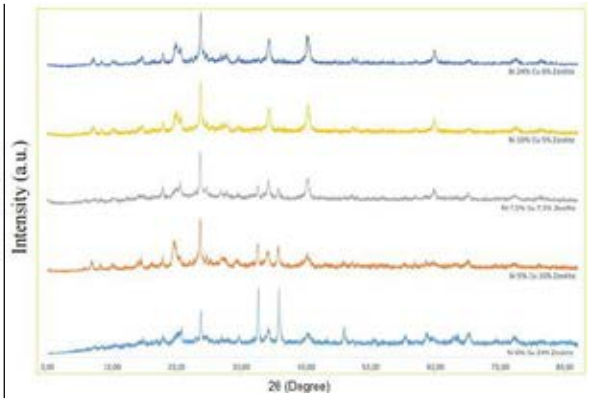


Fig.3. XRD Results of Catalysts

Fig.3 shows that the catalysts have NiO characteristic peaks at 2θ=37.18°, 43.12°, 63.08°, 64.32° and 79.74°, CuO characteristic peaks at 2θ=16.72°, 32.5°, 48.94°, 56.82°.

Catalyst activities were determined in the methanol steam reforming and the effect of catalyst loading ratios and temperature on hydrogen yield is given in Figure 4.

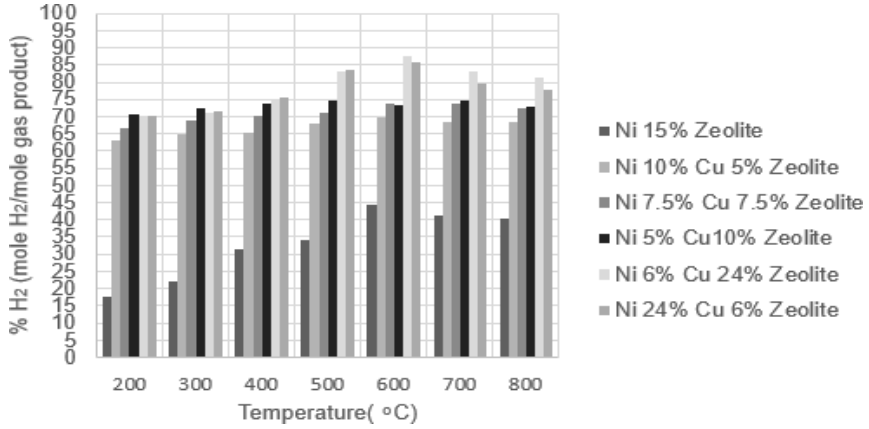


Fig.4. Effects of the catalyst and temperature on the moles of hydrogen in gas product (LHSV=0.012L/h.gcat. / S:C=3:1)

According to Fig.4 keeping the S:C ratio, LHSV value, and catalyst amount constant, the effect of catalyst and temperature on hydrogen production was examined in this work. While the conversions were 94.92% at low temperatures, 100% methanol conversion was achieved in all catalysts at high temperatures. All catalysts had the highest hydrogen molar content at 600°C. Since the highest hydrogen content was reached at 600°C, hydrogen selectivity and yield were calculated at this temperature.

Catalysts' selectivity and yield were specified in Tab. 3 at constant reaction conditions of at 600°C, LHSV=0.012L/h.gcat. / S:C=3:1.

Tab.3: Catalysts' selectivity and hydrogen yield

Catalysts	Selectivity % (mole H_2 prod. / total moles of H_2 in the gas prod.)	Yield % (mole H_2 prod. / mole methanol feed)
15% Ni / Zeo.	77.94	17.80
10%Ni - 5%Cu / Zeo.	94.44	27.92
7.5% Ni - 7.5% Cu / Zeo.	93.06	29.54
5%Ni - 10%Cu / Zeo.	86.92	29.30
6%Ni - 24%Cu / Zeo.	91.04	34.96
24%Ni - 6%Cu / Zeo.	92.62	34.38

As seen in Tab.3, the highest hydrogen selectivity (94.44% mole H_2 prod./total moles of H_2 in the gas prod.) was achieved with 10%Ni - 5%Cu/Zeolite catalyst, while the highest hydrogen yield (34.96% mole H_2 prod./mole methanol feed) was obtained with 6% Ni - 24% Cu/Zeolite catalyst.

IV. Conclusions

The purpose of this research the investigation of zeolite supported catalysts for the methanol steam reforming. It has been observed that zeolite supported catalysts are effective in hydrogen production from Methanol steam reforming. Due to the composition, acidity and crystal structure of the zeolite, it has been determined that it is a suitable support material for the catalyst to be used in methanol steam reforming. It was determined that Cu among the metals loaded on the support material increased the yield while nickel increased the hydrogen selectivity. As a result, Ni-Cu / Zeolite catalysts have been discovered to be effective in the methanol steam reforming. As a result, Ni-Cu/Zeolite catalysts have been discovered to be effective in methanol steam reforming.

References

Inaba, M., Murata, K., Saito, M., & Takahara, I. Hydrogen Production by Gasification of Cellulose over Ni Catalysts Supported on Zeolites. Energy & Fuels, 20(2), 432–438, (2006).

Iulianelli A., Ribeirinha P., Mendes A., Basile A., Methanol steam reforming for hydrogen generation via conventional and membrane reactors: A review, Renewable and Sustainable Energy Reviews, Vol 29, Pages 355-368, (2014).

Lytkina, A. A., Zhilyaeva, N. A., Ermilova, M. M., Orekhova, N. V., & Yaroslavtsev, A. B., Influence of the support structure and composition of Ni–Cu-based catalysts on hydrogen production by methanol steam reforming. International Journal of Hydrogen Energy, 40(31), 9677–9684, (2015).

Palo D.R., Dagle R.A., Holladay J.D., Methanol Steam Reforming for Hydrogen Production, Chem. Rev., 107, 3992−4021, (2007).

Yao D., Yang H., Chen H., Williams P.T., Investigation of nickel-impregnated zeolite catalysts for hydrogen/syngas production from the catalytic reforming of waste polyethylene, Applied Catalysis B: Environmental, Vol 227, 477-487, (2018).

Fine Tuning the Intrinsic Activity of Layered Iron Nickel Sulphide Nanosheets by Varying Boron Doping to Produce Low Cost and Green Hydrogen

[1*] Esaam Jamil, [2] Begüm Yarar Kaplan [1,2] Selmiye Alkan Gürsel, [2] Alp Yürüm
[1] Sabanci University, Faculty of Engineering and Natural Sciences, 34956 Istanbul, Turkey
[2] Sabanci University Nanotechnology Research and Application Center (SUNUM), 34956, Istanbul, Turkey

*E-mail: ejamil@sabanciuniv.edu

Abstract

The prevalent steam reforming process for producing hydrogen causes green house gas (CO_2) emission and is very energy intensive process. Making fuel cells truly green technology especially for transport applications dictates the need to produce hydrogen fuel by green and efficient methods such as electrochemical water splitting. However, the expensive noble metal platinum is the bottleneck to commercialize this technology among other issues such as hydrogen infrastructure. Herein, we synthesized layered transition metal dichalcogenide (S) electrocatalyst based upon low cost earth abundant metals (Ni, Fe) for hydrogen evolution reaction (HER) for low pH electrolyte. Further, by varying the boron's molar ratios (0%, 2.5%, 5% and 10%), the intrinsic activity is fine tuned to improve the HER performance. Different characterization techniques employed such as XRD, XPS, SEM, and BET verified the desired structure, morphology and chemical composition. HER performance was evaluated by linear sweep voltammetry from which three important parameters: overpotential at 10 mA/cm^2, Tafel slopes and exchange current density were extracted which gave insights into the HER reaction mechanism and electrochemical kinetics. The results showed that the boron doping level of 10% improves the HER performance the most. These layered electrocatalysts can be grown on high surface area and highly conductive surface such as graphene to accelerate the green hydrogen generation.

Keywords: Boron doping, Iron nickel sulphide, Hydrogen evolution reaction, Green hydrogen

Introduction

Over the past few decades, the energy demand is increasing at rates never seen before. The fossil fuel consumption has given us an unprecedented set of problems such as green house gas emission, global warming, and climate change. More countries are adopting renewable energy resources to cater for the extra need and environmental concerns. Among these, green hydrogen production from electrolysis is viable and sustainable option but is often restricted due to expensive noble metal catalyst platinum used both at anode and cathode side (1). There is need to replace this noble metal with earth abundant low-cost metals. Transition metals dichalcogenides based upon iron, nickel and sulphur are among the promising candidates which have shown their potential as HER electrocatalyst along with molybdenum sulphide and tungsten disulphide (2). To further improve the active sites and intrinsic catalytic activity of these electrocatalyst, there are various techniques such as making nanostructures, using support materials, controlling shape, alloying, core-shell, elemental doping, etc. (3). Doping with foreign atoms can change the band gap from insulator to semiconductor to metallic behaviour. Hence, in this study, we see the effect of boron doping on iron nickel sulphide which can alter the basal plane to make it active along with the edges. Further, fine tuning the intrinsic activity of nanostructured and layered Fe-Ni-S chalcogenide electrocatalyst structure by varying the boron doping levels and see the improvement in the HER performance.

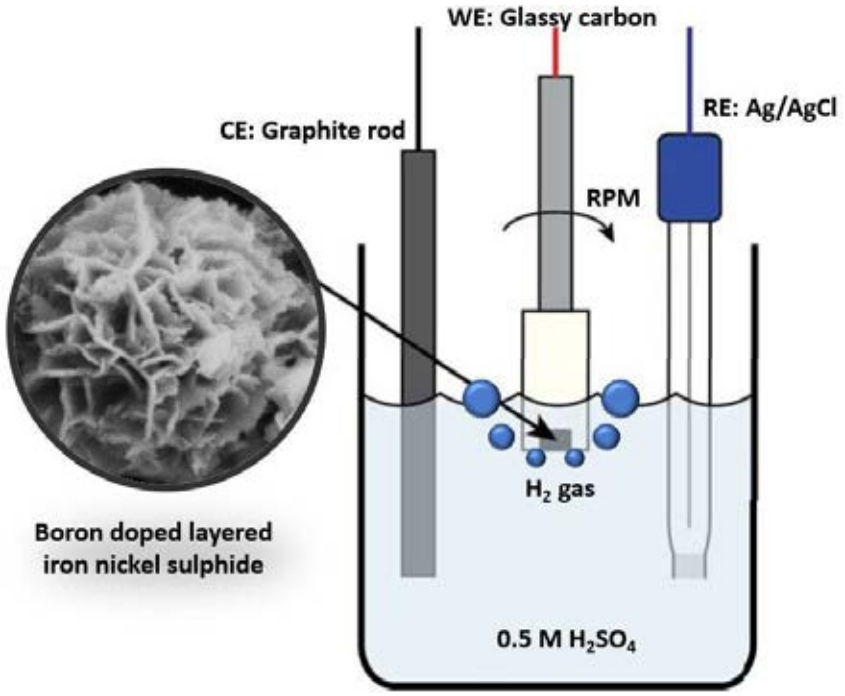


Fig. 1. Three-electrode electrochemical setup for HER performance tests. The inset is the actual SEM image showing morphology of the obtained material.

Materials and Methods

The synthesis was done in a two-step process. Boron doped Fe-Ni layered double hydroxide was produced by hydrothermal process by mixing the respective salts with reducing and chelating agents in DI water and heated for several hours inside Teflon containing autoclave. The obtained material was mixed with sulphur source and sulphidation step was carried by solvothermal process under heat to yield boron doped Fe-Ni sulphide. The resulting materials were washed and dried for further characterizations such as XPS, XRD, SEM, BET and electrochemical characterizations. The formulated electrocatalyst ink was drop-casted on glassy carbon working electrode and dried while graphite and Ag/AgCl were used as counter and reference electrodes (Figure 1). The HER performance was tested in 0.5 M sulphuric acid electrolyte in the hydrogen evolution potential window by linear sweep voltammetry. All the chemicals were obtained from Sigma Aldrich and used without further purification.

Results and Discussion

In this study, facile hydrothermal synthesis was used to produce layered double hydroxide based on iron and nickel. The morphology can be seen in figure 1 inset where the layered nanosheets are visible. The XRD data shows that it has mixed alpha phase and more beta phase. The latter phase has decreased interlayer spacing due to absence of intercalated water molecules (4). The doping of boron doesn't yield phase change and retains its crystalline structure. After sulphidation step, the hydroxide peaks are replaced by sulphide peaks while the SEM images still show open layered structure, but decreased surface area as seen in BET results. Similarly, the doped boron-based hydroxides and sulphide samples yield denser morphology as can be seen in SEM and indicated by BET results. Subsequently, electrochemical characterization tests were performed to evaluate the HER performance in acidic medium. After purging

the electrolyte with nitrogen gas to remove dissolved air, the tests were run by linear sweep voltammetry. Overpotentials were extracted at low and high current densities 10 mA/cm^2 and 100 mA/cm^2. Lower overpotential values mean better electrocatalyst. The LSVs were transformed to Tafel plots. Tafel slopes were measured in the linear region after the onset potential and exchange current densities were extracted by extrapolating method where overpotentials are zero. Lower Tafel slopes and high current densities are indication of high performing catalyst. A general trend was seen in the electrochemical tests that increasing boron doping level makes the electrocatalytic activity better. These results were compared with commercial Pt/C which has to-date the best HER performance with overpotentials as low as 0 mV.

Conclusions

Here we synthesized doped and undoped low cost and earth abundant transition metal chalcogenides (TMDs) by facile hydrothermal/solvothermal methods. These materials are very active for HER in acidic medium due to their balanced strength in proton adsorption and subsequent hydrogen gas evolution. These can be further fine tuned by elemental doping such as boron. The electrochemical results show their potential to replace the expensive noble metal electrocatalyst for green hydrogen generation at low cost. Further, these electrocatalysts can be improved by incorporating 2D carbon based support materials.

Acknowledgement

The research leading to these results has received funding from the Tübitak 1001 – Program for supporting scientific and technological research projects

References

1. Trancik, Jessika E. "Renewable energy: Back the renewables boom." *Nature News* 507.7492 (2014): 300.

2. Wang, Jinsong, et al. "The mechanism of hydrogen adsorption on transition metal dichalcogenides as hydrogen evolution reaction catalyst." *Physical Chemistry Chemical Physics* 19.15 (2017): 10125-10132.

3. Seh, Zhi Wei, et al. "Combining theory and experiment in electrocatalysis: Insights into materials design." *Science* 355.6321 (2017).

4. Hall, David S., et al. "Nickel hydroxides and related materials: a review of their structures, synthesis and properties." *Proceedings of the Royal Society A: Mathematical, Physical and Engineering Sciences* 471.2174 (2015): 20140792.

Effect of Organic Fraction of Municipal Solid Waste Addition to High Rate Activated Sludge System for Hydrogen Production from Carbon Rich Waste Sludge

[1*]Dogukan Tunay, [1]Oznur Yildirim, [1]Bestami Ozkaya, [1]Ahmet Demir
[1] Yildiz Technical University, Faculty of Civil Engineering, Department of Environmental Engineering, Davutpasa Campus Esenler, Istanbul, 34220, Turkey

* E-mail: tunay.dogukan@gmail.com

Abstract
Renewable energy production is a significant part of researches due to the environmental problems and limited energy sources. HRAS is a rapid and less energy consuming process which is resulted with high amount of sludge production. Since the activated sludge consist of dead and living microorganisms, it is not efficient to it for the anaerobic fermentation process. However, these high amount of waste sludge was promoted with organic fraction of municipal solid waste (OFMSW) in order to increase the availability of organic matter for the fermentative bacteria. Thence, solid waste management and wastewater treatment were actualized and hydrogen production rate of the OFMSW was increased.

Keywords: biohdyrogen, activated sludge, dark fermentation, HRAS process

I. Introduction

Water and energy needs have always been an important priority for civilizations. Since water and energy scarcity and global environmental problems have been started in near future, interest of the tendency of renewable sources and efficient wastewater treatment technologies had been increased. Water and wastewater treatment consume high amount of energy. For instance, Approximately, 3 to 4 percent of energy of USA used for water and wastewater treatment (Guven et al., 2017).

High rate activated sludge (HRAS) process is a decent alternative with the less energy and land requirement compared to the conventional activated sludge (CAS) process (Ge et al., 2017). HRAS process has lower hydraulic retention time with the efficient treatment manner; however, it results with more waste sludge production. In HRAS process, particulate, colloidal and soluble COD removed by sedimentation with bioflocculation (Jimenez et al., 2015). For that purpose, increasing the flocculation and the COD removal by addition of food waste is one of the options (Guven et al., 2020).

In this study, HRAS prosess was applied to domestic wastewater with the addition of OFMSW to increase the organic content of the waste sludge. In that purpose, waste sludge was used for the production of hydrogen by the dark fermentation. Thence, wastewater treatment was done with the consuming less energy and area requirement and hydrogen production was occurred in sustainable way.

II. Experimental Set-up and Procedure

In this study, domestic wastewater was used in HRAS process and OFMSW was added to domestic wastewater to increase the COD removal rate and organic fraction of the waste sludge. Properties of the OFMSW was given in Table 1. Total COD and soluble COD concentration of domestic wastewater was 470±16 and 250±20 mg/L. HRAS process was operated with the capacity of 2 L reactor and 10-12 g of OFMSW was added. 2 L/min air was given to the system for the oxygen requirement (Figure 1). Different HRT values were (60, 90, 120 min) tested in HRAS process. Effluent COD concentration and volatile solids (VS) content of sludge was determined for these HRT values.

Tab. 1. Properties of OFMSW

Parametreler	Birim	OFMSW
Moisture	%	50.2
Total Organic Carbon (TOC)	%	26.6
Total Carbon (TC)	%	27.6
Total Nitrogen (TN)	%	1.69
Carbon/Nitrogen (C/N)	-	16.3
Component - Glass	%	20.7
Component - Rock	%	11.3
Component - Plastic	%	0.36
Component - Other	%	67.6

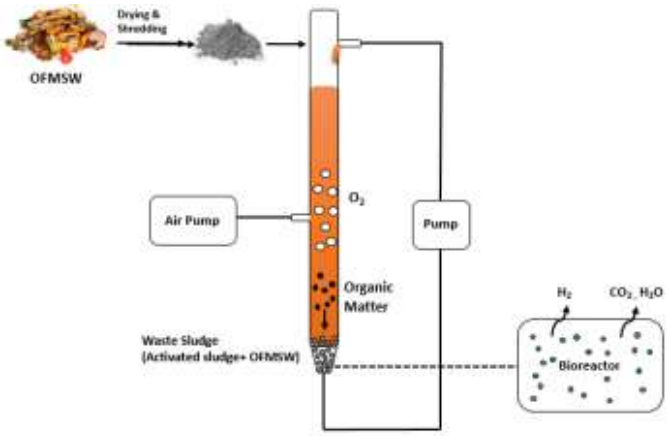


Fig. 1. HRAS system and hydrogen production from waste sludge with dark fermentation

Waste sludge was separated from the domestic wastewater by centrifugation and required trace elements (0.85 g/L KH_2PO_4, 0.75 g/L K_2HPO_4, 0.003 g/L H_3BO_3, 0.2 g/L $MgSO_4 \cdot 7H_2O$, 0.001 g/L $Na_2MoO_4 \cdot 2H_2O$, 0.001 g/L $ZnSO_4 \cdot 7H_2O$, 0.002 g/L $MnSO_4 \cdot 4H_2O$, 0.0001 g/L $Cu(NO_3)_2 \cdot 3H_2O$, 0.001 g/L $CaCl_2 \cdot 2H_2O$, 0.002 g/L EDTA, 0.012 g/L $FeSO_4 \cdot 7H_2O$, 0.004 g/L thiamine, 0.003 g/L biotin, 0.005 g/L p-aminobenzoic acid, 0.0065 g/L nicotinamide, 0.420 g/L glutamic acid, 0.001 g/L resazurin) were added to the bioreactor.

In hydrogen production, autoclave was applied to waste sludge for the elimination of competitive any microorganisms with the dark fermentative microorganisims. Sterilization of the waste sludge was performed in the conditions of 120 ^oC and 1 atm pressure.

III. Analysis

COD and volatile solids measurements were done according to the standard methods (Miner, 2006). Hyrogen measurements were occurred with the gas chromatograph (Shimadzu GC 2014, Tokyo, Japan) with a thermal conductivity detector (TCD) and a 2 m length, 1 mm inner diameter packed column (Restek, USA). The operating temperatures of the column,detector and injector were 80, 200 and 110 ^oC, respectively.

IV. Results and discussions

According to the activated sludge itself, HRAS system increased the hydrogen production due to the increasing COD level and food waste addition. Since the activated sludge is consist of microorganisms which is not readily biodegradable source of carbon, waste sludge mixes with the primary sludge in wastewater treatment plants for biogas production. In same way, readly biodegradable organic fraction of sludge was increased in this study for the hydrogen production succesfully.

V. Conclusions

In the study, sustainable and efficient domestic wastewater treatment was achieved by the HRAS process. Although the use of organic compounds in hydrogen production by dark fermentation has been a process that has been practiced for a long time, increasing the organic fraction of MSW with the wastewater treatment and usage of this waste stream for the hydrogen production offers an innovative approach.

References

Ge, H., Batstone, D.J., Mouiche, M., Hu, S., Keller, J., 2017. Nutrient removal and energy recovery from high-rate activated sludge processes – Impact of sludge age. Bioresour. Technol. 245, 1155–1161. https://doi.org/10.1016/j.biortech.2017.08.115

Guven, H., Eriksson, O., Wang, Z., Ozturk, I., 2020. Corrigendum to "Upgrading options of a preliminary wastewater treatment plant including food waste addition: A detailed life cycle assessment from a systems perspective" [Water Res. (2018) 145 518-530](S0043135418306912)(10.1016/j.watres.2018.08.061). Water Res. 169, 115408. https://doi.org/10.1016/j.watres.2019.115408

Guven, H., Ersahin, M.E., Dereli, R.K., Ozgun, H., Sancar, D., Ozturk, I., 2017. Effect of Hydraulic Retention Time on the Performance of High-Rate Activated Sludge System: a Pilot-Scale Study. Water. Air. Soil Pollut. 228. https://doi.org/10.1007/s11270-017-3598-8

Jimenez, J., Miller, M., Bott, C., Murthy, S., De Clippeleir, H., Wett, B., 2015. High-rate activated sludge system for carbon management - Evaluation of crucial process mechanisms and design parameters. Water Res. 87, 476–482. https://doi.org/10.1016/j.watres.2015.07.032

Miner, G., 2006. Standard methods for the examination of water and wastewater. Am. Water Work. Assoc. J. 98, 130.

Hydrogen and Ammonia as Fuels for the Decarbonization of Shipping

[1]*Omer Berkehan Inal, [1]Burak Zincir, [1]Cengiz Deniz

[1]Istanbul Technical University, Maritime Faculty, Marine Engineering Department, Istanbul, Turkey

*E-mail: inalo@itu.edu.tr, bzincir@itu.edu.tr, denizc@itu.edu.tr

Abstract

Maritime transportation is the most efficient transportation type. Despite, maritime transportation is an effective way to transport goods and passengers, fossil fuels are still in use. Ammonia and hydrogen are promising alternative fuels for the complete decarbonization of maritime transportation with their zero-carbon content and they are also suitable fuels for fuel cells. In this study, ammonia and hydrogen were compared by using safety, reliability, technical, and economic criteria to find which one is the best possible fuel option for fuel cells in terms of use for the shipping industry.

Keywords: Ammonia, Hydrogen, Maritime Transportation, Zero-carbon Shipping, Fuel Cells

I. Introduction

Maritime transportation is the most efficient transportation type and it was done by 98,140 commercial ships of 100 gross ton and above in January 2020 (UNCTAD, 2020). Despite, maritime transportation is an effective way to transport goods and passengers, fossil fuels are still in use. According to the study of the International Maritime Organization (IMO), 300 million tons of fossil fuels are consumed annually (IMO, 2015). Depending on the fossil fuel consumption, there are in increment at total greenhouse gas (GHG) emissions (CO_2, methane, and nitrous oxide) from 977 million tons to 1,076 million tons, and an increment at CO_2 emissions from 962 million tons to 1,056 million tons from the year 2012 to 2018 (IMO, 2020). Maritime transportation is responsible for approximately 3.1% of the total worldwide CO_2 emissions, but the predictions of IMO show that CO_2 emissions will increase between 50% and 250% by 2050 (IMO, 2015) if there will be no mitigation plan or strategy.

IMO set up an Initial Greenhouse Gas Strategy in 2018 which has two aims for maritime transportation (IMO, 2018). The first aim is to diminish CO_2 emissions per transport work at least 40% by 2030 and 70% by 2050, compared to 2008. And the second aim is to decrease GHG emissions from maritime transportation to 50% below the 2008 levels in 2050. To achieve these aims, the short- (2018-2023), the mid- (2023-2030), and the long-term (2030-…) candidate measures were announced under the Initial GHG Strategy. Although there are various ways and combined measures to achieve decarbonized maritime transportation, alternative fuel usage is a common candidate measure in all terms of the Strategy. Alternative fuels with lower carbon content than conventional marine fuels, such as liquefied natural gas (LNG) and methanol, are in use in maritime transportation in the short-term measures and will continue to be used at the mid-term measures. However, the long-term measures involve zero-carbon fuels and electric ships (IMO, 2018). Thus, ammonia and hydrogen are promising alternative fuels for the complete decarbonization of maritime transportation with their zero-carbon content (Inal & Deniz, 2018; Zincir, 2020). Ammonia and hydrogen are suitable fuels for fuel cells (Wan et al., 2021) which will be used for full-electric propulsion as a long-term measure.

The aim of this paper is to find suitable power generation sources with possible fuel options to achieve zero-carbon shipping. In this context, fuel cells, diesel engines, batteries, and renewable energy sources were considered as power sources for marine propulsion systems. Ammonia, diesel oil, fuel oil, hydrogen, methanol, and LNG were fuel options for fuel cells while the same fuels except hydrogen were fuel options for diesel engines. Renewable energy sources were assumed as solar and wind energy. A preliminary evaluation was conducted to find the best ways for zero-carbon shipping. After the preliminary evaluation,

ammonia and hydrogen were compared to find which one is the best possible fuel option for fuel cells. At the end of the study, a discussion was done for sustainable decarbonization of maritime transportation towards zero-carbon shipping.

II. Preliminary Evaluation of Pathways for Zero-carbon Shipping

There are different methods for powering the ships, and in conformity with the scope and the aim of this paper, elaboration of the options which offer a zero-carbon shipping are demonstrated in Figure 1. At the first stage, power sources are given as different main titles such as fuel cells, diesel engines, renewable energy, and battery. Then, these options have been clustered with their sub-titles according to their fuel usages.

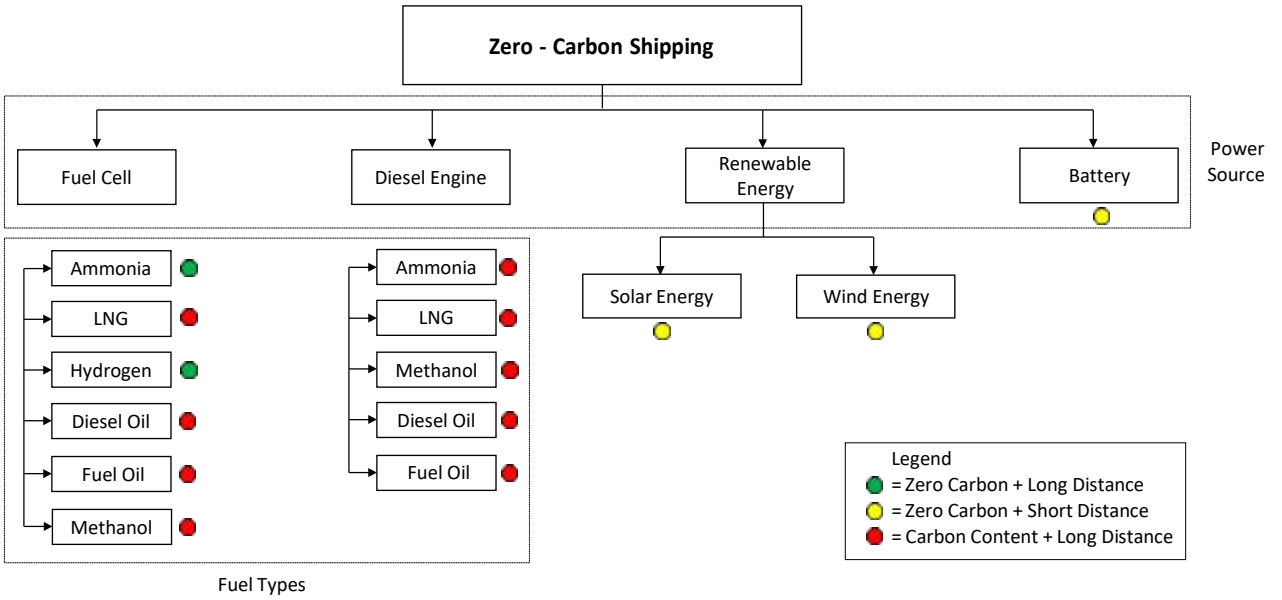


Figure 1: Pathways for Zero-carbon Shipping.

III. Comparison of Ammonia and Hydrogen for Fuel Cells

Ammonia and hydrogen are the most suitable fuels for fuel cells to reach zero-carbon shipping. Both fuels have different properties and it affects shipboard equipment and procedures which are required. To find which fuel is more suitable for shipboard usage a comparison is made by considering various criteria about different aspects. The criteria are determined by benefiting from previous studies in the literature. Table 1 shows the comparison criteria of previous studies. The criteria in this paper are safety, reliability, technical, and economic.

Table 1: Comparison criteria of previous studies in the literature.

Year	Criteria	Study Area	Authors
2016	Safety, applicability, feedstock, maturity, reliability, efficiency, cost	Onboard Hydrogen Production	Zincir & Deniz
2016	Safety, global availability, bunker capability, durability, adaptability, the effect on engine performance, effect on engine emissions, comply with emission regulations, the effect on combustion chamber components, commercial	Alternative fuels	Deniz & Zincir

	effects, costs		
2017	Environmental, economic, technological, social	Alternative fuels	Ren & Liang
2019	Economic, technical, environmental, social	Alternative fuels	Hansson et al.
2020	Cost, fuel types, efficiency, emissions, size, safety, power capacity, lifetime	Fuel cells	Inal & Deniz

IV. Conclusion

Ammonia and hydrogen are essential fuels for zero-carbon shipping and they can be used at fuel cells. The most suitable fuel between them for fuel cells is settled by using comparison criteria and giving points to ammonia and hydrogen at each criterion.

References

Deniz, C. & Zincir, B. (2016). Environmental and economical assessment of alternative marine fuels. *Journal of Cleaner Production, 113,* 438-449.

Hansson, J., Mansson, S., Brynolf, S., & Grahn, M. (2019). Alternative marine fuels: prospects based on multi-criteria decision analysis involving Swedish stakeholders. *Biomass and Bioenergy, 126,* 159-173.

International Maritime Organization (IMO). (2015). Third IMO Greenhouse Gas Study 2014.

International Maritime Organization (IMO). (2018). Adoption of the Initial IMO Strategy on Reduction of GHG Emissions from Ships and Existing IMO Activity Related to Reducing GHG Emissions in the Shipping Sector.

International Maritime Organization (IMO). (2020). Forth IMO Greenhouse Gas Study 2020.

Inal, O. B., & Deniz, C. (2018). Fuel Cell Availability for Merchant Ships. *3rd International Naval Architecture and Maritime Symposium*, 907–916.

Inal, O. B., & Deniz, C. (2020). Assessment of fuel cell types for ships: based on multi-criteria decision analysis. *Journal of Cleaner Production, 265,* 121734.

Ren, J., & Liang, H. (2017). Measuring the sustainability of marine fuels: a fuzzy group multi-criteria decision making approach. *Transportation Research D, 54,* 12-29.

United Nations Conference on Trade and Development (UNCTAD). (2020). Review of Maritime Transport 2020.

Wan, Z., Tao, Y., Shao, J., Zhang, Y., & You, H. (2021). Ammonia as an effective hydrogen carrier and a clean fuel for solid oxide fuel cells. *Energy Conversion and Management, 228,* 113729.

Zincir, B., & Deniz, C. (2016). Comparison of hydrogen production methods for shipboard usage. *10th Symposium on High-Performance Marine Vehicles (HIPER16)*, 193-201.

Zincir, B. (2020). A short review of ammonia as an alternative marine fuel for decarbonised maritime transportation. *International Conference on Energy, Environment and Storage of Energy*, 373-380.

Investigation and thermodynamic analysis of a new geothermal energy system for hydrogen and other valuable outputs

[1]Burak Tekkanat, [2*]Yunus Emre Yuksel, [1]Murat Ozturk
[1] Isparta University of Applied Sciences, Faculty of Technology, Department of Mechatronics Engineering, Cunur West Campus, Isparta, 32200, Turkey
[2] Afyon Kocatepe University, Bolvadin Vocational School, Electricity and Energy Department, Afyonkarahisar, 03300, Turkey

* E-mail: yeyuksel@aku.edu.tr

Abstract
In this study, a geothermal energy-based multigeneration system is designed and analyzed by using thermodynamic and parametric analyses. Power, hydrogen, heating and cooling, fresh water, hot water, and drying are the multiple outputs of the designed system. For this purpose, a Kalina cycle, an organic Rankine cycle, a hydrogen production unit, a fresh water production unit, a greenhouse heating system, and a dryer unit are integrated together. According to the thermodynamic analysis results, the overall plant's energy and exergy efficiencies are found as 59.53% and 53.17%, respectively. Parametric analyses indicate that an increase in the ambient temperature, the mass flow rate of geothermal water, and the geothermal fluid temperature positively impact both the overall system and hydrogen production's energy and exergy efficiency. However, as the vapor generator's pinch point temperature difference increases, the system's efficiency decreases slowly.

Keywords: Geothermal, multigeneration, exergy analysis, hydrogen, thermodynamic

I. Introduction

There are many disadvantages of using fossil fuels to generate power and other by-products (Kåberger, 2018). For this reason, renewable energy sources are an excellent alternative to fossil fuels for power generation (Brockway, et al., 2019). In this study, a geothermal energy source is selected as a prime driver of the designed multigeneration system producing power, hydrogen, fresh water, heating, and drying.
Multigeneration energy systems have gained some popularity after cogeneration and tri-generation systems have high performance results. By using the waste heat of any system, another system can be operated. Hence by integrating systems together, higher energy and exergy efficiencies can be gained.
Ebadollahi et al. (2019) have proposed a geothermal-based multigeneration system for cooling, heating, power, and hydrogen energy. They designed the system to utilize geothermal energy and LNG cold energy. The exergy efficiency of the overall plant is found as 28.91%. Islam and Dincer (2017) have offered solar and geothermal energy-based multigeneration systems producing power, drying, heating, and cooling. The energy and exergy efficiencies of the overall plant are calculated as 51% and 62%, respectively. Hence they have concluded that integrating systems for the multigeneration purpose has increased the system performance. Rostamzadeh et al. (2018) have proposed a novel multigeneration system using both biogas and geothermal energy sources. Thermal efficiency and the exergy efficiency of the proposed system are 62.8% and 74.9%, respectively. Besides, the condenser is found as the most exergy destructive component in the proposed multigeneration system.

II. Experimental Set-up and Procedure

In this study, a geothermal-based energy system is designed for multigeneration purposes such as power, hydrogen, heating, cooling, fresh water, hot water, and drying. The schematic diagram of the developed system is presented in Figure 1. The geothermal fluid is extracted from the well with stream 1 and directed to the vapor generator. The high pressured vapor enters the separator of the Kalina cycle. Then stream 8 enters the Kalina turbine to generate electricity. The stream goes to heat exchanger 1 (HEX-1) after completing its process in the Kalina sub-system. After HEX-1, the high pressured stream enters the organic Rankine cycle (ORC) turbine to generate power. Then waste heat energy is transferred to the PEM electrolyzer and hot water storage tank via 3 way valve-3. PEM electrolyzer produces hydrogen and oxygen. Hydrogen is stored in the hydrogen storage tank. On the other hand, oxygen can be used directly in hospitals to support people suffering from low oxygen levels. The waste heat of ORC is used in the desalination unit to produce fresh water. The stream exiting from HEX-3 goes through a greenhouse to transfer heat energy. Finally, the greenhouse's waste heat is utilized in HEX-4 to heat the air, which is further used in drying applications.

III. Analysis

In this subchapter, the integrated system is examined thermodynamically using the energetic and exergetic assessments to evaluate the system performance. Calculations are made using the EES software program to investigate both energetic and exergetic efficiencies for plant components and irreversibility rates. The general assumptions accepted for the simulation can be listed as given below:

- Steady-state mechanism is assumed for the system units.
- The HEXs, pumps, and turbines are adiabatic.
- Kinetic and potential exergetic terms are neglected for all system units.
- The reference temperature and pressure are constant (i.e., To=25°C and Po=101.3 kPa)

- The ideal gas characteristics are chosen for air to make an assessment.
- The pressure losses are negligible.

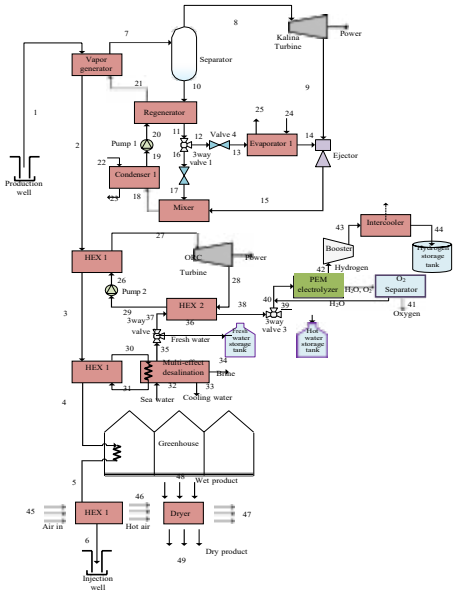


Fig. 1. The schematic diagram of the geothermal energy based multigeneration system

To perform thermodynamic assessment, the general mass, energy, entropy, and exergy balance equalities can be written as;

$$\sum \dot{m}_{in} = \sum \dot{m}_{ex} \quad (1)$$

$$\sum \dot{m}_{in} h_{in} + \sum Q_{in} + \sum W_{in} = \sum \dot{m}_{et} h_{et} + \sum Q_{et} + \sum W_{et} \quad (2)$$

$$\sum m_{in}\, s_{in} + \sum \left(\frac{Q}{T}\right)_{in} + S_{gen} = \sum m_{et}\, s_{et} + \sum \left(\frac{Q}{T}\right)_{et} \quad (3)$$

$$\sum \dot{m}_{in}\, ex_{in} + \sum Ex^{Q}_{in} + \sum Ex^{W}_{in} = \sum \dot{m}_{et} ex_{et} + \sum Ex^{Q}_{et} + \sum Ex^{W}_{et} + Ex_d \quad (4)$$

where in and et show inlet and exit conditions, respectively, Q represents heat transfer rate, W is the work rate, s and h show entropy, and enthalpy, respectively, $\dot{m}$ is the mass flow rate, $\dot{S_{gen}}$ and Ex_D show entropy generation and exergy destruction rate, respectively.

$$Ex_d = \dot{S_{gen}} T_o \quad (5)$$

In Eq. (4), Ex^Q and Ex^W represent thermal exergy flow rate and exergy transfer rate associated with work, respectively;

$$Ex^Q = Q\,(1 - \frac{T_o}{T}) \quad (6)$$

$$Ex^W = W \quad (7)$$

In Eq. (4), ex is the specific exergy, if we ignore the potential and kinetic exergies, specific exergy can be defined as given below;

$$ex = ex_{ph} + ex_{ch} \quad (8)$$

$$ex_{ph} = h - h_o - T_o(s - s_o) \quad (9)$$

$$ex^{ch}_{mix} = \sum y_i ex^{o}_{ch} + RT_o \sum y_i ln y_i \quad (10)$$

where y_i shows the mole fraction, and ex^{o}_{ch} illustrates the standard specific chemical exergy.

IV. Results and discussions

In this study, a new geothermal-based multigeneration system is developed and analyzed. Table 1 presents the overall plant's energy and exergy efficiencies and its sub-systems with exergy destruction rates. As seen from the table, the overall plant's energy and exergy efficiencies are calculated at 59.53% and 53.17%, respectively.

Table 1. Energy and exergy efficiencies with exergy destruction rate of the overall plant and its sub-systems

	η	ψ	Ex_D (kW)
Geothermal process	0.4837	0.5245	5448
Kalina cycle with cooling	0.2142	0.1769	5975
ORC	0.2534	0.2181	4593
Fresh water production	0.4438	0.3626	5154
Hydrogen production	0.7047	0.6718	7856
Greenhouse heating	0.8124	0.7813	4987
Dryer plant	0.7307	0.7635	4069
Overall plant	0.5953	0.5317	38082

After completing the thermodynamic analysis, a parametric study is also performed to figure out how some parameters affect the system performance. The first parameter is the mass flow rate of geothermal water, of which effects are presented in Figure 2. As seen from Figure 2a, while the mass flow rate of geothermal water rises from 125 kg/s to 225 kg/s, all sub-systems' exergy efficiencies and the overall plant increase. Therefore, it can be interpreted that a higher mass flow rate has a positive effect on system performance; hence, useful product generation will increase too. Figure 2b supports this idea as seen. As geothermal water's mass flow rate increases 125 kg/s to 225 kg/s, hydrogen production goes up from 0.0014 kg/s to 0.0016 kg/s.

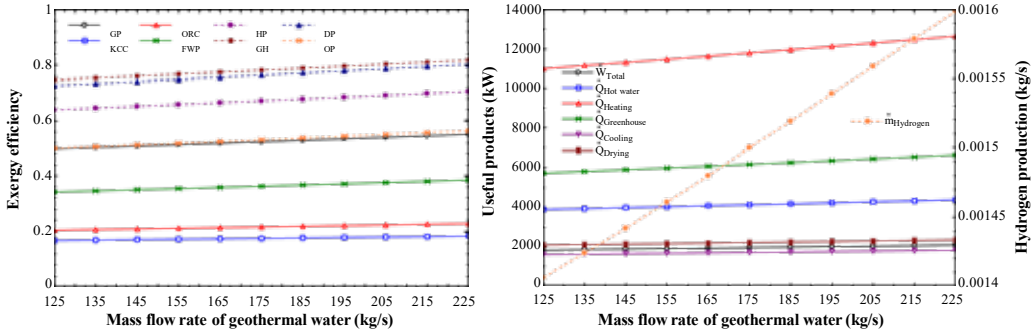


Fig. 2. The effect of the mass flow rate of geothermal water on (a) exergy efficiencies and (b) useful product and hydrogen production

The other parameter investigated in this study is the effect of geothermal water temperature ranging from 180°C to 220°C. For this change, exergy efficiencies of all sub-systems and the overall plant increase as given in Figure 3a. Figure 3b presents the useful product rate and hydrogen production rate with respect to geothermal water temperature.

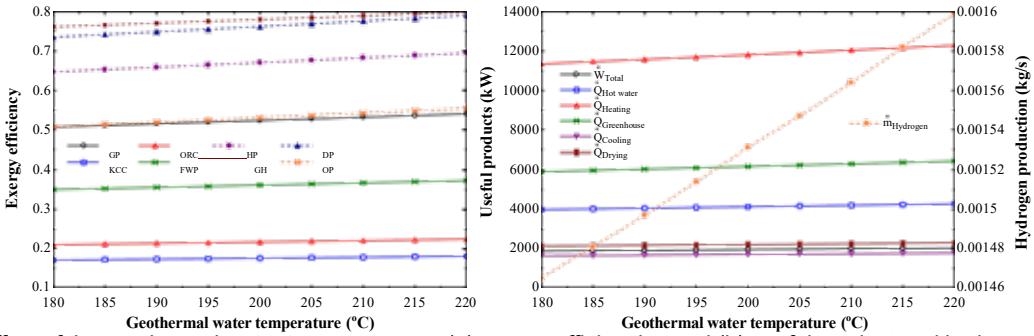


Fig. 3. The effect of the geothermal water temperature on (a) exergy efficiencies and (b) useful product and hydrogen production

V. Conclusions

In this study, a thermodynamic analysis is performed to evaluate the designed geothermal-based multigeneration system. The energy and exergy efficiencies of the overall plant are calculated as 59.53% and 53.17%, respectively. The most effective exergy destruction rate occurs in the hydrogen production system with 7856 kW. Moreover, the total exergy destruction rate of the overall plant is computed as 38082 kW. Parametric analysis results reveal that as the mass flow rate of geothermal water and the geothermal water temperature increase, energy and exergy efficiencies of sub-systems and the overall plant increase.

References

Brockway, P. E., Owen, A., Brand-Correa, L. I. & Hardt, L., 2019. Estimation of global final-stage energy-return-on-investment for fossil fuels with comparison to renewable energy sources. Nature Energy, 4(7), pp. 612-621.

Ebadollahi, M. ve diğerleri, 2019. Proposal and assessment of a new geothermal-based multigeneration system for cooling, heating, power, and hydrogen production, using LNG cold energy recovery. Renewable Energy, Cilt 135, pp. 66-87.

Islam, S. & Dincer, I., 2017. Development, analysis and performance assessment of a combined solar and geothermal energy-based integrated system for multigeneration. Solar Energy, Cilt 147, pp. 328-343.

Kåberger, T., 2018. Progress of renewable electricity replacing fossil fuels. Global Energy Interconnection, 1(1), pp. 48-52.

Rostamzadeh, H., Gargari, S. G., Namin, A. S. & Ghaebi, H., 2018. A novel multigeneration system driven by a hybrid biogas-geothermal heat source, Part I: Thermodynamic modeling. Energy Conversion and Management, Cilt 177, pp. 535-562.

Thermodynamic Optimization of the Scimitar Engine with Fixed Nozzle Geometry

[1*]Tayfun Tanbay, [2]Ahmet Durmayaz
[1] Bursa Technical University, Faculty of Engineering and Natural Sciences, Department of Mechanical Engineering, Yıldırım Campus, Bursa, 16330, Turkey
[2] Istanbul Technical University, Energy Institute, Maslak, Istanbul, 34469, Turkey

* E-mail: tayfun.tanbay@btu.edu.tr

Abstract
Scimitar engine is a novel hydrogen-fueled aero-engine that is designed to propel the LAPCAT A2 vehicle. This study deals with the thermodynamic optimization of the Scimitar engine at hypersonic cruise conditions with fixed nozzle outlet geometry conditions. In this context, the impacts of core nozzle outlet area together with the hydrogen fuel flow rate on the overall efficiency, exergy efficiency, coefficient of ecological performance, and coefficient of emission based ecological performance are investigated. Results show that there exists an optimum value of nozzle outlet area, which maximizes the objective functions considered, whose value depends on the hydrogen flow rate. At cruise speed and altitude of Mach 5 and 25 km, respectively, and for a hydrogen flow rate of 4.05 kg/s, the overall and exergy efficiencies are maximized for a nozzle outlet area of 6.78 m^2 while the coefficient of ecological performance has its maximum for a nozzle outlet area of 6.40 m^2.

Keywords: Scimitar engine, Hydrogen fuel, Thermodynamic optimization, NO_x emission, Exergy

I. Introduction

Hydrogen fuel is considered as a promising alternative to kerosene in mitigating the greenhouse gas emissions of the aviation industry. In addition to being advantageous to conventional jet fuel in terms of energy efficiency (Verstraete, 2013) in long-range transport, a comparative life cycle assessment has revealed that hydrogen is also the better alternative in terms of environmental impact (Bicer and Dincer, 2017). A novel aero-engine concept utilizing this green fuel is the Scimitar engine designed by Reaction Engines Ltd. to propel the hypersonic LAPCAT A2 vehicle (Jivraj et al., 2007). This engine is a hybrid system incorporating the features of a turbofan, ramjet and turborocket, and it is derived from the Synergistic Air-Breathing Rocket Engine (SABRE). It operates as turbofan and ramjet-turborocket for cruise speeds of Mach 0-2.5 and 2.5-5, respectively, and then switches to a pure turborocket mode for Mach 5. The engine is a three-fluid system. Air is the oxidant, and an ad hoc precooler is designed, for which helium is the working fluid, to transfer heat from the hot incoming air to hydrogen fuel that is kept at cryogenic conditions.

Thermodynamic analysis and optimization of aero-engines through parametric cycle analysis play an essential role in the preliminary design of these systems. There exist several studies on the thermodynamic analysis of the Scimitar engine. The exergetic performance of the Scimitar engine is performed by Villace and Paniagua (2013) with the EcoSimPro software to determine the thermal effectiveness and propulsive efficiency. A thermodynamic model is proposed by Tanbay et al. (2020) to investigate the nitrogen oxide (NO_x) emission characteristics of the Scimitar engine. In another recent study, an exergy and NO_x emission based ecological performance analysis (*CEEP*) is presented by Tanbay and Durmayaz (2020) through a newly defined objective function called coefficient of emission based eceological performance. Ingenito et al. (2015) also considered the NO_x emissions of the Scimitar engine and discussed mitigation strategies. Dong et al. (2018) studied the effect of combustion chamber outlet temperature and pressure ratio of air compressor on the specific thrust and overall efficiency of the Scimitar engine.

Previous studies on the Scimitar engine did not focus on the effect of nozzle geometry on the energetic and exergetic objective functions. For instance, the nozzle is assumed to be adapted, (i.e., the nozzle outlet pressure is equal to the atmospheric pressure) in the analyses given by Villace and Paniagua (2013), Tanbay et al. (2020) and Tanbay and Durmayaz (2020). In this study, a thermodynamic optimization of the Scimitar engine with fixed nozzle geometry is carried out to investigate the impact of nozzle outlet area and hydrogen flow rate on the overall and exergy efficiencies, coefficient of ecological performance (*CEP*) and *CEEP* for the hypersonic flight phase. The optimum value of the nozzle outlet area for different values of hydrogen flow rate are presented.

II. The Scimitar engine

The schematic representation of the Scimitar engine for hypersonic flight conditions is illustarated in Fig. 1. Air at ambient conditions enter the engine through the intake with a cruise speed of Mach 5. The deceleration of air in the intake rises its temperature to approximately 1325 K, and it is cooled to core compressor inlet temperature via the precooler (HX1 and HX2). The compressed air enters the preburner where partial combustion takes place. The purpose of the preburner and HX3 is to keep the inlet temperature of helium turbine T1 at a constant value of 1000 K throughout all flight conditions. Partially burned air enters the combustion chamber, and then the core nozzle to provide the propulsion. Hydrogen fuel enters the cycle at cryogenic conditions. Its temperature is increased by the heat extracted from air with the precooler which is transferred to hydrogen through heat exchangers HX4L, HX4H and HX5. The thermal coupling between air and hydrogen is provided via a helium regenerator, which comprises of a low and a high temperature section.

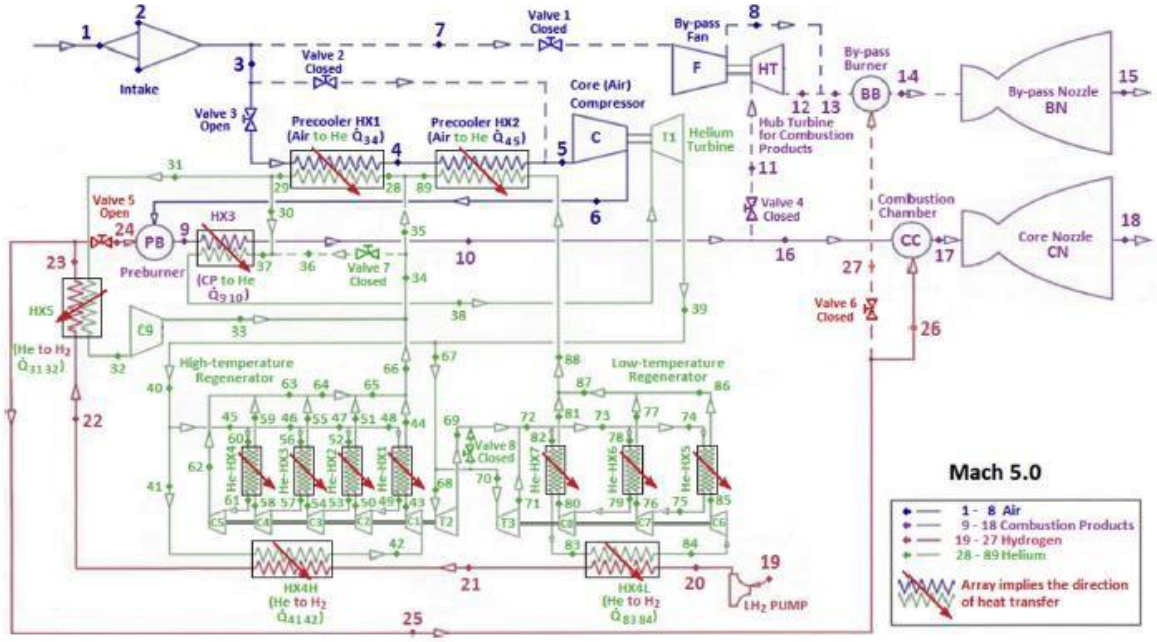


Fig. 1: Schematic representation of the Scimitar engine for hypersonic flight conditions (Tanbay et al. (2020))

III. Core nozzle calculations and objective functions

The energy analysis through a thermodynamic model of the Scimitar engine, which yields a nonlinear system of 82 equations, is presented in detail by Tanbay et al. (2020). The solution of these equations reveals the enthalpies at all stations, and the emissions of the core nozzle. On the other hand, the exergy analysis of the system is given by Tanbay and Durmayaz (2020). The only difference between the model presented in Tanbay et al. (2020) and this study is the calculation methodology of the core nozzle. The outlet conditions are determined by applying conservation of mass and energy equations together with the entropy change equation (Eqs. (30) and (31) in Tanbay et al. (2020)). However, instead of assuming a fixed outlet pressure of $P_{18} = P_1$ yielding an adaptive nozzle, the core nozzle outlet conditions are determined by choosing a fixed outlet area A_e and letting P_{18} vary accordingly.

The objective functions, on which the impact of core nozzle area is investigated, are the overall efficiency, exergy efficiency, *CEP*, and *CEEP* are expressed, respectively by

$$\eta_O = \frac{\dot{W}_P}{\dot{Q}_{LHV}} \tag{1}$$

$$\eta_{II} = \frac{\dot{W}_P}{\dot{X}_{expended}} \tag{2}$$

$$CEP = \frac{\dot{W}_P}{X_{dest,tot}} \tag{3}$$

$$CEEP = \frac{\dot{W}_P}{\dot{m}_{NO,18} + \dot{m}_{NO_2,18}} \tag{4}$$

where W_P is the propulsive power of the engine, Q_{LHV} is the lower heating value, $X_{expended}$ is the expended exergy rate that comprises of the physical and kinetic exergies of incoming air and the chemical exergy of hydrogen fuel, and $X_{dest,total}$ is the total exergy destruction rate of the engine. Explicit expresssions for $X_{expended}$ and $X_{dest,total}$ are given by Tanbay and Durmayaz (2020) while Q_{LHV} is calculated as in Tanbay et al. (2020). Propulsive power for the underexpanded nozzle ($P_{18} > P_1$) is determined by

$$W_P = v_1(\dot{n}_{CP_{CC,18}} M_{CP_{CC,18}} v_{18} - \dot{n}_{air,1} M_{air} v_1) + A_e(P_{18} - P_1) \tag{5}$$

where $\dot{n}$ is molal flow rate, M is molar mass and v is velocity, while subscript CC refers to combustion chamber.

IV. Results and discussions

This study investigates the impact of core nozzle outlet area together with the hydrogen flow rate on the energetic and exergetic performance of the Scimitar engine. The cruise speed and altitude of the engine are Mach 5 and 25 km, respectively. Calculations are performed with MATHEMATICA 11.

Fig. 2 shows the variation of overall efficiency and coefficient of ecological performance with core nozzle outlet area for four values of hydrogen fuel flow rate. All objective functions have a maximum value with respect to A_e.

The optimum value of A_e increases with hydrogen flow rate; for instance the maximum value of η_o is observed for $A_{e,opt} = 6.78m^2$ when $\dot{m}_{H_2} = 4.05\,kg/s$, while for a hydrogen flow rate of $4.17\,kg/s$ the optimum value of A_e is $7.02m^2$. Therefore, an increase in hydrogen flow rate causes a weight penalty for optimum performance. Maximum values of η_o, η_{ex} and $CEEP$ are obtained at the same value of $A_{e,opt}$, however the optimum value of A_e yielding the maximum value of CEP is lower than the one that gives $\eta_{o,max}$, $\eta_{ex,max}$ and CEP_{max}. For the case of $\dot{m}_{H_2} = 4.05\,kg/s$ the maximum value of *CEP* is seen when $A_{e,opt} = 6.40m^2$. Results also show that, unlike the other objective functions, exergy efficiency tends to have a higher value as hydrogen fuel flow rate increases, when a large core nozzle (e.g. $A_e = 10m^2$) is used. Finally, it should be noted that the nozzle area does not have an effect on NO_x emissions, and the change in *CEEP* with respect to A_e is due to the variation of propulsive power with the nozzle outlet area.

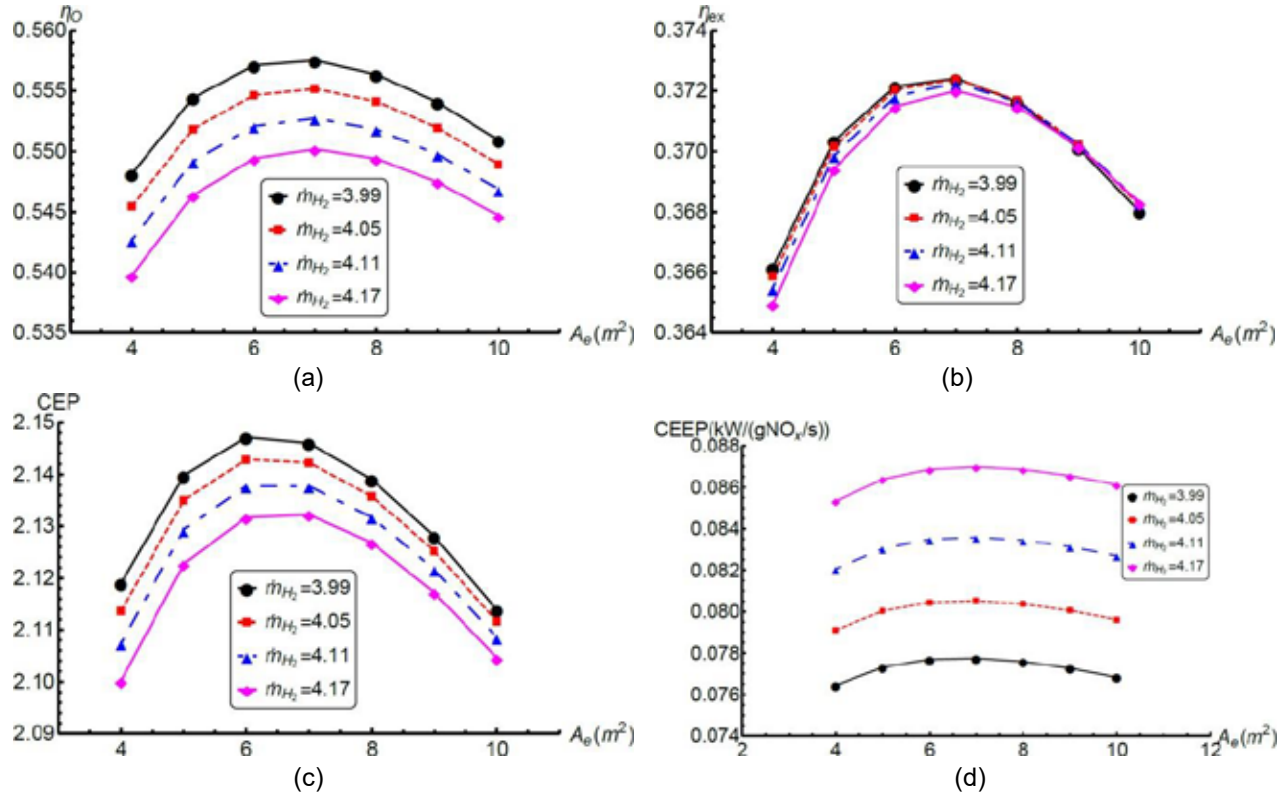


Fig. 2: Impact of core nozzle outlet area on (a) η_O, (b) η_{ex}, (c) CEP and (d) CEEP of the Scimitar engine.

V. Conclusions

Scimitar engine is a hydrogen-fueled aero-engine concept, and parametric cycle analysis of such a novel design is essential to improve its performance. A thermodynamic optimization is carried out in this work to investigate the impact of core nozzle outlet area on the energetic and exergetic performance of the Scimitar engine. Optimum outlet area values for different hydrogen fuel flow rates that maximize the overall and exergy efficiencies, and coefficient of ecological and emission based ecological performance are determined. The results provide valuable information for further research and development activities.

References

Bicer Y, Dincer I., Life cycle evaluation of hydrogen and other potential fuels for aircrafts, International Journal of Hydrogen Energy, 42, 10722-10738, (2017).
Dong P., Tang H., Chen, M., Study on Multi-Cycle Coupling Mechanism of Hypersonic Precooled Combined Cycle Engine, Applied Thermal Engineering, 131, 497-506, (2018).
Ingenito A., Agresta A., Andriani R., Gamma, F., NO_x reduction strategies for high speed hydrogen fuelled vehicles, International Journal of Hydrogen Energy, 40, 5186-5196, (2015).
Jivraj F., Varvill R., Bond A., Paniagua G., The SCIMITAR precooled Mach 5 engine. In: 2nd European conference for aerospace sciences (EUCASS), 3-6 July, Belgium: Universite libre de Bruxelles, (2007).
Tanbay T., Durmayaz A., Exergy and NO_x emission based eceological performance analysis of the Scimitar engine, Journal of Engineering for Gas Turbines and Power, 142, 081008, (2020).
Tanbay T., Uca M.B., Durmayaz A., Assessment of NOx Emissions of the Scimitar Engine at Mach 5 Based on a Thermodynamic Cycle Analysis, International Journal of Hydrogen Energy, 45, 3632-3640, (2020).
Verstraete D., Long range transport aircraft using hydrogen fuel, International Journal of Hydrogen Energy, 38, 14824-14831, (2013).
Villace V. F., Paniagua G., On the exergetic effectiveness of combined-cycle engines for high speed propulsion, Energy, 51, 382-394, (2013).

A new multigeneration plant for useful outputs including hydrogen

[1*]Yunus Emre Yüksel, [2]Murat Öztürk, [3]Ibrahim Dincer
[1] Afyon Kocatepe University, Bolvadin Vocational School, Electricity and Energy Department, Afyonkarahisar, 03300, Turkey
[2] Isparta University of Applied Sciences, Faculty of Technology, Department of Mechatronics Engineering, Cunur West Campus, Isparta, Turkey
[3] Faculty of Engineering and Applied Science, Ontario Tech. University, 2000 Simcoe Street North, Oshawa, Ontario, Canada
* E-mail: yeyuksel@aku.edu.tr

Abstract
In this study, a novel solar energy-based multigeneration system with nine useful outputs, including hydrogen, is designed and analysed thermodynamically. The present system can produce power, heating, cooling, fresh water, hot water, hydrogen, ammonia, methane, and urea. Also, energy and exergy efficiency analyses are performed on all sub-systems and the overall plant. Besides, a parametric study is implemented to find out how some parameters affect the system performance. According to the analysis results, the overall plant's energy and exergy efficiencies are 66.12% and 61.56%, respectively.

Keywords: Solar energy; multigeneration; exergy analysis; hydrogen; methane; ammonia.

1. Introduction

The usage of fossil fuels causes many environmental and ecological problems. With many advantages, renewable energy sources are a very beneficial solution for these environmental and ecological problems. The importance of solar energy increases with each passing day, and its use is expected to increase gradually in the future (Al-Sulaiman, 2014). Especially considering that the world population will increase to 9.7 billion by 2050, it concludes that we need to use energy very efficiently (Mahmood and Al-Ansari, 2021). The gradual replacement of fossil-based energy systems with solar energy is considered a promising energy alternative in reducing CO_2 emissions (AlZahrani, and Dincer, 2018). Therefore, solar power is preferred for this study to supply heat energy to other sub-systems.In a study conducted by Khalid et al., useful outputs were produced using two renewable energy sub-systems, geothermal and solar. They calculated the energy and exergy efficiencies of these systems. In addition, they demonstrated by simulation that 2.7 kg/s of hydrogen could be produced in the electrolyzer (Khalid et al., 2017). Habibollahzade et al. (2018) investigated the energy and exergy analyses of a combined parabolic trough solar collectors (PTSC) with three different cycles: a thermoelectric generator (TEG), a Rankine cycle, and a proton exchange membrane (PEM). They showed that the system's exergy efficiency and total cost under the optimum operating conditions were 12.76% and 61.69 $/GJ, respectively. Alirahmi et al. (2020) designed a geothermal and solar energy-based integrated system to generate hydrogen, freshwater, electricity, cooling load, and hot water. They calculated the exergy efficiency and cost ratio as 21.63% and 63.89 $/h, respectively.

2. System design and description

The schematic representation of the designed multigeneration plant is presented in Figure 1. The prime mover of the system is solar energy via parabolic trough collectors. Produced heat energy is sent to 3-way valve 1 firstly. Some part of heat energy is stored in the hot storage tank to be used when needed. Heat energy is transferred to the Rankine cycle then the organic Rankine cycle to produce power. The remaining heat energy enters the PEM water heater to heat the water to 80°C.

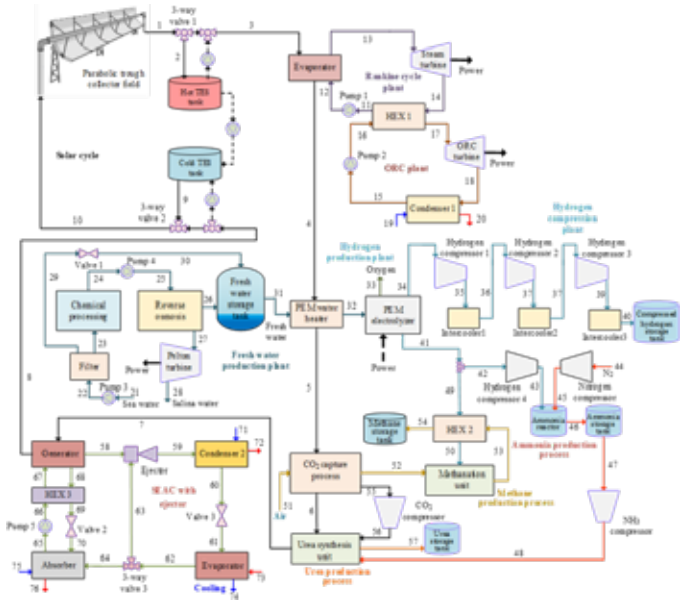


Fig. 1: The schematic representation of the designed multigeneration plant.

Then PEM electrolyzer produces oxygen and hydrogen. Produced hydrogen is then sent to the hydrogen compressor for storage. A part of the hydrogen is used to produce ammonia in an ammonia reactor. Produced ammonia can either be used directly or can be used in the urea production unit. The urea synthesis unit's remaining waste heat goes to the absorption cooling system and produces a cooling effect. Finally, waste heat from here enters the fresh water generation unit to have fresh water and power.

3. Analysis

In this subchapter, the integrated system is examined thermodynamically using the energetic and exergetic assessments to evaluate the system performance. Calculations are made using the EES software program to investigate energetic and exergetic efficiencies for plant components and irreversibility rates. The general assumptions accepted for the simulation can be listed as given below:

- Steady-state process is assumed for the system units.
- The HEXs, pumps, and turbines are adiabatic.
- Both kinetic and potential energy changes are negligible..
- The reference temperature and pressure are constant (i.e., To=25°C and Po=101.3 kPa)
- The ideal gas characteristics are chosen for air to make an assessment.
- The pressure losses are negligible.

For the thermodynamic assessment of the multigeneration system, the general mass, energy, entropy, and exergy balance equalities can be written as;

$$\sum \dot{m}_{in} = \sum \dot{m}_{ex} \quad (1)$$

$$\sum \dot{m}_{in} h_{in} + \sum Q_{in} + \sum W_{in} = \sum \dot{m}_{et} h_{et} + \sum Q_{et} + \sum W_{et} \quad (2)$$

$$\sum m_{in} s_{in} + \sum \left(\frac{Q}{T}\right)_{in} + S_{gen} = \sum m_{et} s_{et} + \sum \left(\frac{Q}{T}\right)_{et} \quad (3)$$

$$\sum \dot{m}_{in} ex_{in} + \sum Ex^{Q}_{in} + \sum Ex^{W}_{in} = \sum \dot{m}_{et} ex_{et} + \sum Ex^{Q}_{et} + \sum Ex^{W}_{et} + Ex_d \quad (4)$$

where in and et show inlet and exit conditions, respectively, Q represents heat transfer rate, W is the work rate, s and h show entropy, and enthalpy, respectively, $\dot{m}$ is the mass flow rate, $\dot{S_{gen}}$ and Ex_d show entropy generation and exergy destruction rate, respectively.

$$\dot{E}x_d = \dot{S}_{gen} T_o \quad (5)$$

Here, Ex^{Q} and Ex^{W} represent thermal exergy flow rate and exergy transfer rate associated with work, respectively;

$$Ex^{Q} = Q\ (1 - \frac{T_o}{T}) \quad (6)$$

$$Ex^{W} = W \quad (7)$$

In addition, ex is the specific exergy, if we ignore the potential and kinetic exergies, specific exergy can be defined as given below;

$$ex = ex_{ph} + ex_{ch} \quad (8)$$

$$ex_{ph} = h - h_o - T_o(s - s_o) \quad (9)$$

$$ex^{ch}_{mix} = \sum y_i ex^{o}_{ch} + RT_o \sum y_i ln y_i \quad (10)$$

where y_i shows the mole fraction, and ex^{o}_{ch} illustrates the standard specific chemical exergy.

4. Results and discussion

In this study, thermodynamic analysis and a parametric analysis are performed to evaluate the designed multigeneration system. Table 1 presents the energy and exergy efficiency results of sub-plants and the overall system. According to the analysis results, the smallest exergy values occur in the SEAC unit and ORC plant with 12.09% and 23.17%. The energy and exergy efficiencies of the overall system are 66.12% and 61.56%. With the selected base parameters, the total power production reaches 62360 kW, hydrogen mass flow rate of production is 2.78 kg/s, and the mass flow rate of produced ammonia is 10.73 kg/s.

Tab. 1: The energy and exergy analyses values for solar energy based integrated plant

Sub-plants/whole plant	Energy efficiency (%)	Exergy efficiency (%)
Solar cycle	45.97	38.25
Rankine cycle plant	36.08	31.42
ORC plant	26.93	23.17
Hydrogen production plant	74.16	68.45
Hydrogen compression plant	64.83	59.34
Ammonia production plant	65.28	60.92
Methane production plant	60.74	55.37
Urea production plant	62.59	56.83
SEAC with ejector	14.86	12.09
Fresh water production plant	79.24	75.62
Overall system	66.12	61.56

In the parametric analysis part, the effect of two parameters is evaluated, which are dead state temperature and solar radiation intensity. As seen from Fig. 2a, as dead state temperature increase from 0°C to 50°C, exergy efficiencies of all sub-plants and the overall system increases slightly. By defining the exergy, as the difference between the environment and the system decreases, exergy destruction rates decrease. Hence, exergy efficiencies increase. For this reason, applicable product generation rates increase with increasing dead state temperature. The second parameter, which is more effective than dead state temperature, is solar radiation intensity as solar radiation intensity varies from 400 W/m^2 to 1000 W/m^2, exergy efficiencies of all sub-systems, and the overall system increases. For instance, the overall system's exergy efficiency ranges from about 58% to nearly 62%. Similarly, as solar radiation intensity rises, production rates also increase. Hydrogen production is about 2 kg/s at 400 W/m^2, it becomes 3 kg/s at 1000 W/m^2.

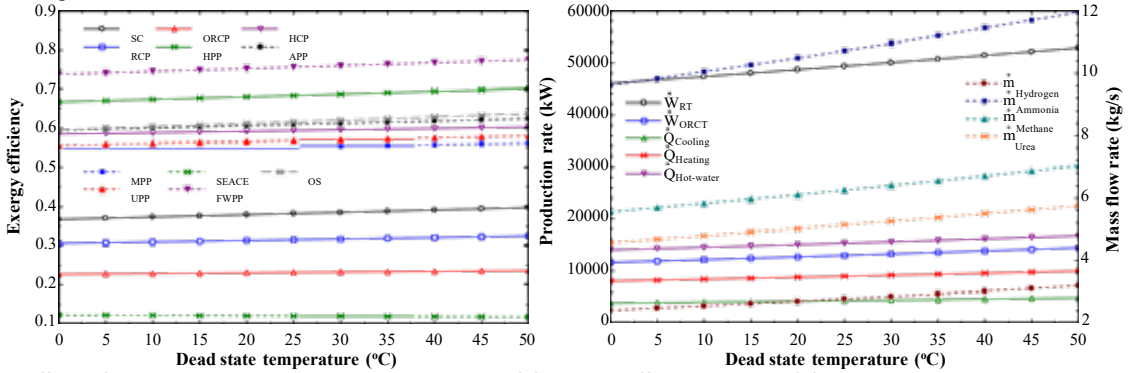


Fig. 2: The effect of the dead state temperature change on (a) exergy efficiencies and (b) power production rates

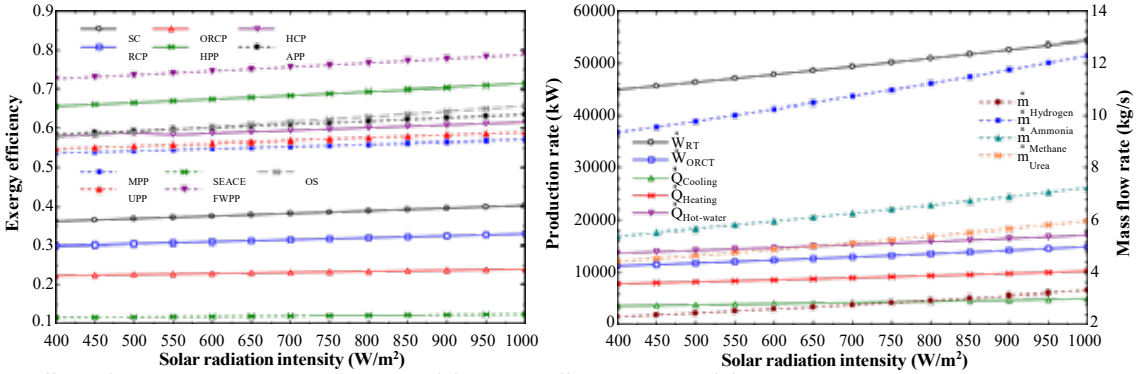


Fig. 3: The effect of the solar radiation intensity on (a) exergy efficiencies and (b) power production rates

5. Conclusions

The thermodynamic analysis along with a parametric study reveal that the present multigeneration system is efficient and effective due to the advantages, including utilizing waste heat. Also, solar radiation intensity is an important factor for the effectiveness of the system. Such a study is helpful to system designers and practicing engineers for developing sustainable communities. The future studies will cover the optimization and economic analyses.

References

Al-Sulaiman, F. A., 2014. Exergy analysis of parabolic trough solar collectors integrated with combined steam and organic Rankine cycles. Energy Conversion and Management, 77, 441-449.

Alirahmi, S. M., Rostami, M., and Farajollahi, A. H., 2020. Multi-criteria design optimization and thermodynamic analysis of a novel multigeneration energy system for hydrogen, cooling, heating, power, and freshwater. International Journal of Hydrogen Energy, 45(30), 15047-15062.

AlZahrani, A. A., and Dincer, I., 2018. Energy and exergy analyses of a parabolic trough solar power plant using carbon dioxide power cycle. Energy conversion and management, 158, 476-488.

Habibollahzade, A., Gholamian, E., Ahmadi, P., and Behzadi, A., 2018. Multi-criteria optimization of an integrated energy system with thermoelectric generator, parabolic trough solar collector and electrolysis for hydrogen production. International journal of hydrogen energy, 43(31), 14140-14157.

Khalid, F., Dincer, I., and Rosen, M. A., 2017. Techno-economic assessment of a solar-geothermal multigeneration system for buildings. International Journal of Hydrogen Energy, 42(33), 21454-21462.

Mahmood, F., and Al-Ansari, T. A., 2021. Design and thermodynamic analysis of a solar powered greenhouse for arid climates. Desalination, 497, 114769.

Energy and exergy analyses of a new geothermal energy-based tri-generation plant

[1*]Murat Koc, [2]Yunus Emre Yuksel, [3]Murat Ozturk
[1] Isparta University of Applied Sciences, Technical Sciences Vocational School, Electricity and Energy Department, Cunur West Campus, Isparta, Turkey
[2] Afyon Kocatepe University, Bolvadin Vocational School, Electricity and Energy Department, Kirkgoz Campus, Afyonkarahisar, Turkey
[3] Isparta University of Applied Sciences, Faculty of Technology, Department of Mechatronics Engineering, Cunur West Campus, Isparta, Turkey
* E-mail: muratkoc@isparta.edu.tr

Abstract
Due to environmental and ecological concerns, new, clean and cheap energy sources are necessary for sustainable development. In this study, a geothermal energy source is selected for the basis of the designed tri-generation plant. The developed tri-generation plant produces power from the Kalina and organic Rankine cycles, hydrogen from PEM electrolyzer, and cooling effect from ejector cooling plant. The tri-generation plant's overall energy and exergy efficiencies are found as 42.08% and 45.39, respectively. Parametric analysis results reveal that the dead state temperature, the geothermal water temperature, and the geothermal water mass flow rate positively impact the system performance.

Keywords: energy, exergy, geothermal, tri-generation

I. Introduction

The energy demand is increasing day by day with the increase of the population and technology development. Although fossil fuels are the primary energy source, their use causes serious environmental problems such as ozone depletion and acid rain. Considering the harmful effects of fossil fuels, renewable energy sources attract more attention (Mohammadi and Mehrpooya, 2017). Geothermal resources are one of the most potential resources in terms of using cleaner technologies with their features such as energy-saving and renewability (Dincer and Acar, 2017). Also, geothermal energy is an excellent renewable energy source, especially for integrated systems operating at low temperatures. Since geothermal energy is both a sustainable and environmentally friendly carbon-free energy source, it is used in hybrid integrated systems (Bonyadi et al., 2018; Olabi et al., 2020).

Behnam et al. (2018), the performance of a small-scale trigeneration system operated by low-temperature geothermal sources to generate fresh water, heating, and electricity were thermodynamically investigated. They concluded that when geothermal water at 100°C is used, system performance is improved. The second-law efficiencies of the Kalina Cycle (KC) and organic Rankine cycle (ORC) of the tri-generation system analyzed by Zare (2016) found as 58.97% and 36.13%, respectively. The energetic and exergetic efficiencies of a geothermal-based integrated system, made by Yuksel et al. (2018), were calculated as 42.59% and 48.24%, respectively. In the literature review presented, it is seen that geothermal energy sources can be used effectively in integrated systems (Akrami et al., 2017). In this study, energy and exergy analysis of trigeneration systems based on geothermal energy are presented.

II. System Definition

Geothermal energy source, a type of renewable energy source, is selected for the prime mover of the designed tri-generation system. As seen in Figure 1, high-temperature geothermal fluid first enters the heat exchanger (HEX) 1 to transfer its heat energy to the Kalina cycle. The Kalina cycle produces power by using heat energy and then transfers its remaining heat energy to the ORC plant via HEX 3. Similar to the Kalina cycle, ORC generates power. On the other hand, a part of the heat energy coming from a geothermal source enters a proton exchange membrane (PEM) water heater from HEX 1. Then, in the PEM water electrolyzer, the Kalina turbine's power is used to generate hydrogen from water. The final hydrogen product is stored in the hydrogen storage tank. Finally, the PEM sub-plant's remaining waste heat enters the HEX 2 of the ejector cooling plant to produce a cooling effect. The fluid exiting from HEX 2 turns back to the injection well to complete the cycle.

III. Analysis

To perform a thermodynamic assessment, the general mass, energy, entropy, and exergy balance equalities can be written as:

$$\sum \dot{m}_{in} = \sum \dot{m}_{ex} \quad (1)$$

$$\sum \dot{m}_{in} h_{in} + \sum \dot{Q}_{in} + \sum \dot{W}_{in} = \sum \dot{m}_{et} h_{et} + \sum \dot{Q}_{et} + \sum \dot{W}_{et} \quad (2)$$

$$\sum \dot{m}_{in}\, s_{in} + \sum \left(\frac{\dot{Q}}{T}\right)_{in} + \dot{S}_{gen} = \sum \dot{m}_{et}\, s_{et} + \sum \left(\frac{\dot{Q}}{T}\right)_{et} \quad (3)$$

$$\sum \dot{m}_{in}\, ex_{in} + \sum \dot{E}x^{Q}_{in} + \sum \dot{E}x^{W}_{in} = \sum \dot{m}_{et} ex_{et} + \sum \dot{E}x^{Q}_{et} + \sum \dot{E}x^{W}_{et} + \dot{E}x_{d} \quad (4)$$

where in and et show inlet and exit conditions, respectively, $\dot{Q}$ represents heat transfer rate, $\dot{W}$ is the work rate, s and h show entropy, and enthalpy, respectively, $\dot{m}$ is the mass flow rate, $\dot{S}_{gen}$ and $\dot{E}x_D$ show entropy generation and exergy destruction rate, respectively.

$$\dot{E}x_d = \dot{S}_{gen} T_o \quad (5)$$

In Eq. (4), $\dot{E}x^Q$ and $\dot{E}x^W$ represent thermal exergy flow rate and exergy transfer rate associated with work, respectively;

$$\dot{E}x^Q = \dot{Q}\left(1 - \frac{T_o}{T}\right) \quad (6)$$

$$\dot{E}x^W = \dot{W} \quad (7)$$

In Eq. (4), ex is the specific exergy, if we ignore the potential and kinetic exergies, specific exergy can be defined as given below;

$$ex = ex_{ph} + ex_{ch} \quad (8)$$

$$ex_{ph} = h - h_o - T_o(s - s_o) \quad (9)$$

$$ex^{ch}_{mix} = \sum y_i ex^o_{ch} + RT_o \sum y_i ln y_i \quad (10)$$

where, y_i shows the mole fraction, and ex^o_{ch} illustrates the standard specific chemical exergy.

These equations are then assigned to all streams found in the tri-generation design. Engineering equation solver (EES) software program is used to perform thermodynamic and parametric analyses.

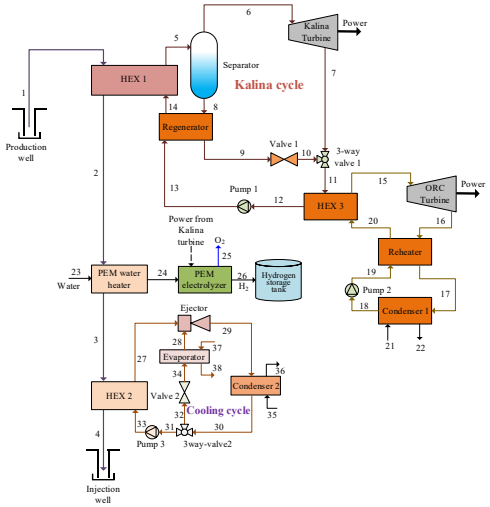


Fig. 1: The schematic representation of the designed tri-generation system

IV. Results and discussions

Thermodynamic analysis results reveal the energetic and exergetic performances of sub-plants and the overall tri-generation system, which are presented in Table 1. According to the analysis results, the highest energy and exergy efficiency belongs to the hydrogen production plant with 72.57% and 67.34%, respectively. The smallest energy and exergy efficiencies occur in the ORC plant with 13.29% and 10.46%, respectively. The overall energy and exergy efficiencies of the tri-generation plant are 42.08% and 45.39%, respectively.

Tab. 1: The energetic performance, exergetic performance, and the exergy destruction rates of sub-plants and the overall system

Sub-systems/whole system	Energetic performance (%)	Exergetic performance (%)	Exergy destruction rate (kW)
Geothermal process	0.3927	0.4164	2862
Kalina power process	0.3613	0.3229	1846
ORC plant	0.1329	0.1046	927
Hydrogen production plant	0.7257	0.6734	1189
Ejector cooling plant	0.1547	0.1108	753
Overall system	0.4208	0.4539	7577

Figure 2a represents the energy and exergy efficiency variations concerning dead state temperature change from 0ºC to 40ºC. As seen from the figure, as dead state temperature rises, all sub-plants' energy and exergy efficiency values and the overall plant increase, too. The increase in dead state temperature closes the gap between the system working temperature and the environmental temperature. Hence, exergy destruction rates caused by irreversibilities decrease.

Figure 2b indicates the effect of geothermal water temperature variation from 150ºC to 200ºC on the energy and exergy efficiency values. Because any increase in geothermal water temperature causes enthalpy rise, it is expected that growth in geothermal water temperature makes the system improved.

Similar to the geothermal water temperature, geothermal water mass flow rate has a positive impact on the system performance due to enthalpy increase as presented in Figure 2c, while geothermal water mass flow rate rises from 38 kg/s to 48 kg/s, sub-plants' and the overall system's energy and exergy efficiencies increase.

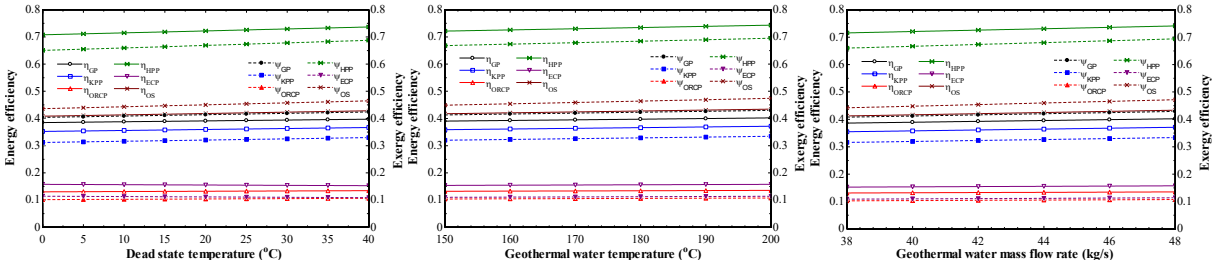


Fig. 2: The effect of (a) the dead state temperature, (b) geothermal water temperature, and (c) geothermal water mass flow rate on energy and exergy efficiencies

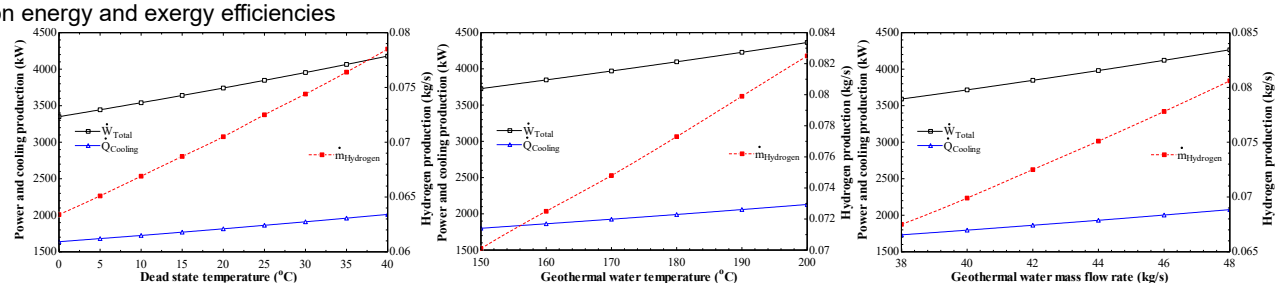


Fig. 3: The effect of (a) the dead state temperature, (b) geothermal water temperature, and (c) geothermal water mass flow rate on power and cooling production rate

Figure 3a shows the effect of dead state temperature variations on power, hydrogen and, cooling production rates. As expected, as dead state temperature increases, total power, hydrogen, and cooling production rates rise, too. The effect of geothermal water temperature on the total power, hydrogen, and cooling production rates are given in Figure 3b. according to the figure, as geothermal water temperature increases from 150ºC to 200ºC, total power production goes up from 3750 kW to nearly 4400 kW. For the same variation, hydrogen production rate increases from 0.070 kg/s to 0.082 kg/s. As the final parameter, the geothermal water mass flow rate effect is presented in Figure 3c. As seen from the figure, as the geothermal water mass flow rate varies from 38 kg/s to 48 kg/s, total power production increases from 3600 kW to 4300 kW. The hydrogen production rate increases from 0.068 kg/s to 0.081 kg/s and the cooling rate rises from 1700 kW to 2000 kW.

V. Conclusions

For a sustainable solution to the energy crisis, a novel tri-generation system using a geothermal source is designed and analyzed both thermodynamic and parametric. Before analysis of the system, some assumptions have been accepted. For selected assumptions, the system's total power output rate is 3847 kW, hydrogen generation mass flow rate is 0.0725 kg/s, and cooling production rate is 1863 kW. The highest exergy destruction rate occurs in geothermal plant with 2862 kW, then in Kalina power plant with 1846 kW. These two plants are vulnerable to improvement in the future. Parametric analysis results show that the dead state temperature, geothermal water temperature, and geothermal water mass flow rate have a positive effect on the system performance.

References

Akrami, E., Chitsaz, A., Nami, H., and Mahmoudi, S. M. S., 2017. Energetic and exergoeconomic assessment of a multi-generation energy system based on indirect use of geothermal energy. Energy, 124, 625-639.

Behnam, P., Arefi, A., and Shafii, M. B., 2018. Exergetic and thermoeconomic analysis of a trigeneration system producing electricity, hot water, and fresh water driven by low-temperature geothermal sources. Energy conversion and management, 157, 266-276.

Bonyadi, N., Johnson, E., and Baker, D., 2018. Technoeconomic and exergy analysis of a solar geothermal hybrid electric power plant using a novel combined cycle. Energy Conversion and Management, 156, 542-554.

Dincer, I., and Acar, C., 2017. Smart energy systems for a sustainable future. Applied Energy, 194, 225-235.

Mohammadi, A., and Mehrpooya, M., 2017. Energy and exergy analyses of a combined desalination and CCHP system driven by geothermal energy. Applied Thermal Engineering, 116, 685-694.

Olabi, A. G., Mahmoud, M., Soudan, B., Wilberforce, T., and Ramadan, M., 2020. Geothermal based hybrid energy systems, toward eco-friendly energy approaches. Renewable Energy, 147, 2003-2012.

Yuksel, Y. E., Ozturk, M., and Dincer, I., 2018. Thermodynamic analysis and assessment of a novel integrated geothermal energy-based system for hydrogen production and storage. International Journal of Hydrogen Energy, 43(9), 4233-4243.

Zare, V., 2016. A comparative thermodynamic analysis of two tri-generation systems utilizing low-grade geothermal energy. Energy Conversion and Management, 118, 264-274.

Thermodynamic analysis of a power and liquid hydrogen production plant using waste heat

[1*]Murat Koc, [2]Yunus Emre Yuksel, [3]Murat Ozturk
[1] Isparta University of Applied Sciences, Technical Sciences Vocational School, Electricity and Energy Department, Cunur West Campus, Isparta, Turkey
[2] Afyon Kocatepe University, Bolvadin Vocational School, Electricity and Energy Department, Kirkgoz Campus, Afyonkarahisar, Turkey
[3] Isparta University of Applied Sciences, Faculty of Technology, Department of Mechatronics Engineering, Cunur West Campus, Isparta, Turkey
* E-mail: muratkoc@isparta.edu.tr

Abstract
Alternative energy generation options are taking attention to eliminate the disadvantages and dangerous effects of fossil fuels usage. The waste heat of any system is released into the environment unless it is used. In this study, a novel integrated approach utilizing the nuclear reactor's waste heat is designed and analyzed. For this purpose, a supercritical CO_2 cycle and a trans-critical CO_2 cycle with a thermoelectric generator are integrated into the nuclear reactor. On the other hand, for hydrogen production PEM electroylzer, for liquefaction of produced hydrogen hydrogen liquefaction system is used. Employing these sub-plants, the overall efficiency of the system improves. The integrated plant's thermodynamic analysis results indicate that the overall energy and exergy efficiencies are 46.59% and 42.87%. Besides, it can be concluded that the nuclear reactor exit temperature and nuclear plant sub-cooled liquid mass flow rate are two crucial parameters affecting the system performance.

Keywords: Integrated system, exergy analysis, thermodynamic, waste heat, liquid hydrogen

I. Introduction

More and more people have accepted that nuclear power plants are reliable sources that respond to growing energy needs (Hannum, et al., 2005; Dincer and Rosen, 2013). However, nuclear power plants should be evaluated very well in thermodynamics, considering their environmental problems. For example, approximately 33% of the thermal energy generated in the nuclear reactions is converted into electricity, while the remaining amount is released to the environment as waste heat (Nisan, et al., 2003; Obara and Tanaka, 2021). Waste heat released from power plants may increase lake and river waters' temperature, endangering the vitality in that region. Therefore, recovering the waste heat in nuclear power plants is very important subject to improve energy efficiency. Instead of releasing this waste heat to the environment such as the ocean, rivers, and air, it is used in applications such as climate-controlled agricultural systems, fish farms, hydrogen production and obtaining drinking water from seawater, and it does not apply to new energy sources for such applications and contributes to reducing environmental problems (Miernicki, et al., 2020; Obara and Tanaka, 2021). With the help of heat exchangers (HEX), nuclear waste heat can be converted back to power in partial condensation trans critical CO_2 (T-CO_2) and recompression supercritical CO_2 (S-CO_2) cycles (Kim, et al., 2012). In this study, it is targeted to produce power and hydrogen by using the waste heat of a nuclear reactor. Therefore, hydrogen production and liquefaction, thermo-electric generator (TEG), T-CO_2 and S-CO_2 cycles for nuclear waste heat are thermodynamically evaluated. The energy efficiency and the whole system's exergy efficiency are 46.59% and 42.87%, respectively.

II. System description

In this study, the waste heat of the small modular nuclear reactor power plant is used as prime mover. The small modular nuclear reactor's waste heat is about 322°C and 15200 kPa with a mass flow rate of 357 kg/s, as seen in Figure 1 with stream 1. Then stream 1 enters heat exchanger 1 (HEX) to transfer its heat to the fluid of the supercritical CO_2 sub-plant. Stream 7 exiting from HEX 1 enters the S-CO_2 turbine to generate power with 310°C and 25000 kPa. This sub-plant's waste heat is re-utilized in a trans-critical CO_2 sub-plant with a thermoelectric generator (TEG). t-CO_2 sub-plant produces power by using the heat energy of the fluid, as seen in stream 12. The stream 12 is 158 °C and 10000 kPa with a 217 kg/s mass flow rate. Thermoelectric generator integrated to t-CO_2 produces heating effect by using the waste heat of the t-CO_2 turbine. Then stream 10 turns back to cooler through pump 2. Therefore, the cycle in the t-CO_2 sub-plant completes. On the other hand, the water entering the HEX 1 carries heat energy to the PEM electrolyzer with stream 17 to heat water up to 80ºC. PEM electrolyzer produces hydrogen and oxygen by splitting up water. Produced hydrogen enters hydrogen liquefaction system and goes through eight HEX and three catalyst bed to be liquefied. Then liquid hydrogen at point 32 enters liquid hydrogen storage tank.

III. Analysis

To perform thermodynamic assessment, the general mass, energy, entropy, and exergy balance equalities can be written as;

$$\sum \dot{m}_{in} = \sum \dot{m}_{ex} \quad (1)$$

$$\sum \dot{m}_{in} h_{in} + \sum \dot{Q}_{in} + \sum \dot{W}_{in} = \sum \dot{m}_{et} h_{et} + \sum \dot{Q}_{et} + \sum \dot{W}_{et} \quad (2)$$

$$\sum \dot{m}_{in}\, s_{in} + \sum \left(\frac{\dot{Q}}{T}\right)_{in} + \dot{S}_{gen} = \sum \dot{m}_{et}\, s_{et} + \sum \left(\frac{\dot{Q}}{T}\right)_{et} \quad (3)$$

$$\sum \dot{m}_{in}\, ex_{in} + \sum \dot{E}x^{Q}_{in} + \sum \dot{E}x^{W}_{in} = \sum \dot{m}_{et} ex_{et} + \sum \dot{E}x^{Q}_{et} + \sum \dot{E}x^{W}_{et} + \dot{E}x_{d} \quad (4)$$

where in and et show inlet and exit conditions, respectively, $\dot{Q}$ represents heat transfer rate, $\dot{W}$ is the work rate, s and h show entropy, and enthalpy, respectively, $\dot{m}$ is the mass flow rate, $\dot{S}_{gen}$ and $\dot{E}x_D$ show entropy generation and exergy destruction rate, respectively.

$$\dot{E}x_d = \dot{S}_{gen} T_o \quad (5)$$

In Eq. (4), $\dot{E}x^{Q}$ and $\dot{E}x^{W}$ represent thermal exergy flow rate and exergy transfer rate associated with work, respectively;

$$\dot{E}x^{Q} = \dot{Q}\left(1 - \frac{T_o}{T}\right) \quad (6)$$

$$\dot{E}x^{W} = \dot{W} \quad (7)$$

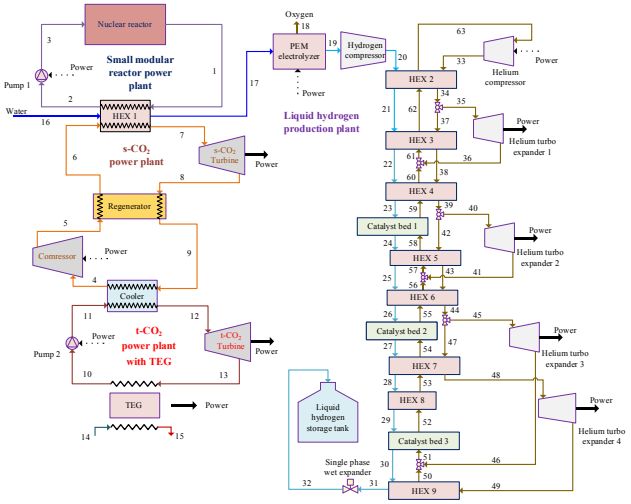


Fig. 1: The schematic diagram of the power and liquid hydrogen production system

IV. Results and discussions

In this study, a novel power and liquid hydrogen production system is designed and evaluated in terms of thermodynamic and parametric analyses. According to the thermodynamic analysis, energy and exergy efficiency values of sub-plants and the whole system are presented in Table 1. As seen from the table, the highest exergy efficiency occurs in small modular nuclear reactor power plant and the minor exergy efficiency belongs to the TEG sub-system. The energy and exergy efficiencies of the whole system are 46.59% and 42.87%, respectively.

Tab. 1: The energy and exergy efficiencies of the sub-systems and the whole system

Sub-systems/whole system	Energy efficiency (%)	Exergy efficiency (%)
Small modular reactor power plant	56.73	48.61
s-CO_2 power plant	36.94	33.75
t-CO_2 power plant	11.26	8.93
TEG sub-system	5.18	2.64
Liquid hydrogen production plant	67.35	52.18
Overall plant	46.59	42.87

Tab. 2: The nuclear power plant outputs rates and exergy destruction rate

Plant outputs	Values
Power production from the S-CO_2 power plant, $\dot{W}_{s-CO_2}$	40654 kW
Power production from the t-CO_2 power plant, $\dot{W}_{t-CO_2}$	4750 kW
Power production from TEG, $\dot{W}_{TEG}$	2903 kW
Total exergy destruction rate, $\dot{E}x_{D,total}$	64375 kW
Liquid hydrogen production rate, $\dot{m}_{H_2}$	0.8925 kg/s

Table 2 reveals the power production rates of the sub-plants. As indicated in the table, the S-CO_2 sub-plant can produce up to 40654 kW, t-CO_2 sub-plant can produce 4750 kW. TEG sub-system, on the other hand, generates 2903 kW. The total exergy destruction rate is 64375 kW. Liquid hydrogen production rate reaches 0.8925 kg/s.

.The effect of the nuclear reactor exit temperature is given in Figure 2. As seen in Figure 2a, while the nuclear reactor exit temperature increases from 300°C to 380°C, the overall plant's exergy efficiency goes up from 42% to 45%. For this nuclear reactor exit temperature change, the total power production increases from about 46000 kW to nearly 52000 kW. Besides, the total exergy destruction rate decreases from 65400 kW to 61400 kW. When analyzed hydrogen production rate versus nuclear reactor exit temperature, it is seen that H_2 production rate increases from 0.83 kg/s to nearly 1.1 kg/s.

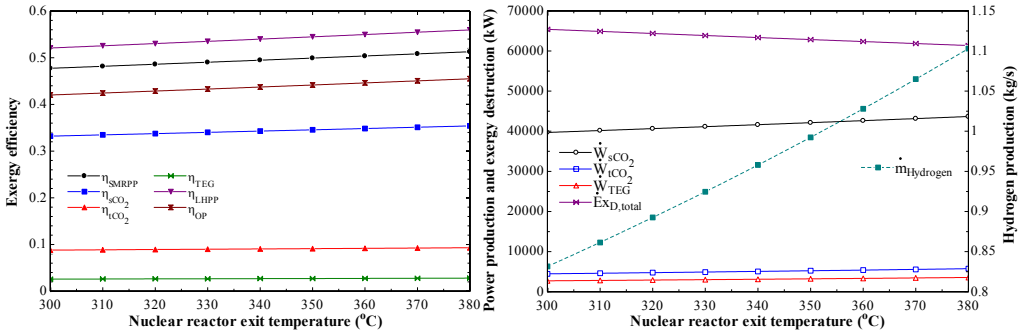


Fig. 2: The effect of the nuclear reactor exit temperature on (a) exergy efficiency and (b) power and hydrogen production and the total exergy destruction rate

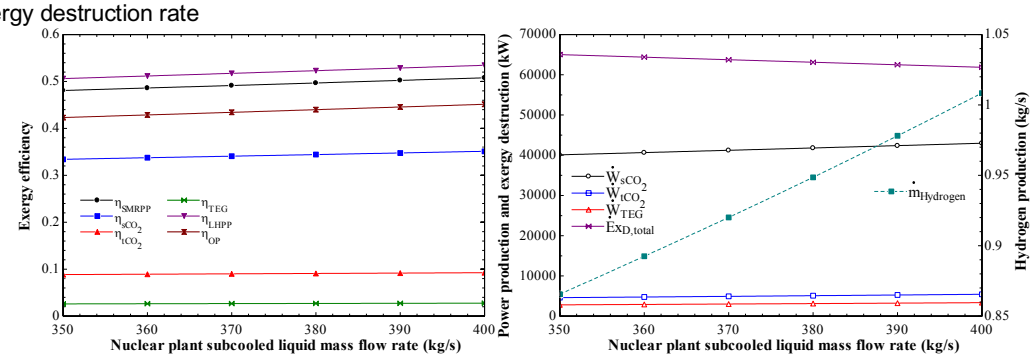


Fig. 3: The effect of the nuclear plant subcooled liquid mass flow rate on (a) exergy efficiency and (b) power and hydrogen production and the total exergy destruction rate

Figure 3a presents the effect of the nuclear plant subcooled liquid mass flow rate on exergy efficiency changes. As the nuclear plant subcooled liquid mass flow rate increases the exergy efficiencies of all sub-plants and the overall plant increase due to higher enthalpy flow per second. The overall plant's energy and exergy efficiencies increase about 10% as the mass flow rate of the subcooled liquid varies from 350 kg/s to 400 kg/s. Figure 3b clearly indicates that the exergy destruction rate sharply decreases as the subcooled liquid's mass flow rate increases. Therefore, total power production rates increase from 46000 kW to 51000 kW, and the hydrogen production rate goes up from 0.87 kg/s to 1.01 kg/s.

V. Conclusions

Nuclear power plants are high-capacity power plants requiring to exhaust their high temperature. Therefore, usually, water is used to cool down nuclear power plants. This study is aimed to utilize this waste heat of nuclear power plants to produce a valuable product. For this reason, S-CO_2, t-CO2, TEG and hydrogen production and liquefaction sub-plants are integrated into the nuclear reactor. In the analysis section, thermodynamic and parametric analyses have been used to evaluate the sub-plants and the overall plant. The overall plant's energy and exergy efficiencies are found at 46.59% and 42.87%, respectively. Parametric analysis results indicate that the nuclear reactor exit temperature and nuclear plant subcooled liquid mass flow rate are two crucial parameters that affect the system positively. This study may be helpful for decision-makers in the future.

References

Dincer, I., Rosen, M.A., 2013. Exergy: Energy, Environment and Sustainable Development. Elsevier B. V, second edition, Amsterdam, Netherlands.

Hannum, W. H., Marsh, G. E., and Stanford, G. S., 2005. Smarter Use of Nuclear Waste. Scientific American, Vol. 293, No. 6, pp. 84-91.

Kim, Y. M., Kim, C. G., and Favrat, D., 2012. Transcritical or supercritical CO_2 cycles using both low-and high-temperature heat sources. *Energy*, *43*(1), 402-415.

Miernicki, E. A., Heald, A. L., Huff, K. D., Brooks, C. S., and Margenot, A. J., 2020. Nuclear waste heat use in agriculture: History and opportunities in the United States. *Journal of Cleaner Production*, 121918.

Nisan, S., Caruso, G., Humphries, J. R., Mini, G., Naviglio, A., Bielak, B., Alonso, O. A., Martins, N., and Volpi, L., 2003. Seawater desalination with nuclear and other energy sources: the EURODESAL project. *Nuclear engineering and Design*, *221*(1-3), 251-275.

Obara, S. Y., & Tanaka, R., 2021. Waste heat recovery system for nuclear power plants using the gas hydrate heat cycle. *Applied Energy*, 116667.

Effect of External Heater Operating Duration on Cold Start Performance of PEM Fuel Cell

[1*]Alparslan Topcu, [2]Kadir Aydın, [3]Selahattin Çelik
[1] Alanya Alaaddin Keykubat University, Rafet Kayış Faculty of Engineering, Department of Mechanical Engineering, Alanya, Antalya, 07425, Turkey
[2] Çukurova University, Faculty of Engineering, Department of Mechanical Engineering, Sarıçam, Adana, 01330, Turkey
[3] Niğde Ömer Halisdemir University, Faculty of Engineering, Department of Mechanical Engineering, Merkez, Niğde, 51240, Turkey

* E-mail: alparslan.topcu@alanya.edu.tr, kdraydin@gmail.com, scelik@ohu.edu.tr

Abstract
In this study, the effect of external heater operating duration on the cold start time was investigated. For this reason, an experimental setup was constituted and cold start tests were performed at -10 °C. The single-cell stack was used in tests and the stack was heated up thanks to an externally heated coolant circulation cycle. Ethanol was preferred as a heating (working) fluid that can operate at subzero temperatures. Ethanol was warm-up thanks to an external electric heater (1.8 kW-powered) with different durations (10, 15, and 20 s) and delivered to the stack, at the same time. A pump (12V-DC) was used to drive the ethanol cycle and time was recorded with the circulation of ethanol. Temperature measurements were carried out thanks to thermocouples placed to the inlet and the outlet points of bipolar plates. Time-temperature graphs were obtained for each external heating durations.

Keywords: PEM fuel cell, cold start, assisted, heater duration.

I. Introduction

PEM (proton exchange or polymer electrolyte membrane) fuel cells, one of the most efficient energy transformation devices, are widely preferred in many industries such as automotive, aviation, material handling, heavy-duty trucks, rail, and marine transportation (Ozden et al., 2019). However, the cold start which means start-up at subfreezing temperatures problem is needs improvement still (Mu et al., 2017). Department of Energy (DOE) unit of the USA publishes technical achievements and targets for the cold start, periodically. In 2020 targets, the cold start time was aimed from -20 °C ambient temperature in 30 seconds (DOE, 2020). In addition, -30 and -40 °C temperatures were assigned as ultimate targets for the unassisted and assisted cold start techniques, respectively. Therefore, cold start techniques are divided into two main groups which are unassisted and assisted approaches.

Before these explanations, it should be noted that the cold start can solve with 'Keep Warm' strategy apart from the aforementioned techniques. The Keep Warm strategy aims to keep the stack above zero to inhibit freeze (Amamou et al., 2016). The stack can warm up owing to internal (low-power stack operation, hot air blowing, etc.) and external (electric heater, battery, catalytic burner, phase change materials, etc. heating sources. Besides, thermal insulation materials are very useful to keep warm the stack. Sasmito et al. (2013) designed an innovative concept and used phase change materials (paraffin, n-eicosane, and Rubitherm27) and insulator material (polyurethane foam) to delay the cooling period of the stack. They simulated insulator material thickness (and also thermal conductivity) and different PCM types (and their thickness) and investigated the effects of these parameters on keeping the warm capacity of the stack. Finally, it was reported that the stack can be kept above zero for around 48 hours thanks to the proposed concept. However, the keep warm strategy requires energy continuously and brings about excessive energy consumption although it disallows freezing the stack. Therefore, solutions are needed at startup which is called 'Thaw at Start' (Amamou et al., 2016).
'Thaw at Start' strategy can maintain with either assisted or unassisted techniques as aforesaid. Some unassisted procedures such as material optimization or optimization of the operating parameters can cope with the cold start problem. But, the achieved improvements are not at the desired level and approaches need to develop still. On the other hand, assisted techniques can ensure quick start-up even if consume more energy and required extra accessories. The major assisted cold start techniques included catalytic H_2/O_2 reaction, coolant heating, electric heating, and antifreeze agent solutions.

Guo et al. (2016) implemented the catalytic reaction and investigated using a three-dimensional model, numerically. Firstly, the numerical model was validated with the experimental data, after constituted twelve different simulation cases considering the galvanostatic, potentiostatic modes, and air inlet mole fraction. They were noted that a successful cold start is possible from -20 °C in the galvanostatic mode. In another catalytic reaction study, Luo et al. (2015) modeled a 30-cell stack and evaluated different startup modes such as maximum power, constant current, and constant power modes (at -25, and -40 °C). A successful cold start from -25 °C was achieved within 13 s with the maximum power mode. Besides, it was reported that the design parameters have a strong effect on cold start. The electric heating method is another heating mechanism for the cold start process and has the power supply and the applied power flexibilities advantages (Matsuoka, 2006). On the other hand, some antifreeze agents can provide opportunities at the startup stage of PEMFC. Because a fast startup is possible with antifreeze without freezing (Knorr et al., 2019). But, it was reported that the antifreeze material (methanol) should be removed from the channels to achieve high power densities (Knorr et al., 2019).

However, limited studies were carried out related to the coolant heating method although this way ensures homogeneous temperature distribution and quick warm-up. Besides, there are a lot of different parameters to affect the performance and energy consumption levels of this approach. Therefore, the effect of heater operation

duration on the cold start performance of PEMFC was investigated in the current study. An experimental mechanism was set up and cold start tests were carried out at -10 °C. The heater was operated in different durations (10, 15, 20 s), and the effect of the initial heating mechanism temperature was determined and compared using time-temperature graphs.

II. Experimental

An experimental setup was constituted before the tests. An electrical circuit was established to drive the heater, pump, and thermostat. A temperature and humidity-controlled conditioning chamber (ESPEC Corp, SH-221, Japan) was used to reach subzero temperatures. Ethanol was selected as a coolant (heating) fluid because of the operation ability and low freezing point at subzero temperatures. Cold ethanol was heated by a 1.8 kW powered instant electric heater and delivered to the back of the stack. External serpentine channels were machined to the back of the anode and the cathode sides of the bipolar plates, and ethanol was circulated thanks to these channels. Therefore, a closed ethanol cycle was established and the stack was heated by both sides. The 12V-DC pump operated to drive the ethanol cycle and it delivered a 0.65 lt/min flow rate ethanol in total. The heating fluid was prorated to the anode and the cathode sides of the stack. Preliminary tests were performed to prove this, and the temperature pursues of the anode and the cathode sides were followed by thermocouples which were placed at the inlet and the outlet points of the bipolar plates.

H_2 and air gases are sent to the anode and cathode departments, respectively at normal PEMFC operating conditions. However, chemical H_2/O_2 reactions and heat production have occurred in the cathode section. Thus, cathode temperature distribution and management are very important to achieve a successful cold start. Consequently, five thermocouples were placed into the mid-section of the cathode bipolar plate, symmetrically, and the temperature was followed.

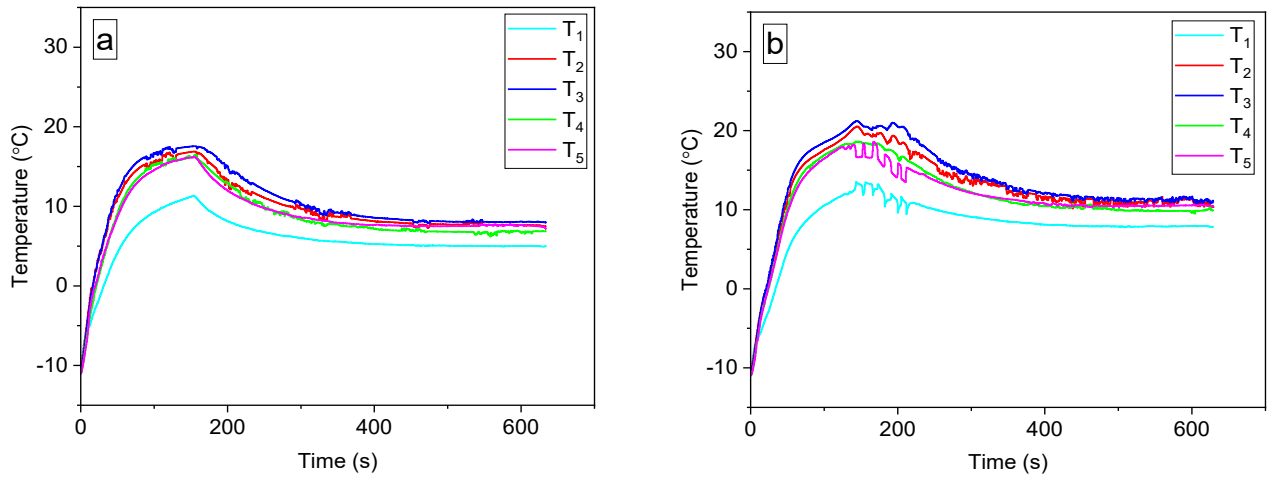
A single-cell stack was used in the tests, and a Nafion-based membrane (25 cm^2 active area, activated) was preferred. Bipolar plates and end plates were made from stainless steel 316L material. Cold start tests were implemented at -10 °C and the temperature-controlled cabinet was conditioned to the -10 °C and the stack was kept 1 h at this temperature. Cold start tests were performed after the system temperature was stabled. Four different case studies were carried out:

1. 10 s heater, 150 s pump was operated.
2. 15 s heater, 150 s pump was operated.
3. 20 s heater, 150 s pump was operated.
4. 15 s heater, 262.5 s pump was operated.

The electric heater consumed 1800 W power to heat the ethanol. Nevertheless, the heater operating duration is crucial in terms of the energy consumption level of the assisted technique. Therefore, the effect of the heater operation duration on the temperature profile was investigated in the first case studies. On the other hand, the pump consumed only 80 W power and 22.5 s pump operation power is equal to the 1 s heater operation. For this reason, the energy consumption levels of the second and third case studies were balanced with the increase of pump operation. Thusly, the comparison of pump operation or heater duration was revealed in the fourth case study. At the same time, 0.5 lt/min H_2 and 1.5 lt/min air were sent to the stack, and the current was collected at 0.4 constant voltage when cold start tests were performing.

III. Results and discussions

Time-temperature graphs of the case studies were presented in Fig. 1. It was observed that the temperature increase rate of the inlet (T_1) and outlet (T_5) points were decreased with time. T_1 was seen as the coldest line among other measurement points although it was the inlet point. On the other hand, the mid-section (T_2, T_3, and T_4) of the bipolar plate was performed warmer behavior according to inlet and outlet points.



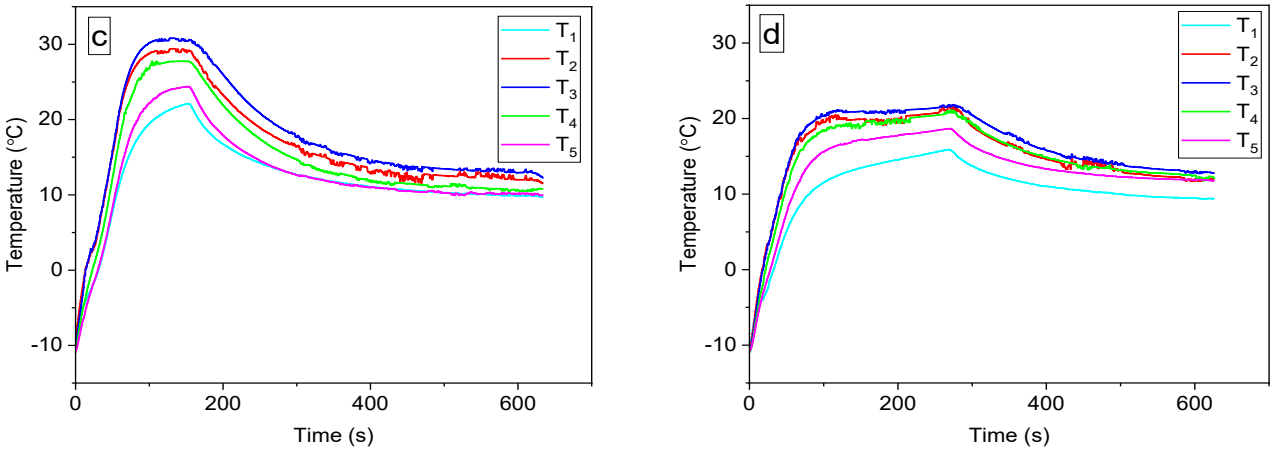


Fig. 1: Time-temperature graphs of the case studies

The chemical reactions that intensively occurred in the mid-section of the cell contributed to the temperature increase in these regions, especially. It was seen the cell maintained its position at 10 °C levels after the heater and the pump shut down. The temperature level was increased with the increase of the heater operation duration, as expected. However, the energy consumption level is increased with the increase of heater operation duration. The short operation durations were found applicable since the cell operated properly. A significant performance difference was not discovered when compared the Fig. 1-c and Fig. 1-d. Nonetheless, a more feasible temperature profile can obtain with the longer pump operation instead of a long-term heater operation.

IV. Conclusions

The coolant heating approach, which is one of the most effective cold start methods, was considered, and the effect of the heater power on cold start temperature distribution was investigated. The heater was operated during 10, 15, and 20 s, and time-temperature profiles of the case studies were followed for 600 s. The cell operated properly and produced current during the performed all cold start cases. Thus, the importance of the applied assisted method was exhibited. Warmer temperature profiles were achieved with the increase of heater operation duration, as expected. Nevertheless, the cell maintained operation around 12~13 °C for all cases. For this reason, it was noted that the longer heater operation leads to excessive energy consumption to heat the stack. Also, the longer pump operation may prefer since offered more smooth and proportional temperature distribution.

Acknowledgments

This research was supported by the Office of Scientific Research Projects of Çukurova University under Contract No. FDK-2020-12750.

References

Amamou A.A., Kelouwani S., Boulon L., Agbossou K., A comprehensive review of solutions and strategies for cold start of automotive proton exchange membrane fuel cells, IEEE Access, 4, 4989-5002, (2016).

DOE technical targets for fuel cell systems and stacks for transportation applications, https://www.energy.gov/eere/fuelcells/doe-technical-targets-fuel-cell-systems-and-stacks-transportation-applications, [Accessed on 04.02.2021].

Guo Q., Luo Y., Jiao K., Modeling of assisted cold start processes with anode catalytic hydrogen-oxygen reaction in proton exchange membrane fuel cell, International Journal of Hydrogen Energy, 38(2), 1004-1015, (2013).

Knorr F., Sanchez D.G., Schirmer J., Gazdzicki P., Friedrich K.A., Methanol as antifreeze agent for cold start of automotive polymer electrolyte membrane fuel cells, Applied Energy, 238, 1-10, (2019).

Luo Y., Jia B., Jiao K., Du Q., Yin Y., Wang H., Xuan J. Catalytic hydrogen-oxygen reaction in anode and cathode for cold start of proton exchange membrane fuel cell, International Journal of Hydrogen Energy, 40, 10293-10307, (2015).

Matsuoka N., Warm-up of fuel cell power plant, US Patent, US 7 108 928 B2, Sep. 19, (2006).

Mu Y-T., He P., Ding J., Chen L., Tao W-Q., Numerical study of the gas purging process of a proton exchange membrane fuel cell, Energy Procedia, 105, 1967-1973, (2017).

Ozden A., Shahgaldi S., Li X., Hamdullahpur F., A review of gas diffusion layers for proton exchange membrane fuel cells - With a focus on characteristics, characterization techniques, materials and designs, Progress in Energy and Combustion Science, 74, 50-102, (2019).

Sasmito A.P., Shamim T., Mujumdar A.S., Passive thermal management for PEM fuel cell stack under cold weather condition using phase change materials (PCM), Applied Thermal Engineering, 58, 615-625, (2013).

Optimization of Pretreatment of Olive Tree Biomass using Response Surface Methodology for Biological Hydrogen Production

[1*]Oznur Yildirim, [1]Dogukan Tunay, [1]Bestami Ozkaya, [1]Ahmet Demir
[1] Yildiz Technical University, Civil Engineering Faculty, Environmental Engineering Department, Istanbul, Turkey

* E-mail: y.oznur2014@gmail.com

Abstract
Lignocellulosic biomass is a promising biofuel source that is studied for recent years. However, the biofuel potential of lignocellulosic biomass relies on the pretreatment performance directly and sugar recovery yields and the pretreatment processes required to achieve that yield is significant. Therefore, pretreatment conditions were optimized with resonse surface methodology for biological hydrogen production. This study investigated the best pretreatment conditions for olive tree biomass to produce bio-hydrogen.

Keywords: Bio-hydrogen, olive tree biomass, clostridium sp., pretreatment, response surface methodology

I. Introduction

Energy consumption and benergy demand are also increasing due to the rapidly increasing population and excessive use of resources. Most of the energy in the world is derived from fossil fuels. However, interest in renewable energy has increased due due to both the environmental damage and the depletion of fossil resources (Raj and Singh, 2012). As a result of the use of hydrogen as a fuel, only water vapor is released. In addition, with zero carbon emissions, hydrogen is one of the most environmentally friendly fuels. Biological hydrogen production can be carried out by different methods such as fermentative hydrogen production, biophotolysis and photodecomposition (Das and Veziroglu, 2008). The most preferred one is the fermentative bio-hydrogen production method. Mostly *Clostridium* sp. Microorganism was used for fermentative hydrogen production (Lin et al., 2007; Wei et al., 2021).

Lignocellulosic wastes are valuable raw materials for biofuel production due to their affordable and low cost. They do not interfere with the food chain and have high energy potential. Although their composition varies according to the type of biomass, they generally contain 40% cellulose, 25% hemicellulose and 15% lignin (Jana et al., 2017). Olive tree biomass (OTB) is one of these lignocellulosic wastes. OTB, which is formed as a result of olive harvest and pruning of olive trees, is burned in small settlements and harms the environment. In addition, the incineration process is prohibited under circular economy directives. However, the cell wall of lignocellulosic wastes is recalcitrance. The reduction of cellulose and hemicellulose in biomass to sugar that can be used by microorganisms requires special pretreatment processes.

Response Surface Methodology (RSM) is a statistical analysis method which is used for the determination of the effect of different variables on the response variables. (Fonseca et al., 2020; Martínez-Patiño et al., 2019; Oliva et al., 2020). Various RSM designs help by allowing limited experimental studies to produce statistically significant results. RSM has many sub-models and the central composite design (CCD) is one of them.

The aim of this study was to evaluate the bio-hydrogen potential of chemical pretreated OTB. In this study, design expert software will be used and the data will be used to develop an experimental model that will increase the amount of reducing sugar. Three independent variables were selected for acid pretreatment and the effect of these variables on sugar yield were investigated.

II. Experimental Set-up and Procedure

Raw Material

Harvested Olive tree biomass were sampled from Balıkesir, Turkey. OTB was collected and dried at 40 degrees Celsius to extract moisture. The size of the dried wastes was reduced by shredding. Some of the shredded waste was used for characterization studies. The rest were stored in a dark and dry conditions for pretreatment and fermentation test sets. Moisture, ash, total solids, extractives, acid-soluble, and acid-insoluble lignin were all determined using National Renewable Energy Laboratory (NREL) techniques.

Pretreatment Procedure

Organic acid pretreatment was applied to OTB.The pretreatment tests of the raw materials were carried out at 10% w / v solid liquid ratio and the chemical concentration, pretreatment temperature and hydrolysis time ranged 1-5% v / v, 100-140 ºC and 20-60 min, respectively. During the pretreatment experiments, the biomass was subjected to high temperature and pressure using an autoclave. After the pretreatment process, the liquid phase and solid biomass mixture are separated by filtration. The solid residue was washed at least three times with distilled water and dried. The dried solid phase was stored for further studies. The liquid fraction called hydrolyzate was used for fermentation.

Response Surface Methodology

Experimental design is a mathematical method that predicts the change in the dependent variable called

"response variables" by replacing the conditions with several independent variables called "input variables". As a result of entering the data obtained as a result of the experiments into the software, a model is created by the software. Thus, the effect of the independent variables on the response variable is interpreted statistically. In this study, the optimization of the pretreatment conditions was done with the Central Composite Design (CCD) tool of the Response Surface Methodology (RSM). Three independent variables were chosen as acid concentration, pretreatment temperature and pretreatment time. The response variable was total reducing sugar.

Fermentation

Clostridium sp. was isolated previously (Koroglu et al., 2019) was used for bio-hydrogen production via dark fermentation. The stock culture was precultivated at 35°C an pH 7, in Reinforced Clostridial Medium (RCM) containing meat extract 10 g/L, peptones 5 g/L, yeast extract 3 g/L, D (+) glucose 5 g/L, starch 1 g/L, NaCl 5 g/L, sodium acetate 3 g/L, l-cysteine chloride 0.5 g/L, and agar–agar 1 g/L in distilled water. During precultivation, cells used to inoculate the fermentation reactor were harvested based on optical density of 0.2 at 600 nm (OD_{600}).

Batch experiments were carried out in serum bottles. The pretreatment hydrolysates were used as a glucose source. The bio-hydrogen production medium containing 0.85 g/L KH_2PO_4, 0.75 g/L K_2HPO_4, 0.003 g/L H_3BO_3, 0.2 g/L $MgSO_4 \cdot 7H_2O$, 0.001 g/L $Na_2MoO_4 \cdot 2H_2O$, 0.001 g/L $ZnSO_4 \cdot 7H_2O$, 0.002 g/L $MnSO_4 \cdot 4H_2O$, 0.0001 g/L $Cu(NO_3)2 \cdot 3H_2O$, 0.001 g/L $CaCl_2 \cdot 2H_2O$, 0.002 g/L EDTA, 0.012 g/L $FeSO_4 \cdot 7H_2O$, 0.004 g/L thiamine, 0.003 g/L biotin, 0.005 g/L p-aminobenzoic acid, 0.0065 g/L nicotinamide, 0.420 g/L glutamic acid, 0.001 g/L resazurin. The medium was flushed with oxygen-free nitrogen gas for 5 min. The reactors were stirred at 120 rpm and the temperature of 35°C. The prodced biogas were measured by syringes. All experiments were performed in triplicate.

III. Analysis

Total reduced sugar determination

For the achievement of pretreatment process was measured with the total sugar concentration and phenol sulfiric acid method was used (Suzanne N.S., 2010). Since the phenol sulfiric acid method was carried out with spectrophotometer, calibration curve was created. In this method, 5 mL of sulfuric acid and 50 µl of 80 % phenol (w/v) were added to 1:2 diluted samples (1 mL of sample+1 mL of DW) with distilled water. After addition of all reagents final solution was mixed with the vortex in a glass tube. After end of mixing, solution was waited in 10 minutes for cooling and after that it was kept in water bath (25 °C) during 10 minutes. Absorbance values were read in 490 nm and depending on created calibration curve concentration of the samples were determined.

Hydrogen measurement

In the study, hydrogen measurements were carried out by the gas chromatograph (GC) (Shimadzu GC2014, Tokyo, Japan). GC includes 2 m length and 1 mm inner diameter packed column (Restek, USA) with the thermal conductivity detector (TCD). In the measurements, argon gas was used as a carrier gas having 10 mL/min of flowrate. The detector, injector and column temperatures were operated in 200,110, and 80 °C respectively.

V. Conclusions

OTB is a promising renewable raw material for second generation biofuel production. The characterization of these feedstocks showed having high amounts of sugar inside them. In this study, CCD of RSM was applied for the optimization of pretreatment conditions to overcome the recalcitrance of lignocellulose and to enhance sugar recovery yield.

References

Das, D., Veziroglu, T.N., 2008. Advances in biological hydrogen production processes. Int. J. Hydrogen Energy 33, 6046–6057.

Fonseca, B.G., Mateo, S., Roberto, I.C., Sánchez, S., Moya, A.J., 2020. Bioconversion in batch bioreactor of olive-tree pruning biomass optimizing treatments for ethanol production. Biochem. Eng. J. 164. https://doi.org/10.1016/j.bej.2020.107793

Jana, A., Ghosh, D., Dasgupta, D., Mohapatra, P.K. Das, Mondal, K.C., 2017. Lignocellulosic Biomass Production and Industrial Applications.

Koroglu, E.O., Ozdemir, O.K., Ozkaya, B., Demir, A., 2019. An integrated system development including PEM fuel cell/biogas purification during acidogenic biohydrogen production from dairy wastewater. Int. J. Hydrogen Energy 44, 17297–17303. https://doi.org/10.1016/j.ijhydene.2019.01.291

Lin, P.-Y., Whang, L.-M., Wu, Y.-R., Ren, W.-J., Hsiao, C.-J., Li, S.-L., Chang, J.-S., 2007. Biological hydrogen production of the genus Clostridium: metabolic study and mathematical model simulation. Int. J. Hydrogen Energy 32, 1728–1735.

Martínez-Patiño, J.C., Gullón, B., Romero, I., Ruiz, E., Brnčić, M., Žlabur, J.Š., Castro, E., 2019. Optimization of ultrasound-assisted extraction of biomass from olive trees using response surface methodology. Ultrason. Sonochem. 51, 487–495. https://doi.org/10.1016/j.ultsonch.2018.05.031

Oliva, J.M., Negro, M.J., Álvarez, C., Manzanares, P., Moreno, A.D., 2020. Fermentation strategies for the efficient use of olive tree pruning biomass from a flexible biorefinery approach. Fuel 277. https://doi.org/10.1016/j.fuel.2020.118171

Suzanne N.S., 2010. Food Analysis Laboratory Manual.

Wei, X., Feng, J., Cao, W., Li, Q., Guo, L., 2021. Photo-biological hydrogen production by a temperature-tolerant mutant of Rhodobacter capsulatus isolated by transposon mutagenesis. Bioresour. Technol. 320, 124286.

Optimum Heating Method for the Assisted Cold Start Technique of PEM Fuel Cell

[1*]Alparslan Topcu, [2]Ahmet Özkan Kocamanoğlu, [3]Kadir Aydın, [4]Selahattin Çelik
[1] Alanya Alaaddin Keykubat University, Rafet Kayış Faculty of Engineering, Department of Mechanical Engineering, Alanya, Antalya, 07425, Turkey
[2] Hitit University, Faculty of Arts and Sciences, Department of Mathematics, Çorum, 19030, Turkey
[3] Çukurova University, Faculty of Engineering, Department of Mechanical Engineering, Adana, 01330, Turkey
[4] Niğde Ömer Halisdemir University, Faculty of Engineering, Department of Mechanical Engineering, Niğde, 51240, Turkey

* E-mail: alparslan.topcu@alanya.edu.tr, ahmetozkankocamanoglu@gmail.com, kdraydin@gmail.com, scelik@ohu.edu.tr

Abstract
The improved cold start capability of the PEM fuel cell is required for further commercialization. In the present study, the optimum heating strategy for the coolant circulation-assisted cold start technique was investigated. A single cell stack was used in the cold start tests, and tests were carried out at -10 °C. The stack was heated thanks to an external coolant circulation cycle by the anode side, the cathode side, and both sides. At the same time, the stack was operated with 0.5 lt/min H_2, and 1.5 lt/min air gases, and temperature distribution along the cathode bipolar plate was followed. Self anode heating strategy heated the cathode side until 10 °C. On the other hand, the self cathode heating approach was denoted as more effective in terms of quick temperature rise. As an overall conclusion, double side heating ensured homogeneous and smooth temperature increase and distribution.

Keywords: PEM fuel cell, cold start, assisted, heating strategy.

I. Introduction

PEM fuel cell temperature cannot increase by itself when operated at below zero temperature. The generated heat is not adequate level to rise the cell temperature above zero. Therefore, occurred water particles freeze without remove from the cell, and cover the catalyst surface. The chemical reactions decelerate and stop after a while due to the ice accumulates exist in the reaction areas. This phenomenon is known as 'cold start' which means start-up ability at subzero temperatures is a key barrier to the use of PEM fuel cell extensively (Zhou et al., 2014). Many assisted approaches are evaluated to improve cold start capability such as catalytic H_2/O_2 reaction, electric heating, coolant heating, etc. (Li et al., 2011). Moreover, the problem can solve with unassisted techniques by the optimization of operating parameters and stack components. For instance, numerical analysis was carried out by Wei et al. (2019, 2020) and effects of coolant flow rate, coolant capacity, and ambient temperature (Wei et al., 2019), flow stoichiometry, initial water distribution (Wei et al., 2020) on the cold start performance of PEMFC stack were investigated. Cold start tests were performed at -20 and -30 °C and coolant flow rate and tank capacity were found to insignificant effects on cell voltage (Wei et al., 2020). In other respects, a more uniform temperature distribution was ensured with higher flow rates. Li et al. (2021) studied the water management characteristics of the electrospun micro-porous layer (MPL), and electrospun MPL found better for water removal from the catalyst layer at cold start conditions. Similarly, electrospun catalyst specifications were studied by Liu et al. (2021).

Rapid and safe solutions can ensure via assisted applications although they required extra accessories (Ryu et al., 2012). St. Pierre et al. (2005) considered methanol combustion and reactant starvation approaches. They followed the temperature increase to 50 °C and noted that the heat losses may occur during startup. Besides, they applied gas purging at shutdown using dry hot and cold air. An experimental study was carried out by Li et al. (2011). They investigated the capability of coolant heating and insulator. Insulator material protected the stack for more than 1 day above zero. Also, they operated a coolant cycle with different power densities, and fast warm-up was supplied at high powers, as expected.

However, the coolant heating method needs energy balances although supply quick and homogeneous temperature dispersion. Otherwise, it leads to overconsumption (Luo and Jiao, 2018). In addition, it should respect the energy limitation targets assigned by DOE, (2020). For this reason, experimental studies were performed to determine the optimum heating strategy for the coolant circulation-assisted cold start technique, in the current study. The stack was heated thanks to an external coolant circulation cycle by the anode side, the cathode side, and both sides. Therefore, the effect of the heating side on the cold start performance was investigated by temperature pursue which was placed into the cathode bipolar plate.

II. Experimental

An electric heater (1.8 kW powered), thermostat, single-cell (25 cm^2 active area) stack, conditioning chamber equipment were used in the experimental set. The stack was placed into the temperature-controlled environmental cabinet, and ethanol (working fluid) coolant was heated by the heater and sent to the stack. The temperature was followed by five thermocouples which were placed into the cathode bipolar plates. A computer-controlled data logger (Measurement Computing, TracerDAQ Pro) was used to collect temperature data. The schematic of the thermocouple layout was illustrated in Fig. 1. T_1, T_3, and T_5 terms are assigned as temperature measurement points for the inlet, middle, and outlet sections of the cathode bipolar plate. T_2 and T_4 points are the other measurement points placed between T_1, T_3, and T_5 terminals, symmetrically.

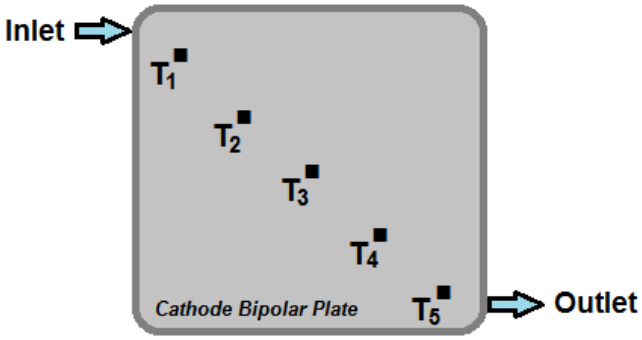


Fig. 1: Thermocouple measurement points

Three case studies were considered which are self anode heating, self cathode heating, and both sides heating techniques after the experimental installation was completed. At the same time, the stack was operated with 0.5 lt/min H_2 and 1.5 lt/min air, synchronously with the coolant cycle. The heater and pump were operated respectively 20 and 150 seconds when the cold start tests were begun. Thus, temperature magnitudes were recorded during the tests.

III. Results and discussions

Temperature distributions for case studies were presented in Fig. 2. The temperature was increased at 10 °C levels in self anode heating approach. The reactions that occurred in the stack maintained the cell temperature at ~6-7 °C grades. Self cathode heating was found better than self anode heating. The temperature reached ~26-27 °C levels instantly. Besides, the cell preserved its temperature above 10 °C. On the other hand, double side heating was supplied more smooth and homogeneous temperature distribution as seen in Fig. 2-c. The temperature achieved 30 °C degrees at the mid-section of the cell during warm-up. The cell kept its position at 15 °C levels after the pump shutdown.

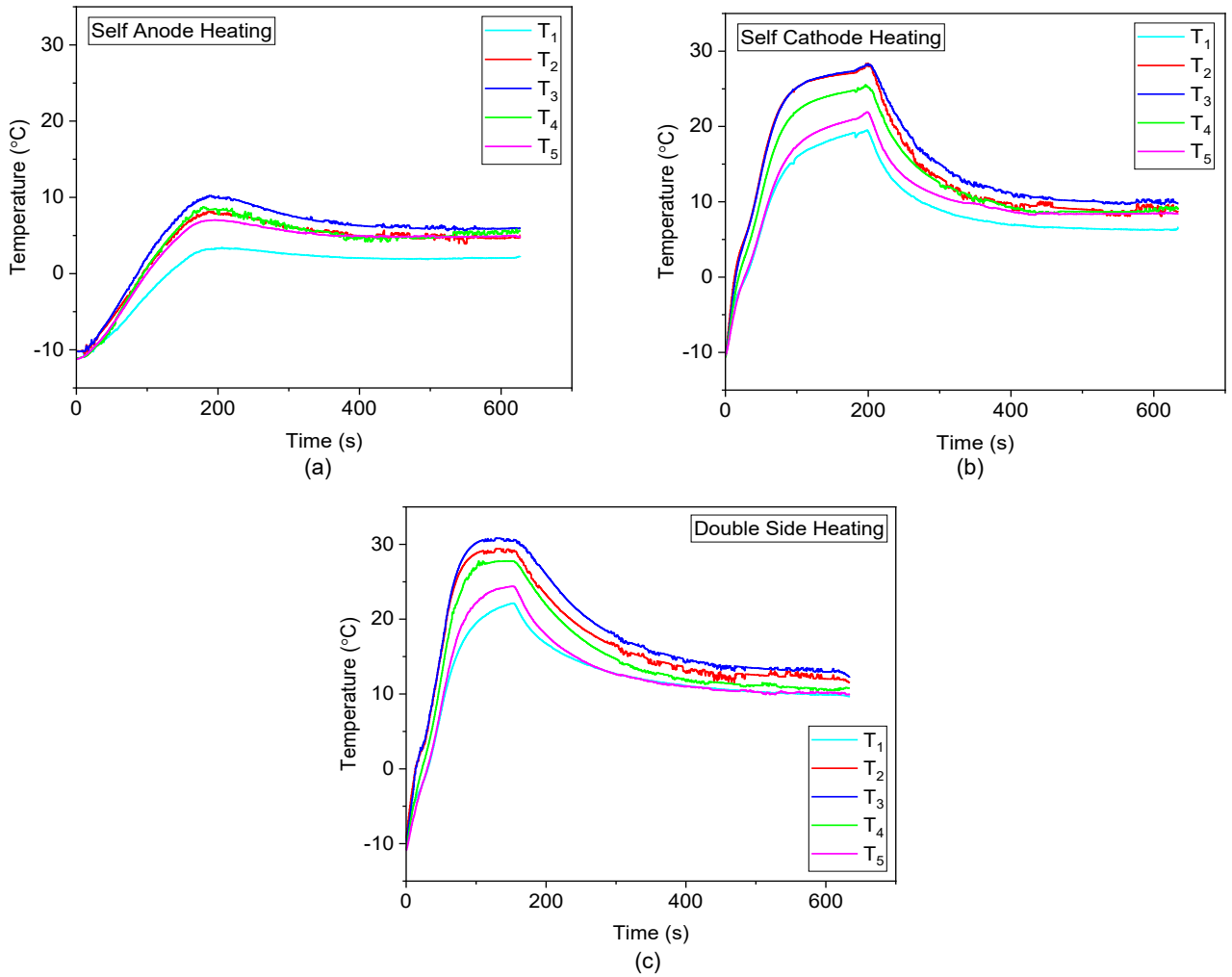


Fig. 2: Temperature distribution of cathode bipolar plate; a) self anode heating, b) self cathode heating, c) double side heating

The mid-sections are warmer than the side-sections for each case study. This indicated that the chemical reactions occurred at mid-region of the active area intensively. However, the cell successfully operated in three cases, too.

IV. Conclusions

Energy management strategies are needed to hinder excessive energy consumption to heat the stack. The application point of the heating mechanism was evaluated, in the current study. The cell was successfully operated under all three conditions. Self cathode heating strategy was found more effective than self anode heating approach, as expected. Directly heat the cathode side is easier than the transfer of heat from the anode side. Nevertheless, double side heating is useful to achieve uniform temperature dispersing. The temperature achieved 30 °C degrees at the mid-section of the cell during warm-up. The cell kept its position at 15 °C levels after the pump shutdown.

Acknowledgments

This research was supported by the Office of Scientific Research Projects of Çukurova University under Contract No. FDK-2020-12750.

References

DOE technical targets for fuel cell systems and stacks for transportation applications, https://www.energy.gov/eere/fuelcells/doe-technical-targets-fuel-cell-systems-and-stacks-transportation-applications, [Accessed on 04.02.2021].

Li C., Si D., Liu Y., Zhang J., Liu Y., Water management characteristics of electrospun micro-porous layer in PEMFC under normal temperature and cold start conditions, International Journal of Hydrogen Energy, 46(19), 11150-11159, (2021).

Li Y., Xu S., Yang Z., Li Y., Experiment and simulation study on cold start of automotive PEMFC, IEEE, International Conference on Electric Information and Control Engineering, (2011), DOI: 10.1109/ICEICE.2011.5776891.

Liu H., Si D., Ding H., Wang S., Zhang J., Liu Y., Cold start capability and durability of electrospun catalyst layer for proton exchange membrane fuel cell, International Journal of Hydrogen Energy, 46(19), 11140-11149, (2021).

Luo Y., Jiao K., Cold Start of proton exchange membrane fuel cell, Progress in Energy and Combustion Science, 64, 29-61 (2018).

Ryu S.P., Park S.S., Lee N.W., Kwon S.U., Choi S.H., Kim D.W., Current collector of end plate for fuel cell and method for controlling the same, US Patent, US 8 178 253 B2, May 15, (2012).

St-Pierre J., Roberts J., Colbow K., Campbell S., Nelson A., PEMFC operational and design strategies for Sub zero environments, Journal of New Materials for Electrochemical Systems, 8, 163-176, (2005).

Wei L., Dafalla A.M., Jiang F., Effects of reactants/coolant non-uniform inflow on the cold start performance of PEMFC stack, International Journal of Hydrogen Energy, 45(24), 13469-13482, (2020).

Wei L., Liao Z., Suo Z., Chen X., Jiang F., Numerical study of cold start performance of proton exchange membrane fuel cell with coolant circulation, International Journal of Hydrogen Energy, 44(39), 22160-22172, (2019).

Zhou Y., Luo Y., Yu S., Jiao K., Modeling of cold start processes and performance optimization for proton exchange membrane fuel cell stacks, Journal of Power Sources, 247, 738-748, (2014).

Synthesis and characterization of $NiFe_2O_4$-TiO_2 photocatalysts and their use for photocatalytic hydrogen production

[1*]Irem Firtina-Ertis, [2]Ozge Kerkez-Kuyumcu

[1] Bahçeşehir University, Faculty of Engineering and Natural Sciences, Energy Systems Engineering Department, Beşiktaş, İstanbul, 34353, Turkey
[2] Marmara University, Faculty of Engineering, Chemical Engineering Department, Göztepe, İstanbul, 34722, Turkey

* E-mail: irem.firtina@eng.bau.edu.tr

Abstract

In this study, magnetically separable $NiFe_2O_4$-TiO_2 photocatalysts were prepared by vapor thermal (VT) and solid-state (SS) methods. Ag^+ was also doped to modify the photocatalytic properties of the material. The characterization of the catalysts was performed with UV-Visible Diffuse Reflectance Spectroscopy (UV-Vis DRS), X-Ray Diffraction (XRD) and, Photoluminescence (PL). The photocatalytic methanol/water splitting was performed by using TiO_2, $NiFe_2O_4$, $NiFe_2O_4$-TiO_2, and $NiFe_2O_4$-TiO_2-Ag^+ photocatalysts under solar light irradiation. $NiFe_2O_4$-TiO_2-VT-Ag^+ showed enhanced photocatalytic behavior; it was obtained approximately 125 µmol H_2 / g-cat after 5 h reaction.

Keywords: $NiFe_2O_4$, TiO_2, photocatalysis, hydrogen

I. Introduction

Semiconductors have received comprehensive attention due to their potential application in photocatalytic H_2 production from water. Among the several semiconductors, TiO_2 is considered an excellent photocatalyst because of its high oxidizing power, high photosensitivity, good stability, nontoxicity, etc (Laokul et al., 2011) However, it has wide-bandgap for effective visible-light absorption, which significantly limits its application due to its fast recombination rate of electron (e-)/hole (h+) pair minimize the photocatalytic activity (Komaraiah et al., 2020). Therefore, it is needed to modify the catalyst to minimize the (e-)/(h+) pair recombination, reduce its bandgap to extend the optical absorption into the visible range. Hematite (α-Fe_2O_3) as one of the promising visible-light-responsive photocatalysts can be doped to TiO_2 due to its narrow bandgap but this is not enough for high conversion efficiency. At this point, spinel ferrites MFe_2O_4 (e.g. M= Ca, Cu, Co, Ni, Zn, or Mg) have been considered for the photocatalytic reactions due to their soft magnetism and narrow bandgap. Spinel ferrites have also great potential in combination with wide bandgap semiconductors such as TiO_2 to enhance the visible-light-responsive photoactivity due to their unique optical, electrical, and magnetic properties (Peng et al., 2012). Besides, these ferrite composites are proposed as magnetically separable catalysts to address the problem of photocatalyst separation (Kim et al., 2014).

In this study, $NiFe_2O_4$(NF), TiO_2, $NiFe_2O_4$-TiO_2 (NF-TiO_2), and $NiFe_2O_4$-TiO_2 -Ag^+ (NF-TiO_2-Ag^+) were synthesis by solid-state (SS) and vapor thermal (VT) method. The photocatalytic methanol/water splitting was performed by using the photocatalysts under solar light irradiation.

II. Experimental Procedure

A) Synthesis of $NiFe_2O_4$

$Fe(NO_3)_3.9H_2O$ and $Ni(NO_3)_2.6H_2O$ (2:1 = molar ratio) were dissolved in distilled water by a magnetic stirrer. Then, PEG 20000 was added to the above solution. After stirring, the NaOH solution was dropped until the pH value reached 11. The solution was kept under the ultrasonication for 30 min and then heated to 70°C and retained 1 h. Finally, the black precipitates cleaned with distilled water several times and dried at 70℃, calcined at 500 ℃ for 2 h.

B) Synthesis of TiO_2

A mixture of propanol and TEA (Triethanolamine) was prepared under magnetic stirring; TISOP (Titanium isopropoxide) was added slowly to this mixture (the molar ratio of Ti: TEA = 1:2). The vessel that contains the prepared solution was placed in a water bath in the stainless-steel autoclave and retained at 160℃ for 24 h, called the vapor thermal method (VT). The autoclave was cooled to room temperature, precipitation filtered, cleaned with propanol, and dried at 100℃. At the end, TiO_2 was calcined at 500 ℃ for 2 h.

C) Vapor Thermal (VT) Method for $NiFe_2O_4$-TiO_2:

As prepared $NiFe_2O_4$ was dispersed in propanol solution under ultrasonication for 10 min. Then, 0.5 ml NH_3 solution was added and kept under ultrasonication for 30 min (Solution A). A mixture of propanol and TEA was prepared under magnetic stirring; TISOP was added slowly to this mixture (Solution B). Solution B was dropped slowly to solution A and again kept ultrasonic water bath for 30 min. The same procedure was applied mentioned as the VT method for bare TiO_2 in the previous section. The amount of $NiFe_2O_4$ was chosen as 4% wt in the catalyst. As-prepared catalysts in this manner called NF-TiO_2-VT.

D) Solid-State Method (SS) for $NiFe_2O_4$-TiO_2:

As-prepared $NiFe_2O_4$ was dissolved in ethanol for 10 min. After the dispersion of the $NiFe_2O_4$, bare TiO_2 was added to this solution at a certain amount. This solution was kept under ultrasonication for 1 h. The mixture was collected. Powder catalyst was dried at 100℃ and calcined at 500 ℃ for 1 h. The amount of $NiFe_2O_4$ was chosen as 4% wt in the catalyst. As-prepared catalysts in this manner called NF-TiO_2-SS.

E) Ag^+ Impregnation:

Specific amounts were taken from NF-TiO_2-VT and NF-TiO_2-SS. $AgNO_3$ aqueous solutions were prepared to dope 1% wt Ag^+ to the catalysts by the impregnation. As-prepared catalysts in this manner are called NF-TiO_2-VT-Ag^+ and NF-TiO_2-SS-Ag^+.

III. Photocatalytic hydrogen production

Photocatalytic hydrogen production reactions were done in a homemade quartz reactor. Asahi Spectra MAX-303 Xenon device was used as a light source during the measurements. The light source was adjusted to 1000 Wm^2 by located the distance between the light source and the catalyst layer. Photocatalysts were suspended in a methanol/water mixture and let to settle down for 1 h, as a pretreatment procedure. After 3 h light irradiation, H_2 production was observed and collected throughout the following 2 h. The quantitative analysis was performed by replacing the hydrogen gas with water in the burette (Tanisik et. al., 2020).

IV. Results and discussions

In the literature, several methods have been used for the synthesis of $NiFe_2O_4$-TiO_2 such as mechanical mixing, solid-state dispersion, sol-gel, hydrothermal, etc. (Police et. al.,2014). In this study, a novel complex assisted vapor thermal (VT) method and solid-state method were used. After 5 h reaction time, NF-TiO_2-SS-Ag^+ showed 81 µmol H_2 / g-cat while NF-TiO_2-VT-Ag^+ showed 125 µmol H_2 / g-cat. According to the photocatalytic H_2 production results, the catalysts prepared by Ag+ doping for both methods have shown higher photocatalytic activity as seen in Fig. 1. Among the as-prepared catalysts, NF-TiO_2-VT-Ag^+ showed the best activity due to better contact between $NiFe_2O_4$ and TiO_2 by using the VT method. Moreover, Ag^+ doping has retarded e^- - h^+ recombination.

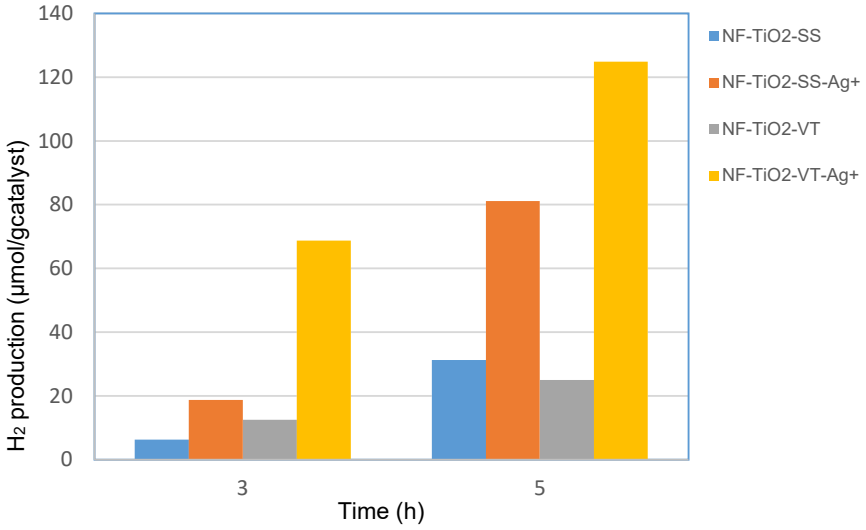


Fig. 1: Photocatalytic hydrogen production via NF-TiO_2 based catalysts.

V. Conclusions

$NiFe_2O4$-TiO_2 based photocatalysts are promising for photocatalytic H_2 production since they have three main properties: narrow bandgap, slow e^- - h^+ recombination rate, magnetic separation. For this reason, different wt% amounts of $NiFe_2O_4$ in the photocatalyst will be investigated in future work.

Acknowledgments

This work was supported by TUBITAK (Project Number: 216M386). The authors would like to thank Prof. Dr. Atıf Koca (Marmara University) for the experimental equipment support.

References

Kim, H. S. *et al.* (2014) 'Synthesis of magnetically separable core at shell structured NiFe2O4 at TiO2 nanomaterial and its use for photocatalytic hydrogen production by methanol/water splitting', *Chemical Engineering Journal*, 243, pp. 272–279. doi: 10.1016/j.cej.2013.12.046.

Komaraiah, D. *et al.* (2020) 'Photoluminescence and photocatalytic activity of spin coated Ag+ doped anatase TiO2 thin films', *Optical Materials*, 108(August), p. 110401. doi: 10.1016/j.optmat.2020.110401.
Laokul, P. *et al.* (2011) 'Characterization and magnetic properties of nanocrystalline CuFe 2O4, NiFe2O4, ZnFe2O 4 powders prepared by the Aloe vera extract solution', *Current Applied Physics*, 11(1), pp. 101–108. doi: 10.1016/j.cap.2010.06.027.
Peng, T. *et al.* (2012) 'Preparation of NiFe 2O 4 nanoparticles and its visible-light-driven photoactivity for hydrogen production', *Catalysis Communications*, 28, pp. 116–119. doi: 10.1016/j.catcom.2012.08.031.
Police, A. K. R. *et al.* (2014) 'CaFe2O4 sensitized hierarchical TiO2 photo composite for hydrogen production under solar light irradiation', *Chemical Engineering Journal*, 247, pp. 152–160. doi: 10.1016/j.cej.2014.02.076.
Tanişik, İ. *et al.* (2020) 'Solar-hydrogen production with reduced graphene oxide supported CdxZn1-xS photocatalysts', *International Journal of Hydrogen Energy*, 45(60), pp. 34845–34856. doi: 10.1016/j.ijhydene.2020.04.035.

Investigation of Effective Promoters and Iron Precursors in FT Synthesis over TiO_2 Supported Iron Catalysts

[1,2]Utku Burgun, [1,2]Hadi Zonouz, [1,2]Hasan Can Okutan, [1,2]Husnu Atakul, [2,3]Selim Senkan,[1,2]Alper Sarioglan, [1,2]Gamze Gumuslu Gur

[1] Istanbul Technical University, Chemical Engineering Department, 34467 Istanbul,Turkey
[2] ITU-SENTEK, ITU Synthetic Fuels and Chemicals Technology Center, 34467 Istanbul,Turkey
[3] University of California, Los Angeles, Chemical Engineering Department, LA, USA

* E-mail: utku.burgun@itu.edu.tr

Abstract
Light olefins are significant key intermediates which are used much in daily modern life. Traditionally their production can be obtained by steam cracking of naphtha which indicates dependence of petroleum source (Torres, 2013). Fischer Tropsch synthesis provides an alternative technology to produce light olefins directly. For this purpose, 90 Fe-based TiO_2 supported catalysts with different promoters were synthesized. In synthesis, two different Fe precursors were used; Ammonium Iron Citrate and Iron Nitrate. Performance screening experiments were performed at atmospheric pressure using a High Throughput Catalyst Test System. The results showed that Bi, Ga and W precursors lead to higher FT-Olefin performance and Fe source was a significant parameter altering the performance.

Keywords: Light olefins, High Throughput, atmospheric pressure, Fischer-Tropsch

I. Introduction

Conventional energy production routes utilize natural gas, petroleum and coal. Among them, it is estimated that petroleum might be depleted by 2050 with the increase of the human population and petroleum-based product demand. In order to provide sustainability in modern life, new/alternative routes have been developed to produce renewable liquid fuels and petroleum-based products (Gholami, 2017). In this regard, Fischer Tropsch (FT) synthesis emerges as a route that converts the synthesis gas ($CO+H_2$) derived from biomass, coal or alternative feedstocks into liquid fuels and value-added chemicals such as light olefins (Barrios, 2020). Light olefins such as ethylene, propylene and butylene are key ingredients of chemical industry (Torres Galvis, 2013). By using FT method, products can be obtained free from undesirable aromatics, nitrogen and sulphur (Barrios, 2020).

Fe, Co and Ru are known as highly active metals in FT synthesis. Among these metals, Fe is mostly selected for light olefins production because of its cost, higher activity, higher selectivity to light olefins, and lower selectivity to methane (Nie, 2019). Electronic and structural promoters are used to increase light olefins selectivity, activity, active metal reducibility and dispersion. Alkali metals, transition metals, rare earth metals, post transition metals can be used to enhance the activity of Fe. (Torres Galvis, 2013).

In this study, we focused on investigating the effect of promoters to enhance the selectivity to light olefins using a High Troughput Catalyst Test System (HTC). HTC is an effective tool that provides catalyst performance tests rapidly by requiring small amount of catalyst and thus it facilitates the discovery of new promosing catalysts. The aim of this study is to explore the effect of different amounts of Mn, Zn, Bi, Ga, W, Cu, Ho, La and Ce metals on TiO2 suppported Fe catalysts by screening in HTC. In catalyst preparation, catalysts were divided into two groups with respect to the iron precursor which are Ammonium Iron Citrate and Iron Nitrate.

II. Experimental Set-up and Procedure

HTC is a compact test system which has 8 mass flow controllers, a mass spectrometer (MS), a micro GC, 4 reactor blocks surrounded with heaters each having 20 micro reactors as shown in Figure 1 and 2. HTC facilitates testing of 80 catalysts sequentially. Dimensions of reactor block are 75 x 36 mm and diameter of micro reactor is 4 mm. Thus, it only requires 10-20 mg of catalysts to be tested.



Fig 1: HTC test system



a) b)

Fig 2: a) Reactor chamber b) reactor block

The product range of FT synthesis starts from lower chain hydrocarbons to long chain hydrocarbons. A Micro GC integrated to the system was used to analyse the productsMicro GC is equipped with Q-Bond and Molecular Sieve,and requires 3 min of analyse time.

In catalyst preparation, TiO_2 was used as support material. The following metal precursors were used as promoter source in catalyst synthesis: $Mn(NO_3)_2.4H_2O$, $Zn(NO_3)_2.6H_2O$, $Zn(C_5H_7O_2)_2.xH_2O$ (zinc acetylacetonate, $Zn(acac)_2$)), $Bi(NO_3)_3.5H_2O$, $Ga(NO_3)_3$,xH_2O, WO_3, $Cu(NO_3)_2.3H_2O$, $C_4H_8CuO_5$ (cupric acetate monohydrate, CuAc), $Ho(NO_3)_3.5H_2O$, $La(NO_3)_3.6H_2O$, $Ce(NO_3)_3.6H_2O$. In order to investigate the effect of active metal precursors, two different iron precursors, Ammonium Iron Citrate (AIC) and Iron Nitrate, were used. Active metal and promoter precursors were firstly dissolved in appropriate amount of Nitric Acid added deionized water. Then, the metal solutions were impregnated onto TiO_2 support. Prepared mixtures were stirred for 2 h at room temperature by using ultrasonic bath and stirring rod. After that, catalyst solutions were dried at 100 °C overnight and then calcined at a heating rate of 5 °C/min with dry air to the set point of 430 °C by holding for 3 h. Total number of promoted and unpromoted catalysts prepared as described above was 90. While Fe content in catalyst was kept 20 wt. %, promoter contents were ranged 0.1, 0.5, 1 and 2 wt. %.

Prior to FT reaction, catalysts were reduced at 350 °C under H_2:N_2=1:1 atmosphere for 4 h. The activity tests were performed under 310 °C, 1 bar and H_2:CO= 2:1. Since performance trends of all catalysts were levelled off at 6th h, results at this point have been considered.

III. Analysis

The results obtained from the FT reaction were analysed and it was found that all catalysts have similar CO conversion (around ~6 %) at atmospheric pressure. For this reason, conventional selectivity calculations could not be applied. Instead, equation (1) and (2) were taken into account that to compare the performance of catalysts.

$$\frac{\text{Produced Hydrocarbon (HC)}}{CH_4 + CO_2} \text{ x } 100 \quad (1)$$

$$\frac{\text{P roduced Light Olefins } (C_2^{=} - C_3^{=})}{Total\ Product} \text{ x } 100 \quad (2)$$

IV. Results and discussions

The results obtained from 90 catalysts are shown in the figure 3. According to the results, it was explicitly seen that AIC catalysts showed higher performance than FeN in most promoters. In this map, 1 wt. % of Bi, Ga, W on AIC/TiO_2 showed higher performance among 90 catalysts regarding both ratios of $HC/(CH_4 + CO_2)$ and ($C_2^{=}$-$C_3^{=}$)/Total Product. The Bi promoted catalyst results are consistent wih the the study of Gu (2018). It was reported that Bi promoted Fe/CNT catalyst showed higher activation both at atmospheric pressure and 10 bar. In case of Ga promoter, it was reported that addition of Ga onto unsupported Fe catalyst had reverse effect on the iron carbidization which is known as the active phase in FT synthesis. Lowering the iron carbide phase resulted in decreased CO conversion and lowered olefin selectivity (Beasley, 2018). Our results can be interpreted as TiO_2 support might have suppressed the reverse effect of Ga. W pomoters has been studied by Barrios (2020) on Fe/SiO2 catalyst. It was reported that addition of W metal improved the CO conversion (Barrios, 2020). But there is lack of detailed information about selectivity to hydrocarbons on W promoted Fe catayst in literature.

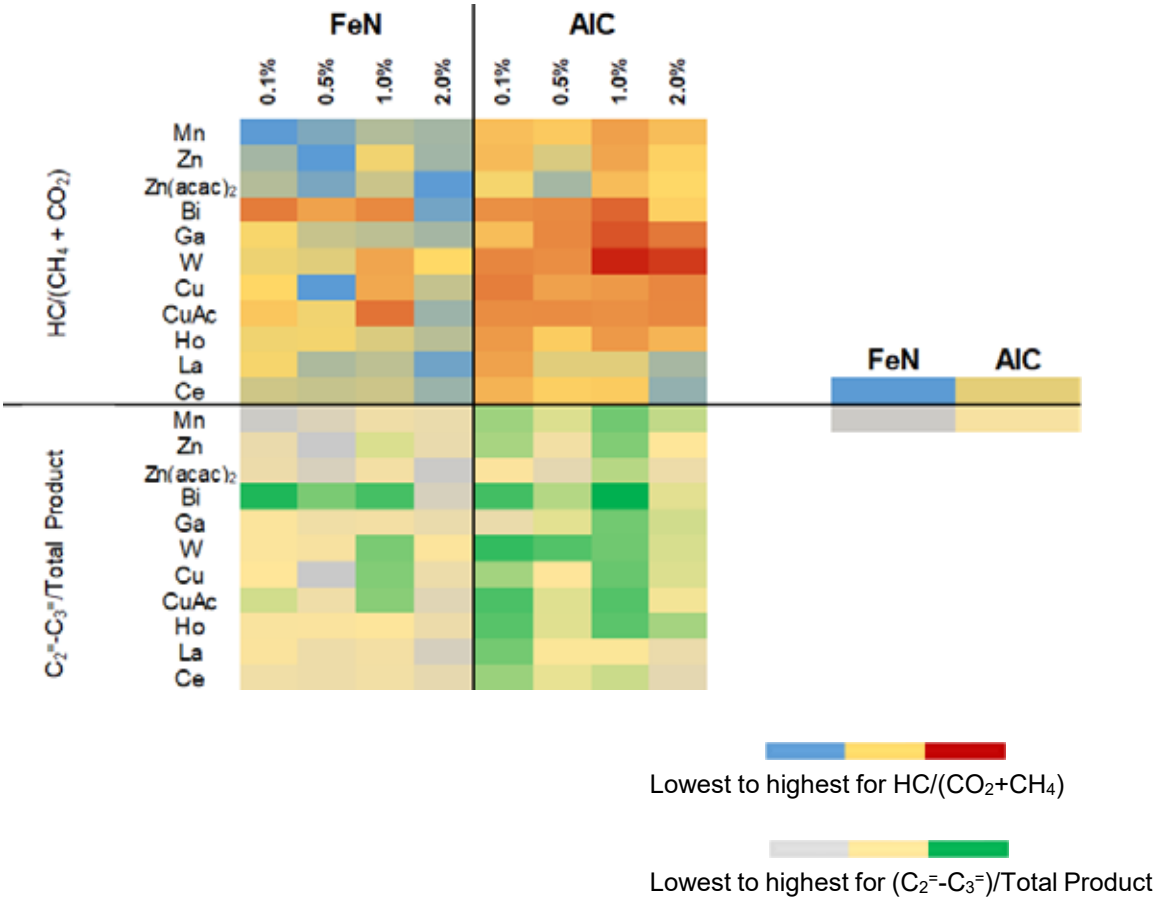


Fig 3: Experimental results (310 °C, 1 bar and H2:CO= 2:1, 7 mL/min)

V. Conclusions

90 catalysts were tested at atmospheric pressure in HTC. Among them, Bi, Ga and W promoted AlC/TiO_2 catalyst have showed higher performance. In further studies, these catalysts will be tested at pressurized conditions so that the effect of pressure and the catalyst performance at FT conditions could be understood. Screening catalysts in HTC is a significant way to discover new promising catalyst.

Acknowledgements

This research was supported by the TÜBİTAK ARDEB 1003 Program, project no 217M924.

References

Barrios A.J., Gu B., Luo Y., Peron D.V., Chernavskii P.A., et al. Identification of efficient promoters and selectivity trends in high temperature Fischer-Tropsch synthesis over supported iron catalysts, Applied Catalysis B: Environmental, 273, 119028, (2020).

Beasley C., Gnanamani M.K., Hamdeh H.H. et al. Effect of Gallium Additions on Reduction, Carburization and Fischer–Tropsch Activity of Iron Catalysts. Catal Lett 148, 1920–1928 (2018).

Gholami Z, Asmawati Mohd Zabidi N. Gholami F., Ayodele O.B. and Vakili M. The influence of catalyst factors for sustainable production of hydrocarbons via Fischer-Tropsch synthesis, Reviews in Chemical Engineering, 33, 4, 337-358, (2017).

Gu B., Ordomsky V. V., Bahri M., et al., Effects of the promotion with bismuth and lead on direct synthesis of light olefins from syngas over carbon nanotube supported iron catalysts, Applied Catalysis B: Environmental, 234, 153-156, (2018).

Nie C., Zhang H., Ma H. et al. Effects of Ce Addition on Fe–Cu Catalyst for Fischer–Tropsch Synthesis. Catal Lett 149, 1375–1382 (2019).

Torres Galvis H. M., de Jong K. P., Catalysts for Production of Lower Olefins from Synthesis Gas: A Review, 3, 9, 2130-2149, (2013).

Kinetic Study of Ni-Co/Al_2O_3 Catalyst Used in Hydrogen Rich Gas Production from Olive Pomace with Thermogravimetric Analysis

[1]Fahriye Dönmez, [1]Vildan Aker, [1*]Nezihe Ayas
Eskişehir Technical University, Engineering Faculty, Department of Chemical Engineering, Eskişehir, 26555, Turkey

* E-mail: nazcan@eskisehir.edu.tr

Abstract
This study focused on the investigation of olive pomace pyrolysis without catalyst and with Ni-Co/Al_2O_3 catalyst by thermogravimetric analysis method. Thermogravimetric (TG) and Derivative Thermogravimetry (DTG) curves were obtained at different heating rates (5, 10 and 15°C/min) between 30-900°C. TG thermogram profiles were drawn to determine kinetic parameters using the model-free method. Activation energies at different conversion rates were calculated by Flynn-Wall-Ozawa (FWO) method and average activation energies without catalyst and Ni-Co/Al_2O_3 were found as 166.72 kJ/mol and 154.40 kJ/mol, respectively.

Keywords: Biomass, Olive Pomace, Pyrolysis, Kinetics, Ni-Co/Al_2O_3

I. Introduction

Biomass is a clean, renewable, and sustainable resource that is one of the alternatives to fossil fuels. The utilization of biomass as a raw material contributes to the diversification of energy production methods and the reduction of greenhouse gases (Alves etal. 2019). Biomass is converted into useful products through various conversion processes such as pyrolysis, combustion, liquefaction, and gasification. Among these processes, pyrolysis is the thermochemical conversion in which organic materials are converted into solid char, liquid, and gas in the absence of oxygen (Ghouma etal. 2017). The amount of solid, liquid, and gas products depends on reaction parameters such as temperature and heating rate etc. Above 500 °C, CO, H_2, methanol and acetone are formed from the reaction of carbon and water vapor (Kabakçı and Aydemir, 2013). Kinetic model allows determination of thermolysis behavior, design of necessary equipment, determination of reaction conditions, saving time and cost (Özveren and Özdoğan, 2013). Thermoanalytical techniques, especially thermogravimetric analysis (TGA) and derivative thermogravimetry (DTG) provide this information simply and accurately (Aboulkas etal. 2009). While TGA results are used for kinetic analysis of thermolysis processes, activation energy is calculated by iso transformation methods such as Friedman (FR), Flynn - Wall - Ozawa (FWO), Kissinger - Akahira - Sunose (KAS), Starink (STK), and Vyazovkin (VYA) (Alves etal. 2019. In literature, numerous works describe TGA based kinetics of biomass such as apricot kernel (Manic etal. 2020), rice husk (Kumar etal. 2020), fine-fruit shell (Alves etal. 2019), hazelnut husk (Ceylan and Topçu, 2014), olive pomace with Refuse Derived Fuel (Ghouma etal. 2017), and olive oil pomace (Özveren and Özdoğan, 2013, Kabakçı and Aydemir, 2013). Although there are studies on the kinetics of olive pomace, there is no thermochemical kinetic study of olive pomace with a catalyst. In this study, olive pomace as a biomass source and Ni-Co/Al_2O_3 catalyst synthesized by impregnation method was used. The activation energy was determined by the kinetic study (FWO method) performed with the data obtained by thermogravimetric analysis.

II. Experimental Set-up and Procedure

Olive pomace was obtained from an olive oil factory in Turkey. Before experimental studies, it was ground with the mill. The Ni-Co/Al_2O_3 catalyst used in the study was synthesized and characterized by our authors in the previous study (Aker and Ayas, 2019).

Thermogravimetric analysis: The thermal behavior of olive pomace was examined with a Perkin Elmer STA 6000 TG analyzer. Approximately 10 mg of sample for each test was placed on the analyzer with a ceramic pan. The catalyst rate was chosen 20% by weight and the nitrogen flow rate was kept constant at 50 mL/min. Analyzes were performed at three different heating speeds (5, 10 and 15°C/min) at the temperature range of 30-900°C and the mass loss of the sample was recorded as TG and DTG.

Kinetic analysis: The data obtained result of the thermogravimetric analysis were used to calculate the kinetic parameters. The pyrolysis process of biomass is a decomposition reaction and the products obtained by pyrolysis of biomass are coke, volatile substances (can be liquefied) and gases. The rate equation of this thermal degradation reaction is calculated by Eq. 1.

$$\frac{d\alpha}{dt} = K(T)f(\alpha) \quad (1)$$

Where K(T) is a temperature-dependent reaction rate constant and f(α) is a dependent kinetic model function. According to Eq. 2, there is a dependence like Arrhenius between K(T) and temperature.

$$K(T) = A\exp\left(-\frac{Ea}{RT}\right) \quad (2)$$

Where A is the pre-exponential factor (generally assumed to be temperature independent), Ea is the apparent activation energy, T is the absolute temperature, and R is the gas constant. Conversion is calculated by Eq. 3.

$$\alpha = \frac{m_0 - m}{m_0 - m_f} \quad (3)$$

Where, m_0, m and m_f are the initial amounts of biomass, the amount of biomass at time t and the final amount of biomass, respectively. For non-isothermal conditions, when the temperature changes over time with a constant heating rate β=dT/dt, Eq. (1) is changed as follows:

$$\beta \frac{d\alpha}{dt} = A \exp\ (-\frac{Ea}{RT}) f(\alpha) \quad (4)$$

Kinetic analysis techniques are classified into three groups: model fitting, iso-conversional (i.e. model-free), and nonlinear regression analysis. In model-free methods, kinetic parameters are determined without knowledge of the reaction mechanism. This method assumes a constant degree of conversion that the reaction rate depends solely on temperature. The iso conversion method proposed by Flynn and Wall and Ozawa (FWO) is given by Eq. 5.

$$ln\beta = ln\frac{AEa}{Rg(x)} - 5.331 - 1.052\frac{Ea}{RT} \quad (5)$$

For x = constant, the lnβ vs (1/T) plot from thermograms recorded at various heating rates should be a straight line its slope can be used to evaluate the apparent activation energy (Aboulkas etal. 2009).

III. Results and discussions

The thermal behavior of olive pomace during the thermochemical process was investigated with TG analyser at different heating rates (5, 10 and 15°C/min). Fig. 1 shows that the thermogram curves showed similar behavior at different heating rates and the mass change was quite low after about 500 °C. The similarity of the TG curves indicates that the degradation reaction of olive pomace is independent of the heating rate and the use of catalysts increased the formation of char.

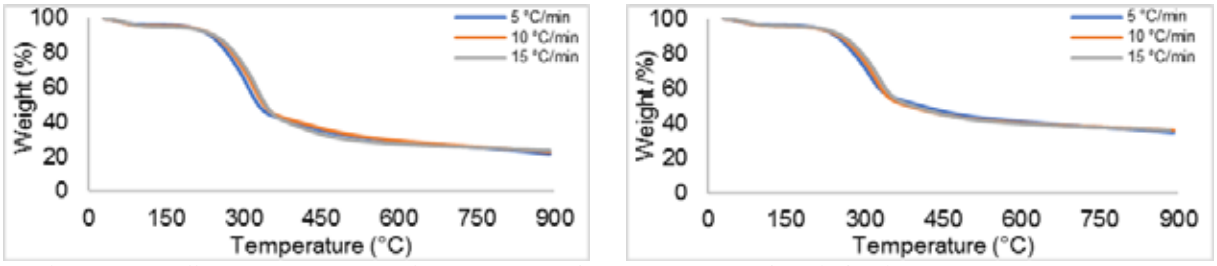


Fig. 1. TG curves at different heating rates of olive pomace a) without catalyst b) Ni-Co/Al_2O_3

DTG curves give more precise results in determining the points at which the reaction reaches its start, end, and maximum mass loss rate. Figure 2.a-b shows that the rate of mass loss increases with the increase of the heating rate in the experiments with and without catalyst. According to Figure 2.a, when the heating rate increased from 5°C/min to 15°C/min, the rate of mass loss from 2.89 to 6.83 %/min. When the catalyst was used (Figure 2.b), a decrease in the rate of mass loss was observed. For both cases, the starting, ending and peak temperature values increased as the heating rate increased.

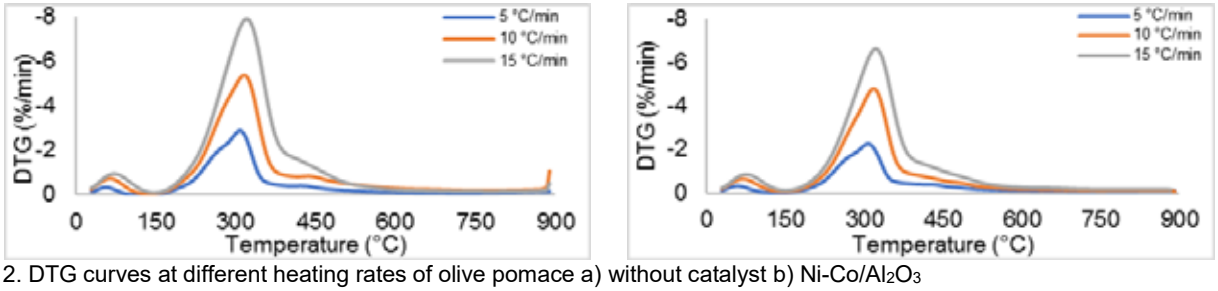


Fig. 2. DTG curves at different heating rates of olive pomace a) without catalyst b) Ni-Co/Al_2O_3

The activation energy was calculated by FWO method using Eq. 5. Due to the low correlation values in the conversion degrees, values above 0.7 are not included. -Ea/R values are derived from the slope of the linear graphs in Figure 3. The activation energies of kinetic study performed with and without catalyst are listed in Table 1.

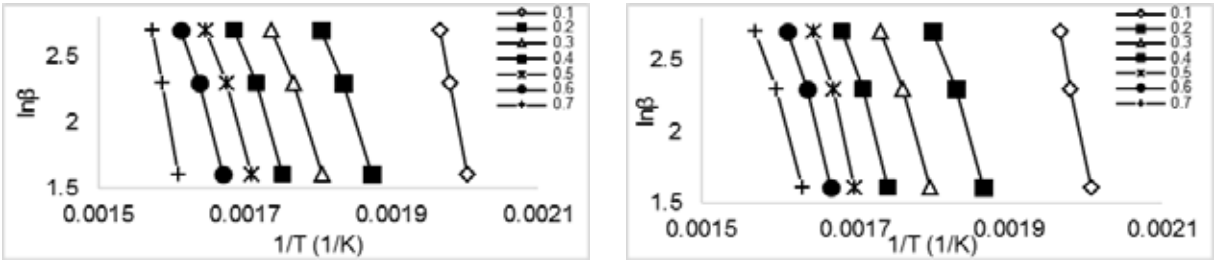


Fig. 3: Linear regression graphs using the FWO method a) without catalyst and b) Ni-Co/Al_2O_3.

Tab. 1: Activation energy for olive pomace

Method	Without catalyst		Ni-Co/Al_2O_3	
α	R^2	Ea (kJ/mol)	R^2	Ea (kJ/mol)
0.1	*0.9995*	*239.09*	*0.9989*	*214.50*
0.2	*0.9934*	*125.56*	*0.9916*	*133.51*
0.3	*0.9898*	*125.73*	*0.9923*	*134.32*
0.4	*0.9872*	*133.34*	*0.9872*	*144.87*
0.5	*0.9908*	*141.38*	*0.9838*	*158.94*
0.6	*0.9933*	*154.80*	*0.9900*	*153.49*
0.7	*0.9994*	*247.14*	*0.9943*	*141.17*
Mean		***166.72***		***154.40***

Kinetic analysis results showed that activation energy is highly conversion dependent and biomass pyrolysis is a complex process consisting of different reactions. When the Ea values calculated with the FWO model were examined, the Ea value increased continuously with the increase of the 'α' value in the experiments without catalyst. On the other hand, in the experiments with catalysts, while the value of 'α' increased from 0.2 to 0.5, the value of Ea increased, and after 0.5 the value of Ea decreased. The Ni-Co/Al_2O_3 catalyst reduced the activation energy from 166.72 kJ/mol to 154.40 kJ/mol. Weihong et al., in their study with sawdust using KOH and K_2CO_3 as catalysts, have been reported to reduce the activation energy of the catalyst (Weihong etal. 2019). Kumar et al., examined the kinetic mechanism of rice husk and the mean Ea value calculated from FWO method was 224.71 kJ/mol (Kumar etal. 2020). Manic et al., reported the average Ea values for the apricot kernel as 193.06 kJ/mol (Manic etal. 2020). The mid-activation energy values calculated for olive pomace (166.72 kJ/mol) in this study show that it can be used as a potential biomass fuel. Furthermore, it is clear that the Ni-Co/Al_2O_3 catalyst reduce the activation energy.

IV. Conclusions

In this study, pyrolysis of olive pomace was carried out by thermogravimetric analysis and its kinetic studies were examined with the data obtained from TG analysis. According to the results; The Ni-Co/Al_2O_3 catalyst reduced the activation energy from 166.72 to 154.40 kJ/mol. These kinetic data will be useful for modeling, designing and developing the thermochemical system for olive pomace. In addition, in the previous work of our authors, the characterization of Ni-Co/Al2O_3 catalyst synthesized by the impregnation method was investigated and the activity studies were achieved in the production of hydrogen-rich gas by olive pomace gasification. Future studies aim to conduct an experimental study of the pyrolysis of olive pomace and characterize the resulting products, as well as develop the study with other models and compare it with the gasification kinetics of olive pomace.

References

Aboulkas A., Nadifiyine M., Benchanaa M., Mokhlisse, A., Pyrolysis kinetics of olive residue/plastic mixtures by non-isothermal thermogravimetry, Fuel Processing Technology, 90(5), 722-728, (2009).

Aker V., Ayas N., Ni-Co Bimetallic Catalyst Synthesis by Co-impregnation Method for Hydrogen Rich Gas Production from Olive Pomace, International Journal of Materials, Mechanics and Manufacturing, 7(1), 16-20, (2019).

Alves J. L. F., Da Silva J. C. G., da Silva Filho V. F., Alves R. F., de Araujo Galdino W. V., Andersen S. L. F., De Sena R. F., Determination of the bioenergy potential of Brazilian pine-fruit shell via pyrolysis kinetics, thermodynamic study, and evolved gas analysis, BioEnergy Research, 12(1), 168-183, (2019).

Ceylan S., Topçu Y., Pyrolysis kinetics of hazelnut husk using thermogravimetric analysis, Bioresource technology, 156, 182-188, (2014).

Ghouma I., Jeguirim M., Guizani C., Ouederni A., Limousy L., Pyrolysis of olive pomace: degradation kinetics, gaseous analysis and char characterization, Waste and biomass valorization, 8(5), 1689-1697, (2017).

Kabakcı S. B., Aydemir H., Pyrolysis of olive pomace and copyrolysis of olive pomace with refuse derived fuel, Environmental Progress & Sustainable Energy, 33(2), 649-656, (2014).

Kumar M., Mishra P.K., Upadhyay S.N., Thermal degradation of rice husk: Effect of pre-treatment on kinetic and thermodynamic parameters, Fuel, 268, 117164, (2020).

Manić N., Janković B., Pijović M., Waisi H., Dodevski V., Stojiljković D., Jovanović V, Apricot kernel shells pyrolysis controlled by non-isothermal simultaneous thermal analysis (STA), Journal of Thermal Analysis and Calorimetry, 1-15, (2020).

Özveren U., Özdoğan Z. S., Investigation of the slow pyrolysis kinetics of olive oil pomace using thermo-gravimetric analysis coupled with mass spectrometry, Biomass and Bioenergy, 58, 168-179, (2013).

Weihong Z., Bin B., Guanyi C., Longlong M., Beibei Y. Thermogravimetric characteristics and kinetics of sawdust pyrolysis catalyzed by potassium salt during the process of hydrogen preparation. International Journal of Hydrogen Energy, 44(30), 15863-15870, (2019).

The Novel Synthesis Route Of $BIVO_4$ And Photocatalitic Activity On Water Splitting

[1] Fatih Tezcan, [2] Meltem Kahya Düdükcü, [2] Gülfeza Kardaş*
[1] Mersin University, Science and Letters Faculty, Chemistry Department, Çiftlikköy, Mersin, Turkey
[2] Çukurova University, Science and Letters Faculty, Chemistry Department, Balcalı, Adana, Turkey

*E-mail: fatihtezcan3935@gmail.com

ABSTRACT

Highly efficient photoelectrodes play a key role for photoelectrochemical hydrogen production via solar irradiation. One of the most promising $BiVO_4$ semi-conductor as a photoanode in photoelectrochemical cells. In this paper, $BiVO_4$ is obtained, Bi metal is originally synthesized with potentiostatic deposition containing 5.0 mM $Bi(NO_3)_3$, 0.1 M citric acid (pH =4,7) at different temperature (30, 40, 50 and 60 °C) on ITO, which is coated $VO(acac)_2$ by drop casting, and calcinated at 500 °C for 2 hours. The various electrode surface morphology is depicted FESEM images, and the crystalline structure is examined by XRD analysis. $BiVO_4$ electrodes flat band potential is obtained by Mott-Shottky measurement. The light absorption, bonding vibration and photocatalytic performance is performed by Uv-vis spectroscopy, Raman spectroscopy and lineer sweep voltammetry under 100 mW cm^{-2} solar light in 0.1 M Na_2SO_3 and 0.1 M phosphate buffer (pH=7), respectively. $BiVO_4$ electrodes crystal structure is defined monoclinic phase by XRD. $BiVO_4$ 30 °C photoelectrode is shows the utmost photocurrent response of 0.803 mA cm^{-2} vs. NHE under simulated solar light.

Keywords: Photoelectrochemical Hydrogen Production, $BiVO_4$, Water Splitting,

INTRODUCTION

Global warming has reached irreversible level for our earth because of carbon emission has dramatically increased due to huge fossil-based energy consumption by humankind. Hydrogen can be altered the dreadful condition in favour of photoelectrochemical hydrogen production by solar power. The eco-friendly process is produced zero CO_2 emission and it is enable to use renewable solar energy resource. Photoelectrochemical cells (PECs) produce hydrogen with solar irradiation as a clean energy process and ıt is consist of photoanode and photocathode in mild/alkaline electrolyte. In the literature, a lot of research groups have studied various binary transition metal-oxide such as TiO_2 [1], ZnO[2], Fe_2O_3[3], Cu_2O[4] in PECs. Although, the both of TiO_2 and ZnO are robust and simply synthesis methods, solar-to-hydrogen conversion efficiency (STH) is quite low value of %1.5, %1.2 [5]. Furthermore, Fe_2O_3 and Cu_2O are cheaper, visible absorption solar light and more photocatalytic response on water splitting, but they suffer from photocorrosion, which is reduced photoelectrode lifetime in PECs. Therefore, researches have canalized multinary semiconductors owning to related drawbacks of binary metal-oxide. Multinary semiconductors have obtained proportional combination of metals with various synthesis technique, such as $BiVO_4$[6], $CuWO_4$[7], $FeVO_4$[8], $CuInS_2$[9] $NiGa_2O_4$[10]. One of the most advantage of multinary semiconductors is increased the valance band (VB) energy level due to non-metals participate into the lattice of the metal oxide semiconductors. Consequently, shifting energy level of VB enhances photochemical decomposition of water to hydrogen evolution reaction (HER) and oxygen evolution reaction (OER). $BiVO_4$ is a n-type semiconductor and absorption of the solar spectrum in visible region, thermodynamically stable monoclinic phase, relatively more negative flat band potential compare with HER energy level, maximum theoretical photocurrent density of 7.5 mA cm^{-2}.vs NHE, promising electrode utilize as a photoanode in PECs. $BiVO_4$ have obtained with diverse synthesis technique, including spin coating[11] , electrospray deposition [12], hydrothermal [13] and electrochemical deposition [14]. $BiVO_4$ synthesis via electrochemical offers benefit surface morphology modification and thickness control of the electrode at nano scale.

The main aim of the paper is appear to $BiVO_4$ photocatalytic performance synthesized from Bi metal on ITO at different temperature (30, 40, 50 and 60 °C) by cathodic electrochemical deposition. In addition, the electrochemical deposition bath is applied the first time including, 5.0 mM $Bi(NO_3)_3$ and 0.1 M citric acid (pH =4,7).

EXPERIMENTAL

Bismuth(III) nitrate pentahydrate ($Bi(NO_3)_3.5H_2O$), citric acid, nitric acid, vanadylacetylacetonate ($VO(acac)_2$), and dimethyl sulfoxide were purchased from Sigma-Aldrich, and were used without further purification. Transparent conductive glasses is ITO for substrate.

$BiVO_4$ synthesis

ITO substrate was cleaned with detergent, acetone, ethanol and distilled water, respectively. Bi film deposition bath was involved of 5.0 mM $Bi(NO_3)_3$, 0.1 M citric acid (pH =4,7) at different temperature (30, 40, 50 and 60 °C). Conventional three electrode system the consisting of ITO, Pt sheet (2 cm^2) and Ag/AgCl (3.0 M KCl) was used for working electrode, counter electrode and reference electrode, respectively. Potantiostatic deposition was conducted to apply 1.0 V on ITO, which was coated with 150 mM $VO(acac)_2$ by drop casting method, and calcinated at 500 °C for 2 hours.

Characterization of $BiVO_4$

The surface morphology of $BiVO_4$ photoelectrodes were depicted by using a field emission scanning electron microscope (FEI Quanta 650 Field Emission SEM). The effect of temperature on grown process of $BiVO_4$ crystal phase investigated by XRD (Panalytical empyrean) with Cu-Kα radiation, 2θ degree between 15° and 70°. The optical properties and bonding vibration in metal oxides were monitored by UV-vis spectrometer (Model: Thermo-Scientific-

Genesys 10S) and Raman spectroscopy (Renishaw Model: In Via Qontor).

Photocatalytic performance

Lineer sweep voltammetry (LSV) was carried out applied potential range from 0.2 to 1.6 V (vs. NHE) at 5 mV s^{-1} scan rate under simulated the solar irradiation of 100 mW cm^{-2} (Model: SunliteTM Solar Simulators; M-SLSS) light in 0.1 M Na_2SO_3 and 0.1 M phosphate buffer (pH=7).

RESULTS AND DISCUSSION

The surface nanostructure of various $BiVO_4$ photoelectrode is depicted in Fig. 1. Bi deposition bath relatively alters surface morphology of electrodes. As seen Fig. 1, nanoparticles form and grown with homogeneity on surface 30 °C $BiVO_4$, but these nanoparticles decay to different particles for 30 °C $BiVO_4$. In addition, a grown process comparatively changes with agglomeration of nanoparticles for 50 °C $BiVO_4$ and 60 °C $BiVO_4$. It can be suggest that Bi electrochemical deposition bath temperature dramatically effect on photoelectrode nanostructure morphology.

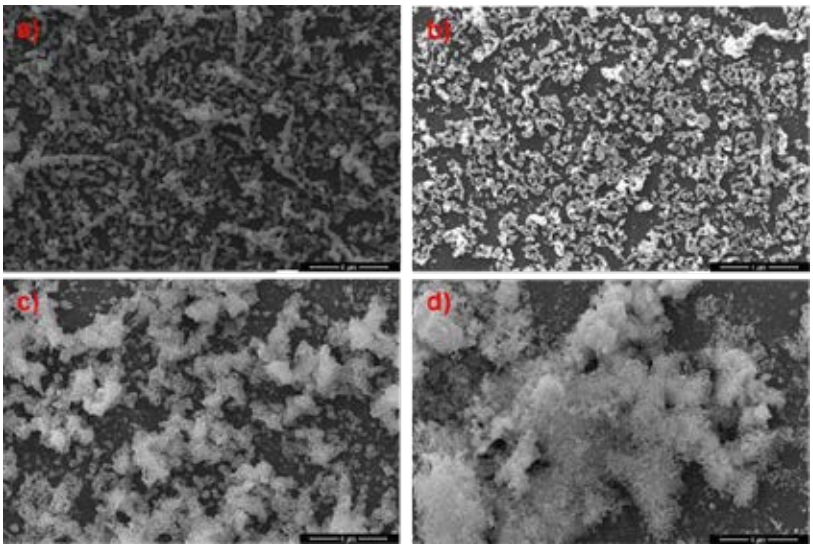


Fig. 1. FESEM images of 30 °C $BiVO_4$ (a), 40 °C $BiVO_4$ (a), 50 °C $BiVO_4$ (c) and 60 °C $BiVO_4$ (d) photoelectrodes.

The crystal phase of electrodes is defined by XRD measurement, is given Fig. 2 (a). The obtained 2θ° peaks of 18.82°, 28.85°, 30.45°, 34.83°, 39.88° and 42,33° can be ascribed to hkl parameters of (011), (112), (004), (020), (121) and (015), respectively. According to JCPDS NO-98-010-060, the main peaks are 18.82° and 28.85° conform to schelit monoclinic phase for all $BiVO_4$ electrodes. Furthermore, the $BiVO_4$ peaks indicate that V_2O_5 and B_2O_3 impurities are not contained in $BiVO_4$ crystal phase. Fig. 1 (b) shows the Uv-vis spectrum of $BiVO_4$ photoelectrodes between 400 and 700 nm. The various temperature $BiVO_4$ absorption begin 520 nm, ıt is compatible with counterpart paper. As seen in Fig. 2 (b), the highest absorption is obtained for 30 °C $BiVO_4$, ıt can be suggest more photocatalytic electrode for water splitting under solar irradiation. Raman spectrum of $BiVO_4$ photoelectrodes are given in Fig. 2 (c). The all electrodes demonstrate maximum intensity of symmetric V–O stretching at 827 cm^{-1} due to disorder for average vanadate species and the weak band at 711 cm^{-1} is correspond to the anti-symmetric V–O stretching. In addition, the symmetric and anti-symmetric of V–O stretching are 369 cm^{-1} ve 327 cm^{-1} at bending modes. According to Raman spectrum, ıt can be proposed $BiVO_4$ synthesis at different deposition temperatures. Finally, Fig. 2 (d) demonstrates $BiVO_4$ photoelectrodes LSV measurement under 100 mW cm^{-2} solar light. The photocatalytic response of $BiVO_4$ electrodes increases within order 60, 50, 40 and 30 °C respectively. 30 °C $BiVO_4$ is the most active photoelectrode for photoelectrochemical water splitting. It means that an efficient charge transfer and separation in electrode surface boundary and decreasing the electron–hole recombination for OER.

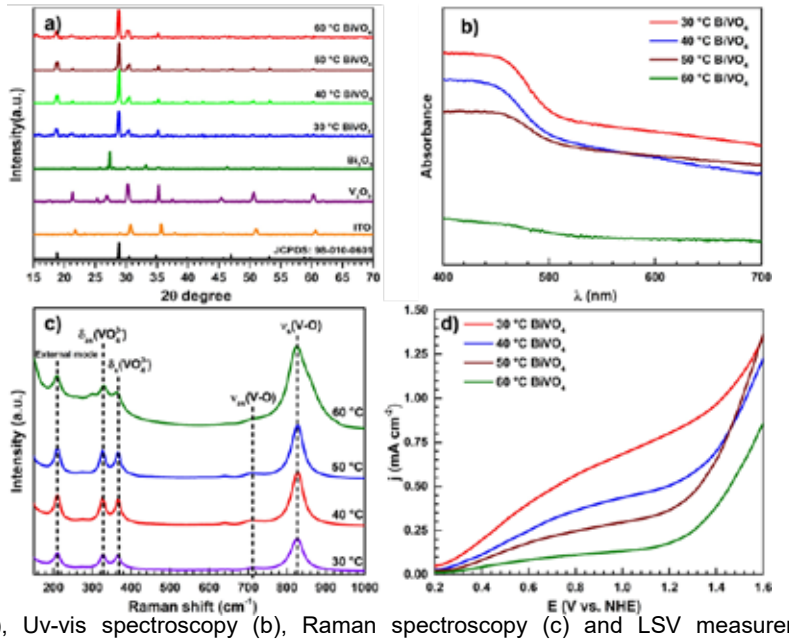


Fig. 2 XRD pattern (a), Uv-vis spectroscopy (b), Raman spectroscopy (c) and LSV measurement of various $BiVO_4$ photoelectrodes

CONCLUSIONS

In this study, we have successfully obtained $BiVO_4$ by electrochemical deposition method and drop casting. The effect of Bi film deposition bath temperature was invastigated with XRD, Raman and Uv-vis spectroscopy, LSV measurement. FESEM images indicate deposition condition affect to surface nanostructure. Acording to Uv-vis spetroscopy and LSV results, the increasing of Bi film depositon bath temperature is decresed absortion of light and photocataytic response of $BiVO_4$ photoelectrodes.

ACKNOWLEDGEMENT

The authors acknowledge the financial support of the The Scientific and Technological Research Council of Turkey under (TUBITAK-BİDEB) 2218- National Postdoctoral Research Fellowship Programme.

REFERENCES

[1] Solakidou M, Giannakas A, Georgiou Y, Boukos N, Louloudi M, Deligiannakis Y. 2019. Efficient photocatalytic water-splitting performance by ternary CdS/Pt-N-TiO_2 and CdS/Pt-N,F-TiO_2: Interplay between CdS photo corrosion and TiO_2-dopping. Applied Catalysis B-Environmental. 254:194-205.
[2] Zhang Z, Choi M, Baek M, Deng Z, Yong K. 2017. Corrosion-Assisted Self-Growth of Au-Decorated ZnO Corn Silks and Their Photoelectrochemical Enhancement. ACS Appl Mater Interfaces.
[3] Zhang H, Park JH, Byun WJ, Song MH, Lee JS. 2019. Activating the surface and bulk of hematite photoanodes to improve solar water splitting. Chemical Science.
[4] Zhang J, Ma H, Liu Z. 2017. Highly efficient photocatalyst based on all oxides WO_3/Cu_2O heterojunction for photoelectrochemical water splitting. Applied Catalysis B: Environmental. 201:84-91.
[5] Jian J, Jiang G, van de Krol R, Wei B, Wang H. Recent advances in rational engineering of multinary semiconductors for photoelectrochemical hydrogen generation. Nano Energy. 2018;51:457-80.
[6] Tang G, Li H, Cheng C. 2019. Au nanoparticles embedded in $BiVO_4$ films photoanode with enhanced photoelectrochemical performance. Nanotechnology. 30:445402.
[7] Gupta R, Boruah B, Modak JM, Madras G. 2019. Kinetic study of Z-scheme C_3N_4/$CuWO_4$ photocatalyst towards solar light inactivation of mixed populated bacteria. J Photochem Photobiol, A. 372:108-21.
[8] Li N, Wu X, Wang M, Huang K, He J, Ma W, et al. 2019. Facile preparation of $BiVO_4$/$FeVO_4$ heterostructure for efficient water-splitting applications. Int J Hydrogen Energy. 44:23046-53.
[9] Kaowphong S, Choklap W, Chachvalvutikul A, Chandet N. 2019. A novel $CuInS_2$/m-$BiVO_4$ p-n heterojunction photocatalyst with enhanced visible-light photocatalytic activity. Colloids Surf, A. 579:123639.
[10] Zhang M, Piao C, Wang D, Zhang Z, Wang J, Song Y. 2020. Bimetal Cu and Pd decorated Z-scheme $NiGa_2O_4$/$BiVO_4$ photocatalyst for conversion of nitride and sulfide dyes to $(NH_4)_2SO_4$. Separation and Purification Technology. 231:115890.
[11] Huang L-W, Vo T-G, Chiang C-Y. 2019. Converting glycerol aqueous solution to hydrogen energy and dihydroxyacetone by the $BiVO_4$ photoelectrochemical cell. Electrochim Acta. 322:134725.
[12] Kim M-W, Samuel E, Kim K, Yoon H, Joshi B, Swihart MT, et al. 2018.Tuning the morphology of electrosprayed $BiVO_4$ from nanopillars to nanoferns via pH control for solar water splitting. J Alloys Compd. 769:193-200.
[13] Samsudin MFR, Bashiri R, Mohamed NM, Ng YH, Sufian S. 2019. Tailoring the morphological structure of $BiVO_4$ photocatalyst for enhanced photoelectrochemical solar hydrogen production from natural lake water. Appl Surf Sci. 144417.
[14] Cho SK, Park HS, Lee HC, Nam KM, Bard AJ. 2013. Metal Doping of $BiVO_4$ by Composite Electrodeposition with Improved Photoelectrochemical Water Oxidation. The Journal of Physical Chemistry C. 117:23048-56.

The Influence of Ni/Dolomite Catalyst for Production of Hydrogen from $NaBH_4$ Hydrolysis

[1]Burcu KİREN, [1*]Nezihe AYAS
[1]Eskişehir Technical University, Faculty of Engineering, Department of Chemical Engineering, İki Eylül Campus, Eskişehir,26000, Turkey

*E-mail: nazcan@eskisehir.edu.tr

Abstract
Hydrogen is expected to play a significant role as an energy carrier in the future energy systems of the globe, as it is abundant element in the universe, generates no toxic by products as well as being versatile in terms of supply and use. Hydrolysis of sodium borohydride is a promising method for on-board hydrogen supply, especially, for fuel cells and other portable devices. Hydrogen evolution in the catalytic hydrolysis of sodium borohydride is a promising and feasible method therefore, catalyst research is of a great importance in the development of this technology. In the present study, Ni/Dolomite catalyst was synthesized by wet impregnation and employed in the hydrolysis reaction. Eventually, the catalyst with 40 wt.% Ni content was assigned as the most suitable catalyst, attaining H_2 production of 100% with rate of 734.28 mL/g_{cat}.min at 60 °C with 5 mL of 0.25 M NaOH, 100 mg $NaBH_4$, 100 mg Ni/Dolomite.

Keywords: Sodium borohydride, hydrolysis, catalyst, Ni/Dolomite, hydrogen

I. Introduction

As a result of overconsumption of fossil fuels, mankind has been stuck on major issues such as environmental pollution, climate change, and energy security (Martin etal., 2020). Due to aforementioned serious issues, hydrogen is one of the most promising choice for addressing the energy crisis and environmental emissions (Ishaq and Dincer, 2019). Metal hydrides have high gravimetric hydrogen storage densities and are attractive means of hydrogen generation for mobile applications. Metal borohydrides including lithium borohydride ($LiBH_4$), potassium borohydride (KBH_4) and sodium borohydride ($NaBH_4$) are highly attractive for hydrogen storage and production as they offer high gravimetric hydrogen density, remain stable in alkaline solution, more importantly, dehydrogenate at moderate temperatures and pressures (Narasimharao etal., 2021). $NaBH_4$ displays non-flammable, non-toxic nature along with being able to store approximately 10.8 wt.% hydrogen (Dönmez and Ayas, 2020).

$$NaBH_4 + (x+2)H_2O \rightarrow 4H_2(g) + NaBO_2 \cdot xH_2O + 4H_2 \;\; \Delta H = -75 \;\; kJ/mol\, H_2 \quad (1)$$

The hydrolysis of sodium borohydride occurs very slowly in a non-catalytic environment; therefore, the reaction can be sped up by the incorporation of catalysts (Cai etal., 2016). In order to increase the rate of hydrogen production in the hydrolysis of sodium borohydrides, a number of catalysts have been investigated by Abdelhamid (2021), Dönmez and Ayas (2020), Manna etal. (2014).

In accordance with our literature research, this study will be the first examination investigating the effect of dolomite supported nickel catalysts to be used in the hydrolysis reaction of sodium borohydride. The synthesized catalyst characterizations were carried out on different techniques such as XRF, XRD, TGA and FT-IR analysis. The activities of catalysts in the hydrolysis of sodium borohydride reaction were investigated.

II. Experimental Set-up and Procedure

The chemicals used in this study (nickel (II) nitrate hexahydrate (97%, Sigma Aldrich), sodium hydroxide (98.8%, VWR Chemicals and sodium borohydride (98%, Sigma Aldrich)) were of analytical purity and were not pre-treated. Dolomite, the support material used in the catalyst synthesis, was purchased as a raw material from a private mining company in Turkey. Before starting the catalyst synthesis, dolomite was ground in powder form (<50 µ) and calcined at 950 °C for 6 hours in dry air atmosphere using split furnace (Xu etal., 2019).

Ni/Dolomite catalysts were prepared by using the wet impregnation method. To load different proportions of Ni on dolomite, a certain amount of nickel nitrate hexahydrate salt was dissolved in a proper amount of distilled water, then mixed in a beaker with pre-calcined dolomite. Then, using magnetic stirrer, the mixture was stirred at 80 °C for 6 hours. The paste obtained was dried at 105 °C for 24 hours in the oven and followed by grinding to reduce its grain size. Finally, the prepared sample was calcined at 400 mL/min in dry air at 1000 °C for 4 hours. The synthesized catalysts were reduced for 1 hour with a flow rate of 400 mL/min H_2/N_2 (20% H_2 volume) at 550 °C before being tested in the hydrolysis reaction.

III. Analysis

Hydrolysis experiments were carried out in a three-necked 250 mL glass flask to examine the activities of the synthesized catalysts. Firstly, the catalyst was added to the flask, then the mixture obtained with sodium hydroxide solution and sodium borohydride was placed into the flask. The generated hydrogen volume was determined using

the water-gas displacement method in a graduated cylinder during the hydrolysis reaction. The effect of reaction temperature (30-60 °C) and metal loading ratio (10,20,30,40 wt.%) on the hydrogen generation were investigated.

IV. Results and discussions

XRF (X-ray fluorescence) results of the synthesized catalysts are given in Table 1.

Tab. 1: XRF results of synthesized catalysts

Ni/ Dolomite Loading ratio (wt./wt.)	NiO	MgO	Al_2O_3	SiO_2	CaO	Fe_2O_3	LOI*
10/90	11.2	30	0.376	0.891	49.9	0.884	6.745
20/80	23.4	27.6	0.465	0.732	45	0.883	1.92
30/70	36.4	23.8	0.524	0.745	35.5	0.623	2.4
40/60	46.1	18	0.512	0.475	31.9	0.703	2.31

* loss of ignition

As it is seen in Table 1, XRF results of catalysts are given in the form of oxide compounds as percentage wt./ wt. According to the results of the XRF, the Ni amounts to be loaded were successfully loaded onto the dolomite.

XRD patterns, FT-IR spectrum and TGA results of Ni/Dolomite are given in Fig. 1-3, respectively.

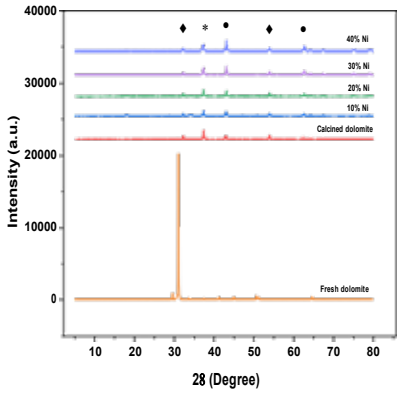


Fig. 1: XRD patterns of Ni/Dolomite. (♦:CaO, ●: MgO, *: NiO)

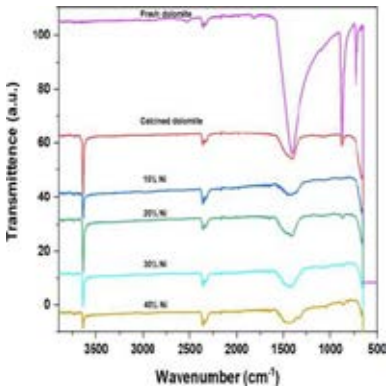


Fig. 2: FT-IR spectrum of Ni/Dolomite.

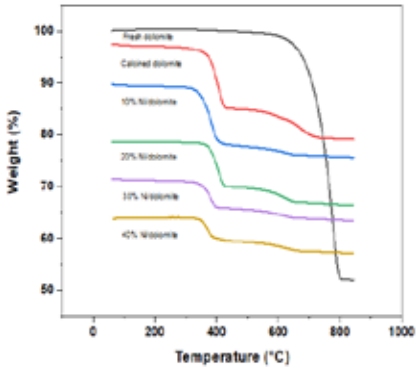
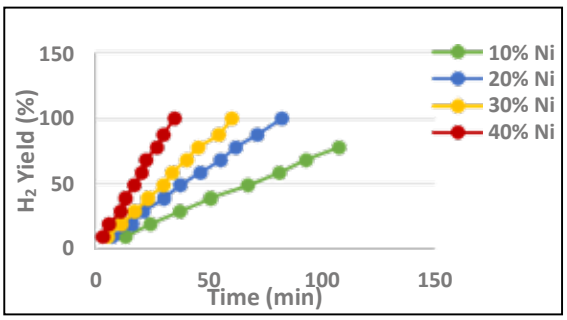


Fig. 3: TGA results of Ni/Dolomite

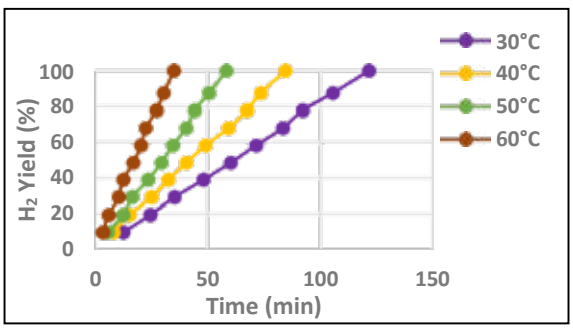
XRD patterns of dolomite and Ni-loaded catalysts with different ratios are given in Figure 1. Depending on the 2θ values, the components of the peaks were determined (CaO: 2θ = 31.06 °, at 50.54 °; MgO 2θ = 31.06 °, at 50.54 °; NiO 2θ = 42.96 °, 43.06 °, 43.48 °). It was observed that the intensity of NiO peaks increased depending on the loaded Ni ratio.

As it is seen in the FT-IR spectrum (Fig.2), OH groups exhibit a sharp tensile vibration due to the stress of CaO and MgO at the catalyst surface at 3650 cm^{-1}. Peaks in the range of 600–800 cm^{-1} are M-O vibrations represented by Ca, Mg and Ni metals. According to Fig.3, while fresh dolomite begins to lose its mass at 700 °C and reaches a constant mass at 800 °C. However, calcined dolomite and Nickel-loaded catalysts start to lose their weights at the temperature around 380 °C and remain constant mass at 400 °C. The reason for this is that the components that are desired to be removed during the pre-calcination process have been removed.

The activities of the catalysts at different Ni loading rates were determined in the hydrolysis experiments of $NaBH_4$. For this purpose, the effect of Ni ratios and time on hydrogen yield is given in Figure 4.a and the effect of temperature and time on hydrogen yield is given in Figure 4.b.



(a) 60 °C, 100 mg $NaBH_4$, 100 mg Ni/Dolomite, 5 mL 0.25 M NaOH



(b) 100 mg $NaBH_4$, 100 mg 40% Ni/Dolomite, 5 mL 0.25 M NaOH

Fig. 4. The influence of (a) Ni content of Ni/Dolomite catalyst and (b) hydrolysis temperature of 40% Ni/Dolomite on hydrogen yield.

It is seen in Fig. 4a that as the nickel ratio increases, the time to reach 100% hydrogen yield decreases. Hydrogen yield at the rate of 10% Ni, it reached 78%, while it reached 100% at 40% Ni. As shown in Fig. 4b, it is clear that the reaction time for 100% hydrogen yield shows a downward trend with increasing reaction temperature. In order to achieve 100% hydrogen yield, it was observed that the reaction time, which was 121 minutes at 30 °C, dropped to the 35 minutes at 60 °C.

V. Conclusions

The present study focused on developing effective catalyst in the generation of hydrogen from sodium borohydride based on varying catalysts and reaction parameters. To this aim, the activity of dolomite supported Ni with various Ni ranging from 10 to 40 wt.% was tested at temperatures within 30 to 60 °C with 10 °C increment. It was concluded that catalysts with Ni loading of 20 wt.% and above were resulted in 100% hydrogen yield. The next main point of current study is that the reaction temperature was another significant parameter. The 100% hydrogen yield was obtained at 30 °C for 121 min. However, with increasing reaction temperature to 60 °C, the completion time was dramatically reduced to 35 min. It is seen that the results obtained from many research papers using different catalysts to produce hydrogen by the hydrolysis of $NaBH_4$ and the results found in this study are compatible. This study will make a new contribution to the gap in the literature, as the results obtained by using dolomite-supported catalysts in hydrolysis reaction is the first study. This research will be developed by testing the parameters of $NaBH_4$ and NaOH concentration, catalyst amount, catalyst reusability and kinetic studies of the reaction mechanism.

References

Abdelhamid H. N., A review on hydrogen generation from the hydrolysis of sodium borohyride, International Journal of Hydrogen Energy, 46, 726-765, (2021).

Liu H., Liu L., Chen Q., Lu P., Dong J., Ni-polymer nanogel hybrid particles: A new strategy for hydrogen production from the hydrolysis of dimethylamine-borane and sodium borohydride, Energy, 99, 129–135, (2016).

Dönmez F., Ayas N., Synthesis of Ni/TiO_2 Catalyst by Sol-gel Method for Hydrogen Production from Sodium Borohydride, International Journal of Hydrogen Energy, (2020).

Ishaq H., Dincer I., Comparative assessment of renewable energy-based hydrogen production methods, Renewable and Sustainable Energy Reviews, 135, 110192, (2021).

Manna J., Roy B., Vashistha M., Sharma P., Effect of Co+2/BH4- ratio in the synthesis of Co-B catalysts on sodium borohydride hydrolysis, International Journal of Hydrogen Energy, 39, 406–413, (2014).

Martin A., Agnoletti M. F., Brangier E., Users in the design of Hydrogen Energy Systems: A systematic review, International Journal of Hydrogen Energy, 45, 11889–11900, (2020).

Narasimharao K., Abu-Zied B. M., Alfaifi S. Y., Cobalt oxide supported multi wall carbon nanotube catalysts for hydrogen production via sodium borohydride hydrolysis, International Journal of Hydrogen Energy, 46, 6404–6418, (2021).

Xu T., Xiao B., Xu F., Moyo G. G., Li F., Chen Z., Wang X., Hu Z., Liu S., Hu M., Syngas production via chemical looping reforming biomass pyrolysis oil using NiO/dolomite as oxygen carrier, catalyst or sorbent, Energy Conversion and Management, 198, (2019).

Xu T., Xu F., Moyo G. G., Sun Y., Chen Z., Xiao B., Wang X., Hu Z., Comparative study of MxOy (M=Cu, Fe and Ni) supported on dolomite for syngas production via chemical looping reforming with toluene, Energy Conversion and Management, 199, (2019).

Synthesis and Characterization of Phase-Pure Perovskite Type Oxides - The Case of $BaZr_{0.80}Y_{0.20}O_{3-\delta}$ and $SrCe_{0.95}Yb_{0.05}O_{3-\delta}$

[1]Ömer Özcan, [1*]Fatih Pişkin
[1] Muğla Sıtkı Koçman University, Faculty of Engineering, Department of Metallurgical and Materials Engineering, Muğla, 48000, Turkey

* E-mail: fatihpiskin@mu.edu.tr

Abstract
In this study, a systematic work was carried out to determine the ideal synthesis parameters for the production of phase-pure perovskite type oxides, namely $BaZr_{0.80}Y_{0.20}O_{3-\delta}$ and $SrCe_{0.95}Yb_{0.05}O_{3-\delta}$. The effect of chelating and polymerization agents on the production of $BaZr_{0.80}Y_{0.20}O_{3-\delta}$ and $SrCe_{0.95}Yb_{0.05}O_{3-\delta}$ powders was investigated in detail. As chelating agents, ethylenediaminetetraacetic acid and citric acid were employed with different fractions, while ethylene glycol was preferred as the polymerization agent. In the current work, the effect of calcination temperature ranging between 1000°C and 1200°C was also investigated so as to eliminate the secondary phase formation during the syntheses.

Keywords: Perovskite-type oxides, proton-conducting oxides, Pechini synthesis.

I. Introduction

Perovskite-type oxides based on $SrCeO_3$ and $BaZrO_3$ have been extensively studied due to their mixed protonic and electronic conductivity (Hashim et al. 2018). Among the $SrCeO_3$ and $BaZrO_3$ oxide families $BaZr_{0.80}Y_{0.20}O_{3-\delta}$ (BZY) and $SrCe_{0.95}Yb_{0.05}O_{3-\delta}$ (SCY) are particularly attractive due to their superior protonic conductivity (Hossain et al. 2017). Additionally, thermo-mechanical stability of these oxides especially in reducing atmospheres such as CO_2 makes them an essential component in several applications such as proton-conducting solid oxide fuel cells (Fabbri et al. 2009) and hydrogen separation membranes (Zhang et al. 2013).

The mixed protonic and electronic conductivity in perovskite-type oxides is typically obtained by p-type or n-type doping resulting in a complex oxide structure (Fish et al. 2015). In order to provide this complex oxide structure, there are several methods such as solid-state reaction (Taglieri et al. 1999), sol-gel (D'Epifanio et al., 2007), and the Pechini method (Pechini 1967). However, the formation of the phase-pure oxides can be problematic regardless of the preferred method. The possible impurities such as oxides derivates of the compounds can be formed during the synthesis and could result in performance degradation (Iguchi et al. 2009) or chemical instability (D'Epifanio et al. 2007) in the perovskite-type oxides. Thus, controlling the synthesis conditions is quite critical for the elimination of possible impurities.

The current study involves a systematic work on the determination of synthesis parameters for the production of BZY and SCY by the Pechini method (Pechini 1967). In the study, the effect of chelating and polymerization agents on the production of SCY and BZY powders was investigated. As chelating agents, ethylenediaminetetraacetic acid (EDTA) and citric acid (CA) were employed with different fractions, while ethylene glycol (EG) was preferred as the polymerization agent. Besides the chelating and polymerization agents, the effect of calcination temperature was also investigated in order to eliminate the secondary phase formation during the syntheses.

II. Experimental

$SrCe_{0.95}Yb_{0.05}O_{3-\delta}$ and $BaZr_{0.80}Y_{0.20}O_{3-\delta}$ were synthesized via Pechini method. Commercial reagents; $Sr(NO_3)_2$ (Alfa Aesar 99.0%), $Ce(NO_3)_3.6H_2O$ (Merck ≥98.5%), $Yb(NO_3)_3.14H_2O$ (Alfa Aesar 99.9%), $Ba(NO_3)_2$ (Merck ≥99.0%), $ZrO(NO_3)_2.xH_2O$ (Sigma Aldrich %99.0) and $Y(NO_3)_3.6H_2O$ (Sigma Aldrich %99.8), citric acid (Carlo Erba 99.5%), EDTA (Carlo Erba ≥99.0%) and ethylene glycol (Carlo Erba ≥99.5%) were employed during the syntheses.

During the synthesis, the stoichiometric amounts of nitrate salts were initially dissolved in a minimum volume of de-ionized water in a beaker by mechanical stirring. The desired molar ratio of the total metal cation (TM), CA, EDTA, and EG were utilized as shown in Tab. 1 and Tab. 2 for BZY and SCY, respectively. The pH of the solution was adjusted to 8 using $NH_3.H_2O$ and the solution was stirred at 300rpm until the viscous gel formed. Subsequently, the viscous gel was heated at 70°C overnight in a drying oven to remove the excess water. The gel was then dried at 250°C for 2h in a drying oven and was ground in a mortar before the calcination. SCY and BZY black powders obtained were calcined for 5 hours at temperatures ranging between 1000°C and 1200°C in an air atmosphere to remove residual organics and to form the perovskite structure.

III. Analysis

A Rigaku SmartLab X-ray diffractometer was used for the crystal structure analysis of synthesized powders. X-ray diffraction (XRD) analyses were performed with Cu-Kα radiation (λ= 1,5406 Å) in Bragg-Brentano geometry between 20°-100° 2θ angles with a scan rate of 0.02°/min. During the analyses, X-ray tube voltage and current were set at 40kV and 30mA, respectively. A JEOL JSM-7600F scanning electron microscope (SEM) was used in

secondary electron imaging mode at accelerating voltage ranging between 10kV and 20kV for investigation of microstructure and morphology of the oxides. Elemental analysis was performed with an energy dispersive spectrometer (EDS) that is integrated into the SEM.

IV. Results and discussions

BZY and SCY powders were synthesized using a different molar ratio of CA, EDTA, and EG with respect to the total metal cations (TM) shown in Tab. 1 and Tab. 2, respectively. Each synthesis was calcined in stagnant air at temperatures ranging between 1000˚C and 1200˚C for 5h.

Tab. 1: The fractions of TM, CA, EDTA, and EG used in BZY synthesis.

Synthesis	TM	CA	EG	EDTA
1	1	2	2	-
2	1	2	-	2
3	1	2	-	-
4	1	-	-	2

Tab. 2: The fractions of TM, CA, EDTA, and EG used in SCY synthesis.

Synthesis	TM	CA	EG	EDTA
1	1	2	2	-
2	1	2	-	2
3	1	2	-	-
4	1	3	-	-

Tab. 3: The secondary phases analyzed in BZY powders synthesized and calcined under different conditions.

Synthesis	Calcination for 5h TMCA		
	1000°C	**1100°C**	**1200°C**
TM:CA:EG 1:2:2	BaO_2, $BaCO_3$	BaO_2, $BaCO_3$	BaO_2, $BaCO_3$
TM:CA:EDTA 1:2:2	BaO_2, $BaCO_3$	BaO_2, $BaCO_3$	-
TM:CA 1:2	BaO_2, $BaCO_3$	BaO_2, $BaCO_3$	BaO_2, $BaCO_3$
TM:EDTA 1:2	BaO_2, $BaCO_3$	BaO_2, $BaCO_3$	BaO_2

Tab. 4: The secondary phases analyzed in SCY powders synthesized and calcined under different conditions.

Synthesis	Calcination for 5h TMCA		
	1000°C	**1100°C**	**1200°C**
TM:CA:EG 1:2:2	Sr_2CeO_4, CeO_2	Sr_2CeO_4, CeO_2	Sr_2CeO_4, CeO_2
TM:CA:EDTA 1:2:2	Sr_2CeO_4, CeO_2	Sr_2CeO_4	Sr_2CeO_4, CeO_2
TM:CA 1:2	Sr_2CeO_4	Sr_2CeO_4	Sr_2CeO_4
TM:CA 1:3	Sr_2CeO_4	-	CeO_2

XRD analyses for BZY and SCY powders synthesized under different conditions are given in Fig. 1. The analyses show that phase-pure BZY perovskite structure was obtained with the synthesis having the fraction of TM:CA:EDTA 1:2:2, and calcination at 1200°C for 5h. In the case of SCY, the single-phase perovskite structure was obtained with TM:CA 1:3 ratio in the synthesis and the calcination at 1100°C for 5h.

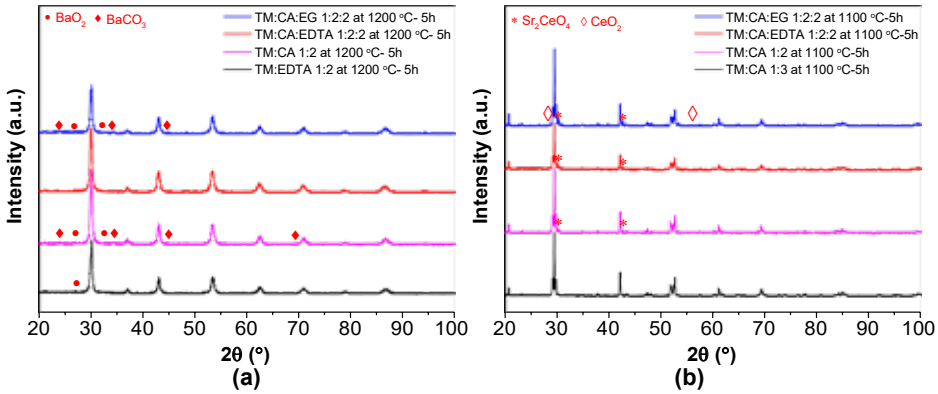


Fig. 1: (a) XRD results of BZY synthesized under different conditions and calcined at 1200 °C for 5h. (b) XRD patterns of SCY powders synthesized under different conditions and calcined at 1100 °C for 5h.

V. Conclusions

In the current work, the Pechini method was employed with different chelating and polymerization agents in order to synthesize phase-pure BZY and SCY powders. As chelating agents, EDTA and citric acid were used with different fractions, while ethylene glycol was preferred as the polymerization agent. The effect of calcination temperature ranging between 1000°C and 1200°C was also investigated so as to eliminate the secondary phase formation during the syntheses. Pure BZY perovskite structure was obtained with the synthesis having the fraction of TM:CA:EDTA 1:2:2, and calcination at 1200°C for 5h. In the case of SCY, the single-phase perovskite structure was obtained with TM:CA 1:3 ratio in the synthesis and the calcination at 1100°C for 5h.

Acknowledgements
This work is supported by the Scientific and Technological Research Council of Turkey (TUBITAK) under project number 119M065, which the authors gratefully acknowledge. During the course of this work, Ömer Özcan is also supported by the TUBITAK 2210-C Domestic Graduate Scholarship Programme Intended for Priority Area, No. 1649B022000693.

References

D'Epifanio A., Fabbri E., Di Bartolomeo E., Licoccia S., Traversa E., $BaZr_xY_{1-x}O_{3-\delta}$ and $BaCe_{1-x}$-$Zr_xY_zO_{3-\delta}$ Proton Conductors For Intermediate Temperature Solid Oxide Fuel Cells (IT-SOFCs), ECS Transactions 7, 2337–2342, (2007).

Fabbri E., Oh T., Licoccia S., Traversa E., Wachsman E. D., Mixed Protonic/Electronic Conductor Cathodes for Intermediate Temperature SOFCs Based on Proton Conducting Electrolytes. Journal of the Electrochemical Society 156, 38–45, (2009).

Fish J. S., Ricote S., O'Hayre R., Bonanos N., Electrical Properties and Flux Performance of Composite Ceramic Hydrogen Separation Membranes. Journal of Materials Chemistry, 3, 5392–5401, (2015).

Hashim S. S., Somalu M. R., Loh K. S., Liu S., Zhou W., Sunarso J., Perovskite-Based Proton Conducting Membranes for Hydrogen Separation: A Review, International Journal of Hydrogen Energy, 43, 15281–15305, (2018).

Hossain S., Abdalla M. A., Jamain S. N. B., Zaini J. H., Azad A. K., A Review on Proton Conducting Electrolytes for Clean Energy and Intermediate Temperature-Solid Oxide Fuel Cells, Renewable and Sustainable Energy Reviews 79, 750–764, (2017).

Iguchi F., Tsurui T., Sata, N., Nagao Y., and Yugami H., The Relationship between Chemical Composition Distributions and Specific Grain Boundary Conductivity in Y-Doped $BaZrO_3$ Proton Conductors, Solid State Ionics 180, 563–568, (2009).

Pechini M. P., Method of Preparing Lead and Alkaline Earth Titanates and Niobates and Coating Method Using the Same to Form a Capacitor, (1967).

Taglieri G., Tersigni M., Villa P. L., Mondelli C,. Synthesis by the Citrate Route and Characterisation of $BaZrO_3$, a High Tech Ceramic Oxide: Preliminary Results." International Journal of Inorganic Materials, 1, 103-110, (1999).

Zhang C., Li S., Liu X., Zhao X., He D., Qiu H., Yu Q., Wang S., Jiang L., Low Temperature Synthesis of Yb Doped $SrCeO_3$ Powders by Gel Combustion Process, International Journal of Hydrogen Energy 38, 12921–12926, (2013).

Determination of the Synthesis and Activity of the Sepiolite Supported Catalyst Used in the Production of H_2 from Methane

[1]Tuğçe Başara, [1*] Nezihe Ayas
[1] Eskişehir Technical University, Engineering Faculty, Department of Chemical Engineering, Eskişehir, 26555, Turkey

* E-mail: nazcan@eskisehir.edu.tr

Abstract

The aim of this study was to prepare Ni-containing catalyst by using sepiolite, a natural mineral, as a support material, and to investigate the efficiency of the catalyst in hydrogen recovery by steam reforming of methane. Ni/sepiolite catalyst was prepared by impregnation method with 10% by weight Ni loading. The characterizations of the prepared catalyst were carried out by X-ray fluorescence (XRF), X-ray diffraction (XRD) and thermogravimetric analysis (TGA). Methane steam reforming studies were carried out at different temperatures (500, 550, 600, 650, 700 °C), atmospheric pressure, 3:1 steam:methane ratio and12 L/g.cat.h Gas Hourly Space Velocity (GHSV). The composition of the gas mixture was determined online by µGC (micro gas chromatography) analysis.

Keywords: Methane, catalyst, Ni/Sepiolite, steam reforming, hydrogen

I. Introduction

Today, energy production is mostly supplied from fossil fuels. Environmental concerns from the release of greenhouse gases and increasing global energy demand have contributed to the spread of alternative energy generation options (Nahar etal., 2017). The world needs a clean, safe and reliable energy sources that can provide a high and sustainable quality of life. As a global energy resource, natural gas has been widely used in recent years as a result of high oil prices, the need for energy diversity and supply security, and the increasing global awareness of environmental problems. Such reasons also form the basis for considering hydrogen as a future energy vector (Izquierdo etal., 2012). Hydrogen is produced by steam reforming (SR) of natural gas for industrial and commercial use and the accompanying water-gas shift (WGS) reactions. Great importance is attached to H_2 as a clean energy carrier for future energy systems, due to its zero-air pollutant emission and inherently high calorific value during combustion (Chen etal., 2019).

The Steam Methane Reforming (SMR) process is characterized by multi-stage reactions. SMR is a catalytic process involving the reaction between natural gas or other light hydrocarbons and steam (Barelli etal., 2008). There are three main reactions that govern the SMR process and the products formed as a result of these reactions are hydrogen, carbon monoxide, carbon dioxide and water (Anzelmo etal., 2018 and Barelli etal., 2008). These reactions:

$$CH_4 + H_2O \leftrightarrow CO + 3H_2 \qquad \Delta H°_{298K} = 206 \text{ kJ/mol} \qquad (1)$$

$$CH_4 + 2H_2O \leftrightarrow CO_2 + 4H_2 \qquad \Delta H°_{298K} = 165 \text{ kJ/mol} \qquad (2)$$

$$CO + H_2O \leftrightarrow CO_2 + H_2 \qquad \Delta H°_{298K} = -41 \text{ kJ/mol} \qquad (3)$$

For catalytic steam reforming reactions, Ni-based catalysts are widely preferred due to their affordable price and exhibit high activity (dehydrogenation capacity) to break down C-C and C-H bonds. The catalytic activity for SR processes significantly depends on the types and properties of the supports, because they can increase the dispersion of the active metal and metal support interaction and could also participate in the catalytic reaction thus affecting reaction pathways and product selectivity. Sepiolite, which offers many advantages such as affordability, non-toxicity and inherently superior hydrothermal stability have been increasingly attracting the interest of researchers. It is a fibrous phyllosilicate mineral composed mainly of magnesium silicate along with varying amounts of Al^{3+}, K^{+}, Ca^{2+}, Fe^{2+} and Fe^{3+} ions, and it is rich in structural channels running parallel to the length of the fiber. These unique structural properties give it high adsorptive properties, provide more reactive sites for reactants and effectively increase the dispersion of active metals on its surface (Chen etal., 2019). There are a number of studies in the literature on methane steam reforming using different of catalysts (Zhai etal., 2011, Izquierdo etal., 2012, Liu etal., 2013 and Anzelmo etal., 2018) However, there has been no study conducted with Ni loaded catalyst on Sepiolite.

In this study, after the synthesis and characterize of Ni/sepiolite catalysts, steam reforming activity tests of methane were carried out in order to obtain H_2 rich gas mixture.

II. Experimental Set-up and Procedure

II.I. Catalyst preparation

The Ni/Sepiolite catalyst was prepared using the impregnation method. First, the catalyst support material sepiolite was pretreated (Liu etal., 2013). The nickel nitrate hexahydrate salt aqueous solution was added on the sepiolite and impregnated at 60 °C for 3 hours then followed by aged for 24 hours. Thereafter, it was dried in an oven at 110 °C. Finally, the prepared catalyst was calcined at 600 °C in 0.3 L/min dry air flow.

III.I. Catalyst characterization

Characterization of the calcined catalyst was carried out by XRF, XRD and TG analysis. Catalyst composition with XRF, crystal size of catalyst composition with XRD, change in catalyst mass with temperature with TGA was observed. XRF was performed on Rigaku ZSX Primus brand analyzer (Tab.1). XRD was performed in Rigaku Rint 2200 brand analyzer at 40 kV, 15 mA, 0,02° step range, 4°/min at 2θ=15-85°range (Fig.1). TGA was made in Perkin

Elmer STA 6000 brand analyzer within the temperature range from 30 to 900 °C with heating value of 10 °C/min under 50 mL/min nitrogen flow.

III.II. Catalytic activity test

The activity of 0.2 g Ni/Sepiolite catalyst prepared by impregnation method with 10% nickel content by weight was tested in methane-steam reforming reaction and the relationship between temperature and CH_4 conversion, H_2 yield, H_2, CO and CO_2 selectivity was investigated. Activity tests were performed in PID Eng&Tech brand and Micro Efficiency model microactivity reactor system, which is an automatic computer controlled catalytic reactor system in order to determine the activity and selectivity of the synthesized catalyst. Prior to the activity tests, the catalyst was reduced at 750 °C for 45 minutes using a mixture of 30 mL/min H_2 and 30 mL/min N_2. A standard feed mixture under constant conditions consisting of 12 L/gcat.h GHSV and H_2O:CH_4:N_2=3:1:1 (molar ratio) was fed to the reactor system at the atmospheric pressure. The experiment was conducted by varying the reaction temperature from 500 °C to 700 °C at the interval of 50 °C before each experiment. The measured parameters are defined as follows:

Methane conversion: $$X_{CH_4}(\%) = \frac{[CH_4]_{in}-[CH_4]_{out}}{[CH_4]_{in}}.100 \quad (4)$$

Hydrogen yield: $$Y_{H_2}(\%) = \frac{2.[H_2]_o}{4.[CH_4]_i+2.[H_2O]_i+6.[C_2H_6]_i+8.[C_3H_8]_i+10.[C_4H_{10}]_i+12.[C_5H_{12}]_i}.100 \quad (5)$$

Hydrogen selectivity: $$S_{H_2}(\%) = \frac{[H_2]_o}{[CH_4]_o+[CO]_o+[CO_2]_o+[C_2H_4]_o+[C_2H_6]_o+[C_3H_6]_o+[C_3H_8]_o+[H_2]_o}.100 \quad (6)$$

CO selectivity: $$S_{CO}(\%) = \frac{[CO]_o}{[CH_4]_o+[CO]_o+[CO_2]_o+[C_2H_4]_o+[C_2H_6]_o+[C_3H_6]_o+[C_3H_8]_o+[H_2]_o}.100 \quad (7)$$

CO_2 selectivity: $$S_{CO_2}(\%) = \frac{[CO_2]_o}{[CH_4]_o+[CO]_o+[CO_2]_o+[C_2H_4]_o+[C_2H_6]_o+[C_3H_6]_o+[C_3H_8]_o+[H_2]_o}.100 \quad (8)$$

IV. Results and discussions

Chemical analysis of the Ni/Sepiolite catalyst was carried out by XRF. From Table 1, as a result of the pre-treatment applied to natural sepiolite, some impurities in the sepiolite content were removed and Ni loading was successfully performed in the form of NiO on the sepiolite at a rate approaching to the theoretically calculated nickel ratio by weight. It was observed that the sepiolite composition did not change significantly after pre-treatment (Menor etal., 2017). In the XRD diffraction pattern in Fig. 1, the peaks belonging the calcined 10% Ni/Sepiolite (wt/wt%) catalyst at 2θ=37.2°, 43.3°, 62.8°, 75.2° and 79.0° correspond to NiO (Menor et al., 2017 and El Samrout etal., 2020). Since sepiolite is a type of silicate clay, it can produce silicon oxides with different crystallinity during the calcination process at 600 °C. Therefore, reflections at 2θ=26,5°, 28° and 31,5° in the (wt/wt%) 10% Ni content catalyst could be attributed to the characteristic refractive peak of siliconoxide (Chen etal., 2019).

Tab. 1: *XRF results of natural sepiolite, pretreated sepiolite and (w/w) 10% Ni/sepiolite catalyst.*

(% w/w) Composition	SiO_2	MgO	Al_2O_3	Fe_2O_3	CaO	K_2O	Cr_2O_3	TiO_2	NiO	SO_3	P_2O_5	*Loi
Natural β-Sepiolite	*58.48*	*21.55*	*4.40*	*2.56*	*0.60*	*0.48*	*0.25*	*0.18*	*0.12*	*0.02*	*0.02*	11.30
Active β-Sepiolite	*69.70*	*21.00*	*3.63*	*1.95*	*0.34*	*0.32*	*0.16*	*0.19*	*0*	*0*	*0*	*2.72*
%10 Ni/Sep.	*62.61*	*17.61*	*3.43*	*2.17*	*0.24*	*0.28*	*0.15*	*0.22*	*11*	*0*	*0*	*2.30*

*(*Loi: Loss of ignition)*

As shown in Fig. 2, a sudden mass loss of 1% is observed in the 30-100 °C temperature range, and this is probably due to the loss of surface water. The mass loss step (1% by weight) between 63 °C and 241 °C corresponds to the zeolitic water loss, the mass loss step between 476 °C and 707 °C (1% by weight) to the coordination water (bound water) loss. Mass loss continues up to 707°C. For 10% Ni/Sepiolite catalyst, the total mass loss is around 4%. Since the desorption of H_2O proceeds in two separate steps, the first is related to the partial folding of the nano-channels, the second to the irreversible folding of the sepiolite crystal, followed by the complete collapse of the structure (Kurtoğlu etal., 2018).

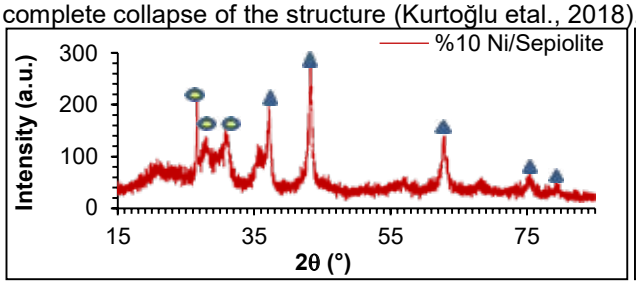


Fig. 1: XRD diffraction pattern of Ni/Sepiolite catalyst (▲: *NiO*, ⬭:*SiO_2*)

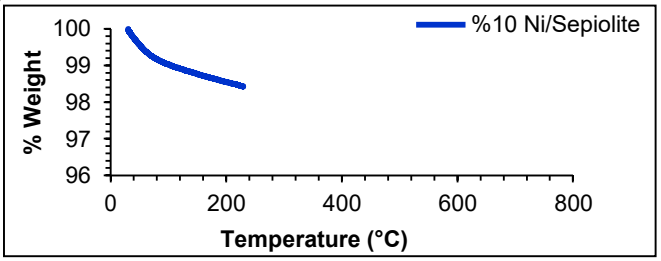


Fig. 2: TGA diagram of Ni/Sepiolite catalyst.

The catalyst characterizations have shown that the high performance of the Ni/Sepiolite catalyst is closely related to the good dispersion of the active ingredient (Zhai etal., 2011).

In this study, the relationship between temperature and CH_4 conversion, H_2 yield, H_2, CO and CO_2 selectivity in methane-steam reforming reaction in the presence of 0.2 g Ni/Sepiolite catalyst with 10% nickel by weight was

investigated. At T=600-650 °C, the highest CH_4 conversion was obtained as 99.99% mol. At T=600 °C, the highest hydrogen yield and selectivity values of 1.62% and 97.20%, as well as the lowest CO_2 and CO selectivity were achieved. Since the methane-steam reforming reaction is an endothermic reaction, it was known that the temperature would have a positive effect, but when the temperature was increased to T=650 °C, there was a 56.27% decrease in the value of H_2 selectivity. Further raising the temperature to 700 °C, there was a drop in hydrogen selectivity up to 56.27% and a rise in CO_2 selectivity to 12.30%. In this study, the optimum temperature for methane steam reforming was determined as T=600 °C in the presence of Ni/Sepiolite catalyst.

Tab. 2: *Results of methane-steam reforming experiments with %10 Ni/Sepiolite catalyst*.

Catalyst Type	Temperature (°C)	CH_4 Conversion (%)	H_2 Yield (mol H_2/mol CH_4)	H_2 Selectivity (%)	CO Selectivity (%)	CO_2 Selectivity (%)
Ni/Sepiyolit	*500*	*98.75*	*1.46*	*88.10*	*0.08*	*1.29*
	550	*99.98*	*1.57*	*94.70*	*0.06*	*0.39*
	600	***99.99***	***1.62***	***97.20***	***0***	***0.19***
	650	*99.99*	*1.59*	*95.90*	*0*	*0.44*
	700	*99.98*	*0.93*	*56.27*	*0*	*12.30*

V. Conclusions

The performance of Ni/Sepiolite catalyst synthesized by the impregnation method using sepiolite support has been investigated in methane-steam reforming reaction at constant S/C ratio and GHSV, under atmospheric pressure, in the temperature range of 500-700 °C. The sepiolite catalyst, which was modified by pre-treatment and loaded with nickel showed a high catalytic activity. The reason for this is thought to be due to the fact that the sepiolite surface area was enhanced by applying pre-treatment and that the nickel is loaded on these surfaces well, thus exhibiting a large active metal surface area. Therefore, during the methane-steam reforming reaction in the presence of Ni/Sepiolite catalyst, maximum values of 99.99% and 97.20%, respectively in methane conversion and hydrogen selectivity were achieved under the following conditions: T=600 °C, S/C=3 and GSHV=12 L/gcat.h.

References

Anzelmo, B., Wilcox, J., & Liguori, S. Hydrogen production via natural gas steam reforming in a Pd-Au membrane reactor. Comparison between methane and natural gas steam reforming reactions. *Journal of Membrane Science*, *568*, 113-120, (2018).

Barelli, L., Bidini, G., Gallorini, F., & Servili, S. Hydrogen production through sorption-enhanced steam methane reforming and membrane technology: a review. *Energy*, *33*(4), 554-570, (2008).

Chen, M., Li, X., Wang, Y., Wang, C., Liang, T., Zhang, H., ... & Wang, J. Hydrogen generation by steam reforming of tar model compounds using lanthanum modified Ni/sepiolite catalysts. *Energy Conversion and Management*, *184*, 315-326, (2019).

El Samrout, O., Karam, L., Jabbour, K., Massiani, P., Launay, F., & El Hassan, N. Investigation of new routes for the preparation of mesoporous calcium oxide supported nickel materials used as catalysts for the methane dry reforming reaction. *Catalysis Science & Technology*, *10*(20), 6910-6922, (2020).

Izquierdo, U., Barrio, V. L., Cambra, J. F., Requies, J., Güemez, M. B., Arias, P. L., ... & Arraibi, J. R. Hydrogen production from methane and natural gas steam reforming in conventional and microreactor reaction systems. *International Journal of hydrogen energy*, *37*(8), 7026-7033, (2012).

Kurtoğlu S. F., Sarp S., Akkaya C. Y., Yağcı B., Motallebzadeh A., Soyer-Uzun S., & Uzun A. COx-free hydrogen production from ammonia decomposition over sepiyolite-supported nickel catalysts. *International Journal of Hydrogen Energy*. 43 (21). 9954-9968, (2018).

Liu S., Chen M., Chu L., Yang Z., Zhu C., Wang J., & Chen M. Catalytic steam reforming of bio-oil aqueous fraction for hydrogen production over Ni-Mo supported on modified sepiyolite catalysts. *International Journal Of Hydrogen Energy.* 38 (10). 3948-3955, (2013).

Menor M., Sayas S. and Chica A. Natural sepiyolite promoted with Ni as new and efficient catalyst for the sustainable production of hydrogen by steam reforming of the biodiesel by-products glycerol. *Fuel.* 193. 351–358, (2017).

Nahar, G., Mote, D., & Dupont, V. Hydrogen production from reforming of biogas: Review of technological advances and an Indian perspective. *Renewable and Sustainable Energy Reviews*, *76*, 1032-1052, (2017).

Zhai X., Ding S., Liu Z., Jin Y., Cheng Y. Catalytic performance of Ni catalysts for steam reforming of methane at high space velocity. *International Journal of Hydrogen Energy*. 36 (1). 482-489, (2011).

Analysis and Assessment of a Novel Biomass Gasification Based Integrated System with Hydrogen Generation Process

[1]*Mehmet Altınkaynak, [2]Murat Ozturk
[1]Isparta University of Applied Sciences, Faculty of Technology, Department of Mechanical Engineering, 32200, Isparta/Turkey
[2]Isparta University of Applied Sciences, Faculty of Technology, Department of Mechatronics Engineering, 32200, Isparta/Turkey
E-mails: mehmetaltinkaynak@isparta.edu.tr, muratozturk@isparta.edu.tr

Abstract:
In the proposed paper, a new configuration of the novel biomass gasification based integrated system with hydrogen generation is proposed and analyzed based on the thermodynamic perspective. The modeled system produces useful products which are power, hydrogen, ammonia and absorption cooling. Power generation of the new biomass gasification-based integrated system of gas turbine, Rankine turbine and thermoelectric generation are 12.29 MW, 4.41 MW and 625 kW, respectively. The energy and exergy efficiencies of the new biomass gasification-based integrated system with the hydrogen production process is 56.01% and 49.93%, respectively. The components that make up multiple production systems in terms of energy efficiency, BPP, GTPP, RPP, HPP, HCP, APP, SEACS are calculated as 73.41%, 40.82%, 36.85%, 76.64%, 46.51%, 53.52% and 16.57%, respectively. In terms of exergy efficiency, these subsystems are 66.03%, 38.56%, 32.74%, 70.33%, 41.36%, 48.27% and 12.61% respectively. Hydrogen and ammonia production capacities are 0.0658 kg/s and 1.843 kg/s, respectively. The rise in the pressure of the combustion chamber has a positive effect on the system's performance.
Keywords: Energy; exergy; biomass, ammonia; hydrogen.

I. Introduction

Fossil fuels are being replaced by renewable energy sources day by day. Because air pollution from fossil fuels and global warming has become a major problem (Saravanan et al., 2018). CO_2 emissions from fossil fuels increased by 2.5% compared to the last year (Roy et al., 2019). Biogas is preferred among these renewable energy sources (Korberg et al., 2020). In addition, it has been stated that with integrated systems, existing systems can be used in a more useful (Yuksel et al., 2021) In the literature, studies of integrated systems and biogas-supported power generation systems are found in large numbers.

Bamisile et al. (2020) stated that discrete renewable energy is one of the challenges faced in multiple renewable energy-supported production systems. As a solution, they proposed an integrated system design with biogas support. They also conducted energy and exergy analyses of this integrated system. As a result of the analysis, the overall energetic efficiency of the system considering all the case studies ranges from 64.91% to 71.06%, while the exergetic efficiencies range from 31.80% to 53.81%. The CO_2 emission analysis results show that the system is environmentally friendly. Zare (2020) considered a closed gas turbine (CCGT) cycle with biomass-fuelled in its proposed design. He examined the compressor inlet air from a thermodynamical point of view as two systems with and without cooling. He stated that compressor inlet cooling is more performance both thermodynamically and economically. In these conditions, he stated that the system will provide a nearly 30.1% increase in energy and exergy efficiencies. Khan et al. (2021) have proposed and analyzed a novel solar-driven multigenerational system producing electricity, cooling, hydrogen and freshwater. The system consists of the parabolic dish collector with hybrid nanofluids, re-compression S-CO_2 Brayton cycle, proton exchange membrane (PEM) electrolyzer, desalination unit and double effect lithium-bromide/water absorption cycle. The results in the analysis indicate that the overall energy and exergy efficiencies of the proposed system are 31.59% and 30.02%, respectively; while the production of fresh water and cooling load are 1.564 kg/s and 196.1 kW, respectively. In this study, the aim of this study was to examine the thermodynamic performance of power generation from biomass-assisted gas turbine and multi-generation system useful outputs from exhaust gas. It is also designed as an integrated system to use the fuel required for the gas turbine in power production by taking it from these biomass. Additional power was also targeted from gas turbine exhaust gas with the Rankine cycle. In the multi-system integrated production model, power, hydrogen production-compression, ammonia production, and single effect absorption cooling will be performed.

II. System Description

A schematic diagram of the proposed comprehensive system for multi-generation is displayed in Fig. 1. This system consists of 7 subsystems which are; biogas system, Brayton cycle system, Rankine cycle system, thermo-electric generation, hydrogen production-compression, ammonia production and single effect absorption cycle. Poultry manure and corn silage are compared in certain proportions in the mixture bunker. As a homogeneous mixture, it enters the digester and enters the gasification process with the waste heat of the gas turbine. Here, the biogas in the fuel state is sent to the combustion chamber of the gas turbine (stages 1 through 5). As a result of the energy generated by combustion in the gas turbine, power is obtained from the turbine (6-10 stage). The end-of-combustion gases first enter the digester with the gas holder and then into the Rankine cycle heat exchanger Hex1. Saturated water pressed by a pump passes into steam in a heat exchanger. Power generation is achieved by passing steam through the Rankine turbine. High-energy steam at the turbine output passes through the Teg, providing additional power generation while liquefying in its Steam so that the cycle can be repeated (stages 16-23). The exhaust gas of the gas turbine coming out of HEX 1 is sent to the PEM. From here, heated water from PEM electrolysis is decomposed into hydrogen and oxygen. Some of the resulting hydrogen is compressed in the hydrogen

compression process and sent to the storage tank (stages 24-25 and 32 through 40). The other part is also sent to the ammonia production process and ammonia production is done (stages 27 through 31). Finally, the exhaust gas coming out of the PEM kettle enters the generator of the single-acting absorption cooling cycle, providing cooling thanks to ejector cooling (stages 14-15 and 41 to 59).

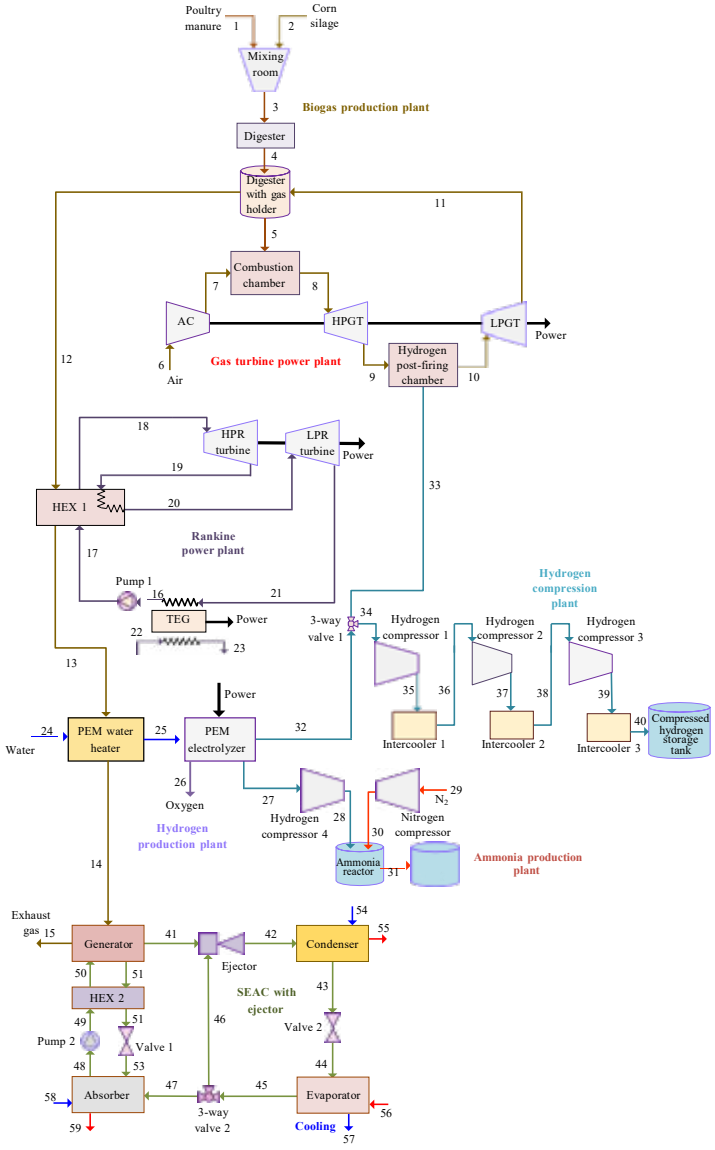


Fig.1 Schematic diagram of biomass gasification based integrated plant for hydrogen generation

III. Analysis

In the modeled plant, it has been thermodynamically examined using energetic and energy efficiency methods for sustainable hydrogen production. In this context, taking into account the first and second laws of thermodynamics, four fundamental equations of mass, energy, entropy and exergy equilibrium can be given as follows (Dincer & Rosen, 2012);

$$\dot{m}_i = \dot{m}_e \quad (1)$$

$$\dot{Q}_i + \dot{W}_i + \sum \dot{m}_i h_i = \dot{Q}_e + \dot{W}_e + \sum \dot{m}_e h_e \quad (2)$$

$$\sum \left(\frac{\dot{Q}}{T}\right)_{in} + \sum \dot{m}_i s_i + S_{gen} = \sum \left(\frac{\dot{Q}}{T}\right)_e + \sum \dot{m}_e s_e \quad (3)$$

$$\dot{E}x^{\dot{Q}_{in}} + \dot{E}x^{\dot{W}_{in}} + \sum \dot{m}_i ex_i = \dot{E}x^{\dot{Q}_e} + \dot{E}x^{\dot{W}_e} + \sum \dot{m}_e ex_e + \dot{E}x_{des} \quad (4)$$

Here, the subscripts “I” and “e” describe the streams inlet and exit the components. Also, h and s explain the enthalpy and entropy terms, respectively. The heat and work exergy rates can be defined as:

$$\dot{E}x^{\dot{Q}} = \dot{Q}\left(1 - \frac{T_0}{T_{source}}\right) \quad (5)$$

$$\dot{E}x^{\dot{W}} = \dot{W} \quad (6)$$

IV. Results and Discussion

Detailed performance analysis of the new design model, whose schematic representation is given above, is handled by determining the exergy destruction rates together with the energy and exergy efficiencies. Before moving on to these calculations, the assumptions presented in Table 1 in the system are made and the kinetic and potential energy changes of the whole system are neglected. Besides, the whole plant and components are modeled as a steady-state flow. The results of this parametric study carried out with a package program called EES (Klein, 2020) are illustrated in Table 2 below.

Table .1 Working conditions for combined system.

Parameters	Values
Combustion chamber temperature, T_{CC}	835 °C
HPGT working pressure, P_{HPGT}	794.2 kPa
LPGT working temperature, T_{LPGT}	790 °C
LPGT working pressure, P_{LPGT}	279.4 kPa
HPRT working temperature, T_{HPRT}	525 °C
HPRT working pressure, P_{HPRT}	8000 kPa
LPRT working temperature, T_{LPRT}	400 °C
LPRT working pressure, P_{LPRT}	1200 kPa

Table 2. Production of useful outlets

Useful outputs	Values
Power production from HPGT, W_{HPGT}	6456 kW
Power production from LPGT, W_{LPGT}	5831 kW
Power production from HPRT, W_{HPRT}	2517 kW
Power production from LPRT, W_{LPRT}	1891 kW
Power production from thermoelectric generator, W_{TEG}	625 kW
Cooling production rate, $Q_{Cooling}$	2834 kW
Heating production rate, $Q_{Heating}$	3627 kW
Hydrogen production rate, $\dot{m}_{Hydrogen}$	0.0658 kg\s
Ammonia production rate, $\dot{m}_{Ammonia}$	1.843 kg\s

Figs. 2, 3 and 4 shows the effect of the change in dead state temperature on the energy and exergy efficiency of the novel biomass gasification based integrated system and on the performance of power generation, hydrogen production and compression, absorption cooling and ammonia production. As can be seen in the energy and exergy graphs, power generation and heating increase with increasing dead-state temperature. However, the energy and exergy efficiency of the absorption cooling system decreases. The reason for this is that the efficiency decreases due to the increase in the condenser load.Looking at the useful outputs, the highest trend of increase has been in gas turbine and ammonia production.Increasing the dead-state temperature caused an increase in ammonia production from 1.377 kg/s to 2.195 kg/s.

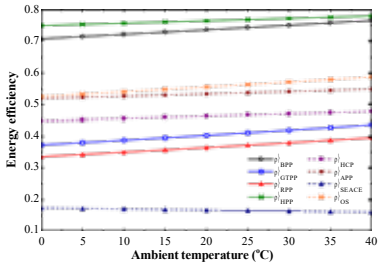


Fig.2. Effect of ambient temperature on the energy efficiencies.

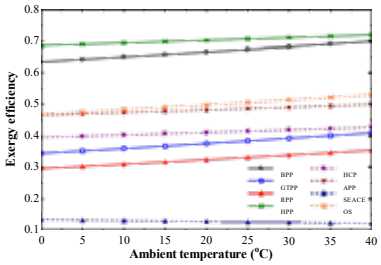


Fig.3. Effect of ambient temperature on the exergy efficiencies.

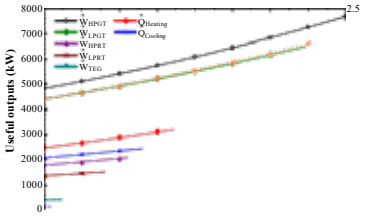


Fig.4. Effect of ambient temperature on the useful outputs.

V. Conclusion

The new configuration of the ovel biomass gasification based integrated system is proposed and analyzed based on the thermodynamic perspective. The modeled system produces useful products which are power, hydrogen production and compreesion, ammonia production and absorption cooling. Calculated and determined of some important results can be briefly summarized as below;

- The energy efficiencies of the BPP, GTPP, RPP, HPP, HCP, APP, SEACS and overall plant are 73.41%, 40.82%, 36.85%, 76.64%, 46.51%, 53.52% 16.57% and 56.01%, respectively.
- The exergy efficiency of subsystems, whcih given before, and overall plant are campoted as 66.03%, 38.56%, 32.74%, 70.33%, 41.36%, 48.27%, 12.61% and 49.93%, respectively.
- Hydrogen generation capacity and ammonia production capacity is 0.0658 kg/s and 1.843 kg/s, respectvily.
- The rise in the pressure of the combusstion chamber has a positive effect on the system's performance.

Reference

Bamisile, O., Huanh, Q., Li, J., Dagbasi, M., Kemena, A. D., Abid, M., Hu, W. (2020). Modelling and performance analysis of an innovative CPVT, wind and biogas integrated comprehensive energy system: An energy and exergy approach. *Energy Conversion and Management*, *209*, *112611*.

Dincer, I., & Rosen, M. A. (2012). *Exergy: energy, environment and sustainable development*. Newnes.

Khan, M. S., Abid, M., Bashir, A. M., Amber, K. P., Khanmohammadi,S., Yan, M. (2021). Thermodynamic and exergoeconomic analysis of a novel solar-assisted multigenerational system utilizing high temperature phase change material and hybrid nanofluid. *Energy Conversion and Management*, *236*, *113948*.

Klein, S. A., (2020). EES-engineering equation solver. *F-chart software*. V10.8353

Korberglva, A. D., Skov, I. R., VadMathiesen, B. (2020). The role of biogas and biogas-derived fuels in a 100% renewable energy system in Denmark. *Energy*, *199*, *117426*.

Roy D, Samanta S, Ghosh S. (2019). Techno-economic and environmental analyses of a biomass based system employing solid oxide fuel cell, externally fired gas turbine and organic Rankine cycle. *Journal of Cleaner Production*, 225, 36–57.

Saravanan, A.P., Mathimani, T., Deviram, G., Rajendran, K., Pugazhendhi, A. (2018). Biofuel policy in India: a review of policy barriers in sustainable marketing of biofuel. *Journal of Cleaner Production*, 193, 734–747.

Yuksel, Y. E., Ozturk, M., & Dincer, I. (2021). Evaluation of a new geothermal based multigenerational plant with primary outputs of hydrogen and ammonia. *International Journal of Hydrogen Energy*.

Zare, V. (2020). Performance improvement of biomass-fueled closed cycle gas turbine via compressor inlet cooling using absorption refrigeration; thermoeconomic analysis and multi-objective optimization. *Energy Conversion and Management, 215, 112946.*

Hydrogen from Poppy Seed Gasification over Co-La/Sepiolite Catalyst

[1]Alattin ÇAKAN, [1]Burcu KİREN, [1*]Nezihe AYAS
[1]Eskişehir Technical University, Faculty of Engineering, Department of Chemical Engineering, İki Eylül Campus, Eskişehir, 26000, Turkey

* E-mail: nazcan@eskisehir.edu.tr

Abstract
The air gasification of poppy seed (PS) using a series of Co catalysts supported on calcined sepiolite with ranging lanthanum (La) loadings was investigated. The experiments were carried out in a fixed bed tubular reactor and operated in the temperature range of 550 to 850 °C. The results disclosed that the hydrogen content of gas product was strongly impacted and significantly enhanced with increasing temperature in absence of catalyst, producing 3.89 mol H_2/kg poppy seed at 850 °C. Besides, the catalyst doped with 10 wt.% La drastically enhanced the catalytic activity resulting extraordinarily high combustible gas production. The gaseous products obtained at 550 °C include H_2 (2.58 mol/kgPS), CO (13.30 mol/kgPS), CO_2 (0.57 mol/kgPS) and CH_4 (1.17 mol/kgPS) with 10 wt.% loading of Co/La-SEP catalyst.

Keyword: Poppy seed, Co/xLa-SEP catalyst, gasification, syngas, hydrogen

I. Introduction

The rapid population expansion and unprecedented industrial growth has been resulted in relentless exploitation of fossil based fuels. Thus, over-utilizing of this non-renewable sources is escalating the greatest environmental threats the globe face recently; such as, releasing a great deal of anthropogenic CO_2 emission and harmful gases that make a huge contribution to greenhouse effect (Deepak etal., 2021). Therefore, the move to curb this trend is now being investigated through utilizing many alternative sources of energy, out of which biomass, its ample availability and its reasonable cost along with facilitating the production of renewable liquid transportation fuels, chemicals, increases the share of biomass to susbstitute fossil fuels (Safarian etal., 2020). It is considered that biomass might have a substantial stake for the realisation of hydrogen economy in near future (Samimi etal., 2020).

Biomass gasification is a multi-step process that includes drying, devolatilization, gasification and char burn-out to transform biomass into a combustible gas fuel in the presence of various gasifying agent, namely air, steam, carbon dioxide and the mixture of these gases as well. Although syngas derived biomass gasification could be fired on a gas engine or utilized in steam turbine, combined heat and power (CHP) and integrated gasification combined cycle (IGCC) are the most pervasive approach for use in industrial scale power generation (Situmurang etal., 2020). Due to its broad set of applications ranging from refinery industries to electrified transportation technologies, the demand for hydrogen has made a threefold jump since 1975. To fulfill this demand, gasification is one of the primary conversion routes for producing hydrogen. Hydrogen production via gasification is economically competitive with natural gas reforming. Water-gas-shift (WGS) reaction and steam reforming reaction play predominant role in determining hydrogen concentration during gasification process (Rauch etal., 2014).

To our knowledge, the assesment of PS in the gasification was not reported in the literature. In the current study, Co/xLa-SEP (x=0, 4, 6, 8, 10 wt.%) catalysts was synthesized by precipitation method and employed in the air gasification of PS with the objective of enhanced hydrogen production and tar reduction with the variation of different reaction parameters.

II. Experimental Set-up and Procedure

Material

The biomass utilized in the current study is PS, which supplied from alkaloid factory located at the Bolvadin, Turkey. PSs were crushed with a stainless steel rod as fine as possible before introducing to the gasifier.
Sepiolite (SEP) was procured from a commercial company and utilized as a support material for catalysts after being crushed and sieved to obtain particle size below 50 µm. All chemicals including $Co(NO_3)_2{\cdot}6H_2O$ (Merck, 99%), $La(NO_3)_3{\cdot}6H_2O$ (Abcr GmbH, 99%) and NaOH (VWR Chemicals, 98.8%) were of sufficient purity and were used as received without further purification. All aqueous solutions were prepared with deionized water (Milli-Q treated).

Catalyst preparation

First of all, the raw sepiolite was treated with 5 mol/L HNO_3 aqueous solution and then followed by calcination according to the procedure described in the literature [6]. Thereafter, predetermined amount of $Co(NO_3)_2{\cdot}6H_2O$ and $La(NO_3)_3{\cdot}6H_2O$, used as the precursor of Co and La, respectively, was dissolved in 250 mL deionized water. The cobalt content of all of the catalysts was fixed at 10 wt.%. Then, the fixed amount of sepiolite was added to the mixture, and the obtained suspension was continuously stirred with a magnetic bar, at 60 °C for 2 h. Afterward, the precipitating agent (5 M NaOH) was slowly added drop by drop until the mixture reached a pH of ~10 under constant stirring. The solution was maintained at 60 °C under continuous stirring for 2 h. The obtained suspension was aged at 60 °C for 12 h and washed with deionized water until the pH reached 7. After filtration, the sediment was dried at 105 °C and then calcined at 700 °C for 4 h (Chen etal., 2019).

Experimental set-up

In this study, the experiments were performed in a fixed bed tubular reactor under the condition of restricted air

atmosphere, by varying the reaction parameters over a wide range. The reactor is 316 stainless steel whose internal diameter and height are 10 mm and 900 mm, respectively. Heating was maintained by means of external source and ceramic insulator was harnessed for the insulation of the reactor vessel. By installing a flow regulator, the flow of high purity dry air was controlled prior to subjecting to reactor bottom. Removal of gas mixture from liquid was achieved in gas-liquid separator, and liquid free gas mixture was directed to the moisture and particle trap for further cleaning before being collected in a gas-sampling bag.

The quantitative analysis of gas mixture was performed on a gas chromatograph (μ-GC 3000, Agilent) fitted with a thermal conductivity detector (TCD) and molecular sieve MS5A and PPQ (PolarPlot Q) columns, with Helium and Argon as the carrier gases.

III. Analysis

Characterization of catalysts

FT-IR spectra of the synthesized catalysts were obtained using the Thermo Fisher Scientific-Nicolet iS10 FTIR spectrometer (Waltham, MA, USA), at a resolution of 4 cm^{-1} after 16 scans in the 4000-600 cm^{-1} by the conventional ATR disk tablet method. The spectra were recorded and analysed using Omnic 9 Spectra Software.

Thermo-gravimetric and differential thermal analysis (TG/DTA) measurements were performed using a Perkin Elmer STA 6000 equipment, in the 30-850 °C temperature range (heating rate=10 °C/min) under nitrogen atmosphere with flow of 50 mL.

Experimental procedure of PS

The catalytic and noncatalytic gasification of PS were conducted to elucidate the influence of temperature, various loading of La loadings on the distribution gaseous product. To this objective, 3 g of PS was loaded into the reactor to see the effect of the variation of temperature (550, 650, 750, 850 °C) for 15 min. High purity dry air was employed for the initiation of gasification reactions with the flow rate of 3 L/h. For the catalytic activity tests, the same procedure was applied with addition of varying La (0, 4, 6, 8 ,10 wt.) doped Co/xLa-SEP with the catalyst to biomass ratio of 20 wt./wt. at 550 °C. After the completion of the gasification, the received gas was identified with the μ-GC and then followed by its volume determination through water-displacement technique. The liquid product was discharged from gas-liquid separator. The spent catalyst was removed from solid residue and after being dried at 105 °C, it is utilized for further analysis.

IV. Results and discussions

Characterization of catalysts

Infrared spectroscopy of prepared catalysts is shown in Fig. 1. The FTIR spectrums show prominent peaks at 780-810, 1085-1050 and 2349 cm^{-1}, which are attributed the stretching vibration of the C-H, C-O and CO_2, respectively.

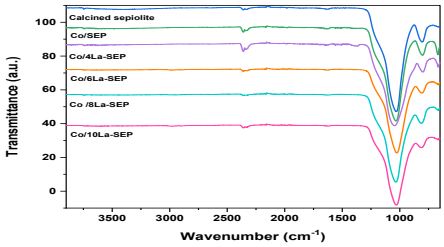


Fig. 1: FT-IR Spectra of the calcined sepiolite and synthesized catalysts,

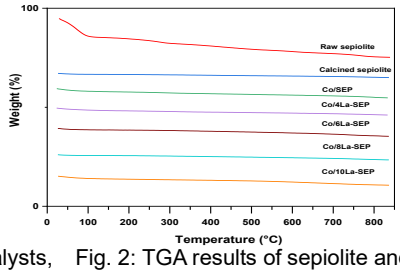


Fig. 2: TGA results of sepiolite and synthesized catalysts

As shown in Fig. 2, during the thermal degregation of raw sepiolite, a single major mass loss was observed at 100 °C accompanying by mass loss percentage of 10%. This is probably due to the removal of zeolitic or channel water. However, calcined sepiolite and catalysts with various La doping amounts show excellent thermal stability, for this reason they preserve their properties.

Gasification of PS

The influence of temperature

Temperature appears to have a significant influence on heating value and syngas composition and according to Le Chatelier's principle, the thermodynamic behavior of exothermic and endothermic reactions taking place during gasification depending on temperature manages the gaseous product and their characteristic behavior (Sansaniwal etal., 2017).

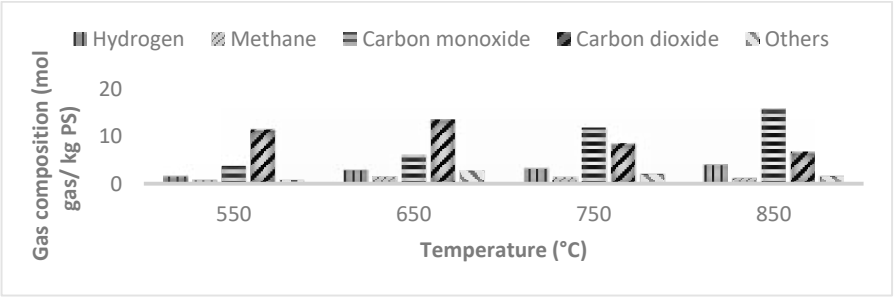


Fig. 3: Effect of temperature on gaseous product distribution (without a catalyst, 3 L/h air flow rate, 15 min. reaction time)

As demonstrated in Fig. 3, ranging temperature from 550 °C to 850 °C considerably improved H_2 content of syngas, increasing from 1.5 to 3.89 mol H_2/kg PS. CO concentration, on the other hand, enhanced dramatically from 3.80 to 15.89 mol H_2/kg PS, significantly exceeding hydrogen content with elevated temperature. However, the amount of CO_2 and CH_4 and other gaseous including ethane and propane increased up to temperature of 650 °C, thereafter, displayed opposite trend with raising temperature.

The influence of various La loading content

In order to evaluate the impact of La promoter and find the most convenient loading of La promoter content in Co/Sep, the PS were firstly gasified with catalysts having different La loadings at 550 °C for 15 min, and the corresponding results were given in Fig. 4.

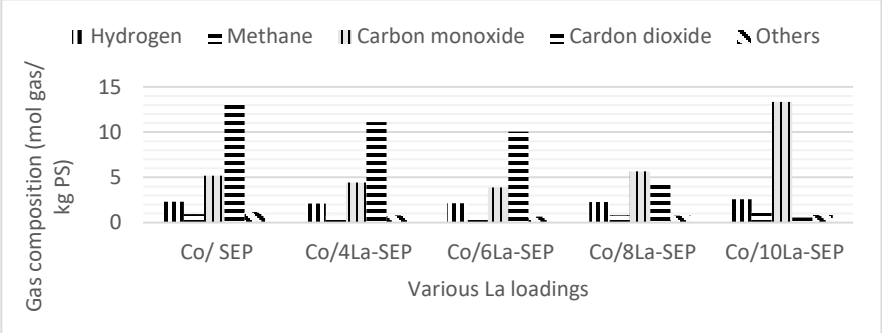


Fig. 4: Effect of different La loadings on gaseous product distribution (550 °C, 20 wt. % catalyst ratio, 3 L/h air flow rate, 15 min. reaction rate)

As shown in Fig. 4, raising La content in the catalyst enhanced the composition of syngas, and the highest hydrogen yield was achieved in the case of 10 La wt.% loading. The similar findings was observed from research done by Su etal. (2020). On the other hand, addition of 10% La led to a significant diminution in CO_2 content, dwindling from 13.25 to 0.83 mol gas/kg PS. Although the fraction of CO showed a decreasing trend at low La loading (0-6 wt.%), it has started to display an upward tendency at high La loadings.

V. Conclusions

In the current study a series of promoter with various La loadings in Co/xLa-SEP were evaluated in the gasification of PS. According to the findings obtained, the composition of combustible gases including H_2 an CO are in dependence of temperature within 550-850 °C. It was also found that the syngas composition was profoundly affected by loading of La that increase catalytic activity of catalyst. Co/10La-Sep exhibited the superior performance, generating 2.58 mol H_2/kg PS at relatively low temperature. For the illimination of synergic relation of Co and La, the inclusion of various reaction parameters such as higher reaction temperature, varying catalyst ratio as well as different residence time may be the future direction of present study.

Acknowledgements

This research was financially supported by Eskisehir Technical University Scientific Research Project Fund through project no 20ADP107.

References

Chen M., Wang C., Wang Y., Tang Z., Yang Z., Zhang H., Wang J., Hydrogen production from ethanol steam reforming: Effect of Ce content on catalytic performance of Co/Sepiolite catalyst, Fuel, 247, 344–355, (2019).

Deepak S., Sampath K., Sujit S., Feasibility studies of coconut shells biomass for downdraft gasification, Materials Today: Proceedings, (2021).

Rauch R., Hrbek J., Hofbauer H., Biomass gasification for synthesis gas production and applications of the syngas, Wiley Interdisciplinary Reviews: Energy and Environment, 3, 343–362, (2014).

Safarian S., Saryazdi S.M.E., Unnthorsson R., Richter C., Artificial neural network integrated with thermodynamic equilibrium modeling of downdraft biomass gasification-power production plant, Energy, 213, 118800, (2020).

Samimi F., Marzoughi T., Rahimpour M. R., Energy and exergy analysis and optimization of biomass gasification process for hydrogen production (based on air, steam and air/steam gasifying agents), International Journal of Hydrogen Energy, 45, 33185–33197, (2020).

Sansaniwal S.K., Rosen M.A., Tyagi S.K., Global challenges in the sustainable development of biomass gasification: An overview Renewable and Sustainable Energy Reviews, 80, 23–43, (2017).

Situmorang Y.A., Zhao Z., Yoshida A., Abudula A., Guan G., Small-scale biomass gasification systems for power generation (<200 kW class): A review, Renewable and Sustainable Energy Reviews, 117, 109486, (2020).

Su H., Kanchanatip E., Wang D., Zhang H., Antoni, Mubeen I., Huang Z., Yan M., Catalytic gasification of food waste in supercritical water over La promoted Ni/Al_2O_3 catalysts for enhancing H_2 production, International Journal of Hydrogen Energy, 45, 553-564, (2020).

Thermodynamic Modeling of a Combined Plant for Clean Hydrogen Generation using High Pressure Air Storage Plant

[1]*Mehmet Altınkaynak, [2]Murat Ozturk,
[1]Isparta University of Applied Sciences, Faculty of Technology, Department of Mechanical Engineering, 32200, Isparta/Turkey
[2]Isparta University of Applied Sciences, Faculty of Technology, Department of Mechatronics Engineering, 32200, Isparta/Turkey
E-mails: mehmetaltinkaynak@isparta.edu.tr, muratozturk@isparta.edu.tr

Abstract:
In the proposed research, a new configuration of compressed air storage based multigeneration plant is proposed and analyzed based on the thermodynamic perspective. The modeled system produces useful products which are power, hydrogen, hot water, and absorption cooling. The operation of air storage tank coupled to the gas turbine, and the use of waste heat in the multiple generation model caused an increase in power generation by 39.4%.In terms of energy efficiency for ORC 1, ORC 2, BC, sCPPP, HPP and SEACS calculated as 18.44%, 16.99%, 41.17%, 14.96%, 62.77%, 15.78% and 30.65%, respectively.In terms of exergy efficiency for these sub-systems are 16.39%, 14.27%, 36.99%, 11.95%, 57.99%, 12.47% and 24.77%, respectively. Hydrogen generation capacity is 0.0726 kg/s.The rise in the pressure level of air storage tank has a positive effect on the system's performance.
Keywords: Analysis; energy; exergy; air storage; hydrogen.

I. Introduction

The use of fossil fuels is still ongoing. But from the perspective of environmental impact and global warming, most countries are moving away from these levels. Instead, the focus on renewable energy sources is growing rapidly. Looking at renewable energy sources, power generation from solar, wind, geothermal, hydraulic and waste heat has started to gain importance. Waste heat exists at very high temperatures and high flow rates in the industry and in solid or gas-fired power generation plants. From the point of view of energy use, transport with air, use air, process air, etc. Facilities are available for use. Compressors are used for the preparation and pressurization of the process and use air. High energy consumption occurs in compressors. Compressors can be fed with renewable energy to prevent or reduce this consumption. In addition, compressed air can be provided more economically with air storage systems. In the literature, a rapid concentration is observed on integrated systems that provide power generation from air storage and waste heat. Cavallo (2007), stated that compressed air storage systems can be used in intermittent wind energy, hybrid wind/compressed air energy storage (CAES) systems. Bagdanavicius and Jenkins (2014), conducted an energy and exergy analysis for a compressed air storage system. In their study, they tried to show that the compression energy can benefit from the heat. At this stage, they proposed two types of systems. They found CAES and CAES-TG respectively. Energy efficiency 48% and 86%, respectively. Patil and Ro (2020) proposed a design with 500m depth and 2MWh capacity, which they call the Ocean compressed air energy storage (OCAES) system. These have examined the efficiencies of all their ingredients for OCAES. As a result of the examination, they stated that in increasing the air storage depth, the dpeolama volume requirement decreased. In the literature, this stored compressed air is generally used in power generation. Zare V. and Hasanzadeh M. (2016) conducted an energy and exergy analysis of a closed Brayton cycle integrated into the solar tower. As a result of the analysis, they stated that the exergy efficiency is higher than 30% for the power plant. Additionally, the proposed power cycles were reported to have better performance than other researched RC and supercritical CO2 systems.

Ghaebi et al. (2018) suggested a new multigeneration plant that consists of the absorption process, Kalina cycle, humidification-dehumidification desalination plant, and hot water production process. Based on the optimization of their proposed plant shows that the energy and exergy efficiencies are 94.84% and 47.89%, and also, the total unit cost of the product is 89.95 $/GJ. Yuksel et al. (2019) examined a new solar tower that supported the multigeneration system with hydrogen-generating. According to applied different operating parameters, they computed the energetic and exergetic effectiveness of their system are 65.17% and 62.35%.

In this study, it is planned to store the energy of air preparation systems with high energy consumption based on the power provided from renewable energy (wind and solar supported). Additional power generation will also be provided with two ORCs in the decolonization applied in the air storage systems. It is also designed as an integrated system to use the air required for the gas turbine in power production by taking it from these tanks. Additional power is also targeted from the gas turbine exhaust gas with the S-CO_2 Brayton cycle. In the integrated production model for multigeneration, hydrogen production, liquefaction and single effect absorption cooling are performed.

II. System Description

In this study, a multi-power generation model from power generation and waste heat with air storage assisted gas turbine is given in Figure 1. The electrical energy required for air storage is provided by wind turbines and solar panels. Here, power is produced with ORC turbines using HEX 1 and HEX 2 from the heat released during air pressurization. Compressed air is sent to the gas turbine and used as combustion air. The air entering the gas turbine with the fuel comes out as waste gas after the power generation is achieved. This waste gas first transfers its heat in the S-CO_2 (supercritical carbon dioxide) heat exchanger named HEX 3. From here, the S-CO_2 enters the turbine and the power generation is ensured in the S-CO_2 turbine. Additional electricity generation is provided by using TEG as a condenser function at the turbine outlet. The waste gas, whose energy is reduced a little, enters the PEM water heater. The water heated here enters the PEM electrolyzer for hydrogen production and is sent to

the storage tank with the generated hydrogen booster. The waste gas from the PEM water heater enters the generator of the absorption cooling system. Here, cooling is performed with the single effect absorption cooling system.

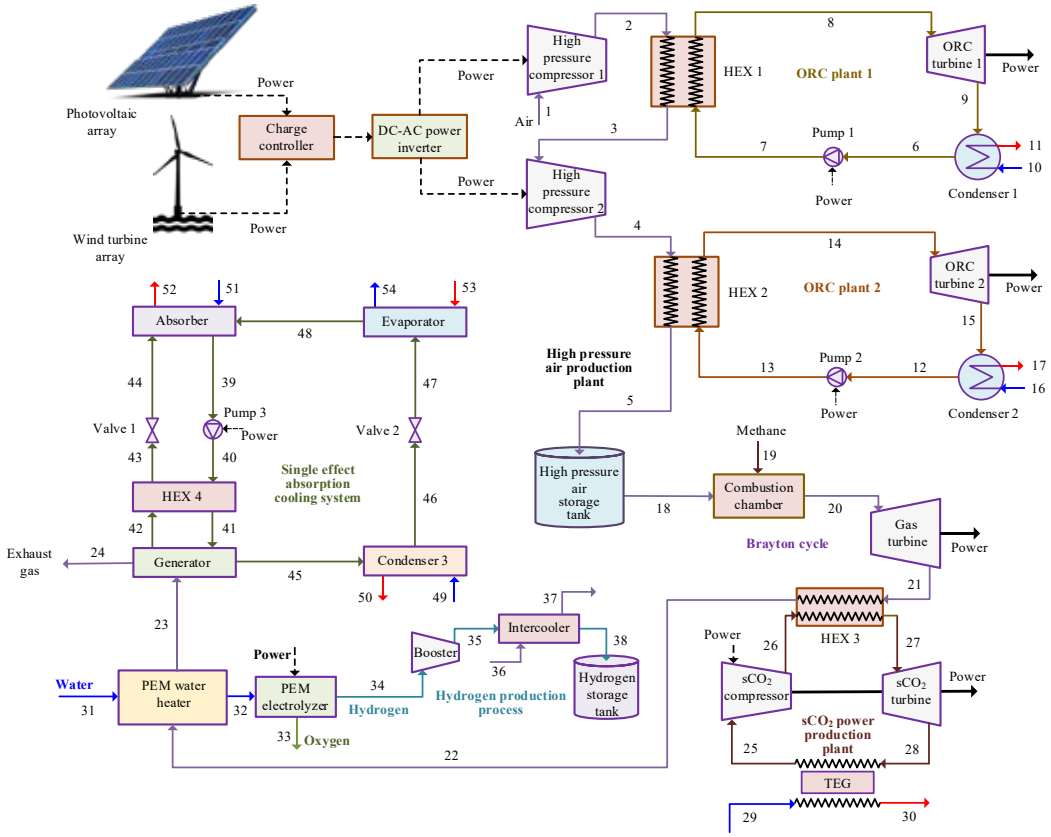


Fig. 1. The schematic diagram of the compressed air storage based multigeneration plant.

III. Analysis

In the modeled plant, it has been thermodynamically examined using the energetic and energy efficiency methods for sustainable hydrogen production. In this context, taking into account the first and second laws of thermodynamics, four fundamental equations of the mass, energy, entropy and exergy equilibrium can be given as follows (Cengel & Boles, 2007; Dincer & Rosen, 2012);

$$\dot{m}_i = \dot{m}_e \quad (1)$$

$$\dot{Q}_i + \dot{W}_i + \sum \dot{m}_i h_i = \dot{Q}_e + \dot{W}_e + \sum \dot{m}_e h_e \quad (2)$$

$$\sum \left(\frac{\dot{Q}}{T}\right)_{in} + \sum \dot{m}_i s_i + \dot{S}_{gen} = \sum \left(\frac{\dot{Q}}{T}\right)_{e} + \sum \dot{m}_e s_e \quad (3)$$

$$\dot{E}x^{\dot{Q}_{in}} + \dot{E}x^{\dot{W}_{in}} + \sum \dot{m}_i ex_i = \dot{E}x^{\dot{Q}_e} + \dot{E}x^{\dot{W}_e} + \sum \dot{m}_e ex_e + \dot{E}x_{des} \quad (4)$$

Here, the subscripts i and e describe the streams inlet and exit the components. Also, h and s explain the enthalpy and entropy terms, respectively. The heat and work exergy rates can be defined as:

$$\dot{E}x^{\dot{Q}} = \dot{Q}\left(1 - \frac{T_0}{T_{source}}\right) \quad (5)$$

$$\dot{E}x^{\dot{W}} = \dot{W} \quad (6)$$

After writing the general balance equation, the specific exergy term can be writed as:

$$ex = (h - h_0) - T_0(s - s_0) \quad (7)$$

IV. Results and Discussion

Detailed performance analysis of the new design model, whose schematic representation is given above, is handled by determining the exergy destruction rates together with the energy and exergy efficiencies. Before moving on to these calculations, the assumptions presented in Table 1 in the system are made and the kinetic and potential energy changes of the whole system are neglected. The reference temperature and pressure are taken as 25 °C and 101.3 kPa, respectively. Besides, the whole plant and components are modeled as a steady-state flow. The results of this parametric study carried out with a package program called EES (Klein, 2020) are illustrated in Table 2 below.

Figs. 2, 3 and 4 shows the effect of the change in dead state temperature on the energy and exergy efficiencies of the multi-generation system and on the performance of power generation, heating, absorption cooling and hydrogen production. As can be seen in the energy and exergy graphs, power generation and heating increase with increasing dead-state temperature. However, the energy and exergy efficiency of the absorption cooling system decreases. The reason for this is that the efficiency decreases due to the increase in the condenser load.Increasing the dead-state temperature caused an increase in hydrogen production from 0.061 kg/s to 0.081 kg/s. Considering the power generation processes, the highest power increase occurs in the gas turbine unit.

Table .1 Input variables for the designed system

Parameters	Values
Pressure of compressed air storage, P_{CAS}	1013 kPa
ORC turbine 1 inlet temperature, T_8	78.18 °C
ORC turbine 1 inlet pressure, P_8	1001 kPa
ORC cycle 1 working fluid	n-pentane
ORC turbine 2 inlet temperature, T_{14}	142.3 °C
ORC turbine 2 inlet pressure, P_{14}	1456 kPa
ORC cycle 2 working fluid	n-pentane
Combustion chamber temperature, T_{CC}	800 °C
Gas turbine inlet pressure, P_{20}	1013 kPa
Natural gas mass flow rate, $\dot{m}_{ng}$	2.18 kg/s
sCO_2 turbine inlet temperature, T_{27}	272.6 °C
sCO_2 turbine inlet pressure, P_{27}	22600 kPa

Table 2. Proposed system analyses results

Useful outputs	Values
Power production from ORC turbine 1, $\dot{W}_{ORCT1}$	4142 kW
Power production from ORC turbine 2, $\dot{W}_{ORCT2}$	6873 kW
Power production from gas turbine 1, $\dot{W}_{GT}$	39605 kW
Power production from sCO_2 turbine, $\dot{W}_{ST}$	1869 kW
Cooling production rate, $\dot{Q}_{Cooling}$	2361 kW
Heating production rate, $\dot{Q}_{Heating}$	4035 kW
Hydrogen production rate, $\dot{m}_{H_2}$	0.0726 kg\s

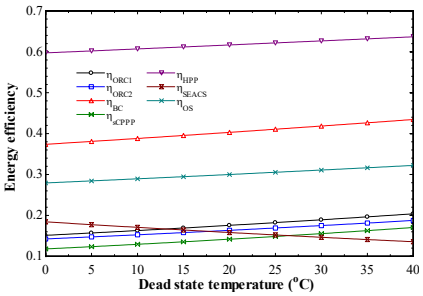


Fig.2. Effect of the dead state temperature on the system and its subsystems exergy efficiencies.

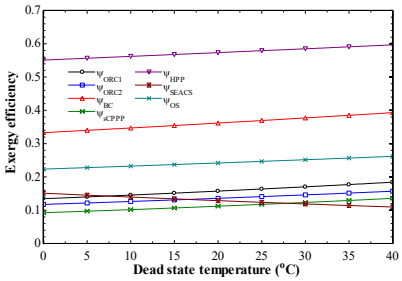


Fig.3. Effect of the dead state temperature on the system and its subsystems exergy efficiencies.

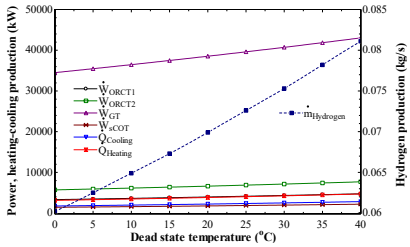


Fig.4. Effect of the dead state temperature on the useful productions.

V. Conclusion

The new configuration of the compressed air storage based multigeneration plant is proposed and analyzed based on the thermodynamic perspective. The modeled system produces useful products which are power, hydrogen, hot water, and absorption cooling. Calculated and determined of some important results can be briefly summarized as below;

• The operation of the air storage tank coupled to the gas turbine and the use of waste heat in the multiple generation model caused an increase in power generation by 39.4%.

• In terms of energy efficiency, ORC 1, ORC 2, BC, sCPPP, HPP and SEACS are 18.44%, 16.99%, 41.17%, 14.96%, 62.77%, 15.78% and 30.65%, respectively.

• In terms of exergy efficiency, ORC 1, ORC 2, BC, sCPPP, HPP and SEACS are calculated as 16.39%, 14.27%, 36.99%, 11.95%, 57.99%, 12.47% and 24.77%, respectively.

• Hydrogen generation capacity is 0.0726 kg/s.

• The rise in the pressure level of the of air storage tank has a positive effect on the system's performance.

Reference

A Cavallo, Controllable and affordable utility-scale electricity from intermittent wind resources and compressed air energy storage (CAES), Energy 32 (2007) 120–127.of an integrated flash-binary geothermal power plant with reverse osmosis desalination and absorption refrigeration for multi-generation. *Geothermics*, *89*, 101949.

A. Bagdanavicius, N Jenkins, Exergy and exergoeconomic analysis of a Compressed Air Energy Storage combined with a district energy system, Energy Convers. Manag. 77 (2014) 432–440.Barbier, E. (1997). Nature and technology of geothermal energy: a review. *Renewable and sustainable energy reviews*, *1*(1-2), 1-69.

Patil, V.C., & Ro, P.I. (2017). Modeling of liquid-piston based design for isothermal ocean compressed air energy storage system Journal of Energy Storage, 31, 101449.

V. Zare, M Hasanzadeh, Energy and exergy analysis of a closed Brayton cycle-based combined cycle for solar power tower plants, Energy Convers. Manag. 128 (2016) 227–237.

Ghaebi, H., Namin, A.S., Rostamzadeh, H. (2018). Performance assessment and optimization of a novel multi-generation system from thermodynamic and thermoeconomic viewpoints. *Energy Conversion and Management,* 165,419-439.

Yuksel, Y.E., Ozturk, M., Dincer, I. (2019). Energetic and exergetic assessments of a novel solar power tower based multigeneration system with hydrogen production and liquefaction. *International Journal of Hydrogen Energy*, *44*(26), 13071-13084.

Cengel, Y. A., & Boles, M. A. (2007). *Thermodynamics: An Engineering Approach 6th Editon (SI Units)*. The McGraw-Hill Companies, Inc., New York.

Dincer, I., & Rosen, M. A. (2012). *Exergy: energy, environment and sustainable development*. Newnes.

Klein, S. A., (2020). EES-engineering equation solver. *F-chart software*. V10.8353.

H_2 Release from $NaBH_4$ with Novel Catalyst

[1]* Aybüke Ayşe Ertürk, [2]Tugba Akkas Boynuegri, [3]Metin Gürü
[1*,3] Gazi University, Faculty of Engineering, Department of Chemical Engineering, Maltepe, Ankara, Turkey
[2]Eti Maden, Technology Development Department, Ankara, Turkey

* E-mail: erturkaybuke@gmail.com

Abstract

In this paper, the dehydrogenation reaction of $NaBH_4$ was performed in the presence of the co-catalyst involving Co and Ni metal sources. For this purpose, heterogenous catalyst was prepared by using a supporter material and metal sources, Cr MIL-101, CoF_2 and NiF_2, respectively. This metal organic framework (MOF), Cr MIL-101, was selected to obtain higher catalytic activity because of its larger specific surface area, 2 504 m^2 g^{-1}, than that of active carbon, ɣ-Al_2O_3 etc. For three different catalyst pellets consisting of %10, 20, 30 metal cites, volumes of released hydrogen from $NaBH_4$ were found as 103, 104 and 82 mL, respectively. Dehydrogenation reactions of $NaBH_4$ were carried at room temperature and optimal catalyst recipe was determined according to this produced hydrogen amount and also its endurance. The study is orginal as for prepared and used catalyst in the hydrogen release reactions of borohydrides. It is known that MOFs are promising novel materials synthesized various aims. Here, we tried to indicate its different usage area in catalytic reactions.

Keywords: Sodium borohydrides**,** catalyst, metal organic frameworks.

Energy and Exergy Analyses of a Concentrated Solar Power Generation System Integrated with a Biomass-based Hydrogen Production Process

[1*]Mehmet Emre Burulday, [1]Nader Javanı, [2]Mehmet Selçuk Mert
[1] Yildiz Technical University, Faculty of Mechanical Engineering, Besiktas, Istanbul, TR-34349, Turkey
[2]Yalova University, Faculty of Engineering, Energy Systems Engineering Department, Yalova, TR-77200, Turkey

* E-mail: memrebrldy@gmail.com

Abstract
In the present study, a concentrated solar power generation system integrated to biomass-based hydrogen production process has been investigated. It is aimed to provide required energy for the hydrogen production process and to generate extra electrical power. The high-purity hydrogen is obtained from a biomass-derived synthesis gas through thermochemical processes. The integrated model is simulated by using Aspen HYSYS software. The performance of the hybrid system is investigated in terms of energy and exergy analyses. The exergy efficiencies of the hydrogen production process and power generation system are found to be 55.8% and 39.6%, respectively. Based on an annual operating time of 7,500 hours, the amount of hydrogen gas production in the integrated system is 7,912.5 ton/year with a flow rate of 10.8 ton/h synthesis gas, while a net 38.89 MWe power output.

Keywords: Hydrogen production, Solar thermal energy, Energy and exergy analyses

I. Introduction

Hydrogen gas, which can be produced from various sources using different technologies, stands out as an alternative fuel, although it is not widely found in nature molecularly. Among the biomass conversion technologies, gasification process is preferred in biofuel production because it is an efficient and cleaner technology instead of direct combustion (Adamson, 2004). High purity hydrogen can be produced by using synthesis gas obtained as a product of gasification of biomass and tar removal. Hydrogen is regarded as a potential fuel of the future due to its environmentally friendly and sustainable character and high energy carrying capacity (Granovskii et al., 2007). The existence of rich biomass waste potentials in some regions of our country constitutes a source for the production of hydrogen gas, which is an energy carrier. At the same time, the use of domestic and renewable energy sources such as solar, geothermal and wind existing in these regions also enables clean and independent energy production. In this study, an integrated renewable power generation system with the hydrogen generation process from biomass synthesis gas based on gasification technology has been modelled, and the energy and exergy analyses of the system has been made. In the proposed system, it is aimed to produce high purity hydrogen as well as energy production, and the total efficiency of the system was examined.

II. Materials and Method

Exergy can be described as a measure of the distance of the system state to the environment, based on the first and second laws of thermodynamics. It can also be defined as the maximum useful work that can be obtained from a system. The general exergy balance for steady-flow, stable and open systems can be written as:

$$Ex_Q + \sum_i E\,x_i = \sum_o Ex_o + E\,x_W + E\,x_L + E\,x_D \quad (1)$$

Here; Ex_i , $E\ x_o$, $E\ x_Q$, Ex_W , Ex_L ve Ex_D refer respectively to inlet stream exergy, outlet stream exergy, heat transfer exergy, work transfer exergy, exergy loss and exergy destruction.

Exergy equivalence for a process unit k can be written as follows (Bejan et al., 1996; Mert et al., 2012):

$$Ex_{F,k} = E\,x_{P,k} + Ex_{L,k} + Ex_{D,k} \quad (2)$$

Here; F, P, L, and D indices define fuel, product, loss and destruction, respectively. While the total fuel exergy is the exergy of the streams entering the system, the total product exergy is the exergy of the streams coming out of the system. Total exergy loss is the total amount of exergy transferred from the system to the environment due to the temperature difference and thermodynamically lost. Total exergy destruction refers to the exergy loss caused by irreversibility within the system boundaries (Mert et al., 2012).

Exergy efficiency (ε_k) for a system or a process unit (k) is defined as the ratio of exergy of products to exergy of fuels and can be expressed as follows (Bejan et al., 1996):

$$\varepsilon_k = E\,x_{P,k}/Ex_{F,k} = 1 - (Ex_{D,k}/E\,x_{F,k}) \quad (3)$$

III. Simulation and Analysis

Synthesis gas, which is purified especially from tar, sulfur and unwanted particulate matter, is processed in a water gas shift (WGS) reactor. The WGS process is used to increase the amount of hydrogen in the gas by reacting CO in a gas stream with steam, and is a very common industrial process. The working principle of the PSA system, which is then used for high purity hydrogen separation, is based on the physical binding of gas molecules to the adsorbent material. A typical PSA system designed to produce purified product gas includes the processes in which the reactor containing adsorbent or a series of reactors are pressurized repeatedly by a compressor and the pressure reduction steps are performed (Xebec, 2014).

An integrated solar thermal power generation system model has been developed in order to meet the electrical energy required by the hydrogen generation system. Solar thermal systems are included in renewable and sustainable systems where there is no combustion process and fuel cost. In addition, organic Rankine cycle (ORC) systems, which can be integrated into solar thermal systems and provide efficient electricity generation in low heat-sourced systems, are considered as a power system that can be easily integrated for the hydrogen generation process (Guzović et al., 2014). Figure 1 shows the block flow diagram of the proposed hybrid hydrogen and power generation system. Combining the ORC-1 integrated hydrogen production process with the solar thermal power system modeled using the Rankine cycle and ORC-2 in power block, electricity and hydrogen production are carried out together.

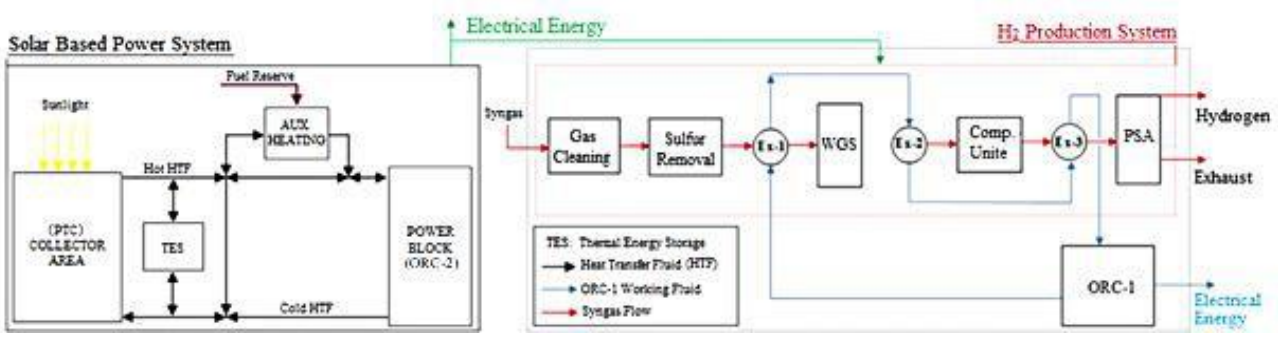
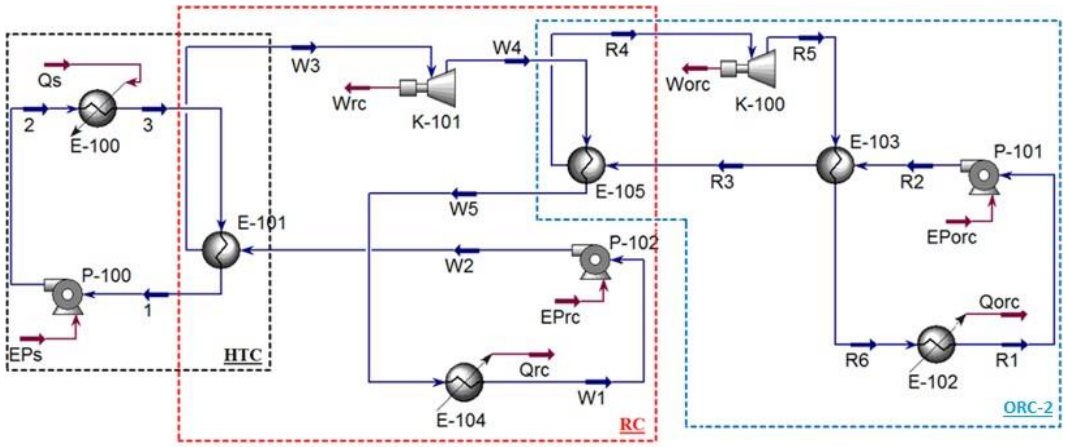


Fig. 1: Block flow diagram of hybrid hydrogen and solar thermal power generation system

IV. Results and discussions

The solar power system has been simulated using Aspen HYSYS software and the simulation screenshot is given by Figure 2. The power system consists of heat transfer cycle (HTC), rankine cycle (RC) and an organic rankine cycle (ORC-2). Also T-s diagram of power cycles (RC and ORC-2) are shown in Figure 3.



Equipment	Equipment Description	Equipment	Equipment Description	Equipment	Equipment Description
P-100	HTF Feed Pump	*E-101*	Evaporator-1 (PTC-RC)	*E-105*	Evaporator--2 (RC-ORC)
P-101	R-134a Feed Pump	*E-102*	ORC-3 Condenser	*E-106*	RC Recuparator
P-102	Su Feed Pump	*E-103*	ORC-3 Recuparator	*K-100*	ORC-3 Turbine (Expander)
E-100	PTC Heater	*E-104*	RC Condenser	*K-101*	RC Turbine

Fig. 2: Simulation screenshot of the solar based power generation system

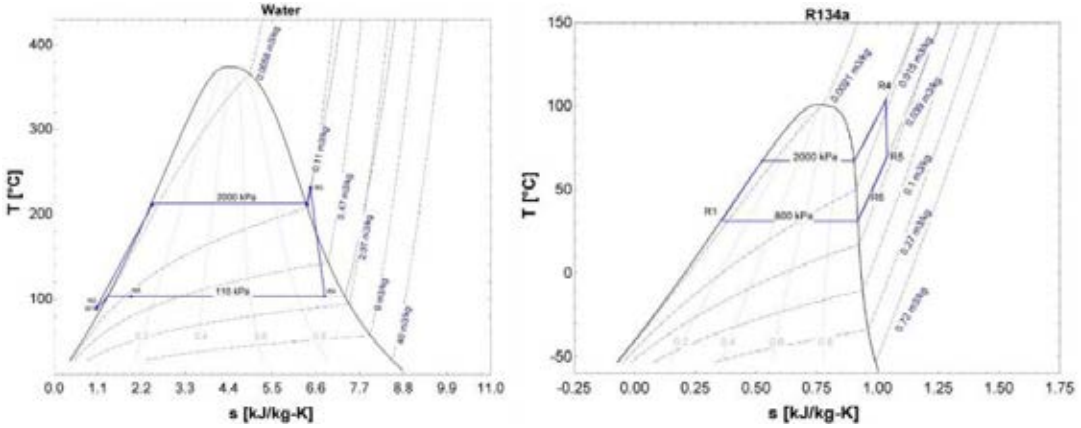
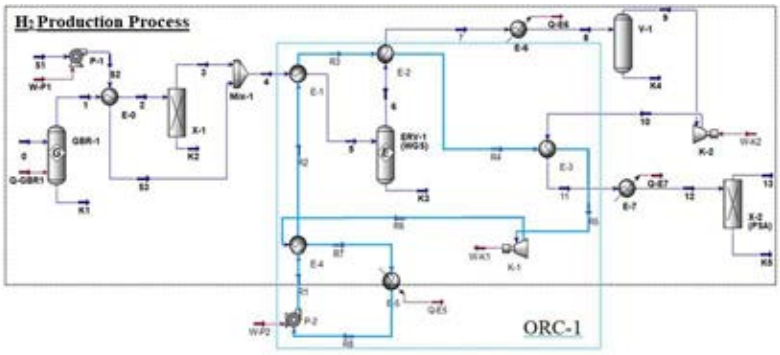
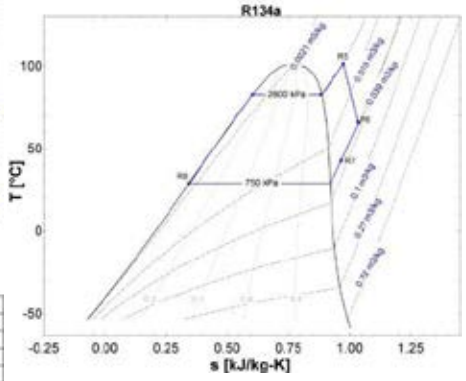


Fig. 3: T-s diagrams of Rankine and organic Rankine cycles in solar-based power system

In our previous study, ORC-1 integrated hydrogen process with a geothermal source was examined and approximately 47.6 MWe was produced. The simulation screenshot of the ORC-1 integrated hydrogen production process and the T-s diagram of the ORC-1 are shown in Figure 4 (Mert et al, 2019). In the present study, with the evaluation of the solar system, a total of 40.77 MWe was generated from the turbines.





Equipment	Equipment Description	Equipment	Equipment Description	Equipment	Equipment Description
P-1	WGS Feed Water Pump	Mix-1	Mixer	E-3	3th Heat Exchanger (ORC-1)
P-2	R-134a Feed Pump	K-1	ORC-1 Turbine (Expander)	E-4	Recuparator (ORC-1)
X-1	Sulfur Removal	K-2	Compressor	E-5	Condenser (ORC-1)
X-2	Pressure Swing Adsorption (PSA)	E-6	Heat Exchanger (WGS)	E-6	Cooler
ER1-1	Equilibrium Reactor (WGS)	E-1	1st Heat Exchanger (ORC-1)	E-7	Cooler
V-1	Separator	E-2	2nd Heat Exchanger (ORC-1)	GBR-1	Gibbs Reactor

Fig. 4: Simulation screeshot of hydrogen production process and T-s diagram of integrated ORC-1 (Mert et al., 2019).

Solar energy and synthesis gas with 100,970 kW and 54,974.58 kW exergy values are fed as fuel to the modeled integrated hydrogen and power generation system, respectively. On the other hand, 38,890 kWe net power and 35,213.79 kW exergy value of hydrogen gas are obtained as a product from the system. When the systems are operated together, the total exergy efficiency has been observed as 47.5% in reference operating conditions.

V. Conclusions

As a result, the solar power generation system consisting of RC and ORC-2 and the hydrogen production process with ORC-1 has been integrated as a hybrid system. It is evaluated that renewable biomass and solar resource energies can be used and besides, hydrogen gas, which is a high-energy carrier, can be obtained efficiently.

Acknowledgements

This study was carried out within the scope of the project titled "Hydrogen Production Technology by Gasification from Biomass" (Project no: 213M368) supported by TÜBİTAK-1003 Priority Areas R&D Projects Support Program. We would like to thank TÜBİTAK for their support. This work was also supported by Yalova University within the scope of a Master's Thesis Project (Project No: 2018/YL/009).

References

Adamson, K. (2004), "Hydrogen from renewable–the hundred year commitment", Energy Policy, 32, 1231-1242.

Bejan, A., Tsatsaronis, G., & Moran, M.., (1996). Thermal Design Optimization, John Wiley & Sons, USA.

Granovskii, M., Dincer, I., & Rosen, M. A., (2007). Greenhouse gas emissions reduction by use of wind and solar energies for hydrogen and electricity production: Economic factors. International Journal of Hydrogen Energy, 32, 927–931.

Guzović, Z., Sakoman, I. & Lončar, D., 2014. Influence of Working Fluid on ORC with Low Temperature Geothermal Source – Case Study Geothermal Power Plant "Babina Greda". 10th International Conference on Heat Transfer, Fluid Mechanics and Thermodynamics, Orlando, Florida, USA: Temmuz 14-16.

Khalid F., Dincer İ., Rosen M.A. (2017), ''Thermoeconomic analysis of a solar-biomass integrated multigeneration system for a community'', Applied Thermal Engineering 120 (2017) 645–653.

Mert, M.S., Dilmaç, Ö. F., Özkan S., Karaca F., & Bolat, E., (2012). Exergoeconomic analysis of a cogeneration plant in an iron and steel factory. Energy, 46, 78-84.

Mert, M.S., Yüksel, F., Burulday, M.E., (2019). Modeling of an Integrated Power System to Hydrogen Production from Biomass-Derived Synthesis Gas), Erzincan University Journal of Science and Technology, 12 (2), 607-619.

Xebec, (2014). What is PSA, <http://www.xebecinc.com/technology-what-is-psa.php> Erişim tarihi: 20.06.2018.

The stability and corrosion behavior of binary NiPd electrocatlysts in alkaline electrolysis system

[1*]Ramazan Solmaz

[1]Bingöl University, Health Sciences Faculty, Occupational Health and Safety Department, Bingöl 12000, Turkey

[*]E-mail: rsolmaz@bingol.edu.tr; rsolmaz01@gmail.com

Abstract
The physical and electrochemical stabilities of the electrode materials in electrolysis conditions are very improtand for the practical applications. Although, electrochemical stability of the electrodes in electrolysis system were tested frequently, their corrosion behavious is mostly avoided. But, corrosion is very important problem, specifiacally at open circuit conditions. Searching for new and efficient as well as time-stable electrocatalysts is another one of the most popular topic. In this study, we have studied electrochemical stability and corrosion behavious of an efficient binary electrocatalyst, NiPd which was fabricated over a Ni-modified C-felt (C) electrode. The tests were performed in KOH solution. For this aim electrochemical impedance stectroscopy, linear polarization resistance and polarization studies were used. It was found that the electrocatalyst retains its catalytic activity after electrolysis and corrosion resistance was quite high even after the electrolyses.

Keywords: Electrolysis, corrosion, electrochemical stability, electrochemical deposition, NiPd-modified electrode

I. Introduction

The most important energy carrier alternative to fossil fuels, which constitute the majority of the energy source used today, is hydrogen due to its superior properties (Veziroğlu and Şahin 2008; Veziroğlu and Barbir 1992). High purity and large amount of hydrogen can be obtained by electrolysis. Energy input, which constitutes a significant part of the cost in this method, can be obtained from primary energy sources such as solar and nuclear. Better anode and cathode studies are continuing to increase efficiency and performance by reducing overvoltages in the system. Platinum and platinum group metals are the best metals that catalyze the splitting of water. But these metals are expensive and have limited reserves on the earth (Habibi et all 2008; Mandegarzad et all 2016; Nunes et all 2020). Binary alloys of large numbers of transition metals or their alloys with platinum group metals have yielded promising results for this aim. Depositing small amounts of platinum group metals on catalytic surfaces having large surface area results promising results. We have reported that co-deposition of low amount of Ni and Pd over the Ni-modified C provides superior hydrogen evolution performance (Solmaz 2017). However, these electrodes have time-stability problems and corrosion in the electrolysis conditions. On the other hand, low corrosion resistance of electrodes under electrolysis conditions has not been studied sufficiently. Corrosion decreases the life of catalysts as well as their efficiency during the operations (Solmaz and Kardaş 2005; Solmaz et all 2009).

In this study, the stability and corrosion resistance of NiPd alloy, which is one of the important catalysts in alkaline electrolysis conditions during the operation were investigated. For this aim, electrochemnical studies were used.

II. Experimental Set-up and

ProcedureFabrication of electrodes

The details of fabricating NiPd-modified C/Ni was given elsewehere (Solmaz 2015; Solmaz 2017). In summary; the working electrode was prepared from 5 mm thick carbon felt by cutting it in 10mmx10mm dimensions (Average weight 0.05 g). The cut carbon felt samples were washed thoroughly with distilled water, kept in pure water for 2 hours, then dried in an oven at 105° C for 12 hours and kept in a desiccator. Working electrodes were prepared by passing the dried C electrodes to Pt (or Ni coated Pt) wires. The C surface was modified by precipitation of 1 g Ni / 1 g C Ni over the C (C/Ni), and then Ni and Pd (total 20 mg) were co-deposited over the Ni-modified surface (C/Ni-NiPd). The optimization of Ni and Pd ratios were reported before (Solmaz 2017). Before the tests, the electrodes were activated by applying a constant 100 mA constant cathodic current in 1 M KOH solution.

Characterization of the electrodes

The surfaces of the prepared electrodes were examined by SEM. Metal proportions of the catalyst and the distribution of metals on the electrode surface (EDX-mapping) were determined by EDX.

Electrochemical stability and corrosion tests

The electrodes were used as cathode in 1 M KOH solution at 25 ° C in 1 M KOH solution. A Pt electrode (10mmx10mmx01mm), and Ag/AgCl (3 M KCl) were used as counter and reference electrodes, respectively. Electrochemical measurements were performed using a computer controlled CHI 660D or CHI 6096E Electrochemical Analysers. -100 mV overpotential was applied to the electrolysis system for 5 days. Before and after the electrolysis, the catalytic performance of the electrode was investigated using EIS and polarization studies. Also, corrosion behavior of the electrode was investigated before starting and ending of the electrolysis with the help of linear polarization resistance and EIS studies at open circuit conditions. After 5 days electrolysis, the elecytode was exposed to the same electrolyte for 24 h at open circuit conditions, then the electrolysisis was continued for one additional day and its performance was also tested. Polarization measurements were performed between -1.8 V and open circuit potential at a scan rate of 5 mV s^{-1}. EIS measurements were perfomed at different overpotentials from 100 kHz to 0.01-0.1 Hz. The amplitude was 5 mV. Linear polarization measurements were performed at 0.001 V/s at ± open circuit conditions.

III. Results and discussions

The surface morphologies of the bare and C/Ni-NiPd electrodes are given on Fig. 1. The distribution and chemical of composition of the film over the surface was examined with EDX and provided on the same figure. The SEM images clearly indicate that C has quite large volumes and high surface area. The Ni-NiPd deposit almost homogenously deposited over the C surface and the deposit has large surface area. The deposit was adhesive and compact, which provides advantages for catalytic activity of the water splitting since this reaction is a surface process and depends on the real surface area. SEM and EDX results showed that Ni and Pd metals almost homogenously distributed over the surface and the surface has large surface area.

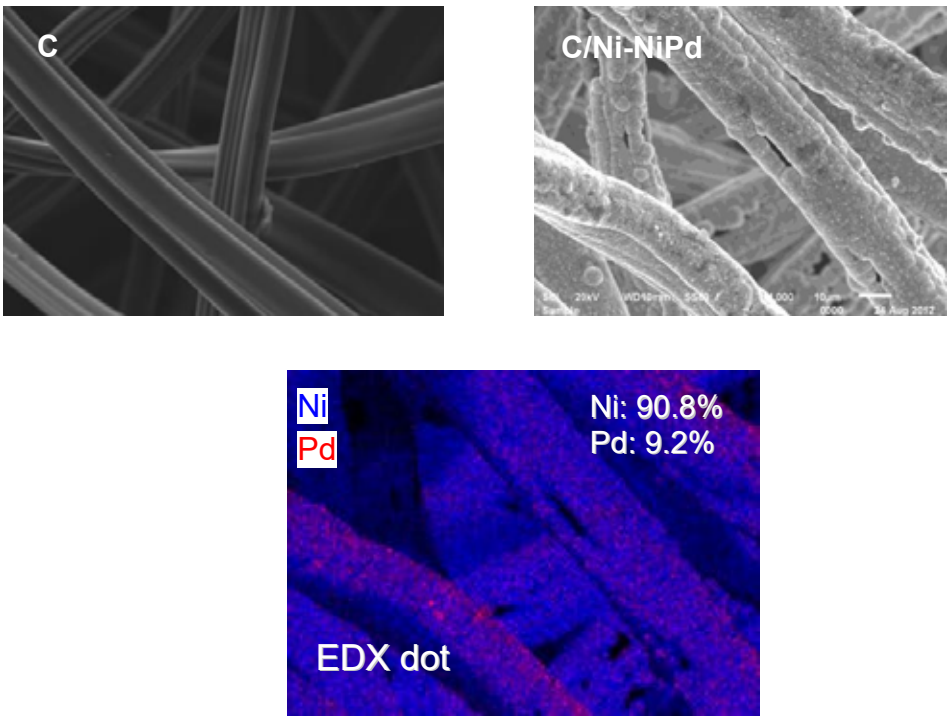


Fig. 1. The SEM images of bare and C/Ni-NiPd electrodes, EDX mapping image of the surface of C/Ni-NiPd electrode

The electrodes were acvtivated in electrolysis conditions and polarization plots were obtained before and anfter the electrolysis. EIS studies were performed at -100 mV overpotential, which was determined form polarization studies at where hydrogen evolution takes place, to determine electrochemical performance of the electrodes. In order to determine effect of corrosion on the water splitting performance of the electrodes, after 24 h electrolysis the electrode was kept at open circuit conditions for 24 h, then electrolysis was performed once again for an additional 24 h. The data obtained at -100 mV overpotential are shown on Fig. 2 a and b. Apperently, the electrocatytic activity of the electrode does not reduce during the electrolysis. Moreover, the performance of the catalysts increased slightly most probably due to the evolution of hydrogen gas and activating the surface. Exposing the electrode to the electrolyte at open circuit conditions reduses activity slightly, which can be assign to corrosion of the electrode. However, the activity of the electrode was quite high. Therefore, it is apperant that the corrosion affect water splitting performance and must be taken into account in the fabricating electrodes and during the electrolysis.

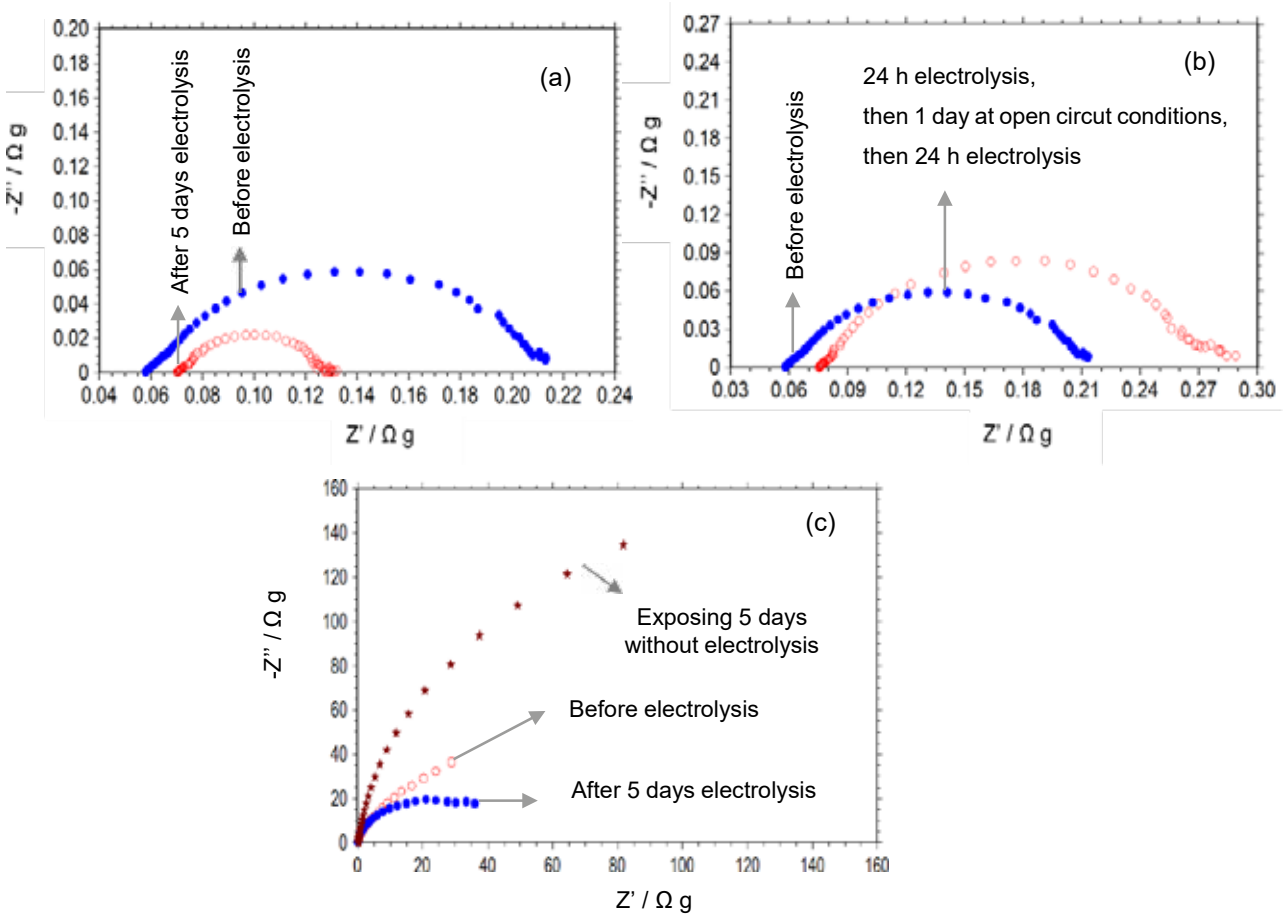


Fig. 2. Nyquist plots of C/Ni-NiPd electrode at -100 mV overpotential before and after electrolysis (a), before and after 24 h exposing to the electrolyte at open circuit conditions (c), at open circuit potential before, after and without electrolysis

Corrosion resistance of the electrode was determined with EIS and linear polarization resistance. Nyquist plots obtained at open circuit conditions before and after electrolysis as well as the electrode exposed to the electrolyte for 5 days without electrolysis are shown on Fig. 2c. It is seen that the corrosion resistance slightly reduced after the electrolysis. But, it is still quite high. On the other hand, the highest corrosion resistance was observed at the electrode, which was only exposed to the electrolyte due to formation of oxide/hydroxides over the surface.

IV. Conclusions

The electrocatalytic activity of C/Ni-NiPd electrode was very stable during the electrolysis. Corroson can affect water splitting performance of the electrodes. The corrosion process must be controlled during the electrolysis, specifically at the open circuit conditions. The electrode tested in this study has high corrosion reistance after 120 h electrolysis. Therefore, C/Ni-NiPd can be used for the pacticall applications for water splitting.

Acknowledgements

The author is greatly thankful to Bingöl University Scientific Research Projects Coordination Unit (BÜBAP) for financial supporting and Bingöl University Central Laboratory for characterization measurements.

References

Veziroğlu TN, Şahin S. 21st century's energy hydrogen energy system. Energ Convers Manage, 49: 1820 – 31 (2008)
Veziroğlu TN, Barbir F. Hydrogen: the wonder fuel. Int J Hydrogen Energy, 17: 391 – 404 (1992)
Solmaz R, 2nd International Hydrogen Technologies Congress, Abstract Book, 38 pp., Adana, Turkey, March 15-18, 2017
Habibi B, Pournaghi-Azar MH, Razmi H, Abdolmohammad-Zadeh H, Int J Hydrogen Energy 33: 2668 – 78 (2008).
Mandegarzad S, Raoof JB, Hosseini SR, Ojani R, Electrochimica Acta 190: 729–736 (2016).
Nunes M, Fernandes DM, Morales MV, Rodríguez-Ramos I, Guerrero-Ruiz A, Freire C, Catalysis Today 357: 279 – 290 (2020).
Solmaz R, Kardaş G, Energ Convers Manag 48: 583 – 591 (2007)
Solmaz R, Döner A, Şahin İ, Yüce AO, Kardaş G, Yazıcı B, Erbil M, Int J Hydrogen Energy 34: 7910 – 7918 (2009)
Solmaz R, Ulusal Hidrojen Teknolojileri Kongresi, 181-187 pp., İstanbul, Türkiye, 20-23 Aralık 2015.

Pd-modified polyrhodanine thin films as cathode electrocatalysts for water splitting

Ramazan Solmaz[1,2*], Dursun Öztürk[2,3]

[1]Bingöl University, Health Sciences Faculty, Occupational Health and Safety Department, Bingöl 12000, Turkey
[2]Bingöl University, Renewable Energy Systems Division, Bingöl 12000, Turkey
[3]Bingöl University, Engineering and Architecture Faculty, Electrical Engineering Department, Bingöl 12000, Turkey

E-mail: rsolmaz@bingol.edu.tr; rsolmaz01@gmail.com

Abstract
High-quality polyrhodanine (pRh) thin films were electrochemically synthesized on a Pt surface. The films were then modified with small amount of Pd particles to be used as electrocatalyst for alkaline water electrolysis. Since rhodanine (Rh) has many active centers it is expected that the polimerized form of this molecule could distribute Pd particles well, and high electrical conductivity provides good charge transfer. The data obtained showed that the the Pd particles homogenously distributed over the polymer film. Water splitting performance of the metal-organic composite film was tested in 0.5 M H_2S0_4 solution using electrochemical techniques. It was found that, the Pd-modified composite thin films enhances hydrogen evolution activity of the electrode; the observed water splitting activity of this electrode is better than Pt electrode. The electrode also has high time stability in 0.5 M H_2SO_4 solution.

Keywords: Polyrhodanine, Pd-modified films, electrocatalysts, cathode, water electrolysis

I. Introduction

Hydrogen gas has almost all the properties desired in alternative energy sources and is recommended as the energy carrier of the future (Veziroğlu and Şahin 2008; Veziroğlu and Barbir 1992). Although hydrogen gas is obtained by many methods, one of the most important methods is the electrolysis of water. The most important disadvantages of this method are the anode and cathode kinetics, the dissolution of metals especially in acidic environments, overvoltages in the system and cost of the system. Pt and Pt group metals are the better catalysts for the electrolysis of water (Habibi et all 2008; Mandegarzad et all 2016; Nunes et all 2020). Since these metals are expensive, alloy electrodes from cheaper transition metals are also tested. However, most of these metals dissolve in acidic environments. In order to overcome this disadvatages we are proposing a novel method, covering surface of the electrode with a stable polymer, pRh. Formerly, we have firstly reported SAM films of Rh for this aim (Solmaz and Salcı, 2019). We also reported that, pRh has high physical, thermal and electrochemical stability (Solmaz and Kardaş, 2007).

In this study, pRh thin polymer films were electrochemically fabricated on Pt and small amount of Pd was deposted over the film. The fabricated composite electrode was tested as cathode for water splitting reaction in 0.5 M H_2S0_4 solution. For this aim, electrochemical techniques were used.

II. Experimental Set-up and Procedure

Electrochemical synthesis of polyrhodenine

The synthesis of polymer films has been previously detailed elsewhere (Solmaz ve Kardaş, 2007). In summary, the pRh thin films were synthesized a Pt sheet (10mmx10mmx1mm) from 0.01 M monomer containing 0.3 M ammonium oxalate solution using cyclic voltammetry technique by potential cycling between 0.00 V ad 1.40 V at a scan rate 100 mV s^{-1}. A Pt electrode and Ag/Ag/AgCl (1 M KCl) were used as counter and reference electrodes respectively. Totally 200 segments were applied. This electrode was named as Pt/pRh. After synthesis, the films were washed with pure water and followed with ethanol, dried under nitrogen gas and kept in a desicator until the tests. The mechanism of polymerization was reported elsewhere (Solmaz ve Kardaş, 2007).

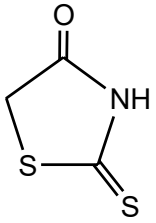


Fig. 1. Chemical structure of Rhodanine

Fabricationg Pd-modified polymer

The surface of pRh was modified by depositing 1 mg cm^{-2} Pd in order to improve its water splitting activity. For this aim, the deposition was carried aout in 5 mg $PdCl_2$ containing 0.1 M HCl solution. For this aim, Pt/pRh electrode was used as cathode and 10 mA cathodic current was applied to the system for 363 s. In this way, theoretically 1 mg cm^{-2} Pd was deposited over the polimer surface. This modified electrode was named as Pt/pRh-Pd. Before electrochemical measurements the surface of the modified electrode was electrochemically activated in the test solution by applying -50 mA cathodic current for 3600 s.

Characterization of the electrodes

The surfaces of the prepared electrodes were examined by SEM. Their electrochemical stability were also tested electrochemically.

Water splitting performance of the Pd-modified polymer

Water splitting performance of the composite electrode was investigated in an acidic media, 0.5 M H_2SO_4 solution. For this aim, cyclic voltammety (CV), electrochemical impedance spectroscopy (EIS) and polarization studies were performed. Electrochemical measurements were performed using computer controlled CHI 660D or CHI 6096E Electrochemical Analysers. The counter electrode was a Pt sheet having 2 cm^2 total surface area. An Ag/AgCl (3 M KCl) was used as referenced electrode. Polarization measurements were performed between -0.8 V and open circuit potential at a scan rate of 5 mV s^{-1}. EIS measurements were perfomed at different cathodic overpotentials from 50 kHz to 0.01-0.1 Hz. The amplitude was 5 mV.

III. Results and discussions

The surface morphology Pd-modified pRh thin films are shown on Figure 1. Apparently, the film was homogenous and cover all the surface. Spherical Pd particles were distributied homogeously over the surface. The surface also is very porous. These properties provides enhancement of electrocatalytic activity for water splitting. Surface photograph of pRh is shown on the same figure. By comparing with the un-coated Pt, it is very clear that a very homogenous and dark-purple colored film is synthesized on the electrode. The film is also very adherent to the surface which provides an advantage of stability during the excess gas evolution.

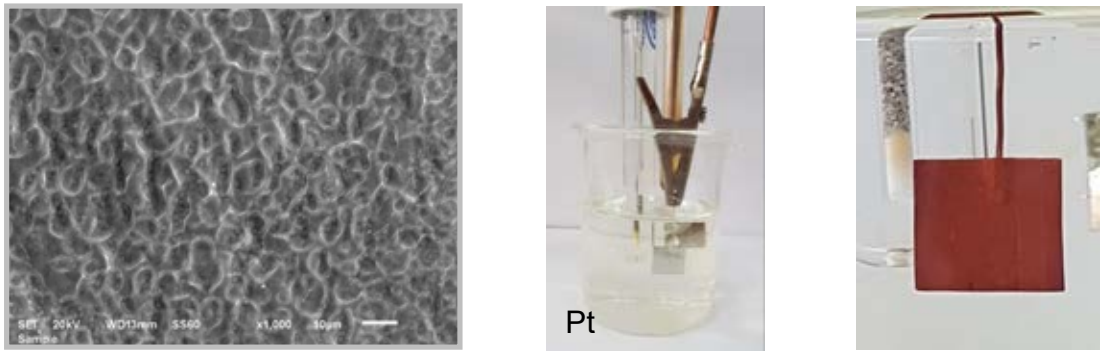


Figure 2. SEM image of Pt/pRh-Pd, surface photograph of bare Pt and the pRh film synthesized on the Pt after 200 segment

Cathodic semi logarithmic current - potential curves of the electrodes obtained in H_2S0_4 solution are presented in Figure 3a. It is seen that pRh films are quite well for charge transfer reaction in this media. However, the main aim of the study was not using this film directly for hydrogen production. It is aimed that improving an organic film which is suitable for depositing small amount of platinum group metals and lowering cost of the electrode by lowering using these metals. Modifying pRh surface by Pd significantly enhances the water splitting activity, which is better than Pt. EIS studies were performed at -200 mV overpotential, which was determined form polarization studies at where hydrogen evolution takes place, to determine electrochemical performance of the electrodes and the data obtained are given on Figure 3b. EIS data agree well with the polarization studies and clearly indicates that Pd-modified pRh composite electrocatalysts enhances hydrogen evolution performance. The enhanced activity of the catalyst can be assigned to the enlarged real surface area, synergistic effect between the conductive polymer and the Pd particles as well as high intrinsic activity of the Pd.

Electrochemical stability of the composite electrode was tested by CV technique and the data obtained are shown on Figure 3c. From the data it is appearent that the composite Pd-modified pRh films are very stable in this conditions.

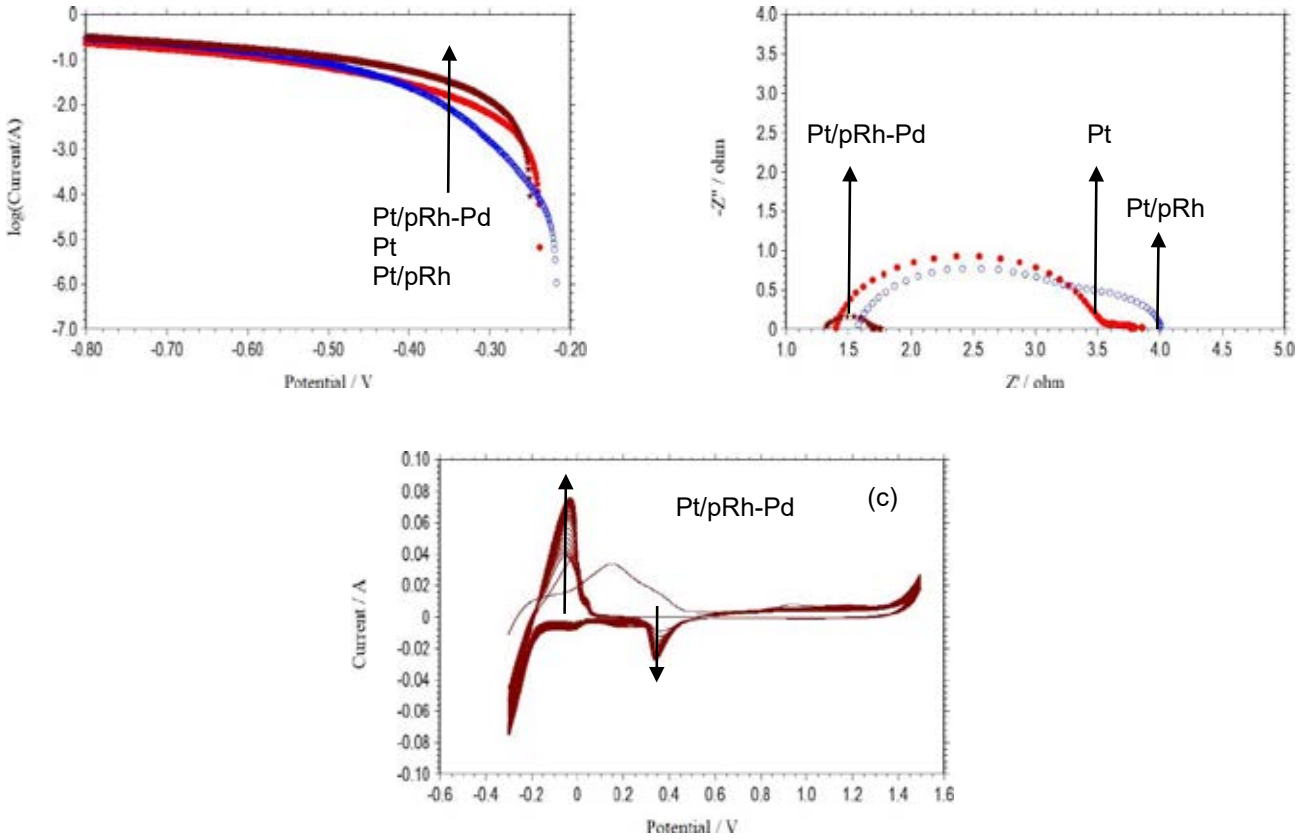


Fig. 3. Semi logarithmic current-potential cureves (a), Nyquist plots obtained at -200 mV and CV (200 segment) of the electrodes obtained in 0.5 M H_2S0_4 solution

IV. Conclusions

The Pd-modified pRh composite electrodes were electrochemically fabricated on Pt and tested for water splitting activity in 0.5 M H_2S0_4 solution. It was found that the film was homogenously prepared on Pt. The film was very adherent and electrochemically stable. The Pt/pRh-Pd electrode has very good hydrogen evolution activity which is better than Pt. The enhanced activity was related to the enlarged real surface area, synergistic effect between the conductive polymer and the Pd particles as well as high intrinsic activity of the Pd.

Acknowledgements

The author is greatly thankful to Bingöl University, Health Sciences Faculty, Occupational Health and Safety Department and Bingöl University Central Laboratory for characterization measurements.

References

Veziroğlu TN, Şahin S. 21st century's energy hydrogen energy system. Energ Convers Manage, 49: 1820 – 31 (2008)
Veziroğlu TN, Barbir F. Hydrogen: the wonder fuel. Int J Hydrogen Energy, 17: 391 – 404 (1992)
Habibi B, Pournaghi-Azar MH, Razmi H, Abdolmohammad-Zadeh H, Int J Hydrogen Energy 33: 2668 – 78 (2008).
Mandegarzad S, Raoof JB, Hosseini SR, Ojani R, Electrochimica Acta 190: 729–736 (2016).
Nunes M, Fernandes DM, Morales MV, Rodríguez-Ramos I, Guerrero-Ruiz A, Freire C, Catalysis Today 357: 279 – 290 (2020).
Salcı A, Solmaz R, Hydrogen Evolution Reaction Activity of Rhodanine Self Assembled Monolayer Films, 4th International Hydrogen Technologies Congress, Proceedings Book, 192-195 pp., June 20-23, 2019, Edirne, Turkey
Kardaş G, Solmaz R, Electrochemical synthesis and characterization of a new conducting polymer: Polyrhodanine. Applied Surf Sci 253, 3402–3407, (2007)

Autonomous Hydrogen Production System Design

[1] Feride Cansu İskenderoğlu, [2*] Mustafa Kaan Baltacıoğlu, [2] Çağlar Conker, [1] Hasan Hüseyin Bilgiç
[1] İskenderun Technical University, Faculty of Engineering and Natural Science, Mechanical Engineering Department, Hatay, 31200, Turkey
[2] İskenderun Technical University, Faculty of Engineering and Natural Science, Mechatronics Engineering Department, Hatay, 31200, Turkey

* E-mail: mkaan.baltacioglu@iste.edu.tr

Abstract
A hydrogen generator prototype has been developed for fuel cell systems used in portable applications. This generator is designed based on the use of hydrides with high hydrogen storage capacity in the catalytic hydrolysis reaction. Some using problems such as unstable hydrogen production, one-off service life, heavy or large-volume storage system, and short duty time can be avoided in moveable applications when the use of the produced prototype. Designed of this system consists of water reservoir, liquid pump, fuel reservoir, reaction chamber and control unit. In this study, details about the operating system and performance of a portable and autonomous prototype with 4 parts and 1 hour hydrogen production capacity are given.

Keywords: Sodium Borohydride, Hydrogen Production, Autonomous Systems, Portable Power Generator

I. Introduction

Conventional fossil fuel sources, such as coal, oil, and natural gas, which meet most of the world's energy demand, are being consumed rapidly. Additionally, their combustion products are causing global problems, such as the greenhouse effect and pollution. Therefore, many countries have published their strategy plans to achieve net zero-emissions targets by 2050. Thus, there is a movement towards renewable energy sources, which are environmentally friendly, more efficient power production, zero emissions, over the world. Renewable energy technologies such as solar, wind, hydropower and heat pumps are widely preferred for increasing energy demand (Hansu,2020). Today, battery technologies have been more popular to be used in applications that have a large share of carbon emissions such as portable applications and transportation applications. However, the batteries fail to satisfy the energy required for developing technologies, their weights increase the energy consumption of the systems and create transport problems. One of the developed systems, which based on renewable energy sources, to supply the required energy is the fuel cells. The fuel cells have the potential of achieving much higher specific energy densities than any advanced battery systems. Fuel cells, which can operate in light, quiet and grid-independent environments, high energy conversion efficiency, high power density and zero pollutant emission, provide an alternative way to obtain the energy required by portable applications (Barbir, 2005). At this point, alternative energy sources appear as a solution. Hydrogen is an excellent alternative to meet the growing demand for efficient and clean energy sources (Sahiner,2016). As an energy carrier, hydrogen is expected to play an important role in future energy systems. As the lightest element, hydrogen has many advantages such as environmental friendliness and the highest energy capacity per unit weight (Abdalla,2018).

Besides, hydrogen is a very difficult gas to store. The most common method of hydrogen stored is to obtain compression and storage of hydrogen gas in high-quality tanks (at least 200 bar), but this method increases costs and causes high energy consumption. In addition to cost, hydrogen is a volatile and flammable gas, which creates disadvantages in terms of safety (Rivarlo,2018). Nowadays, research is being done to use hydrogen stored in different chemical compounds to reduce these disadvantages. For example, various hydrides such as Lithium Hydride (LiH), Calcium Hydride (CaH_2), Magnesium Hydride (MgH_2), Lithium Borohydride ($LiBH_4$), Lithium Aluminum Hydride ($LiAlH_4$), Sodium Borohydride ($NaBH_4$), Ammonia Borane (NH_3 BH_3) are used sources of hydrogen (Balbay,2018). Among the boronhydrides defined as reducing substances and used in the formation of many hydrolysis reactions, $NaHB_4$ is the most known. $NaHB_4$ is a strong reductant and can react with many organic and inorganic compounds. $NaBH_4$ is considered a potential candidate for hydrogen storage due to its high hydrogen storage density and controllable hydrogen release through hydrolysis at room temperature. As a result of the reaction of $NaBH_4$ with water, hydrogen is released and $NaBH_4$ can be synthesized again from Sodium Metaborate ($NaBO_2$), which is a by-product. In this case, it reveals that $NaBH_4$ is a renewable product. Reaction of $NaBH_4$ with water (Eqn.1) progresses very slowly under room conditions. A catalyst need to used to accelerate this reaction and increase the yield (Schlesinger,2018).

$$NaBH_4 + 2H_2O \rightarrow NaBO_2 + 4H_2 \quad (1)$$

In this study focused on a new designs of hydrogen generators that are using hydrides for based hydrogen/fuel cells aplications. Hydrogen was produced in a chemical reaction between water and sodium boron hydride with the Co nano powder as a catalyst. This design allows high energy density, cheap design, low cost, high applicability, and fast to use, refill or clean. A small prototype design was built, examined and characterized, then this design will

be developed for big-scale using.

II. Experimental Set-up and Procedure

The schematic view of the experimental setup is shown in Figure 1. It consists of a hydrogen generator, a heater, a moisture trap, Alicat Scientific brand flowmeter, thermocouple and Arduino Uno. Hydrogen production took place in 3 part hydrogen generator as shown in Figure1.

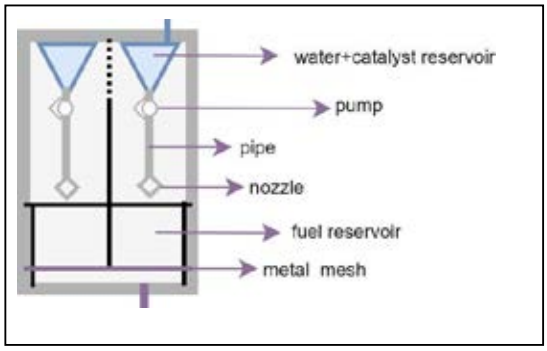


Fig. 1: The design of the hydrogen generator system

The developed reactor is intended to be made of plexiglass material. All connections of the generator were pasted with chloroform adhesive to prevent possible hydrogen leakage, providing a high sealing environment. The fuels will be discharged from their respective chambers into the reservoir where the reaction takes place. The 20 ml water + catalyst mixture will be added with the help of a pump to on the $NaBH_4$ particles that are in the fuel reservoir. The reaction is expected to occur rapidly at room temperature. The hydrogen gas produced as a result of the hydrolysis reaction taking place in the reactor was transferred through the humidifier to the flow meter. The pressure, temperature and production amounts taken from the flow meter collected by the microcontroller will be monitored and will be realized with an automatic control system for sustainable electricity generation. The algorithm of the autonomous control system will be designed depending on the changes in reactor pressure. A test station will be installed in this way; the system tests such as pressure, temperature and the performance of H_2 production are planned in this system. The electronic operating performance of systems and autonomous systems requirements of the system will also be evaluated. After optimal results obtained from these experimental tests, a prototype of the size that will be integrated into a stack of the fuel cell will be prepared. It is planned to conduct performance tests of the generator using the autonomous control system for 6, 12 and 24 hours of different working phases and to record the test results.

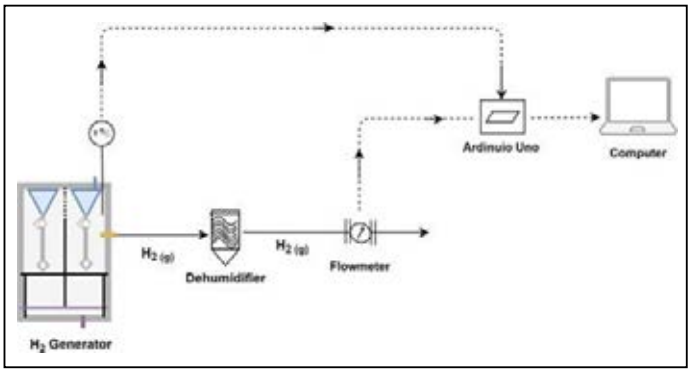


Fig. 2: The schematic view of the generator system

IV. Results and discussions

Experiments have been carried out in order to record hydrogen production and reaction conditions such as hydrogen flow, reactor temperature, and pressure) and to evaluate the prototype's feasibility, efficiency and performance. Figure 3a. is show relatively constant on-demand hydrogen flow (of about 17,5 L/min) for 20 min. The experiments of hydrolysis reactions were carried out using 2 g of $NaBH_4$, 20 ml of distilled water and Co nanopowder as a catalyst was used in 2 different amounts as 0.2 g- 0.5 g. In the experiment with 0.2 g and 0.5 g of Co nanopowder, the total flow rates are 343.46 L and 361.17 L, respectively. The hydrolysis reactions of the Co nanopowder end suddenly, the total hydrogen amounts of the 0.2 g and 0.5 g Co powders are very close to each other, but the reaction using 0.5g of Co powder ends 2 times faster. As can be seen in Figure 3.a and 3.b, the reaction time shortened with the increase in the amount of catalyst, however, the hydrogen production rate decreased. In the graph shown in figure 3, each part of the 4-segment generator was started at different times. A working cycle is designed to have a maximum instantaneous hydrogen production of 3 L / min.$g_{catalyst}$ continuously for 1 hour. In this working cycle, the amount of hydrogen produced instantaneously decreases to 1 L / min.$g_{catalyst}$ from time to time. This situation can be adjusted by increasing the amount of $NaBH_4$ used according to the instantaneous hydrogen

requirement of the system to which the generator will be connected.

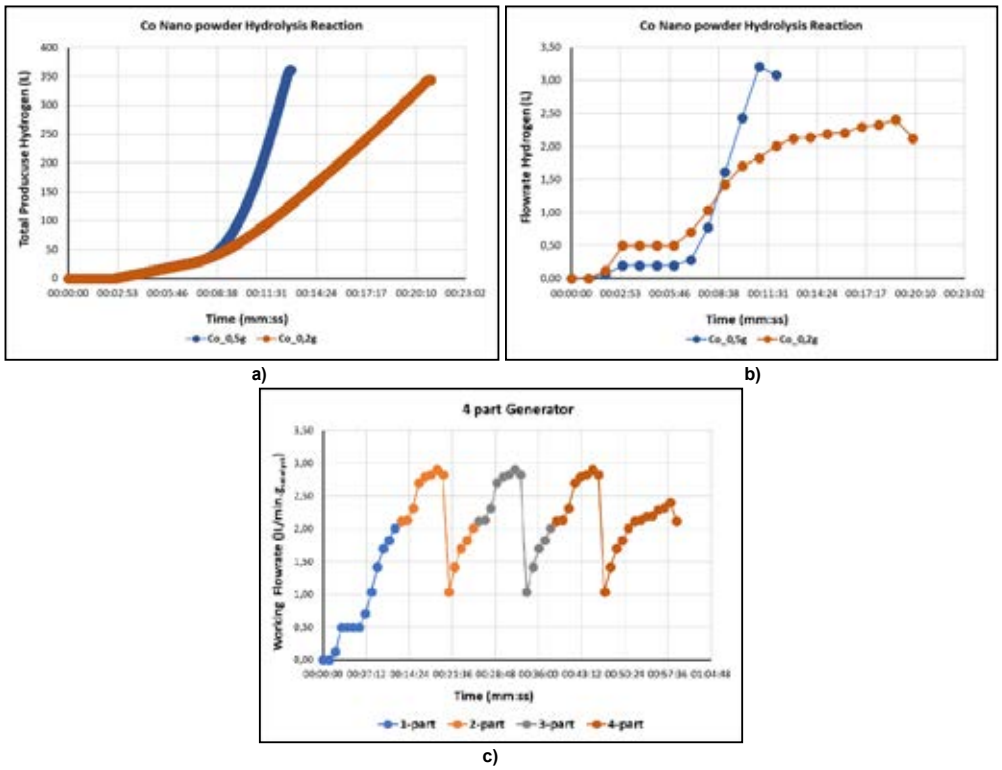


Fig. 3: Total hydrogen production, flowrate and 4 working times variation of the Co nanopowder versus time.

V. Conclusions

The system to be developed as a result of this study can be used efficiently in portable applications. Thus, the energy capacity problems of traditional energy sources and batteries used will be solved. The fuel cells can continue to operate, as long as fuel continuity is maintained. Fuel cells are a very light energy solution compared to batteries. However, the storage of hydrogen gas in tanks does not eliminate the weight problem. Therefore, it is important for future technologies to develop new methods for fuel continuity for systems. However, this study shows a NaBH4 hydrolysis reaction based on Co nanopowder that is satisfactory fuel conversion and high hydrogen production rate at ambient temperature. Pure Co nano powder is not used in hydrolis experiments in the literature. In addition to the hydrogen generator design, the use of pure Co powder as a catalyst in experiments is very important in terms of contributing to the literature.

Acknowledgements

This research was supported by TUBITAK and Prof. Dr. Ertuğrul Baltacıoğlu.

References

Abdalla, A., Hossain, S., Nisfindy, O.B., Azad, A.T., Dawood, M.M., Azad, A., Hydrogen production, storage, transportation and key challenges with applications: A review, Energy Conversion and Management, 165, 602-627, (2018).

Balbay, A., Saka, C., Effect of phosphoric acid addition on the hydrogen production from hydrolysis of NaBH4 with Cu based catalyst, Energy Sources, Part A: Recovery, Utilization, and Environmental Effects, 40 (7), 794-804, (2018).

Barbir F., PEM Fuel Cells, (2005). https://doi.org/10.1016/B978-0-12-078142-3.X5000-9.

Hansu, T. A., Caglar, A., Sahin, O., Kivrak, H., Hydrolysis and electrooxidation of sodium borohydride on novel CNT supported CoBi fuel cell catalyst., Mater Chem Phys, 239,122031, (2020).

Rivarolo, M., Improta, O., Magistri, L., Panizza, M., Barbucci, A., Thermo-economic analysis of a hydrogen production system by sodium borohydride (NaBH4), International Journal of Hydrogen Energy, 40(7), 794-804, (2018).

Sahiner, N., Demirci, S., Very fast H2 production from the methanolysis of NaBH4 by metal-free ploy (ethylene imine) microgel catalysts, International Journal of Energy, 41(5), 736-746, (2016).

Schlesinger, H. I., Brown, H. C., Finholt, A. E., Gilbreath, J. R., Hoekstra, H. R., Hyde, E. K., Sodium borohydride, its hydrolysis and its use as a reducing agent and in the generation of Hydrogen, Journal of the American Chemical Society, 75(1), 215-219, (1953).

Development of LPG Powered Micro-Tubular Solid Oxide Fuel Cell System for Unmanned Aerial Vehicles

[1*] Ugur Aydin, [1] Ibrahim Pamuk, [1] Kerem Talu, [1] Omer Erdemir, [2] Cigdem Timurkutluk, [2,3] Selahattin Celik, [2,3] Bora Timurkutluk
[1] Vestel Defense Industry, Titanium Block 17/B, ODTU, Teknokent, 06800 Ankara, Turkey
[2] Nigde Omer Halisdemir University, Prof. Dr. T. Nejat Veziroglu Clean Energy Research Center, Nigde, 51245, Turkey
[3] Nigde Omer Halisdemir University, Mechanical Engineering Department, Nigde, 51245, Turkey

* E-mail: uguraydin@vestel.com.tr

Abstract
Micro tubular solid oxide fuel cells (mT-SOFCs) defined as tubular cells with diameters in the millimeter range are favorable in terms of thermal stress resistance and simplified sealing compared to those in planar geometry. They can easily be fed by reformate gas produced from most hydrocarbons. mT-SOFC devices can achieve higher energy density values along with a small volume needed for mobile applications. Besides, mT-SOFC is suitable for electrolyzer operation. However, mT-SOFC incurs performance penalties derived from the current collection, cell thermal expansion-contraction issues that have to be addressed before commercialization. The main objective of this study is to design a portable power system based on mT-SOFCs for unmanned aerial vehicles (UAVs) including an LPG burner, LPG steam reformer and 100 Watt mT-SOFC stack working with reformate gas. mT-SOFC production and power measurements, CFD analyses for two different stacks, LPG catalyst production and, compact burner, reformer and stack designs are completed and reported in this study.

Keywords: Microtubular solid oxide fuel cell; LPG steam reforming; unmanned aerial vehicles.

I. Introduction

There are two main solid oxide fuel cell (SOFC) geometric configurations, i.e. tubular and planar. Planar SOFC performance is higher than that of tubular one, because of the reduced in-plane ohmic resistance. Also, tape casting and other mass-production techniques, for example, spray methods or screen printing can easily be applied for planar SOFC production, thus making possible a substantial reduction in the production cost. On the other hand, the tubular configuration may solve the problems related to cracking, thermal-cycling, start-up time, and sealing due to its circular geometry (Sammes, Du and Bove, 2005). Therefore, planar SOFCs are mostly used in stationary or semi-stationary applications due to long startup time required to prevent mechanical failure of the ceramic cells. Nevertheless, the main advantage of SOFC is to be able to work with hydrogen-rich gas beside pure hydrogen, unlike polymer electrolyte membrane fuel cells. Furthermore, SOFC based combined heat and power (CHP) systems can reach overall efficiencies above 90% (Mai et al, 2013). On the other hand, the main disadvantage of planar type SOFC is that it has to be heated up slowly because of different thermal expansion coefficients of the materials used for building a stack. Other than two main SOFC geometry, mT-SOFCs, having a diameter less than 5mm in general, have been received great attention recently. Micro tubular SOFC systems have shown many desirable characteristics over planar SOFC systems (Steele, 2000). It was reported that small-scale tubular SOFCs endured thermal stress caused by rapid heating up to operating temperature. It is also possible to design SOFC stacks with high volumetric power density by using micro tubular SOFCs (Toshio et al., 2007). For mT-SOFCs, the current collection is typically achieved by winding a non-oxidizing metal wire like Au or Pt on both anode and cathode sites. Silver wire can be used also because oxidized silver is still an electronic conductor. This issue makes the mT-SOFC stack lighter and compact, beside the fast startup, high thermal shock resistance and quick response to dynamic loads.
In this study, mT-SOFC based system is developed as a power unit for UAVs. For this purpose, 72mm long anode supported mT-SOFC is fabricated by extrusion method. After the extrusion, YSZ electrolyte and LSM cathode are applied by dip coating in an order. For the performance measurement, 0,4mm silver wire is selected as a current collector material and Aremco Ceramabond 571 is used as a sealing material. LPG is one of the most used gas all around the world and has no logistical difficulties. Producing hydrogen-rich gas from hydrocarbon gases is relatively unchallenging compared to that from liquid hydrocarbons. Therefore, it is selected as a fuel in this study. %5 NiO impegnated Al_2O_3 steam reforming catalyst is also developed. However, a commercial catalyst is used for removing the sulpfur from LPG to maintain the lifetime of the stack. A reformer made of SUS 316 is designed, fabricated and tested at 800°C under 0,1L/min LPG and 0,8mL/min water. A propane burner is also designed to heat up the system components up to the desired operating temperatures. All system components are brought together to have a compact design which is one of the most important issues for unmanned aerial vehicles.

II. Experimental

The first step in the experimental studies is to prepare mT-SOFC for the performance evaluation. mT-SOFC is first brush-coated with commercial alcohol-based silver paste to reduce the contact resistance. Next, pure silver wire of 0,4mm diameter is winded around on both anode and cathode surfaces. mT-SOFC is then placed in a steel tube, sealed with Aremco Ceramabond 571, cured at 100°C for 2,5 h followed by curing at 200°C for 2 hours (Fig. 1). The performance of single mT-SOFC at an operating temperature of 800 °C is given in Fig. 2. The peak power density is measured to be ~0.45 W/cm^{-2} (~2,2 W).



Fig. 1. mT-SOFC experimental setup

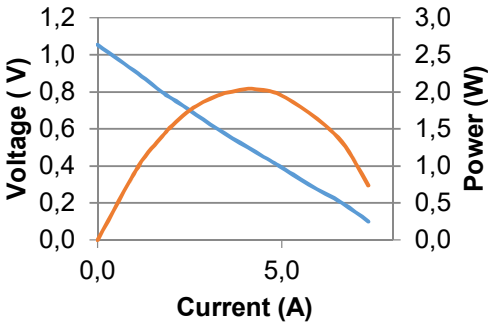


Fig. 2. I-V curve of single mT-SOFC

Based on this results, two stacks having 50 cells connected in serial (~100W) are designed to examine how the gas distribution changes with the flow direction of the gas feeding pipe (Fig.3 and Fig. 4). Also, the gravimetric direction is changed to investigate its effect on the flow. The stack is designed as open cathode and air is fed to the furnace directly.



Fig. 3. First 50 mT-SOFC stack design



Fig. 4. Second 50 mT-SOFC stack design

The outer diameter of the stack is designed to be 150mm. The main reason for this diameter selection is to apply the sealing material between the tubes easily. Like in the similar studies in the literature, the inner diameter of the gas feeding pipe is selected as 8mm and the gas outlet pipe inner diameter is set to 4mm. 5 wt.% NiO impegnated Al_2O_3 steam reforming catalyst is produced for the reformer and tested. Volumetric flowrate of LPG and steam fed to the reformer is selected as 0.1 NL/min ve 0.8 sccm/min, respectively. The tests are ended after 25.5 h and gas analyses are performed by a gas chromatography.

III. Results and discussions

The flow simulation for two mT-SOFC stack designs is performed by Solidworks flow simulation. It is seen that the first stack design cannot provide a homogenous gas distribution (Fig. 5-a). On the other hand, the second design, where flow direction is changed, offers better gas distribution as shown in Fig.5-b. LPG steam reforming catalyst performance is evaluated by GC and the results are listed in Table 1. It is found out that the developed catalyst provides almost stable operation and more than 80 mol% hydrogen content at the exit. The amount of gases other than CO, CO_2 and H_2 at the reformer outlet is found negligible.The general view of the entire system is depicted in

Fig.6. The innermost unit is the LPG burner where the heat is generated to heat the system to operating temperature of 800°C. The steam reformer is installed on the LPG burner because the steam has to be fed and the endothermic reforming reaction process needs heat energy. The outmost unit is the mT-SOFC stack where the electricity is generated. Water is fed by the serpentine steel tube at the exhaust as the reformer needs a water stream and the waste heat is utilized to improve the system efficiency.

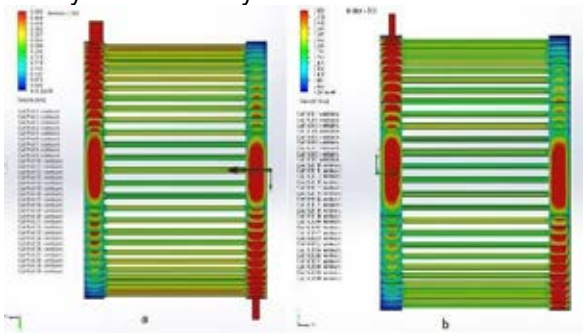


Fig. 5. CFD analysis of the stacks: (a) First design, (b) Second design

Table 1. GC analysis of LPG reforming process

Formula	Units	1. analysis (t=120. min.)	2. analysis (t=22. hour)	3. analysis (t=25.5 hour)
CH_4	mol%	0.13	0.99	1.95
C_2H_6	mol%	0.01	0.03	0.04
C_2H_4	mol%	0.02	0.14	0.27
C_3H_8	mol%	0.37	0.35	0.03
C_3H_6	mol%	0.00	0.00	0.00
H_2	mol%	82.67	82.64	81.60
CO_2	mol%	12.84	11.68	11.93
CO	mol%	3.96	4.16	4.18

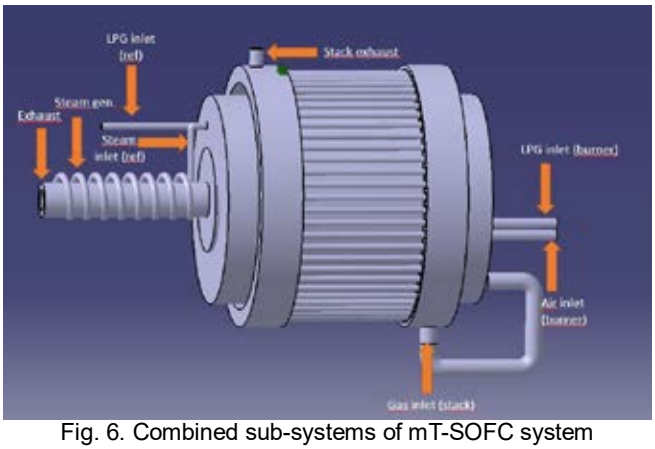


Fig. 6. Combined sub-systems of mT-SOFC system

V. Conclusions

In this study, mT-SOFC based power unit fed by LPG is developed for UAVs. Single mT-SOFC is fabricated first and the performance is measured. The results show that 50 single mT-SOFC are required to obtain the desired power output of100W. NiO catalyst is also developed for LPG steam reformer. The hydrogen yield is found to be suitable to feed the SOFC stack. Two different stacks are designed and flow analyses are performed to compare the resultant gas distribution. Finally, a compact system design is provided for the mT-SOFC system to power unmanned air vehicles. The manufacturing and efficiency improvement studies are still underway.

Acknowledgments

The equipment and materials support of this research by TUBITAK under a project number of 9180030 is gratefully acknowledged.

References

A. Mai et al. “Hexis’ SOFC System Galileo 1000 N – Lab and Field Test Experiences.” In: ECS Trans. 57.1, 73–80, (2013).
Sammes N.M., Du Y., Bove R., Design and fabrication of a 100 W anode supported micro-tubular SOFC stack, J. Power Sources 145 (2005)
Steele B. C. H., Solid State Ionics 129, 95–110 (2000)
Toshio S., Toshiaki Y., Yoshinobu F., Masanobu A., Current collecting efficiency of micro tubular SOFCs, Journal of Power Sources 163, 737-742, (2007).

Performance Assessment of Vanadium Chlorine Thermochemical Cycle

[1*] *Mustafa Tolga Balta,* [2]*M.Zahit Keleş*

[1] Uşak University, Faculty of Engineering, Department of Mechanical Engineering, Uşak, Turkey

[2] Necmettin Erbakan University, Graduate School of Natural and Applied Science, Department of Mechanical Engineering, Konya, Turkey

*E-mail: mustafa.balta@usak.edu.tr

ABSTRACT

Energy production and utilization lead several environmental problems that can have various consequences. Hydrogen generation through renewable based thermochemical water splitting cycles can play a key role in reducing accelerate of global warming and also may offer many opportunities for getting better environment and sustainability. This study is related with the thermodynamic performance assessment of hydrogen production through vanadium chlorine thermochemical cycle. The performance of V-Cl cycle is analysed through in terms of energy and exergy. In this context, this study has shown that V-Cl thermochemical cycle has higher exergetic efficiency than that of other thermochemical cycles.

Keywords*:* Energy, Exergy, Hydrogen production, Thermochemical cycle, Vanadium Chlorine.

I. Introduction

Today, fossil fuels are the main energy source that is still over consumed in the world. The excessive use of fossil fuels to meet this energy demand has led to several environmental consequences. In addition to these environmental consequences also there are other substantial concerns (energy, economics and politics. The significant consequences of the non-renewable based hydrogen production technologies are discussed in detail at (Dincer, 2002). Among the given solutions, it is important to highlight that implementing the hydrogen economy is one of the crucial solution to ensure a sustainable future if hydrogen is achieved through renewable. Main advantages of the implementing the hydrogen economy are given in (Acar and Dincer, 2014). Thermochemical cycles are one of the hydrogen production methods that only using heat to decompose water into hydrogen and oxygen via series of endothermic and/or exothermic chemical reactions and substances. Many researchers and scientists (Brown et al., (2000) and (2003), Abanedes, (2019) have published many papers and reports related with thermochemical cycles over the past 40 years. Brown et al., (2000) analyzed the several potential thermochemical cycles and mentioned that only 25 cycles have been practically feasible (Lewis and Masin (2009). This study is related with the thermodynamic performance assessment of hydrogen production through vanadium chlorine (V-Cl) thermochemical cycle. The performance of V-Cl cycle is analysed through in terms of energy and exergy.

II. Process Description and Performance Assessment

The reactions in the V-Cl cycle are using solely heat to split water into hydrogen and oxygen at a maximum reaction temperature of 525 °C. In the literature, this cycle is reported as the highest efficiency in the chlorine family cycles (Knoche and Schuster (1984), Knoche et al., (1984). In addition, Amendola (2005) proposed two different V-Cl cycles which consists three chemical reactions. The proposed cycles can be examined in two processes such as dry and wet. In the first reaction of the dry process, VCl_3 is decomposed to VCl_2 and Cl_2 at 525 °C which is the maximum cycle temperature. Cl_2 obtained from the first step is reacted with H_2O to produce O_2 and HCl. As the last step, HCl is reacted with VCl_2 to produce H_2 and VCl_3.

Further details on the processes and steps of this V-Cl cycle are given elsewhere (Amendola, 2005).

$$2VCl_3(s) \Rightarrow 2VCl_2(s) + Cl_2(g) \quad (525\ ^oC)$$

$$Cl_2(g) + H_2O(g) \Rightarrow 2HCl(g) + \tfrac{1}{2}O_2(g) \quad (Co\ catalyst)\ (100\ ^oC)$$

$$2VCl_2(s) + 2HCl \Rightarrow 2VCl_3(s) + H_2(g) \quad (300\ ^oC)$$

The performance of V-Cl cycle is analysed through in terms of energy and exergy. Schematic concept of the V-Cl cycle is given in Fig.1.

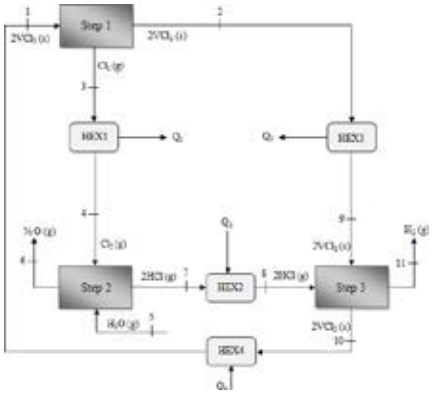


Fig. 1. Schematic layout of V-Cl cycle (adapted from Amendola, 2005)

Mass, energy and exergy balance equations are applied to each steps of the cycle. The following assumptions are taken into consideration;
(i) Dead state values are taken as 298 K for reference temperature (T_o), 100 kPa for reference pressure (P_o), (ii) The heat gains and losses from the cycle are disregarded,(iii) In all steps, the reactions take place at the given reaction temperatures and a pressure of 100 kPa. In these reactions, all chemicals are at the reaction temperature. (iv) Whole process runs steady-state and steady-flow. (v) The effects of the potential and kinetic energies are negligible.
Mass cannot be created or destroyed in a chemical reaction. Hence, the mass balance equation using molar quantities is defined with,

$$\sum n\overline{m}_{\mathrm{R}} = \sum n\overline{m}_{\mathrm{P}} \quad (1)$$

"R" and "P" represents reactants and products, respectively. The generalized energy balance can be expressed as

$$\overline{E}_{in} - \overline{E}_{out} = \Delta\overline{E}_{s} \quad (2)$$

Under the steady state and steady flow condition, the heat transfer for each step can be defined as follows

$$\dot{Q} = \sum n_{P}\left(\overline{h}_{f}^{o} + \overline{h} - \overline{h}^{o}\right)_{P} - \sum n_{R}\left(\overline{h}_{f}^{o} + \overline{h} - \overline{h}^{o}\right)_{R} \quad (3)$$

where $\overline{h}_{f}^{o}$ denotes for the standard enthalpy of formation. Enthalpy and entropy values of each chemical substance are determined using Shomate equations as follow:

$$\bar{h} - \bar{h}_{0} = AT + B\frac{T^{2}}{2} + C\frac{T^{3}}{3} + D\frac{T^{4}}{4} - E\frac{1}{T} + F - H \quad (4)$$

$$\bar{s} = A * \ln(T) + B * T + C * \frac{T^{2}}{2} + D * \frac{T^{3}}{3} E * \frac{1}{2T^{2}} + G \quad (5)$$

$$Cp(T) = A + B(T) + C(T^{2}) + D(T^{3}) + \frac{E}{T^{2}} \quad (6)$$

where T is 1/1000 of the temperature (in K). Enthalpy and specific heat as a function of temperature for VCl_2 are given, respectively by King (1948), Rogers (2015).

$$\overline{h}(T) - \overline{h}_{0} = (17.25)T + (1.36\,\mathrm{x}\,10^{-3})T^{2} + (0.71\mathrm{x}\,10^{5})T^{-1} - 5502 \quad (7)$$

$$Cp(T) = 17.25 + (2.72\,\mathrm{x}\,10^{-3})T - (0.71\mathrm{x}\,10^{5})T^{2} \quad (8)$$

Table 1. Enthalpy of formation, reference entropy and Shomate coefficients for chemical compounds (NIST 2015).

Compounds	$\overline{h}_{f}^{o}$ (kJ/mole)	$\overline{s}_{0}$ (J/mole-K)	A	B	C	D	E	F	G	H
H_2O (g)	-241.83	188.84	-203.606	1523.290	-3196.413	2474.455	3.855326	-256.5478	-488.7163	-285.8304
Cl_2 (g)	0	223.08	33.05060	12.22940	-12.06510	4.385330	-0.1594940	-10.83480	259.02900	0
O_2	0	205.15	31.32234	-20.23531	57.86644	-36.50624	-0.007374	-8.903471	246.7945	0
H_2 (g)	0	130.68	33.066178	-11.363417	11.432816	-2.772874	-0.158558	-9.980797	172.707974	0
HCl (g)	-92.310	186.90	32.12392	-13.45805	19.86852	-6.853936	-0.049672	-101.6206	228.6866	-92.31201

Enthalpy and specific heat as a function of temperature for VCl_3 are given as respectively by,

$$\overline{h}(T) - \overline{h}_{0} = (22.99)T + (1.96\,\mathrm{x}\,10^{-3})T^{2} + (1.68\,\mathrm{x}\,10^{5})T^{-1} - 7592 \quad (9)$$

$$Cp(T) = 22.99 + (3.92\,\mathrm{x}\,10^{-3})T - (1.68\,\mathrm{x}\,10^{5})T^{2} \quad (10)$$

where T is temperature (in K) of VCl_2 and VCl_3, the specific enthalpy change between the standard states is in units of calories/mole and Cp is the specific heat in units of calories/mole-K. Enthalpy formation and entropy values for VCl_2 and VCl_3 at reaction temperatures are given in Table 2.

Table 2. Enthalpy of formation and entropy values for VCl_2 and VCl_3 (NIST, 2015; King, 1948; Rogers, 2015).

Compounds	$\overline{h}_{f}^{o}$ (kJ/mole)	$S_T - S_{298.15}$ (J/mole-K)
VCl_2	-452.17	0.04930
VCl_3	-581.13	0.06462

In the literature, calculation of standard chemical exergy of substances is defined in detail by elsewhere for reference environment (Valero and Valero, 2015). And also standard chemical exergy tables can be found in literature, as listed in Table 3.

Table 3. Standard chemical exergy of compounds (Valero and Valero, 2015).

Compounds	Standard chemical exergy (kJ/mole)	Compounds	Standard chemical exergy (kJ/mole)
Cl_2 (g)	124.02	H_2 (g)	236.1
H_2O (g)	9.34	VCl_2 (s)	439.35
HCl (g)	84.73	VCl_3 (s)	395.85
O_2 (g)	3.97		

The exergy balance equation can be written for a system as follows,

$$\Delta\mathrm{Ex}_{\mathrm{sys}} = \sum \dot{\mathrm{E}}\mathrm{x}_{\mathrm{in}} - \sum \dot{\mathrm{E}}\mathrm{x}_{\mathrm{out}} - \dot{\mathrm{E}}\mathrm{x}_{\mathrm{dest}} \quad (11)$$

where subscripts "sys", "in", "out" and "dest" represents system, inlet, outlet and destruction, respectively. For a steady state and steady flow system, $\Delta\mathrm{Ex}_{\mathrm{sys}}$ is equal to zero, hence Eq. (11) becomes;

$$\dot{\mathrm{E}}\mathrm{x}_{\mathrm{Q}} - \dot{\mathrm{E}}\mathrm{x}_{\mathrm{W}} + \dot{\mathrm{E}}\mathrm{x}_{\mathrm{mass,in}} - \dot{\mathrm{E}}\mathrm{x}_{\mathrm{mass,out}} = \dot{\mathrm{E}}\mathrm{x}_{\mathrm{dest}} \quad (12)$$

Energy,exergy and step efficiencies are given in Table 4 with Eqs.(13-15).

Table 4. Energy, exergy and step efficiencies of the cycle

	Step	Energy	Exergy	Equation No
Efficiency	$\psi_{step} = \frac{\overline{ex}_{out}}{\overline{ex}_{in}}$	$\eta_{overall} = \frac{LHV_{H_2}}{\sum Q_{in}}$	$\psi_{overall} = \frac{\sum Ex_{H_2}}{\sum Ex_{in}}$	(13,14,15)

The LHV of hydrogen which is taken as 239.92 kJ/mole (Lewis et al., 2009). The exergy efficiency of the cycle is defined as the ratio of the exergy of the hydrogen (H_2), over the total exergy input, which can be determined from with Eq.(15) .

III. Results and discussions

In this study, performance analysis of the vanadium-chlorine thermochemical cycle through energy and exergy is analysed. Energy and exergy efficiencies of the considered cycle are examined and and performance results are presented for comparison purposes. Overall energy and exergy efficiencies of the considered cycle are presented in Fig. 2., depending on the given assumptions and parameters. Energy and exergy efficiencies of the V-Cl cycle calculated as 41.80% and 77.28%, respectively. As can be seen in this figure, exergy efficiency increases with the reference environment temperature increase 273 K to 298 K, although energy efficiency of this cycle remains constant as expected. The reaction heat demand, inlet and outlet exergy rates and exergy destruction rates of the reactions for the V–Cl cycle are calculated and listed in Table 5. An endothermic reaction takes place in the first and second steps of the cycle while an exothermic reaction occurred for the last step of the cycle.

Table 5. Reaction heat demand, inlet and outlet exergy rates and exergy destruction rates of the steps.

Step	Temperature (K)	Reaction heat demand (kJ/mole H_2)	Exergy inlet rate (kJ/mole H_2)	Exergy outlet rate (kJ/mole H_2)	Exergy destruction rate (kJ/mole H_2)
1	798	349.6	1174.00	1053.00	121.00
2	373	70.77	183.90	172.00	11.90
3	573	-88.72	1061.09	1004.00	57.09

IV. Conclusions

The following main conclusions drawn from the present study are, (i) V-Cl cycle needs to be further improvement to compete with the most prominent cycles. (ii) The energy and exergy efficiencies of the V-Cl cycle are calculated as 41.80% and 77.28%, respectively. (iii) This cycle is reported as the highest efficiency in the chlorine family cycles so there is a need for further research and development for better design, analysis and performance assessment.

References

Abanades S. 2019. Metal Oxides Applied to Thermochemical Water-Splitting for Hydrogen Production Using Concentrated Solar Energy, ChemEngineering 3:63:1-28.

Acar C, Dincer I. 2014. Comparative assessment of hydrogen production methods from renewable and non-renewable sources, International Journal of Hydrogen Energy 39(1): 1-12.

Amendola S. 2005. Thermochemical hydrogen produced from a vanadium decomposition cycle, U.S. Patent Application 20050013771.

Beghi GE. 1986. A decade of research on thermochemical hydrogen at the Joint Research Centre, ISPRA. International Journal of Hydrogen Energy 11(12):761–771.

Brown LC, Besenbruch GE, Lentsch RD, Schultz KR, Funk JF, Pickard PS, Marshall AC, Showalter SK. 2003. High efficiency generation of hydrogen fuels using nuclear power, General Atomics Project 30047, Final Technical Report GA- A24285.

Brown LC, Funk JF, Showalter SK. 2000. Initial screening of thermochemical water-splitting cycles for high efficiency generation of hydrogen fuels using nuclear power: GAA23373. San Diego, CA.

Carty RH, Mazumder MM, Schreider JD, Pangborn JB. 1981. Thermochemical hydrogen production. Chicago, IL: Gas Research Institute for the Institute of Gas Technology; 1-4: GRI-80/0023.

Dincer I. 2002. Technical, environmental and exergetic aspects of hydrogen energy systems. International Journal of Hydrogen Energy 27(3):265–285.

King EG. 1948. Heat contents at high temperatures of vanadium dichloride and vanadium trichloride, Journal of the American Chemical Society 70(6): 2154-2155.

Knoche KF, Schuster P. 1984. Thermochemical production of hydrogen by a vanadium/chlorine cycle. Part 1: an energy and exergy analysis of the process. International Journal of Hydrogen Energy 9:452–472.

Knoche KF, Schuster P, Ritterbex T. 1984. Thermochemical production of hydrogen by a vanadium/chlorine cycle. Part 2: experimental investigation of the individual reactions. International Journal of Hydrogen Energy 9:473–482.

Lewis MA, Masin JG. 2009. The evaluation of alternative thermochemical cycles – Part II; the down-selection process, International Journal of Hydrogen Energy 34: 4125–4135.

Lewis MA, Masin JG, O'Hare PA. 2009. Evaluation of alternative thermochemical cycles-Part I. The methodology, International Journal of Hydrogen Energy 34(9):4115–24.

Rogers CM. 2015. Vanadium trichloride thermochemical solar energy storage system analysis, University of Louisville, Electronic Theses and Dissertations Paper 1660.

NIST. 2015. National Institute of Standards and Technology, http://webbook.nist.gov/chemistry/ [access date 02.07.15].

Valero A, and Valero A. The Exergy Calculator. Online tool available at the Exergoecology Portal. www.exergoecology.com. [access date:02.07.2015]

Investigation of Contact Problem in Planar Solid Oxide Fuel Cells

[1, 2*] Sezer Onbilgin, [1,3] Cigdem Timurkutluk, [1, 2] Bora Timurkutluk, [1, 2] Selahattin Celik

[1] Nigde Omer Halisdemir University, Prof. Dr. T. Nejat Veziroglu Clean Energy Research Center, Nigde, 51245, Turkey
[2] Nigde Omer Halisdemir University, Mechanical Engineering Department, Nigde, 51245, Turkey
[3] Nigde Omer Halisdemir University Department of Energy Science and Technologies, 51245, Nigde, Turkey

* E-mail: sezeronbilgin@ohu.edu.tr

Abstract
Solid oxide fuel cells (SOFCs) are electrochemical devices that convert the energy of a fuel into heat and electrical energy at high operating temperatures with high efficiency. The contact pressure has a significant effect on the current collection in SOFCs. Since the contact resistance decreases as the contact pressure increases, it causes an increase in performance. However, it should be carefully selected to avoid mechanical failure of the ceramic cells. In this study, the effect of contact pressure on the performance of electrolyte-supported planar SOFCs are experimentally investigated. In this respect cells with 1, 9, 16, 81 and 150 cm^2 active areas were produced and tested under different contact pressures. It is found that 0.486, 0.308 and 0.231 W/cm^2 maximum power density is obtained under the same contact pressure from the cells with an active area of 1, 9 and 16 cm^2, respectively. On the other hand, when the impedance results are considered, it is seen that as the active area of the cell increases under the same pressure, the contact resistance increases significantly. On the other hand, when the pressure is adjusted according to the active area, a similar power density of approximately 0.4 W/cm^2 is obtained from all three cells. Moreover, almost similar performance is obtained from all five cells when a portion of cells with 1 cm^2 active is cut and tested under 0.2 MPa contact pressure.

Keywords: Solid oxide fuel cell; electrolyte; contact pressure; contact resistance; electrochemical performance.

I. Introduction

One of the biggest problems in improving the performance of SOFCs is the contact resistance between metallic interconnect and electrodes. The contact resistance depends on properties such as the interconnection area, the resistance of the current collector mesh, the interactions between the metallic interconnection and the electrode, and the contact pressure (Z. Yang et al., 2006). It is well known that as the active area of the cells increases, the performance decreases. On of the possible reason for this can be that as the cell active area increases, the applied contact pressure becomes insufficient, leading to poor contact between the metallic interconnection and the electrode decreases, thus insufficient current collection or increased contact resistance. In a study by Tapobrata Dey et al. (2013) for planar type SOFCs, contact resistances formed between electrodes and intermediate connectors were investigated under different compressive loads. In their experiments carried out in the range of 600 - 800 ^oC indicated that while the contact resistance on the cathode side decreased as the temperature increased, whereas the contact resistance on the anode side increased with increasing temperature. The contact resistance was obtained as 33.3 $m\Omega.cm^2$ under 0.064 MPa compression load for the cathode side at 800 ^oC operating temperature. On the other hand, for the anode side, the contact resistance was obtained as 48 $m\Omega.cm^2$ under a compressive load of 0.074 MPa under the same operating temperature. Kennouche et al. (2018), investigated the electrolyte, contact and polarization resistances for standard 37.8 cm^2 and reduced 24.5 cm^2 cathode contact areas in SOFC stacks. It was reported that the ohmic resistance of the SOFC stack with a cathode contact area of 24.5 cm^2 decreases due to the decrease in ionic and electronic conductivity as the temperature decreases. Moreover, while 51% of the total resistance of the standard SOFC stack at 800 ^oC operating temperature is the contact resistance, this ratio is given as 39% for the reduced size SOFC stack. In this study, a contact problem that can be encountered during the scale-up studies for SOFCs is experimentally studied.

II. Experimental

In this study, the electrolyte of the cells is manufactured by tape casting method. In the production of electrolyte-support layer; YSZ ($(Y_2O_3)_{0.08}(ZrO_2)_{0.92}$) powder was mixed with appropriate amounts of binder, plasticizer, solvent, and dispersant. The YSZ solution was then ball milled for 24 hours with zirconia balls in polyethylene bottles. After that, the resulting YSZ slurry was cast with a doctor blade gap of 190 µm on a Mylar strip via a tape casting device. The tapes were then stacked and pressed to complete the lamination. Next, the laminate is sintered after cutting with the desired geometry. Then, one side of electrolyte was coated with anode functional and anode current collecting layers via screen printing method. After co-sintering of anode layers, cathode functional and cathode current collection layers were coated similarly. Following the cathode sintering, solid oxide fuel cells with 1 cm^2, 9 cm^2, 16 cm^2, 81 cm^2 and 150 cm^2 active areas were produced. After the production, the performance and impedance tests of the cells were carried out at 700, 750 and 800 ^oC operating temperatures under different contact pressures. The main structure of the single cells is given in Fig.1. First the cells with 1, 9, 16, 81 and 150 cm^2 active areas were

tested under 0.2 MPa contact pressure. Then, the cells with 1, 9 and 16 cm^2 active area were tested under a contact pressure of 0.04, 0.36 and 6.4 MPa, which are decided according to the active area of each cell providing the same load per unit active area. Finally, 1cm^2 parts are cut from the cells and tested.

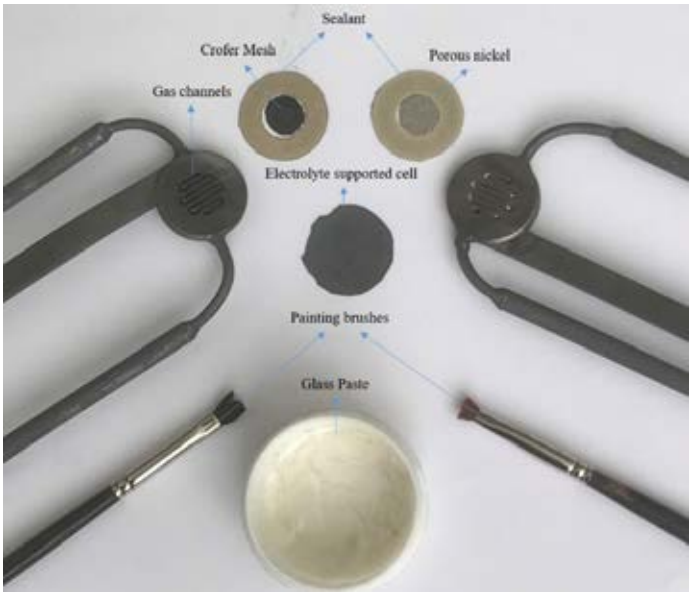


Fig. 1: Experimental installation

III. Results and discussions

The performance and impedance results of the cells at an operating temperature of 800 °C are shown in the Fig 2 - Fig. 4.

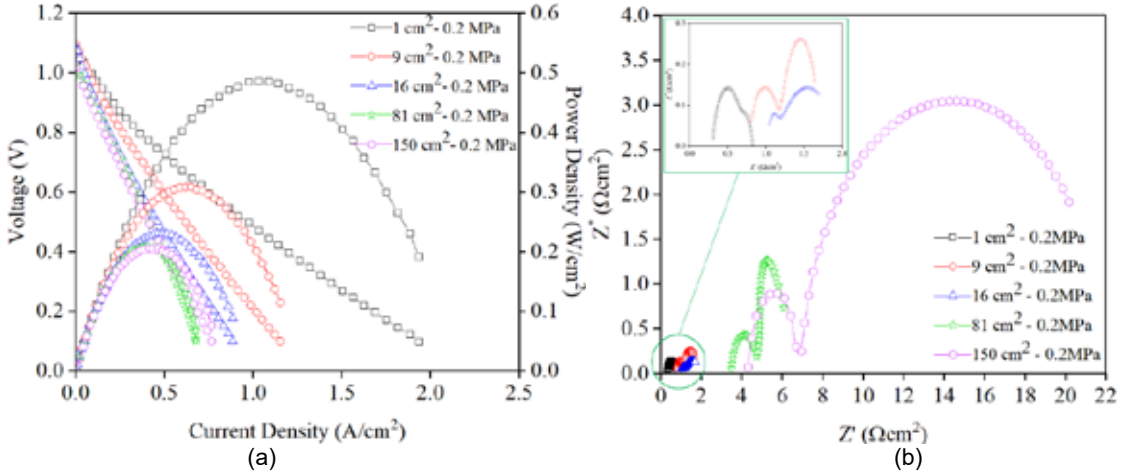


Fig. 2: Effect of the contact resistance on the performance (a) and impedance (b) of the different size cells

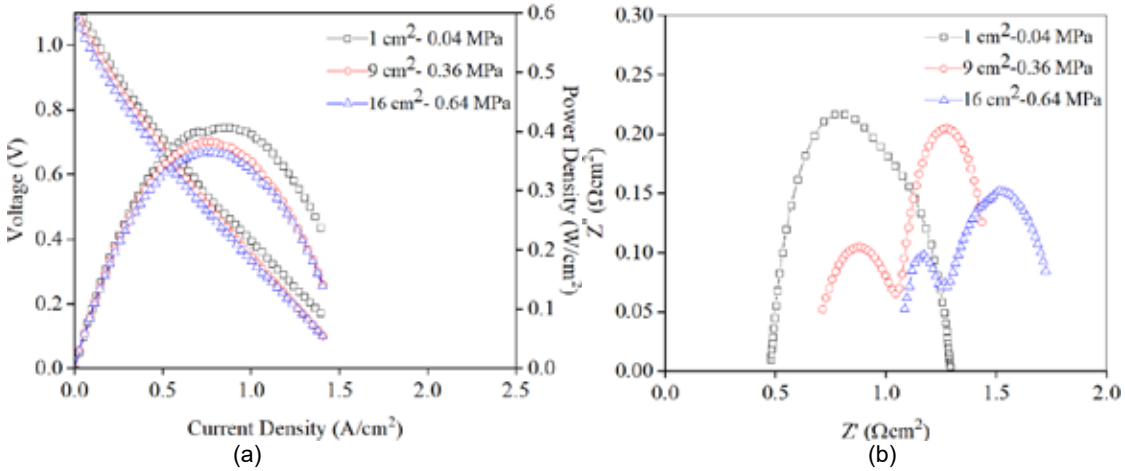


Fig. 3: Effect of the contact pressure on the performance (a) and impedance (b) of the different size cells

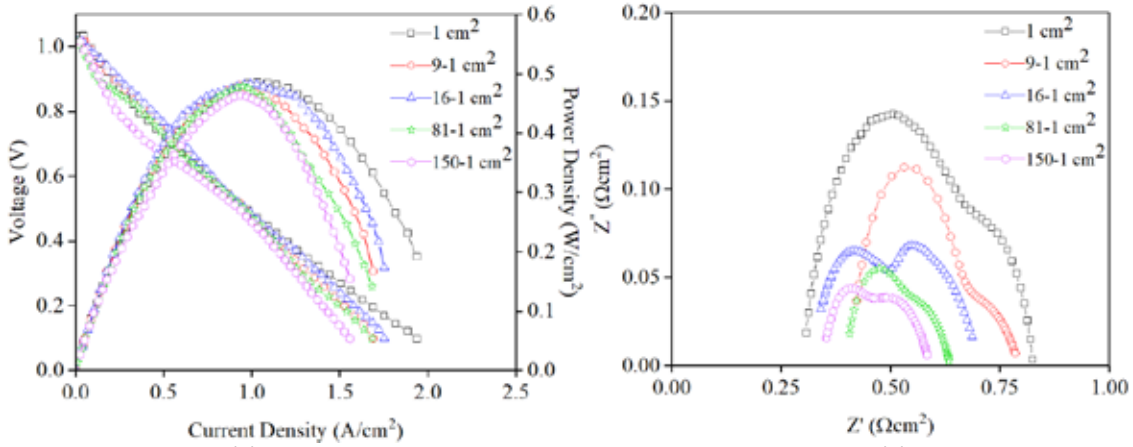


Fig. 4: Effect of the contact pressure on the performance (a) and impedance (b) of the same size cells

As can be seen in Fig. 2, 0.486, 0.308 and 0.231 W/cm^2 maximum power density is obtained under the same contact pressure of 0.2MPa from the cells with the active area of 1, 9 and 16 cm^2, respectively. When the impedance results are considered, as the active area of the cell increases under the same pressure, the contact resistance increases significantly. On the other hand, as seen in Fig.3, when the pressure is adjusted considering the active area, a similar peak power density of approximately 0.4 W/cm^2 is measured from these cells, indicating that the applied load should be selected according to the active area. To prove this, a part of cells with 1 cm^2 active area is cut and tested also. The performance results under 0.2 MPa contact pressure are compared in Fig.4. It is seen that all cells provide almost the same peak power density of around 0.5W/cm^2.

IV. Conclusions

In this study, SOFC single cells with 1, 9, 16, 81 and 150 cm^2 active areas are produced. The performance and impedance tests of the cells were carried out at 700, 750 and 800 ^{o}C operating temperatures and different contact pressures. It is seen that at 800 ^{o}C operating temperature the cells with the active areas of 1, 9 and 16 cm^2 exhibits a maximum power density of 0.486, 0.308 and 0.231 W/cm^2 under the same contact pressure of 0.2MPa, respectively, while that of the cells having different contact pressure shows a relatively similar peak power density (0,4 W/cm^2). The impedance results show that as the active area of the cell increases under the same contact pressure, the contact resistance increases significantly. Therefore, the main reason for different performance values under the same pressure when the active area increases is due to inadequate contact. To prove this, 1cm^2 active area parts are cut from the cells and tested. Almost the same peak power of ~0.5 W/cm^2 is obtained. This result indicates that the decrease in the cell performance with increasing the cell size is not due to the experimental procedures followed in increasing cell size that may lead to cells with different properties but the insufficient contact. Therefore, the contact load should be selected depending on the cell active area.

References

Zhenguo Y., Guanguang X., Prabhakar S. and Jeffry W. S., Electrical contacts between cathodes and metallic interconnects in solid oxide fuel cells, Journal of Power Sources 155, 246-252, (2006).

Tapobrata D., Debanand S., Manaswita B., Rajendra N.B. and Prakash C.G., Study of contact resistance at the electrode-interconnect interfaces in planar type Solid Oxide Fuel Cells, Journal of Power Sources 233, 290-298, (2013).

Kennouche D., Fang Q., Blum L.and Stolten D., Analysis of the Cathode Electrical Contact in SOFC Stacks, Journal of The Electrochemical Society, 165(9), F677-F683, (2018).

Automatic PEM Water Electrolyzer Control System (PEMECS) Design For Cell Testings

[1,2] Emre Özdoğan, [1,2]Ebubekir Tuncay, [1,2]İlayda Nur Uzgören, [1,2]Murat Kıstı, [1,2]Süleyman Uysal, [1,2]Bulut Hüner, [1,2]Nesrin Demir and [1,2,*] Mehmet Fatih Kaya,
[1] Erciyes University, Engineering Faculty, Energy Systems Engineering Department, Heat Engineering Division, 38039, Kayseri, Türkey
[2] Erciyes University H2FC Hydrogen Energy Research Group, 38039, Kayseri, Turkey
* E-mail: kayamehmetfatih@erciyes.edu.tr

Abstract
Polymer Electrolyte Membrane Water Electrolysis (PEMWE) is one of the most preferred method among hydrogen production methods. In PEMWE systems, during the hydrogen evolution reactions, some losses occur like activation, ohmic and concentration polarizations. The effect of temperature, flow control and cell design is very important to overcome these losses. In this study, an automatic PEMWE control system (PEMECS) is designed to arrange constant temperature during the electrolysis process. To control the cell and water tank temperature, a control system is designed with an Arduino and sensor systems. The control system has some functions like; controlling the temperature of the water, the temperature of the PEMWE test cell and the amount of water in the water tank chamber where the water is heated, instantly. Moreover, the accuracy of the temperature applied to the system is tested using multiple temperature measurement systems. Error factor for the measurement temperature of the system is calculated as ± 0.5 °C. Thanks to this system, water level and the homogeneous water temperature is obtained sensitively.

Keywords: PEM electrolysis, Temperature control, Efficiency.

I. Introduction

The increasing need for energy in developing countries has also increased the use of fossil-based fuels. However, greenhouse gases (CO_2, SO_2, NO_x) generated by the use of fossil fuels are cause environmental pollution. (Kampa and Castanas, 2008) Castanas (2008). To reduce greenhouse gases, researchers have turned to alternative energy sources, which are clean and renewable. Hydrogen, as an energy carrier, has a high energy density and it is one of the most promising fuels due to its high energy conversion by the help of fuel cells. (Ghosh et al., 2003). Among the electrolysis of water methods, PEMWE is a promising method for energy storage systems. Because it can be used with renewable energy sources such as wind and solar for continuous hydrogen production (Yigit and Selamet, 2016, Mayousse et al., 2011, Carmo et al., 2013). PEMWE basically consists of anode and cathode current collectors, membrane, gas diffusion layer, and flow channels. In PEM electrolyzers, water is supplied by the anode. Then, water is reached the anode catalyst layer and it is separated into oxygen gas, hydrogen ions, and electrons. While the oxygen gas is thrown out of the cell, hydrogen ions (H^+) pass through the electrolyte to the cathode. Electrons move from the anode to the cathode in the external circuit and combine with hydrogen ions in the cathode catalyst layer to form hydrogen gas. In the electrolysis of PEM water, the effects of operating parameters such as current density, activation, ohmic, and mass losses on cell voltage are changed depending on the temperature. Thus, it is possible to reduce the temperature-based losses by keeping water supply and temperature of the system in constant value with an automatic control unit.

II. Materials and Methods

In this study, temperature, and water level control for the PEM electrolyzer was performed using the central Arduino system control unit. In addition, the instantaneous temperature changes were measured by the sensors and the amount of hydrogen production. Hydrogen production could be transferred to the computer by communicating between the Arduino and the computer. In this way, the effect of the temperature factor on hydrogen production could be seen in real-time in experimental studies. In long-term experimental studies, it could allow automatic adjustment of the water reservoir temperature, cell temperature and water level of the chamber. When the temperature level was reached the determined level, water was sent to the electrolysis cell through the peristaltic pump. The water temperature could be measured from many places simultaneously and temperature measurement accuracy could be ensured. Measurements were made from the outlet of the water tank and the inlet of the electrolysis cell. In addition to heating the water, the electrolysis cell could also be heated up to the specified level in the same controlling unit. Simultaneously, the amount of hydrogen production could be measured so that the temperature effect can be fully examined. Figure 1 shows the PEMWE control system diagram.

Task of the PEMECS can be listed as below:

- Heating the pure water in the heating water tank to the specified temperature level and keeping it constant at the specified temperature level. Keeping the system temperature constant when adding fresh water.
- To keep the test cell constant at the desired level by heating it up to the determined temperature level.
- Measuring the level of pure water in the heated water tank.
- If the water level has fallen below the specified value, the solenoid valve is opened to provide water supplementation to the tank.

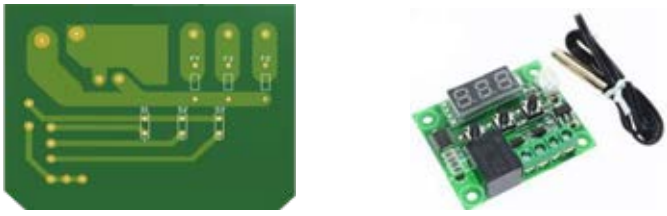
- Instant measurement and saving of the water output temperature from the tank with the over-the-line thermocouple located at the exit of the heating water tank.



Fig.1: PEMWE control system diagram

- Instant measurement and saving of the water temperature entering the cell with the over-the-line thermocouple located at the entrance of the heating electrolysis test cell.
- Recording the instantaneous amount of hydrogen measured with the hydrogen flow meter and calculating the total hydrogen production.
- Instant transfer of measurement data to the computer.

In Figure 2 the power circuit can be seen for 1500W heating element and other heaters. This circuit is designed withstand the high currents to be applied to it. In addition, one of the possible problems that may occur in heat control systems is relay failure. It is suitable for replacing with Solid State Relay (SSR) when necessary, in case of relay failure. In addition, fuses and circuit breakers are used in case of any leakage or danger. In this study, two heat control systems are used. In addition, a three-channel heat control device is designed due to the possibility of using additional heaters in the future studies. This heat control unit works separately from the Arduino central processing unit. A thermostat circuit is used due to its simplicity.



(a) (b)

Fig. 2: (a) PEMECS power transmission circuit (b) heat controller

After the electrical designs of the system are completed, PEMECS heat controller's design and production is made by a 3D printer. The outer body design and the printed controllers of PEMECS are shown in Figure 3. The controller body parts, and electrical circuits produced using a 3D printer are assembled on the body. There are heat control devices, power input outputs, sensor input outputs, on/off buttons on the body.



(a) (b)

Fig. 3: (a) PEMECS three-channel heat controller body design, (b) 3D printed controller with its control equipment

III. Results and Discussions

In Figure 4, temperature-time graph of the PEMECS can be seen for water tank and the PEMWE cell.

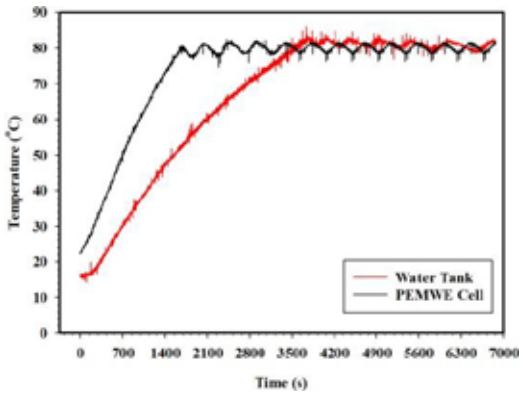


Fig. 4: PEMWE and water tank temperature-time graph in PEMECS

As seen in Figure 4, temperature in water tank reached to 80 °C in 60 minutes. In 60 minutes, water is transferred from the reservoir to the PEMWE cell via the pump. When water level was decreased in the tank, the solenoid valve is opened, and water has added to the water tank from deionized water device. Thus, the temperature of the water is reduced by about 10 °C due to the addition of water. The temperature of the PEMWE had reached 80 °C after 30 minutes. In addition, when the fresh water is supplied to tank, the temperature fluctuations are occurred. Polarization curve (I-V) of PEMWE in different temperature is shown as Figure 5 from our previous studies:

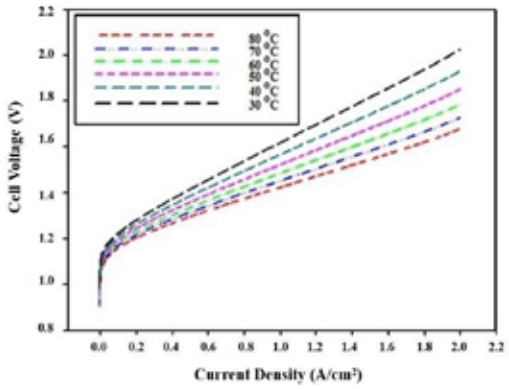


Fig. 5: Polarization curve of the cell at different temperatures

IV. Conclusion

When the PEMWCS is used in PEMWE tests, constant current density is obtained due to the stable cell and temperature-water controlling. In long-term experiments, remote control of system data ensured to follow-up the experimental study. Experimental study results are automatically recorded by the system like temperature-time, water level-time. The level of water temperature is balanced between 45-50 minutes depending on the ambient temperature. When water is added slowly to the water chamber, the fluctuation of the temperature occurs between 3-7°C, and then the temperature is again stabilized between 1 and 3 minutes. Thanks to PEMECS system, it will be possible longer testing time for PEMWE to overcome durability problems.

Acknowledgments

The authors would like to thank TUBITAK 1001 (grant number 120M324) and Erciyes University BAP (FDK-2020-10548 and FYL-2020-10547) for their financial support.

References

Carmo, M., D. L. Fritz, J. Mergel & D. Stolten, A Comprehensive Review on PEM Water Electrolysis, International Journal of Hydrogen Energy, 38, 4901-4934, (2013).

Ghosh, P., B. Emonts, H. Janßen, J. Mergel & D. Stolten, Ten years of operational experience with a hydrogen-based renewable energy supply system, Solar Energy, 75, 469-478, (2003).

Kampa, M. & E. Castanas, Human health effects of air pollution, Environmental pollution, 151, 362-367, (2008).

Mayousse, E., F. Maillard, F. Fouda-Onana, O. Sicardy & N. Guillet, Synthesis and characterization of electrocatalysts for the oxygen evolution in PEM water electrolysis, International Journal of Hydrogen Energy, 36, 10474-10481, (2011).

Yigit, T. & O. F. Selamet, Mathematical modeling and dynamic Simulink simulation of high-pressure PEM electrolyzer system, International Journal of Hydrogen Energy, 41, 13901-13914, (2016).

Fuzzy- Analytical Hierarchy Process (F-AHP) Based Material Selection for Solid Oxide Fuel Cell Electrolyte

[1*]Siamak Alipour, [2]Emrah Sagir, [1]Arash Sadeghi
[1] Depertment of Chemical Engineringg, Faculty of Engineering, University of Maragheh, 55181-83111, Maragheh, Iran
[2] Department of Biology, Faculty of Arts and Sciences, Osmaniye Korkut Ata University, 80000, Osmaniye, Turkey

* E-mail:s.alipour@maragheh.ac.ir

Abstract
Solid oxide fuel cells (SOFC) initially was shown to operate effectively at high temperatures (~1000°C), reducing the operating temperature to less than 600°C provides chances of implementing various material in construction of Low Temperature SOFC (LT-SOFC). Stabilized ZrO_2, doped CeO_2, Bi_2O_3-based, ABO_3-based, and other oxides are among types of electrolytes used in LT-SOFC construction. Electrolyte, as one of the main constituent, efficiency influenced the performance of a LT-SOFC. In this study, the most appropriate type of electrolyte that allows oxygen transfer in a LT-SOFC is determined. To achieve this purpose, The Fuzzy-Analytical Hierarchy Process (F-AHP) is assisted. The scalability, stability, and conductivity were considered as judgment criteria. Then available alternatives for electrolyte were prioritized. Based on the results, stability was the most important criterion in the decision making process. Besides, with respect to the goal, Ceria-based electrolytes had the highest preference compared to other alternatives.

Keywords: Fuell Cell, Low Temperature Solid Oxide Fuel Cells, F-AHP, Electrolyte, Oxygen-Ion Conducting

I. Introduction

Ever-increasing world energy demands high rates of energy sources exploitation. Fossil fuels have been utilized as a reliable source for decades. However, these are exhaustible sources, and their usage negatively impacts the planet's environment, i.e., climate change, global warming, rising water levels in the ocean, and emission of greenhouse or pollutant gases. In order to address these issues, renewable and sustainable sources should be implemented (Sagir and Alipour, 2021). Fuel cells as an alternative approach can be used to produce energy in electricity form. Among different fuel cell types, solid oxide fuel cells (SOFC) are promising energy sources due to flexibility in consuming various fuels, low or zero-emission of pollutant gases (i.e., sulfur and nitrogen compounds) zero noise pollution. Besides, SOFC has no electrolyte leakage problem since its structure is entirely solid (Shi etal. 2020). Initially, SOFC has performed energy production at approximately 1000 °C that makes their applications and material used in their construction limited. Decreasing working temperature to below 600 °C not only overcomes these issues, but also makes the low-temperature SOFC (LT-SOFC) cost-effective. In general, the LT-SOFC consists of three major elements, namely cathode, anode, and electrolyte. The electrolyte position is between the two electrodes, and it should be capable of conducting ions. Electrolytes are constructed mainly from ceramic material(s) capable of conducting ions which can be an oxide ion or proton. The electrolyte should possess properties to perform its tasks, majorly including: (i) it should have a high order of proton or oxide ion conductivities. (ii) It should be a low electronic conductivity medium. (iii) The Electrolyte should have high thermal stability and mechanical strength to resist stresses efficiently (Su and Hu, 2020).
Therefore, selecting a viable electrolyte requires a systematic multi-criteria decision-making (MCDM) approach to investigate the advantages and disadvantages of the introduced material as an electrolyte. This approach generally provides pairwise comparisons between choices based on criteria and ranks them, and then a decision will be made. As a most preferred MCDM method, Analytical Hierarchy Process (AHP) assesses the issue by defining goal(s), criteria and alternatives. It has been used for complex issues to make decisions in the chemical engineering field (Pirdashti etal. 2009). It has been shown that by implementing fuzzy theory on AHP principles, personal judgment will decrease significantly (Ayhan, 2013). This study aims to judge the various materials as the electrolyte that just transfers oxygen ions in a LT-SOFC and determine the appropriate material assisting F-AHP, which is one of the MCDM approach.

II. Experimental Set-up and Procedure

In the F-AHP process, the pairwise comparison of criteria and alternatives is conducted using parameters presented by Ayhan (2013). The analysis is performed by assigning Triangular Intuitionistic Fuzzy Numbers (TIFN's) corresponding to linguistic variables. Then the pairwise comparison inconsistency is calculated to validate results. If this value is less than 0.1, the pairwise comparison is considered acceptable (Gogus and Boucher, 1998). In order to perform F-AHP and assess different materials as electrolyte conductivity, scalability and stability are selected as criteria. Stabilized ZrO_2, doped CeO_2, Bi_2O_3- based materials, ABO_3 based materials (i.e. perovskites), and other oxides (i.e. materials considered in any of these types) are considered as alternatives. The decision structure is presented in Figure 1.

III. Analysis

The weights of material selection were prioritized based on the author's experience and investigating various

sources. Then a proposal was prepared and reviewed by experts from academia and industry. Calculations were made as described by Promentilla et al. (2018).

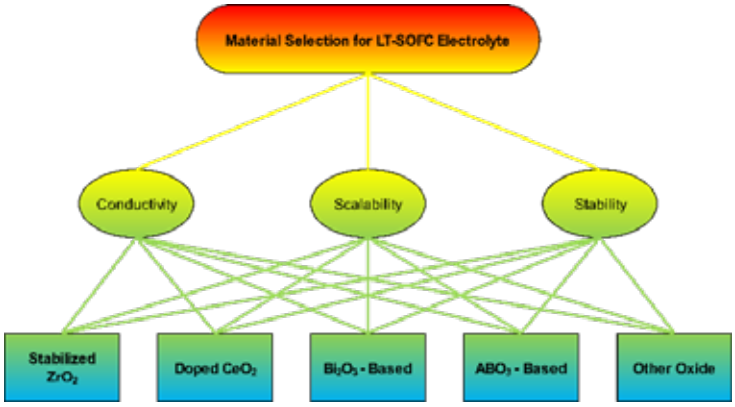


Fig. 1: Decision structure for selecting the appropriate material for the electrolyte of the LT-SOFC

IV. Results and discussions

The fuzzy evaluation matrix concerning to the goal results is presented in Table 1. According to the result of the fuzzy evaluation of criteria illustrated in Figure 2, the stability criteria with 71% importance are the main criteria for the goal. In the following priorities, scalability and conductivity have importance in prioritizing the selecting material as electrolyte with 22% and 7%, respectively. The 0.05 inconsistency, which is less than <0.1, indicates the pairwise comparison of criteria is logical.

Tab. 1: Pairwise comparison matrix for criteria using Fuzzy AHP for material selection for LT-SOFC electrolyte

Criteria	Conductivity	Scalability	Stability	Averaged weight (M_i)
Conductivity	(1, 1, 1)	($^1/_3$, $^1/_4$, $^1/_5$)	($^1/_7$, $^1/_8$, $^1/_9$)	0.071
Scalability	(3, 4, 5)	(1, 1, 1)	($^1/_3$, $^1/_4$, $^1/_5$)	0.224
Stability	(7, 8, 9)	(3, 4, 5)	(1, 1, 1)	0.713
Inconsistency= 0.05				

The final scores of F-AHP for material selection as electrolyte for an LT-SOFC are illustrated in table 2. Among different alternatives, doped CeO_2 has the highest score of 0.425. Results indicate that the stabilized ZrO_2 has a 0.298 final score which is higher compared to other alternatives. ABO_3 based, other oxides, and Bi_2O_3 based materials have the final score of 0.132, 0.075, and 0.069, respectively. Besides, the overall inconsistency is 0.03 that shows the F-AHP results are valid and reliable.



Fig. 2: Priorities of criteria according to importance concerning to the goal

Tab. 2: Final scores of F-AHP for material selection for LT-SOFC electrolyte

Criteria / Alternatives	Conductivity (0.071)	Scalability (0.224)	Stability (0.713)	Final Scores
Stabilized ZrO_2	0.044	0.473	0.269	0.298
Doped CeO_2	0.469	0.271	0.469	0.425
Bi_2O_3 – Based	0.075	0.045	0.075	0.069
ABO_3 – Based	0.142	0.098	0.142	0.132
Other Oxide	0.269	0.113	0.044	0.075
Overall Inconsistency= 0.03				

V. Conclusions

In order to mitigate negative impacts of fossil fuels consumption as an energy source, SOFC has been considered as a sustainable and clean source. The LT-SOFC is a promising alternative due to various benefits. In this study, the appropriate type of electrolyte were investigated and determined by F-AHP. In order to perform the decision making process, scalability, stability, and conductivity were considered as judgment criteria and alternatives for electrolyte were prioritized. The stability was the major important criteria and Ceria-based electrolytes had highest preferences compared to other alternatives.

Acknowledgements

Authors acknowledge supports from the Univeristy of Margheh and Dr. A. Karimi for helpful discussions.

References

1. Ayhan, M. B., A fuzzy AHP approach for supplier selection problem: A case study in a Gear motor company, International Journal of Managing Value and Supply Chains, 4, 11-23, (2013).
2. Gogus, O., Boucher, T. O., Strong transitivity, rationality and weak monotonicity in fuzzy pairwise comparisons, Fuzzy Sets and Systems, 94, 133-144, (1998).
3. Pirdashti, M., Ghadi, A., Mohammadi, M., Shojatalab, G., Multi-criteria decision-making selection model with application to chemical engineering management decisions, World Academy of Science, Engineering and Technology, 49, 54-59, (2009).
4. Promentilla, M. A. B., Aviso, K. B., Lucas, R. I. G., Razon, L. F., Tan, R. R., Teaching Analytic Hierarchy Process (AHP) in undergraduate chemical engineering courses, Education for Chemical Engineers, 23, 34-4, (2018).
5. Sagir, E., Alipour, S., Photofermentative hydrogen production by immobilized photosynthetic bacteria: Current perspectives and challenges, Renewable and Sustainable Energy Reviews, 141, 110796, (2021).
6. Shi, H., Su, C., Ran, R., Cao, J., Shao, Z., Electrolyte materials for intermediate-temperature solid oxide fuel cells, Progress in Natural Science: Materials International, 30, 764-774, (2020).
7. Su, H., Hu, Y. H., Progress in low-temperature solid oxide fuel cells with hydrocarbon fuels, Chemical Engineering Journal, 402,126235, (2020).

A Unique Hydrogen Energy System Developed for Data Centers in Arctic Regions with Heat Recovery

[1*]Mert Temiz, [1]Ibrahim Dincer
[1]Clean Energy Research Laboratory (CERL), Faculty of Engineering and Applied Science, Ontario Tech. University, 2000 Simcoe Street North, Oshawa, Ontario L1H 7K4, Canada
* E-mail: mert.temiz@uoit.ca

Abstract
A unique, solar-driven hydrogen energy system is developed for data centers in this study. A bifacial PV plant is integrated with an ammonia trilateral Rankine cycle heat recovery system, proton-exchange membrane electrolyzer and fuel cell systems, and additional cooling stream. A case study is carried out for an 11.2 MW capacity data center in Norilsk, Russia. A transient analysis is performed with hourly meteorologic and simulation data by considering commercially available solar components and actual meteorological measurements. Both energy and exergy approaches are applied for the thermodynamic analysis. For the average conditions, the overall energy and exergy efficiencies are calculated as 23.42% and 24.33%, respectively. 2920.7 tons of hydrogen is produced, and 2728.7 tons of hydrogen is consumed during an average year. 92.2 GWh electricity is consumed by the data center, and 172.3 GWh total annual energy demand is met by 175 MWp bifacial PV plant, 11.6 MW fuel cell, 109. electrolyzer, 375 kWp heat recovery systems.

Keywords: Hydrogen energy, heat recovery, arctic, bifacial photovoltaics, data center, thermal energy conversion.

1. Introduction

The explosive growth in communication technology and digital transformation in almost all areas and sectors brings increasing electricity demand of data centers. Global energy consumption share of data centers is increasing as well. Electronic processes generate heat as an unavoidable byproduct; therefore, the cooling process is another significant part of the energy consumption of data centers. The electricity usage of communication technology is expected to contribute 23% of the global greenhouse gas emissions by 2030, according to the study by Andrae and Edler (2015).In order to meet the electricity demand without carbon emissions, renewable-driven energy systems are an alternative solution. However, the intermittent characteristic of renewables should be compensated by an energy storage system. There are various alternatives for energy storage options in the literature. According to Acar et al. (2019), solar-powered hydrogen production methods have a key role in order to achieve global goals.

A unique solar-driven data center energy system with hydrogen storage and ammonia trilateral Rankine cycle heat recovery systems is developed in this study. The key novelty of this study can be described as the overall system integration for a data center and heat recovery with an energy conversion system.

2. System Description

A bifacial photovoltaic system with a 0.8 albedo field is used as the primary electricity generation process. The excess electricity is exploited in the proton-exchange membrane (PEM) electrolyzer to produce hydrogen for energy storage purposes. The produced hydrogen is used once the electricity is required. Moreover, the rejected heat from the electronic devices is used in the heat recovery system with the ammonia trilateral Rankine cycle. A data center with 11.2MW capacity in Norilsk, Russia, is considered in the case study.

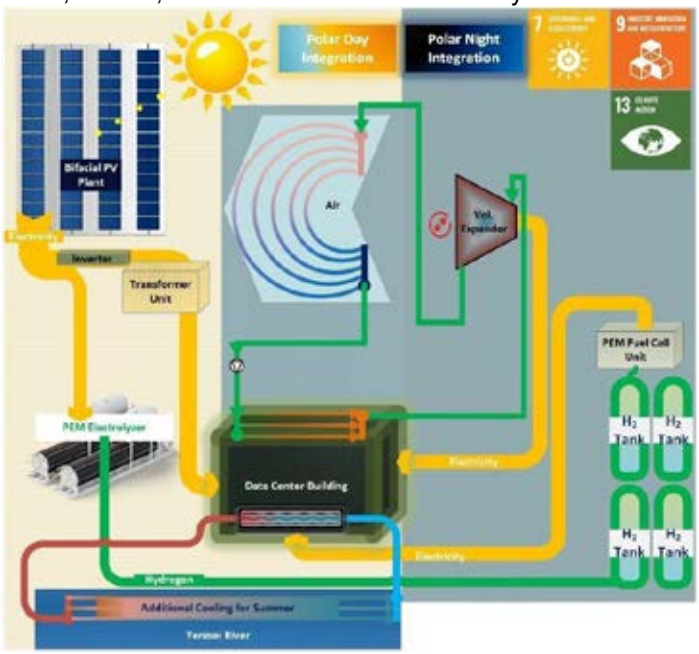


Fig. 1: Simplified layout of the proposed system

3. Analysis

Each component of the overall system is analyzed with the mass, energy, entropy, and exergy balance equations introduced by Dincer and Rosen (2021). The mass, energy, entropy and exergy balance equations can be expressed in the general form as follows:

$$\sum_i \dot{Q}_i + \sum_i \dot{W}_i + \sum_i \dot{m}_i \left(h_i + \frac{V_i^2}{2} + gZ_i\right) = \sum_o \dot{Q}_o + \sum_o \dot{W}_o + \sum_o \dot{m}_o \left(h_o + \frac{V_o^2}{2} + gZ_o\right) \quad (1)$$

$$\sum_i m_i s_i + \sum_{net} \frac{\dot{Q}_{net}}{T_S} + S_{gen} = \sum_o m_o s_o \quad (2)$$

$$\sum_i \dot{E}x_{Q_i} + \sum_i \dot{W}_i + \sum_i \dot{m}_i ex_i = \sum_o \dot{E}x_{Q_o} + \sum_o \dot{W}_o + \sum_o \dot{m}_o ex_o + \dot{E}x_d \quad (3)$$

The overall system can be evaluated with the following overall energy and exergy efficiencies:

$$\eta_{en,ov} = \frac{\dot{W}_{El,net}}{\dot{Q}_{GHI,BiPV}} \quad (4)$$

$$\eta_{ex,ov} = \frac{\dot{W}_{El,net}}{(\dot{Q}_{GHI,BiPV})\left(1-\frac{4}{3}\frac{T_o}{T_{sun}}(1-\cos\delta)^{1/4}+\frac{1}{3}\left(\frac{T_o}{T_{sun}}\right)^4\right)} \quad (5)$$

where T represents the temperature, $\dot{Q}_{GHI}$ represents the global horizontal irradiation input, $\dot{W}_{el,net}$ denotes the net electrical work, δ denotes the half-angle of the cone of the sun.

4. Results and Discussion

The proposed integration is developed according to the 11.2MW data center in Norilsk. The overall system, each component and subsystems are thermodynamically analyzed. The solar system is simulated via PVSyst software. A transient analysis is carried out with obtained data. According to the calculations, over an average year, 235 GWh electricity is produced by 175MWp bifacial PV, 11.6MW PEM fuel cell, 375kWp heat recovery systems. The excess electricity is exploited via a 109.1MW electrolyzer to produce 2920 tons of hydrogen annually. 2728tons of hydrogen is consumed in an average year to generate electricity by PEM fuel cell. 73.8GWh heat is recovered by the ammonia trilateral Rankine cycle to produce 2GWh electricity. The overall system possessed 23.42% energy and 24.33% exergy efficiencies for the average ambient and working conditions. Fig. 2 dynamically shows each energy generation system's capacity ratios, irradiation ratio, the overall energy and exergy efficiencies, and the ambient temperatures for an average year.

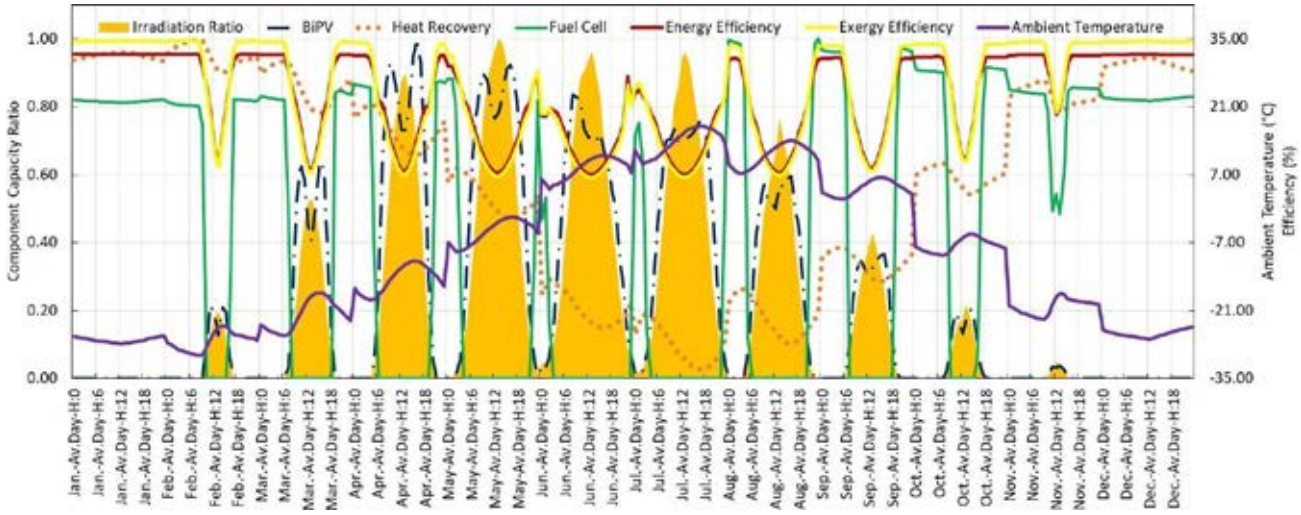


Fig. 2: The capacity ratios of each energy generation system and ambient conditions with the overall energy and exergy efficiencies for an average year

5. Conclusions

The overall system possessed 100% self-sufficiency by exploiting the solar resource only. The cooling load of the data center is transformed into an energy generator with the proposed integration. For the average ambient and working conditions, the proposed system's energy and exergy efficiencies are calculated as 23.42% and 24.33%, respectively.

References

Acar, C., et al., Transition to a new era with light-based hydrogen production for a carbon-free society: An overview, International Journal of Hydrogen Energy, 44.47 25347-25364 (2019).

Andrae, Anders SG, and Tomas E., On global electricity usage of communication technology: trends to 2030, Challenges 6.1 117-157 (2015).

Dincer, I., and Rosen Marc., Exergy, Elsevier, London (2021).

Development of Ceramic-Fiber Reinforced Sealants for Solid Oxide Fuel Cells

[1, 2*]Cigdem Timurkutluk, [1, 3]Gamze Atalmıs, [1, 3]Sezer Onbilgin, [1, 3]Furkan Toruntay and [1, 3]Bora Timurkutluk

[1] Nigde Omer Halisdemir University Prof. Dr. T. Nejat Veziroglu Clean Energy Research Center, 51245, Nigde, Turkey
[2] Nigde Omer Halisdemir University Department of Energy Science and Technologies, 51245, Nigde, Turkey
[3] Nigde Omer Halisdemir University, Mechanical Engineering Department, 51245, Nigde, Turkey

* E-mail: cigdemtimurkutluk@ohu.edu.tr

Abstract
Sealing material in solid oxide fuel cells (SOFCs) is applied between ceramic cells and interconnectors in the stack to prevent direct contact of fuel and oxidizing gases. In this respect, glass-ceramic materials are frequently used as solid oxide fuel cell sealing materials. Partial crystallization achieved after a high temperature forming process provides a gas-tight sealing, while the remaining glassy phase offers self-healing ability. However, crystalline formation increases depending on the number of thermal cycles, operating period and temperature. The thermal expansion mismatch between the resultant crystalline phases and the cell components can cause a mechanical failure, even under small temperature gradients during the operation. In this study, the effects of adding glass ceramic fiber to the glass ceramic material to prevent the flow during the operation are experimentally investigated for microtubular SOFCs. The results reveal that cast ceramic fiber provides the best sealing performance. The cell with ceramic bulk fiber, ceramic rope, ceramic blanket, ceramic fiber rope gasket, glass rope reinforced ceramic paste and glass ceramic paste provides an open curciut voltage of 1.103V, 0.928V, 0.968V, 1.020V, 0,950V and 0.988V, respectively.

Keywords: Solid Oxide Fuel Cell (SOFC), Micro-tubular Ceramic Fiber, Glass- Ceramics, Sealing**.**

I. Introduction

A typical sealant for solid oxide fuel cells (SOFCs) should provide gas-tight sealing and electrical insulation in both oxidizing and reducing environments of SOFCs together with acceptable chemical stability and compatible coefficient of thermal expansion with other SOFC components. Glass-ceramics have been considered to be an appropriate sealing material for SOFCs since they can be designed to meet those requirements above by modifying the composition (Brochu, 2006). One of the challenges for the implementation to solid oxide fuel cells is the development of hermetic sealant materials, which is used to separate the air and fuels gasses and to combine SOFC components. The sealants should have a high electrical resistance and must be thermochemically and mechanically compatible with other SOFC materials, which are solid electrolyte, metallic interconnect, anode and cathode (Ayawanna, 2019). SOFCs are being developed for a wide range of applications such as automobiles and power generators (Lea, 2007). Planar-typeSOFCs are superior to those having tubular designs because of their simple manufacturing process and the promise of a higher power density (Taniguchi, 2000). Good brazing between the current collector and the tube can be achieved to avoid leakage in tubular SOFCs. Glass and glass-ceramics which have stable performance during high-temperature operation are currently a favorable candidate for sealing the components in SOFCs. In the glass and glass-ceramic systems developed for SOFCs, silicate glass systems with alkaline-earth modifiers are among the favorites because of their stable characteristics. In addition, a self-healing feature of some glass systems has attracted more attention for SOFCs. With a suitable viscosity, a self-healing glass seal can restore its mechanical properties on being reheated to the stack operating temperature by healing the cooling-induced damages/cracks pre-sent at room temperature (Lin, 2013). Ceramic fibers are used as an additive to glass ceramic sealing material in this study. Ceramic fiber is an insulator made of an alumina–silica composition. It resists oxidation and is easy to fabricate and install with an elastic recovery higher than 93.35%. It can be used for extended periods of time and is also used in furnace insulation and high temperature gaskets. Most of its characteristics meet the demands for SOFC sealing. However, its porosity is higher than 90% and infiltration is required for its application to SOFC sealing to reduce the leak rates (Lea, 2007). In this work we present the sealing performance of glass paste-ceramic fiber types. Mixtures of two different compositions are used to produce fiber types-glass paste mixtures and their sealing performances at 800 °C are evaluated by measuring open circuit potential of microtubular cells. The influence of the composition of mixtures on high temperature sealing behavior is discussed and the microstructure of the composite ceramic fiber-paste is observed after the operation.

II. Experimental Set-up and Procedure

V1649 Commercial glass-ceramic powders (Ceradyne Inc., Washington, USA) were used as a sealing material. In order to prepare sealing paste, these powders were mixed with terpineol solvent and ethyl cellulose binder at suitable ratios. The mixture was then ball milled for 24h and the homogenization of the paste was made via three rolls mill. Commercially available non-crystal silica/alumina (SiO, 47-60 wt.% + AlO, 45-60 wt.%+Fe_2O_3,0-1.5 wt%+ ZrO_2, 0-19 wt%+ TiO_2 0-1.9 wt%) fiber types (Kiltaş, Haksan Industrial Materials, Turkey) were used as the ceramic fiber. The effects of adding different ceramic fibers (ceramic bulk fiber, ceramic rope, ceramic fiber paper, ceramic fiber rope gasket, glass rope) into glass-ceramic paste to prevent flowing of the glass-ceramic for microtubular

SOFCs were experimentally investigated. Two different mixtures were prepared for each fiber type. They were applied to the hydrogen inlet and outlet channels of the microtube for sealing tests. It is determined that appropriate amount of ceramic fiber types in the paste with desired properties should be 1.25 wt. %. The photos of the ceramics fibers used are given in Figure 1.

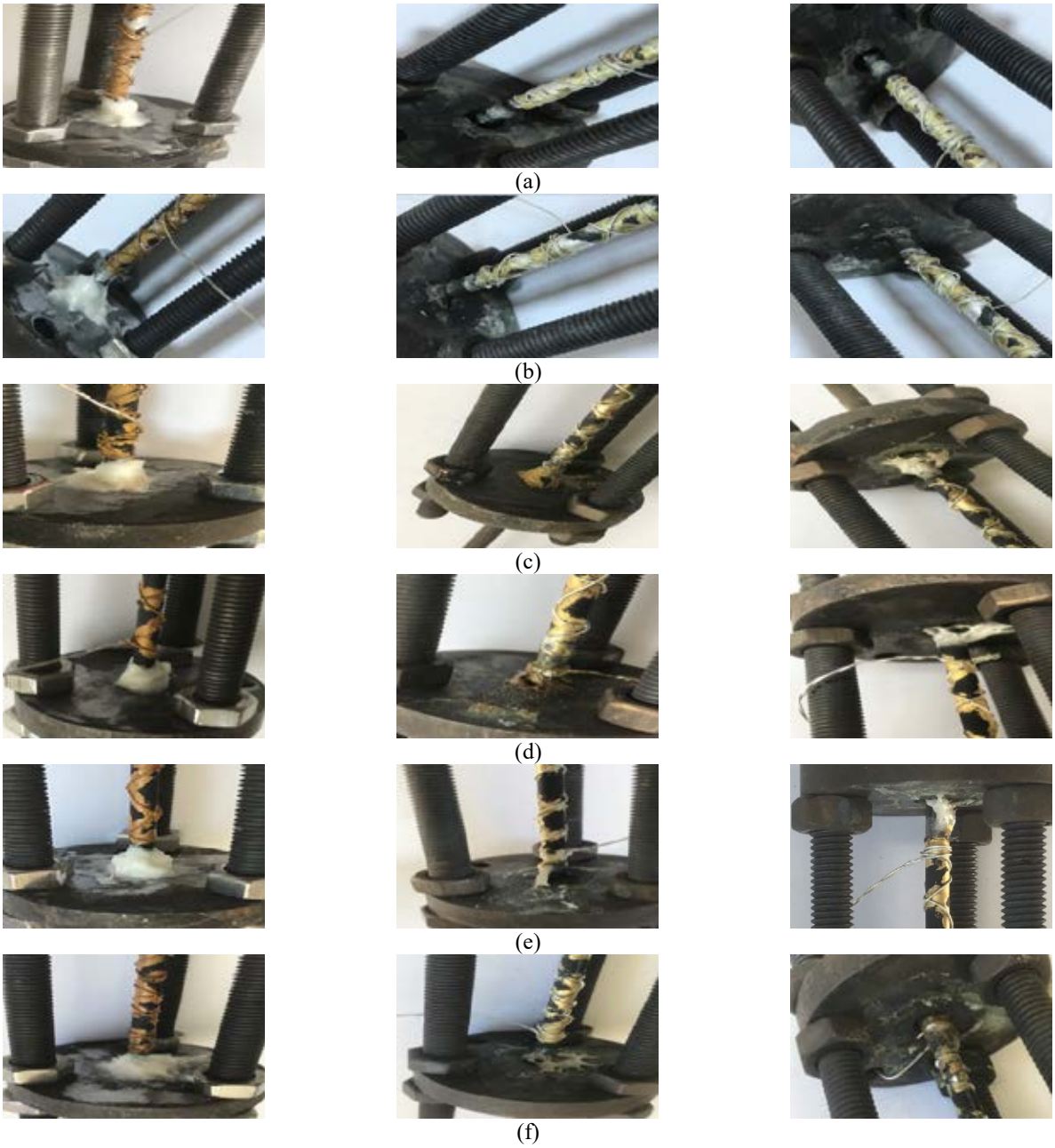


(a) (b) (c) (d) (e)

Figure 1: Ceramic fibers employed: (a) bulk fiber, (b) ceramic rope, (c) ceramic blanket, (d) ceramic fiber rope gasket and (e) glass rope

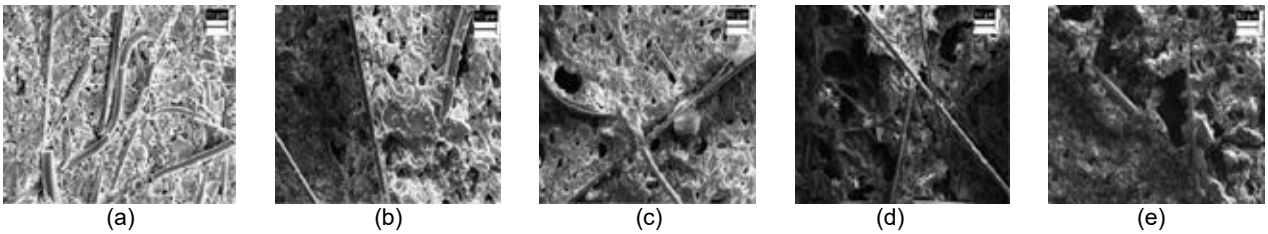
III. Results and discussions

After mixing with various chemicals, glass paste for each case is obtained. The composite sealings were applied to the inlet and outlet channels of the microtube with a suitable wt. % determined. The same processes were repeated for each glass paste ceramic fiber sealings (ceramic bulk fiber, ceramic rope, ceramic blanket, ceramic fiber rope gasket, glass rope). Photographs of each sealings before and after performance tests are given in Figure 2, while SEM images are shown in Figure 3.



(a) (b) (c) (d) (e) (f)

Figure 2. Photos of glass-ceramic sealing paste before (left) and after (middle and right) tests: (a) without any additive (b) with bulk fiber, (c) with ceramic rope, (d) with ceramic blunket, (e) with ceramic fiber rope gasket and (f) with glass rope



(a) (b) (c) (d) (e)

Fig. 3: SEM images of glass-ceramic pastes with bulk fiber (a), ceramic rope (b), ceramic blunket (c), ceramic fiber rope gasket(d) and glass rope (e)

It is seen that in general adding fibers can limit flowing of the glass-ceramic during the operation thus improves the sealing performance. It is more obvious in Figure 4, which compares the cell performance together with open circuit potentials. The highest open circuit potential thus the sealing performance is obtained from the cell sealed with a paste made of glass-ceramic and bulk fiber.

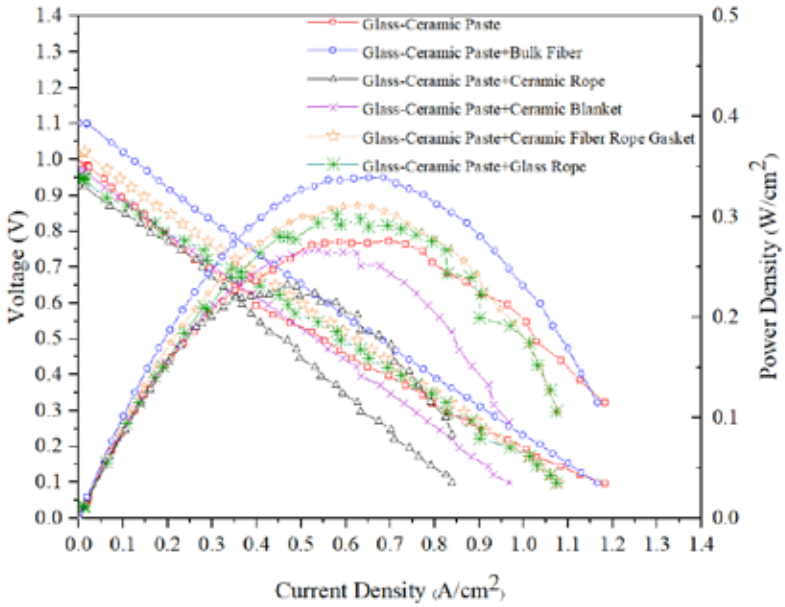


Fig. 4: Performance curves of NiO-YSZ anode supported micro-tubular SOFCs

IV. Conclusions

In this study, various ceramic fibers are added to glass-ceramic paste as a reinforcement material and their sealing performances are evaluated for microtubular SOFCs by measuring open circuit potential. The results show that the bulk ceramic fiber- glass ceramic paste mixture provides the best sealing performance. SEM images indicate that this fiber can be distributed more homogeneously in the paste than other fiber types. The improvement in the sealing performance is attributed to restricted flow of the glass-ceramic during the operation by adding fiber into the structure.

References

Ayawanna J., Kingnoi N., and Laorodphan N., Effect of bismuth oxide on crystallization and sealing behavior of barium borosilicate glass sealant for SOFCs, Journal of Non-Crystalline Solids, 509, 48-53,(2019).

Lea S., Suna K., Zhang N., Shao Y., Ana M., Fua Q., Zhua X., Comparison of infiltrated ceramic fiber paper and mica base compressive seals for planar solid oxide fuel cells, Journal of Power Sources ,168, 447–452, (2007).

Lin C.K., Lin K.L., Yeh J.H., Shiu W.H., Liu C.K., Lee R.Y., Aging effects on hightemperature creep properties of a solid oxide fuel cell glass-ceramic sealant, Journal of Power Sources, 241,12–19, (2013).

Brochu M., Gauntt B.D., Shah R., Loehman R.E., Comparison between micrometerand nano-scale glass composites for sealing solid oxide fuel cells, Journal of the American Ceramic Society, 89, 810–816, (2006).

Taniguchi S., Kadowaki M., Yasuo T., Akiyama Y., Miyake Y., Nishio K., Improvement of thermal cycle characteristics of a planar-type solid oxide fuel cell by using ceramic fiber as sealing material ,Journal of Power Sources 90 ,163–169, (2000).

A RENEWABLE ENERGY BASED WASTE-TO-ENERGY SYSTEM WITH HYDROGEN OPTIONS

[1*]B. Gungor and [1]I. Dincer
[1]Clean Energy Research Laboratory, Faculty of Engineering and Applied Science Ontario Tech. University2000 Simcoe Street North, Oshawa, Ontario L1H 7K4, Canada
*E-mail: bogachan.gungor@ontariotechu.net, ibrahim.dincer@uoit.ca

Abstract
In this study, a pressurized gasification combined system is integrated with geothermal energy to produce hydrogen rich syngas. This system uses dewaterized sludge, which leaves the primary and secondary sedimentation tanks in the biological wastewater treatment facility as a feedstock to produce energy in the form of hydrogen and transform it in a PEM Fuel Cell. This system incorporates a wind energy-based hydrogen storage system to meet with societies' energy need when the energy demand fluctuates. The Greater Toronto area is chosen as the reference location for the case study, and a thermodynamic is completed on the Aspen Plus and EES softwares. The hot water produced, and the total energy delivered to the community is calculated to be 1296 tonnes and approximately 2.1G Wh during its operation in a day. In addition, hydrogen to fuel ratio at the gasification system is found to be 0.12 through the sludge utilization. The overall energy and exergy efficiency of this system is recorded as 33% and 37%, respectively.

Keywords: Sustainable community, waste to energy, hydrogen, energy, exergy, efficiency.

1. Introduction

In 2020 the worlds energy consumption dropped by about 5% compared to 2019 but it is seen that the energy demand was mostly met using non-renewable energy resources. Even though the use of non-renewable energy has a overall decreasing trend over the last few years, there is still much improvement needed in the utilization of renewable energy and waste. (World Energy Outlook, 2020).

There are several studies completed to investigate the environmental impact and thermodynamic analysis of waste to energy systems through thermodynamic modeling and life cycle assessments. A study conducted by Evangelisti et al. aimed to improve traditional waste management systems where the final disposal of the waste ends up in landfilling and mass burn incineration. The advanced technology included gasification and plasma gas cleaning system with a capacity of 20MWe net energy output. This system was compared with traditional system and was recorded to have lower environmental impact in global warming potential and acidification potential categories. (Evangelisti et al., 2015). Another study by Ishaq et al. considered a hydrogen storage system and integrated this system with a wind farm to create a sustainable community. This study aimed to store the excess electricity in the form of hydrogen when the energy demand is low and transform the hydrogen into electricity through a fuel cell system when the energy demand is high. This shows economical advantage of hydrogen storage systems (Ishaq et al., 2018). These literature reviews demonstrates that waste can be utilized as a source to produce energy and with a proper waste to energy technology and storage system, self-sustainability can be achieved for communities.

2. Materials and Methods

A comprehensive thermodynamic analysis has been completed for this proposed system. For the thermodynamic simulation of this waste to energy system, both Aspen Plus and EES were used. As a property method, RK-SOAVE was selected, and the energy and exergy analysis of the overall system and subsystems were completed. The gasification unit was modeled using two different reactors, RYIELD and RGIBBS, to be able to simulate pyrolysis and gasification stages. For the RYIELD reactor, a FORTRAN Code was used to calculate the mass yield through a calculator block. Proximate and ultimate analysis of the dewaterized sludge used in the gasification system are given in Table 1. Dewaterized sludge was used as a feedstock in this pressurized gasifier with the presence of steam and limited oxygen to produce energy in the form of hydrogen. The wind farm was modeled on RetScreen software and the reference location was selected to be Greater Toronto Area for the calculation of wind speed and net energy outputs. The hydrogen produced was compressed in three stages to 3 MPa in the hydrogen tank and this storage unit was modeled on the Aspen Plus.

In this regard, the following equation is used to calculate chemical exergy of the organic matters and fuels used within this integrated system:

$$\dot{E}_{OM} = \dot{m}.ex_{ch,CO_2} + \frac{q}{2}.ex_{ch,H_2O} + \frac{q}{2}.ex_{ch,N_2} + r.ex_{ch,SO_2} - (m + r + \frac{n}{4} - \frac{p}{2}).ex_{ch,O_2} - \Delta G_r^0(kj.kg^{-1}) \quad (1)$$

where the stoichiometric equation used to calculate the coefficients is

$$C_mH_nO_qN_qS_r + (m + r + \frac{n}{4} + \frac{p}{2})O_2 \rightarrow mCO_2 + \frac{n}{2}H_2O + \frac{q}{2}N_2 + rSO_2 \quad (2)$$

The hydrogen production rate in the electrolyzer is calculated as follows:

$$\eta = \frac{LHV_{H_2}.\dot{m}_{H_2}}{W} \quad (3)$$

The total energy delivered to the community is found by using Formula 4:

$$\eta = \frac{W}{LHV_{H_2}.\dot{m}_{H_2}} \quad (4)$$

Table 1. Proximate and Ultimate Analysis of Dewaterized Sludge (Ibrahim et al., 2019)

Heating Value	Ultimate Analysis (%wt)							Proximate Analysis (%wt)			
HHV (MJ/kg)	C	O	H	N	Cl	S	Ash	Moisture	FC	VM	Ash
16.84	34.29	25.8	5.2	5.8	0	3.12	25.79	0	18.79	55.42	25.79

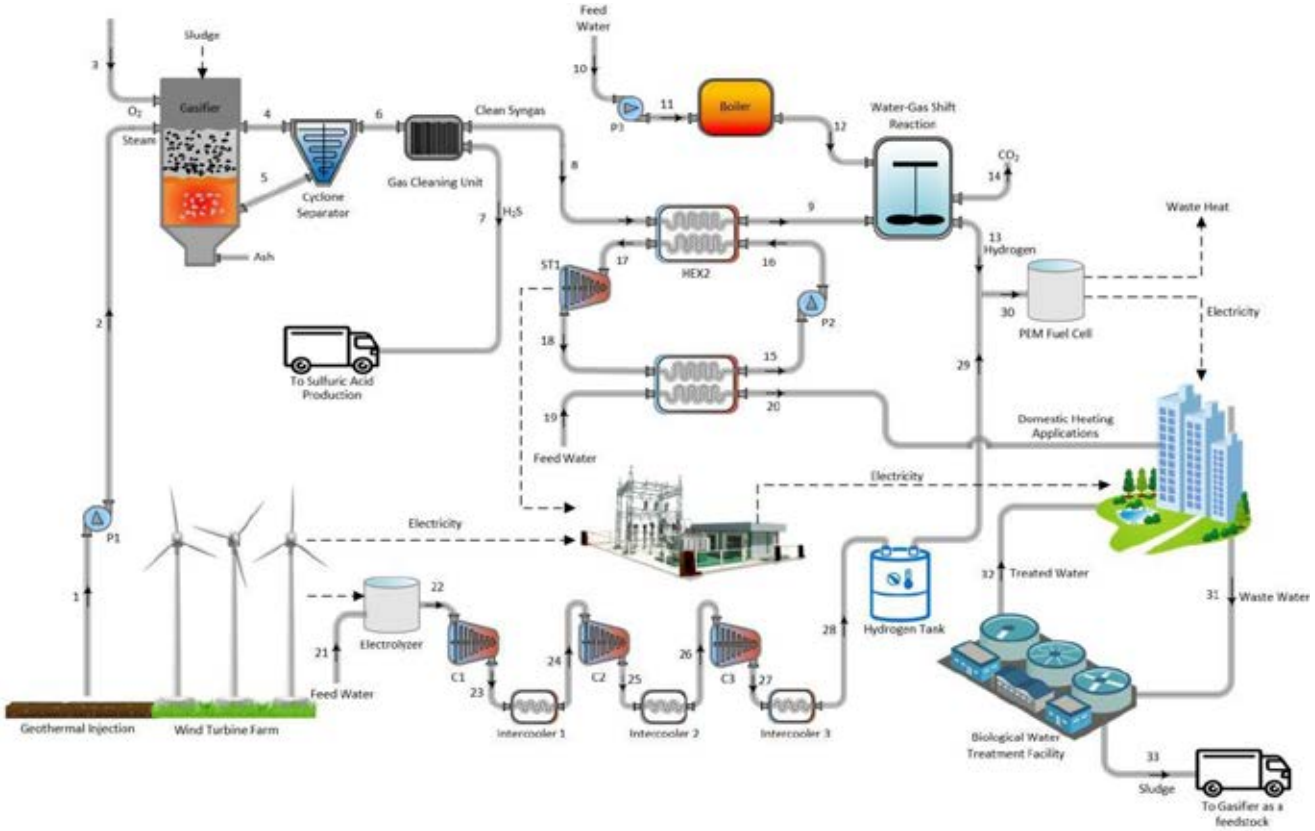


Fig.1. Proposed Advanced Waste-to-Energy System with a Hydrogen Storage Option for Energy Production

3. Results and Discussion

For the overall system and subsystems, a thermodynamic modeling was completed on ASPEN PLUS. For each unit, exergy destruvtion rates were complete and gasification unit was recorded to have the highest exergy destruction rate. According to RK-SOAVE property method, energy and exergy efficiencies of the overall system were calculated and stated to be 33% and 37%, respectively. The hydrogen to dewaterized sludge rate was found to be 0.078 and 0.12 at the gasifier and WGSR respectively. The daily total energy delivered to the community and the stored hydrogen were found to be 2.1GWh and 9180kg/d, in this order.

4. Conclusions

The thermodynamic assessment was completed for the proposed advanced WtE system and energy and exergy efficiencies of the integrated system was found to be 33% and 37%, respectively. LCA Analysis should be completed to investigate environmental impact of this integrated system for a sustainable community.

References

Evangelisti, S, Tagliaferri, C., Clift, R., Lettieri, P., Taylor, R., and Chapman, C. Life cycle assessment of conventional and two-stage advanced energy-from-waste technologies for municipal solid waste treatment. *J. Clean. Prod.*, 100, 212–223, (2015).

Ishaq, H., Dincer, I., and Naterer, G. Performance investigation of an integrated wind energy for co-generation of power and hydrogen. *International Journal of Hydrogen Energy,* 43, 9153-9164, (2018).

Ibrahim, A. B. A., Akilli, H Fuel Characterization and Simulation Study of Dewatered Domestic Wastewater Sludge Gasification Using ASPEN Plus. *7thInternational Symposium on Innovative Technologies,* 2, 954-963, (2019).

World Energy Outlook. https://www.iea.org/reports/world-energy-outlook-2020. Accessed on April 22nd, 2021.

Cold Sintering of 8YSZ Electrolytes for Solid Oxide Fuel Cells

[1*]Tuğçe Ucun [2]Murat Murutoğlu [3]Aligül Büyükaksoy [4]Yahya Kemal Tür [5]Hüseyin Yılmaz
[1]Gebze Technical University, Materials Science and Engineering Department, Gebze 41400, Kocaeli, Turkey.
* E-mail: tucun2018@gtu.edu.tr

Abstract

In this study, the fabrication of $Zr_{0.84}Y_{0.16}O_2$ (YSZ) electrolyte via cold sintering technique was investigated. Being an ultra-low temperature process, cold sintering has significant advantages over the conventional sintering techniques, in terms of energy cost, process simplicity and equipment requirements. YSZ electrolytes that are normally sintered at high temperatures (1400-1500°C) were sintered at lower temperatures (≤1225°C) after cold sintering process. The microstructural, electrical and electrochemical characterization of these ceramics have been carried out.

Keywords: SOFC, Cold sintering, YSZ

I. Introduction

Cold sintering is a recently developed low temperature densification process for ceramics. Using this approach, many ceramic powders can be sintered into high density ceramics at temperatures below their conventional sintering temperature.(Guo *et al.*, 2019) Cold sintering is a process that is carried out at temperatures just above the boiling point of water (100-200°C) and at pressures up to 450MPa. This process had been mentioned in the literature earlier and was referred to as “hydrothermal hot pressing” (Yamasaki *et al.*, 1986). Recently, it has been re-introduced to the literature by Randall et al (J. Guo *et al.*, 2016)(H. Guo *et al.*, 2016a) (H. Guo *et al.*, 2016b) and is referred to as “cold sintering”. According to Randall et al, the mechanisms during cold sintering resembles those that occurs in liquid phase sintering.

A solid oxide fuel cell (SOFC) is an energy conversion device that generates electricity directly from the fuel.(Minh, 2004). SOFCs based on ceramic membranes with high density, high ionic conductivity and low electronic conductivity. Y_2O_3 stabilized ZrO_2 (YSZ) is a common material used in SOFCs, and it divides the fuel cell into two compartments as anode and cathode, where fuel gas and oxygen gas will be sent. When oxygen and fuel gases are blown into the cathode and anode chambers respectively, a chemical potential difference occurs in these two chambers. This chemical potential difference spontaneously transforms into an electrical potential difference (voltage) in accordance with Nernst's equation (Equation 1) (Singhal and Kendall, 2003).

$$E = E^0 + \frac{RT}{nF}\ ln\left(\frac{p_{H_2}p_{O_2}^{\frac{1}{2}}}{p_{H2O}}\right) \qquad \text{Equation (1)}$$

High processing temperatures of SOFCs cause high energy costs, also the refractory and heating elements of the furnaces must be made from special and expensive materials. Cold sintering has the potential to be an environmentally friendly processing technology and become a widely used one. Production of SOFCs by cold sintering will provide process simplicity, reduced costs and contribute to their commercial production.

II. Experimental Set-up and Procedure

In this study, YSZ powders were filled into a steel die at specified amounts and pressed under pressure up to 450 MPa at temperatures 150-200°C and cold sintered for 1,5 and 12 hours. In addition, YSZ powders mixed with organic acids such as maleic acid, oleic acid and lactic acid to investigate their effect on cold sintering. Following the cold sintering process, YSZ electrolytes that are normally sintered at high temperatures such as 1400-1500°C, were sintered at lower temperatures of such as 1200 and 1225°C. Ceramics produced by cold sintering were subjected to a secondary heat treatment (post sintering) at much lower temperatures than known, in order to improve their physical and chemical properties. The microstructural, electrical and electrochemical characterizations of YSZ electrolytes have been carried out.

III. Analysis

Cold sintered densities of electrolyte samples were calculated from the macroscopic geometry and mass of the disc shaped ceramics. After cold sintering, the samples reached to ~57% of their theoretical density. Cold sintered 8YSZ ceramics were then post sintered at 1200°C and 1225°C for 2 and 4 hours in conventional furnaces and optimum conditions that resulted in densities > 90% of their theoretical value were found. After post sintering at 1200°C for 4 hours, ~90% theoretıcal density values were achieved. However, just to be on the safe side for SOFC applications, ceramics were post sintered at 1225°C instead of 1200°C to achieve ~95% theoretıcal density value.

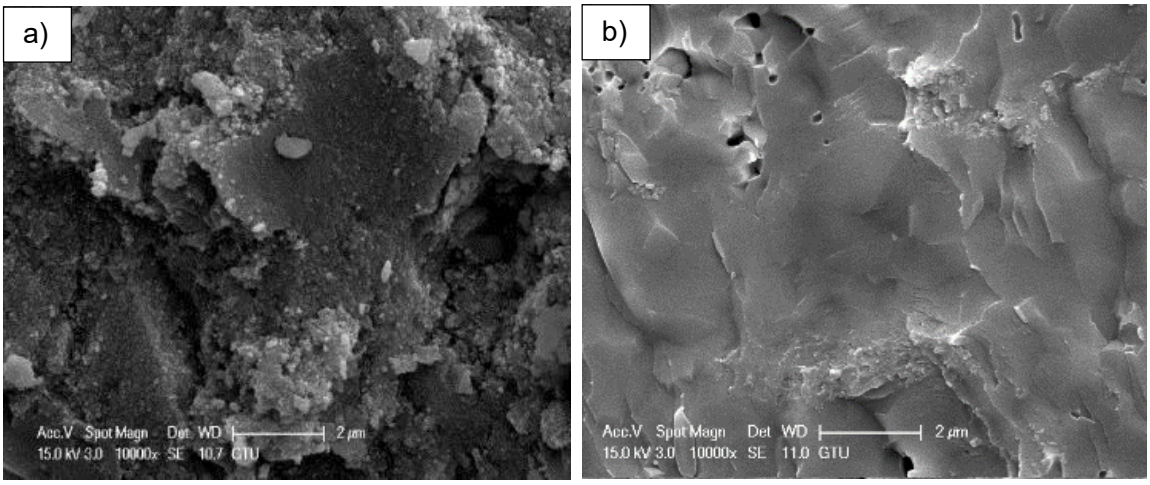


Figure.1: SEM images of a) cold sintered b) post sintered YSZ electrolyte from fracture surface at 10000x magnification

IV. Results and discussions

Electrochemical measurements were carried out on the cold sintered YSZ electrolytes at 800°C. The electrolyte impedance values were obtained from the ES measurements. The measured electrical conductivity of ceramics at 800°C has been calculated as 1.70 $\times 10^{-2}$S/cm. The electrical conductivity of cold sintered YSZ ceramics is close to the value of 1.6 $\times 10^{-2}$ S/cm which is obtained from traditional sintering YSZ ceramics at 750°C in the literature.(Kwon and Choi, 2006)(Brune *et al.*, 1998). Also electrical conductivity of YSZ electrolytes showed Arrhenius-type behavior and the activation energy found as 1.06 eV, in accordance with the literature data (Sındıraç, Büyükaksoy and Akkurt, 2019). Furthermore, a satisfactory open circuit potential(OCV) value of 0.9V at 600°C was obtained from the YSZ electrolytes. This value was considered very promising because it was the first-time an open circuit potential was reported from the YSZ electrolyte produced by cold sintering method. Studies are currently made to further improve the electrolyte performances.

V. Conclusions

YSZ electrolytes cold sintered at 200°C for 1 hour and then post sintered at 1225°C for 4 hours and resulted in ceramics which suitable for SOFC applications. Ceramics reached to ~95% of their theoretical density value at these conditions. Structural and electrical measurements revealed that they are promising materials for SOFC applications. Cold sintering process is a new and alternative way of processing ceramics and has a lot of advantages over conventional sintering in terms of process simplicity and cost reduction.

References

Brune, A. *et al.* (1998) 'The electrical conductivity of yttria-stabilized zirconia prepared by precipitation from inorganic aqueous solutions', *Solid State Ionics*. doi: 10.1016/s0167-2738(97)00486-4.
Guo, H. *et al.* (2016a) 'Cold Sintering Process: A Novel Technique for Low-Temperature Ceramic Processing of Ferroelectrics', *Journal of the American Ceramic Society*. doi: 10.1111/jace.14554.
Guo, H. *et al.* (2016b) 'Protocol for Ultralow-Temperature Ceramic Sintering: An Integration of Nanotechnology and the Cold Sintering Process', *ACS Nano*. doi: 10.1021/acsnano.6b03800.
Guo, J. *et al.* (2016) 'Cold Sintering: A Paradigm Shift for Processing and Integration of Ceramics', *Angewandte Chemie - International Edition*. doi: 10.1002/anie.201605443.
Guo, J. *et al.* (2019) 'Cold Sintering: Progress, Challenges, and Future Opportunities', *Annual Review of Materials Research*, 49, pp. 275–295. doi: 10.1146/annurev-matsci-070218-010041.
Kwon, O. H. and Choi, G. M. (2006) 'Electrical conductivity of thick film YSZ', *Solid State Ionics*. doi: 10.1016/j.ssi.2006.07.039.
Minh, N. Q. (2004) 'Solid oxide fuel cell technology - Features and applications', *Solid State Ionics*. doi: 10.1016/j.ssi.2004.07.042.
Singhal, S. C. and Kendall, K. (2003) *High-temperature Solid Oxide Fuel Cells: Fundamentals, Design and Applications*, *High-temperature Solid Oxide Fuel Cells: Fundamentals, Design and Applications*. doi: 10.1016/B978-1-85617-387-2.X5016-8.
Sındıraç, C., Büyükaksoy, A. and Akkurt, S. (2019) 'Electrical properties of gadolinia doped ceria electrolytes fabricated by infiltration aided sintering', *Solid State Ionics*. doi: 10.1016/j.ssi.2019.115020.
Yamasaki, N. *et al.* (1986) 'A hydrothermal hot-pressing method: Apparatus and application', *Journal of Materials Science Letters*. doi: 10.1007/BF01748104.

Hydrogen Powered Cities: A Perspective on Urban Planning

[1*]Munevver Ozge Balta, [2]Mustafa Tolga Balta
[1] Uşak University, Arthitecture and Design Faculty, Department of City and Reginol Planning, Uşak, 64200,Turkey
[2] Uşak University, Engineering Faculty, Department of Mechanical Engineering, Uşak, 64200,Turkey

* E-mail: munevver.balta@usak.edu.tr

Abstract
In recent years, the concept of sustainable cities has attracted much more important due to the unpreceded challenges. Especially, globalisation, population growth, environmental and economic problems have become more apparent and increasingly important. In this regard, planning for sustainable cities becomes increasingly complex. New and sustainable approaches are needed for implenting the urban plans should establish for green and smart cities. For creating a carbon free cities should be planned in a sustainable way for considering the needs of the 21st century. In this context, hydrogen powered cities are one of the solution to preventing to these problems. In this study, various planned hydrogen powered cities are reviewed and the projects of some cities have been examined.

Keywords: Cities, Hydrogen, Renewable Energy, Sustainable, Urban Planning.

I. Introduction

Today, more than half of the global population of the world lives in urban areas due to ongoing urbanization, industrialization, and population growth. The urban population which was 751 million in 1950 has reached 4.2 billion in 2018 with a rapid increase. According to UN research, approximately two-thirds of the world's population will live in urban areas by 2050 (UN, 2019). We are encountering a rapid increase in population in urban areas. Migration from rural areas to cities continues, exponentially. This global transition is accelerating day by day with the industrialization and urbanization. Also, urban growth rate is increasing very dramatically. This rapid increase has led several environmental and substantial concerns such as growing demand for food, water and energy and also deforestation, land degradation. Energy consumption of the transportation, utilizations in the buildings and also industrial has an important effect on the urban development. This increasing demand in cities is met mostly with fossil fuels. Fossil fuels are still the main source of energy consumed in the world. The excessive use of fossil fuels to meet these demands has also caused several environmental problems, including an increase in greenhouse gas concentration in the atmosphere and climate change. However, the most important environmental issue is climate change that needs to be taken into account. The environmental issues of the cities mentioned above can be solved with an energy system that complies with the parameters given below;

- optimized
- sustainable
- efficient
- self-sufficient
- resilient
- accessible
- affordable
- adequate
- eco-friendly and environmental-benign

In this regard, effective, efficient and also environmentally friendly renewable based systems will play utmost important role to ensure sustainable urban environment. An effective solution to address the challenge of these environmental and economic problems is to transition to the carbon free economy. In this regard, transition to carbon free economy presents various opportunities. One of the effective solution to address the challenge is hydrogen-based energy supply system. In this context, evaluating the hydrogen economy may offer many opportunities. Some of the major benefits of transitioning to the hydrogen economy can be given as;

(i) to revitalize the economic activities at cities
(ii) to improve the quality of environment conditions for city dwellers,
(iii) to ensure sustainable urban future,
(iv) to ensure the energy security of the cities,
(v) to combat the environmental and other consequences,

In recent years, there has been an increasing interest in energy management systems and energy conservation systems of cities. Most studies in the field of smart and/or sustainable cities have solely focussed on transportation, infrastructure planning or energy utilization in the buildings, separately. In the literature, there has been significant number of studies on smart and/or sustainable cities although there is no more paper on hydrogen powered cities which is conducted on perspective on urban planning. First studies on the concept of the hydrogen cities is published by Lodhi (1987). The purpose of this paper is to review recent research on hydrogen powered cities.

II. Hydrogen Cities

Energy systems of the cities are changing due to global warming. Cities have a crucial role in reducing the greenhouse gas emissions and transition to the green energy system. Countries are looking to create a hydrogen society in the near future. In this regard, many city authorities want to build a "first hydrogen city" which use hydrogen and related technologies, in the world. In recent decades, many countries have become interested in hydrogen energy systems that use renewable energy sources in various scales from a small to large settlements. Therfore, many countries have various projects to build the first hydrogen city. Recent projects on hydrogen cities are briefly defined below;

- **South Korea**

South Korea want to be seen as a leader in green technology by creating a hydrogen powered society. Promotion strategy of the first hydrogen pilot city was declared by the South Korean Ministry of Land, Infrastructure, Transport and Tourism (Bergenson, 2021). Decleration at ministerial level shows their attention to importance of the hydrogen cities. This pilot city is planned to build in 2022, for testing the hydrogen associated technologies in transportation and residential sectors. The strategy of the South Korea was powered the 10% of the country's cities, counties, and towns by hydrogen by 2030 (Zuid, 2019). In this project, cities will use hydrogen as a power source for heating, cooling and electricity. Related infrastructure, such as 9.9 MW fuel cells, 670 hydrogen fuel-cell electric passenger vehicles and 30 hydrogen buses, will be available in the planned cities (KH, 2019). Hydrogen based transportation system is also considered for this project. This project includes a hydrogen charging station for vehicles that will be installed in a transfer center, parking lot, and bus garage either in the city itself or near it. South Korea has a goal for 2040, in which 40% of local governments will be hydrogen powered cities and operate12000 hydrogen buses and 825000 hydrogen cars (Bergenson, 2021). The hydrogen market was expected to reach 70 trillion won by 2050, according to the South Korean government's hydrogen road map (KH, 2019). A concept plan for pilot city can be found in detail at Zuid (2019).

- **Danish Dream City (H2PIA)**

A number of group of Danish companies have released a visionary concept called as H2PIA which will build up for achieving a fully sustainable lifestyle, free of addiction to oil, coal and gas in the date of 2050. H2PIA was announced as a project for urban communities based on renewable energy, and hydrogen technologies as the sources of energy. This concept is extended worldwide due to its sustainability (Paul, 2006; Emad et al, 2018). In this project, renewable based hydrogen was planned to produce through dissocation of water via solar energy and wind power. Residents will have a number of options for their home: Plugged, Unplugged, Hybrid. Although, H2PIA appears an utopia, but the designers make a point of that is not a fantasy (Paul, 2006).

- **Wuhan, China**

According to Wuhan city development plan, Wuhan will build itself into a "hydrogen city" through developing hydrogen energy industry. The goal of the city is build up to 20 hydrogen fueling stations from 2018 to 2020 to support the running of about 3,000 hydrogen fuel cell-powered vehicles. In this project, a hydrogen energy industrial park is expected to be built in the city gathering the fuel cell automakers and associated companies. The city is planned to advance research and development of hydrogen technologies such as core technology of hydrogen production, storage and transport, and improve hydrogen infrastructure in the next decades (CD, 2018). Chinese government stated that, hydrogen offers a significant way towards meeting the decrease in the affects on the climate change and pollution goals without increasing reliance on imported non-renewable fuels. China is expected that hydrogen will account for 10% of the Chinese energy system by 2040 (Brasington, 2019).

- **Harumi Flag, Japan**

Harumi Flag is originally being built as the Olympic Village for the Tokyo 2020 Games as a residential complex being built on 18 hectares with a full scale hydrogen infrastructure system which is located in Tokyo. This project will be expected to complete by the year of 2024. A hydrogen station is planned to be built near the town. Hydrogen will deliver to the residental complex by the underground pipelines. The hydrogen pipelines were planned to be connect to hydrogen fuel cell generators that will be installed in residental complex. Transition to the hydrogen economy is an very important tool for providing the energy security and decrease in the accelerate of the global warming. In this regard, The Japanese government aims to produce hydrogen from carbon free emission sources by 2040. A concept plan for hydrogen supply system of Harumi Flag can be found in detail at (Panasonic, 2019).
This project has three main goal to achive the sustainability; (i) Self-sustained energy supply; (ii) Life comfort with low emission; and (iii) A model city of advanced sustainability (Panasonic, 2019).

- **Ornkey Island, Scotland**

On the Orkney Islands, is under implementation of an H2 Valley concept. The implementation of a fully integrated concept for hydrogen production from renewables is considered for this project. Renewable electricity from wind and tidal turbines is used to produce green hydrogen in two electrolysers on two different islands with a total capacity

of 1.5 MW. Energy demand for heat, power and mobility applications meet from green hydrogen. A concept plan of the hydrogen production on the Orkney Islands can be found in detail at (Ruf, 2018). In this project, annual H2 demand is calculated at about 10-15 tons for heat, power and mobility applications while total annual H2 production capacity is at about 100-150 tons, but it has a potential to be increase to 200 tons (Ruf, 2018).

- **Glasgow, Scotland**

A project is designed for Glasgow city, for providing a carbon free economy and supporting the country's efforts to achieve net zero by 2045 which wants to become the first net-zero city. Renewable electricity obtained from wind and solar is used to operate 10 MW electrolyser to produce green hydrogen. one of the aim of this project is supply hydrogen to the commercial market within the next two years (ITM-Power, 2020).

- **Noem, Saudi Arabia**

A project will be constructed in Saudi Arabia as a sustainable and smart city which is called NOEM. This project has a capacity of around 650 tons of hydrogen per day as well as 1.2 million tons of green ammonia each year. 4 GW energy capacity is required for this project which will be powered up by solar, wind coupled up with battery storage. The project will be completed by the year of 2025. With this project will reduce the CO2 emissionsof the world by 3 million tons, annually (SE, 2020).

III. Conclusions

The main conclusions that can be drawn from this study are given below,

(i) One of the transitional solution is creating a carbon free future by meeting the energy demand of the cities with renewable energy based hydrogen.

(ii) Cities should consider the energy efficient urban planning and design which can contribute to the decrease of the CO_2 emissions and thus reduce the accelerate of the global warming.

(iii) Regions and cities see the importance of the hydrogen and hydrogen associated systems which can play a crucial role in their future green energy systems and transition strategies.

References

Bergenson A., South Korea has big plans to create hydrogen cities, https://www.hydrogenfuelnews.com/south-korea-has-big-plans-to-create-hydrogen-cities/8538904/, Accessed date: 10.March. 2021.

Brasington L., Hydrogen in China, China Energy & Power, Hydrogen, (2019), https://www.cleantech.com/hydrogen-in-china/, Accessed date: 10.March. 2021.

China Daily, Hydrogen city' to be built in central China, https://www.chinadailyhk.com/articles/108/12/246/1516590980444.html, (2018), Accessed date: 10.March. 2021.

Emad A., El-Shimy M., Mohamed G., Super Sustainability through Hydrogen Cities –An Overview, The 2nd International Conference on New Trends for Sustainable Energy (ICNTSE 2018), Alexandria –Egypt, (2018).

ITM Power, Green Hydrogen for Scotland, (2020) https://www.itm-power.com/news/first-project-to-deliver-a-10mw-electrolyser-to-glasgow-facility

Korea Herald, S. Korea to build 3 hydrogen-powered cities by 2022, http://www.koreaherald.com/view.php?ud=20191010000806, (2019), Accessed date: 10.March. 2021.

Lodhi M., Hydrogen city, International Journal of Hydrogen Energy, 12(11), 783-803, (1987).

Panasonic, Harumi Flag, The City That Brings The Future to Today's Tokyo, Towards 2020, Beyond 2020, Part 2,(2019), https://news.panasonic.com/global/stories/2019/71600.html, Accessed date: 10.March. 2021.

Paul R., World's First Hydrogen City, https://inhabitat.com/worlds-first-hydrogen-city/136168706_2610b7c915/, (2006), Accessed date: 10.March. 2021.

Ruf Y., Lange S., Pfister J., Droege C., Kaufmann M., Heieck F., A Study for the Fuel Cells and Hydrogen Joint Undertaking, Fuel Cells and Hydrogen for Green Energy in European Cities and Regions, FCH, 61, (2018).

Solar Edition, World's Largest Green Hydrogen Project Will build in NOEM Smart City, Saudi Arabia, SE2020, No:973,(2020) https://solaredition.com/worlds-largest-green-hydrogen-project-will-build-in-noem-smart-city-saudi-arabia/ Accessed date: 10.March. 2021.

United Nations, World Urbanization Prospects: The 2018 Revision (ST/ESA/SER.A/420), Department of Economic and Social Affairs, Population Division, New York, (2019).

Zuid J., Hydrogen-Powered Cities: Who, Where, How? https://www.whatsorb.com/community/building-hydrogen-powered-cities-who-where-how, Accessed date: 10.March. 2021.

Development of Multi Phase Cathodes for IT-SOFCs via Thermal Plasma

[1,3] Havva Eda Aysal, [2,3]*Gülhan Çakmak, [1,3] Tayfur Öztürk,
[1] Middle East Technical University, Faculty of Engineering, Department of Metallurgical and Materials Engineering, Ankara, Turkey [2] Muğla Sıtkı Koçman University, Department of Metallurgical and Materials Engineering, Mugla, Turkey
[3] ENDAM, Center for Energy Materials and Storage Devices, Middle East Technical University, Ankara, 06800, Turkey
* E-mail: gulhancakmak@mu.edu.tr

Abstract
The composition and microstructure of cathode materials have a large impact on the performance of solid oxide fuel cells (SOFCs). The main goal in SOFC research is to develop cathodes with a sufficiently low electrochemical resistance (~0.15 Ω.cm2) at operating temperatures significantly below 800°C. The focus has been shifted to particularly mixed conducting perovskites of which La1-xSrxCoO3—δ (LSC) family has attracted considerable interest. Baumann (2005). The current study examines the possibility of producing these materials via thermal plasma synthesis.
Keywords: IT-SOFCs, Thermal Plasma, Multi-Phase Cathodes,

I. Introduction

The composition and microstructure of cathode materials have a large impact on the performance of solid oxide fuel cells (SOFCs). The main goal in SOFC research is to develop cathodes with a sufficiently low electrochemical resistance (~0.15 Ω.cm2) at operating temperatures significantly below 800°C. The focus has been shifted to particularly mixed conducting perovskites of which La1-xSrxCoO3—δ (LSC) family has attracted considerable interest. Baumann (2005).

Following Crumlin and Sase that hetero-interfaces enhances ORR kinetics, composite cathodes have attracted considerable attention. Thus it was shown that mixed (La0.8Sr0.2)CoO3/(La0.5Sr0.5)2CoO4 (LSC113/LSC214) had superior ORR performance in the temperature range from 700oC-500 oC. Torunoglu 2018. Furthermore, we have recently shown that the sputter-deposited dual-phase cathode yields the best performance at mid-compositions where hetero-interfaces were expected to be the most dominant. Sari (2018). Interestingly the mixture obtained as a result of this sputter deposition had an amorphous structure.

A striking feature of these structures was that they were highly stable and resisted crystallization at low temperatures and that when recrystallized, e.g. prolonged use at 700oC, formed an ill-defined nanocrystalline structure where the crystal size was not more than 10nm. Sari (2019). Furthermore, this amorphous/ nanocrystalline structure was resistant to strontium segregation, and thus, LSC113/LSC214 composite could be used as a cathode for IT-SOFCs operating at temperatures as low as 575oC. Sari (2019).

The current study examines whether or not the favourable properties obtained via sputter deposition can be obtained through other methods. Thermal plasma would enable the synthesis of powders at the nanoscale, and therefore it might be an alternative to sputter deposition.

II. Experimental Set-up and Procedure

LSC powder was synthesized from precursor solutions prepared by mixing nitrates, namely La(NO3)3.6H2O, Sr(NO3)2 and Co(NO3)2.6H2O according to the targeted stoichiometric proportions and fed to thermal plasma reactor. The powder synthesized via thermal plasma was structurally analyzed with SEM and XRD, and its electrochemical performance was characterized with Electrochemical Impedance Spectroscopy on symmetric cells.

,

IV. Results and discussions

A total of five runs were synthesized with different intended compositions. In each case, the EDS analysis of the resulting powder yielded a composition of LaxSryCox, which is quite close to the targeted composition. Rietveld refinement of XRD patterns shows that the resulted phases were LSC 113, LSC 214 and the combination of these two structures. A typical SEM micrograph taken from powders is given in Fig.1.

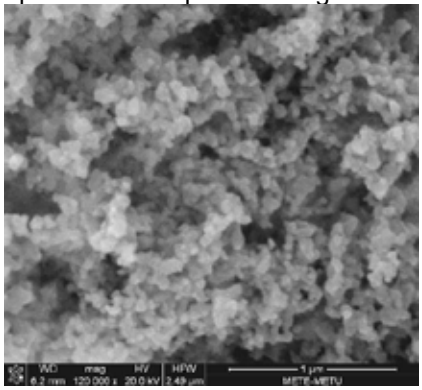


Fig.1: SEM image of LSC113

Symmetric cells of LSC113-LSC214 cathodes coated with screen-printing were analyzed with electrochemical impedance spectrum (EIS). The analysis is continuing for the measurement of cathode resistance and area-specific resistance of composite cathodes in 350-700 °C temperature intervals.

V. Conclusions

The study includes the thermal plasma-based production of La1-xSrxCoO3—δ based multi-phase powders for IT-SOFC purposes. Compositions with different LSC 113/LSC214 ratios were successfully synthesized using various precursor amounts. LSC113/LSC214 structurally characterized using X-ray Diffraction and SEM, and their electrochemical properties are under investigation for cathode purposes.

Acknowledgements

This work was supported by TÜBITAK (The Scientific and Technological Research Council of Turkey) (Project Number 217M628), which the authors gratefully acknowledge.

References

Baumann FS., Fleig, J. , Konuma, M. Starke, U., Habermeier H-U., Strong performance improvement of la 0.6Sr 0.4Co 0.8Fe 0.2O 3-δ SOFC cathodes by electrochemical activation, J. Maier, J. Electrochem. Soc., 152(2005) A2074,.

Crumlin E. J. et al., Surface strontium enrichment on highly active perovskites for oxygen electrocatalysis in solid oxide fuel cells, Energy Environ. Sci., 5,. 2012. 6081,

Sase M. et al., Enhancement of oxygen surface exchange at the hetero-interface of (La,Sr) CoO3 / (La,Sr) 2 CoO4 with PLD-layered films., Electrochem. Soc.,155,2008, B793,.

Torunoglu ZC, Sari, D Demircan, O Kalay, YE Ozturk T., Kuru, Y. One-pot synthesis of (La,Sr)CoO3/(La,Sr)2CoO4 for IT-SOFCs cathodes, Int. Journal of Hydrogen Energy 43(2018) 18642-18649

Sari, D Piskin, F Torunoglu, ZC Yasar, B Kalay YE, Ozturk T., Combinatorial development of nanocrystalline/amorphous (La, Sr) CoO3-(La, Sr) 2CoO4 composite cathodes for IT-SOFCs Solid State Ionics, 326, 2018,124–130,

Sari, D Yasar, B Piskin, F Kalay YE, Ozturk T, Segregation Resistant Nanocrystalline/Amorphous (La, Sr) CoO3-(La,Sr)(2)CoO4 Composite Cathodes for IT-SOFCs, Journal of The Electrochemical Society, 166 2019 F1157-F1163

Development Of Sustainable Multigeneration System with Recompression sCO_2 Brayton Cycle For Hydrogen Production

[1*]Serpil Celik Toker, [1]Gamze Soyturk, [1]Onder Kizilkan
[1] Isparta University of Applied Sciences, Technology Faculty, Department of Mechanical Engineering, Isparta, 32000, Turkey

* E-mail: serpilcelik@isparta.edu.tr

Abstract
In this paper, an multigeneration power plant based on the solar dish collector has been designed to produce hydrogen production and beneficial outputs. The proposed solar energy-based multigeneration power system consists of five different sub plants, such as solar dish collector, recompression sCO_2 (supercritical carbon dioxide) Brayton cycle, hydrogen generation, ejector cooling cycle, and hot water preparation. The first and second law analyzes of thermodynamics are conducted to examine multigeneration system performance. Various parameter studies have been carried out to examine the effect of solar radiation on the system. The parametric results show that; net power generation, refrigeration, hot water preparation, and hydrogen production are increased with the rise of solar radiation. Moreover, based on the thermodynamic assessment outputs, the energy and exergy efficiencies of 4.6 % and 47 % are computed for the multigeneration system with solar energy, respectively.

Keywords: Solar dish collector, recompression sCO_2 Brayton cycle, PEM electrolyzer, ejector cooling cycle

I. Introduction

Worldwide energy consumption is increasing significantly with population growth and industrialization. Among the energy consumption, conventional fossil fuels still dominate the energy sector. The use of fossil fuels has led to increased CO_2 emissions and environmental problems. Therefore, more efficient and greener energy systems are desired (Jradi and Riffat, 2014). Poly-generation systems have various advantages on energy conversion, including higher thermal efficiency, lower costs, and fewer emissions compared with separated production systems (Kavvadias and Maroulis, 2010). These systems not only generate power but also utilize the waste heat to produce the supplementary electricity, heating, cooling, and hydrogen production. Many technologies, such as solar tower, parabolic collector, gas turbine cycle, sCO_2 cycle, heat recovery steam generator (HRSG), absorption chiller, ejector cooling system, organic Rankine cycle (ORC), hydrogen production, etc., have been employed to realize the poly-generation procedures.

In recent years, the sCO_2 Brayton power generation technology with solar energy-based has attracted significant research attention. The sCO_2 Brayton cycle uses environmentally friendly and nontoxic sCO_2 as the working fluid. Compared with a steam Rankine cycle, the sCO_2 Brayton cycle has advantages in terms of power conversion efficiency in the turbine inlet temperature range of 773–1173 K, and it can safely operate at higher turbine inlet temperatures (Crespi et al., 2017). Also, the thermo-physical properties of CO_2 present sharp changes near the critical state, which reduces the compression power consumption and consequently promotes its cycle efficiency (Hami et al., 2017). By adding sub-cycles to the solar-powered sCO_2 Brayton cycle, such as the transcritical CO_2 Rankine cycle, the ORC, the ejector cooling cycle, and hydrogen generation, the efficiency of the system can be further increased.

More recently, some researchers investigated the poly-generation system with the solar energy-based sCO_2 Brayton cycle. Wang et al. (2012) proposed a new CCHP (combined cooling, heating, and power) system utilizing a CO_2 Brayton cycle and a transcritical CO_2 refrigeration cycle driven by solar thermal power. By analyzing the influence of several key thermodynamic parameters on the system performance, they found that the system efficiency is reduced when increasing the turbine inlet pressure and ejector inlet temperature and improved when increasing the turbine back pressure and turbine inlet temperature. Wu et al. (2017) proposed a novel CCHP system that combined with a sCO_2 recompression Brayton cycle and an absorption refrigeration cycle. The performances of the system were optimized and compared from the viewpoints of the first law, second law, and exergoeconomics. It was concluded that the proposed system could not only enhance the thermal and exergy efficiencies but also improve the exergoeconomic performance. Huang et al. (2019) developed a CCHP system comprising a CO_2 Brayton cycle, a dual-pressure ORC, and an ejector refrigeration cycle. The single-objective optimization was carried out by means of a genetic algorithm to obtain the minimum levelized exergy cost of the system product. Al-Zahrani and Dincer (2016) integrated the solar tower with a solid oxide fuel cell (SOFC) and CO_2 Brayton cycle to generate electricity and hydrogen. According to the results, they concluded that the working performance of the electrolyzer has a significant effect on the efficiency of the integrated system.

In this work, a multigeneration plant is proposed to offer multiple useful products and to increase the system performance, therefore, to help to decrease harmful emissions. For the driving source of the proposed multigeneration system, solar energy is selected. By using Engineering Equation Solver (EES) software, together with thermodynamic analysis, parametric assessments are made to examine the effect of solar radiation on the system.

II. System Description

A representation picture of the solar energy combined multigeneration plant is given in Fig. 1. This combined plant includes the solar dish, recompression sCO_2 Brayton cycle, hydrogen production, ejector cooling cycle, and hot water preparation. Solar radiation is the main power supply for the multigeneration system, and solar radiation can be collected by using the solar dish. Therminol VPI salt solution, the heat transfer fluid used in the solar collector, absorbs the solar energy and transfers its heat to the CO_2 fluid used in the HEX1 of the Brayton cycle. Subsequently, heat transfer fluid enters the HEX2 to heat the electrolyzer water. Then, electricity coming from the gas turbine and the hot water enters the PEM electrolyzer and, in this process, the water is separated into H_2 and O_2. A part of the heat of the fluid coming out of HEX2 is used in the ejector cooling system to obtain cooling, and some part is used in hot water preparation.

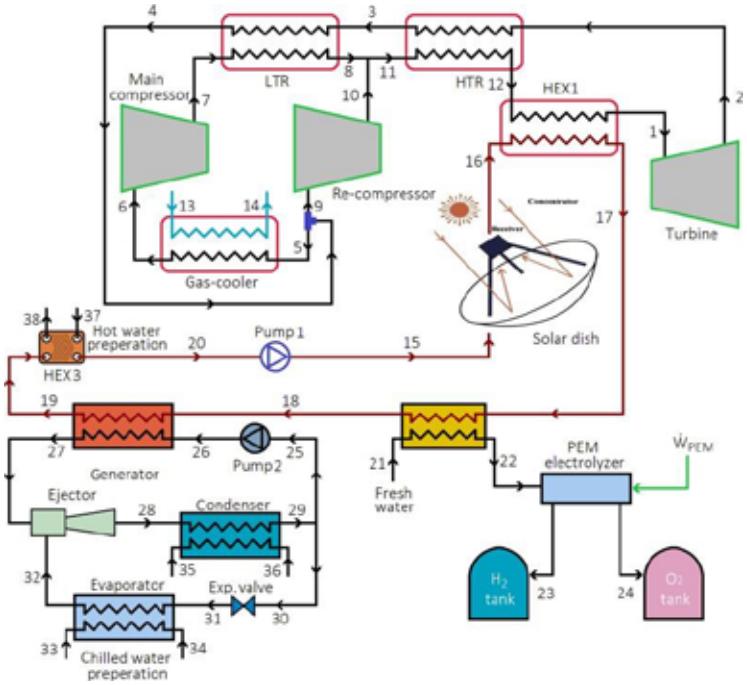


Fig. 1. Schematic diagram of solar dish assisted multigeneration plant with hydrogen generation and ejector cooling cycle

The general mass balance, the general energy- exergy balance equations, and energy-exergy efficiency used for thermodynamic analysis can be written as follows equations ([Çengel, 2015; Bejan, 1996; Dincer, 2013):

$$\sum \dot{m}_{in} = \sum \dot{m}_{out} \quad (1)$$

$$\dot{Q} + \sum \dot{m}_{in} h_{in} = \dot{W} + \sum \dot{m}_{out} h_{out} \quad (2)$$

$$\dot{E}x_Q - \dot{E}x_W = \sum \dot{m}_{out} e_{out} - \sum \dot{m}_{in} e_{in} + \dot{E}x_{dest} \quad (3)$$

$$\dot{E}x_{dest} = T_0 \dot{S}_{gen} \quad (4)$$

In the above equation, $\dot{m}$ is the mass flow rate, the subscripts in and out stand for inlet and outlet, $\dot{Q}$ is the rate of heat, $\dot{W}$ is the rate of work, and h is the specific enthalpy, $\dot{E}x_Q$ and $\dot{E}x_W$ are the energies of heat and work, e is the specific exergy and $\dot{E}x_{dest}$ is exergy destruction.

The amount of hydrogen produced by the electrolyzer can be obtained using the following equation:

$$\dot{m}_{H_2} = \eta_{elec} \, x \, \frac{\dot{W}_{elec}}{HHV_{H_2}} \quad (5)$$

here, η_{elec} is the efficiency of the electrolyzer, $\dot{W}_{elec}$ is the amount of power fed to the electrolyzer and HHV_{H_2} represents the higher heating value of hydrogen.

IV. Results and discussions

The main purpose of this work to assess the energetic and exergetic performances of solar energy-assisted multigeneration plants. For this purpose, The Engineering Equation Solver (EES) packet program is used for thermodynamic and parametric analyses. The influence of solar radiation on the multigeneration system outputs is demonstrated in Fig. 2 and 3. It is evidently seen that the outputs of integrated plants, which are including net power generation, refrigeration, and hot water generation, increase with the rise of solar radiation. In parallel with this rise, the hydrogen generation rate increases by approximately 0.12 kg/h.

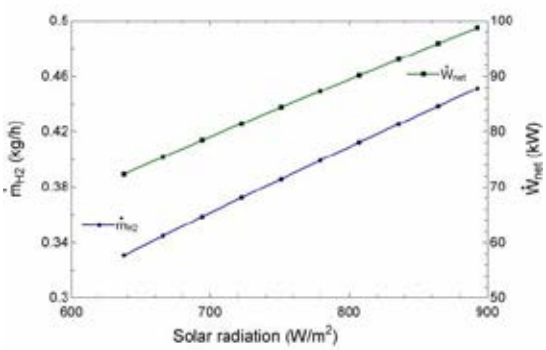


Fig. 2. Variation of multigeneration system net power generation and mass flow rate of hydrogen with respect to solar radiation

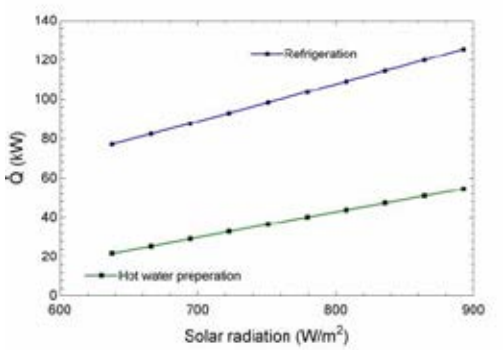


Fig. 3. Variation of multigeneration system refrigeration and hot water production with respect to solar radiation

In addition, another important parameter is that the influence of solar radiation on cycle efficiency because solar energy is the main heat source in this study. Fig. 4 displays the change in energetic and exergetic efficiency of the combined cycle with respect to solar radiation. The energetic and exergetic performance of the multigeneration system increases with the increase of solar irradiation from 600 to 900 W/m^2. The increasing solar irradiation has a constructive effect on the energetic performance of the integrated cycle. Likewise, the reason for the exergetic efficiency increase is that the increase in the power and heat production rates obtained from the multigeneration system. Fig. 5. displays the exergy destruction rates of the components of examined multigeneration system. As seen from the figure, the highest exergy destruction rate is found to be in the solar dish, with almost 70% of the total irreversibility.

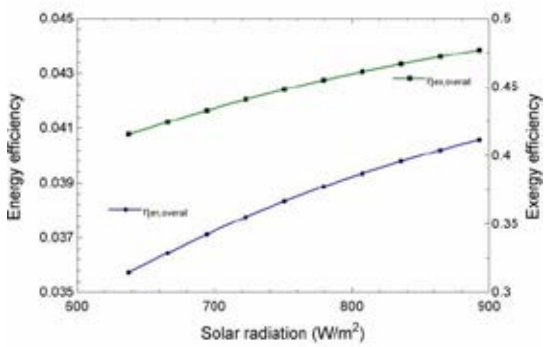


Fig. 4. Variation of energetic and exergetic performance of multigeneration system with respect to solar radiation

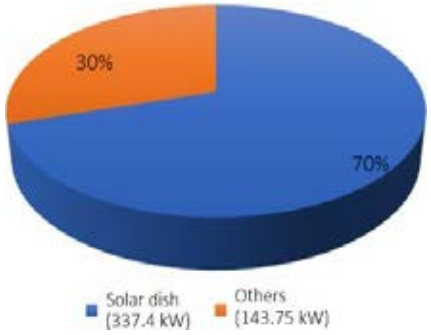


Fig. 5. Exergy destruction rates of the components of multigeneration system

V. Conclusions

In this paper, as an alternative, clean and sustainable solution, a solar-based multigeneration power plant is designed and studied both thermodynamically and parametrically. According to the results of the study, while the net power generation of the system are calculated to be 94.48 kW, the cooling capacity was calculated to be 117.4 kW and hot water capacity was calculated to be 49.1 kW. The hydrogen production and hot water preparation rate are calculated as 0.432 kg/h and 0.31 kg/s. The energy and exergy efficiency of the multigeneration plant is 4.6 % and 47 %, respectively. Also, parametric studies have shown that as solar radiation increases, hydrogen production, net power generation, refrigeration, and hot water preparation increase.

References

Jradi M., Riffat S., Tri-generation systems: Energy policies, prime movers, cooling technologies, configurations and operation strategies, Renewable and Sustainable Energy Reviews, 32, 396–415 (2014).

Kavvadias K.C., Maroulis Z.B., Multi-objective optimization of a trigeneration plant, Energy Policy, 38, 945–954 (2010).
Crespi F., Gavagnin G., Sánchez D., Martínez G.S., Supercritical carbon dioxide cycles for power generation: A review, Applied Energy, 195, 152-183 (2017).

Nami H., Mahmoudi S.M.S., Nemati A., Exergy, economic and environmental impact assessment and optimization of a novel cogeneration system including a gas turbine, a supercritical CO2 and an organic Rankine cycle (GT-HRSG/SCO 2), Applied Thermal Engineering, 110, 1315-1330 (2017).

Wang J.F., Zhao P., Niu X.Q, Dai Y.P., Parametric analysis of a new carbon dioxide transcritical power cycle using a low temperature source, Applied Energy, 94, 58–64 (2012).

Wu C., Wang S.S., Feng X.J., Li J., Energy, exergy and exergoeconomic analyses of a combined supercritical CO2 recompression Brayton/absorption refrigeration cycle, Energy Conversion Management, 148, 360-377 (2017).

Coolant Selection for the Enhanced Cold Start Capability of PEM Fuel Cell

[1*]Alparslan Topcu, [2]Kadir Aydın, [3]Selahattin Çelik, [3]Mikail Yağız
[1] Alanya Alaaddin Keykubat University, Rafet Kayış Faculty of Engineering, Department of Mechanical Engineering, Alanya, Antalya, 07425, Turkey
[2] Çukurova University, Faculty of Engineering, Department of Mechanical Engineering, Sarıçam, Adana, 01330, Turkey
[3] Niğde Ömer Halisdemir University, Faculty of Engineering, Department of Mechanical Engineering, Merkez, Niğde, 51240, Turkey

* E-mail: alparslan.topcu@alanya.edu.tr, kdraydin@gmail.com, scelik@ohu.edu.tr, yagizmikail.1071@gmail.com

Abstract
In this study, different coolant substances which can operate at sub-zero temperatures were evaluated in terms of heating rate to reach enhanced cold-start capability of PEM fuel cell. Water solutions of the ethanol, methanol, and ethylene glycol fluids (80% wt.) were circulated thanks to a closed coolant loop. Tests were performed at -10 °C and a conditioning cabinet was used to achieve this temperature. A pump and a heater were used to drive and heat the coolant, respectively. The heater was warm up the coolant for 20 s while the pump was operated 150 s. At the same time, the single-cell stack was operated at 0.4 V constant voltage, and current drawn during the tests. As a result, the stack properly operated in three coolant circulation, too. Nevertheless, ethanol-assisted circulation was found more successful compared to the methanol and ethylene glycol cycles.

Keywords: PEM fuel cell, cold start, assisted, coolant, optimization.

I. Introduction

A few automakers released their fuel cell vehicle (FCV) models to the market with the commercialization of the PEM fuel cell-powered vehicles (Sankar and Jana, 2018). The cold start issue remains its existence and plays a critical role in the full commercialization of PEM fuel cells (Jiang et al., 2020). Cold start failure is derived from the freezing of the water particles that hindered the reaction areas on the catalyst layer. Therefore, water droplets covered the surface, and the cell cannot generate electricity. Indeed, the understanding of the cold start mechanism is difficult due to the supercooled water existence in the reaction fields. However, the solution is easy although it should be applicable and sustainable. External heat is required to heat the stack and warm-up above zero, immediately. This heat can supply by itself of the stack and an external energy source. Solutions are named as unassisted and assisted based on the self-stack operation and external resource, respectively (Luo and Jiao, 2018). There are a lot of parameters that affect the cold start performance is endured not only characteristics of the stack components but also operating conditions and warm-up style (Zhan et al., 2018). Wu et al., (2020) studied the effect of hydrogen flow arrangement and flow field on the cold start performance, numerically. The numerical results were found to match with the experimental data, and counter-flow geometry generated much less ice than the co-flow pattern. Besides, off-gas recirculation anode (ORA) was pointed out as the best flow arrangement owing to its better start up capability, better output performance, and higher hydrogen utilization. In another similarly structured study performed by Liao et al., (2021), and compared the cold start capabilities of zigzag and straight channel types. They established 3D non-isothermal model with coolant circulation and validated their model with experimental data. They remarked that the zigzag channel at a smaller w/h ratio (more zigzagged structure) was further capacity although slightly less heat was generated. Zang and Hao, (2020) proposed a 1D transient model and investigated four different current density operating modes which were constant, gradually increasing, stepwise increasing, and zigzag modes. They compared the cold start characteristics of the proposed approaches at -30 °C, and gradually and stepwise increasing modes were found better than the constant and zigzag modes.

On the other hand, the coolant heating technique which is an approach to the assisted cold start process provides quick start-up and homogeneous temperature distribution. Wei et al. (2019) investigated the effects of coolant heating strategy parameters which are coolant flow rate, coolant capacity, and ambient temperature, numerically. Similarly, the flow stoichiometry and initial water distribution effects on the cold start performance were studied by Wei et al. (2020). The effects of tank capacity and coolant flow rate parameters were found relatively low (Wei et al., 2020), and it was pointed out that the higher flow rates were supplied a more uniform temperature distribution. However, the effect of the coolant type was never studied in the literature. For this reason, different coolant substances which ethanol, water solutions of the ethanol, methanol, and ethylene glycol were evaluated in terms of heating rate on the cold-start capability for PEM fuel cell. Temperature distribution characteristics were compared under the same operating conditions depends on time.

II. Experimental

The experimental setup was constituted using coolant loop components. A heater was used to heat the coolants, and a pump was operated to deliver coolants to the stack. The circulated coolant turned back to the coolant tank, and therefore a closed coolant cycle was designed. The physical specifications of the coolants used in this study were given in Tab. 1. The melting points of the ethanol and methanol are quite enough to level for the cold start operation except for ethylene glycol (-13 °C), as seen in Tab. 1. On the other hand, the boiling points of the ethanol and methanol coolants are not satisfied the requirements for the operating of PEM fuel cells at normal conditions

(65-75 °C).

Tab. 1: Physical specifications of the substances

Substance	Chemical Composition	Melting Point (°C)	Boiling Point (°C)	Density (kg/m^3)
Ethanol	C_2H_5OH	*-114*	*78*	*0.789*
Methanol	CH_3OH	*-97*	*65*	*0.792*
Ethylene Glycol	$C_2H_6O_2$	*-13*	*197*	*1.11*

On the other hand, these substances can solve in the water, homogeneously, and the water content affects the melting and boiling of the substances. The whole substances were mixed with pure water at 20% (80% coolant – 20% pure water) proportions. 80% rate was selected in order to compare the specifications of the coolants without losing their features. Otherwise, a 50% solution would have been preferred. Each mixture ratio will result in a different profile, naturally. The freezing points of the prepared aqueous solutions of the substances are presented in Tab. 2. It is understood that the aqueous solutions of the substances are satisfied the necessities at normal and cold start operations of the PEMFCs.

Tab. 2: Freezing points of the prepared coolants

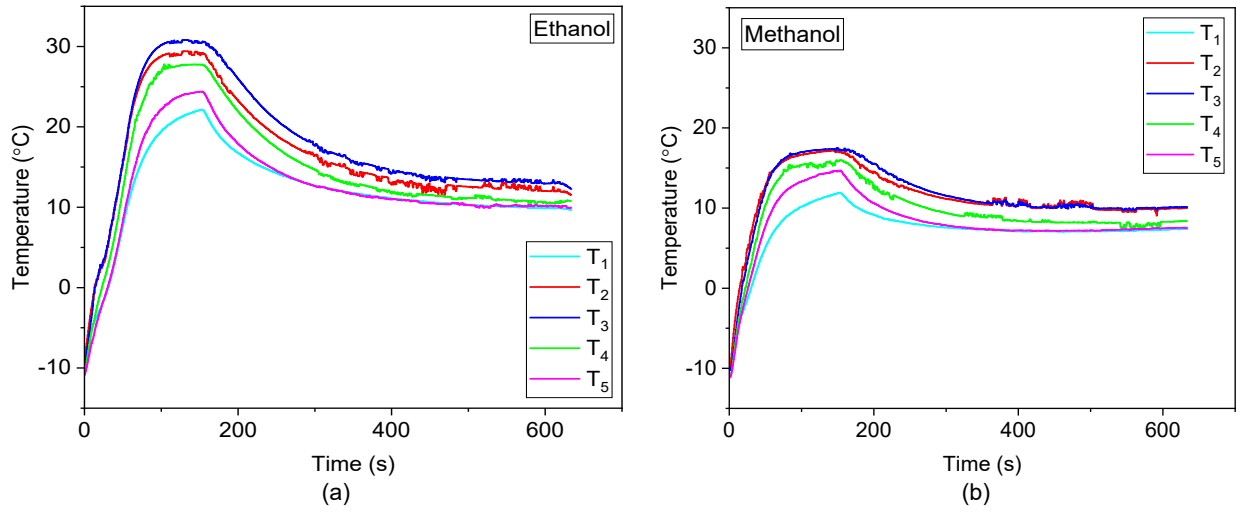
Aqueous Solution (80% Substance – 20% Water)	Freezing Point (°C)
Ethanol	*-70*
Methanol	*-87*
Ethylene Glycol	*-45*

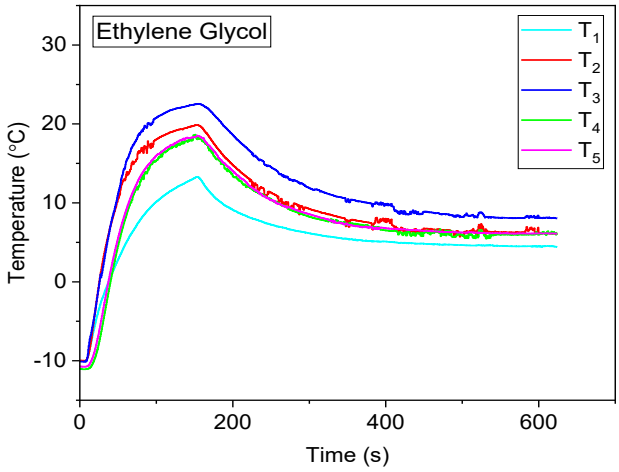
The cold start tests were performed at -10 °C using three different coolants under the same operating conditions. A conditioning cabinet was used to achieve cold start temperatures. The heater and the pump were operated for 20 and 150 seconds, respectively. At the same time, the cell was generated electricity with 0.5 lt/min H_2 and 1.5. lt/min air gases. Thermocouples are placed into the cathode bipolar plate and the time depended temperature was followed during the tests.

III. Results and discussions

Time-temperature graphs of the coolant cycles were illustrated in Fig. 1. The temperature was raised especially at the mid-section of the cell with the effect of the heated coolant circulation as seen in each figure. The warm-up profile continued a while more after the shutdown of the heater (20 s). And, the temperature maintained its position during the pump operation. Then, the temperature gradually decreased after the pump shutdown. Nevertheless, the generated heat by the cell accelerated with time and protected the cell position when the effect of the coolant cycle was decreased. Thus, the cell successfully operated with the help of coolant cycles.

The ethanol cycle was found as the better warm-up cycle as seen Fig.1-a. The temperature rose at 30 °C levels at the mid-section. The cell preserved its status around 15 °C after pump shutdown and temperature stabled. The methanol coolant, on the other hand, has performed a worse temperature increase profile than the ethanol cycle. The temperature raised 17-18 °C grades maximum, and then the generated heat by the cell operation kept the cell temperature at ~10 °C. Nonetheless, the most stable temperature profile was supplied by methanol coolant. The ethylene glycol coolant has performed a performance between ethanol and methanol cycles. Also, temperature differences at the inlet-middle-outlet regions were found higher than the other temperature profiles.





(c)

Fig. 1: Time-temperature graphs of the coolants; a) ethanol, b) methanol, c) ethylene glycol

IV. Conclusions

The specifying of the optimum coolant can accelerate the warm-up profile for the cold start operation. For this purpose, cold start tests were performed with three different coolants (aqueous solutions of the ethanol, methanol, and ethylene glycol at 80% in wt.) under the same conditions to determine optimum coolant that the quickest and homogeneous temperature profile. The ethanol cycle was found to the better warm-up cycle owing to its high warm-up capability. The methanol coolant has performed the worst performance although supply the most stable temperature profile. On the other hand, the rapid warming profile could not be achieved with ethylene glycol at the initial stage of cold start. This situation may be due to the high density of ethylene glycol relative to ethanol and methanol.

Acknowledgments

The authors wish to thank the Office of Scientific Research Projects of Çukurova University for funding this study under Contract No. FDK-2020-12750.

References

Jiang H., Xu L., Struchtrup H., Li J., Gan Q., Xu X., Hu Z., Ouyang M., Modeling of fuel cell cold start and dimension reduction simplification method, Journal of The Electrochemical Society, 167, 044501, (2020).

Liao Z., Wei L., Dafalla A.M., Suo Z., Jiang F., Numerical study of subfreezing temperature cold start of proton exchange membrane fuel cells with zigzag-channeled flow field, International Journal of Mass and Heat Transfer, 165, 120733, (2021).

Luo Y., Jiao K., Cold Start of proton exchange membrane fuel cell, Progress in Energy and Combustion Science, 64, 29-61 (2018).

Sankar K., Jana A.K., Nonlinear multivariable sliding mode control of a reversible PEM fuel cell integrated system, Energy Conversion and Management, 171, 541-565, (2018).

Wei L., Dafalla A.M., Jiang F., Effects of reactants/coolant non-uniform inflow on the cold start performance of PEMFC stack, International Journal of Hydrogen Energy, 45(24), 13469-13482, (2020).

Wei L., Liao Z., Suo Z., Chen X., Jiang F., Numerical study of cold start performance of proton exchange membrane fuel cell with coolant circulation, International Journal of Hydrogen Energy, 44(39), 22160-22172, (2019).

Wu K., Xie X., Wang B., Yang Z., Du Q., Xuan J., Zu B.,, Liu Z., Jiao K., Two-dimensional simulation of cold start processes for proton exchange membrane fuel cell with different hydrogen flow arrangements, International Journal of Hydrogen Energy, 45(30), 17795-17812, (2020).

Zang L., Hao L., Numerical study of the cold-start process of PEM fuel cells with different current density operating modes, Journal of Energy Engineering, 146(6), 04020057, (2020).

Zhan Z., Yuan C., Hu Z., Wang H., Sui P.C., Djilali N., Pan M, Experimental study on different preheating methods for the cold-start of PEMFC stacks, Energy, 162, 1029-1040, (2018).

Machine learning analysis of gas phase photocatalytic CO_2 reduction for hydrogen production

Dilara Saadetnejad[1], Burcu Oral[1], Elif Can[1], Ramazan Yıldırım[1*]
[1]Bogazici University, Department of Chemical Engineering, Istanbul, 34342, Turkey
*E-mail: yildirra@boun.edu.tr

Abstract

In this work, the gas phase photocatalytic CO_2 reduction was analyzed via machine learning, and the results were compared with those obtained in liquid phase process. 549 data points (268 for gas and 281 for liquid phase) were extracted from 80 published papers for this purpose. Simple descriptive statistics was used to analyze the general trends while the random forest was used for predictive models; the decision tree (DT) classification was also used to deduce heuristics rules for higher CO_2 reduction rates. It was found that H_2, CO and CH_4, are the main products in gas phase while CH_3OH production is more dominant in liquid phase. Decision tree analysis showed that the type of co-catalysts is the major factor followed by the semiconductor type in gas phase while the additives for reaction medium, type of semiconductors, and temperature were more deterministic for high gas production in liquid phase.

Keywords: Photocatalytic CO_2 reduction, hydrogen production, machine learning, random forest, decision tree

I. Introduction

The world's energy consumption has been continuously increasing due to the rapid growth of world population and the energy consumption per capita; the rate of global energy demand is estimated to increase to 25–27 TW by 2050 (Severin,2013) Today, most of the world energy supply is coming from non-renewable fossil fuels, which are the main reasons of global warming; about 30.4 Gt of carbon dioxide is annually emitted to the atmosphere (Kohsuke, 2012). CO_2 can be utilized as a raw material, and converted into more valuable chemicals such as hydrogen, methane and methanol (Mirza, 2011). This may help to reduce the net carbon emission to the atmosphere. Since solar radiation provides an almost infinite amount of energy, the CO_2 reduction using solar energy seems to be an excellent solution to control the CO_2 emission. There are two main approaches to reduce CO_2 via solar energy. First, the photovoltaic cells may be used to convert the solar radiation into electricity; then CO_2 is reduced electrochemically on metal electrodes. In the second approach, CO_2 is photocatalytically reduced in the presence of some reductants such as H_2O. This process can be performed in both gas and liquid phases; the gas phase process mainly produces H_2, CO and CH_4 while the liquid process mainly leads to CH_3OH.

In this work, a dataset containing 268 case for gas phase CO2 reduction was analyzed using random forest and decision tree techniques to determine the critical factors on the total gas production rate (mainly H_2, CO and CH_4), and compared with the results of analysis of 281 data points for the liquid phase process.

II. Method

The dataset was constructed from 80 experimental papers, which were published between 1993-2019, available in online sources including Elsevier, Wiley Online Library, American Chemical Society and Royal Society of Chemistry. The dataset contained 549 instances (268 for gas phase and 281 for liquid phase processes); the gas and liquid phase data were analyzed separately due to the differences in the input variables and the products. The data contained information about the semiconductors and co-catalysts characteristics, including preparation methods, and reaction parameters as the input variables. Decision tree algorithm was used for the classification of data based on total gas production rates; the *rpart* (CRAN "rpart", 2021) package in RStudio was used for this purpose. The total gas production rates were divided into three equal sized classes as high (class A), intermediate (class B), and low (class C) production rates for gas and liquid phase systems separately. 5-fold cross validation was applied to determine the best model hyper parameters (complexity parameter and minsplit). Random forest algorithm was applied to predict the total gas production rate; the *randomForest* (CRAN "randomForest", 2021) package in RStudio was used for this purpose. The nodesize and tree number(ntree), as the model hyper parameters, were optimized by 5-fold cross validation; the root mean square error (RMSE) was used in the selection of these parameters.

III. Analysis

Both gas and liquid phase datasets were analyzed by using simple descriptive statistics to determine the product distributions and possible significant descriptors. As an example, the distribution of average production rates of major products (H_2, CH_4, CO and CH_3OH) in the publications covered in the dataset is given in Figure 1.a; the visible light seems to produce mainly syngas (H_2+CO) while H_2 and CH_4 are the major products under UV light irradiation. Although H_2 production is significant in both cases, the results in visible light irradiation is more relevant because the solar irradiation, which is mainly in visible range, has to be the energy source in future when this technology is commercialized. The liquid phase process usually produces CH_3OH as the main product while H_2, CH_4, and CO are also produced. Similar analysis was also performed for the input variables to identify the similarities and differences in preferences and performances of various variables like semiconductor, co-catalyst and dopants between the gas and liquid phases processes as well as the visible and UV irradiation.

IV. Results and Discussion

TiO_2 is the most commonly used semiconductor in both phases; in the gas phase, 130 data points involving TiO_2 were taken under UV light sources while 84 data points were studied under visible light conditions. ZrO_2 is the best semiconductor in gas phase even though it was studied under UV irradiation while $SrTiO_3$ and ZnS also performed better than TiO_2. The visible light performance of ZnO is much better than the other semiconductor regardless of lighting conditions. The most commonly used co-catalysts in the dataset are Cu, CuO, Ag, AgBr, Pt and In_2O_3 while the cases with no co-catalyst is still the highest group in both phases. Au seems to be the best in the gas phase (under UV) while NiO has the highest average performance in liquid phase (under UV). The hydrothermal synthesis is the most commonly employed method (159 data points; 80 for gas, 79 for liquid phase) to prepare semiconductors. It is interesting that commercial materials have the highest production rate under UV light conditions in both phases while the thermal synthesis and the sol-gel seems to be better under the visible light irradiation in liquid phase process. Incipient to wetness seems to be the best choose for the UV tests while the photocatalysts prepared by sol-gel gave much better performance under visible light. The decision tree models resulted in 79 % precision in classification of high production class as shown in Figure 1.b indicating that co-catalyst and semiconductor are the major factors. The overall test accuracies were 0.72 for gas phase and 0.7 for liquid phase models. Random forest gave root means square error of 29.49 for gas phase and 41.99 for liquid phase models.

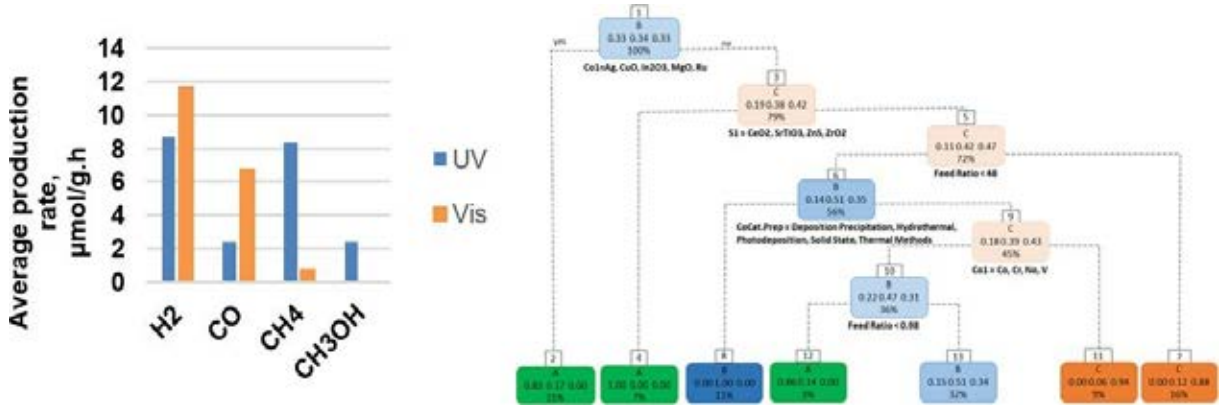


Fig.1 a) Products in gas phase CO_2 reduction, b) Decision tree model for the gas phase CO_2 reduction

V. Conclusions

The production rate of all major products, except hydrogen, are higher in the liquid phase. CH_3OH and CO productions are higher in UV (liquid phase) while higher H_2 (in gas phase) and CH_4 (in liquid phase) are produced under visible light irradiation. TiO_2 (324 instances) is the most common semiconductor as expected. The most commonly used co-catalysts are Cu (96 instances), Ag (40 instances) and Pt (30 instances); Au gives the most efficient result in gas phase (under UV) whereas NiO is better in liquid phase reactions (also under UV). Preparation methods of catalysts are also important for the performance. Decision tree analysis showed that the co-catalysts (Ag, CuO, In_2O_3, MgO or Ru) are the major factor followed by the semiconductor (CeO_2, $SrTiO_3$, ZnS and ZrO_2) determining the total gas production rates in gas phase processes. In the liquid phase, on the other hand, the additive, coupled with semiconductors, and temperature selection seems to be more deterministic for high gas production rates.

References

CRAN, randomForest: Classification and Regression Based on a Forest of Trees Using Random Inputs, https://cran.r-project.org/web/packages/randomForest/randomForest.pdf, (accessed April 2021).

CRAN, rpart: Recursive Partitioning and Regression Trees, https://cran.r-project.org/web/packages/rpart/rpart.pdf, (accessed April 2021).

Kohsuke M., Hiromi Y., and Masakazu A., Photocatalytic reduction of CO2 with H2O on various titanium oxide photocatalysts. RSC Advances, 2, 3165-3172, (2012) https://doi.org/10.1039/C2RA01332K

Mirza C., Christian B., Bernhard R., Wolfgang H., and Fritz K., Transformation of Carbon Dioxide with Homogeneous Transition-Metal Catalysts: A Molecular Solution to a Global Challenge?. Angewandte Chemie International Edition 50, 8510-8537, (2011) https://doi.org/10.1002/anie.201102010

Severin H., Lukas S.M., and Jacek S., Photocatalytic reduction of CO2 on TiO2 and other semiconductors. Angew Chem Int Ed Engl, 52, 7372-408, (2013) https://doi.org/10.1002/anie.201207199

Hydrogen Energy Systems for Underwater Applications

[1, 2*] Berna Sezgin, [3] Yılser Devrim, [1] Tayfur Öztürk, [4] Inci Eroglu
[1]Middle East Technical University, Faculty of Eng., Dept. of Metallurgical and Materials Eng., Çankaya 06800, Ankara, Turkey
[2]Roketsan Missiles Inc., Dept. of Next Generation Propulsion Tech., Elmadağ 06790, Ankara, Turkey
[3]Atılım University, Faculty of Engineering, Dept. of Energy Systems Engineering, İncek 06830, Ankara, Turkey
[4]Middle East Technical University, Faculty of Engineering, Dept. of Chemical Engineering, Çankaya 06800, Ankara, Turkey

* E-mail: berna.sezgin@metu.edu.tr, berna.sezgin@roketsan.com.tr

Abstract
In recent years, the most important development in conventional underwater applications is to use Air Independent Propulsion (AIP) Systems. PEM fuel cell powered AIP systems are getting more interest all over the world since they offer to have many advantages such as longer endurance time without going to the surface for 2-3 weeks or without snorkeling with an average speed, perfectly silent operation, environmentally friendly process, high efficiency and low thermal dissipation under water. PEM fuel cells require a continuous source of hydrogen and oxygen as fuel and oxidant to sustain a chemical reaction to produce electrical energy. Hydrogen storage is the key challenge in terms of quality of supplied hydrogen, system weight and volume. The aim of this study is to compare metal hydride integrated PEM fuel cell with reformed hydrogen integrated PEM fuel cell hydrogen energy systems for underwater applications.

Keywords: Hydrogen energy, PEM fuel cells, AIP, underwater applications

I. Introduction

Usage and development of technology brings out a drastic increase in energy consumption in all areas of life. It is known that today's energy supplies mainly depend on the combustion of fossil fuels, which cannot be continued forever due to depletion of them and environmental concerns. The need for more energy, decrease in available sources and the rise in the awareness of environmental issues attracts many groups in the area of research on alternative energy sources. Hydrogen is one of the alternative energy carriers that can replace fossil fuels. Although hydrogen is not a primary energy source, there are many different hydrogen sources in our planet such as water and hydrocarbons. Fuel cells are the most convenient way to gain energy from hydrogen to produce electricity. Fuel cells are electrochemical devices that converts chemical energy of fuel, hydrogen, into electrical energy directly. The reaction is basically the combustion of hydrogen, which results only with water and heat as products. There are several types of fuel cells such as PEM fuel cells, solid oxide fuel cells, alkaline fuel cells, direct methanol fuel cells and so on. Among various types of fuel cells, PEM fuel cells, also known as proton exchange membrane fuel cells, are the most promising candidate as next generation power sources for many applications, especially for vehicular applications.

PEM fuel cell can be used as power source for many applications since their power range can alter from watts to hundreds of kilowatts. The most common area that PEM fuel cells are preferred is transportation or vehicular applications. There are several reasons of this preference such as short start-up time, simple mechanical design, compactness and robustness, suitable building materials. Automobiles, buses, forklifts, trains, trucks, motorcycles, planes, drones, boats, space shuttles and so on can be clarified as the transportation applications of PEM fuel cells. Among all these applications, underwater vehicles powered with a PEM fuel cell system have gain interest under the umbrella of Air Independent Propulsion (AIP) systems for both civilian and military purposes. The use of unmanned underwater vehicles (UUVs) has become widespread in both civilian and military purposes in recent years. Whereas the civilian purposes of using UUVs are generally exploration/rescue missions, deep ocean exploration, documentary shooting, abutment controlling and cable/pipe laying, the military purposes are intelligence/surveillance, mine diagnosis, weapon carrying, submarine rescue and critical area security. Especially in recent years, academic and industrial studies aim to increase the capability of UUVs to access to smaller areas and extending the duty period by increasing the duration of submersion without putting human life at risk. UUVs are classified into two types; remotely operated underwater vehicles (ROVs) and autonomous underwater vehicles (AUVs), as shown in Fig.1.

For any underwater applications, optimization of hydrogen storage system is very critical since the volume of AIP system have many effects on the vehicle such as ability to move, execute a maneuver and endurance time, while oxygen is generally stored in pressurized tanks in the gas form [2]. Many hydrogen storage technologies are presently being developed to satisfy the requirements of optimization. Types of hydrogen storage techniques are compressed hydrogen storage in the gas form, metal hydride based hydrogen storage in solid form, cryogenic hydrogen storage, chemical hydride based hydrogen storage, reformed hydrogen and so on. However, not all of them can be built and integrated within a UUV because of operational reasons. The aim of this study is to compare compressed hydrogen storage, metal hydride based hydrogen storage and reformed hydrogen storage that are

built already existing underwater applications.

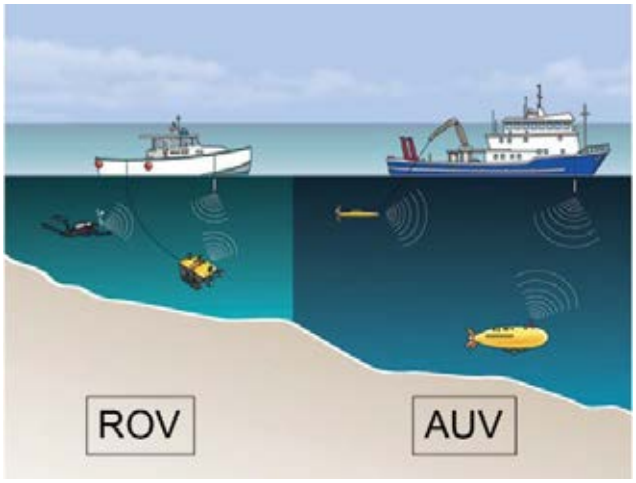


Fig. 1: Schematic representation of ROV and AUV [9]

II. Underwater Vehicle Applications of Hydrogen and PEM Fuel Cell

The main purpose of hydrogen storage for fuel cell powered UUV is to be able to store hydrogen at the highest possible volumetric density. There are two major hydrogen storage techniques exists in building UUV; compressed hydrogen storage in the gas form and metal hydride storage in solid form. Compressed hydrogen storage requires a steel or composite tank with pressure up to 700 bar, commercially. Although this technique has low volumetric density, it offers very low weight. The reason why compressed hydrogen is preferred in a UUV is not the low weight, but the simplicity of processing and low cost. On the other hand, usage of metal hydride based hydrogen storage for UUVs overrides other storage methods in terms of volume advantage. Metal hydrides can store 100 times more hydrogen than compressed hydrogen gas storage tank with the same volume. The only disadvantage of this storage method is heavy weight, meaning that having low gravimetric density which creates no operational problem since underwater vehicles require high amount of bile weight for diving. In addition, the reason why they are preferred in underwater applications is being very safe storage methods due to low operation temperature and pressure.

Tab. 1: Properties of fuel cell powered underwater vehicles [1, 5, 6]

	Vehicle	Power (kW)	Range (km)	Mission (hr)	Hydrogen Storage
Urashima	UUV	4	317	56	Metal Hydride
Urashima 2	UUV	10	3000	600	Metal Hydride
DeepC	UUV	3.6	-	60	Metal Hydride
MUN Explorer	AUV	1.2	80	10	Compressed
IDEF	UUV	1.5	300	24	Compressed
Dragon	UUV	0.1	-	-	Compressed
Seahorse	AUV	0.4	482	72	Compressed

III. Submarine Applications of Hydrogen and PEM Fuel Cell

Pure hydrogen can be stored in metal hydride tanks, compressed tanks or cryogenic tanks. On the other hand, hydrogen can be produced from the reforming of liquid fuels are considered for fuel, and the compressed/liquid oxygen or hydrogen peroxide are considered as oxidant for submarine applications. Compressed hydrogen offers the simplest and least expensive storage solution [7]. However, liquid storage of the hydrogen is more efficient and has the lowest weight and volume. On the other hand, it requires low temperature, high cost and greater system complexity. Generally, submarines with fuel cells are based on hydrogen storage in metal hydride storage cylinders. This technology offers many advantages regarding the special requirements of submarines. The hydrogen stored in hydride form with alloys is heavy, only a limited number of metal hydride storage cylinders can be carried by submarines. This technology is therefore limited to small to medium sized submarines. Liquid fuels have high volumetric and gravimetric energy density and are easy to handle. Ethanol, methanol and diesel are the alternative choices for the liquid fuels [3, 5]. Therefore, liquid fuel reforming technology is developed to obtain hydrogen for the fuel cell powered submarine. The liquid fuel has great influence on the reformer design and also on the whole submarine design and performance. The liquid fuel reforming process applied to submarines must have low acoustic noise level, low magnetic signatures, and high efficiency/low heat transfer to the seawater, easy maintenance and low exhaust gas signature [4].

Tab. 2: Properties of liquid fuel reformer and fuel cell powered submarines [4, 5, 8]

	Fuel	Oxidant	Power (kW)
S-80	Ethanol	Oxygen	300
U-216	Methanol	Oxygen	480
FC2G	Diesel	Oxygen	180

IV. Conclusions

For Unmanned Underwater Vehicles (UUV), including both Remotely Operated Vehicles (ROV) and Autonomous Underwater Vehicles (AUV), compressed hydrogen storage and metal hydride based hydrogen storage is preferably used. It has been showed that for any UUV having a larger power capacity up to 3-10 kW is encapsulated with metal hydride based hydrogen storage tanks because larger power capacities would require larger amounts of hydrogen to store. By applying metal hydride storage, larger amounts of hydrogen can be stored in very small volumes, compared to the volume that compressed hydrogen tank would occupy. Therefore, it makes sense that compressed hydrogen storage technology is favored for UUVs with lower power capacity up to 2-3 kW since the required hydrogen amount to be stored is quite few.

For submarines, as another underwater application, metal hydrides and compressed hydrogen storage are suitable for small to medium size submarines. However, methanol-reforming technology, which provides on-board hydrogen production, combined with PEM fuel cell is decidedly suitable for large-scale submarines as Air Independent Propulsion system. This technology is tested for a long time, and now it is fully submarine-proven system available on the market.

References

1. Albarghot MM, Iqbal MT, Pope K and Rolland L., Dynamic modeling and simulation of the MUN Explorer autonomous underwater vehicle with a fuel cell system, AIMS Electronics and Electrical Engineering, 4(1),114-131, (2019).

2. Baumert R and Epp D., Hydrogen storage for fuel cell powered underwater vehicles, Proceedings of OCEAN ’93, 2, II/166-171, (1993).

3. Han G, Bae M, Cho S and Bae J., Start-up strategy of a diesel reformer using the decomposition heat of hydrogen peroxide for subsea applications, Journal of Power Sources, 448(2020), 227465, (2019).

4. Krummrich S and Llabrés J., Methanol reformer–The next milestone for fuel cell powered submarines, International Journal of Hydrogen Energy, 40, 5482-5486, (2015).

5. McConnell VP., Now, voyager? The increasing marine use of fuel cells, Fuel Cells Bulletin, 5, 12-17, (2010).

6. Mendez A, Leo TJ and Herreros MA., Fuel cell power systems for autonomous underwater vehicles: state of art, Proceedings of 1st International e-Conference of Energies, (2014).

7. Tsourapas V, Sun J and Nickens A., Modeling and dynamics of an autothermal JP5 fuel reformer for marine fuel cell applications, Energy, 33, 300–310, (2008).

8. Retrieved from www.cfc.forces.gc.ca/259/290/405/192/summers.pdf., Accessed on March 11,(2020).

9. Retrieved from www.edgetech.com/product/usbl-broadband-acoustic-tracking-system-bats/, Accessed on March 5, (2020).

A New Off-Grid Autonomous Energy System Structure and Improved Controller

[1*]Süleyman Yıldız, [2]Burak Yıldırım, [3]Mahmut Temel Özdemir,
[1] Mus Alparslan University, Vocational School of Technical Sciences, Electrical and Energy, Mus, 49000, Turkey
[2] Bingol University, Vocational School of Technical Sciences, electronics and automation, Bingol, 12000, Turkey
[3] Firat University, Engineering Faculty, Electrical and Electronics Engineering, Elazig, 23000, Turkey
* E-mail: s.yildiz@alparslan.edu.tr

Abstract

This study provides an approximate model of a microgrid including photovoltaic, biogas, bio-diesel generators, and battery unit consisting of fuel cell with an electrolyzer for load-frequency analysis. In cases where the energy produced from renewable sources exceeds consumption, the excess energy is converted into hydrogen using an electrolyzer and stored. When needed, the stored hydrogen is converted into electrical energy in the fuel cell. Due to the unpredictability of renewable energy supply-demand, a new PI-PD controller was demonstrated and incorporated with an innovative Improved Salp Swarm Algorithm (ISA) for the designed model. Additionally, in order for the controller to effectively perform load frequency control, a double-input interval type-2 fuzzy logic (DIT2-FL) controller was designed to adjust the controller gains specified through optimization. The performance of the proposed cascade DIT2-FL controller (C-DIT2-FLC) was examined with real-world scenarios. The results are comparatively presented and the performance of the control mechanism was demonstrated.

Keywords: Electrolyzer; Fuel cell; Renewable microgrid; Improved salp swarm algorithm, Double-input interval type-2 fuzzy logic controller (DIT2-FLC), C-DIT2-FLC

I. Introduction

Increasing population and industrialization increase the global energy demand day by day. Fulfillment of the increasing energy demand using conventional sources harms the nature. Additionally, many consumers of conventional electrical power systems are removed from production points and the transportation of energy to consumers is both costly and has negative effects on the environment (Özdemir, 2020). Microgrids that can generate sustainable green energy from biodegradable wastes, harvested energy crops, wind and the sun provide great opportunities to overcome these negative effects (Barik and Das, 2018)

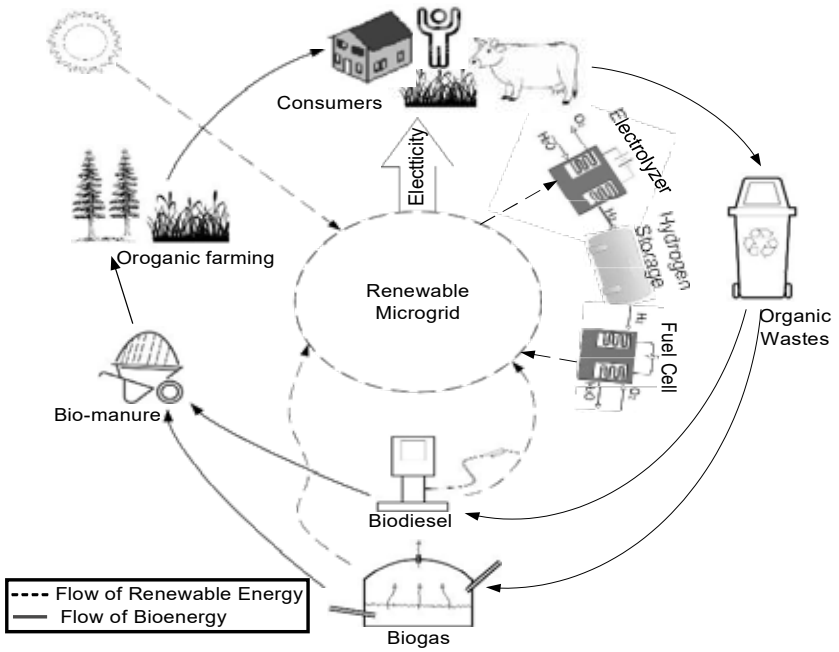


Fig. 1: Conception of proposed microgrid

Renewable energy sources (RESs) such as solar panels and wind turbines are intermittent and relying on weather changes (Yildirim, 2020). For this reason, diesel engine generators (DEG) are widely used in renewable isolated microgrids to sustain energy continuity (El-Fergany and El-Hameed, 2017). Diesel fuel pollutes the atmosphere and emits toxic emissions. Energy consistency must be built with alternative, green methods (Singh et al., 2021). As a consequence, we need eco-friendly renewable alternatives such as bioenergy. It will also be very beneficial to convert excess energy into hydrogen in cases where energy production in microgrids exceeds consumption, and into electrical energy in the fuel cell operating as a backup generator in cases where RESs are unable to meet energy demand.

In the present study, a microgrid that generates energy from biogas generators, biodiesel generators and solar

panels, converts excess energy into hydrogen using an electrolyzer and stores it, and converts the stored hydrogen into electrical energy when needed was modelled. Figure 1 shows the microgrid designed.

The present study proposes a strong control strategy for load frequency control in the microgrid. For this purpose, a cascade double-input interval type-2 fuzzy logic PI-PD (C-DIT2-FLC) controller was developed for LFC control in the microgrid. The gains of the controller were determined using the Improved Salp Swarm Algorithm (ISSA), a new optimization algorithm. Some important features of the present study can be listed as follows.

- A fuzzy-based C-DIT2-FLC controller design is presented as the central control to perform LFC in the sustainable green energy based MG.
- Real solar data were used rather than constant power changes in the PV system.

II. Experimental Set-up and Procedure

A microgrid structure aiming the optimal use of the renewable sources of the off-grid area was proposed. Figure 2 shows the LFC model of the microgrid containing a biogas turbine generator (BGTG), biodiesel engine generator (BDEG), photovoltaic (PV), fuel cell (FC) and electrolyzer system (ES).

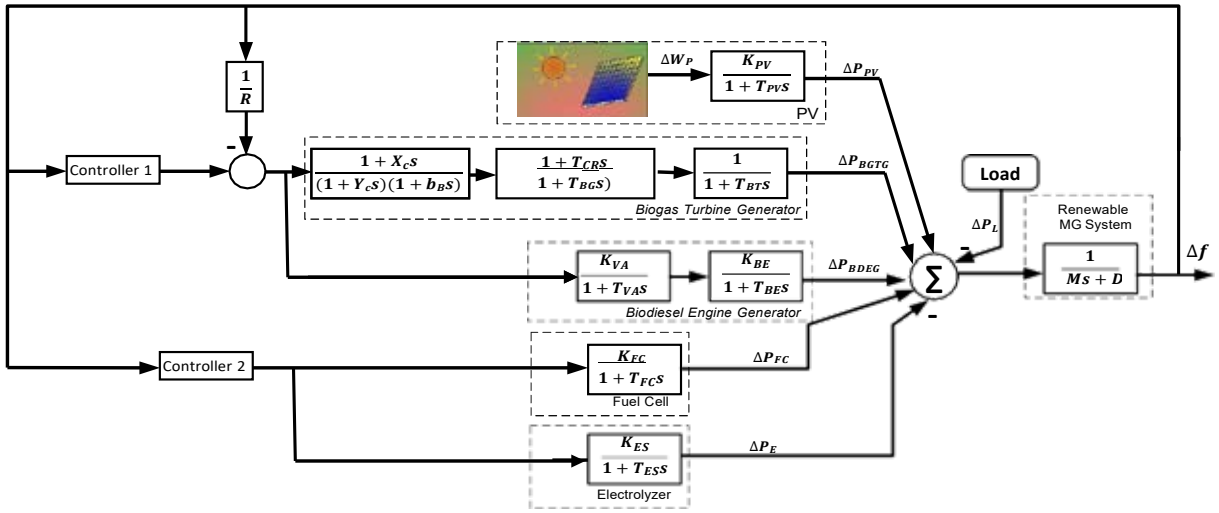


Fig. 2: Renewable MG's LFC model

Table 1 shows the parameters of the microgrid modeled in MATLAB/Simulink.

Tab. 1: MG System's Parameters

Parameters	Values	Parameters	Values	Parameters	Values
K_{PV}, T_{PV}	*1, 1.8 s*	K_{VA}, T_{VA}, K_{BE}, T_{BE}	*1,0.05s, 1, 0.5s*	K_{ES}, T_{ES}	*0.002, 0.5s*
X_c, Y_c, b_B, T_{CR}, T_{BG}, T_{BT}	*0.6,1s, 0.01s, 0.23s, 0.2s*	K_{FC}, T_{FC}	*0.01, 4.0s*	**M, D, R**	*0.2s, 0.012, 2.4*

A PI-PD cascade controller was designed to eliminate the frequency deviations in the microgrid. The gains of the controller are determined using ISSA. Gains of the PI controller are adjusted for the best response of the microgrid's LFC using DIT2-FL. Figure 3 shows the structure of the proposed C-DIT2-FLC.

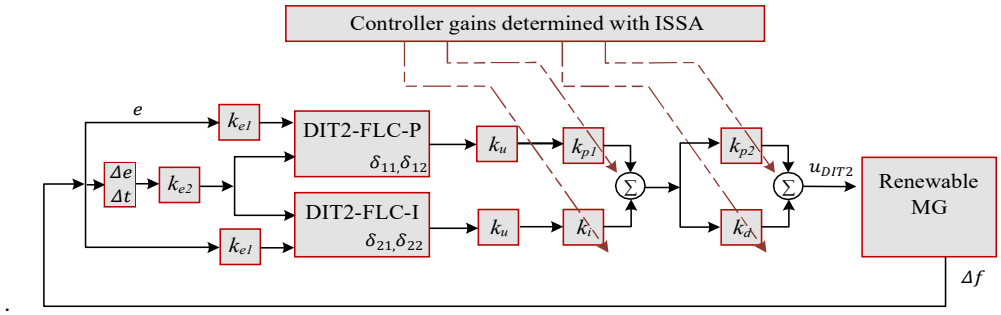


Fig. 3: The schematic diagram of the C-DIT2-FLC

III. Analysis

Simulation studies were carried out in MATLAB/Simulink. Figure 4 shows the real solar radiation data and the load change scenario.

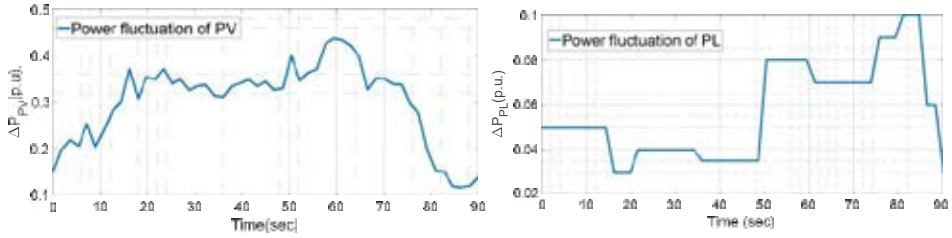


Fig. 4: Power variations of PV and load

Table 2 shows the controller gains determined with ISSA.

Tab. 2: Controller gains

	Controller 1				Controller 2			
Gain	k_{p1}	k_i	k_{p2}	k_d	k_{p1}	k_i	k_{p2}	k_d
Value	*0.843*	*2.043*	*-4.690*	*-2.104*	*-2.513*	*0.517*	*1.861*	*-1.299*

IV. Results and discussions

Figure 5 shows the frequency response of the microgrid under solar radiation and load change conditions. The performance of the controlled proposed in Figure 5 was compared with the performances of the Fuzzy Type1-FLC and Classic PI-PD cascade controllers. The results clearly show the success of the C-DIT2-FLC controlled in the LFC of the microgrid.

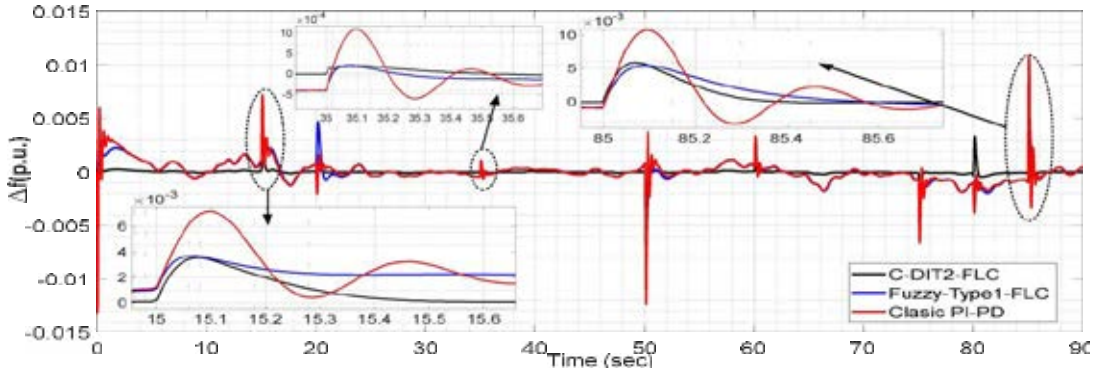


Fig. 5: Frequency responses of the renewable microgrid

V. Conclusions

Hydrogen energy provides great convenience in overcoming the problems in the integration of renewable sources into the grid. In the present study, a microgrid containing a solar panel, biogas generator and biodiesel generator was modeled. The system was estimated to convert excess energy into hydrogen through an electrolyzer and use the stored hydrogen in the fuel cell operating as the backup generator unit. A new C-DIT2-FLC controller was designed to perform the frequency control of the microgrid. First, gains of the controller were determined with ISSA. Afterwards, controller gains were adjusted to obtain the best frequency response of the microgrid using DIT2-FL. The present study offers a unique approach to the LFC problems of renewable microgrids. Despite the extremely variable structure of renewable energy sources, the controller proposed successfully performed the load-frequency control of the microgrid.

References

Özdemir M. T., The effects of the FOPI controller and time delay on stability region of the fuel cell microgrid, Int. J. Hydrogen Energy, 45, 35064-35072, (2020).

Barik A., Das D., Expeditious frequency control of solar photovoltaic/biogas/biodiesel generator based isolated renewable microgrid using grasshopper optimisation algorithm, IET Renewable Power Generation, 12, 1659-1667, (2018).

Yildirim, B., Advanced controller design based on gain and phase margin for microgrid containing PV/WTG/Fuel cell/Electrolyzer/BESS, International Journal of Hydrogen Energy, (2020).

El-Fergany, A.A., El-Hameed, M.A., Efficient frequency controllers for autonomous two-area hybrid microgrid system using social-spider optimiser, IET Generation, Transmission & Distribution, 11, 637–648, (2017).

Singh K., Gope S., Pradhan N., Firefly Algorithm-Based Optimized Controller for Frequency Control of an Autonomous Multi-Microgrid, Advances in Intelligent Systems and Computing, 437-451, (2021).

New and Future Approach Technologies on Hydrogen Fuel Cell Applications with Marine Vehicles

[1*]Meryem Gizem Sürer, [2]Hüseyin Turan Arat
[1]Iskenderun Technical University, Faculty of Engineering and Natural Sciences, Mechanical Engineering, Central Campus, Hatay, 31200, Turkey
[2]Iskenderun Technical University, Faculty of Engineering and Natural Sciences, Mechatronics Engineering, Central Campus, Hatay, 31200, Turkey

* E-mail: hturan.arat@iste.edu.tr

Abstract
With the increasing population and demands, Maritime industry has led renewable energy sources for the more green environment. Hydrogen is one of the most popular of these renewable energy sources and one of the most researched worldwide. The aim of this study is to give a brief overview of the production and storage methods of hydrogen, which is seen as an important potential in maritime transport for a cleaner environment, its usage in marine vehicle's propulsion system and its development history and future perspective.

Keywords: Hydrogen, Marine Vehicles, Greenhouse Gas

I. Introduction

Maritime transport has a huge share in world trade due to the fact that it is less costly than other transportation methods. The increase in this share with the increasing population has brought many disadvantages. One of these disadvantages is the carbon emission, which has become more important with the increasing environmental sensitivity. It is expected that greenhouse gases generated by maritime transport, which is responsible for approximately 2.8% of annual greenhouse gas emissions in 2015, will increase by 50-250% by 2050 (IMO, 2018;IRENA,2020). The aim of this study is to give a brief overview of the current perspective and future perspective of hydrogen usage on marine vehicles.

II. Hydrogen Production and Storage Methods

Hydrogen Production: Although hydrogen can be produced with many energy sources, IRENA (International Renewable Energy Agency) uses a common color code terminology. Today, 95% of hydrogen production is obtained from fossil fuels (IRENA,2020). In Table 1, you can see hydrogen production methods according to this color code terminology. Additionally, Figure 1 shows the inputs and outputs of common production methods to produce 1.1 tonnes of hydrogen.

Tab. 1: Hydrogen production methods according to common color code terminology [Gathered from (IRENA,2020)].

Color	Process	Source	Explanation
Grey Hydrogen	SMR(steam methane reforming) or gasification	Methane or coal	* The use of gray hydrogen produced from fossil fuels releases CO2 and does not give hope for the future. * SMR is currently the cheapest industrial hydrogen source.
Blue Hydrogen	SMR or gasification with carbon capture (85-95%)	Methane or coal	*The only difference from gray hydrogen is the use of carbon capture and storage [CCS] system in its production. * It has additional costs for CO2 transportation and storage. * The CCS system means that 5-15% of the CO2 is still emitted. * It is seen as a short-term transition.
Turquoise Hydrogen	Pyrolysis	Methane	* The carbon in methane turns into solid carbon. * Solid Carbon can be stored more easily than gaseous CO2. * Currently, turquoise hydrogen is still in pilot phase.
Green Hydrogen	Electrolysis	Renewable electricity	* Green hydrogen produces from renewable energy resources. * The most common method is water electrolysis.

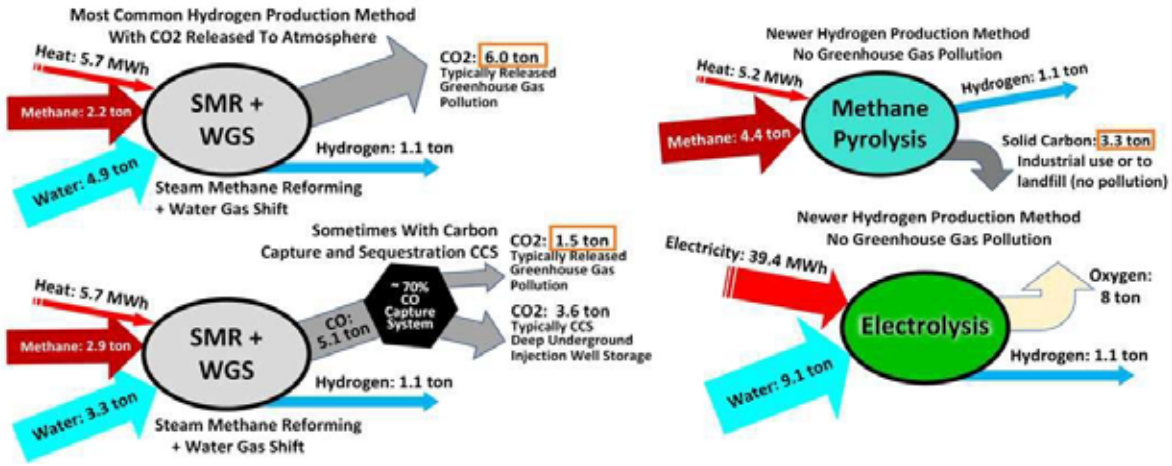


Fig. 1: The inputs and outputs of common production methods to produce 1.1 tonnes of hydrogen[Vikipedia,2021]

Hydrogen Storage: The most common storage methods used in marine vehicles research are compressed H_2 storage and liquid H_2 storage. Though other methods needs more technology level, all methods have problems to be solved . One of the most important of these problems is the low volumetric energy density of hydrogen. You can find the advantages and disadvantages of these two common methods in the table 2 below.

Tab. 2: Advantages and disadvantages of gasous and liquid hydrogen storage [Gathered from ()].

Storage Method	Advantages (Other methods)	Disadvantages(Other methods)
Compressed H2 Storage	*more simpler *more economical *more efficient	*Although the pressure increase has a positive effect on increasing density, very high pressures make it difficult to refuel. *The most important problem is weight.(due to having low volumetric energy density)
Liquid H2 Storage	*High liquid density (Nearly two times the density of hydrogen gas) *Because of having much lighter and smaller as volume, the weight problem has improved.	* It requires special storage techniques. Because liquid hydrogen is stored at 21 K. * Fuel system components is more (such as liquid fuel pumps, fuel lines, heat exchangers etc..) *Hydrogen loses due to boil off.

III. Usage and Development of Fuel Cell Applications in Marine Vehicles

Fuel cell systems have been used for many years in the main propulsion power and APU applications in maritime transportation. Using hydrogen as a fuel, the PEM fuel cell has been popular in aircraft and cars as well as in marine vehicle project. Features such as having relatively mature technology, partly less cost, ability to operate at low temperatures, rapid response to load changes, and partially higher power density have made PEM ahead of other fuel cells. The major disadvantage of PEMFC technology is that it is sensitive to impurities in hydrogen and requires a complex water management system (both gas and liquid).(Sürer and Arat,2020) An example fuel cell propulsion system for the ship is given in figure 2(Yuan,2014). The system consists fuel cell stacks, reactants control unit, inverter, necessary power/electricity supply components and etc.

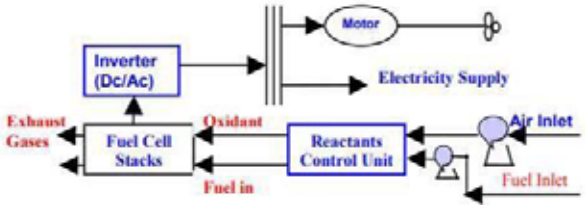


Fig. 2. Schematic setup of fuel cell system for a ship. (Yuan,2014)

Tab. 2: Examples of the development of fuel cell based marine vehicles in historical order. [Gathered from (Tronstad et all ,2017)].

Prototype	Project Name/Partners	Year	Fuel Cell Type/ Fuel	Capacity	Explanatory
	Nemo H2/Rederij Lovers etc	2012- present	PEMFC/ hydrogen	60 kW	*Hydrogen storage in 8 cylinders at 350 bar *Hybrid system of PEM fuel cell and batteries on a passenger vessel
	SF-BREEZE/Sandia National Lab., Red and White Fleet	2015 - present	PEMFC/ Liquid hydrogen	120 kW per Modul. Total power 2.5MW	* The project aims to design a 150 passenger high-speed hydrogen fuel cell passenger ferry using a PEMFC and L H2.
	ZemShip - Alsterwasser – Elektra/Proton Motors, GL, Alster Touristik GmbH, Linde Group etc.	2006-2013	PEMFC/ hydrogen	96 kW	*Two PEM A 50 maritime fuel cell systems (48 Kw peak power each) and seven lead gel battery pack with a total capacity of 560V and 360Ah delivered by Proton Motor. *compressed hydrogen in twelve 350-bar pressure tanks

	**Hornblower Hybrid / Hornblower**	2012- present	PEMFC/ hydrogen	32 KW	* 600 passenger ferry *Hybrid ferry with diesel generator, batteries, PV, wind and fuel cell * 32 kW, combined with diesel, wind, solar and batteries
	**Cobalt 233 Zet/Zebotec, Brunnert-Grimm**	2007 - present	PEMFC/ hydrogen	50 kW	* Sports boat employing hybrid propulsion system using batteries for peak power * 24 Kw Fuel cell
	**Hydrogenesis**	2012 - present	PEMFC/ hydrogen	12 kW	* 12 passenger ferry * 11 m long

IV. Future Perspect

There are some actions that need to be taken for hydrogen applications to become more common in the future.These are:

- Costs should be reduced by developing methods of production technology from renewable energy.
- All storage methods have their own disadvantages. The problems experienced, especially due to the low volumetric density of hydrogen, should be solved with developing technology.
- To improve the understanding of green hydrogen, a green hydrogen market must be created. Policies should be prepared to accelerate this development.

V. Conclusions

Hydrogen is currently one of the best choice that can provide a solution against global warming. In the hydrogen economy, the production of low-cost hydrogen using renewable energy sources plays an important role. However, due to the high production costs of hydrogen today, it can be said that it has not reached the mature technological level that can literally replace fossil fuels. Therefore, studies on this subject must be increased and it should be aimed to reach technological maturity as soon as possible.

References

Efcan, V., & Gürgen, E. Gemilerin Sevk/Tahrik Sistemlerinde Kullanilebilecek Alternatif Enerji Kaynakları ve Güncel Yaklaşımlar. *8. Ulusal Lojistik Ve Tedarik Zinciri Kongresi* , 25.(2019)

Hydrogen Production, Vikipedia, [Last Access: https://en.wikipedia.org/wiki/Hydrogen_production].

IMO(International Maritime Organization), Note by the International Maritime Organization to the UNFCCC Talanoa Dialogue, (2018) [Last Acces: 10.04.2021: https://unfccc.int/sites/default/files/resource/250_IMO%20submission_Talanoa%20Dialogue_April%202018.pdf]

International Renewable Energy Agency (IRENA) , Green Hydrogen A guide to policy making, (2020)

Lim, Chee Kuan, et al. "High-temperature electrolysis of synthetic seawater using solid oxide electrolyzer cells." *Journal of Power Sources* 342 (2017): 79-87.

Sürer, Meryem Gizem, and Hüseyin Turan Arat. "State of art of hydrogen usage as a fuel on aviation." *European Mechanical Science* 2.1 (2018): 20-30.

Tronstad, Tomas, et al. "Study on the use of fuel cells in shipping." *European Maritime Safety Agency* (2017).

Ship Technology, Hydrogenesis Passenger Ferry, [Last Acces: https://www.ship-technology.com/projects/hydrogenesis-passenger-ferry/)

Yuan, Jinliang, et al. "Marine applications of fuel cell technology." *International Conference on Fuel Cell Science, Engineering and Technology*. Vol. 41650. (2004).

A novel chaos embedded particle swarm optimization based on stability boundary locus for delayed fuel cell microgrid with PI controller

Vedat Çelik [1] Mahmut Temel Özdemir [2]
[1,2] Firat University, Faculty of Engineering, Department of Electrical and Electronics Engineering, Elazig, 23119, Turkey

* E-mail: celik@firat.edu.tr, mto@firat.edu.tr

Abstract
In this paper, a new approach is proposed for load frequency control (LFC) optimization in the off-grid mode of the delayed fuel cell microgrid with PI controller system. For this purpose, a new approach which is chaos embedded particle swarm optimization (CEPSO) based on stability boundary locus (SBL) is proposed. In the proposed optimization, the search is performed only among the PI control parameters that would keep the system stable. Therefore, both the stability of the system is guaranteed by SBL and the PI controller parameter optimization in the stable region is carred out. In addition, optimization results are obtained with classical CEPSO. When the obtained results are compared, the superiority of the proposed method in terms of iteration history, fitness value and time response of the system is revealed.
Keywords: Fuel cell microgrid, Renewable energy, Chos embedded particle swarm optimization, PI controller Stability boundary locus.

I. Introduction

The use of renewable energy sources in microgrids has become a popular topic recently. Microgrids consist of different types of sources such as micro sources, micro turbines, wind turbines, PV solar panels and fuel cells. Microgrids can be used on-grid or off-grid mode. However, the realization of load frequency control (LFC) of microgrids is a more important issue in off-grid mode. Because the energy generation units, which are wind and solar energy of microgrids, cannot meet the desired demand instantly and demand changes constantly, the stability of off-grid systems inculdes uncertainty. In other words, these systems cannot guarantee their users necessary and sufficient power when wind and solar energy are insufficient. The elimination of the mentioned problem can be achieved by realizing the LFC of the system. One of the methods used to provide LFC in off-grid mode is to add hydrogen fuel cell to the system. There are also delays caused by communication in this control system, and design of controllers should be made by considering this time delay. These microgrids are called delayed fuel cell microgrids. One of the most important purposes in control systems is to keep stable the system. Another of the most important purposes in control systems is to achieve a controller design to provide the desired output. There are many metaheuristic optimizations proposed for this aim. In (Özdemir, 2021), a new approach is proposed for controller design that provides an AVR system to operate at the desired performance using particle swarm optimization (PSO). In the mentioned study, the parameter space of the PI controller that keeps the system stable is obtained by using stability boundary locus (SBL) and the search with PSO is carried out in the stable region. Thus, the obtained control parameters ensure the stability of the system in any case, shorten the optimization time and provide a better system response.
In this study, it is aimed to optimize the LFC of the delayed fuel cell microgrid system with a new approach using PI controller that is widely used in the industry for the first time in the literature. For this purpose, optimization is performed using chaos embedded particle swarm optimization (CEPSO), which is more efficient than PSO in the stable PI controller parameter space obtained with SBL. In addition, a search is performed with classical CEPSO and compared with the proposed method in terms of iteration history, fitness value and time response. Thus, the superiority of the proposed method in terms of iteration history, fitness value and time response is shown.

II. Delayed Fuel Cell Microgrid with PI Controller

Off-grid delayed fuel cell microgrid with PI controller for LFC is illustrated in Figure 1.

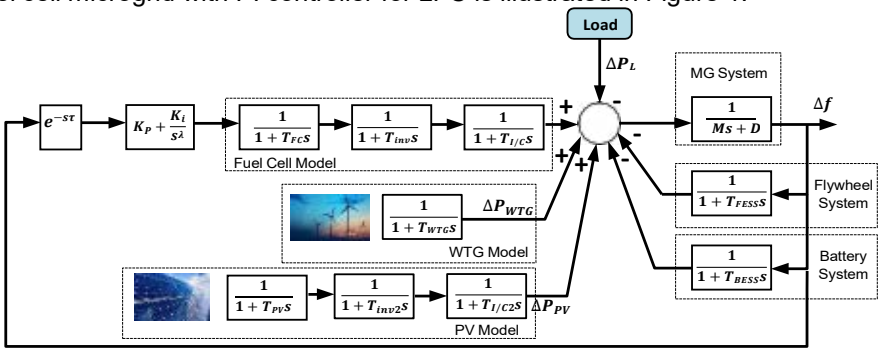


Fig. 1: Delayed Fuel Cell Microgrid Model with PI controller

The system consists of fuel cell (FC) which is main power plant, wind turbine generator (*WTG*), photovoltaic (*PV*), battery energy storage system (*BESS*) and flywheel energy storage system (*FESS*). *FOPI* controller controls the *FC* according to the load changes in the system and power changes generated by *WTG* and *PV* systems.

III. A novel chaos embedded particle swarm optimization based on stability boundary locus

CEPSO is propsed to increase the success level of the PSO algorithm (Alatas, et al.). The weights values in the speed function are taken from chaotic maps. Therefore, it improves global search capability of the algorithm by escaping local solutions. In the proposed new optimization approach, CEPSO will be performed in the stable parameter space obtained for the system with PI controller. Thus, it will be possible to search for controller parameters that would keep the system stable. For this case, the pseudocode of the proposed optimization approach would be as follows:

1. **Start**
2. ***Calculate the stability boundary locus and set the boundaries of the search space***
3. ***Randomly initialize pozition within the stable region*** and velocity of Particles: X_i (0) and V_i (0)
4. **while** terminating condition is not reached do
5. **for** *i* = 1 to *number of particles* **do**
6. Calculate the fitness value *f(ITSE/IAE/ISE/ITSE etc.)*
7. Update personal best and global best of each particle
8. Velocity update: $\boldsymbol{V(t+1)= CM1 \times V(t) + c_1 \times CM2 \times (X_{pbest} - X(t)) + c_2 \times CM3 \times (X_{gbest} - X(t))}$
9. Position update: $\boldsymbol{X (t+1) = X(t) + V(t+1)}$
10. ***If K_{system}, τ_{system} 0 (there is a change in the system parameters)***
11. ***Calculate the $I(\omega, K_p, K_i)$ and set the boundaries of the search space***
12. ***end if***
13. ***If X_i $I(\omega, K_p, K_i)$ (the particle is outside the stable region)***
14. ***move to position into the stable region and update the position and velocity***
15. ***end if***
16. **end for**
17. **end while**
18. **Stop**

IV. Results and discussions

The parameters of the off-grid delayed fuel cell microgrid with PI controller system are considered as given in (Özdemir, 2020) for the application. The stable PI controller parameter space change depending on the time delay of the system for these system parameters. The stable region is obtained with SBL as in Figure 2 for different time delays.

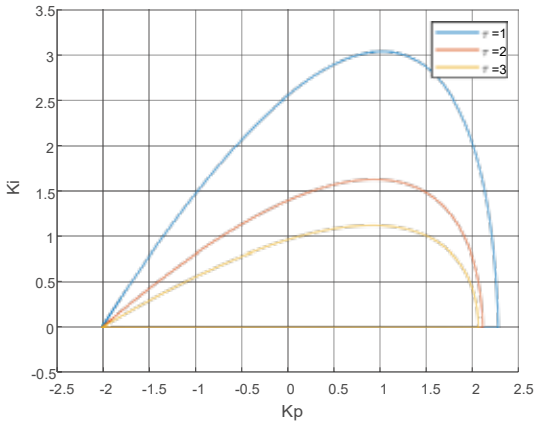
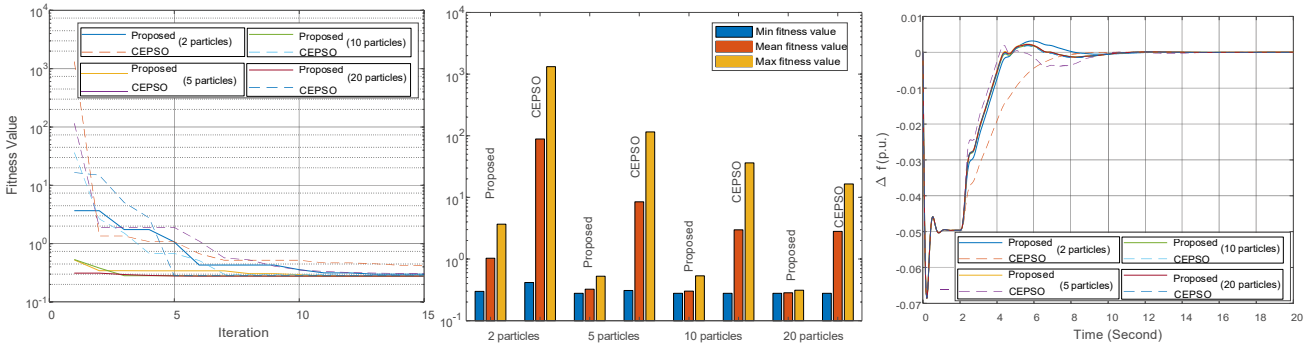


Fig.2: Stable regions obtained for different time delays

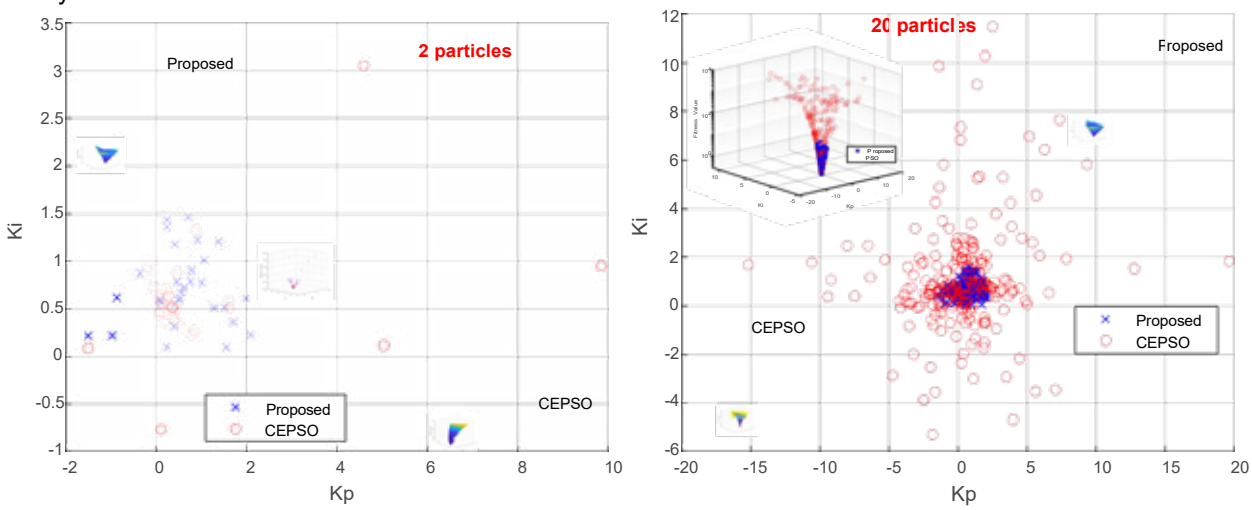


a) Iteration histories b) min, mean and max of Iteration histories c)Time responses

Fig. 3: Obtained optimization results with proposed CEPSO and classical CEPSO

In this study, where a PI controller is designed by optimizing the controller parameter, the time delay is considered as τ = 2 s. Some optimization results of the application are given in Figures 3 and 4.

For 2, 5, 10 and 20 particles, the iteration history, their minimum, maximum and average values and, the time responses of the system according to the optimized controller gains of the proposed and classical CEPSO optimizations are shown in Figures 3.a, 3.b and, 3.c respectively. Considering the changes in global best value (lowest fitness value in iteration) in the optimizations, the proposed approach finds the lowest cost value under all conditions. The proposed approach under the same conditions is shown a superior performance compared to classical CEPSO for its low, average and maximum values. This result can also be seen from the time responses of the system.



a) For 2 particles b) For 20 particles

Fig. 4: Positions of particles in solution space

The effect of the number of particles in optimizations is shown in Figure 4 for the proposed and classical CEPSO. Figure 4.a shows two and three-dimensional positions of particles in the solution space for 2 particles. Figure 4.b also shows two and three-dimensional positions of particles in the solution space for 20 particles. 3D graphics are included in the figures to show the exact positions of the particles. According to the results obtained in Figure 4, the increase in the number of particles does not affect the performance of the proposed approach much. However, it is significantly to increase the performance of the classic CEPSO. A large number of particles means an increase in the total processing time, which is not preferred. It is also seen from the results that the proposed approach reduces the processing time.

V. Conclusions

In this study, a new optimization approach is proposed for the first time in the literature to find the best performance of the delayed fuel cell microgrid system. PI controller is used for control and stable PI controller parameter space is obtained for different time delay values with SBL for optimization. The controller is designed for different numbers of particles with the proposed approach and classical CEPSO. As a result, the important results obtained in this study for the proposed approach are as follows:

- ✓ The system is guaranteed to remain stable for all time delays and controller parameters,
- ✓ The best performance that satisfies the stability condition is found,
- ✓ Fewer particles and less iterations advantage is provided, which means shorter processing time.

The above results show that the proposed approach for the delayed fuel cell migrogrid system achieves high performance results with fewer processes and provides a PI controller design that will keep the system stable. Thus, real-time optimizations can be performed for the delayed fuel cell migrogrid system.

References

Dong C., Gao Q., Xiao Q., Yu X., Pekař L., Jia H., Time-delay stability switching boundary determination for DC microgrid clusters with the distributed control framework. Appl. Energy. 228, 189–204 (2018). https://doi.org/10.1016/j.apenergy.2018.06.026.
Hatziargyriou N., Asano H., Iravani R., Marnay C., Microgrids, (2007). https://doi.org/10.1109/MPAE.2007.376583.
Khalil A., Rajab Z., Alfergani A., Mohamed O., The impact of the time delay on the load frequency control system in microgrid with plug-in-electric vehicles. Sustain. Cities Soc. 35, 365–377 (2017). https://doi.org/10.1016/j.scs.2017.08.012.
Li X., Song Y.-J., Han S.-B., Frequency control in micro-grid power system combined with electrolyzer system and fuzzy PI controller. J. Power Sources. 180, 468–475 (2008). https://doi.org/10.1016/j.jpowsour.2008.01.092.
Özdemir M.T., Öztürk D., Eke İ., Çelik V., Lee K.Y., Tuning of Optimal Classical and Fractional Order PID Parameters forAutomatic Generation Control Based on the Bacterial Swarm Optimization. IFAC-PapersOnLine. 48, 501–506 (2015).
Veronica A.J., Kumar N.S., Internal Model Based Load Frequency Controller Design for Hybrid Microgrid System. Energy Procedia. 117, 1032–1039 (2017). https://doi.org/10.1016/j.egypro.2017.05.225 .
Ozdemir, M.T., (2020). The effects of the FOPI controller and time delay on stability region of the fuel cell microgrid, International Journal of Hydrogen Energy, https://doi.org/10.1016/j.ijhydene.2020.05.211
Ozdemir, M.T., (2021). A novel optimum PI controller design based on stability boundary locus supported particle swarm optimization in AVR system, Turk J Elec Eng & Comp Sci 29 (1), 291-309 doi:10.3906/elk-1910-81
Alatas B., Akin E., Ozer A.B., (2009). Chaos embedded particle swarm optimization algorithms. Chaos, Solitons Fractals, 40: 1715-1734.

Energy, Exergy and Economic Analyses and Multiobjective Optimization of a Novel Solar Multigeneration System for Production of Green Hydrogen and Other Utilities

[1*]Mert Colakoglu, [1]Ahmet Durmayaz
[1]Istanbul Technical University, Energy Institute, Maslak, Istanbul, 34469, Turkey

*E-mail: mertcolakoglu@gmail.com , durmayaz@itu.edu.tr

Abstract
A novel solar-based triple power cycle driven multigeneration plant is developed for the production of green hydrogen as the main product. Solar tower-based open Brayton cycle (BC) with intercooling, regeneration and reheat (IRR) is coupled with a regenerative Rankine cycle (RRC) and a Kalina cycle-11 (KC11) as a novel triple power cycle. Significant portion of the produced electricity is utilized in an electrolyzer (EL) to produce green hydrogen. A single-effect absorption refrigeration cycle (SEARC) and two domestic hot water heaters (DHWHs) are also integrated to the plant to produce green hydrogen, power, cooling and domestic hot water. A thermal energy storage system (TES) and two auxiliary external combustion chambers (ECC) are incorporated into the BC to ensure continuous operation. System performance is investigated with energy, exergy and economic analyses. A rigorous parametric analysis is conducted. Multiobjective (MO) optimization is carried out to determine the optimum design point of the system.

Keywords: Green hydrogen production, solar energy, multiobjective optimization, multigeneration, energy analysis, exergy analysis, economic analysis

I. Introduction
Multigeneration (MG) systems have become an important research topic due to their superiority over conventional power generation systems (Ahmadi et al., 2013). Role of hydrogen as a crucial energy vector in storing, transporting and using clean energy has been recognized thoroughly in the last decade and incorporation of hydrogen production in solar systems has become a significant focus area (Demir and Dincer, 2017). Hogerwaard et al. (2017) analyzed a MG system based on solar tower (ST) by using a combined cycle composed of an intercooling-regenerative (IR) open air BC and an organic Rankine cycle (ORC) to produce power, heating, cooling and fresh water. El-Emam and Dincer (2018) studied a ST MG system with reheat RC to produce green hydrogen with an EL in addition to power, heating, cooling and fresh water. Pourrahmini and Moghimi (2019) proposed a combined power cycle driven MG system with a simple BC and an ORC based on ST and included an EL to produce hydrogen, power and cooling. Yilmaz et al. (2020) analyzed a ST MG system for production of green hydrogen, power, heating, cooling and drying and used a BC with IR, and incorporated a high temperature steam EL. Colakoglu and Durmayaz (2021) proposed a MG plant using an IR ST gas turbine cycle (IR-SGTC) coupled to an ORC at exhaust and a Kalina cycle-34 (KC34) at intercooling to produce power, including an EL within intercooling stage for hydrogen production, in addition to heating, cooling, and DHWHs. In the literature, no study investigated a MG system based on a solar tower-driven triple power cycle composed of an intercooling-regenerative-reheat open air BC (IRR-SGTC), a regenerative RC and a KC11 and no study is focused on the effects of the power size of the EL in the overall performance of the MG system. Hence, this study aims to fulfill this lack in the literature, by proposing a novel ST triple power-cycle MG system for green hydrogen production as the main product with energy, exergy and economic analyses and multiobjective optimization. Effect of the EL size on the overall performance of the MG system is also investigated in addition to a detailed parametric analysis of design variables.

II. System Description
System consists of an IRR-SGTC with TES and two ECCs to compensate for the intermittent character of solar energy, a RRC, a KC11, a SEARC, two DHWHs and an EL to produce green hydrogen with the significant portion of the produced power. RRC and KC11 utilize the waste exhaust heat of the IRR-SGTC to enhance power generation. MG products of the system are green hydrogen and power, cooling and domestic hot water. The proposed novel MG system is illustrated in Fig.1.

III. Analysis
General mass, energy, concentration and exergy balance equations are used to construct the thermodynamic model of the proposed system. Total cost rate for economic analysis consists of the cost rates of components, fuel and environmental pollution as

$$\dot{C}_{total} = \sum \dot{Z}_k + \dot{C}_{fuel} + \dot{C}_{env} \quad (1)$$

Performance indicators used in the parametric analysis and MO optimization are

$$\eta_{en} = \frac{\dot{W}_{net,MG} + \dot{Q}_{DHW} + \dot{Q}_{cool} + \dot{m}_{H_2} LHV_{H_2}}{\sum_{j=1}^{n} \dot{Q}_{solar,in,j}} \quad (2)$$

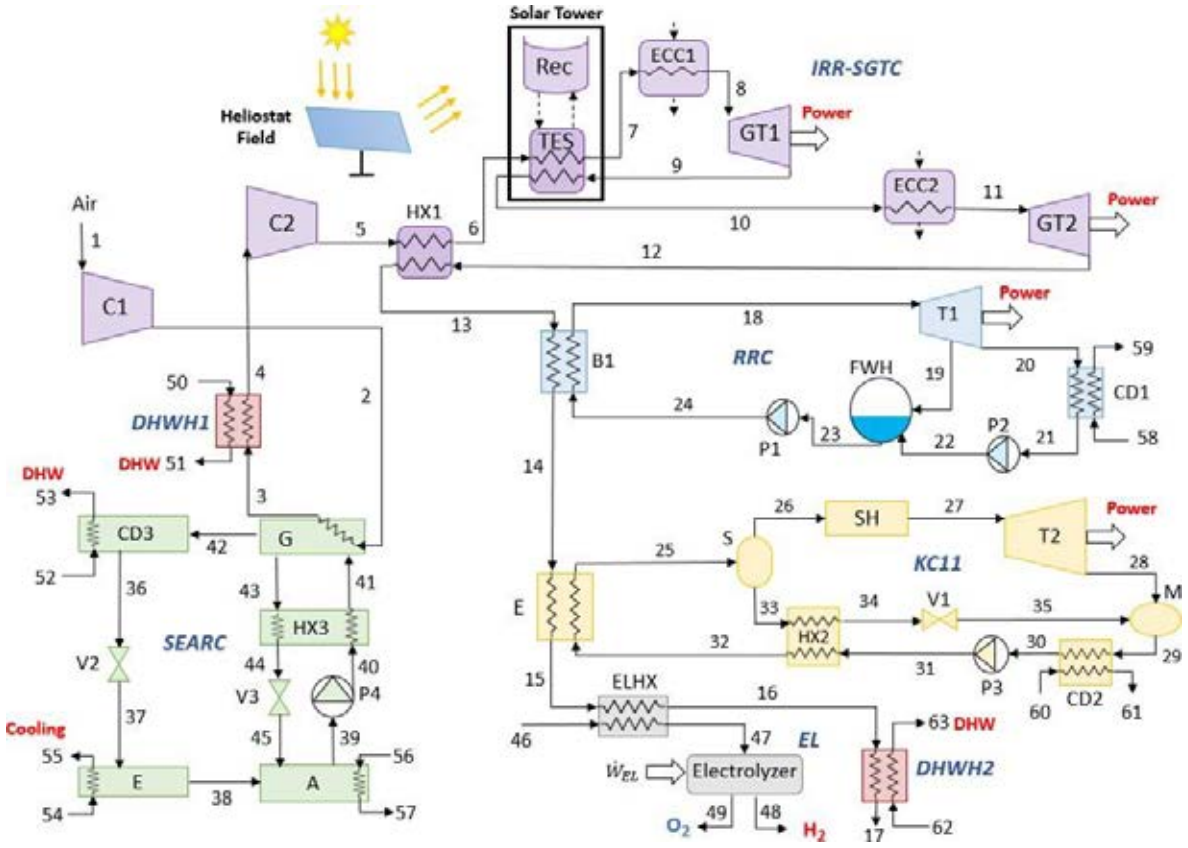


Fig. 1: Schematic representation of the proposed multi-generation system

$$\eta_{ex} = \frac{W_{net,MG} + Ex_{DHW} + Ex_{cool} + Ex_{H2}}{\sum_{j=1}^{n} Ex_{solar,in,j}} \quad (3)$$

$$c_{prod,ex} = \dot{C}_{total} / \dot{E}x_{prod} \quad (4)$$

where η_{en}, η_{ex} and $c_{prod,ex}$ represent energy efficiency, exergy efficiency and unit exergy product cost of the proposed MG system and are named as f_{en}, f_{ex} and f_{econ}, respectively. $\dot{E}x_{prod}$ denotes the total exergy rate of useful products. Multiobjective function (MOF) for the MO optimization of the system is written as

$$Min(MOF) = \sqrt{\left(\frac{f_{en}^{max} - f_{en}^{j}}{f_{en}^{max} - f_{en}}\right)^2 + \left(\frac{f_{ex}^{max} - f_{ex}^{j}}{f_{ex}^{max} - f_{ex}^{min}}\right)^2 + \left(\frac{f_{econ}^{j} - f_{econ}^{min}}{f_{econ}^{max} - f_{econ}^{min}}\right)^2} \quad (5)$$

Selected decision variables for the MO optimization are total pressure ratio of compressors, $r_{P,total}$, expansion coefficient of gas turbines, n, feed water pressure of Rankine cycle, P_{19}, turbine inlet pressure of Kalina cycle, P_{25}, and fraction of the EL power to the total power output of MG system, f_{EL}, which is defined as

$$f_{EL} = W_{EL} / W_{Total} \quad (6)$$

IV. Results and discussions

Effect of variation of design parameters on the performance indicators are presented in Fig. 2. Fig. 2a shows that η_{ex} reaches the maximum point at $r_{P,total}$ = 18.25, while $c_{prod,ex}$ reaches its minimum at $r_{P,total}$ = 21.75. Fig. 2b shows that as f_{EL} increases in the MG system, η_{en} and η_{ex} of the system decrease, while $c_{prod,ex}$ increases.

Results of MO optimization is presented in Tab.1.It shows that $r_{P,total}$, n, P_{19}, and P_{25}, are optimized at 19.24, 0.5855, 2.667 bar and 30.44 bar, respectively. Fraction of the electrolyzer power to the total system power, f_{EL}, is optimized at 0.4 instead of the base case value of 0.5 due to high losses and irreversibility of the electrolysis process.

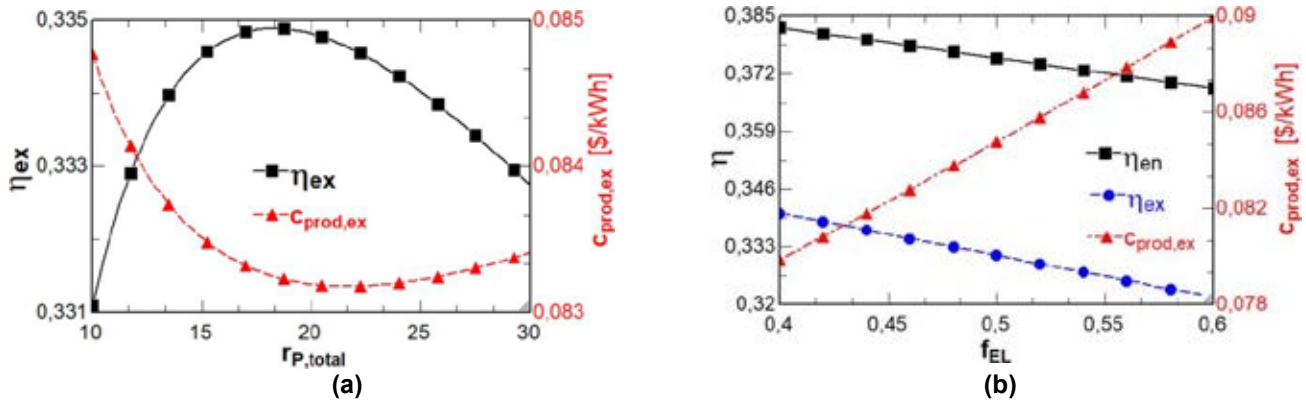


Fig. 2: Effect of variation of (a) $r_{P,total}$ on η_{ex} and $c_{prod,ex}$, (b) f_{EL} on η_{en}, η_{ex} and $c_{prod,ex}$

Tab. 1: Results of the MO optimization in comparison with the base case values

Parameters	Base Case	MO Optimum
$r_{P,total}$	10	19.24
n	0.55	0.5855
P_{19} (bar)	2	2.667
P_{25} (bar)	20	30.44
f_{EL}	0.5	0.4
η_{en}	37.55%	40.63%
η_{ex}	33.11%	34.52%
$c_{prod,ex}$ ($/kWh)	0.08477	0.07822

Tab.1. indicates that MO optimization results provide 8.02%, 4.26% and 7.27% better η_{en}, η_{ex} and $c_{prod,ex}$ compared to that of the base case, hence, performance of the optimized system is considerably higher.

V. Conclusions

It is concluded in this study that as fraction of the electrolyzer power to the total system power increases, energy, exergy and economic performance indicators of the MG system decrease due to high level of losses and irreversibility of the electrolysis process.

The most significant design parameters that has the largest effect on the performance indicators are total pressure ratio of compressors, expansion coefficient of gas turbines and fraction of the electrolyzer power to the total system power.

The proposed novel MG system can produce 23.34 kg/h green hydrogen, 1534 kW net power, 225.5 kW cooling and 6.453 kg/s domestic hot water.

References

Ahmadi P., Dincer I., Rosen M.A., Thermodynamic modeling and multi-objective evolutionary-based optimization of a new multigeneration energy system, Energy Conversion and Management, 76, 282-300, (2013).

Colakoglu M., Durmayaz A., Energy, exergy and environmental-based design and multiobjective optimization of a novel solar-driven multi-generation system, Energy Conversion and Management, 227, 113603, (2021).

Demir M.E., Dincer I., Development of a hybrid solar thermal system with TEG and PEM electrolyzer for hydrogen and power production, International Journal of Hydrogen Energy, 42, 30044-30056, (2017).

El-Emam R.S., Dincer I., Development and assessment of a novel solar heliostat-based multigeneration system, International Journal Hydrogen Energy, 43, 2610-2620, (2018).

Hogerwaard J., Dincer I., Naterer, G.F., Solar energy based integrated system for power generation, refrigeration and desalination, Applied Thermal Engineering, 121, 1059-1069, (2017).

Pourrahmani H., Moghimi M., Exergoeconomic analysis and multi-objective optimization of a novel continuous solar-driven hydrogen production system assisted by phase change material thermal storage system, Energy, 189, 116170, (2019).

Yilmaz F., Ozturk M., Selbas R., Development and performance analysis of a new solar tower and high temperature steam electrolyzer hybrid integrated plant, International Journal Hydrogen Energy, 45, 5668-5686, (2020).

A New Signal Processing-Based Islanding Detection Method for Reliable Grid Integration of Solid Oxide Fuel Cell-Based Distributed Generators

[1]Alper Yılmaz, [1]*Gökay Bayrak
[1] Bursa Technical University, Faculty of Engineering and Natural Sciences, Department of Electrical and Electronics Engineering, 16300, Bursa, Turkey

* E-mail: gokay.bayrak@btu.edu.tr

Abstract

This paper presents a new signal processing-based islanding detection method for fuel cell (FC)-based distributed generators (DGs). In the study, the undecimated wavelet transform (UWT)-based islanding detection method was proposed for reliable grid integration of the Solid Oxide FC-based DG system (SOFCDG). The proposed method was analyzed under different load conditions on the simulated test system. Besides, the developed WT-based islanding detection method (IDM) is tested in the presence of electrical noise. The proposed method reduces the oscillations in the voltage signal; noise sensitivity is lower than other wavelet transform (WT)-based methods and helps to select threshold values. The results also show that the proposed un-decimated WT-based method is more reliable than current WT-based islanding detection methods, even in noisy conditions. The non-detection zone (NDZ) is almost zero, and the detection time is under the IEEE 929-2000 standards in the proposed method.

Keywords: Fuel cell power generation system, Islanding detection, SOFC, Wavelet transform, Distributed generation

I. Introduction

Distributed generators (DGs) have been widespread worldwide, and hydrogen energy is the most promising renewable energy source in the DGs (Uyar, 2017). Besides, rapid development in Fuel Cell (FC) technology has made grid-connected FC systems more popular. Therefore, the integration of FC systems, whose number is rapidly increasing, into the grid has become an important issue (Lin, 2020).

The most crucial criterion in ensuring the power system's safety and reliability, together with the high-power quality, is the islanding condition. The island mode is defined as the condition in which the power flow is provided by the currently disconnected DG system when the system is electrically isolated from the grid (Bayrak, 2014). IEEE 929-2000 defines some rules for grid-connected FCs to provide the power system's stability. The islanding condition is also a crucial problem if DG systems are reliably operated with the main grid. Unintentional islanding condition in a DG causes several damages for both the consumers and the electrical equipment in a DG system. Thus, the detection of islanding in time is the most necessary protection precaution for a DG system.

Islanding detection methods can be classified as remote, local, and intelligent methods (Raza, 2015). Local methods can be examined in three groups as passive, active, and hybrid. Passive methods contain a large non-detection zone (NDZ), and this ratio is not sufficient in FC-based systems (Bayrak, 2018). In active methods, the power quality of the system decreases as noise is injected into the grid. Although NDZ is low in remote methods, the cost is very high (Bayrak, 2018). The disadvantage of intelligent methods is the necessity to use a hybrid method, the difficulties in a real-time application, and the studies remain only in the simulation's size.

Signal processing-based islanding detection methods use components of the time and frequency of a signal. Thus, this is a valuable property to detect islanding comparing to conventional methods (Yılmaz, 2019). Wavelet transform (WT) (Paiva,2020), Fourier transform (FT), Hilbert-Huang transform, curvelet transform, and s-transform constitute the signal-analysis-based methods for the detection of islanding conditions (Raza, 2015). WT methods have advantages over other signal processing methods to locally investigate sudden changes and discontinuities in high-level derivatives (Singh, 2018). The most significant disadvantage of conventional WT methods is their sensitivity to noise. Also, the continuous wavelet transform (CWT) method has implementation problems, and the discrete wavelet method (DWT) leads to the loss of information. These drawbacks have been improved with the proposed un-decimated wavelet transform (UWT)-based method.

In this study, the Solid Oxide FC- based DG system (SOFCDG) from the point of common coupling (PCC) to the three-phase grid was modeled, and the UWT-based island mode detection method was analyzed under different load conditions on the simulated test system. While applying the method, the voltage signal at the PCC point was used. With the proposed method utilizing only the voltage information, the loss in measurement time and calculation load was kept low. The islanding was detected according to the threshold value determined by the decomposition process with UWT. The proposed method's significant advantages are that the islanding detection time is fast and has no NDZ.

II. Test System and Proposed Method

The modeled test system configuration is shown in Fig. 1. In the modeled test system, the output of the SOFC is connected to the IGBT inverter (Zhu, 2002). The inverter provides grid synchronization, and it uses hysteresis switching and controls. The inverter output is filtered, it is connected to the grid via a circuit breaker (CB), and there is a parallel RLC load at the PCC. The performance of the UWT-based method has been tested with different islanding conditions. Since the SOFCDG system operated the unity power factor, a parallel RLC load at 50 Hz (resonance frequency) can be considered the worst-case scenario to detect islanding conditions.

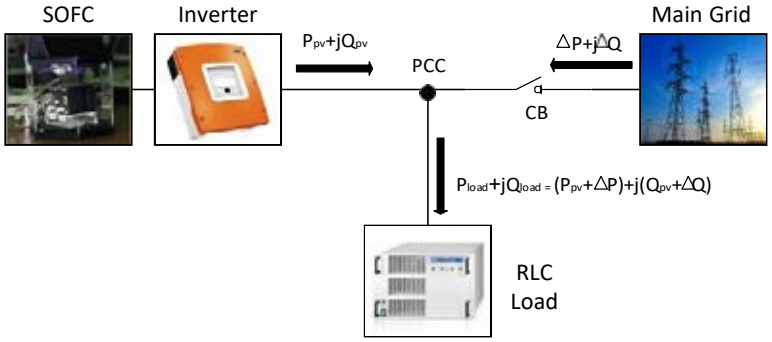


Fig. 1: Test system configuration

The flowchart of the proposed UWT-based islanding detection method has shown in Fig. 2. The two levels of the decomposition process performed with db8 and not reduced the number of samples. The last stage is decided whether the fault is island mode or another disturbance according to the determined threshold value. Different simulation studies have been conducted. The most appropriate parameters have been determined by selecting the type of wavelet, sampling frequency, wavelet level, and threshold value used in the UWT-based method for islanding detection. The computational time is reduced using the db8 mother wavelet containing a few samples and a short wavelet type. The voltage signal is acquired at 1 kHz sampling frequency.

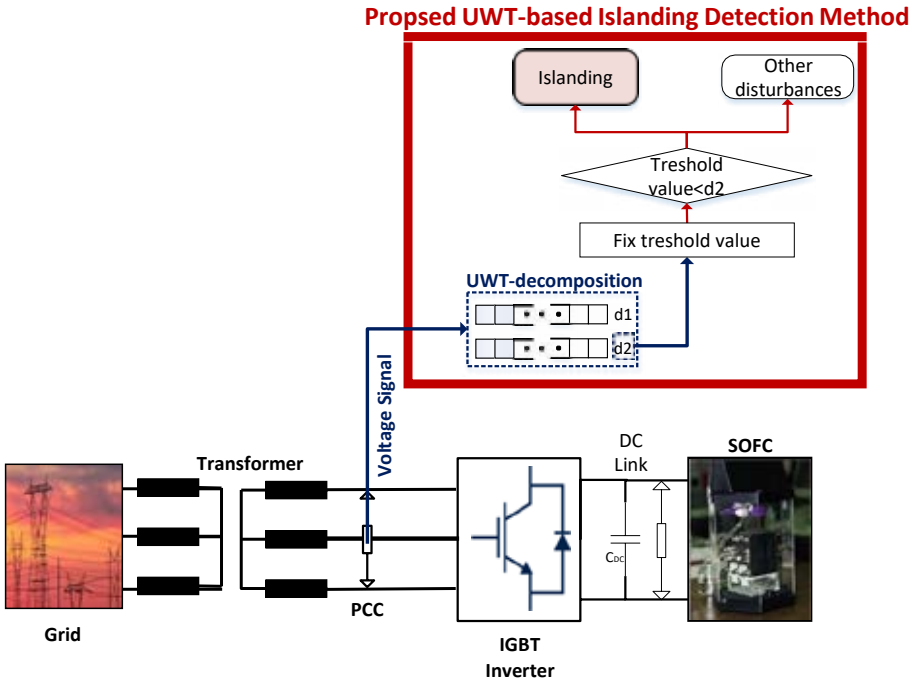


Fig. 2: The flowchart of the proposed UWT-based islanding detection method

III. Results

Case 1: The performance of the UWT-based method has been tested islanding condition with no power imbalance. The power mismatch (ΔP) / P_{Load} is 0%. The islanding condition in Fig. 3.a starts at the 120th millisecond. Also, the performance of the UWT-based method is shown.

Case 2: In this condition, the parameters of the test system are the same as in Case 1, and the voltage signal has noise (signal-to-noise-ratio (SNR) =20 dB). The islanding condition with the noisy environment is shown in Fig. 3.b and the UWT-based islanding detection method's performance in the developed software. This case, which remained in the NDZ region in conventional methods, could be detected reliably with the proposed method.

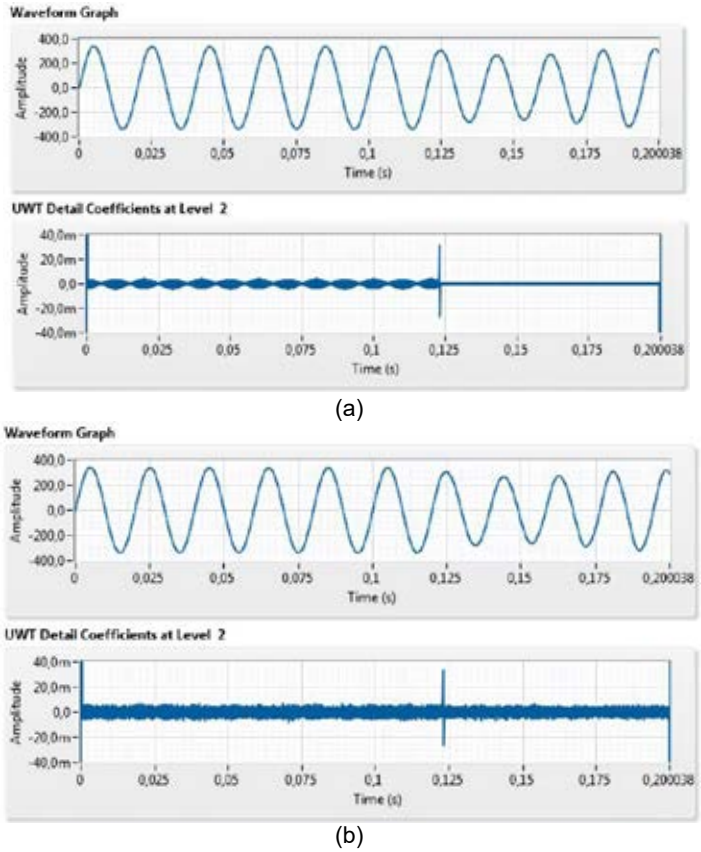


Fig. 3: Islanding detection with proposed method for Case 1 (a), and Case 2 (b)

V. Conclusions

In this study, the islanding conditions in the grid-connected SOFCDG-based microgrids are investigated, and a new UWT-based IDM is proposed. The UWT-based method overcomes the implementation problems and performance limitations of WT-based methods. The performance of islanding conditions under noise has been dramatically improved with UWT. The proposed method detects islanding conditions under the IEEE 929-2000 standards with almost zero NDZ. As a result, the UWT-based method is most suitable to detect islanding in SOFCDGs.

References

Uyar, T. S., and Beşikci D., Integration of hydrogen energy systems into renewable energy systems for better design of 100% renewable energy communities, International Journal of Hydrogen Energy 42.4: 2453-2456, (2017).

Lin, Rong-Heng, Ying-Ying Zhao, and Bu-Dan Wu., Toward a hydrogen society: Hydrogen and smart grid integration, International Journal of Hydrogen Energy 45.39: 20164-20175, (2020).

Bayrak, G., & Cebeci, M., A novel anti-islanding detection method for grid-connected fuel cell power generation systems. International Journal of Hydrogen Energy, 39(16), 8872-8880, (2014).

Raza, S., Mokhlis, H., Arof, H., Laghari, J. A., & Wang, L., Application of signal processing techniques for islanding detection of distributed generation in distribution network: A review, Energy Conversion, and Management, 96, 613-624, (2015).

Bayrak, G., Wavelet transform-based fault detection method for hydrogen energy-based distributed generators, International Journal of Hydrogen Energy, 43(44), 20293-20308, (2018).

Yılmaz, A., & Bayrak, G., A real-time UWT-based intelligent fault detection method for PV-based microgrids. Electric Power Systems Research, 177, 105984, (2019).

Paiva, S. C., de Araujo Ribeiro, R. L., Alves, D. K., Costa, F. B., & Rocha, T. D. O. A., A wavelet-based hybrid islanding detection system applied for distributed generators interconnected to AC microgrids, International Journal of Electrical Power & Energy Systems, 121, 106032, (2020).

Singh, R., Mohanty, S. R., Kishor, N., & Thakur, A., Real-time implementation of signal processing techniques for disturbances detection, IEEE Transactions on Industrial Electronics, 66(5), 3550-3560, (2018).

Zhu, Y., & Tomsovic, K., Development of models for analyzing the load-following performance of microturbines and fuel cells, Electric Power Systems Research, 62(1), 1-11, (2002).

Biohydrogen and Bioethanol Production Routes from Pyrolysis Gas

[1]Simge Sertkaya, [2]Gozde Duman, [3]Haris Nalakath Abubackar, [4]Nuri Azbar, [2]Jale Yanık,[5*]Tugba Keskin
[1]Ege University, Center for Environmental Studies, Izmir, 35100, Turkey
[2]Ege University, Faculty of Science, Chemistry Department, Izmir, 35100, Turkey
[3]Chemical Engineering Laboratory, Faculty of Sciences and Centre for Advanced Scientific Research (CICA), University of La Coruña, Rúa da Fraga 10, 15008 – La Coruña, Spain
[4]Ege University, Faculty of Engineering, Bioengineering Department, Izmir, 35100, Turkey
[5]Izmir Democracy University, Department of Environmental Protection, Izmir, 35140, Turkey

* E-mail: tugba.keskingundogdu@idu.edu.tr

Abstract
Syngas fermentation technology for biofuel production is gaining importance. Bioethanol is the most studied product of these technologies, but it is known that biohydrogen can also be produced from C1 gases (CO, CO_2) by water gas shift reaction. Another known technology that uses lignocellulosic material for renewable energy production is pyrolysis and biochar production. The outlet gas of pyrolysis contains C1 gases which can be converted into bioethanol and biohydrogen using syngas technologies. Similar amounts of bioethanol and acetate values were observed using commercial syngas and pyrolysis gas (up to 140 mg/L ethanol; 160 mg/L acetate). In this study, an energy-intensive, zero-waste approach for biofuel production from lignocellulosic biomass is evaluated based on small-scale laboratory study findings. Two different routes for biohydrogen production, biohydrogen production options using pyrolysis gas directly or acetate for photofermentative biohydrogen production, were suggested.
Keywords: Bioethanol, biohydrogen, pyrolysis, syngas fermentation,

I. Introduction

To mitigate the vast greenhouse gas emissions sourced by fossil fuels and cope with growing global energy demands, a widespread replacement of these fuels with renewable energy carriers became very important. Hydrogen is one of the most prominent sustainable energy carrier with the advantageous properties of being non-pollutant and carbon neutral (Aghbashlo et al., 2016). The current hydrogen production technologies from natural gas, oil, and coal are unsustainable (Coche et al. 2011). Using renewable energy sources instead of fast-depleting non-renewable resources will be a more environmentally friendly and sustainable option (Hosseini et al., 2015). Hydrogen can also be produced by WGS (Water Gas Shift) reaction which is the reaction of CO with water (Hosseini et al. 2015).

$$H_2O + CO \rightarrow CO_2 + H_2$$

The microorganisms used in water gas shift reactions conserve metabolic energy with producing H_2. In this process CO serves as electron donor, carbon and energy source. Bioethanol is predominantly produced through the fermentation of easily degradable carbohydrate substrates, such as corn starch and sugar cane. Alternatively, fermentable sugars can be obtained through the acid or enzymatic pretreatment of insoluble cellulosic biomass. However, most biomass sources like straw and wood contain a large proportion of material that cannot be converted to ethanol by microorganisms. An alternative might be to gasify organic biomass and use the produced synthesis gas (or syngas) as a feedstock to synthesize ethanol and other valuable compounds. Syngas, formed by the gasification or reforming of coal, natural gas, or biomass, is a crucial intermediate in producing synthetic fuels. The most studied acetogenic microorganisms for bioethanol production are *Clostridium ljungdahlii, C. ragsdalei, C. carboxydivorans, C. autoethanogenum*. Reducing air pollution, syngas fermentation is an outstanding and promising technology (Abubackar et al., 2015). Pyrolysis is one of the effective methods producing biochar. The pyrolysis gas can be used to produce ethanol and hydrogen because of its composition, including CO and CO_2 by syngas fermentation. H_2 production from CO and syngas technologies can be achieved by different anaerobic microorganisms. The mainly used microorganisms are *Rhodopseudomonas palustris, Rhodospirillum rubrum Citrobacter Y19* (Kerby et al. 1995). In this study, the potential of hydrogen production by photofermentation with sequential reactor system with syngas fermentation using pyrolysis gas is considered. Different options of the combination of hydrogen production with syngas fermentation and pyrolysis are evaluated.

II. Experimental Set-up and Procedure

Microorganisms and Media

Syngas fermentation studies were done with two bacteria*, Clostridium ljungdahlii,* and *Clostridium ragsdalei.* *C. ljungdahlii* DSM 13528 was supplied from the Deutsche Sammlung von Mikroorganismen und Zellkulturen GmbH (Braunschweig, Germany), DSMZ medium 879 was used. *C. ragsdalei* ATCC BAA622 was obtained from the American Type Culture Collection (ATCC, USA). The lyophilized cultures were activated by growing in ATCC Media at 30°C for 24 h. Before inoculation, the cultures were kept active by transferring into new media, including fructose, every 2 weeks. 10% (v/v) of active inoculum was used in growth media.

Compositions of commercial syngas and pyrolysis gas

A local gas company prepared syngas as 10 L with composition*;* 60% CO, 10% CO_2, 20% N_2 and 10% H_2. The composition of pyrolysis gas is as follows; 20.73% CO, 49.20% CO_2, 29.74% N_2, 0.06% H_2. Pyrolysis experiments

were performed in a laboratory-scale fixed bed pyrolysis reactor (V = 1 L) at 350°C. The reactor loaded with 30 g of sunflower stalk was placed in a vertical furnace. The method was described before elsewhere(Duman et al. 2013). The mass yields of biochar (carbon rich solid product), bio-oil (liquid product) and gas were found to be 40.3%, 34.6% and 25.1%, respectively.

Analytical methods

Ethanol and acetic acid concentrations in the fermentation broth were analyzed using a High Pressure Liquid Chromatography (HPLC) instrument (Thermo Fisher Scientific, MA, USA) equipped with a Refractive Index Detector (RID) (Keskin and Duman 2020). The quantitative analysis of pyrolysis gases was carried out with the Refinery Gas Analyzer (RGA) with Agilent 7890B model gas chromatography (Duman et al. 2013).

Syngas fermentation with batch reactors for ethanol and acetate production

After growth of microorganisms, the effect of syngas and pyrolysis gas was compared for different conditions which were determined in our previous studies. The best alternative fermentation medium compositions from *C. ljungdahlii* were, using 30 g/L whey powder (WP) instead of trace element solution and 5 mL glycose syrup (GS) instead of trace element solution (Gunay et al. 2020). The same conditions were applied for *C. ragsdalei* for comparison. All alternative medium were also compared with DSMZ medium for *C. ljungdahlii* and ATCC medium for *C. ragsdalei*. All batch reactors were capped with rubber and clamped with Al ring. After flushing the headspace with 100% N_2 to supply anaerobic condition 20 ml commercial syngas and pyrolysis gas were injected to the headspace of all reactors.

IV. Results and discussions

Clostiridum ljungdahlii and *Clostridium ragsdalei* are the most studied microorganisms for bioethanol production with syngas fermentation. Ethanol and acetate are the main products of Wood-Ljungdahlii pathway (Abubackar et al. 2015). Batch reactors were operated for 14 days. After a rapid growth phase, acetate and ethanol production started.

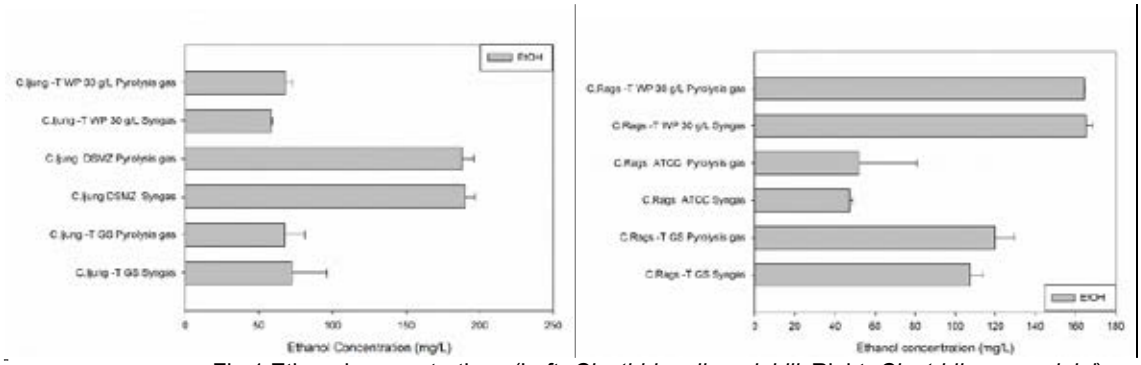


Fig.1 Ethanol concentrations (Left: *Clostiridum ljungdahlii*; Right: *Clostridium ragsdalei*)

Figure 1 represents the ethanol production values of *C. ljungdahlii* and *C. ragsdalei*. For all batch reactors, ethanol production values were approximately the same with commercial syngas and pyrolysis gas. The reason for these similar production values is that *C. ljungdahlii* and *C. ragsdalei* can convert C1 gases into acetate and ethanol. Up to 200 mg/L ethanol production was observed with DSMZ medium using *C. ljungdahlii* and WP medium using *C. ragsdalei*. Alternative mediums showed better performance for *C. ragsdalei* the opposite trend was observed for *C. ljungdahlii*.

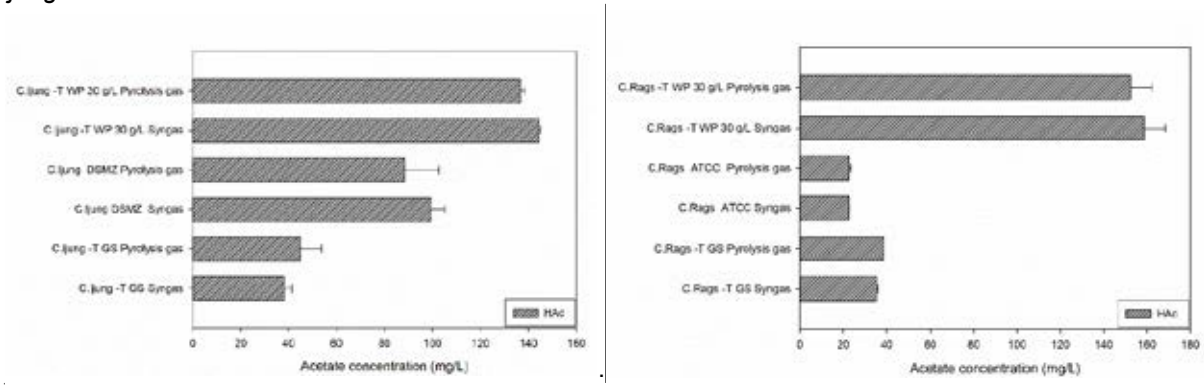


Fig. 2 Acetate concentrations (Left: *Clostiridum ljungdahlii*; Right: *Clostridium ragsdalei*)

The second main product of syngas fermentation is acetate which is one of the best organic substrate for photofermentative hydrogen production. High concentrations of acetate (140 mg/L) was observed for WP medium for both microorganisms. The concentrations of acetate are close to each other while using commercial syngas and pyrolysis gas (Figure 2).

Syngas technologies can also be used for biohydrogen production. Zhao et al.(2011) studied bioconversion of syngas using a continuous hollow fiber membrane bioreactor(MBR) with *Carboxydothermus hydrogenoformans*. Carbon monoxide was used as a carbon source, and 0.46 mol/d hydrogen production rate were 33.5 mmol/L biohydrogen was produced by batch reactor systems using locally isolated photosynthetic bacterium *Rhodopseudomonas palustris* PT. CO-rich syngas was converted into biohydrogen through a water-gas shift (WGS) reaction. (Pakpour et al., 2014). Aghbashlo et al. (2016) performed exergy-based multi-objective fuzzy optimization using a continuous photobioreactor for biohydrogen production from syngas via waster-gas-shift reaction by *Rhodospirillum rubrum.* 21.66% exergy efficiency and 85.65% rational exergy efficiency values were the optimum values for 13.35 mL/min syngas flow rate with 383.34 rpm agitation speed. Hosseini et al. (2015) studied exergy analysis of batch biohydrogen production through WGS reaction using *Rhodospirillum rubrum* for the first time. Acetate was identified as the most appropriate carbon source for biohydrogen production.
Based on the findings of our study it is clearly understood that commercial syngas and pyrolysis gas can be used for biohydrogen production with syngas technologies with same yields. Another important finding is; bioethanol production can be integrated with biohydrogen production with photo-fermentation because of the high acetate concentrations. There are two options to use syngas fermentation technologies for biohydrogen production. First one is directly usage of pyrolysis gas and produce biochar and biohydrogen. The second option is to integrate these two systems with sequential bioreactors; at first stage syngas fermentation from pyrolysis gas for ethanol and acetate production and at second stage biohydrogen production using the media with acetate after separating ethanol for photo-fermentative biohydrogen production.

V. Conclusions

There are several routes of biofuel productions from lignocellulosic biomass. The first one is to produce biochar from waste and ethanol from the waste gas (pyrolysis gas); as a second option, biohydrogen can be produced by water gas shift reaction using pyrolysis gas. The third one is to produce biochar, bioethanol, and biohydrogen simultaneously, which will be the energy-intensive and zero-waste approach. At the first stage, biochar can be produced from lignocellulosic biomass; at the second stage, bioethanol and acetate can be produced from waste gas of biochar production (pyrolysis gas), a third stage after separating ethanol, the remaining medium, including acetate, can be used for biohydrogen production by photo-fermentation.

Acknowledgements

TK, GD and HNA would like to acknowledge the Scientific and Technological Research Council of Turkey (TUBITAK-CAYDAG) [grant number 118Y305] for the financial support. TK and HNA would like to acknowledge TUBITAK-CAYDAG [grant number 120Y069] for the financial support. HNA also thanks the Xunta de Galicia (Spain) for his postdoctoral fellowship (ED481D 2019/033).

References

Abubackar H. N., Veiga, M. C., Kennes C., Ethanol and acetic acid production from carbon monoxide in a Clostridium strain in batch and continuous gas-fed bioreactors, International Journal of Environmental Research and Public Health 12,1029 (2015).

Aghbashlo S., Tabatei M., Sina S., Ghasem H., Najafpour G., Younesi H., An exergetically-sustainable operational condition of a photo-biohydrogen production system optimized using conventional and innovative fuzzy techniques, Renewable Energy 94, 605-618 (2016).

Cohce M.K., Dincer I., Rosen M.A., Energy and exergy analyses of a biomass based hydrogen production system, Bioresource Technology, 102, 8466-8474 (2011).

Duman G., Pala M., Ucar S., Yanik J., Two-step pyrolysis of safflower oil cake, Journal of Analytical and Applied Pyrolysis, 103, 352 (2013).

Günay B., Azbar N., Keskin T., The effect of corn syrup and whey on the conversion process of CO to ethanol using *Clostridium ljungdahlii,* Chemosphere, 261, 127734 (2020).

Kerby R.L., Ludden P.W., Roberts G.P., Carbon monoxide dependent growth of *Rhodospirillum rubrum*. Journal of Bacteriology, 177, 2241-2244 (1995).

Keskin T., Duman G., Bioethanol production by syngas fermentation from pyrolysis gas using mixed culture: Heat-pretreatment effect, Pamukkale University Journal of Engineering Sciences 26, 1299-1307 (2020).

Pakpour F., Najafpour G., Tabatabei M., Tohidfar M., Younesi H. Biohydrogen production from CO-rich syngas via a locally isolated *Rhodopseudomonas palustris* PT. Bioprocess and Biosystems Engineering 37, 923-930 (2014).

Sina S., Aghbashloa M., Tabataberi M., Younes H., Najafpour G. Exergy analysis of biohydrogen production from various carbon sources via anaerobic photosynthetic bacteria (*Rhodospirillum rubrum*) 93, 730-739 (2015).

Zhao Y., Liu Z., Guiot R., Continuous biohydrogen production from syngas fermentation in a hollow fiber membrane reactor Xiandai Huagong/Modern Chemical Industry 31, 71-74+76 (2011).

Mathematical Modeling of a Solid Oxide Fuel Cell (SOFC) Based Micro-CHP System for Residential Applications

[1*]Merve Atilmis, [2]C Ozgur Colpan,
[1]Dokuz Eylul University, School of Natural and Applied Sciences, Mechanical Engineering Department, Buca, Izmir, 35000, Turkey
[2] Dokuz Eylul University, Faculty of Engineering, Mechanical Engineering Department, Buca, Izmir, 35000, Turkey

* E-mail:merveatilmis@windowslive.com

Abstract
Micro combined heat and power (micro-CHP) systems can be used to meet the necessary electricity demands of the houses such as lighting, heating and the necessary thermal energy demands of the houses such as space heating or domestic hot water (DHW). Micro gas turbines, stirling engines or fuel cells are the technologies can be used for the production of electricity in these systems. Among of these systems, fuel cell-based systems are quite notable for building applicatiıns due to their properties such as low emission, high electrical efficiency and low noise operation. Building cogeneration systems (also known as micro cogeneration systems) have gained importance with increasing global energy demands and greenhouse emissions. They are designed to meet the energy needs of a single-family house or a small commercial building. Fuel cell (FC) based micro-cogeneration systems are one of the key technology options for improving building energy efficiency and reduce emissions. Among the several FC types, SOFC-mCHP is one of the best choices for energy production among the fuel cell technologies due to their high efficiency, low environmental pollution, and fuel flexibility (Kazempoor, 2010).
In residential applications, it is important to match the energy generated by the micro-CHP system with the instantaneous electricity and heat demand. In a typical building, electricity consumption increases at certain times of the day. In addition, when space heating is required, higher heating loads are required and instantaneous heating loads occur when DHW is required (Liso, 2014). The thermal and electricity load is directly dependent on the climate conditions.
The main objectives of the model developed in this study is to meet the heat and electrical energy demands of a building through the energy analysis conducted for three climate zones. The methane (CH_4) -fueled SOFC system used with the air heat pump increase the performance in periods of high heating and cooling demands. The first part of the analysis includes the energy analysis of the building, and the second part involves the analysis of the SOFC based micro cogeneration system.

Five-floor building as shown Fig. 1 is modelled according to ASHRAE 189.1-2009 standards. The building is modelled using SketchUp and simulated using OpenStudio software. Each floor has four apartments and number of people living is four for each apartment. Three climate zones were selected using ASHRAE climate zone map.

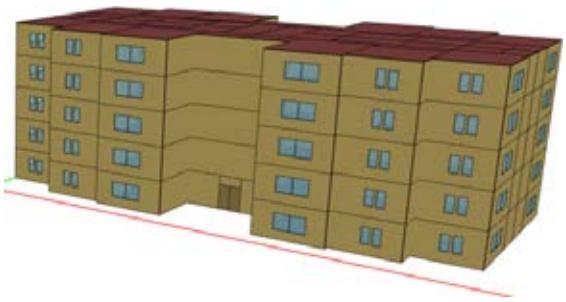


Fig. 1: Building Geometry

The results of annual energy simulation analysis is given in Fig.2. System analysis is done using the Matlab and SIMULINK programs. As a result of the MATLAB/SIMULINK analysis of the system, it is aimed to meet the loads obtained from the energy analysis.

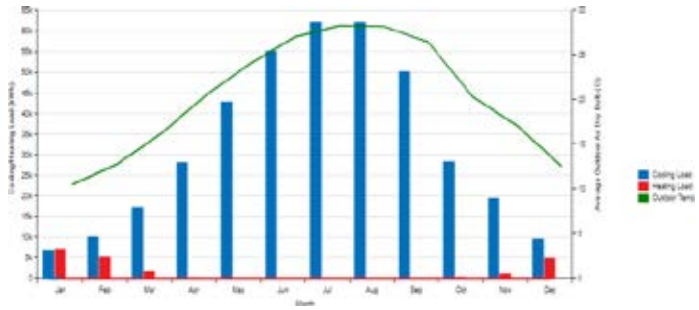


Fig.2: HVAC Loads for 2A climate zone

Keywords: mCHP, SOFC, building, energy simulation

References

Pejman Kazempoor*, Viktor Dorer, Andreas Weber, Modelling and evaluation of building integrated SOFC systems, International Journal of Hydrogen Energy, 36, 13241-13249, (2011).

Vincenzo Liso, Yingru Zhao, Wenyuan Yang, Mads Pagh Nielsen, Modelling of a Solid Oxide Fuel Cell CHP System Coupled with a Hot Water Storage Tank for a Single Household, Energies, 8, 2211-2229,(2015).

An Experimental Study to Validate Optimum Distance Between Metal Hydride Tanks With Staggered Arrangement for Effective Thermal Management

[1*]İsmail Hilali, [2]Ahmet Akbaş, [3]Vehbi Balak, [3]Dursun Akaslan
[1] Harran University, Department of Mechanical Engineering, Sanliurfa, 63000, Turkey
[2] Elif Engineering Co, Sanliurfa, 63330, Turkey
[3] Harran University, Department of Computer Engineering, Sanliurfa, 63000, Turkey

* E-mail:ihilali@gmail.com

Abstract
The aim of this work is to validate the results of numerical calculations for staggered metal hydride banks with the pitch-to-diameter ratio of 0.06 and 0.07 at the Reynolds number of 6000 and 12000. The optimized metal hydride tank array frames as per the results of theoretical study have been fabricated and experimental tests are carried out on the designed system. The effects of operating parameters such as tank pressure, ambient temperature and equilibrium on system performance were studied. The experimental results are compared with the theoretical model and validation is found between the two. It is also experimentally demonstrated that metal hydride storage tanks are strongly affected by the array geometry for maximum heat transfer, especially for small pitch arrays at high Reynolds numbers. The results show good agreement with the available theoretical data. The thermal behavior results for the given parameters showed that the metal hydride reservoirs placed with optimum spacing have heat transfer capability of more than 75% of their theoretical capacity. It was experimentally shown that the overall efficiency of the fuel cell-metal hydride system can potentially be increased by simple geometrical arrangements. In addition, it is important to consider the potential contribution to commercially available work such as automotive.

Keywords: Metal Hydride, Optimization, Heat Management, Thermal Imaging, Experimental validation

I. Introduction

Metal hydrides have been extensively used in green vehicles due to good energy density and low operating pressure. Their performance and life cycle are related by temperature. If possible, more than one tank should prefer to obtain effective heat management because of the extra heat transfer area. Additionally, when one tank is used, the system's performance will be affected by the performance of the metal hydride tank. For this reason, it is important to use as more as possible the tanks. Also, occupied space and investment costs should be considered and competed economically with cheap hydrocarbons for mobile applications. Because end-users want economic and reliable vehicles in terms of price.

All the work on this subject has been made in consideration of a single tank. Omrani at al. designed and positioned horizontally the nine metal hydride tanks in two parallel rows in a well-insulated air box. Mahmoodi at al. was studied experimentally to increase the desorption performance of a metal hydride tank using new novel geometric configuration of heat pipes. They focused especially effects of heat pipe number and fin in metal hydride tank. Kumar at al. studied absorption/desorption characteristics of a metal hydride tank with 99 cooling tubes. Tarasov at al. used multiple metal hydride tanks in experiments. Lototskyy at al. developed an assembly of the metal hydride containers staggered with heating/cooling tubes. But it does not contain any data related to tank arrangements. Almost all did not focus on the effect of array geometry of metal hydride tanks.

The goal of the current study is to prove experimentally that ideal distance exists in metal hydride array according to the results of theoretical study (Hilali et al., 2018).

II. Experimental Set-up and Procedure

In the present study, the LaNi5 alloy filled with metal hydride tanks with staggered arrangement as shown in Fig. 1 are considered.

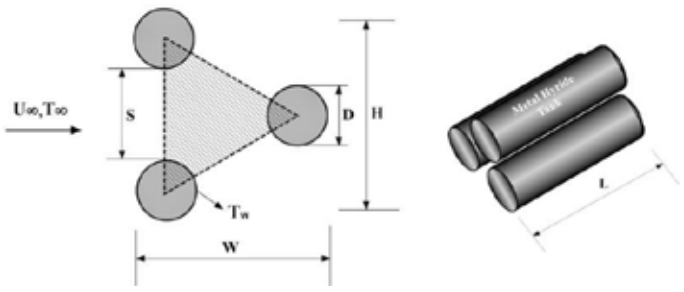


Fig. 1: Schematic of the staggered arrangement

Hilali et al. found the existence of an ideal distance for the largest heat transfer rate. The heat transfer rate is formulated for the extreme distances, i.e., large distance and small distance. Then the ideal distance is found by balancing the formulas.

$$\left(\frac{S_{opt}}{D}\right) \cong 4.\mathrm{Re}_D^{-0.47}.\mathrm{Pr}^{-0.21} \quad (1)$$

As shown in Fig. 2 and 3, the experimental setup consists of an axial fan with frequency controller, an air heater with temperature controller, an air flow meter, a fuel cell system, metal hydride storage tanks, black coated aluminum plates and a thermal imaging camera with SuperResolution. The fuel cell system is based on the 1200 W Nexa power source including energy management module and electronic loader.

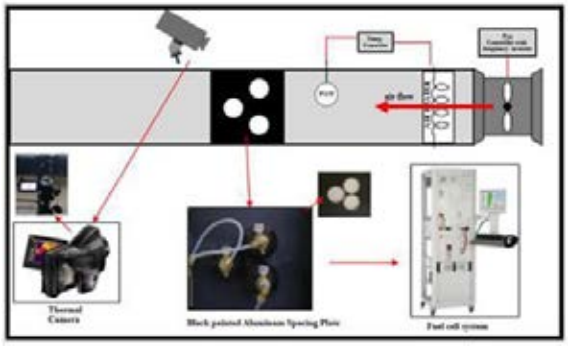


Fig. 2: Schematic of the experimental setup



Fig. 3: Photograph of the experimental setup

The present study consists of two stages determined by perforated plates; each of them evaluates the heat transfer rate separately based on different ambient temperatures (300 K & 310 K), Reynolds numbers (6000 & 12,000) and equilibrium pressures (60 kPa & 120 kPa). In each of the two stages, two plates were used with a spacing of 5 and 6 mm between the tanks. These plates were selected according to previous results of theoretical study. The tank pressures were obtained by operating the fuel cell up to the specified values under the constant load using an electronic loader.

III. Results and discussions

The solid lines drawn on the plate in Fig. 4 were used to plot the temperature profile using the thermal image data along the lines to compare the results of the theoretical study. The contours in Fig. 5 show the temperature distribution over the plate area according to the solid lines for relevant variables. The results of CFD and the experimental results are shown on the left side and the right side of Fig. 6, respectively.

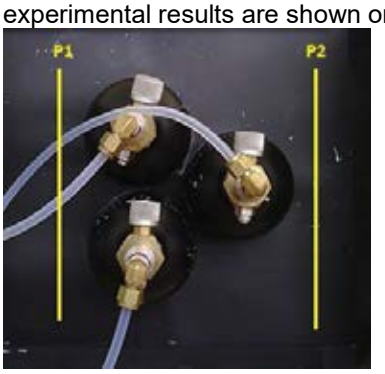
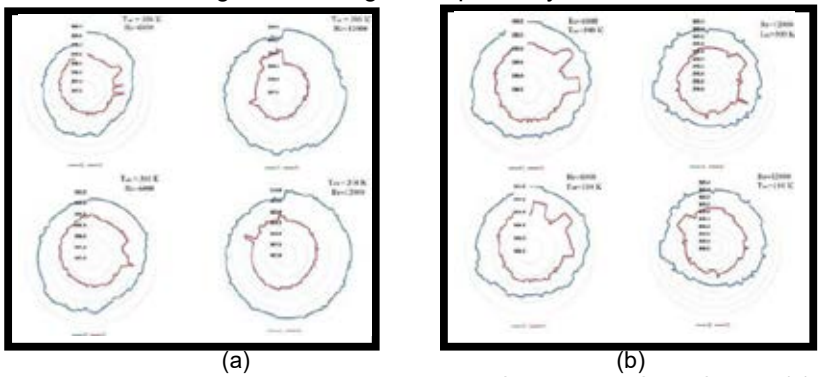


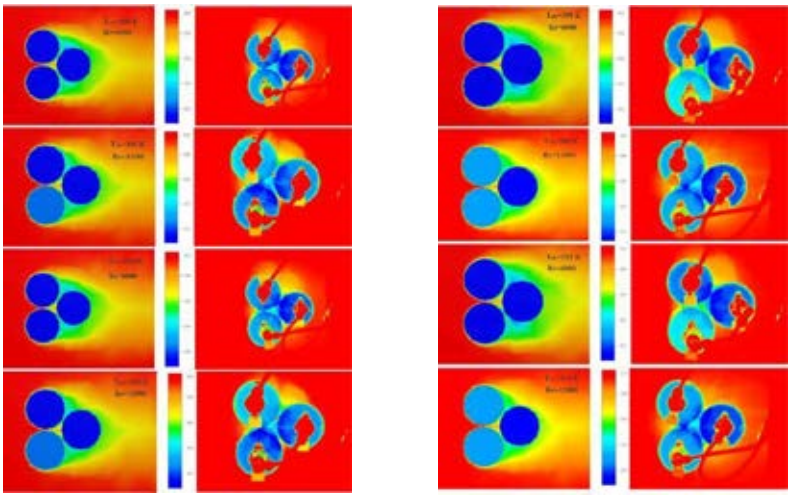
Fig. 4: Measurement planes on the plates



(a) (b)

Fig. 5. The captured temperature profiles over the face of plates (a) for Peq=60 kPa (b) for Peq=120 kPa

Fig.5 shows the temperature distributions on the surface of the plate along each vertical line (P1&P2) at Peq=60 kPa and 120 kPa, respectively. The blue counter indicates the inlet air temperature, and the red counter indicates the outlet air temperature. The difference between the blue and red counters indicates the heat transfer rate of the metal hydride reservoirs. As the figures show, the temperature difference is approximately between 0.5 and 1 K depending on the Reynolds number. As the Reynolds number increases, the temperature difference increases. These results are in agreement with the results of another study by the author. Fig. 6 states that both contours agree well, thus verifying the validity of the model. As can be seen, both contours agree and the small differences are a consequence of the thermal camera measurements and the many uncertainties associated with the experimental setup, since the simulated values are calculated under ideal conditions.



(a) (b)

Fig. 6. The visual comparison of CFD results and experimental results (a) for Peq=60 kPa (b) for Peq=120 kPa

V. Conclusions

The thermal management of metal hydride storage devices (MH) separated by the ideal distance is discussed In this study.The varying inputs namely air velocity, pressure and ambient temperature were considered as the main parameters to affect the temperature distribution during discharge. The data output as a result of the thermal response for the input parameters discovered the importance of optimizing an ideal spacing between the metal hydride tanks, as it plays a critical role in the ability to transfer heat above 75% of the theoretical capacity. Therefore, the study concludes that an optimal spacing between the metal hydride storage devices has positive effects on the thermal conductivity of the proposed system as it critically improves the effective thermal management. The main conclusions of this study imply through our experiments that the heat transfer is directly related to the optimal spacing. The experimental and theoretical results of this work can provide a direction for the characterization of a metal hydride storage system.

References

Hilali, İ., Karadag, R., Bulut, H., & Aktacir, MA. A study on ideal distance between staggered metal hydride tanksniforced convection. International Journal of Hydrogen Energy, 43(38), 17970–17977 (2018).

Kumar, A., Raju, N. N., Muthukumar, P., & Selvan, P. V. Experimental studies on industrial scale metal hydride based hydrogen storage system with embedded cooling tubes. International Journal of Hydrogen Energy, 44(26), 13549–13560 (2019).

Lototskyy, M., Tolj, I., Klochko, Y., Davids, M. W., Swanepoel, D., & Linkov, V. Metal hydride hydrogen storage tank for fuel cell utility vehicles. International Journal of Hydrogen Energy, 45(14), 7958–7967 (2020).

Mahmoodi, F., & Rahimi, R. Experimental and numerical investigating a new configured thermal coupling between metal hydride tank and PEM fuel cell using heat pipes. Applied Thermal Engineering, 178, 115490 (2020).

Omrani, R., Nguyen, H. Q., & Shabani, B. Thermal coupling of an open-cathode proton exchange membrane fuel cell with metal hydride canisters: An experimental study. International Journal of Hydrogen Energy, 45(53), 28940–28950 (2020).

Automated Classification of Power Quality Disturbances in a SOFC&PV-based Microgrid Using a Hybrid Machine Learning Method with High Noise Immunity

[1]Alper Yılmaz, [2]Ahmet Küçüker, [1]*Gökay Bayrak

[1]Bursa Technical University, Faculty of Engineering and Natural Sciences, Department of Electrical and Electronics Engineering, 16300, Bursa, Turkey

[2]Sakarya University, Faculty of Engineering, Department of Electrical and Electronics Engineering, 54187, Sakarya, Turkey

* E-mail: gokay.bayrak@btu.edu.tr

Abstract

In this study, the performance of a developed hybrid machine learning (ML) method is investigated for the classification of the power quality disturbances (PQDs) by using an un-decimated wavelet transform (UWT)-based feature extraction method for fuel cell (FC) and photovoltaic (PV)-based hybrid distributed generation (DG) system. The UWT method is used and investigated with the Gradient Boosting Decision Tree (GBDT) classifier in the literature for the first time to classify PQD signals for a Solid Oxide FC-based DG system (SOFCDG). The proposed method reduces the oscillations in the voltage signal; noise sensitivity is lower than other wavelet transform (WT)-based methods. The results obtained show that the combination of the (UWT-GBDT) method can classify with high accuracy as 99.85%. Besides, it is observed that the features extracted with the UWT method provide much more successful results in classification than the existing discrete wavelet transform (DWT) methods in the literature. The proposed method was also tested under noisy conditions with a 30dB and 40dB signal-to-noise ratio (SNR). Even the UWT-GBDT method's noise sensitivity performance is much better than other conventional wavelet algorithms.

Keywords: Fuel cell power generation system, Power quality, SOFC, Wavelet transform, GBDT

I. Introduction

The depletion of fossil fuels has made clean and sustainable renewable energy sources (RES) an important alternative. Weather dependence of RES such as photovoltaic (PV) systems and wind energy systems can be eliminated by the use of fuel cell (FC) technologies (Wang, 2021). Therefore, the integration of FC systems, whose number is rapidly increasing, and its effects on power quality (PQ) have become an important issue (Lin, 2020). (Lin, 2020).

Power quality is directly related to voltage and current characteristics, and a problem that leads to deviation from the ideal waveform is called the power quality disturbance (PQD). The PQD definitions can be found in detail in the reference (IEEE std. 1159-2009) of voltage sag/swell, voltage interruption, current and voltage harmonics, transient regime events, notch formation, flickers, and voltage imbalances in the system. The problems occurring in the Solid Oxide FC (SOFC)-PV-based microgrids show similar features to conventional systems. However, PQDs in micro-grid applications are more challenging to identify than traditional power systems (Wang,2019). As with conventional systems, short circuit faults, switching of large, powerful loads and large capacitor banks, presence of drive systems, and transformers energization will lead to transients, sudden current/voltage rises, voltage fluctuations, harmonics, etc. in the micro-grid such as SOFC-PV-based systems. On the other hand, some situations cause PQDs specific to microgrids, such as enabling or disabling DGs, the presence of nonlinear loads, inverter control strategies, and operating mode switching. It is clear that the microgrid structure is the most crucial part of the smart grid, and it has become imperative to create a high accuracy PQD detection and classification method.

Conventional methods can be applied easily. They have many disadvantages, such as difficulty selecting threshold values, uncertainty caused by working conditions, involving undetected areas, and being easily affected by noise. Many signal processing-based (Khokhar, 2015) and artificial intelligence-based methods related to PQD detection and classification have been proposed in recent years, differing from conventional approaches to eliminate these disadvantages (Chawda, 2020) AI-based detection and classification methods for PQDs constituted of neural-network (NN)-based classifiers, support vector machine (SVM)-based classifiers, fuzzy expert system-based classifiers, decision tree (DT), random forest (RF) classifiers, and deep learning (DL)-based classifiers (Mishra, 2019). Some hybrid methods in literature have high accuracy, but they have no information about classification accuracy under low-level noise and high-level noise conditions. Also, utilizing many features can increase classification performance, but it also increases the computational time. Wavelet transform (WT) is used in many studies, but it has many deficiencies, especially in the analysis of noisy signals (Yılmaz, 2019). This shortcoming in the literature has been eliminated with the proposed UWT and GBDT-based hybrid method.

In this study, a new hybrid, UWT-based feature extraction method using a GBDT is proposed to classify PQDs in the Solid Oxide FC-based DG system (SOFCDG) grid-connected PV system-based microgrid. For the first time in

the literature, a UWT method was performed in SOFCDGs. The UWT technique was used to feature extraction of PQDs, and these events' features were obtained. The overall recognition test accuracy for the PQDs is 99.59% for the proposed UWT and GBDT-based hybrid method. The classification accuracy under low-level noise and high-level noise conditions is 99.50% and 99.29%, respectively. UWT-GBDT method produces reliable and easily usable results in the classification of PQDs in SOFC-PV-based microgrids.

II. SOFC and PV-based Test System and Proposed UWT-GBDT Method

The schematic view of the studied SOFC-PV-based microgrid has shown in Fig. 1. The system consists of a PV system, SOFCDG system, a delta/star connected step down two windings transformer, linear and nonlinear loads, capacitor bank, induction motor, and circuit breakers (CBs). Sags, swells, transients, harmonics, flickers, and notches are generated by these loads, such as a parallel RL load, capacitor bank, single-phase induction machine, and variable speed drive a three-phase induction motor. The simulated PQDs are shown in Tab. 1.

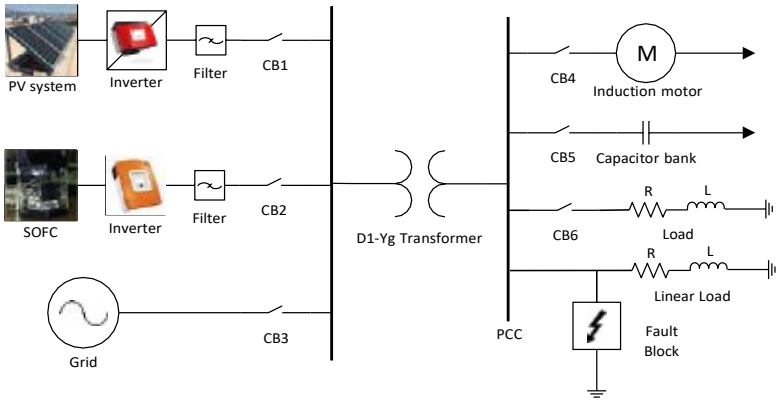


Fig. 1: SOFC-PV-based microgrid test system

Tab. 1: PQD signals

Class	PQD Signals	Class	PQD Signals
C1	Nominal	**C6**	Flicker
C2	Sag	**C7**	Oscillatory transient
C3	Swell	**C8**	Impulsive transient Spike
C4	Interruption	**C9**	Notch
C5	Harmonics		

In the proposed method, UWT coefficients are obtained by an 8-level decomposition method after pre-processing signals received from the point of common coupling (PCC). The average value, standard deviation, variance, entropy, and energy of each level coefficient obtained are calculated, and a feature dataset is created with these values calculated for all levels. Feature dataset used to train the GBDT. This process flowchart is shown in Fig. 2.

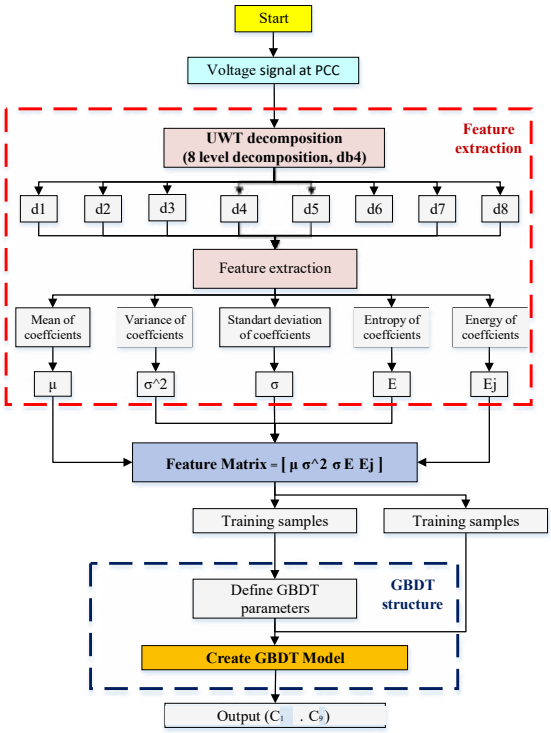


Fig. 2: Proposed UWT and GBDT-based method flowchart

III. Results

The test performance scores of the proposed method are given in Tab. 2. Various noise conditions are verified to verify the effect of the proposed hybrid UWT-GBDT under different noise levels. GBDT classifier gives successful results even in high noise PQD signals if the features obtained from UWT coefficients are used. The performances of the proposed UWT-based feature extraction process and the conventional discrete wavelet transform (DWT) method were also compared.

Tab. 2: Test Data Performance (% acc) of GBDT-based classifier

	Pure		30db		40db	
Classifier	**UWT**	**DWT**	**UWT**	**DWT**	**UWT**	**DWT**
GBDT	**99.59**	97.61	**99.29**	95.01	**99.50**	96.66

As shown in Tab. 3, the PQDs classification accuracy corresponding to the UWT and GBDT-based algorithm is higher than all the other investigated methods. The classification accuracy under low-level noise and high-level noise conditions is 99.50% and 99.29%, respectively, for the proposed method.

Tab. 3: Performance comparison of existing methods

Method	Accuracy (%)		
	Pure	40 dB	30 dB
EWT and SVM (Thirumala, 2019)	97.22 (25-55 dB mixed data)		
DWT and PNN (Khokhar, 2017)	**99.87**	98.6	95.2
Proposed method	99.59	**99.50**	**99.29**

V. Conclusions

In this study, a new hybrid, UWT-based feature extraction method using a GBDT is proposed to classify PQDs in the SOFC-PV-based microgrid. The performance of the GBDT, which is developed based on DWT but has low performance under noise, has been dramatically improved with UWT. The proposed method classification accuracy for PQDs under different noise levels and no noise conditions are higher than the other methods. As a result, the UWT and GBDT-based method are most suitable to classify PQDs in SOFCDGs.

References

Wang, F. C., Lin, K. M., Yang, Y. Z., & Liu, H. W., Fuel-cell sharing for a distributed hybrid power system, International Journal of Hydrogen Energy, 46(1), 1174-1187, (2021).

Lin, Rong-Heng, Ying-Ying Zhao, and Bu-Dan Wu., Toward a hydrogen society: Hydrogen and smart grid integration, International Journal of Hydrogen Energy 45.39: 20164-20175, (2020).

IEEE, IEEE recommended practice for monitoring electric power quality, IEEE Std 1159-2009 (Revision of IEEE Std 1159-1995) c1-8, (2009).

Wang, S., & Chen, H., A novel deep learning method for the classification of power quality disturbances using deep convolutional neural network, Applied Energy, 235, 1126-1140, (2019).

Khokhar, S., Zin, A. A. B. M., Mokhtar, A. S. B., & Pesaran, M., A comprehensive overview on signal processing and artificial intelligence techniques applications in the classification of power quality disturbances, Renewable and Sustainable Energy Reviews, 51, 1650-1663, (2015).

Chawda, G. S., Shaik, A. G., Shaik, M., Padmanaban, S., Holm-Nielsen, J. B., Mahela, O. P., & Kaliannan, P., Comprehensive review on detection and classification of power quality disturbances in utility grid with renewable energy penetration, IEEE Access, 8, 146807-146830, (2020).

Mishra, M., Power quality disturbance detection and classification using signal processing and soft computing techniques: A comprehensive review. International transactions on electrical energy systems, 29(8), e12008, (2019).

Yılmaz, A., & Bayrak, G., A real-time UWT-based intelligent fault detection method for PV-based microgrids. Electric Power Systems Research, 177, 105984, (2019).

Thirumala, K., Pal, S., Jain, T., & Umarikar, A. C., A classification method for multiple power quality disturbances using EWT-based adaptive filtering and multiclass SVM, Neurocomputing, 334, 265-274, (2019).

Khokhar, S., Zin, A. A. M., Memon, A. P., & Mokhtar, A. S., A new optimal feature selection algorithm for classification of power quality disturbances using discrete wavelet transform and probabilistic neural network, Measurement, 95, 246-259, (2017).

A Road Map to Ammonia Deployment as a Green Fuel in the Land Transportation Sector of Qatar

[1*]Mohammed Al-Breiki, [1]Yusuf Bicer
[1] Division of Sustainable Development (DSD), College of Science and Engineering (CSE), Hamad Bin Khalifa University (HBKU), Qatar Foundation (QF), Education City, Doha, Qatar
* E-mail:malbreiki@hbku.edu.qa

Abstract
Ammonia is more widely known for its potential global use as an essential fertilizer and cooling agent. However, new ammonia applications are currently being developed for heavy transport (shipping and aviation), road transport, electricity generation, and fuel supply. This work focuses on the employment of ammonia as a carbon-free fuel in the land transportation sector in Qatar. A roadmap is implemented based on 2°C degree increase of global temperature to limit the global warming. Generated emissions from the fossil fuel-based land transportation sector are estimated and compared with the transition to ammonia-fueled land transportation sector. Ammonia-fueled buses are the first vehicle types to be deployed in the land transportation. In contrast, small/medium cars take the most extended deployment duration from 2030 to 2050 due to technology readiness and social acceptance. Additionally, ammonia-fueled transportation modes reduce emissions by 80% in 2050, with an estimation of about 4.98 million tonnes of CO_2 eq.

Keywords: Carbon-free; Energy Carrier; Fuel; Renewable

I. Introduction

Ammonia and hydrogen have tremendous potential as carbon-free fuels for decarbonizing energy and transportation systems. Hydrogen has created significant expectations for a carbon-free economy, but storage, delivery, and infrastructure deployment problems have delayed its complete adoption. In contrast, ammonia is a highly effective energy vector with high energy density and presents a scalable and a stable infrastructure to mitigate the core disadvantages of hydrogen. These challenges and wide implementation of renewable energy sources have led to the exploitation of the transformation from fossil-fuels to ammonia as a next viable energy-generating fuel solution. In this respect, the transportation industry will benefit from ammonia-fueled internal combustion engines as one of the key reasons of carbon emissions. Thus, a need for a roadmap to deploy ammonia as a fuel for transportation modes is required for different regions of the world.

Several studies have been published related to the development of ammonia roadmaps. For example, the research was conducted to present a roadmap for the ammonia economy in (MacFarlane et al. 2020). The roadmap assessed three technologies for ammonia production: Haber-Bosch process using fossil fuel sources (Generation 1), Haber-Bosch process using renewable sources (Generation 2), and electrochemical processes (Generation 3). The roadmap also presented issues and challenges specifically for the electrochemical processes and their scale up. Ammonia utilization in marine engines, vehicle engines, power generators, gas turbines, and fuel cells is briefly discussed, followed by potential environmental impacts of an extraordinarily increased use of ammonia (MacFarlane et al. 2020). Another recent research was published related to the roadmap to the ammonia economy (Morlanés et al. 2021). The research presented possible utilization of ammonia either as a hydrogen carrier or direct utilization of ammonia. The study also included restrictions that prevent the development of a feasible ammonia-based energy system as a significant energy carrier, hence further effort is needed for the development of electrochemical ammonia production, and environmental impacts when using ammonia as a direct fuel in power generation systems (Morlanés et al. 2021).

As noticed in the literature, published roadmaps to the ammonia economy focus on ammonia production pathways and restrictions that prevent the development of the ammonia economy. Therefore, this study emphasizes implementing a practical ammonia roadmap to deploy ammonia as fuel in the land transportation sector to limit global warming targets to 2°C scenario.

II. Methodology

Deployment of ammonia in land transportation sector is driven by limiting global average temperature rise to 2°C. Thus, current emissions generated from land vehicles powered by fossil fuel (small/medium car, trailer, motorcycle, buses, and heavy equipment and machinery) will be estimated and then compared with generated emissions when ammonia is deployed as fuel in these vehicles. Deployment of ammonia as a fuel in each vehicle type will be implemented based on technology readiness level, availability of feedstock, and social acceptance.

Since Qatar is taken as a case study, all the required data to implement the ammonia roadmap will be taken from Qatar. Therefore, vehicle types and the total number of vehicles are estimated from Planning and Statistics Authority in Qatar (Transport and Communication Statistics 2019). Ammonia deployment is run from 2021 until 2050. Therefore, the rate of increase in Qatar's number of vehicles is accounted for, in addition to other policies including deployment of electric car in the transportation sector in Qatar. For example, it is planned to have 10% electric vehicle of all vehicles in Qatar by 2030.

Produced greenhouse gas emissions, based on GHG-10, from the vehicles powered by fossil fuel in Qatar are calculated by knowing the paid emission rate for each vehicle type (kg/ton). The emissions rates for

small/medium cars, trailers, motorcycles, buses, and heavy equipment and machinery are determined using the Greenhouse Gases, Regulated Emissions, and Energy Use in Technologies Model (GREET) software. Argonne National Laboratory develops GREET to estimate emissions from transportation modes (Argonne National Laboratory 2012). The total emissions without the use of ammonia in the Qatari land transport sector will be presented. The roadmap of ammonia deployment in each transportation mode is dependent on technology readiness level, availability of feedstock, and social acceptance.

III. Results and Discussion

The roadmap provides a systemic view of ammonia technology's potential as an energy vector for various road transport applications. The perspective is optimistic yet practical. It does not focus on unknown technological advances but on systems that show their feasibility. This is not about imaginary solutions but the scaling of current systems and the valuable linkage and virtue of ammonia technology in the energy sector. It also does not encourage ammonia but finds it along with other low-carbon technologies as a winner-taking option. To realize this vision, active use of technology is necessary.

Currently, land transportation modes in Qatar are small/medium car, trailer, motorcycle, buses, and heavy equipment and machinery. The number of small and medium vehicles in Qatar is dominating, and they are fueled by gasoline and diesel, which increase the global warming. Table 1 presents estimated emissions in 2021, 2030, and 2050 from the transportation modes driven by fossil fuels and ammonia in Qatar.

Table 1: Transportation modes statistics in Qatar and generated emissions while the use of fossil fuel and ammonia fuel

Vehicle statistics in Qatar			**CO_2 eq. emissions (mT) with fossil fuel deployment**			**CO_2 eq. emissions (mT) with ammonia deployment**		
Type of Vehicle	Number (Transport and Communication Statistics 2019)	Current Emission Rate (ton/year) (Argonne National Laboratory 2012)	2021	2030	2050	2021	2030	2050
Small/Medium Car	1455280	3.8	5.53	6.03	7.18	5.53	6.03	4.98
Trailer	46217	46.23	2.14	2.34	2.76	2.14	2.14	0.00
Motorcycles	26233	6.295	0.17	0.32	0.62	0.17	0.32	0.00
Buses	2900	22.48	0.07	0.07	0.08	0.07	0.06	0.00
Heavy Equipment and Machinery	125070	8.8	1.10	1.17	1.32	1.10	1.06	0.00
Total Emissions (mT)			9.00	9.93	**11.97**	9.00	9.61	**4.98**

The total generated emissions from transportation modes increase about 33% in 2050 even though 10% of small/medium electric cars are included in 2030. This indicates that employment of carbon-free fuels is necessary to reach to 2°C target especially in the land transportation sector. In this work, ammonia is proposed to be used as fuel for transportation modes. No carbon emissions are generated when combusting ammonia. Possible produced noxious as a result of incomplete combustion of ammonia can be treated before it is sent to the atmosphere similar to selective catalytic reduction currently in use.

Employment of ammonia as fuel is implemented for each type of vehicle-based on technology readiness level and availability of feedstock. Currently, the technology readiness level (TRL) for ammonia fueled engine is (4 – 5), which is at the technology development level (IEA 2020). Ammonia production capacity in Qatar is about 3.7 mT, and an increase in ammonia production capacity is estimated to be 2% per year from the year 2020-2050 (Trevor 2018). In road transportation, ammonia-powered engines are currently or will be eligible for commercial use in medium and large cars, busses, motorcycles within the coming years. For these segments, fuel cell vehicles (FCVs) best follow the criteria for efficiency and convenience. In the next wave, prices are expected to fall, enabling ammonia to operate in some segments including smaller cars. Therefore, deployment roadmap of ammonia as a fuel in variety of transportation modes based on the previous parameters is demonstrated in Fig. 1.

Buses used for public transport are owned and operated by the State of Qatar under an enterprise called Karwa. These buses are stationed in specific locations in Qatar, which can support fueling the buses efficiently. Thus, buses are estimated as the first vehicle type to use ammonia as fuel. The employment duration of fueled ammonia buses starts from 2021 to 2030. After the year 2030, it is considered that all buses in Qatar are fueled by ammonia. The same approach is used for other transportation modes. Gradual employment of small/medium fueled ammonia cars start from the year 2030 until 2050. Employment of ammonia in these transportation modes results in the reduction of emissions by 80% in 2050. The generated emissions from the land transportation sector are about 4.98 mT which allows reaching 2°C targets. In comparison, greenhouse gas emissions in the land transportation sector are estimated to increase by 25% in 2050 reaching 11.97 mT compared to generated emissions in 2021, estimated to be 8.99 mT.

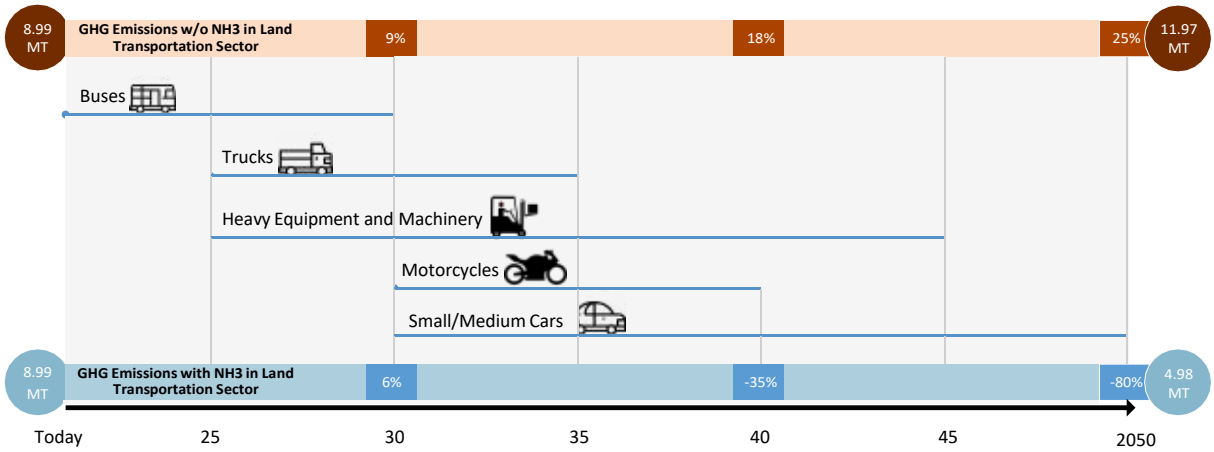


Fig. 1: Ammonia deployment roadmap in the land transportation modes in Qatar

V. Conclusions

A roadmap of deployment of ammonia as fuel in the land transportation sector in Qatar is presented to limit global warming to 2°C targets. Small/medium cars, trailers, motorcycles, buses, and heavy equipment and machinery are the land transportation modes used in this study. Estimated emissions from these modes are determined and then compared to estimated emissions when ammonia is deployed as a fuel. Employment of ammonia in each transportation mode is dependent on technology readiness level, feedstock availability, and social acceptance. Buses and trucks are considered to be the first transportation modes to deploy ammonia in their combustion engines due to easiness in the fueling infrastructure in specific locations. In contrast, small/medium cars take the most extended duration due to social acceptance and a low technology readiness level.

Acknowledgments

The authors acknowledge the support provided by the Hamad Bin Khalifa University, Qatar Foundation, Qatar (210009034)

References

Argonne National Laboratory. 2012. “Argonne GREET Model Webpage.” http://greet.es.anl.gov/.

IEA. 2020. “ETP Clean Energy Technology Guide.” *International Energy Agency*. https://www.iea.org/articles/etp-clean-energy-technology-guide.

MacFarlane, Douglas R. et al. 2020. “A Roadmap to the Ammonia Economy.” *Joule* 4(6): 1186–1205.

Morlanés, Natalia et al. 2021. “A Technological Roadmap to the Ammonia Energy Economy: Current State and Missing Technologies.” *Chemical Engineering Journal* 408.

Transport and Communication Statistics. 2019. Doha. https://www.psa.gov.qa/en/statistics/StatisticalReleases/Economic/TransportCommunications/2019/10_Transport_and_Communication_AE_2019.pdf.

Trevor, Brown. 2018. “What Drives New Investments in Low-Carbon Ammonia Production? One Million Tons per Day Demand - Ammonia Energy Association.” *Ammonia Energy Association* . https://www.ammoniaenergy.org/articles/what-drives-new-investments-in-low-carbon-ammonia-production-one-million-tons-per-day-demand/ (April 18, 2021).

Local Green Hydrogen Production Potentials for Turkey with Solar Energy

[1] Gorkem Kubilay Karayel, [1*]Nader Javani, [2,1] Ibrahim Dincer,
[1] Faculty of Mechanical Engineering, Yildiz Technical University, Besiktas, Istanbul, Turkey
[2]Faculty of Engineering and Applied Science, University of Ontario Institute of Technology, Oshawa, Ontario, Canada
E-mail: njavani@yildiz.edu.tr

Abstract
The transition to renewable energy systems requires alternative energy sources and well-established energy storage and distribution systems. The current study investigates the renewable-based hydrogen production potential in Turkey, based on the provided official data. Solar energy, which is a principal renewable energy source, is considered for this purpose. For the photovoltaic systems, mono and polycrystalline solar cells are considered and the transmitted electric energy is directed to an electrolyser. The output of generated hydrogen is described in detail for each region in Turkey, showing a clear picture of possibly solar-driven hydrogen generation potentials. This, in turn, can be considered in the context of the current policies for the energy supply of the country.

Keywords: Alkaline Electrolyser, Green hydrogen, Solar energy, Solar panel

Introduction

The switch to renewable energy for a sustainable future is unavoidable. To pave the road for this transition, the produced energy should be stored or transported properly (Vivas et al (2018)). Green hydrogen is considered a promising solution for improving renewable energy generation. In line with the growing renewable energies market in Turkey, Dincer et al (2021) proposed a road map for hydrogen energy technology development in Turkey. There are different methods for hydrogen production including electrolysis, photoelectrolysis, and thermochemical water splitting and renewable sources (Nikolaidis and Poullikkas (2017)). Among the renewable energy sources, solar energy has a high potential in Turkey which is the sunniest country in Europe as announced by European Comission (2021). The main idea of the current research is to show Turkey's hydrogen potential based on the solar energy intensity in different regions of the country. It is also expected that the presented results can be exploited in designing the energy supply network of the country, with an emphasis on hydrogen technology.

System Description and Analysis Procedure

Electrolysis is an easily applicable industrial approach for producing pure hydrogen. Water electrolysis is based on the movement of electrons, which are supported by an external circuit (Godula-Jopek (2015)). Alkaline, solid oxide (SOE) and polymer membrane (PEM) are among the most common electrolysis types for hydrogen production. Table 1 gives the specifications and differences among these three types of electrolysis as considered for the study..

Tab.1. Typical specifications of alkaline, polymer membrane (PEM), and solid oxide electrolyser (SOE)

Specification	Alkaline	PEM	SOE
Cell temperature, °C	60-80	50-80	900-1000
Cell pressure, bar	<30	<30	<30
Current density, A/cm²	0.2-0.4	0.6-2.0	0.3-1.0
Cell voltage, V	1.8-2.4	1.8-2.2	0.95-1.3
Power Density, W/cm²	Up to 1.0	Up to 4.4	-
Specific system energy consumption, kWh/Nm³	4.5-7.0	4.5-7.5	2.5-3.5
Hydrogen production, Nm³/h	<760	<300	-
System lifetime, yr	20-30	10-20	-
Hydrogen purity, %	>99.8	>99.999	-

In the current study, an alkaline electrolyser with an efficiency of 70% have been considered for hydrogen production. Turkey's average solar radiation changes between 1400 to 2000 KWh/m²year as announced by the Ministry of Energy and Natural Resources of Turkey (2021). From North to South of the country, this value increases. Sunny hours are also known as sunbathing hours differs from 4 to 12 hours a day, depending on the season. In this study, two main types of photovoltaic, namely monocrystalline and polycrystalline solar panels are taken into account with 15% and 20% efficiencies, respectively.

Solar power produced from a 100-m² area for both mono and polycrystalline PV panels is considered in the calculations. A total of 117,650 kJ energy is required to produce 1 kg hydrogen from the electrolysis. Likewise, the efficiency of the electrolyser is considered as 70%. Consequently, the required energy would be calculated as follows:

$$W_{actual} = \frac{117{,}650\ kJ}{0.7} = 168{,}071\ kJ \quad (1)$$

Subsequently, solar power output based on the monocrystalline PV panels is used as the input energy for the alkaline electrolyser. Following the solar energy potential calculations for all cities, the output electric power is used as a power source for alkaline electrolyser's to produce hydrogen. The solar irradiation data is taken from the Ministry of Energy and Natural Resources.

Results and Discussion

The produced green hydrogen potential in Turkey, using solar energy potential is listed in Table 2.

.

Table 2. Solar radiation and photovoltaic electricity production

No.	City	Solar Panels Output Power (kWh-yr/100m²)	Hydrogen Production (kg)	No.	City	Solar Panels Output Power (kWh-yr/100m²)	Hydrogen Production (kg)
1	Adana	22000-26000	471-557	41	Kocaeli	19000-22000	407-471
2	Adıyaman	23000-27000	493-578	42	Konya	24000-27000	514-578
3	Afyon	22000-26000	471-557	43	Kütahya	22000-25000	471-535
4	Ağrı	23000-26000	493-557	44	Malatya	24000-27000	514-578
5	Amasya	20000-23000	428-493	45	Manisa	22000-25000	471-535
6	Ankara	21000-25000	450-535	46	Maraş	24000-27000	514-578
7	Antalya	24000-27000	514-578	47	Mardin	23000-26000	493-557
8	Artvin	21000-23000	450-493	48	Muğla	24000-27000	514-578
9	Aydın	23000-26000	493-557	49	Muş	23000-27000	493-578
10	Balıkesir	21000-24000	450-514	50	Nevşehir	23000-26000	493-557
11	Bilecik	21000-24000	450-514	51	Niğde	24000-27000	514-578
12	Bingöl	23000-27000	493-578	52	Ordu	20000-23000	428-493
13	Bitlis	24000-27000	514-578	53	Rize	21000-23000	450-493
14	Bolu	21000-24000	450-514	54	Sakarya	19000-22000	407-471
15	Burdur	24000-27000	514-578	55	Samsun	19000-22000	407-471
16	Bursa	21000-23000	450-493	56	Siirt	23000-27000	493-578
17	Çanakkale	20000-23000	428-493	57	Sinop	19000-22000	407-471
18	Çankırı	21000-24000	450-514	58	Sivas	22000-26000	417-557
19	Çorum	21000-24000	450-514	59	Tekirdağ	19000-22000	407-471
20	Denizli	23000-27000	493-578	60	Tokat	21000-24000	450-514
21	Diyarbakır	22000-25000	471-535	61	Trabzon	20000-23000	428-493
22	Edirne	19000-22000	407-471	62	Tunceli	23000-26000	493-557
23	Elazığ	24000-27000	514-578	63	Urfa	23000-26000	493-557
24	Erzincan	23000-26000	493-557	64	Uşak	22000-26000	417-557
25	Erzurum	22000-26000	471-557	65	Van	24000-27000	514-578
26	Eskişehir	22000-25000	471-535	66	Yozgat	22000-25000	471-535
27	Gaziantep	23000-26000	493-557	67	Zonguldak	19000-22000	407-471
28	Giresun	21000-24000	450-514	68	Aksaray	23000-26000	493-557
29	Gümüşhane	22000-25000	471-535	69	Bayburt	22000-26000	417-557
30	Hakkari	24000-27000	514-578	70	Karaman	24000-28000	514-600
31	Hatay	24000-27000	514-578	71	Kırıkkale	21000-25000	450-535
32	Isparta	24000-27000	514-578	72	Batman	23000-26000	493-557
33	Mersin	24000-27000	514-578	73	Şırnak	24000-27000	514-578
34	Istanbul	19000-22000	407-471	74	Bartın	19000-22000	407-471
35	Izmir	22000-25000	471-535	75	Ardahan	22000-25000	471-535
36	Kars	22000-25000	471-535	76	Iğdır	22000-25000	471-535
37	Kastamonu	20000-23000	428-493	77	Yalova	19000-23000	407-493
38	Kayseri	24000-27000	514-578	78	Karabük	20000-23000	428-493
39	Kırklareli	19000-22000	407-471	79	Kilis	23000-26000	493-557
40	Kırşehir	22000-25000	471-535	80	Osmaniye	23000-26000	493-557
				81	Düzce	20000-23000	428-493

Conclusions

The process to switch from fossil fuels to renewable energies is an irreversible process. Turkey also has to invest in this sector, using its renewable energy resources. Possessing a high potential for solar energy makes this transition possible for the country. The results of the current study show that solar energy potentials are alluring for hydrogen production in different regions of Turkey. Data is taken from the Turkish Government's official commentary. Monocrystalline solar panels with an efficiency of 20% provide the required electricity to be used by the electrolyser for hydrogen production. Results of this study show the hydrogen production range by using solar energy for different locations. This, in turn, can be a deterministic point of view for different sectors, involved with the energy profile of the country.

References

Dıncer I., Eroglu I., Ozturk M., Hydrogen Technologies Road Map for Turkey, Hydrogen Technologies Association, Istanbul, (2021)

European Commission, Meteorological data from ECMWF models, Retrieved date 01.05.2021, from https://marswiki.jrc.ec.europa.eu/agri4castwiki/index.php/Meteorological_data_from_ECMWF_models

Godula-Jopek A. Hydrogen Production by Electrolysis. Germany: Wiley-VCH, (2015)

Ministry of Energy and Natural Resources, Renewable Energy General Directorate, Retrieved date: 01.05.2021, from gepa.energy.gov.tr/MyCalculator

Nikolaidis P., Poullikkas A. A comparative overview of hydrogen production processes, Renewable and Sustainable Energy Reviews, 67, 597-611, (2017)

Vivas, F.J., De las Heras, A., Segura, F. Andújar, J.M., A review of energy management strategies for renewable hybrid energy systems with hydrogen backup. Renewable and Sustainable Energy Reviews, 82, 126-155, (2018)

Effect of Anode Functional Layer Material on the Performance of Anode Supported Micro-tubular SOFCs

[1, 2*]Cigdem Timurkutluk, [3]Keremhan Bilgil, [3]Ali Celen, [1, 4]Sezer Onbilgin, [1, 4]Tolga Altan and [4,5]Ugur Aydin

[1] Nigde Omer Halisdemir University Prof. Dr. T. Nejat Veziroglu Clean Energy Research Center, 51245, Nigde, Turkey
[2] Nigde Omer Halisdemir University Department of Energy Science and Technologies, 51245, Nigde, Turkey
[3] Erzincan Binali Yildirim University, Department of Mechanical Engineering, Erzincan 24100, Turkey
[4] Nigde Omer Halisdemir University, Mechanical Engineering Department, 51245, Nigde, Turkey
[5] Vestel Defense Industry, Titanium Block 17/B, ODTU, Teknokent, 06800 Ankara, Turkey

* E-mail: cigdemtimurkutluk@ohu.edu.tr

Abstract
In this study, anode supported micro-tubular solid oxide fuel cells are fabricated by extrusion method and the effect of anode functional layer material on the electrochemical performance is experimentally investigated. For this purpose, four different commercial NiO powders are tested as anode functional layer. The performance tests are performed at an operating temperature of 800°C under hydrogen and air. The maximum power density of 0.41 W/cm^2 is obtained from the cell having an anode functional layer prepared by J.T. Baker powders. In addition to the performance tests, electrochemical impedance spectroscopy measurements are conducted. It is seen that the same cell has the minimum total polarization resistance compared to those of others.

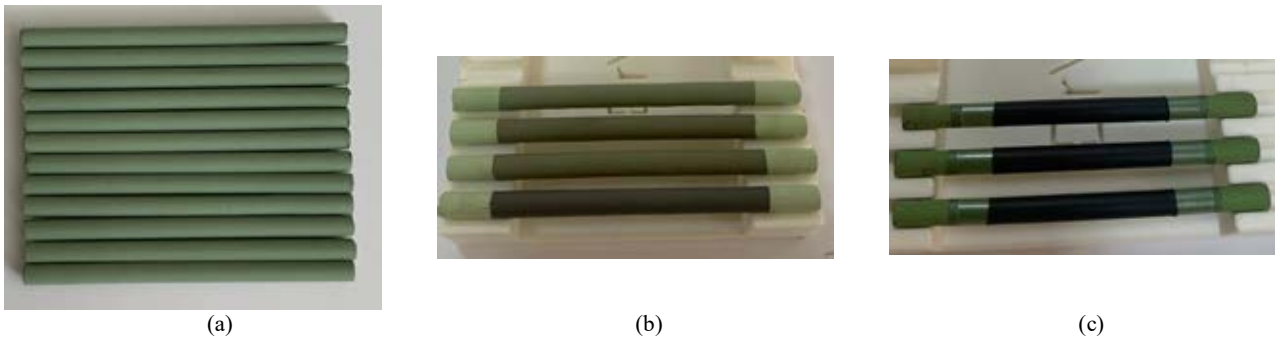
Keywords: Solid oxide fuel cell; Micro-tubular; Anode supported; Extrusion.

I. Introduction

Solid oxide fuel cells (SOFCs) are one of the promising fuel cell types because of their high efficiency and fuel flexibility. They can also be considered as noiseless energy conversion devices as other fuel cells since there are no moving parts required for the electricity generation. SOFCs are generally classified in two groups according to the geometry, which are planar and tubular. Since tube diameter has a significant effect on the cell performance, tubular SOFCs are also classified by considering tube diameter. The tubular SOFCs having diameter lower than or almost equal to 5 mm are called micro-tubular SOFCs. The concept of micro-tubular SOFCs was firstly proposed by Kendall (2010) and some studies on this subject have been performed by many researchers such as Chen et al. (2011), Monzón et al. (2014), Jamil et al. (2015), Mat et al. (2016), Timurkutluk et al. (2018) and Timurkutluk et al. (2020). In application, micro-tubular SOFCs offer some advantages such as fast start-up and higher thermal shock resistance compared to planar ones. Generally, the anode support layer of micro-tubular SOFCs is manufactured by extrusion method. These tubes are subjected to sintering process and they are coated by electrolyte and cathode layers in an order by means of dip coating followed by sintering. In this study, anode supported micro-tubular SOFCs are fabricated by using extrusion method and the effect of the powder type commercially available used in the anode functional layer on the cell performance is experimentally investigated. Beside the performance and empedance measurements, the microstructures of the cells are also visualized by scanning electron microscope (SEM).

II. Fabrication of micro-tubes

In order to manufacture anode support micro-tubes, commercial NiO (NiO-A, Novamet, New Jersey, USA) and YSZ (Tosoh, Tokyo, Japan) powders were mixed with some amounts of dispersant (fish oil) and solvent (methyl ethyl ketone and ethanol). The mixture ball milled for 24 hours and suitable amounts of binder (butvar) and plasticizer (polyethylene glycol) were then added. After the second ball milling stage, the slurry stirred for 3 hours by means of a magnetic stirrer. The final slurry which had desired viscosity was obtained by adding appropriate amounts of stearic acid and paraffin wax. Next, an extrusion machine with a die having an outer/inner diameter of 5.25/4 mm is used for the extrusion of the slurry and extruded anode support tubes were dried during 2 hours in air atmospheric conditions.



(a) (b) (c)

Fig. 1: The fabricated anode supported micro-tubular cells (a) anode support micro-tubes, (b) anode functional layer coated micro-tubes before sintering, (c) cathode layer coated micro-tubes

Later, they were sintered at a temperature of 1400ºC for 4 h. Anode support micro-tubes are given in Fig. 1(a). Similarly, anode functional layer (AFL) was dip-coated by using four different commercial NiO powders, i.e. NiO (Fisher Chemical), NiO (J. T. Baker), NiO (Novamet) and NiO (Fuel Cell Materials). Fig. 1 (b) illustrates AFL coated microtubes before sintering at a temperature of 1100 ºC. Finally, YSZ electrolyte and LSM-YSZ cathode layers were produced by again dip-coating method followed by sintering. The electrolyte layer was sintered at the temperature of 1400°C during 4h whereas the sintering of the cathode layer was achieved at 1100°C during 2h. The final anode supported micro-tubular cells can be seen in Fig. 1(c). The performance of the cells is measured at an operating temperature of 800 °C under hydrogen (0.6 NL/min) and air (1.2 NL/min). The impedance data is also obtained just after the performance measurements. The microstructures of the cells are also determined via SEM.

III. Results and discussions

SEM images of the fabricated anode supported micro-tubular cells are presented in Fig. 2. All fabricated cells have almost the same anode functional layer thickness and a good adhesion between all layers is ensured without any delamination or crack. Since the cells with Novamet powders were damaged after the cathode sintering stage, they could not be tested.

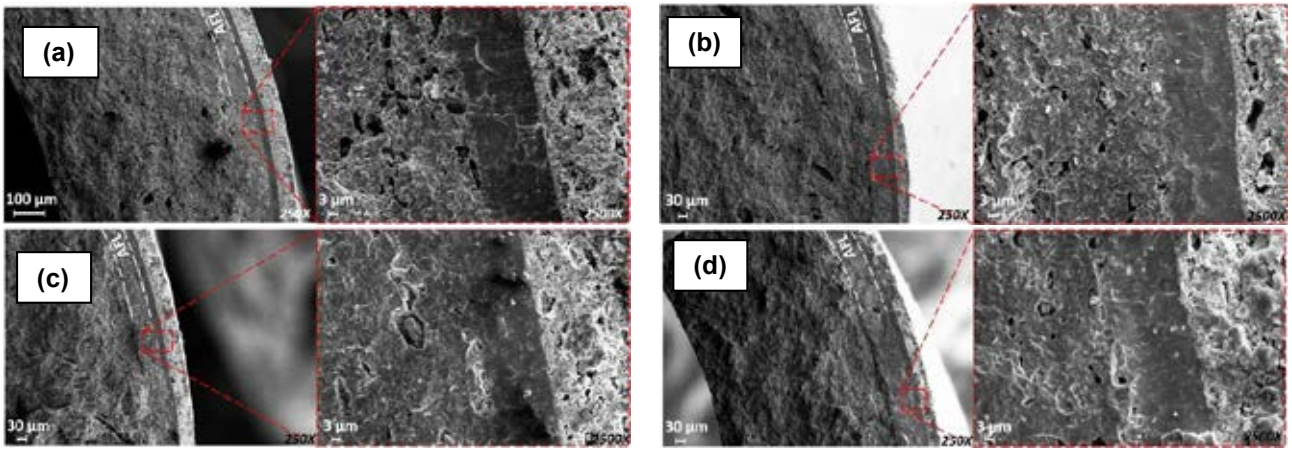


Fig. 2: SEM images of fabricated anode supported micro-tubular cells having anode functional layer material of (a) Fisher Chemical, (b) J.T. Baker, (c) Novamet and (d) Fuel Cell

The performance of the micro-tubular cells with various AFL powders is compared in Fig. 3. It can be seen that the maximum power densities are obtained as 0.41 W/cm^2, 0.37 W/cm^2 and 0.34 W/cm^2 from the cell having J.T. Baker, Fisher Chemical and Fuel Cell NiO powders, respectively. This result reveal that relatively high number of triple-phase boundaries are achieved with J.T. Baker NiO in the anode functional layer. Moreover, it is observed that the anode functional layer material has not a significant effect on the open circuit potential although the electrolyte layer is coated on this layer.

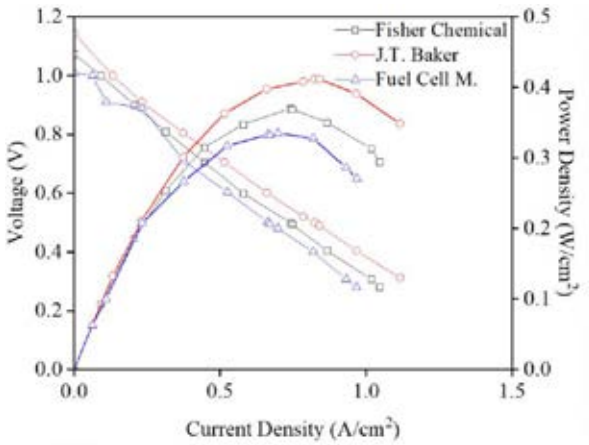


Fig. 3: The effect of anode functional layer material type on micro-tubular cell performance

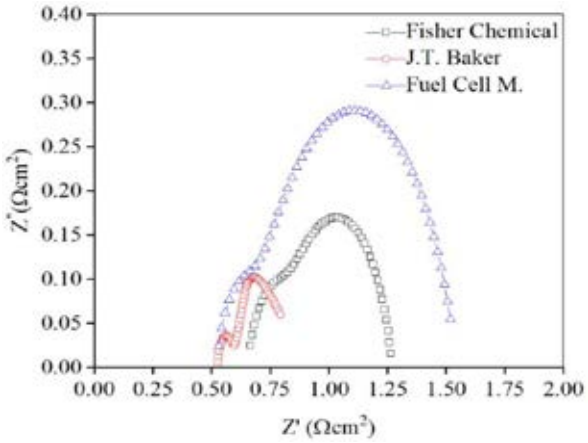


Fig. 4: Electrochemical impedance spectroscopy results for fabricated micro-tubular cells

Fig. 4 compares impedance spectroscopy results of the micro-tubular cells under the open circuit voltage at 800°C. The overall polarization resistance of micro-tubular cell having J. T. Baker NiO is found to be lower than that of the other ones, confirming the performance measurements.

IV. Conclusions

In this study, the influence of anode functional layer material on the performance of anode supported micro-tubular SOFCs is experimentally investigated. Among the cases considered, the cell fabricated with commercial NiO powders in the anode functional layer provided by J.T. Baker exhibits the highest power density of 0.41 W/cm^2. The improved performance is attributed to the increased TPB length as confirmed by the impedance tests.

References

Chen, C., Liu, M., Yang, L., Liu, M., Anode-supported micro-tubular SOFCs fabricated by a phase-inversion and dip-coating process, International Journal of Hydrogen Energy, 36(9), 5604-5610, (2011).

Jamil, S. M., Othman, M. H. D., Rahman, M. A., Jaafar, J., Ismail, A. F., Li, K., Recent fabrication techniques for micro-tubular solid oxide fuel cell support: A review, Journal of the European Ceramic Society, 35(1), 1-22, (2015).

Kendall, K., Progress in microtubular solid oxide fuel cells, International Journal of Applied Ceramic Technology, 7(1), 1-9, (2010).

Mat, A., Canavar, M., Timurkutluk, B., Kaplan, Y., Investigation of micro-tube solid oxide fuel cell fabrication using extrusion method, International Journal of Hydrogen Energy, 41(23), 10037-10043, (2016).

Monzón, H., Laguna-Bercero, M. A., Larrea, A., Arias, B. I., Várez, A., Levenfeld, B., Design of industrially scalable microtubular solid oxide fuel cells based on an extruded support, International Journal of Hydrogen Energy, 39(10), 5470-5476, (2014).

Timurkutluk, B., Timurkutluk, C., Toros, S., Kaplan, Y., Influence of sintering support design on the properties of NiO-YSZ anode support micro-tubes, Ceramics International, 44(5), 5587-5593, (2018).

Timurkutluk, C., Timurkutluk, B., Kaplan, Y., Experimental optimization of the fabrication parameters for anode-supported micro-tubular solid oxide fuel cells, International Journal of Hydrogen Energy, 45(43), 23294-23309, (2020).

Fabrication of micro-tubular solid oxide fuel cells by tape casting method

[1, 2*] Tolga Altan, [1,3] Cigdem Timurkutluk, [1, 2] Bora Timurkutluk, [1, 2] Selahattin Celik
[1] Nigde Omer Halisdemir University Prof. Dr. T. Nejat Veziroglu Clean Energy Research Center, 51245, Nigde, Turkey
[2] Nigde Omer Halisdemir University, Mechanical Engineering Department, 51245, Nigde, Turkey
[3] Nigde Omer Halisdemir University Department of Energy Science and Technologies, 51245, Nigde, Turkey

* E-mail: tolgaaltan@ohu.edu.tr

Abstract
In this study, micro-tubular solid oxide fuel cells are produced with two different methods, i.e. conventional extrusion and newly proposed tape casting. The mechanical properties of the cells produced by standard extrusion and tape casting method are experimentally investigated and the results are compared. Measured flexural strengths values of cells via three-point bending reveal that micro-tubular anode supports fabricated by tape casting exhibit ~64% higher flexural strength than those manufactured by the common extrusion method.

Keywords: SOFC, micro-tubular, tape casting, extrusion, method comparison.

I. Introduction

Solid oxide fuel cells (SOFCs) can be produced in many different geometries and designs compared to other fuel cells due to the use of solid material in all cell components. Many geometries and designs are suggested in the literature, but common geometries are planar and tubular cells. Recently, tubular cells having 5 mm or less in diameter have been taken great attention since the cell performance is inversely related to the tube diameter. This geometry is known as micro-tubular and was first introduced by Kendall (1992). There can be found several studies on the micro-tubular SOFCs in the literature (Monzón et al., 2014; Suzuki et al., 2009; Sumi et al., 2012; Timurkutluk et al., 2020). Micro-tubular cells have many advantages over planar cells like higher thermal shock resistance due to their cylindrical structure, enabling fast start-up which is crucial for mobile applications. However, one of the advantages of planar cells over micro-tubes is that they can be produced with standard and easy production methods such as tape casting and screen printing. In this respect, planar SOFCs can offer time and cost-effective production. For micro-tubular SOFCs, on the other hand, the extrusion is method is frequently employed to fabricate the support layer, while other layers are coated by dip coating in general. In this study, to the best knowledge of the authors, the tape casting method is proposed to fabricate anode support micro-tubes as an alternative method to extrusion first time in the literature. The mechanical properties of the anode support micro-tubes produced by standard extrusion and tape casting method are experimentally investigated. The porosities of the support tubes are also determined by Archimedes method. In addition, micro-tubular single cells are fabricated and, their electrochemical performances are measured and compared.

II. Fabrication of micro-tubes

In this study, micro-tubes were produced by extrusion and tape casting. The production steps for both methods are shown in Fig.1 for comparison. It is seen that there are many similarities between them.

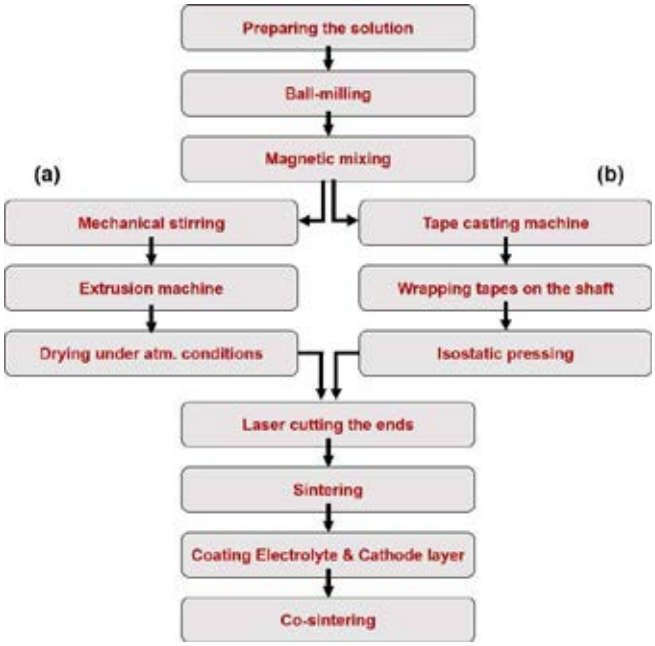


Fig. 1: Micro-tubular cell production steps: (a) extrusion (b) tape casting

To prepare the extrusion/tape casting slurry of anode support micro-tubes, commercially available NiO (NiO-A, Novamet, New Jersey, USA) and YSZ (Tosoh, Tokyo, Japan) powders were mixed with appropriate amounts of solvent (methyl ethyl ketone and ethanol) and dispersant (fish oil). After 18 hours of ball milling with zirconia balls, suitable amounts of binder (butvar) and plasticizer (polyethylene glycol) were added. At the end of the other ball milling process for 18 hours, the slurry was moved to a magnetic stirrer and stirred for 3 h. After this step, two different routes were followed for the extrusion and tape casting method. For the extrusion method, a transmission-type mechanical mixer was used to obtain the final slurry viscosity by adding proper amounts of paraffin wax and stearic acid. Then the slurry was extruded by an extrusion machine with a die having an inner and outer diameter of 4 mm and 5.25 mm, respectively. Extruded microtubes were dried in air atmosphere for 2 hours. For the tape casting method, after the magnetic stirrer step, the slurry was cast into tapes with a doctor blade gap of 300 µm thickness. Next, the tapes were simply wrapped on the shaft with a desired thickness. Although any shaft size can be selected, for an accurate comparison 4 mm diameter shaft was selected in this study which is the same as the inner diameter of the die used in the extrusion process. Then the structure was laminated under an isostatic pressure of 70 MPa for 4 min. Finally, the anode support was obtained by removing the laminated tapes from the shaft. The sintering of the anode support micro-tubes prepared by extrusion and tape casting is achieved at 1400 °C for 4 h. These structures are subjected to three-point bending tests to evaluate their flexural strengths. In addition, full cells are fabricated after coating of NiO-YSZ anode functional, YSZ electrolyte and LSM-YSZ cathode layers by dip-coating method in an order followed by sintering. In this respect, anode functional and electrolyte layers are co-sintered at 1400°C for 4h, while the cathode is sintered at 1000 °C for 2h. Fig.2 shows the micro-tubes produced by both methods. It is seen that neither crack nor warpage is available.

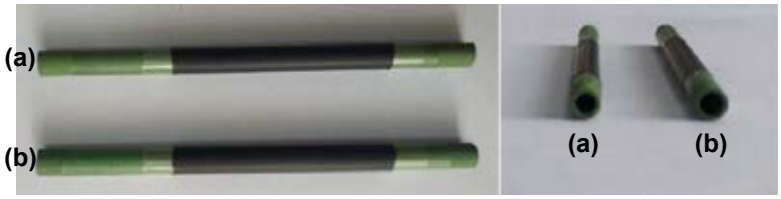


Fig. 2: Photos of the produced micro-tubular cells: (a) extrusion (b) tape casting

III. Results and discussions

The microstructures of anode support micro-tubes fabricated by tape casting are investigated by scanning electron microscopy. For these tubes, it is important to have a fully laminated structure without any delamination. It can be seen in Figure 3 that there is good adhesion without any delamination at the interfaces. Also, for both methods, anode support porosity measurement was performed by Archimedes method. They exhibit very close open porosity values such that the open porosity of the unreduced anode supports was measured as 22.6% for extrusion and 21.1% for tape casting.

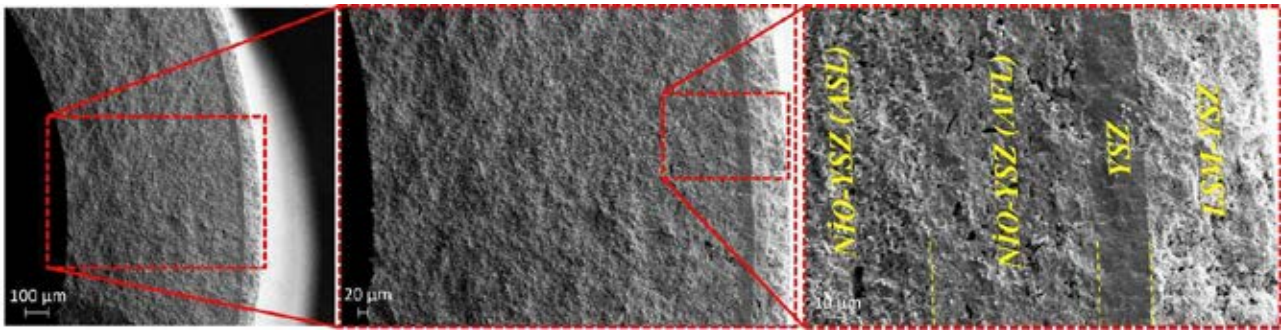


Fig. 3: SEM images of tape casting micro-tubular cell

The three-point bending test can be used to evaluate both the ductility and strength of materials. The flexural strengths of the anode support micro-tubes are measured via three-point bending test to compare the influence of the production method on the mechanical properties of anode support micro-tubes. The details of the test apparatus can be found elsewhere (Timurkutluk et al., 2018). The radius of the support and loading cylinder is 15 mm and 5 mm respectively. The distance between the support cylinders is adjusted to 50 mm and the specimen length is enough (64 mm) for overhanging on each end of the support span. The speed of the loading cylinder is set to 1 mm/min and deflection values are measured until the fracture occurs. Analysis of 15 samples prepared by both methods to increase the reliability of the test results was performed. The reliability curves of the flexural strength data are also obtained via two-parameter Weibull distribution method (Weibull, 1951). The results are shown in Figure 4. It is found out that NiO-YSZ anode support micro-tubes manufactured by the tape casting method suggested in this study provide relatively higher flexural strength values at all reliability values. The average flexural strength at a reliability of 70 % is measured as 149.18 MPa and 244.03 MPa for the extruded and tape cast samples, respectively. The improvement in the flexural strength, despite the similar porosity values and composition used, can be attributed to the compactness and better adhesion provided by isostatic pressing.

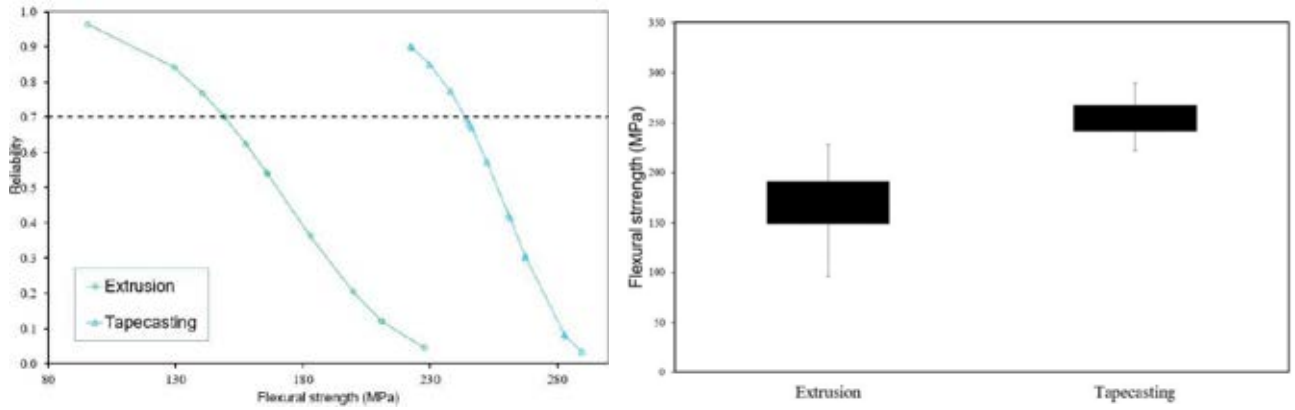


Fig. 4: Mechanical properties of fabricated micro-tubular cells: (a) the reliability plots of the flexural strengths measured and (b) the measured flexural strengths of the micro-tubes.

The performance comparison of the micro-tubular SOFCs at an operating temperature of 800 °C is depicted in Fig.5. The peak performances seem to be relatively lower than those of similar reports in the literature. This behaviour is found reasonable since no structural or compositional optimization was performed in this study. It is also seen that the cell, whose anode support layer was fabricated by tape casting, shows slightly lower performance than that of the cell manufactured by extrusion. This small difference is explained by the relatively lower porosity of the anode support layer in the tape cast samples, which may lead to an increase in the gas diffusion resistance.

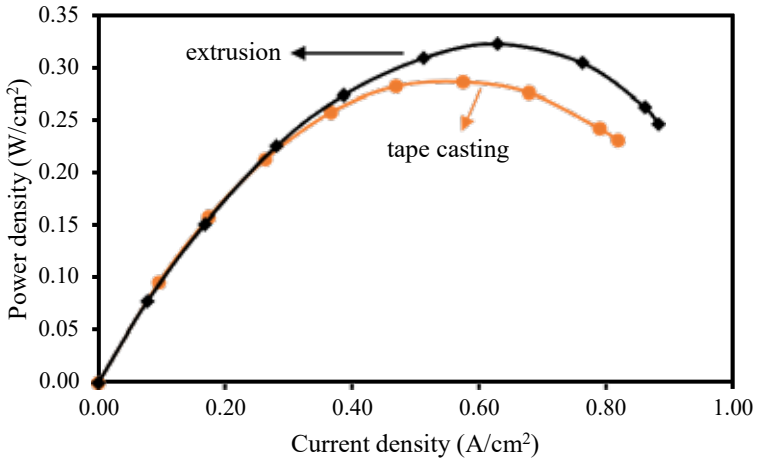


Fig. 5: Electrochemical performance of fabricated micro-tubular cells

V. Conclusions

In this study, tape casting method is proposed to fabricate micro-tubular anode support layers as an alternative to traditional extrusion. The anode supports with tape casting exhibit ~64% better average flexural strength. In addition, the cell fabricated by tape casting provides a performance close to that of the extruded cell. This performance can be improved by systematic optimization studies especially considering the fabrication and process parameters, which will be performed within the scope of future studies.

References

- Kendall K., Development of microtubular solid oxide fuel cell, In Proceedings of the International Forum on Fine Ceramics, p. 143-148, (1992).
- Monzón H., Laguna-Bercero M. A., Larrea A., Arias B. I., Várez A., Levenfeld B., Design of industrially scalable microtubular solid oxide fuel cells based on an extruded support, International journal of hydrogen energy, 39, 5470-5476, (2014).
- Suzuki T., Funahashi Y., Yamaguchi T., Fujishiro Y., Awano M., Effect of anode microstructure on the performance of micro tubular SOFCs, Solid State Ionics, 180, 546-549, (2009).
- Sumi H., Yamaguchi T., Hamamoto K., Suzuki T., Fujishiro Y., Matsui T., Eguchi K., AC impedance characteristics for anode-supported microtubular solid oxide fuel cells, Electrochimica acta, 67, 159-165, (2012).
- Timurkutluk B., Timurkutluk C., Toros S., Kaplan Y., Influence of sintering support design on the properties of NiO-YSZ anode support micro-tubes, Ceramics International, 44, 5587-5593, (2018).
- Timurkutluk C., Timurkutluk B., Kaplan Y., Experimental optimization of the fabrication parameters for anode-supported micro-tubular solid oxide fuel cells, International Journal of Hydrogen Energy, 45, 23294-23309, (2020).
- Weibull W., A statistical distribution function of wide applicability, Journal of applied mechanics, 18, 293-297, (1951).

Effects of adding graphene oxide to glass ceramic for solid oxide fuel cells

[1, 2*] Tolga Altan, [1, 2] Mikail Yagiz, [1, 2] Selahattin Celik, [3, 4] Recep Zan
[1] Nigde Omer Halisdemir University, Prof. Dr. T. Nejat Veziroglu Clean Energy Research Center, Nigde, Turkey
[2] Nigde Omer Halisdemir University, Mechanical Engineering Department, 51245, Nigde, Turkey
[3] Nigde Omer Halisdemir University, Nanotechnology Application and Research Center, Nigde, Turkey
[4] Nigde Omer Halisdemir University, Department of Physics, 51240, Nigde, Turkey

* E-mail: tolgaaltan@ohu.edu.tr

Abstract
In this study, the effect of adding GO (graphene oxide) to solid oxide fuel cell (SOFC) glass-ceramic sealing material on mechanical properties is investigated. Four different GO additive glass-ceramics (1, 3, 5, and 10 wt.% of GO with respect to the total powders) were prepared. Also, for comparison purposes, glass-ceramics sealant without GO is prepared as a base case. For each case, 20 samples were prepared and subjected to mechanical testing. The mechanical performances of the fabricated sealants are investigated via tensile tests.

Keywords: SOFC, glass-ceramics, graphene oxide, bonding performance, tensile tests.

I. Introduction

Solid oxide fuel cell (SOFC) generates electrical energy directly from the chemical energy of the fuel. However, high operating temperatures (800-1000 °C) are required. As the temperature increases, the electrochemical reaction kinetics and thus efficiency increase, and high power density can be obtained. On the other hand, high temperature brings along the problems of suitable sealing material. The sealant is used to gas-tighten ceramic and metal components and prevent fuel and air from mixing during fuel cell operation. Sealing is important for solid oxide fuel cell performance and safety, as leaks may cause problems such as insufficient fuel supply and internal combustion as a result of fuel/air mixture. Due to the high operating temperature, conventional sealants such as polymers and organic adhesives cannot be used. Several different sealing approaches have been developed for the sealing of SOFCs: metallic, compression, and rigidly bonded seals. Among them, the most effective approach for SOFC sealing has been to use glass / glass-ceramics with transition temperatures close to the operating temperature. However, due to the fragile nature of glass and glass-ceramic, studies on mechanical strength enhancement are widely carried out. In this context, adding different additives to the glass-ceramic content is a widely used method in the literature. Among these studies, Alizadeh et al. (2004) studied the addition of Fe_2O_3 as nucleant agent and experimental results show that the addition of 5.0 wt.% Fe_2O_3 to the glass produces a sinterable glass-ceramic with high mechanical strength. Wei et al. (2015) found that reinforcing the glass-ceramic with silver particles improves the mechanical behavior of sealant. Heydaria et al. (2012) found that the mechanical properties of glass-ceramic sealant improve with the addition of zirconia nanoparticles. Results show that with the addition of zirconia nanoparticles up to vol.10%, the flexure strength of glass-ceramic is increased. Also, there are many studies in the literature studying the effect of different additives materials such as TiO_2 (Zhou et al., 2021), Na_2O (Shi et al., 2018), Al_2O_3 (Xia et al., 2014; Arcaro et al., 2017), and YSZ (Timurkutluk et al., 2015) on the mechanical properties of glass-ceramic sealant. In addition to these materials, graphene oxide is a material that has come to the fore with its mechanical properties in recent years. Therefore, in this study, similarly, the effect of adding GO to SOFC glass-ceramic sealing material on mechanical properties was investigated.

II. Materials and Methods

Glass-ceramic sealing materials were produced using the tape casting method. Firstly, tape casting slurries were prepared. In order to investigate the effects of GO content, four different mixtures with 1–10 wt.% GO (G01–G10) with respect to the total powders were prepared. For this purpose, commercially available glass-ceramic powders V1649 (Ceradyne Inc., Washington, USA) were mixed with GO powders. Then, powders were mixed with appropriate amounts of solvent (methyl ethyl ketone and ethanol) and dispersant (fish oil). After 18 hours of ball milling with zirconia balls, appropriate amounts of binder (butvar) and plasticizer (polyethylene glycol) were added. At the end of the other ball milling process for 18h, the slurry was cast into tapes of 190-micron thickness by the doctor blade gap. The tapes were dried in an air atmosphere for 30 min. Figure 1 shows the slurries before casting and the detailed compositions of all slurries are listed in Table 1.



Fig. 1: Views of tape casting slurries before casting

Tab. 1: Compositions of the tape casting slurries

Sealant name	GP (g)	GO (g)	Solvent (g)	Dispersant (g)	Binder (g)	Plasticizer (g)
G00	*15*	*0*	*15*	*0,5*	*1,5*	*1,5*
G01	*14.85*	*0,15*	*15*	*0,5*	*1,5*	*1,5*
G03	*14.55*	*0,45*	*15*	*0,5*	*1,5*	*1,5*
G05	*14.25*	*0,75*	*15*	*0,5*	*1,5*	*1,5*
G10	*13.5*	*1,5*	*15*	*0,5*	*1,5*	*1,5*

Then, a total of 8 glass-ceramics tapes were stacked together and laminated under an isostatic pressure of 50 MPa for 10 min. The laminated sealants were cut with a laser cutter to dimensions 4.7 mm x 12.5 mm suitable for Crofer tensile test plates. 20 samples for each case were prepared and were placed into a high-temperature furnace with SiC block as a deadweight load to improve the joining. All samples were subjected to the same glass formation heating regime. Besides, the heating procedure was carried out in the same furnace to minimize the experimental errors. After the cooling down to the room temperature with a cooling rate of 1°C/min, the fracture strengths of the samples were measured via a tensile test machine (Shimadzu Autograph AG-IS, Kyoto, Japan) with suitable apparatus. The details of the tensile test plates, tensile test apparatus, and heating regime can be found elsewhere (Altan and Celik, 2020).

III. Results and discussions

After the heating regime, joined samples view is given in Fig. 2 as an example. It can be concluded that dead weight load provides almost homogenous load distribution for each sample. Similar results are also obtained from the other cases considered. For each case, an analysis of 20 samples was performed to increase the reliability of the test results. The reliability curves of the fracture strength data are also obtained via the two-parameter Weibull distribution method (Weibull, 1951). The results are shown in Figure 3. Also for all cases, fracture strength data for different reliability levels are summarized in Table 2.



Fig. 2: Appearance of the joined GC with GO added sample after heating regime

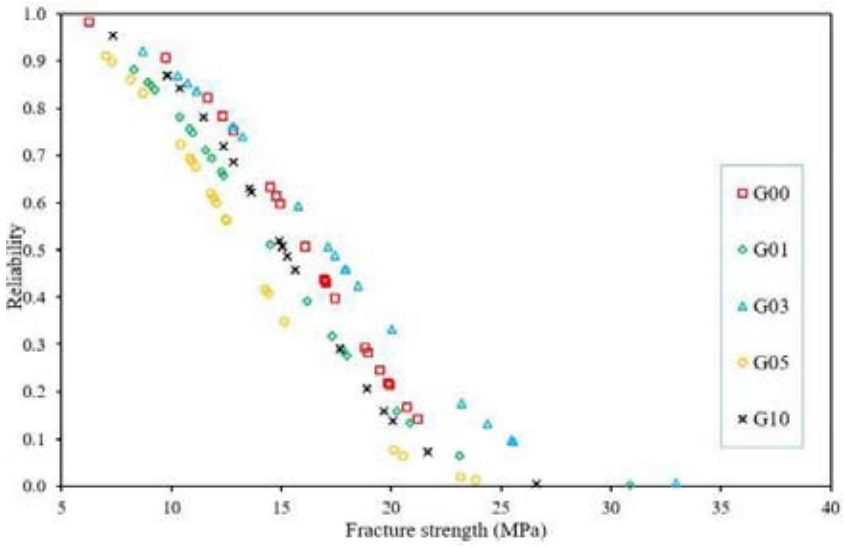


Fig. 3: The effect of adding graphene oxide to glass-ceramic on the reliability curves of fracture strength

Tab. 2: Summary of the tensile test results

Sealant name	Fracture strength (MPa)			Average fracture strength (MPa)
	50% reliability	60% reliability	70% reliability	
G00	*16.18*	*14.94*	*13.56*	*16.02*
G01	*14.63*	*13.2*	*11.72*	*14.72*
G03	*17.26*	*15.64*	*13.9*	*17.36*
G05	*13.27*	*12.04*	*10.74*	*13.33*
G10	*13.94*	*13.92*	*12.63*	*15.08*

V. Conclusions

In this study, graphene oxide (1-10 wt.%) / glass-ceramic composites sealants were prepared with the purpose of studying the influence of adding GO on mechanical properties. According to the experimental results, the addition of 3 wt.% GO to the glass-ceramic was exhibited higher fracture strength data for all reliability levels. The average flexural strengths value of GC with 3 wt.% GO exhibits 8.4% higher fracture strength than the base case. Effects of adding graphene oxide to glass-ceramic on thermal and electrical properties will be studied in future works.

References

Alizadeh P., Yekta B. E., Gervei A., Effect of Fe2O3 addition on the sinterability and machinability of glass-ceramics in the system MgO–CaO–SiO2–P2O5, Journal of the European Ceramic Society, 24, 3529-3533, (2004).

Altan T., Celik S., Effect of surface roughness of the metallic interconnects on the bonding strength in solid oxide fuel cells, International Journal of Hydrogen Energy, 45, 35118-35129, (2020).

Arcaro S., Moreno B., Chinarro E., Salvador M. D., Borrell A., Nieto M. I., de Oliveira A. N., Properties of LZS/nanoAl2O3 glass-ceramic composites, Journal of Alloys and Compounds, 710, 567-574, (2017).

Heydari F., Maghsoudipour A., Hamnabard Z., Farhangdoust S., Mechanical properties and microstructure characterization of zirconia nanoparticles glass composites for SOFC sealant, Materials Science and Engineering: A, 552, 119-124, (2012).

Shi J., He F., Xie J., Liu X., Yang H., Effects of Na2O/BaO ratio on the structure and the physical properties of low-temperature glass-ceramic vitrified bonds, Ceramics International, 44, 10871-10877, (2018).

Timurkutluk B., Ciflik Y., Korkmaz H., Strength evaluation of glass–ceramic composites containing yttria stabilized zirconia after thermal cycling, Ceramics International, 41, 6985-6990, (2015).

Wei J., Pećanac G., Malzbender J., Mechanical behavior of silver reinforced glass–ceramic sealants for solid oxide fuel cells, Ceramics International, 41, 15122-15127, (2015).

Weibull W., A statistical distribution function of wide applicability, Journal of applied mechanics, 18, 293-297, (1951).

Xia Q., Zhong C. W., Luo J., Low temperature sintering and characteristics of K 2 O–B 2 O 3–SiO 2–Al 2 O 3 glass/ceramic composites for LTCC applications, Journal of Materials Science: Materials in Electronics, 25, 4187-4192, (2014).

Zhou R. C., Liu X. P., Wan L., Gao P. Z., Liao M. Y., Zhu Y. L., Influence of TiO2 amount on the interfacial wettability and relevant properties of vitrified bond CBN composites, Journal of the European Ceramic Society, 41, 300-309, (2021).

Effects of increasing the electrolyte surface area on the electrochemical performance

[1,2*] Cigdem Timurkutluk, [1, 3] Tolga Altan, [1, 3] Fuat Yildirim, [1, 3] Sezer Onbilgin, [1, 3] Mikail Yagiz,
[1, 3] Bora Timurkutluk, [1, 3] Selahattin Celik
[1] Nigde Omer Halisdemir University Prof. Dr. T. Nejat Veziroglu Clean Energy Research Center, 51245, Nigde, Turkey
[2] Nigde Omer Halisdemir University Department of Energy Science and Technologies, 51245, Nigde, Turkey
[3] Nigde Omer Halisdemir University, Mechanical Engineering Department, 51245, Nigde, Turkey

* E-mail: cigdemtimurkutluk@ohu.edu.tr

Abstract
In this study, the effects of increasing yttria stabilized zirconia (YSZ) electrolyte support surface area on the electrochemical performance are investigated. Metal mesh is used to increase the electrolyte surface area. Mesh geometry is printed on the YSZ electrolyte surface by means of co-isostatic pressing. Profilometer is used to determine the surface topography and a 3D map of the YSZ surface after sintering is created. Finally, performance tests are conducted after the anode and cathode layer are coated on the patterned YSZ electrolytes. The peak electrochemical performance of the patterned electrolyte is measured to be 11% higher than that of the base case.

Keywords: Solid oxide fuel cell; SOFC; YSZ electrolyte; surface area; mesh pressing; increasing TPBs.

I. Introduction

Solid oxide fuel cells (SOFCs) are devices that produce clean energy from the chemical energy of the fuel with high efficiency. Electrochemical reactions take place in regions called triple-phase boundaries (TPBs) where electrolyte-pore-electrode phases meet. The cell performance improves as the number and the length of these regions increase. Therefore, it is reasonable to increase the interface area between the electrodes and the electrolyte layers in order to increase TPBs. Increasing the surface area by patterning the electrolyte surface is a method applied in the literature and various methods were employed for this purpose. Among the studies in the literature, Xu et al. (2013) created micro patterns onto the interface between the electrolyte and anode by the micro powder imprinting (μPI) method. The patterns increased the reactive area and the patterned electrolyte showed better performance than the flat one. Wang et al. (2010) modified the YSZ electrolyte surface by depositing semi-melted YSZ particles via flame spraying methods. According to the results, the cathode activation polarization of the cell was found to decrease by about 30-43% than that of a flat electrolyte. Another method used in surface patterning, in which cell performance is significantly improved, is laser machining (Larrea et al., 2011; Timurkutluk et al., 2012). In this study, on the other hand, surface patterning process was performed using a simple mesh pressing method. Metallic meshes used in pressing process have advantages such as easy supply, offering options in terms of shape and size, and reusable after surface patterning. The proposed method is also a suitable method considering the mass production as it easily creates a patterned surface.

II. Experimental

Electrolyte supports were fabricated using a tape-casting technique. To prepare the alcohol-based tape casting slurry, first YSZ (with 8 mol% Y_2O_3) powders (Tosoh, Tokyo, Japan) were mixed with certain amount of dispersant (fish oil, Sigma–Aldrich, Munich, Germany) and solvent (mixture of ethanol and ethyl methyl ketone). After ball milling for around 18 h, organic binder (butvar, Sigma-Aldrich) and plasticizer (polyethylene glycol, Sigma-Aldrich) were added with suitable ratios. Then, the mixture was ball milled again for another 18 h. The slurry was moved to a magnetic stirrer and stirred there for 3 h. Next, the slurries were tape cast by a laboratory scale tape casting equipment on a Mylar film with a blade gap of 190 μm. The tapes were dried under atmospheric air for 30 min. A single tape thickness was measured as 41 μm after drying. Then, eight tapes were stacked for all cases and pressed according to the conditions given in the table 1. For surface patterning, metal mesh was placed on the electrolyte in the isostatic press stage and the structure pressed together to pattern one of the electrolyte surfaces. In none of the cases, patterning process was carried out in the mechanical press stage.

Tab. 1: Conditions applied during the electrolyte patterning

Cases	Uniaxial press	Isostatic press	Uniaxial press parameters	Isostatic press parameters
Base	√	*Warm*	*200 bar, 4 min.*	*50 MPa, 4 min, 70 °C*
Case1	√	*Cold*	*200 bar, 4 min.*	*50 MPa, 4 min, 25 °C*
Case2	*X*	*Cold*	-	*50 MPa, 4 min, 25 °C*
Case3	√	*Warm*	*200 bar, 4 min.*	*50 MPa, 4 min, 70 °C*
Case4	*X*	*Warm*	-	*50 MPa, 4 min, 70 °C*

After the pressing step, the laminate is subjected to two stages of sintering. Firstly, the electrolytes are heated to 1000 °C with 2 °C/min temperature increment and held for 2 h at this temperature to remove the organic additions. In the second sintering stage, to obtain fully dense electrolyte, pre-sintered electrolyte sintered at 1400 °C for 5 h

with a rate of 3 °C/min. After the sintering process, the roughness of the electrolyte surface was measured with a profilometer (Bruker Nano Surfaces Dektak XT, Santa Barbara, USA) device. Next, anode and cathode layers are screen printed on the electrolyte which has the highest surface area to investigate the effect of the patterns created on the electrolyte surface on the cell performance. For this purpose, two cells are fabricated by coating the patterned surface with anode and cathode. In addition, a cell without any patterning process was also manufactured and tested similarly for comparison.

III. Results and discussions

Surface topography analysis was carried out for each case listed in Table 1. 100 mm^2 (10 mm × 10 mm) selected area for all cases was scanned for this purpose. The resultant 3D maps of the electrolyte surface are shown in Fig.1. Also, surface characterization parameters such as average roughness (R_a) and height of the formed hills (Δz) are measured by contact stylus profilometer. Case3 provides the highest surface area among the cases examined. Therefore, a cell based on this electrolyte support was fabricated and tested together with the base case, whose electrolyte has no pattern.

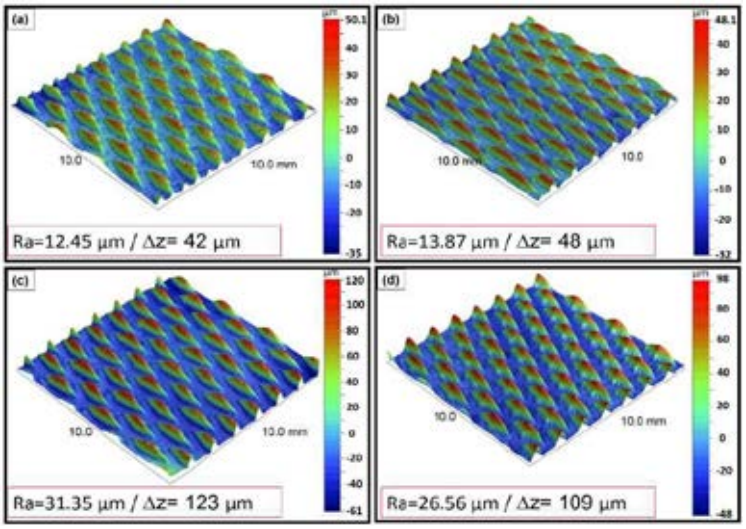


Fig. 1: Surface map and measured surface characterization parameters of patterned YSZ: (a) case1, (b) case2, (c) case3 and (d) case4

It is seen that applying a preliminary uniaxial press is not effective in creating patterns on the YSZ surface. On the other hand, the process temperature during the isostatic press is quite effective in patterning the surface. It can be seen from Fig.1. that the surface of the electrolyte via warm isostatic press has approximately 2 times higher average roughness value than that of the cold pressed. This result indicates that the pressing temperature improves the formability of YSZ tapes. Along with the high surface area for an improved cell performance, the lamination is also significant since the electrolyte support should be pinhole and crack-free. For this purpose, the microstructures of patterned electrolytes are investigated by scanning electron microscopy and the results are shown in Fig.2. It is seen that there is no delamination available and the electrolytes seem to have a dense structure in all cases. Especially the microstructures of the cases where pre-mechanical press is not applied indicate that the isostatic press is sufficient for the lamination step under the conditions considered in this study.

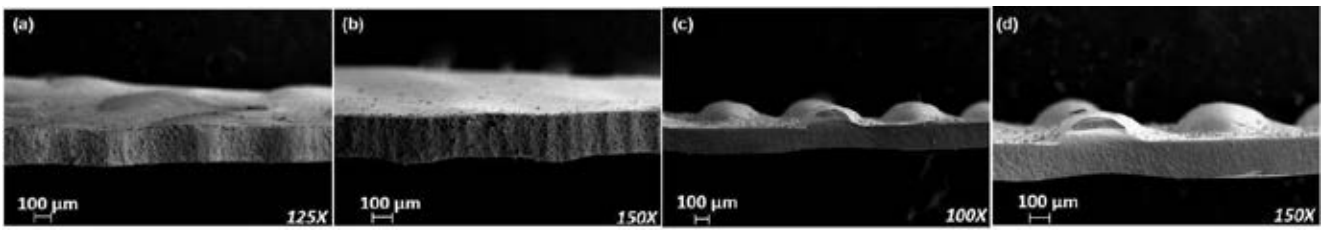


Fig. 2: SEM image of the fracture cross-section of cases: (a) case1, (b) case2, (c) case3, (d) case4

Fig.3. compares the surface topography and a 3D map of the patterned and opposite YSZ surface for Case 3, which shows the highest surface area after the mesh patterning. Although the mesh is placed on one YSZ surface during the patterning process, the opposite surface also seems to have some patterns with relatively low roughness and depth/surface area. This behaviour is considered reasonable and elucidated by the residual stresses during the isostatic pressing. The photos of the cells with Case 3 electrolyte but the patterned surface is coated with different electrodes are given in Fig.4. The performance comparison for an operating temperature of 800 °C, on the other hand, is depicted in Fig.5. The patterned electrolyte exhibits relatively higher peak power compared to that of the base case having unpatterned electrolyte regardless of the electrode material coated on the patterned surface.

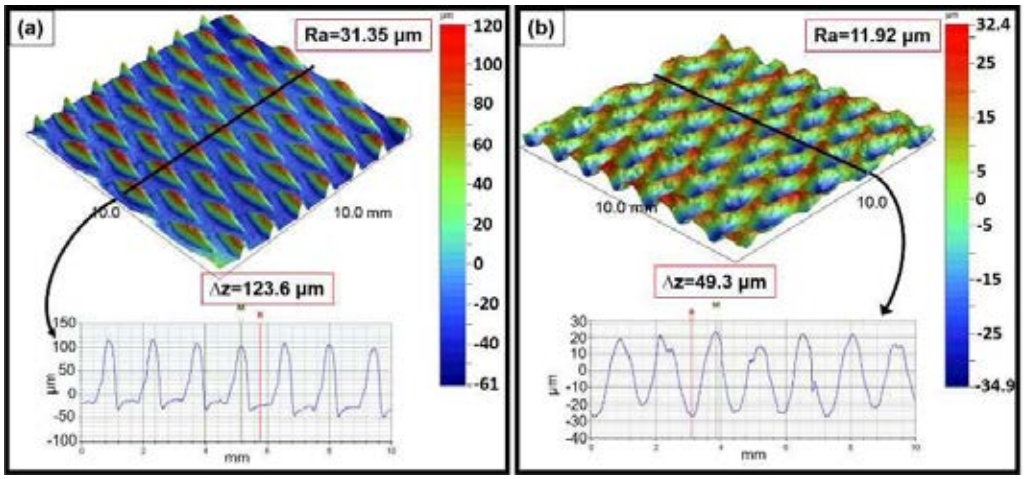


Fig. 3: Surface profile of case 3: (a) front and (b) back surface

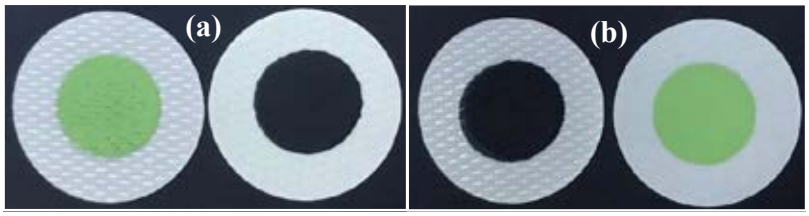


Fig. 4: Cells fabricated with Case 3 electrolyte: (a) anode on the patterned surface and (b) cathode on the patterned surface

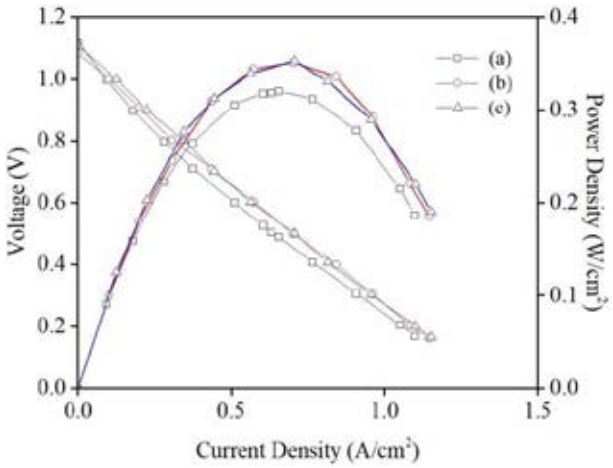


Fig. 5: Electrochemical performance of cases: (a) base cell, (b) cathode on the patterned surface and (c) anode on the patterned surface

V. Conclusions

In this study, to increase the cell performance YSZ electrolyte patterning is carried out by simply placing a metallic mesh on one of the YSZ surface and pressing under various conditions. SEM images indicate that all electrolytes are crack and delamination-free. The electrolyte structure offering the highest surface area is used to fabricate single cells with anode and cathode coated on the formed surface. The cells with patterned electrolyte produce 11% higher power density than that of the cell with the unpatterned flat electrolyte. The improved performance is attributed to the increased contact area between the electrolyte and the electrodes providing relatively higher TPBs. In the future studies, the effects of surface patterning on the mechanical properties of YSZ electrolyte will be examined. Besides, the bonding performance between the patterned electrolyte and glass-ceramic will be studied and compared to that for the base cell.

References

- Larrea A., Sola D., Laguna-Bercero M. A., Peña J. I., Merino R. I., Orera V. M., Self-supporting thin yttria-stabilised zirconia electrolytes for solid oxide fuel cells prepared by laser machining, Journal of The Electrochemical Society, 158, B1193, (2011).
- Timurkutluk B., Celik S., Timurkutluk C., Mat M. D., Kaplan Y., Novel structured electrolytes for solid oxide fuel cells, Journal of Power Sources, 213, 47-54, (2012).
- Wang X. M., Li C. J., Li C. X., Yang G. J., Microstructure and electrochemical behavior of a structured electrolyte/LSM-cathode interface modified by flame spraying for solid oxide fuel cell application, Journal of thermal spray technology, 19, 311-316, (2010).
- Xu Y., Tsumori F., Osada T., Miura H., Improvement of solid oxide fuel cell by imprinted micropatterns on electrolyte, Micro & Nano Letters, 8, 571-574, (2013).

Modeling of Sheet Hydroforming of Metallic Interconnectors for Solid Oxide Fuel Cells

[1,2*] Habip G. Korkmaz, [1,2] Emre Ucar, [1,2] Serkan Toros, [1,2] Bora Timurkutluk

[1] Nigde Omer Halisdemir University Prof. Dr. T. Nejat Veziroglu Clean Energy Research Center, 51245, Nigde, Turkey
[2] Nigde Omer Halisdemir University, Mechanical Engineering Department, 51245, Nigde, Turkey

* E-mail: hkorkmaz@ohu.edu.tr

Abstract
Sheet metal forming, instead of conventional machining, is an effective method for the fabrication of interconnectors in solid oxide fuel cells with desired design features, for which both the weight and volume are very important. In this respect, hydroforming is one of the suitable methods providing several advantages over traditional sheet metal forming methods. It is possible to obtain the desired geometry by using relatively thinner sheets via hydroforming. In this study, the formability of metallic interconnectors with different channel width is investigated numerically by using 0.2 mm thick Crofer 22 APU material. As a result of the modeling via LS-DYNA finite element analysis program, it is found out that it is not possible to manufacture even the interconnector with 0.5 mm channel depth and 1.5 mm channel width by hydroforming method due to the limitations of the material formability. However, the maximum depth for this channel depth and width, at which the sheet can be safely formed without neck formation, is measured as 0.23 mm.

Keywords: Solid Oxide Fuel Cells; Interconnector; Crofer 22 APU; Hydroforming.

I. Introduction

Membrane electrode assembly (MEA) of a solid oxide fuel cells (SOFCs) consists of an anode and a cathode electrode coated on both surfaces of an electrolyte. As long as fuel and oxidizer are supplied to the anode and to the cathode, respectively, MEA continuosly generates electrical and heat energy as a result of the electrochemical reactions occurring in the electrodes. On the other hand, interconnectors, required to connect the single cells electrically in a stack, play an important role in collecting the current produced in MEA. Interconnectors are also ceramic or metallic system components that distribute the necessary fuel and oxidizer to the system homogeneously through the flow channels generally formed by traditional machining. Cell performance changes with the interconnector design, as the geometry of these flow fields significantly affects the transfer of species, heat and momentum (Saied M. at al., 2018, Kong W. at al., 2020). In this respect, interconnectors, subjected to both reduction and oxidation at high operating temperature, are as significant as MEA. Due to the high operating temperatures, high temperature resistant alloys are used as interconnector materials in SOFCs (Yang Z. at al., 2003, Quadakkers W. J. at al., 2003). One of these alloys is Crofer 22 APU. The conventional Crofer 22 APU interconnector with flow channels is manufactured by machining the bulk material. In addition to long-term channel processing on precision CNC machines, grinding for effective current collection increases the production costs of conventional interconnectors. On the other hand, thick materials should be used to prevent mechanical damage during channel processing. This increases the material cost and the resulting interconnectors are both heavy and big in size. Therefore, the specific (W/kg) and volumetric (W/m^3) power densities of SOFC stacks with conventional interconnectors are low. The production of interconnector plates by sheet metal forming instead of machining helps to significantly reduce both the weight and volume of SOFC stack. The system weight and volume can be reduced by using thin sheets. In this study, it is suggested to use the hydroforming method, which was reported to improve the formability of sheet materials compared to classical forming methods (Bell C. at al., 2020). Therefore, the formability of SOFC interconnectors with different dimensional geometries by hydroforming is numerically investigated in this study.

II. Analysis

Dies with 0.5 mm channel depth and 0.5, 1 and 1.5 mm channel width are designed for interconnector sheets with 0.2 mm thickness. Forming simulations are performed in 3D using the commercial finite element analysis program LS-DYNA. In order to save analysis time, the fully symmetrical system is modeled as a quarter model. Figure 1.a contains a visualization of the system in the program, showing the sheet to be formed, die, blank holder, imaginary pressure and symmetry planes. The entire domain has 22273 mesh elements at the beginning, where the elements on the sheet are coarse to save the analysis time. ADAPTIVE card is enabled and 6 levels of refining mesh are performed. This further divides each mesh in the critical regions into 4 each and repeats this division upto 6 times if required until suitable mesh sizes are achieved. The mesh size, which is 0.75 mm at the beginning, can be reduced to 0.0234 mm, especially in the filleted regions at the end of the analysis (Figure 1.b). MASK card is used in order to model hydroforming in the system and a liquid pressure of 150 MPa, which is considered suitable for the forming process, is applied as perpendicular to the normal of the sheet elements to be shaped.

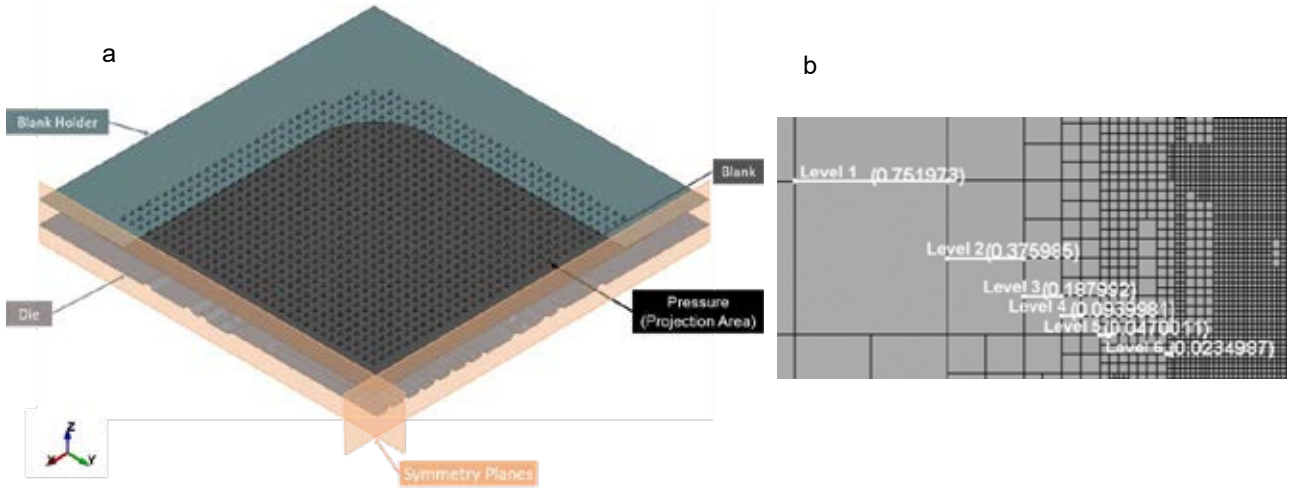


Fig. 1: (a) Tools in used Finite Elemant Model (b) An example for mesh refining

In the forming analysis, the 3_PARAMETER_BARLAT (MAT36) material model is used. The mechanical properties of the material are given in Table 1 and the stress strain curve is given in Figure 2.a. The tear control of the sheet is performed using the Forming Limit Diagram (FLD). FLD obtained for 0.2 mm thick material is shown in Figure 2.b. RIGID (MAT20) material model is used for the blank holder and die, both defined as steel.

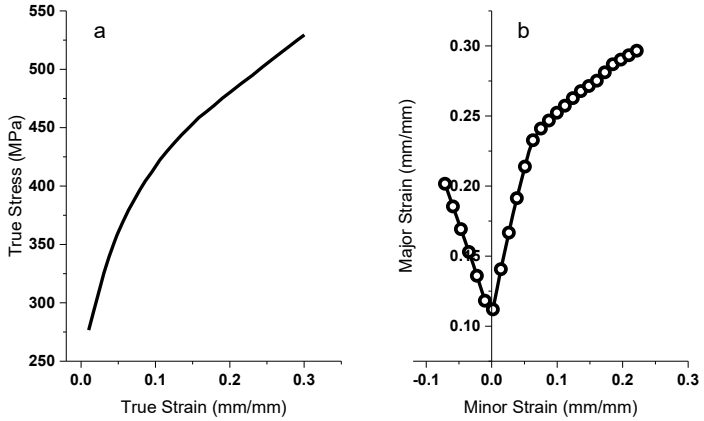


Fig. 2: (a) Stress-Strain Curve for Crofer 22 APU (b) FLD curve for Crofer 22 APU

Tab.1: Mechanical properties of 0.2 mm thick Crofer material

Young Modulus (GPa)	Strength Coefficient K (MPa)	Strain Hardening Exponent n	R_0	R_{45}	R_{90}
207	*670.3*	*0.2*	*1.86*	*1.65*	*1.14*

In the analysis, a blank holder force of 100kN is applied and FORMING_ONE_WAY_SURFACE_TO_SURFACE contact type is used between the blank and the die, and between the blank and the blank holder. The friction coefficient of 0.08 between lubricated metal-metal in forming simulations is selected, which is generally preferred in the literature.

III. Results and discussions

According to the simulation results, the desired profile cannot be obtained in the die design with channel width of 0.5 mm, and the desired profile is not fully formed, although relatively better results are obtained for the die design with 1 mm channel width. As can be seen from the comparative cross-sectional views given in Figure 3, the channel geometries can be transferred providing a better match to the die geometry with increasing the channel width thus among the studied channel widths, 1.5 mm width is found to be more appropriate for the forming of the desired final geometry. The designs for relatively lower channel widths can also be formed by increasing the fluid pressure, but since the highest pressure value of 150 MPa is defined for the test device, analysis at higher pressures are not performed. The tear controls with FLD of the formed parts with a constant channel depth of 0.5 mm and 0.5 mm, 1 mm and 1.5 mm channel width are shown in Figures 4(a-c), respectively. As can be seen from the figures, the parts of all designs are teared under the channel depth value of 0.5 mm. The damage occurring on a formed part with a depth of 0.36 mm is given in Figure 4.d. The tears are still available in the structure. The maximum depths that can be reached for each channel width studied are computed as 0.13 mm, 0.19 mm and 0.23 mm for 0.5 mm, 1 mm and 1.5 mm channel width, respectively, as shown in Fig.5 (a-c).

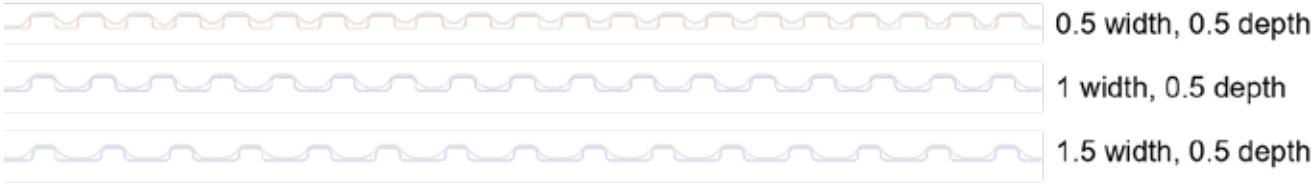


Fig.3: Cross sectional views of forming simulation results of die designs with different widths

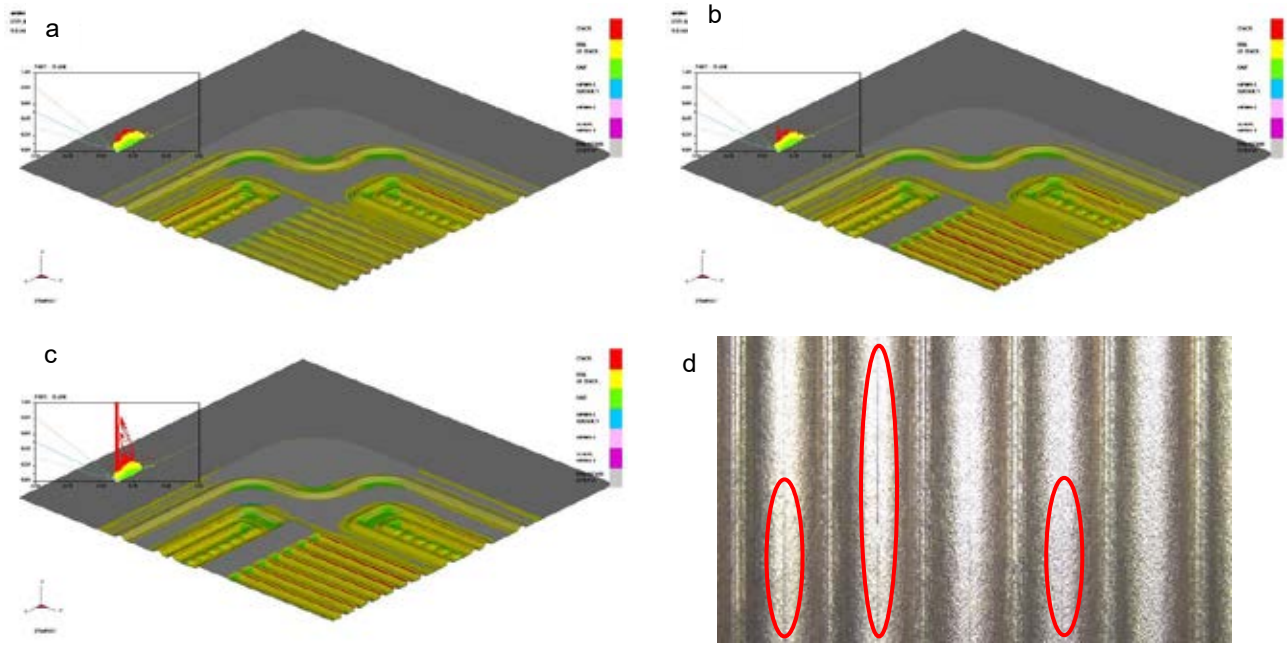


Fig. 4: Tear control with FLD (a) 0.5 width (b) 1 width (c) 1.5 (d) Necked sheet at a depth of 0.36 mm

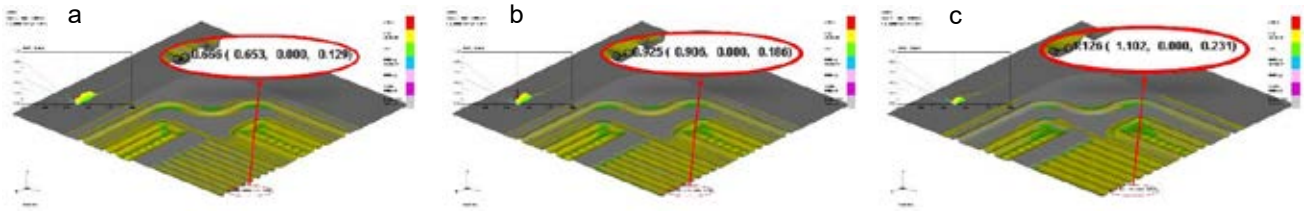


Fig. 5: Depth measurements without necking on the material (a) 0.5 width (b) 1 width (c) 1.5 width

IV. Conclusions

In this study, forming simulations are carried out in order to investigate the formability of Crofer 22 APU as an interconnector for SOFCs having 0.5 mm, 1 mm and 1.5 mm channel width and 0.5 mm channel depth via hydroforming method. The tearing of the formed sheets is controlled using the FLD curve of the materials. From the simulation results, it is concluded that manufacturing of Crofer 22 APU thin sheet interconnector plates of 0.2 mm thick with the channel depth and width considered in this study is not possible by hydroforming. On the other hand, it is seen that the channel depth of 0.13 mm, 0.19 mm and 0,23 mm can be formed for the channel width of 0.5 mm, 1 mm and 1.5 mm, respectively.

References

Bell C., Corney J., Zuelli N., Savings D., A state of the art review of hydroforming technology, International Journal of Material Forming, 13, 789-828, (2020).
Kong W., Han Z., Lu S., Gao X., Wang X., A novel interconnector design of SOFC, International Journal of Hydrogen Energy, 45, 20329-20338, (2020).
Quadakkers W. J.,Piron-Abellan J., Shemet V., Singheiser L., Metallic interconnectors for solid oxide fuel cells - a review, Materials at High Temperatures, 20, 115-127, (2003).
Saied M., Ahmed K., Nemat-Alla M., Ahmed M., El-Sebaie M., Performance study of solid oxide fuel cell with various flow field designs: numerical study, 43, 20931-20946, (2018).
Yang Z., Scott W. K., Paxton D. M., Stevenson J. W., Selection and evaluation of heat-resistant alloys for SOFC interconnect applications, 150, A1188-A201, (2003).

Cold sintering of GDC electrolyte for SOFCs applications

[1*]Murat Murutoğlu, [1]Tuğçe Ucun, [1]Aligül Büyükaksoy, [1]Yahya Kemal Tür [1]Hüseyin Yılmaz
[1] Gebze Technical University, Department of Material Science and Engineering, InstituteAddress, Kocaeli, 41400, Turkey
* E-mail: m.murutoglu@gtu.edu.tr

Abstract

The effect of the cold sintering process (CSP) on the electrochemical properties of 20 mol% Gd-doped ceria (GDC) was investigated. Nanoscale GDC powder was sintered via a cold sintering process (CSP) at room temperature followed by post-annealing at 1100 °C. The result of CSP ceramics exhibits high relative density (> 95%) with a fine grain size of ~500 nm. Samples illustrate comparable electrochemical properties with the performance of the conventionally prepared ones in the literature.

Keywords: cold sintering, SOFCs, electrolyte, ceria

I. Introduction

Recently, cold sintering process (CSP) was developed to densify ceramics at substantially reduced temperatures (Guo et al., 2016a). The CSP is a transient liquid phase sintering method aided by pressures ranging from 100 to 600 MPa at low temperatures (Guo et al., 2016b). Even thoug it is still not fully understood yet, the densification mechanism in CSP could be divided in two; thermodynamically, the ceramic particles are partially dissolved in the presence of liquid phase (mostly water) and then evaporation of the liquid leads to supersaturated liquid from which precipitation takes place, at the final stage enhanced diffusion densifies the ceramic (Guo et al., 2016b, Guo et al., 2017). In the last five years, a wide range of materials for different applications, including piezoelectric, semiconductors (Funahashi et al., 2017) and ionic conductors (Guo et al., 2017) have been successfully fabricated using this new technique.

Cerium Oxide (CeO_2) is an electroceramic oxide with a centrosymmetric cubic fluorite structure (Esposito and Traversa, 2008). Due to its excellent mechanical, electrical and chemical properties such as high ionic conductivity, catalytic redox properties and chemical resistance it has been studied comprehensively for SOFC applications (Kabir et al., 2020). Because of their significant contribution to ionic conductivity, ceria is commonly doped with Gd^{3+} or Sm^{3+} (Wang et al., 2020). However, since ceria based ceramics have high melting point (aproximatelly 2450 °C), full densification typically demands a high sintering temperature of 1500-1600 °C (Ni et al., 2015). These elevated processing temperatures cause increased diffusion and, more specifically, segragation of the rare-earth dopant, as well as unwanted chemical reactions within the substance and atmosphere (Zaengle et al., 2020).

In this study, these drawbacks were reduced by sintering the gadalonium doped cerium oxide (GDC) electrolytes at lower temperatures by applying CSP. For this pupose, the GDC samples were first cold sintered, and then post-heat-treatment for further densification. Moreover, microstructure and electromechanical properties were investigated.

II. Experimental Set-up and Procedure

Commercial 20 mol% Gd-doped ceria (GDC20) powders (Fuellcell Materials, 5-10 nm, USA) with specific surface area of 95 m^2/g, were used in this experiment. Cold sintering was carried out between RT-200°C and 150-550 MPa. A custom-made hydraulic press (100 Tons, HIDROTIM, Turkey) equipped with a PID controlled heating furnace that tightly covers the steel die, was used to carry out cold sintering process. GDC powder was placed in a steel die with a 15 mm inner diameter and pressed at room temperature for 1 hour under a uniaxial pressure of 450 MPa. The green density of cold sintered samples was measured roughly 53%. To study the sintering behavior of GDC ceramics, cold sintered samples were monitored by an optical dilatometer (MISURA 3, Expert System Solutions, Italy) up to 1380°C at 10°C/min heating rate.The sample was post-annealed at 1100 °C for 2 hours at a heating rate of 10 °C/min to reach final density.

III. Analysis

The densities of cold sintered samples were measured from geometry and their mass. Theoretical density of GDC was taken to be 7.246 g/cm^3. Phase analysis was done by using an X-Ray diffractometer (Rigaku D-Max 2200) with Cu-K_α radiation and particle and crystalline sizes were calculated from the x-ray peak broadening using silicon powders (Rigaku Standard Reference Powder) as standard. Microstructural analysis was done using a scanning electron microscope (SEM) (Philips XL 30 SFEG, Eindhoven, Netherlands) from the broken surfaces of cold sintered and post annealed samples. The electrochemical impedance spectroscopy (EIS) measurements of the GDC electrolyte were carried out by a Gamry Reference 3000 potentiostat/galvanostat/ZRA analyzer.

IV. Results and discussions

Due to the continuous mass loss of GDC powders with the increasing temperature, dilatometer analysis couldn't be used to determine the post annealing temperature since it was not possible to distinguish the shrinkage due to the mass. Densities of post-annealed samples were found to be higher than 95% of their theoretical density.

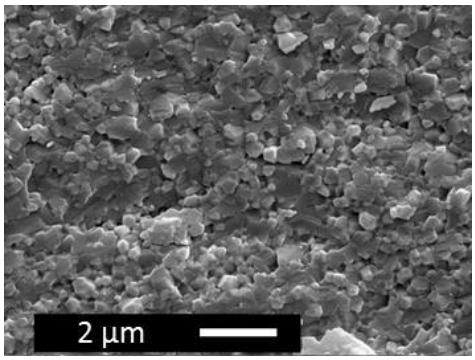


Figure 1: Scanning electron microscope (SEM) image of the GDC pellet, cold sintered at room temperature under 450 MPa and then, post-annealed at 1100 °C for 2 h.

Microstructural images taken from the fracture surfaces of GDC electrolytes calcined at 600°C for 5 hour and cold sintered at 25°C and then post sintered at 1100°C are shown in Figure 2. The microstructure was very dense (> 95% of theoretical density). Grain size was found to be less than 500 nm.
The electrical conductivity of cold sintered GDC electrolytes were calculated as 2.30×10^{-2} S / cm at 800°C. The electrical conductivity of GDC electrolytes was observed to show Arrhenius type behavior and the activation energy was found to be 0.69 eV. Open cell potentials were measured to be 0.97 - 0.88 V at 600 and 800 °C, respectively. Electrochemical results were promising for an electrolyte that was processed with a new method at much lower temperatures than the conventional ones (Sındıraç, Büyükaksoy and Akkurt 2019).

V. Conclusions

In short, this study demonstrates the effect of the cold sintering process (CSP) on the properties of 20 mol% Gd-doped ceria (GDC) electrolytes. It is observed that CSP enhanced densification (> 95 of theorical density) of the GDC at a lower sintering temperature of 1100°C.

References

Guo H., Guo J., Baker A., Randall CA., Hydrothermal-Assisted Cold Sintering Process: A New Guidance for Low-Temperature Ceramic Sintering, ACS Applied Materials Interface, 8, 32, 20909-20915, (2016).

Guo H., Baker A., Guo J. and Randall C.A., Cold Sintering Process: A Novel Technique for Low-Temperature Ceramic Processing of Ferroelectrics, Journal of American Ceramic Society, 99, 3489-3507, (2016).

Guo H., Bayer TJM., Guo J., Baker A., Randall CA., Current progress and perspectives of applying cold sintering process to ZrO_2-based ceramics, Scripta Materialia, 136, 141-148, 1359-6462, (2017).

Funahashi S, Guo J, Guo H, et al., Demonstration of the cold sintering process study for the densification and grain growth of ZnO ceramics, Journal of American Ceramic Society, 100, 546–553, (2017).

Esposito V. and Traversa E., Design of electroceramics for solid oxides fuel cell applications: Playing with ceria, Journal of American Ceramic Society, 91, 1037–1051, (2008).

Kabir A., Ke D., Grasso S., Merle B., Esposito V., Effect of Cold Sintering Process (CSP) on the Electro-Chemo-Mechanical Properties of Gd-doped Ceria (GDC), Journal of the European Ceramic Society, 40, 15, 5612-5618, (2020).
Sındırac C., Büyükaksoy A., Akkurt S., Electrical properties of gadolinia doped ceria electrolytes fabricated by infiltration aided sintering, Solid State Ionics, 340, 115020, 0167-2738, (2019).

Ni DW., Florio DZ., Marani D., Kaiser A., Tinti VB., and Esposito V., Effect of chemical redox on Gd-doped ceria mass diffusion, Journal of Materials Chemistry A, 3, 18835–18838, (2015).

Zaengle TH., Ndayishimiye A., Tsuji K., et al., Single-step densification of nanocrystalline CeO_2 by the cold sintering process, Journal of American Ceramic Society, 103, 2979–2985, (2020).

Wang Z., Ye Z., Zhang Y., Li C., Zeng Y., Fluorite-doped Gd0.1Ce0.9O1.95 polycrystalline electrolytes with extraordinarily enhanced oxide ionic conductivities controlled by depletion degree of oxygen vacancies at grain boundaries, Journal of Power Sources, 480, 229118, (2020).

IHTEC 2021

www.ihtec2021.org

5th International HYDROGEN TECHNOLOGIES Congress

May 26-28, 2021
Niğde Ömer Halisdemir University, Niğde, Turkey

ORGANIZATION SECRETARIAT

BROS
Congress, Incentive and Events

Esentepe Mah. Sağlam Fikir Sok. Esen Palas Apt. A Blok No:2 D:9
Esentepe / Şişli - İstanbul / TURKEY
Tel: + 90 212 296 66 70 / **Fax:** + 90 212 296 66 71
alen.demirel@brosgroup.net / www.brosgroup.net

ISBN: 978-605-70717-0-5